Structures in Fire

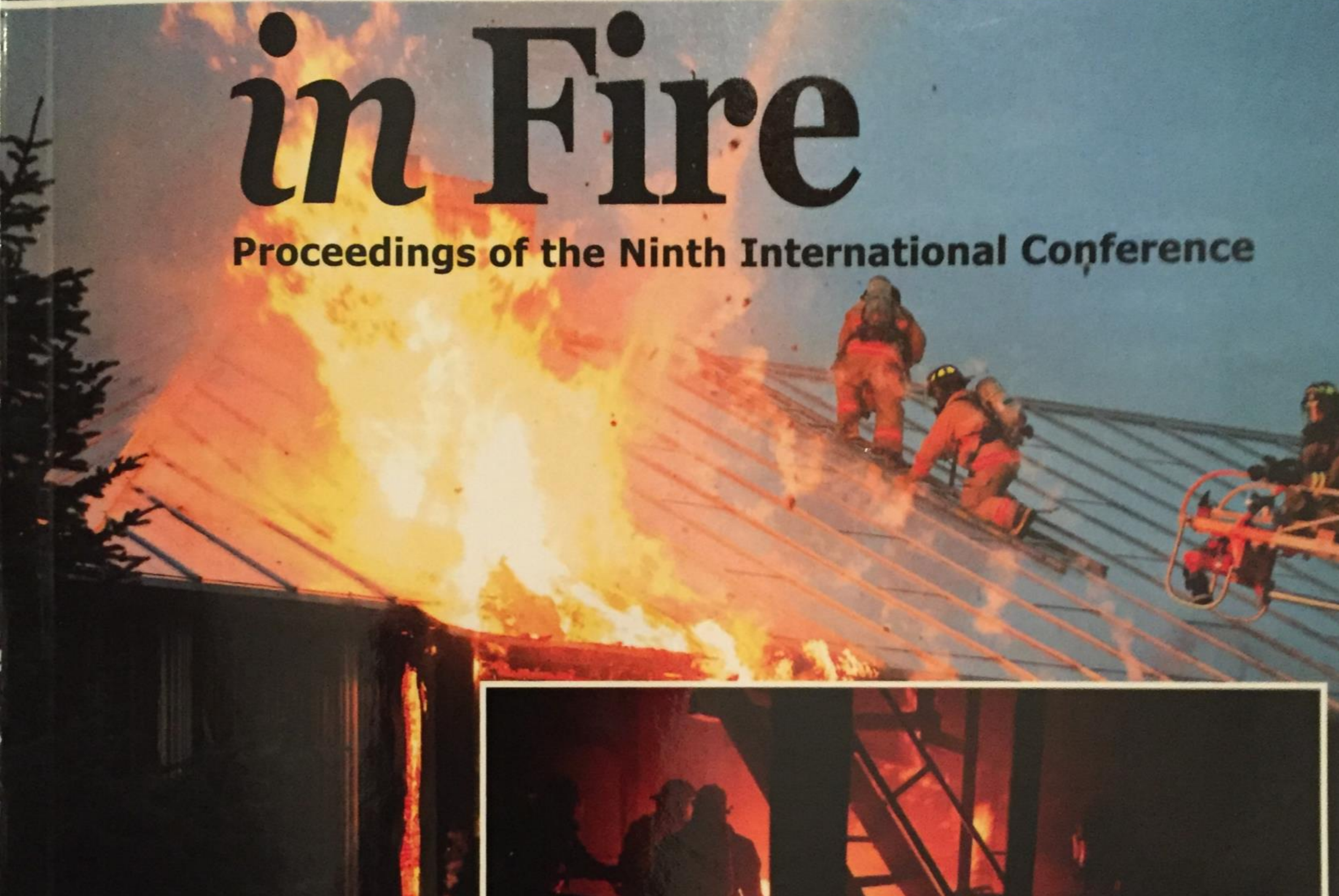

Proceedings of the Ninth International Conference

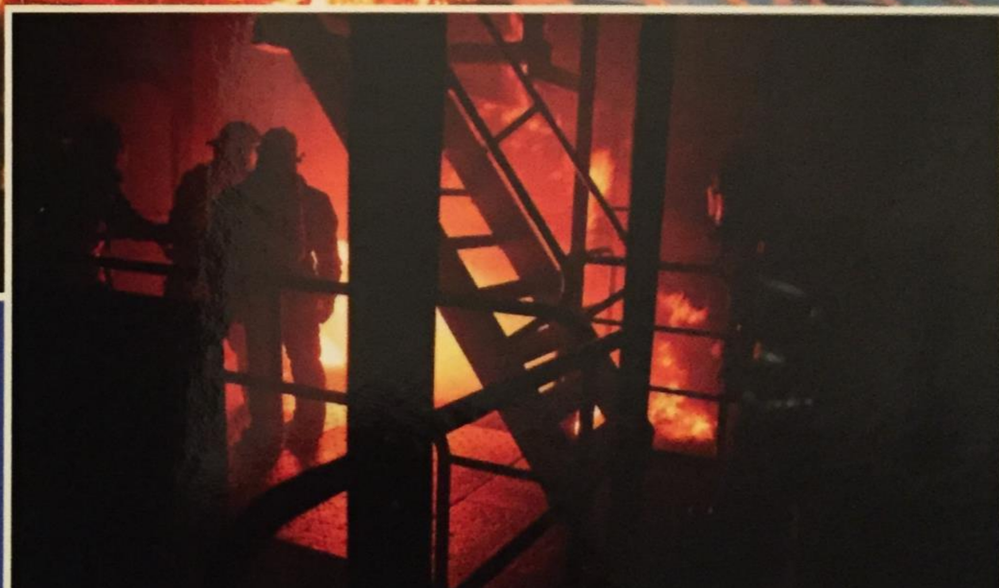

Edited by

Maria E. Moreyra Garlock

Venkatesh K. R. Kodur

Structures *in* Fire

Proceedings of the Ninth International Conference

Organized by Princeton University

Edited by

Maria E. Moreyra Garlock
Venkatesh K.R. Kodur

DES*tech* Publications, Inc.

Structures in Fire

DEStech Publications, Inc.
439 North Duke Street
Lancaster, Pennsylvania 17602 U.S.A.

Copyright © 2016 by DEStech Publications, Inc.
All rights reserved

No part of this publication may be reproduced, stored in a retrieval system, or transmitted, in any form or by any means, electronic, mechanical, photocopying, recording, or otherwise, without the prior written permission of the publisher.

Printed in the United States of America
10 9 8 7 6 5 4 3 2 1

Main entry under title:
Structures in Fire (Proceedings of the Ninth International Conference)

A DEStech Publications book
Bibliography: p.
Includes index p. 1141

ISBN: 978-1-60595-320-5

HOW TO ORDER THIS BOOK

BY PHONE: 1-877-500-4337 or 717-290-1660, 9AM–5PM Eastern Time

BY FAX: 717-509-6100

BY MAIL: Order Department
DEStech Publications, Inc.
439 North Duke Street
Lancaster, PA 17602, U.S.A.

BY CREDIT CARD: American Express, VISA, MasterCard, Discover

BY WWW SITE: http://www.destechpub.com

Table of Contents

CONCRETE STRUCTURES: FIBER REINFORCEMENT AND STRENGTHENING

CONCRETE STRUCTURES: MATERIAL BEHAVIOR

METAL STRUCTURES: MATERIAL BEHAVIOR

TIMBER STRUCTURES

EXPERIMENTAL METHODS

PROBABILISTIC APPROACHES AND APPLICATIONS OF FIRE SAFETY

NUMERICAL MODELING

Preface

The “Structures in Fire” (SiF) specialized workshop series was conceived in the late 1990’s with the first international workshop hosted in Denmark in 2000. SiF workshops followed every two years: New Zealand (2002), Canada (2004), and Portugal (2006). These events were renamed as International *Conferences* on Structures in Fire and held in Singapore (2008), the United States (2010), Switzerland (2012) and Shanghai (2014). Princeton University, USA, was selected to host the 2016 SiF International Conference (SiF’2016) from June 8 to June 10.

The main mission of SiF conferences is to provide an opportunity for researchers, practitioners and engineers to share their “Structures in Fire” research, technology, and expertise with their peers in an international forum. Allowing papers to be submitted only two months before the conference permits the most current scholarship to be presented. In addition to high quality state-of-the-art presentations, the 2016 SiF conference places significant value on discussions at the conference, both formally following presentations, and informally through social gatherings.

SiF’2016 received about 250 abstracts for consideration. The Scientific Committee made three reviews of each abstract, and based on their recommendations about 150 papers were invited for publication, from which 135 accepted the invitation. These proceedings represent those 135 papers, and collectively they represent the international state-of-the art in fundamental knowledge and practical applications of structural fire safety. Twenty-six countries from around the globe have contributed to the knowledge contained in this book.

In these proceedings, the papers are grouped into the following categories:

- Concrete Structures
- Concrete Structures: Fiber Reinforcement and Strengthening
- Concrete Structures: Material Behavior
- Metal Structures
- Metal Structures: Connections and Composite Floors
- Metal Structures: Material Behavior
- Composite Columns
- Timber Structures
- Material Behavior

- Bridges and Non-buildings Structures
- Experimental Methods
- Probabilistic Approaches and Applications of Fire Safety
- Numerical Modeling
- Fire Protection

We hope that the work presented in these proceedings will lead to safer, more economical, and more elegant fire designs for structures.

We extend a sincere 'thank you' to the Steering Committee for their guidance in making important decisions regarding the program format and proceedings. Our appreciation also goes to the members of the Scientific Committee for dedicating their time reviewing the abstracts. We are grateful to the Organizing Committee who was instrumental in developing the conference program and website. We also appreciate the work of Conference Services at Princeton University, in particular Lucy Weise, for managing registrations, classroom reservations, catering, etc. A huge thank you goes to the staff in the Civil and Environmental Engineering Department at Princeton University, in particular Jillian Hoffman and Islam Elnaggar, for supporting abstract and paper submissions, visa letters, attending to emails and a lot of other secretariat support.

Of course, SiF'2016 would not be possible without the proceeding's authors and conference participants. To you, we extend our greatest appreciation for making SiF'2016 a success.

Maria E. Moreyra Garlock
Chair, Organizing Committee
Princeton University

Venkatesh K. R. Kodur
Chair, Scientific Committee
Michigan State University

Scientific Committee

Chairman: Venkatesh Kodur, Michigan State University, USA

Tony Abu, University of Canterbury, New Zealand
Faris Ali, University of Ulster, Ireland
Pradeep Bhargava, Indian Institutes of Technology, Roorkee, India
Luke Bisby, University of Edinburgh, Scotland
Florian Block, Buro Happold, Germany
Andy Buchanan, University of Canterbury, New Zealand
Ian Burgess, University of Sheffield, England
Suwen Chen, Tongji University, China
Frank Dehn, Leipzig University, Germany
Dionis Dhima, Centre Scientifique et Technique du Batiment (CSTB), France
Michael D. Engelhardt, University of Texas at Austin, USA
Roberto Felietti, Politecnico di Milano, Italy
Mario Fontana (Track Leader), Swiss Federal Institute of Technology in Zurich, Switzerland
Massimo Fragiacomo, University of Sassari, Italy
Andrea Frangi, Swiss Federal Institute of Technology in Zurich, Switzerland
Jean-Marc Franssen, University de Liège, Belgium
Pietro Gambarova, Polytechnic University of Milan, Italy
Leroy Gardner, Imperial College, England
Maria Garlock, Princeton University, USA
Martin Gillie, University of Manchester, England
Mark Green, Queen's University, Canada
John Gross, National Institute of Standards and Technology (NIST), USA
Ralph Hamerlinck, Bouwen met Staal, Netherlands
Linhai Han, Tsinghua University, China
Zhaohui Huang, Brunel University, England
Basam Izzuddin, Imperial College, England
Marc Janssens, South West Research Institute, USA
Ann Jeffers, University of Michigan, USA
Daniel Joyeux, Efectis, France
Markus Knobloch, Swiss Federal Institute of Technology in Zurich, Switzerland
Susan Lamont, Arup, England
Angus Law, The University of Queensland, Australia
Guo Quiang Li (Track Leader), Tongji University, China
Mahen Mahendran, Queensland University of Technology, Australia
C. S. Manohar, Indian Institute of Science, India
Vasanth Matsagar, Indian Institutes of Technology, Delhi, India
Ali Nadjai, University of Ulster, Ireland
Emidio Nigro, University of Naples Federico II, Italy
Jyri Outinen, Ramboll, Finland
Spencer Quiel, Lehigh University, USA

João Paulo Rodrigues, Universidade de Coimbra, Portugal
Peter Schaumann, University of Hannover, Germany
Joachim Schmid, SP Technical Research Institute, Sweden
Mahmood Tabaddor, Underwriters Laboratory, USA
Luc Taerwe, University of Ghent, Belgium
Didier Talamona, University of Newcastle, Australia
Philip Tan Kang Hai (Track Leader), Nanyang Technological University, Singapore
Asif Usmani (Track Leader), Brunel University, England
Amit Varma, Purdue University, USA
Olivier Vassart, Arcelor Mittal, Luxembourg
Paulo Vila Real (Track Leader), University of Aveiro, Portugal
Frantisek Wald, Czech Technical University in Prague
Yong C. Wang, University of Manchester, England
Bo Wu, South China University of Technology (SCUT), China
Yao Yao, Northwestern Polytechnic University, USA
Raul Zaharia, University of Timisoara, Romania
Bin Zhao (Track Leader), Centre Technique Industriel de la Construction Métallique (CTICM), France
Huang Zhaohui, Brunel University, England

Organizing Committee

Maria E. Moreyra Garlock, Chair, Princeton University, USA
Jonathan Glassman, Exponent Failure Analysis Associates, USA
Negar Elhami Khorasani, University at Buffalo-SUNY, USA
Spencer Quiel, Lehigh University, USA

Steering Committee

Andy Buchanan, University of Canterbury, New Zealand
Jean-Marc Franssen, University of Liege, Belgium
Paulo Vila Real, University of Aveiro, Portugal
Venkatesh Kodur, Michigan State University, USA

Acknowledgements

CONCRETE STRUCTURES

Glass Fibre Reinforced Polymer (GFRP) Reinforced Concrete Slabs with Low Cover in Fire

HAMZEH HAJILOO[1], MARK F. GREEN[1],
NOUREDDINE BÉNICHOU[1] and MOHAMED SULTAN[2]

SUMMARY

One of the main safety requirements in the design of buildings is ensuring safe and appropriate fire endurance of the structures. To fill the knowledge gap on the fire resistance of fibre reinforced polymer (FRP) reinforced concrete members, comprehensive experimental and analytical studies are underway at Queen's University with collaboration from industry and the National Research Council of Canada (NRC). As a part of the program, two full-scale glass FRP (GFRP) reinforced concrete slabs were tested under exposure to the ASTM-E119 standard fire. The slabs were identical except that they were reinforced with different types of GFRP and tested to examine the adequacy of 40 mm of clear concrete cover. Currently, CSA-S806 allows a simplified method to design concrete slabs with FRP reinforcement and this results in a requirement for clear concrete cover of approximately 60 mm to achieve a 2 hour fire resistance rating. The test results showed that the slabs endured beyond 3 hours of fire exposure while resisting a high level of sustained load that was higher than the expected service load.

INTRODUCTION

It is generally supposed that concrete elements with FRP reinforcing bars have lower fire resistance than equivalent conventionally reinforced concrete with steel. In fact, until last year, the *ACI Guide for the Design and Construction of Concrete Reinforced with FRP Bars* [1] did not recommend FRP reinforcement for structures in which fire resistance was vital to maintain structural integrity. Design of FRP reinforced concrete members to resist fire incidents has been challenging since the available standards such as CSA-S806 [2] propose thicker concrete cover than the required cover for steel reinforced elements. Given the higher short-term construction cost of FRP reinforced structures than for steel reinforced ones, thicker concrete cover to ensure fire resistance, which leads to inefficient material use in FRP reinforced

[1]NRC-construction, National Research Council Canada, Ottawa, ON, Canada
[2]Civil Engineering, Queen's University, 58 University Avenue, Kingston ON Canada

construction, has limited applications of FRP reinforcement in structures where fire is a concern. This uncertainty excludes FRP reinforcement from many applications such as parking garages where FRP reinforcement can ensure durability of the structures. FRP reinforcement is a competitive replacement for steel in bridge construction; however, recent fire incidents have also created needs to consider fire in bridge design.

The authors, in collaboration with industry partners, have launched an extensive research program on the evaluation of FRP material behaviour at elevated temperatures and FRP reinforced concrete flexural elements to address these issues. As a part of this project, two full-scale slabs were tested in the floor furnace at the National Research Council (NRC) facilities. The slabs were designed and fabricated to represent common FRP reinforced concrete slabs such as those found in a typical parking garage but with only 40 mm of clear concrete cover.

EXPERIMENTAL PROGRAM

The intent of this experiment was to achieve two hours of fire endurance with 40 mm cover for simply supported unrestrained slabs under standard fire exposure. The slabs were heavily instrumented to collect the thermal field data in exposed and unexposed areas of slabs. Strain gauges were installed on the longitudinal reinforcing bars to measure strain before fire test and during the early stages of the fire test.

Two concrete slab specimens were fabricated for this experimental test; each was reinforced with reinforcing bars from a different manufacturer, which are designated as Slab-A and Slab-B hereafter. The slabs were conservatively tested without end restraints and were free to rotate and expand. Table I provides the details of the specimens.

The slabs were 3900 mm long, 1200 mm wide, and 200 mm thick which is typical for slabs in parking garages. The clear concrete cover to the bottom of longitudinal reinforcing bars was 40 mm. The centre-to-centre clear spacing of the bottom and top longitudinal reinforcement was 150 and 220 mm, respectively. The transverse reinforcing bars were placed in 200 mm intervals at the bottom and top meshes to control shrinkage and thermal cracks. Concrete with carbonate aggregate was used in the fabrication of slabs with the average 28 day compressive strength of $f_c' = 34$ MPa.

The GFRP reinforcing bars for the slabs had a nominal diameter of 16 mm. Rebar-A had sand coating on the surface which was applied on the hardened reinforcing bar following the pultrusion process. Rebar-B had a helical braid of fibres was in addition to a sand coating. This braid created surface deformations to enhance bond. Properties of the GFRP reinforcing bars are given in Table II.

Table I. FABRICATION DETAILS FOR THE SLABS.

Slab ID	Thickness (mm)	Cover (mm)	Reinforcement	Aggregate	f_c' (MPa)
Slab-A	200	40	Rebar-A	Carbonate	34
Slab-B	200	40	Rebar-B	Carbonate	34

Table II. MANUFACTURER SPECIFIED MATERIAL PROPERTIES.

Properties	Units	Rebar-A	Rebar-B
		#5	#5
Nominal Diameter	(mm)	16	16
Nominal Cross Sectional Area	(mm^2)	198	199
Nominal Tensile Strength	(MPa)	1720	1290
Nominal Modulus of Elasticity	(MPa)	64100	62600
Glass transition temperature	°C	119	114

Test Configuration and Procedure

The NRC's floor furnace can accommodate two centered slabs next to each other with the space between them filled by ceramic insulating blankets. The uniformly distributed load was applied by a loading system comprised of six jacks located on each slab. The superimposed load was constant during the fire test until failure occurred. The slabs were tested under a sustained distributed load of 19.1 (kN/m) which resulted in a bending moment equal to approximately 45 kN.m, which corresponded to 45 % of the ultimate flexural capacity of the slabs based on the tested 28 day strength of the concrete.

In most fire experiments, the ASTM E119 [3] or the ISO-834 [4]standard fire curves are used to evaluate the fire resistance of reinforced concrete members incorporating FRPs. Both curves are suitable for fire testing of structural elements. In this project, the ASTM E119 standard fire curve was used, and the temperatures inside of furnace were monitored using nine thermocouples located as close as possible to the bottom surface of the specimens. Following closely the ASTM E119 fire curve, the temperature increases rapidly during their early stages and stabilizes at around 1000 °C, reaching 1050 °C after three hours.

TEST RESULTS

Both concrete and reinforcing materials are influenced when subjected to fire. Although the degradation of concrete and steel reinforcement in conventional reinforced concrete elements is a matter of concern, concrete is not as much of a concern for FRP reinforced members since the degradation of the FRP material takes at lower temperatures than those that negatively affect concrete.

The thermal distribution in the slabs was recorded using 29 thermocouples placed in each slab. The temperatures throughout the concrete depth at midspan of Slab-B are shown in Figure 2.

Thermocouple T21 was located very close to the bottom surface of the slabs and hence the highest temperatures were recorded by T21. The recorded temperatures in the first five minutes of the fire were close to the internal furnace temperatures and reached 135 °C in 5 minutes. A notable spike in T21 at 75 minutes was due to local spalling of concrete leaving the thermocouple with less cover. The second thermocouple, T22, located 20 mm deep into the slab, reached 135 °C in 11 minutes. T23, located at the level of the reinforcing bars, showed that temperature on the bars was 365 °C after 2 hours of fire exposure. Material tests have shown that the FRP reinforcing bars retain approximately 40 % of their room temperature strength at a temperature of 365 °C [5].

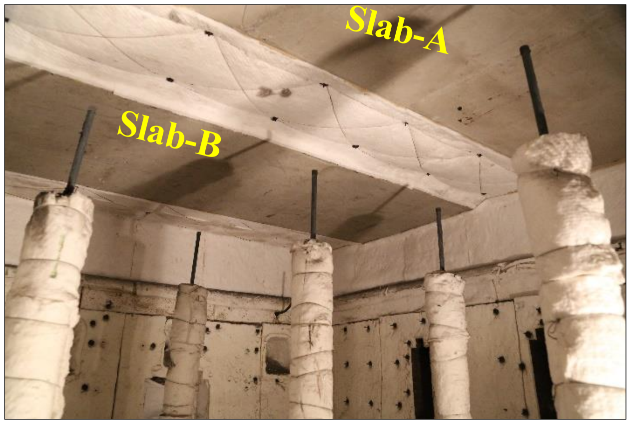

Figure 1. Testing furnace and setup

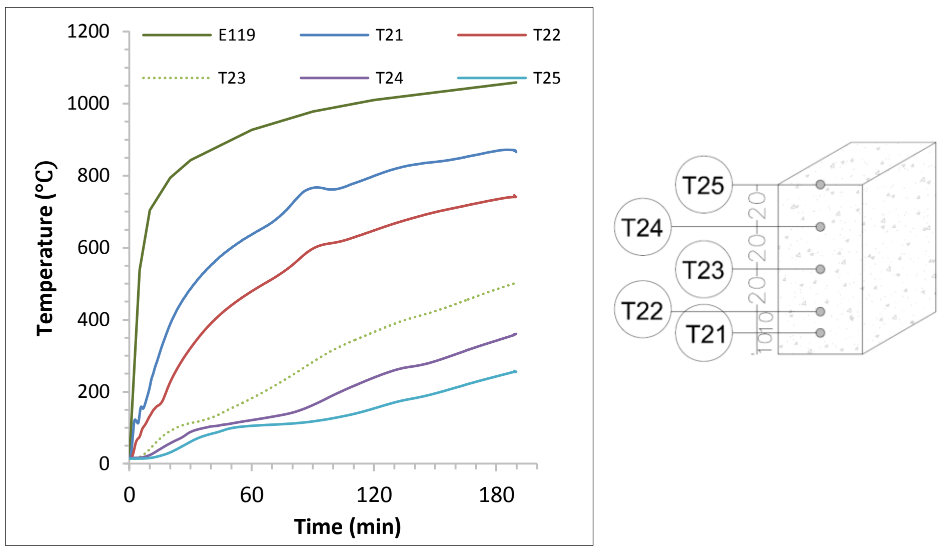

Figure 2. Temperatures within the thickness of Slab-B.

T23 and T24 were located at 40 and 60 mm from the exposed bottom surface of slab, respectively. Considering that the outer diameter of the reinforcing bars was approximately 20 mm, the readings of T23 and T24 were representative of temperatures at the bottom and top surfaces of the reinforcing bars. While the temperature increased in the bottom of the lower reinforcement layer to 365 °C after two hours of exposure, thermocouple T24 (close to the top surface of the reinforcing bars in the bottom of the slab) showed only 240 °C demonstrating a thermal gradient of approximately 125 °C across the reinforcing bars. Such differences between temperatures on the top and bottom surfaces of the reinforcing bars were observed during the entire fire exposure.

In steel reinforced structures, the bond strength variation at elevated temperature is quite similar to the variation in the compressive strength of the concrete [6]. However, the bond of FRP reinforcement to concrete deteriorates at lower temperatures and when the temperature at the FRP to concrete interface reaches about 170 °C, the remaining bond strength is approximately 10% of the bond strength at room temperature for both Rebar-A and Rebar-B [7]. Thus, the most informative thermal data were collected from the anchor zone where eight thermocouples were aligned along 200 mm of the anchor zone (Figure 3). These thermocouples recorded the thermal gradients along the reinforcing bars in the anchor zone. These areas of interest were heavily instrumented since the failure of the slabs was expected to initiate by bond degradation between the FRP and concrete based on a previous set of fire tests on GFRP reinforced slabs [8]. All of the thermocouples illustrated in Figure 3 were installed at a depth of 40 mm into the thickness of the slab at the bottom surface of the reinforcing bars. The first thermocouple was placed 25 mm from the end of slabs and the rest of thermocouples were located every 25 mm; the last sensor (T11) was located on the boundary of the exposed and protected area.

The thermal field in the anchor zone at the ends of Slab-A and Slab-B is shown in Figure 4. The recorded results in Figure 4 show that the temperatures remained below 100 °C at 75 mm (T16) from the ends of Slab-A during the test; the maximum temperature at the same location for Slab-B was 116 °C. At these temperatures, the bond strength between the concrete and the FRP was approximately 30 % of the room temperature strength.

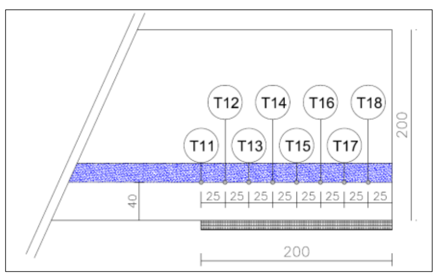

Figure 3. Thermocouples placed in the anchor zone of each slab.

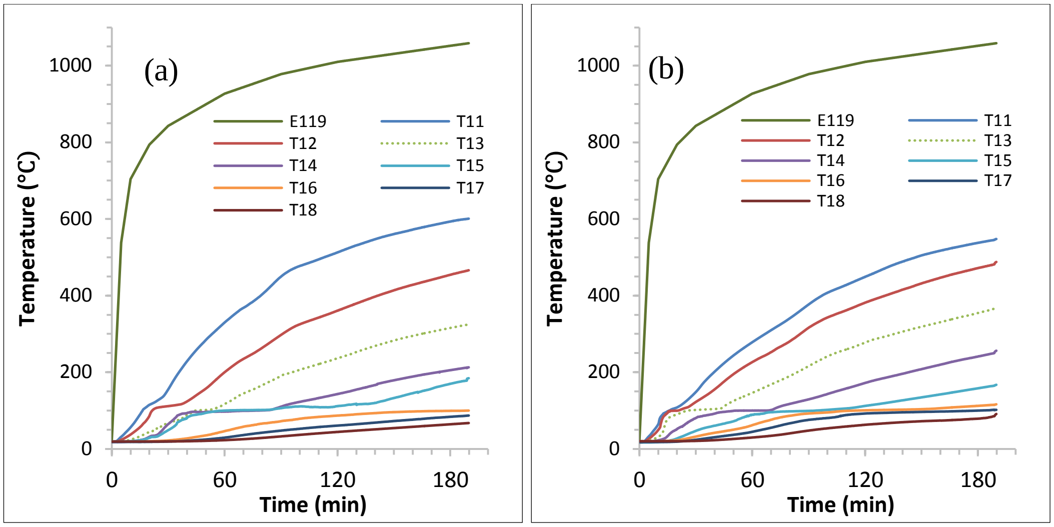

Figure 4. Temperature variations in the anchor zone; (a) Slab-A; (b) Slab-B.

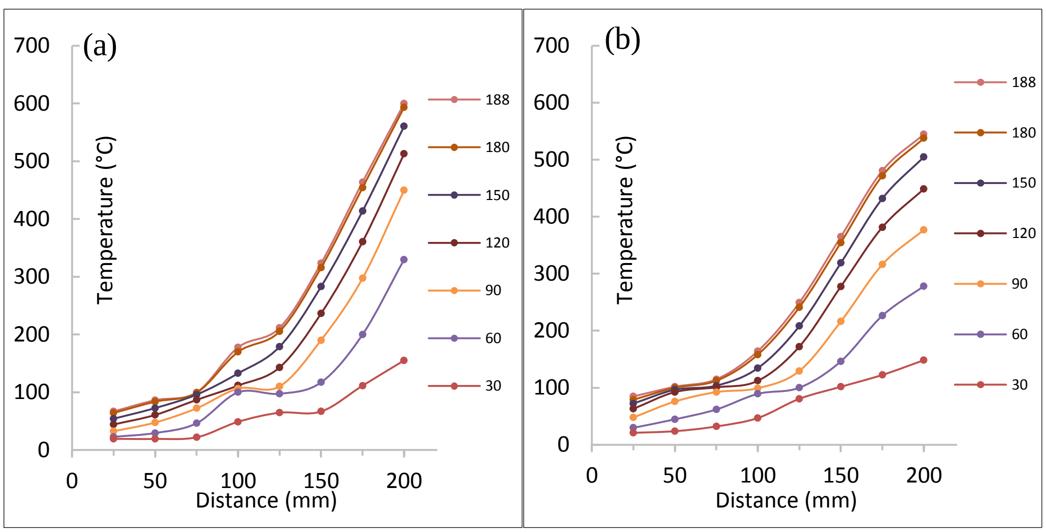

Figure 5. Temperature gradients along the anchor zone; (a) Slab-A; (b) Slab-B.

Figure **5** shows thermal gradients in the anchor zone. Temperatures drop significantly from the edge of the exposed zone towards the unexposed zone, especially between the 200 mm and 125 mm away from the end of the slabs. The thermal field becomes uniform in the last 100 mm strip of the slabs.

Failure modes

According to ASTM E119-15 [3], the average temperature rise of the unexposed surface of the slab with respect to the room temperature has to remain below 139 °C. In addition, passage of flame through the slab is not permitted. None of these failure criteria associated with thermal behaviour occurred during the fire exposure.

Both slabs were able to carry a high level of superimposed load for more than 180 minutes. It should be noted that the load applied on the slabs during fire exposure was well beyond the expected load on the slabs in a real fire incident. Since serviceability governed the design of the slabs, the corresponding expected service moment was 23.4 kN.m. Despite this, the slabs endured more than three hours of fire exposure under a higher sustained moment of 45 kN.m that corresponded to 45 % of the ultimate flexural capacity of the slabs based on the tested 28 day strength of the concrete.

The slabs were simply supported at the ends and unrestrained axially and rotationally before load application and during fire exposure. Figure 6 shows the time–deflection behaviour of the slabs after the start of the fire. Uneven thermal fields in the lower and top layers of concrete caused the slabs to bow downward. The deflection shown in Figure 6 consisted of the heat-induced bowing deflections and deflections due to the fact that the concrete and FRP reinforcing bars were degrading as a result of elevated temperatures during fire exposure. The changes in temperatures at the lower layers of concrete too place quickly. As shown in Figure **6**, thus, there was a rapid deformation in first 20 minutes of the onset of fire. Then, the time-deflection curve reached an almost stable region. After 60 minutes, the temperatures at the bottom of the reinforcing bars reached 180 °C, and as mentioned earlier from the material tests [7], the remaining bond strength of the reinforcing bars in the centre of the slabs was small. However, the relatively short embedment of the reinforcing bars into the anchor zone still provided sufficient bond strength between the reinforcing bars and concrete. In other words, the slabs were anchored from both ends acting like a tied arch. This change in structural behaviour from a bonded to an unbonded system caused rapid increase in the deflection.

After two hours, the slabs deformed at a relatively higher rate, especially Slab-B. Right after three hours (at 188 minutes), Slab-B failed due to excessive deflection, and the test was stopped to prevent it from falling into the furnace. Figure 7 shows the excessive residual deflection of Slab-B after the fire test.

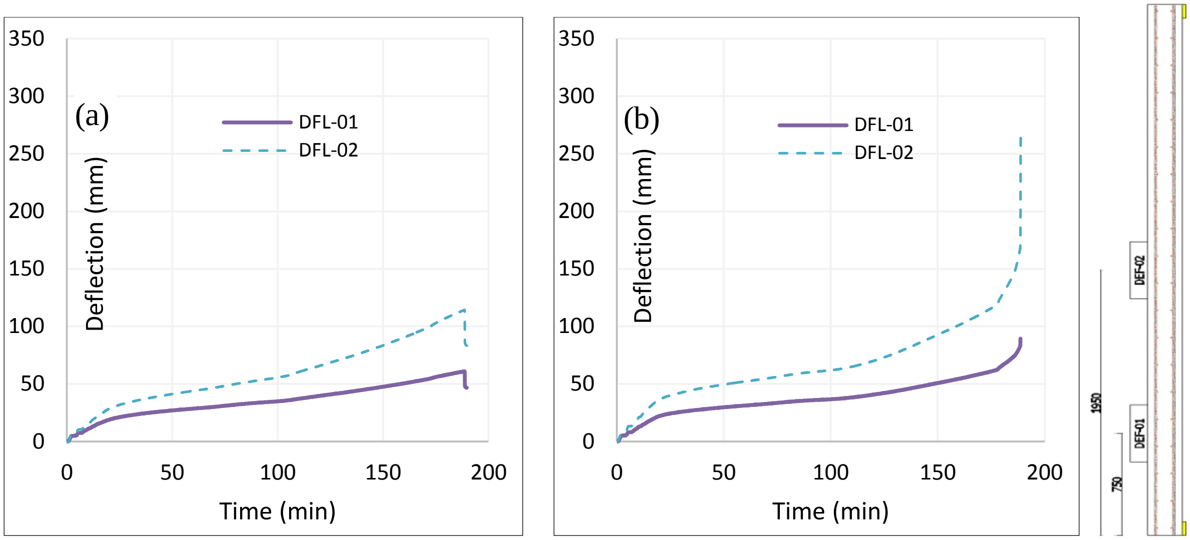

Figure 6. Deflection vs time; (a) Slab-A and (b) Slab-B.

Figure 7. Excessive deflection of Slab-B.

CONCLUSIONS

By virtue of the results of these fire tests, another step was taken towards constructing FRP reinforced concrete structures with more certainty by demonstrating safe applications of FRP reinforcing bars with relatively low concrete cover. The tests investigated the fire safety of the very efficient practice of GFRP reinforcement in flexural elements with only 40 mm of clear concrete cover. The results proved that FRP flexural elements can endure more than three hours and that 200 mm embedment of the bars into the support is sufficient to prevent early failure due to bond loss.

ACKNOWLEDGEMENTS

The authors would like to thank the Natural Sciences and Engineering Research Council of Canada (NSERC), Pultrall Inc. and BP Composite for their financial and material support. The authors also appreciate the contributions of Patrice Leroux and the other technical staff of the Fire Research Laboratory at NRC, the insightful advice of Dr. B. Benmokrane, and the cooperation of Dr. H. Mohammad and the technical staff at the University of Sherbrooke. The assistance of Dr. J. Gales (Carleton University) and Dr. M. Noël (University of Ottawa) is also appreciated.

REFERENCES

1. ACI-440.1R-15, Guide for the Design and Construction of Concrete Reinforced with FRP Bars in *American Concrete Institute*, *Detroit*, *Michigan*. 2015.
2. Canadian Standards Association, Design and construction of building components with fiber-reinforced polymers, in *Canadian Standards Association. Mississauga, Ontario, Canada:* 2012.
3. ASTM E119-15, Standard Test Methods for Fire Tests of Building Construction and Materials. 2015: ASTM International, West Conshohocken, PA.
4. ISO 834-11. Fire resistance tests- Elements of building construction. International Organization for Standardization.
5. Hajiloo, H., J. Gales, M. Noël, and M.F. Green. "Material Characteristics of Glass Fibre Reinforced Polymer (GFRP) Bars at High Temperature," presented at Protect 2015. 2015. Michigan, USA. pp. 94-104.
6. Harmathy, T.Z., *Fire safety design and concrete*. 1993: John Wiley & Sons, New York.
7. Hajiloo, H. and M.F. Green. "Bond Strength of Glass Fibre Reinforced Polymer Bars in Concrete at High Temperature," presented at CSCE-2015. 2015. REGINA, SK.
8. Hajiloo, H., M.F. Green, N. Bénichou, and M. Sultan. "Fire Performance of FRP reinforced concrete slabs " presented at 7th International Conference on Advanced Composite Materials in Bridges and Structures. 2016. Vancouver, Canada.

The Effect of LITS on Punching Shear in Fire

RWAYDA AL HAMD, MARTIN GILLIE, GIACOMO TORELLI,
HOLLY SMITH, TIM STRATFORD and YONG WANG

ABSTRACT

Several recent sets of experimental results on the punching shear behavior of flat slabs in fire have produced apparently anomalous deflections results, where the slab deflections on heating are in the opposite direction to that expected. Using numerical analysis, this paper shows that the results are explained by load induced thermal strains (LITS). Using two independent modelling approaches, the profound effect of LITS on deflection behavior is demonstrated. Analysis of the strain state near column connections identifies significant differences when LITS is included in analyses. By contrast for the unrestrained slabs considered here, stress states do not change much. The potential implications of these findings for design are noted.

INTRODUCTION

Flat plate concrete structures are an economical type of building frame commonly used for offices and similar structures. They are easy to construct, offer flexible column arrangements and are relatively cheap to build. However, they are susceptible to a type of failure known as "punching shear" (Figure 1), where columns pierce floor slabs, leading to collapse. This is a particularly dangerous type of failure as it is brittle and occurs suddenly. Punching shear occurring at high temperatures, such as in fire, is a concern [1]. This condition has been studied experimentally but to date there has been little numerical investigation of the topic. This paper presents a numerical study of the mechanics of punching shear failure at elevated temperatures, with a focus on the role of load induced thermal strain (LITS), which is shown to explain some apparently anomalous experimental results.

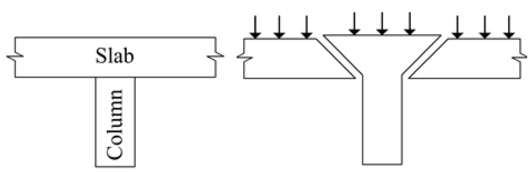

Figure 1 Schematic diagram of a flat plate structure and the punching shear failure mechanism.

After the car park collapse in Gretzenbach, Switzerland in 2004 due to fire [1], various experimental studies investigated punching shear in heated slabs. These included Salem, et al. [2], Annerel et al. [3,4] and Liao et al. [5]. More recently, Smith et al. [6–8] investigated punching behavior under fire by testing 15 slabs with different heating and support conditions (laterally and rotationally restrained and unrestrained). They noted that the deflections of the slabs when heated were in the opposite direction to that expected – away rather than towards the heat source, as a simple thermo-mechanical analysis would predict (Figure 2).

Rwayda Al Hamd, University of Manchester.
Martin Gillie, University of Manchester.
Giacomo Torelli, University of Manchester.
Holly Smith, AECOM.
Tim Stratford, University of Edinburgh.
Yong Wang, University of Manchester.

This finding could not be explained directly from the experimental results but was in line with the work of Liao et al. [5] who observed the same effect. It is a behavior that the present study focuses on and explains using a numerical approach.

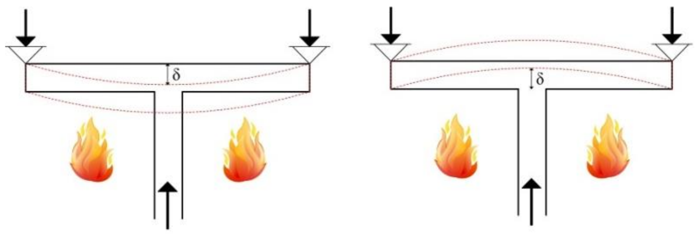

a. The expected deflection b. The experimental deflection

Figure 2 (a) An expected deflection reponse to heating and (b) the deflection response seen in Smith's tests [6–8].

LOAD INDUCED THERMAL STRAIN (LITS)

A key aspect of the behavior of the heated concrete slab discussed below was found to be LITS. LITS can be thought of as an additional plastic strain that develops under combinations of temperature and stress [9][10]. Under suitable conditions, it can result in an apparent thermal contraction on first heating of concrete, behavior at odds with that of most materials and intuitive expectations. Several analytical models have been proposed to represent LITS [9]. In this study the model proposed by Anderberg and Thelandersson [11] is adopted, where LITS in compression, ε_{ts} is given by:

$$\varepsilon_{ts}=-k_{tr}\frac{\sigma}{\sigma_{u0}}\varepsilon_{th} \qquad \text{for } T \leq 550 \text{ °C}$$

$$\frac{\partial\varepsilon_{ts}}{\partial T}=-0.0001\left(\frac{\sigma}{\sigma_{u0}}\right) \qquad \text{for } T > 550 \text{ °C}$$

where σ_{u0} is the compressive strength of concrete at ambient temperature, k_{tr}, and ε_{th} is the free thermal strain.

MODELLING APPROACH

The finite element package Abaqus was used in the majority of this study. First, models of a single column and associated area of floor slab (Figure 3) were developed and validated against ambient temperature experimental results [12–14] for punching shear. The models used 8-noded hexahedral solid elements with reduced integration for all concrete parts, together with truss elements to represent the reinforcement. Full bond between the two materials was assumed. Concrete was represented using the damaged plasticity model provided within Abaqus, with the uniaxial compressive stress-strain relationship taken from Eurocode 2 [15]. Uniaxial tension behavior was taken from Wang and Hus [16]. Steel behavior was taken from results of coupon tests and modelled using a von Mises yield criterion. Details of the validation for ambient temperature can be found in [13] .

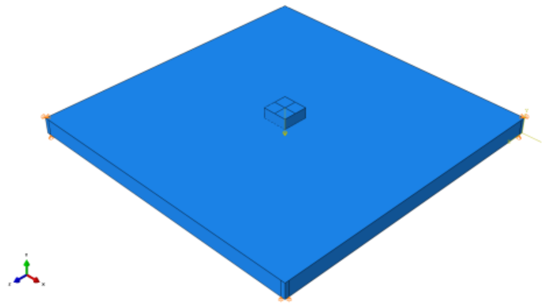

Figure 3 Abaqus finite element model developed.

RESULTS

The same modelling approach was then adopted to model the high temperature behavior of Smith's slabs. For the main Abaqus study, a slab was chosen that had simple supports at all edges (no vertical movement but free to rotate) with a thickness of 75mm. Only tension reinforcement was present. Heating was provided in Smith's experiments by radiant panel heaters, with a peak surface temperature of around 380°C being reached. The surface temperatures in the slabs were measured by Smith and those used in this paper are shown in Figure 4. Based on this data, a numerical thermal analysis provided predicted temperatures at all depths within the slab through time.

It was found that simply introducing elevated temperatures, together with thermal expansion and degradation of material properties, to the ambient temperature model was not sufficient to reproduce Smith's [6–8] experimental results (Figure 5). Instead, a response as might be expected from a simple consideration of thermal expansion was seen (Figure 2). However, the addition of LITS to the model had a large effect on the predictions and re-produced the experimental results accurately. The stark effect of LITS is also shown in Figure 5.

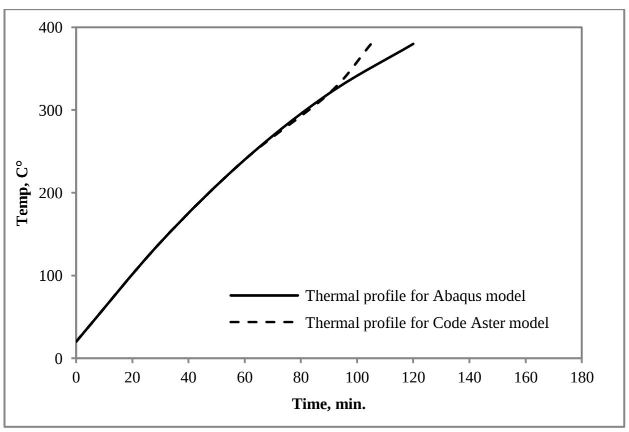

Figure 4 Temperature-time data for the heated surface.

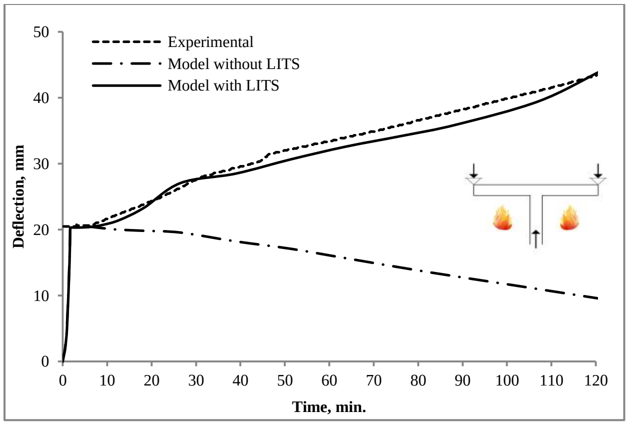

Figure 5 Deflection time response for Abaqus model.

To confirm these results, another of Smith's experimental results was modelled with the FE package Code Aster. This experiment had no steel reinforcement and a 100 mm slab thickness. A similar material behavior law incorporating elasticity, thermal expansion and the Anderberg and Thelandersson's [11] LITS model was implemented and used to evaluate the deflection of the slab when heated. As in the Abaqus model, significantly better deflection predictions result when LITS is included (Figure 6). Taken together, the results shown in Figures 5 and 6 give a high level of confidence that the previously inexplicable experimental results are due to LITS dominating deflections at high temperatures.

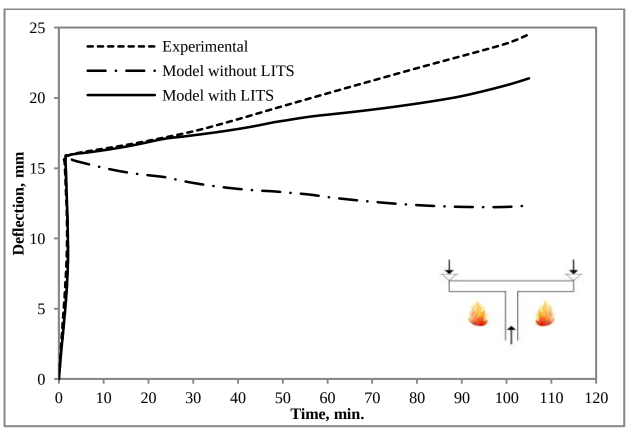

Figure 6 Deflection time response for the Code Aster model.

With this finding, the effect of LITS on the stresses and strains within the heated slab were examined using the results from the Abaqus model. These are presented in the Figures 7 and 8, where quantities are plotted along a line extending at 45^o from the slab-column interface (distance =0mm) to the unheated surface (distance =~105 mm). This line approximates the line along which a punching shear crack would develop (Figure 1). Quantities are plotted at the end of the heating phase of the predictions.

The shear stress distribution in the slab is shown in Figure 7. The difference between the case when LITS is present and when it isn't is relatively small. This is explained by the slab being close to determinate (no in-plane restraint and free to rotate at the supports). For this situation, stresses are largely independent of the stiffness of the structure and thermal expansion. The differences that are apparent are due to large deflection effects.

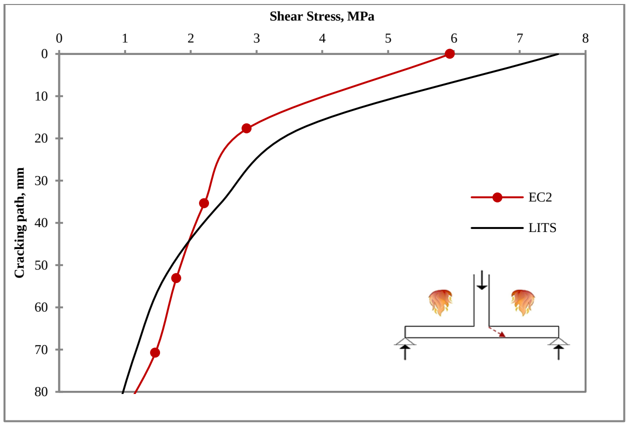

Figure 7 Stress distribution predictions for the LITS and non-LITS (EC2) Abaqus models.

The predicted in-plane strain distributions along the expected crack path at various time (=temperature) steps are shown in Figure 8. There is marked difference between the LITS and non-LITS predictions here, with greater strains predicted when LITS is included in the model. This behavior corresponds to the increase in compressive strains predicted by the LITS material model when concrete is heated under stress, with the discrepancy being greater at higher temperatures. In-plane strains are largely a result of bending behavior in the slab. Therefore, for reasons of compatibility, the tensile strains increase with line with the compressive strains and the neutral axis moves away from the heated surface as heating progresses.

Figure 9 shows the evolution of the maximum principal strain as heating progresses for the two cases. Principal strains develop roughly normal to the expected crack direction and will be a better predictor of shear-crack development than in-plane strains as they are affected less by bending behavior. In both the upper and lower portions of the slab, there is an increase in strain as a result of included LITS behavior in the model.

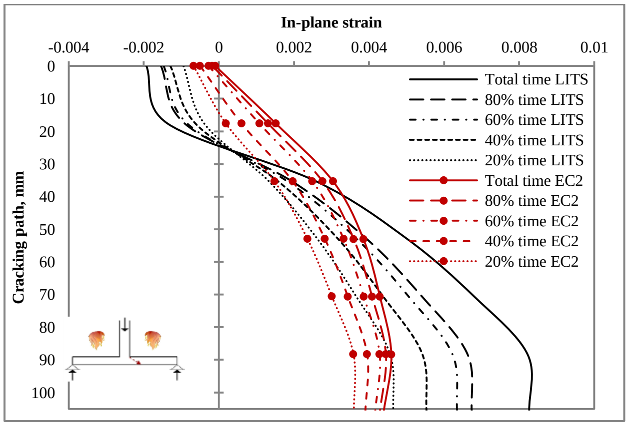

Figure 8 In plane mechanical strain distributions for LITS and non-LITS cases.

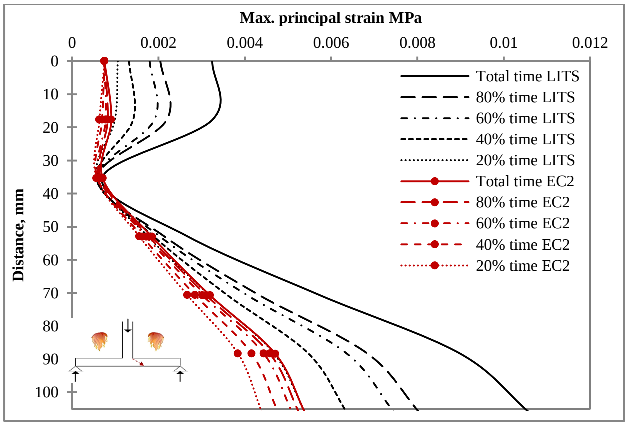

Figure 9 Maximum principal strain distribution predictions for the LITS and non-LITS cases.

CONCLUSIONS

The results clearly show that LITS accounts for the apparently anomalous experimental deflection results seen in punching shear experiments in fire. For the load cases presented here, the consequences of this finding are mainly relevant to deflection predictions and strain distributions, with little effect on predicted stresses. The consequences of this finding for the design of slabs in punching shear in fire should be determined. In particular the implications of the predictions for the recently developed critical shear crack theory [17] should be identified. This approach to calculating punching shear strength relies on estimates of the rotation of slabs to predict initiation of cracking. Larger deflections (and hence rotations), as seen experimentally and now explained numerically, may mean the method needs additional calibration for fire loading.

Further numerical studies should be undertaken to identify the likely effects of LITS on stresses when in-plane restraint is present, as is likely in real floor plates. Compressive in-plane stresses serve to increase punching shear capacity and a simple analysis would suggest restrained thermal expansion produces highly compressive in-plane stresses. However, if, as appears likely, LITS results in lower compressive (or even tensile) in-plane stresses, this would reduce the punching shear capacity below that anticipated by current design approaches.

ACKNOWLEDGEMENTS

The authors acknowledge the support of The Higher Committee for Education and Development in Iraq (HCED) for the financial support that made this work possible.

REFERENCES

[1] Ghoreishi M, Bagchi A, Sultan MA. Review of the Punching Shear Behavior of Concrete Flat Slabs in Ambient and Elevated Temperature. Structural Fire Engineering 2013;4:259–80.

[2] Salem H, Issa H, Gheith H, Farahat A. Punching shear strength of reinforced concrete flat slabs subjected to fire on their tension sides. HBRC Journal 2012;8:36–46.

[3] Annerel E, Lu L, Taerwe L. Punching Shear Tests on Flat Concrete Slabs Exposed to Fire. Fire Safety Journal 2013;57:83–95.

[4] E. Annerel , L. Taerwe, B. Merci , D. Jansen , P. Bamonte RF. Thermo-Mechanical Analysis of an Underground Car Park Structure Exposed to fire. Fire Safety Journal 2013;57:96–106.

[5] Liao J-S, Cheng F-P, Chen C-C. Fire Resistance of Concrete Slabs in Punching Shear. Journal of Structural Engineering 2014;140:04013025. doi:10.1061/(ASCE)ST.1943-541X.0000809.

[6] Smith HKM, Stratford T, Bisby L. Deflection Response of Reinforced Concrete Slabs Tested in Punching Shear in Fire. Applicatons of Structural Fire Engineering, Dubrovnik, Croatia: 2015.

[7] Smith HKM, Stratford TJ, Bisby LA. Punching Shear of Restrained Reinforced Concrete Slabs under Fire Conditions. 8th International Conference on Structures in Fire, Shanghai, China: 2014.

[8] Smith HKM, Stratford T, Bisby L. The Punching Shear Mechanism in Reinforced-Concrete Slabs under Fire Conditions, East Langsing, Michigan: 2015, p. PROTECT conference. doi:10.1126/science.1247727.

[9] Law A. The Assessment and Response of Concrete Structures Subjected to Fire. The University of Edinburgh, 2010.

[10] Law A, Gillie M, Pankaj P. Incorporation of Load Induced Termal Strain in Finite Element Models. Application of Structural Fire Engineering 2009;49:19–20.

[11] Anderberg Y, Thelandersson S. Stress and deformation characteristics of concrete at high temperature: 2. Experimental investigation and material behaviour model. Bulletin No 46 1976:86.

[12] Salman RK. Behavior of Flat Plates under Eccentric Loading Using Shearhead Reinforcement. Al Mustansiriya University, 2012.

[13] Al Hamd RKS, Gillie M, Wang Y, Rasheed MM. Punching Shear – Eccentric Load and Fire Conditions. CONFAB 2015 Conference Proceedings, Glasgow , United Kingdom: ASRANet Ltd; 2015, p. 201–9.

[14] Salman RK, Rasheed MM, Al-Amier JSA, Jamal Saeed Abd Al-Amier Asst Mohammed Rasheed AM, Khdier Salman R. Effect of Steel Shearhead on Behaviour of Eccentrically Loaded Reinforced Concrete Flat Plate. Journal of Engineering and Development 2013;17:14–27.

[15] Eurocode 2. Design of Concrete Structures, Part 1-1: General Rules and Rules for Buildings. vol. 3. 2004.

[16] Wang T, Hsu T. Nonlinear Finite Element Analysis of Concrete Structures Using New Constitutive Models. Computers & Structures 2001;79:2781–91.

[17] Muttoni A. Punching Shear Strength of Reinforced Concrete Slabs. ACI Structral Journal 2008;105:440–50.

Concrete Edge Failure of Headed Stud Anchors under Fire and Post-Fire Conditions: Verification of a 3D FE Code

KAIPEI TIAN, JOŠKO OŽBOLT and GORAN PERIŠKIĆ

ABSTRACT

Fire tests were conducted at University of Stuttgart to investigate the capacity of headed stud anchors under shear load perpendicular to free edge of concrete members. The headed stud anchors were cast in concrete with various edge distances, embedment depths and diameters. The specimens were specially designed so that the anchors could be loaded in shear after 90 min (hot state) of fire according to ISO 834. Reference tests and post-fire tests on the corresponding anchors were also conducted to make comparative analysis. More importantly, numerical analyses based on a three-dimensional thermo-mechanical constitutive model for concrete that was implemented into a three-dimensional finite element code were performed to simulate experimental tests. The main aim of the paper is to verify numerical model based on the performed experimental tests. It is shown that the numerical analysis is able to predict the thermal and structural response of headed stud anchors cast in concrete close to edge very well. Based on the experimental results and numerical verification, the modification of the current formula according to Eurocode 2 for concrete edge failure of headed stud anchors under 90 min of fire is proposed.

INTRODUCTION

Numerous investigations on concrete edge failure of headed stud anchors at room temperature have been performed so far [1, 2]. However, the load-bearing behavior at elevated temperatures, such as in case of fire, has barely been investigated. In ACI318 code anchorages under fire are not considered, and in Eurocode 2 there is only a general informative note. Although in most fire cases steel failure might be the governing failure mode, due to the softening of steel at high temperature, fastener or fastener groups close to edge of concrete structure may fail by concrete edge breakout when the steel part is protected or specially designed. Moreover, after cooling steel

Kaipei Tian, PhD student; Joško Ožbolt, Professor.
Institute for Construction Materials, University of Stuttgart, Pfaffenwaldring 4, 70569 Stuttgart, Germany.
Goran Periškic, PhD., Nolasoft GbR, Hermannstrasse 9, 70178 Stuttgart, Germany.

resistance is recovered and concrete resistance not, with the consequence that concrete failure can become relevant. It is known that fire tests are rather demanding, expensive and it is not easy to get relevant information from the test. Therefore to better understand the behavior of fasteners under fire it is important to have objective numerical tool. Recently fire tests on single headed stud anchors loaded in shear towards concrete edge were conducted to verify the numerical model, which is subsequently used in the numerical parametric studies of anchors loaded under fire.

EXPERIMENTAL PROGRAM

Headed stud anchors cast in concrete with different edge distances $c = 50$ mm, 100 mm, and 150 mm, embedment depths $h_{ef} = 45$ mm and 95 mm, and stud diameters $d = 16$ mm and 25 mm, were loaded towards the concrete edge both, under 90 min of fire according to ISO 834, and after naturally cooling down to room temperature. The fire exposure on one and two sides of concrete edge, respectively, was considered (see Fig. 1). The one side of fire exposure was realized by attaching a fire protection board on the front face of the concrete block as shown in Fig. 1a. Tests under fire were performed by using the specimen as shown in Fig. 2a, in which the anchors could be loaded from the top and outside of the furnace. The length of the free edge was 5 times the edge distance c. The temperature distribution around the anchors (see Fig. 2b), load-displacement curves, and the failure patterns were recorded.

NUMERICAL PROGRAM

Numerical simulations of each anchor tested under fire and after cooling down were conducted using three-dimensional thermo-mechanical model for concrete that was implemented into a three-dimensional finite element code [3, 4]. The mechanical constitutive law for concrete is the temperature dependent microplane model [5]. The Finite element discretizations were performed following exactly specimen geometry and boundary conditions of experimental set up (see Fig. 3). Figure 3a shows the FE discretization for fire exposure on one side of the concrete edge by employing a layer

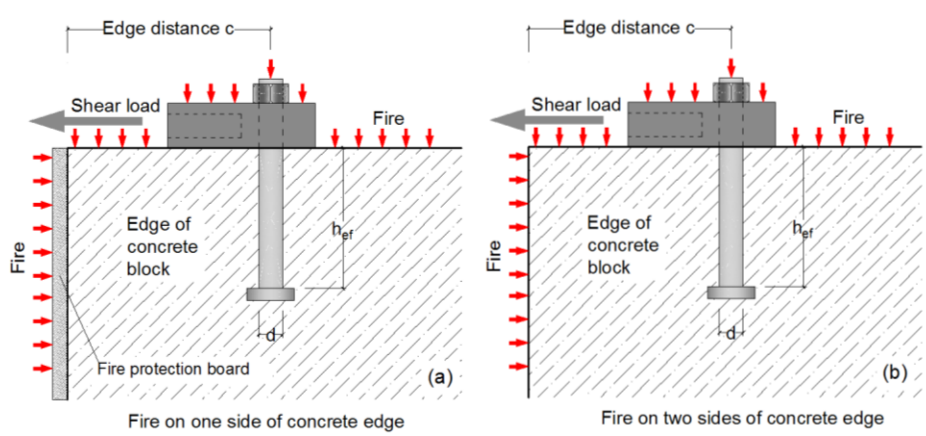

Figure 1. Sketch of single anchor loaded in shear and subjected to fire: (a) on one side of concrete edge and (b) on two sides of concrete edge.

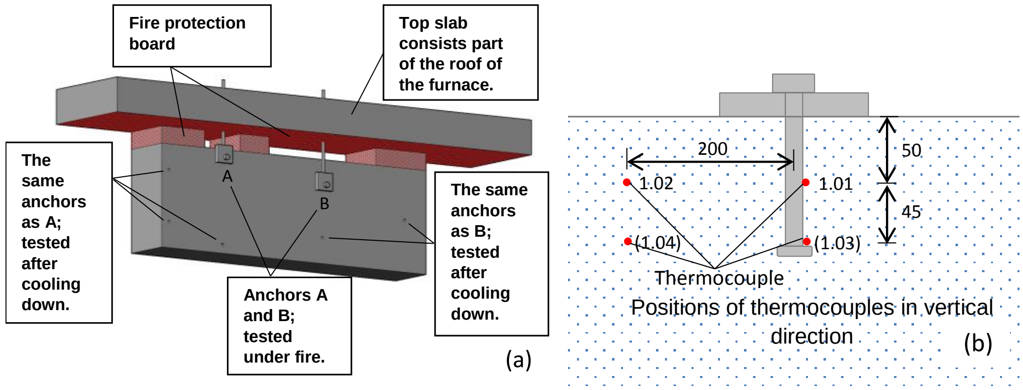

Figure 2. Concrete specimen used in the fire tests.

of elements to model the fire protection board. For the analysis of fire exposure on two sides of the concrete edge, this layer of elements was removed. Note that the top slab from Fig. 3a was not exposed to fire. Considering the confinement effect that comes from the top slab the FE discretization shown in Fig. 3b, with no confinement effect, was employed to verify the numerical results with experimental results at ambient temperature and after cooling down of the concrete slab to ambient temperature. It was also employed to calculate the shear resistance of anchor under fire in the framework of the parametric study. The distance of the supports on the front face were taken as 7 times of the edge distance.

VERIFICATION ANALYSIS

Verification of Temperature Profiles

Temperature history curves obtained from the experiments and the finite element analysis (FE discretization from Fig. 3a) for anchors c150h95d25 (edge distance c = 150 mm, embedment depth h_{ef} = 95 mm and diameter d = 25 mm) and c50h95d16 are shown in Fig. 4. It can be seen that the FE analysis reasonably well predicts temperature profile of concrete slab subjected to fire. The disagreement exists only in

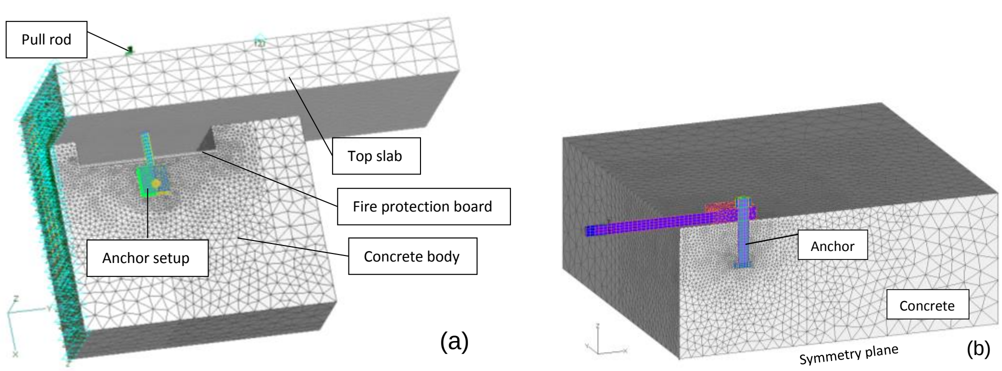

Figure 3. Finite element discretization of experimental test set-ups for (a) 90 min of fire and (b) cold state and ambient temperature.

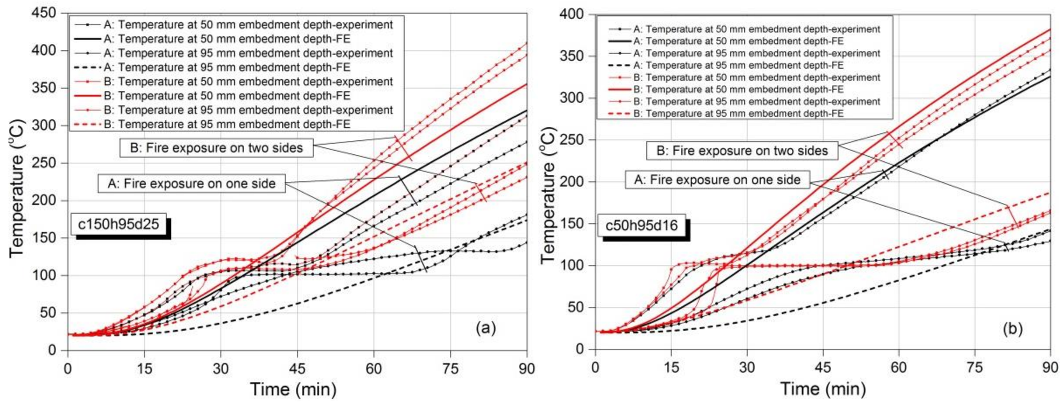

Figure 4. Comparison between experimentally and numerically obtained temperature profiles.

the temperature range in which there is evaporation of free water from the concrete, which cause change of its thermal properties. This effect is not a part of the thermal model for concrete. However, it is important that for higher temperatures the agreement between experimental measurements and analysis is good since for these temperatures the reduction of material mechanical properties is relevant.

Verification of Damage

Figure 5 shows the crack pattern of the anchor c50h95d16 at ambient temperature, both numerically and experimentally obtained. It is obvious they agree with each other very well. The failure pattern is typically of a semi-cone shape. In Fig. 6 is shown the comparison between the crack patterns for the anchor c150h95d25 loaded in shear in hot state after 90 min of fire exposure. As it is shown in Fig. 6a and b, not only are the cracks around the anchor due to shear loading agree with each other very well, but also the thermal cracks due to heating at the right down side of the specimen nicely correlate with each other. Both numerically and experimentally, the cracks are initiated at the back side of the anchor and propagate towards the free corners. In Fig. 6a on the back side of the anchor significant damage can be observed, which is also observed in the experimental tests (see Fig. 6c). The half-cone diameter B (see Fig. 6d) is approximately 5 times of the edge distance and its depth H at the front face is approximately 1.5 times of the edge distance. The angle of the concrete half-cone measured with respect to the free edge is around 30 degrees.

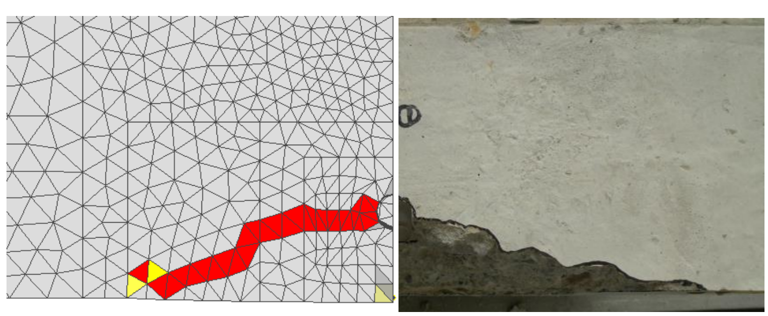

Figure 5. The crack pattern at peak load for the anchor c50h95d16 at ambient temperature.

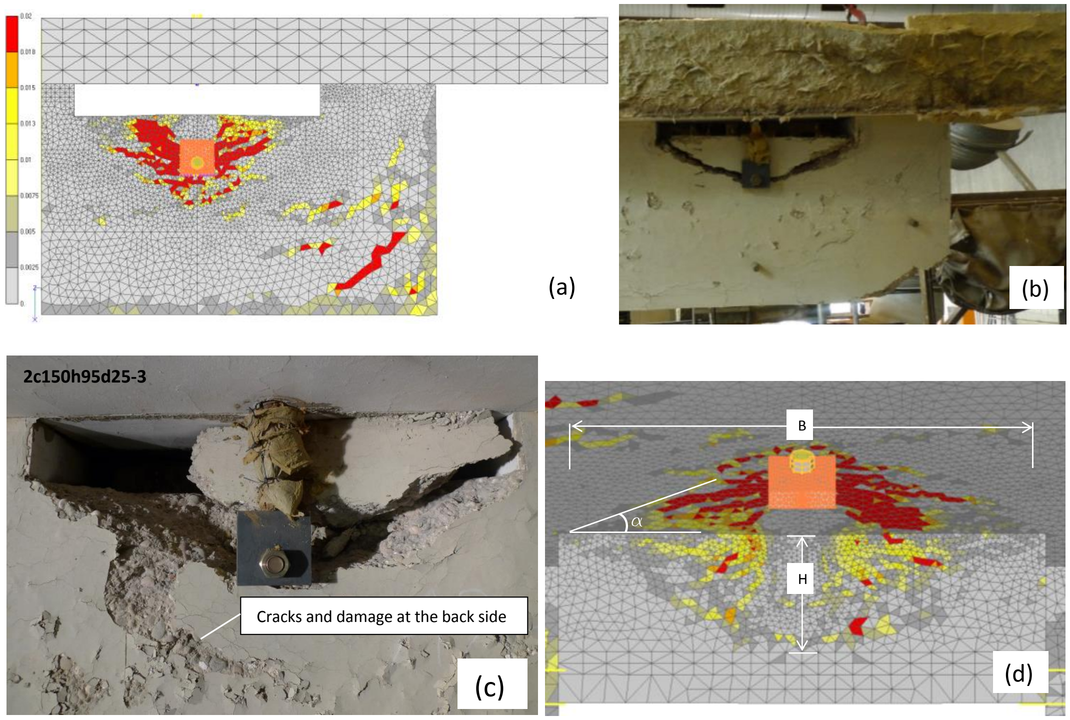

Figure 6. Comparison of the crack patterns for the anchor c150h95d25 exposed to fire on two sides of the concrete edge (one symmetry plane, red zone = crack width greater than 0.02 mm).

Verification of Resistance

Figure 7 shows the comparison of the load displacement curves for anchors loaded in shear at ambient temperature and after cooling down from 90 min of fire. At ambient temperature, as shown in Fig. 7a, the numerical prediction is stiffer than observed in the experimental tests. This can be attributed to the local damage of concrete, which is not accounted for in the macroscopic finite element analysis. In the case of cooling down (see Fig. 7b), the load displacement curves obtained numerically agree well with the experimentally obtained curves. The heating and cooling processes cause damage to the concrete and consequently reduction of stiffness and resistance. Nevertheless, as can be seen from Fig. 8, both at ambient temperature and after cooling down the numerically predicted resistance agrees reasonably well with the experimentally obtained peak loads.

In the numerical analysis for hot state the anchors were first loaded by allowable actions and subsequently exposed to elevated temperature. After fire exposure of 90 min the anchors were loaded further until failure. The failure loads obtained are compared with experimental results, as shown in Fig. 8a. Note that the values obtained for the anchors with diameter of 25 mm were normalized to the corresponding values for the anchor diameter of 16 mm. For relatively smaller edge distance, the numerically obtained values are slightly lower than experimental ones. However, for larger edge distances there is a relative good agreement between numerical and experimental results. They show that the numerical simulation is able to realistically replicate experimental tests. Note that the analysis indicated relatively large compressive stresses parallel to the free edge of concrete specimen. This is the reason

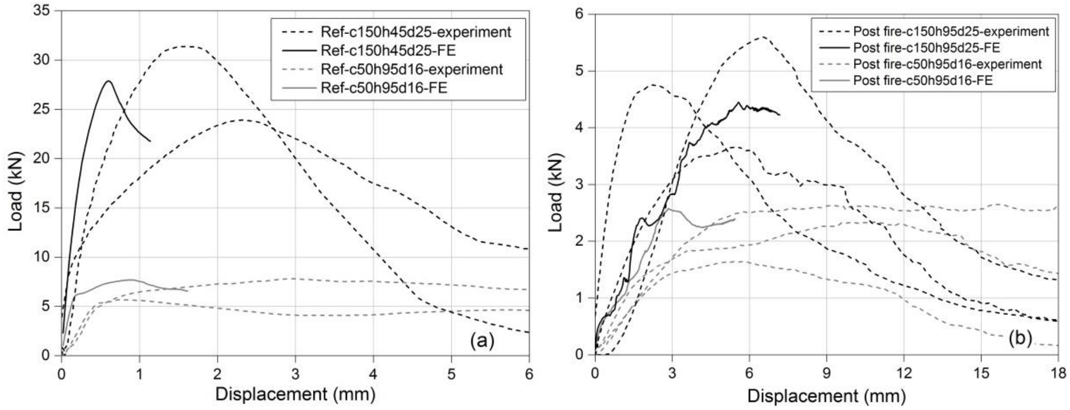

Figure 7. Load displacement curves for anchors loaded in shear: (a) ambient temperature and (b) after cooling down.

for relative low reduction of shear capacity observed in the experimental tests for hot state.

The above analysis without confinement effect was carried out also for the cold state. As in the experiment, the concrete specimen was after heating cooled down to the ambient temperature. Subsequently the anchors were loaded up the failure. The results are shown in Fig. 8a. It can be seen that there is very good agreement between experimental and numerical results. Furthermore, it is obvious that for the cold state the reduction of the resistance is much higher than that for the hot state. Finally, it can be seen that the prediction according to Eurocode 2 shows much better agreement with the peak loads obtained for the cold state.

Figure 8b shows the influence of embedment depth on shear capacity. It can be seen that its influence is small for reference tests at room temperature and post fire tests after cooling. In hot state, here considering only one side of fire exposure, it is shown the decrease of capacity of anchor with 45 mm embedment depth is more distinct than that of anchor with 95 mm embedment depth. This is reasonable since with smaller embedment depth after 90 min of fire temperature over the whole embedment depth is relatively high, which creates severe damage of concrete around the entire anchor.

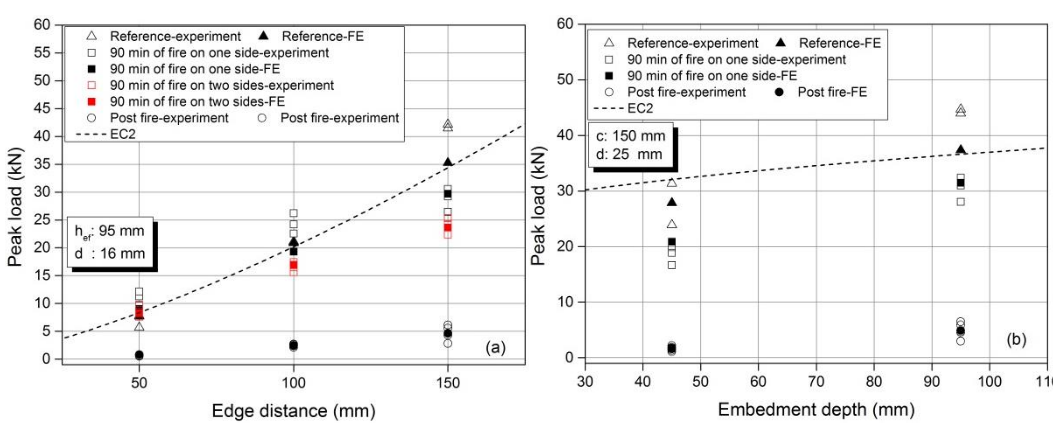

Figure 8. (a) Peak load as a function of edge distance and (b) embedment depth.

Nevertheless, the numerical results show very good agreement with the experimental results, i.e. the used numerical model is objective and can be employed in further parametric studies.

DISCUSSION

Based on the convincing verification analysis, the FE discretization shown in Fig. 3b was employed to calculate the shear capacity of anchors for 90 min of fire in order to eliminate the confinement effect. It can be seen (see Fig. 9) that these resistances are much lower than the experimentally and numerically obtained peak loads for hot state with confinement. This confirms that for the hot state the confinement effect in the experimental tests was rather strong. However, the resistance without confinement effect is higher than the prediction according to Eurocode 2. The numerically predicted resistances are approximately 40% of the references at ambient temperature, rather than 25% of the values according to the current Eurocode 2, Part 4, Annex D (EN 1992-4 2015) [6]. The prediction formula according to Eurocode 2 reads:

$$V^0_{u,c,fi(90)} = 0.25 \cdot 3 \cdot d^{\alpha}_{nom} \cdot l^{\beta}_{f} \cdot \sqrt{f_{cc,200}} \cdot c^{1.5} \tag{1}$$

where $\alpha = 0.1 \cdot \left(\frac{l_f}{c}\right)^{0.5}$, $\beta = 0.1 \cdot \left(\frac{d_{nom}}{c}\right)^{0.2}$ and l_f is the embedment depth.

For anchors with small embedment depths the above equation actually overestimates the residual capacity after cooling of concrete (see Fig. 9b). For both, one and two side of fire exposure, it can be seen that the difference for the hot state is not obvious and both values are much larger than the peak loads according to Eq. (1). However, for cold state the prediction according to Eq. (1) is un-conservative, especially for smaller embedment depths close to edge, and should be improved.

CONCLUSIONS

In the present paper the results of experimental and numerical investigations on

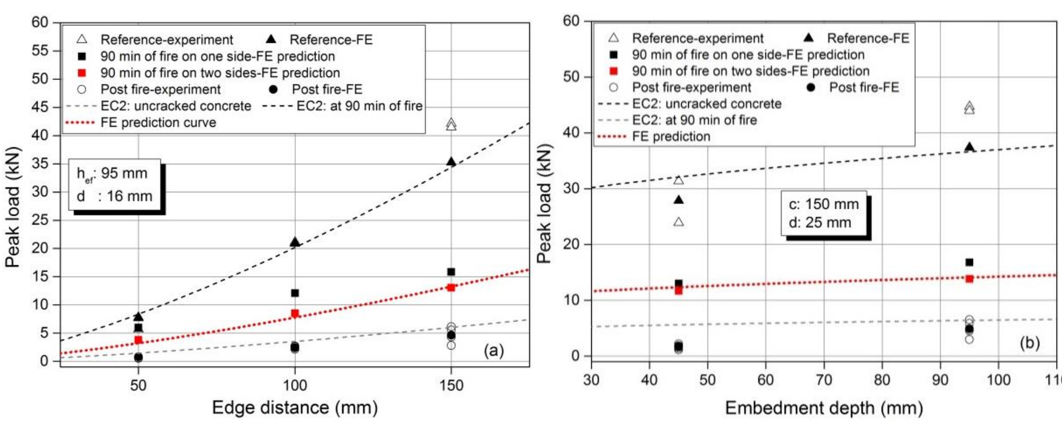

Figure 9. Shear resistance of anchors for ambient, hot and cold state without confinement effect as a function of: (a) edge distance and (b) embedment depth.

single headed stud anchors close to concrete edge loaded in shear under elevated temperature are presented and discussed. Reference test at ambient temperature, the tests at 90 min of fire (hot state) and tests after 90 min of heating and subsequent cooling are performed (cold state). The experimental tests were numerically simulated in order to verify the numerical model. Based on the presented results the following can be concluded. (1) The employed numerical model is able to realistically replicate experimental tests. This is observed for the temperature distribution, failure mode and resistance. (2) The failure load of reference test at room temperature agrees very well with the design code formula according to Eurocode 2, numerical and experimental results. (3) It was found that for the anchors with relative small edge distance, tested in hot state, the resistance is even larger than for the reference test at room temperature. As confirmed in the numerical study, the reason is due to the influence of the confinement compressive stresses that are due to thermal strains and the corresponding confinement effects from the test set-up. The same analysis without confinement effect exhibited stronger reduction of the peak load. (4) The analysis shows that the shear resistance of anchors in the hot state is higher than the resistance in the cold state. (5) The design prediction formula underestimates resistance for the hot state. However, for cold state it overestimates the resistance and this is especially true for the anchors with small embedment depth. (6) The results of the study indicate that for the shear concrete resistance cold state is relevant. Therefore, it would be possible that for the hot state failure of steel is relevant, however, for the cold state failure of concrete can be more critical.

ACKNOWLEDGEMENTS

The authors would like to thank the German Research Foundation (DFG) and the China Scholarship Council for providing funding for this project.

REFERENCES

1. Grosser, P. R. 2012. "Load-Bearing Behavior and Design of Anchorages Subjected to Shear and Torsion Loading in Uncracked Concrete, " PhD Dissertation, Institute for Conctruction Materals, University of Stuttgart.
2. Hofmann, J., W. Fuchs, and R. Eligehausen. 2004. "Behavior of Anchorages Arranged Close to the Edge and Loaded Towards the Edge," Beton und Stahlbetonbau, 99(10):806-812.
3. Ožbolt, J., G. Periškic, and H. W. Reinhardt. 2008. "Numerical Analysis of Spalling of Concrete Cover at High Temperature," Comput. Concr., 5(4):279-293.
4. Ožbolt, J., I. Kožar, R. Eligehausen, and G. Periškić. 2005. "Transient 3D Thermo-mechanical for Concrete ". Beton und Stahlbetonbau, 100(1):39-51.
5. Ožbolt, J., Y. Li, and I. Kožar. 2001. "Microplane Model for Concrete with Relaxed Kinematic Constraint ". Int. J. Solids Struct., 38(16):2683-2711.
6. European Standard (FprEN 1992-4: 2015) Eurocode 2 Design of Concrete Structures - Part 4 Design of Fastenings for Use in Concrete.

Rational Design Approach for Predicting Fire Resistance of Hollowcore Slabs

ANUJ M. SHAKYA and VENKATESH K. R. KODUR

ABSTRACT

A rational approach is proposed for evaluating fire resistance of PC hollowcore slabs. The proposed approach comprises of two main steps; namely, evaluating cross-sectional temperatures in the slab, and then evaluating degrading moment and shear capacity at any given duration of the fire exposure. Fire resistance is evaluated by comparing the sectional moment and shear capacity at any given fire exposure time against applied moment and shear force. A simplified approach is also proposed for predicting sectional temperatures in hollowcore slabs under fire exposure by utilizing data obtained from numerical studies performed on wide range of hollowcore slabs.

INTRODUCTION

In recent years, prestressed concrete (PC) hollowcore slabs are being increasingly used in building applications due to numerous advantages, such as cost-effectiveness, architectural aesthetics, speedy construction, space utilization, and low maintenance costs, they offer over other floor systems. Structural fire safety is one of the primary considerations in building applications and hence, building codes generally specify fire resistance ratings for these hollowcore slabs. The prevalent method of evaluating fire resistance of hollowcore slabs is through prescriptive methods, as specified in ACI 216.1 [1], PCI [2] and Eurocode 2 [3]. The prescriptive methods are derived based on standard fire tests, and prescribe tabulated fire resistance ratings linked to concrete cover thickness and effective slab depth of hollowcore slabs. These prescriptive methods do not account for critical influencing factors such as, realistic fire scenarios and failure limit states, especially shear failure criterion, and thus might not yield realistic fire resistance of PC hollowcore slabs. To overcome some of these drawbacks, a rational approach is proposed in this paper for evaluating the fire resistance of PC hollowcore slabs.

Anuj M. Shakya, Michigan State University, Department of Civil and Environmental Engineering, USA. Email: shakyaan@msu.edu
Venkatesh K. R. Kodur, Michigan State University, Department of Civil and Environmental Engineering, USA. Email: kodur@egr.msu.edu

As structural behavior of PC hollowcore slabs is mainly governed by flexural and shear response, fire resistance of PC hollowcore slab is to be evaluated by checking failure under both flexural and shear limit states. The proposed approach comprises of two main steps, wherein in the first step, cross-sectional temperature is to be evaluated and in the second step, moment and shear capacities are to be evaluated by accounting for the degradation in material properties. Since, the moment capacity at a critical section of hollowcore slab is mostly dependent on the strand and the shear capacity is mostly dependent on the web concrete, temperatures at strand and web locations need to be evaluated during fire exposure. Knowing the temperatures in prestressing strand and web concrete, flexural and shear capacities at any given fire exposure time is evaluated by accounting for temperature dependent material properties. Fire resistance can then be evaluated by comparing the moment and shear capacities at any given time with the applied bending moment and shear force.

APPROACH FOR PREDICTING SECTIONAL TEMPERATURES

The first step in evaluating fire resistance is evaluating sectional temperatures in PC hollowcore slabs. Thus, a simplified approach for predicting sectional temperature in PC hollowcore slabs exposed to fire is proposed.

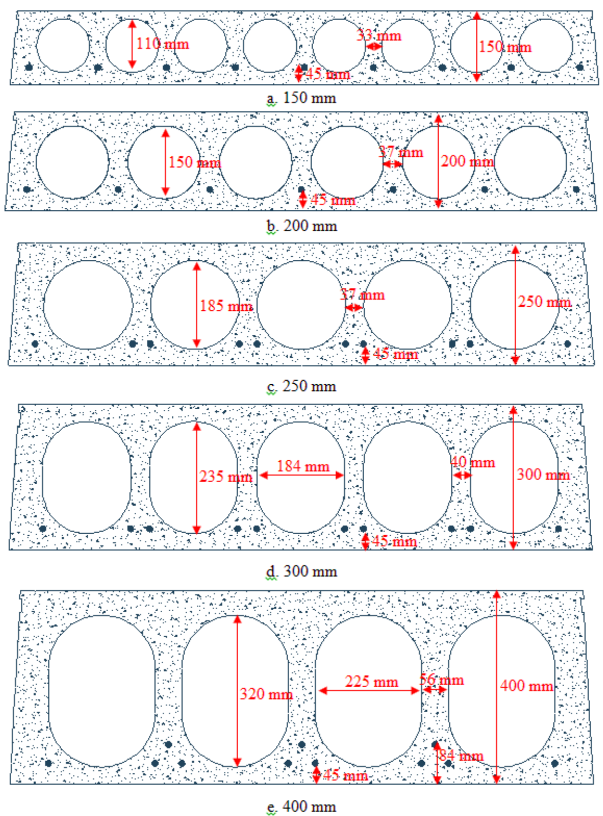

Figure 1. Cross-sectional configurations of standard PC hollowcore slabs specified by PCI.

General procedure

There are very few simplified approaches in the literature for predicting sectional temperatures in fire exposed concrete members. Kodur et al. [4] recently proposed a simplified approach for evaluating sectional temperatures in concrete members. However, this approach is not directly applicable to hollowcore slabs due to presence of void cores. Thus, the approach developed by Kodur et al. [4] is extended for evaluating sectional temperatures in hollowcore slabs.

To account for hollow cores in slabs, regression analysis is carried out on temperature data generated on numerous slabs for obtaining necessary coefficients in the simplified approach proposed by Kodur et al. [4]. The regression analysis is carried out based on temperature data generated from numerical analysis on wide range of PC hollowcore slabs of various thicknesses and configurations, as shown in Figure 1. The sectional temperature is dependent on the slab depth and core size, and thus, the coefficients need to be individually calibrated for temperatures at different concrete layers. Thus, two sets of coefficients are calculated for predicting temperatures in hollowcore slabs at two critical locations; strand and mid depth, required for evaluating moment and shear capacity.

Further, there is large variability in cross-sectional core configurations in hollowcore slabs from one manufacturer to another and one country to another. Thus, it is extremely difficult to develop a unified regression-based simplified approach for predicting sectional temperatures for all possible cross-sectional configurations. Thus, proposed simplified approach for evaluating sectional temperatures is established based on core configurations commonly used in the United States, with depths ranging from 150 mm to 400 mm, as illustrated in Figure 1.

Nonlinear regression analysis

For deriving temperature coefficients, a large amount of temperature data is generated through numerical analysis on wide range of PC hollowcore slabs. The numerical analysis is performed utilizing a previously developed finite element model in ANSYS [5]. A nonlinear regression analysis on the temperature data, with corresponding fire-exposed time and cross-sectional locations, was carried out using “solver” function in Microsoft Excel [6]. The “solver” function is able to calculate the optimum coefficients to match the original data with a given format of formula and applied “constraint” criteria. The coefficients are calibrated by minimizing the sum of square of error between the predictions and original data, which is highly dependent on the format of formula and constraint criteria. Thus, a general format of the equations and constraint criteria was adopted from the equation proposed by Kodur et al. [4] for solid concrete slabs, before undertaking regression analysis. Since the heat transfer through hollowcore slabs is one directional, the temperature equations are proposed for 1-dimentional heat transfer only. The general format for the 1-dimensional heat transfer equation can be expressed as:

$$T_z = c_1 \cdot \eta_Z \cdot (a \cdot t^n) \quad (1)$$
$$\eta_z = a_1 \cdot \ln\left(\frac{t}{z^{1.5}}\right) + a_2 \cdot \sqrt{z} + a_3 \quad (2)$$

where, T_z is the temperature resulting from 1-D heat transfer in °C, η_Z is the heat transfer factor induced through one fire-exposed surface, c_1 is the coefficients to account for concrete type, t is the fire exposure time in hours, z is the distance from the point in concrete section to fire exposure surface in meters, and a_1, a_2 and a_3 are the coefficients to be traced in the regression analysis. $(a.t^n)$ is the temperature under standard fire exposure [4]. For ASTM E119 fire, a = 910 and n = 0.148 and the default values of c_1 for high strength carbonate aggregate concrete is 1.01 [4].

The regression parameters (a_1, a_2 and a_3) are chosen to fit the data points in the critical range with the smallest discrepancy, and that have reasonable match in other regions using "constraint" criteria. The compressive strength of concrete and yield strength of prestressing steel are typically not influenced up to 200°C, and that these strengths become negligible after reaching 800°C [1], [3]. Therefore, the regression result has to be highly reliable and slightly conservative in temperature-sensitive zone of 200-800°C. Further, the regression results in 20-200°C could be set as a secondary target since the variation in this temperature range does not significantly influence the strength of concrete and steel reinforcement.

Equations for sectional temperatures

With the above developed equations and constraints, a regression analysis was conducted for 1-D equation for temperatures at strand and mid-depth level. The final formulae used for calculating temperature at a given point in a hollowcore slab are obtained as follows.

$$T_z = c_1 \cdot \eta_Z \cdot (a \cdot t^n) \quad (3)$$
$$\eta_z = a_1 \cdot \ln\left(\frac{t}{z^{1.5}}\right) - a_2 \cdot \sqrt{z} - a_3 \quad (4)$$

where regression coefficient a_1, a_2 and a_3 are evaluated to be 0.222, 0.425 and 0.634 for strand temperature and 0.233, 0.579 and 0.356 for mid-depth temperature respectively.

APPROACH FOR PREDICTING SECTIONAL CAPACITY UNDER FIRE CONDITIONS

Knowing sectional temperatures in PC hollowcore slabs, flexural and shear capacity at critical sections can be evaluated at any given fire exposure time.

General procedure

Once sectional temperatures at various steps into fire exposure is known, temperature dependent strength properties of strand and concrete can be evaluated at any given time into fire exposure. These temperature dependent strength properties of prestressing strand and concrete can be evaluated using strength degradation relations specified in Eurocode 2 [3]. Then, capacity equations specified in Eurocode 2 [3] for ambient conditions can be modified to evaluate reduced flexural and shear capacities of slabs under fire exposure by accounting for temperature dependent strength properties.

Flexural and shear capacity under fire conditions

The ambient temperature flexural and shear capacity equations specified in Eurocode 2 [3] are utilized to evaluate degrading flexural and shear capacity at given fire exposure time. The modified equations for evaluating flexural capacity under fire conditions are.

$$M_{nT} = A_{ps} f_{psT}\left(d - \frac{a_T}{2}\right) \tag{5}$$

in which, $f_{psT} = f_{puT}\left[1 - \frac{\gamma_p}{\beta_1}\left(\frac{\rho_p f_{puT}}{f'_{cT}}\right)\right]$, $a_T = \frac{A_{ps} f_{psT}}{0.85 f'_{cT} b}$, $\beta_1 = 0.85 - \left(\frac{f'_{cT}(\text{in psi}) - 4000}{1000}\right) \times 0.05$ and $\rho_p = \frac{A_{ps}}{b d_p}$

where, M_{nT} = flexural capacity under fire conditions, kN-m, A_{ps} = area of prestressed reinforcement in m^2, f_{psT} = stress in prestressed reinforcement under fire conditions in Pa (or N/m^2), f_{puT} = tensile strength of prestressing steel under fire conditions in Pa (or N/m^2), f'_{cT} = compressive strength of concrete under fire conditions in Pa (or N/m^2), γ_p = factor for type of prestressing strand (0.28 for low relaxation strand), β_1 = factor relating depth of equivalent rectangular compressive stress block to neutral axis depth, ρ_p = ratio of prestressed reinforcement, d = distance from extreme compression fiber to centroid of prestressed reinforcement in m, a_T = depth of equivalent compression stress block under fire conditions in m.

Similarly, the modified equations for evaluating degrading shear capacity of hollowcore slabs under fire conditions can be expressed as:

$$V_{Rd,c,fi} = \left[C_{Rd,c} k \left(100 \rho_{l,fi} f_{c,fi,m}\right)^{\frac{1}{3}} + k_1 \sigma_{cp,fi}\right] b_w d \tag{6}$$

in which, $k = 1 + \sqrt{(200/d)} \leq 2.0$, $\rho_{1,fi} = \frac{A_{sl}}{b_w d} \leq 0.02$, $k_1 = 0.15$, and $\sigma_{cp,fi} = N_{Ed}/A_c$

where, $V_{Rd,c,fi}$ = shear capacity in regions un-cracked in flexure under fire conditions in N, $C_{Rd,c} = 0.18/\gamma_c$ (γ_c is partial safety factor for concrete), $f_{c,fi,m}$ = average compressive strength of concrete under fire conditions in MPa, d = effective depth at ambient temperature measured in mm, $\rho_{1,fi}$ = force-equivalent ratio of longitudinal reinforcement, A_{sl} = area of the tensile reinforcement (prestressing strands in mm^2), b_w = smallest width of the cross-section in the tensile area measured in mm, N_{Ed} = axial force in the cross-section due to loading or prestressing in N, and A_c = area of concrete cross-sectional measured in mm^2.

VALIDATION OF PROPOSED APPROACH

The proposed approach is validated by comparing predicted sectional temperatures and fire resistance with that obtained from fire tests and finite element approach. Further, predicted moment and shear response is also compared with that obtained from finite element approach.

TABLE 1. SUMMARY OF SLAB DETAILS AND TEST PARAMETERS.

Test slab	Agg. type	Dimensions length (m) ×width (m) ×depth (mm)	Cross sectional configurations	Test day comp. strength (f'_c), MPa	Applied loading (% of capacity)	Support conditions	Fire expo-sure
Slab 6 [7]	Carbo-nate	3.65×1.2 ×200	6-150 mm cores 7-12.5 mm strands	75	60	SS	ASTM -E119
Slab G6 [8]	Carbo-nate	3.9×1.2 ×265	5-167 mm × 200 mm cores 7-9.5 mm strands	56	70	SS	ISO 834

Note: SS = simply supported

Verification of temperature equation

The validation of the proposed equations (Eqns. 3 and 4) is established by comparing predicted temperatures with that measured in fire tests and that obtained from finite element approach [9]. For this purpose fire tests conducted on two hollowcore slabs namely; Slab 6 tested by Shakya and Kodur [7] and Slab G6 tested by Janzse et al. [8] are selected. In tests, Slab 6 was exposed to ASTM-E119 standard fire [10], whereas Slab G6 was exposed to ISO834 standard fire [11]. Details of slab configuration and fire exposure conditions are tabulated in TABLE 1.

The predicted temperatures at strand and at mid-depth concrete for Slab 6 and Slab G6 are compared with that measured in the tests and that obtained from finite element approach in Figure 2. It can be seen that the predicted temperatures are mostly in good agreement with the measured data in the tests. However, in Figure 2(b) for Slab G6, it can be seen that there is higher discrepancy at the mid depth temperatures, as compared to that in Slab 6, as shown in Figure 2(a). This is mainly due to the fact that the equations are calibrated for slab core configurations and depths typically used in the United States. The Slab G6 has a depth of 265 mm and has slightly lower core area to gross area (ratio) than those found in the US. Because of higher cross-sectional concrete area, the temperatures in the inner layers increase at a slightly slower rate than that predicted by the proposed temperature equations. However, the effect of core configuration is less significant on the strand temperature, as strand lies closer to the fire exposed surface.

Further, the verification of the proposed equations is also illustrated by comparing strand temperature obtained from the proposed approach with these obtained from finite element approach at 1 hr, 2 hr and 3 hr into fire exposure in TABLE 2.

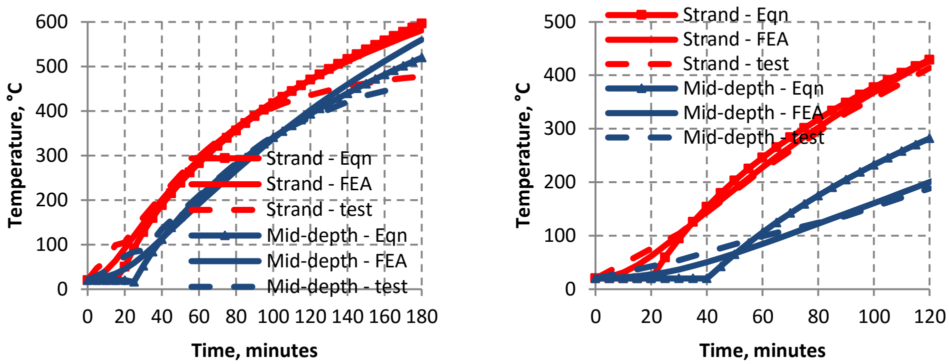

a. Slab 6 b. Slab G6

Figure 2. Comparison of predicted temperature in Slab 6 with that obtained from test conducted by Shakya and Kodur.

Validation of predicted fire resistance

The validity of the proposed capacity equations (Eqns. 5 and 6) is established by comparing predicted response of tested slabs (Slab 6 and Slab G6) with results from fire tests. Since the variation of moment and shear capacities with fire exposure time cannot be directly measured in fire tests, degradations of moment and shear capacity evaluated utilizing proposed equations are compared with that obtained from the finite element approach in Figure 3. Further, the predicted fire resistance (failure times) obtained from the proposed approach are compared with that measured during tests in TABLE 3. The comparison shows that the proposed approach provides reasonable predictions of fire resistance of PC hollowcore slabs. It is to be noted that the proposed approach best works for slabs having cross sectional configuration similar to that commonly used in the US. In the case of Slab 6, proposed equation predicts fire resistance of 130 minutes which is slightly conservative than that measured in the test. Results from the proposed approach also show that Slab 6 fails through flexural limit state, as observed in the test.

TABLE 2. COMPARISON OF TEMPERATURE IN PRESTRESSING STRAND AT 1, 2 AND 3 HOURS OF FIRE EXPOSURE.

Test slab	Strand temperature, °C					
	FEA			Proposed approach		
	1 hr	2 hr	3 hr	1 hr	2 hr	3 hr
Slab 6 [7]	290	469	580	284	469	596
Slab G6 [8]	227	427	n.a.	245	429	n.a.

Note: ‘n.a.’ = not available

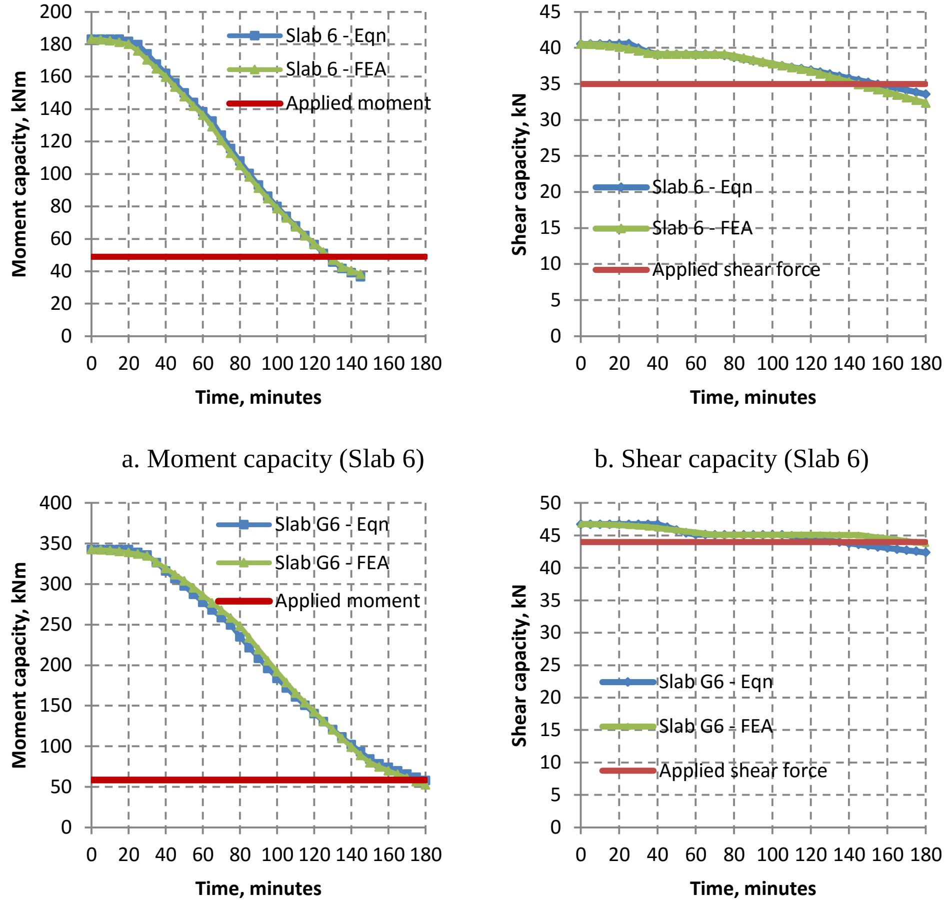

a. Moment capacity (Slab 6) b. Shear capacity (Slab 6)

c. Moment capacity (Slab G6) d. Shear capacity (Slab G6)

Figure 3. Comparison of moment and shear capacity degradation using proposed equations and FEA in tested Slab 6.

Similarly, in the case of Slab G6, failure did not occur at 120 minutes of fire exposure during the test, when fire exposure on slab was terminated. The proposed approach predicts a fire resistance of 135 minutes for Slab G6, showing that the slab does not fail until 120 minutes. The proposed approach also predicts that failure in Slab G6 occurs through shear limit state and this concurs with test observations, wherein Slab G6 failed through shear cracking when loading was increased at 120 minutes.

TABLE 3. COMPARISON OF PREDICTED AND TEST FIRE RESISTANCE.

Test slab	Dimensions length (m) ×width (m) ×depth (mm)	Fire resistance, minutes			
		Test		Proposed approach	
		Flexure	Shear	Flexure	Shear
Slab 6 [7]	3.65×1.2×200	140	n.f.	130	150
Slab G6 [8]	3.9×1.2×265	>120	>120	180	135

Note: ‘n.f.’ = not failed

The proposed approach provides a rational approach to predict fire resistance of PC hollowcore slabs. However, the proposed approach is only validated over certain range of design parameters, and this approach can be applied only for simply supported PC hollowcore slabs exposed to standard fires. Also, the proposed approach predicts fire resistance more accurately in slabs having core configurations similar to those specified in PCI manual [2] (prevalent in the US). Moreover, the proposed temperature equations for predicting temperatures in strand and mid-depth concrete does not account for uncertainty factors such as fire-induced spalling and cracking of concrete.

SUMMARY

This paper presents a rational approach for assessing fire resistance of PC hollowcore slabs exposed to standard fire. The approach is developed by applying similar design analogy as that at room temperature, but by accounting for the temperature induced strength degradation in strands and concrete. Simplified equations are also proposed for predicting sectional temperatures in hollowcore slabs at any fire exposure duration. The validity of the proposed approach is established by comparing predicted cross sectional temperatures, moment and shear capacity and failure times with those obtained from fire tests and finite element analysis. Overall, the proposed approach provides a simple and rational tool for evaluating fire resistance of fire exposed PC hollowcore slabs.

REFERENCES

[1] ACI 216.1-14, *Code requirements for determining fire resistance of concrete and masonry construction assemblies*. Farmington, MI: American Concrete Institute, 2014.

[2] PCI, *PCI Design Handbook*, 7th ed. Chicago, IL: Precast Prestressed Concrete Institute, 2010.

[3] Eurocode 2, “Design of concrete structures, Part 1-2: General rules-structural fire design. ENV 1992-1-2,” CEN: European Committee for Standardization, UK, 2004.

[4] V. K. R. Kodur, B. Yu, and M. M. S. Dwaikat, “A simplified approach for predicting temperature in reinforced concrete members exposed to standard fire,” *Fire Saf. J.*, vol. 56, pp. 39–51, Feb. 2013.

[5] V. K. R. Kodur and A. M. Shakya, “Modeling the response of precast prestressed concrete hollowcore slabs exposed to fire,” *Prestress. Concr. Inst. J.*, vol. 59, no. 3, Jul. 2014.

[6] Microsoft Excel, *Microsoft Excel*. Microsoft Corporation.

[7] A. M. Shakya and V. K. R. Kodur, “Response of precast prestressed concrete hollowcore slabs under fire conditions,” *Eng. Struct.*, vol. 87, pp. 126–138, Mar. 2015.

[8] W. Jansze, A. V. Acker, B. D. Bella, R. Klein-Holte, G. Lindstrom, A. Nitsch, J. P. Py, F. Robert, and M. Scalliet, “Fire resistance of hollowcore floors regarding shear and anchorage capacity,” in *Structures in Fire Sif ’12*, Zurich, Switzerland, 2012.

[9] M. B. Dwaikat and V. K. R. Kodur, “Hydrothermal model for predicting fire-induced spalling in concrete structural systems,” *Fire Saf. J.*, vol. 44, no. 3, pp. 425–434, Apr. 2009.

[10] ASTM, “Standard test methods for fire tests of building construction and materials. Test Method E119,” American Society for Testing and Materials, West Conshohocken, PA, 2011.

[11] International Standard (E), “Fire resistance tests: Elements of building construction. Part 1: General Requirements. ISO834-1-1999,” International Organization for Standardization, Geneva, Switzerland, 1999.

Shear and Torsion in R/C Structural Members in Fire

PATRICK BAMONTE, PIETRO GAMBAROVA,
NATAŠA KALABA and SERGIO TATTONI

ABSTRACT

Seldom structural designers are required to design from scratch or to check existing R/C structures or members in fire, under pure shear or torsion, because the structural response is in most cases controlled by either bending (with/without an axial force) or by shear with some bending. Furthermore, there is hardly a single test under prevailing shear or torsion in fire. How to design or to check a shear- or torsion-sensitive R/C member in fire is, therefore, an open issue, which needs a reasonable answer based on the available design models and on the knowledge of the shear-resistant mechanisms active in reinforced concrete. In this rather general paper, the design models well-known in the calculations at the ultimate limit state in ordinary environmental conditions are recalled and their use in fire is discussed, with reference to both *solid* and *thin-walled open* sections. Both the *effective-section* method and the *zone* method are treated, as well as the fire-sensitivity of the various shear-transfer mechanisms, active in both shear and torsion, related to concrete-struts bending, aggregate interlock and dowel action along the cracks, not to mention the stirrups. On the whole, what stands out clearly in fire is the increasing role played by the stirrups in shear and that played by the rather cold concrete core in torsion.

INTRODUCTION

Shear and torsion as such very rarely occur in R/C structures, as in most cases other – and larger – internal forces (like bending moments and axial forces) come into play on extended parts of the span [1-4]. Shear, however, tends to be the controlling force in certain localized zones (D-zones [5-8]), while torsion tends to be a critical issue more for the whole construction, than for each single member.

In the case of torsion, neglecting its effect in ordinary design is justified by at least two further reasons: (a) traditional R/C structures consist of parallel 2D

Patrick Bamonte, Pietro G. Gambarova and Nataša Kalaba, Department of Civil and Environmental Engineering
Sergio Tattoni, Department of Architecture, Built Environment and Construction Engineering
Politecnico di Milano, Piazza Leonardo da Vinci 32, Milan 20133, Italy

frames connected by one-way slabs – or systems of joists and slabs – which transmit shear and bending to the beams of the frames, but little or negligible torsion, and (b) the static redundancy typical of most R/C structures generally provides alternative resisting paths inducing extra shear and extra bending, which do not require torsion to ensure equilibrium (*secondary* or *compatibility* torsion, as opposed to *primary* torsion whenever torsional resistance is instrumental in guaranteeing equilibrium).

Another more general and somewhat tricky reason is that basically the resistance is a sectional issue in bending, as one or more cracked sections provide resistance in accordance with a statically-determined mechanism (a couple of forces). On the contrary, in both shear and torsion the resistance is provided by several mechanisms, which develop over portions of the structural members and are – on the whole – statically redundant. Such reasons are valid also in fire conditions, as all the resisting mechanisms active at room temperature continue to be active in fire.

Within this context, the design models provided by the codes for shear and torsion in R/C are first recalled in this paper, and then are adjusted to fire conditions.

In shear, the validity of the *reduced*- or *effective-section method* is discussed for solid sections (where the thermal field is far from uniform), while the *zone method* is shown to be instrumental in analyzing thin-walled members (where the thermal field tends to be rather uniform throughout the thickness).

In torsion, the *hollow-prism* or *tube* analogy still provides a reasonable and viable model, though it neglects the contribution of the *core*, which may play a sizable role at high temperature, being in most cases below the reference temperature (500°C) for the entire fire duration. (At room temperature, the share of the twisting moment taken by the core in the elastic domain may range from 8-10% to 15-20%, depending on section size and reinforcement).

For both shear and torsion, the contribution of the various shear-transfer mechanisms and some examples are presented and discussed.

SHEAR AND TORSION IN FIRE-EXPOSED CONCRETE MEMBERS

The behavior of R/C members exposed to high temperature or fire is similar to the behavior in ordinary environmental conditions, as concrete remains a rather brittle material even at high temperature. (The tensile strength is more affected by high temperature than the compressive strength, but less than the elastic modulus). Concrete, therefore, fails in tension, and cracks are controlled by principal stresses.

As for the reinforcement, its elastic-plastic-hardening behavior tends to become elastic-plastic and even mostly plastic at very high temperatures (above 500°C).

Cracks tend to be initially at 45° to the axis if shear or torsion prevail over the other internal forces. In the case of shear, however, the cracks tend to become vertical close to the intrados in tension and increasingly horizontal the closer they are to the neutral axis (i.e. close to the top fibers in compression).

In shear, the cracks at roughly 45° typical of transversely-reinforced R/C beams suggest the formation of a 2D truss system (Mörsch-Ritter truss system, Fig1a left), while the rather flat cracks typical of transversely-unreinforced R/C beams suggest an arch-and-tie behavior (Fig. 1a right).

In torsion, only transversely-reinforced members make sense; the cracks tend to develop according to spirals inclined by 45° (or less, should a compressive force be applied), with the formation of a 3D truss system (Fig. 1b).

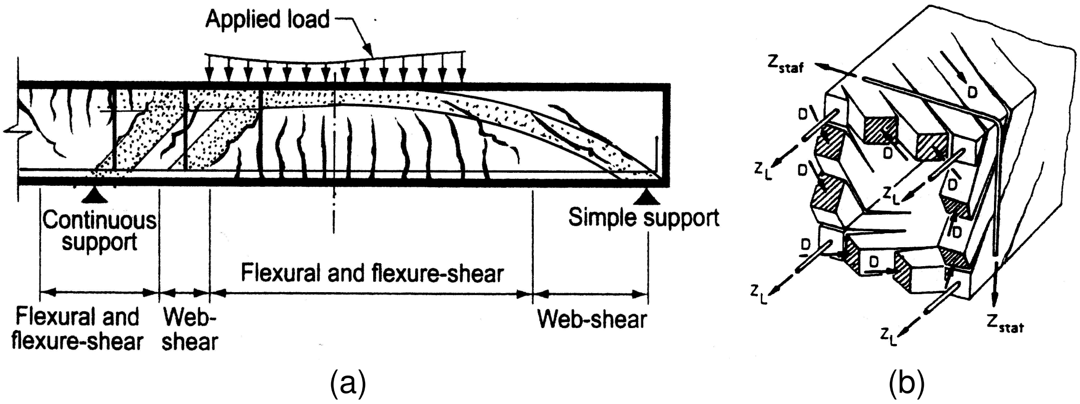

Figure 1. R/C beam (a) in shear, with the formation of a truss system (left) or of an arch-and-tie system (right) in transversely-reinforced/unreinforced sections, respectively (adapted from ACI 318M-08, Chapter 11); and (b) in torsion with the formation of a 3D truss system (Fuchssteiner, see Leonhardt in "Spannbeton für die Praxis", Ernst Verlag, Berlin, 1973).

DESIGN MODELS IN SHEAR AND TORSION

The same models introduced for shear and torsion in ordinary environmental conditions may be used in fire, provided that the mechanical properties of the materials and/or the geometry of the section be updated.

The models used in ordinary environmental conditions, however, have not been validated in fire conditions (*«shear – and torsion – failures due to fire are very uncommon….the calculation methods …. are not fully verified», Annex D, EN 1992-1-2:2004*). In shear, the simple approach based on a *reduced section* or *effective section* can be used; its assumptions are:

- no damage at all in both concrete and reinforcement enveloped by a *reference isotherm* (generally the 500°C isotherm in ordinary concrete);
- full damage (*no strength*) in the concrete outside the reference isotherm;
- in each reinforcing bar outside the reference isotherm, the strength should be that corresponding to the actual temperature provided by thermal analysis.

This approach was initially used for the bending under the standard fire, but was later shown to be reliable – and conservative - under eccentric axial forces.

A conceptually similar, but more refined approach is based on the subdivision in *zones* which leads to the evaluation of an *effective thickness* by subdividing the section into a number of zones, each at uniform temperature, as dictated by thermal analysis; in each zone, steel and concrete properties depend on the mean temperature of the zone itself.

In the checks for fire resistance in shear, both approaches can be used, provided that the temperature of the stirrups be evaluated in the most stressed point (*reference point P*, Fig. 2a), according to the thermal field. The key aspect of the problem is how to identify the reference point, since both the temperature and the stress in the stirrups are not uniform. As a matter of fact, the temperature tends to decrease towards the top of the section so that the mean temperature of the stirrups is lower than that of the surrounding concrete. In EN 1992-1-2 it is suggested to use the point located at the limit a-a (Fig. 2a) between the effective tension area and the rest of the section [5,9].

As for the longitudinal bars, their mechanical properties should be updated in accordance with the local temperature yielded by thermal analysis.

In torsion, the analogy with the *hollow prism* – or *tube* – can still be used in fire; the entire reinforcement (stirrups – or ties – and longitudinal bars) and the inclined concrete struts are involved in resisting the applied torque (Fig. 2b). The point P (Fig. 2b) may be chosen in the mid sections of the sides (chord a-a).

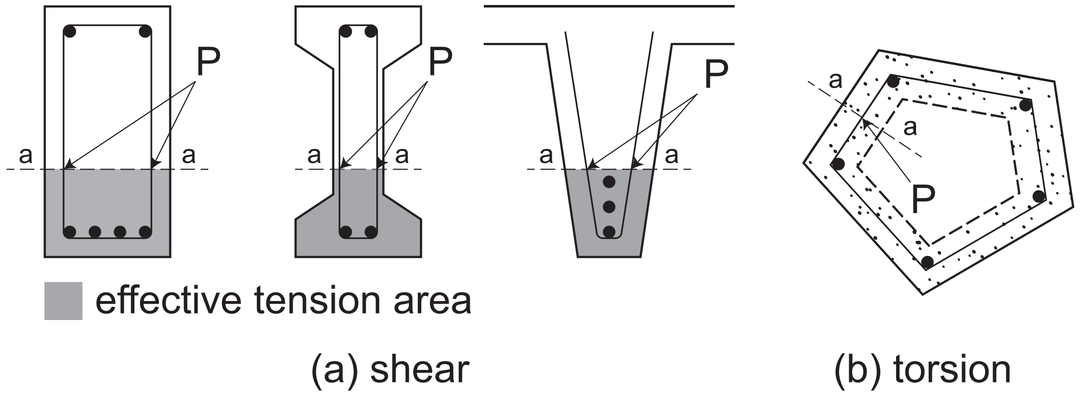

Figure 2. Identification of the reference temperature.

For the evaluation of the bearing capacity in shear and in torsion, the equations provided in EC2 (2005) are presented below ($\gamma_c = \gamma_s = 1$; reference isotherm 500° when requested; not all the limits of validity of the equations are reported):

Shear in transversely-unreinforced R/C beams:

$$V_{Rc,fire} = [C_{R,c}\ k\ (100\ \rho_l{*}\ f_{ck}^{20})^{1/3}]\ b_{w,fire}\ d \quad \text{with } k = 1 + (200/d)^{1/2} \le 2 \qquad (1)$$

where $C_{R,c} = 0.18$; $b_{w,fire}$ = reduced width of the effective section; $\rho_l{*} = \rho_l\ (f_{ctk}^{T}/f_{ctk}^{20})$

Shear in transversely-reinforced R/C beams ($\theta = 45°$).

$$V_{R,fire} = V_{Rs,fire} = (A_{sw}/s)\ z\ f_{ywk}^{T} \le V_{Rc,fire} = ½\ \alpha_{cw}\ b_{w,fire}\ z\ \nu\ f_{ck}^{20} \qquad (2a,b)$$

where $\nu = 0.6\ (1 - f_{ck}^{20}/250)$; $\alpha_{cw} = 1$ (no axial force in compression); A_{sw} = section of each stirrup x no. of the legs (only external legs); s = stirrup spacing; z = internal lever arm (= 0.9 d); note that all the external legs are assumed to be at the same temperature.

Torsion in transversely-reinforced R/C beams ($\theta = 45°$)

$$T_{R,fire} = \mathrm{Min}\ (T_{Rl,fire}\ ,\ T_{Rw,fire}\ ,\ T_{Rc,fire}) \qquad (3)$$

where:

$T_{Rl,fire}$ = bearing capacity of the longitudinal reinforcement = $2\ A_k\ (A_{sl}/u_k)\ f_{ylk}^{T}$

$T_{Rw,fire}$ = bearing capacity of the transverse reinforcement = $2\ A_k\ (A_{sw}/s)\ f_{ywk}^{T}$

$T_{Rc,fire}$ = bearing capacity of the concrete struts = $\nu_{fire}\ \alpha_{cw}\ A_k\ t_{eff}\ f_{ck}^{T*}$

where A_k = area enveloped by the mean line of the section of the hollow prism; A_{sw} = section of each stirrup x no. of the legs (inside each sub-region of the hollow prism); u_k = length of the mean line of the section of the hollow prism; t_{eff} and f_{ck}^{T*} = effective thickness and mean temperature of the hollow prism; f_{ck} and $f_{ctk}/f_{ylk}/f_{ywk}$ = characteristic strengths of concrete/longitudinal reinforcement/transverse reinforcement; all the longitudinal bars are assumed to be at the same temperature, and so all the stirrups.

REINFORCED AND UNREINFORCED BEAMS IN SHEAR

Solid sections

A rectangular section exposed to the standard fire along three sides has been analyzed with/without transverse reinforcement, by using Eq.1 and Eq.2a, respectively. The dimensions and reinforcement are: b × h = 200 × 400 mm; 4∅16 mm-bars in tension; 2∅14 mm-bars in compression; two-leg stirrups 1∅10 mm/150 mm; ρ_l = 1.21%; ρ_w = 0.52%. As should be expected, in the transversely-unreinforced section the strength V_R’ is controlled by concrete decay, while in the transversely-reinforced section the strength V_R” is controlled by the stirrups and by steel decay. In the case of long-duration fires, the strengths V_R’ and V_R” tend to get closer and closer.

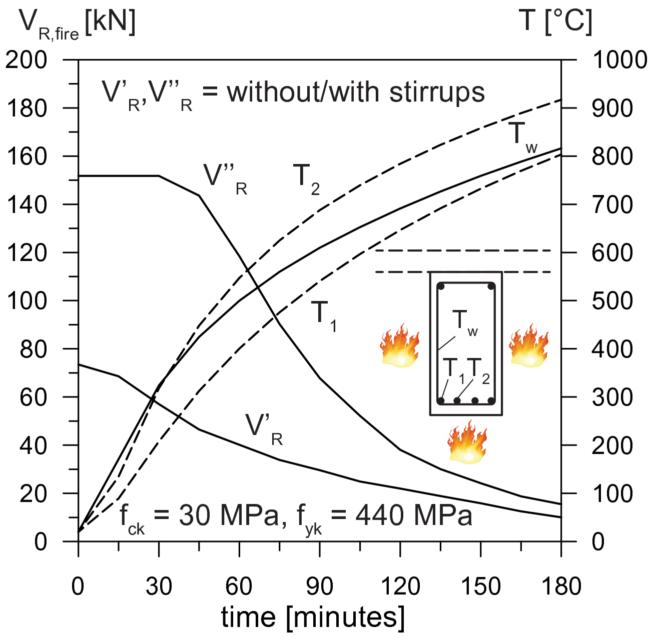

Figure 3. Shear capacity and temperature versus fire duration for a reinforced concrete section in shear, with and without transverse reinforcement (V_R”; V_R’); stirrup / bar cover = 21/34 mm.

Open thin-walled sections

An indirectly-supported inverted-V pre-tensioned beam has been studied to evaluate its fire resistance under the standard fire (Fig. 4a; thermal properties from EC2).

The main geometric characteristics are: support-to-support span = 12 m, width and depth = 2.4 and 1.6 m; thickness of the wings and angle to the horizontal axis = 90 mm and 51°. Beside the 7-wire 0.5 in-strands (26 in all), the wings are reinforced with stirrups and bars, which form two nets of bars.

Because of the small thickness of the wings, their effective section goes rapidly to zero (Fig. 4a), and the zone method must be applied (Fig. 4b).

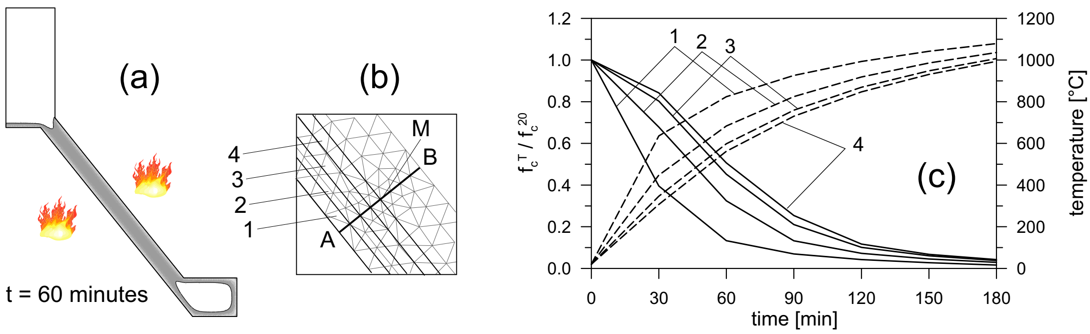

Figure 4. Isotherm 500°C for t = 60 minutes (a); subdivision into 4 + 4 zones of the wings (b); and plots of the strength decay and of the temperature in the 4 + 4 zones or layers (c).

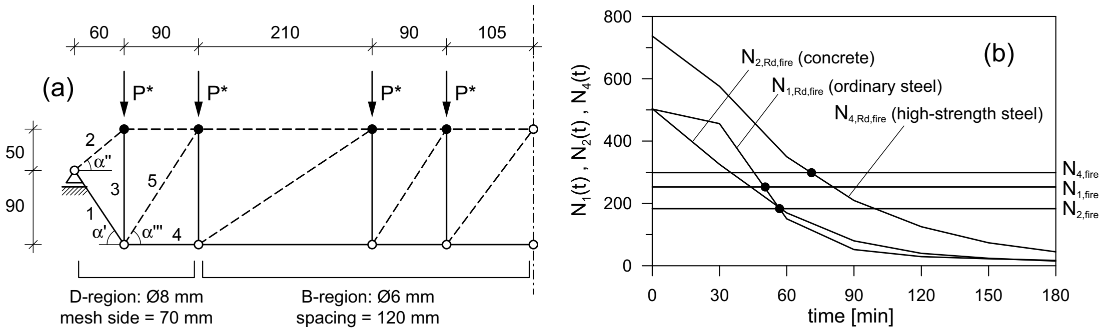

Figure 5. Truss or strut-and-tie system adopted to model each wing (a); and strength decay and temperature in the main members of the D-region; P* (own weight included) = 82 kN.

The normalized strength and the temperature of each of the 4+4 layers are plotted in Fig. 4c. The reinforcement and the concrete were modelled by means of a truss or strut-and-tie system (Fig. 5a). The strength decrease of the main members (Strut 2, and Ties 1 and 4) is plotted in Fig. 5b. The fire resistance is close to 50 minutes in the D-region (Fig. 5b) and to 60 minutes in the B-region [7].

REINFORCED MEMBERS IN TORSION

A transversely-reinforced rectangular section exposed to the standard fire along four sides (Fig. 6) has been analysed by using Eq.3. The three resisting moments provided by the stirrups (T_{Rw} and T_{Rw}*), by the longitudinal bars (T_{Rl}) and by the 45°- concrete struts (T_{Rc}) are plotted in Fig. 6 as a function of fire duration (standard fire), together with the average temperatures T_w, T_l and T_c.

Note that (a) only with the higher stirrup amount the strength decay is controlled by concrete (T_{Rc}) for t < 80-85 minutes, and (b) in the former case the longitudinal and transverse reinforcements are almost balanced (ρ_l = 1.95%; ρ_w = 1.92%).

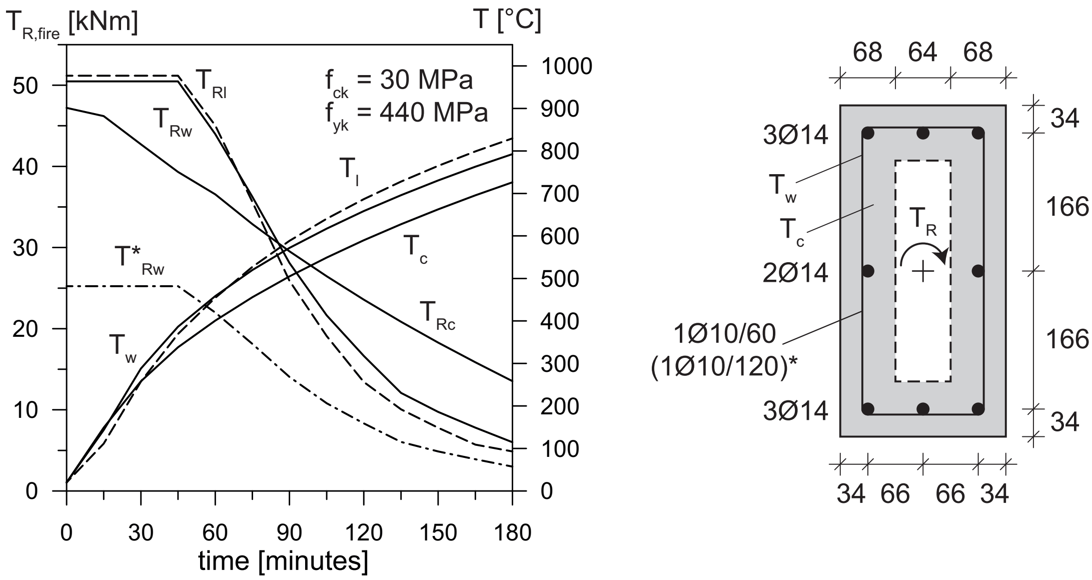

Figure 6. Resisting twisting moments T_{Rw}, T_{Rw}*, T_{Rl} and T_{Rc}, and temperatures T_w, T_c and T_l vs. fire duration for a rectangular R/C section subjected to torsion: l, w (w*) = longitudinal, transverse reinforcement; c = concrete struts; stirrup/bar cover = 22/34 mm.

SHEAR-TRANSFER MECHANISMS

To understand properly the mechanical decay in fire of a R/C member subjected to shear stresses (be they due to a shearing force or to a twisting moment), the local mechanisms contributing to shear transfer should be analyzed in the context of high temperature and fire, to justify the rather indirect and simplified way these mechanisms are taken care of in the design equations.

Let us consider the case of Fig. 7, where the I-section introduced by di Prisco and Gambarova (J. Struct. Eng – ASCE, Dec. 1995) is shown. Two different kinematics were adopted along the inclined cracks, with the bottom chord cracked (R/C) or uncracked (P/C), respectively, while the thin web was assumed to be cracked in both cases. The various shear-resistant mechanisms were modelled (aggregate interlock INT, dowel action DWL, bending in the diagonal concrete struts BND, stirrups STR), as well as tension-stiffening in the stirrups. In the end, a rather complex system of equations was written, taking care of sectional and local equilibriums, compatibility and constitutive behavior. By extending the analytical formulations of the shear-transfer mechanisms to high temperature [8], the normalized contributions to shear capacity can be worked out (Figs. 7a,b), as a function of fire duration (Standard Fire ISO 834; thermal properties from EC2). Contrary to the R/C section (Fig. 7a), dowel action is not active in the P/C section (Fig. 7b).

The two major contributions are those related to the stirrups (70-75% of the shear capacity at room temperature) and to aggregate interlock (20-25%). The former is not affected by the fire as long as bar temperature remains below 400°C (hot-rolled stirrups), and later starts decreasing. The latter starts decreasing earlier, primarily because of crack kinematics, as crack opening tends to increase in fire more than crack slip; as for concrete deterioration, its effect on aggregate interlock is minimal.

The contributions of dowel action (close to 2% in R/C at room temperature) and strut bending (close to 3% in both R/C and P/C at room temperature) are definitely less relevant at any temperature, but V_{DWL} is totally lost after 30 minutes primarily because of heat-induced damage in the cover, while V_{INT} decreases regularly both in R/C and P/C sections, but more in the former case (Fig. 7a) than in the latter (Fig. 7b).

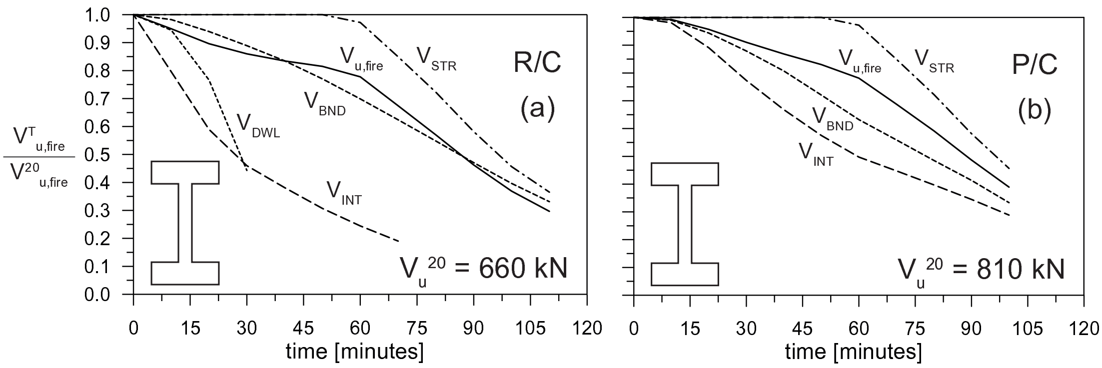

Figure 7. Example of a I shear-sensitive section (h = 1100 mm; chords: 600 × 200 mm; web thickness = 120 mm): normalized contributions to shear transfer: (a) crack inclination α_{cr} = 40°, f_{ck} = 30 MPa, ρ_l = 2%, $\varnothing_l$ = 18 mm and stirrup spacing s = 100 mm; and (b): α_{cr} = 30°, f_{ck} = 45 MPa and s = 150 mm; stirrup $\varnothing_{st}$ = 8 mm (2 legs in both cases), f_{yk} = 440 MPa and max. aggregate size d_a = 20 mm.

CONCLUDING REMARKS

- The well-established design models for shear and torsion (beam-end section and 2D-truss models in shear, and 3D-truss model in torsion) are still consistent with crack evolution at high temperature, and can easily be extended to fire design; experimental evidence is, however, badly needed.
- In shear, the rather cold core of solid structural members always prevents concrete struts from crushing in fire; in torsion, large solid sections provide extra strength in a prolonged fire thanks to the cold core, whose contribution is generally negligible at room temperature, but may be substantial at high temperature.
- The reduced/effective section method is adequate for solid sections, where the thermal field is highly variable and the reference temperature of 500°C is a sort of mean temperature in the more or less heated concrete.
- The zone method is more general and covers also the cases in which the thermal field in the concrete tends to be rather uniform, as in thin-walled members.
- Among the shear-transfer mechanisms, the contributions of the stirrups and of the comb-like mechanism of the struts decrease regularly, the former in accordance with the yielding of the steel and the latter keeping always very small values. On the contrary, the contribution of aggregate interlock decreases sharply because of crack opening, and the that of dowel action (only in R/C sections and rather small) rapidly goes to zero, because of the heat-induced damage in the cover; on the whole, even in fire stirrups and aggregate interlock remain the main actors, but the latter loses much of the relevance it has at room temperature.

REFERENCES

1. Kordina, K. 1979. "Über das Brandverhalten von Bauteilen und Bauwerken (On Fire Behavior of Structural Members and Constructions)", *Rhein.-Westfäl. Akademie dere Wissenschaften*, Report No. 281.
2. Hertz, K. (1985). "Analyses of Prestressed Concrete Structures Exposed to Fire". *Report No.174, Institute of Building Design, Technical University of Denmark*, Lyngby (DK): 152 pp.
3. Ellingwood, B., and Lin, T.D. 1991. "Flexure and Shear Behavior of Concrete Beams during Fires", *ASCE – Journal of Structural Engineering*, V.117, No.2: 440-458.
4. Kodur, V.K.T., and Hatinger, N.R. 2011. "A Performance-Based Approach for Evaluating Fire Resistance of Prestressed-Concrete Double T-Beams", *Journal of Fire Protection Engineering*, V.8: 185-222.
5. Campanale F. 2005. On the Shear Resistance of R/C Members in Fire Based on Available Experimental and Numerical Results" (in Italian). *MS Dissertation supervised by Professor Sergio Tattoni, Politecnico di Milano,* April 2005: 175 pp.
6. Felicetti, R., and Gambarova, P.G. 1999. "Residual Capacity of HSC Thermally-Damaged Deep Beams", *ASCE – Journal of Structural Engineering*, V.125, No.3: 319-327.
7. Bamonte, P., Felicetti, R., and Gambarova P.G. 2011. "On Fire Safety of Thin-Walled P/C Beams Subjected to Cracking and Corrosion. *ACI – SP 279*: 137-169.
8. Campi, G.A., and Spirio, D.A. 2012. "On the Shear Behavior of R/C and P/C Thin-Walled Members Exposed to high Temperature" (in Italian). *MS Dissertation supervised by Dr. Patrick Bamonte, Politecnico di Milano*, December 2012: 170 pp.
9. Tattoni, S. 2005 "Fire Resistance of Precast Elements: Research Activity within the Italian National Project ULISSE". Proc. Workshop on "Fire Design of Concrete Structures: What's Now? Whats Next?", Milan (Italy), 2-4 December 2004: 307-310.

Fire Behavior of Two-Way Post-Tensioned Concrete Slabs Provided with Bonded Tendons: An Experimental Study

LI ZHANG, YA WEI, FRANCIS TAT KWONG AU and JING LI

ABSTRACT

Fire tests of three reduced-scale two-way post-tensioned concrete slabs with bonded tendons were carried out. This study was intended to investigate the influence of the layout of prestressing tendons, prestressing force and concrete spalling on the structural response of two-way post-tensioned concrete slabs with bonded tendons in fire. The material used to fabricate the specimens, the phenomena observed during the tests, the temperature distributions, the deflections and occurrence of concrete spalling were investigated.

INTRODUCTION

Post-tensioned concrete slabs are common structural components in buildings to achieve large span-to-depth ratios and economy. They may be one-way or two-way. A typical one-way slab has an aspect ratio of 2 or above and is usually supported at the two longer opposite sides. A two-way slab has an aspect ratio below 2 but there may be more variations. It may be supported by beams at all four sides of the perimeter or supported by columns at the four corners as in the case of flat slab.

Previous studies have provided comprehensive knowledge of the behavior of one-way post-tensioned concrete slabs in fire [1-5]. Work has also been done on the structural fire performance of two-way reinforced concrete slabs [6] and two-way post-tensioned slabs with unbonded tendons [7], but little of such work has been done on two-way post-tensioned concrete flat slabs with bonded tendons. The present experimental study aims to explore the structural behavior of two-way bonded post-tensioned concrete slab at elevated temperatures with particular attention to concrete spalling, failure mode, etc.

Li Zhang, Department of Civil Engineering, the University of Hong Kong, Pok Fu Lam Road, Hong Kong.
Ya Wei, Department of Civil Engineering, the University of Hong Kong, Pok Fu Lam Road, Hong Kong.
Francis Tat Kwong Au, Department of Civil Engineering, the University of Hong Kong, Pok Fu Lam Road, Hong Kong.
Jing Li, School of Civil Engineering and Transportation, South China University of Technology, Wushan Road, Guangzhou, Guangdong Province, China

TEST PROGRAM

Dimensions and Material Properties of Specimen

Three specimens of post-tensioned two-way concrete flat slab provided with bonded tendons were fabricated for fire testing. The specimens were designed to a reduced scale mainly according to ACI318-08 [8] and BS EN 1992-1-1 [9] to satisfy the available space inside the furnace. Each slab specimen comprised a central rectangular area bounded by four columns at the corners of that area and cantilever panels outside the rectangular area as shown in Figure 1. The slab thickness and concrete cover were 95mm and 10mm respectively. Linear variable differential transducers (LVDTs) and thermocouples were placed at critical locations to measure the displacements and temperature distributions respectively.

The tendons were provided with curved profiles as shown in Figure 2. For the distributed-distributed tendon arrangements, tendons X1 to X6 employed were given “Profile-A1”. Tendons Y1, Y2, Y5 and Y6 employed were given “Profile-A2” while Y3 and Y4 employ were given “Profile-A3”. For the distributed-banded tendon arrangements, tendons X1 to X6 employed were given “Profile-B1”. Tendons Y1, Y2, Y5 and Y6 employed were given “Profile-B2” while tendons Y3 and Y4 employed were given “Profile-B3”. The tendons were stressed to the target levels expressed as percentage of the corresponding “yield strength” as shown in Table 1. The tendon arrangement and design load ratio are also given in Table 1.

C40 and C60 concrete mixes were used in the base and columns respectively. Grade 1860 prestressing steel strands to GB/T 5224 with diameter of 12.7 mm and nominal cross sectional area of 98.7 mm^2 were employed as prestressing tendons. Circular corrugated steel ducts originally with diameter of 40 mm, thickness of 0.3 mm and yield strength 195 MPa were flatted before use. The concrete used in the fabrication of the slab was C60 self-consolidating concrete with aggregate size of 5-10mm. The 28-day cube strength and the moisture content were shown in Table 2. The grout was produced with 42.5R cement with water to cement ratio of 0.4, providing a 28-day compressive strength of 42.6 MPa.

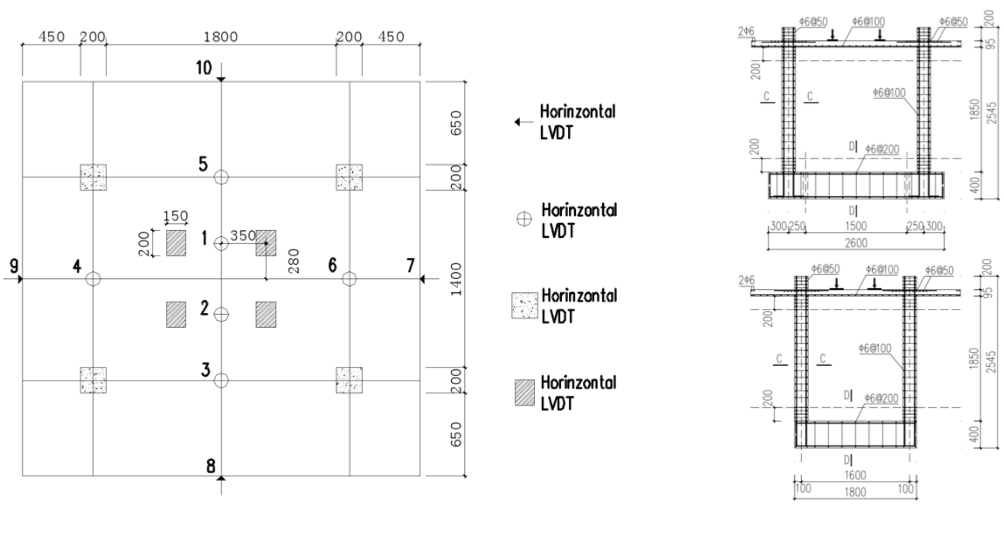

(a) Plan view (b) Side view

Figure 1. Dimensions of specimen (unit: mm)

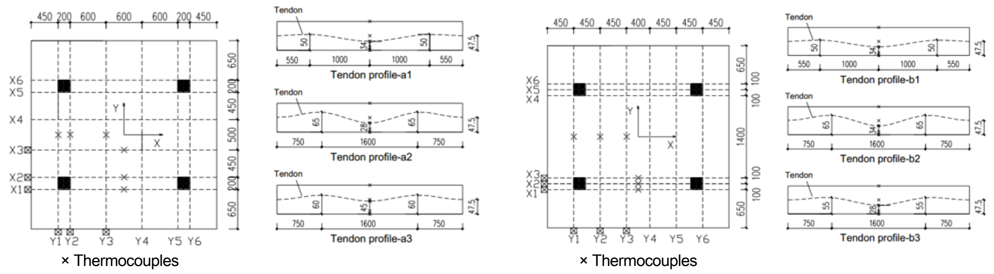

(a) Distributed-distributed (b) Distributed-banded

Figure 2. Tendon distribution and profile (unit: mm)

TABLE 1. DESIGN TEST CONDITIONS OF SPECIMENS

Specimen	Tendon arrangement	Bond condition	Target prestressing level	Design load ratio
1	Distributed-distributed	Bonded	37%	25%
2	Distributed-distributed	Bonded	50%	50%
3	Distributed-banded	Bonded	50%	25%

TABLE 2. PROPERTIES OF SPECIMENS

Specimen	Force of tendons		Load (kN)	Concrete strength (kN)		Concrete moisture content (%)
	Target force (kN)	Measured force (kN)		28-day	Test day	
1	67.9	64.7	43.4	61.5	53.9	2.49
2	91.8	94.5	85.7	61.5	53.0	2.10
3	91.8	94.8	43.4	61.5	53.2	2.02

Test Facilities

The temperature in the furnace was controlled by a computer and monitored by 12 thermocouples to ensure the required temperature. The load applied by a hydraulic jack was transferred through steel beams onto 4 loading areas on the slab by 4 spreaders as shown in Figure 1(a). Ten LVDTs were placed at different locations as shown in Figure 1(a). The vertical LVDTs were denoted as VD-1 to VD-6 and the horizontal LVDTs were denoted as HD-7 to HD-10. Positive LVDT measurements refer to either the vertical downward displacement or horizontal outward displacements.

The thermocouples were denoted according to their locations as shown in Figure 2. Taking the thermocouples at the middle of tendon Y3 for example, Y3-T, Y3-M, Y3-B, Y3-P, Y3-S, Y3-Dt and Y3-Db denoted the thermocouple located at the top surface, the mid-depth, the bottom surface, the prestressing tendons, the reinforcing steel, the top surface of the duct and the bottom surface of the duct respectively. Centroid-B denoted the thermocouple located at the bottom surface of the centroid of the panel.

Test Procedure

The test setup was shown in Figure 3. The soffit of the central panel within the rectangle defined by the four columns will be heated while the cantilever parts, the columns and the base of the specimens were protected with fireproof material after the fabrication of specimens. The transient state method was adopted where the load was constantly acting on the specimen when the temperature of the specimen was elevated until structural failure. The measured temperature curves of tests were compared to the standard fire curve of ISO 834 as shown in Figure 3(c).

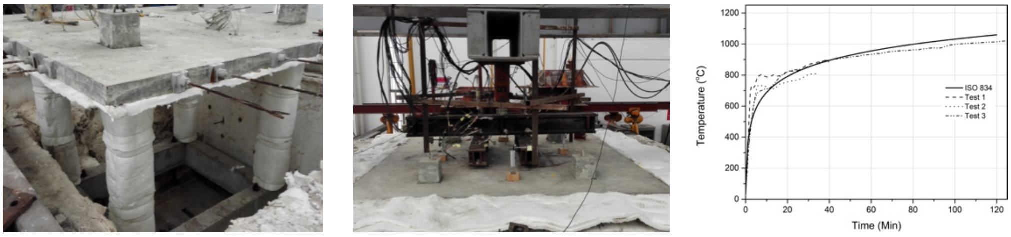

(a) Furnace (b) Loading setup (c) Temperature curves

Figure 3. Test Setup and measured temperature curves

RESULTS AND DISCUSSIONS

Observations

In test 1, continuous noise due to concrete spalling was heard from 5 minutes after ignition to the end of the test. Cracks were first observed in line with tendons X3 and Y4 near the load spreader accompanied by water seepage due to evaporation. At around 40 minutes, a "big bang" was heard and a through hole was observed at the intersection of tendons X4 and Y4, after which the test was terminated.

In test 2, similar to test 1, continuous noise due to concrete spalling was heard from 5 minutes after ignition to the end of the test except that the noise due to concrete spalling was more intensive. A "big bang" was heard due to the crushing of part of the concrete at the top surface at 34 minutes.

In test 3, the test was relatively quiet compared to the previous tests. Noise was first heard at 7 minutes. All the noise due to concrete spalling occurred in the first 19 minutes. The first crack was observed parallel to and near tendon Y4. At 50 minutes, all the water at the top surface had evaporated. The specimen was heated for 120 minutes without apparent concrete spalling at the top surface, which exceeded the design fire resistance of 90 minutes in accordance with BS EN 1992-1-2 (2004) [9].

3.2 Temperature Distribution

Figure 4 shows the temperature-time curves of the thermocouples in the central slab panel. Comparing the temperatures at different levels, e.g. X3-B, X3-S, X3-P, X3-M and X3-T in Figure 4(a), shows different heating rates depending on the distance from the slab soffit, which clearly reflects the poor thermal conductivity of concrete. The temperatures of X3-P in Figures 4(a)-(c) were higher than those of Y3-P because of the smaller distance of X3-P to the soffit compared with that of Y3-P. In particular, the temperature of X3-B in Figure 4(a) was higher than that of Y3-B because of more severe continuous concrete spalling at the corresponding location, leading to thinner concrete cover.

Figures 4(a)-(b) show sharp increases of temperatures around 10 to 15 minutes after ignition, which indicate the occurrence of severe concrete spalling at the soffit, almost directly exposing the thermocouples to fire. The temperature curves in Figure 4(c) are relatively smooth and free of any sudden jump because of the milder concrete spalling of specimen 3 as compared to the first two specimens. Moreover, the heating rates of the top surface of specimens also increased gradually because of the concrete spalling and hence shorter path of heat transfer.

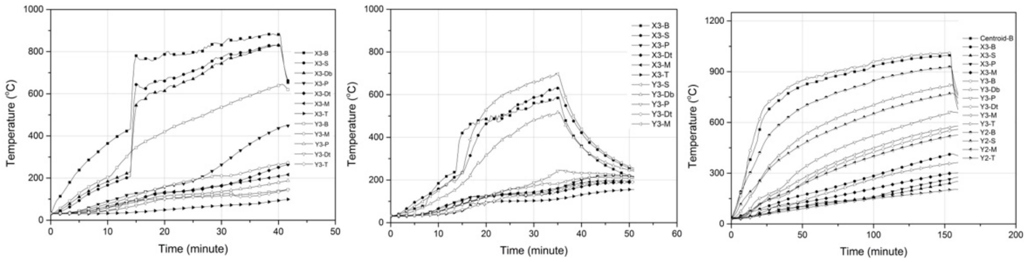

(a) Specimen 1 (b) Specimen 2 (c) Specimen 3

Figure 4. Temperature distributions of specimens

3.3 Structural Responses

The vertical displacements at critical locations are used to describe the structural responses of the specimens. The vertical responses were dominated by thermal bowing caused by the thermal gradients across the depth of the slab and hence differences in thermal expansion [10] combined with the thermal thrust forces provided by restraints [11]. The horizontal displacements were dominated by thermal expansion of the specimens. Furthermore, the variations of vertical and horizontal displacements were related to the degradation of mechanical properties of concrete, steel reinforcement and prestressing tendons as well as their thermal relaxation with the increase in temperature. The severity of concrete spalling also contributed to the increase in camber of slab due to loss of self-weight and reduced stiffness as the temperature increased.

Among various vertical displacements of Specimen 1 as shown in Figure 5(a), displacements VD-1 and VD-2 had a relatively rapid increase in the first 6 minutes due to increasing thermal gradient as temperature rose, while VD-3, VD-4 and VD-6 had relatively slower increase, showing that thermal gradient dominated the vertical displacements at this stage. Afterwards, the rate of increase of vertical displacements reduced gradually while the thermal gradient decreased and the thermal thrust increased. The vertical displacements reached the peak at around 10 minutes and started to decrease until the end of the test, probably because severe concrete spalling led to reduced self-weight and stiffness of the slab. The curved prestressing tendons gradually dominated the load carrying mechanism and caused more camber.

The vertical displacements of Specimen 2 as shown in Figure 5(b) have similar trends as those of Specimen 1. The LVDT measurements indicate relatively symmetrical deformation pattern of the specimen. The vertical displacements at VD-3 and VD-5 were larger than those at VD-4 and VD-6 because of the larger span in the X direction and hence smaller flexural stiffness. The maximum vertical

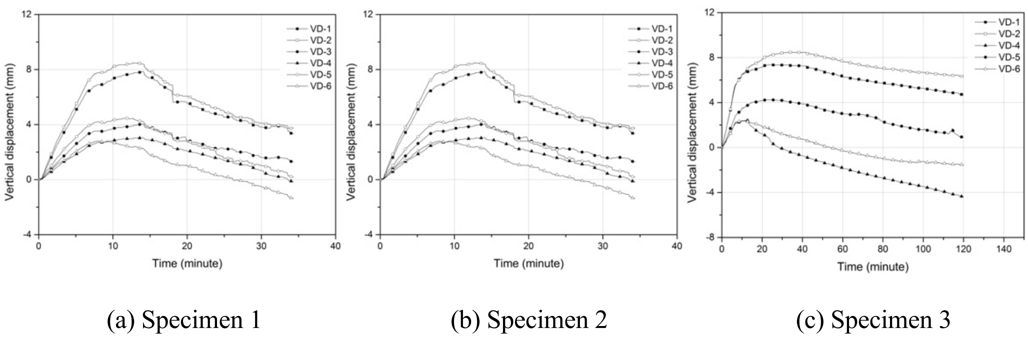

(a) Specimen 1 (b) Specimen 2 (c) Specimen 3

Figure 5. Vertical displacements of specimens

displacements were reached at around 13 minutes when sudden increase in temperature of X3-B occurred as shown in Figure 4(b), confirming the effects of concrete spalling on the structural response.

Figure 5(c) shows the vertical displacements of Specimen 3 that has undergone a fire test of over 120 minutes. The vertical displacements of VD-1 and VD-2 rose in the first 30 minutes and dropped afterwards. The vertical displacements of VD-1, VD-2 and VD-5 remained positive at 120 minutes while those of VD-4 and VD-6 were negative, implying that the camber effect was more significant at VD-4 and VD-6. This was consistent with the tendon layout as shown in Figure 2(b), since there were 3 tendons close to VD-4 and VD-6, but fewer tendons close to VD-1, VD-2 and VD-5. The localized upward pressure provided by the three adjacent tendons caused the upward displacements of VD-4 and VD-6.

3.4 Concrete Spalling

After the fire tests, the cracks and concrete spalling were closely examined. Figure 6 shows the concrete spalling at the soffit of Specimens 2 and 3. Both Specimens 1 and 2 had severe concrete spalling, while that of Specimen 3 was less severe. Concrete spalling at elevated temperature obviously influenced the structural integrity and temperature distribution, possibly causing premature failure.

The lost area at the soffit of Specimen 2 caused by concrete spalling accounted for more than 60% of the central panel while the depth of concrete spalling in most part was over 50mm, as shown in Figure 6(a). The majority of reinforcing bars and tendons X3, X4 and Y4 were exposed to fire. As no ruptured reinforcing bars were found, the tensile stresses in the bars should be relatively low at the corresponding temperatures. The through hole occurred near the intersection between tendons X4 and Y4 where one of the load spreader sat. Obviously before the formation of through hole by severe spalling, the concrete depth of the heated area was reduced, thus weakening the concrete seriously. Afterwards the adjacent concentrated load failed the thin layer of the concrete by combined flexure and shear.

The severity of concrete spalling in Specimen 3 as shown in Figure 6(b) was much less severe as compared to Specimen 1 and 2. The depth of concrete spalling was around the thickness of concrete cover (i.e. 10mm) and cracks in line with tendons X3 and X4 were also found at the soffit. A few reinforcing bars were exposed but the tendons were still well protected.

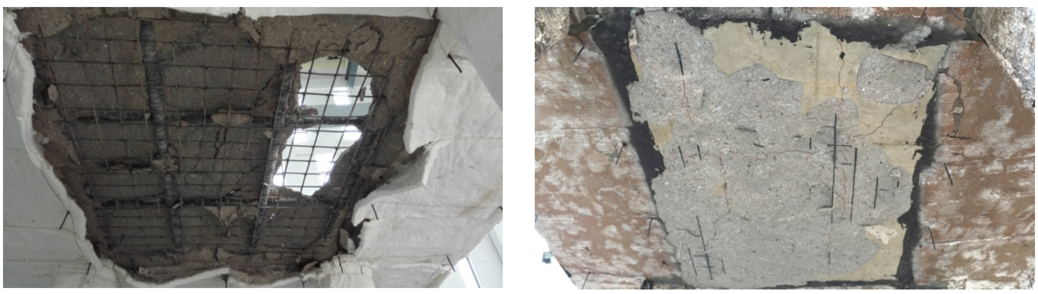

(a) Test 2 (b) Test 3

Figure 6. Concrete spalling of Tests 2 and 3

3.4 Discussions

The integrity of post-tensioned concrete slab is a major concern as it affects the structural behavior. The top surface of Specimen 1 to 3 sustained the fire for 40 minutes, 34 minutes and over 120 minutes respectively, while the soffit suffered different degrees of concrete spalling.

Only Specimen 3 sustained the desirable structural fire resistance with satisfactory integrity. One of the critical factors contributing to massive concrete spalling was probably the highest heating rate of test 2 at the early stage as shown in Figure 3(b). The higher the heating rates, the greater the probability of concrete spalling as concluded in previous studies on the fire resistance of concrete structures [12-14].

Another factor affecting the possible loss of concrete integrity at the soffit was the compressive concrete stresses at the soffit of panel center induced by restrained thermal expansion and post-tensioning. Specimens with distributed-banded tendon layout had tendons Y3 and Y4 located near the center of central panel while the other specimens with distributed-distributed tendon layout had tendons X3, X4, Y3 and Y4 located near the center. Additionally, with the interweaving ducts near the center of specimen with distributed-distributed tendon layout, the reduced depth of concrete at duct intersections weakened the slab there to certain extent.

The difference between the largest displacement and the displacement at the end of the test can be considered to result from spalling and stiffness. Specimens 1, 2 and 3 had displacement differences of 7.95, 4.57 and 2.39mm. The value of Specimen 3 was the smallest because its stiffness was the largest among the specimens, which restrained the deformation of the bonded tendons.

The increased camber helped reduce the tensile stress in the reinforcing bars so that they could survive the reduction in tensile strength at elevated temperatures. The upper layer of concrete was mainly under tension perpendicular to the tendon as proven by the crack appearance in line with the tendons.

4 CONCLUSIONS

Three specimens of post-tensioned concrete flat slab with bonded tendons were tested at elevated temperatures. The specimens were designed with different load ratios, prestress levels and tendon layouts. The first two specimens suffered severe concrete spalling while the other one retained satisfactory integrity. Based on the test results, some conclusions can be drawn as follows:

(a) Concrete spalling at elevated temperatures severely affected the integrity of structure and gave rise to temperature and stress redistribution, which could lead to progressive concrete spalling.
(b) Further camber occurred after severe concrete spalling and hence partial loss of self-weight, thus releasing the constraints of the bonded tendons and weakening the stiffness of slab.
(c) The concrete spalling at the soffit can be attributed to the reduced compressive strength of concrete at elevated temperature coupled with the increasing compressive stress in concrete as induced by retrained thermal expansion and prestressing.
(d) While prestressing can contribute to concrete spalling by inducing large compressive stresses at the soffit, later in the heating process it can also reduce the tension in reinforcing bars thereby protecting them to certain extent.

REFERENCES

[1] Bailey, C.G. and E. Ellobody. 2009. "Fire tests on unbonded post-tensioned one-way concrete slabs," *Magazine of Concrete Research*, 61(1), 67-76.

[2] Bailey, C.G. and E. Ellobody. 2009. "Fire tests on bonded post-tensioned concrete slabs," *Engineering Structures*, 31(3), 686-696.

[3] Bailey, C.G. and E. Ellobody. 2009. "Comparison of unbounded and bonded post-tensioned concrete slabs under fire conditions," *The Structural Engineer*, 87(19), 23-31.

[4] Ellobody, E. and C.G. Bailey. 2009. "Modelling of unbonded post-tensioned concrete slabs under fire conditions," *Fire Safety Journal*, 44(2), 159-167.

[5] Ellobody, E. and C.G. Bailey. 2008. "Modelling of bonded post-tensioned concrete slabs in fire," *Structures and Buildings*, 161(6), 311-323.

[6] Moss, P. J., R. P. Dhakal, G. Wang, and A. H. Buchanan. 2008. "The fire behaviour of multi-bay, two-way reinforced concrete slabs," Engineering Structures 30(12), 3566-3573.

[7] Wei, Y., F.T.K. Au, J. Li and N.C.M. Tsang, 2014. "Structures in Fire," presented at the 8th International Conference on Structures in Fire, June 11-13, 2014.

[8] ACI 318-08. 2008. *Building Code Requirements for Structural Concrete and Commentary*. ACI Standards, American Concrete Institute, Farmington Hills, MI, U.S.A.

[9] BS EN 1992-1-2. 2004. *Eurocode 2: Design of concrete structures - Part 1-2: general rules – structural fire design*. British Standards Institution, London, UK.

[10] Usmani A.S., J.M. Rotter, S. Lamont, A.M. Sanad and M. Gillie. 2001. "Fundamental principles of structural behaviour under thermal effects," *Fire Safety Journal*, 26(8), 721-744.

[11] Lim, L., A. Buchanan, P. Moss and J. Franssen. 2004. "Computer modelling of restrained reinforced concrete slabs in fire conditions," *Journal of Structural Engineering*, 130(12), 1964-1971.

[12] Ali F., A. Nadjai, G. Slikock and A. Abu-Tair. 2004. "Outcomes of a major research on fire resistance of concrete columns," *Fire Safety Journal*, 39(6), 433-445.

[13] Chung J.H. and G.R. Consolazio. 2005. "Numerical modeling of transport phenomena in reinforced concrete exposed to elevated temperatures," *Cement and Concrete Research*, 35(3), 597-608.

[14] Gamal A. and J. Hurst. 1995. "Modeling the behavior of concrete slabs subjected to the ASTM E119 standard fire condition," *Journal of Fire Protection Engineering*, 7(4), 125-132.

Insights into the Complexity of Structural Fire Response from Repeated Heating Tests on Post-Tensioned Concrete

JOHN GALES and LUKE BISBY

ABSTRACT

This paper extends discussion of previous research presented by the authors on post-tensioned (PT) concrete flexural elements in fire. Tests on two monostrand, continuous PT concrete slabs (one with an unbonded tendon and the other bonded) exposed to constant incident heat fluxes while under sustained load are reviewed and discussed. During testing these slabs demonstrated a distinct time-deflection response in heating and cooling consisting of five phases. For the first time, this paper gives the results from these unique slab tests during a second thermal cycle. The novelty of this study is that it was performed in an attempt to observe and better understand the thermal straining effects that contributed to the observed five-phase deflection response under first heating – illustrating many inter-related mechanisms that contribute to the complexity of the observed deflection responses. The resulting discussion is provided to advance the overall understanding of the response of real concrete structures (as opposed to isolated elements) in fire, and will hopefully assist structural fire modelers to validate (or otherwise) their modelling capabilities.

INTRODUCTION AND MOTIVATION

Performance based structural fire design methodologies for steel-concrete composite structures have greatly advanced in recent years. Such approaches are possible because comprehensive data sets exist from a range of large-scale structural fire experiments; these enable practitioners to support computational model(s) use to undertake performance assessments, analyses, and designs with relative confidence. As a result, the number of full frame fire-engineered steel-composite structures continues to grow, with enhanced safety and optimized protection measures [1]. However, other structural typologies such as reinforced concrete frames and shear wall structures lack a similar amount of large-scale structural fire test data needed to

John Gales, Civil and Environmental Engineering, Carleton University, Ottawa, Canada
Luke Bisby, School of Engineering, University of Edinburgh, Edinburgh, United Kingdom

inform model development, validation, and verification. This may limit the advancement of performance based structural fire design solutions for concrete structures. To shed light in this area, specifically for post-tensioned (PT) concrete flat slab structures, a series of loaded, three-span continuous PT concrete slabs were tested under sustained load and exposure to high temperatures at the University of Edinburgh between 2011 and 2014 [2]. The test series included both an unbonded and bonded monostrand stressed prestressing steel tendons (embedded at the centre of the slabs and parabolically draped for an eccentric prestressing force) and to the knowledge of the authors are the first such tests to incorporate axial, vertical and rotational restraint across multiple spans, whilst still accounting for bonded or unbonded tendon configurations [3]. The tests included as many complexities of real PT concrete construction as possible. A test schematic is shown in Figure 1; slab reinforcement details are given in Figure 2. The slabs were heated in their central spans using radiant panels that imposed a localized and constant incident heat flux.

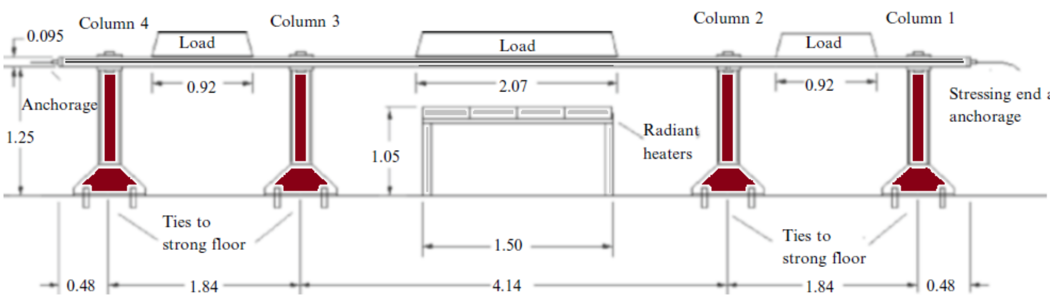

Figure 1. Test set up and geometry (front elevation, dimensions in m).

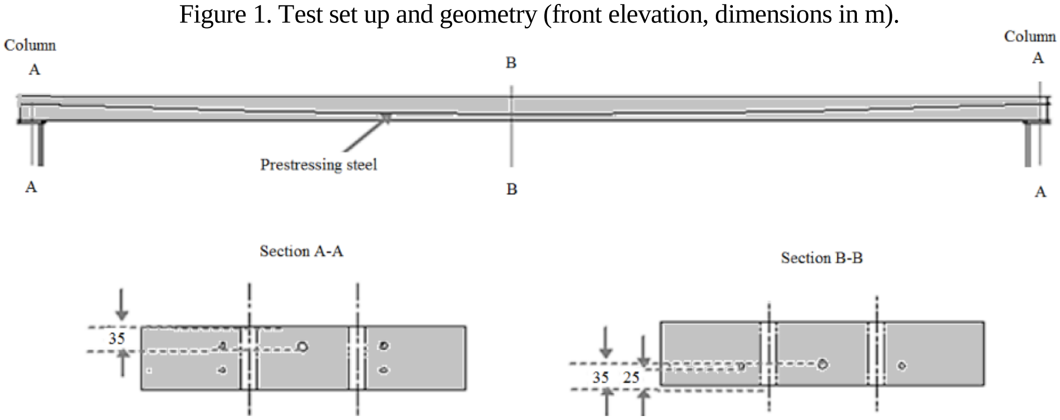

Figure 2. Steel reinforcement profile in concrete slabs (elevation and sections, dimensions in mm).

During testing the slabs demonstrated a complex, five-phase response (in heating and cooling); this is shown in idealized form in Figure 3. A detailed discussion of each phase has been given previously [3] and should be reviewed for additional context.

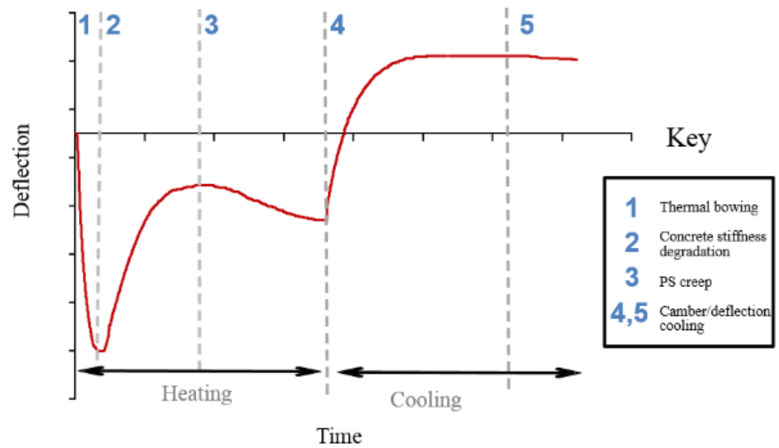

Figure 3. Idealized central span deflection vs time for constant incident heat source (+ive = camber).

Modelling the observed behavior is clearly challenging. The test deflection patterns were hypothesized as being influenced by a range of thermal and physical mechanisms, including load-induced thermal straining (LITS) [2]. LITS involves straining induced by stress concrete when exposed to high temperatures during the first exposure to heating [4]. As such, LITS strain effects should be absent under repeated heating, provided that the stress and heating levels are not exceeded. LITS is of significant interest to the structures in fire community, both qualitatively and quantitatively [4-8]. The practical significance of LITS for structural fire response has been debated within the modelling community, as has its impact on structural performance of concrete in fire tests. There is consensus that thermal straining under load (stress) involves a combination of plastic strains, and that these must incorporate 'transient' straining mechanisms [8]. A detailed discussion of LITS is available elsewhere [7, 8]. One primary motivation of the current study is to use previously performed but unpublished testing performed by the authors to highlight the potential significance of LITS effects in concrete structures exposed to fire. The hope is that this might help to advance the understanding of concrete structures in real fires, and might assist in the development of advanced, validated computational modelling capabilities. It is widely accepted that LITS occurs only under load and during a first heating cycle, and thus that it is absent should a material be heated for a second time. The authors previously presented fire tests on PT concrete slabs [2]; however two of these slabs were allowed to cool before experiencing any obvious signs of structural failure, and were subsequently subjected to a second fire exposure. This was done for one unbonded and one bonded PT concrete slab (with a total testing time of only 48 hours). The slabs were allowed to cool to ambient after the first heating test. They were then heated again to observe the impact of thermal straining effects and to try to better understand the other physical mechanisms at play which contributed to the observed five-phase deflection response in first heating (see [3]). These second heating tests are presented here for the first time.

EXPERIMENTAL PROGRAM AND METHODOLOGY

Reference [2], related to the first heating tests on the noted slabs, provides a detailed overview of the test set up, preparation, and information pertaining to instrumentation, overall dimensioning, and ambient material parameters. The important information pertaining to the second heating is repeated herein where necessary. At all stages of experimentation: temperatures were recorded using K-type thermocouples, which were predominately located in the central span (Figure 1) at mid span, quarter points of the slab and near columns; these were distributed over the slab depth at soffit, steel reinforcement, and top surface; a thermal camera was used to measure soffit temperatures; axial and rotational restraint from the supporting steel columns was monitored by calibrated foil strain gauges mounted on the column faces; tendon stress levels were monitored through two load cells at both dead and live slab ends; deflection was measured using five string pot displacement gauges; and three digital SLR cameras were used to monitor movement of columns and slab deflections by digital image correlation. As-constructed drawings are given in Figures 1 and 2. The concrete was C40/50 with predominately limestone aggregates, mild steel reinforcement was of 600 MPa yield strength, 10 mm diameter deformed bars with 25 mm axis distance concrete cover, and prestressing steel was 1860 MPa grade 12.5 mm diameter strand at 35 mm axis distance concrete cover. All slabs were loaded on all three spans using lead weights leading to a test load ratio of 0.32 and 0.42 for the bonded and unbonded slabs, respectively. The bonded slab, although constructed similarly, has higher ambient strength due to strain compatibility assumptions.

FIRST HEATING CYCLE

Both slabs were heated (in both heating cycles) by imposing a constant incident radiant heat flux of about 35 kW/m^2 using a radiant heating array. The slabs were first heated until the internal prestressing steel reached approximately 350^{o}C (the critical temperature for prestressing steel in Europe), and were then allowed to cool to ambient over 24 hours. After first heating and cooling both slabs exhibited a degree of damage, as shown schematically in Figure 4. This damage is important in understanding the observed response during second heating. Transverse cracking occurred adjacent to the supports, this was nearly twice as deep in the unbonded slab (extending 60 mm from the unexposed surface at a total depth of 95 mm) as opposed to the bonded slab (extending 30 mm from the unexposed surface at a 95 mm depth). The bonded slab developed a longitudinal crack that arrested outside the heated zone, and included a small spalled zone. In both slabs a transverse crack developed on the boundary of the heated soffit of the slab; all cracks were less than 1 mm wide.

Figure 4. Exaggerated schematic of slab damage after first heating for each slab (crack widths <1 mm).

SECOND HEATING CYCLE

Once cooled to ambient temperature, the slabs were again heated (under the same sustained imposed load) until the prestressing steel reached a temperature of 427^{o}C (the critical temperature for prestressing steel in North America). The slabs were then allowed to cool and were unloaded and de-stressed. The resulting deflection response during second heating (noting that both slabs were exposed to the same heating intensity) is illustrated for both slabs and both first and second heating cycles in Figure 5. No remarkable observations were made during cooling other than those discussed previously [2], and therefore only the heating portion is shown. The slabs recovered deflection of their thermal bowing deformation during cooling.

The second heating deflection response (mostly) followed the expected idealized five phase deflection responses seen during the first heating cycles (see Figure 3). During second heating the slabs showed: (1) a slower thermal bowing deflection rate during the initial stages of heating; (2) greater deflection of the unbonded PT concrete slab in the thermal bowing stage than the bonded slab, (3) a downward deflection increase after two hours for the unbonded configuration; and (4) a marked reduction in the upward deflection trends for both slabs after initial thermal bowing.

These differences highlight the complexity of physical and thermal behavior in PT concrete in fire, they are discussed sub-sequentially below.

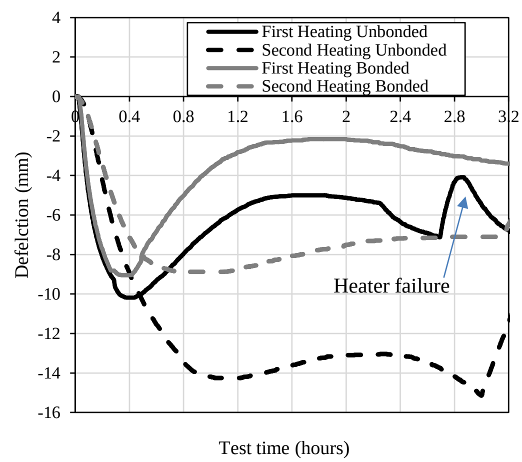

Figure 5. Deflection response of central span of PT concrete slab exposed to two repeat heats (note that downward deflection (-ve) is relative to test start).

(1) Slower Rate of Thermal Bowing during Initial Stages of Heating

Concrete during first heating loses moisture. This was visually confirmed by migration of pore water to unheated (cooler) portions of the concrete. This migration behavior was absent in the second heating cycle as most of the free moisture had evaporated. The reduced moisture also results in a more rapid rise in temperature at the level of the prestressing tendon.

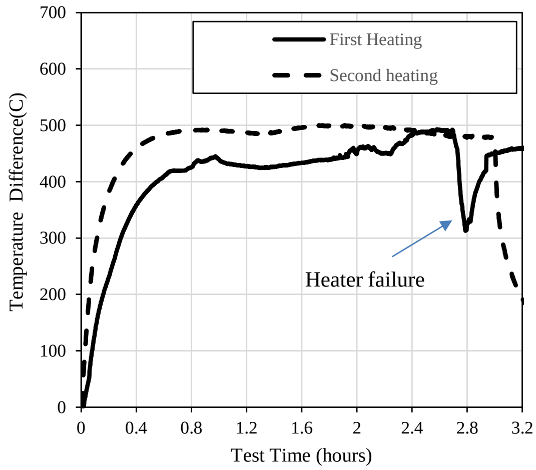

Figure 6. Maximum difference in temperature of exposed soffit and unexposed surface for the unbonded PT concrete slab at mid span for both heats.

One might expect that the more rapid rise of temperature should indicate a faster climb in deflection from a steeper temperature difference between the exposed soffit and unexposed surface of the slab (thermal gradient) in second heating at mid span (see Figure 6). That action was not directly observed for both repeat heating tests. The deflection rate response of the concrete was less in second heating (Figure 5). While this behavior influences the deflection response of the slab, it does not appear to dominate the deflection behavior at the start of the test. The behavior instead appears dominated by a lower thermal expansion of the thermally pre-damaged concrete. This can be hypothesized as less thermally stable concretes (those with limestone for example which these slabs were) will have a reduced thermal expansion [4] and consequently here, less bowing deflection. This is also made more profound when the consideration of reduced stiffness of thermally damaged concrete (see [9] for material testing using this and similar concretes) is considered. The aggregate and concrete type clearly can have a dominating influence on the initial stages of deformation of a heated concrete slab.

(2) Greater Deflection of the Unbonded PT Slab during Thermal Bowing

The unbonded slab illustrated considerably more deflection than the bonded slab during the second heating cycle. Upon cooling, both slabs recovered much of the bowing deflections. After both heating cycles, unloading, and prior to distressing, the unbonded slab showed significantly more remaining camber than the bonded slab (differing by about 2 mm), despite the same tendon drapes (as physically verified after testing). The deflections observed during thermal bowing represent a recoverable response of both the concrete and the embedded reinforcing steels – but this response between slabs obviously differs, and the only difference between the slabs, are their tendon bond and prestress relaxation states. The differences can be explained by considering that the bonded slab only experienced localized tendon stress relaxation effects due to the local placement of radiant heaters; with stresses shed to the bonded steel (non-prestressed) reinforcement. This occurred over less than half of the center span of the slab. While the bonded tendon was afforded some relaxation where it was heated (which cannot be directly measured or quantified), outside the heated region the tendon may maintain the majority of its original prestress (as partly confirmed by no observed changes in load cell readings at either the dead or live and anchorages, and post-testing confirmation that full grouting of the tendon duct had indeed occurred).

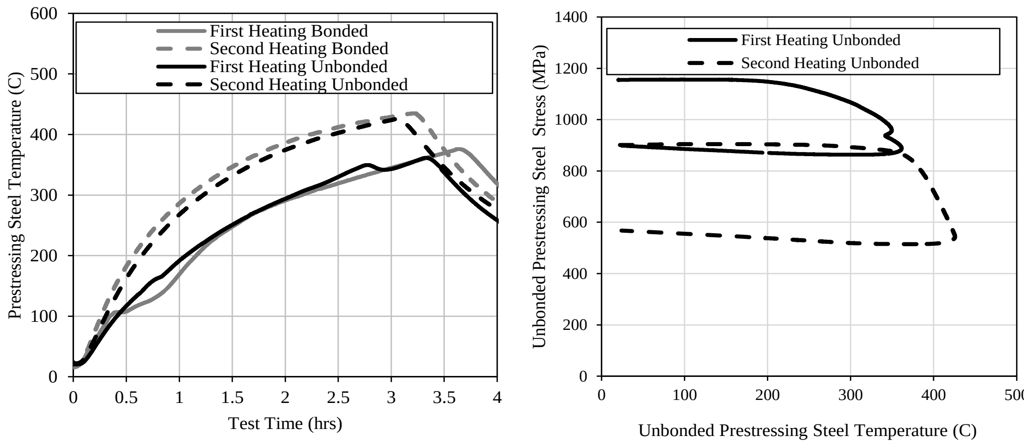

Figure 7. (a) Prestressing steel temperatures during heating, and (b) unbonded prestress relaxation of during repeat heating (bonded slab data not shown as there were no observable prestress relaxation).

The bonded tendon was therefore capable of balancing more load in areas outside the heated regions, where the unbonded slab tendon uniformly relaxed over the full length of the entire slab (including unheated regions) being unable to balance as much load, and hence expected to have greater overall deflection. The slab end-to-end stress relaxation for both heating cycles for the unbonded slab are shown in Figure 7b. This is a key difference between the two bond types slab behavior in fires. Additionally, since the unbonded slab experiences more damage at the supports of the slab (likely as a result of the central span deflecting more), it is also hypothesized that the unbonded concrete slab had less rigid connections at the column supports during the second heating cycle; this in turn promoted more deflection.

(3) Downward Deflection Increase of the Unbonded PT Slab after two Hours

Figure 7 illustrates that in both the bonded and unbonded tests the prestressing steel reached approximately the same temperatures with time. Likewise during repeat heating – indicating good test control, repeatable thermal exposures, and accurate placement of the instrumentation. These data also confirm that in the unbonded concrete slab, the prestress showed negligible relaxation effects until it reached its previous maximum exposure temperature (seen during the first heating cycle). After reaching that point the steel subsequently began again to relax. This relaxation (which reduces the ability to balance load) promotes more deflection of the slab. If the prestress state of the tendon was less than the original level during first heating, and below the maximum exposure temperature, it is expected that there should appear minimal creep relaxation deformation in Figure 7b. Once the temperature exceeds its previous maximum, the creep relaxation appears to pick up where it last finished during the first heating cycle, and downward deflection dominates again. A comprehensive creep model to describe the prestressing steels used for this study has concurrently been developed [10], which helps to show the importance of explicit consideration of prestressing steel creep in any future UPT concrete structural fire modelling endeavors. In any case, these data show that thermal straining effects for prestressing steel can dominate the behavior of PT concrete slabs in fire.

(4) Reduction in the upward deflection trends for both slabs after the initial thermal bowing

In the first heating cycle there was an upward deflection trend that followed the thermal bowing phase. In second heating there was not as much of this upward deflection as observed in Figure 5. As hypothesized, if the maximum temperature of the concrete from the first heating cycle were not exceeded in the second cycle, this deformation camber action – if it is influenced by LITS – would be expected to be absent in the second heating cycle. In both slabs there is minimal upward deflection trends at any time that occurs in the second heating; this is less than 2 mm after the thermal bowing phase. In comparison to first heating, where the value was about 7 mm. The action of an upward deflection trend (after the initial thermal bowing) in the slabs can also be influenced from the neutral axis of the concrete shifting. This can be a result of a reduced concrete stiffness of the thermally damaged concrete – this was seen in the first heating and is discussed in [2]. That action would not be expected to contribute much in second heating, since the neutral axis has already largely shifted during the first heating cycle. The contribution of both thermal straining effects and the neutral axis shift appear negligible beyond the initial stages of heating in the second cycle, but do appear to dominate in the initial heating cycle. That is before they are apparently overtaken in importance by the effects of creep of the prestressing steel.

CONCLUSIONS AND DISCUSSION

Repeat buildings fires in the same location are certainly not frequent; the second heating cycles imposed herein were intended not to simulate any practical reality, but rather to interrogate the physical reasons for the observed deflection histories for PT concrete slabs of both bonded and unbonded configurations [3], and further illustrates the complexity of PT concrete structures (or perhaps concrete structures in general) in fire. The predominant form of thermal straining effect (in the current case) was shown to be creep of prestressing steel. Once prestressing steel creep begins to accelerate, in all heating cycles, the slabs begin to deflect downward at pace. However, in the early stages of heating, deformation from thermal straining effects in concrete, possibly from LITS or from different coefficients of thermal expansion (although these two effects are complex, and hard to unpick, particularly for stressed and heated concrete) seem to play in this test programme a larger role than tendon creep.

With the requisite data now available, attempts could be made to computationally model the presented tests; however, the complexity of these systems still prohibits even certain qualitative explanation of physical and thermal mechanisms described herein, let alone quantitative analysis. It may therefore be questionable if available structural fire modelling techniques are yet able to demonstrate a capability to capture these complexities, and how these complexities might be interrelated.

Currently, simple prescriptive fire resistance tests are typically extrapolated from small scale isolated member tests to describe a full system behavior for PT concrete. The thermal and physical mechanisms observed in the testing presented herein represent many of the factors that could be expected to play roles in real PT concrete structures. Prescriptive rules – regardless of tendon bond – cannot possibly capture these complex mechanisms and interactions. More realistic structural testing of PT concrete needs to be performed to confirm the severity and degree of impact thermal straining effects on concrete.

ACKNOWLEDGEMENTS

We would like to acknowledge NSERC, Arup, and The Ove Arup Foundation for their support during the period in which this research undertaken.

REFERENCES

1. Gales, J., Maluk, C., and Bisby, L. 2012. Large-scale structural fire testing - how did we get here, where are we, and where are we going? in ICEM 15 - Porto, 2012, pp. 1-22.
2. Gales, J., Hartin, K., and Bisby, L. 2016. Structural Fire Performance of Contemporary Post-tensioned Concrete Construction. Springer Briefs in Fire. 91 pp.
3. Gales, J., and Bisby, L. 2014. Deformation and response of continuous and restrained post-tensioned concrete slabs at high temperatures. 8th International Conference on Structures in Fire. 305-312.
4. Khoury, GA. 2006. Strain of Heated Concrete during Two Thermal Cycles. Part 2: Strain during First
   Cooling and Subsequent Thermal Cycle. Magazine of Concrete Research, 58, 387-400.
5. Gernay, T., 2012. Effect of Transient Creep Strain Model on the Behaviour of Concrete Columns Subjected to Heating and Cooling; Fire Technology 48: 313-329.
6. Mindeguiaa JC, Hagerb I, Pimienta P, Carre H, Borderie C., 2013. Parametric study of transient thermal strain of ordinary and high performance concrete. Cement and Concrete Research 48: 40-50.
7. Lange, D. and Jansson R., 2014. A comparison of an explicit and an implicit transient strain formulation for concrete in fire. Fire Safety Science 11: 572-583.
8. Wang Y. (et al). 2013. Performance- Based Fire Engineering of Structures. Spon CRC Press.
9. Gales, J., Parker, T., Cree, D., and Green, M. 2016. Fire Performance of Sustainable Recycled Concrete Aggregates: Mechanical Properties at Elevated Temperatures and Current Research Needs. Fire Technology. 29 pp. in press.
10. Gales, J., Robertson, L., Bisby, L. 2016. Creep of Prestressing Steels in Fire. Fire and Materials. 21pp. in press.

Quantifying the Effect of Temperature Induced Bond Degradation on Fire Resistance of RC Beams

ANKIT AGRAWAL and VENKATESH KODUR

ABSTRACT

This paper presents the effect of temperature induced bond degradation on fire resistance of reinforced concrete (RC) beams. Results from experimental and numerical studies, both at material and structural level, on temperature induced bond degradation in RC beams are presented. As part of material level tests, high temperature double tension pull-out (DTP) tests on normal strength concrete (NSC) and high strength concrete (HSC) specimens were conducted in a customized setup to ensure presence of longitudinal tensile stress in concrete surrounding the ribs. Data from tests is utilized to propose a simplified temperature dependent bi-linear bond stress-slip relationship. Furthermore, a finite element based numerical model is developed in ABAQUS that accounts for temperature induced bond degradation in evaluating response of RC beams under fire conditions. The model is applied to quantify the effect of temperature induced bond degradation on fire resistance of RC beams.

INTRODUCTION

Reinforced concrete (RC) structural members, when exposed to fire, experience loss of structural capacity as a result of temperature induced degradation in mechanical properties of reinforcing steel and concrete. This temperature induced degradation in strength properties and elastic modulus, accompanied with differential thermal expansion, can result in loss of interfacial bond between reinforcing steel and concrete. Indeed, limited data from bond tests reported in literature indicate that temperature induced bond degradation to occur faster than the strength degradation in reinforcing steel [1]. This stress transfer between concrete and rebar, and hence the moment (or shear) capacity of a reinforced

---

Ankit Agrawal, Ph.D. Candidate, Department of Civil and Environmental Engineering, Michigan State University, East Lansing, Michigan 48823, U.S.A.
Venkatesh Kodur, Professor, Department of Civil and Environmental Engineering, Michigan State University, East Lansing, Michigan 48823, U.S.A.

concrete beam, is influenced by the extent of bond deterioration. Therefore, high temperature interfacial stresses that develop at the interface of reinforcing steel and concrete during fire exposure influence the resulting fire resistance in an RC beam. Moreover, this degradation in bond also influences the residual capacity of fire exposed RC members as well [2,3].

In current practice, flexural (or shear) capacity of RC beams under fire conditions is determined based on the assumption of perfect bond between steel reinforcement and concrete. This is largely due to the fact that there are no reliable guidelines for incorporating temperature induced bond degradation in fire resistance analysis of RC beams. Also, this simplification is based on the rationale that bond degradation is implicitly accounted for in the tensile strength degradation of concrete [4].

Only a limited number of publications have appeared on this problem [4–6]; and a fundamental understanding of the relationship between bond and temperature is still lacking. A majority of reported studies utilized concentric pullout tests, which are now known to be unrepresentative of the stress state that occur in a flexural member [1]. Numerous numerical models have also been developed to trace the response of RC structures in fire [7–10]. However, in all these numerical models, except those by Huang [9] and Gao et al. [10], a perfect bond has been assumed between steel rebars and concrete throughout the fire exposure duration.

To address these knowledge gaps, experimental and numerical investigations, both at material and structural level are presented in this paper. Temperature induced bond degradation in both NSC and HSC is studied through tests on double-pull out specimens in a customized setup. Data from these tests is utilized to develop a simplified bilinear bond stress-slip relationship for a range of high temperatures, typically experienced during a fire event. Subsequently, a numerical model is developed using the general purpose finite element program ABAQUS [11], and is applied to undertake numerical studies to quantify effect of bond degradation of fire resistance of RC beams. The effect of utilizing varied local stress-slip relationships, including the one proposed in this study, on resulting fire resistance is also discussed.

TESTS TO EVALUATE BOND DEGRADATION

In order to develop a thorough understanding of the bond stress-slip relationship at elevated temperatures, high temperature tests are being conducted at Michigan State University. Details of specially fabricated double tension pull-out (DTP) test specimen, together with some preliminary results from high temperature bond tests are presented in this section.

Experimental program and test setup

DTP specimens, fabricated different concrete types, were tested at various high temperatures. Two concrete strengths of 40 MPa (for NSC) and 90 MPa (for HSC) and ribbed bars of diameter 19 mm with having yield strength of 420 MPa were considered in the study. The direct tension pullout DTP specimen used in this study comprises of a concrete prism (178 mm X 178 mm X 254 mm) with a concentric test rebar, anchored end to end, with four threaded anchor bars, at each corner on the other end (Fig. 1a). Normal tensile stresses are transferred to the surrounding concrete, as the test rebar is gradually pulled in tension. This ensures presence of a longitudinal tensile stress, in the cover away from the ribs, unlike the direct compression present parallel to the rebar axis, in a classical pullout test. The specimen is stressed to 30 percent of the measured room temperature strength, before exposing to a target temperature. The target temperature was maintained for 30 minutes before the specimens were allowed to cool down inside the furnace. The specimens were tested 48 hours after cooling down to room temperature. The test setup for both room temperature and high temperature tests is shown in Fig. 1a-b.

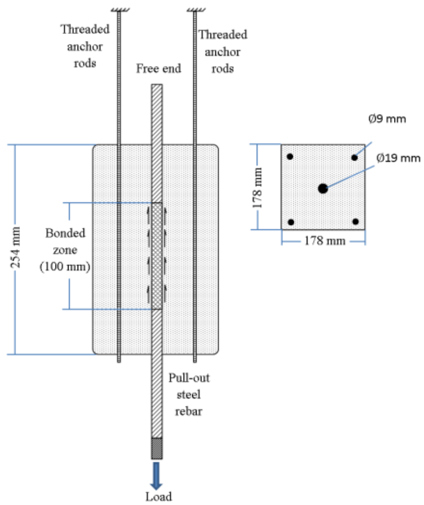

(a) Schematic diagram of DTP test

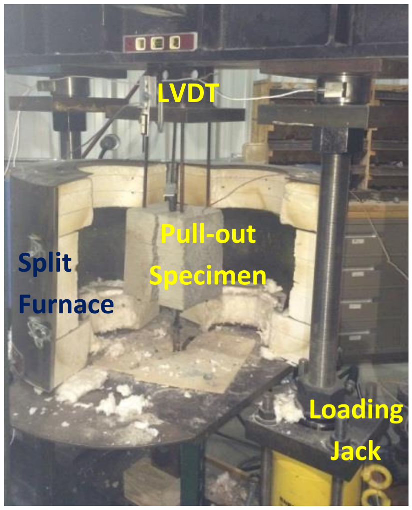

(b) High temperature set up

Figure 1. Test setup for bond (pull-out) tests at elevated temperatures.

Results from high temperature bond tests

Results from tests show that bond strength degradation in high strength concrete (HSC) specimens occurs at a faster rate than that in normal strength concrete (NSC) specimens. A significant reduction in bond strength is seen (Fig. 2a) in both HSC and NSC specimens when the exposure temperature is greater than 400°C. It should be noted that the bond degradation trends in the current study suggest that previous tests utilizing classic pull-out tests [1,12] tend to be un-conservative. Bond stress free-end-slip was also measured during these tests. It can be clearly seen in the typical bond stress-free-end-slip (BS-FES) relationships plotted in Fig.2b, that temperature induced bond degradation in NSC and HSC specimens is markedly different. Maximum slip increases for NSC specimens at higher temperatures whereas it remains almost the same for HSC specimens. This indicates that failure of HSC specimens to occur in a brittle pattern than that of NSC specimens after exposure to high temperature.

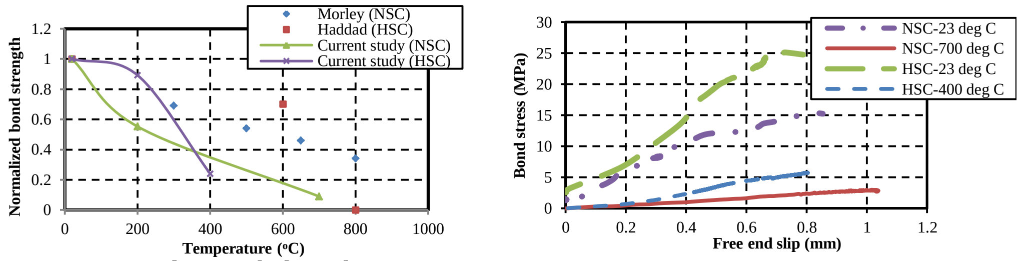

(a) Bond strength degradation (b) Bond stress-slip relationships

Figure 2. Test data from DTP tests after exposure to high temperature for NSC and HSC.

Furthermore, the failure mode changes in both NSC and HSC specimens with increasing temperatures (Fig.3a-b). A longitudinal crack develops in the specimen due to differential expansion between rebar and concrete. This crack causes loss of bond and causes a subsequent reduction in bond strength. This type of splitting failure can also be attributed to lack of any confining reinforcement within the specimen.

(a) Normal strength concrete (NSC) specimens

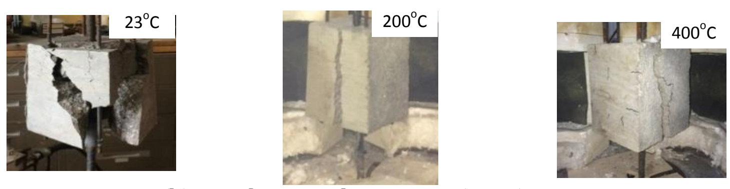

(b) High strength concrete (HSC) specimens

Figure 3. Failure modes in NSC and HSC specimens at different temperatures.

Temperature dependent bond stress-slip relationship

Based on data obtained from these tests simplified bilinear bond stress-slip relationships are proposed. These relationships account for degradation in bond strength and bond stiffness with increasing temperatures. Firstly, the degradation in bond strength with temperature is developed using a polynomial equation, which is a function of temperature and expressed as:

For NSC,

$$\frac{\tau_{max,T}}{\tau_{max,20}} = 1.0589 - 3 \times 10^{-3}T + 2 \times 10^{-6}T^2 \; (20^oC \le T \le 700^oC) \tag{1}$$

For HSC,

$$\frac{\tau_{max,T}}{\tau_{max,20}} = 0.984 + 9 \times 10^{-4}T - 7 \times 10^{-6}T^2 \; (20^oC \le T \le 400^oC) \tag{2}$$

where, $\tau_{max,T}$ is the bond strength at temperature ‘T’ and $\tau_{max,20}$ is the bond strength at room temperature.

Secondly, a bilinear bond-stress-slip relationship is proposed based on a general relationship developed by Ulaga and Vogel [13], with suitable modifications for high temperature [14]. The slip at maximum stress is assumed constant for all temperatures, which is consistent with previous models [9,10,14]. The generalized relationship bond stress-slip relationship is given as:

$$\boldsymbol{\tau_{b,T}} = \begin{cases} \boldsymbol{\tau_{max,T}}\left(\frac{s}{s_1}\right) & \mathbf{0 \le s \le s_1} \\ \boldsymbol{\tau_{max,T}} & \mathbf{s_1 < s \le s_2} \end{cases} \quad (3)$$

where, $\tau_{b,T}$ represents bond stress, s represents slip in mm, s_1 represents slip at maximum bond stress (1 mm for NSC and 0.5 mm for HSC) and s_1 represents ultimate slip (3 mm for NSC and 2 mm for HSC) [14]. The bond strength at room temperature is calculated using the generalized expression proposed by Aslani and Samali [14].

FINITE ELEMENT MODEL

To illustrate the influence of interfacial bond between steel rebar and concrete on response of RC beams under fire conditions, a finite element model was developed using general purpose finite element program ABAQUS [11]. This model is employed to study the response of a typical RC beam exposed to fire using the proposed models, for both NSC and HSC.

Input parameters and discretization

Various input parameters such as geometric characteristics of the beam, load distribution, boundary conditions, fire scenarios and high temperature material properties are required to carry out different stages of fire resistance analysis. The load distribution and boundary conditions of the beam are applied at the beginning of the analysis and maintained constant during fire exposure.

Two sub-models are needed to carry out fire response analysis of RC beams, namely, structural and thermal model. The structural model utilizes C3D8 (8 node linear brick) element for discretizing concrete while longitudinal reinforcement and stirrups were discretized using T3D2 (truss) element available in ABAQUS library. A damage based plasticity model defined within the framework of ABAQUS was used to model non-linear behavior of concrete. The constitutive definition of reinforcing steel was based on a rate independent metal plasticity model with isotropic hardening available in ABAQUS [11].

For the thermal model, the concrete section is discretized using DC3D8 element (8 node linear brick element) and the steel reinforcement and stirrups are discretized using DC1D2 element (2 node link element) with nodal temperature as the only active degree of freedom.

Modelling interfacial bond

In the present study, the interfacial bond between concrete and reinforcing steel is taken into account using zero thickness bond-link elements consisting of two orthogonal springs to transfer shear and normal forces in the transition zone between rebar and concrete. The force-displacement relationship of the non-linear bond-link element is derived for different cases based on the proposed relationship in the current study (Eq. 1-3). A discretized view of the beam is depicted in Fig. 4.

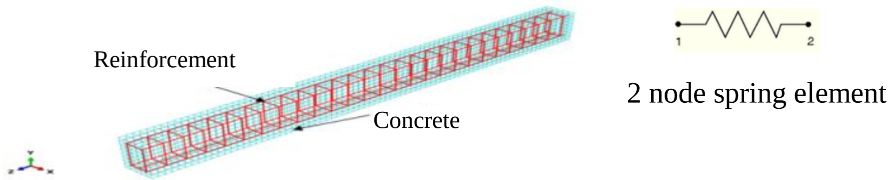

Figure 4. Discretized view of the selected beam for numerical simulation

Output results and failure criteria

Displacement, stress and temperature fields are the primary output variables that are generated during different stages of analysis. During fire resistance analysis, the output from the thermal analysis, namely nodal temperatures, is applied as a thermal body load on the structural model to evaluate the mechanical response of RC beam under fire exposure. Also, temperatures experienced at each node during thermal analysis are used to evaluate temperature dependent mechanical properties of reinforcing steel, concrete and the interfacial bond.

Fire resistance is evaluated from the output results based on thermal, strength failure criteria according to ASTM E119. A deflection or rate of deflection criteria, suggested by BS 476, is also employed to assess failure of the beam based on the displacement profile obtained for the beam during fire exposure.

QUANTIFYING EFFECT OF BOND DEGRADATION ON FIRE RESISTANCE

To establish the validity of the numerical model, one of three identical RC beams tested under fire exposure at Tianjin Fire Research Institute, China [15], was selected. The details of the beam are presented in Fig. 5.

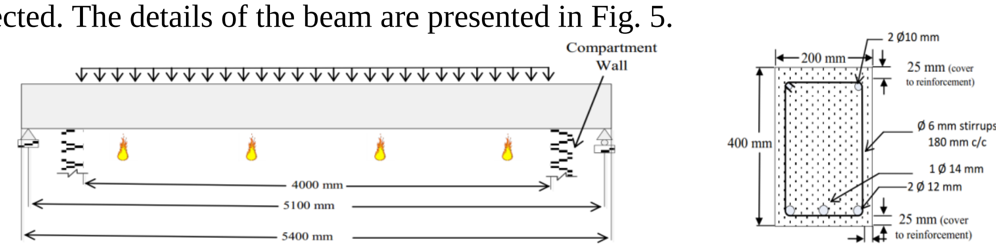

(a) Elevation (b) Cross-section

Figure 5. Dimensions, loading and reinforcement details of RC beams selected for validation.

Model validation

Predictions from the model are compared with measured response parameters from fire tests in Fig. 6a-b. A comparison of predicted temperatures (Fig. 6a) at various locations in the beam with test data indicates a close agreement, except during the first 40 minutes of fire exposure. During first 40 minutes, the temperature at 100 mm from the bottom face is somewhat underestimated. This is due to migration of moisture towards inner part of the beam, which has not been modeled explicitly.

Furthermore, experimentally measured mid-span deflections and predictions from FE model are depicted in Fig. 6b. A close examination of the predicted response against test data indicates that the developed model is capable of capturing the response, as well as failure of the RC beam, under fire exposure with sufficient accuracy.

Effect of temperature induced bond degradation

Results from the FE model are plotted in Fig. 6b to illustrate the effect of temperature induced bond degradation on fire resistance of RC beams. The three predicted curves in Fig. 6b correspond to three different assumptions for the bond behavior between steel and concrete: (a) perfect bond; (b) bond-slip model proposed in the current study for NSC bond degradation with temperature, and (c) lower-bound bond-slip model proposed by Gao et al. [10].

It can be seen that different assumptions for interfacial bond between rebar and concrete has an influence on the fire response of RC beams. The fire resistance of RC beam is reduced by almost 10% when temperature dependent bond slip is included. Significant difference occurs in the predicted response in the two cases after approximately 60 minutes or when rebar temperature exceeds 400°C. This can be attributed to the nature of bond stress-slip relationships incorporated in the model, which assume significant loss in bond beyond 400°C. Furthermore, it should be noted that although fire resistance predicted by Gao et al. [10] is similar to the predictions made in the current study, the deflection profile is markedly different. This clearly infers that the nature of adopted bond stress-slip relationships has an influence on the global response of an RC beam under fire exposure.

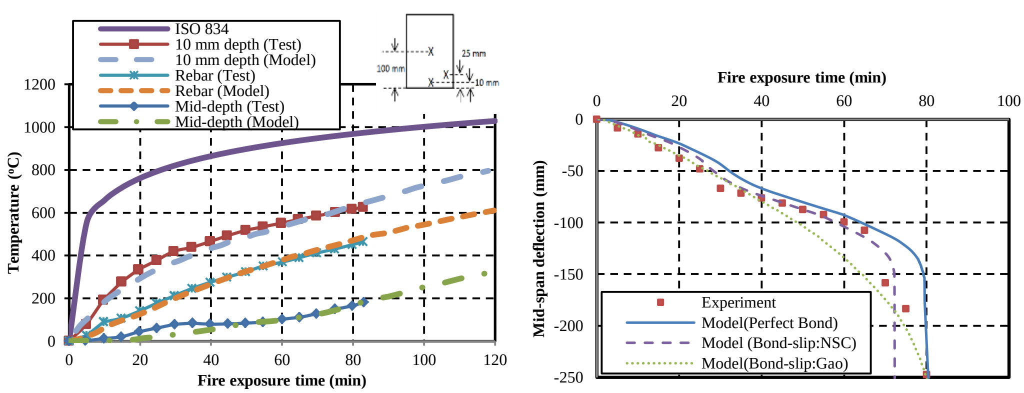

(a) Predicted and measured temperatures at various locations

(b) Predicted and measured mid span deflections for different bond conditions

Figure 6. Comparisons of the RC beams tested by Wu et al. [15] and results using numerical analysis.

SUMMARY AND CONCLUSIONS

The main findings from experimental and numerical analysis presented are:

- Interfacial bond between reinforcement and concrete deteriorates significantly at temperatures above 400^{o}C; more so for high strength concrete, wherein the rate of degradation is much faster than NSC.
- Preliminary bond tests using DTP specimens at high temperatures indicate a faster rate of bond degradation with temperature than conventional pull-out tests, owing to presence of longitudinal stresses in the concrete surrounding pull-out rebar.
- A simplified bi-linear relationship proposed to account for temperature induced bond degradation in RC members.
- Interfacial bond plays a crucial role on fire resistance of RC beams. Accounting for temperature induced bond degradation will lead to lower fire resistance prediction by about 10 %. The adopted bond stress-slip relationship has significant influence on global response of the RC beam.

ACKNOWLEDGEMENT

The authors wish to acknowledge the support of United States Agency for International Development (through Pakistan-US Science and Technology Cooperative Program grant PGA-2000003665) and Michigan State University for undertaking this research. Any opinions, findings, conclusions, or recommendations expressed in this paper are those of the author and do not necessarily reflect the views of the institution.

REFERENCES

[1] Morley P, Royles R. The influence of high temperature on the bond in reinforced concrete. Fire Saf J 1980;2:243-55.

[2] Kodur VKR, Agrawal A. Critical Factors Governing the Residual Response of Reinforced Concrete Beams Exposed to Fire. Fire Technol 2015.

[3] Kodur VKR, Agrawal A. An approach for evaluating residual capacity of reinforced concrete beams exposed to fire. Eng Struct 2016;110:293-306.

[4] Pothisiri T, Panedpojaman P. Modeling of bonding between steel rebar and concrete at elevated temperatures. Constr Build Mater 2012;27:130-40.

[5] Haddad RH, Abendeh RM. Effect of thermal cycling on bond between reinforcement and fiber reinforced concrete. Cem Concr Compos 2004;26:743-52.

[6] Haddad RH, Al-Saleh RJ, Al-Akhras NM. Effect of elevated temperature on bond between steel reinforcement and fiber reinforced concrete. Fire Saf J 2008;43:334-43.

[7] Kodur VKR, Dwaikat M. A numerical model for predicting the fire resistance of reinforced concrete beams. Cem Concr Compos 2008;30:431-43.

[8] Kodur VKR, Dwaikat M, Raut N. Macroscopic FE model for tracing the fire response of reinforced concrete structures. Eng Struct 2009;31:2368-79.

[9] Huang Z. Modelling the bond between concrete and reinforcing steel in a fire. Eng Struct 2010;32:3660-9.

[10] Gao WY, Dai JG, Teng JG, Chen GM. Finite element modeling of reinforced concrete beams exposed to fire. Eng Struct 2013;52:488-501.

[11] Hibbitt, Karlsson & Sorensen I. ABAQUS standard user's manual 2012.

[12] Haddad RH, Shannis LG. Post-fire behavior of bond between high strength pozzolanic concrete and reinforcing steel. Constr Build Mater 2004;18:425-35.

[13] Ulaga T, Vogel T. The bi-linear stress slip model: Theoretical background and significance. In: Tan KH, editor. 6th Int. Symp. Fibre-Reinforced Polym. Reinf. Concr. Struct., World Scientific; 2003, p. 8-10.
[14] Aslani F, Samali B. Predicting the bond between concrete and reinforcing steel at elevated temperatures. Struct Eng Mech 2013;48:643-60.
[15] WU H, Lie T, Hu J. Fire resistance of beam-slab specimens-experimental studies. Canada: 1993.

Modelling of Bond-slip between Prestressed Strands and Concrete at Elevated Temperatures

JAMAL KHALAF and ZHAOHUI HUANG

ABSTRACT

In this paper a new analytical model has been developed to simulate the average bond stress-slip relationship between strand and concrete for prestressed concrete structural members. Two different bond-slip curves have been proposed to represent the bond-slip characteristics for the three-wire and seven-wire strands. The model is able to take into account the type of strand surface, smooth or indented. The degradation of materials and bond characteristic at elevated temperatures are also considered in the model. The proposed model is validated against previous experimental results at ambient and elevated temperatures.

1. INTRODUCTION

Prestressed concrete (PC) construction has obtained wide popularity in current building construction. PC beams can be constructed by utilizing unbounded or bonded strands. For bonded PC beams, the force is transferred from strand to concrete through end anchors, together with the bond between strand and concrete. Bonded beams are more robust structural members at ambient temperature. However, previous research indicated that compared to normal reinforcing steel, prestressed steel wires are more sensitive to elevated temperatures due to the stress level in prestressing wires is very high.

At present, a number of investigations has been conducted to study the bond behaviour between prestressed strands and concrete at ambient temperature [1-3]. However, there are very limited researches conducted for investigating the bond-slip characteristic between prestressed strands and concrete at elevated temperatures. Hence, the main objective of this paper is to develop a robust model for modelling the bond-slip characteristic between prestressed strands and concrete under fire conditions.

Jamal Khalaf & Zhaohui Huang, Department of Mechanical, Aerospace and Civil Engineering, Brunel University, Uxbridge, Middlesex, UB8 3PH, UK.

2. ANALYTICAL MODEL

When concrete is casted around a strand in prestressed concrete structures, the concrete forms an envelope or sleeve surrounding the strand. The hardened concrete mimics the shape of the strand. When the strand is pulled through the concrete, movement is resisted by the concrete keys acting on the outside wires of the strand. As shown in Figure 1, this resistance is called mechanical interlocking. The mechanisms that contribute to the bond strength between prestressed steel and surrounding concrete are chemical adhesion, friction and mechanical interlocking. The mechanical interlocking is the largest contributor to the bond strength.

When the cracks are formed in the concrete surrounding a strand, the strand's slip is occurred for some small finite distance on either side of the crack to preserve compatibility of the strand. When the bond's slip is occurred, the mechanical interlocking is activated by the reaction of the interlocking of outside wires with the concrete envelope. The bond's slip is caused mainly by the crushing of the concrete in front of the strand's ridges. The high pressure on the concrete in front of the ridges causes tensile stresses in the concrete surround the strand, which in turn create the internal inclined cracks. These inclined cracks are initiated at relatively low bond stresses at the point of contact between the strand and concrete. With increasing induced slip, the concrete in front of the ridges will be crashed; then, the shear cracks in the concrete keys between strand ridges are initiated. At maximum bond resistance, these concrete keys are sheared off [4].

In the proposed model, the shear force resistance of the concrete in front of strand ridges V_c (as shown in Figure 1) can be calculated as:

$$V_c = v_c A_{sh} n \tag{1}$$

Where, v_c is the shear strength of the shear keys in the concrete mass; n is the number of the outer wires and A_{sh} is the shear area of the cracked surface, which is the area of the concrete keys between two ridges of the strand and equal to the diameter of the outer wires d_w by the length of wires l_w (Figure 1) as:

$$A_{sh} = d_w l_w \tag{2}$$

Then, the force F along the length of the wires can be found as:

$$F = F_1 + F_2 \tag{3}$$

$$F_1 = \mu V_c \tag{4}$$

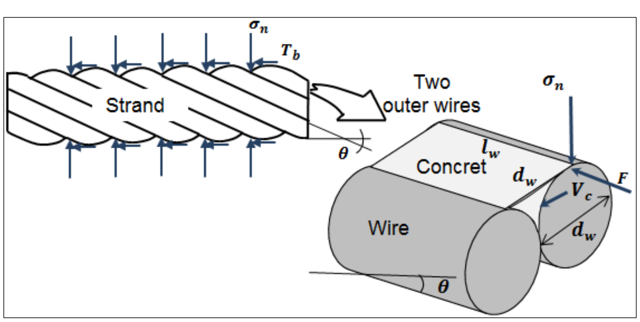

Figure 1. The interaction between the outer wires of strand and concrete.

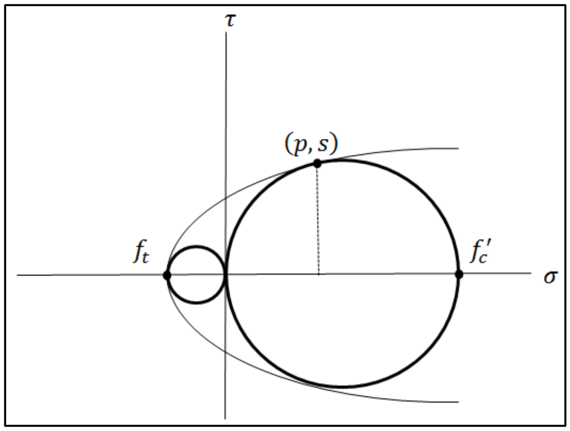

Figure 2. Parabolic Mohr envelope [7].

The second part of bond stress is achieved by the cohesion and friction between strand and concrete as:

$$F_2 = (0.6\pi d_w) l_w (C + \mu\sigma_n) n \tag{5}$$

Where, C is the cohesion between concrete and steel and μ is the coefficient of friction between steel and concrete. Based on References [1, 5, 6], for three-wire and seven-wire smooth strands C = 1.3 and $\mu = 0.4$; for three-wire indented strand C = 1.7 and $\mu = 0.6$; for seven-wire indented strand C = 1.6 and $\mu = 0.5$. In this proposed model, the value of μ is assumed to be the same at ambient and elevated temperatures and the cohesion C is assumed to be zero when temperature > 400^{o}C. The maximum bond force in the direction of the strand T_b is calculated as:

$$T_b = F / \cos(\theta) \tag{6}$$

Where, θ is the pitch angle of the outer wires which can be taken as θ = 9^{o} [6].

The shear strength of the concrete mass v_c in Eq. (1) should not be greater than $0.2 f_c^{'}$ [4]. The value of the shear strength of the concrete keys v_c can be calculated by using Parabolic Mohr Envelope [7]. Figure 2 shows a parabolic fit to Mohr circles for the uniaxial compression and tension test results [7]. From Figure 2, the shear strength envelope is defined as follows:

$$\tau^2 = \left[f_c^{'} - 2 f_t \left(-1 + \sqrt{1 + \frac{f_c^{'}}{f_t}} \right) \right] (\sigma_n + f_t) \tag{7}$$

If $\sigma_n = 0$ then

$$\tau = c = v_c = f_t \left(\frac{f_c^{'}}{f_t} + 2 - 2\sqrt{1 + \frac{f_c^{'}}{f_t}} \right)^{1/2} \tag{8}$$

Where: τ is the peak shear strength ($v_c = \tau$); $f_c^{'}$ is the concrete compressive strength; f_t is the concrete tensile strength; σ_n is the normal stress perpendicular to strand axes. If $\sigma_n \neq 0$, which means that there is a pressure effect which is normal to the axes of the strand inside concrete, σ_n can be found based on the stress-strain relation defined in the Eurocode 2 for non-linear structural analysis as $\sigma_n = \sigma_c$, that is:

$$\sigma_n = \sigma_c = f_{cm} \frac{k\eta - \eta^2}{1 + (k-2)\eta} \tag{9}$$

$$\eta = \varepsilon_c / \varepsilon_{c1} \tag{10}$$

$$\varepsilon_{c1} = 0.7 f_{cm}{}^{0.31} \leq 2.8 \tag{11}$$

Where, ε_{c1} is the strain at peak stress; ε_c is the concrete strain defined in Eq. (15);

$$k = 1.05 E_{cm} \,|\varepsilon_{c1}| / f_{cm} \tag{12}$$

Normal pressure σ_n in prestressed concrete can be generated from the effect of Poisson ratio (Hoyer effect). This is due to the released prestressed strand after concrete casting, the nominal diameter of the strand is increased due to the effect of Poisson ratio. This radial expansion generates normal stresses in the concrete surrounding the strand. These stresses give extra confinement to the strand and result in increasing of the bond stress between the strand and concrete. The expansion of the strand diameter can be calculated as:

$$\frac{P_1}{A_s E_s} = \varepsilon_{s1} \tag{13}$$

$$\frac{P_2}{A_s E_s} = \varepsilon_{s2} \tag{14}$$

$$\varepsilon_c = \varepsilon_{sl} = \frac{P_1 - P_2}{A_s E_s} v = |\varepsilon_{s1} - \varepsilon_{s2}| v \tag{15}$$

Where, P_1 is the initial tension force on the strand, usually to be $0.75 f_u$ (0.75 ultimate stress); P_2 is the force after the force of strand to be released; A_s is the nominal area of strand; E_s is the modulus of elasticity of strand; v is the Poisson ratio of steel; ε_{s1} is the first strain of strand at P_1; ε_{s2} is the second strain of strand at P_2; ε_{sl} is the lateral strain of strand due to Poisson ratio; ε_c is the strain of concrete generated by the strand lateral pressure. As shown in Figure 3, the average bond stress-slip relationship between concrete and deformed bar defined by CEB-FIP Model code [8] has been adopted in this study.

In Figure 3, τ is the average bond stress; $\tau_{\max}$ is the maximum bond stress; S is the slip between strand and concrete. In current model, $\tau_{\max}$ can be calculated as:

$$\tau_{\max} = \frac{T_b}{A_b} \tag{16}$$

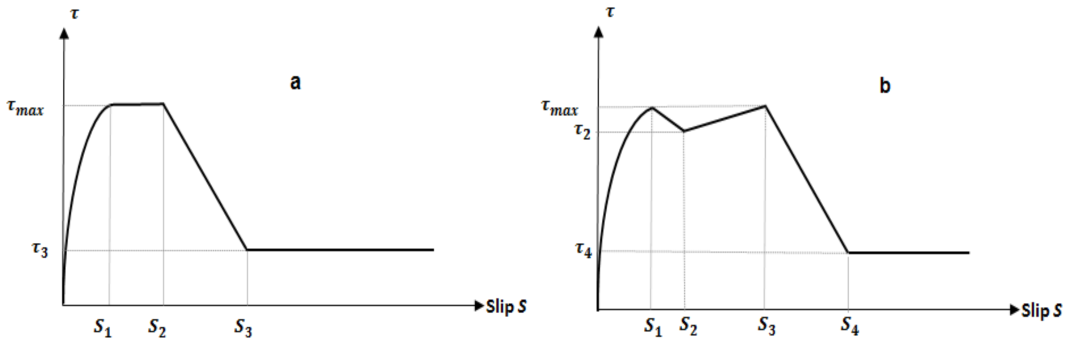

Figure 3. Bond stress-slip curves used: (a) Three-wire smooth and indented strands, and seven-wire indented strands; (b) Seven-wire smooth strands.

Where, T_b is the maximum bond force which can be calculated from Eq. (6) and A_b is the contact area between the strand and concrete as:

$$A_b = \pi \, d_s \, L_b \tag{17}$$

Where, d_s is the nominal diameter of strand and L_b is the embedded length of strand.

The values of parameters S_1, S_2, S_3 and S_4 are assumed based on the statistical analysis of the experimental results from the previous researches [2, 3]. In the Figure 3(a), for three-wire smooth strand $S_1 = S_2 = 0.5$, $S_3 = 5.0$, $\tau_3 = 0.35\tau_{\max}$; for three-wire indented strand $S_1 = 1.0$, $S_2 = 3.5$, $S_3 = 5.0$, $\tau_3 = 0.65\tau_{\max}$; for seven-wire indented strand $S_1 = 1.0$, $S_2 = 3.5$, $S_3 = 6.0$, $\tau_3 = 0.35\tau_{\max}$. In the Figure 3(b), for seven-wire smooth strand $S_1 = 0.25$, $S_2 = 0.5$, $S_3 = 3.5$, $S_4 = 8.0$, $\tau_2 = 0.75\tau_{\max}$, $\tau_4 = 0.35\tau_{\max}$.

3. EFFECT OF ELEVATED TEMPERATURES

In this research the effect of high temperature on the bond characteristics is considered by taking into account the degradation of concrete properties at elevated temperatures. The compressive strength and elastic modulus of concrete at elevated temperatures are calculated based on Eurocode 2 [9]. However, the degradation of the tensile strength of concrete at elevated temperatures is calculated using the model proposed by Aslani and Bastami [10].

4. VALIDATION

There are two parts for presenting the validation of the proposed model. The first part is to validate the bond stress-slip curve at ambient temperature and the second part is to validate the bond-slip curve at elevated temperatures.

4.1. Validation of bond stress–slip curve at ambient temperature

Vázquez-Herrero et al. [2] conducted a test on the bond stress-slip between strand and concrete. In this test, a seven-wire smooth strand and a cylinder specimen of normal concrete with dimensions of 150 × 300 mm were used. The

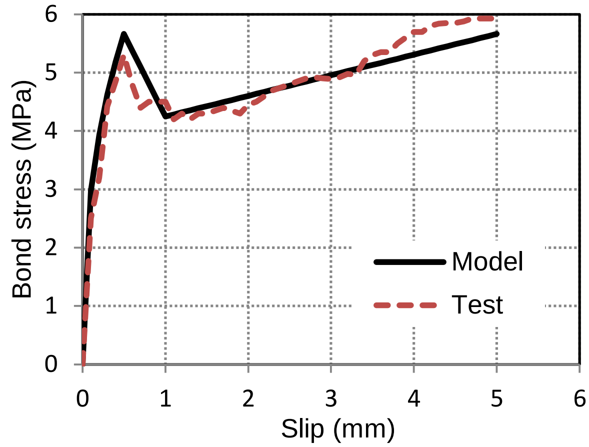

Figure 4. Comparison of predicted and tested bond stress–slip curves at ambient temperature [2].

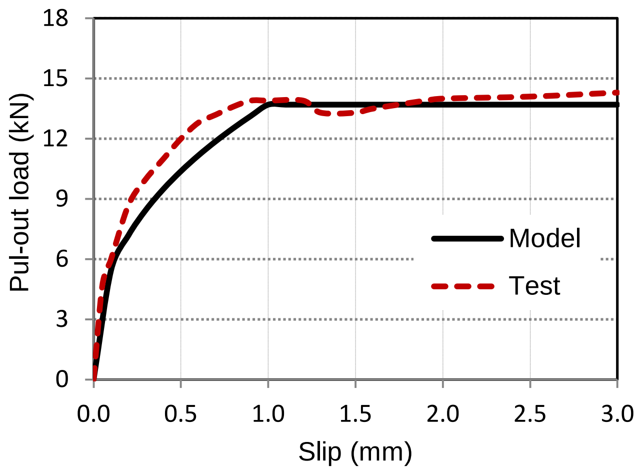

Figure 5. Comparison of predicted and tested pull-out load-slip curves at ambient temperature [3].

tested material properties of concrete are: compressive strength = 49 MPa, tensile strength = 2.9 MPa. The properties of seven-wire smooth strand are: nominal diameter = 15.2 mm, average elastic modulus = 197.4 GPa, breaking strength = 260 kN, and cross section area = 142 mm^2. Figure 4 shows the predicted bond stress-slip curve together with the test results. It is evident that good agreement was achieved between the predictions and test results.

A pull-out test of seven-wire indented strand was conducted by Lundgren [3] to investigate the bond behaviour of this type strand. The diameter of the strand is 12.9 mm. The tested concrete properties are: compressive strength = 63 MPa and Young's modulus = 36 GPa. Figure 5 presents the comparison of predicted pull-out load versus bond slip curve against the test results. It can be seen that good agreement between the predictions and test results was achieved.

Gustavson [11] studied the bond characteristics of three-wire smooth and indented strands. In this study two types of bond test were conducted which were pull-out and push-in tests. For the push-in test, the indented strand used was 3×3.0 mm EU 138/6 with nominal diameter of 6.5 mm. The strand was prestressed with a

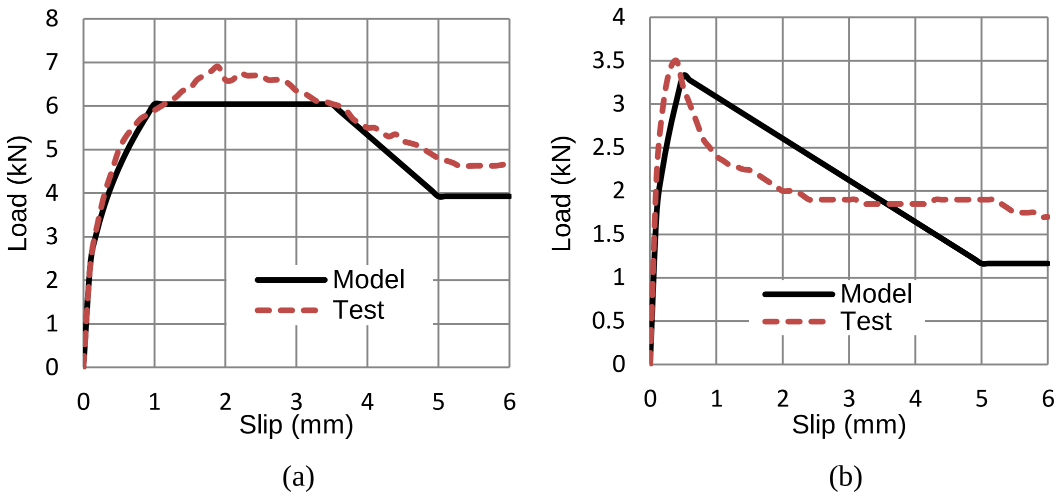

Figure 6. Comparison of predicted and tested load–slip curves at ambient temperature: (a) Push-in test; (b) Pull-out test.

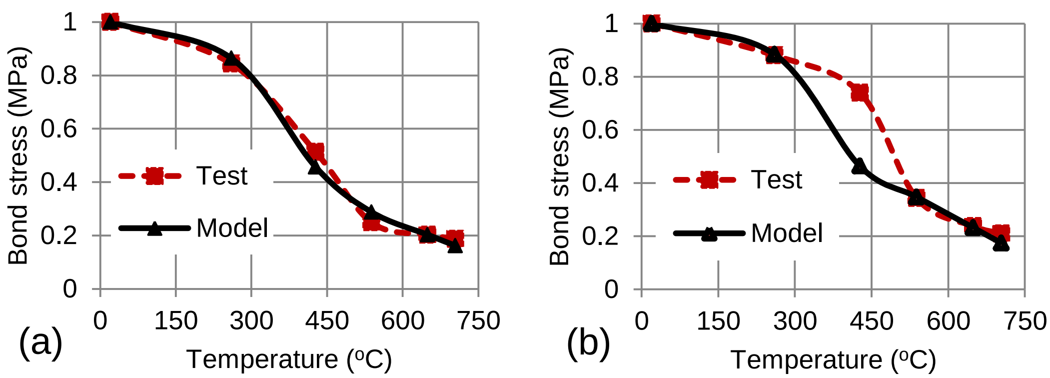

Figure 7. Comparison of predicted and tested bond stresses with different concrete compressive strengths at elevated temperatures: (a) 77.4 MPa; (b) 98.8 MPa.

force of 28 kN, corresponding to a prestress of 1320 MPa. The tested concrete compressive strength was 25 MPa. For the pull-out test, the smooth strand with 6.5 mm diameter was used. The tested concrete compressive strength was 55 MPa. Figure 6(a) shows the comparison of predicted and tested load–slip curves for the push-in test. Figure 6(b) illustrates the comparison of predicted and tested load-slip curves for the tests. It is clear that reasonable agreements were obtained for both tests.

4.2. Validation of bond stress–slip characteristic at elevated temperatures.

Moore [12] studied the flexural bond-slip characteristics of strands at elevated temperatures. Seven-wire low relaxation smooth strands with grade 270 were used in this investigation. The diameter of the strands was 12.7 mm. Two types of concrete with different compressive strengths were used in the tests. They were 77.4 MPa and 98.8 MPa, respectively. Pull-out specimens were $152.4 \times 152.4 \times 101.6\ mm$ with embedded length of 101.6 mm. The specimens were heated with a heating rate of 4.4 ^{o}C/min. Six temperatures of 20, 260, 427, 538, 649 and 704 ^{o}C were adopted. The specimens were heated until the designated temperatures were reached. Figure 7 shows the comparisons of the bond degradation at elevated temperatures between the predicted and tested results. Again, reasonable agreements were achieved.

5. CONCLUSION

This paper presents a new analytical model for predicting the bond stress-slip between strands and concrete in prestressed concrete at elevated temperatures. The developed model is based on the mechanical interlocking between the prestressed strands and surrounding concrete as well as the effect of Poisson ratio (Hoyer effect). The model takes into account the variation of concrete properties and strand's geometries. The degradation of bond strength at elevated temperatures is related to the concrete material properties changed with temperature. A series of validations has been conducted using the previous tested data generated by different researchers and reasonable agreements have been achieved between the model's predictions and tested results. The model is able to predict the bond-slip characteristic between concrete and smooth or indented three-wire and seven-wire strands at elevated temperatures. The model can be integrated into the finite element software for modelling of prestressed concrete structures under fire conditions.

ACKNOWLEDGMENTS

The authors gratefully acknowledge the financial support of the Ministry of Higher Education and Scientific Research of Iraqi government for this PhD project.

REFERENCES

1. Bolmsvik R. and Lundgren K. 2006. "Modelling of bond between three-wire strands and concrete," Magazine of concrete research, 58(3), 123-133.
2. Vázquez-Herrero C. and Martínez-Lage I. 2013. "Evaluation of strand bond properties along the transfer length of prestressed lightweight concrete members," Engineering Structures, 49, 1048-1058.
3. Lundgren K. 2002. "Steel-Encased Pull-Through Tests of Seven-Wire Strands," Report No. 02:13, Chalmers University of Technology, Sweden.
4. Choi O. C. and Choi H. J. 2010. "Bearing angle model for bond of fractioning bars to concrete," Korea Concrete Institute, Seoul.
5. Brown C. J., Darwin D. and McCabe S. L. 1993. "Finite element fractures analysis of steel-concrete bond," SM Report No. 36, University of Kansas Center for Research.
6. CEB-FIP 2000, "Bond of reinforcement in concrete", Bulletin 10.
7. Curtis D. D. 2011. "Estimated shear strength of shear keys and bonded joints in concrete dams", 31st Annual USSD Conference, San Diego, California, 11-15.
8. CEB-FIP, fib Bulletin 55, Model code 2010, First complete draft, Volume 1.
9. EN 1992-1-2. Eurocode 2. 2004. "Design of Concrete Structures – Part 1-2: general rules structural fire design". British Standards Institution, London.
10. Aslani F and Bastami M. 2011. "Constitutive relationships for normal-and high-strength concrete at elevated temperatures", ACI Material Journal, 108(4), 355-64.
11 Gustavson R. 2004. "Experimental studies of the bond response of three-wire strands and some influencing parameters," Materials and Structures, 37, 96-106.
12. Moore W. L. 2008. "Performance of fire-damaged prestressed concrete bridges," Masters Theses, Missouri University of Science and Technology.

Performance Comparison Between Rectangular and Circular Cross-section Columns in Fire Situation, Using Tabulated Methods

ALZIRA RAMALHO and MIGUEL GONÇALVES

ABSTRACT

It is presented, in this study, a performance comparison between rectangular and circular cross-section' columns in fire situation, using tabulated methods. For this purpose it appealed to the statistical analysis of the fire behaviour of 13129 columns inserted in the structures of 63 buildings carefully selected so that it corresponded to a representative sample of the licensed buildings in Portugal, covering different types of occupation. From these columns, 12243 presented a rectangular cross-section and 886 a circular cross-section. The fire resistance required for these columns was analysed using the methods presented in the form of tables in EN 1992-1-2 [1]. It was found that these methods were not applicable to a large number of columns (up to 45,8% in rectangular columns and 45,6% in circular columns) and, when applicable, led to a reduced number of columns that checked the fire resistance (up to 24,6% in rectangular columns and 36,5% in circular columns). It also concludes that the application of these methods to the circular columns leads to substantially less conservative results than when applied to the rectangular columns.

INTRODUCTION

The fire behaviour of 12243 rectangular and 886 circular cross-section concrete columns was studied, applying the methods presented in the form of tables in EN 1992-1-2 [1]. The values of the reduction factor for load combination, η_{fi}, and of the load level at normal temperature, n, were calculated, to know the most frequent project values of these parameters. The fire resistance of those columns was analysed, considering η_{fi} with project values and η_{fi}=0,7, a conservative simplification pointed in that European Standard, and the consequences of adopting this simplification were studied. It was also considered the concrete cover provided in the respective structures designs and the minimum concrete cover determined considering the requirements pointed in EN 206-1/2000 [2] and in EN 1992-1-1 [3].

Maria Alzira Ramalho
Miguel Chichorro Gonçalves, Building Division, Faculty of Engineering, University of Porto, Rua Doutor Roberto Frias. 4200-465 Porto, Portugal.

ANALYSED COLUMNS CROSS-SECTIONS

Considering the analysed columns, 70% have a rectangular cross-section, 24% a quadrangular cross-section and 6% a circular cross-section. The percentages of the different columns cross-sections provided in the projects are shown in Figure 1 (a) to the quadrangular columns, in Figure 1 (b) to the circular columns and in Figure 2 to the rectangular columns. The percentages are calculated assuming the total number of columns (13129). In Figure 2 the columns with cross-sections that presented percentages lower than 1% of the universe of rectangular columns are inserted into "Others".

DISTRIBUTION OF THE ANALYZED COLUMNS BY FIRE RESISTANCE LEVELS

The distribution of the columns by fire resistance levels is shown in Figure 3. The quadrangular section columns were inserted in the rectangular columns' group. As it can be seen in Figure 3 (a), the largest number of rectangular columns are inserted in the fire resistance level R90 (44,6%), followed by level R120 (31,7%) and R60 (19,2%). For circular columns, Figure 3 (b), the higher percentage is at level R120 (58,8%), followed by levels R90 (26,3%) and R60 (14,0%). Figure 4 shows the distribution of the 12243 rectangular columns by fire resistance levels, for each value of the smallest dimension of its cross-section, *b*, and Figure 5 the distribution of the 886 circular columns by fire resistance levels, for each value of the diameter of its cross-section, Φ.

METHOD A APPLICATION

The project values of the reduction factor, η_{fi}, for each value of the combination factor, ψ_1, are shown in Figure 6. Figure 7 shows the percentage distribution of the 114 types of buildings use (use-types) for the different values of η_{fi}. The results of Method A application to the rectangular columns are shown in Figure 8 and to the circular columns in Figure 9.

METHOD B APPLICATION

The design values of the load level at normal temperature conditions, *n*, are shown in Figure 10 for the rectangular columns and in Figure 11 for the circular columns. The results of Method B application to the rectangular columns are shown in Figure 12 and to the circular columns in Figure 13.

METHOD C APPLICATION

The results of Method C application to the rectangular columns are shown in Figure 14 and to the circular columns in Figure 15.

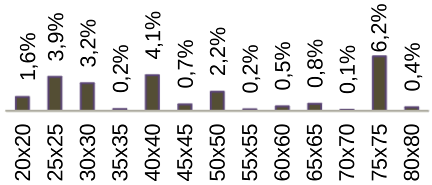

(a) Quadrangular sections.

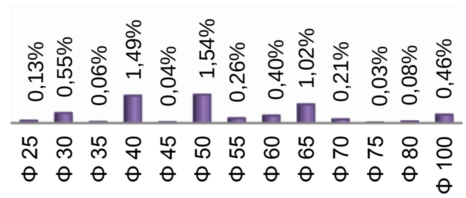

(b) Circular sections.

Figure 1. Quadrangular and circular columns' cross-sections [cm].

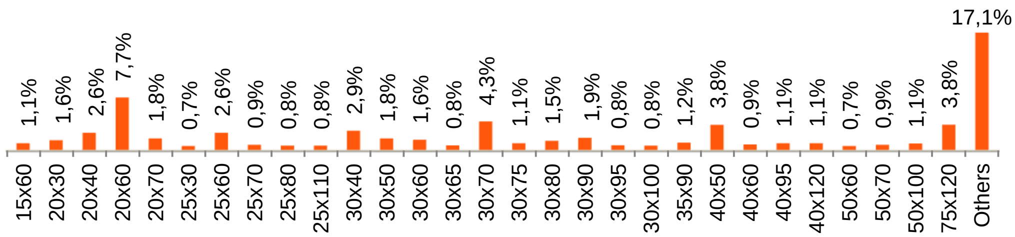

Figure 2. Rectangular columns' cross-sections [cm].

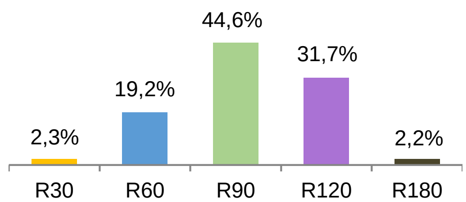

(a) Rectangular cross-section columns (12243).

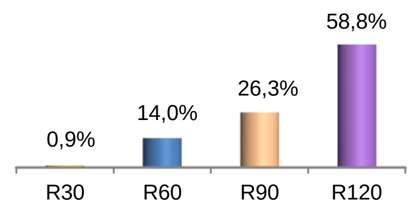

(b) Circular cross-section columns (886).

Figure 3. Distribution of the 12243 rectangular columns and the 886 circular columns by fire resistance levels.

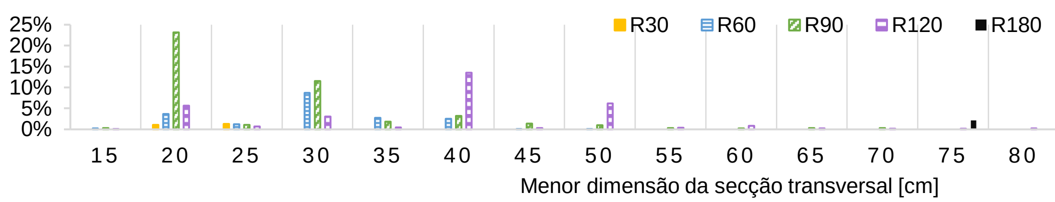

Figure 4. Distribution of the 12243 rectangular columns by fire resistance levels, in function of their width, *b*.

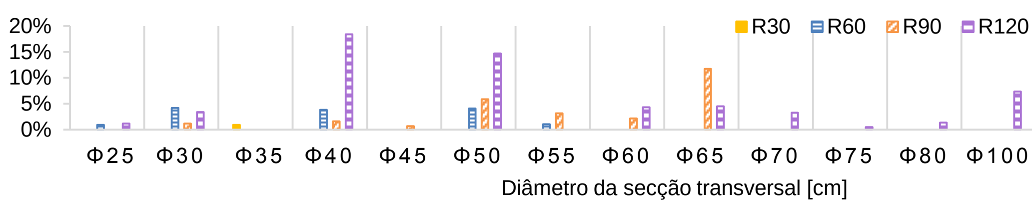

Figure 5. Distribution of the 886 circular columns by fire resistance levels, in function of their diameter, *Φ*.

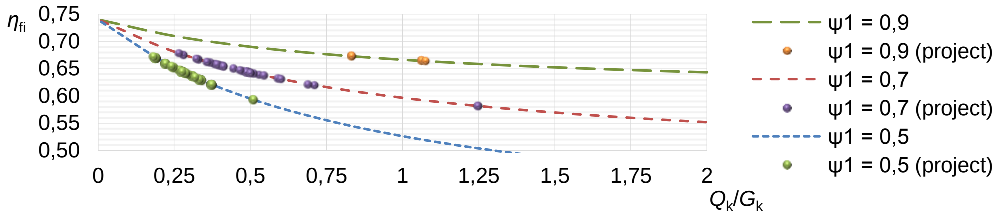

Figure 6. Project values of the reduction factor for load combination, η_{fi}, inserted in Figure 2.1 of EN 1992-1-2 [1].

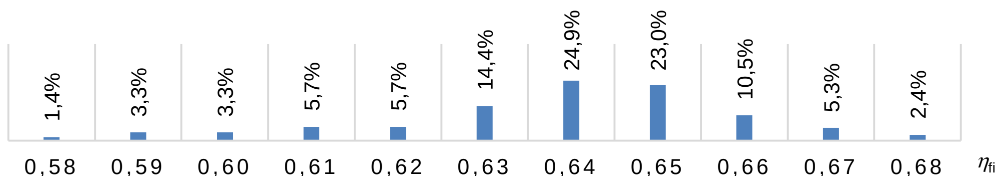

Figure 7. Percentage distribution of use-types by the different values of η_{fi}.

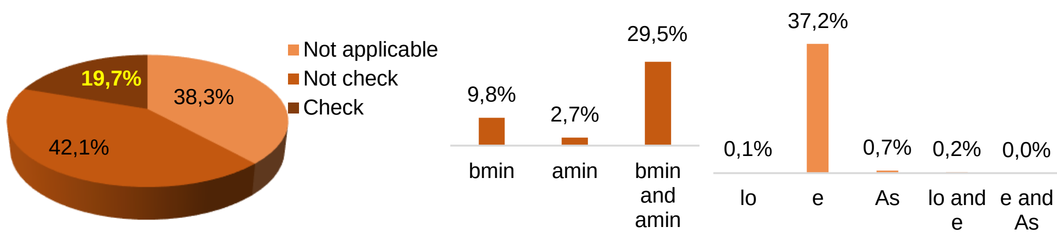

(a) Check, not check, not applicable. (b) Not check. (c) Not applicable.

Figure 8. Results of Method A application to the analysed rectangular columns, considering project values of η_{fi} and the minimum normative concrete cover.

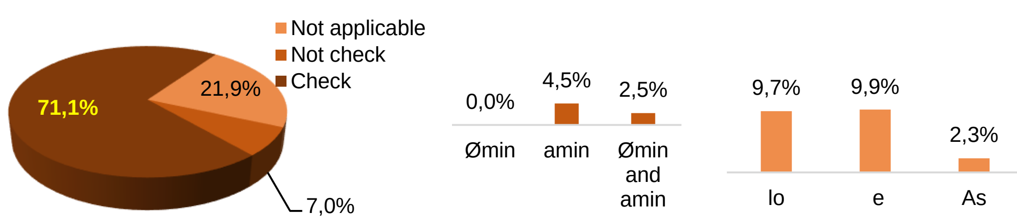

(a) Check, not check, not applicable. (b) Not check. (c) Not applicable

Figure 9. Results of Method A application to the analysed circular columns, considering project values of η_{fi} and the minimum normative concrete cover.

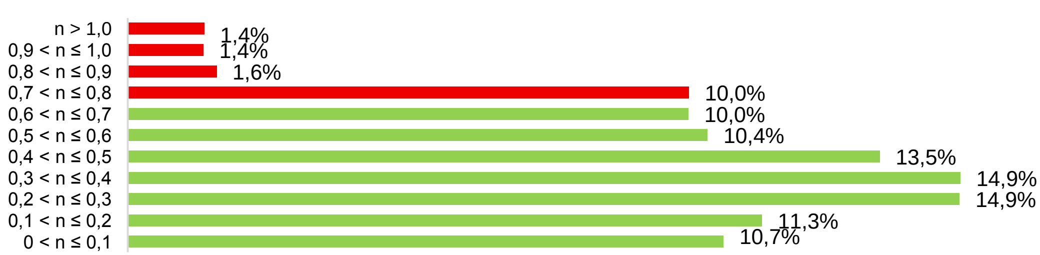

Figure 10. Distribution of rectangular columns by the different intervals of *n*.

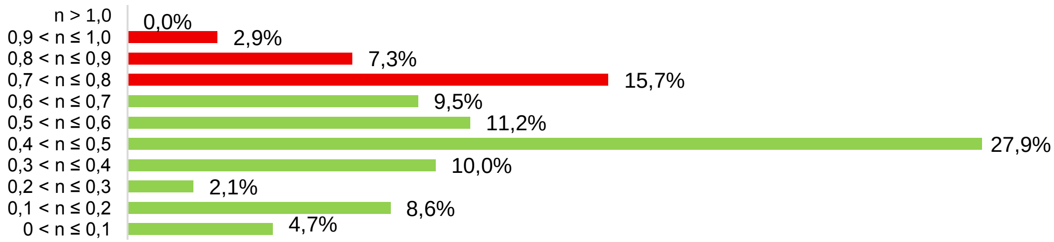

Figure 11. Distribution of circular columns by the different intervals of *n*.

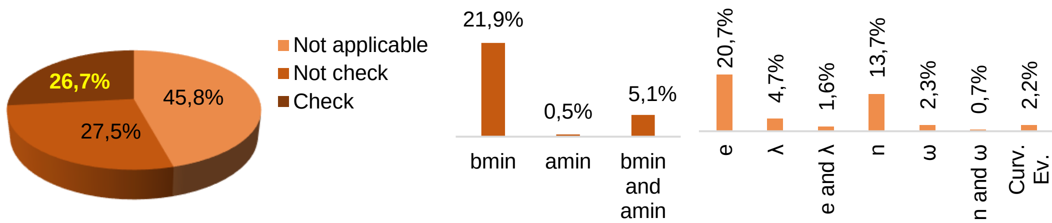

(a) Check, not check, not applicable. (b) Not check. (c) Not applicable.

Figure 12. Results of Method B application to the analysed rectangular columns, considering project values of η_{fi} and the minimum normative concrete cover.

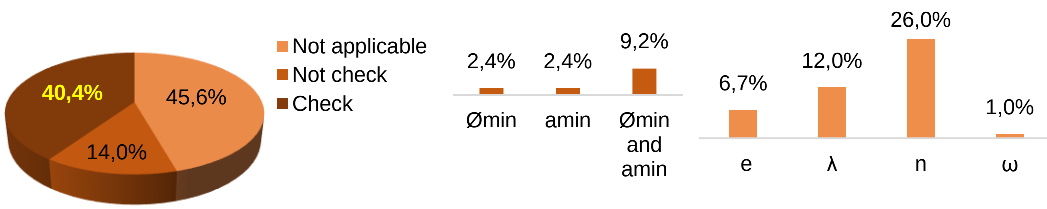

(a) Check, not check, not applicable. (b) Not check. (c) Not applicable.

Figure 13. Results of Method B application to the analysed circular columns, considering project values of η_{fi} and the minimum normative concrete cover.

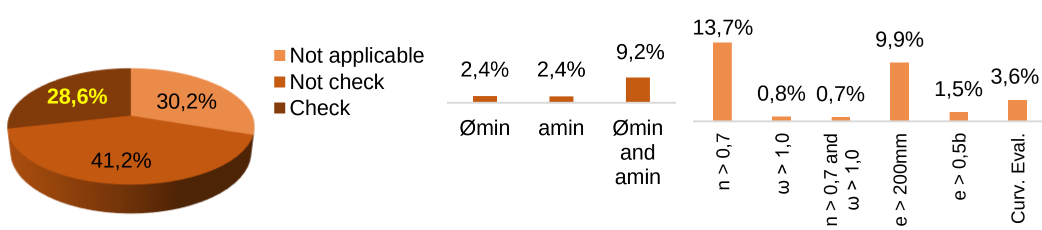

(a) Check, not check, not applicable. (b) Not check. (c) Not applicable.

Figure 14. Results of Method C application to the analysed rectangular columns, considering project values of η_{fi} and the minimum normative concrete cover.

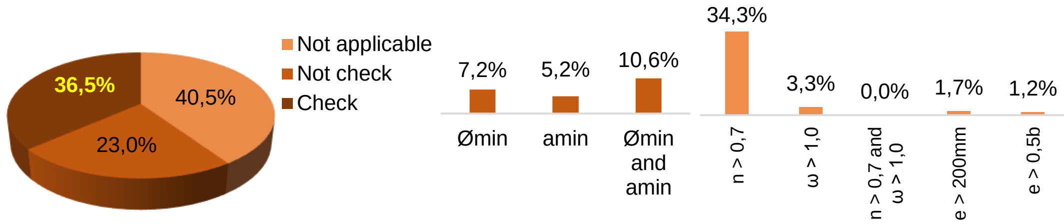

(a) Check, not check, not applicable. (b) Not check. (c) Not applicable.

Figure 15. Results of Method C application to the analysed circular columns, considering project values of η_{fi} and the minimum normative concrete cover.

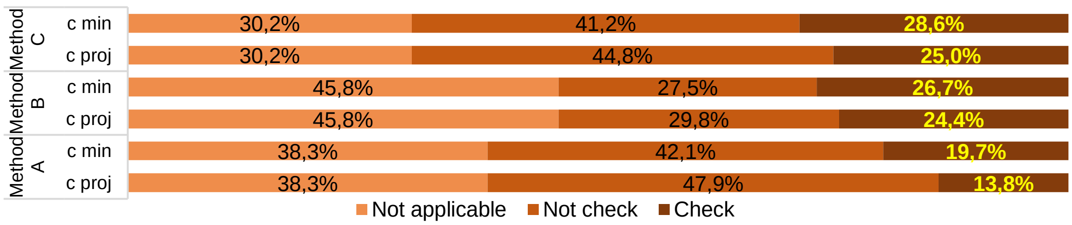

Figure 16. Results of the three methods application to the rectangular columns, considering project values of η_{fi} and, for the calculation of a, the project cover, c_{proj}, and the minimum concrete cover, c_{min}.

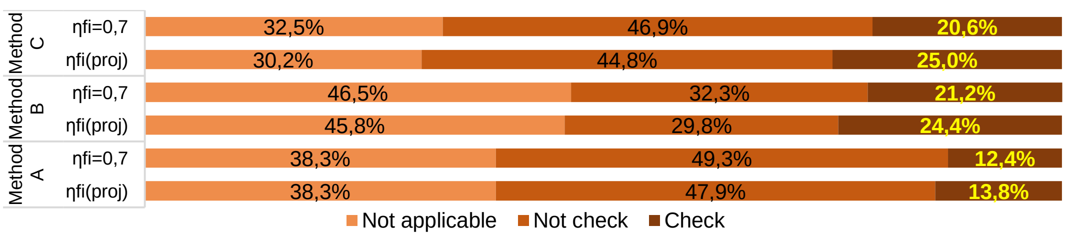

Figure 17. Results of the three methods application to the rectangular columns, considering project cover, project values of η_{fi} and η_{fi}=0,7.

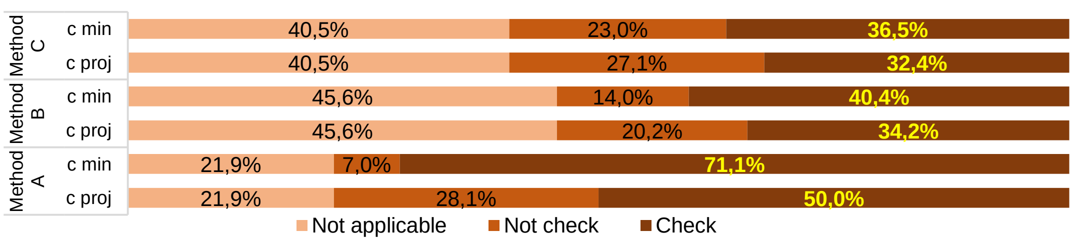

Figure 18. Results of the three methods application to the circular columns, considering project values of η_{fi} and, for the calculation of a, the project cover, c_{proj}, and the minimum concrete cover, c_{min}.

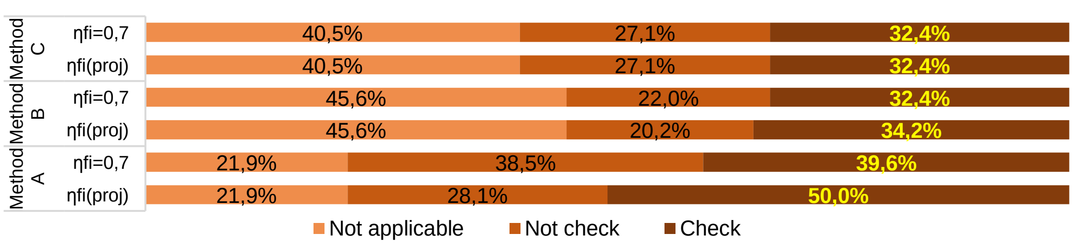

Figure 19. Results of the three methods application to the circular columns, considering project cover, project values of η_{fi} and η_{fi}=0,7.

CONCLUSIONS

Observing the figures presented, the following conclusions can be formed:

- Considering project values of η_{fi} and the minimum concrete cover, 19,7% of the rectangular columns check the required fire resistance when using Method A, 26,7% when using Method B and 28,6% when using Method C. For circular columns, 71,1% check the fire resistance when using Method A, 40,4% when using Method B and 36,5% when using Method C;

- In current buildings, the reduction factor for load combination, η_{fi}, varies between 0,58 and 0,68. Therefore, it is recommended the use of values in this range in the calculation of the initial axial load in fire situation ($N_{Ed,fi}=\eta_{fi}.N_{Rd}$), in experimental fire tests. The most frequent values are η_{fi}=0,64 (24,9% of the use-types) and η_{fi}=0,65 (23,0% of the use-types);

- The conservative simplification of considering η_{fi}=0,7 has significant repercussions in rectangular columns when using Method C (reduction in 4,4% of the columns that checked the required fire resistance) and not significant when using Method A (reduction in 1,4%). When considering the evaluation of circular columns, this simplification has very significant repercussions when using Method A (reduction in 10,4% of the columns that check fire resistance), with no impact when using Method C (Figure 17 and Figure 19);

- In rectangular columns, the most frequent values of the load level at normal temperature, n, are included in the ranges $0,2<n\leq0,3$ and $0,3<n\leq0,4$ (14,9% of columns in each range) followed by values in the range $0,4<n\leq0,5$ (13,5%). In the circular columns, the most frequent values of n are included in the range $0,4<n\leq0,5$ (27,9%), followed by $0,7<n\leq0,8$ (15,7%, in a range of values that leads to inapplicability);

- It was found that the fact of considering the minimum normative reinforcement cover, in the calculation of a, led to an increase of 5,9% in the number of rectangular columns that checked the fire resistance when Method A was applied, 3,6% with Method C and 2,3% with Method B. In the circular ones, the number of columns that verified the fire resistance increased 21,1% when Method A was used, 6,2% with Method B and 4,1% with Method C. Thus, it is considered appropriate to recommend to the structures' designers a particular attention in the definition of the cover adoption (Figure 16 and Figure 18);

- Method A, Method B and Method C leads to substantially more conservative results when applied to the rectangular columns than when applied to circular ones. In rectangular columns Method C is the one which leads to less conservative results and Method A in the case of circular columns.

REFERENCES

1. CEN, EN 1992-1-2: Eurocode 2: Design of concrete structures: Parte 1-2: General rules - Structural fire design. European Standard, December 2004.
2. CEN, EN 206-1: "Concrete - Part 1: Specification, performance, production and conformity", European Standard, December 2000.
3. CEN, EN 1992-1-1: Eurocode 2: Design of concrete structures: Parte 1-1: General rules and rules for buildings. European Standard, December 2004.

Fire Resistance of Reinforced Concrete Columns Subjected to Standard Fire—Comparison of an Advanced and a Simplified Method

MARCUS ACHENBACH, THOMAS GERNAY and GUIDO MORGENTHAL

ABSTRACT

For designing concrete columns subjected to a standard fire exposure, the Eurocode permits the use of simplified or advanced calculation methods. For the designer, the question of the respective advantages of these two types of methods arises. Which situations demand the use of an advanced method? When does a simple method provide sufficient accuracy? In this paper, laboratory tests are recalculated using Finite Element Modeling (FEM) as an advanced and Extended Zone Model (EZM) as a simple method in order to investigate these questions. The recalculations indicate that the simple EZM is of sufficient accuracy for symmetric heated columns without restraints. In contrast, the mechanical behavior of columns heated on three sides demands an advanced method such as FEM to be properly described.

INTRODUCTION

Designers who follow the Eurocode EN 1992-1-2 [1] for designing concrete members subjected to a standard fire exposure are left with several options regarding the method to apply. Among the calculation methods, they can opt for simplified methods developed for specific types of members, or for advanced methods, for instance based on Finite Element Modeling (FEM). The objective of this research is to recalculate laboratory tests on concrete columns using an advanced and a simplified method, in order to compare the respective capabilities and advantages of these methods.

Marcus Achenbach, LGA KdöR, Tillystraße 2, 90431 Nürnberg, Germany, marcus.achenbach@lga.de
Thomas Gernay, University of Liège, Allee de la Decouverte 9, 4000 Liège, Belgium, Thomas.Gernay@ulg.ac.be
Guido Morgenthal, Bauhaus Universität Weimar, Marienstraße 13, 90431 Weimar, Germany, guido.morgenthal@uni-weimar.de

Advanced FEM requires the use of proper material models for simulating the behavior of the materials at elevated temperature. The model given in EN 1992-1-2 [1] for concrete includes the transient thermal strains implicitly, which means that these strains are assumed not to depend on the stress-temperature history. This simplification has been criticized and an advanced material model with an explicit formulation for the transient thermal strains has been proposed [2]. The parameters of the proposed stress-strain curves have been chosen to match the parameters of EN 1992-1-2 under constant compression and monotonously increasing temperature. This model is called "Explicit transient creep model" (ETC). In this paper, FEM with ETC material model is used as the advanced method for the comparative analysis. It is referred to as "ETC method".

On the other hand, more simplified analysis methods are under development. The Zone Method proposed by Hertz has been extended [3] using the stress-strain curves from EN 1992-1-2, keeping the assumption that thermal strains can be neglected. The proposed method is called "Extended Zone Method" (EZM) and is suitable for the implementation in commercial design software.

APPLIED METHODS

Recalculated laboratory tests

Four columns from TU Braunschweig [4, 5], which have been heated on all sides, are used for recalculation. The pin ended columns have been subjected to a constant load $|N_0|$ with constant eccentricity e_0 and have been heated until failure. The parameters of the columns are given in Figure 1 and Table I.

To study the effect of unequal thermal strains, three tests performed by Anderberg [6] are also recalculated. The columns have been heated on three sides and the deformations of the columns in the mid span have been measured. The parameters of the tests are documented in Figure 2 and Table II.

The concepts of the applied methods are explained briefly in the following paragraphs. Detailed information on the assumptions and limits are given in the literature [2, 3].

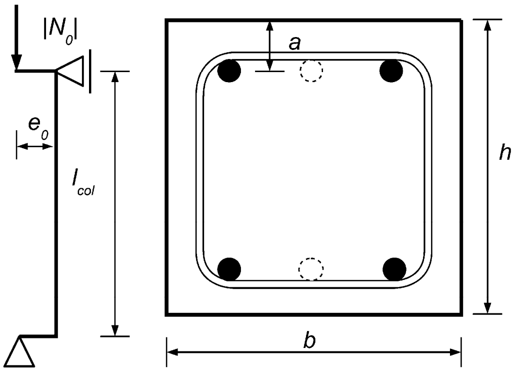

Figure 1. Structural system and cross section for the laboratory tests from TU Braunschweig

TABLE I. PARAMETERS OF TESTS FROM TU BRAUNSCHWEIG

Nr.	l_{col} (cm)	b=h (cm)	$A_{s,tot}$ (mm)	a (cm)	f_c (MPa)	f_y (MPa)	e_0 (mm)	$\|N_0\|$ (kN)	t_{exp} (min)
SFB5	476	30	6∅20	3.8	37	462	15	740	85
SFB12	376	20	4∅20	3.8	29	487	0	420	58
SFB13	376	20	4∅20	3.8	29	487	0	420	66
SFB46	470	30	6∅20	3.8	38	526	150	465	50

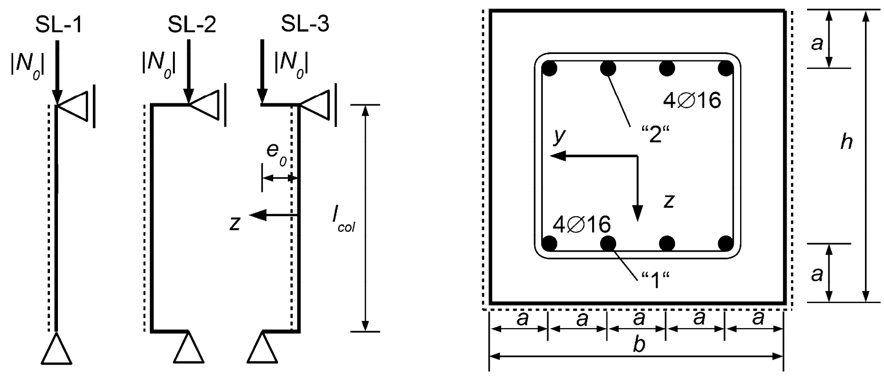

Figure 2. Structural system and cross section for the laboratory tests by Anderberg

TABLE II. PARAMETERS OF TESTS BY ANDERBERG

Nr.	l_{col} (cm)	b=h (cm)	$A_{s,tot}$ (mm)	a (cm)	f_c (MPa)	f_y (MPa)	e_0 (mm)	$\|N_0\|$ (kN)	t_{exp} (min)
SL-1	200	20	8∅16	4.0	46	453	0	900	52
SL-2	200	20	8∅16	4.0	46	453	-60	600	30
SL-3	200	20	8∅16	4.0	46	453	+60	300	120

"Explicit transient creep model" (ETC)

The stress-strain curves given in EN 1992-1-2 include transient thermal strains implicitly. The "mechanical strains" ε_m considered in the equations consist of the stress related strains ε_σ and transient thermal strains ε_{tr}. In ETC, both components are treated separately. The stress related strains ε_σ are derived from steady-state laboratory tests. Transient thermal strains ε_{tr} are indirectly obtained as the difference in strain between a steady-state test and a transient test. It is assumed that the transient thermal strains can be calculated by:

$$\varepsilon_{tr}(\theta,\sigma) = \phi(\theta)\frac{\sigma}{f_{ck}}. \tag{1}$$

The temperature dependent creeping function ϕ is derived from laboratory tests to fit the stress-strain curves of EN 1992-1-2 for a material first-time heated under constant stress. The transient thermal strains are dependent from the load history, hence the corresponding stresses and strains must be traced in the numerical analysis. The ETC model is implemented in the nonlinear finite element software SAFIR® [7], which is used for recalculation.

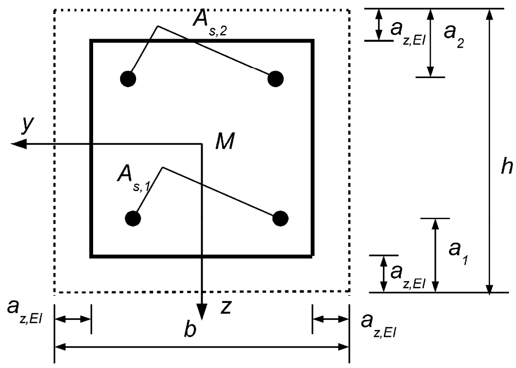

Figure 3. Cross section for the Extended Zone Method

"Extended Zone Method" (EZM)

The basic principle of the Extended Zone Method is to keep as much as possible from the method proposed by Hertz and to introduce modifications only where necessary. The proposed modifications are to use the stress-strain curves for concrete and reinforcing steel given an EN 1992-1-2 and to model the effect of the hindered thermal extension of the compressed reinforcement by a reduced strength. Background information on the validity of these extensions and the assumptions by Hertz are given in detail by Achenbach and Morgenthal [3].

The principles of the Extended Zone Method for a concrete cross section exposed to fire on all four sides, as displayed in Fig. 3, can be described by:

- thermal stains and stresses can be neglected,
- the concrete cross section is reduced by $a_{z,EI}$,
- the concrete is represented with a constant temperature θ_M using the stress-strain curves of EN 1992-1-2,
- the peak strain of the concrete $|\varepsilon_{c1,\theta}|$ is at least 3.5 ‰,
- the stress-strain curves of EN 1992-1-2 are used for the reinforcement,
- the strength of the compressed reinforcement is reduced by $\eta_s(\theta)$.

For a rectangular cross section with $b < h$, the mean strength of the concrete is calculated for a section through the centroid parallel to y:

$$k_{c,m} = \frac{\int_{-b/2}^{b/2} k_c(\theta)\,\mathrm{dz}}{b} \quad , \tag{2}$$

with $k_c(\theta) = f_{c,\theta} / f_{ck}$, $f_{c,\theta}$ = concrete strength at temperature θ. The height of the "damaged" zone $a_{z,EI}$ for the compressed cross section is defined by:

$$a_{z,EI} = \frac{b}{2} \cdot \left(1 - \left(\frac{k_{c,m}}{k_c(\theta_M)} \right)^{4/3} \right) . \tag{3}$$

The area of the compressed reinforcement is multiplied by

$$\eta_s(\theta) = \begin{cases} 1.0 \text{ for } \theta \leq 100\text{ °C} \\ 0.5 \text{ for } \theta \geq 400\text{ °C} \end{cases} \tag{4}$$

to model the effect of the hindered thermal extension, values for 100 °C < θ < 400 °C can be interpolated linearly. The strength of reinforcement is not reduced for rebars under tension.

It is not necessary to trace the load history in EZM, each time step can be solved independently. This is useful in a design situation for a given fire resistance, because only the desired "end point" must be solved.

The proposed method is verified by the recalculation of laboratory tests [8]: the calculated results are close to those of the Advanced Calculation Method given in EN 1992-1-2. The Extended Zone Method is implemented in the computer algebra system Mathcad for this paper, using a transfer matrix method for the calculation of the state of strain.

Parameters for recalculation

The physical properties according to EN 1991-1-2 [9] and EN 1992-1-2 [1] are used for the thermal analysis. The considered parameters are given in Table III.

The yield strength of reinforcement f_{yk} is taken from the measured values for f_y. Hot rolled reinforcement, as documented in the reports [4-6], is taken in the recalculation. Siliceous aggregates are assumed for both test series. The concrete strength f_c at the age of test has been measured using 200 mm cubes. The documented concrete strength f_c is transformed into the corresponding 150 mm cylinder strength f_{ck} according to the recommendations by Schnell and Loch [10]:

$$f_{ck} = k_{150} \cdot k_{cyl} \cdot k_{cure} \cdot f_c = 1.05 \cdot 0.8 \cdot 0.92 \cdot f_c = 0.77 \cdot f_c \tag{5}$$

where: k_{150} = strength of 150 mm cubes / 200 mm cubes, k_{cyl} = strength of cylinders / cubes, k_{cure} = strength of wet cured / dry cured concrete.

For the centrically loaded columns heated on all four sides (SFB 12 and 13), an initial curvature of l_{col} / 2000, as recommended by Haß [11], is applied in the recalculation. It is assumed that all columns are perfectly pin ended.

The thermal strains of concrete and reinforcement are disregarded in EZM. Therefore curvatures, which may be caused by asymmetric heating, must be estimated. In this paper, the differences in thermal strains of the rebars are used for this simple approach. The curvatures κ_{th} are calculated by

$$\kappa_{th} = \frac{\varepsilon_{th,s}("1") - \varepsilon_{th,s}("2")}{h-2a} \tag{6}$$

with the nomenclature given in Figure 3.

TABLE III. PARAMETERS OF THERMAL ANALYSIS

Parameter	value	unit
α	25 / 4	[W/m²K]
ε	0.7	[-]
ρ	2400	[kg/m³]
u	3	[%]
λ_c	lower limit	[W/mK]

RESULTS OF RECALCULATION

Tests from TU Braunschweig – symmetric heated columns

The calculated times to failure $t_{cal,ETC}$ and $t_{cal,EZM}$ - using the advanced method ETC and the simplified EZM - are given in Table IV. It must be pointed out that the load history is not considered in the implementation of EZM. The results for columns SFB 12 and SFB 13, which have both identical parameters but different experimental times to failure, are dependent from the applied initial curvature.

Comparing the results for both methods reveals that both methods are able to predict the experimental time to failure with comparable deviations. Using the advanced method ETC does not increase the accuracy of the calculated time to failure. But to generalize this statement, a larger database of laboratory tests should be considered to allow a statistical evaluation.

Tests by Anderberg – asymmetric heated columns

Results for the Anderberg tests are plotted in Figure 4-6. The plots show the horizontal deflections at mid-span of the columns calculated with the EZM and ETC methods, as well as the measured ones.

Test SL-1 must be considered carefully. It was reported [6] that the column exploded early, probably due to the high moisture content of u = 6 % and the high level of applied loads. Hence the effect of spalling cannot be fully ignored for SL-1. As shown in Figure 4, the measured deflections in the middle of the column are towards the fire for the first 25 min of the test, which can be explained by thermal curvatures. After 25 min, the column moves away from the fire. This may be caused by the proceeding deterioration of the concrete, which causes a shift of the neutral axis of the cross section. This effect can be explained by EZM, because the cross section is only reduced at the heated surfaces. Both ETC and EZM with simplified curvatures overestimate the deflections towards the fire and the time to failure. It is noted that spalling is not captured by either method.

For SL-2, the calculated deflections for ETC and EZM with simplified thermal curvatures are close to the measured results, as displayed in Figure 5. There are only experimental results for the first 30 min reported, because the test has been interrupted due to a support failure. The thermal strains and the eccentricity of applied loads cause a deflection towards the fire. In this case, the accuracy of the calculated deflections using EZM can be improved with the simple estimation of thermal curvatures given by Eqn. (6).

TABLE IV. RESULTS OF TESTS FROM TU BRAUNSCHWEIG

Nr.	t_{exp} (min)	$t_{cal,ETC}$ (min)	$t_{cal,EZM}$ (min)
SFB5	85	74	89
SFB12	58	49	44
SFB13	66	49	44
SFB46	50	54	51

For SL-3, the eccentricity of the load is partly balanced by the deflections due to unequal thermal strains. This effect is visible in in the measured deflections displayed in Figure 6. The observed deformations can be reproduced with satisfying accuracy using ETC. The limits of the simple EZM become clear for SL-3: disregarding the thermal strains leads to an underestimation of the deflections, while the consideration of simplified thermal curvatures leads to an overestimation.

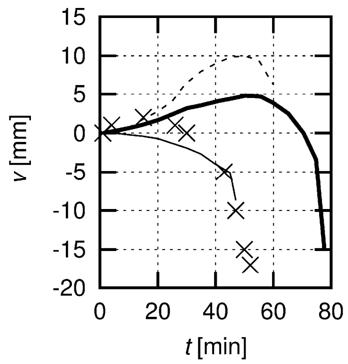

Figure 4. Calculated deflections for SL-1 using ETC (▬), EZM (—), EZM (- - -) with simplified thermal curvatures and measured deflections (×)

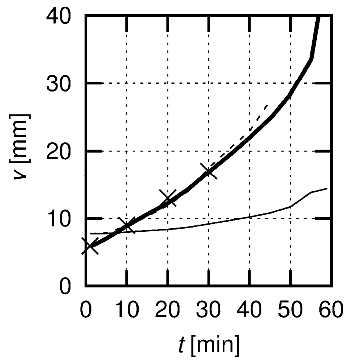

Figure 5. Calculated deflections for SL-2 using ETC (▬), EZM (—), EZM (- - -) with simplified thermal curvatures and measured deflections (×)

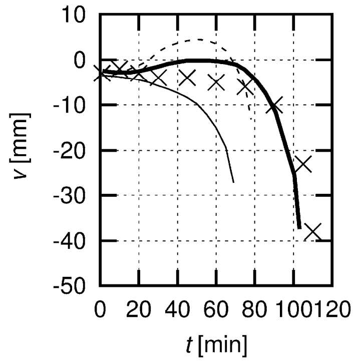

Figure 6. Calculated deflections for SL-3 using ETC (▬), EZM (—), EZM (- - -) with simplified thermal curvatures and measured deflections (×)

CONCLUSIONS

The first series of recalculations indicate that the simplified EZM is of sufficient accuracy for the calculation of unrestrained columns subjected to a standard fire on all four sides. In this situation, which is the standard design situation used in a single member design, the advanced ETC method can also be used but it does not provide any significant improvement in terms of accuracy for the calculated time to failure. The limits of EZM become clear when the effects of non-uniform heating have to be considered. In this case, the advanced ETC is more able to describe the observed behavior of the tested columns. In future, this research will be extended to include a larger database of tests to allow for a statistical evaluation of the different methods.

REFERENCES

1. EN 1992-1-2. Eurocode 2: Design of concrete structures - Part 1-2: General rules - Structural fire design, December 2004.
2. Gernay, T. and Franssen, J.-M. A formulation of the Eurocode 2 concrete model at elevated temperature that includes an explicit term for transient creep. *Fire Safety Journal*, 51:1–9, 2012.
3. Achenbach, M. and Morgenthal, G. Extension of the Zone Method of Eurocode 2 for reinforced concrete columns subjected to standard fire. *Journal of Structural Fire Engineering*. Accepted for publication.
4. Klingsch, W., Haksever, A. and Walter, R. Brandversuche an Stahlbetonstützen - Versuchsergebnisse und numerische Analyse. In *Sonderforschungsbereich 148 - Brandverhalten von Bauteilen - Arbeitsbericht 1975 / 77, Teil I.* Technische Universität Braunschweig, pp. A 1-2-1 – A-1-2-18, 1977.
5. Haß, R. Brandversuche an Stahlbeton- und Verbundstützen. In *Sonderforschungsbereich 148 - Brandverhalten von Bauteilen – Arbeitsbericht 1984-1986, Teil I/A.* Technische Universität Braunschweig, pp. 80-99, 1987.
6. Haksever, A. and Anderberg, Y. Analytical predictions of structural response for reinforced concrete columns in fire, tested in Sweden. In *Sonderforschungsbereich 148 - Brandverhalten von Bauteilen - Arbeitsbericht 1978-1980, Teil I*, pages 197–210. Technische Universität Braunschweig, 1980.
7. Franssen, J.M. SAFIR: A thermal/structural program for modeling structures under fire. *Engineering Journal* , 42(3): 143-158, 2005.
8. Achenbach, M. and Morgenthal, G. Recalculation of laboratory tests with the Extended Zone Method. In F. Wald, I. Burgess, M. Jelčić Rukavina, D. Bjegović, and K Horová, editors, *Applications of Structural Fire Engineering - Proceedings of the International Conference in Dubrovnik, 15-16 October 2015*, pages 31–36. Czech Technical University, 2015.
9. EN 1991-1-2. Eurocode 1: Actions on structures - Part 1-2: General action – Actions on structures exposed to fire, November 2002.
10. Schnell, J. and Loch, M. Umrechnung historischer Baustoffkennwerte auf charakteristische Werte. *Der Prüfingenieur* 34, pp. 50-61, 2009.
11. Haß, R. *Zur praxisgerechten brandschutztechnischen Beurteilung von Stützen aus Stahl und Beton.* Ph.D. Thesis, Technische Universität Braunschweig, 1986.

Buckling Strength of Slender Reinforced HSC and VHSC Columns in Fire

MASAKI KATO, SHINTARO MICHIKOSHI, SHIGEAKI BABA and KAZUMASA IMAI

ABSTRACT

In fire, it is anticipated that slender RC columns would be more vulnerable to buckling failure than to cross sectional failure because of thermal degradation in the cover concrete. This paper presents the main results from an experimental and analytical study of this phenomenon in slender RC columns using high-strength concrete (HSC) and very high-strength concrete (VHSC) under fire conditions. The parameters in the fire resistance tests were concrete strength, cross-sectional shape, axial force and the ratio of column height to cross-sectional diameter, and we consequently obtained fire-resistance time and failure mode. For analysis, a finite-element method with an assumption of the Bernoulli-Euler theory was applied. The analysis, using a method proposed by the authors based on tangent-modulus theory, evaluates the buckling strength under fire conditions. A comparison of the experimental and analytical results shows that the proposed analysis method offers a good approximation of both fire-resistance time and failure mode.

1 INTRODUCTION

Reinforced concrete columns formed with high-strength concrete have been developed for use as axial force carrying members [1]. They have a reduced cross section compared with conventional "short" columns and are known as "slender" columns. These columns allow for larger building interior spaces and offer architectural space with good visibility.

Under Japan's current Building Standard Law, an extra coefficient of stress is set where the ratio of column height to cross-section diameter of an RC column exceeds 15. The room temperature structural design is established by ensuring that the value obtained by multiplying this extra coefficient by the design stress is within an allowable stress [2]. However, there is no structural design method for slender RC columns in the case of fire. Therefore the fire-resistance performance required of slender RC columns for actual projects has been confirmed by tests.

The Young's modulus of concrete decreases more rapidly than compressive strength at high temperatures. When slender RC columns are thermally loaded by fire,

Technology Center, Taisei Corporation, 344-1, Nase-cho, Totsuka-ku, Yokohama-shi, Kanagawa, Japan.

the temperature of the cover concrete increases earlier than that of core concrete. For this reason, it is anticipated that slender RC columns would be more vulnerable to buckling failure than to cross sectional failure. This paper presents the main results from an experimental and analytical study of slender RC columns made with HSC and VHSC under fire conditions. The results lead to a discussion of fire performance, including fire-resistance time and failure mode. The authors have proposed an evaluation method for the buckling strength of RC columns exposed to thermal loading in fires, and the validity of this method is examined in this paper.

2 FIRE RESISTANCE TEST

2.1 Test program

An outline of the fire resistance test is given in Table I while Figure 1 shows the cross sections of the specimens used. Fire resistance tests were carried out on eleven specimens. The parameters in the tests were concrete strength (120, 270 and 300

TABLE I. TEST OUTLINE.

<table>
<tr><th rowspan="4">Name</th><th rowspan="3">Compressive Strength of Concrete σ_B</th><th colspan="5">Outline of Specimens</th><th colspan="3">Concrete Mix Proportioning</th></tr>
<tr><th rowspan="2">Column Height</th><th colspan="2">Cross-Section</th><th rowspan="3">Column Height/ One side or Column Height/ Diameter</th><th rowspan="3">Axial Force Ratio * $N / (\sigma_B A)$</th><th rowspan="2">Water /Binder</th><th rowspan="2">Poly-Propylene Fiber</th><th rowspan="2">Steel Fiber</th></tr>
<tr><th rowspan="2">Shape</th><th>One side (square) or Diameter (circle)</th></tr>
<tr><th>[N/mm^2]</th><th>[mm]</th><th>[mm]</th><th>[%]</th><th colspan="2">[kg/m^3]</th></tr>
<tr><td>C120-20s15</td><td rowspan="4">126</td><td rowspan="3">5000</td><td rowspan="4">square</td><td rowspan="4">250</td><td rowspan="3">20.0</td><td>0.15</td><td rowspan="4">22.5</td><td rowspan="4">1.5</td><td rowspan="4">0</td></tr>
<tr><td>C120-20s20</td><td>0.20</td></tr>
<tr><td>C120-20s33</td><td>0.33</td></tr>
<tr><td>C120-14s20</td><td>3570</td><td>14.3</td><td>0.20</td></tr>
<tr><td>C270-11c07</td><td>271</td><td rowspan="5">4550</td><td rowspan="3">circular</td><td rowspan="5">400</td><td rowspan="5">11.4</td><td>0.07</td><td rowspan="5">12.0</td><td rowspan="5">2.5</td><td>117</td></tr>
<tr><td>C270-11c15</td><td>273</td><td>0.15</td><td>78</td></tr>
<tr><td>C270-11c25</td><td>290</td><td>0.25</td><td>78</td></tr>
<tr><td>C270-11s25</td><td>286</td><td rowspan="2">square</td><td>0.25</td><td>117</td></tr>
<tr><td>C270-11s20</td><td>295</td><td>0.20</td><td>78</td></tr>
<tr><td>C300-16c22</td><td>302</td><td>3400</td><td rowspan="2">circular</td><td>220</td><td>15.5</td><td>0.22</td><td rowspan="2">12.0</td><td rowspan="2">0.0</td><td rowspan="2">67</td></tr>
<tr><td>C300-14c22</td><td>304</td><td>3400</td><td>250</td><td>13.6</td><td>0.22</td></tr>
</table>

* N: Axial force, A: cross-section area

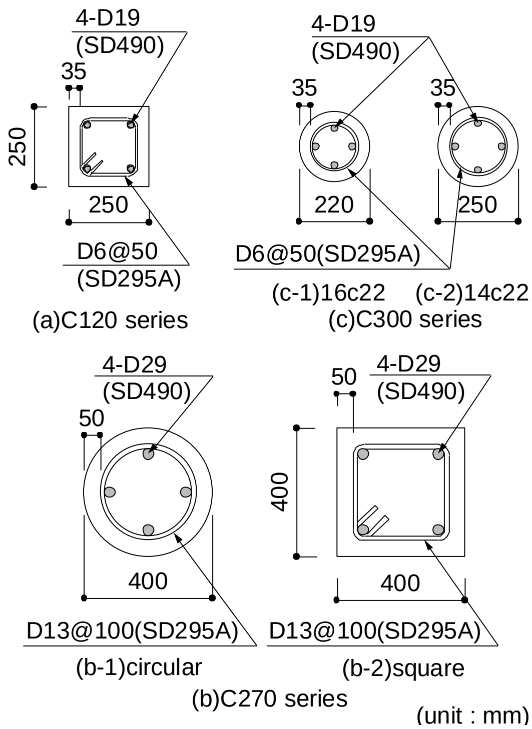

Figure 1. Cross section of specimens.

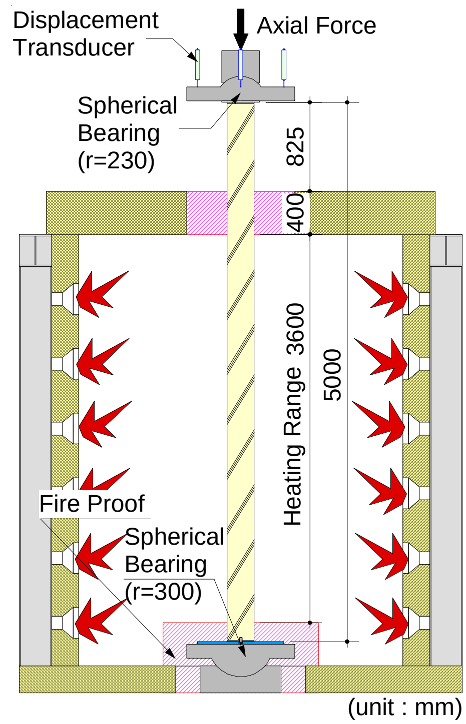

Figure 2. Test setup (An example of C120-20 series).

N/mm^2), cross-sectional shape (square and circular), axial force ratio (with values from 0.07 to 0.33) and the ratio of column height to cross-section diameter (with values from 11.4 to 20.0). The values of axial force ratio are set in the range of practical use. Steel fibers and polypropylene fibers are mixed into the concrete for the purpose of raising compressive strength and preventing spalling, respectively. During concrete placement in the formwork, the formwork is set vertically in the case of the circular section and horizontally in the case of the square section. The concrete used in the C300 series does not incorporate polypropylene fibers in consideration of the small cross-sectional diameter and the poorer workability of the concrete. Cross-section and reinforcement arrangement are uniform in the height direction of the specimens.

2.2 Test setup

The test apparatus is shown in Figure 2. Specimens were subjected to a fire temperature history as specified in ISO834 [3] after loading with the predefined axial force at the top of the column. An example shown loaded in Figure 2 is one of the C120-20 series. A steel stub is placed under the lower spherical bearing for specimens measuring less than 4000mm in height. The height of the steel stub is 1000mm (C120-14s20) and 1380mm (C300 series). In the case of the C300 series specimens, the spherical bearing is not in contact with the specimen; rather these specimens are placed directly on the stub.

Vertical displacement at the top of the column and temperatures in the furnace were measured during the tests. Additionally, in the case of the C120 series, internal temperatures were measured using another similar specimen 900mm in height; a separate specimen was used so as to avoid partial loss of sectional area by introduction of the thermocouples. This specimen was subjected to the fire temperature history as specified in ISO834 without axial force.

2.3 Test results

The state of certain specimens after testing is shown in Photo 1. Specimens with a higher ratio of column height to cross-section diameter and subjected to lower axial loading (C300 series, C120-20s15 and C120-20s20) tended to fail by buckling, while other specimens suffered compressive failure.

Vertical displacement at the column top for all specimens and temperatures for the only C120 series are plotted in Figure 3. The temperatures in Figure 3(a) include the thermal conductivity analysis result evaluated in the next chapter.

Spalling was not observed in the C120 and C270 series. Slight spalling and cracking were observed in the C300 series during testing, but the cover concrete did not fall away because steel fibers contained the concrete comprising the C300 series are hold on cover concrete. All specimens expanded axially just after the start of heating, then they contracted and lost capacity to bear axial force. In comparing C270-11s25 with C270-11c25, which are similar but with different cross-sections, the time history of vertical deformation is approximately the same. However, the time to failure (fire-resistance time) is shorter with the square cross-section than with the circular cross-section. This variation is thought to depend on the difference in concrete confinement by the shear reinforcement.

In C270-11c07 and C270-11c15, a gradual increase of the axial force began at 216min. and 300min. respectively, at which points axial stiffness and residual strength were measured. Axial stiffness decreased about 30% and 25% in the two cases compared to room temperature, and the specimens failed at axial force ratios 0.15 and 0.18. The corresponding fire-resistance times were 236min. and 310min., respectively.

In these tests, the spherical bearing was set directly at either end of all specimens except the C300 series. The spherical bearing rotates when a moment is generated. Under centric axial force, little moment is generated at the bearing, so the mechanical

20s15 20s20 20s33 14s20 11c07 11c15 11c25 11s25 11s20 16c22 14c22

(a) C120 series (b) C270 series (c) C300 series

Photo 1. Specimens after tests.

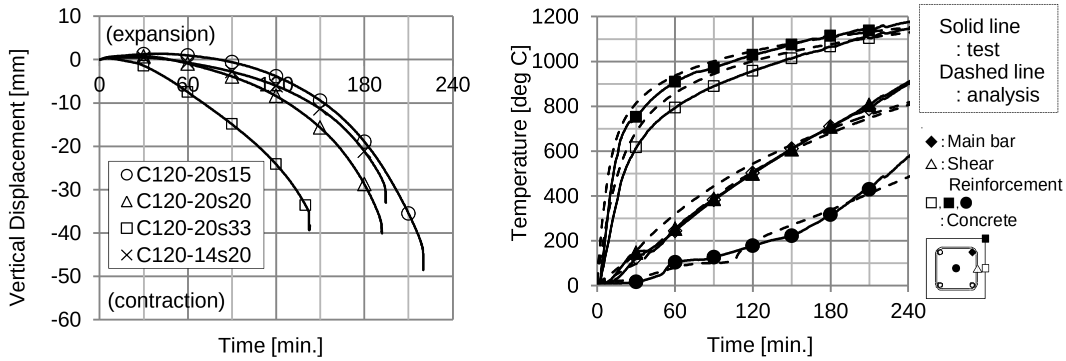

(a) C120 series

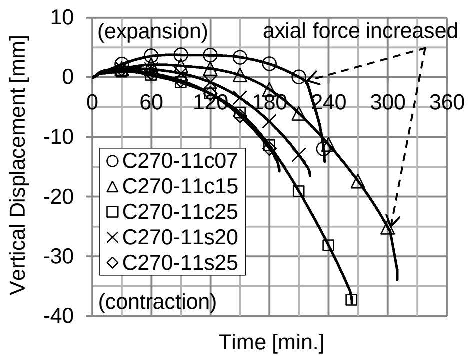

(b) C270 series

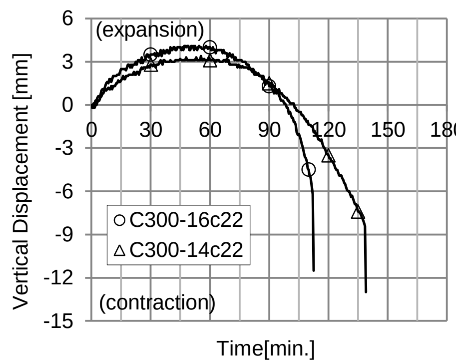

(c) C300 series

Figure 3. Vertical displacement at column top versus temperature.

boundary conditions at the specimen ends will be fixed; in this situation, the buckling length is half of the column height before heating. However, in the tests, bending stiffness was non-uniform in the height direction during heating because the specimens had areas of greater and lesser heating. As a result there were temperature gradients between these areas in these specimens. The influence of the resulting non-uniform bending stiffness on buckling length is a subject of future investigation.

3 ESTIMATION OF FIRE RESISTANCE

3.1 Analysis outline

Thermal conductivity analysis was conducted and the results were used as the basis for an analysis of thermal stress. The thermal conductivity analysis was conducted with the versatile finite-element method program “ABAQUS” using Solid elements. The thermal stress analysis was conducted using Beam elements in a method suggested in the literature [4].

The analysis targets were the C120 series that suffered two kinds of failure mode (cross-sectional failure and buckling). Test results were compared with the analysis results.

3.1.1 METHOD OF ESTIMATING BUCKLING STRENGTH

Using a method proposed by the authors based on tangent-modulus theory, the buckling strength was analyzed under fire conditions moment by moment from the bending stiffness of the slender RC columns. Tangent-modulus theory has a long history of study in the field of steel structures. In this case, it was applied to slender RC columns that have large temperature gradients over the cross-section in a fire.

The thermal stress analysis with an assumption of the Bernoulli-Euler theory of total strain ε_{tot} (composed of mechanical strain ε_σ, free thermal strain ε_{th} and transient strain ε_{tr}) was applied. The authors propose equation (1) for buckling strength based on tangent-modulus theory using tangent-stiffness on $\sigma-\varepsilon_\sigma$ relationship of each element.

$$E_t \cdot I = \int_A E_{t,i}\,(T,\varepsilon_\sigma)\, y^2 dA \qquad (1)$$

Where, $E_{t,i}$ (T, ε_σ) : tangent-stiffness on σ - ε_σ relationship,
(element i ,temperature T, stress σ, mechanical strain ε_σ)
y : distance from centroid axis to element i,
dA : cross-sectional area of element i

3.1.2 ANALYSIS MODEL

The analysis was conducted for slender RC columns fabricated using high-strength concrete with a compressive strength of 120N/mm^2 (C120 series). The cross-sectional model and the high-temperature characteristics of the concrete for analysis are shown in Figure 4 and Figure 5, respectively. The concrete mix proportioning for C120 was approximately the same as the mix proportioning for this concrete (Table I) in reference [5] (Note: the water-binder ratio given in the literature is 23.0%.) Thermal properties were taken from reference [6]. The assumed models for the σ - ε_σ relationship of concrete and main bar are as given in references [7] and [8], respectively. The σ - ε_σ relationship used for the concrete takes into account the influence of axial confinement effect (axial force ratio: 0.20) during heating.

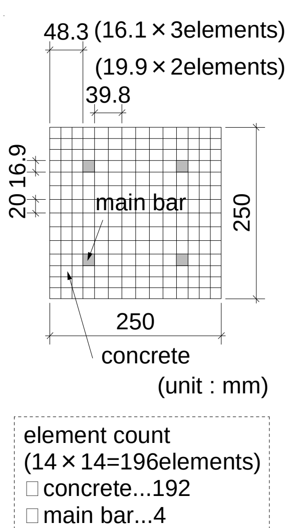

Figure 4. Cross-sectional model.

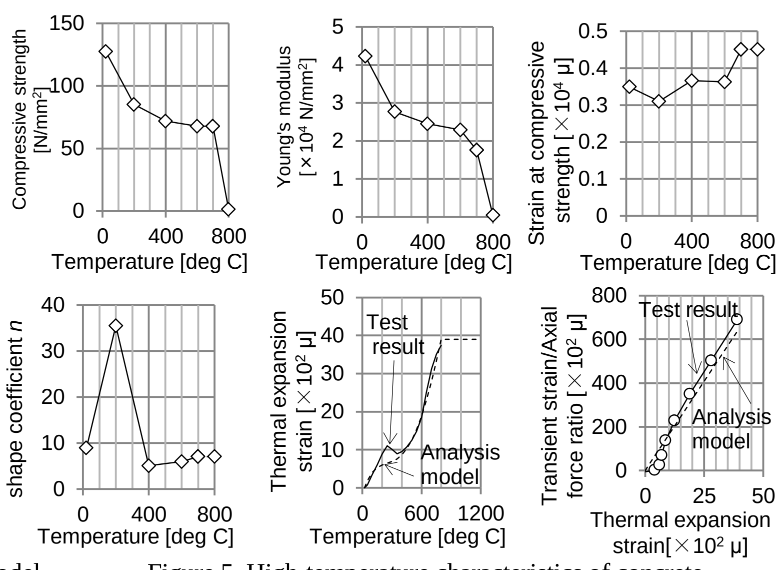

Figure 5. High-temperature characteristics of concrete.

3.2 Thermal conductivity analysis results

The thermal conductivity analysis results are shown in Figure 3. A comparison of the experimental and analytical results shows good matching up to 220 minutes. Beyond 220 minutes, the analysis gives a lower temperature than measured in the tests. Thermal stress analysis was conducted using these results for thermal conductivity, because the fire-resistance times of the C120 series are all less than 220 minutes.

3.3 Thermal stress analysis results

3.3.1 RATE OF BENDING STIFFNESS

The time history of bending stiffness $E_t \cdot I$ is shown in Figure 6. In this figure, the cross-section is divided into three elements consisting of the cover concrete, core concrete and main bar. Bending stiffness decreased considerably due to thermal degradation of the cover concrete and compressive yielding of the main bar. The core concrete had little impact on bending stiffness, because the Young's modulus of the core concrete decreased more slowly than that of the cover concrete while the second moment of area I is very small.

3.3.2 FAILURE MODE AND FIRE-RESISTANCE TIME

The analytical relationship between axial force ratio and fire-resistance time is shown in Figure 7. The buckling strength P_{cr} of the slender RC columns under fire conditions moment by moment was obtained by substituting the bending stiffness calculated by equation (1) into equation (2). The fire-resistance time in this analysis was defined as the time until this buckling strength decreased to the axial force. As previously described, the buckling length was the half of the column height, because the mechanical boundary conditions at ends of the specimens were fixed.

In this analysis, the model with lower axial loading tended to fail by buckling, in line with the test results. A comparison of the experimental and analytical results

$$P_{cr} = \pi^2 \cdot \frac{E_t \cdot I}{l_k^2} \tag{2}$$

Where, $E_t \cdot I$: bending stiffness (calculated by equation (1)), l_k: buckling length

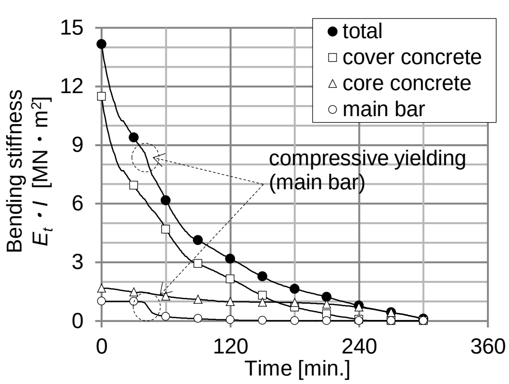

Figure 6. Bending stiffness (axial force ratio: 0.1).

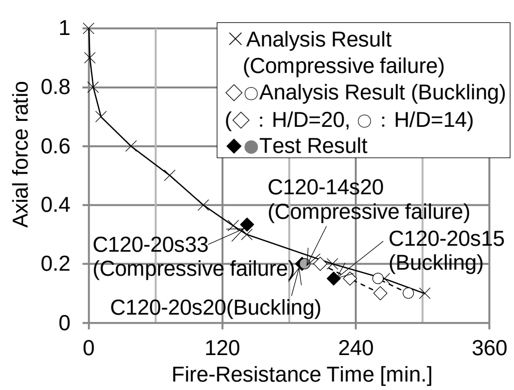

Figure 7. Fire-resistance time.

shows that the proposed analysis method offers a good approximation of both fire-resistance time and failure mode.

4 CONCLUSION

Fire-resistance tests were conducted on slender RC columns made with HSC and VHSC and their performance in fire, including fire-resistance time and failure mode, was obtained. For specimens of the shape and materials, those under lower axial loading tended to fail by buckling. Further, fire-resistance time is found to be shorter with a square cross-section than a circular cross-section due to confinement effect of the shear reinforcement.

The authors have proposed an evaluation method based on tangent-modulus theory for the buckling strength of RC columns exposed to thermal loading in fires, and the validity of this method was examined. A comparison of experimental and analytical results showed that the proposed method offers a good approximation of both fire-resistance time and failure mode. Bending stiffness was shown to decrease considerably due to thermal degradation of the cover concrete and compressive yielding of the main bar.

In these tests, bending stiffness was non-uniform in the height direction during heating, because the specimens had areas with greater and lesser heating. Additionally, although the tangent-modulus theoretical value indicates the force at which the columns start to bend, real buckling strength should be calculated using Shanley's theory [9]. These are subjects for future investigation.

REFERENCES

1. T. Korenaga, K. Imai, K. Yamamoto, S. Michikoshi, T. Komuro and A. Hattori, "Development of Slender Columns Using Ultra High Strength Concrete (Part 1~5)" (in Japanese), *Summaries of Technical Papers of Annual Meeting*, Architectural Institute of Japan, pp.547-556, 2013.8.
2. Architectural Institute of Japan, "AIJ Standard for Structural Calculation of Reinforced Concrete Structures" (in Japanese), pp.144-147, 2010.2.
3. ISO/FDIS 834-1, 1999. "Fire-resistance tests - Elements of building construction - Part1 General requirements."
4. H. Uesugi and H. Koike, "THERMAL STRESS OF STEEL STRUCTURES OF TALL BUILDINGS IN FIRE: Part 1. Computer analysis method of tall structures exposed to compartment fire" (in Japanese), *Journal of Structural and Construction Engineering*, No.381, pp.73-80, 1987.11.
5. M. Kato, S. Michikoshi, S. Baba, S. Kuroiwa and H. Jinnai, "Compressive Tests of 100N/mm2 High Strength Concrete in High Temperature and After Heating Conditions" (in Japanese), *Summaries of Technical Papers of Annual Meeting*, Architectural Institute of Japan, A-2, pp.13-14, 2011.8.
6. S. Michikoshi and Y. Kobayashi, "Mechanical Properties of High Strength Concrete At High Temperatures" (in Japanese), *Summaries of Technical Papers of Annual Meeting*, Architectural Institute of Japan, A-2, pp.79-80, 2004.8.
7. Sandor Popovics, "A Numerical Approach to the Complete Stress-Strain Curve of Concrete", *CEMENT and CONCRETE RESEARCH*, Vol.3, pp.583-599, 1973
8. K. Nagao, H. Eto, H. Niwa and H. Uesugi, "The Results of Elevated Temperature Tensile Tests of Reinforcing Bars" (in Japanese), *Summaries of Technical Papers of Annual Meeting*, Architectural Institute of Japan, A-2, pp.75-76, 2000.9.
9. F. R. Shanley, "Inelastic Column Theory", *Journal of the Aeronautical Sciences*, Vol.14, No.5, pp.261-268, 1947.5.

Effects of Localised or Non-Uniform Heating on Reinforced Concrete Columns

JAMIE MACLEAN, VADIMS GOREMIKINS, LUKE BISBY and TIM STRATFORD

ABSTRACT

This paper describes a research project being conducted to shed light on the response of concrete columns to non-uniform heating, and on the ability to credibly model the response of realistic concrete structures during non-standard fires. A series of 48 one-third scale reinforced concrete (RC) columns are being tested under sustained eccentric axial loading, and exposed to a localised radiant heat source to observe their response, to provide validation data for full-frame structural fire modelling, and to determine the "damage" caused by non-standard fire exposures. All 48 columns are being loaded eccentrically and exposed to a constant incident heat flux at their mid height by means of a propane-fired radiant panel. This paper describes the project, including; the objectives and expected outputs of the project, the experimental test series which is underway, and initial *a priori* modelling results obtained using the commercially available Finite Element Software ATENA, which will be compared against the results of the experiments once these data are available.

INTRODUCTION AND MOTIVATION

In addition to life-safety concerns during building fires, uncontrolled fires within buildings have the potential to cause extensive structural damage. Current design guidance for structures in fire, however, focuses almost exclusively on the life safety of the occupants within buildings. This is generally achieved by specifying a defined fire resistance period during which structural integrity must be maintained and fire spread must be prevented, to ensure that the building's egress routes are not compromised until all occupants have escaped from the building and fire-fighting operations have been completed. Designers are not typically required to explicitly consider the residual, post-fire effects of fires on structures – nor the associated direct and indirect repair costs associated with fire induced damage to the building itself. Only particularly enlightened consultants or clients will demand that fire damage to the building be explicitly considered during design.

Maclean J., Bisby L., Stratford T., The University of Edinburgh, School of Engineering, Sanderson Building, Robert Stevenson Road, The Kings Buildings, Edinburgh, UK, EH9 3FB.
Goremikins V., Riga Technical University, Faculty of Civil Engineering, Azenes Street 16/20, Riga, LV 1048, Latvia.

Historically, concrete buildings have performed relatively well in fires, and concrete structures can often be repaired after a fire event [1]. It is, however, challenging to predict the response of concrete structures during heating, and even more challenging to quantify their residual structural performance after cooling. Little validated computational modelling work is available in the literature, particularly for non-standard fire exposures. This paucity of information makes holistic, performance-based, full frame design and analysis of concrete structures difficult, since the total damage (and thus true costs) from uncontrolled fires cannot currently be quantified.

To better understand how concrete structures may react in fires, both non-standard fire tests on concrete structural elements and validated numerical modelling techniques are essential. In recent years a number of studies have presented attempts to computationally model the behavior of concrete structures at high temperature, as well as during the cooling phase and residually [2-4]. Such studies have required the development of material and numerical models to predict the response of concrete under load, both during and after elevated temperature [3-4]. These models may offer engineers additional analysis capability during design, however further validation work is needed before they can be confidently applied on a widespread basis in design.

This paper presents a project aiming to better understanding the thermal, and more importantly structural, response of concrete columns subjected to loading and non-standard, non-uniform fire conditions. Both numerical and experimental studies are being undertaken, with the objective of increasing the pool of data available from tests on concrete structures under non-standard arrangements. Such data are essential for comparisons against computational model predictions. A total of 48 square one-third scale reinforced concrete (RC) columns have been constructed. These are being exposed to localised heating at their mid-height using a constant incident radiant heat flux from propane-fired radiant panels, and subjected to varying degrees of sustained axial loading eccentricity. The data gathered during the transient thermal experiments includes: the internal temperatures through the columns using 18 thermocouples; vertical and lateral deflections; and strains using digital image correlation.

The parameters being investigated in the test series include: the magnitude of loading; the degree of eccentricity of loading; the number of sides heated (1 or 2); the severity of the incident heat flux; and the concrete compressive strength. In addition to the experimental test procedure, this paper gives results of *a priori* finite element (FE) modeling undertaken in accordance with thermal and mechanical property relationships suggested by Eurocode 2 [5]. All FE models have been developed before the tests are carried out to ensure that the authors' modelling ability is genuinely interrogated without temptation to vary model input parameters to match the experimental results (as would occur in an engineering design office).

The vast majority of the available research investigating the performance of concrete columns subjected to elevated temperatures has concentrated on the performance of columns when subjected to uniform heating over the full (or almost full) length of the column and over all four sides simultaneously [3]. In addition, the columns are almost always exposed to the ISO 834 standard fire curve (or similar) within a fire testing furnace [2-3]. Furnace testing, although useful for comparative testing of different columns and materials, is not very useful to observe or quantify the precise thermal exposure and structural response, which makes use of such tests problematic for validation of structural fire analysis software. To address this shortcoming, radiant panels are being used in the current study to induce a constant incident heat flux to the columns; this can be directly controlled, measured, and used as a well-defined thermal boundary condition for computational models being developed and validated on the basis of the experiments.

It is well documented that concrete is sensitive to elevated temperatures [1-7]. In real fires, when a concrete column is subjected to heating on one side only, thermal gradients will be induced within. This will result in the development of thermal deformations and thermal stresses within the column, resulting in a section with differing strength and stiffness over its cross-section. The effect of these factors is being investigated by exposing the columns to different severities of heat fluxes on one face only. Standard heating, e.g. ISO 834 [6], is not being considered, since the goal is to understand response and validate modelling capability, rather than simply to provide simplistic fire resistance ratings, which do not help to evaluate the time history of structural fire response or the structural damage that might be expected after a fire. It is hoped that this will help inform post-fire analysis of RC columns for use by engineers and insurers to provide property protection and quantified probabilistic structural fire engineering design in the future.

TEST SPECIMENS AND PROCEDURES

Columns and Instrumentation

Figure 1 gives section and elevation schematics of the design of both the columns and the testing frame to be used. Forty-eight geometrically identical reinforced concrete columns have been cast in two sets of twenty-four. All of the columns are 150mm x 150mm in cross-section and 1400mm long, longitudinally reinforced with four 10mm diameter deformed reinforcing bars and 5mm diameter deformed steel ties spaced at 140mm on center. The design of the columns follows Eurocode 2 [5]. One set of concrete columns is lower strength (32MPa at 28 days) and second set was cast

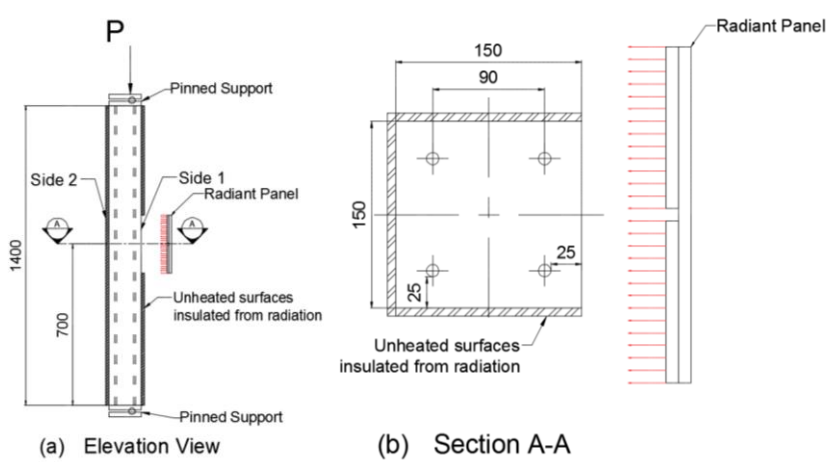

Figure 1. Detailed of reinforced concrete column design, heating regime, and testing configuration.

using higher strength concrete (52MPa at 28 days). It is noteworthy that both mixes include 2kg/m^3 of polypropylene (PP) fibers for spalling mitigation during the tests.

The test setup has been specifically designed such that the thermal exposures experienced by the columns can be accurately controlled, compared, and modelled. A total of 18 thermocouples have been cast into each concrete column at mid-height, 900mm (the top of the radiant panel) and 950mm (50mm above the top of the radiant panel) from the base of the column respectively. The thermocouples are being used to quantify the thermal exposure on the surface of the columns and to validate the thermal models being developed in conjunction with the tests. The samples have been cured unsealed and open to the atmosphere at 50% relative humidity and 23^{o}C, for a period of 6 months.

Experimental Procedure

The test setup is illustrated in Figure 1. Tests have four distinct stages:

1. Columns are placed in the testing frame and loaded to the desired sustained load. This load is maintained constant during steps 2 and 3;
2. Columns are exposed to a localised incident radiant heat flux over a defined area at their mid heights. The incident heat flux is applied instantaneously and maintained constant for 30 or 60 minutes;
3. After 30 or 60 minutes of heating, provided the column has not failed, the heating is removed and the column is allowed to cool to ambient temperature, with its mechanical response during cooling also monitored;
4. The sample is tested residually to failure to determine its residual response.

This test procedure allows the entire sequence of elevated temperature heating, cooling, and potentially post-heating residual response, to be interrogated and modelled. The parameters being investigated include:

1. The strength of the concrete (32MPa or 52MPa);
2. The number of sides heated (front face only, or both front and back faces);
3. The severity of the thermal exposure (60kW/m^2 or 80kW/m^2);
4. The eccentricity of the sustained axial load (5mm or 25mm); and
5. The magnitude of the load during heating (20% or 60% ambient capacity).

Table I shows the full testing matrix for the current study, along with the associated parameters being varied.

A PRIORI FINITE ELEMENT MODELLING

Model Description

An *a priori* FE model of the column tests was developed using the commercial FE code Atena 5 Science with the GID 12 preprocessor. Concrete was modelled using 3D brick elements applying a nonlinear fracture-plastic material model. The concrete model includes post-cracking and post-crushing softening phases. Steel bars and ties (see Figure 2a) were modelled using 1D bar elements. The steel base plates and rollers (Figure 2b), which were used during testing to provide well-defined pinned-pinned column end conditions, were included in the FE models to capture the precise load application used in the tests, rather than the load application that might occur in a real building. The material models used account for changes in the mechanical and thermal properties of the steel and concrete due to increases of temperature; this is done in accordance with the Structural Eurocodes [6].

TABLE I. REINFORCED CONCRETE COLUMN TEST MATRIX.

No.	Conc. Strength f_c (MPa)	Side Heated (see Fig. 1)	Heat Flux (kW/m^2)	Duration (min)	Eccentricity (mm)	Load (% amb. cap.)
1	32	1	80	30	5mm	20%
2	32	1	80	30	5mm	60%
3	32	1	80	30	25mm	60%
4	32	1	80	60	5mm	20%
5	32	1	80	60	5mm	60%
6	32	1	80	60	25mm	60%
7	32	1	60	60	5mm	20%
8	32	1	60	60	5mm	60%
9	32	1	60	60	25mm	60%
10	32	2	80	60	25mm	60%
11	32	2	60	60	5mm	60%
12	32	2	60	60	25mm	60%
13	32	1&2	80	30	5mm	60%
14	32	1&2	80	30	25mm	60%
15	32	1&2	80	60	5mm	60%
16	32	1&2	80	60	25mm	60%
17	32	1&2	60	60	5mm	60%
18	32	1&2	60	60	25mm	60%
19	52	1	80	30	5mm	20%
20	52	1	80	30	5mm	60%
21	52	1	80	30	25mm	60%
22	52	1	80	60	5mm	20%
23	52	1	80	60	5mm	60%
24	52	1	80	60	25mm	60%
25	52	1	60	60	5mm	20%
26	52	1	60	60	5mm	60%
27	52	1	60	60	25mm	60%
28	52	2	80	60	25mm	60%
29	52	2	60	60	5mm	60%
30	52	2	60	60	25mm	60%
31	52	1&2	80	30	5mm	60%
32	52	1&2	80	30	25mm	60%
33	52	1&2	80	60	5mm	60%
34	52	1&2	80	60	25mm	60%
35	52	1&2	60	60	5mm	60%
36	52	1&2	60	60	25mm	60%
37	32	N/A	N/A	N/A	5mm	100%
38	32	N/A	N/A	N/A	5mm	100%
39	32	N/A	N/A	N/A	25mm	100%
40	32	N/A	N/A	N/A	25mm	100%
41	52	N/A	N/A	N/A	5mm	100%
42	52	N/A	N/A	N/A	5mm	100%
43	52	N/A	N/A	N/A	25mm	100%
44	52	N/A	N/A	N/A	25mm	100%
45	52	TBC	TBC	TBC	TBC	TBC
46	52	TBC	TBC	TBC	TBC	TBC
47	52	TBC	TBC	TBC	TBC	TBC
48	52	TBC	TBC	TBC	TBC	TBC

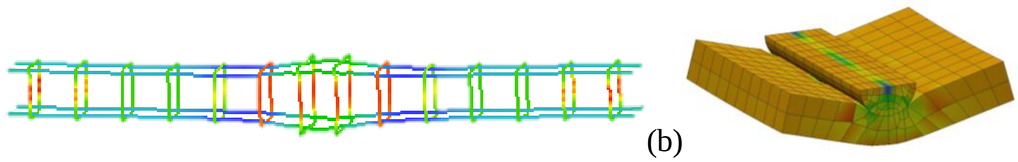

(a) (b)

Figure 2. Schematics showing (a) steel bars and ties and (b) steel base plate and roller end conditions applied during FE modelling (exaggerated deformations).

The analyses were carried in two steps. In the first step the three-dimensional thermal fields were calculated within the columns. Since it is not possible to apply an incident surface heat flux in ATENA, as will be applied by the radiant panels during the experiments, the incident heat flux was converted to a convection and radiation boundary condition. In the second step the mechanical analyses were performed with the thermal fields taken as inputs. The columns were loaded during the analyses first by applying the sustained mechanical loading; new thermal fields were then applied in each subsequent time step, with the mechanical loads held constant.

Modelling Results

A range of the testing scenarios listed in Table I has been modeled computationally. However, it should be noted that concrete strengths of 40MPa and 80MPa were used since these were the specified concrete strengths specified during casting of the test columns (these were not achieved and the models now require refinement for comparison against the tests, when performed). Figure 3 shows the predicted ambient response of the columns when loaded monotonically to failure. Using this response as a baseline, the response of the columns has been compared when subjected to a localised heat heating and sustained eccentric axial load.

The predicted capacity of the columns is roughly 1400kN and 1000kN for the C80 concrete for 5mm and 25mm eccentric loads, respectively, whereas for C40 concrete it is 1100kN and 700kN, respectively. As expected, lower concrete strength results in predicted decreases in axial load-bearing capacity, and additional loading eccentricity results in considerable increases in predicted lateral deflections.

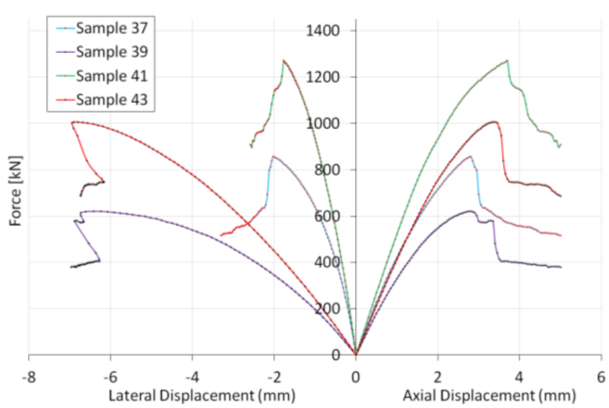

Figure 3. Selected RC column responses at ambient temperature (see Table I).

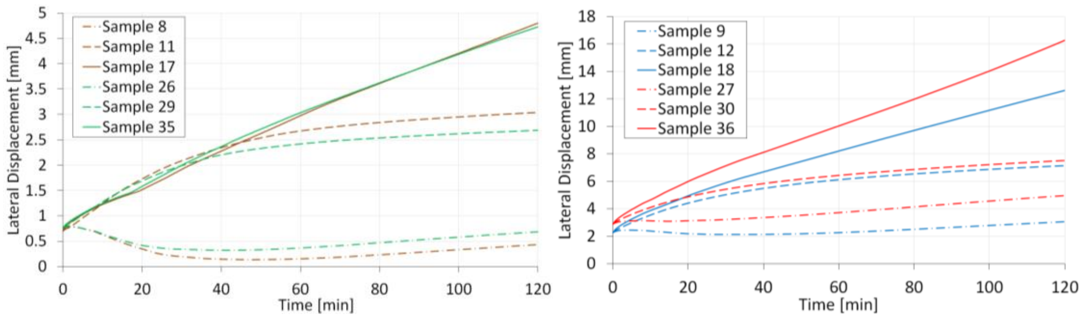

Figure 4. Selected predicted lateral displacements of columns with time of exposure to 60kW/m^2 of localised incident heat flux (see Figure 1 and Table I); effect of sides heated; (a) 5 mm eccentricity; (b) 25 mm eccentricity.

Figure 4 shows the predicted response of selected columns listed in Table I, subjected to a localised incident heat flux of 60kW/m^2 for 120 minutes. All columns shown were loaded to 60% of their ambient capacity. Figure 4 shows that, when the 'tension' (i.e. least compressed) face of the eccentrically loaded columns is subjected to heating, horizontal deflections in the column are predicted to increase continuously during heating. Obviously this can be attributed to thermal expansion of the concrete on the tension face (thermal bowing), which increases lateral deflections and exacerbates secondary moments. If, however, the 'compression' face of the eccentrically loaded column is heated, the horizontal deflections in the column initially decrease for both 5mm and 25mm eccentricities; this is later followed by increasing deflections with further heating, as a consequence of deterioration of mechanical properties of concrete on the more highly compressed face. This confirms that thermal expansion of the concrete plays a key role in the response of asymmetrically heated RC columns, particularly in the early stages of heating. In the later stages of heating, however, the reduced mechanical properties of the concrete dominate the response.

Columns heated on both faces initially experience similar deflections to columns heated on the tension face only; however they experience greater deflections in the later stages of heating, again once reduced mechanical properties begin to dominate the response. Higher eccentricities are predicted to lead to an overall response which is more dominated by material property reductions, particularly under two-sided heating.

Figure 5 shows the predicted vertical displacements of the columns subject to an

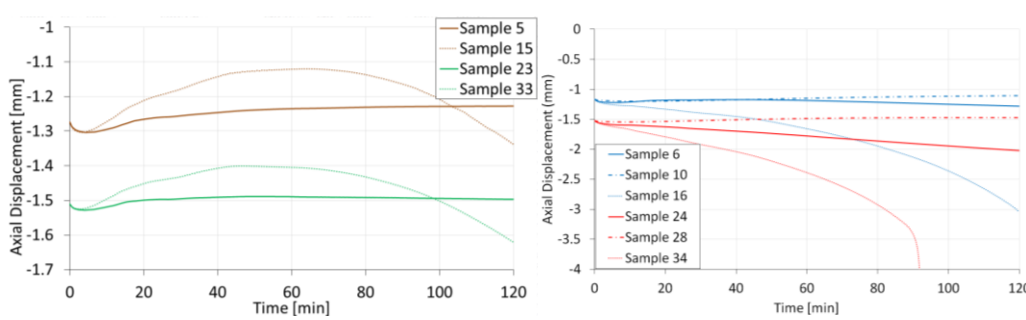

Figure 5. Predicted axial displacements of selected columns subjected to an 80kW/m^2 localised incident heat flux, heated on one or two faces (see Table I); (a) 5 mm eccentricity; (b) 25 mm eccentricity.

80kW/m^2 heat flux loaded to 60%. It can be seen that, as the concrete temperatures increase, the vertical displacements increase until failure. However, where the load eccentricity is small (i.e. 5mm), similar to the horizontal deflections, the vertical displacements initially decrease as a result of thermal expansion. This suggests that the lower the load eccentricity, the larger relative influence thermal expansion will have on the structural response of the columns (and consequently, the overall structural frame in real concrete buildings. These tests (see Table I) will provide the opportunity to compare the above (and other) computational predictions against ad-hoc non-standard fire testing of concrete columns.

CONCLUSIONS

Based on the *a priori* modelling completed for the RC columns described in Table I of this paper, the response of the concrete columns is seen to depend on the thermal gradient through the depth of the column and on the specific loading scenario applied. This in turn places a higher degree of importance on the location and time history of the fire itself. Testing and analysis of RC structural elements under standard fire testing procedures is therefore not necessarily conservative for assessing either the element response or the full structural response to heating. Additional research work, currently underway, is required to support analysis and design of concrete columns under non-standard heating regimes, and to validate models' ability to predict "real" structural behavior in fire. Based upon the simulations completed, the following conclusions can be drawn on the response of RC columns to localised heating:

1. As the thermal wave passes through concrete columns exposed to elevated temperatures non-uniformly, the structural response is predicted to depend considerably on the thermal gradients and, in turn, the fire severity and location.
2. When the most compressed column face is exposed to elevated temperatures, thermal expansion of the concrete opposes the thermal bowing of the column, and results in decreased horizontal displacements during the initial heating stages. The opposite is predicted if the least compressed face is heated.
3. The lower the moment (i.e. load eccentricity) applied to a column, the more influence thermal expansion has on the response in the initial stages of heating.

REFERENCES

1. Block, F., Clarke, J., Cole, B., Deeny, S., Heise, A., Ingham, J., & Pierce, N. (2013). TR68 Assessment, Design and Repair of Fire-Damaged Concrete Structures, Concrete Society.
2. Jau, W.-C., & Huang, K.-L. (2008). A study of reinforced concrete corner columns after fire. *Cement and Concrete Composites*, *30*(7), 622-638.
3. Chen, Y.-H., Chang, Y.-F., Yao, G. C., & Sheu, M.-S. (2009). Experimental research on post-fire behaviour of reinforced concrete columns. Fire Safety Journal, 44(5), 741-748.
4. Chang, Y. F., Chen, Y. H., Sheu, M. S., & Yao, G. C. (2006). Residual stress–strain relationship for concrete after exposure to high temperatures. Cement and Concrete Research, 36(10), 1999–2005.
5. Youssef, M.A., & Moftah, M. (2007). General stress–strain relationship for concrete at elevated temperatures. Engineering Structures, 29(10), 2618-2634.
6. CEN. (204a). EN 1992-1-1: Eurocode 2: Design of concrete structures – Part 1-1: General rules for buildings. Brussels, Belgium.
7. ISO 834-1: 1999, Fire-resistance tests - Elements of building construction. General requirements. International Standards Organisation, Geneva, Switzerland.

Modelling the Thermal and Structural Performance of a Concrete Column Exposed to a Travelling Fire – Tisova Fire Test

DAVID RUSH[1], DAVID LANGE[2], JAMIE MACLEAN[1], and EGLE RACKAUSKAITE[3]

SUMMARY

The Tisova Fire Test was a large real scale fire test conducted in the Czech Republic in January 2015 inside of a 4-storey concrete frame building, with concrete and composite deck floors. The ground floor test compartment had a total area of ca. 230m^2 with a height of 4.4m. The fire compartment included four columns from the original 1958 concrete construction, one of which was instrumented retroactively for temperatures, chosen due to its higher likelihood of observable thermal and structural response. This paper presents selected results from the thermal environment around, and the thermal response of, the column showing the variability of temperatures through the compartment height. The paper proceeds to model the thermal response of the column from 1) the real fire scenario, and 2) equivalent areas under the standard fire curve. These thermal profiles are then used to assess the reduction of the columns cross-sectional capacity, and shows that using equivalent fire durations is not an appropriate method to calculate the thermal and structural response of concrete columns exposed to a travelling fire.

INTRODUCTION

Current fire engineering design guidance (e.g. [1]), in general, assesses single structural elements and their response to fire on a pass/fail assessment usually consisting of prescribed fire resistance criteria and times. This assessment is usually based on a standard fire that represents only one fire out of a range of possible fires which may occur, and may not represent the most onerous (or more realistic) fire insult that a structure might experience [2]. The tests are also limited in their ability to represent fires within large compartments such as a travelling fire, and so representation of fire severity have been developed (i.e. [3]).

Modelling of concrete elements and structures to non-standard fires has shown that long durations of some travelling fires [4] or parametric fires [5] can have significant effects on the response of concrete structures. However the validity of these models

[1]BRE Centre for Fire Safety Engineering, University of Edinburgh, UK.
[2]Technical Institute of Sweden SP, Boras, Sweden
[3]Imperial College London, UK

remains in question due to the lack of experimental data, with very few tests conducted in large compartments with travelling fires. The Tisova Fire Test aimed to generate experimental data on some of the modelling uncertainties namely; travelling fires; the thermal and structural response of composite slabs, concrete slabs, and concrete columns to real fires. This paper considers one aspect of the Tisova Fire Test – the thermal response of a concrete column to a travelling fire and in turn an assessment of the columns structural performance.

FIRE TEST

The Tisova Fire Test was carried out in January of 2015 by a team from SP, the University of Edinburgh, Imperial College London, Luleå Technical University, and Technical University Ostrava, Majaczech, CSTB and CERIB. The fire test was conducted inside of a real building, Figure 1, which was scheduled for demolition. The building was constructed in 1958 and comprised of a reinforced concrete frame and slab construction. In 1980 the buildings use was changed and additional floorslabs were added using composite slab construction tied in to the original frame. The aim of the test was to achieve a structurally challenging travelling fire.

Figure 1. Left – Southwest corner of test building, and Right – fire compartment.

The test compartment shown in Figure 2 was on the ground floor and the fire compartment had a total area of approximately 230m^2 and was 4.4 m high from floor to slab soffit. The layout was generally open, with a series of large rooms enclosing one side as well as one corner, centered on a lift shaft. Four columns were fully within the fire compartment. The smallest 30 x 30 cm column (C1) indicated in Figure 2 was chosen to be examined due to its slenderness and was therefore most likely to experience higher core temperatures and damage during the fire test.

The size and layout of the compartment meant that it was ideal for testing the travelling fires methodology developed by Stern-Gottfried & Rein [6]. The fuel was laid out as a uniform single fuel bed across the whole floor, apart from a 0.5 – 1 m path around the perimeter of the floor area. The fuel bed load was 40kg/m^2 of spruce timber conditioned to a targeted 11% moisture content equating to approximately 680MJ/m^2. The fire was well ventilated to ensure that fire was fuel load controlled and not controlled by ventilation, and the fire was ignited at location *FI* in Figure **2** using organic fuel soaked in lighter fuel within the crib.

Fire temperatures within the compartment were recorded using 56 thermocouple (TC) trees incorporating Type-K Inconel sheathed thermocouples hung from the ceiling. Figure 2 shows four thermocouple trees within a 2.5m radius of the column C1, named NE, NW, SE, and SW TC trees, respectively. Each thermocouple tree had 6 thermocouples at heights below the soffit of the slab of: 5cm, 65cm, 140cm, 205cm, 260cm, and 370cm, respectively. The top of the fuel bed was approximately 40cm off the floor. The SW and SE TC trees are shown in Figure **3** a).

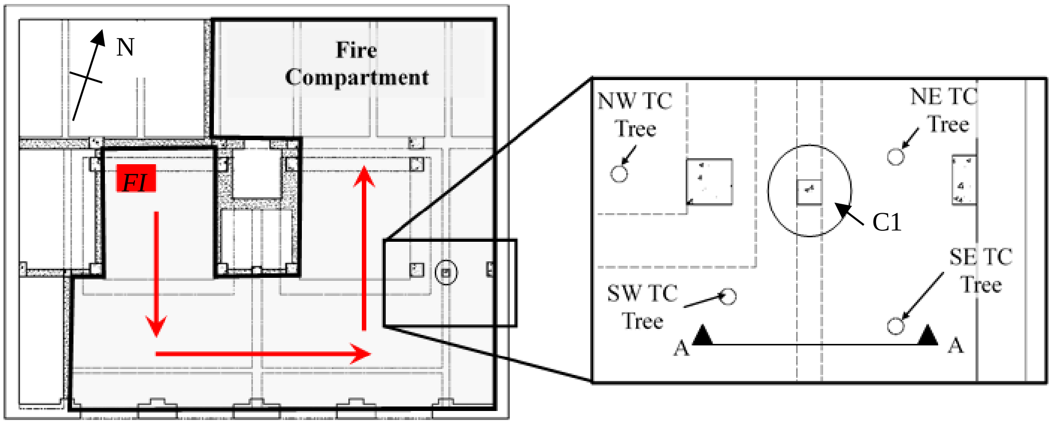

Figure 2. Fire compartment showing fire ignition point (*FI*) and path of travel (arrows), and column C1 and associated TC tree locations.

Column C1 was instrumented with 6 thermocouples at two heights, 1.5m above the floor and 3m above the floor, unfortunately the thermocouples 1.5m above the floor suffered from a failure early on in the test and all data was corrupted and will not be discussed any further in this paper. Figure **4** b) shows the locations of the thermocouples at the 3m height of the column, with four TCs which placed 6 cm from each of the four faces, and two TCs which were placed 10 cm from the North and West faces. Plate thermometers (PT) was placed 10 cm from each of the North (N), East (E), South (S), and West (W) column faces with their centers at the same 3m height from the floor.

Results

The fire was successfully ignited as planned however it soon became evident that fire spread rate was very slow with the flame length along the path (shown in Figure 2) of approximately 1 m with a flame height between 1.5 – 2 m. The resulting temperatures in the compartment, especially near the ceiling, were not high enough for a structurally challenging fire, i.e. well below 100^{o}C. To encourage fire growth during the test the ventilation was reduced and a 10 litre 1:1 mixture of gasoline to diesel was poured over the fuel bed along the southern perimeter 2.5 hrs into the test. This resulted in a more severe fire covering cribs in that region. However, as the fire started to move north (Figure 2), the intensity of the fire reduced and the fire spread further into the compartment slowed significantly. The reason for the poor severity of the fire was mainly due to the moisture content of the wood, which when controlled specimens were tested after the fire, showed a moisture content between 18-22% rather than 11%. Higher moisture contents results in more energy being absorbed in the evaporation of water rather than into the fire environment, and reduces the rate of flame spread [7].

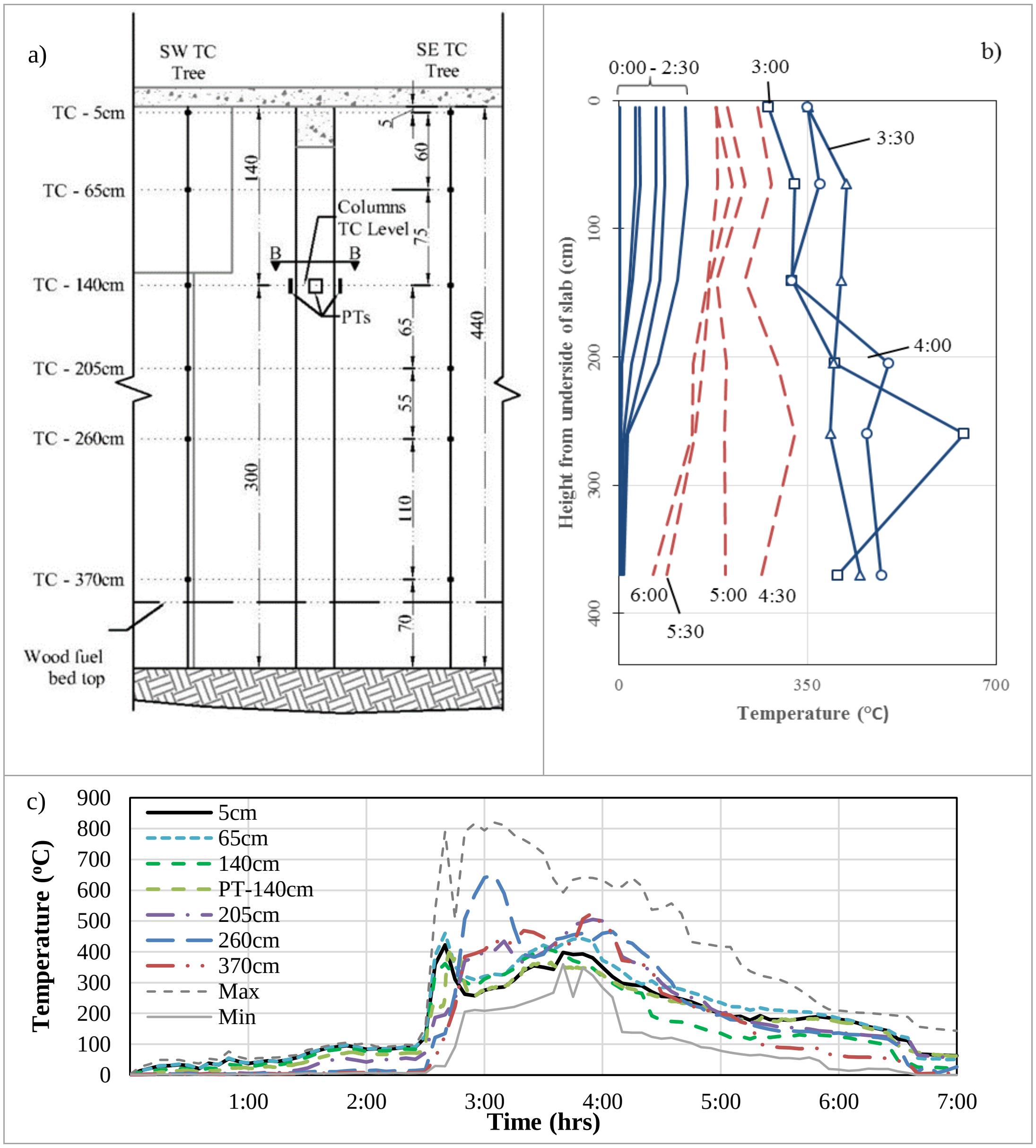

Figure 3. a) TC tree thermocouple layout, and column TC and PT height [Section A-A]; b) variation in temperature over the height of the compartment at 30 minute intervals; and c) averaged time-temperature curves at each of the 6 TC and PT heights below the soffit of 5cm, 65cm, 140cm, 205cm, 260cm, and 370cm.

TEMPERATURES IN REGION OF COLUMN

Figure 3 shows the recorded temperatures during the fire test with respect to the height below the soffit. Figure 3 c) shows the clear jump in temperatures after 2:30 hrs due to the addition of gasoline to the fire compartment to encourage the growth of the fire. It can also be seen from Figure 3 c) that there is a marked temperature differential between the maximum *single* TC recorded temperature and the minimum *single* TC recorded temperatures across the four TC trees (NW, NE, SW, and SE). Maximum *average* temperatures experienced in the top 140cm of the fire compartment were in the region of 400-450^{o}C. In contrast the temperatures further away from the ceiling were more varied but in general hotter than those near the ceiling, with average temperatures peaking at 500^{o}C, 635^{o}C, and 510^{o}C, at 205cm, 260cm, and 370cm from the ceiling, respectively. This is clearly shown in Figure 3 b) which shows the variation in temperature over the height of the compartment at 30 minute intervals, with the maximum temperatures, after the gasoline was added at 2:30 hrs, consistently observed within the lower half of the compartment for over two hours.

Figure **3** b) shows that there is a great deal of variation within the fire environment through the height of the compartment. However the temperature measurements were at a not insignificant distance from the column C1 which is being investigated. To understand the thermal boundary for the column at 3m above the floor, four plate thermometers (PT) were installed around the perimeter of the column (Figure **4** b)). Figure **3** c) shows that the average recorded temperatures from the PTs correlate will with the average TC-140cm temperature data. Any future modelling of the heat transfer to the column can be confident of the thermal boundary present in the tests.

COLUMN TEMPERATURE

Figure **4** a) shows the data recorded at 3m above the floor (140cm below the ceiling soffit), and shows an increase in structural temperatures at around 2:40 which increase relatively linearly until 4:30 at approximately 1^{o}C/min. The very slow heating rate causes very similar temperatures to be observed within the cross-section. As the maximum observed temperatures are well below those that would be considered structurally significant, little to no damage would have been experienced by the concrete material. As previously stated, temperatures at 1.5m above the floor were corrupted, so comparisons of the heat transfer to the column from the maximum temperatures recorded within the compartment cannot be made.

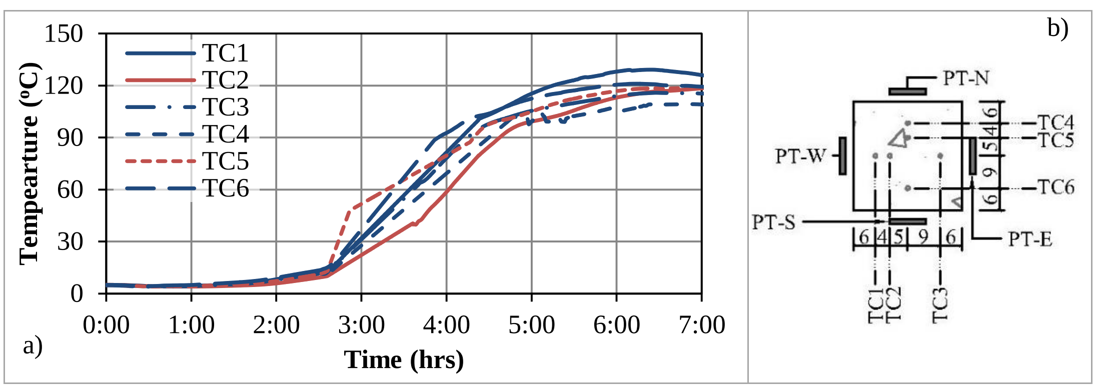

Figure 4. a) Column TC recorded temperatures; and b) location of PT and TC within the column at 140 cm below ceiling soffit.

MODELLING OF TEMPERATURE PROFILES

The aim of the modelling within this paper is to investigate whether the equivalent fire area concept (i.e. [3]) is an appropriate method to represent the thermal and mechanical response for concrete sections exposed to a travelling fire. The concrete cross-section at 140cm below the slab soffit was modelled using ABAQUS, employing thermal boundary properties (ε_{tot}=0.7, α_c=25 W/m^{2}K), the recorded time-temperature history, and concrete thermal properties (upperbound thermal conductivity, 3% moisture content) from EC1 [8] and EC2 [9], respectively. As can be seen in Figure 5, the modelled temperatures are in general slightly greater compared to the averaged recorded temperatures. The average error over the 7 hours is -1.0°C and +7.7°C, with maximum absolute errors of 15°C and 17°C, for TC's 2 & 5 and TC's 1, 3, 4, & 6 respectively. These relatively small errors are likely due to inaccuracies of retrofit placement of the thermocouples within the column, lack of accurate data on the thermal properties of the real concrete column, and modelling a 3D environment in 2D. However these errors are within expected levels experimental and modeling errors.

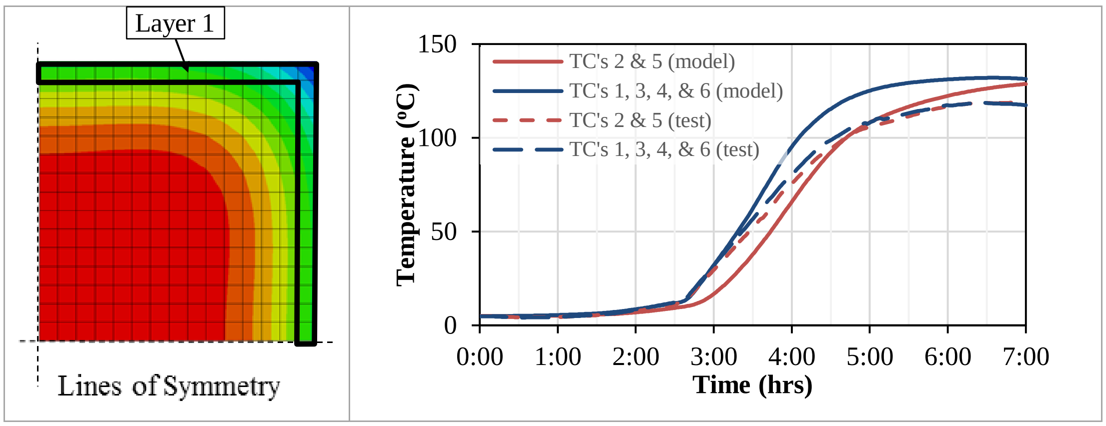

Figure 5. a) quarter cross-section of column at 7hrs of heating; and b) comparison of modelled and recorded average temperatures within cross-section.

Using the thermal model, two subsequent thermal model assessed the thermal profile of the cross-section at different depths below the soffit, 65cm due to the time-temperature curve having the greatest area under the fire curve and 260cm due to the highest recorded temperatures. The cross-section was also modelled to equivalent times under the ISO-834 time-temperature curve with three levels of equivalency being assessed; the total area under the curves; the total area above 150°C [3]; and the total area under the curve above 400°C [5]. Table **I** shows the area under the recoded time-temperature curves for the three different levels of equivalent area and the equivalent time under the ISO-834 fire curve to achieve the same area under the curve.

In terms of thermal response, Figure **6** compares the averaged maximum temperature at the centroid of the cells for each layer of cells at a perpendicular distance from the centroid (schematic shown for layer 1 in Figure **5** a)), determined using recorded gas phase temperatures (Real) or equivalent durations of the ISO-834 fire using either the total area under the curve, area under the curve above 150°C, or area under the curve above 400°C. Figure **6** clearly shows that any of the equivalent area methods do not accurately predict the thermal gradients experienced within the concrete column when it is exposed to a travelling fire.

From the thermal models, an assessment of the reduction in strength relative to the characteristic strength of the concrete and steel rebar is made by taking the weighted average of temperature dependent reduction factors for each layer of cells at a perpendicular distance from the centroid as shown in Table **I**. Two assumptions have been made in this assessment due to lack of other pertinent data; 1) that the concrete is made with siliceous aggregates; and 2) that the steel rebar has a cover of 30mm.

Table **I** shows that the column loses 3%-10% of its capacity in the concrete under the real traveling fire scenario, with the maximum loses of capacity occurring at 260cm below the soffit, and loses no strength in the steel reinforcement. The loss in strength when the section is modelled using the total equivalent area under the fire curves is between 37% - 43%, and 17% - 36% for the concrete and steel, respectively. For equivalent areas above 150^{o}C, losses in the concrete are between 18% - 28%, and it is only when the equivalent areas above 400^{o}C is used that we get close to what is modelled, in terms of strength loss, from the real travelling fire scenario. This shows the significance of both the area and maximum temperatures of the time-temperature history of the travelling fire when trying to create an equivalent time of exposure to the ISO-834 standard fire. However, whilst the strength loss is somewhat accurate, the calculated thermal profile for equivalent areas above 400^{o}C bears little resemblance to those determined using recorded gas phase temperatures (Real).

Table I. Area under fire curves, equivalent times under ISO-834 fire, and averaged strength reduction factors for concrete and steel.

Depth below soffit *(cm)*	**Recorded temperatures area under the curve** *(Temp.mins)*			**Equivalent time under ISO-834** *(mins)*			**Average cross-section reduction factors**							
							Concrete				Steel			
							$f_{c\theta}/f_{ck}$				$f_{s,\theta}/f_{yk}$			
								ISO equivalent area				ISO equivalent area		
	total	>150^{o}C	>400^{o}C	total	>150^{o}C	>400^{o}C	Real	total	>150^{o}C	>400^{o}C	Real	total	>150^{o}C	>400^{o}C
65	82785	35374	1772	95	46	4	0.94	0.57	0.74	1.00	1.00	0.64	1.00	1.00
140	64824	22849	146	77	32	0	0.97	0.63	0.82	1.00	1.00	0.83	1.00	1.00
260	76529	39418	9083	89	51	15	0.90	0.59	0.72	0.96	1.00	0.70	1.00	1.00

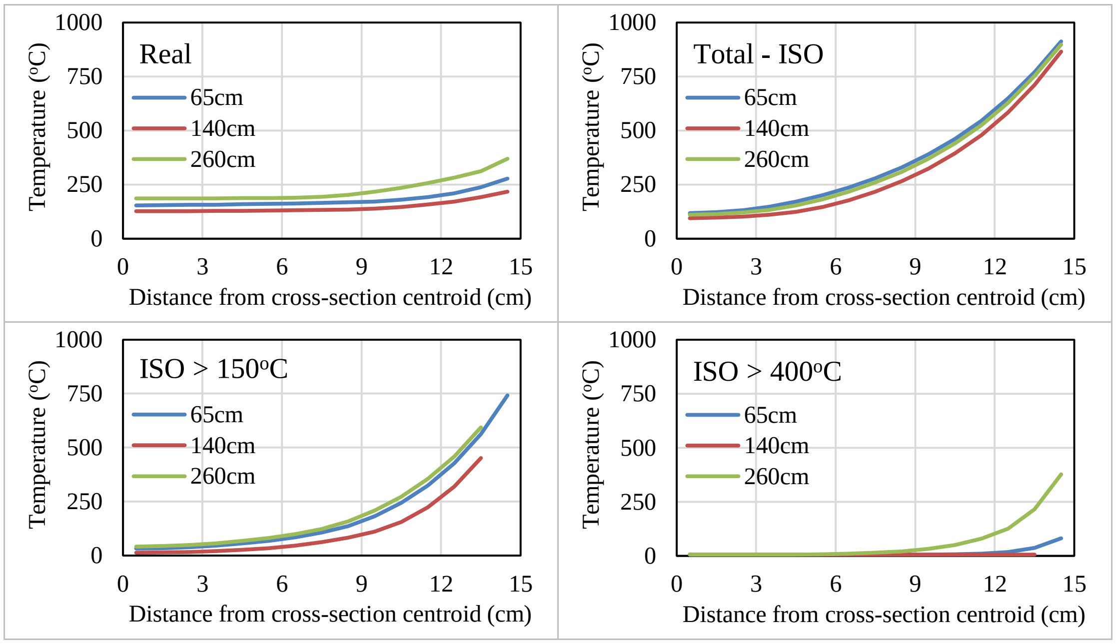

Figure 6. Maximum temperature profiles under real travelling fire, and equivalent times under the ISO-834 fire curve.

CONCLUSIONS

This paper has presented selected results and modelling from the large scale Tisova Fire Test conducted in the Czech Republic in January 2015, from which we can conclude:

- The moisture content of wood severely retarded the fire severity, and even after a gasoline/diesel mix was introduced, temperatures struggled to get above 500°C for any prolonged amount of time within the compartment.
- Temperatures within compartment were found to be hotter in the lower half of the compartment (i.e. nearer the flames) rather than near the ceiling, with potential implications for the design of columns within such compartments.
- Thermal profiles calculated using equivalent areas under the ISO-834 standard fire curve represented very poorly thermal profiles within the concrete section determined using recorded gas phase temperatures.
- The greatest determined strength loss of the concrete within the column occurred at the combination of high temperatures and large area under the fire curve, rather than just due to the latter.
- Strength loss in concrete due to travelling fires was poorly predicted when using equivalent area under fire curves.
- The equivalent are method is not an appropriate method to predict temperature or structural capacity for columns exposed to travelling fires, and a new method may be required for future design purposes.

ACKNOWLEDGMENTS

The authors would like to thank the fire and rescue service in Carlsbad for their enthusiastic support, the Swedish Fire Research Board (Brandforsk), and from the Engineering and Physical Sciences Research Council in the UK (EPSRC).

REFERENCES

[1] CEN, "BS EN 1992-1-2:2004 - Eurocode 2 : Design of concrete structures — Structural fire design," Brussels, Belgium, 2010.

[2] J. Gales, C. Maluk, and L. Bisby, "Large- scale structural fire testing- How did we get here, Where are we, and where are we going?," in *15th ICEM*, 2012, pp. 1-22.

[3] S. H. Ingberg, "Tests of the severity of building fires," *NFPA Q.*, vol. 22, no. 1, pp. 43–61, 1928.

[4] A. Law, J. Stern-Gottfried, M. Gillie, and G. Rein, "The influence of travelling fires on a concrete frame," *Eng. Struct.*, vol. 33, no. 5, pp. 1635-1642, 2011.

[5] D. Rush, L. Bisby, I. Ioannou, and T. Rossetto, "Towards fragility analysis for concrete buildings in fire: residual capacity of concrete columns," in *8th SiF*, 2014, pp. 467-474.

[6] J. Stern-Gottfried and G. Rein, "Travelling fires for structural design-Part II: Design methodology," in *Fire Safety Journal*, 2012, vol. 54, pp. 96-112.

[7] W. L. Fons, H. B. Clements, and P. M. George, "Scale effects on propagation rate of laboratory crib fires," *Symp. Combust.*, vol. 9, no. 1, pp. 860-866, 1963.

[8] CEN, "BS EN 1991-1-2:2002 Eurocode 1- Actions on structures; Part 1-2: General Actions - Actions on structures exposed to fire," Brussels, Belgium, 2009.

[9] CEN, "BS EN 1992-1-2:2004: Eurocode 2: Design of concrete stuctures; Part 1-2: General rules - Structural fire design," Brussels, Belgium, 2008.

An Analytical Approach for Predicting the Deformed Configuration of High Rise Concrete Walls Subjected to Fire Loading Conditions

MINGGUAN YANG, SAMIR MEHAL, DUC TOAN PHAM, PATRICK DE BUHAN and JEAN-VIVIEN HECK

ABSTRACT

This contribution presents an analytical approach for predicting the deformed configuration of high rise concrete walls subjected to fire loading conditions. The approach is based on the thermo-elastic analysis of a 2D plate model taking the geometry change of the plate due to its deflection, into account. A first illustrative application to the particular configuration of infinitely wide panel is performed leading to first conclusive results regarding the thermal-induced out-of-plane change of geometry of the wall.

INTRODUCTION

High rise concrete walls are large size reinforced concrete structures for which the analysis of fire resistance requires a more sophisticated approach than for conventional, *i.e.* smaller size structures. Indeed, the sole degradation of the stiffness and strength properties of reinforced concrete due to severe temperature increase, cannot explain as such the collapse of these structures. Due to the thermal-induced deformations, such slender structures exhibit important out-of-plane (horizontal) displacements, which in turn lead to an eccentricity of the gravity load (self-weight) with respect to the initial plane. As a consequence, bending moments are generated in the wall in addition to the pre-existing compressive axial force distribution, which is usually known as a second order (or P-delta) effect. As the eccentricity increases, the moment due to self-weight eccentricity also increases, thus subjecting the wall to still higher bending moments and associated curvature deformations. Simultaneously, but independently, elevated temperature leads to a degradation of constituent materials. Consequently, it is the combined effect of fire-induced material strength degradation and developing bending effects due to geometry change, which may trigger the overall failure of the structure.

Mingguan YANG, Samir MEHAL, Duc Toan PHAM, Jean-Vivien HECK, Université Paris-Est, Centre Scientifique et Technique du Bâtiment (CSTB), 84 avenue Jean Jaurès, Champs-sur-Marne, 77447 Marne-la-Vallée Cedex 2, France.
Patrick de BUHAN, Université Paris-Est, Laboratoire Navier (Ecole des Ponts ParisTech, IFSTTAR, CNRS UMR 8205), 6-8 avenue Blaise Pascal, Cité Descartes, Champs-sur-Marne, 77455 Marne-la-Vallée Cedex 2, France.

Relying on a simplified 1D beam-like schematization of the problem (figure 1(*a*)), an approach based on the yield design theory ([1]) has recently been developed for analyzing the potential failure of high rise walls (that are larger than the dimensions of experimental test furnaces) under fire conditions (see [2] for more details). The main limitation of the previous approach lies in its inability to still provide reliable predictions as soon as the simplified 1D beam model is no more valid. This is for instance the case of rectangular reinforced concrete panels the lateral vertical sides of which are simply supported, thus preventing out-of-plane displacements along the wall four edges. The structure is then to be adequately schematized as a 2D plate (or slab) (figure 1(*b*)). However, unlike for the simple 1D beam model, the structure is no longer *statically determinate*, and the issue of thermal-induced change of geometry has to be considered in a much more complex framework.

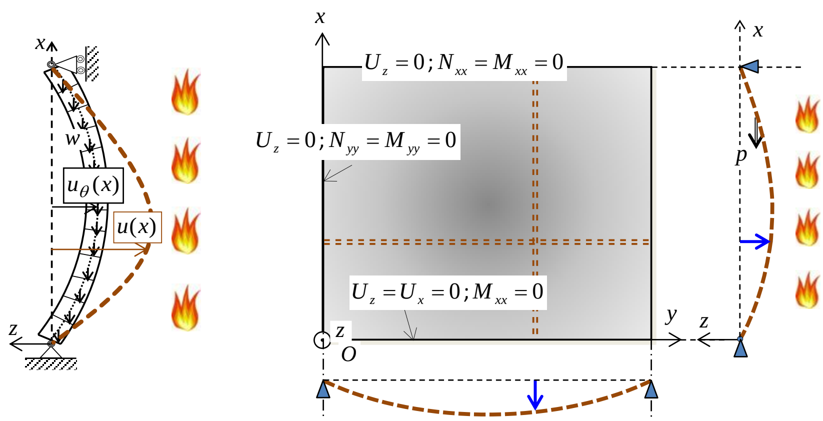

(*a*) (*b*)

Figure 1. (*a*) Simplified 1D beam model and (*b*) 2D plate model of the wall.

It should be noted that, the determination of membrane forces-bending moments yield strength capacities of any wall cross-section as a function of the prescribed temperature gradient, as it has been done for heterogeneous periodic plates ([3]), is completely independent from the preliminary determination of the wall deformed configuration. In this context, the purpose of the present contribution is only focused on predicting the deformed configuration of the wall, regarded as a 2D plate, under the combined action of thermal gradient and in-plane loading due to the self-weight. The application of the yield design approach in order to analyze the global stability of high rise walls, taking the geometry changes induced by the thermal loading into account, is currently under way.

STATEMENT OF THE PROBLEM AND GENERAL EQUATIONS

Prior to the application of thermal loading, the wall is schematized as an initially flat vertical rectangular plate of height H and width L contained in the Oxy-plane as shown in figure 1 (*b*), where the different boundary conditions corresponding to situations encountered in practice, are specified. In short, the wall is simply supported along its four edges (free rotation along these edges), while the other prescribed kinematic conditions indicate that the wall is free to translate both horizontally and vertically along its upper edge, horizontally and vertically upwards along the lower edge, and vertically and horizontally to the right (resp. to the left) along the left (resp. right) hand lateral side.

Thermo-elastic constitutive equations

The wall is uniformly exposed to fire on one side as well as to its self-weight. Following the standard curve of temperature versus time advocated by design codes [4] for modelling the action of a fire on a structure, a heat transfer analysis may be firstly carried out on the wall. In the case of a simple structure such as that considered here, one-dimensional heat propagation across the wall thickness suggests that the field of temperature increase resulting from such a thermal loading will depend on the thickness-coordinate only:

$$\theta(x,y,z)=\theta(z) \tag{1}$$

the corresponding thermal strain being of the form:

$$\varepsilon_{ij}^{\ th}(x,y,z)=\alpha(z)\theta(z)\delta_{ij} \tag{2}$$

where $\alpha(z)$ is the coefficient of thermal expansion of the concrete material located at level z in the wall thickness.

Under fire loading conditions, the thermo-elastic constitutive behavior of concrete subjected to temperature increase must take the so-called Load Induced Thermal Strain (LITS: see for example [5]) into account. This is achieved here by considering that the concrete Young's modulus is a decreasing function of the temperature increase; that is, by applying a reduction factor to the modulus at ambient temperature. Thus, a linear thermo-elastic behavior of the concrete material can be expressed by the following constitutive relationships corresponding a plane state of stress:

$$\begin{aligned}
\sigma_{xx}(x,y,z)&=\frac{E_c(\theta(z))}{1-\nu^2}\left(\varepsilon_{xx}(x,y,z)+\nu\varepsilon_{yy}(x,y,z)-(1+\nu)\alpha(z)\theta(z)\right)\\
\sigma_{yy}(x,y,z)&=\frac{E_c(\theta(z))}{1-\nu^2}\left(\varepsilon_{yy}(x,y,z)+\nu\varepsilon_{xx}(x,y,z)-(1+\nu)\alpha(z)\theta(z)\right)\\
\sigma_{xy}(x,y,z)&=\frac{E_c(\theta(z))}{1+\nu}\varepsilon_{xy}(x,y,z)
\end{aligned} \tag{3}$$

where $E_c(\theta(z))$ denotes the concrete Young's modulus which, as mentioned above, is a function of the temperature increase $\theta(z)$, while ν is the Poisson's ratio which is assumed to remain unaffected by the temperature increase.

Equilibrium equations

The local stresses appearing in the left hand members of the constitutive relationships (3) are in equilibrium with the resultant in-plane (membrane) forces and bending and twisting moments per unit length of the plate:

$$i, j = x, y : N_{ij} = \int_{-h/2}^{h/2} \sigma_{ij} dz \quad \text{and} \quad M_{ij} = \int_{-h/2}^{h/2} - z\sigma_{ij} dz \tag{4}$$

where h is the thickness of the wall along the Oz-axis.

The field of membrane forces must satisfy the following equilibrium equation:

$$\begin{aligned} &\frac{\partial N_{xx}}{\partial x} + \frac{\partial N_{xy}}{\partial y} - p = 0 \\ &\frac{\partial N_{yy}}{\partial y} + \frac{\partial N_{yx}}{\partial x} = 0 \end{aligned} \tag{5}$$

where p is the weight of the plate *per unit area*.

As illustrated in figure 2, the moment equilibrium equation must take the geometry change of the plate due to its large deflection into account (see [6] for more details), thus giving:

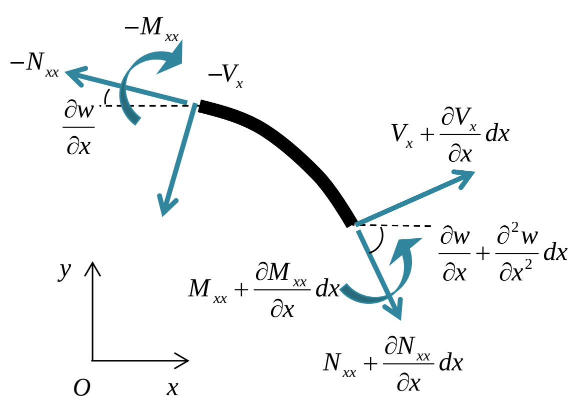

Figure 2. Equilibrium of plate element in its deformed configuration (rotations have been exaggerated for the sake of clarity).

$$\begin{aligned} &\frac{\partial^2 M_{xx}}{\partial x^2} + 2\frac{\partial^2 M_{xy}}{\partial x \partial y} + \frac{\partial^2 M_{yy}}{\partial y^2} - N_{xx}\frac{\partial^2 w}{\partial x^2} - N_{yy}\frac{\partial^2 w}{\partial y^2} - 2N_{xy}\frac{\partial^2 w}{\partial x \partial y} + \\ &-\frac{\partial w}{\partial x}\left(\frac{\partial N_{xx}}{\partial x} + \frac{\partial N_{xy}}{\partial y}\right) - \frac{\partial w}{\partial y}\left(\frac{\partial N_{yy}}{\partial y} + \frac{\partial N_{yx}}{\partial x}\right) = 0 \end{aligned} \tag{6}$$

where w is the transverse displacement of the middle surface (z=0).

Equations of geometrical compatibility

Let u and v, be respectively the displacement components along the x and y directions of the middle surface (z=0) of the plate. It follows that the in-plane strains in any point may be written as:

$$\varepsilon_{xx}(x,y,z) = \frac{\partial u}{\partial x} + \frac{1}{2}\left(\frac{\partial w}{\partial x}\right)^2 - z\frac{\partial^2 w}{\partial x^2}$$

$$\varepsilon_{yy}(x,y,z) = \frac{\partial v}{\partial y} + \frac{1}{2}\left(\frac{\partial w}{\partial y}\right)^2 - z\frac{\partial^2 w}{\partial y^2} \tag{7}$$

$$\varepsilon_{xy}(x,y,z) = \frac{1}{2}\frac{\partial u}{\partial y} + \frac{1}{2}\frac{\partial v}{\partial x} + \frac{1}{2}\frac{\partial w}{\partial x}\frac{\partial w}{\partial y} - z\frac{\partial^2 w}{\partial x \partial y}$$

which takes the out-of plane displacement w into account. This relies on the following assumptions:

- second order terms $(\partial u/\partial x)^2$ (resp. $(\partial v/\partial x)^2$) and $(\partial u/\partial y)^2$ (resp. $(\partial v/\partial y)^2$) can be neglected,
- first order terms $(\partial u/\partial x)$ and $(\partial v/\partial y)$ are of the same order as $(\partial w/\partial x)^2$ and $(\partial w/\partial y)^2$.

Under such assumptions, the geometrical compatibility of in-plane deformations at the middle surface (z=0) of the plate may be written as:

$$\frac{\partial^2 \varepsilon_{xx}}{\partial y^2} + \frac{\partial^2 \varepsilon_{yy}}{\partial x^2} - 2\frac{\partial^2 \varepsilon_{xy}}{\partial x \partial y} = \left(\frac{\partial^2 w}{\partial x \partial y}\right)^2 - \frac{\partial^2 w}{\partial x^2}\frac{\partial^2 w}{\partial y^2} \tag{8}$$

Combining equations (6) and (8) with the constitutive thermos-elastic equations (3) leads to a system of coupled fourth order differential equations, the solution of which must include the prescribed boundary conditions.

APPLICATION TO THE PARTICULAR CONFIGURATION OF INFINITELY WIDE PANEL

The present section will demonstrate how it is possible to obtain an analytical solution for the deflection of the wall in the particular case when the panel width become very large. In such a particular configuration, membrane forces as well as bending moments depend on the vertical coordinate x only, so that equations (5) simplify to:

$$\frac{\mathrm{d}N_{xx}}{\mathrm{d}x} - p = 0 \tag{9}$$

so that, on account of the boundary conditions along the top of the wall (figure 1(b)):

$$N_{xx} = p(x - H) = 0 \tag{10}$$

On the other hand, equation (6) becomes:

$$\frac{\mathrm{d}^2 M_{xx}}{\mathrm{d}x^2} - N_{xx}\frac{\mathrm{d}^2 w}{\mathrm{d}x^2} - \frac{\mathrm{d}w}{\mathrm{d}x}\left(\frac{\mathrm{d}N_{xx}}{\mathrm{d}x}\right) = 0 \tag{11}$$

and taking (10) along with the thermo-elastic constitutive relationships into account, the following fourth order differential equation is finally derived:

$$\left(C-\frac{B^2}{A}\right)\frac{\mathrm{d}^4 w}{\mathrm{d}x^4}-p(x-H)\frac{\mathrm{d}^2 w}{\mathrm{d}x^2}-p\frac{\mathrm{d}w}{\mathrm{d}x}=0 \tag{12}$$

where A, B, C are calculated as follows:

$$A=\frac{1}{1-\nu^2}\int_{-h/2}^{h/2}E_c(z)dz\,;\,B=\frac{1}{1-\nu^2}\int_{-h/2}^{h/2}E_c(z)zdz\ \text{ and }C=\frac{1}{1-\nu^2}\int_{-h/2}^{h/2}E_c(z)z^2dz \tag{13}$$

The solution to the governing equation (12), on account of the boundary conditions, is searched in the form:

$$w(x)=\left[\sum_{n=1}^{\infty}a_n\sin\left(\frac{n\pi x}{H}\right)\right]+\frac{1}{2}\frac{BD-AE}{AC-B^2}(x^2-Hx) \tag{14}$$

where D and E are additional constants calculated as:

$$D=\frac{1+\nu}{1-\nu^2}\int_{-h/2}^{h/2}E_c(z)\alpha(z)\theta(z)dz\quad;\quad E=\frac{1+\nu}{1-\nu^2}\int_{-h/2}^{h/2}E_c(z)\alpha(z)\theta(z)zdz \tag{15}$$

It is clearly apparent that such an out-of-plane displacement is kinematically admissible with the boundary conditions. Making use of the Galerkin procedure for the first term of the series (14) (n=1), the following estimate can be found for the wall deflection:

$$w(x)=a_1\sin\left(\frac{\pi x}{H}\right)+\frac{1}{2}\frac{BD-AE}{AC-B^2}(x^2-Hx) \tag{16}$$

where

$$a_1=\left(\frac{4H^2}{\pi^3}\frac{BD-AE}{AC-B^2}\right)\left(1-\frac{2\pi^2}{pH^3}\frac{CA-B^2}{A}\right)^{-1} \tag{17}$$

ILLUSTRATIVE EXAMPLE

For illustrative purpose, the following example will help clarify the thermal-induced out-of-plane change of geometry of the wall which generates bending moments in addition to pre-existing compressive loads.

Assuming that the wall is exposed to an ISO 834 fire [4] on one of its faces with different time durations (60, 90 and 120 min), the following set of quite representative data has been selected:

- The wall is H=10m high and h=15cm thick.

- The wall is made of a normal weight concrete with siliceous aggregates, exhibiting the following stiffness characteristics at ambient temperature: (20 °C): E_c = 19.2 GPa, ν=0.2.
- Material properties are considered to be temperature dependent according to experimental curves provided by Eurocode 2-Part 1-2 [7].
- Weight of the plate per unit area: p = 3.75 kN/m^2.

A preliminary heat transfer analysis, aimed at evaluating the temperature increase distribution across the wall thickness, should be first conducted. Figure 3 displays the temperature profiles across the wall thickness obtained for instance by the SAFIR computer program [8], corresponding to 60 and 120 min fire durations.

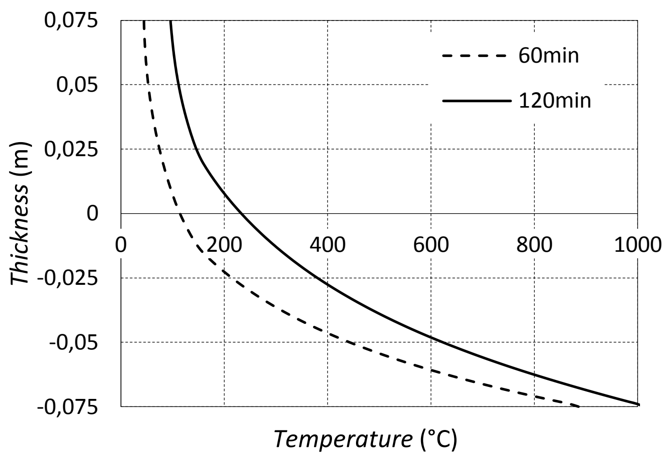

Figure 3. Calculated temperature profiles across the wall thickness for different fire exposures.

Introducing these temperature profiles into the above described calculation procedure, the corresponding deformed configuration can be determined as shown in figure 4.

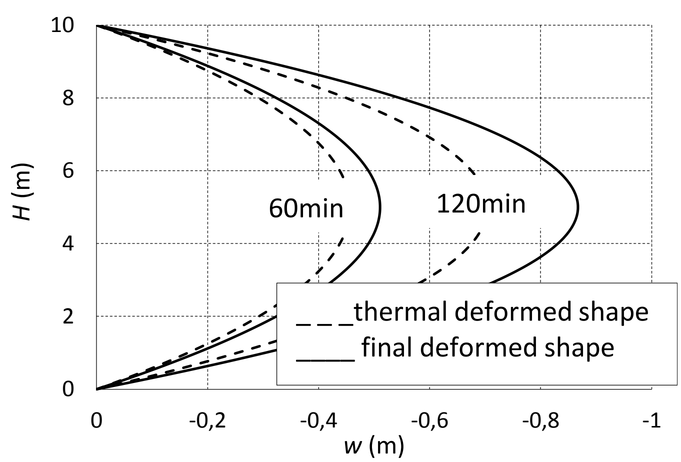

Figure 4. Initial thermal-induced and final equilibrated deformed configurations of a wall.

As it can be clearly seen from figure 4, the difference between the initial thermal-induced deformation and the fully equilibrated configuration is becoming increasingly significant with the time duration.

CONCLUDING REMARKS

Based on a 2D plate modelling of the problem, this paper has proposed and developed a consistent approach for evaluating the deformed configuration of high rise concrete walls subjected to fire loading conditions. The main original feature of the present work lies in the fact that the geometric configuration of the high rise wall is determined from a preliminary thermo-elastic calculation accounting for geometrically non-linear second order effects. The calculation procedure has been performed on a particular configuration of infinitely wide panel illustrating the thermal-induced out-of-plane change of geometry of the wall.

To that end, developments are currently under way concerning both the formulation of a strength criterion of the plate expressed in terms of in-plane membrane forces and bending moments, and the application of this strength criterion on the deformed configuration in order to analyze the global stability of high rise walls.

REFERENCES

1. Salençon, J. 2013. *Yield design.* John Wiley.
2. Pham, D. T., de Buhan, P., Florence, C., Heck, J. V., and Nguyen, H. H. 2015. "A Yield design-based analysis of high rise concrete walls subjected to fire loading conditions," *Engineering Structures,* 87:153-161.
3. Bleyer, J., Pham, D. T., de Buhan, P., and Florence, C. 2015. "Yield design of periodically heterogeneous plates," in *Direct Methods for Limit and Shakedown Analysis of Structures*, Fuschi, P., Pisano, A. A., Weichert, D., eds. eBook: Springer International Publishing, pp. 143-158.
4. EN1991-1-2. 2002. Eurocode 1: Actions on structures-Part 1–2: General actions - Actions on structures exposed to fire.
5. Law, A. and Gillie, M. 2008. "Load induced thermal strain: implications for structural behavior," in *Proc. of the 5th international conference on Structures in Fire,* Singapore. p. 488–96.
6. Ventsel, E. and Krauthammer, T. 2001. *Thin Plates and Shells - Theory, Analysis, and Applications.* Marcel Dekker, Inc.
7. EN1992-1-2. 2004. Eurocode 2: Design of concrete structures-Part 1–2: General rules-structural fire design.
8. Franssen, J.-M. 2005. "SAFIR: A thermal/structural program for modeling structures under fire," *Engineering Journal-American Institute of Steel Construction Inc*, 42(3), 143-158.

A Thermo Mechanical Experimental Investigation on 3 Loaded Concrete Walls Exposed to ISO 834-1 Fire

MD JIHAD MIAH, NICOLAS PINOTEAU and PIERRE PIMIENTA

ABSTRACT

This paper describes the thermo mechanical experimental response of three full-scale ordinary concrete (fc 28 days = 32 MPa) wall specimens (3.0 x 1.2 x 0.2 m^3) subjected to thermal and mechanical loading. The wall specimens were heated on one side over the full length and height of the wall with the ISO 834-1 fire curve, while simultaneously being subjected to a constant uniaxial compressive load at the bottom of the wall. Walls 1, 2 and 3 were loaded at 0, 10 and 110 tons, respectively. The aim of this research is to provide the experimental results on the structural behavior of load bearing concrete walls in a fire situation. No spalling was observed on any of the 3 walls. It has been found that the deflections of the walls decreased with the increased applied mechanical loading. A thermo mechanical modeling benchmark has been organized. Eight laboratories have participated. It is encouraged for whoever wishes to carry out a simulation of the 3 walls in order to compare the calculated deflections with the experimental measurements presented in this paper.

INTRODUCTION

The structural safety of buildings exposed to fire is one of the today's major issues in the design and construction. The reinforced concrete bearing wall system has been widely used in the residential buildings due to the effective roles of bearing walls both in resisting loads and in partitioning the space [1]. With the increasing use of load-bearing concrete walls in modern construction today, it is important to know the fire resistance behavior and the time of failure of concrete walls. For a certain duration of fire, concrete walls should present the ability to limit the temperature rise of the unexposed face of wall (provide an adequate barrier between a fire compartment and an adjacent compartment), integrity of the wall (ensuring that hot gases and flames are not transmitted through the member by means of cracks, fissures), and adequate load bearing capacity (ability to support the imposed loads without collapsing) [2].

Md Jihad Miah[1, 2], Nicolas Pinoteau[1] and Pierre Pimienta [1]
[1]Université Paris Est, Centre Scientifique et Technique du Bâtiment (CSTB), France
[2]Université de Pau et des Pays de l'Adour – SIAME – Anglet, France
Jihad.miah@cstb.fr, nicolas.pinoteau@cstb.fr, pierre.pimienta@cstb.fr

3 walls were exposed to ISO 834-1 fire with 3 different levels of uniaxial mechanical loading. The test results including temperature and deflections of the walls are presented.

This experimental data can be used for future modeling and the development of appropriate design guidelines on the stability of concrete walls when exposed to fire and external mechanical loading. A thermo mechanical modeling benchmark has been organized. Eight laboratories from different countries have participated. The benchmark results have been analyzed [3-4]. It is encouraged for whoever wishes to carry out a simulation of the 3 walls in order to compare the calculated deflections with the experimental measurements presented in this paper. For this purpose, entry data is referenced in this paper and numerical deflection values are intentionally not displayed. Contact person in CSTB is the third author.

EXPERIMENTAL PROGRAM

The experimental program was designed to analyze the thermo mechanical behavior of an ordinary concrete (fc 28 days = 32 MPa) walls. The tests involved 3 reinforced concrete walls of section 1.2 m width x 0.2 m thick and 3.0 m height. Each wall was reinforced by a steel mesh (rebar ø 5.5 mm, mesh 11.9 x 11.9 mm²) positioned at 5 cm from the shuttered surface. All the walls were tested at the age of 2 years. Thermal and mechanical properties of the tested concrete were determined in the previous research work [5]. The tests were performed on the cylindrical samples (104 mm in diameter and 300 mm long) under thermal loads of 120, 250, 400 and 600 °C reached with a slow heating rate of 1 °C/min. The thermal and mechanical properties of the tested concrete are shown in figure 1 and table 1.

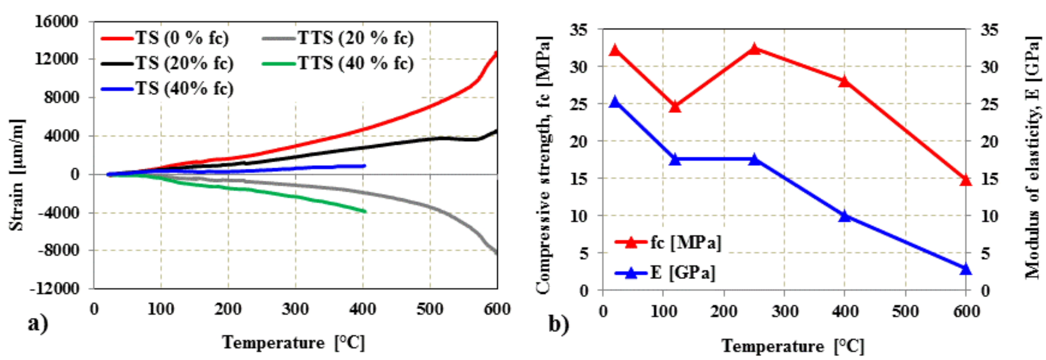

Figure 1. (a) Thermal strain under different levels of compressive stress (TS = Thermal strain, TTS = Transient thermal strain) and (b) hot mechanical properties of concrete as a function of temperature.

TABLE 1. THERMAL EXPANSION COEFFICIENT (α) OF THE TESTED CONCRETE.

T [°C]	< 100 °C	< 200 °C	< 300 °C	< 400 °C	< 500 °C	< 600 °C
α (0 % fc) [µm/m/°C]	8	11	14	19	28	63
α (20 % fc) [µm/m/°C]	7	5	8	11	11	13
α (40 % fc) [µm/m/°C]	4	1	5	3	-	-

The wall specimens were placed vertically in a furnace and heated on one side over the full length and height of the wall with the ISO 834-1 fire time-temperature curve for 2 hours. Each wall was equipped with three lines of thermocouples at different heights. In each line, thermocouples were positioned at 10, 20, 30, 40, 50, 60, 100 and 150 mm depths from the exposed surface. Ten linear variable differential transformers (LVDTs) were positioned at 5 cm from the edges in two rows on the wall height to determine the deflection (Uz), see figure 2 left. Four rotation sensors were positioned on the wall specimens to measure the rotation at the top and the bottom. 2 LVDTs were also positioned on the bottom loading beam for the measurement of the longitudinal movement of the loading beam. A reaction beam at the top of the wall ensured that the wall was loaded in compression.

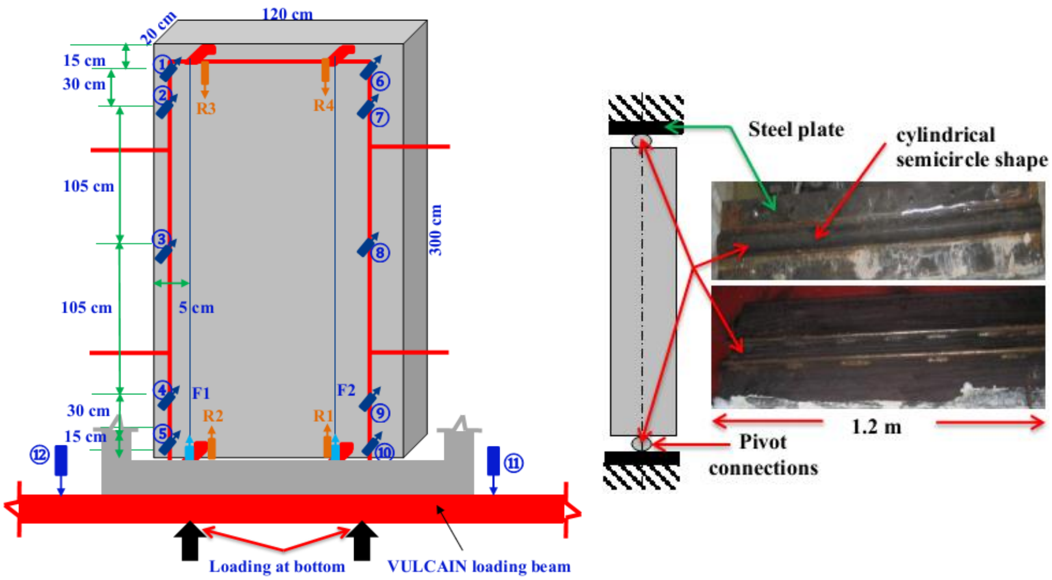

Figure 2. The position of displacement and rotation sensors on the wall specimen (left) and pivot connections between the wall and the frame (right).

A constant compression load was applied at the bottom of the wall before the fire test and then the load was maintained constant throughout the fire test. Walls 1, 2 and 3 were loaded at 0, 10 and 110 tons, respectively. The boundary conditions at the top and the bottom of the walls 2 and 3 were pivot connections centered on the thickness allowing only rotation along the length horizontal axis, see figure 2 right. For wall 1, the top of the wall was allowed to displace under increasing temperatures (free from mechanical loading/restraint). The bottom of that wall was connected by a pivot connection. A cylindrical semicircle shape metal plate was used to create the pivot boundary conditions in order to allow the rotation of the wall during the fire tests.

RESULTS AND DISCUSSION

GENERAL OBSERVATIONS

After about 11 to 18 minutes of fire exposure, water started to appear on the unexposed surface of the walls through the micro-cracks. It has been observed that the appearance of water occurred earlier in the case of the unloaded wall than the loaded walls (11 min for the unloaded wall and 18 min for both loaded walls). This observation suggests that the development of micro-cracks occurred earlier in the unloaded wall than the loaded walls, since the opening of cracks is more restrained by the compressive stress [6]. This observation is consistent with the measured higher deflection of the unloaded wall, see figure 6. None of the walls spalled during and after the test. Some detachment of the surface mortar after cooling could nevertheless be seen in figure 3. This result is mainly explained by the low strength and the low water content of the tested walls. The long drying period of the samples (over 2 years) could have favored the absence of spalling.

Exposed face	Exposed face	Exposed face	Unexposed face after 2 hours of fire
Wall 1 (0 ton)	Wall 2 (10 tons)	Wall 3 (110 tons)	

Figure 3. Exposed and unexposed faces of the three walls loaded at 0, 10 and 110 tons.

THERMAL RESPONSE OF THE WALLS

Figure 4a presents the evolutions of temperatures along the three thermocouple lines in the third wall which was loaded with 110 tons, together with the target ISO 834-1 fire time-temperature curve. Figure 4b presents the same data during the 1st hour. It can be seen that the furnace control temperature followed the target ISO 834-1 fire curve very closely (the variation of temperature is less than 4.5 %). The maximal scatter of temperatures is lower than 90 °C near 500 °C (at 30 mm). The temperatures at 10 mm present lower scatter (< 70 °C near 600 °C). These scatters may be partly explained by the uncertainty of the thermocouple position (due to technical offsets during installation). In all measuring depths, a slight temperature plateau has been observed. The temperature plateau is caused by the water phase change (vaporization). This transformation is endothermic and consumes part of the energy that is brought by heating. As a consequence, the temperature rise of the concrete sample is slowed down. Almost constant temperature was observed in the plateau phase, see figure 4b. It can be emphasized that water vaporization can induce additional temperature gradients [7]. The temperature increased again once all the moisture evaporates and the concrete becomes dry.

The thermal responses of the three walls measured at 10, 20, 30, 40, 50, 60, 100 and 150 mm from the exposed surface are shown in figure 5. The temperature was determined as the average of the three temperatures measured at a given depth. Almost similar development of temperatures has been measured in the 3 walls.

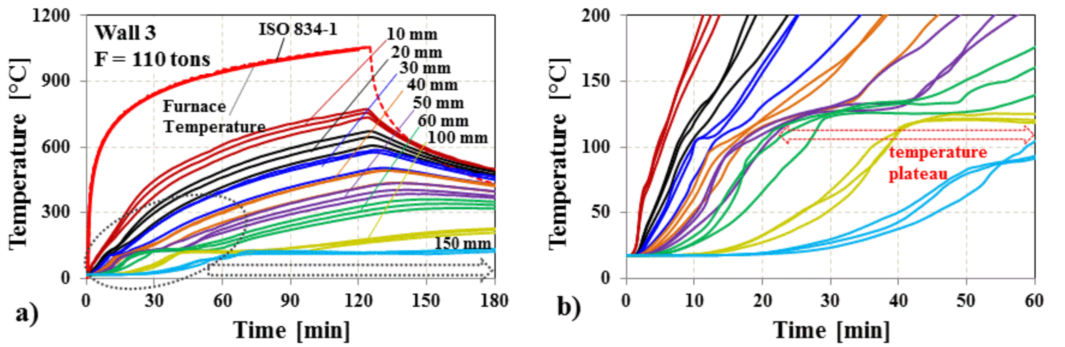

Figure 4. (a) Evolution of the temperatures along three thermocouple lines displayed at different heights along the diagonal of the wall 3; (b) Zoom of the circle point of figure 4a to show detail in data.

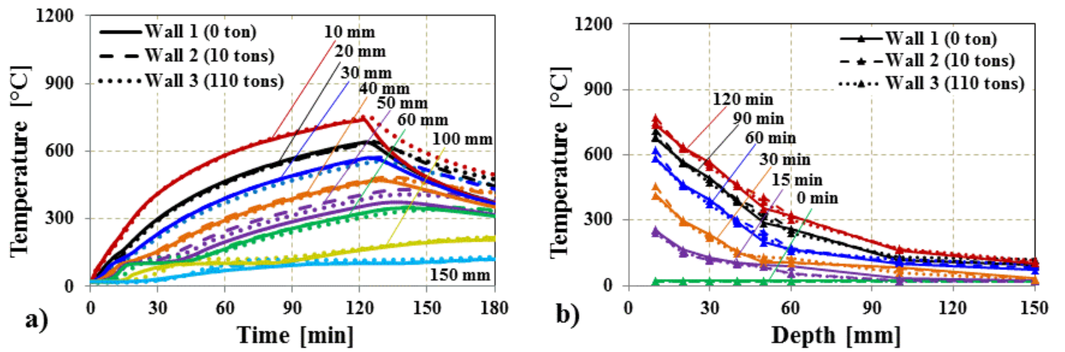

Figure 5. Evolution of the temperatures inside the 3 walls as a function of time and depth (triangular symbols markers on each curve depict the measurement depths of temperature).

Steep thermal gradients were observed near the heated surface of concrete walls, while thermal gradients were lower in the inner depths of concrete walls, see figure 5b. The thermal gradients rose rapidly during the first 60 min of fire when the furnace temperatures were increasing rapidly, see ISO 834-1 curve in figure 4a. The maximum thermal gradient between the first two thermocouple depths (10 mm and 20 mm from the exposed surface) of walls 1, 2 and 3 are respectively, 12, 16 and 12 °C/mm for the first hour of fire and 10, 14, 12 °C/mm for the second hour of fire.

HORIZONTAL DEFLECTION OF THE WALLS

Figure 6 shows the horizontal deflection (Uz) of the walls at three different levels of mechanical loading. As mentioned before, the plots are presented without the deflection numerical values. However, the plots are at the same scale. The positive deflection (Uz) corresponds to displacements towards the fire. The represented displacements were determined from the average of the LVDT sensor measurements on each side of the wall. From these values along the height, the wall profile was plotted at each time using a parabolic curve (which corresponds to a constant curvature along the height). The square markers on each curve depict the measurement points of the displacements (corresponding to the heights of the LVDT sensors). Additionally, the rotation angles at the top and the bottom (averaged 2 by 2 with the inclinometer measurements on each side) are represented with vectors. It can be seen that the deflection of the walls measured by the LVDTs is quite well fitted with the rotation angles measured by the rotation sensors at the top and bottom of the wall. On the Y-axis representing the height of the wall, 0 m corresponds to the bottom and 3 m corresponds to the top of the wall. During the first 30 min of fire, there was an initial rapid bowing of all walls. Beyond that time, a slower rate of deflection was observed.

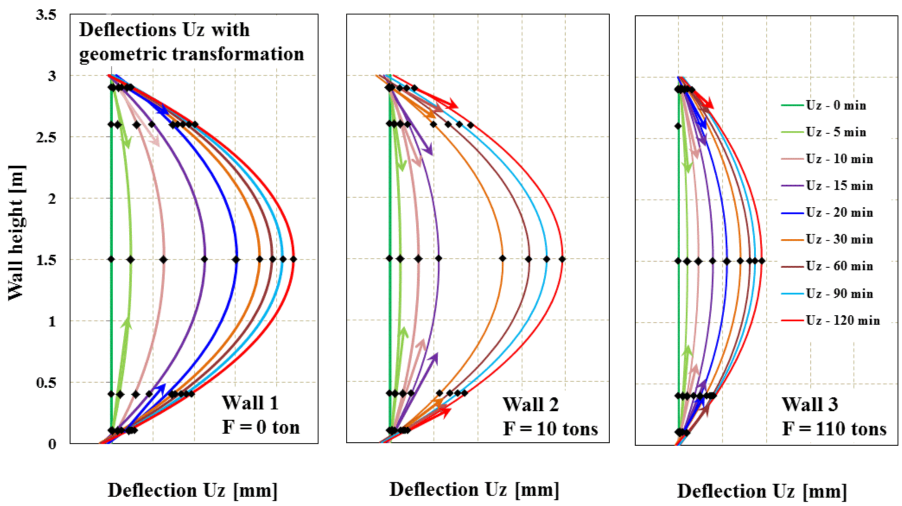

Figure 6. Horizontal deflection of the 3 walls loaded at 0, 10 and 110 tons (plots are at the same scale).

An important observation from figure 6 is that higher deflections were measured for lower applied loads. We can observe that a low level of external mechanical loading (Wall 3 = 4.5 MPa or 14 % of fc at room temperature) can lead to a deflection more than two times lower than the one measured on the walls 1 and 2.during the fire test.

The curvature is linked to two main thermo mechanical phenomena.

i) First, **differential thermal dilatation** (caused by the temperature gradient through the thickness of the wall) will induce a positive deflection (towards the fire). At a given position, the thermal dilatation depends on the temperature and the applied load. This dilatation is often decomposed as 2 terms: **Free Thermal Strain** (depending only on the temperature) and **Transient Thermal Strain** (TTS) (depending on the temperature and the applied stress).

Free thermal strain is common to many materials and induces an expansion. Transient Thermal Strain (TTS) is specific to concrete and induces negative strain (opposing an expansion). The resulting strain (free TS + TTS) is a thermal expansion strain lower than free TS (and that decreases with increasing applied stress).

The thermal curvature is generated by the temperature gradient and the thermal strain. For wall 1, in absence of loading, the thermal strain is close to free thermal strain. Some TTS may be induced by auto stress in the material (due to differential expansion). For wall 2, the load of 10 Tonnes induces TTS which leads to lower thermal expansion than for wall 1, thus creating a lower curvature than for wall 1. For wall 3, the higher load of 110 Tonnes induces more TTS which leads to lower thermal expansion than wall 2, thus creating a lower thermal curvature.

ii) Secondly, **<u>differential the loss of stiffness</u>** (caused by the decrease of modulus of elasticity with temperature) will induce a negative curvature (away from the fire). The fibres close to the exposed surface present high temperatures and low stiffness while the fibres away from the fire present low temperatures and high stiffness. The load applied on the wall is distributed on the entire thickness. Therefore, under similar applied external stress, the compression mechanical strains near the exposed surface will be higher than the compression strains away from the exposed surface. This difference of strains may cause mechanical curvature (influenced thermally by elasticity loss), oriented away from the fire.

Additional phenomena may occur during the fire that could influence the curvature such as creep, cracking or second order effects.

- **Creep** could be seen as a loss of stiffness with time which occurs faster at higher temperatures. With the similar analysis on <u>differential stiffness loss</u>, it could be expected that creep induces a negative curvature away from the fire.
- **Cracking** or material damage occurring near the exposed surface will result in stress redistribution through the wall thickness (by increasing the stress in the cooler areas). With the similar analysis on <u>differential stiffness loss</u>, it could be expected that material damage near the exposed surface favours a positive curvature (towards the fire).
- A **second order effect** may occur during the bending of loaded walls due to the eccentricity of the applied load (known as the P-delta effect). However, studies have shown that the influence of the P-delta effect on deflection can be neglected for walls lower than 6 m high [8].

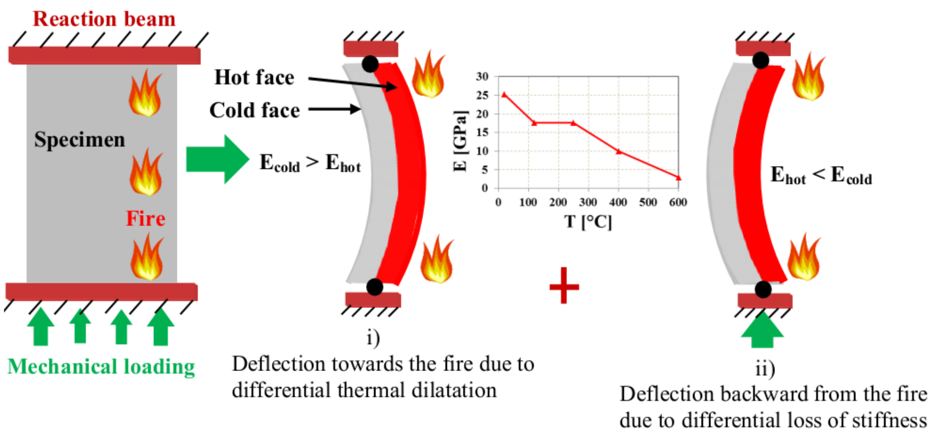

Figure 7. Schematic diagram of the deformed shape of the loaded wall.

CONCLUSIONS

Three full-scale concrete wall test specimens subjected to one-sided fire under three different levels of uniaxial mechanical loading are discussed. This experimental data can be used for future modeling and the development of appropriate design guidelines on the stability of concrete walls when exposed to fire and external mechanical loading. The following conclusions can be drawn based on the results presented in this study.

None of the walls spalled during and after the test, except some detachment of the surface mortar after cooling.

The experimental test results have shown that the mechanical loading has an influence on the deflections of the wall. The deflections of the walls decreased with the increased applied mechanical loading.

It is worth noting that a low level of external mechanical loading (Wall 3 = 4.5 MPa or 14 % of fc at room temperature) can reduce more than half of the deflection of the wall in a fire situation.

These results tend to show that the external mechanical loading induces a number of phenomena directly affecting the deflection. Some of these phenomena are: differential thermal dilatation and differential loss of stiffness. The influence of each phenomenon could be quantified with numerical simulations. It I encouraged whoever wishes to compare simulation to these test results to participate to the modeling benchmark.

ACKNOWLEDGMENTS:

Authors wish to express gratitude to the University of Liege Belgium, Politecnico di Milano, University of Edinburgh, SP Technical Research Institute of Sweden, Institut national des sciences appliquées de Rennes (INSA), University of Bordeaux and Brno University of Technology for their participation in the modeling benchmark. Special thanks are also given to Toan Pham from CSTB for his valuable insight and discussions on the interpretation of the test observations.

REFERENCES

1. Lee, S., Lee, C. (2013). "Fire Resistance of Reinforced Concrete Bearing Walls Subjected to all-sided Fire Exposure," Materials and Structures (2013), 46:943-957.
2. Buchanan, A., Munukutla, V.R. (1991). "Fire Resistance of Load-Bearing Reinforced Concrete Walls," Fire Safety Science-Proceedings of the Third International Symposium, 1991, pp. 771-780.
3. Miah, M. J., Pimienta, P., and Pinoteau, N. (2015). "Comparison of the Measured and the Calculated Temperatures," Benchmark on the Vulcain tests on 3 Walls, Document 3, 2015, CSTB.
4. Miah, M. J., Pimienta, P., and Pinoteau, N. (2015). "Comparison of the Measured and the Calculated Displacements," Benchmark on the Vulcain tests on 3 Walls, Document 5, 2015, CSTB.
5. Mindeguia JC. (2009). "Contribution Expérimental a la Compréhension des risqué d'Instabilité Thermiques des Béton," PhD Thesis (French), Université de Pau et des Pays de l'Adour, France.
6. Castillo, C. and Durrani, A. J. (1990). "Effect of Transient High Temperature on High-Strength Concrete," ACI Materials Journal, V. 87, No. 1, pp. 47-53.
7. Mindeguia, JC., Pimienta, P., Noumowé, A., and Kanema, M. (2010). "Temperature, Pore Pressure and Mass Variation of Concrete Subjected to High Temperature-Experimental and Numerical Discussion on Spalling Risk," Cement and Concrete Research (2010), Vol. 40, pp. 477-487.
8. Pham, D, T., Buhan, Pd., Florence, C., Heck, JV., Nguyen, H, H. (2015). "Yield Design-based Analysis of High Rise Concrete Walls Subjected to Fire Loading Conditions," Engineering Structures 87 (2015) 153-161.

On the Effect of Design Parameters and Boundary Conditions on the Post-Earthquake Fire Performance of RC Structural Walls

ANNA C. BIRELY and SHUNA NI

ABSTRACT

The post-earthquake fire (PEF) behavior of reinforced concrete (RC) structural walls investigated using finite element analysis. Damage due to an earthquake consists of damage to the concrete and steel at the heavily reinforced end regions of the wall. The loss of cover increases the spread of thermal damage through the wall, impacting the thermal fire resistance of the wall and damaging the material for load-bearing fire resistance. This paper investigates the influence of key wall characteristics (geometry, reinforcement ratios, and axial load demand) on the fire resistance. Results indicate that, for damaged RC walls, i) at low axial loads, the insulation criterion controls the fire resistance, ii) higher reinforcement ratios contribute to increased load-bearing fire resistance, and iii) longer boundary regions can have accelerate the rate of heat transfer through a damaged wall.

INTRODUCTION

Post-earthquake fire (PEF) can have a significant impact on the structural performance of a building due to the increased likelihood of fire ignition and extended fire duration resulting from damage to fire suppression systems and/or the inability of emergency responders to access the structure. The potential disaster resulting from extended fire duration times are compounded by the possible damage to the structure due to the earthquake as the damaged or missing concrete can enable a more rapid transfer of heat through the walls and there is less material available for the resistance of loads.

Mousavi et al. [1] provide a detailed review of PEF, including the history, major factors, strategies for mitigation, and methods for evaluation of building performance. Evaluation of building performance requires two key steps: 1) seismic analysis and post-processing to determine effects on characteristics impacting fire resistance and 2) thermal and/or thermal-mechanical analysis to assess fire resistance. Mousavi et al. list a key research need as experimental and analytical studies to inform development of

Anna C Birely, 3136 TAMU, College Station, TX 77843-3136, U.S.A.
Shuna Ni, 3136 TAMU, College Station, TX 77843-3136, U.S.A.

guidelines for assessing PEF performance of structures. The work presented in this paper is focused on numerical analysis of reinforced concrete (RC) structural walls.

RC walls are critical components for the resistance of lateral loads generated by earthquakes and often serve the dual purpose of serving as fire barriers. Further, RC walls are very common lateral load resisting systems and can be found in both steel and concrete buildings. Consequently, the PEF performance of these components is critical to understanding the performance of many buildings. Damage to RC walls from an earthquake include cracks (horizontal and diagonal), loss of cover concrete, crushing of core concrete in boundary regions (heavily reinforced regions at the extreme compression/tension ends of the walls), and buckling/fracture of reinforcing bars. These physical changes to the wall can have a significant impact on the fire resistance of RC walls because they enable a more rapid transfer of heat through the walls and there is less material available for the resistance of lateral loads.

In this research, finite element models are used to conduct uncoupled thermal-mechanical analysis of reinforced concrete walls. The work builds on previous work by the authors in this area and specifically focus on boundary conditions for the walls and key wall characteristics (thickness, reinforcement amount and layout, and axial load ratio). The fire resistance is evaluated by both the insulation criterion (Criterion I) and the load-bearing criterion (Criterion R).

PRELIMINARY INVESTIGATION

Ni and Birely [2] conducted a preliminary investigation of the impact of fire resistance of earthquake damaged reinforced concrete walls using numerical models. The models were created using ABAQUS. For heat transfer analysis, 8-node linear heat transfer brick elements were used for concrete and 2-node heat transfer link elements were used for reinforcement. Tie connections were used for heat transfer between the steel and concrete. For mechanical analysis, 8-node linear brick elements were used to model the concrete and 2-node linear 3-D truss elements were used to model the reinforcing bars. Reinforcement was embedded with the assumption of perfect bond.

The models were validated by comparing the results to experimental data of simply supported walls subjected to fire only (Crozier and Sanjayan [3]). The walls were 75, 100, and 150 mm thick, which is thinner than most lateral load resisting walls found in mid- to high-rise buildings on the west coast of the United States. Results of the heat transfer analysis were consistent with the experimental measurements. Minor discrepancies arose due to lack of environmental temperatures, inconsistencies in furnace temperatures relative to intended loading used in models, and uncertain material properties. Results of the mechanical analysis provided reasonable deformations in the walls. Discrepancies arose due to uncertainties in material properties and failure of the model to capture fracture of the concrete, a failure mode that controlled in some tests. Post-processing of the data to capture this was successful.

In considering the damage due to earthquakes, the loss of cover is considered to be the most critical damage as it allows for a more rapid transfer of heat through the wall. To investigate PEF behavior of RC walls, Ni and Birely simulated the loss of cover concrete in the models by significantly reducing the thermal and mechanical properties to be sufficiently small that the impact of the concrete was similar to results for no concrete. This was chosen over the conducting a lateral load analysis using ABAQUS/STANDARD for two reasons. First, ABAQUS is not an ideal software for accurately capturing the response of walls subjected to cyclic lateral loads. Second, the aim of the investigation was to investigate the impact of different damage levels. By manually forcing these damage levels, the impact of damage characteristics can be directly evaluated. The sizes (length and height) of the concrete damage considered were selected based on damage characteristics of reverse-cyclic lateral load tests documented by Birely [4]. One of these experimental tests were used as the basis for investigating the PEF response of walls. The wall was considered to be a cantilever (fixed at bottom, free at top).

Ni and Birely found that the fire resistance of cantilever walls was influenced more by the length of the damage relative to the length of the wall than it was by the height of the damage relative to the height of the wall. Increase in the axial load ratio from 2.5% to 5.0% was found to have a minimal influence on the fire resistance. In all cases, the fire resistance measured by the load bearing criteria was found to control over the thermal insulation criteria. Short comings of the investigation by Ni and Birely are i) the use of cantilever walls, when most walls in buildings are likely to have some degree of restraint, and ii) limited wall characteristics investigated.

OVERVIEW OF PARAMETRIC STUDY

To build on the findings of Ni and Birely [2], the work presented here investigates the PEF performance of RC structural walls with different boundary conditions and different wall design characteristics that are known to have influence on the fire and/or seismic response of walls.

The RC walls investigated are based on a prototype walls considered to fall within a range of representative buildings characteristics and low- to mid-rise buildings. The prototype wall is four stories tall, with floor heights of 10 ft. The wall length is 10 ft. Classification of walls for lateral load resistance is based on one of two measures for the relative height to length. The first, aspect ratio (wall height to wall length ratio), is a function of geometry only. The second, shear span ratio is a function of the wall geometry and the assumed lateral load distribution. Walls with low aspect ratios or shear span ratios are considered to be squat walls and have response and failure dominated by shear. Walls with high aspect ratios or shear span ratios are considered to be slender walls and have response and failure dominated by flexure. The prototype wall in this study is at the low end of slender walls and earthquake damage would be expected to have the characteristics similar to the damage modeled.

The thickness of the wall is a key property for both fire and lateral load resistance. For fire resistance, the thickness impacts heat transfer analysis and stability for axial load bearing resistance; walls are typically classified based on an out-of-plane aspect ratio of the unbraced height to the thickness of the wall. For lateral load resistance, the thickness impacts the cross-sectional aspect ratio (wall length divided by wall thickness). The cross-sectional aspect ratio has been shown to influence the ductility of the walls (Birely [4]). Two wall thicknesses are considered in this study: 8 inch (200 mm) and 12 inch (300 mm).

A cross-section for one of the walls studied is shown in Figure 1. A typical design of walls is to have reinforcement concentrated near the extreme compression/tension fibers. These heavily reinforced regions, typically called boundary elements, have closely spaced confining reinforcement to improve the ductility of the walls. This confining reinforcement often also contains cross-ties between pairs of bars on opposite faces of the wall. The length of the boundary element relative to the length of the wall is a parameter that can impact the performance of a wall subjected to seismic loads, thus, the length is introduced as a variable in this study. Three boundary element lengths are considered, 10, 15, and 20% of the wall length. The area between the boundary elements is typically referred to as the web of the wall and contains code minimum longitudinal reinforcement. The total area of longitudinal reinforcement divided by the wall area is the reinforcement ratio, ρ; reinforcement ratios of 1.2% and 1.9% are considered in this study. Transverse reinforcement spanning the length of the wall contributes to the shear strength of the wall; impact of this variable is not considered in this study.

The final parameter considered in this study is the axial load ratio of the wall. In most walls, an axial load ratio, λ_N, of up to10% is reasonable for design and analysis, although larger axial loads up to 30% are possible. In this study, axial load ratios of 2.5%, 6.25%, 12%, and 25% are considered. Table I provides a summary of all walls considered in this study.

The material properties were kept consistent for all walls considered in the parameter study. For concrete, a compressive strength of 6,000 psi (42 MPa) was used and for reinforcing steel, yield strength of 75 ksi (525 MPa) was used. The size of the expected damage was not varied in this study, as this was explored by Ni and Birely (2014). The damage was modeled on both ends of the wall and extended a length of one-quarter the wall length and one-tenth the wall height. The depth of the damage was considered to be the cover concrete only. This damage is a worst case scenario for the surface area extent of damage.

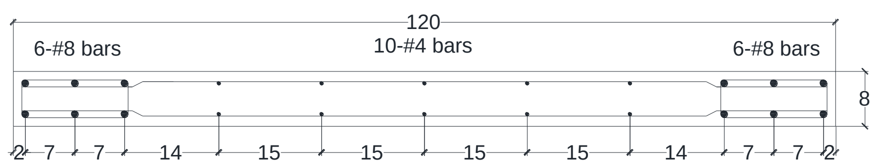

Figure 2. Cross-section of Wall 1 *t8-be15%-ρ1.2%* walls. Dimensions shown in inches.

TABLE I. MATRIX OF NUMERICAL ANALYSES.

Number	Name	t_w, in	L_B/L_w	ρ	λ_N
1(ref)	t8-be15-ρ1.2-λ2.5	8	0.15	1.2%	2.5%
2	t12-be15-ρ1.2-λ2.5	12	0.15	1.2%	2.5%
3	t8-be10-ρ1.2-λ2.5	8	0.10	1.2%	2.5%
4	t8-be20-ρ1.2-λ2.5	8	0.20	1.2%	2.5%
5	t8-be15-ρ1.9-λ2.5	8	0.15	1.9%	2.5%
6	t8-be15-ρ1.2-λ0.5	8	0.15	1.2%	0.5%
7	t8-be15-ρ1.2-λ6.25	8	0.15	1.2%	6.25%
8	t8-be15-ρ1.2-λ25	8	0.15	1.2%	25%

Uncoupled thermal-mechanical analysis of the walls was conducted in ABAQUS/Standard following the method used by Ni and Birely (2014), summarized earlier in this paper. The thermal properties of the concrete and steel were modeled in accordance with EC2-02. All models had one face of the bottom floor exposed to fire, with the other surfaces exposed to room temperature, as shown in Figure 2. For the fire-exposed surface, both heat radiation and heat convection were considered; for all other surfaces, only radiation was considered. The heat transfer parameters for the fire-exposed side are: film coefficient = 25 $W/m^2/K$ and emissivity = 0.7; for other surfaces, emissivity=0.9. The fire exposed side is heated following the standard ASTM E119 time-temperature curve. For the mechanical analysis, two boundary conditions were considered: cantilever walls, similar to those used in previous studies, and a cantilever wall with a roller at the top. Realistically, some lateral restraint should be expected at each floor level, but use of a restraint only at the top provides an extreme on the potential load-bearing fire resistance while providing a more realistic restraint than a cantilever wall. The region of damage concrete was modeled by directly removing the concrete in that region.

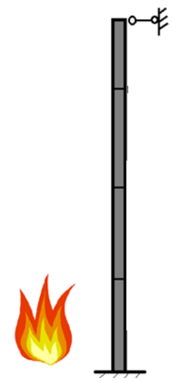

Figure 3. Schematic of boundary conditions and fire location.

SUMMARY OF RESULTS

Thermal Analysis

The results of the heat transfer analysis are independent of the axial load applied to the wall and the boundary conditions used for the mechanical analysis, resulting in five unique models to consider. The fire resistances for the damaged and undamaged walls are presented in Table II. The fire resistance is based on the insulation criteria; that is the average temperature rise over the whole non-exposed surface is limited to 140 K (252^{o}F) and the maximum temperature rise at any point of that surface does not exceed 180 K (324^{o}F). Underlined numbers indicate the value (average or minimum) that controls the fire resistance; for all walls considered in this study, maximum temperature increase determines the fire resistance.

As expected, walls with a larger thickness are less impacted by the earthquake damage. In part this is due to the depth of damage being the same for both thicknesses used. Unexpected results were the influence of the boundary element length on the damage. These differences are driven in part by the mesh sensitivity of the maximum temperature and the location of the maximum temperature in the walls with different reinforcing steel layout. However, it is clear that there is an influence of the amount of steel, which can increase the rate at which the heat is transferred to the unexposed face. This is consistent with the impact of reinforcement ratio on the decrease in fire resistance as a function of damage.

TABLE II. FIRE RESISTANCE (INSULATION) OF WALLS.

Numbers	Name	Undamaged		Damaged		% Decrease
		Avg., hrs	Max, hrs	Avg., hrs	Max., hrs	
1, 6-8	t8-be15-ρ1.2	6.46	<u>6.19</u>	5.73	<u>2.53</u>	59
2	t12-be15-ρ1.2	15.32	<u>14.43</u>	14.30	<u>8.27</u>	43
3	t8-be10-ρ1.2	6.47	<u>5.95</u>	6.15	<u>4.02</u>	32
4	t8-be20-ρ1.2	6.46	<u>5.26</u>	5.79	<u>3.11</u>	41
5	t8-be15-ρ1.9	6.18	<u>5.63</u>	5.45	<u>2.65</u>	53

Mechanical Analysis

The results of the mechanical analysis for walls with the boundary conditions shown in Figure 2 are presented in Table III. The time to failure, determined by instability of the model and failure to support load, is provided for the damaged and undamaged walls.

The impact of the boundary conditions used is significant. In the cantilever wall results presented by Ni and Birely, small axial load did not impact on the fire resistance of the wall, which was controlled by mechanical failure. In the walls considered in this study, small levels of axial have minor impact on the load bearing fire resistance of the walls. Although cantilever data is not provided in Table III, it is important to note that the boundary conditions have a significant impact on the fire resistance. For example, damaged Wall 1 has a fire resistance of approximately 3.5 hours for a cantilever boundary condition, controlling over the insulation fire resistance time. If damaged Wall 1 has a roller support at the top, the load-bearing fire resistance is approximately 5.6 hours and the insulation fire resistance controls.

For Walls 1-7, the earthquake damage decreases the load-bearing fire resistance by no more than 20%, however, it is important to note that for all of these, the insulation fire resistance of the damaged wall controls the fire resistance. It is only with an increase in the axial load that the mechanical. For Wall 7, the axial load ratio is 6.25% and the load-bearing fire resistance comes close to controlling over the insulation fire resistance. At higher axial load ratios, it follows that the load-bearing criteria will control; this is the case for Wall 8 (25% axial load), which has a fire resistance that is controlled by the load-bearing criterion.

Other variable considered in this study are the amount of longitudinal reinforcement and the length of the boundary element relative to the wall length. Both have a less significant influence on the reduction in load-bearing resistance of damaged walls. An increase in the total longitudinal reinforcement ratio for walls increases the fire resistance (Wall 5 compared to Wall 1). Conversely, the load resistance of the walls with longer boundary elements is decreased. It is believed that this is due to a larger volume of steel exposed to the fire loads (the confining reinforcement has smaller spacing than the transverse reinforcement in the wall web). This is consistent with the larger decrease observed in the insulation fire resistance for these walls. It is important to note that all other parameters varied were done so only at low axial load ratios and the impact at higher axial load levels may be more pronounced.

TABLE III. FIRE RESISTANCE (MECHANICAL) OF WALLS.

Number	Name	Undamaged, hrs	Damaged, hrs	% Decrease
1	t8-be15-ρ1.2-λ2.5	6.92	5.55	20
2	t12-be15-ρ1.2-λ2.5	>8	>8	-
3	t8-be10-ρ1.2-λ2.5	6.83	6.67	3
4	t8-be20-ρ1.2-λ2.5	6.98	5.33	24
5	t8-be15-ρ1.9-λ2.5	>8	>8	-
6	t8-be15-ρ1.2-λ0.5	>8	>8	-
7	t8-be15-ρ1.2-λ6.25	3.91	3.13	20
8	t8-be15-ρ1.2-λ25	1.64	1.25	24

CONCLUSIONS

This study investigated the impact of wall boundary conditions (cantilever vs cantilever with roller support) and wall design and load characteristics, on the fire resistance of reinforced concrete structural walls damaged by earthquakes. Fire resistance was evaluated on the basis of the insulation and load-bearing criteria. Results indicate that typical wall axial loads (i.e. less than 10%), the fire resistance of damaged walls is controlled by the insulation criterion, with significant decreases in the fire resistance compared to undamaged walls. Key influences on the severity of the decrease were the wall thickness and the volume of reinforcing steel in the wall. At large axial loads, the load-bearing criteria controls for both damaged and undamaged walls, although the percentage decrease in the fire resistance due to the damage is not much more severe than it is for walls with low axial loads. For large axial load ratios, a more accurate representation of boundary conditions (i.e. restraint at all floors) may be informative in assessing the true risk to building exposed to post-earthquake fire.

It is important to emphasize that this study investigate the impact of earthquake damage assumed to be the worst-case scenario for damage to cover concrete and does not represent a detailed exact representation of damage in a wall. That is, the impact of residual cracks and reduced mechanical properties of reinforcing steel and concrete are not considered. The results provide a preliminary examination of the impact of earthquake damage on the fire resistance of walls.

REFERENCES

1. Mousavi, S., A. Bagchi, and V.K.R. Kodur. 2008. "Review of Post-Earthquake Fire Hazard to Building Structures," *Canadian Journal of Civil Engineering,* 35: 689-698.
2. Ni, S. and Birely, A.C. 2014. presented at the 10th U.S. National Conference on Earthquake Engineering, July 21-25, 2014, Anchorage, Alaska, USA.
3. Crozier, D.A., and J.G. Sanjayan. 2000. "Tests of Load-Bearing Slender Reinforced Concrete Walls in Fire," *ACI Structural Journal*, 97(2): 243-253.
4. Birely, A.C. 2012. "Seismic Performance of Slender Reinforced Concrete Walls," Ph.D. Dissertation, University of Washington, Seattle, WA.

CONCRETE STRUCTURES: FIBER REINFORCEMENT AND STRENGTHENING

Effects of Polypropylene and Steel Fibers on Permeability of Ultra-high Performance Concrete at Hot State

Y. LI and K. H. TAN

ABSTRACT

Permeability of concrete is identified as one of the key parameters controlling explosive spalling. Measurements of permeability were performed on ultra-high performance concretes (UHPC) at elevated temperature ranging from ambient temperature to 300 °C. The effects of polypropylene fibers and steel fibers were investigated. The results show that plain UHPC and UHPC with steel fibers exhibit steady increase in permeability with increasing temperature. UHPC with polypropylene fibers exhibits a sudden increase of permeability at 150 °C. The microstructure of UHPC before and after exposure to elevated temperature was investigated by conducting Field Emission Scanning Electron Microscope (FESEM) observation. The results confirm that both the channels caused by melted polypropylene fibers as well as the generated micro crack network are the major factors causing a significant increase in permeability.

1. INTRODUCTION

Compared with normal strength concrete, ultra-high performance concrete (UHPC) has superior performance such as high strength, high toughness and impact resistance, high abrasion resistance, high durability, etc. These excellent properties are due to dense microstructure on concrete. Due to superior performance, UHPC has been increasingly utilized in many civil engineering structures such as high-rise buildings, tunnels, and bridges. However, the dense microstructure makes UHPC even more vulnerable to explosive spalling in fire condition [1, 2]. Explosive spalling results in partial loss of concrete cross section and exposure of steel reinforcements to fire, which significantly compromises the load-bearing capacity of structures [3, 4].

School of Civil and Environmental Engineering, Nanyang Technological University, Singapore 639798, Singapore

High pore pressure is one of the governing factors for explosive spalling. Permeability is assumed to be the parameter controlling moisture transport and pore pressure build-up inside the heated concrete. It is a useful parameter for UHPC when assessing its performance under fire condition. Majority of experimental studies on permeability were performed in the residual state, after the specimens have cooled down to ambient temperature from heating. At this state, differential thermal expansion between concrete matrix and aggregates caused mismatch and polypropylene fibers may recrystallize and regain stiffness in the concrete matrix at the residual state. Therefore, the measured residual permeability values at ambient temperature will be different from the actual values at the hot state. Moreover, a long duration is necessary for drying the water caused by dehydration of cement paste. Thus, residual state permeability tests cannot eliminate the influence of water and the intrinsic permeability cannot be measured. To gain a deeper understanding of spalling mechanism, it is imperative to have the permeability measurements performed at the hot state. However, there are very few experiments on permeability at elevated temperatures. The purpose of the present study was to investigate the effects of PP fibers and steel fibers on permeability of UHPC at elevated temperature, which could be used as input parameters in numerical modelling. Moreover, microstructure of UHPC before and after heating was investigated to better understand the mechanism of changing permeability and its effect on explosive spalling.

2. EXPERIMENTAL PROGRAM

2.1. Mix Proportions and Specimens Preparation

The control mix proportion was chosen based on UHPC mechanical property research. PP fibers and steel fibers were selected as key factors. Their influences on permeability were investigated. TABLE I shows the mix proportions of ultra-high performance concrete in which UHPC-P-control serves as the control specimen with no polypropylene or steel fibers, UHPC-P-PP has only 3.0 kg/m^3 of polypropylene fibers, while UHPC-P-steel has 2.5% of steel fibers in volume. The cube compressive strength of UHPC-P-control, UHPC-P-PP, and UHPC-P-steel is 149.6 MPa, 159.7 MPa, and 172.1 MPa respectively ($50\times50\times50$ mm^3 cubes were used).

The cement used in this research was ASIA@ CEM II 52.5 R. Steel fibers were supplied from Dramix@. Their aspect ratio is equal to 81. Their length is 13 mm and diameter is 0.16 mm. The steel fibers have tensile strength no less than 2000 MPa. The monofilament polypropylene fibers were supplied by DFL and they have tensile strength between 550-600 MPa. Their length is 12-19 mm and diameter is 18-60 μm. A third generation polycarboxylic type superplasticizer Sika@ ViscoCrete@-2044 was used in all concrete mixtures. Natural river sands were used as aggregates in concrete mix design. The maximum aggregate size was 0.6 mm.

Specimens were cast in cake-shape polyester molds with a depth of 45 mm. After 24 hour curing in molds, the specimens were demolded and stored in lime-saturated water at ambient temperature for 28 days. After curing, the discs were grinded from both sides to 40 mm thick and smoothened. Since the present tests are to evaluate intrinsic permeability of UHPC, the effect of humidity had to be

TABLE I. Mix Proportions.

Mix Design	PP fiber (kg/m^3)	Steel fiber (V_f,%)	Relative weight ratio to cement						f_c (MPa)
			SF	AG	C	SP	SS	W/B	
UHPC-P-control	**0.00**	**0.00**	**0.25**	**1.1 (0.6 mm)**	1.00	0.03	0.25	0.22	149.6
UHPC-P-PP	**3.00**	**0.00**	**0.25**	**1.1 (0.6 mm)**	1.00	0.03	0.25	0.22	159.7
UHPC-P-steel	**0.00**	**2.50**	**0.25**	**1.1 (0.6 mm)**	1.00	0.03	0.25	0.22	172.1

SF: silica Fume
AG: biggest aggregate sizes in mm are shown in the table.
C: cement
SP: superplasticizer
SS: Silica sand
W/B: water binder ratio
f_c: Compressive strength after 28 days

eliminated. All the specimens were dried in oven at 105 °C until constant mass was reached. High-temperature silicone was smeared all around the side face of the specimens to prevent air leakage.

2.2. Measurements of Gas Permeability

Apparent gas permeability was calculated based on Darcy's law as modified by Hagen-Poiseuille relation [5]:

$$k_{\mathrm{a}} = \frac{Q}{A}\frac{2\mu L p_{\mathrm{atm}}}{\left(p_{\mathrm{i}}^2 - p_{\mathrm{atm}}^2\right)} \tag{1}$$

where k_{a} [m^2] is the apparent permeability, Q [m^3/s] is the gas flow rate, A [m^2] is the specimen cross sectional area, p_i [Pa] is the inlet pressure, p_{atm} [Pa] is the outlet pressure (atmospheric pressure), L [m] is the length of a specimen, μ [Pa·s]is the dynamic viscosity of the gas used.

During gas transport through UHPC, the contribution of Knudsen diffusion might be very significant due to the average pore size is of the same order of magnitude as the mean free path of gas molecules [6]. Pressure will influence the mean free path of gas molecules. Hence, the permeability measured would depends on the pressure applied. In order to get intrinsic permeability, Klinkenberg suggested a method to correct the apparent permeability. The intrinsic permeability is regarded as a measurement independent of applied pressure. It can be obtained by:

$$k_a = k_{\mathrm{int}}\left(1 + \frac{b}{p_m}\right) \tag{2}$$

where k_{int} [m^2] is the intrinsic permeability, b [Pa]is the Klinkenberg constant, and $p_m = \left(p_i + p_{\mathrm{atm}}\right)/2$ [Pa] is the average value of the inlet and outlet pressures (atmospheric pressure) on the two sides of the specimen.

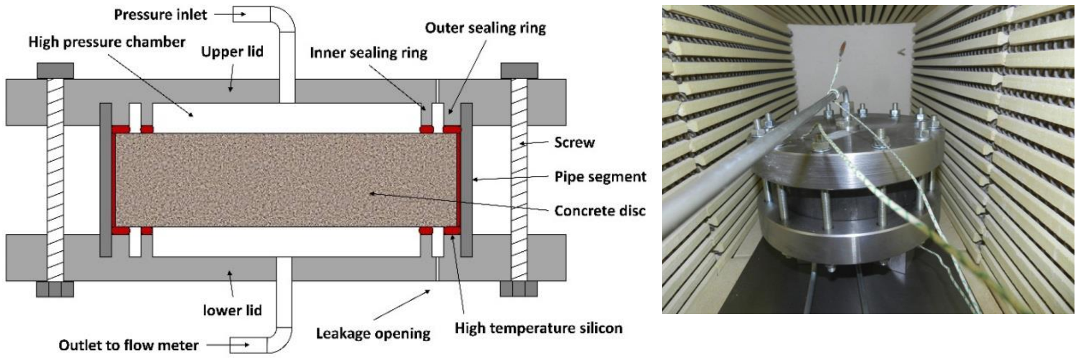

Figure 1. Experimental setup to measure gas flow of specimens.

Experimental Setup and Testing Procedure

Figure 1 presents the experimental setup to measure gas flow through a specimen at the hot state. The device consists of two lids with two sealing rings and a pipe segment. The concrete disk is placed between the two lids and sealed with high-temperature silicone. The entire device is placed inside an electric furnace. A compressor supplies compressed air into the upper chamber of the device and the velocity of air penetrating the concrete disc is measured from the outlet tube.

Specimens were uniformly heated up to target temperature levels of 30 °C, 105 °C, 150 °C, 175 °C, 200 °C, 250 °C, and up to 300 °C, as spalling is most active within this range of temperature. The heating rates are lower than 1 °C/min to prevent undesirable thermal stress developing inside the specimens. At each temperature level, three pressure levels (i.e. 9 bar, 6 bar, and 3 bar) were applied (1 bar=100000 Pa) to calculate intrinsic permeability. Airflow rate Q [m^3/s] was used to calculate permeability until it reached a stable state. One complete measurement of the specimen took about 48 to 96 hours as the permeability measurements only ceased after three consecutive readings were almost the same to ensure consistency of test results.

3. RESULTS AND DISCUSSION

3.1. Permeability at Elevated Temperature

The relations between the measured permeability and temperature are plotted in Figure 2. The mix designs have lower initial permeability values than reported values of permeability of concrete from other studies due to a more compact matrix in UHPC compared to NSC and HPC [7-11]. With increasing temperature, the control mix did not show a significant increase in permeability from 30 °C to 105 °C. The mechanism is due to the drying of specimens at 105 °C. 30 °C is just a residual state. Without drying, saturated water inside the concrete specimens clogs the porous network. Due to very small values, permeability at ambient temperature without drying could not be detected by this set-up. With temperature rising beyond 105 °C, permeability increased more than two orders of magnitude. This is because in this temperature range, physical absorbed water was gradually lost and the C-S-H gel dehydrated. Consequently, the microstructure became more porous [12].

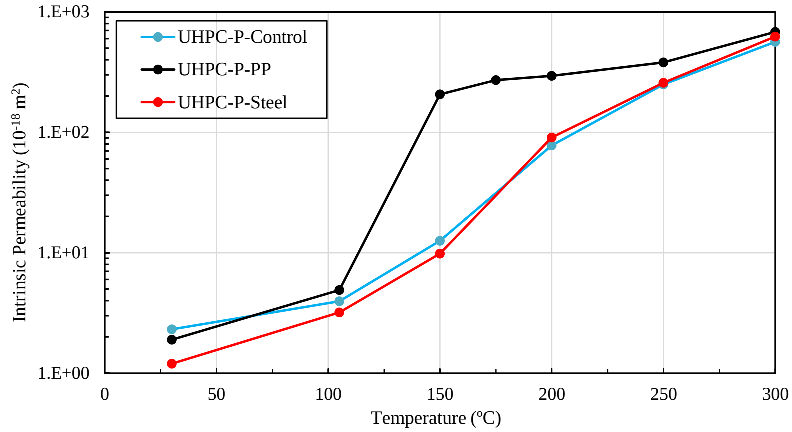

Figure 2. Permeability of concretes as a function of temperature.

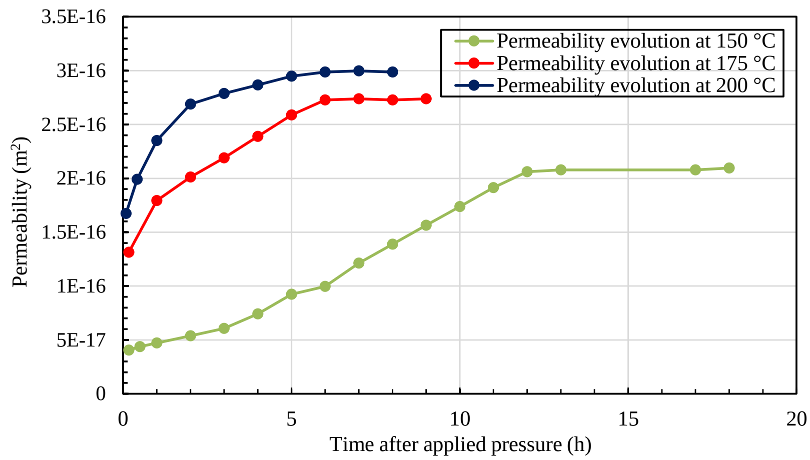

Figure 3. Permeability increases with time at 150 °C, 175 °C, and 200 °C.

The initial permeability of UHPC-P-PP with PP fibers was similar to that of concrete without PP fibers. Compared to UHPC-P-control, the permeability of UHPC-P-PP increased significantly at 150 °C. At 150 °C, the permeability of UHPC-P-PP was more than one order of magnitude larger than UHPC-P-control. The increase in permeability was possibly due to formation of micro cracks, softening of PP fibers, and pressure-induced tangential space (PITS) [2].

It is worth noting that at 150 °C, permeability measurements took 12 hours to reach a steady state (Figure 3). A linear increase of nearly one order of magnitude was observed. At 200 °C, permeability increased faster with time. A possible explanation is that at this temperature, melted PP fibers with a lower viscosity were “pushed” into micro cracks and porous matrix by applied air pressure with lesser effort. This phenomenon indirectly supported the transport theory of melted PP fibers through UHPC matrix.

Compared UHPC-P-steel with UHPC-P-control shows that steel fibers do not have significant contribution to changes of permeability at elevated temperature. The steel fibers affect spalling by enhancing mechanical properties of UHPC and bonding UHPC matrix together. The microstructure analysis is presented in Section 3.2.

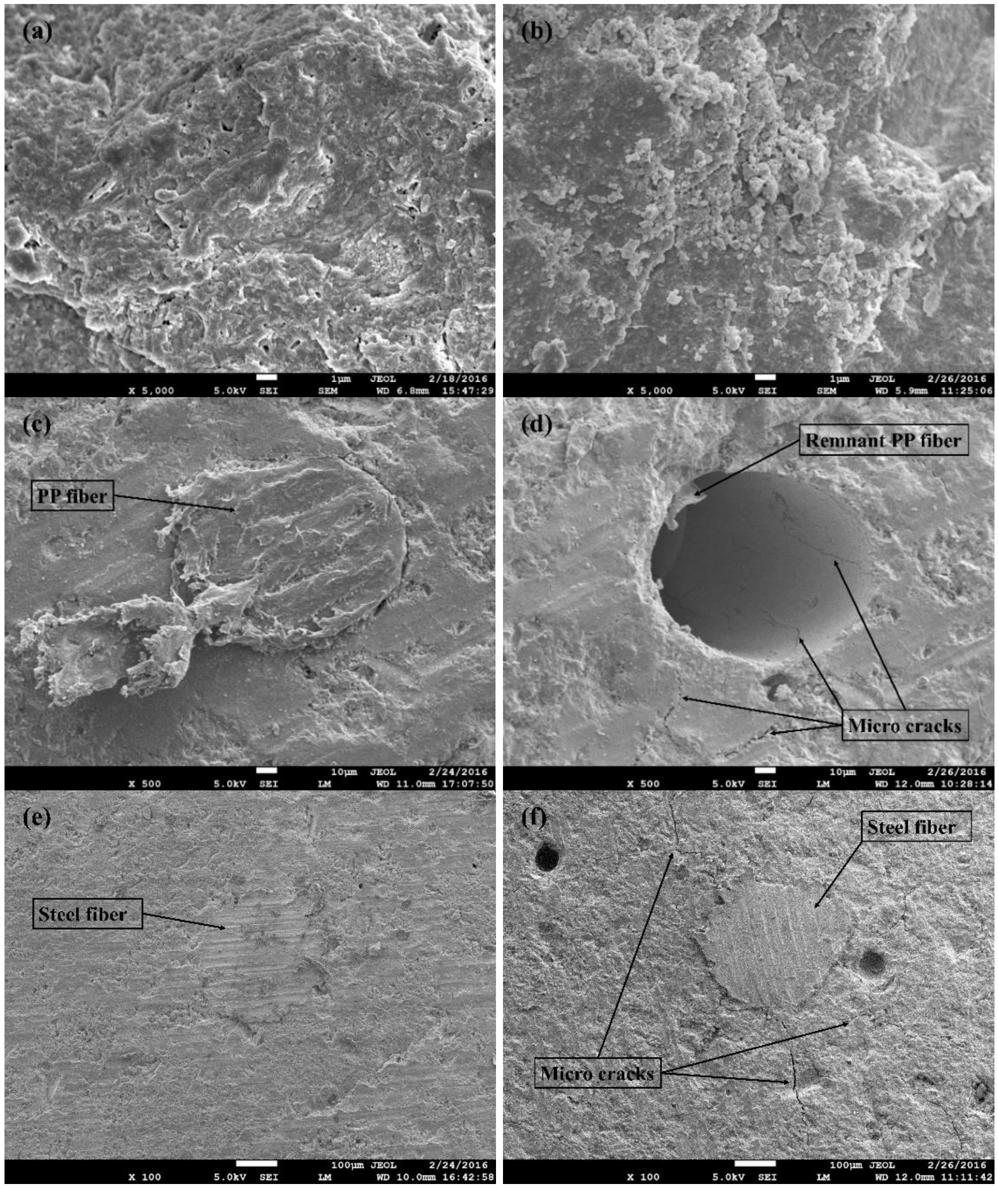

Figure 4. FESEM photos of the microstructure of UHPCs before and after heat treatment. (a) and (b): matrix of UHPC before and after exposure to 250 °C. (c) and (d): single polypropylene fiber inside UHPC before and after exposure to 175 °C for 20 hours. (e) and (f): single steel fiber inside UHPC before and after exposure to 250 °C.

3.2. Microscopic Investigation

Thin square specimens cut to around $10\times10\times4$ mm^3 by a diamond saw were used to conduct Field Emission Scanning Electron Microscope (FESEM) observation. The specimens before and after exposure to high temperature were studied. Figure 4 (a) and (b) shows the hydrates before and after exposure to 250 °C. No CH crystals was observed due to pozzolanic reaction of silica fume. The microstructure was dense with a small amount of scattered micro pores (diameter<1 μm). After exposure to 250 °C for 4 hours, coarsen of C-S-H was identified. The change was primarily due to dehydration reaction [12].

Figure 4 (c) shows one polypropylene fiber in cross section before exposed to high temperature. The fiber was nicely dispersed in the UHPC matrix. There was no interfacial transition zone (ITZ) around the PP fiber. This explains the similar permeability values to UHPC-P-control at low temperature. The same specimen was then heated up to 175 °C at a heating rate of 10 °C/min. After 20 hours, it could be observed in Figure 4 (d) that only a very small piece of PP fiber remained. This shows that the melted polypropylene was absorbed by the porous structure of UHPC and transported into a network of micro cracks. In Josipa Bošnjak's research, after 2 days of heating under 200 °C, there was still a large part of remaining PP fibers inside the channel. This is due to fibers used in his tests possess very low viscosity (40 to 50 times greater than for the standard fibers) [13]. Several micro cracks formed around the fiber channel as well as inside the channel wall. The width of micro cracks were smaller than 5 μm. Contradictory to Josipa Bošnjak's observation [13], there were neither flaws (notches) nor initial cracks in the region around the formed channel. Therefore, even without initial flaws, thermal expansion of polypropylene could cause micro cracks.

Figure 4 (e) and (f) shows steel fibers reinforced UHPC before and after exposure to 250 °C for 4 hours. Many micro cracks were observed around the steel fibers, due to differences of expansion between steel and UHPC matrix. The width of cracks ranges from 1 μm to 5 μm. In terms of the number and density of micro cracks created around one single fiber, PP fibers have similar effect as steel fibers. However, steel fibers do not melt and migrate into cement matrix. It can be concluded that, the channels left from the melting of PP fibers are crucial for increasing permeability.

4. CONCLUSIONS

This paper presents the permeability measurements of UHPC under elevated temperature. Permeability values from 30 °C to 300 °C were measured. The effects of PP fibers and steel fibers were analyzed. FESEM observation was conducted to analyze changes in microstructure with and without exposure to high temperature. For lower temperature, no significant difference was observed between plain UHPC and UHPC with PP fibers and steel fibers. This is attributed to the dense microstructure of UHPC. No ITZ was observed. For UHPC-P-control and UHPC-P-steel, permeability increased nearly linearly (semi-log scale) from 105 °C to 300 °C. However, permeability of UHPC-P-PP showed a sudden increase at 150 °C. FESEM observation shows the disappearance of PP fibers and newly-formed networks comprising of micro cracks. Steel fibers also initiated micro cracks. However, since they did not melt, permeability did not increase much.

ACKNOWLEDGEMENT

This material is based on research/work supported by the Land and Liveability National Innovation Challenge under L2 NIC Award No. L2NICCFP1-2013-4.

DISCLAIMER

Any opinions, findings, and conclusions or recommendations expressed in this material are those of the author(s) and do not necessarily reflect the views of the L2 NIC

REFERENCES

1. Kodur, V. *Spalling in high strength concrete exposed to fire—concerns, causes, critical parameters and cures*. in *Proceedings, ASCE Structures Congress, Philadelphia, PA*. 2000.
2. Bangi, M.R. and T. Horiguchi, *Pore pressure development in hybrid fibre-reinforced high strength concrete at elevated temperatures.* Cement and Concrete Research, 2011. **41**(11): p. 1150-1156.
3. Klingsch, E.W.H., *EXPLOSIVE SPALLING OF CONCRETE IN FIRE*. 2014, ETH: Zurich.
4. Kodur, V. and L. Phan, *Critical factors governing the fire performance of high strength concrete systems.* Fire Safety Journal, 2007. **42**(6): p. 482-488.
5. Gallé, C. and J. Sercombe, *Permeability and pore structure evolution of silicocalcareous and hematite high-strength concretes submitted to high temperatures.* Materials and Structures, 2001. **34**(10): p. 619-628.
6. Sun, H., et al., *Gas transport mode criteria in ultra-tight porous media.* International Journal of Heat and Mass Transfer, 2015. **83**: p. 192-199.
7. Zeiml, M., et al., *Identification of residual gas-transport properties of concrete subjected to high temperatures.* Cement and Concrete Research, 2008. **38**(5): p. 699-716.
8. Picandet, V., A. Khelidj, and H. Bellegou, *Crack effects on gas and water permeability of concretes.* Cement and Concrete Research, 2009. **39**(6): p. 537-547.
9. Noumowe, A.N., R. Siddique, and G. Debicki, *Permeability of high-performance concrete subjected to elevated temperature (600°C).* Construction and Building Materials, 2009. **23**(5): p. 1855-1861.
10. Loosveldt, H., Z. Lafhaj, and F. Skoczylas, *Experimental study of gas and liquid permeability of a mortar.* Cement and Concrete Research, 2002. **32**(9): p. 1357-1363.
11. Hoseini, M., V. Bindiganavile, and N. Banthia, *The effect of mechanical stress on permeability of concrete: A review.* Cement and Concrete Composites, 2009. **31**(4): p. 213-220.
12. Lin, W.-M., T. Lin, and L. Powers-Couche, *Microstructures of fire-damaged concrete.* ACI Materials Journal, 1996. **93**(3).
13. Bošnjak, J., J. Ožbolt, and R. Hahn, *Permeability measurement on high strength concrete without and with polypropylene fibers at elevated temperatures using a new test setup.* Cement and Concrete Research, 2013. **53**: p. 104-111.

Numerical Study on Steel Fiber Reinforced Concrete Columns Subjected to Fire

VENKATESH KODUR[1], PRATIK BHATT[2]
and VASANT MATSAGAR[3]

ABSTRACT

This paper presents a finite element (FE) based numerical approach to predict the thermal and mechanical response of steel fiber reinforced concrete (SFRC) columns subjected to fire. A sequentially coupled nonlinear thermo-mechanical analysis is carried out using ABAQUS® to obtain the temperature distribution and deformation profile in reinforced concrete (RC) columns subjected to simultaneous mechanical and thermal loading. The material and geometric nonlinearities, along with the temperature dependent thermal and mechanical properties of the reinforcing steel and the SFRC, are duly incorporated in the FE model. The thermal and mechanical response quantities predicted by the FE model are compared with that measured from the fire tests on the SFRC columns. The comparison shows that the developed FE model is capable of predicting the response of the SFRC columns subjected to thermal and mechanical loading with adequate accuracy. The developed FE model can be used to undertake detailed parametric study for quantifying the influence of critical factors on fire resistance of the SFRC columns.

Keywords: concrete columns, fire resistance, nonlinear finite element model, steel fiber reinforced concrete

INTRODUCTION

Columns form the most important load bearing member of the skeletal structures and hence, provision of appropriate fire resistance to the columns is one of the major design requirement. This is mainly due to the fact that structural integrity is the last line of defense in the event of fire. The concrete members, made from normal strength concrete (NSC), typically exhibit satisfactory performance under fire exposure [1 and 2].

However, observations made during tests have revealed that high strength concrete (HSC) members when exposed to fire experiences significant deterioration due to rapid degradation of strength and stiffness properties. In addition, the HSC is

[1] Professor, Department of Civil and Environmental Engineering, Michigan State University (MSU), East Lansing, Michigan (MI), USA.
[2] PhD Research Scholar, Department of Civil and Environmental Engineering, Michigan State University (MSU), East Lansing, Michigan (MI), USA.
[3] Associate Professor, Department of Civil Engineering, Indian Institute of Technology (IIT) Delhi, Hauz Khas, New Delhi, India (matsagar@civil.iitd.ac.in).

inherently brittle and has much lower permeability as compared to the NSC that lead to explosive spalling during fire exposure [3 and 4]. To overcome these drawbacks and improve the fire resistance of the HSC, various researchers [5-7] have suggested addition of polypropylene (PP) or steel fibers (SF).

Investigations have shown that addition of the steel fibers in plain concrete enhances the tensile and flexural strengths of the composite and improves ability to resist cracking under service conditions. Further, it improves resistance to material deterioration as a result of fatigue, impact, shrinkage, and thermal stresses and makes the concrete ductile [8 and 9]. The steel fibers bridge the cracks that develop in the structural members upon loading; this bridging action provides the SFRC structures with higher ultimate tensile strength and toughness [9]. Owing to these advantages, the SFRC is used in numerous real-life applications at an escalating rate to improve the performance of the structural members and to reduce their section thickness [10]. Various researchers [6-8, and 11] in their investigations on the SFRC subjected to elevated temperatures observed that addition of the steel fibers has minimal effect on the thermal properties of the concrete. However, mechanical properties of the concrete are altered significantly due to the addition of the steel fibers as well as with the type of aggregate used. Kodur et al. [5] in their investigations on the performance of different types of columns observed that fire resistance of the NSC column is higher than that of the HSC column, with the former showing ductile behavior whereas latter showing brittle behavior. The addition of the steel fibers improves fire resistance of the HSC columns significantly. Steel fibers help to mitigate spalling during fire in the HSC members by increasing the tensile strength [4 and 5].

Although, the thermal and mechanical properties of the SFRC at elevated temperatures have been studied at material level mostly, the performance of the structural elements such as beams, columns, or an assemblage of these structural elements such as portal frame structures made of the SFRC at elevated temperature is required to be thoroughly investigated. In order to reduce cost-intensive fire tests in the laboratories, extensive parametric investigation conducted by means of rigorous finite element (FE) simulations is helpful. The present study addresses this need by providing a detailed FE modeling approach and numerical analysis of the SFRC columns subjected to fire.

In this paper, the behavior of the SFRC columns when subjected to fire is analyzed by means of a 3D nonlinear transient thermo-mechanical finite element analysis (FEA), using commercially available software package ABAQUS® and the results are compared with the response recorded in the past experimental studies. The temperature and deformation induced in the cross-section due to the thermo-mechanical loading are investigated. Moreover, the reduction in the axial load carrying capacity of the column due to increase in temperature is also computed.

FINITE ELEMENT (FE) MODEL

The thermo-mechanical analysis consists of heat transfer and mechanical analyses. Three different modes of heat transfer namely conduction, convection, and radiation are considered. The temperature of the outermost exposed surface of the column rises due to the heat exchange between the surrounding environment and the column by means of convection and radiation. Within the structural member, conduction is responsible for heat transfer.

The heat transfer analysis is carried out by solving the governing equation for the isotropic material; in transient heat conduction it is given as:

$$\nabla(k\nabla T) + Q - \rho c \frac{\partial T}{\partial t} = 0 \tag{1}$$

with the initial condition defining the temperature distribution at the beginning of the heat transfer analysis by:

$$T = \bar{T}(x, y) \text{ on } \Gamma_T \tag{2}$$

where, T is the temperature, ∇ is the differential operator, k is the thermal conductivity, c is the specific heat, ρ is the density, t is the time, Q is the heat generated internally per unit volume per unit time, and $\bar{T}$ is the prescribed value of temperature on the boundary Γ_T.

The boundary conditions responsible for the convective and radiative heat transfers at the column surface are given by:

$$-k\frac{\partial T}{\partial n} = h_c(T - T_f) \tag{3}$$

$$-k\frac{\partial T}{\partial n} = \varepsilon_s \varepsilon_f \sigma\left[(T-273)^4 - (T_f - 273)^4\right] \tag{4}$$

where, h_c is the convective heat transfer coefficient, n is the outward surface normal, T_f is the furnace temperature, ε_s is the emissivity of the surface in consideration (varying between 0 and 1), ε_f is the emissivity of the fire (usually taken as 1 for standard fire condition), and $\sigma = 5.67 \times 10^{-8}$ W/(m^{2}K^4) is the Stefan-Boltzmann constant.

Galerkin-Ritz discretization of the above partial differential equation leads to the following matrix equation:

$$[K]\{a\} + [C]\{\dot{a}\} = \{F\} \tag{5}$$

where, $[K]$ is the global heat conduction/convection matrix, $[C]$ is the global heat capacity matrix, $\{F\}$ is the global heat input vector, and $\{a\}$ is the global nodal temperature vector.

In a similar manner, equations at element level are obtained and assembled at global level to obtain the nodal displacement response.

$$[K_s]\{u\} = \{f\} \tag{6}$$

where, $[K_s]$ is the global stiffness matrix, $\{u\}$ is the global nodal displacement vector, and $\{f\}$ is the global load vector. The mechanical response incorporates the effect of thermal strains (ε_t) as well as mechanical strains (ε) on the stresses calculated using:

$$\{\sigma\} = [D]\{\varepsilon - \varepsilon_t\} \tag{7}$$

where, $\{\sigma\}$ is the stress vector, $[D]$ is the constitutive matrix, and $\{\varepsilon\}$ is the strain vector computed as:

$$\varepsilon = \varepsilon_{el} + \varepsilon_{pl} + \varepsilon_{sh} + \varepsilon_{cr} \tag{8}$$

where, ε_{el} is the elastic strain, ε_{pl} is the plastic strain, ε_{sh} is the shrinkage strain, and ε_{cr} is the creep strain. It should be noted that at present very scarce data is available on the shrinkage and creep strains developed in the SFRC at elevated temperature. Therefore, for the analysis presented in this paper these strains are neglected.

Discretization

In order to capture the thermo-mechanical response of the high strength SFRC columns, the concrete and steel rebars are modeled using C3D8T and T3D2T elements, respectively. The C3D8T is an 8-node brick element and the T3D2T is a 2-node truss element for coupled temperature-displacement analysis. The truss element is tied to the surrounding concrete region using *TIE* constraint option available in ABAQUS®.

Material Properties

The variation of the thermal and mechanical properties of the steel reinforcement and concrete with temperature are suitably considered in the FE formulation. The variation of thermal and mechanical properties of the concrete with temperature depends significantly on the strength of concrete as well as the type of aggregate used. Investigations [7, 8, and 11] on the SFRC when subjected to fire suggest that addition of the steel fibers have negligible effect on the thermal properties of concrete; however, mechanical properties are enhanced considerably. The thermal and mechanical properties of the constituent materials, such as concrete and steel, used in the FE model are discussed here.

CONCRETE

The thermal conductivity (k), specific heat capacity (c), and thermal expansion coefficient (α) considering their variation with temperature are defined according to Eurocode-2 [13] for the NSC, i.e. $f_c' < 83\,\text{MPa}$. For the HSC and high strength SFRC, these thermal properties are defined using the equations proposed by Kodur et al. [11]. The variation of thermal conductivity, specific heat, and thermal expansion with temperature for the NSC, HSC, and high strength SFRC are shown in Figures 1(a), 1(b), and 1(c), respectively.

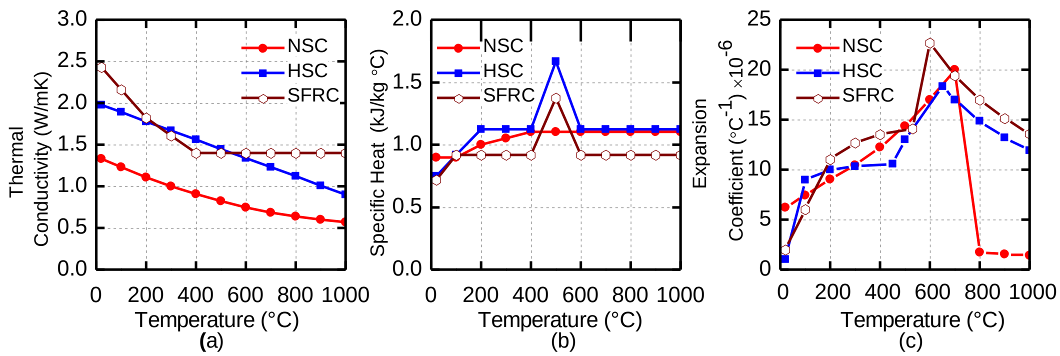

Figure 1. Variation of thermal properties with temperature for different types of siliceous aggregate based concrete: (a) thermal conductivity, (b) specific heat, and (c) expansion coefficient.

The degradation in the compressive strength and elastic modulus with temperature for the NSC is defined using the reduction factors given in [13]. For the HSC and SFRC the reduction factors given in [6 and 8] are used to define the degradation in the compressive strength and elastic modulus with temperature. These reduction factors for the compressive strength and elastic modulus for the NSC, HSC, and SFRC are shown in Figures 2(a) and 2(b), respectively. The concrete is modeled as an elasto-plastic material with strain softening. For modeling the compressive behavior of the NSC, the stress-strain relations available in [13] are used. For the SFRC, the presence of the steel fibers in the concrete is accounted implicitly in the FE model by modifying the stress-strain relationship of the concrete in compression. The stress-strain relationships used for modeling the compressive behavior of the HSC and SFRC are referred respectively from [6 and 8].

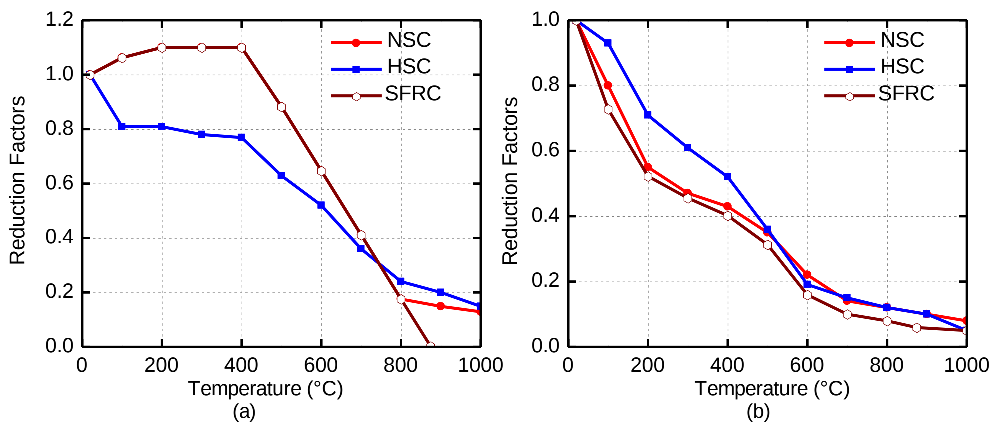

Figure 2. Reduction factors for different types of siliceous aggregate based concrete: (a) compressive strength, and (b) elastic modulus.

The nonlinear behavior of concrete due to crack formation and propagation is modeled using concrete damaged plasticity (CDP) model available in ABAQUS® wherein the effect of tension softening and tension stiffening is duly considered. The parameters of the CDP model includes dilation angle (ψ) interpreted as internal friction angle that controls the amount of volumetric strain developed during plastic shearing and it usually varies between 30° and 40° [14]. Eccentricity parameter ($\in$) is the ratio of tensile strength to compressive strength. Its value depends on the type of concrete; for the NSC it is 0.1 whereas for the HSC and high strength SFRC, it varies from 0.06 to 0.08. The shape of the yield surface is determined by a user-defined parameter (K_c) and is set to unity, which corresponds to using the traditional Drucker-Prager yield criterion, i.e. conical shape. The parameter defining the ratio of biaxial compressive strength to uniaxial compressive strength is considered as 1.16. The viscosity parameter (μ) is used for the visco-plastic regularization of the concrete constitutive equations. The default value of μ is 0.0, which means that a strain rate-independent analysis is carried out. The details of the yield surface and non-associative flow rule used in the CDP model can be referred from [15].

The behavior of the concrete in tension is characterized into two parts: pre-cracking stage and post-cracking stage. In the first part, i.e. the pre-cracking stage, stress varies linearly with strain up to the ultimate tensile strength (f_t) of the concrete at which it cracks. The second part, i.e. the post-cracking stage, consists of a nonlinear softening branch wherein, the stress decreases with increased strain until the zero stress level for the NSC and HSC. However, in case of the SFRC, in the post-cracking stage, the stress reduces up to the residual stress and then remains constant for further increase in the strain. Such constitutive relation for the SFRC is referred from [16].

STEEL REINFORCEMENT

The temperature variation of various thermal and mechanical properties of reinforcing steel is incorporated as specified in Eurocode-2 [13]. The post-yielding behavior of the steel reinforcement is incorporated using metal plasticity model available in ABAQUS®. The model utilizes the von-Mises yield criterion with associated plastic flow and isotropic hardening.

Loading and Boundary Conditions

The FEA is carried out in two steps for mechanical and thermal analyses. In the first step, a mechanical load of about 50% of the ultimate capacity is applied on the top surface of the columns to simulate the dead and live loads at ambient temperature. In the second step, a heat transfer analysis coupled with stress displacement analysis is carried out. The column is subjected to an initial ambient room temperature of 20°C. Transient thermal load resulting from fire is applied to the exposed portion of the columns in the form of transient time-temperatures curves. The standard time-temperature curve as specified in ASTM E119 [17] is used to simulate the fire on the exposed surface of the column.

The radiation boundary condition on the exposed surface of the column is modeled using emissivity of the surface (ε_s) as 0.8 and the emissivity of the fire (ε_f) as 1. The convective heat transfer coefficient (h_c) for the exposed surface is specified as 25 W/m^2K to model the convection on the exposed surface of the column. The convective heat transfer coefficient used for the unexposed surface is 0.8 W/m^2K. The mechanical load is kept constant throughout the duration of the application of fire.

Failure Criteria and Numerical Convergence

A strength failure criterion is applied to evaluate the fire resistance, and the column is assumed to have failed at any given time step when the applied load exceeds the capacity. The “analysis = discontinuous” parameter is invoked using the *CONTROLS* option. It prevents the discontinuity due to the discontinuous nonlinear behavior of the high strength SFRC and thus improves the efficiency of the analysis as it allows the program to perform relatively large number of iterations prior to checking for convergence rate. A line search algorithm (with line search parameter = 5) is employed in order to increase the rate of convergence and to stabilize convergence behavior. A tolerance of 1×10^{-6} and 5×10^{-2} (typical range of 0.05 to 0.2) respectively on the temperature and displacement norms are defined as convergence criteria at all the time steps for the transient thermo-mechanical analysis.

FE MODEL AND EXPERIMENTS

The analyses results obtained from the developed FE model are compared with the results of the full-scale fire resistance tests carried out on various types of reinforced concrete (RC) columns at NRC Canada reported in [5]. Four columns selected from these fire tests for the purpose of comparative assessment are denoted as TNC1, THC4, THS10, and THS11. The column TNC1 was a NSC column, THC4 was a HSC column whereas, THS10 and THS11 were the SFRC columns.

Geometry of Column

Elevation, cross-section, and FE discretization of a typical column considered in the present analysis are shown in Figure 3. The chosen four columns were 3810 mm in length and had a square cross-section of 305 mm sides. All the columns had four longitudinal steel rebars of 25 mm diameter welded to the end plate. The rebars were attached with lateral ties of 10 mm diameter at spacing of 75 mm in 650 mm length near the supports and 145 mm spacing in the middle of the column height. The longitudinal reinforcing rebars and the lateral ties had yield strength of 420 MPa and 280 MPa, respectively. The other test parameters, such as, 28-day cylinder compressive strength, test day strength, ultimate resistance, applied load, load intensity, and fire resistance (observed experimentally and predicted by the model) of these four columns are summarized in Table I. All four columns were made from siliceous aggregate and exposed to fire on four faces along the height. Detailed test specifications of the concrete strength, aggregate type, fiber type, load applied, instrumentation of the column furnace, testing procedure, and results of temperature variation and deflection can be referred from Kodur et al. [5].

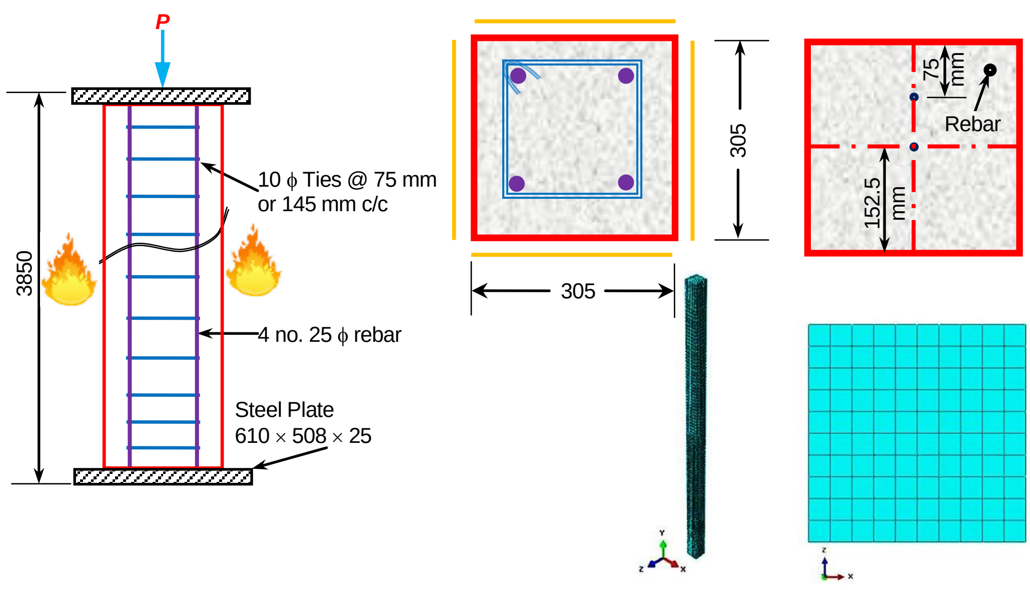

Figure 3. Geometrical details and discretization of columns of tested columns selected for numerical assessment.

Analysis Details

The geometry, loading, and boundary conditions of the columns are modeled similar to that of the aforementioned experimental program [5]. The end conditions are fixed-fixed for all columns. Initially, static mechanical load (*P*) of about 50% of the ultimate capacity of the column is applied on the top surface and kept constant. Fire is applied on all four sides for a length of 3000 mm by means of varied temperature according to the ASTM E119 standard time-temperature curve. The temperature is measured at center and quarter points of the cross-section at the mid-height of the column as well as at the rebar as shown in Figure 3. Temperature variation at these selected locations in the column cross-section, axial deformation as well as the fire resistance time of the selected four columns are used for comparing the results of the developed 3D finite element (FE) model.

TABLE I. PARAMETERS CONSIDERED AND RESULTS FOR THE FIRE TESTS ON DIFFERENT TYPES OF COLUMNS.

Name of Column	Compressive Strength of Concrete (f_c') (MPa)		Type of Column	Test Day Capacity (P_u) (kN)	Applied Load (P) (kN)	Load Intensity (P/P_u)	Fire Resistance (minutes)	
	28 Day	Test Day					Tests	Model
TNC1	27.8	40.2	NSC	1728	930	0.54	278	282
THC4	60.6	99.6	HSC	3697	2000	0.54	202	202
THS10	63.2	89.1	High Strength SFRC	3349	1800	0.54	239	245
THS11	63.2	89.1	High Strength SFRC	3349	2200	0.66	206	212

RESULTS AND DISCUSSION

Thermal Response

Predicted responses from the developed FE model at the center and quarter points of the cross-section at the mid-height of the column as well as at the rebar are compared with that of the experimentally reported results. Figures 4(a), 4(b), and 4(c) show such comparison for the columns TNC1, THC4, and THS10, respectively. As expected, the temperature near the surface is the highest and it reduces towards the center of the column cross-section. The temperature in the steel rebars is higher than that in the concrete. Moreover, due to relatively higher conductivity in steel as compared to the concrete, the rate of increase in temperature in steel is higher than that in the concrete. Further, the type of concrete used, i.e. NSC, HSC, or SFRC, shows negligible effect on the temperature rise. It is evident from Figure 4 that good agreement is achieved between the predicted and measured temperatures throughout the fire test. Hence, the developed finite element (FE) model can suitably be used to predict with sufficient accuracy the thermal response of different types of the RC (NSC, HSC, and SFRC) columns and to undertake detailed parametric study for quantifying the influence of the critical factors on the fire resistance of the SFRC columns.

Mechanical Response

In order to assess the mechanical response of the RC columns, the axial deformation predicted by the 3D finite element (FE) models for each of the four columns considered in the present study is compared with the response measured during the fire tests of the columns. Also, the fire resistance time of each column is compared with the experimentally measured fire resistance time by assessing the reduction in the axial load carrying capacity of the columns.

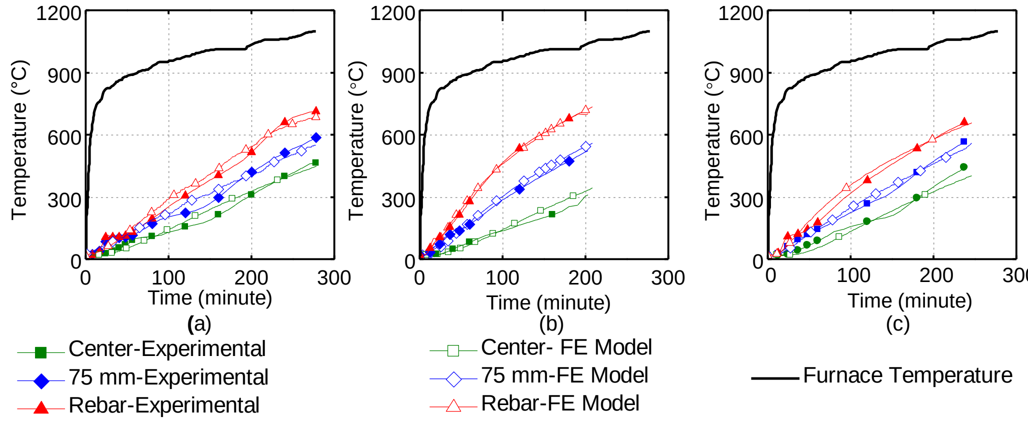

Figure 4. Thermal response: comparison of predicted and measured temperatures at various locations in cross-section at mid-span of columns: (a) TNC1, (b) THC4, and (c) THS10.

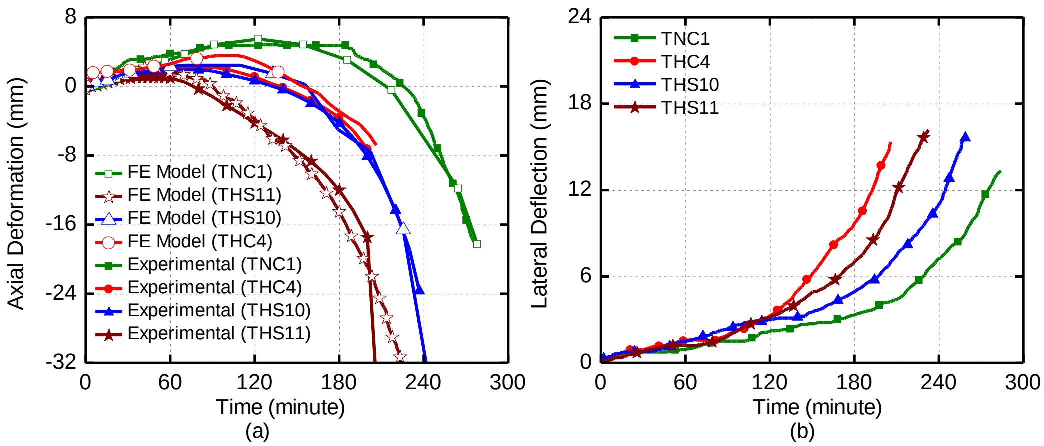

Figure 5. Mechanical response: (a) comparison of predicted and measured axial deformation, and (b) predicted lateral deflection of various RC columns.

The comparison of the predicted and measured axial deformations for four columns (TNC1, THC4, THS10, and THS11) is shown in Figure 5(a). Data from various experimental studies on the behavior of the RC columns when subjected to fire show that, both concrete and steel reinforcement in an RC column expand initially at the start of fire load owing to the increase in the thermal strains and then contract with the reduction in the strength and stiffness of the concrete and steel due to increase in the temperature. As the steel reinforcement possess higher thermal conductivity and is placed at concrete cover distance from the outer face, the increase in temperature of the steel is rapid as compared to the increase in temperature in the inner core of the concrete; hence, steel loses strength and stiffness much earlier than concrete. In [18], the contraction is attributed to the rise of creep and transient strain components. This behavior of the RC columns under fire is traced with sufficient accuracy through the present 3D finite element (FE) model. It is clear from Figure 5(a) that the axial deformation predicted by the FE model is in good agreement with the measured experimental response for all the four columns considered herein.

The predicted lateral deformation of the four columns, TNC1, THC4, THS10, and THS11, is shown in Figure 5(b). Note that, in Figure 5(a) the axial deformation initially increases (expands) and then decreases (contacts); in contrast to this, in Figure 5(b), the lateral deformations increase monotonically during the entire fire exposure duration. A sharp increase is further observed after about 120 minutes fire exposure in each of these columns.

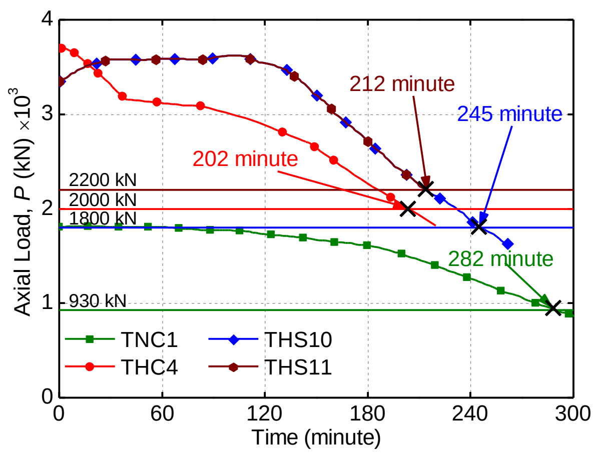

Figure 6. Reduction of axial load carrying capacities in the four RC columns considered.

The reduction of the axial load (P) carrying capacities of the four columns, TNC1, THC4, THS10, and THS11, is shown in Figure 6. This is used to evaluate the fire resistance time of these columns using the developed 3D finite element (FE) model and compare it with the experimentally measured fire resistance time. The time at which the applied loading exceeds the axial load carrying capacity of a column is considered as the fire resistance time of the column. The reduction of the axial load carrying capacity of the column is computed using the average temperature of the section and the equation proposed in ACI 318.08 [19] for computing the ultimate capacity of the columns (P_u). The fire resistance time for each column is compared in Table I. It is observed that the use of steel fibers enhances the fire resistance of the HSC by about 21%. Further, it can be seen from Table I that the fire resistance time predicted by the proposed 3D finite element (FE) model for various columns is fairly close to the experimentally observed time. Hence, the proposed 3D finite (FE) element modelling approach may be used to predict the mechanical response of various types of the RC (NSC, HSC, and SFRC) columns subjected to fire with sufficient accuracy.

CONCLUSION

The performance of the SFRC columns subjected to fire is evaluated by developing a 3D finite element (FE) model in ABAQUS® and suitably incorporating the geometric and material nonlinearities. The numerical results obtained from the FE model are compared with the experimental studies. The thermal and mechanical response of the columns subjected to fire predicted using the proposed 3D finite element (FE) model are in agreement with the experimentally observed response. The proposed finite element (FE) approach is capable of tracing the thermal and mechanical response of the high strength SFRC columns subjected to fire with sufficient accuracy necessary for all practical purposes. It is concluded that the use of steel fibers enhances the fire resistance of the HSC by about 21%.

The results of this numerical study on the performance of the SFRC columns at elevated temperatures are crucial because limited 3D finite element (FE) based studies are available in the literature to evaluate the performance of the SFRC columns subjected to fire. The FE modeling approach presented herein may suitably be used to carry out investigations on the performance of the SFRC column under different design fire scenarios, durations of fire, and exposed surfaces. These investigations can serve as a basis for economic performance-based design of columns subjected to fire and develop rational fire safety design guidelines.

ACKNOWLEDGEMENTS

The research presented in this paper is carried out during the exchange visits of researchers sponsored by the "Indo-US Science and Technology forum" (IUSSTF) under the research project "Establishment of Indo-US Virtual Fire Center for Advancing Research and Education in Structural Fire Engineering". The authors are thankful to the IUSSTF for providing the financial support for the exchange visits. Any opinions, findings, and conclusions or recommendations expressed in this paper are those of the authors and do not necessarily reflect the views of the sponsors.

REFERENCES

[1] Arioz, O. (2007). "Effects of Elevated Temperatures on Properties of Concrete." Fire Safety Journal, 42(8), 516-522.
[2] Fletcher, I. A., Welch, S., Torero, J. L., Carvel, R. O., and Usmani, A. (2007). "Behavior of Concrete Structures in Fire." Thermal Science, 11(2), 37-52.
[3] Phan, L. T. (1996). ''Fire Performance of High-Strength Concrete: A Report of the State-of-the-Art.'' NISTIR 5934, National Institute of Standards and Technology (NIST), Gaithersburg, Maryland (MD), USA.
[4] Kodur, V. K. R., and McGrath, R. (2003). "Fire Endurance of High Strength Concrete Columns." Fire Technology - Special Issue, 39(1), 73-87.
[5] Kodur, V., Cheng, F., Wang, T., and Sultan, M. (2003). "Effect of Strength and Fiber Reinforcement on Fire Resistance of High-Strength Concrete Columns." Journal of Structural Engineering, ASCE, 129(2), 253-259.
[6] Cheng, F. P., Kodur, V. K. R., and Wang, T. C. (2004). "Stress-Strain Curves for High Strength Concrete at Elevated Temperatures." Journal of Materials in Civil Engineering, ASCE, 16(1), 88-94.

[7] Khaliq, W., and Kodur, V. (2011). “High Temperature Properties of Fiber Reinforced High Strength Concrete.” ACI Special Publication: Innovations in Fire Design of Concrete Structures, ACI SP No. - 279, 3.1-3.42.
[8] Lie, T. T., and Kodur, V. (1996). “Thermal and Mechanical Properties of Steel Fiber Reinforced Concrete at Elevated Temperatures.” Canadian Journal of Civil Engineering, 23(4), 511-517.
[9] Altun, F., Haktanir, T., and Ari, K. (2007). “Effects of Steel Fiber Addition on Mechanical Properties of Concrete and RC Beams.” Construction and Building Materials, 21(3), 654-661.
[10] Poon, C. S., Shui, Z. H., and Lam, L. (2004). “Compressive Behavior of Fiber Reinforced High Performance Concrete Subjected to Elevated Temperatures.” Cement and Concrete Research, 34(12), 2215-2222.
[11] Kodur, V. K. R., and Sultan, M. A. (2003). “Effect of Temperature on Thermal Properties of High-Strength Concrete.” Journal of Materials in Civil Engineering, ASCE, 15(2), 101-107.
[12] Rafi, M. M., Nadjai, A., and Ali, F. (2009). “Finite Element Modeling of Carbon Fiber-Reinforced Polymer Reinforced Concrete Beams under Elevated Temperatures.” ACI Structural Journal, 105(6), 701-710.
[13] Eurocode-2 (2004). “EN 1992-1-2 Design of Concrete Structures, Part 1-2: General Rules - Structural Fire Design.” European Committee for Standardization, Brussels, Belgium.
[14] Kmiecik, P., and Kaminski, M. (2011). “Modeling of Reinforced Concrete Structures and Composite Structures with Concrete Strength Degradation Taken into Consideration.” Archives of Civil and Mechanical Engineering, 11(3), 623-636.
[15] ABAQUS (2014). “ABAQUS User’s Manual, Version 6.14.” Hibbitt, Karlsson and Sorensen, Inc., Pawtucket, Rhode Island (RI), USA.
[16] Lok, T. S., and Xiao, J. R. (1999). “Flexural Strength Assessment of Steel Fiber Reinforced Concrete.” Journal of Materials in Civil Engineering, ASCE, 11(3), 188-196.
[17] ASTM E119 (2002). “Standard Test Methods for Fire Tests of Building Construction and Materials.” ASTM International, West Conshohocken, Pennsylvania (PA), USA.
[18] Bratina, S., Čas, B., Saje, M., and Planinc, I. (2005). “Numerical Modeling of Behavior of Reinforced Concrete Columns in Fire and Comparison with Eurocode-2.” International Journal of Solids and Structures, 42(21-22), 5715-5733.
[19] ACI 318-08 (2008), “Building Code Requirements for Reinforced Concrete and Commentary.” American Concrete Institute (ACI), Farmington Hills, Michigan (MI), USA.

Experimental Study of Ultra-high Performance Fibre Reinforced Concrete under ISO 834 Fire

CHARLES KAHANJI, FARIS ALI and ALI NADJAI

ABSTRACT

Ultra-high performance fibre reinforced concrete (UHPFRC) is a relatively new construction material that possesses favourable mechanical properties over ordinary concrete. Although enormous strides have been achieved in understanding the performance and behaviour of UHPFRC at ambient temperature, there's little literature and experimental data on their behaviour when submitted to fire. This study presents experimental results of four, 2m long, singly reinforced UHPFRC beams subjected to an ISO 834 fire curve for 60 minutes under a constant load. Two beams contained steel fibres with 2% volumetric ratio while the other set had 4%. Two load ratios of 0.4 and 0.6 were imposed prior to heating and kept constant throughout the fire test. Spalling was observed in all beams, being more severe in beams with steel dosage of 2%. The failure modes, displacement patterns, temperature profiles and corresponding fire endurance for each beam have been presented in this study.

INTRODUCTION

Ultra-high performance fibre reinforced concrete (UHPFRC) is a recently developed construction material ideally suited for high strength applications due to its exceptional mechanical properties in comparisons to normal strength concrete (NSC) and high-performance concrete (HPC). While research on behaviour and performance of UHPFRC at ambient temperature has progressed massively, fire tests on UHPFRC material are few and far between. A large number of fire tests, however, have focussed more on residual mechanical properties and have largely been conducted on cylinders, cubes and on small unstressed elements [1-4]. Fire tests that have been conducted on concrete with low permeability like HPC, have always been accompanied by high levels of explosive spalling [5-9]. UHPFRC, typically do not contain coarse aggregates, which gives rise to more densely packed concrete matrix with lower permeability than HPC [10, 11]. Spalling occurs when temperatures rise rapidly, causing vapour pressure in capillary pores to rise. Due to the absence of connected gateways from the pores to the surface, when the pore pressure exceeds the

FireSERT, Built Environment Research Institute, School of the Built Environment, Ulster University, Shore Road, BT37 0QB, United Kingdom
e-mails: kahanji-c@email.ulster.ac.uk; f.ali@ulster.ac.uk; a.nadjai@ulster.ac.uk

concrete's tensile strength, concrete breaks into pieces and this process is usually accompanied by violent noise and pieces of concrete are scattered at high speeds. Spalling, therefore, reduces the cross-sectional area of structural elements and thus their load carrying capacity is diminished. Although most fire-related research has primarily centred on NSC and HSC, there are a few fire tests that have been conducted on the full-size element of building construction of UHPFRC. Lee [12], conducted standard fire tests on columns with compressive strengths of up to 200 MPa. The test columns which had a hybrid combination of steel, nylon and polypropylene fibres showed superior fire resistance with reduced spalling. Pimienta and Behloul [4, 13] also conducted tests on two industrial prestressed I-shaped beams made from commercially marketed UHPFRC, Ductal©-AF which were subjected to a standard fire. One beam had an imposed load, the other was unloaded. Both beams did not record significant material loss. The unloaded beam had minor spalling while the loaded beam recorded no spalling at all. This paper presents experimental findings of testing UHPFRC beams that were exposed to ISO 834 fire curve for a duration of one hour. The aims of the project were to study the influence of two parameters; i.e., the loading levels and fibre content in the beams and their effects on the fire performance and behaviour.

EXPERIMENTAL STUDY

Material

The concrete mix proportion used in this research programme is given in Table I. All the beams contained steel fibres, manufactured by Bekaert. Two beams had fibre dosage of 2% per volume while the remainder had 4% volumetric ratio. These fibres were straight, 13mm long and a diameter of 0.2mm. Only fine sand with a maximum size of 0.6mm was used, no coarse aggregates were added. Silica fume used had particle size of less than 1µm and were the granular materials with smallest particle size. The portland cement (CEM I 52.5N) used had a mean particle size of 5-30µm. In order to obtain hardened concrete with high compressive strength, it was necessary to use low water/binder (w/b) ratio of 0.2. Superplasticiser (HRWR) complemented the low w/b ratio, enabling it to attain good workability.

TABLE I. MIX PROPORTION.

Unit weight (kg/m^3)						
Cement	**Silica fume**	**Sand**	**HRWR**	**Water**	**Steel fibres (2%)**	**Steel fibres (4%)**
967	251	675	77	244	158	316

Experimental tests were conducted on four UHPFRC beams measuring 2000mm long, 200mm deep and 100mm wide. Each beam was reinforced with two traditional H16 steel reinforcement bars in the tension region and an all-round cover of 20mm was provisioned. The beam notations shown in Table 2, contain 3 letters RLF, followed by the numerical values 2 or 4. These represent the steel fibre dosage of 2% and 4% used in the respective beams. The two-digit number 40 and 60 at the end represents the imposed as a percentage of the beam's ambient ultimate bending strength. The ultimate strength was estimated at 125kN and was obtained experimentally from the UHPFRC beam with 2% fibres, previously tested at ambient temperature [14]. This was supported by moment capacity computation based on

Eurocode 2. The beam had 28-day and test-day compressive strengths of 126MPa and 150MPa respectively.

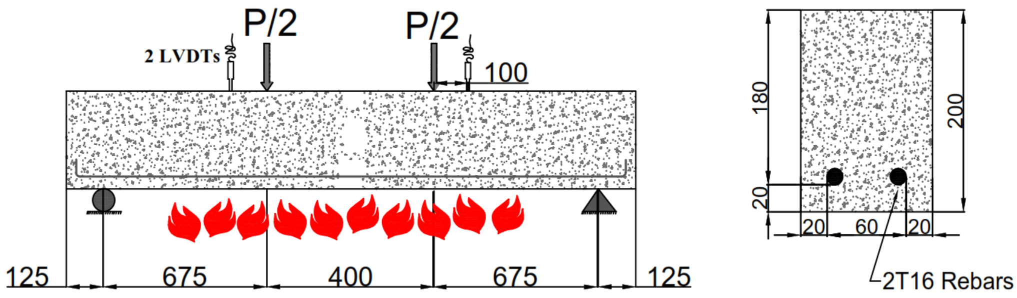

Figure 1. Layout of the beam.

TABLE 2. BEAM DESIGNATION AND DETAILED PARAMETERS.

Steel Fibre Dosage	Beam ID	Load Ratio [%]	Applied load [kN]	Beam age [Days]	f_c - 28days [Mpa]	f_c –test day [Mpa]
(2%)	RLF2-40	0.4	50	234	131.1	163.4
	RLF2-60	0.6	75	238	155.0	178.7
(4%)	RLF4-40	0.4	50	248	148.5	166.8
	RLF4-60	0.6	75	252	155.9	173.8

Furnace and instrumentation

The tests were carried out in a furnace with an internal chamber measuring 1500mm x 1500mm x 1500mm. The beams were supported on two steel rollers which were embedded into the furnace walls. A four-point constant load was imposed on the beam 30 minutes before the fire test and kept constant throughout the test. Because of the furnace chamber size, only the 1500mm middle section of the beam was heated. Only the bottom half of this section was initially exposed to heat, the top half including the top surface were not exposed to heat. But as the beam deformed due to applied load and thermal stress, the lateral sides were slowly getting exposed to fire. Two linear variable differential transformers (LVDTs) were attached to the beam to measure the deflection. Their positions are shown in Figure 1. Thermocouples of type K-310 with stainless steel sheath material were fixed at various locations in the beams to monitor the temperature distribution across the beams' depth and on the rebars. The exact positions of the six thermocouples, marked TC1, TC2, TC3, TC4, TC5 and TC6 are shown in Figure 2.

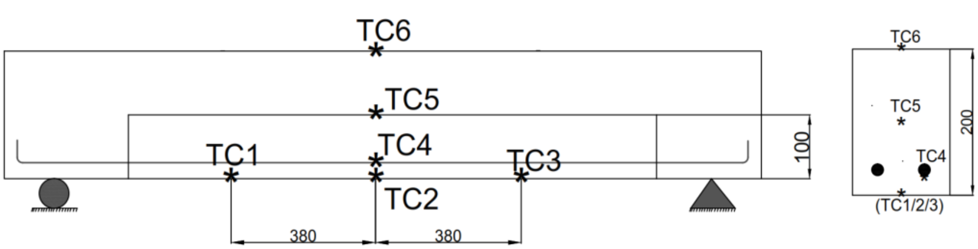

Figure 2. Positions of thermocouples.

RESULTS

The beams were successfully tested in the furnace for one hour. The results relating to failure mode, displacement and failure time are recorded in Table 4. Figure 3 and Figures 4 show photos of beams after the fire test. The mode of failure of each beam and the extent of spalling are clearly visible from the photos. All the beams failed before the designated one-hour duration. Failure of beams under the load ratio of 0.6 (RLF2-60 and RLF4-60) was sudden and with little warning. They snapped into two pieces, prompting the furnace to be switched off immediately, to protect instruments above it. For beams under 0.4 load ratio failure was gradual and exhibited some ductility. Once a sudden dip in deflection was observed, the load was then removed but the beam continued to be heated until the 60th minute.

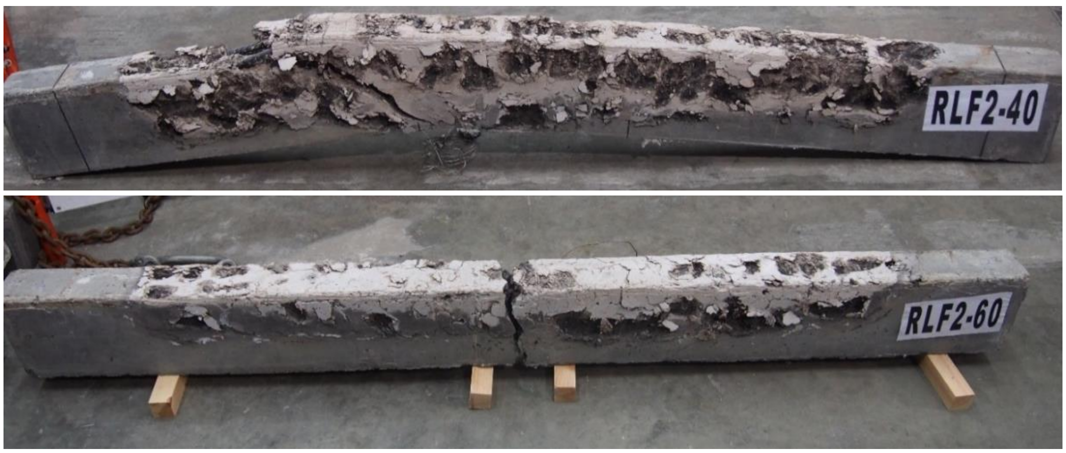

Figure 3. Beams with 2% steel fibres after fire test.

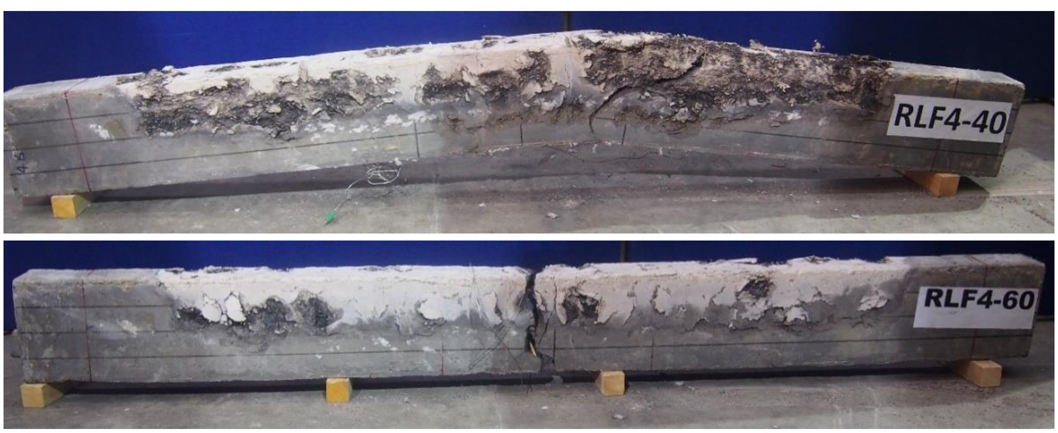

Figure 4. Beams with 4% steel fibres after fire test.

TABLE 4. ENDURANCE AND FAILURE MODE RESULTS.

Beam ID	Failure Time [min]	Endurance [min]	Failure mode	Initial deflection [mm]	Final deflection [mm]	Spall fragments [kg]
RLF2-40	49	30	Shear	2.0	76.0	6.0
RLF2-60	53	30	Flexure	4.3	35.5	1.5
RLF4-40	52	30	Shear	2.2	74.8	3.2
RLF4-60	54	30	Flexure	4.7	33.9	0.9

Explosive Spalling

All the beams experienced spalling as they were heated. Explosive sounds of spalling started after about 10 minutes and went for the next 15 to 20 minutes. At the time spalling commenced, the surface of the beams had attained an average temperature of 275°C. The concrete pieces that came off from each beam and scattered on the furnace floor were weighed and graphically presented in Figure 5. The RLF2-40 beam was the worst affected, losing 6 kg as fragments of spalling. The cross section area of the tension region was gravely reduced and as a consequence, its load carrying capacity was markedly reduced. The least affected in terms of spalling was the RLF4-60, shedding off just less than a kilogramme in fragmentations. The possible explanation for this is that cracks only developed in beams loaded with 75kN. No visible cracks were observed in the beams under the 50kN load prior to heating. These cracks created connected channels up to the surface of the beam through which the gases under high pressure would escape. The pore pressure of concrete within the crack vicinity was therefore reduced. Reduction in pore pressure, therefore, reduces the likelihood of spalling. Explosive spalling sounds resumed towards the end of the test and were more pronounced in the RLF2-40 and RLF4-40. This was due to the fact that fresh parts of the top half of the beam, previously unexposed to heating were now exposed to heating. Figure 6 shows the deflection patterns of the beams and it clearly shows the two beams deforming rapidly towards the end of the test.

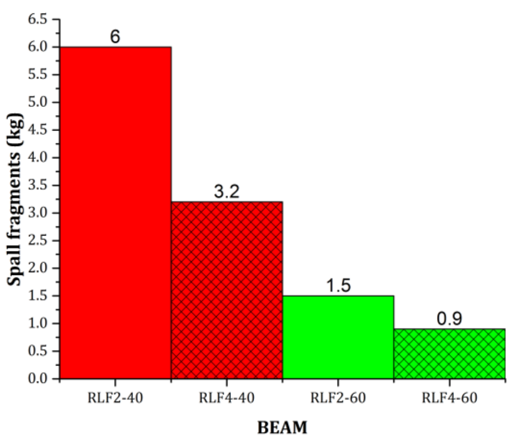

Figure 5. Mass of concrete fragments lost in beams.

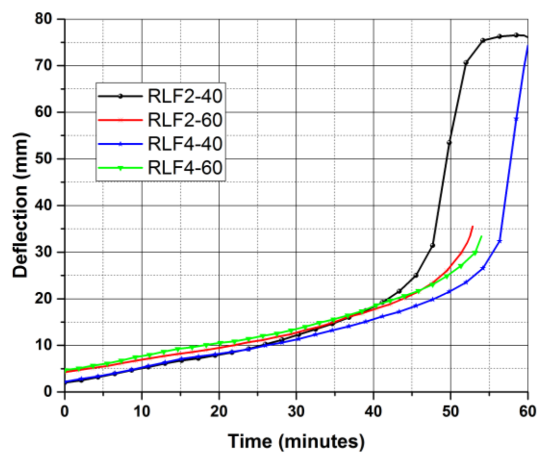

Figure 6. Deflection pattern of beam.

Thermal behaviour

Since UHPFRC is a new material, monitoring the temperature distribution of the structural member across its depth when exposed to high temperature can offer a better understanding of material's thermal properties. Thermocouples were attached to the bottom surface, the rebar, the centre and on the top surface. A discussion of the temperature history of the four locations is presented.

BOTTOM SURFACE

Three thermocouples, TC1, TC2 and TC3 were affixed to the bottom surface of the beams at different locations to read the temperature during the entire fire test. The temperature profiles for the bottom surface of the beam, monitored by one thermocouple are presented in Figure 7(a). Also included is the average gas temperature of the furnace chamber which was the same for all the tests since it followed the ISO 834 fire curve. Visual inspections at the end of the tests revealed that most of the thermocouples were detached from the concrete surface primarily due to spalling. Spalling commenced after 10 minutes and peaked around the 20th minute. The worst affected were the RLF2-40 and RLF4-40 beams, where all three thermocouples in each beam were detached. The surface temperature of both beams rose dramatically after 15 minutes, providing some indication when the thermocouples were detached from the concrete surface and started to read the furnace gas temperature.

BEAM CENTRE TEMPERATURE

The temperature profile at the centre of the four beams as measured by their respective thermocouples, TC5 are presented in Figure 7(b). The general picture is that RLF2-40 recorded the highest temperature at the centre throughout the test with a maximum of 350°C after 60 minutes compared to 200°C average temperature for the other beams. The severity of spalling in the RLF2-40 beam saw the loss of concrete mass on the lateral and bottom surfaces up to 30mm in depth. Therefore, the heat was able to travel a shorter distance to the centre of the beam.

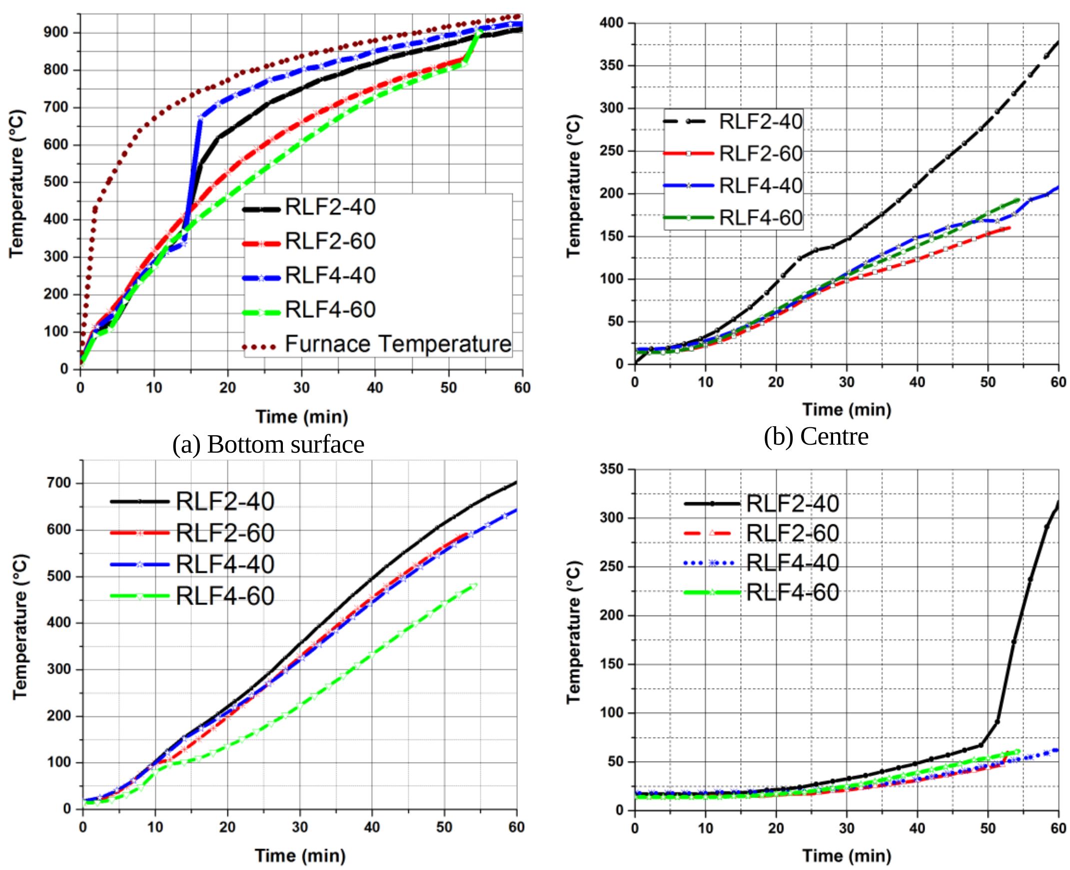

(a) Bottom surface

(b) Centre

(c) Rebars

(d) Top (unexposed) surface

Figure 7. Temperature development of various location of the beam.

STEEL REINFORCEMENT

Figure 7(c) presents temperature distribution in the reinforcement bars for all the four beams monitored by their respective TC4 thermocouples, which were affixed to the rebar during the casting process and left to set with the beam. Three beams that had their concrete cover partially exposed in some areas were the RLF2-40 and RLF4-40. Visual examination of the RLF4-40 beam showed that the loss of concrete cover of reinforcement occurred in more spots than other beams and this explains why it recorded the highest temperature. Spalling is a random process and although some parts of the beam recorded spalling depths of up to 30mm, some of the affected areas were not around the reinforcement bars.

TOP SURFACE

The development of temperature of the top surface that was unexposed to heat was monitored by TC-6 thermocouples. The resulting curves for all the 4 beams are shown in Figure 7(d). The temperature for all the beams remained within room temperature range in the first 20 minutes and stayed below 50°C up to the 40th minute. At the end of the test, the average temperature for all the beams was about 60°C except for the RLF2-40. The latter failed after 49 minutes, attaining a deflection of over 50mm, at that instant the top-surface was just about level with the furnace and exposed to the flames, and this explains why the temperature rose rapidly to over 300°C. Overall, the temperature of unexposed surface virtually remained constant irrespective of the magnitude of imposed load.

Parameters influencing fire performance

An analysis of test data and visual observations during and after experimental tests points to some possible factors that might have an influence on fire performance and behaviour of beams and these are briefly explained below.

INFLUENCE OF STEEL FIBRE CONTENT

Within the same load category, spalling was more predominant in beams with 2% steel fibres. Doubling the amount of steel fibres in beams resulted in a remarkable decrease in spalling by 87% and 66% for those in load ratio categories of 0.4 and 0.6 respectively. Steel fibres can increase the bond and tensile strengths of concrete and studies have shown that it can prevent spalling to some degree [15]. Therefore, the beams with 4% fibres had higher tensile strength than those with 2% fibres. This increase in tensile strength could have helped the beams to withstand the vapour pressure that built-up inside concrete due to heating. This, in turn, resulted in reduced spalling in beams with 4% fibres.

INFLUENCE OF LOADING LEVELS

Beams with the same amount of steel fibres had contrasting responses to variations in imposed loads. The two load ratios had dissimilar effects on beams' response to fire. The 0.4 load ratio caused the beam to fail in shear while the two beams with 0.6 ratio failed in bending. The intensity of spalling in beams with 0.4 load ratio was up to four times greater than those under the 0.6 load ratio.

INFLUENCE OF SPALLING

A closer scrutiny of beams having same constituent materials shows a direct relationship between the degree of spalling and fire endurance. The beams which were affected severely by spalling (RLF2-40 and RLF4-40) failed a little bit earlier due to loss of load-carrying capacity. While other factors such as loading levels and fibre content levels had a cumulative effect on endurance, spalling as a single factor can have a devastating effect on flexural element's load bearing capacity.

CONCLUSIONS

Four UHPFRC beams with 2% and 4% steel fibres with compressive strengths of up to 178 MPa were submitted to an ISO 834 fire in the furnace for one hour. two different loading levels of 0.4 and 0.6. Below are some of the key findings:

- Loading levels had an influence on failure criteria. Both beams under 0.4 load ratio failed in shear while those under 0.6 load ratio failed in bending.
- The load levels also influenced the spalling patterns of beams. The intensity of spalling in beams with 0.4 load ratio was up to four times higher than in beams with 0.6 load ratio.
- Steel fibres had an influence on the severity of spalling. Spalling was more severe in beams with 2% fibre ratio. However, doubling the amount of steel fibres resulted in a decrease in spalling by up to 87%.
- All the beams had fire resistance rating of 30 minutes.

REFERENCES

[1] B. Chen and J. Liu, "Residual strength of hybrid-fiber-reinforced high-strength concrete after exposure to high temperatures," *Cem. Concr. Res.,* vol. 34, pp. 1065-1069, 6, 2004.
[2] M. S. Cülfik and T. Özturan, "Effect of elevated temperatures on the residual mechanical properties of high-performance mortar," *Cem. Concr. Res.,* vol. 32, pp. 809-816, 5, 2002.
[3] G. Peng, S. Bian, Z. Guo, J. Zhao, X. Peng and Y. Jiang, "Effect of thermal shock due to rapid cooling on residual mechanical properties of fiber concrete exposed to high temperatures," *Constr. Build. Mater.,* vol. 22, pp. 948-955, 5, 2008.
[4] M. Behloul, G. Chanvillard, P. Casanova, G. Orange and F. F. F. France, "Fire resistance of ductal® ultra high performance concrete," in *1st Fib Congress,* 2002, pp. 421-430.
[5] P. Kalifa, G. Chéné and C. Gallé, "High-temperature behaviour of HPC with polypropylene fibres - From spalling to microstructure," *Cem. Concr. Res.,* vol. 31, pp. 1487-1499, 2001.
[6] P. Kalifa, F. Menneteau and D. Quenard, "Spalling and pore pressure in HPC at high temperatures," *Cem. Concr. Res.,* vol. 30, pp. 1915-1927, 12, 2000.
[7] P. Kalifa, G. Chéné and C. Gallé, "High-temperature behaviour of HPC with polypropylene fibres: From spalling to microstructure," *Cem. Concr. Res.,* vol. 31, pp. 1487-1499, 10, 2001.
[8] V. Kodur, "Spalling in high strength concrete exposed to fire: Concerns, causes, critical parameters and cures," in Anonymous American Society of Civil Engineers, 2000, pp. 1-9.
[9] F. Ali, A. Nadjai and S. Choi, "An experimental and numerical study on the behavior of high strength concrete columns in fire subjected to high restraint," *Journal of Structural Fire Engineering,* vol. 1, pp. 1-16, 2010.
[10] F. de Larrard and T. Sedran, "Optimization of ultra-high-performance concrete by the use of a packing model," *Cem. Concr. Res.,* vol. 24, pp. 997-1009, 1994.
[11] K. Wille, A. E. Naaman and S. El-Tawil, "Optimizing Ultra-High-Performance Fiber-Reinforced Concrete," *Concr. Int.,* vol. 33, pp. 35-41, 2011.
[12] J. H. Lee, Y. S. Sohn and S. H. Lee, "Fire resistance of hybrid fibre-reinforced, ultra-high-strength concrete columns with compressive strength from 120 to 200 MPa," *Magazine of Concrete Research,* vol. 64, pp. 539-550, 06/01; 2016/01, 2012.

[13] P. Pimienta, J. Mindeguia, A. Simon and M. Behloul, "Behavior of UHPFRC at high temperatures," in *Designing and Building with UHPFRC*, F. Toutlemonde and J. Resplendino, Eds. John Wiley & Sons, Inc., 2011, pp. 579-600.
[14] C. Kahanji, F. Ali and A. Nadjai, "Influence of curing regimes on flexural behaviour of ultra-high performance concrete beams," in *Response of Structures Under Extreme Loading*, East Lansing, Miami, USA, 2015, pp. 730-737.
[15] V. Kodur, "Fiber reinforcement for minimizing spalling in Hig Strength Concrete structural members exposed to fire," *ACI Special Publication*, vol. 216, 2003.

Fire Tests on Fiber Sheet Strengthened RC Beams using Geopolymers as Adhesive Agent

HAI YAN ZHANG, SHU LIANG QI, VENKATESH KODUR and HAO RAN LV

ABSTRACT

This study presents experimental results of fire tests on one control beam and four FRP strengthened RC beams, using geopolymers and epoxy resin as adhesive agent, to investigate the influence of temperatures on effectiveness of fiber sheet-geopolymer strengthening systems. The thermal response and deflection evolution of these beams with time were monitored. The test results show that although geopolymer material possess better bond properties than epoxy resin at high temperatures, the beams strengthened by carbon fiber sheet-geopolymer systems did not exhibit good fire resistance as expected, due to the falling off of the thermal insulation. Appropriate measurements to avoid the falling off of the insulation are required.

INTRODUCTION

In the last decades, the construction industry has shown great interest in the use of external bonded fiber-reinforced polymer (FRP) for strengthening concrete structures, due to its superior mechanical performance at ambient temperature. However, FRP material exhibits significant deterioration in mechanical and bond properties, at temperatures approaching the glass transition temperature of the organic polymer matrix, which is typically less than 100^{o}C [1, 2]. In addition, the combustible organic matrix can generate flame spread and toxic smoke under fire. To overcome these concerns, innovative matrix/fiber systems are being developed to enhance high temperature tolerance of FRP. Recently, a new class of material, inorganic geopolymers, has been introduced as a viable alternative to organic polymers. In comparison with organic polymers, inorganic geopolymers have advantages of resistance to high temperature, resistance to UV radiation, minimal toxic smoke under fire exposure, and ease in handling [3, 4].

Hai Yan Zhang, State Key laboratory of Subtropical Architecture Science, South China University of Technology, Guangzhou 510641, P.R. China.
Qi Shu Liang, Department of Civil Engineering, South China University of Technology, Guangzhou 510641, P.R. China
Venkatesh Kodur, Department of Civil and Environmental Engineering, Michigan State University, East Lansing 48823, MI, USA
Hao Ran Lv, Department of Civil Engineering, South China University of Technology, Guangzhou 510641, P.R. China

Experimental data on the mechanical properties at ambient temperature of fiber sheet strengthened concrete members bonded with geopolymers has already been reported in literature [5, 6]. However, there is lack of data on the mechanical performance of RC beams strengthened by fiber sheet-geopolymer systems in fire. In this study, fire tests were conducted on one control RC beam and four FRP strengthened RC beams, using geopolymers or epoxy resin as adhesive agent respectively. Data generated from the tests were utilized to evaluate the effect of temperature on the effectiveness of fiber sheet-geopolymers strengthening systems.

EXPERIMENTAL PROGRAM

The experimental program consists of fire resistance experiments on one unstrengthened control beam and four fiber sheet strengthened RC beams. The test variables include fiber sheet type and layer, and adhesive agent type.

Fabrication of test specimens

Five rectangular RC beams were fabricated for undertaking the fire resistance tests. The beams were of 250 mm width, 400 mm depth, and 5.3 m length. The beams were cast with ready-mixed concrete, produced in a concrete plant. The average cubic compressive strength at an age representative of fire resistance test is 40.4 MPa. The internal longitudinal steel reinforcement, with a cover of 25mm, consisted of two ϕ22 deformed rebars (HRB335), with yielding strength of 363.5 MPa, as flexural reinforcement and two ϕ12 deformed rebars (HPB235), with yielding strength of 420.6 MPa, as compression reinforcement. The stirrups used as shear reinforcement were ϕ8 plain rebars (HPB235) at spacing of 160 mm in the middle pure bending section and two cantilever sections, and at spacing of 80 mm in the shear bending sections. The beams were intentionally overdesigned for shear capacity because the focus of this study was flexural failures.

FRP strengthening

Four of the RC beams (B2–B5) were strengthened with one or two layers of fiber fabrics to enhance their flexural strength capacity, and one beam was unstrengthened as the control beam (B1). Two types of fiber sheets, including carbon fiber (CF) sheets and basalt fiber sheets, with length of 4400 mm and width of 250 mm, were bonded on the beam soffit along the longitudinal direction by organic epoxy resin or inorganic geopolymers, as the strengthening systems. After the strengthening system on the beam soffit was dried, six U-shaped fabrics hoops, with size of 150 mm (width)$\times$ 1050 mm (length), were wrapped on the two sides and the soffit of the beam, and bonded through matrix, to provide the anchorage for the longitudinal strengthening system. Details of the tested beams are summarized in Table 1.

Table I. Details of beam specimens.

Specimen No.	Matrix	Type of fiber fabrics	layer of fiber fabrics	Fire insulation thickness (mm)	Total load (kN)	Load ratio	Fire endurance (min)
B1	-	-	-	-	76	0.5	129
B2	Epoxy resin	BFRP	1	10	90	0.5	193
B3	Epoxy resin	CFRP	1	10	112	0.5	199
B4	Geopolymers	CFRP	1	10	112	0.53	160
B5	Geopolymers	CFRP	2	10	133	0.5	158

The organic matrix was provided by a China supplier. The inorganic geopolymers were prepared by blending metakaolin and fly ash mixture with potassium silicate solution. The detailed preparation procedures of geopolymers can be referred to Zhang et al. [4].

Commercially available carbon fiber sheet and basalt fiber sheet, with unidirectional plain weave, were used. The carbon fiber sheet, with thickness of 0.167mm, has an ultimate tensile strain of 1.73%. The basalt fiber sheet, with thickness of 0.16mm, has an ultimate tensile strain of 1.7%. The tensile strength of CFRP composite was 3455 MPa for organic matrix and 3149 MPa for inorganic matrix. The tensile strength of BFRP composite was 1202 MPa for organic matrix.

Fire Protection

The strengthened beams were cured for 7 days and then were plastered with TB tunnel fire protection system, which was supplied by Guangzhou (China) Taibao Fireproof Material Ltd. This insulation is a non-combustible and a non-flammable lightweight material available in powder form. The density, heat capacity and thermal conductivity coefficient of the insulation is 500 kg/m^3, 1036 J/(kg·^{o}C) and 0.126 W/(m·^{o}C) respectively. The insulation layout was comprised of 10 mm of insulation thickness at the beam soffit, extending 80 or 50 mm on the two sides for beams B2/B3 and B4/B5 respectively.

Instrumentation and test setup

The beams were instrumented with thermocouples at four different sections along the span of the beam to measure the temperatures at various depths in the concrete, reinforcement and FRP/concrete interfaces. A total of 13 thermocouples were installed for each beam. Also, three displacement sensor were installed on each beam, at the 1/4, 1/2 and 3/4 span, to measure the deflections. The locations of thermocouples and displacement sensor are shown in Figure 1.

The fire resistance tests on RC beams were conducted on a fire testing furnace, with chamber of 4400 mm long, 3000 mm wide and 1500 mm high. The beams were simply supported at the ends, and loaded with four point loads. The total load and the ratio of the load to the calculated nominal bearing capacity are listed in Table 1.

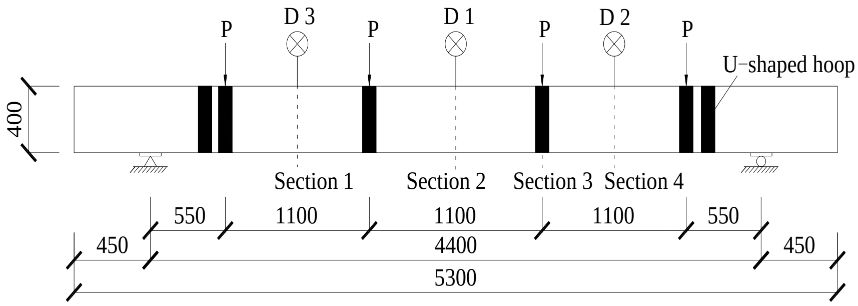

(a) Elevation and location of displacement sensors

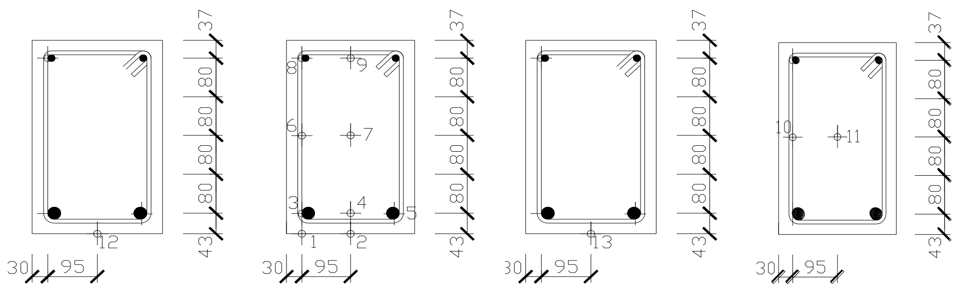

Section 1 Section 2 Section 3 Section 4

(b) Location of thermocouples

Figure 1. Elevation and cross-sectional details of tested strengthened beam.

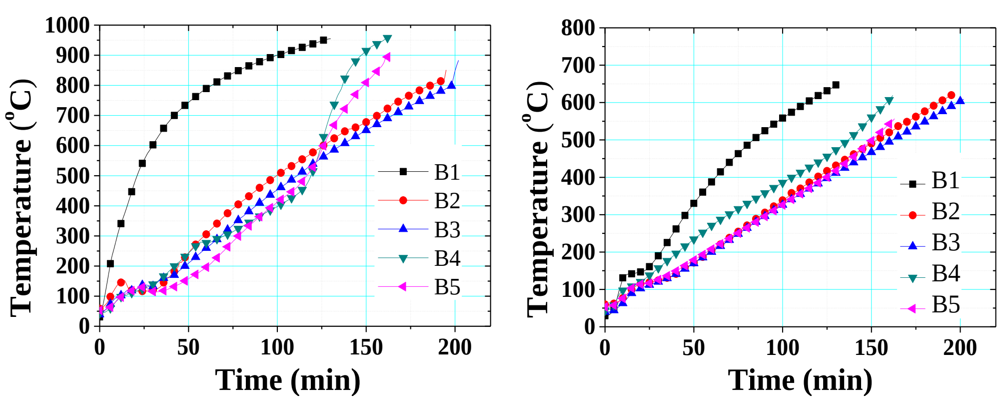

（a）T2 (Concrete/FRP interface) （b）T3 (Corner rebar)

Figure 2. Measured temperatures at different position as a function of fire exposure time.

The load was applied approximately 30 min prior to the start of fire until a steady condition was reached. After 30 min of loading, the beams were exposed to fire from three sides. For the duration of the fire test, the applied load was kept constant. The furnace temperature increased in accordance with the ISO 834 standard fire curve.

During the tests, the temperatures at various locations of the beam cross sections and deflections were recorded at 5 s intervals.

RESULTS AND DISCUSSION

Data generated from the above fire tests, including cross-sectional temperatures at various locations, mid-span deflections, as well as fire endurance, are utilized to evaluate and compare the fire behavior of FRP strengthened RC beams using inorganic geopolymers and organic epoxy resin as adhesive agent.

Thermal response

Figure 2 illustrates the temperatures measured as a function of the time of fire exposure at different positions in five beams. As illustrated in Figure 2(a), the temperature of thermocouple T2, located at the mid-span concrete soffit of beam B1, is much higher than that of beams B2-B4 during the duration of fire exposure, due to no fire protection. The temperatures of T2 in beams B2-B5, representing the temperatures on FRP/concrete interface, increase at a similar rate at the early stage, and exhibiting a small plateau just over 100^{o}C, which is caused by the water vaporization in the surrounding insulation and concrete. However, an abrupt increase was recorded at the FRP/concrete interface of beams B4 and B5 after 120 min of fire exposure. And after 150 min, the temperatures almost approach the highest one that beam B1 (without fire protection) experienced. This rapid increase in temperature after 120 min probably occurred due to the falling off of a portion of insulation.

Figure 2(b) shows the temperature progression in a corner rebar (thermocouple T4) as a function of time for the five tested beams, including the RC control beam. As expected, the temperatures of rebars in FRP-strengthened RC beams with fire protection experienced slower increase for the entire test duration than that of the control beam, which was not insulated. Compared to the other three insulated beams, the measured corner rebar temperatures in beam B4 is 40-70^{o}C higher, after 30 min exposure. This is due to the early minor crack propagation in the two sides of beam B4 before fire test.

Structural response

Figure 3 presents the mid-span deflection evolution of five tested beams as a function of the time of fire exposure. It can be clearly seen from Figure 3(a) that during the entire fire duration, the mid-span deflection of the control beam is higher than that of FRP-strengthened beams, since no thermal insulation was applied on control beam. Before 110 min, the deflection of the control beam increases gradually, but after that it increases at a higher rate. This is due to the higher degradation in stiffness and strength occurred.

The deflection of strengthened beams B2-B5 experienced three phases for the entire duration of fire exposure. The first phase, from the beginning of fire exposure to 55 min (75 min for B5), the mid-span deflections of beams B2-B5 increase at a lower rate. From Figure 2, it can be seen that the temperatures of concrete and rebar were just over 100 and 200^{o}C in 55 min, due to the existing of plateau around 100^{o}C.

Therefore, the thermal-induced degradation on mechanical properties was not significant. When the evaporation of most water in specimens was completed, the deflection evolution entered the second phase. In this phase, the temperatures of concrete and rebars began to increase at a higher rate, which led to higher degradation of stiffness (and strength) and thus quicker increase in deflection. When the temperatures of concrete and rebars exceeded 600°C and 500°C respectively, significant degradation (almost 50% decreases) in strength and elastic modulus of concrete and rebars occurred, and thereafter the mid-span defection of beams grew sharply. The period from the beginning of sharp deflection growth to failure of FRP-strengthened beams can be classified as the third phase.

As illustrated in Figure 3(a), the sharp deflection growth of beams B4 and B5 occurred around 150 min, which is earlier than that of B2 and B3. This is resulted from higher temperature of concrete and rebars developed in beams B4 and B5 after 120 min exposure to fire. Figure 3(b) presents the mid-span deflection evolution of beams B3 and B4 at the early 150 min for comparison. Beams B3 and B4 were subjected to the same load and strengthened by carbon fiber sheets with the same thickness, but through different matrix. It can be seen from Figure 3(b) that beam B4 exhibited lower deflection than beam B3 from the beginning of fire exposure to 150 min, although beam B4 exhibited higher deflection before fire exposure. Especially, from 10 to 50 min, the mid-span deflection of beam B4 almost kept constant, but a higher deflection development was seen on beam B3. This is due to the significant temperature-induced degradation in mechanical properties of organic matrix, when FRP/concrete interface temperature exceeded the glass transition temperature of organic matrix (about 82°C), but geopolymers maintain good bond properties until 300°C [3]. Even though the temperatures on FRP/concrete interface in beam B4 increases abruptly and exceed that of B3 after 120 min (as shown in Figure 2(a)), the mid-span deflection of beam B4 is lower than that of B3 between 120 min to 150 min.

Fire resistance

Table I provides a comparison of the fire-resistance ratings achieved by all five

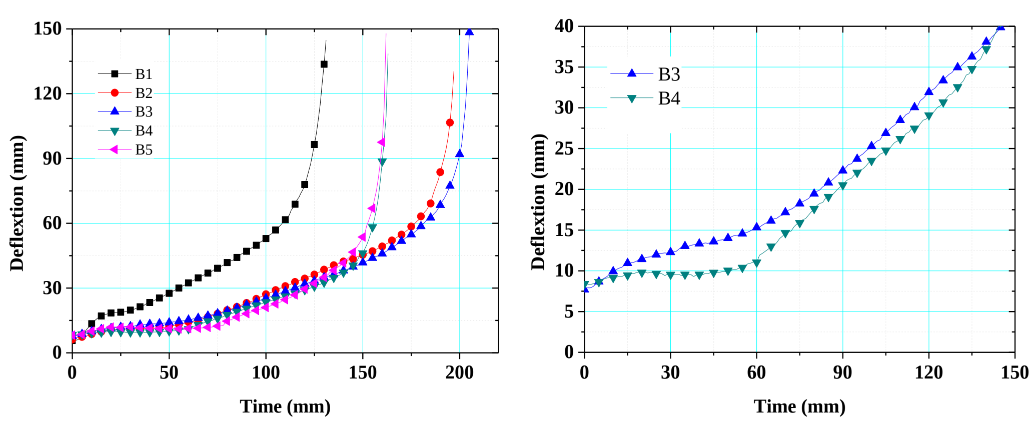

(a) Deflection evolution of beams B1-B5 (b) Deflection comparison of B3 and B4

Figure 4. Mid-span deflection of tested beams.

beams. Apart from the control beam, all FRP strengthened beams had fire endurance of greater than 150 min. Clearly, the superior fire resistance of the strengthened beams, as compared to the control beam, can be attributed to the presence of the fire protection systems. Beams B2 and B3 were strengthened by basalt fiber sheets and carbon fiber sheets respectively, using organic matrix. Although beam B2 was applied a lower load, but B2 had shorter fire endurance than B3. This is due to that the concrete and internal rebars in B2 experienced higher temperatures during the fire tests. Beams B4 and B5 were strengthened by one or two layers of carbon fiber sheets, using geopolymers as adhesive agent. It is reported that geopolymers possess better high temperature performance than epoxy resin. However, beams B4 and B5 did not exhibit higher fire endurance as expected. This is induced by the sudden falling off of the thermal insulation from beams B4 and B5 at 120 min, which leads to rapid increase in temperatures of concrete and rebars, and thus the sharp degradation of mechanical properties. From the post-fire observations, it can be inferred that the failure of beams B4 and B5 was driven by the direct exposure and fracture of tensile rebars, after the falling off of insulation and partial concrete. Therefore, appropriate measurements to avoid the falling off of insulation are required.

CONCLUSIONS

Fire tests were conducted on one control beam and four external FRP strengthened beams in this study. From the test results, the following conclusions can be drawn.

(1) The beams strengthened through bonding carbon fiber or basalt fiber sheets with epoxy resin can achieve acceptable fire endurance, conditional on thermal insulation applied.

(2) Although geopolymer materials possess better high temperature performance than organic matrix, the beams strengthened by fiber sheet-geopolymer system do not exhibit better fire resistance than that strengthened by fiber sheet-epoxy resin system. Appropriate measurements should be taken to avoid the falling off of insulation.

REFERENCES

1. Firmo, J. P., J. R. Correia, and L. A. Bisby. 2015. “Fire behaviour of FRP-strengthened reinforced concrete structural elements: A state-of-the-art review,” *Composites Part B*, 80: 198-216.
2. Ahmed A., V. Kodur. 2011. “The experimental behavior of FRP-strengthened RC beams subjected to design fire exposure,” *Engineering Structures*, 33: 2201-2211.
3. Zhang H. Y., V. Kodur, S. L. Qi, and B. Wu. 2015. “Characterizing the bond strength of geopolymers at ambient and elevated temperatures,” *Cement & Concrete Composites*, 58:40-49.
4. Zhang H. Y., V. Kodur, S. L. Qi, L. Cao, and B. Wu. 2014. “Development of metakaolin－fly ash based geopolymers for fire resistance applications,” *Construction and Building Materials*, 55:38-45.
5. Toutanji H., and Y. Deng. 2007. “Comparison between Organic and Inorganic Matrices for RC Beams Strengthened with Carbon Fiber Sheets,” *Journal of Composites for Construction*, 11 (5):507-513.
6. Toutanji H., L. Zhao, and Y. Zhang. 2006. “Flexural behavior of reinforced concrete beams externally strengthened with CFRP sheets bonded with an inorganic matrix,” *Engineering Structures*, 28: 557-566.

Elevated Temperature Response of RC Beams Strengthened with NSM FRP Bars Bonded with Cementitious Grout

IOLANDA DEL PRETE[1], ANTONIO BILOTTA[2], LUKE BISBY[3] and EMIDIO NIGRO[2]

ABSTRACT

This paper presents the results of 12 tests on small-scale reinforced concrete beams strengthened in flexure with a single near surface mounted (NSM) carbon FRP bar. To improve the performance of the FRP strengthening system at elevated temperature, the specific FRP bar has high values of glass transition T_g and decomposition T_d temperature. Tests are performed to define the resin behavior at elevated temperature. The FRP is bonded using a cementitious grout rather than an epoxy adhesive. Flexural tests have been performed at both ambient and elevated temperatures on both un-strengthened and strengthened beams. Tests at elevated temperature were performed using propane-fired radiant panels rather than a fire testing furnace. Two heating configurations were used: (1) localised heating near midspan only; and (2) global heating over the entire bonded length of the FRP systems. Thermo-structural response was investigated under loads that give typical (i.e. maximum permissible) FRP service loading strain conditions. Internal temperatures, beam displacements, and slip of the FRP strengthening were measured. Bonded foil strain gauges were used to measure the FRP bar strains prior to heating, and digital image correlation (DIC) was also used to study displacements. The tests demonstrated good performance of this novel FRP strengthening system, both under localized (non-bond critical) and global heating (bond critical), and also demonstrated the grout-bonded NSM CFRP strengthening system's ability to maintain structural effectiveness at temperatures up to about 600°C with adequate anchorage. However, similar tests with an epoxy adhesive are needed before the novel system can be confidently stated as being vastly superior to epoxy-adhered NSM systems.

INTRODUCTION

Fibre reinforced polymers (FRP) are widely applied for structural strengthening by bonding them to the exterior of reinforced concrete (RC) structures, usually with epoxy adhesives. However, degradation of mechanical properties of polymer

[1] BuroHappold Engineering, 17 Newman Street W1T 1PD, London - UK
[2] Department of Structures for Engineering and Architecture, University of Naples, via Claudio 21 80125, Naples - Italy
[3] Institute for Infrastructure & Environment, School of Engineering, University of Edinburgh, Mayfield Road EH9 3JL, Scotland UK

adhesives and composites due to various environmental effects, notably including elevated temperatures, is an important factor in application of FRP composite materials in buildings and certain industrial applications. With the near surface mounted (NSM) FRP strengthening technique, the FRP bar/rod/strip is placed in a groove cut into the concrete cover and bonded in place by filling the groove with an epoxy (or, less commonly , cementitious) adhesive. Several studies have demonstrated that NSM bonded with epoxy adhesive exhibits superior bond behavior compared with externally-bonded FRP reinforcement (EBR) ([6], [7], [8]). NSM is also less prone to damage, since the FRP is embedded in a groove and inside adhesive. Despite this, the effectiveness of epoxy adhesive is severely reduced at elevated temperatures. Ambient temperature cure epoxy adhesives are characterized by relatively low glass transition temperatures (T_g), however higher T_g values can be achieved for pultruded FRP which is manufactured at elevated temperature. In NSM applications, using an elevated T_g FRP product bonded with a cementitious grout may result in superior mechanical performance in fire, since cementitious adhesives may perform better than epoxies, whilst also protecting (both mechanically and thermally) the FRP, possibly without the need to apply costly and unattractive supplemental insulation materials to the exterior of the FRP strengthening system [1]. Though epoxy resins are usually used as bonding agents, there have been several recent studies on the behavior of cementitious paste or mortar bonded NSM FRP systems ([1], [3], [4], [5]).

This paper presents an experimental testing program aimed at investigating the performance of a novel high temperature cementitious-bonded NSM CFRP strengthening system for concrete, which has been developed specifically to address the performance of FRP strengthening systems at elevated temperatures.

EXPERIMENTAL PROGRAM

The core experimental program consisted of dynamic mechanic analysis (DMA) and thermos-gravimetric analysis (TGA) tests on the FRP bar, along with twelve four-point bending tests of RC beams and NSM FRP strengthened RC beams, 1450 mm long and 150 mm square in cross-section. The flexural tests were performed both at ambient and elevated temperature. The tests at elevated temperature were executed using propane-fired radiant panels to heat the beams, rather than a standard fire-testing furnace. This has the advantage of being able to provide more direct instrumentation and observation of the beams during heating, whilst still providing severe, however non-standard, heating. Two heating configurations were used: (1) localised heating near midspan only; and (2) global heating over the entire bonded length of the FRP.

The thermo-structural response was investigated under sustained loads sufficient to generate FRP strains that are typical of maximum permissible service strain conditions in the FRP (Service Load (SL) = 40 kN; High Load (HL) = 50 kN). TABLE I summarizes the flexural tests, showing the relevant test beam designations.

Material Properties

DMA and TGA were performed on the novel, high T_g commercial CFRP bars to define T_g and T_d, respectively, for this particular FRP product.

DMA tests were carried out through a DMA analyzer performed according to [9], with 3 tests in a single cantilever configuration and 3 in a three-point bending configuration.

TGA provides the mass of a sample as a function of temperature. TGA tests were carried out through a thermobalance with a horizontal arrangement, with 3 tests performed in Nitrogen (N_2) atmosphere, and 3 tests in air.

TABLE I. EXPERIMENTAL PROGRAM.

Beam designation	Scheme	Load
UN-S_i i=1,2	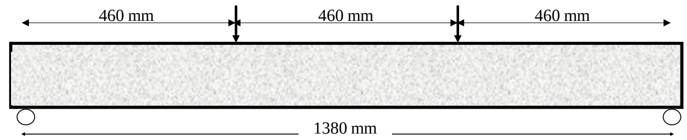	2mm/min
Note:	2 tests at ambient temperature of **UN-S**trengthened beams	
S-i i=1,2,3_cut	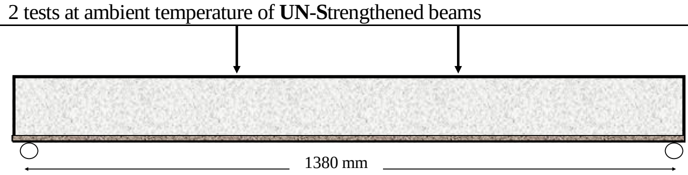	2mm/min
Note:	3 tests at ambient temperature of NSM FRP **S**trengthened beams	
UN-S_GloH_SL_1	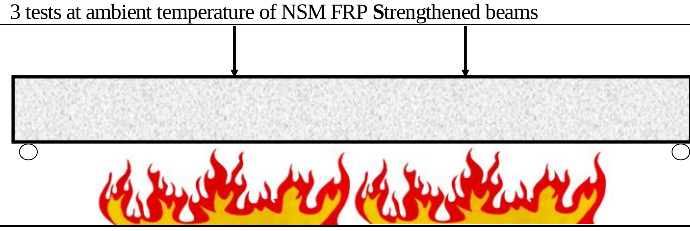	SL=40 kN
Note:	1 test of **UN-S**trengthened beam in **Glo**bal **H**eating configuration, under **S**ervice **L**oad	
S_GloH_SL_i i=1,2	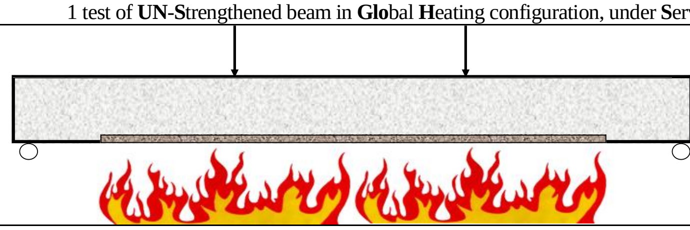	SL=40 kN
Note:	2 tests of NSM FRP **S**trengthened beams in **Glo**bal **H**eating configuration, under **S**ervice **L**oad	
S_LocH_SL_i S_LocH_HL_i i=1,2	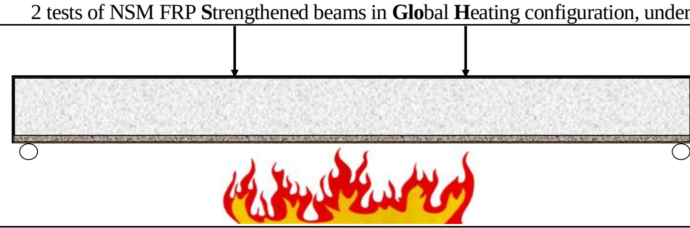	SL=40 kN HL=50 kN
Note:	- 2 tests of NSM FRP **S**trengthened beams in **Loc**alised **H**eating configuration, with **S**ervice **L**oad - 2 tests of NSM FRP **S**trengthened beams in **Loc**alised **H**eating configuration, with **H**igh **L**oad	

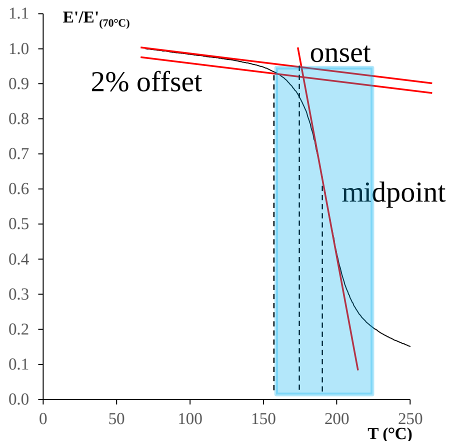

Figure 1. DMA processing methods.

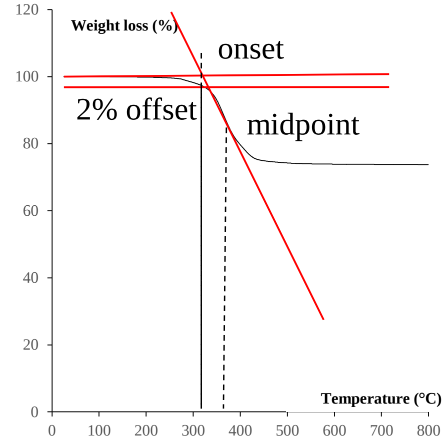

Figure 2. TGA processing methods.

The results of DMA and TGA tests were processed using several techniques available in literature (refer to Figure 1 and Figure 2). The testing outcomes are discussed in greater detail in [11]. The observed T_g values ranged between 160°C ($T_{g,offset}$) and 220°C ($T_{g,max(tan\delta)}$), and T_d values range between 315°C ($T_{d,offset}$) and 360°C ($T_{g,midpoint}$). The variability, which is evident in these , highlights the need for clear standardization of the DMA and TGA test methods' results and the manner in which the resulting test data are processed and interpreted to arrive at suitable (i.e. physically representative) T_g and T_d values for use by designers.

Thermal conductivity tests were performed on the cementitious grout adhesive used in the current study and yielded thermal conductivity values (essentially constant in the temperature range 50-175°C) of 0.55 W/mK; a slightly higher value (0.66 W/mK) was obtained at about 100°C, likely due to the evaporation of water, which led to a greater energy absorption than that needed to maintain the thermal gradient in the sample at other temperatures.

The concrete compressive and tensile strengths at 28 days were 35.6 MPa and 3.83 MPa, respectively. The concrete compressive strength at 76 days was 47.7 MPa. The steel yield strength (tension reinforcing bars) was 525 MPa. The steel ultimate strength (tension reinforcing bars) was 622 MPa. The steel yield strength (compression bars) was 700 MPa. The cementitious mortar compressive strength at 28 days was 90 MPa, and the CFRP tensile strength was 1750 MPa, with a tensile elastic modulus of 136 GPa. It is noteworthy that all the above values have been obtained by testing at least three samples.

Design and Fabrication

All twelve beams had internal flexural reinforcement in the form of two deformed steel reinforcing bars (nominal diameter of 10 mm) on the tension side and two deformed steel reinforcing bars (nominal diameter of 6 mm) in compression (see **Figure 3**b).

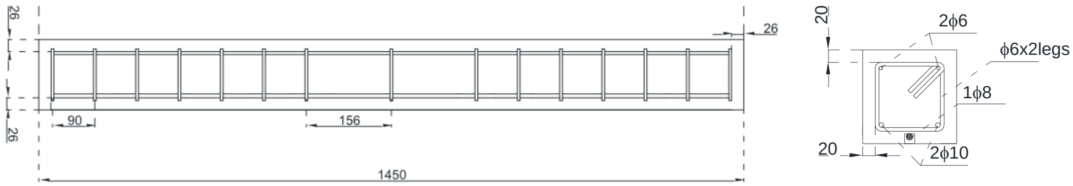

a) Longitudinal section b) Cross section

Figure 3. NSM FRP strengthened RC beam.

The FRP strengthening system consisted of a single CFRP bar (nominal diameter of 8 mm), grouted in place using a cementitious mortar within a groove, 16 mm square in cross-section, that was cut into the concrete cover of the beam using a ‘wall chaser’ fitted with a diamond blade. The shear reinforcement in the beams was designed to ensure that flexural failure would govern. Steel stirrups (with a nominal diameter 6 mm) were spaced at 90 mm on centre (see **Figure 3**a). The design of the RC beams was performed in accordance with EN1992-1 [12] and ACI 318-08 [13]; however the stirrup spacing according to EN1992-1 was adopted in the final design.

The NSM strengthening system was applied after casting and curing of the RC beams. A wall-chasing grinder fitted with two spaced diamond cutting discs was used to cut precise vertical slots in the bottom concrete cover of the beams, and the remaining fin of concrete was removed with a wall-chasing break-out tool. The groove was then made smooth and clean, and the bar was placed and grouted, with the beams in an upside-down configuration (i.e. with gravity used to ensure complete filling of the NSM grooves)..

Instrumentation and Test setup

Linear potentiometers were used during testing to measure the vertical displacement at the beams at midspan (LP100) and the slip of the NSM CFRP bar at both the left hand (LP25-LHS) and right hand (LP25-RHS) ends of the beams (with reference to Figure 4). A bonded foil strain gauge was also placed at the mid length of the CFRP bar before it was installed. A high-resolution digital SLR camera was set to take photos every five seconds; this enabled a DIC monitoring the vertical deflections and flexural strains over the height of the beams. Multiple thermocouples (TCs) were also located in and on the beams, as shown in Figure 4.

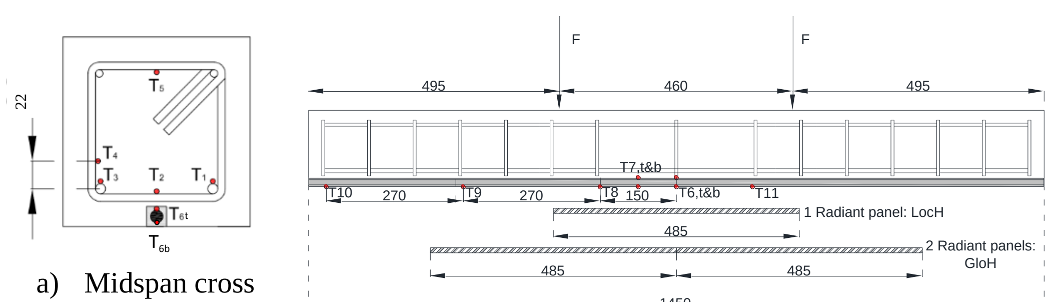

a) Midspan cross section

b) Longitudinal section

Figure 4. Thermocouple locations.

The tests in a local heating configuration (LocH) used a propane-fired radiant heating panel, with plan dimensions of 485x330 mm, located at midspan 120 mm below the beams. The tests in global heating configuration (GloH) were carried out with two such radiant heating panels, ensuring heating over the entire bonded length of the NSM FRP strengthening system, which was 970 mm long for the beams tested in this configuration.

TEST RESULTS

Ambient temperature tests

The flexural tests of the strengthened beams showed that the beam cracked under a load of about 8 kN, as was also observed for un-strengthened beams. Thus, as expected the strengthening did not significantly affect the beams' pre-cracked moment of inertia. The load then linearly increased until the yielding of the internal tensile reinforcement, at about 56 kN (36% greater than the yield load of the un-strengthened beams), and corresponding to a midspan deflection of about 9 mm. After steel yielding, the increasing tensile loading of the CFRP bar led eventually to slippage between FRP bar and the cementitious bonding agent. The load then gradually increased to about 59 kN (19% greater than the failure load of UN-S_1), with periodic slippage of the FRP bar resulting in a significant increase of the midspan deflection, up to about 21 mm, due eventually to complete debonding of the CFRP bar within the cementitious grout. After debonding of the strengthening system, which appeared to occur when the slippage of the bar was measured as about 6 mm, the strengthened beams showed behaviour essentially identical to that exhibited by the un-strengthened beams. Beam 'failure' occurred due to concrete crushing in the compressione zone near midspan. The strain in the CFRP bar, after concrete cracking increased, linearly, up to 5170 $\mu\varepsilon$, until bar slippage initiated. During the gradual slippage and debonding stage the strains in the FRP bar increased up to about 5850 $\mu\varepsilon$, corresponding to a slight increase in load capacity. A full discussion of the ambient temperature tests is given in [15].

Elevated temperature

The elevated temperature tests highlighted the ability of the novel FRP strengthening system to remain effective at elevated temperature, in both global and local heating configurations. The effectiveness of the strengthening system during a fire event and its residual strength depends also on the utilization factor of the member in fire, η_{fi}, being the ratio between the relevant effects of actions in the fire situation at time *t*, $E_{d,fi,t}$, and the design value of the resistance of the member in the fire situation at beginning of thermal transience, $R_{d,fi,0}$ (EN1991-1-2 [14]).

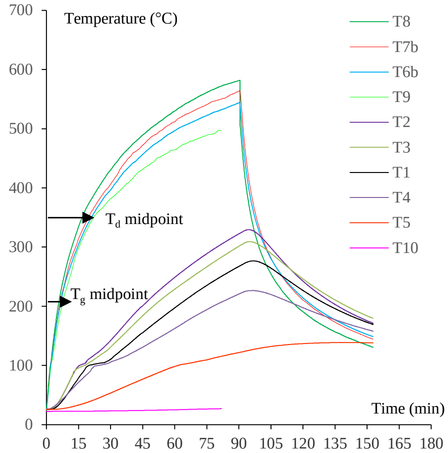

Figure 5. Temperature recorded (GloH).

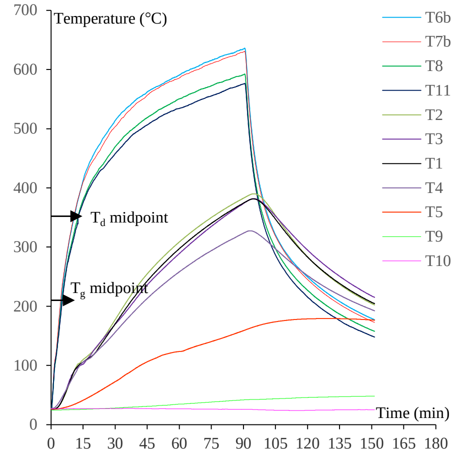

Figure 6. Temperature recorded (LocH).

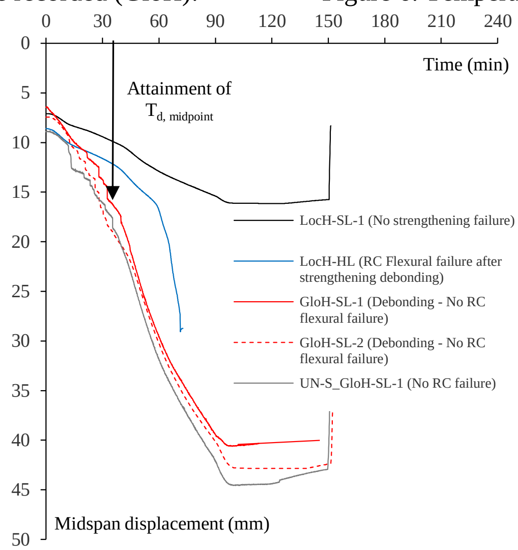

Figure 7. Midspan displacement versus time.

The tests on FRP strengthened beams in a global heating mode were undertaken on beams with a utilization factor equal to about 0.7 (sustained load of 40 kN). These tests showed that attainment of $T_{d,midpoint}$ (360°C in Figure 5) along the overall bonded length of the CFRP bar led to debonding and subsequent loss of effectiveness of the strengthening system. Nevertheless, these beam did not fail after 90 min of heating exposure since the un-strengthened beams were able to carry the applied load without the FRP strengthening system remaining effective, even though very large deflections were exhibited (see Figure 7).

Residual tests, undertaken after the beams had cooled to room temperature, confirmed that the residual failure load was equal to that obtained from testing the un-strengthened beams at ambient temperature (i.e. the pre-existing concrete beams had not been significantly damaged by the heating exposure, despite loss of effectiveness of the FRP system.

The strengthening system of the tested beams with η_{fi} equal to about 0.7, tested in a local heating configuration (i.e. with the anchorage zones of the NSM FRP strengthening system remaining cool during heating) did not fail after 90 min of fire exposure, even though the temperature of the CFRP bar in the heated zone was about 600°C (refer to Figure 6); it is noteworthy that this is a significantly higher temperature than T_d of the polymer matrix of the bar. This suggests that the CFRP bar in the heated zone was likely completely debonded due to softening and decomposition of the epoxy matrix within the heated region. The cold-end anchorage of the NSM FRP system was able to carry the stress transferred from midspan, and the carbon fibres were able to carry the service level tensile stress in the FRP even once the resin had lost effectiveness in the heated zone. Figure 7 shows the beams' deflection versus time of heating, highlighting that in a local heating configuration the deflection of the beams was significantly lower than that observed in global heating, since the thermal gradient, and therefore the thermal curvature, were lower than that induced by global heating.

Beams tested in a local heating configuration with η_{fi} equal to about 0.8 (sustained load of 50 kN), were unable to sustain the stress transferred from midspan when the maximum temperature in the CFRP bar achieved about 600°C, even given that the temperature at the end-anchorages was close to ambient. It is possible that the temperature of the CFRP bar close to the heat-exposed zone may have exceeded T_g due to thermal conduction along the FRP bar and leading to a reduction of the effective end-anchorage length.

The tests performed herein thus demonstrate the importance of cold end-anchorage zones to maintain the effectiveness of this NSM FRP strengthening system in case of fire under sustained loads typical of maximum service strain conditions in the FRP. It is noteworthy that no tensile failures of the CFRP bars were observed in any tests, despite the fact that (i) a temperature of more than 600°C was attained in the bar during heating, and (ii) a significant sustained stress was maintained within the FRP.

CONCLUSIONS

Tests have been presented on a novel cementitious-bonded CFRP NSM strengthening system specifically developed to address the problematic performance of conventional epox adhered FRP strengthening systems at elevated temperatures. Based on the tests presented it can be concluded that:

- T_g ranged between 160°C ($T_{g,offset}$) and 220°C ($T_{g,max(tan\delta)}$) for the CFRP bar used. T_d ranged between 320°C ($T_{d,offset}$) and 360°C ($T_{d,midpoint}$). This highlights the need to standardize T_g and T_d definitions and test configurations.
- When adequately anchored in cool regions with an anchorage length of at least 300 mm, the NSM FRP system studied herein was able to carry tensile stresses typical of in-service conditions at elevated temperatures up to 600°C.
- The capacity of the NSM FRP system depends on the presence of effective cold anchorage, because carbon fibres behave significant strength at elevated temperatures even when the performance of the polymer matrix is compromised; and,
- Local insulation systems placed at the end-anchorages only, instead of insulation along the overall bonded length for the FRP system, may be able to prolong overall system performance in fire; further testing is needed to confirm this.

ACKNOWLEDGEMENT

The authors would like to thank Milliken Infrastructure Solutions for providing the FRP materials and cementitious mortar (marketed under the trade name FireStrong) used in the experimental program.

The authors would like to thank BuroHappold Engineering for supporting the presentation of this paper to the SIF'16 Conference.

REFERENCES

1. Yu B., Kodur V., (2014). Fire behavior of concrete T-beams strengthened with near-surface mounted FRP reinforcement. Engineering Structures. 2014;80:350-361.
2. El-Gamal S., Al-Salloum Y., Alsayed S., Aqel M., (2012). Performance of near surface mounted glass fiber reinforced polymer bars in concrete. Journal of Reinforced Plastics and Composites, 31 (22) 1501-1515. DOI: 10.1177/073168441246408
3. Petri P., Blaszak G., Rizkalla S., (2013). Structural Fire Endurance of an RC Slab Strengthened with High T_g Near Surface Mounted CFRP Bars. ACIC 2013, Edited by Miss Claire. J. Whysall and Prof. Su. E. Taylor, 140-151, Queen's University Belfast on 10 -12 September 2013
4. Burke P.J., Bisby L. A., Green M., (2013). Effects of elevated temperature on near surface mounted and externally bonded FRP strengthening systems for concrete. Cement & Concrete Composites 35 (2013) 190–199
5. Palmieri A., Matthys S., Taerwe L., (2013). Fire Endurance and Residual Strength of Insulated Concrete Beams Strengthened with Near-Surface Mounted Reinforcement. J. Compos. Constr. 2013.17:454-462.
6. El-Hacha R., Rizkalla S: H., (2004). Near-Surface-Mounted Fiber-Reinforced Polymer Reinforcements for Flexural Strengthening of Concrete Structures, ACI Structural Journal, September-October 2004, 717-726
7. Foret G., Limam O., (2008). Experimental and Numerical analysis of RC two-way slabs strengthened with NSM CFRP rods, Construction and Building Materials 22 (2008) 2025-2030.
8. Bilotta A., Ceroni F., Di Ludovico M., Nigro E., Pecce M., (2011). Bond Efficiency of EBR and NSM FRP Systems for Strengthening Concrete Members, J. Compos. Constr. 2011.15:757-772.
9. ISO 6721-1:2011. Plastics - Determination of dynamic mechanical properties - Part 1: General principles.
10. ASTM D 4092 – 07 (2013). Standard Terminology for Plastics: Dynamic Mechanical Properties.
11. Del Prete I., Bilotta A., Bisby L., Nigro E., (2015). NSM FRP strengthened reinforced concrete beams: Benefits in fire of high Tg FRP & cementitious adhesive. Applications of Structural Fire Engineering, 15-16 October 2015, Dubrovnik, Croatia, 331-336.
12. EN1992-1-1 (2004). Eurocode 2: Design of concrete structures - Part 1-1: General rules and rules for buildings
13. ACI 318-08 (2009). Building Code Requirements for Structural Concrete. ACI Committee 318, American Concrete Institute.
14. EN1991-1-2 (2002). Eurocode 1: Actions on structures – Part 1-2: General actions – Actions on structures exposed to fire.
15. Del Prete I., Bilotta A., Bisby L., Nigro E., (2015). Bond tests on NSM FRP strengthening using cementitious matrices for concrete structures. FRPRCS-12 & APFIS-2015 Joint Conference, 14-16 December 2015, Nanjing, China.

Flexural Capacity of NSM FRP Strengthened RC Beams at Elevated Temperature

IOLANDA DEL PRETE[1], ANTONIO BILOTTA[2],
DANIELE DI FIORE[2] and EMIDIO NIGRO[2]

ABSTRACT

This paper presents the thermal and the mechanical analyses, simulating the experimental tests conducted in the recent past on reinforced concrete beams strengthened with the Near Surface Mounted (NSM) FRP system. The thermal analyses were conducted through the software ABAQUS, whereas the mechanical analyses were carried out through the iterative-incremental procedure Moment-Curvature.

The aim of these analyses is, firstly, assess the ability of simulating the experimental results of non-standard fire tests (local and global heating using propane-fired radiant panels) and, then, generalise the experimental results providing a standard time of fire exposure that might lead to the un-effectiveness of the strengthening system due to debonding failure.

The results of the numerical analyses (2D) cross-sectional finite element model (FEM) and 3D FEM were compared with the temperature recorded by the thermocouples during the tests, in order to assess the reliability of the FEM simulating the experimental results. The results of the 3D FEM model enabled also the evaluation of the heat transfer from the exposed to the unexposed zone and, therefore, to assess the length of the effective cold end-anchorage.

Finally, thermal analyses of a 3D FEM of the NSM FRP strengthened RC beam, subjected to the standard ISO834 curve, were conducted in order to define useful fire safety design criteria for this investigated structural typology. The effect of the passive protection of the end-anchorage was also investigated, analyzing the structural element protected at both ends through a fire rated plasterboard with thickness ranging between ten and thirty millimeters.

INTRODUCTION

According to European codes, the fire resistance assessment of a structural member may be performed through experimental tests or applying analytical approaches. In both cases, conventional temperature-time laws of the environment are usually assumed. For instance, for fires characterized mainly by the burning of cellulosic substances, the ISO834 standard curve is suggested by EN1991-1-2. Standard fire tests have many inadequacies, such as the absence of a cooling phase.

[1] BuroHappold Engineering, 17 Newman Street W1T 1PD, London - UK
[2] Department of Structures for Engineering and Architecture, University of Naples, via Claudio 21 80125, Naples - Italy

Localized heating may occur in a real structure due to a single bay fire in a continuous multi-bay structure, a travelling fire, a localized ceiling jet fire [3]. The radiant panels are very useful to simulate localised fire event, but they are also able to simulate global heating configurations, if an arrow of radiant panels is used. Currently, few researchers conducted high temperature tests in non-standard localised [1],[3],[4] and global heating configurations [1],[5]. The results of non-standard experimental tests cannot be used to define a standard time of fire resistance of the structural members, since the heating history can be significantly different to that provided by standard fire curve in terms of temperature growth rate, maximum temperature, duration of the heating stage.

This paper presents the numerical thermal and the mechanical analyses, simulating the experimental tests conducted in the recent past, using propane-fired radiant panels, both in local (LocH) and global heating (GloH) configuration, on reinforced concrete beams strengthened with near surface mounted NSM FRP system ([1]).

With the NSM FRP strengthening technique, the FRP bar/rod/strip is placed in a groove cut into the concrete cover and bonded in place by filling the groove with an epoxy (or, less commonly, cementitious) adhesive. In NSM applications, using an elevated T_g FRP product bonded with a cementitious grout may result in superior mechanical performance in fire, since cementitious adhesives may perform better than epoxies, whilst also protecting (both mechanically and thermally) the FRP, possibly without the need to apply costly and unattractive supplemental insulation materials to the exterior of the FRP strengthening system [6].

The aim of the conducted analyses is, firstly, assess the ability of simulating the experimental results of non-standard fire tests and, then, generalise the experimental results providing a standard time of fire exposure that might lead to the un-effectiveness of the strengthening system due to debonding failure.

NUMERICAL MODEL

Numerical thermal and mechanical analyses were performed through the software Simulia Abaqus on reinforced concrete beams strengthened with NSM FRP system (see Figure 1 and Figure 2), in order to simulate the experimental non-standard fire tests conducted by using propane-fired radiant panels, both in local and global heating configuration (Figure 3 and Figure 4).

Geometry and material properties

The modelled beam was a NSM FRP strengthened RC beam, 1450 mm long (Figure 1) and 150 mm square in cross-section (Figure 2). The beam had internal flexural reinforcement in the form of two deformed steel reinforcing bars (nominal diameter of 10 mm) on the tension side and two deformed steel reinforcing bars (nominal diameter of 6 mm) in compression. The FRP strengthening system consisted of a single CFRP bar (nominal diameter of 8 mm), grouted in a cementitious mortar within a groove, 16 mm square in cross-section. The shear reinforcement in the beam was made of steel stirrups (with a nominal diameter 6 mm), spaced at 90 mm on centre. The thermal and mechanical properties of steel and concrete were defined according to EN 1993-1-2 and EN1992-1-2, respectively. The properties of CFRP and cementitious grout (see Figure 5) were experimentally defined as shown in [12].

For the thermal analysis, the emissivity (ε) was set equal to 0.7, the coefficient of convection on the exposed surface (α_c) equal to 25 W/m^{2}K and the coefficient of convection on the un-exposed surface equal to 4 W/m^{2}K.

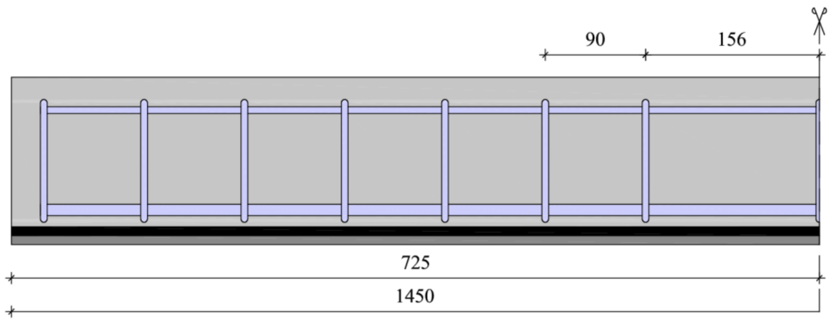

Figure 1. Longitudinal section.

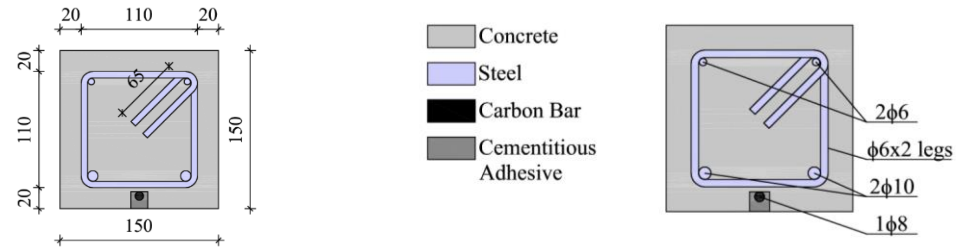

Figure 2. Cross section.

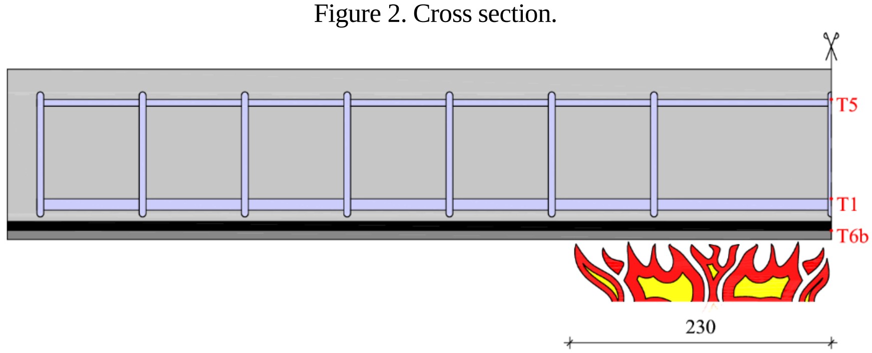

Figure 3. Local Heating configuration (LocH).

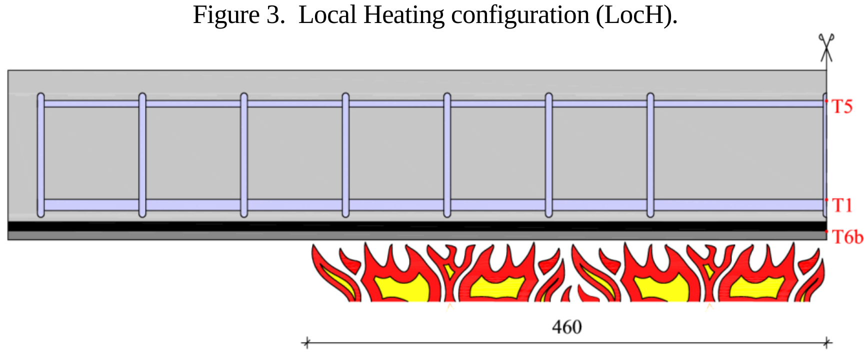

Figure 4. Global Heating configuration (GloH).

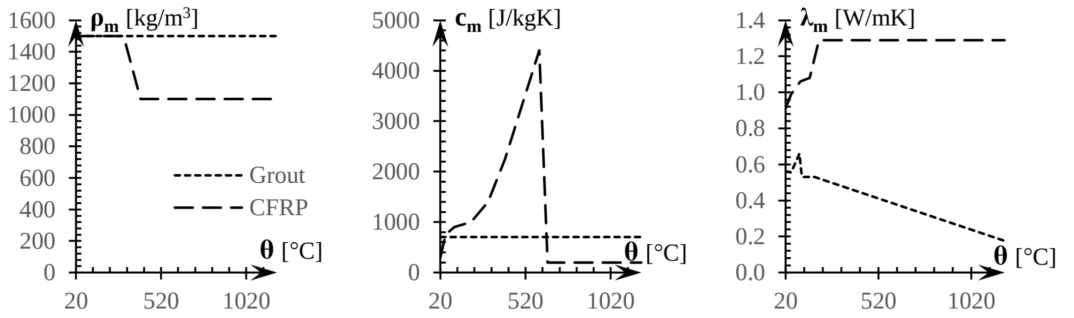

a) Density
b) Specific Heat
c) Conductivity

Figure 5. CFRP and cementitious grout properties.

Validation of the thermal model

The results of the numerical analyses on the 2D cross-sectional finite element model (FEM) were compared firstly with the temperature recorded by the thermocouples during the tests, in order to assess the reliability of the FEM simulating the experimental results. The modelled beam was accurately discretized in order to have the nodes, where the temperature should have been monitored, in the same position of the thermocouples in the real tested beams. Figure 6 shows the monitored nodes in the cross-sectional FEM, which was analysed by imposing to the bottom of the beam, the temperature recorded by the thermocouple at the beam's soffit during the experimental tests in case of local heating configuration (LocH – Figure 3). Figure 7 shows that a fairly good agreement was obtained between experimental and numerical results, therefore the FEM was deemed reliable and the same properties of this model were used in a 3D FEM model, as described in the following section.

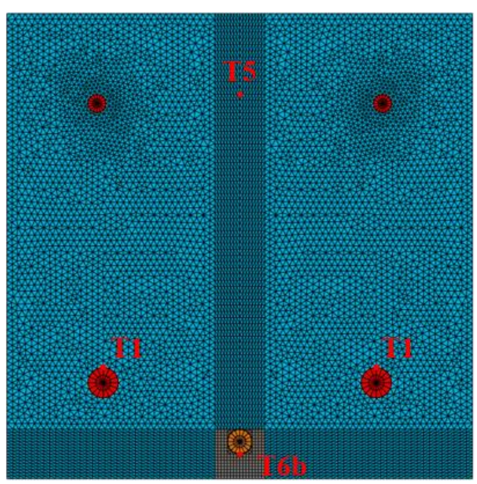

Figure 6. 2D FEM of NSM FRP strengthened RC beam: location of the monitored nodes.

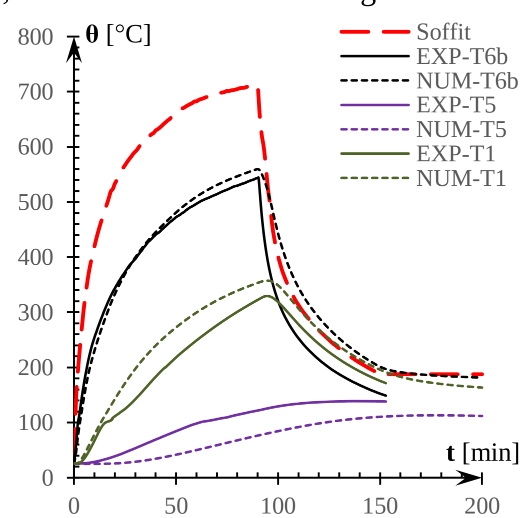

Figure 7. Numerical vs experimental results.

Thermal analyses with the 3D model

The analysis of the 3D FEM model enabled the evaluation of the heat transfer from the exposed to the unexposed zone both in LocH and GloH configuration (Figure 4 and Figure 5), in order to assess the length of the effective cold end-anchorage.

Figure 8 and Figure 9 show the temperature in the CFRP bar along the bonded length of the bar in case of LocH and GloH configuration, respectively.

Figure 8 shows that the effective end anchorage was slightly more than 400 mm in case of LocH, since the glass transition temperature of the bar ($T_{g,\max(\tan\delta)}$=220°C, according to [7]) was not attained along this length, whereas Figure 9 shows that the effective cold end-anchorage was only 200 mm in case of GloH. Moreover, these figures show that the T_g was attained in the exposed zone after about 10 minutes. However, the experimental tests demonstrated that the attainment of this temperature is not critical under loads that give typical (i.e. maximum permissible) FRP service loading strain conditions, when the bar is adequately anchored in cool regions with an anchorage length of at least 300 mm [7] .

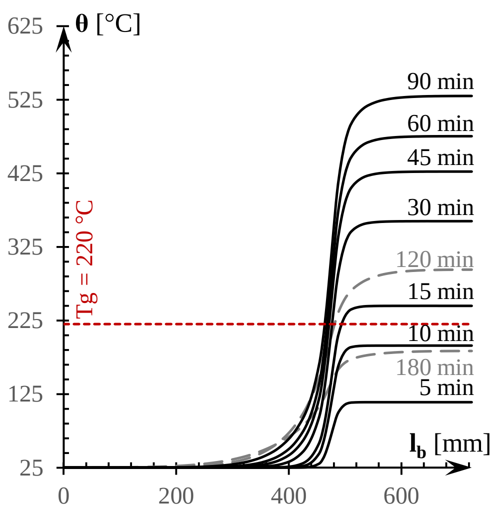

Figure 8. CFRP temperature along the bonded length (LocH).

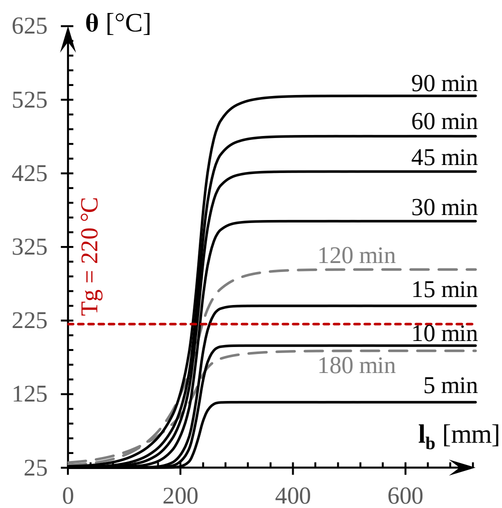

Figure 9. CFRP temperature along the bonded length (GloH).

Simplified mechanical analysis

Assuming that the cold end-anchorage length was sufficient to sustain the mechanical stress transferred by the debonded zone in case of fire, a simplified mechanical analysis was preliminarily conducted through the iterative-incremental procedure Moment-Curvature, shown in [2]. The degradation of the mechanical properties of the CFRP with temperature was modelled according to [9].

Figure 10 shows the bending moment resistance plotted versus the time of fire exposure, showing that the load bearing capacity can be higher than ordinary bearing demand even the contribution provided by the CFRP is expected very low. Indeed, after 90 min of fire exposure the temperature in the CFRP bars was about 550°C (see Figure 9), therefore its strength is lower than its strength at ambient temperature. The simplified model could be used to predict the flexural capacity of simply supported full scale beams in fire, such as bridges, which are often strengthened with FRP systems.

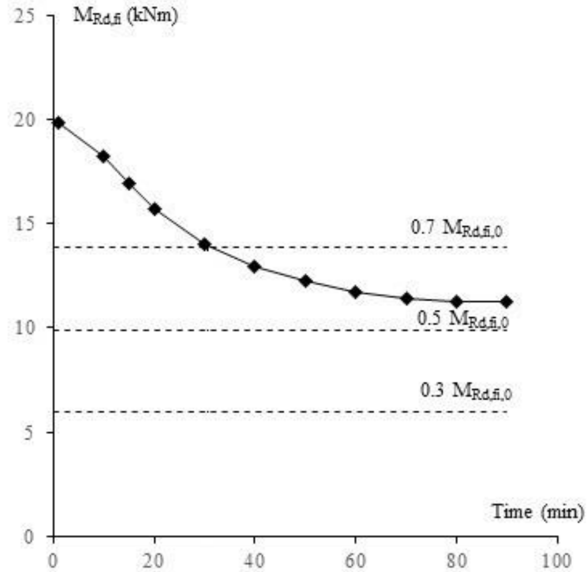

Figure 10. Bending moment resistance versus time of fire exposure (LocH).

THERMAL ANALYSIS OF A FULL-SCALE BEAM

The following section summarizes the results of a thermo-mechanical analysis conducted on a full-scale 300 mm x 500 mm NSM FRP strengthened RC beam, 4200 mm long, aimed to find out useful fire safety design criteria for this investigated structural typology. The beam had internal flexural reinforcement in the form of two deformed steel reinforcing bars (nominal diameter of 20 mm) on the tension side and two deformed steel reinforcing bars (nominal diameter of 16 mm) in compression. The FRP strengthening system consisted of two CFRP bars (nominal diameter of 8 mm), grouted in a cementitious mortar within a groove, 16 mm square in cross-section.

The beam was analyzed in case of three-side standard fire exposure (Figure 11), considering the beam both un-protected and protected with plasterboard, which thickness ranged between 10 and 30 mm. It is noteworthy that the density of the plasterboard (ρ) was assumed equal to 300 kg/m^3, the specific heat (c) equal to 800 J/kgK and thermal conductivity (λ) ranging between 0.15 and 0.20 W/mK, depending on the temperature [8].

In case of un-protected beam, the temperature in the FRP attained the $T_{g,\max(\tan\delta)}$ after about 9 minutes of standard fire exposure (Figure 12). The time up to the attainment of the T_g increased significantly when the beam was protected with a plasterboard: 51 minutes with 10 mm thick plasterboard; 74 minutes with 20 mm thick plasterboard, 87 minutes with 30 mm thick plasterboard (Figure 12).

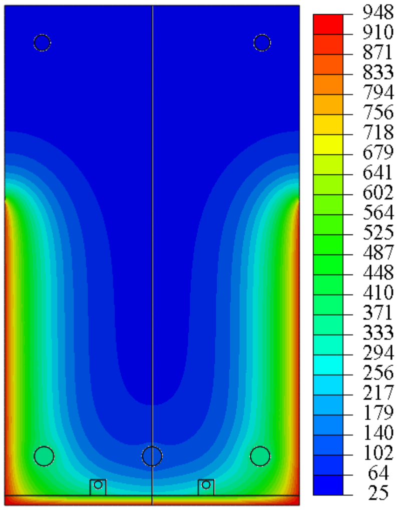

Figure 11. Thermal field in the cross-section (beam protected with 10 mm plasterboard) after 60 min of standard fire exposure.

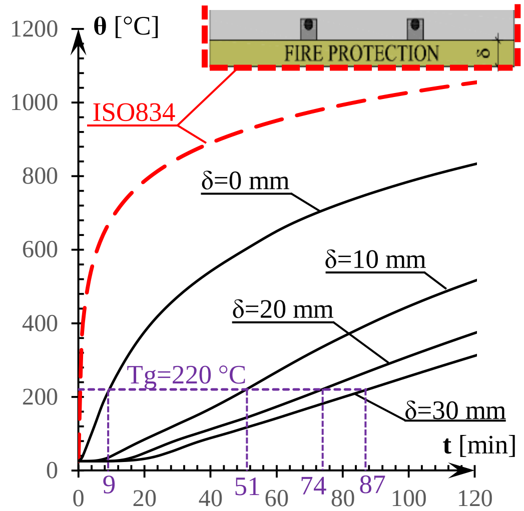

Figure 12. CFRP temperature vs time.

However, the application of supplemental insulation materials to the exterior of the FRP strengthening system along the overall bonded length is unattractive and costly, whereas the provision of a certain cold end-anchorage, guaranteed by a local insulation system at the ends only, is deemed a cost effective solution.

Therefore 3d analysis were performed to evaluate the heat transfer from the exposed to the unexposed zone and, therefore, to assess the length of the effective cold end-anchorage (Figure 13).

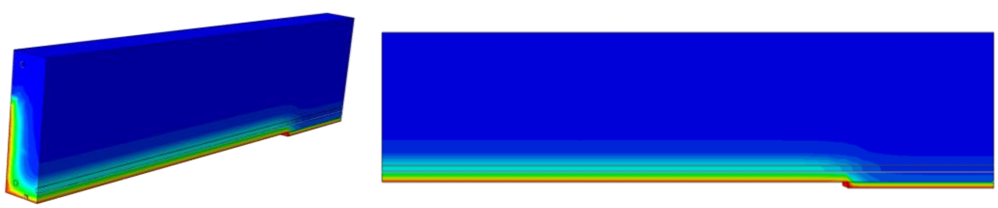

Figure 13. Temperatures in the 3d model.

Figure 14 and Figure 15 show that using a 20 mm thick plasterboard with $\boldsymbol{l_p}$ equal to 300 mm and 500mm, the effective end-anchorage ($l_{b,eff} \approx 200\ mm$) and ($l_{b,eff} \approx 400\ mm$) are retained for 74 minutes in case of standard fire exposure. Therefore the effective anchorage length ($l_{b,eff}$) is equal to the length of the protection system $l_p - (\approx 100\ mm)$. A similar criterion (a constant reduction in length) was obtained for FRP bar reinforcements in [10].

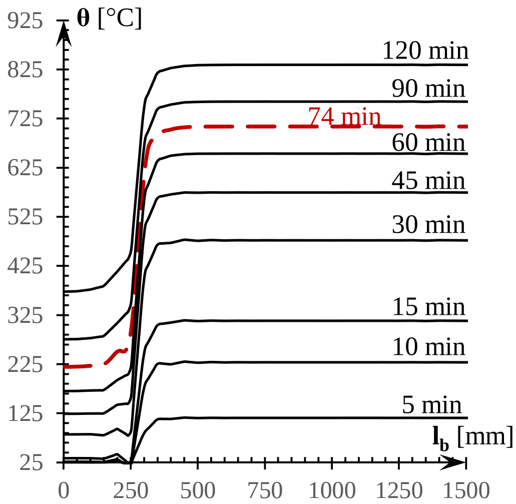

Figure 14. Temperature along the bonded length of the CFRP bar (l_p = 300 mm).

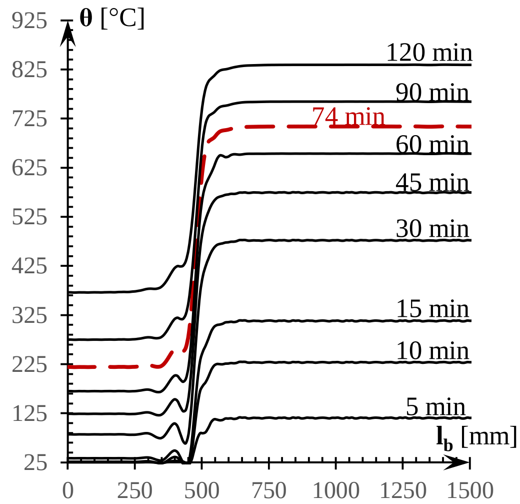

Figure 15. Temperature along the bonded length of the CFRP bar (l_p = 500 mm).

CONCLUSIONS

The analysis shown in this paper demonstrated the ability of the numerical model to simulate with a fairly good agreement the temperature recorded in non-standard fire tests conducted on NSM FRP strengthened RC beams both in local and global heating configuration.

The 3D model of the beam enabled to evaluate the heat transfer from the exposed to the unexposed zone of the beam and to assess the minimum length of the effective cold end-anchorage of the strengthening system, needed to sustain the stress transferred from the exposed debonded zone of the strengthening. This is very useful to avoid the application of supplemental insulation materials to the exterior of the FRP strengthening system along the overall bonded length that is unattractive and costly, whereas the provision of a certain cold end-anchorage, guaranteed by a local insulation system at the ends only, is deemed a cost effective solution.

A preliminary mechanical analysis, conducted assuming that the cold end-anchorage length was sufficient to sustain the mechanical stress transferred by the debonded zone in case of fire, was also shown in this paper. This showed the reduction of the strengthening performance with the increasing temperature. The development of a refined model, taking into account the bond behavior of the bar in the groove, is still in progress and will be shown presented in the future as further development of this work.

REFERENCES

[1] Del Prete I., Bilotta A., Bisby L., Nigro E., (2015a). "*Flexural tests on RC beams strengthened with NSM FRP bars bonded with cementitious grout*". The 12th FRPRCS-12 & The 5th APFIS-2015, 14-16 December 2015, Nanjing, China.

[2] Del Prete I., Bilotta A., Nigro E., (2015b). "*Performances at high temperature of RC bridge decks strengthened with EBR-FRP*". Composites: Part B 68 (2015) 27-37.

[3] Gales J., Bisby L., Gillie M., (2011). "*Unbonded Post Tensioned Concrete Slabs in Fire - Part I: Experimental Response of Unbonded Tendons under Transient Localized Heating*", Journal of Structural Fire Engineering. 2(3):139153.

[4] Carvelli V., Pisani M. A., Poggi C., (2013). "*High temperature effects on concrete members reinforced with GFRP rebars*", Composites: Part B4 (2013) 125–132, http://dx.doi.org/10.1016/j.compositesb.2013.05.013.

[5] Smith H. K.M., Stratford T. J., Bisby L. A:, (2014). "*Punching shear of restrained reinforced concrete slabs under fire conditions*", 8th International Conference on Structures in Fire (SIF), 443-450, Edited by Li G.Q., Kodur V. K. R., Jiang S.C., Jiang J., Chen S.W., Lou G.B., Shanghai, China, June 11-13, 2014.

[6] Yu B., Kodur V., (2014). Fire behavior of concrete T-beams strengthened with near-surface mounted FRP reinforcement. Engineering Structures. 2014;80:350-361.

[7] Del Prete I., Bilotta A., Bisby L., Nigro E., (2015c). NSM FRP strengthened reinforced concrete beams: Benefits in fire of high Tg FRP & cementitious adhesive. Applications of Structural Fire Engineering, 15-16 October 2015, Dubrovnik, Croatia, 331-336.

[8] Hopkin, D.J. (2011). The Fire performance of engineered timber products and systems. EngD Thesis.

[9] Bisby L., Green M. and Venkatesh K.. Response to fire of concrete structures that incorporate FRP. Progress in Structural Engineering and Materials, 136-149.

[10] Nigro E., Cefarelli G., Bilotta A., Manfredi G., Cosenza E. (2012). Performance under fire situations of concrete members reinforced with FRP rods: bond models and design nomograms. Journal of Composites for Construction, vol. 16, p. 395-406.

[11] Chung D.D.L., (2001). "Cement-matrix composites for thermal engineering", Applied Thermal Engineering 21 (2001) 1607-1619.

[12] I. Del Prete (2015). "NSM FRP Strengthening RC beams using high Tg FRPs & cementitious adhesives – Response at ambient and elevated temperature" PhD Thesis.

Fire Testing of Insulated RC Beams Strengthened with Near Surface Mounted FRP Reinforcement

ALESSANDRO PROIA, STIJN MATTHYS, LUC TAERWE
and ANIELLO PALMIERI

ABSTRACT

Seventeen NSM FRP (Near Surface Mounted Fibre Reinforced Polymer) strengthened and insulated full-scale beams, and two unstrengthened and unprotected beams, were subjected to fire tests. Insulation material type and dimensions and the insulation configuration were examined in order to develop practical methods for protecting FRP during fire exposure. Structural testing up to failure at room temperature of the fire tested beams has been carried out in order to evaluate their residual strength after one and two hours of fire exposure. The test program included the design and fabrication of steel reinforced concrete beams with rectangular cross-section. The experimental data demonstrated that all the insulated beams obtained the fire endurance ratings of 2h and 1h by satisfying both thermal and load bearing criteria. The paper will discuss the obtained test results.

INTRODUCTION

In recent decades, FRPs are widely employed as strengthening systems among which Near Surface Mounted (NSM) reinforcement. In NSM systems, bars or strips are embedded in the concrete cover by means of epoxy. Although, this type of adhesive, shows good performance at room temperature, its mechanical properties decrease at elevated temperatures beyond the glass transition temperature. Application of epoxy for polymer bonded systems needs special attention because of external exposure conditions such as fire [1-3]. In this work, seventeen insulated concrete beams strengthened with NSM have been investigated to evaluate their fire endurance. The experimental campaign has involved different types of FRP strengthening (bars and strips), adhesives (epoxy resin and grout) and insulating materials. In order to study the behavior of the insulations under fire exposure, they have been applied to the concrete beams on the basis of several configurations (see Table 2).

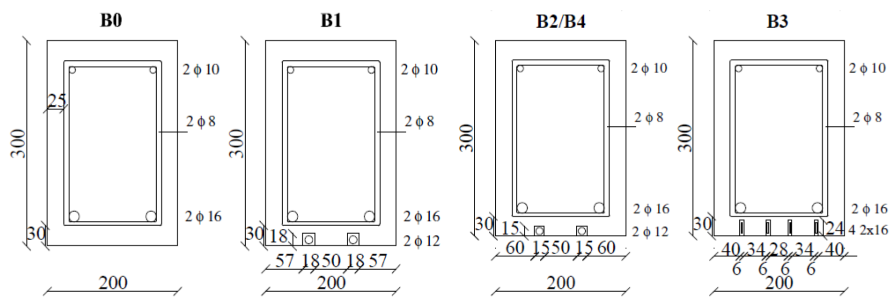

Figure 1. Reference (B0) and NSM strengthened (B1-4) sections.

Table 1. Beam properties and service loads.

Beam	FRP		Adhesive			Concrete	$Q_{serv.}$	Q_{serv}/Q_u
	Type	Dim. mm	Type	f_a MPa	T_g °C	$f_{c,cub}$ MPa	kN	(%)
B0	-	-	-	-	-	48.6	30.5	54
B1	GFRP	12	Sikadur 30	27.0*	62**	48.6	36.0	37
B2	CFRP	9.5	Fortresin CFL	26.5*	65**	51.6	40.5	40
B2	CFRP	9.5	High T_g	30*	82*	51.6	40.5	40
B3	CFRP	2x12	Fortresin CFL	26.5*	65**	51.6	40.5	40
B4	CFRP	9.5	Sikagrout	4.1*	-	44.3	40.5	40

f_a : tensile strength adhesive, $f_{c,cub}$: compressive strength of concrete cubes
$Q_{serv.}$: service load, Q_u: experimental ultimate load at ambient condition
*: provided by manufacturers, **: evaluated by differential scanning calorimetry

SPECIMENS AND MATERIAL PROPERTIES

The fire testing program involved the design and fabrication of 19 steel reinforced concrete beams with rectangular cross-section, two of which were the reference specimens and the others were insulated and strengthened in flexure with three different NSM FRP systems (see Figure 1).

The FRP reinforcement of the NSM FRP strengthened beams consisted of: CFRP sand-coated rods and smooth strips (type Aslan 200 and Aslan 500) with a nominal diameter of 9.53 mm and dimensions of 2mm x16mm respectively and GFRP rods (type Combar) with a nominal diameter of 12 mm. Four different types of adhesive, with different T_g values, were tested as reported in Table 1.

INSULATION

Five fire insulation systems were investigated (Table 2): a glass-fiber cement fire protection board (type Aestuver), two types of calcium silicate protection board (type Promatect- H and Promatect L-500), a two component system under development (type WR-APP C) and one insulation system composed of two ceramic based coatings (type Hot Pipe Coating and Omega Fire). The fire insulation systems were applied to the beams over a length of 2900 mm. In Table 3 the thermal properties of the different fire protection systems are reported as provided by manufacturers.

Table 2. Insulation configurations.

Promatect H

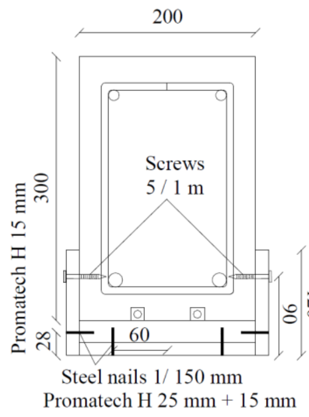

Aestuver

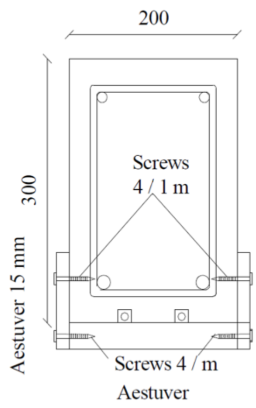

Aestuver 1

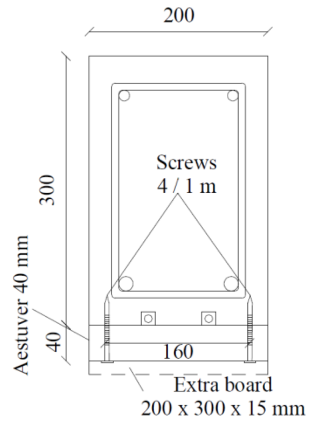

Promatec L 500

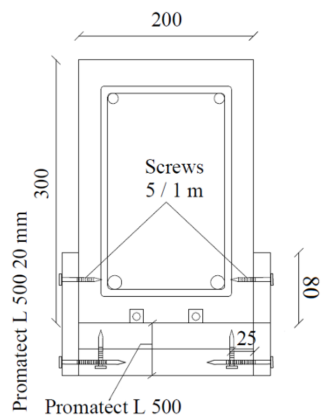

HPC/Omega Fire 1

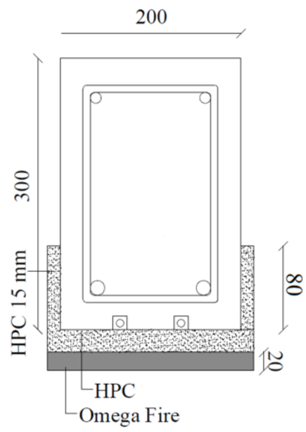

WR-APP

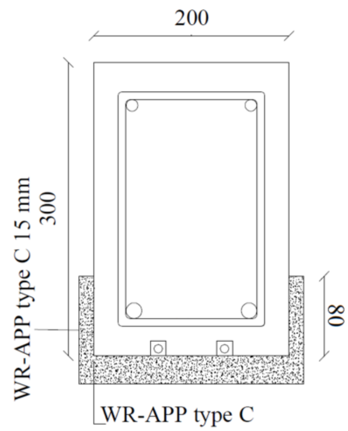

HPC/Omega Fire

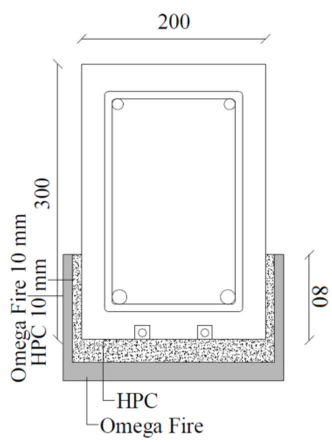

Table 3. Thermal properties of the insulation materials.

Insulation	Density [Kg/m^3]	Thermal Conductivity [W/mK]
Aestuver	680	0.22
Promatect H	870	0.19
Promatect L-500	500	0.08
WR-APP type C	269	0.12
Hot Pipe Coating	599	0.06
Omega Fire	1138	0.25

TEST SETUP AND INSTRUMENTATION

The fire test program consisted of four series with different exposure times. A maximum of 2 h fire exposure was chosen for fire test series 1, 2 and 4 while a maximum of 1 h of fire exposure was chosen for fire test series 3. No axial restraints were provided during the fire tests. The beams were exposed to fire from three sides (bottom of the beams and lateral sides over a height equal to 150 mm) and the top surface was exposed to ambient temperature. Before starting the fire test all the test specimens were loaded, in 4 point bending, to their service load (see Figure 2). The load was applied approximately 30 min prior to the start of the fire. The load were kept constant during the fire test. The furnace temperature was controlled to follow the standard time-temperature curve according to ISO 834 [4]. Twenty thermocouples, type K, were placed inside the concrete at two different cross-sections of the member to measure the temperature distributions (each at a distance equal to 375 mm from the middle of the specimen). In addition a displacement transducer (LVDT) was connected to the unexposed surface of each specimen to measure the deflection at mid-span in the pre-load phase and during fire testing. During the fire tests, also visual observations were made through view ports in the furnace to record the progression of possible cracks or/and localized burning in the insulation as well as possible delamination of the insulation or/and FRP reinforcement system.

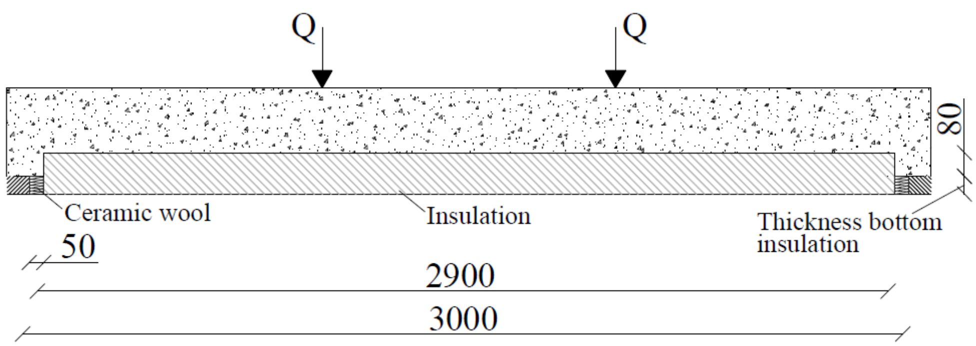

Figure 2. Test set-up.

RESULTS: THERMAL PERFORMANCE

First series

After 2h of fire exposure the lower protection board of B1-F1-1 was still intact (no signs of damage to the adhesive). The insulation of B2-F1-1 partially detached at 70 min and the epoxy adhesive was partially burned off. The insulation of B2-F1-2 and B3-F1-1 completely detached at 34 and 105 min respectively. At 34 and 105 min the temperature at the FRP/epoxy interface increased significantly and the loss in the adhesive strength led to higher deflections (see Figure 3).

Table 3. Performance of fire insulation.

Specimen	Insulation configuration	Thickness		t_{deb}	T_{conc}	T_{steel}	T_{adh}	$t_{Tadh=Tg.}$
		Bottom mm	lateral mm	min	°C	°C	°C	min
B1-F1-1	Promatec H	25+15	15	90	72	310	305 (4.9)	22
B2-F1-1	Aestuver	30	15	70	88	392	631 (9.7)	20
B2-F1-2	Austever 1	40	-	34	94	570	644 (9.9)	20
B3-F1-1	Aestuver	40	15	90	77	318	546 (8.4)	22
B1-F2-1	Promatec L 500	50+50	20	>120	48	135.8	115 (1.8)	60
B1-F2-2	HPC/OmegaFire1	40/20	15/-	100	60	201	282 (4.5)	45
B1-F2-3	HPC/OmegaFire1	25/20	15/-	>120	51	163	158 (2.5)	50
B2-F2-1*	WR-APP	30	15	25	54	223	207 (3.1)	44
B2-F2-2*	WR-APP	40	15	30	53	147	137 (2.1)	58
B1-F3-1	Promatec L 500	50+50	20	>60	34.6	126.4	116 (1.8)	39
B1-F3-2	HPC/OmegaFire	25/20	10/10	>60	33.9	127.4	131 (2.1)	33
B1-F3-3	HPC/OmegaFire	35/20	10/10	>60	33.8	135.4	101 (1.6)	49
B1-F3-4	HPC/OmegaFire	20/15	10/10	>60	34.6	122	101 (1.6)	37
B2-F3-1	Promatec L 500	30+30	20	>60	39.2	135.1	111 (1.7)	38
B4-F3-1	HPC/Omega Fire	10/10	10/10	>60	45	160	163	-
B2-F4-1**	HPC/Omega Fire	25/20	10/10	50	167	630	220 (3.3)	40
B4-F4-1	HPC/Omega Fire	20/10	10/10	>120	77	310	278	-

* High T_g was used as embedding adhesive
** partially insulated, 500 mm from the free end of the FRP at both sides
t_{deb}: loss of composite action, T_{conc}: concrete temperature at the unexposed side after fire exposure
T_{steel}: bottom steel bars temperature after fire exposure, T_{adh}: adhesive temperature after fire exposure (T_{adh} and T_g ratio), $t_{Tadh=Tg.}$: time when the adhesive reached T_g

The bottom longitudinal steel bars in B1-F1-1, B2-F1-1 and B3-F1-1 experienced a steady rise in temperature for the entire test.

Second series

The fire insulation of B1-F2-1 was fully intact after the test (no signs of damage to the adhesive). For B1-F2-2 and B1-F2-3, at 20 min, the layer of Omega Fire detached from HPC. For B1-F2-2 the layer of HPC was consumed and cracked close to the FRP anchorage zone. An abrupt increase of temperature was reached at the FRP/epoxy interface at 110 min due to the partial detachment of the insulation material from the bottom surface of the beam. After the fire exposure, no signs of damage were observed to the adhesive of B1-F2-3. Despite the higher insulation thickness, the recorded longitudinal steel reinforcement temperatures of B1-F2-2 were higher than B1-F2-3. For B1-F2-1 and B1-F2-3 the mid-span deflection increased gradually for the entire test. At 20 min, for B2-F2-1 and B2-F2-2, transversal cracks on the insulation surface were observed (at that time a sudden increase in deflection was observed for both of the beams). The insulation of B2-F2-1 remained attached to the beam during the complete fire exposure but epoxy was locally burned off. For B2-F2-

2 the insulation cracked close to the FRP anchorage zone and detached locally with consequent burning off of the adhesive. For both these beams a slight higher increase of temperature at the FRP/adhesive interface was observed at the measurement sections.

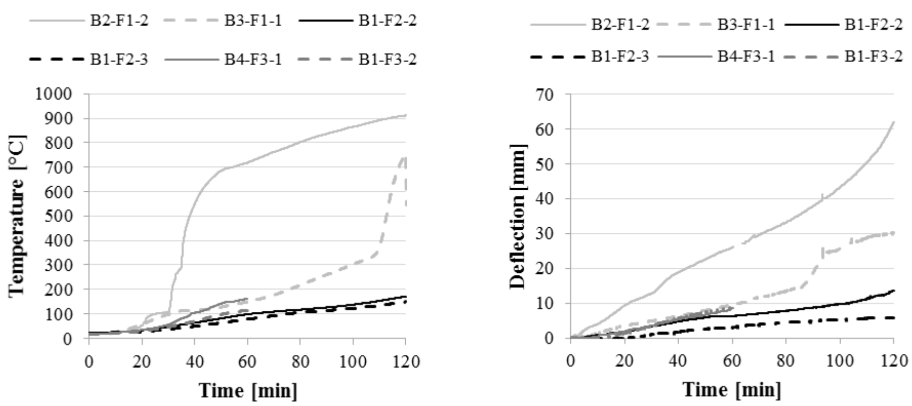

Figure 3. Temperature a FRP/adhesive interface (left) and deflections (right).

Third series

The fire insulation system of B1-F3-1 and B2-F3-1 remained intact and no signs of damage were observed to the adhesive. Despite the different thicknesses, both beams showed the same temperature at the steel rebars and at the FRP/adhesive interface. During the tests on B1-F3-2, B1-F3-3 and B1-F3-4 several cracks were observed on the outer layer Omega Fire at 18min fire exposure. At 30 min the two lateral Omega Fire layers started to detach and at 50 min the Omega Fire detached from the HPC layer at the bottom of the beam. HPC performed well for all the durations of fire exposure. For these beams the thermal performance of the insulation depended heavily on its overall thickness. A different behaviour was observed for B4-F3-1, for which no cracks were observed during the fire test. Despite its lower thickness of insulation the increase of temperature was lower than that of B1-F3-2. After the fire exposure, for all of the beams insulated with Omega Fire and HPC, no signs of damage were observed to the adhesive. No significant changes, in terms of sudden increases of deflection or rate of deflection in the time deflection curves, were observed for all tested beams.

Fourth series

For B2-F4-1 (insulated only at the FRP anchorage zones) the fast increase of temperature in the unprotected area led to a fast increase of temperature into the longitudinal steel with consequently failure of the beam under the applied load. The beam fell into the oven at 118 min. The longitudinal steel reinforcement displayed higher temperatures than the reference B0-F1 due to the smaller concrete cover close to the grooves. The mid-span deflection increased gradually until 50 min because the insulation at the anchorage zone contributed to control the rise of temperature at the FRP/adhesive interface along the protected anchorage zone. Beyond 50 min the deflection increased due to the loss of FRP action. At 15 min several cracks were observed on the outer layer of the Omega Fire of beam B4-F4-1. At 64 min the Omega

Fire was consumed in portion due to the flaming of the product. After the fire exposure Omega Fire was completely consumed but the HPC remained intact (no signs of damage into the adhesive). The bottom steel reinforcement experienced a steady rise in temperature for the entire test duration.

RESIDUAL STRENGTH

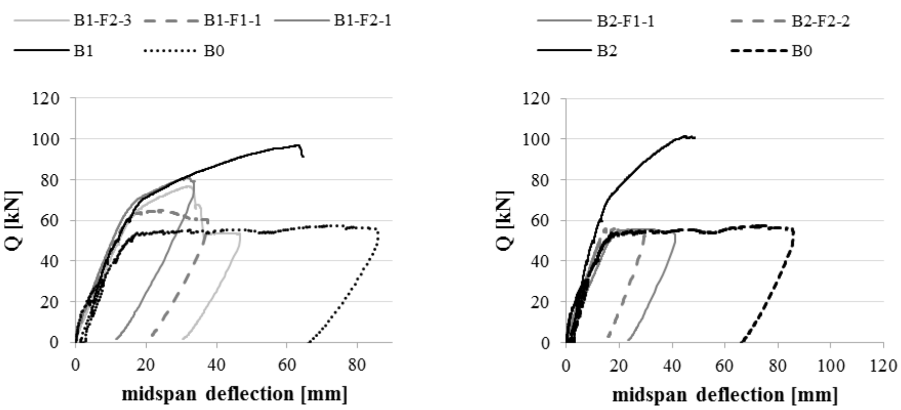

Figure 4. Residual strength: beams B1 (left) and beams B2 (right).

Another potentially important aspect of fire performance of FRP strengthened concrete structures is their residual behaviour after fire exposure. The post-fire residual behaviour of RC members depends on the internal temperatures attained during fire exposure fire, the load experienced by the members in fire, the cooling method (ambient air cooled method for this test program) and the strength recovering time following the cooling period. The experimental load-mid-span deflection curve of B1-F1-1 is initially in close agreement with that of the strengthened B1 until the reinforcement started yielding (see Figure 4). The observed stiffness and yield load was higher than that of the unstrengthened B0 tested in ambient conditions. After yielding of the steel no more contribution of the FRP was observed and failure was due to steel yielding followed by concrete crushing. This behaviour can be explained considering that after 2 h of fire exposure the insulation board was effectively able to maintain relatively low temperatures in the compressive concrete zone and the longitudinal steel reinforcement but the recorded temperature of the adhesive (T_{adh}= 305 °C) was well beyond its T_g value (62°C). The experimental load-mid-span deflection curves of B2-F1-1 and B3-F1-1, in which the fire protection detached at 70 min and 90 min respectively, clearly showed no residual strength of the adhesive after 2 h of fire exposure. Indeed the load-mid-span deflection curves perfectly match the unstrengthened B0. The experimental load-mid-span deflection curves of B1-F2-1 and B1-F2-3 were in close agreement with that of the FRP strengthened B1 tested at ambient conditions until they start failing under the applied loads. The two insulation systems were able to keep, during the fire exposure, the adhesive at relatively low temperature (T_{adh}= 115 °C and T_{adh}= 159 °C respectively for B1-F2-1 and B1-F2-3) so that they retained a significant part of their original strength at room temperature. Despite the higher value of the adhesive temperature

(T_{adh}=1.86T_g and T_{adh}=2.56T_g, respectively for B2-F2-1 and B1-F2-3) with respect to its T_g value (62 °C), the adhesive was still able to transfer stresses from the FRP to the concrete surface. In the same way the experimental load-mid-span deflection curves of B2-F2-1 and B2-F2-2 clearly showed no residual strength of the adhesive after 2 h of fire exposure. Indeed, whereas relatively low temperature increases of the adhesive were recorded (at the two measurement sections), respectively T_{adh}= 207 °C and T_{adh}= 138 °C for B2-F2-1 and B2-F2-2, the tendency of the insulation layer to crack during fire exposure allowed rapid heat ingress at localized areas (close to the FRP anchorage zone) resulting in local burning of the epoxy adhesive.

CONCLUSIONS

Seventeen full scale beams insulated and strengthened with FRP NSM have been exposed to fire action in order to investigate their fire endurance. The following five observations can be drawn.

Temperature at the FRP/adhesive interface represents an important indicator of the fire performance of the FRP-strengthened RC element beams because the adhesive shows a faster strength degradation than steel reinforcement.

Test results reveal that beams can achieve 2 h of fire endurance even after the adhesive temperature exceeds excessively the T_g. Residual flexural strength tests have demonstrated that in some cases the FRP seems to be able to retain bond strength to the concrete for the beams where the adhesive temperature remained less than 2.5 T_g (B1-F2-3, B1-F2-1, B1-F3-X).

The third test series showed the feasibility of providing 1 h fire endurance under service load of the strengthened beams without loss of bond integrity of the FRP, if adequate fire protection is provided.

Residual flexural strength tests show no residual strength of the adhesive in those beams exposed to high temperature at the FRP/adhesive interface along the FRP anchorage zone (even if low temperature increases of the adhesive were recorded at the two monitored sections).

Some beams insulated with the HPC/OmegaFire system did not show a direct correlation between insulation thickness and level of fire protection (B1-F2-2 and B1-F2-3, B1-F3-2 and B1-F3-3).

REFERENCES

1. A. Palmieri. 2012-2013. “Evaluation and Optimization of the Fire Safety of Concrete Elements Strengthened with NSM Reinforcement”, PhD dissertation. Ghent University.
2. A. Palmieri, S. Matthys and L. Taerwe. 2012. “Experimental investigation on fire endurance of insulated concrete beams strengthened with near surface mounted FRP bar reinforcement”. Composites Part B-engineering. 43(3):885-895.
3. A. Palmieri, S. Matthys and L. Taerwe. 2013. “Fire endurance and residual strength of insulated concrete beams strengthened with near surface mounted reinforcement”, 2013. Journal of composites for constructions. 17(4):454-462.
4. ISO 834. 1999. “Fire Resistance Tests – Elements of Buildings Construction –Part I – General Requirements”. International Organization for Standardization.
5. H. Blontrock. 2003. “Analyse en modellering van de brandweerstand van betonelementen uitwendig versterkt met opgelijmde composietlaminaten”, PhD dissertation. Ghent University.

CONCRETE STRUCTURES: MATERIAL BEHAVIOR

Thermal Boundary Conditions When Fire Testing Concrete

CRISTIAN MALUK, ANGUS LAW and JOSE LUIS TORERO

ABSTRACT

Experimental studies of concrete in fire or at elevated temperature have traditionally controlled the thermal boundary condition by controlling the gas temperature in a furnace. Relatively little attention has been given to quantifying the energy delivered to the sample; consequently, the true test severity (in terms of energy imparted to the test specimen and therefore temperature gradient of the structure) remains uncontrolled between different furnaces and different experimental samples. This has implications for test repeatability and consistency between testing facilities. This paper examines the fundamentals of heat transfer when controlling the time-history of temperature inside a furnace (or oven), versus controlling the time-history of incident radiant heat flux at a specimen's exposed surface. It is shown that the definition of the thermal boundary conditions has significant implications for structural behaviour.

INTRODUCTION

Structural fire testing requires one fundamental process above all others: heat transfer. Regardless of the test setup employed when fire testing concrete, energy transferred from the source of heat (e.g. oven, furnace, open flame, radiant burner) to the target exposed surfaces of a specimen is expressed in terms of energy (e.g. joules) per unit time (e.g. seconds) – power (e.g. watts). This is termed the net heat flux, $\dot{q}''_{net}$ and is expressed as follows [1]:

$$\dot{q}''_{net} = -k_s \left.\frac{\partial T}{\partial x}\right|_{x=0} \tag{1}$$

Where k_s is the thermal conductivity of the solid, and $\left.\frac{\partial T}{\partial x}\right|_{x=0}$ represents the in-depth time dependent temperature distribution at the exposed surface. If the thermal exposure is defined by a time-history of temperature inside an oven or furnace, simplified calculations can be used to correlate the gas temperature (T_f) with the net heat flux at the exposed surface of structure by considering heat transfer by radiation and convection, thus:

$$h_c\left(T_f - T_s\right) + F_{f,s}\varepsilon_f\sigma T_f^4 - \alpha_s\sigma T_s^4 = \dot{q}''_{net} \tag{2}$$

Where T_s is the exposed surface temperature of the test specimen. The absorptivity at the exposed surface and the emissivity of the gases inside the compartment are given by α_s and ε_g, respectively. The Stefan-Boltzmann constant, σ, and an average convective heat transfer coefficient, h_c, are used to describe heat transferred towards the exposed surface of the structural element by radiation and convection, respectively.

It is noteworthy that the formulation presented in Equation 2 assumes that the convection and radiation modes of heat transfer at the exposed surface are functions of a single temperature (T_f). This assumption is acceptable for characterizing the boundary conditions when thermal equilibrium within a compartment (e.g. furnace); i.e. there is no radiation exchange between the gas phase and the boundaries of the compartment, and thus gas temperatures can be used to establish radiative heat fluxes. The view factor for radiation heat transfer between the gas and the exposed surface of the test specimen, $F_{f,s}$, is generally assumed as unity [1]. Under certain conditions, the absorptivity of the exposed surface and emissivity of the gases may be considered equal [1]; hence it can be considered that there is an equivalent fire emissivity (ε_f). Equation 2 may then be simplified as:

$$h_c(T_f - T_s) + \varepsilon_f \, \sigma \left(T_f^4 - T_s^4\right) = \dot{q}''_{net} \tag{3}$$

On the basis of Equations 2 or 3, the thermal boundary conditions can be described using a single time-temperature curve, along with an assumption that variations in thermal conditions at the surface of the structural element (i.e. absorptivity, emissivity, and convective heat transfer coefficient) are not significant.

THE CONTROL VARIABLE

The boundary conditions of a thermodynamic system (e.g. furnace test, a compartment fire) are governed by conservation of energy, and must (by definition) be formulated in terms of heat fluxes. This section presents a comparison of thermal boundary conditions defined by controlling the time-history of 'a temperature' inside a furnace (or oven), versus one defined by controlling the time-history of incident radiant heat flux at a specimen's exposed surface.

Control by Temperature

The transient energy inside a furnace can be expressed by equating the energy inputs and outputs. The energy input is defined by the heat of combustion at the burners in the furnace. The output is defined by the energy going into the solid boundaries of the system (i.e. furnace linings and specimen), along with the energy change in the furnace through hot gases leaving the furnace (extraction vents) and fresh (ambient) air coming into the furnace. For a thermodynamic system in which the time-history of temperature $\left(\frac{\partial T}{\partial t}\right)$ inside the control volume (i.e. inside the furnace) is the control variable (or objective function), conservation of energy can be expressed as:

$$\Delta\dot{Q} - \dot{q}''_{net,lining} \cdot A_{lining} - \dot{q}''_{net,s} \cdot A_s = V_g \rho_g C_{p,g} \frac{\partial T}{\partial t} \tag{4}$$

Where the thermal equilibrium is defined by:

- the differential between heat inflow and outflow in the furnace ($\Delta\dot{Q}$);
- the net heat flux ($\dot{q}''_{net,lining}$) and exposed surface area (A_{lining}) of furnace linings;
- the net heat flux ($\dot{q}''_{net,s}$) and exposed surface area (A_s) of the test specimen; and
- the enthalpy associated with gases inside the furnace ($V_g \rho_g C_{p,g} \frac{\partial T}{\partial t}$).

The volume inside the furnace is denoted as V_g. The density and specific heat of the gases inside the furnace are denoted by ρ_g and $C_{p,g}$, respectively. $\Delta\dot{Q}$ is thus defined as:

$$\Delta\dot{Q} = \dot{m}_F \, \Delta H_{c.F} \; - \; \dot{m}_g \, C_{p,g} \, (T - T_{IN}) \tag{5}$$

Where the first term is the increase in energy due to the combustion process at the burners in the furnace, defined by the mass flow of fuel consumed by the burners ($\dot{m}_F$) and the heat of combustion of the fuel ($\Delta H_{c,F}$). The second term is defined as the differential energy between the gases leaving the furnace at temperature T, and the gases coming into the furnace at temperature T_{IN}; where $\dot{m}_g$ and $C_{p,g}$ are the mass flow and specific heat of the gases leaving and entering the furnace, respectively. This is illustrated in Figure 1.

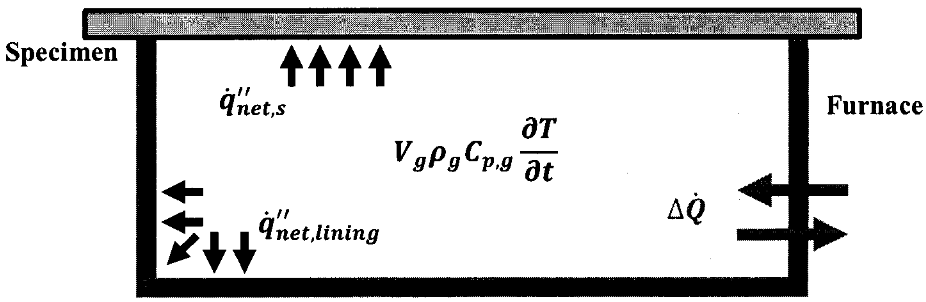

Figure 1. Simplified energy conservation schematic of thermal boundary conditions for which the time-history of temperature is the objective function.

To maintain $\frac{\partial T}{\partial t}$ by controlling a time-history of temperature inside the furnace, the furnace operates by controlling $\dot{m}_F$ (and $\dot{m}_g$ to some extent) so that $\Delta\dot{Q}$ compensates for the changes in the thermodynamic system; for example, changes in the thermal properties of the test specimen. Therefore, the magnitude of the terms that define $\Delta\dot{Q}$ cannot be generalized. In practice, heating the inside of a furnace (or oven) is usually accomplished by forcing hot gases into the furnace using gas-fired burners (or less commonly using electrical heating coils). Equations 4 and 5 assume:

- homogenous temperature inside the furnace (i.e. within the control volume);
- homogenous net heat fluxes at the exposed surfaces of the furnace linings and the specimen;
- heat losses from hot gas extraction vents inside the furnace are neglected; and

- the kinetic and potential energy associated with the transient mass transfer of the gases inside the control volume are neglected.

The thermal boundary conditions at the exposed surfaces of a test specimen thus depend on the thermal conditions on its exposed surfaces, hence on the thermal properties (i.e. thermal inertia) of the materials being tested. Thus, while furnace lining materials, dimensions, temperature gauges, and specific burner types are now reasonably standardized and regulated (e.g. [2]), the thermal boundary conditions at the exposed surfaces of test specimens are inevitably linked to the thermal properties of the test specimen itself; making the comparative usefulness of tests controlled in this manner questionable for materials with different thermal properties [3].

Likewise, adoption of the *plate thermometer* as the standard gauge for temperature control within testing furnaces [2, 4] is also governed by energy conservation inside a furnace; hence it is impossible for a specific type of temperature gauge can fully harmonize the thermal boundary conditions imposed when controlling by a temperature [5, 6].

If energy from the thermodynamic system going into the test specimen can be neglected (refer to Equation 4), the energy conservation in the furnace becomes independent of the test specimen. In a furnace this might be reasonable for materials with very small exposed surface areas (relative to the exposed surfaces of the furnace lining) and similar thermal properties to those of the furnace linings; otherwise this assumption is not valid.

Control by Incident Radiant Heat Flux

For a system in which the control variable is the time-history of incident radiant heat flux ($\dot{q}''_{inc}$) at the exposed surface of the test specimen, the local energy conservation equation can be expressed as:

$$\dot{q}''_{net,s} = \alpha_s\, \dot{q}''_{inc} - \dot{q}''_{losses} \tag{6}$$

where the net heat flux ($\dot{q}''_{net,s}$) is calculated accounting for the absorptivity (α_s) and heat flux losses ($\dot{q}''_{losses}$) at the exposed surface of the test specimen. Hence the time-history of incident radiant heat flux ($\dot{q}''_{inc}$) is an independent control variable.

The heat flux losses at the specimen's exposed surface may be calculated using a direct heat transfer model (analytical or numerical, implicit or explicit). For instance, a simplified formulation for calculating the heat flux losses at the exposed surface is:

$$\dot{q}''_{losses} = h_c(T_s - T_{amb}) + \varepsilon_s\, \sigma\, T_s^4 \tag{7}$$

where constant or temperature dependent values may be considered for the convective heat transfer coefficient (h_c) and emissivity (ε_s).

Control of fire science experiments by incident radiant heat flux is not a novel concept; indeed it has been widely implemented for more than five decades in a wide variety of fire science studies (e.g. [7]). Commercially available fire testing apparatus such as the *Cone Calorimeter* [8] or *Fire Propagation Apparatus* [9] are widely used for small-scale tests with control by incident radiant heat flux. Furthermore, numerous authors have suggested replacing a prescribed time-history of temperature when describing a fire with a time-history of incident radiant heat flux (e.g. [10]). Recent developments in fire testing have employed high performance radiant burners for controlling the incident radiant heat flux at the exposed surface of test specimens (refer to Figure 2).

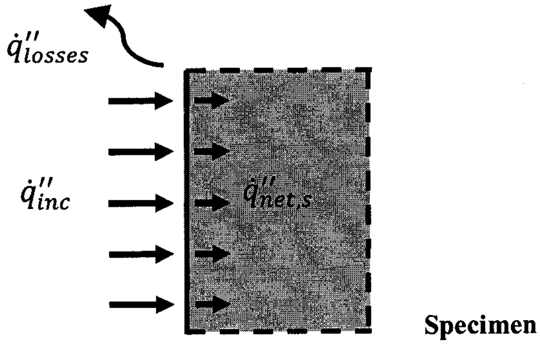

Figure 2. Simplified energy conservation schematic of a thermal exposure for which the time-history of incident radiant heat flux is the objective function.

BIOT NUMBER

Establishing the nature of temperature gradients within a solid remains vital for understanding structural response. The nature of the temperature gradients is defined by the *Biot number*:

$$Bi = \frac{h_T d}{k} \tag{8}$$

Fig. 3 provides a simple schematic showing the influence of the *Biot number* in a one dimensional heat transfer – evidencing the scope for potential simplifications of the heat transfer problem. If the *Biot number* is close to one (case (b) in Fig. 3) temperature gradients in the gas and solid phases are large and therefore Equations 6 and 7 will need to be fully resolved, hence no simplifications are possible. If the *Biot number* is much greater than one (case (c) in Fig. 3) the temperature differences in the gas phase are much smaller than those in the solid phase and it can be assumed that surface and gas temperatures are almost the same. Finally, if the *Biot number* is much smaller than one (case (a) in Fig. 3) then the temperature differences in the solid phase are much smaller than those in the gas phase, therefore temperature gradients in the solid phase can be ignored and a single temperature can be assumed for the solid.

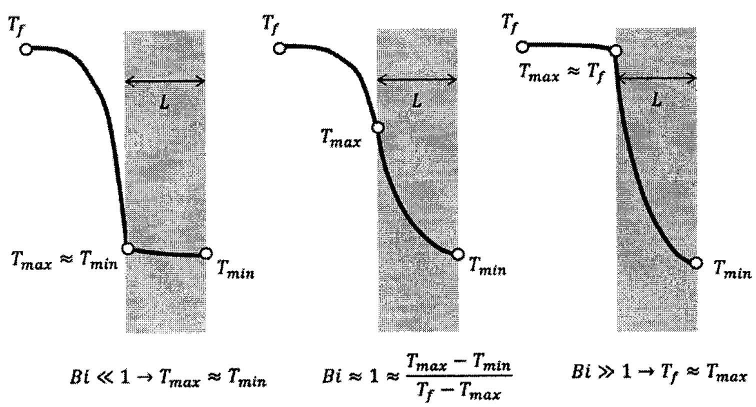

Figure 3. Influence of Biot number on the thermal gradients within a solid

The representation of a structural element by means of a single temperature is therefore only valid if $Bi <<1$. This simplification is called a "lumped capacitance solution" and while it does not resolve spatial temperatures distributions it still requires an adequate definition of the heat transfer between the source of heat (e.g. furnace or 'real' fire) and the solid. An important observation is that for materials with *Biot numbers* much smaller than one, the thermal energy is rapidly diffused through the integrity of the material, so if the density was to be high (see Eq. 6 and 7), then the lumped solid will lag significantly the gas phase temperature (Fig. 2). Heat transfer is therefore dominated by the temperature difference between the solid and the gas phase, and errors in the definition of the heat transfer coefficient become less relevant.

STRUCTURAL BEHAVIOUR

The fire response (or behavior) of the structure is defined by thermally-induced changes of the mechanical properties, and the developments of thermal expansion [11]. However, the interaction of these two parameters has a significant impact on the response of a structure. This interaction is a function of the bulk temperature increase within the material and thermal gradients. The temperatures and thermal gradients are a function of the thermal boundary conditions, thermal properties, and material thickness as examined above.

Where the temperature distribution of an unrestrained structural element is simplified to a one dimensional (through- or in-depth) heat transfer analysis, a linear thermal gradient will result in a member curvature. Where a thermal gradient is non-linear, this will result in the development of internal mechanical strains within the depth of the structural element; these strains (or rather, the force and moment induced by them) must be resolved in order to maintain static equilibrium of the structural element. Assuming that the material remains in the elastic range, the curvature (ϕ) and total axial strain (ε_a) of the structural element can be solved using the following equations:

$$0 = \sum_{i=1}^{i=n} \{(\phi y_i + \varepsilon_a + \alpha T_i) E_i(T_i) y_i A_i\} \tag{9}$$

$$0 = \sum_{i=1}^{i=n} \{(\phi y_i + \varepsilon_a + \alpha T_i) E_i(T_i) A_i\} \tag{10}$$

Where "n" is the number of fibres into which an element is discretized, "y_i" is the distance from the centroid of the section to the centroid of each fibre, "α" is the coefficient of thermal expansion, T_i is the temperature of each fibre, $E_i(T_i)$is the temperature dependent elastic modulus of each fibre, and A_i is the area of each fibre. For a simply supported beam, the axial elongation then becomes:

$$dL = L - \varepsilon_a L - \frac{\sin\left({}^{L\phi}/_{2}\right)}{{}^{L\phi}/_{2}} \tag{11}$$

and the total deflection due to thermal curvature becomes:

$$d = \frac{1}{\phi}\left(1 - \cos\left({}^{L\phi}/_{2}\right)\right) \tag{12}$$

Canonical Example

If the full set of heat transfer equations are solved for an idealized case, this allows the comprehensive study for the effects of the thermal boundary condition, as a function of the *Biot number* on the mechanical behavior of the structural element.

The equations were solved for a unit length, unit width structural concrete element subject on one side to a constant gas temperature of 1,000°C. It was assumed, for the numerical simulations, that $h_i = 35\ W/m^2$, $h_o = 8\ W/m^2$, and $\varepsilon = 0.7$; where these represented the internal and external convective heat transfer coefficients and ε the emissivity for the radiative component (equations 9 and 10). The thermal properties of concrete were in accordance with the Eurocode, and it was assumed that the degradation of elastic modulus was as per the Eurocode. Three material thicknesses were analyzed: 28, 50, and 100 mm. These values correspond to a *Biot number* of 0.5, 1, and 2 (assuming $h_T = 45\ W/m^2$). The analysis was continued until an approximate stead state was achieved after 2 hrs, and the results for a simply supported section in terms of total deflection and total elongation are shown in Fig. 4.

These results demonstrate that, at the steady state, different *Biot numbers* induce different structural behaviors. As the *Biot number* increases, the bulk change in length diminishes as well as the deflections showing an overall less significant effect of heat on the structural element. For lower *Biot numbers* the overall expansion of the structural element results in a greater final deflection. However, the results of the numerical model also demonstrate that highest deflections occur during the transient stages of a fire – indicating that the *Biot number* also has a significant importance on the nature of the transient deformation and potentially early adverse effects.

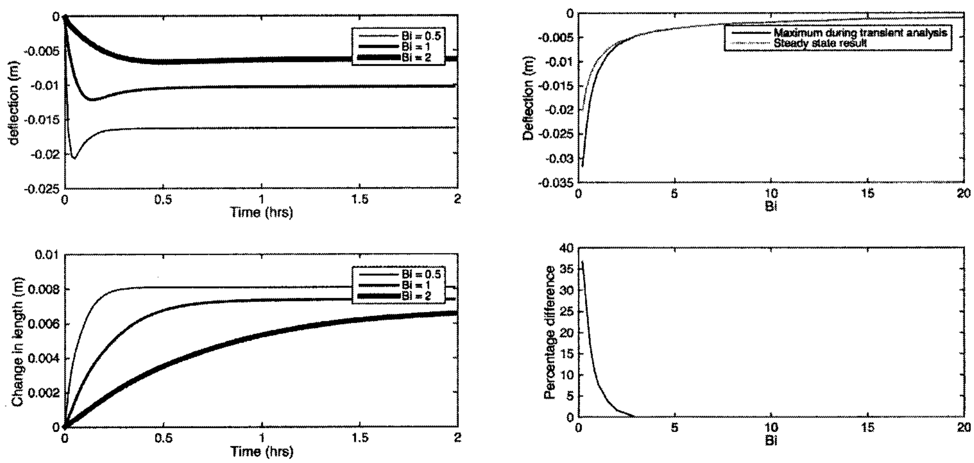

a) b)

Figure 4. a) Resulting transient deflections and elongations; b) Absolute values of deflection obtained from the two analyses (top), and the relative errors associated with the different between the steady state value and the transient analysis (bottom).

The maximum deflections in the steady state and in the transient analysis were calculated for a wide range of *Biot numbers* and the results presented in Figure 4. The results show that, for the canonical structure studied here, above a *Biot number* of approximately three transient and steady state solutions are almost identical, with a negligible error if only a steady state solution was to be applied. For smaller *Biot numbers* the two solutions diverge and given the worst-case deflections of the transient period, a transient analysis is necessary.

CONCLUDING REMARKS

This paper has examined the basis of two heating systems that can be used for fire testing load bearing materials and structural systems it is demonstrated that:

- By using incident radiant heat flux as a control measure, it is possible (and technically possible in practice) to harmonise the thermal boundary conditions at the exposed surface of a test sample, and therefore generate repeatable testing conditions independent of testing equipment or sample properties;
- Defining the thermal boundary conditions in terms of the Biot number allows for varying structural behaviours for different transient and steady state conditions to be considered; and
- The difference between the transient and stead state conditions reduces to zero as Biot increases above 3.0.

REFERENCES

1. Incropera, F.P. & DeWitt, D.P. (2002), *Fundamentals of Heat and Mass Transfer*. Wiley & Sons, New York, NY, US.
2. CEN (2012). Eurocode: Fire Resistance Tests – Part 1: General Requirements (EN 1363-1:2012). *European Committee for Standardization*, Brussels, Belgium, 56 pp.
3. Harmathy T.Z. and Mehaffey J.R. (1982). Normalized Heat Load: A Key Parameter in Fire Safety Design. *Fire and Materials*, 6 (1), 27-31.
4. Wickström U. (1986). A Proposal Regarding Temperature Measurements in Fire Test Furnaces. *Technical Report from the Nordtest Project 355-82*, 37 pp.
5. Cooke G.M.E. (1994). Can Harmonisation Of Fire Resistance Furnaces Be Achieved By Plate Thermometer Control? Proceedings of the *4th International Symposium on Fire Safety Science (IAFSS)*, Ontario, Canada, 1195-1207.
6. Kruppa J. and Curtat M. (1995). Comments on Wickström's "The Plate Thermometer – A Simple Instrument for Reaching Harmonized Resistance Tests". *Fire Technology* (letter to editor), 31 (1), 84-90.
7. Babrauskas V. and Williamson R.B. (1978). The Historical Basis of Fire Resistance Testing – Part II. *Fire Technology*, 14 (4), 304-316.
8. ASTM (2013). Standard Test Method for Heat and Visible Smoke Release Rates for Materials and Products Using an Oxygen Consumption Calorimeter (ASTM E1354). American Society for Testing and Materials (ASTM), 20 pp.
9. ASTM (2002). Standard Test Methods for Measurement of Material Flammability Using a Fire Propagation Apparatus (FPA) (ASTM E2058). American Society for Testing and Materials (ASTM), 30 pp.
10. Pettersson O. (1973). Need For and Some Remarks on Internationally Standardized Fire Test Procedures. *Lund Institute of Technology*, Lund, Sweden, 19 pp.
11. Usmani A.F., Rotter J.M., Lamont S., Sanad A.M., and Gillie M. Fundamental Principles of Structural Behaviour Under Thermal Effects. *Fire Safety Journal*, 36 (8), 721-744, 2001.

Predictive Testing for Heat Induced Spalling of Concrete Tunnels—The Influence of Mechanical Loading

IEUAN RICKARD[1], LUKE BISBY[1], SUSAN DEENY[2] and CRISTIAN MALUK[3]

ABSTRACT

This paper describes Phase II of a project being undertaken to develop a predictive test method to investigate heat-induced explosive spalling of concrete, with a specific focus on concrete used in tunneling applications (but obviously applicable to other applications). The test method seeks to allow careful control of the thermal and mechanical transient conditions influencing the occurrence of heat-induced concrete spalling, thus enabling convenient, representative, repeatable, and comparable testing to be carried out on various concrete mixes under various potentially relevant conditions.

Phase I of the project focused on establishing suitable thermal exposures to use for testing based on the thermal exposures which a sample would be exposed to during a standard furnace test (cellulosic or modified hydrocarbon) in the Promethee testing facility at CERIB in France. The work described in this paper deals with establishing suitable mechanical loading conditions for a spalling test, the focus in the current work is to enable provision of a representative test for precast segmental concrete tunnel linings (as opposed to sprayed or cut-and-cover tunnel linings). With small adaptations the spalling test method could be adjusted to suit other applications. This paper focuses on the motivation for developing the testing method and outlines the testing to be carried out. Tests are currently underway, and the full suite of results will be presented at the conference.

INTRODUCTION

Heat-induced concrete spalling poses a serious risk to the design, construction and operation of concrete structures, both above and below ground. In many well-known fires, for instance those in the Channel and Mont Blanc Tunnels, explosive concrete spalling caused considerable damage to the structures of the tunnels and required substantial, costly, and time-consuming repair works. Severe and rapidly growing fires, in combination with the lateral restraint to thermal expansion which may be present in

[1]BRE Centre for Fire Safety Engineering, The University of Edinburgh, Scotland
[2]Ove Arup and Partners Ltd, Scotland
[3]School of Civil Engineering, The University of Queensland, Australia

some cases, means that all modern concrete structures are potentially susceptible to heat induced concrete spalling, and that tunnel structures have a particularly high risk of spalling in the event of a fire [1].

The project discussed in this paper is motivated primarily by the need for increased knowledge of spalling risk in concrete tunnel projects, and for a convenient and economical testing method to determine the propensity of different concrete mixes for spalling under a range of thermal and mechanical conditions. The work also has relevance to heat-induced concrete spalling building fires, particularly given the current shift toward higher strength, self-consolidating mixes containing silica fume which have shown increase tendency for spalling [2].

Currently there is no validated guidance to enable the design of concrete mixes to prevent spalling, nor is there an established, widely accepted test method available to quantify spalling for a given concrete mix or to demonstrate spalling resistance [2]; even costly and time-consuming large scale furnace testing is performed on an essentially ad-hoc, project-specific basis. As a result, the potential for spalling of candidate concrete mixes continues to pose a serious design risk at all stages of a concrete construction project cycle.

Conventional large-scale fire tests (i.e. ad-hoc standard furnace tests) of concrete structural elements are currently the sole design/compliance method/test for heat induced concrete spalling. Test methods and apparatus typically vary across projects and jurisdictions, thus limiting their usefulness for research and interpretation and their wider international applicability. Coupled with the global growth in infrastructure development, this has created demand from clients, contractors, and designers alike for a convenient predictive test method to quantify spalling risk. Any such test method must be able to accurately and repeatably control the thermal and mechanical exposures, provide known, appropriate loading and restraint conditions, and be cost effective and time efficient.

The project described herein will establish a suitable predictive test method for the explosive spalling of concrete, with a particular focus on tunnel linings. In order to do this, the test method needs to be able to control all the necessary parameters that are known to affect spalling. Defining a suitable thermal exposure and developing a method for accurately and repeatably imposing this thermal exposure on a sample were dealt with in Phase I [3,4]. All tests performed thus far have been carried out on unloaded samples of different sizes and geometries, primarily for the purposes of defining the requisite thermal exposure, however it is well known that mechanical loading and thermal restraint conditions experienced by samples during heating will also significantly influence spalling.

Numerous examples on the influence of loading and restraint in the occurrence of heat-induced concrete spalling are available in current literature [5-8]; based on small and large scale fire tests. The general consensus seems to suggest that increased external compressive loading or increased restraint to thermal expansion (either externally applied, or inherent due to sample thickness) increases the propensity of spalling. To be able to test with relevance to tunnel linings it is necessary to test samples of representative thickness under representative mechanical stresses, and it is therefore necessary to impose large mechanical loads.

FIRE TEST METHODOLOGY

Thermal Boundary Conditions

The testing method is based upon adaptation and extension of a novel testing method and apparatus known as the Heat-Transfer Rate Inducing System (H-TRIS), previously described by Maluk and Bisby [2]. H-TRIS controls the thermal exposure to which a sample is exposed (i.e. the time history of internal thermal gradients within a sample) by varying the incident radiant heat flux imposed at the target exposed surface of the test sample, rather than controlling temperature inside a furnace – as would typically be the case in a standard fire resistance test. The result of this shift in heating method is that the thermal boundary conditions can be more accurately defined, quantified, and reproduced, leading to a more repeatable test method. H-TRIS thus allows multiple repeat tests of candidate concrete mixes under a wide range of potential thermal exposures.

Phase I of the project [3,4], established the appropriate thermal exposure conditions (i.e. time-histories of incident heat flux) for testing under both standard cellulosic (ISO 834) [9] and standard modified hydrocarbon (HCM) [10] fire curves. This was accomplished by testing a large number of heavily instrumented prismatic concrete samples of various sizes and mix designs in the Promethee furnace facility at CERIB, France. The samples varied in surface area from relatively small (350 × 350 mm in plan) to full scale (4380 × 1450 mm in plan), and their thickness was either 100 or 250 mm.

Analysis of the in-depth temperature measurements within the samples tested in Promethee allowed the equivalent net heat flux to be determined [2], and this was subsequently converted into an incident heat flux for reproduction within H-TRIS. This thermal characterisiation of the thermal exposure was a crucial outcome for the overall project but other insights into spalling behavior were also gained. The testing methodology was verified by testing identical concrete samples using H-TRIS and comparing the in depth thermal profiles against the furnace tests. Figure 1 shows the equivalent time histories of incident heat flux followed by the H-TRIS test apparatus to give an equivalent thermal exposure as experienced during the furnace tests.

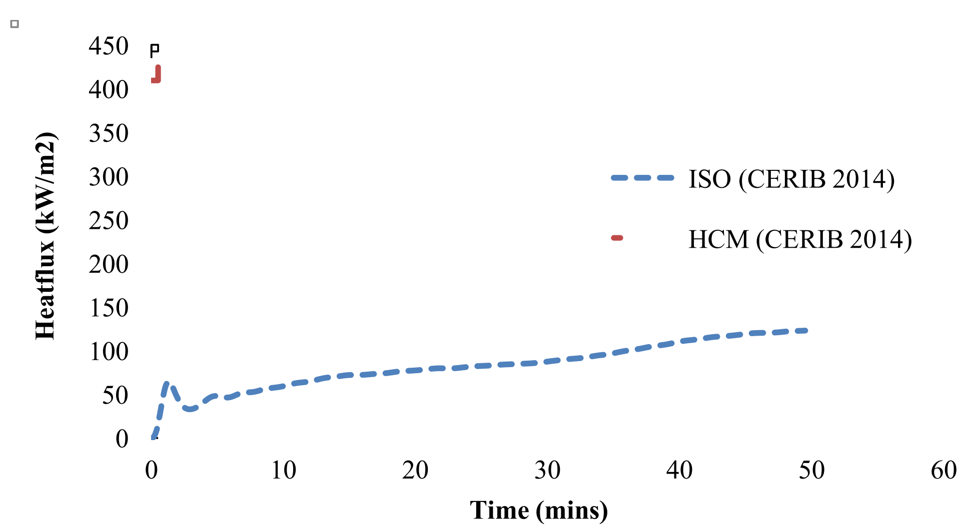

Figure 1. Incident Radiant Heat Flux calculated from in-depth temperature measurements of samples tested during a standard fire resistance test.

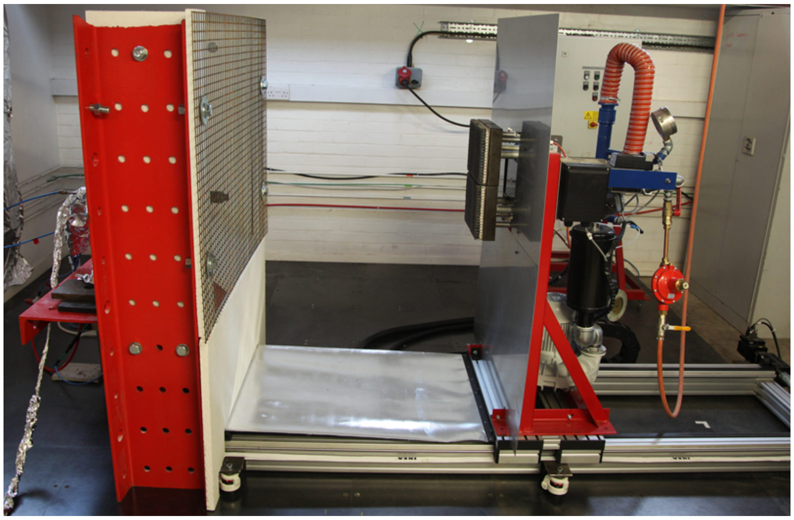

Figure 2. Heat-Transfer Rate Inducing System (H-TRIS) MkII

The current incarnation of the H-TRIS test apparatus (named H-TRIS MkII) is shown in Figure 2. Incident radiant heat flux is varied during testing by varying the standoff distance between the propane fueled radiant panels and the target sample using a computer controlled linear motion system. This method of heating a sample allows superior control and repeatability of the thermal exposure, particularly during the early stages of a test (i.e. within the first five to ten minutes) when standard fire testing furnaces tend to struggle to maintain control (hence the allowable temperature tolerances are much wider, or not existent in available fire resistance testing guidelines). Another advantage the H-TRIS apparatus and methodology is that this method allows for easy, direct observation of spalling times, patterns, and depths.

Loading Conditions

Phase II of the project is being carried out to investigate the influence of sustained compressive loads and localised heating on the propensity for heat-induced concrete spalling. Along with a bespoke 3MN uniaxial loading frame. Figure 3 shows both schematics and photos (during fabrication) of the loading and restraint frame that has been developed. The frame has been designed to allow large concrete samples, with surface areas up to 500 × 500 mm and depths up to 250 mm, to be loaded to up to a sustained level of 20 MPa (and smaller samples to be loaded to much higher stresses).

When used in conjunction with H-TRIS MkII heating rig, the loading frame enables simultaneous, accurate, heating and uniaxial compressive loading of samples of realistic scale. The loading frame uses two 1500kN hydraulic jacks to apply the load to the samples, and these are operated using load control by control of hydraulic pressure. The load on the samples is held constant during testing, and no increase in load due to thermal expansion is permitted. Such an approach has been taken because attempting to 'fully' restrain the samples is impractical and would lead to poorly characterized stress conditions within the concrete (indeed this is a shortcoming of much of the available research to date on spalling).

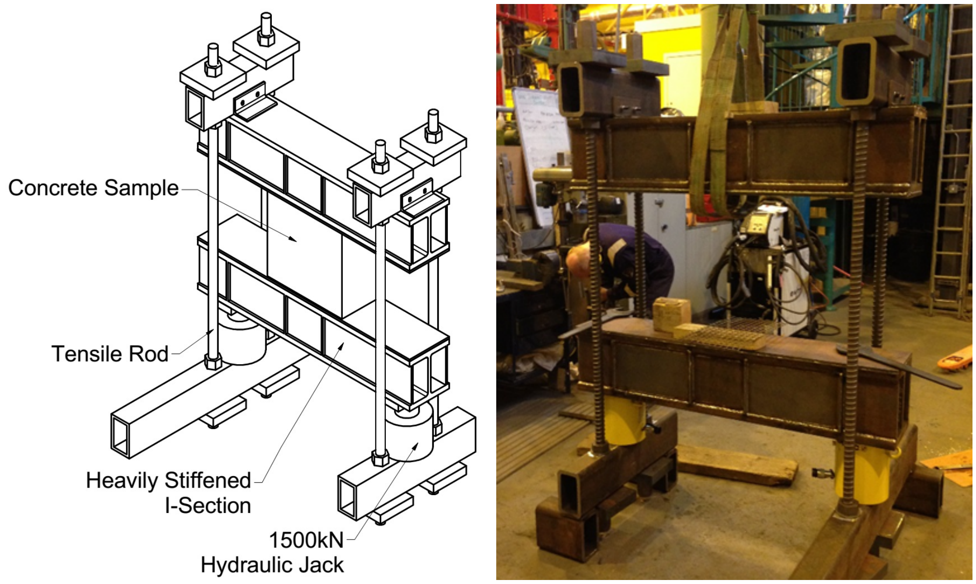

Figure 3. Loading frame design and frame under construction.

PHASE II TESTING PROGRAM

A total of forty-two unreinforced concrete samples, prismatic in shape with plan dimensions of 500 mm square and with various thicknesses (100 mm, 175 mm, and 250 mm), have been cast and conditioned, at room temperature and 50% relative humidity, for more than one year. The samples have been instrumented with thermocouples close to the heat-exposed surface to allow the temperatures within the samples to be monitored and the consistency of heating demonstrated and quantified. The parameters being varied amongst the samples, and the reasons for these choices, are discussed below. The overall testing matrix is shown in Table 1.

Table 1. Test matrix for Phase II testing.

Exposure area (mm)	Heating Curve	Thickness (mm)	Load (% ambient f_c')
400x400	HCM	100	10
400x400	ISO	100	10
400x400	HCM	100	0
400x400	HCM	100	30
400x400	HCM	100	50
400x400	HCM	100	70
400x400	HCM	175	10
400x400	HCM	175	0
400x400	HCM	250	10
400x400	HCM	250	0
100x100	HCM	250	0
150x150	HCM	250	0
200x200	HCM	250	0
300x300	HCM	250	0

* NOTE: Each test to be performed in triplicate

Heating Conditions

The thermal boundary conditions imposed are equivalent to those experienced by concrete test samples during a standard fire resistance test controlled to follow the ISO 834 [9] and HCM [10] time history of temperature inside the furnace. It was observed in Phase I, in agreement with the vast majority of available research on heat-induced concrete spalling, that the more severe HCM fire curve caused more severe spalling; however, tests are being carried out to confirm that this is the case for the Phase II samples. If either no spalling occurs or too much spalling occurs in the initial tests, it may be difficult to determine the influences of the secondary experimental parameters (see discussion below), and it may therefore be necessary to impose a more or less severe heating curve to enable useful comparisons of the influences of additional parameters.

Depth of the Test Sample

Samples with thicknesses of 100 mm, 175 mm, and 250 mm are being testing in Phase II. In Phase I, samples with thicknesses of 100 mm and 250 mm were tested, both in the Promethee furnace and using H-TRIS (MkI). It was observed, particularly during the furnace testing, that when otherwise identical samples that had different depths (thicknesses) were tested together, the 100 mm deep sample experienced almost no spalling, whereas the 250 mm deep sample spalled extensively; regardless of the plan dimensions of the samples. This coincided with the observed thermal bowing of the thinner 100 mm deep samples, and it is therefore hypothesized that thermal bowing allowed restrained differential thermal stresses to be somewhat relieved, resulting in less spalling. In a comparatively thick segmental concrete tunnel lining segment, bowing is highly unlikely to occur in the event of a fire due to both the curvature of the segment and the restraint to deformation provided by the surrounding overburden. Thus, it is important when developing a test method that the concrete be restrained against bowing (to the extent possible). As a result, the loading frame designed and constructed for Phase II imposes uniaxial stress with notional rotationally fixed-fixed end conditions.

Loading Conditions

Previous testing carried out on segments for installation in the Great Belt Tunnel [11] assumed that a realistic in-situ ambient compressive stress of 5MPa was representative of in-service conditions before a fire with relatively little justification. Samples in Phase II are being tested under sustained compressive uniaxial stresses of up to 20MPa. It is well known that the loading/restraint on a concrete sample influences its spalling propensity on heating. It is therefore necessary to determine the relative influence of applied mechanical stress in comparison with other relevant parameters; and to determine the credible worst-case loading to be applied in order to properly test for spalling. In the case of concrete in a precast segmental tunnel lining it is difficult to know the loading state in the tunnel lining (even at ambient temperature) as this depends on a range of uncertain variables, including the ground conditions and factors related to the tunnel's constructability. In the case of fire, the loading in a concrete tunnel segment is likely to depend on, amongst other factors, the in-service ambient loading, the global deformation of the tunnel due to the thermal exposure – which may include the response of the surrounding overburden to tunnel expansion, the tunnel's method of construction – which may influence whether the concrete segments experience biaxial or uniaxial loading, and the effects of localized, rather than global, heating to buoyancy effects or flame impingement.

It should be noted that it is not the aim of the current project to recreate the thermal and physical realities within a real tunnel, but rather to create a test method which provides a credible worst case for heat-induced spalling, which is representative of the range of conditions which could occur in a fire in a tunnel. The goal is to experimentally unpick the importance of the respective parameters, rather than perform simple compliance testing, and eventually to develop the necessary protocols to show that explosive spalling will not occur for any credible combination of loading and heating in a real tunnel such as is needed to undertake performance based fire design of tunnels and tunnel linings.

It should also be noted that the loading frame developed for Phase II imposes uniaxial versus biaxial loading; this has been a conscious decision taken after consultation with structural designers of segmental concrete tunnel lining systems, who stated that longitudinal restraint is likely to be low in an installed segmental concrete tunnel lining in a fire due to the gasketing materials that are placed between the successive tunnel rings. Biaxial applied stress may, however, be appropriate for other structural scenarios.

Heated Surface of the Test Sample

Samples in Phase II are being exposed to heat areas varied between 100×100 mm and 400×400 mm. Whilst making it difficult to quantify the stress state within a sample, a number of authors have experimented with localized heating of concrete in order for the sample to be subjected to a certain degree (however un-quantified) of self-restraint to thermal expansion [12,13]. Thermal expansion of the heated area is restrained by the cooler surrounding concrete, leading to the development of a complex stress state in the concrete surrounding the heated surface and potentially contributing to (or dominating) explosive spalling. Testing with only localized heating could therefore enable testing that requires no applied loading system, and may also capture the effects of non-uniform/localised heating in a real fire. A comparison of tests using different exposed areas is underway to provide better understanding of how important this parameter might be in practice.

FURTHER OUTCOMES AND OBSERVATIONS

In addition to presenting the details of a novel testing method that can be used to assess the propensity of various candidate concrete mix designs to experience heat induced spalling, the testing described herein will enable a more complete understanding of the relative influences of applied loading and sample restraint/geometry on heat-induced explosive spalling. The results will inform the current project as it moves forward into Phase III to test candidate mixes from actual European tunnel lining projects and compare the results against those from conventional full scale tests undertaken on the same concrete mixes in furnaces. Recommendations for the development of an international industry standard for testing for the spalling propensity of concrete mixes will be proposed based on the work undertaken, via the RILEM committee on spalling of concrete due to fire.

CONCLUDING REMARKS

This paper has presented the current status of a project being undertaken at The University of Edinburgh to develop a predictive test method to investigate heat-induced explosive spalling of concrete, with a specific focus on concrete used in tunneling applications. A brief summary of Phase I has been given and the details of and motivations for phase II of the project have been described. The results of the testing which is currently underway will be presented at the conference.

The test method seeks to allow careful control of the thermal and mechanical conditions influencing the occurrence of heat-induced concrete spalling, thus enabling convenient, representative, repeatable, and comparable testing to be carried out on various concrete mixes under various potentially relevant conditions.

ACKNOWLEDGEMENTS

The work described in this paper would not have been possible without the support of the fire engineering and tunnels engineering teams at Arup and CERIB.

REFERENCES

[1] C. Maraveas, A. a Vrakas, and C. M. Partnership, “Design of Concrete Tunnel Linings for Fire Safety,” 2014.

[2] C. Maluk and L. Bisby, “A Novel Test Method for Materials and Structures in Fire,” in *8th International Conference on Structures in Fire (SiF’14)*, 2014, pp. 1063–1070.

[3] I. Rickard, C. Maluk, L. Bisby, and S. Deeny, “Predictive Testing for Heat-Induced Spalling of Concrete,” in *IABSE Conference Geneva, Structural Engineering: Providing Solutions to Global Challenges*, 2015, pp. 929 – 936.

[4] I. Rickard, C. Maluk, F. Robert, L. Bisby, S. Deeny, and C. Tessier, “Development of a Novel Small-Scale Test method to Investigate Heat-Induced Spalling of Concrete Tunnel Linings,” in *4th International Workshop on Concrete Spalling Due to Fire Exposure*, 2015, pp. 195–205.

[5] R. J. Connolly, “The spalling of concrete in fires,” The University of Aston in Birmingham, 1995.

[6] K. D. Hertz and L. S. Sørensen, “Test method for spalling of fire exposed concrete,” *Fire Saf. J.*, vol. 40, no. 5, pp. 466–476, 2005.

[7] C. Meyer-Ottens, “Zur Frage der Abplatzungen an Betonbauteilen aus Normalbeton bei Brandbeanspruchung,” Technischen Universität Carolo-Wilhelmina zu Braunschweig, 1972.

[8] Y. Sertmehmetoglu, “On a Mechanism of Spalling of Concrete Under Fire Conditions,” University of London, King’s College, 1977.

[9] International Organisation for standardization, “ISO 834-1 Fire-resistance tests - Elements of building construction - -Part 1: General Requirements,” vol. 1999. International Organisation for standardization, 1999.

[10] Ministère de l’Equipement, “Circulaire interministérielle no 2000-63 du 25 Aout 2000 relative à la sécurité dans les tunnels du réseau routier français,” Paris, France, 2000.

[11] N. P. Høj, C. Tait, and M. Macdonald, “Great Belt Tunnel Repairs and Refurbishmanet Following a Fire,” *Tunn. Manag. Int.*, pp. 16–22, 1999.

[12] K. D. Hertz, “Limits of spalling of fire-exposed concrete,” *Fire Saf. J.*, vol. 38, no. 2, pp. 103–116, 2003.

[13] S. Werner and A. Rogge, “The effect of various fire-exposed surface dimensions on the spalling of concrete specimens,” *Fire Mater.*, Jun. 2014.

Explosive Concrete Spalling During Large-Scale Fire Resistance Test

CRISTIAN MALUK[1], LUKE BISBY[2]
and GIOVANNI PIETRO TERRASI[3]

ABSTRACT

This paper presents a comprehensive investigation of explosive heat-induced spalling observed during a set of large-scale fire resistance tests (or standard furnace tests) on prestressed concrete slabs. The study, based on data from large-scale tests, examines the influence of numerous design parameters in the occurrence of spalling (age of concrete, inclusion of polypropylene fibres, depth of the slab, and prestressing level). Furthermore, a careful thermal analysis of the tested slabs is presented; a comparison of in-depth temperature distributions inside concrete slabs shows that spalling occurred for slabs with more rapid in-depth temperature increase. The analysis presented herein shows that the scatter of in-depth temperature increase experienced by concrete slabs tested simultaneously has a substantial influence in the occurrence of heat-induced concrete spalling.

INTRODUCTION & BACKGROUND

During (or even after) heating in fire, concrete at the exposed surface of structural elements flakes away in a more or less violent manner. This phenomenon is known as 'heat-induced concrete spalling' [1]. As a consequence, the concrete cover to the internal reinforcement is reduced, resulting in rapid temperature increase of the reinforcement and within the structural element, in addition to a direct influence on load bearing capacity due to the loss of physical or effective cross sectional area.

Two main mechanisms are widely considered to contribute to the occurrence of heat-induced concrete spalling. The first is a thermo-hydraulic mechanism associated with the transport and/or evaporation of free water (or capillary water) within the concrete microstructure; this is postulated to lead to generation of steam pressure and a 'moisture clog', and eventually to spalling. It is almost universally agreed that higher

[1]School of Civil Engineering, The University of Queensland, Australia
[2]BRE Centre for Fire Safety Engineering, The University of Edinburgh, Scotland
[3]Empa, Swiss Federal Laboratories for Materials Science and Technology, Switzerland

moisture content results in increased heat-induced spalling, all other factors being equal [2]. The second is a thermo-mechanical mechanism associated with internal mechanical stresses resulting from in-depth temperature distributions and incompatibilities in the thermal and thermo-mechanical behaviour of the components within the concrete matrix (e.g. coarse and fine aggregates, cement paste, chemically bound water, etc). This mechanism can also be described at the macro-scale, and linked to internal mechanical stresses resulting from external loading, restraining forces, and/or differential thermal stresses arising due to uneven heating, in-depth temperature distributions, and/or the presence of cold areas.

The relative significance of these two mechanisms for a particular concrete mix, under a particular thermal exposure in a given application, are not well known. Regardless of the unquantified risk of spalling, current design and construction guidance for spalling prevention (e.g. [3,4]) is based on prescribing a dose of polypropylene (PP) fibres which is presumed to assure limited spalling in applications with 'relatively high' spalling risk (e.g. high-strength concrete, high in-service moisture content, high in-service compressive stress, rapidly growing fires, etc). For example, European design guidelines for concrete in fire [3] recommends including at least 2 kg of monofilament PP fibres per cubic metre concrete for high-strength (>55 MPa cube compressive strength), high moisture content (>3% by mass) and/or concrete with high inclusion of silica fume (>6% by mass of cement). Australian design guidance for concrete in fire [4] states that the addition of 1.2 kg of 6 mm long monofilament PP fibres per cubic metre concrete has a "dramatic effect in reducing the level of spalling".

Within the scope of the work presented and discussed herein a careful thermal analysis of the tested slabs is done for one of the large-scale fire resistance tests (reefer to Figure 1). A comparison of in-depth temperature distributions inside concrete slabs shows that spalling occurred for slabs with more rapid in-depth temperature increase.

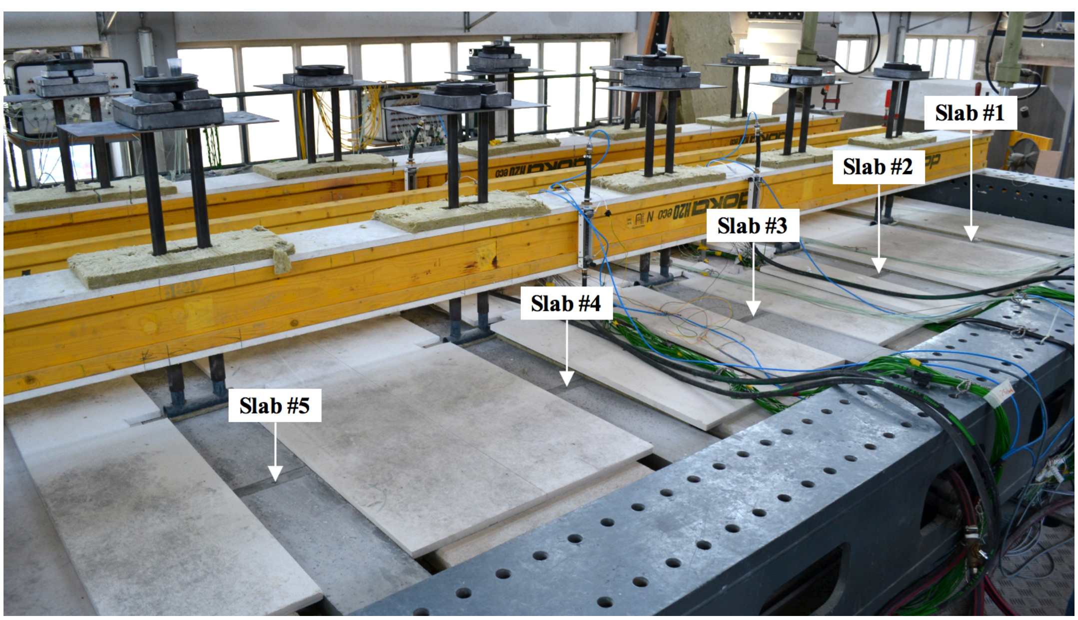

Figure 1. Photo of the fire resistance test setup showing positions of the respective slabs and sustained loading technique used.

TEST PROGRAM

A set of large-scale fire resistance tests were executed, each with five loaded prestressed concrete slabs simultaneously tested in a standard floor furnace test [5]. The design and test program of the prestressed slabs was aimed to evaluate the influence of: age of concrete, inclusion of polypropylene fibres, depth of the slab, and prestressing level. The parameters evaluated for the test examined within this paper is shown in Table 1 (reefer to Figure 1).

Table 1. Evaluated parameters, time-to-failure and failure mechanisms for slabs discussed herein.

Slab #	Concrete mix	Depth of the slab [mm]	Applied load per point [kg]	Slab utilization factor	Time-to-failure [mm' ss'']	Failure mechanism
1	A	45	25.0	0.23	42' 01''	Loss of anchorage
2	A	45	25.0	0.23	12' 37''	**Explosive spalling**
3	A	60	38.4	0.20	22' 10''	**Explosive spalling**
4	B	45	25.0	0.23	50' 27''	Loss of anchorage
5	B	60	38.4	0.20	93' 04''	Loss of anchorage

Test slabs

The tested slabs were similar to those used by the authors in prior research [5]. Their overall length was 3360 mm and they were prestressed with four circular pultruded, quartz sand-coated CFRP tendons stressed to an initial prestress level of 1,000 MPa. Initial prestress level was calculated based on the gross cross-sectional area of the tendons; i.e without considering the layer of sand coating (refer to Section 3.2.2 of this paper).

All CFRP tendons were located at the slab mid-depth, with a tolerance of ±2 mm, to obtain a nominally concentric prestressing force. The slabs were 45 or 60 mm thick (refer to Table 1), leading to clear concrete covers to the prestressed CFRP reinforcement of 19.5 mm and 27 mm, respectively. All slabs were 200 mm wide. Lateral clear concrete cover at the slab edges was 22 mm in all cases, with a tendon-to-tendon clear spacing of 44 mm.

High-Performance, Self-Consolidating Concrete (HPSCC)

All slabs were fabricated from a high-performance, self-consolidating concrete (HPSCC) of strength class C90 (minimum 28 day 150 mm cube compressive strength of 90 MPa). Given the high likelihood of spalling for this mix due to its high strength and the inclusion of microsilica in the mix [3], 2.0 kg of 3 mm long or 1.2 kg of 6 mm long PP monofilament fibres (32 μm in diameter) were included for mixes A and B, respectively. Detailed of both mixes are given in Table 2. Moisture content was measured by dehydration mass loss of control specimens. The average moisture contents at the time of testing were 3.6 and 3.9% by mass, for mixes A and B, respectively. Compressive and splitting tensile strengths were measured at 28 days and 6 months (close to the time of testing).

Table 2. Mix composition and slump flow for the HPSCC mixes.

		Mix #A	Mix #B
Water/(cement + microsilica + fly ash)	[-]	0.31	0.31
Cement (includes 20% microsilica)	[kg/m^3]	475	469
Fly ash	[kg/m^3]	120	120
Limestone aggregate (0-8 mm)	[kg/m^3]	1675	1669
Superplasticizer in % of cement	[%]	1.69%	1.75%
Polypropylene fibres	[kg/m^3]	2.0 (3 mm PPs)	1.2 (6 mm PPs)
Slump flow **Error! Reference source not found.**	[mm]	830	785
Compressive strength (28 days / 6 months)	[MPa]	92.6 / 93.3	96.2 / 98.5
Splitting tensile strength (28 days / 6 months)	[MPa]	5.44 / 5.47	5.49 / 5.57
Moisture content (at the time of testing)	[% by mass]	3.6%	3.9%

TEST SETUP

Thermal Conditions

The setup of the specimens was aimed at assuring one-sided heating from below, so the sides of the specimens were fully insulated. The heating regime was executed according to the requirements of the standard time-temperature curve [6]. During testing, the furnace was instrumented in accordance with European fire test standards [4]; eight standard plate thermometers were positioned inside the furnace. These were used to record and control the temperatures inside the furnace during testing.

Mechanical Conditions

Sustained mechanical loading was applied to simulate an in-service condition for the slabs, in simply-supported four-point bending. The applied load was designed to be sufficient to achieve decompression at the extreme tension fibre within the constant moment region (i.e. $\sigma_{c,bottom} = 0$ [MPa]); this corresponds to a typical design service load condition for a façade element of this type in a real building [5]. Loading was imposed 30 minutes prior to start of heating. Prestressing losses due to elastic shortening, shrinkage and creep of the concrete were considered and calculated based on results from prior experimental studies performed for similar HPSCC mixes [5].

DISCUSSION

Furnace Temperature

Temperature measurements from the eight plate thermometers inside the furnace are shown in Figure 2 along with the objective time-temperature curve. Although compliant with the testing standard [6], the temperature measurements show substantial deviation in the temperature measured inside the furnace, especially during the first 20 minutes (see Figure 3). Due to the obvious technical challenge of precisely controlling the furnace to follow the rapidly growing prescribed time-temperature curve [6] during early stages of the test, most testing standards do not prescribe an allowable deviation during the first 5 minutes (see Figure 3).

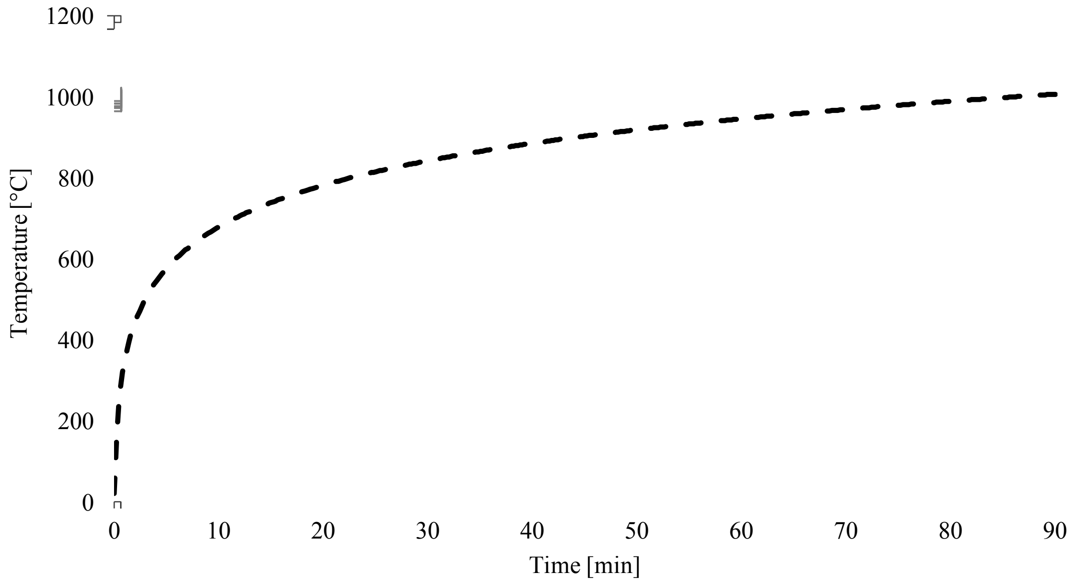

Figure 2. Furnace gas temperatures measured by the plate thermometers along with the objective standard time-temperature curve [6].

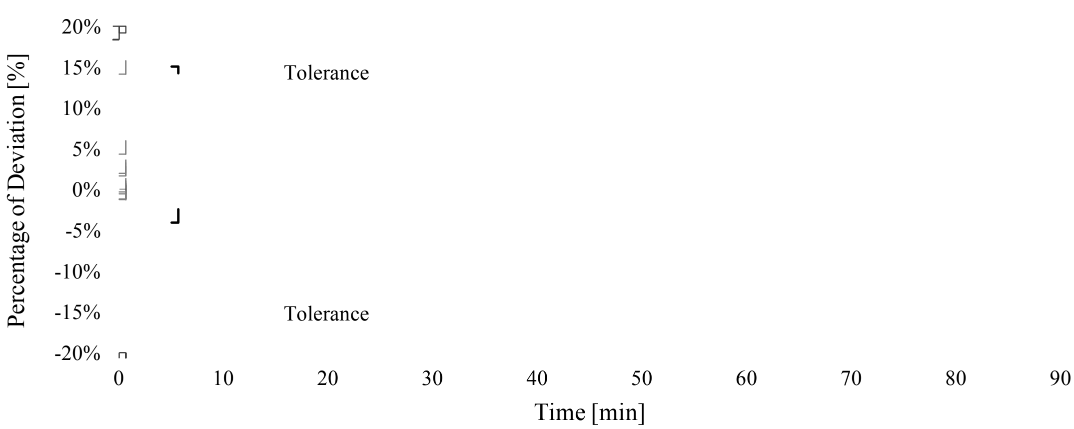

Figure 3. Percentage of deviation of the temperature measured by plate thermometers from that of the objective temperature, and the maximum allowable deviation (tolerance) [6].

Slabs in-depth temperature

In-depth temperature measurements were taken at midspan of the slabs. Temperature was measured in up to eleven positions from the exposed surface of each of the slabs. Special care was taken during the casting process to ensure precise placement of thermocouples at the intended location inside the slabs. A comparison of in-depth temperature distributions measured at midspan is shown in Figures 4. Temperature for the first 12 minutes of a test are shown.

Considerable variation of in-depth temperature distributions was observed for slabs with equivalent thickness, demonstrating poor homogeneity of the thermal exposures for slabs tested simultaneously during a single furnace test; this is despite the temperatures measured by the plate thermometers complying with the test standard (see Figure 3). Slabs with more rapid temperature increase spalled, while slabs with relatively slower temperature increase did not spalled. This suggests the important influence of the thermal exposure, hence transient evolution of thermal gradients, in the occurrence of heat-induced concrete spalling [7].

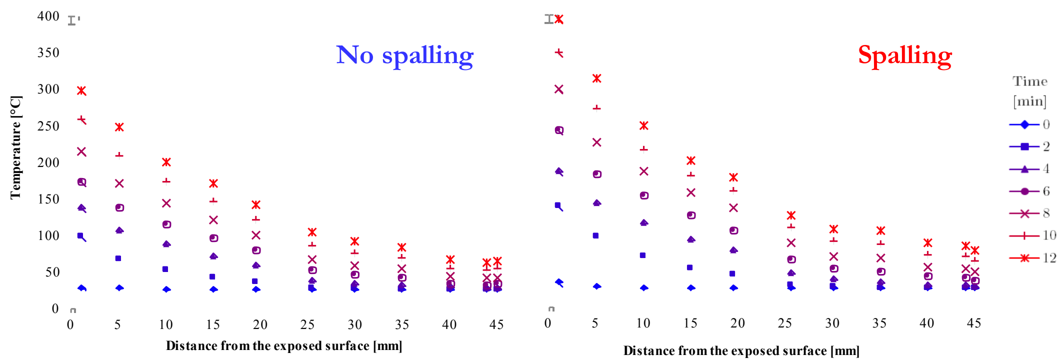

Figure 4. In-depth temperature distribution for identical slabs; Slab #1 (left plot) that did not spalled and Slab #2 (right plot) that spalled 12 minutes from the start of the test (reefer to Table 1).

Failure of slabs #2 and #3 was driven by the occurrence of single explosive concrete spalling events, 12 and 22 minutes from the start of the test, respectively (refer to Table 1). Immediately after spalling, each of these slabs suffered catastrophic failure and collapsed into the furnace. Video stills recorded during testing showed the moment at which spalling occurred (shown for Slab #2 in Figure 19).

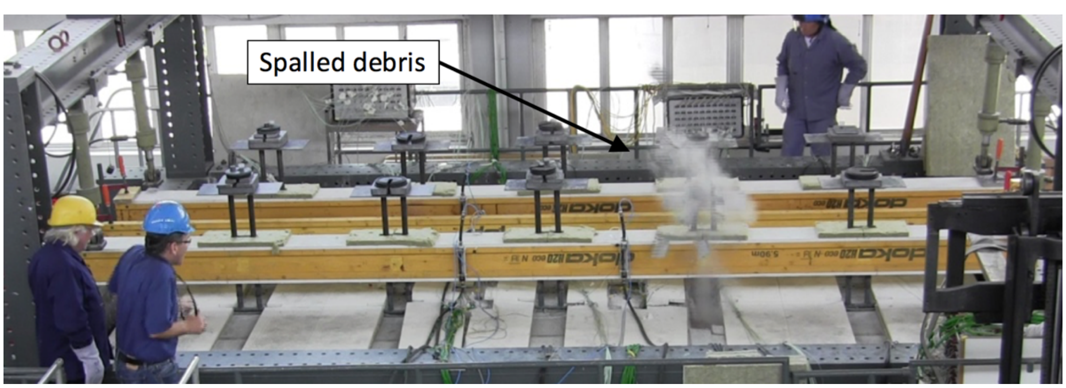

Figure 3. Explosive spalling and immediate collapse of a large-scale slab during a fire resistance test.

Slab #2 failed after 12 minutes, whereas the virtually identical Slab #1 failed due to loss of anchorage after 42 minutes of fire exposure (refer to Table 1); Figure 13 shows that Slab #2 experienced more rapid heating during the early stages of the test. This suggests a possible important influence of the time-history of in-depth temperatures on the occurrence of heat-induced concrete spalling [1]. For instance, Slab #2 spalled when the measured temperature 1 mm from its exposed surface was 400°C, while for Slab #1 the temperature at the same location was only 300°C. The possibility that this was due to misplacement of thermocouples during casting was discarded since equivalent temperature differences between slabs #1 and #2 were observed for temperatures measured at various positions in the slab (e.g. 5, 10, and 15 mm from the exposed surface).

For slabs #4 and #5, both of which were cast from Mix B, no spalling was observed and thus it is not possible to determine whether time-history of in-depth temperatures might influence the occurrence of spalling for this mix. The above demonstrates an inability to properly compare test results for multiple specimens simultaneously tested during a single furnace test when subtle differences in thermal gradients play important roles in the test outcomes.

CONCLUDING REMARKS

Recognizing that it is challenging to draw categorical conclusions on the basis of a limited number of large-scale fire resistance test, the following conclusions can be drawn on the basis of the data and discussion presented herein:

- The fire resistance of CFRP prestressed HPSCC slabs during a standard fire resistance test is influenced by the occurrence of heat-induced concrete spalling, and if no spalling occurs, by loss of anchorage.
- Although all five test specimens were tested simultaneously and exposed to the same notional time-history of temperature inside the furnace, variability was observed in the time-history of in-depth temperatures for essentially identical slabs. This demonstrates the relatively poor, although 'test standard compliant', homogeneity of the thermal loading imposed during a standard furnace test [6]. Interestingly, more rapid in-depth temperature increases were measured for slabs at the centre of furnace, relative to those near its walls.
- Failure of slabs #2 and #3 was driven by the occurrence of a single explosive spalling event leading to sudden failure, while identical slabs did not spalled.
- The occurrence of heat-induced concrete spalling appears to be subtly influenced by the time-history of in-depth temperature within a concrete slab. Comparison of temperature measurements recorded for slabs #1, #2, and #3 (all Mix A) indicated an influence of time-history of in-depth temperatures on the occurrence of heat-induced concrete spalling. More rapid in-depth temperature increases were measured for slabs #2 and #3, which spalled at 12 and 22 minutes, respectively.
- Results suggest that a lower risk of spalling exists for slabs cast with Mix B (containing 1.2 kg/m3 of 6 mm long PP fibres) than for those cast with Mix A (2.0 kg/m3 of 3 mm long PP fibres). This may be related to the short PP fibres (3

mm long) included in Mix A being less effective in mitigating heat-induced concrete spalling. It is noteworthy that existing European (and other) design guidelines for concrete in fire [3] prescribe the inclusion of 2 kg/m3 of monofilament PP fibres to 'avoid' spalling; this is clearly indefensible based on the tests presented herein. Furthermore, these guidelines provide no guidance on the required PP fibre diameter or length.

This work demonstrates the sensitivity of thermal exposure in the occurrence of heat-induced concrete spalling. These findings are based on the comparison of test results from a large-scale fire resistance tests, where it was observed that a 'subtle' differences in thermal gradients can play an important role in the occurrence of spalling; for essentially identical concrete slabs. A proper understanding of the response of these elements is needed before they can be designed and implemented with confidence; this is unlikely to be achieved by performing additional standard fire resistance tests. Conversely, what is needed is scientific understanding of the thermal and mechanical fire behaviour of these elements at the material, member, and system levels; this can be accomplished using a range of conventional and bespoke test methods and procedures, many of which are now being used by the authors (e.g. [1]).

REFERENCES

1. Maluk C. *Development and Application of a Novel Test Method for Studying the Fire Behaviour of CFRP Prestressed Concrete Structural Elements*. PhD Thesis, The University of Edinburgh, UK, 2014, 473 pp.
2. Bailey C.G. and Khoury G.A. Performance of Concrete Structures in Fire – An In-depth Publication on the Behaviour of Concrete in Fire. *MPA - The Concrete Centre*, Ruscombe Printing Ltd, Reading, UK, 2011, 187 pp.
3. CEN. Eurocode 2: Design of Concrete Structures – Parts 1-2: General Rules – Structural Fire Design (EN 1992-1-2). *European Committee for Standardization*, Brussels, 2004, 100 pp.
4. CCAA. Fire Safety of Concrete Buildings. *Cement Concrete & Aggregates Australia (CCAA)*, 2013, 33 pp.
5. Terrasi G.P., Bisby L., Barbezat M., Affolter C., and Hugi, E. Fire Behavior of Thin CFRP Pretensioned High-Strength Concrete Slabs. J. of Composites for Const, 2012, 16(4), 381–394.
6. CEN. Eurocode: Fire Resistance Tests – Part 1: General Requirements (EN 1363-1:2012). *European Committee for Standardization*, Brussels, 2012, 56 pp.
7. Hertz K.D. and Sørensen L.S. Test Method for Spalling of Fire Exposed Concrete. Fire Safety Journal, 2005, 40 (5), 466-476.

Effect of Biaxial Mechanical Loading and Cement Type on the Fire Spalling Behaviour of Concrete

MD JIHAD MIAH, FRANCESCO LO MONTE, PIERRE PIMIENTA and ROBERTO FELICETTI

ABSTRACT

Fire spalling of concrete is a complex phenomenon, which might occur due to pressure build-up in the pores, thermal- and load-induced stresses. In this context, eight mid-size ordinary concrete slabs (4of B40-II and 4 of B40-III concrete: fc28 ≈ 40 MPa) were heated at the bottom face according to Standard Fire curve (ISO 834-1), while a constant biaxial compressive load was applied. Four different levels of biaxial mechanical loading have been investigated on both concretes. The test results showed that the loaded specimens are more prone to spalling than unloaded specimens, with increasing amount of spalling for higher values of applied load. Concrete made with CEM III cement (B40-III: 43 % of slag) exhibited less spalling than CEM II cement concrete (B40-II: 3 % of slag).

INTRODUCTION

Thermal spalling is a sudden and violent breaking away of a surface layer of heated concrete. Fire spalling reduces the cross-sectional area and may lead to the direct exposure of rebars to flame, with a significant reduction of the load bearing capacity [1-2]. Two physical mechanisms are often associated with this phenomenon, namely: the build-up of pore pressure and thermal stresses in the concrete when exposed to a rapidly increasing temperature [1-2]. Despite a large body of literature, controversial opinions exist about the causes of spalling. It is worth noting, however, that a huge number of experimental studies have been reported in the literature on unloaded specimens [1-3], while very limited experimental studies are available on the fire spalling behaviour of concrete under mechanical loading condition [4-9].

Kodur et al. 2007 [4] and Boström et al. 2007 [5] concluded that the type of loading and its intensity have significant influence on fire spalling behaviour

Md Jihad Miah [1], Francesco Lo Monte [2], Pierre Pimienta [1] and Roberto Felicetti [2]
[1]Université Paris Est, Centre Scientifique et Technique du Bâtiment (CSTB), France
[2] Department of Civil and Environmental Engineering, Politecnico di Milano, Milan, Italy
Jihad.miah@cstb.fr,francesco.lo@polimi.it, pierre.pimienta@cstb.fr, roberto.felicetti@polimi.it

of concrete.

of concrete.

Mechanically loaded specimens during heating are more susceptible to spalling than unloaded members [4-5]. Numerical and experimental investigations by Ali et al. 2010 [6] have shown that increasing loading levels enhance the probability of concrete spalling, particularly under low heating regimes. Miah et al. 2015 [7] investigation on uniaxially loaded cubes have shown that the amount of spalling increases with the applied compressive load. The above reported studies clearly proved that the mechanical loading during fire is a key parameter influencing spalling behaviour of concrete. Within this context, a novel test procedure has been design at the Politecnico di Milano to perform fire spalling test under a constant biaxial membrane loading and ISO 834-1 standard fire curve. In a previous experimental campaign on High-Performance Concrete, explosive spalling was observed in plain concrete slab loaded at 10 MPa and the process involved the whole heated area of the specimen [8-9].

The cement industry has recently shown a significant interest in blast furnace slag based cement because of its very good durability performance as low chloride diffusion and lower carbon footprint. The existing literature does not provide detailed investigation of the fire behaviour of concrete made with blast furnace slag based cement (CEM III in Europe), especially spalling process of concrete in fire.

The lack of published test results on the role of mechanical loading and cement type on fire spalling behaviour of concrete provides the motivation for the experimental program in this paper. The test results including spalling volume, pore pressure, and displacements are presented.

EXPERIMENTAL SETUP AND PROGRAM

To investigate the interaction between pore pressure and thermo-mechanical stresses in triggering spalling, mid-size concrete slabs (800 x 800 x 100 mm^3) were subjected to ISO 834-1fire curve at different levels of biaxial membrane loading. Two ordinary concretes (B40-II and B40-III) made respectively with CEM II (CEM II/A-LL 42.5 R CE CP2 NF) and CEM III (CEM III/A 42.5 N CE CP1 NF) cements have been investigated. The CEM II cement contains 85% of clinker, 12% of calcareous fillers and 3% of slag, while the CEM III cement contains 54% of clinker and 43% of slag. The concrete slabs were placed on top of the horizontal furnace, within a loading system consisting in a welded steel frame fitted with hydraulic jacks. Eight mid-size concrete slabs (4 of B40-II and 4 of B40-III) were heated at the bottom face according to ISO 834-1fire curve. In order to limit the temperature in the hydraulic jacks, only the central part of the slab (600 x 600 mm^2) was heated to keep the external concrete rim colder. To reduce the confining effect exerted by this colder rim, 16 radial cuts (around 5 mm thick) were performed, aimed at breaking its mechanical continuity (see figure 1). The furnace was heated by a propane burner with a control system able to strictly follow the ISO 834-1 fire curve. A constant biaxial compressive load was applied with 8 hydraulic jacks (see figure 1) before heating and then the load was kept constant throughout the fire test. Four different levels of biaxial loading (0, 0.5, 5 and 10 MPa for B40-II and 0.5, 1.5, 5 and 10 MPa for B40-III) have been investigated. In order to avoid complete collapse of the specimen and to compare the amount of spalling at different levels of biaxial loading, the tests were stopped after thirty minutes of fire for spalled specimens, while no spall specimen was heated for 1 hour to monitor the flexural behaviour of heated concrete.

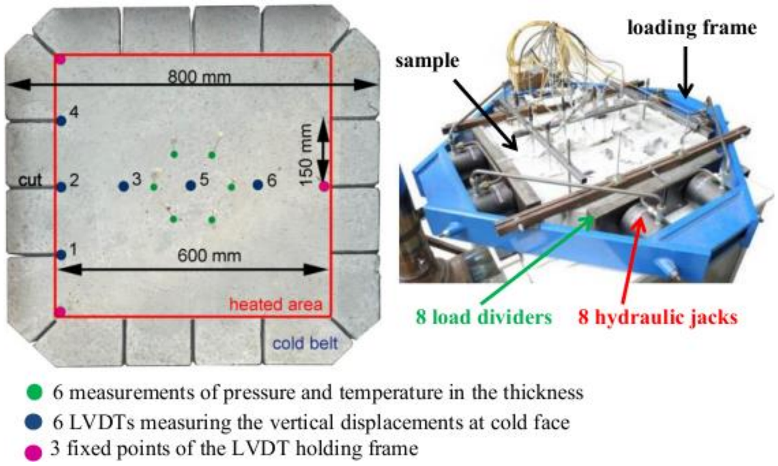

Figure 1. Concrete slab and measuring points (left); biaxial membrane loading system (right).

During the fire tests, both pore pressure and temperature were monitored (according to the system described by Felicetti et al. 2012 [10]) at 6 different depths of 5, 10, 20, 30, 40 and 50 mm from the exposed face of the slab. The flexural behaviour was monitored through 6 Linear Voltage Displacement Transducers (LVDT) placed on one center line and on one edge of the slab to measure the out of plane displacements at the top (cold) face. A more detailed description about the test set-up and the test method is given by Lo Monte et al. 2015 [8-9]. After each test, the thickness profile of the spalled area was measured at room temperature by using a laser profilometer. The compressive strength of both concretes measured on cylinder (Ø 160 mm x h 320 mm) at 28 days and 90 days are 40 MPa and 51 MPa, respectively. Further details about mix design and mechanical properties of these concretes are presented in Miah et al. 2015 [7, 11]. The initial water content of B40-II and B4-III concretes after drying at 80 °C was 4.0% and 5.3 %, respectively. This water content refers to the initial free water of the fire test specimens.

RESULTS AND DISCUSSION

SPALLING

Figures 2 presents the image of the exposed face of B40-II and B40-III concretes slabs exposed to ISO 834-1 fire at 4 different levels of biaxial loading. The experimental results have shown that the loaded specimens are more prone to spalling than unloaded specimens. Similar behaviour has been observed in uniaxially loaded concrete cubes during ISO 834-1 fire tests [7]. Spalling was accompanied by a loud "popping" sound as concrete fragments were released layer-by-layer from the concrete surface. The time of first spall is about 6-10 minutes of fire. The oven temperature at the onset of spalling was 600-650°C, whereas the measured temperature at the depth of 5 mm from the exposed surface was about 130-170 °C. The collapse of the slabs occurred at 29.7 min for the specimen loaded at 5 MPa (B40-II only) and 25.1 / 24.4 min for the specimens loaded at 10 MPa (B40-II / B40-III); then the heating was stopped. Spalling leads to a maximum loss of up to 73% and 87% of the total thickness of B40-II concrete loaded at 5 and 10 MPa, respectively, and 76% of the total thickness of B40-III concrete loaded at 10 MPa (Figure 3 right). Due to early failure behaviour of both concretes loaded at 10 MPa, the spalling volumes are decreased at 10 MPa than the specimens loaded at 5 MPa (see figure 3a). After cool down the furnace, the mass of the concrete spalled fragments were weighed. The mass of the concrete spalled fragments loaded at 5 and 10 MPa are respectively 35.3 kg and 33.1 kg for B40-II and 30.9 kg and 28.6 kg for B40-III concrete. It is interesting to see that the whole heated area of the concrete specimen was spalled, except B40-III concrete slabs loaded at 0.5 MPa and 1.5 MPa. Unfortunately, the temperature of the furnace was lower in B40-III concrete loaded at 1.5 MPa than the target temperature due to a problem in the gas supply after 10 minutes of fire duration. Therefore the amount of spalling was lower in B40-III concrete loaded at 1.5 MPa than the expected, see figures 2 and 3.

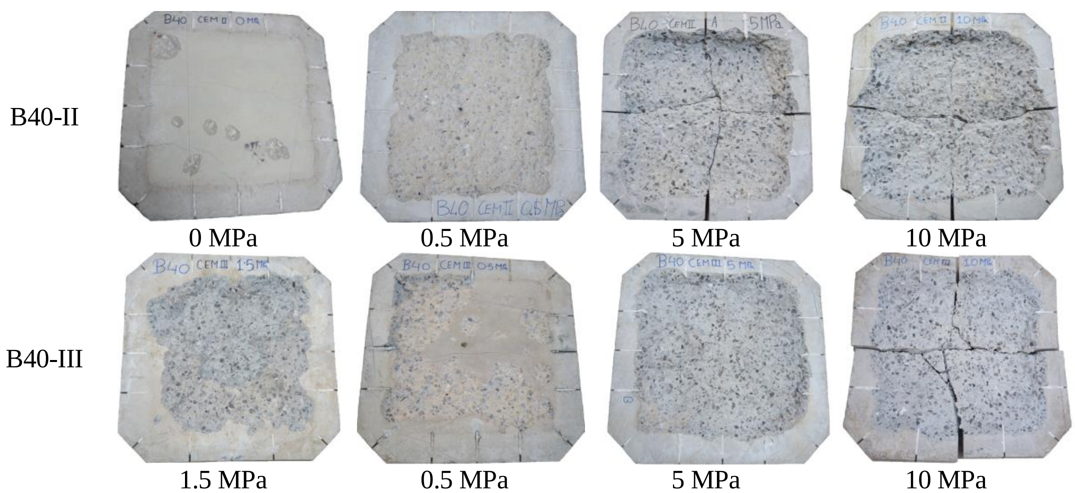

Figure 2. Exposed face of the B40-II and B40-III slabs exposed to ISO 834-1 fire.

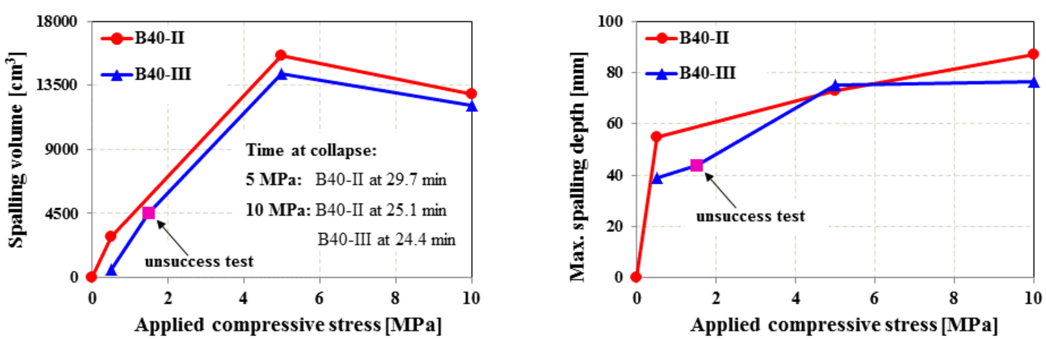

Figure 3. Spalling volume (left) and maximum spalling depth (right) of B40-II and B40-III concretes.

It is worth noting that the spalling behaviour of concrete under very small load (0.5 MPa) and no load (0 MPa) has two different scenarios. On the one hand, a uniform erosion extended to the whole heated area has been observed in B40-II concrete loaded at 0.5 MPa, for an average spalling depth of 16 mm. On the other hand, no spalling has been observed in unloaded B40-II specimen. These results tend to show that very small loads can influence the spalling behaviour of concrete, even though 0.5 MPa stress is small compared to the tensile strength of concrete (tensile strength at 28 days = 4 MPa). This implies that the permeability may play an important role during heating, since the development of cracking is more restricted in loaded than in unloaded specimens [12-13].Indeed, lower permeability reduces transport of water vapour inside the concrete and then induces faster build-up of pore pressures. Higher pore pressure was observed in B40-II specimen loaded at 0.5 MPa than the unloaded specimen (see figure 4c). This higher pore pressure of loaded specimen with the combination of stresses (due to thermal gradients and external load) increased the risk of spalling.

Higher spalling has been observed in B40-II than the B40-III (figures 2 and 3). These results are in good agreement with the uniaxially loaded cube test results [7]. Contrary to B40-II, the B40-III specimen loaded at 5 MPa did not collapse after 30 min heating, also less and non-uniform spalling behaviour has been observed in B40-III specimens loaded at 0.5 MPa compared to B40-II at the same loading level.

TEMPERATURE AND PORE PRESSURE

Temperature trends at 6 different depths along the slab thickness (5, 10, 20, 30, 40 and 50 mm) and at the hot and cold faces are shown in figures4a-b as functions of time for B40-II concrete exposed to ISO 834-1 fire curve under mean biaxial compressive stress of 0 and 10 MPa. It can be seen that the measured air temperature in the furnace followed the target ISO 834-1 fire curve, except after the first spalling event. An initial temperature plateau can be seen at around 150 °C (onset of water vaporization which consumes a significant amount of energy). In principle, the development of temperature within a heated concrete specimen is governed by its thermal diffusivity, i.e. thermal conductivity over heat capacity. The imposition of the external mechanical loading should not have any effect on these properties, except for the rate of mass loss at elevated temperatures due to the formation of cracks and release of hot vapour. The experimental results showed that higher temperatures were exhibited by loaded specimen. This is caused by spalling, since thickness reduction leads to the direct exposure of thermocouples to flame, hence to higher temperature rise.

However, it can be seen that the development of pore pressure seems to be different for specimens with no load or limited load (0.5 MPa). Maximum pore pressures was 0.84 MPa and 1.28 MPa in the former and in the latter case, respectively, for B40-II concrete. Even if the temperature of the furnace was lower after 10 min of fire in B40-III loaded at 1.5 MPa, the maximum pore pressure of 2.2 MPa was measured at 10 mm depth after 17 min of fire. From these values, it seems that there was some effect of loading on permeability of hot concrete which can influence the build-up of pore pressure during heating. The permeability increase is favoured by the thermal incompatibility between cement pastes and aggregates, which brings in tensile stresses in the matrix leading to cracking [1]. As a result, vapour and liquid water can escape from the specimen, this affecting the build-up of pore pressure. As mentioned before, the development of cracking is more limited in loaded specimen than in unloaded specimens [12-13]. In the literature, it was found that the permeability of concrete during heating under compressive loading (stress levels lower than 80% of the strength) is smaller than the permeability measured after unloading [14]. It can be seen that higher load (10 MPa) can affect the build-up of pore pressure during heating. In this case, spalling might take place before the pressure peak reaches the sensors; afterwards pressure build-up is impaired by increased permeability because of cracking.

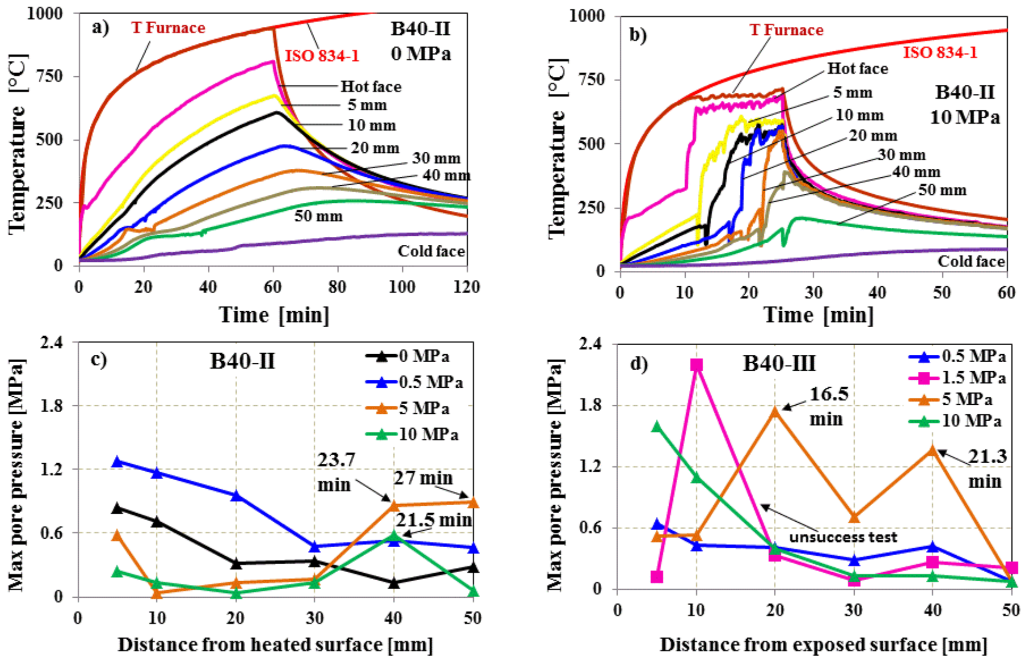

Figure 4. Development of temperature and pore pressure inside the B40-II and B40-III concrete exposed to ISO 834-1 fire at different levels of biaxial compressive loading.

Nevertheless, higher pore pressures were measured in B40-III than B40-II (contrary to 0.5 MPa). Firstly, this could be due to the higher thermal damage of B40-II specimens during heating (higher spalling in B40-II than B40-III), which increase the permeability and then decrease the pore pressure. The second reason is that the initial water content of B40-III concrete is about 1.3 % higher than the B40-II concrete. This higher water content could be leading higher pore pressure in B40-III than the B40-II.

FLEXURAL BEHAVIOUR

Figure 5 presents the deformed shape of the slab specimens in the x and y axes (symbols on each line depict the measurement points). It can be seen that the applied external mechanical loading reduces the displacement of the slabs during heating. When heating concrete, initial sagging curvature towards the fire prevails due to the thermal dilation of the bottom heated face. Afterwards, the decay of concrete stiffness in the hot layers makes the bottom part of the slab more and more deformable. When this layer becomes significantly weaker, a reverse hogging curvature may occur due to the presence of applied external mechanical loading during heating. In fact, the line of action of the applied load remains in the original centre-line of the slab thickness, this resulting in an eccentric force due to the significant degradation of stiffness at the exposed side of the slab. As a consequence, the combined effects (sagging curvature due to thermal loading and hogging curvature due to the presence of mechanical loading caused by eccentric force) lead to lower curvature in the loaded specimen than in unloaded specimens. As a consequence, upward deflections have been observed in the most loaded specimens due to the larger eccentricity caused by the higher reduction of thickness (see figures 5c-d). In the end, a sudden failure was reached in these latter tests due to excessive bending and lack of reinforcement.

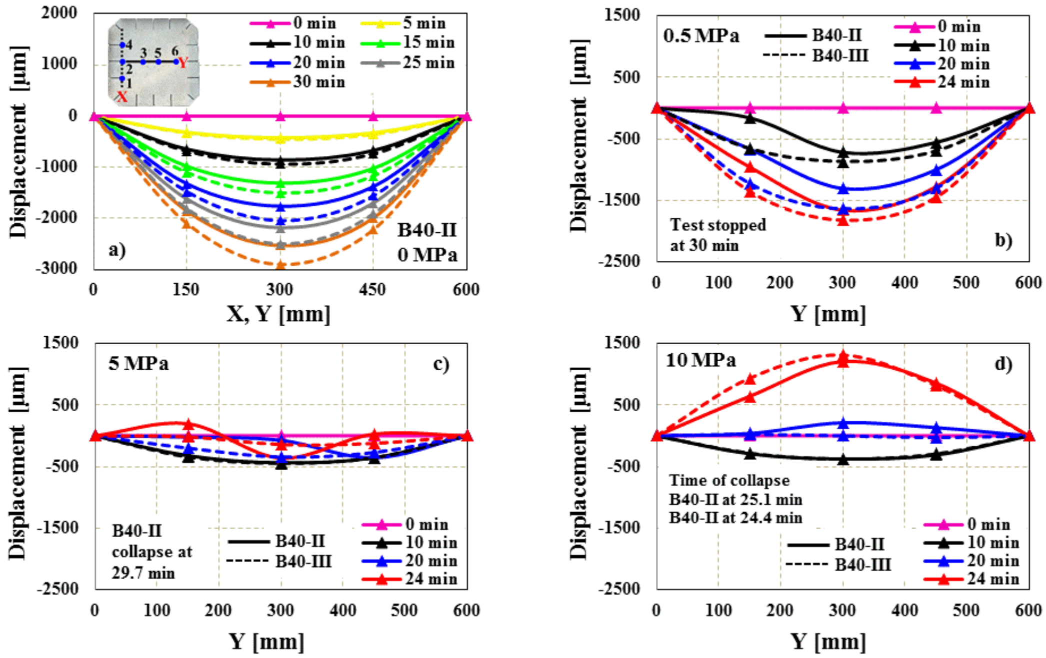

Figure 5. Deformed shape of B40-II slabs in the x and y axes (see top-left plot). Almost similar displacements have been observed in B40-III concrete slabs.

When curvature sign changes in loaded specimens, namely from sagging to hogging, concrete is pressed at the bottom side, this probably closing macro-cracks and then fostering the increase of pore pressure (see figures 4c-d and 5c-d). Due to higher reduction of the slab thickness caused by spalling, higher bending moment could develop due to higher eccentric force. Furthermore, lower displacements have been observed in B40-II than B40-III, see figures 5b-d. Due to higher reduction of thickness caused by spalling, a higher load eccentricity was introduced in B40-II, resulting in lower deflections.

CONCLUSIONS

The fire spalling behaviour of concrete exposed to ISO 834-1 fire under different levels of biaxial loading has been documented. Two ordinary concretes (B40-II and B40-III) made respectively with CEM II and CEM III cements have been investigated. The following conclusions can be drawn based on the results presented in this study.

The experimental test results have clearly shown that the mechanical loading and loading levels have significant influence on the fire spalling behaviour of concrete. Loaded specimens are more susceptible to spalling than unloaded specimens. The amount of spalling was increased by higher values of applied compressive load.

It was found that the stresses due to both thermal gradients and external load in combination with pore pressures can increase the risk of spalling. These results show that the compressive stress is one of the most important parameters that fire resistant design of concrete structures should take into account when considering spalling.

Concrete made with CEM III cement (B40-III: 43 % of slag) exhibited less spalling than CEM II cement concrete (B40-II: 3 % of slag). These results tend to show that the studied B40-III concrete could be less sensitive to fire spalling.

REFERENCES

1. Kalifa, P., Menneteau, FD., and Quenard, D. 2000. "Spalling and Pore Pressure in HPC at High Temperatures," Cement and Concrete Research (2000), Vol. 30, pp. 1915-1927.
2. Khoury G. A., and Anderberg Y. (2000), "Concrete Spalling Review", Fire Safety Design, report submitted to the Swedish National Road Administration, Sweden.
3. Mindeguia JC. (2009). "Contribution Expérimental a la Compréhension des risqué d'Instabilité Thermiques des Béton," PhD Thesis (French), Université de Pau et des Pays de l'Adour, France.
4. Kodur, V. K. R., and Phan, L. (2007). "Critical Factors Governing the Fire Performance of High Strength Concrete Systems," Fire Safety Journal 42, pp. 482-488.
5. Boström L., Wickström, U., and Adl-Zarrabi B. (2007). "Effect of Specimen Size and Loading Conditions on Spalling of Concrete", Fire and Materials, 31, pp. 173-186.
6. Ali, F., Nadjai, A., and Choi, S. (2010). "Numerical and Experimental Investigation of the Behavior of High Strength Concrete Columns in Fire," Engineering Structures 32, pp. 1236-1243.
7. Miah, M. J., Carré, H., Pimienta, P., Pinoteau, N., and La Borderie, C. (2015). "Effect of Uniaxial Mechanical Loading on Fire Spalling of Concrete," Proceedings of 4th International Workshop on Concrete Spalling due to Fire Exposure, October 8-9, 2015, Leipzig, Germany.
8. Lo Monte, F., Felicetti, R., Rossino, C., Piovan, A., and Scaciga, G. (2015). "In-Plane Loaded Concrete Slabs Subjected to Fire: A Novel Test Set-Up to Investigate Spalling," Proceedings of International Fire Safety Symposium, IFireSS 2015, Coimbra, Portugal, 20th to 22nd April 2015.
9. Lo Monte, F., Rossino, C., and Felicetti, R. (2015). "Spalling Test on Concrete Slabs Under Biaxial Membrane Loading," Proceedings of 4th International Workshop on Concrete Spalling due to Fire Exposure, October 8-9, 2015, Leipzig, Germany.
10. Felicetti, R., Lo Monte, F., and Pimienta, P. (2012). "The Influence of Pore Pressure on the Apparent Tensile Strength of Concrete," Proceeding of 7th International Conference on Structures in Fire, June 6-8, 2012, Zurich, Switzerland.
11. Miah, M. J., Pimienta, P., Carré, H., Pinoteau, N., and La Borderie, C. (2015). "Fire Spalling of Concrete: Effect of Cement Type," Proceedings of 4th International Workshop on Concrete Spalling due to Fire Exposure, October 8-9, 2015, Leipzig, Germany.
12. Castillo, C. and Durrani, A. J. (1990). "Effect of Transient High Temperature on High-Strength Concrete," ACI Materials Journal, V. 87, No. 1, pp. 47-53.
13. Jansson, R., and Boström, L. (2013). "Factors Influencing Fire Spalling of Self Compacting Concrete," Materials and Structures, 46, pp. 1683-1694.
14. Choinska, M., Khelidj, A., Chatzigeorgiou, G., Pijaudier-Cabot, G. (2007). "Effects and Interactions of Temperature and Stress-level Related Damage on Permeability of Concrete," Cement and Concrete Research 37 (2007) 79-88.

Effects of Polypropylene Fibers on Preventing Concrete Spalling In Fire

FANGXIA LU and MARIO FONTANA

ABSTRACT

The addition of polypropylene fibers (PP-fibers) has been proved effective to prevent explosive spalling of concrete elements in tests. With PP-fibers, the permeability of concrete will increase significantly above the melting of PP-fibers, as a results, high pore pressure can be prevented. To investigate the effects, the permeability of concrete with PP-fibers has been measured. The effect on explosive spalling of concrete is investigated by experimental and numerical methods. Apart from the amount, the fiber geometry must be taken into account. For the PP-fiber combination investigated by fire test, the recommended amount by Eurocode 2 is effective for these thin PP-fibers. The test result has been simulated by a spalling model. The spalling model considers the influences from the combination of PP-fiber with a simplified increasing factor, the application of other types and amounts of PP-fibers can be evaluated by this model.

INTRODUCTION

High performance concrete (HPC) shows excellent durability at room temperature, however, concrete spalling induced by fire exposure is a major concern in the use of HPC [1]. To eliminate the spalling risk, many protective methods have been investigated [2]. It is shown that the addition of polypropylene fibers (PP-fibers) can reduce the spalling risk by increasing the permeability of concrete at high temperatures [3]. The use of PP-fiber is normally expressed by the ratio of weight per volume, e.g. 2 kg/m^3 as recommended by Eurocode 2. However, fire tests and permeability measurements of concrete with PP-fibers have shown that the amount by weight was not the only factor that could influence the spalling protection [2]. The fiber geometry also affects the increase of permeability.

This paper focuses on the use of PP-fibers to prevent concrete spalling in case of fire. The influences from diameters and amounts of PP-fibers have been investigated by permeability measurement. The combinations of PP-fibers were compared with respect to the increase of permeability. The application of the selected combination of PP-fibers was studied in fire tests. The effect from the PP-fibers has been simulated by a permeability model. Reduced spalling risk in specimen with the selected combination of PP-fibers has been predicted by a spalling model, effects from amounts and fiber geometry are considered by an increasing factor. This simplified method to estimate the use of PP-fibers was developed and a combination of PP-fibers has been proposed.

Dr. Fangxia Lu, IBK ETH Zürich, Stefano-Franscini-Platz 5, 8093 Zürich, Switzerland.
Prof. Mario Fontana, IBK ETH Zürich, Stefano-Franscini-Platz 5, 8093 Zürich, Switzerland.

PERMEABILITY OF CONCRETE WITH PP-FIBERS

In the experimental study of explosive spalling, concrete is treated as a porous medium. The permeability is an important property for the porous medium, which describes the conductivity of concrete with respect to a fluid (vapour or liquid) flow. To study the explosive spalling, various experimental studies have been carried out and the test results have shown that the permeability of concrete varies with temperature, moisture content and pore pressure. Experiments and numerical studies have shown that the low permeability of high performance concrete (HPC) makes it more susceptible to explosive spalling [4]. The use of PP-fibers increases the permeability of concrete above the melting point of PP-fibers, as a result, the high pore pressure in concrete induced by fire exposure is prevented. To investigate the effect from PP-fibers on concrete spalling, the permeability measurement of concrete specimens with various PP-fiber combinations has been carried out.

Figure 1. Residual permeability measuring device according to the Torrent method.

As for the test methods, hot- and residual permeability has been measured at ETH [2]. Test results indicated that both methods could illustrate the permeability change with temperature. However, the current hot permeability-measuring device was not reliable due to leakage because of insufficient sealing or decomposition of the silicone [5]. The Torrent method measures the permeability of the specimens after cooling from high temperatures, therefore is more applicable. As the residual permeability was found similar to the hot permeability [6], the residual permeability-measuring device according to the Torrent method (see Figure 1) was chosen to study the type and amount of PP-fibers. A hot permeability device according to Torrent method is under development, the result of residual permeability will be further compared with the hot permeability in the future.

To study the effects of fibers on the permeability of concrete, two types of PP-fibers with various amounts were added to the concrete mix HPC_1, which is prone to explosive spalling at high temperature (see Figure 4) [2]. PP-fibers with diameters of 32 µm (Type 1) and 16 µm (Type 2) have been studied and the effects from amounts (1, 2 and 3 kg/m^3) on permeability have been compared. The details of mixtures with PP-fibers are listed in TABLE I. Concrete disks (ø = 150 mm, h = 60 mm) with the listed mixtures were dried to constant in mass at 105°C. For the residual permeability measurement, a heating rate of 5 K/min was selected.

TABLE I. MIXTURES USED IN THE PERMEABILITY TEST.

Mixture	Type of PP-fibers	Amount of PP-fibers
HPC_1	Without PP-fibers	-
V2		1 kg/m^3
V3	Type 1: ø = 32 µm, L = 6 mm	2 kg/m^3
V4		3 kg/m^3
V5		1 kg/m^3
V6	Type 2: ø = 18 µm, L = 6 mm	2 kg/m^3
V7		3 kg/m^3

After reaching the target temperature, specimens were conditioned for two hours in the furnace to achieve a homogeneous temperature distribution inside the specimens. The residual permeability measurement was carried out, when the surface temperature decreased to 80°C in ambient temperature. To illustrate the effect from PP-fibers, the results are presented as relative permeability to the initial permeability of the specimen at ambient temperature.

The test results indicated that with the same amount, thin PP-fibers were more effective in increasing the permeability of concrete. Figure 2 shows the relative permeability of HPC_1 (without PP-fibers), V2 (HPC_1 with Type 1) and V5 (HPC_1 with Type 2). Without PP-fibers, there was a drop of permeability in the temperature range from 150 °C to 250 °C, which is attributed to the change of moisture content [7]. With PP-fibers, a significant increase in permeability above the melting point of PP-fibers was observed. It can be seen that the permeability of specimen with 1 kg/m^3 of thin PP-fibers (16 µm) increased more significantly above the melting point of PP-fibers. The drop of permeability was already prevented by 1 kg/m^3 of Type 2 PP-fibers as well. The thin PP-fibers seemed more effective in increasing permeability. However, when the added amount is 2 kg/m^3 or higher, the difference was slight. All the tested PP-fibers with an amount of 2 kg/m^3 induced a similar increase of permeability above their melting points, regardless of the diameters of PP-fibers. As for the influence from the amount of PP-fibers, Figure 3 shows the permeability of HPC_1 with 1 kg/m^3 (V5), 2 kg/m^3 (V6) and 3 kg/m^3 (V7) of Type 2 PP-fibers. It can be seen that higher amount results in more significant increase in permeability. These results were used in the spalling model to evaluate the reduced spalling risk. Details are presented in later section.

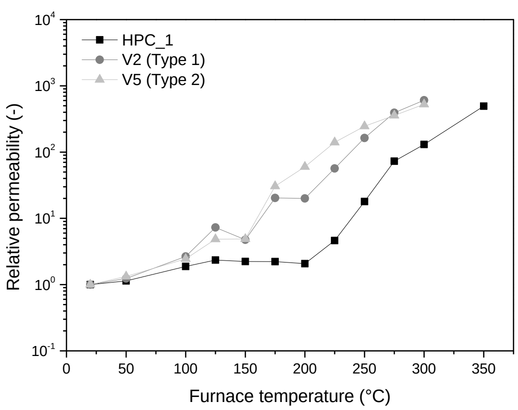

Figure 2. Relative permeability of concretes with Type 1 and Type 2 PP-fibers (1 kg/m^3).

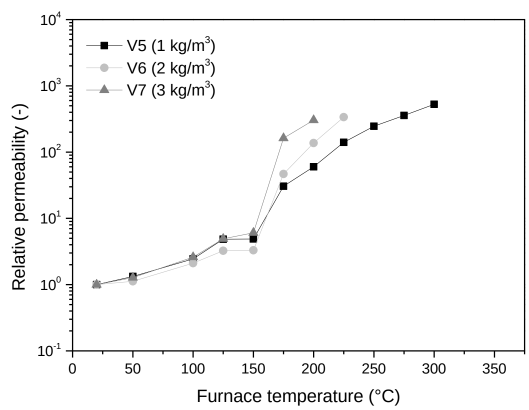

Figure 3. Relative permeability of concrete with various amounts of PP-fibers (Type 2).

FIRE TEST ON HPC SLABS

To investigate the effect of PP-fibers on preventing concrete spalling, fire tests on HPC slabs with and without PP-fibers have been carried out. To investigate the effects from PP-fibers, the dense mixture HPC_1 (TABLE I) was chosen, with a high compressive strength over 120 MPa [2]. A concrete slab made of HPC_1 with dimensions of $l \times w \times h = 1100 \times 900 \times 150$ mm^3 was tested, the ISO fire curve was applied during the heating period. The combinations of Typed 2 PP-fibers were added to the HPC_1 mixture. The amounts of 2 kg/m^3 and 3 kg/m^3 were tested simultaneously on the slab, which consists of two segments, each measuring $l \times w \times h = 1100 \times 450 \times 150$ mm^3.

As for the HPC_1 mixture, explosive spalling was observed in the dense slab without PP-fibers after 14 minutes of ISO fire exposure. The test was stopped manually after 30 minutes for safety reasons. Figure 4 shows the spalled HPC_1 slab after 30 minutes of ISO fire exposure. The concrete cover to the steel reinforcements is removed and the maximum spalling depth was over 60 mm. The severe explosive spalling illustrated the high risk of spalling in HPC_1. Protective method must be applied to reduce the spalling risk in HPC. The test on the slab with Type 2 fibers has shown that the tested combinations of PP-fibers were capable of preventing explosive spalling. No explosive spalling occurred in two hours of ISO fire exposure. Figure 5 shows the slab with Type 2 PP-fibers after 120 minutes. Both segments containing 2 kg/m^3 and 3 kg/m^3 of Type 2 PP-fibers the concrete slab remained intact. No significant difference was noticed between the two fiber combinations. With the amounts of 2 kg/m^3 and 3 kg/m^3, spalling was prevented for 120 minutes.

Figure 4. Spalling in slab made of HPC_1 after 30 min of ISO fire exposure. The spalling was observed after 14 min of heating.

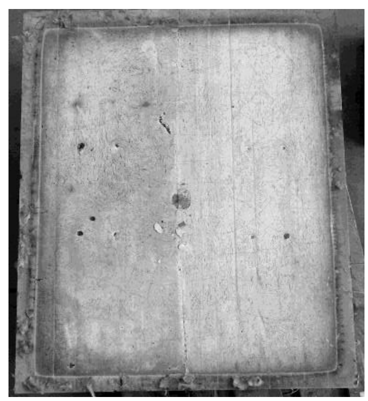

Figure 5. No spalling observed in slab containing Type 2 PP-fibers (left side: 2 kg/m^3, right side: 3 kg/m^3).

The Type 2 PP-fibers with the amount of 2 kg/m^3 have been proved effective to reduce the risk of concrete spalling in HPC. Considering the effects on permeability, the recommended amount of 2 kg/m^3 (Eurocode 2) is considered effective. With this amount, the influence from the types of PP-fibers is limited; the permeability of HPC increased similarly above the melting point of PP-fibers and explosive spalling is prevented. Lower amount of PP-fibers can increase the permeability as well, but the effect must be investigated considering the type of the fibers. To investigate other combinations of PP-fibers to prevent spalling, apart from fire test, a spalling model has been proposed, based on the increase of permeability, the use of other PP-fiber combinations will be investigated against the valid PP-fiber combination.

NUMERICAL INVESTIGATION

In the numerical investigation, the pore pressure was simulated by a thermo-hydro model (TH-model) and the spalling was predicted by a spalling model [3]. The increased permeability caused by the addition of PP-fibers was taken into account by the permeability model; an increasing factor has been applied to consider the effects from various PP-fiber combinations [8]. The results of pore pressure have been investigated against the measured values in the tests [9]. The tests of HPC_1 and V6 (2 kg/m^3 of Type 2 PP-fibers) have been simulated.

Without PP-fibers, the spalling in HPC_1 was predicted after 19 minutes (Test 14 minutes) of ISO fire exposure. As shown in Figure 6, high pore pressure was predicted in HPC_1. At the depth of 5 mm, the pore pressure reached 1 MPa. In the deeper sections, the pore pressure was higher. According to the spalling model, the pore pressure was combined with thermal stresses, the spalling will be predicted when the spalling criterion reaches the temperature dependent tensile strength in the spalling temperature range (from 250 °C to 400 °C, which is plotted as solid lines). In Figure 7, it can be seen that the spalling criterion reached the tensile strength at a depth of 7 mm in the spalling temperature range. The result agreed well with the observation in test, the high spalling risk in HPC_1 has been predicted.

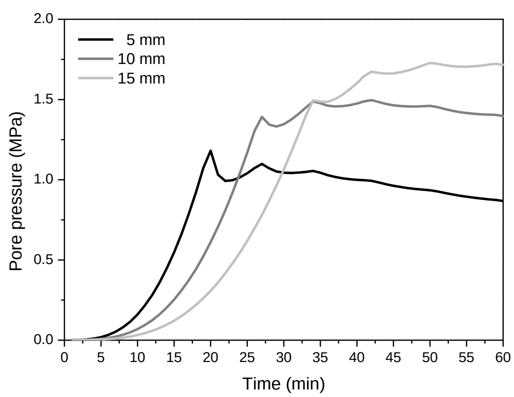

Figure 6. Predicted pore pressure in HPC_1 slab under ISO fire.

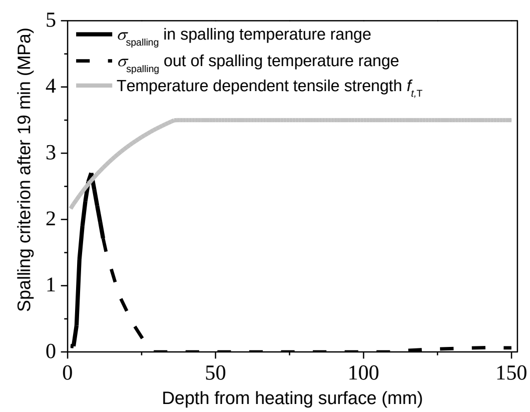

Figure 7. Spalling predicted for the HPC_1 after 19 minutes of ISO fire exposure.

The permeability measurement has shown that the application of 2 kg/m^3 of Type 2 PP-fibers resulted in an increase in permeability. This effect has been simulated by a simplified permeability model using an increasing factor. The increasing factor accounts for the use of the PP-fibers. Based on the permeability measurement, the increasing factor has been proposed to be 20 for this type of PP-fiber. The increased permeability above the melting point of PP-fibers agreed well with the test results, as shown in Figure 8. This result has been used in the TH-model to simulate the pore pressure in V6.

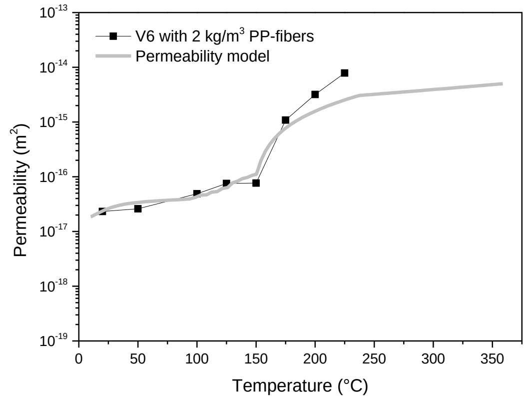

Figure 8. Comparison of predicted and measured permeability of V6 (with 2 kg/m^3 of Type 2 PP-fibers).

The pore pressure predicted by TH-model is shown in Figure 9. It can be seen that in V6, the maximum pore pressure at 15 mm was less than 0.8 MPa, the pore pressured decreased significantly compared to HPC_1. The increase of permeability induced by the melting of PP-fibers above 160 °C further accelerated the drying of moisture in the specimen, preventing high pore pressure.

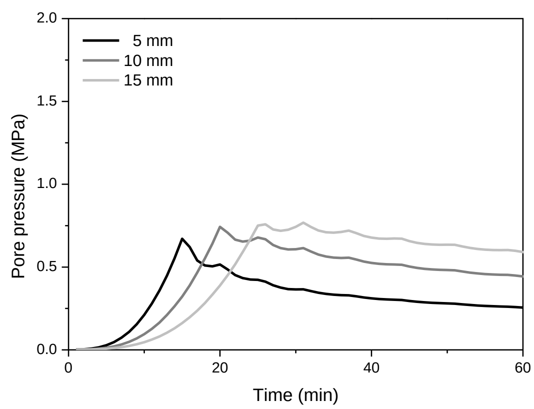

Figure 9. Predicted pore pressure (TH-model) in HPC_1 with 2 kg/m^3 of Type 2 PP-fibers.

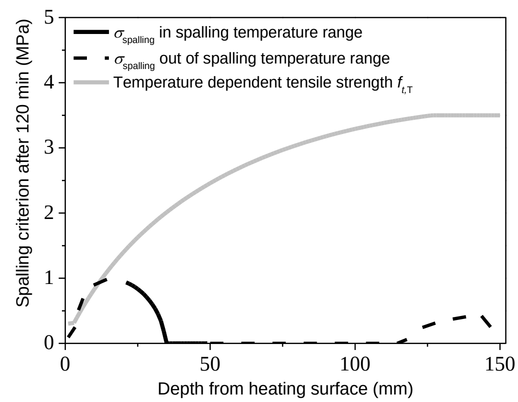

Figure 10. No spalling is predicted by the spalling model after 120 min of ISO fire exposure.

To reduce the risk of spalling, the effect from the addition of 2 kg/m^3 of Type 2 PP-fibers has been considered. No spalling was predicted in 120 minutes by the spalling model. The spalling criterion and the temperature dependent tensile strength are presented in Figure 10. The effect from the validated PP-fiber combination has been taken into account, the spalling criterion reached the tensile strength out of the spalling temperature range, and therefore, no spalling was predicted in two hours.

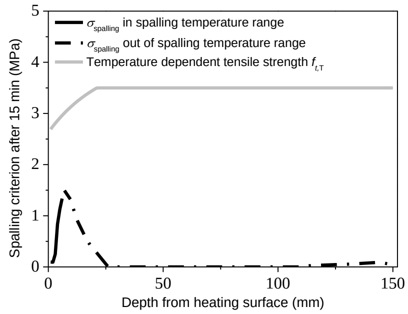

a) Spalling criterion after 15 minutes of ISO fire exposure.

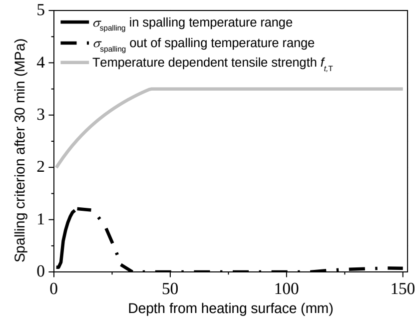

b) Spalling criterion after 30 minutes of ISO fire exposure.

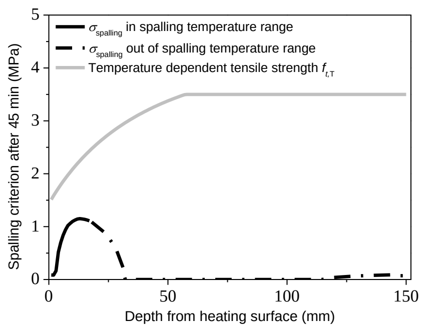

c) Spalling criterion after 45 minutes of ISO fire exposure.

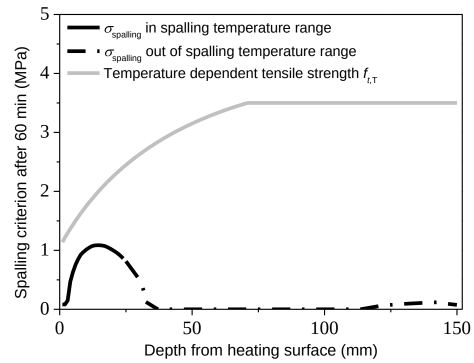

d) Spalling criterion after 60 minutes of ISO fire exposure.

Figure 11. The change of spalling criteria of HPC_1 with 2 kg/m^3 of Type 2 PP-fibers.

As the influence from PP-fibers on the temperature distribution and tensile strength was limited [2], the reduced spalling risk was attributed to the lower pore pressure. The pore pressure in V6 (2 kg/m^3 of type 2 PP-fibers) was predicted lower; accordingly the spalling criterion was lower in the spalling model. The development of spalling criterion in V6 is shown in Figure 11, it can be seen that the spalling criterion is reduced: after 15 minutes of heating, spalling criterion in V6 is about 50 % lower than that of HPC_1. At the later stage of heating, the spalling criterion is still low in V6 and the temperature in the near surface region is out of the spalling temperature range. Therefore, even though the tensile strength decreased to the level of spalling criterion after about 90 minutes, no spalling is predicted. This degradation of concrete due to the high temperature is different from spalling. The concrete cover to the steel reinforcement remained in place and worked as isolation for the reinforcements. The application of PP-fibers can prevent the resistance of a HPC element to decrease markedly due to the rapid temperature rise of reinforcement.

SUMMARY

The experimental and numerical investigations of the application of PP-fibers to prevent concrete spalling have been described. Here are some key conclusions summarized in the context:

- High performance concrete (HPC) is prone to explosive spalling, which may lead to the exposure of reinforcement to fire. The risk of spalling in HPC must be controlled to achieve adequate bearing capacity.

- The effect from PP-fibers has been related to permeability. A higher amount of PP-fibers increases the permeability more significantly. Above 2 kg/m^3, the effect from the type of PP-fibers is reduced and the recommended amount (2 kg/m^3) by Eurocode 2 is considered effective for most types of PP-fibers.
- Fire test have shown that this PP-fiber amount is able to prevent concrete spalling in fire test. With 2 kg/m^3 of Type 2 fibers (ø = 18 µm) no spalling was observed after 120 minutes of ISO fire exposure. This PP-fiber combination has been investigated by fire test.
- The TH-model and spalling model consider the effect from PP-fibers; reduced spalling risk has been predicted. The numerical method will facilitate the use of PP-fibers to prevent concrete spalling. Effects from other PP-fiber combinations will be compared with the validated combination of 2 kg/m^3 of Type 2 PP-fibers.
- Further tests on other PP-fibers combinations are necessary to verify the method for its practical applications in real structures.
- A new experimental setup to measure the hot-permeability is under development.

REFERENCES

1. Kodur V. K. and Phan L. (2007), Critical factors governing the fire performance of high strength concrete systems. Fire Safety Journal, 2007. 42(6-7): p. 482-488.
2. Klingsch E., Frangi A. and Fontana M. (2013), Explosive spalling of concrete in fire, Test report. IBK Tests report No. 352. 2013: Institute of Structural Engineering (IBK), ETH Zurich, Switzerland.
3. Lu F. and Fontana M. (2015), A thermo-hydro model for predicting spalling and evaluating the protective methods, 4th International RILEM Workshop on Concrete spalling due to fire exposure (IWCS), Leipzig, Germany.
4. Khoury G. (2000), Effect of fire on concrete and concrete structures, Progress in Structural Engineering and Materials Volume 2, Issue 4, pp 429-447.
5. Klingsch E, Lu F., Käßmann R. and Tan K. H. (2015), Tests on the hot and residual permeability of concrete at high temperatures, 4th International RILEM Workshop on Concrete spalling due to fire exposure (IWCS), Leipzig, Germany.
6. Bošnjak J., Ožbolz J., Sharma A. and Periškiæ G. (2013), Permeability of concrete at high temperatures and modelling of explosive spalling. 8th International Conference on Fracture Mechanics of Concrete and Concrete Structure, Toledo, Spain, March 10-14.
7. Lu F., Klingsch E., Fontana M. and Fernando D. (2014), Improved Permeability Model For Concrete At High Temperature, 8th International Conference on Structures in Fire Shanghai, China, June 11-13.
8. Lu F., Klingsch E. and Fontana M. (2015), Protection methods against the explosive spalling of concrete, PROTECT 2015—Fifth International Workshop on Performance, Protection & Strengthening of Structures under Extreme Loading, East Lansing, MI, USA, June 28-30.
9. Mindeguia J. C., Pimienta P., Noumowe A.and Kanema M. (2010), Temperature, pore pressure and mass variation of concrete subjected to high temperature – Experimental and numerical discussion on spalling risk, Cement and Concrete Research 40, 2010, 477-487.
10. Dwaikat M.B. and Kodur V.K., (2009), Hydrothermal Model for Predicting Fire Induced Spalling in Concrete Structural Systems, Fire Safety Journal, 44(3), pp. 425-434.

Reuse of Waste Tyre Fibres in Concrete—Fire-Spalling Mitigation

SHUN HEY DAWN HOU[1], SHAN-SHAN HUANG[1], HARRIS ANGELAKOPOULOS[2], KYPROS PILAKOUTAS[1] and IAN BURGESS[1]

ABSTRACT

This paper presents an experimental study investigating the effectiveness of reused tyre polymer fibres (RTPF) and reused tyre steel fibres (RTSF) in high-strength concrete to mitigate fire-induced spalling. Concrete is an inherently fire resistant material due to its low thermal conductivity and non-combustibility. Rapid advances have been made in the last few decades to improve the performance of concrete in large-scale structures (e.g. tunnels), which are driven mainly by factors (e.g. strength, cost and sustainability) other than fire safety. It has been found that modern high performance, high strength concrete is more vulnerable to fire-induced spalling. Many research have been carried out to improve the resistance of such concrete against fire-induced spalling, and the most common solution is the addition of polypropylene fibres (PPF).

Each year in the EU, more than 3.5 million tonnes of tyres reach the end of their lives. These tyres comprise roughly 15% and 5% (by weight) steel and polymer fibre reinforcements, respectively. These fibres are then extracted during the tyre recycling process, but they are mostly landfilled or used as fuel since they are too agglomerated and contaminated by rubber to find alternative use. A series of concrete specimens with RTPF and RTSF were tested under thermo-mechanical loading. The results indicate the potential of replacing the manufactured fibres with these re-used ones to mitigate fire-induced spalling in concrete.

INTRODUCTION

In recent years, the fire safety of tunnels has become an increasingly concerned issue after the occurrence of various fire incidents such as the Mont Blanc Tunnel fire and the Channel Tunnel fire, which posed serious threats to human lives and economy [1][2]. The causes of spalling are generally understood as the differential thermal stresses and excessive pore pressure close to the heated surface of concrete. Severe fire-induced spalling implies potential failure of concrete structures and can result in significant repair costs. High performance (high-strength, self-compacting) concrete is increasingly used to replace normal strength concrete [3]. Such concrete is however more vulnerable to fire spalling, mainly due to its reduced permeability and porosity [4].

[1]Department of Civil and Structural Engineering, University of Sheffield, Sir Frederick Mappin Building, Mappin Street, Sheffield S1 3JD, United Kingdom.
[2]Twincon Ltd., UK

Past research has shown that PPF can be effective in mitigating fire spalling [4][5] and steel fibre could potentially control spalling (i.e. by delaying the spalling time and/or by reducing the spalling depth) by reducing crack propagation in concrete when subjected to high temperature [6]. It is apparent that the combination of PPF and steel fibre could result in desirable thermal stability in concrete. In addition, steel fibres are often used to replace (partially or totally) the conventional steel rebars in tunnel linings. Therefore, the test specimens of this research were all with steel fibres, except the reference plain concrete mix.

In the EU alone, an estimated 63,000 tonnes of polymer fibres are generated each year as a by-product of the recycling (for recovering rubber) of tyres [7]. These fibres are very difficult to store because they are very easily carried away by the wind and due to their large volume and high flammability. Currently, they are mainly landfilled or incinerated [8]. As for re-used tyre steel fibres, their cost can potentially be much lower than industrially produced steel fibres and re-bars. The potential supply of RTSF would also exceed the current demand for steel fibres [9]. All of the above imply the need and possibility of replacing industrialized fibres with the reused ones.

This study examines the feasibility of replacing the manufactured fibres with RTPF and RTSF for the prevention of fire-induced spalling, as part of ANAGENNISI [10], a European collaborative project exploring the reuse of tyre components in concrete.

FIBRE PROCESSING FOR REUSE

Currently, polymer fibres extracted from tyres are too contaminated with rubber and too tangled to be reused as a construction material. Techniques for removing rubber contamination and separating tangled filaments for the large-scale production of RTPF do not exist. In this research, a screening technique (using vibrating sieves) was employed to remove the majority of rubber dusts and particles for the purpose of laboratory testing. In addition, RTPF was integrated into concrete by manually sieving them into concrete then mixing the tangled fibre (remained on top of the sieve) in water with electric mixer, which was proven sufficient to uniformly disperse RTPF in the concrete mix for lab application. RTSF and RTPF used in the experimental testing are shown in Figure 1.

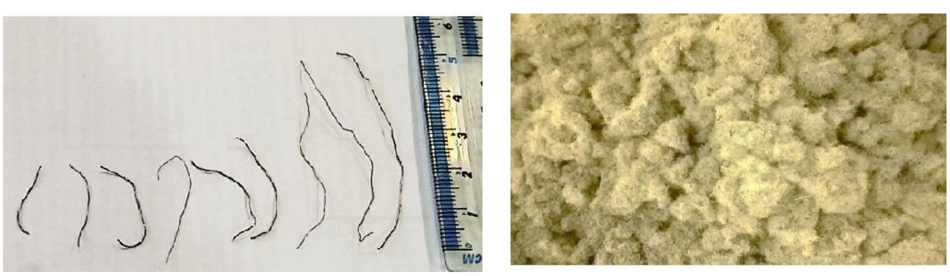

Figure 1. Reused tyre steel fibres (left) and reused tyre polymer fibres (right) after cleaning.

EXPERIMENTAL DETAILS

Studied Parameters

A C70 concrete mix has been chosen for this study. Concrete specimens with steel mesh, RTSF or RTSF/RTPF blends were cast. The size of the specimens is 200mm ×

200mm × 500mm. They are named as PC, SFC, SF2PFC, and SF5PFC, as shown in Table I. PC is the reference plain concrete mix; SFC contains 40 kg/m^3 RTSF; SF2PFC contains 40 kg/m^3 RTSF and 2kg/m^3 RTPF based on the EC2 [11] recommended PPF dosage; SF5PFC contains 40 kg/m^3 RTSF and 5kg/m^3 RTPF. The amount of steel mesh and RTSF used aims to reflect typical weight of steel reinforcement in precast tunnel segments. The steel mesh is of 50mm×50mm spacing, Ø5mm, with a 30mm cover. Thermocouples were cast into specimens at 1mm, 10mm and 50mm from the heated surface of the specimens. All tests were conducted in triplicate. The specimens were cured in the mist room with temperature of approximately 20°C and 60% relative humidity for 28 days to 56 days.

TABLE I. CONCRETE MIX PROPORTIONS.

Type	***W/C***	**Quantity (kg/m^3)**								
	(%)	**CEM**	**CAGG**	**FAGG**	**W**	**PFA**	**SP**	**RTSF**	**RTPF**	**SM**
PC	0.56	300	1281	734	168	99	4	0	0	123.3
SFC	0.56	300	1281	734	168	99	4	40	0	61.5
SF2PFC	0.56	300	1281	734	168	99	4	40	2	61.5
SF5PFC	0.56	300	1281	734	168	99	4	40	5	61.5

* W/C for water/cement ratio, C for cement (CEM II 52.5), G for coarse aggregates (5/10mm), S for fine aggregates (0/5mm), W for water, P for PFA, SP for superplasticizer (Twinflow 05), RTPF for reused tyre polymer fibre, RTSF for reused tyre steel fibre, and SM for steel mesh, respectively.

Explosive Spalling Tests

The specimens were heated using a three-headed blowtorch. The distance of the blowtorch from the sample (i.e. 20cm) has been previously determined by Huang, et al [13] to reproduce an initial heating rate as close to that of a large pool hydrocarbon fire as possible [14]. A thermocouple was placed at the centre of the specimen’s surface to measure the temperature of the fire during each test. Figure 2 shows the test set up.

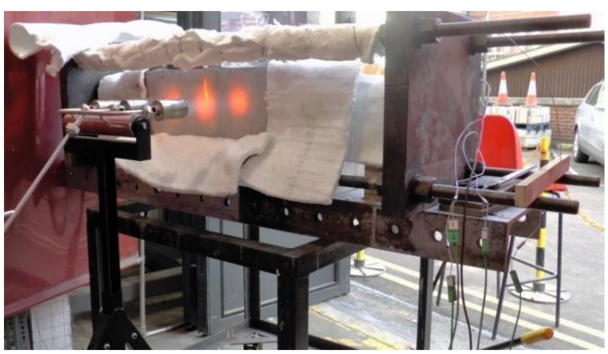

Figure 2. Test setup.

During the spalling tests, the specimens were subjected to a constant load of 6.25MPa, 9% of the ambient-temperature compressive (cube) strength. During heating, the thermal expansion along the loaded axis was restrained and any changes in compressive stress were recorded throughout testing.

Determination of concrete strength and moisture content

Concrete strength was measured from 100mm cubes on the day of each spalling test. For each test specimen, three cubes were cast and tested.

A primary cause of the fire-induced spalling of concrete is the inability of trapped moisture to escape from concrete pores [5]. Therefore, sixteen cylinders were cast in order to monitor moisture content in the specimens at different depths and time. For each concrete mix, four cylinders were prepared and subjected to the same curing condition as for the specimens. After being taken out of the mist room, all cylinders were cut at depths of 10mm, 20mm, 50mm and 100mm. One cylinder of each mix was dried in the oven for 24 hours at 100◦C for the determination of the initial moisture content. The other three cylinders (for each mix) were then sealed with aluminium foil tape to provide one-dimensional drying condition. Plastic tapes were used to seal the gaps between the adjacent layers, as illustrated in Figure 3. Then the change in moisture content with time was monitored by weighing each slice daily.

Figure 3. Cutting of cylinders (left) Wrapping of cylinders (right).

RESULTS AND DISCUSSION

Table II summarizes the compressive strength and moisture content acquired from the cubes and cylinders. The compressive strength at the time of each spalling test was approximately 70 MPa, as expected. Their moisture contents were between 2.59% and 2.98%. EC2 states that spalling is unlikely to occur when the moisture content in concrete is lower than 3% by mass. However, most of the spalled specimens had moisture contents below 3%, indicating the potential risk borne by high-strength concrete.

A summary of the test results is given in Table III. The aftermath of the spalling tests are shown in Table IV. Two of the three plain concrete specimens experienced severe spalling with a maximum depth of spalling up to 14mm. The other plain concrete specimens did not spall but a large crack extended on the top of the, as shown in Figure 4, which could help relieve pore pressure and explains why this specimen did not spall. The three specimens (SFC1, SFC2 and SFC3) with only RTSF barely spalled with very shallow spalling depth (around 1mm). This implies the incorporation of RTSF may not be able to stop fire-induced spalling completely but has the potential to control it. One of the three specimens (SF2PFC1, SF2PFC2 and SF2PFC3) with

RTSF and 2kg/m^3 RTPF spalled. It is worth noticing that the spalled concrete was still attached to the specimen surface as they might be held by the steel fibres. None of the three specimens with RTSF and 5kg/m^3 RTPF (SF5PFC1, SF5PFC2 and SF5PFC3) experienced spalling. In fact, there was barely any surface spalling that the specimens look almost intact after the fire test.

TABLE II. RESULTS OF CUBE TESTS AND MOISTURE CONTENT MEASUREMENTS.

Specimens	Age (days)	Moisture content (day of test) (%)	Strength (day of test) (MPa)
PC1	77	2.98	69.88
PC2	77	2.98	69.88
PC3	77	2.98	69.88
SFC1	77	2.79	73.33
SFC2	77	2.79	73.33
SFC3	78	2.78	72.49
SF2PFC1	73	2.70	65.84
SF2PFC2	71	2.73	66.92
SF2PFC3	73	2.70	65.84
SF5PFC1	51	2.71	68.36
SF5PFC2	51	2.71	68.36
SF5PFC3	51	2.71	68.36

TABLE III. RESULTS OF EXPLOSIVE SPALLING TESTS.

Specimens	Fire Duration (mm:ss)	Spalling	Time taken to spall (mm:ss)	Max Depth of spalling cut (mm)	Total weight loss (kg)	Concrete Loss (kg)
PC1	15:02	Yes	01:12	13	0.49	0.22
PC2	16:21	Yes	00:41	14	0.94	0.67
PC3	16:07	No	-	0	0.25	-
SFC1	15:05	No	-	0	0.32	-
SFC2	16:41	No	-	0	0.34	-
SFC3	15:06	No	-	0	0.30	-
SF2PFC1	22:43	Yes	01:07	8	0.45	0.18
SF2PFC2	36:52	No	-	0	0.93	-
SF2PFC3	18:03	No	-	0	0.39	-
SF5PFC1	15:20	No	-	0	0.27	-
SF5PFC2	15:04	No	-	0	0.23	-
SF5PFC3	15:01	No	-	0	0.22	-

Figure 4. Large crack on top of specimen PC3.

TABLE IV. SPECIMENS AFTER FIRE- INDUCED SPALLING TESTS.

PC	 PC1	 PC2	 PC3
SFC	 SFC1	 SFC2	 SFC3
SF2PFC	 SF2PFC1	 SF2PFC2	 SF2PFC3
SF5PFC	 SF5PFC1	 SF5PFC2	 SF5PFC3

These results are encouraging in showing that RTPF has a potential to replace manufactured fibres for the mitigation of fire-induced spalling. The time taken for initial spalling to occur ranges from 41secs to 1min 12sec. The quantity of spalling was approximated by the measured weight change of the spalled specimens before and after the spalling tests, from which the moisture loss of un-spalled specimens due to heating is deducted, as listed in Table IV. Further research is required to investigate the contribution of reused tyre steel fibres in preventing fire-induced spalling, as well as to determine the optimum amount of RTPF required to protect concrete specimens from fire-induced spalling.

Thermocouples were used to measure the fire temperature very close to the heated surface of the specimen during the tests. Figure 7 plots the temperature-time relationships measured by all thermocouples. The large pool hydrocarbon fire curve is also plotted on this figure to allow comparison. A higher initial heating rate was achieved by using the blowtorch comparing with the large pool hydrocarbon curve.

When spalling occurs, a sudden drop of temperature was captured. For instance, in the PC1 section of Figure 5, the measurements from the thermocouples at depths 1mm and 10mm indicate sudden decreases of temperature when spalling occurs. This is because they were both exposed directly to fire after explosive spalling occurred and so they no longer measured the temperature of concrete but that of the fire. Similar observations were made from the PC2 specimen. Note that a drop of temperature was also measured by the thermocouple at 10mm depth in PC3 specimen at 3 minute, which might be related to the development of internal cracks, triggering the development of the large crack on the top of the specimen, as shown in Figure 4.

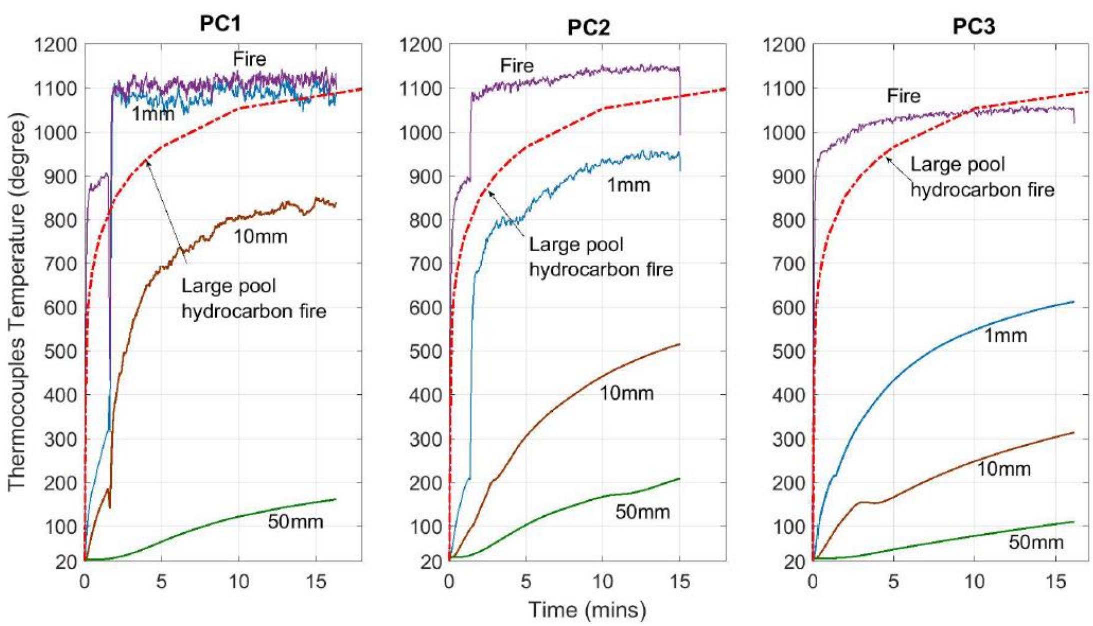

Figure 5. Temperature time curve of thermocouples & large pool hydrocarbon fire curve of PC1, PC2 and PC3.

CONCLUSION

Explosive spalling can be detrimental to structural integrity. This study attempts to investigate the potential of reusing tyre polymer fibre and tyre steel fibres to prevent fire-induced spalling in large structures such as tunnels. Not only could the construction industry potentially benefit from these fibres but also the environment by reducing the disposal of hazardous waste materials. It appears that the combination of RTSF and RTPF (5kg/m^3) was sufficient to prevent fire-induced spalling. Further research is needed to confirm the effectiveness of RTSF and RTPF in preventing spalling, to quantify the optimum dosage of these fibres and to understand their working mechanisms. The development of processing techniques will also be vital in encouraging the replacement of manufactured polypropylene fibre currently used in the industry with RTPF.

ACKNOWLEDGEMENTS

The research leading to these results has received funding from the European Union Seventh Framework Programme [FP7/2007- 2013] under grant agreement N° 603722.

REFERENCES

1. Bailey, C. 2015. “Mont Blanc Tunnel, Italy” University of Manchester, O. S. Engineering.
2. Smith, K. and T. Atkinson, T. 2010. “PP fibres to resist fire-induced concrete spalling,” in *TunnelTalk* .
3. Dwaikat, M. and V. Kodur. 2009. “Hydrothermal model for predicting fire-induced spalling in concrete structural systems,” 44: 425-434.
4. Jansson, R. 2013. “Fire Spalling of Concrete- A historical overview.”
   Kato, M., H. Dobashi, H. Tajima, N. Kawada, and T. Takahama. 2015. “The application of fireproof SFRC segments and cast- in- place fireproof concrete to metropolitan expressway yokohama circular northern route.” M. E. Obayashi Corporation, Ed.
5. Both, K. 2003. “Tunnel Fire Safety.” Retrieved from http://heronjournal.nl/48-1/1.pdf
6. Global Tire Shipments to Reach 1.7 Billion Units by 2015, According to a New Report by Global Industry Analysts, Inc. (2010). Retrieved from http://www.prweb.com/releases/tires_OEM/replacement_tire/prweb4545704.htm
7. Serdar, M., A. Baricevic, M. J. Rukavina, M. Pezer, D. Bjegovic, and N. Stirmer. 2015. “Shrinkage Behavior of Fibre Reinforced Concrete with Recycled Tyre Polymer Fibres.” International Journal of Polymer Science, Croatia: Hindawi.
8. Pilakoutas, K., K. Neocleous, H. Tlemat, Dipl-Ing, and B. Ingenieur. 2004. “Reuse of tyre steel fibres as concrete reinforcement.” Proceedings of the ICE: Engineering Sustainability, University of Sheffield: White Rose, pp. 131-138.
9. Anagennisi Project. Retrieved from http://www.anagennisi.org/
10. CEN. 2004. Eurocode 2: Design of Concrete Structures - Part 1-2: General Rules - Structural Fire Design. Brussels: European Committee on Standardization.
11. Lourenco, L, J. Barros and J. A. Alves. 2011. “Fibre Reinforced Concrete of Enhanced Fibre Resistance for Tunnel Segments”.
12. Huang, S.S., C. Angelakopoulos, K. Pilakoutas and I. W. Burgess. “Reused Tyre Polymer Fibre for Fire-Spalling Mitigation” Proceedings. ASFE 2015, Dubrovnik, Croatia, pp 355-361.
13. PD7974-3: 2003: Application of fire safety engineering principles to the design of buildings. Structural response and fire spread beyond the enclosure of origin (Sub-system 3).

Constitutive Models of Concrete at Elevated Temperatures: Studying the Effect of Temperature Gradients

QUANG XUAN LE, VINH THE NGOC DAO, CRISTIAN MALUK, LUKE BISBY and JOSÉ LUIS TORERO

ABSTRACT

The outbreak of fire can have serious consequences in the structural performance of a load-bearing concrete structure. To assure adequate fire performance, detailed knowledge of fundamental mechanical properties of concrete at elevated temperatures is crucial. This paper first highlights limitations of existing knowledge regarding the mechanical response of concrete at elevated temperatures, including the inconsistent thermal boundary conditions and intentionally-minimised temperature gradients in "standardized" conventional concrete material testing. Accordingly, it is argued that the effect of temperature gradients within concrete on its fire performance has not been extensively or directly addressed.

On this basis, the paper outlines key features of an ongoing research programme at The University of Queensland aimed at studying the performance of concrete in fire using a novel medium-scale testing method. By heating using radiant panels, well-defined and consistently-controlled heat flux boundary conditions on concrete cylinders (ϕ100mm x 200mm) have been achieved. The repeatability, consistency, and uniformity of thermal boundary conditions are demonstrated using measurements of heat flux, temperature profile, and compressive strength.

Analysis of initial obtained data shows that the incident heat fluxes, and thus the associated temperature gradients, have potentially significant effects on concrete properties at elevated temperatures. Further research is thus ongoing to quantify such effects and also to develop models for their inclusion into effective performance-based fire design and analysis of concrete structures.

INTRODUCTION

Despite extensive research over the past decades, current knowledge of fundamental properties of concrete at elevated temperatures remains largely based on

---

Quang X. Le[1,2], Vinh T. N. Dao[1,*], Cristian Maluk[1], Luke Bisby[3], José L. Torero[1].
[1] School of Civil Engineering, The University of Queensland, QLD 4072, Australia.
[2] Faculty of Civil Engineering, The University of Danang–University of Science and Technology, Vietnam.
[3] School of Engineering, The University of Edinburgh, UK.
[*] Corresponding Author. Email: v.dao@uq.edu.au.

data collected from conventional tests in which the thermal loading experienced by concrete specimens is difficult to be consistently controlled [1, 2]. As a result, the effect of temperature gradients within concrete on its fire performance has not been well investigated. The influence of processes linked with temperature gradients, including thermal stresses, moisture transport, and pore pressures, has not been directly addressed. This gap of knowledge is potentially important considering the likely steep temperature gradients within concrete structure subjected to real fires.

Realistic structural fire design of concrete structures thus requires detailed knowledge of fundamental properties of concrete at elevated temperatures, taking due account of the effects of temperature gradients. This is especially true in the context of current movements toward performance-based design for fire-related applications. The success of such an approach hinges on the establishment of reliable numerical models; which, in turn requires realistic constitutive models that should:

- reflect the true behaviour of concrete at elevated temperatures and under realistic thermal gradients; and
- be based on reliable and well-documented results from tests carried out under well-defined and well-controlled conditions.

This paper first highlights shortcomings of standardized conventional tests for concrete in fire, and discusses the potentially important limitations in the resulting currently available constitutive models for concrete at elevated temperatures. The paper then briefs key features of an ongoing research program that aims to re-examine the fire performance of concrete using a novel testing approach.

LIMITATIONS IN CONVENTIONAL TESTS AND THEIR EFFECTS

The increase of temperature in a test specimen is directly related to the incident heat flux on the specimen's surface. When a conventional fire testing furnace/oven is used, the temperature evolution of the gases in the furnace is controlled – if thermocouples are used – and the heat-flux to a plate – if a plate thermometer is used. The net heat flux at the specimen's surface results from a combination of radiation and convection between the furnace environment and the test specimen. This complex heat transfer process is sometimes further complicated by the presence of other test specimens within the testing chamber.

Using an energy balance the heat flux at the specimen's surface $q_s^{"}$ can be approximated as:

$$q_s^{"} = \varepsilon . q_{inc}^{"} - \varepsilon . \sigma . T_S^4 + h(T_H - T_S) \tag{1}$$

where ε: thermal emissivity; T_H, T_S: temperature of gas and of specimen surface, respectively; σ: Stefan-Boltzmann constant; and $q_{inc}^{"}$: incident radiative heat flux (from gases, furnace walls, and other test specimens). The evolution of $q_s^{"}$ in time and space is highly complex and difficult to control accurately or consistently. This has potentially serious implications for concrete samples with a Biot number close to 1, where proper characterisation of thermal boundary conditions is required [2].

Poor definition of $q_s^{"}$ makes it challenging to achieve reliable control of the temperature evolution/gradient in test specimens in furnace tests. This has caused, at least partly, the following issues:

a. Currently available constitutive models for concrete have largely been derived from standardized tests where temperature gradients within the concrete test specimens is intentionally minimized [3, 4], with the aim being to separate, as far as possible, the "material" from the "structural" effects [5]. Limitations of these models include:
   - Mass transfer processes affected by heat are different from typical real fire situations (with higher temperature gradients) because the very slow heating rates do not only allow dissipation of heat through the specimen but also slow dissipation of water vapour with minimal pore pressure increase.
   - Components of the model linked with temperature gradients have not been explicitly addressed, nor have the couplings between different processes linked to temperature gradients (including moisture transport, vapour pressure, and thermal gradient induced stresses).

b. Significant variation in test results regarding both strength deterioration and spalling of concrete upon heating [3, 5]: Different heating rates result in different heating histories. These are complex and generally undefined due to poor thermocouple/sensor resolution. The undefined different heating histories in turn result in unquantifiable variability in the responses of test specimens. The significant variation in test results is likely also due in part to the inherent variation of concrete properties, and partly to possible experimental errors. In conventional tests, as a result of the limitations in thermal loading highlighted above, it is difficult to assess different sources of errors.

The above-discussed shortcomings can be addressed if known heat fluxes, including those representatives of real fire scenarios, can be consistently applied onto test specimens. A research program is thus underway at The University of Queensland to re-examine the thermal and mechanical performance of concrete at elevated temperatures by establishing well-defined and consistently-controlled thermal boundary conditions. This paper reports initial results of material testing of cylinder specimens, forming the basis for revision of constitutive models to reflect the effects of heat flux and associated temperature gradients.

EXPERIMENTAL STUDY

Test specimens and materials

Concrete cylinders of Φ100mmx200mm were adopted due to their common use for establishing uniaxial constitutive models of concrete in compression. The mix design was typical for concrete with 28-day compressive strength of 80 MPa, and is given in Table I. All mixing and casting was done in accordance with relevant Australian standards [6]. To ensure consistent moisture conditions, upon stripping from their moulds one day after casting, test specimens were cured in water at 27^{o}C for four months, and then in air at 27 °C and 70% relative humidity for another three months until testing. The mass loss with time was monitored and found to become negligible after about 40 days. Two series of specimens were prepared:

- Series 1, of 9 specimens with internal thermocouples: Each specimen had 5 thermocouples located on two radial lines at mid-height. Temperatures were measured at three depths (Figure 1): (i) at the specimen's surface and (ii) centreline, and (iii) at 21 mm from the surface; this being the location of the average temperature [7].

- Series 2, of 33 specimens without thermocouples: Specimens were exposed to pre-determined schemes of heat flux boundary condition before testing to failure under compression. Due to good repeatability of heating and curing, temperature profiles in these specimens are assumed the same as corresponding specimens in Series 1.

TABLE I. CONCRETE MIX DESIGN.

Constituents	Quantity (/m^3)
10mm aggregate	925 (kg)
Manufactured coarse sand	600 (kg)
River fine sand	140 (kg)
Cement	580 (kg)
Water	193 (l)
Superplasticiser	4.06 (l)

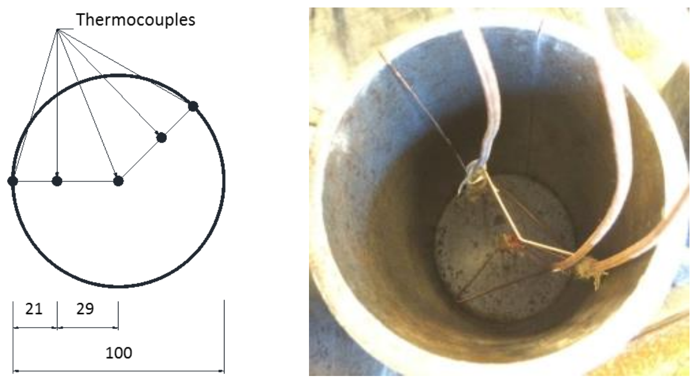

Figure 1. Locations of thermocouples in the cylinder concrete specimen.

Radiant panel heating setup

The heat flux incident on cylinder test specimens was actively controlled using a system of four high performance radiant heating elements (Figure 3). Calibration of heat flux was performed using a Schmidt-Boelter heat-flux sensor as follows:

- The incident heat flux from each of the four panels was determined as a function of the distance between the panel and the target at the start of the testing, and this was repeated upon completion of the test series. The heat flux profiles produced by the four panels were essentially identical (Figure 2), proving that the consistency between the four panels was maintained throughout the testing.
- Two radiant panels were used to determine the degree of uniformity of incident heat flux intensities on the cylinder specimen surface placed at different offset distances (Figure 2). The measured heat fluxes at the three locations (i.e. A, B and C) varied within by 5% for all distances, giving a homogeneous thermal boundary.

Imposed heat fluxes

Following the above calibration process, the incident heat flux intensities in this study were chosen as 20, 30, and 40 kW/m^2. Concrete specimens were first heated under a given incident heat flux level until the target average temperature, as recorded by thermocouples at 21 mm depth from the specimen surface, was reached. The test specimens were then loaded in compression at a rate of 0.25 mm/min until failure.

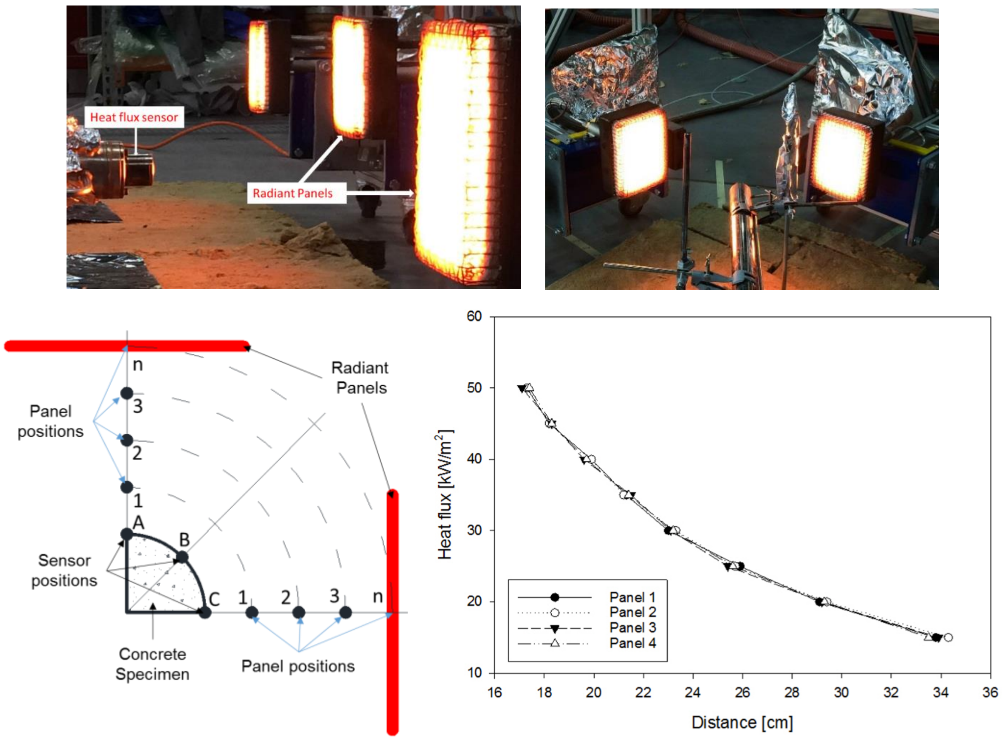

Figure 2. Illustration of heat flux calibration process.

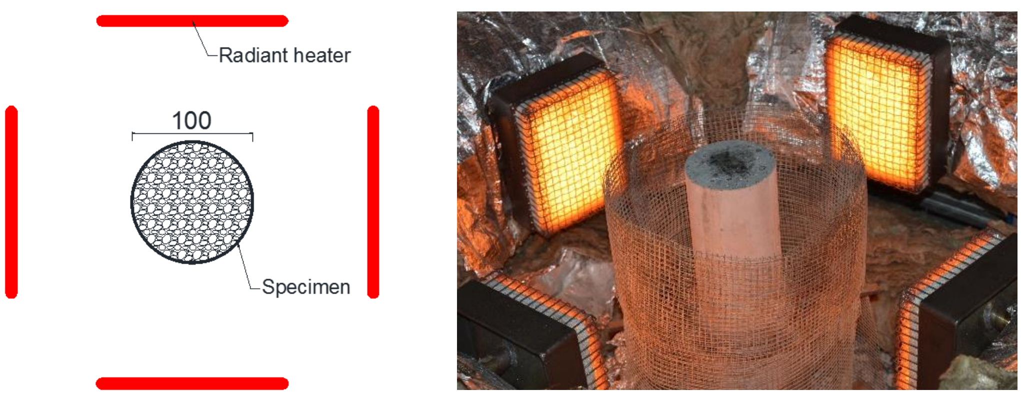

Figure 3. Radiant heaters and specimen.

Mechanical loading preparation

Figure 4 shows a schematic of the test setup for mechanical and thermal loading. Key features of the test setup include:

- Loading crossheads below and above the test specimen: A water-cooling system was designed to maintain the temperature of the crossheads at less than 40°C during testing. The concrete block, as part of the attachment, was made of 100 MPa concrete, acting as an insulator with similar thermal conductivity to that of test specimens.

- A spherical seat ensured that uniaxial compression load was imposed.
- A steel mesh (of 5mm x 5mm grid) was placed around the test specimens to protect the radiant panels from possible explosive spalling.

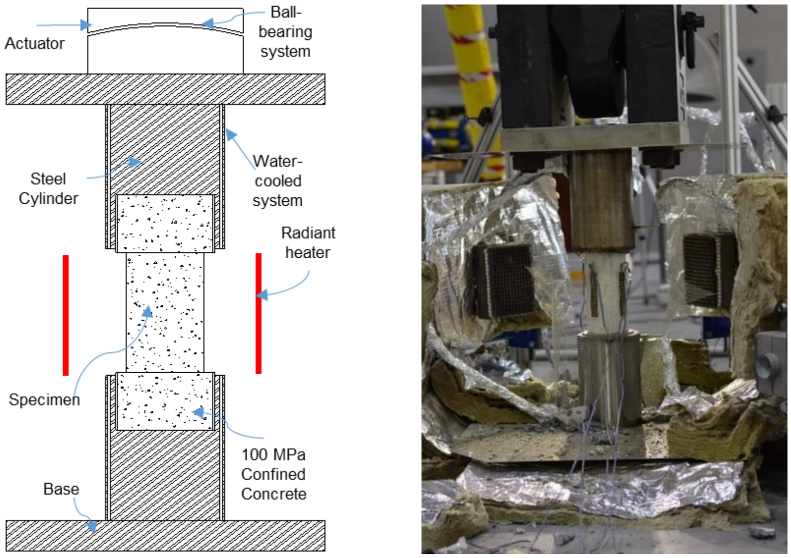

Figure 4. Schematic illustration and photo of test setup.

EXPERIMENTAL RESULTS AND DISCUSSION

Spalling

No spalling was observed during testing of all 39 cylinder specimens, despite the high compressive strength of concrete used, which was about 95 MPa at test date, and the relatively high rate of temperature increase for these specimens, which was between 10 and 20°C/min during the initial stages of heating.

Time evolution of in-depth temperature profiles

The time evolution of in-depth concrete temperature profiles in three test specimens was determined for each of the three incident heat flux levels. A good degree of consistency was observed among the measured temperatures for each heat flux (Figure 5). The recorded temperatures along the two radial lines at corresponding depths (Figure 1) also had good agreement, confirming the uniform heat flux boundary condition.

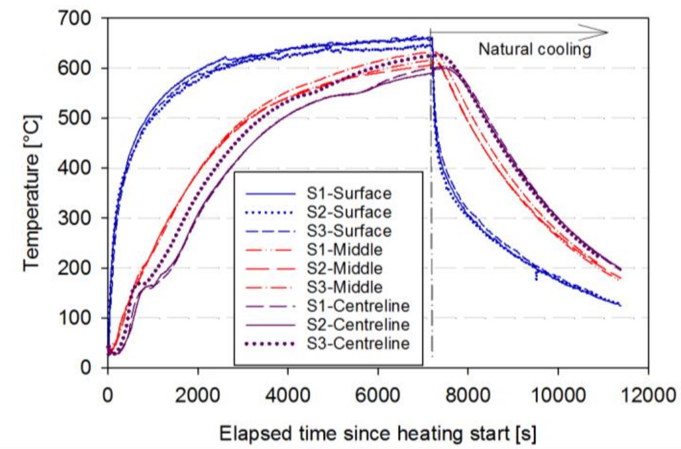

Figure 5. Temperature profiles of 3 specimens subject to HF40.

Strength of concrete at elevated temperatures

Three cylinder specimens were tested for each combination of incident heat flux and target temperature. The average compressive strengths, normalised against corresponding strengths at ambient temperature, are plotted in Figure 6.

It can be seen from Figure 6 that, at a given average elevated temperature, concrete strengths of test specimens subject to different incident heat fluxes vary over a significant range. Such a difference can be explained by linking temperature gradients, heating time, and corresponding physical-chemical processes within concrete specimens. At an average temperature of 300°C, for instance, the temperature ranges within test specimens due to heat fluxes of 20, 30 and 40 kW/m^2 were 233 to 431, 217 to 490, and 212 to 545°C, respectively. As a result, while significant strength recovery was observed in HF20 specimens due to increased surface forces arising from loss of absorbed water [4], such recovery was modest in HF30 and HF40 specimens, possibly due to the counteracting effect of decomposition of $Ca(OH)_2$ [8].

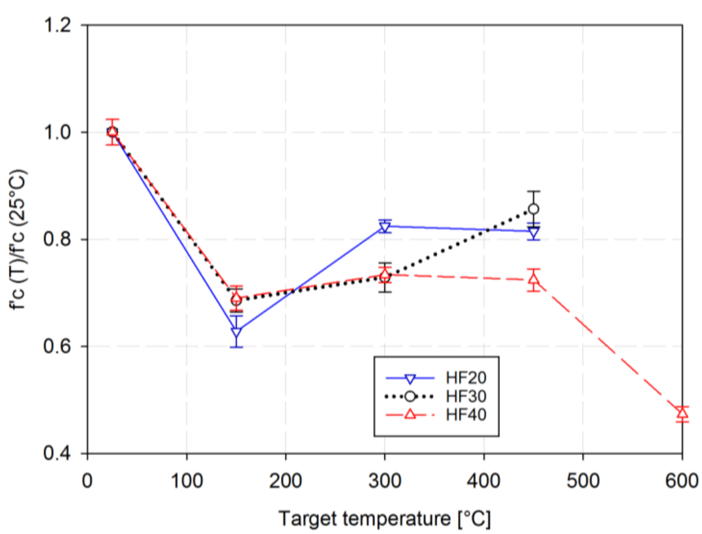

Figure 6. Change of concrete compressive strength at different target temperatures and incident heat fluxes.

Figure 6 thus highlights the potential influence of incident heat fluxes, and thus the associated temperature gradients, on concrete properties at elevated temperatures. The challenging question is to quantify such influence and also to develop methodology to effectively account for it in fire design and analysis of concrete structures.

SUMMARY AND CONCLUSIONS

This paper has outlined the limitations of inconsistent thermal boundary conditions and intentionally-minimised temperature gradients in conventional materials testing of concrete at elevated temperature. Details of a research program aiming to re-examine the fire performance of concrete structures, taking due account of temperature gradients, are given. The test setup for thermal and mechanical loading, using radiant panels to generate well-defined and reproducible heating regimes, is described. The good repeatability, consistency, and uniformity of the thermal boundary conditions on test cylinder specimens are demonstrated.

Using this novel test setup, the measured compressive strengths of concrete specimens at a given average temperature were observed to be influenced by the incident heat fluxes, implying an observable effect of temperature gradients on concrete properties at identical average elevated temperatures. Further research is required to quantify this effect and also to develop models for its inclusion into structural fire design and analysis.

ACKNOWLEDGEMENTS

The authors acknowledge the financial support of Australian Research Council's Discovery Projects funding scheme (DP150102354). The first author is also grateful for the financial support of Australia Awards Scholarships.

REFERENCES

1. Maluk, C., L. Bisby, G. Terrasi, M. Krajcovic and J. Torero. 2012. "Novel fire testing methodology: Why, how and what now?," in *Proceedings of the Mini Symposium on Performance-based Fire Safety Engineering of Structures as part of the 1st International Conference on Performance Based land Life Cycle Structural Engineering,* Hong Kong Polytechnic University: Hong Kong. p. 448-458.
2. Torero, J. 2014. "Assessing the performance of concrete structures in fires," *Concrete in Australia - Special Issue on "Concrete Performance in Fire"*, 40(3):44-49.
3. Phan, L.T. 1996. "Fire performance of high-strength concrete: A report of the state-of-the-art," *The National Institute of Standards and Technology (NIST)*. p. 118.
4. Cheng, F.-P., V.K.R. Kodur, and T.C. Wang. 2004. "Stress-strain curves for high strength concrete at elevated temperatures," *Journal of Materials in Civil Engineering,* 16(1): 84-90.
5. Khoury, G.A., P.J.E. Sullivan, and B.N. Grainger. 1984. "Radial temperature distributions within solid concrete cylinders under transient thermal states," *Magazine of Concrete Research,* 36(128):146-156.
6. Standards Australia. 2014. *AS1012.1:2014 - Methods of testing concrete. Method 1: Sampling of concrete.* Standards Australia Limited: Sydney, NSW 2001.
7. Le, Q.X., V.T.N. Dao, and J.L. Torero. 2015. "Fire performance of concrete: Effect of temperature gradients?," in *PROTECT2015 - The Fifth International Workshop on Performance, Protection, and Strengthening of Structures under Extreme Loading,* V.K.R. Kodur and N. Banthia, eds: Michigan State University. p. 189-196.
8. Khoury, G.A. 1992. "Compressive strength of concrete at high temperatures – a reassessment," *Magazine of Concrete Research,* 44(161):291-309.

Post-cooling Stress-strain Model of Traditional and High-Strength Concrete

EMMANUEL ANNEREL, TOM VAN DEN STEEN
and LUC TAERWE

ABSTRACT

As concrete structures suffer from severe fire damage, but may retain a certain remaining loadbearing capacity, it is important to have material properties for assessment by calculation after fire. This paper proposes a full stress-strain model for post-cooling conditions of a traditional calcareous concrete (TCC) and a high strength siliceous concrete (HSSC).

1. INTRODUCTION

In a compartment fire, concrete structural elements can suffer from severe damage. Nevertheless, after the fire these structures or part of them often can be considered for further use after appropriate assessment, and possible replacement or repair. One way to assess the remaining loadbearing capacity of the elements is by calculation. In structural design codes, such as the Eurocodes, hot strength properties and simplified calculation methods are provided by which the loadbearing capacity can be estimated. However, these tabulated material properties are valid for the design during fire only. Hence, in order to perform an adequate analysis after fire, a database is needed for material properties valid for post-cooling conditions.

The last decades, a lot of research has been performed worldwide in order to understand the remaining strength properties of concrete exposed to fire. It is demonstrated that the post-cooling strength of concrete is complex and depends on the specific conditions during fire, such as heating rate, exposure temperature and

Emmanuel Annerel, Ghent University, Faculty of Engineering and Architecture, Department of Structural Engineering, Magnel Laboratory for Concrete Research, Technologiepark Zwijnaarde 904, B-9052, Ghent, Belgium; PRTC, Bormstraat 24, B-2830, Tisselt, Belgium
Tom Van Den Steen, Ghent University, Faculty of Engineering and Architecture, Department of Structural Engineering, Magnel Laboratory for Concrete Research, Technologiepark Zwijnaarde 904, B-9052, Ghent, Belgium
Luc Taerwe, Ghent University, Faculty of Engineering and Architecture, Department of Structural Engineering, Magnel Laboratory for Concrete Research, Technologiepark Zwijnaarde 904, B-9052, Ghent, Belgium

duration, as well as the existence of an external load [1,2]. After fire, also the cooling rate and specific subsequent environmental storage conditions influence the remaining strength [1,2].

Mostly these influencing parameters after fire result in a further reduction of the compressive strength compared to the strength loss already induced by the temperature. For the HSSC used in this paper, after slowly heating (5°C/min) to uniform temperatures up to 550°C without sustained load, a fast cooling rate by water immersion (13-17°C/min) results in additional strength losses of about 30-35% [2]. And a post-cooling storage in air or under water results in an additional strength loss of 20-30% [2]. The additional loss induced by the cooling rate can be explained by the introduction of a thermal shock in case of a rapid cooling method, resulting in additional cracks and therefore strength loss. The additional strength loss related to post-cooling storage conditions should be related to newly formed portlandite ($Ca(OH)_2$) which is an expansive reaction, and thus literally presses the concrete to failure from the inside.

This paper contributes to the described specific research area by proposing a full stress-strain model for post-cooling compressive strength of a traditional calcareous concrete (TCC) and a high strength siliceous concrete (HSSC). In addition to other research programs found in literature, this paper not only studies the compressive strength, but also the stiffness. Reference is made to section 2.3 to understand the specific test conditions and therefore the application limits of the proposed stress-strain model. The work presented is part of a master thesis [3].

2. TEST PROGRAM

2.1. Concrete mix

Table I presents the composition of the concrete mixes used in present study. A traditional calcareous concrete (TCC) and a high strength siliceous concrete (HSSC) are studied. Cylindrical samples with diameter 106 mm and 320 mm height are casted.

TABLE I. CONCRETE MIXES

Constituent	**TCC**	**HSSC**
Sand [kg/m³]	664	650
Coarse aggregates [kg/m³]	1210	1250
CEM I 52.5N [kg/m³]	350	400
Water [kg/m³]	165	132
W/C [-]	0.47	0.33
Superplasticizer [l/m³]	-	16.5

2.2. Test setup

The test setup consists of an electrical split oven, a loading frame, a measurement system and a PC unit.

The oven has an internal diameter of 220 mm and a height of 550 mm, and can reach temperatures up to 600°C. The concrete sample is positioned inside the oven. Thermocouples K-type are used to measure the temperature at the surface of the concrete at 3 positions, namely 20 mm from the top and bottom of the sample, and at midheight of the sample. The central opening of the oven is sealed with fire protection insulation (PROMAGLAF HTK 1260°C, high temperature glass fibers) to reduce heat losses. To avoid possible damage to the oven due to concrete spalling, the cylinders are surrounded in the oven with an additional steel tube.

The load from the hydraulic jack is transferred to the sample by means of a series of steel cylinders. Loading till target level is performed by a pump, after which the load is sustain during the test by an accumulator.

2.3. Test conditions

The following test conditions are used:

Preparation of samples. Concrete mix and casting is explained in section 2.1. Fire tests show a risk for spalling of the concrete samples due to the sustained load, even when heated at 1°C/min. Hence, to be able to compare material property results in agreement to the scope of the test programme, the concrete samples are pre-dried at 105°C till constant mass is reached.

Target temperature. The concrete samples are heated to uniform target temperatures inside the cylinders of 175°C, 350°C and 550°C. The temperature level of 350°C is chosen as it can be regarded as the onset of strength loss due to loss of chemically bound water, whereas 550°C corresponds to the disintegration of portlandite. It is noted that determining residual properties beyond 550°C exposure are less interesting, as given the expected damage the layers between 300-550°C are already expected to be removed in case of repair of a concrete element.

The heating rate (measured by thermocouples positioned on the concrete) is 1°C/min. This heating rate is slow to avoid additional internal damage due to large differences in thermal expansion over the cross section of the concrete samples.

For the residual properties, uniform temperature over the cross section of the sample is required. Dummy tests with registration of the temperature in the center of the samples, together with thermal FEM calculations are performed to determine the exposure time needed to obtain uniform temperature distribution inside the samples. The required time is 7h of heating after reaching the target temperature.

Loading, cooling and post-cooling conditions. Two type of tests are performed, for which each test condition is executed twice per concrete type:

Test 1 comprises heating of the samples under a compression load ratio of 0, 20 or 30% of the initial compressive strength (further in the text referred to as ‘loading from start’). Cooling is slow in a closed oven under sustained load, reaching a temperature drop from 550°C till 100°C over 8 hours.

Test 2 consists of heating without load till target temperature, from where additional 3 hours of heating is performed under the same load ratios as stated above (further in the text referred to as ‘delayed loading’). Cooling is fast, but naturally, by immediately opening of the oven after the test. In this way, a temperature drop from 550°C to 100°C is found at the surface of the concrete within 1 hour.

The samples of all tests are further stored for 5 weeks in a climate chamber at temperatures of 20±1°C and 60% R.H. without load, after which they are tested for

Young's modulus (displacement controlled test, according to B15203-1990: 0.002 mm/s).

It is noted that the difference between both test conditions explains the possible effect of delayed loading during heating, as can be expected in some cases from restraint actions in a real fire.

The load is not sustained after cooling. Hence, the possible influence of this parameter is not taken into account in the proposed stress-strain model. However, the expected influence with respect to a post-cooling storage without load is a significant increase of the Young's modulus, but without effect on the compressive strength. This estimation is based on experiments of heating a similar concrete as TCC (but with siliceous aggregates) to 500°C under the same conditions as Test 1, but by also keeping the 20% load level for the 12 weeks post-cooling storage in ambient air [2]. Nevertheless, attention is necessary as increasing the load level to 40% results in failure after a few days during the post-cooling storage under load.

3. RESULTS

3.1. Sargin model at ambient temperatures

Equation 1 describes the non linear stress-strain relationship of concrete at ambient conditions, as proposed by Sargin and adopted in EN1992-1-1.

$$\frac{\sigma}{f_{cm}} = \frac{k \cdot \eta - \eta^2}{1 + (k-2) \cdot \eta} \tag{1}$$

With:

$\eta = \varepsilon/\varepsilon_{c1}$; $k = 1.05 \cdot E_{cm} \cdot |\varepsilon_{c1}|/f_{cm}$

ε_{c1} is the strain at peak stress ($= 0.7\ f_{cm}^{0.31} < 2.8$)

ε_{cu1} is the nominal ultimate strain

$\varepsilon_{cu1} = 2.8 + 27\ [(98 - f_{cm})/100]^4$ $\quad f_{ck} \geq 50$ N/mm²

$\varepsilon_{cu1} = 3.5$ $\quad f_{ck} < 50$ N/mm²

f_{cm} is the average cylinder compressive strength at age of 28 days [N/mm²]

Samples of TCC and HSSC are tested at an age of 28 days for Young's modulus. Table II summarizes the mechanical properties of both concretes with respect to the Sargin model.

TABLE II. MECHANICAL PROPERTIES AT AMBIENT TEMPERATURE

Concrete	**$f_{ccub150}$ [N/mm²]**	**$f_{ccil106x320}$ [N/mm²]**	**ε_{c1} [10^{-3}]**	**$E_{ccil106x320}$ [N/mm²]**	**k_{sargin} [-]**
TCC	59.04	47.96	2.02	36750	1.62
HSSC	74.06	70.83	1.98	45270	1.33

3.2. Modified Sargin model for post-cooling fire conditions

For post-cooling fire conditions, the model of Sargin (section 1) is modified as given in Equation 2, by adopting the parameters $f_{c,T}$, $\varepsilon_{c1,T}$ and k as function of temperature which are tabulated in Table III.

$$\frac{\sigma}{f_{c,T}} = \frac{k \cdot \eta - \eta^2}{1 + (k-2) \cdot \eta} \qquad \text{with} \quad \eta = \varepsilon/\varepsilon_{c1,T} \quad ; \qquad \text{for } T \leq 550°\text{C} \tag{2}$$

TABLE III. PARAMETERS MODIFIED SARGIN MODEL (VALID T ≤ 550°C)

Concrete	Test	α [%]	$\varepsilon_{c1,T}/\varepsilon_{c1}$ [-] ; $f_{c,T}/f_c$ [-] ; k [-]
TCC	1	0	$\varepsilon_{c1,T}/\varepsilon_{c1} = 7.195 \cdot 10^{-6} \cdot T^2 - 1.165 \cdot 10^{-3} \cdot T + 1.023$; $f_{c,T}/f_c = 3.230 \cdot 10^{-7} \cdot T^2 - 1.516 \cdot 10^{-3} \cdot T + 1.046$; $k = -7.752 \cdot 10^{-4} \cdot T + 1.455$
		20	$\varepsilon_{c1,T}/\varepsilon_{c1} = 4.205 \cdot 10^{-6} \cdot T^2 - 1.332 \cdot 10^{-3} \cdot T + 1.031$; $f_{c,T}/f_c = 3.174 \cdot 10^{-7} \cdot T^2 - 1.389 \cdot 10^{-3} \cdot T + 1.024$; $k = -6.195 \cdot 10^{-4} \cdot T + 1.430$
		30	$\varepsilon_{c1,T}/\varepsilon_{c1} = 2.990 \cdot 10^{-6} \cdot T^2 - 6.365 \cdot 10^{-4} \cdot T + 9.906 \cdot 10^{-1}$; $f_{c,T}/f_c = 6.998 \cdot 10^{-7} \cdot T^2 - 1.615 \cdot 10^{-3} \cdot T + 1.043$; $k = -7.660 \cdot 10^{-4} \cdot T + 1.482$
	2	20	$\varepsilon_{c1,T}/\varepsilon_{c1} = 5.821 \cdot 10^{-6} \cdot T^2 - 6.041 \cdot 10^{-4} \cdot T + 1.007$; $f_{c,T}/f_c = 2.476 \cdot 10^{-7} \cdot T^2 - 1.447 \cdot 10^{-3} \cdot T + 1.031$; $k = -9.682 \cdot 10^{-4} \cdot T + 1.530$
		30	$\varepsilon_{c1,T}/\varepsilon_{c1} = 5.995 \cdot 10^{-6} \cdot T^2 - 7.201 \cdot 10^{-4} \cdot T + 9.623 \cdot 10^{-1}$; $f_{c,T}/f_c = 3.428 \cdot 10^{-7} \cdot T^2 - 1.535 \cdot 10^{-3} \cdot T + 1.047$; $k = -6.809 \cdot 10^{-4} \cdot T + 1.446$
HSSC	1	0	$\varepsilon_{c1,T}/\varepsilon_{c1} = 8.220 \cdot 10^{-6} \cdot T^2 - 2.170 \cdot 10^{-4} \cdot T + 1.056$; $f_{c,T}/f_c = -2.368 \cdot 10^{-7} \cdot T^2 - 1.341 \cdot 10^{-3} \cdot T + 1.057$; $k = -3.398 \cdot 10^{-4} \cdot T + 1.228$
		20	$\varepsilon_{c1,T}/\varepsilon_{c1} = 4.392 \cdot 10^{-6} \cdot T^2 - 1.421 \cdot 10^{-4} \cdot T + 1.059$; $f_{c,T}/f_c = -6.453 \cdot 10^{-7} \cdot T^2 - 9.850 \cdot 10^{-4} \cdot T + 1.026$; $k = -4.170 \cdot 10^{-4} \cdot T + 1.262$
		30	$\varepsilon_{c1,T}/\varepsilon_{c1} = 4.481 \cdot 10^{-6} \cdot T^2 - 1.391 \cdot 10^{-4} \cdot T + 1.031$; $f_{c,T}/f_c = -4.478 \cdot 10^{-7} \cdot T^2 - 1.105 \cdot 10^{-3} \cdot T + 1.038$; $k = -3.785 \cdot 10^{-4} \cdot T + 1.244$
	2	20	$\varepsilon_{c1,T}/\varepsilon_{c1} = 9.179 \cdot 10^{-6} \cdot T^2 - 4.484 \cdot 10^{-4} \cdot T + 1.076$; $f_{c,T}/f_c = -4.225 \cdot 10^{-8} \cdot T^2 - 1.469 \cdot 10^{-3} \cdot T + 1.053$; $k = -4.426 \cdot 10^{-4} \cdot T + 1.259$
		30	$\varepsilon_{c1,T}/\varepsilon_{c1} = 5.253 \cdot 10^{-6} \cdot T^2 - 8.609 \cdot 10^{-4} \cdot T + 1.005$; $f_{c,T}/f_c = -3.913 \cdot 10^{-7} \cdot T^2 - 1.276 \cdot 10^{-3} \cdot T + 1.043$; $k = -4.421 \cdot 10^{-4} \cdot T + 1.276$

Figure 1 shows the experimental stress-strain test result, as well as the fit of the proposed stress-strain model. Generally, a good agreement is found between the experimental value and the proposed model. For target temperatures of 550°C, a smaller Young's modulus is often found for the experiments with respect to the proposed model. Probably, this should be related to the development of micro-cracking induced by the heating process. For instance: differences in thermal expansion between the aggregates and the cement matrix. Given this observation, although not further examined, it is expected that the proposed model will lose accuracy when adopted for temperatures much higher than 550°C.

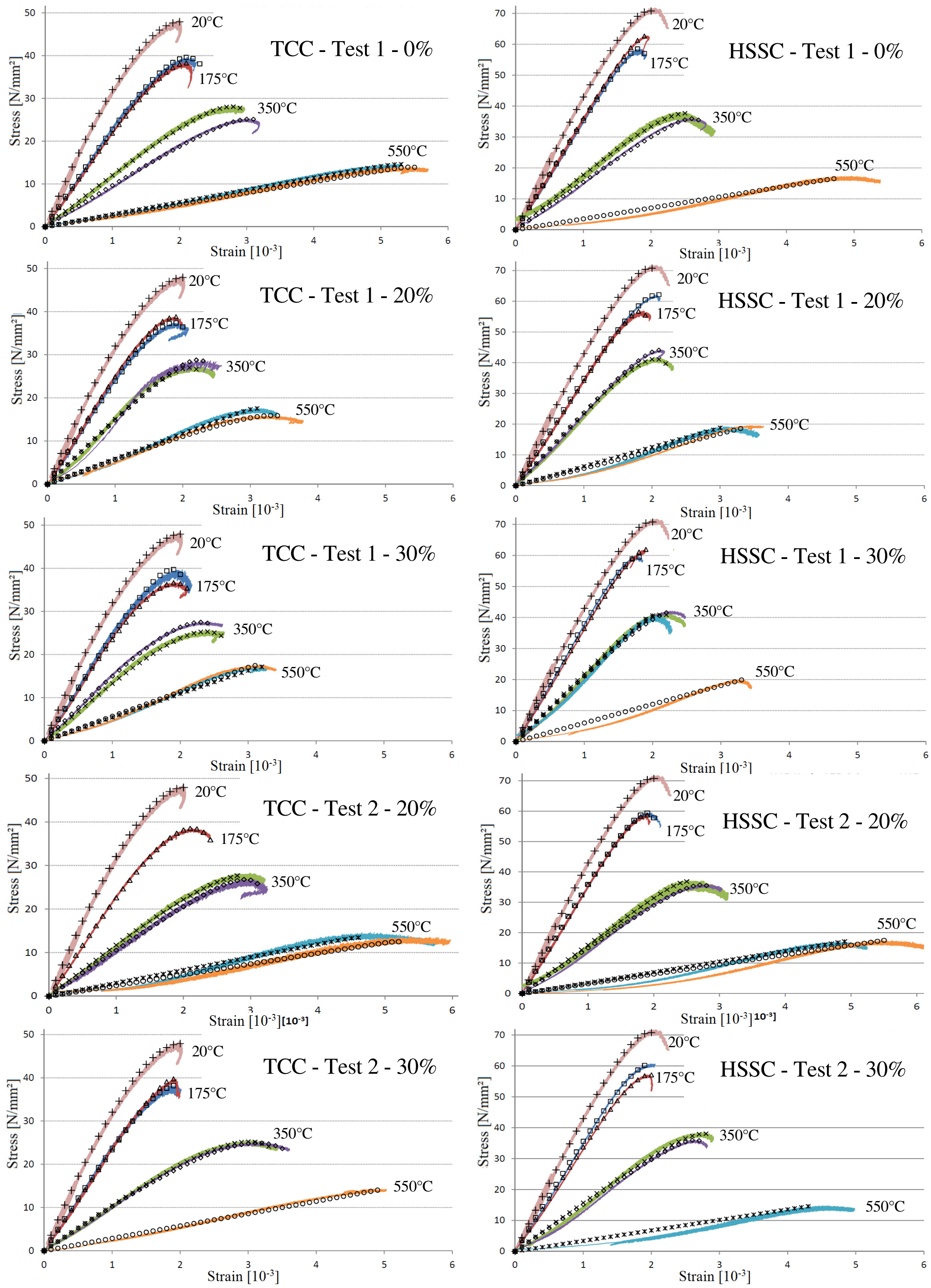

Figure 1. Stress-strain curve for TCC (left column) and HSSC (right column) for temperatures 20°C, 175°C, 350°C and 550°C. Full lines: experimental data; Shape designations: modified Sargin model.

3.3. Analysis of material properties

Figure 2 illustrates the reduction curves of compressive strength and Young's modulus for both concretes, as can be derived from the proposed model. Table IV presents the influence of the type of loading with respect to the values found for 0% loading of Test 1. Positive values indicate that the reduction with temperature is less than this reference.

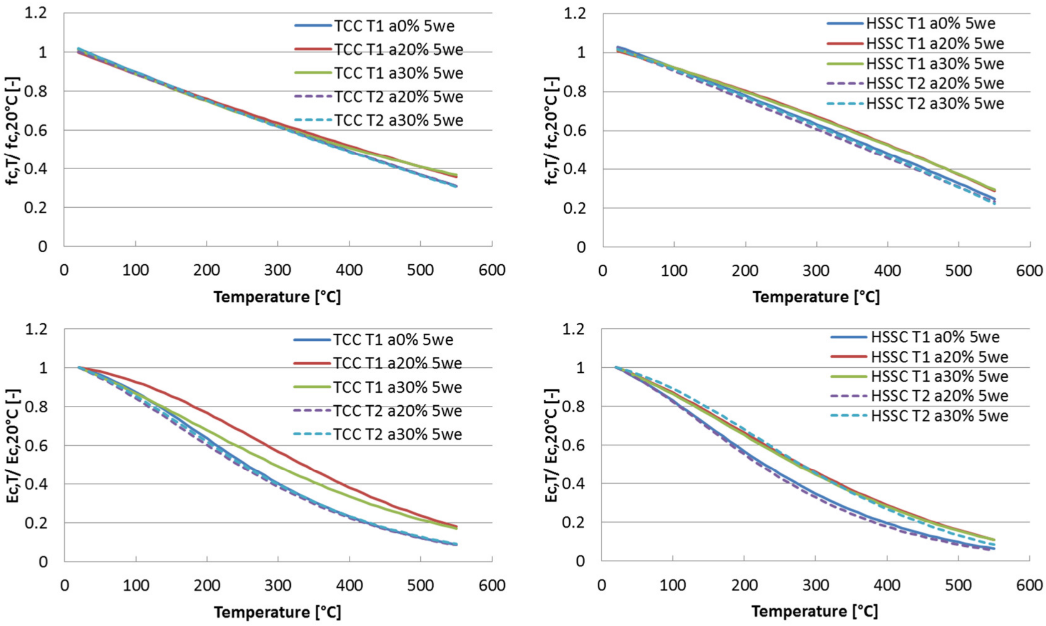

Figure 2. Reduction curves of compressive strength (top row) and Young's modulus (bottom row). Left column: TCC; right column: HSSC.

TABLE IV. INFLUENCE OF LOADING, WITH RESPECT TO 'TEST 1 – 0% load'

concrete	temp. [°C]	$f_{c,T}/f_{c,20°C\_T1/2\text{-}x\%}$ - $f_{c,T}/f_{c,20°C\_T1\text{-}0\%}$ [%]				$E_{c,T}/E_{c,20°C\_T1/2\text{-}x\%}$ - $E_{c,T}/E_{c,20°C\_T1\text{-}0\%}$ [%]			
		load from start		delayed loading		load from start		delayed loading	
		20%	30%	20%	30%	20%	30%	20%	30%
TCC	100	-0.9	-0.9	-0.9	-0.1	5.4	-0.5	-3.0	-1.8
	200	0.3	-0.8	-0.4	-0.2	13.2	4.3	-3.2	-1.7
	300	1.6	0.1	-0.1	-0.3	16.6	8.9	-1.7	-0.6
	400	2.8	1.8	0.1	-0.3	15.0	10.3	-0.6	0.2
	500	4.0	4.2	0.1	-0.4	11.2	9.3	-0.2	0.5
HSSC	100	0.1	0.2	-1.5	-0.9	4.1	3.5	-0.5	6.3
	200	2.4	2.0	-2.2	-0.7	9.5	8.3	-1.6	11.2
	300	3.9	3.3	-2.5	-0.8	11.1	9.9	-2.0	10.7
	400	4.6	4.2	-2.4	-1.3	9.3	8.5	-1.8	7.3
	500	4.5	4.6	-1.9	-2.0	6.2	6.0	-1.2	3.6

Figure 2 shows no large differences between the different test conditions for the reduction of the compressive strength, whereas for the Young's modulus significant differences are notable. Table IV presents an increase of both compressive strength and Young's modulus when load is applied from the start of the heating. On the other hand, delayed loading introduces a (limited) decrease for both properties, with exception of Young's modulus of HSSC 30% load. Observed differences can be explained by the activation of transient strain in case load is applied from the start.

Assuming a spread of 5% as being significant (corresponding to the spread found on compressive strength tests at ambient conditions), Table IV presents only significant differences for the Young's modulus. An increase is found for both TCC and HSSC, which is temperature dependent and has a maximum of respectively 16.6% and 11.1% at 300°C in the case of 20% loading applied from the start. For the 30% load, the increase is smaller.

Table V presents the difference in reduction with temperature of compressive strength and Young's modulus between both concretes. Negative values indicate that the reduction with temperature is larger for HSSC. Regarding the compressive strength, about 300-400°C can be observed as a shift from HSSC having less to more reduction with temperature than TCC. For the Young's modulus, larger differences are found, indicating a steeper reduction of stiffness of HSSC for all test conditions, except delayed loading and 30% load level.

TABLE V. DIFFERENCE OF MATERIAL PROPERTIES BETWEEN HSSC AND TCC

Temp. [°C]	$f_{c,T}/f_{c,20°C\_HSSC} - f_{c,T}/f_{c,20°C\_TCC}$ [%]					$E_{c,T}/E_{c,20°C\_HSSC} - E_{c,T}/E_{c,20°C\_TCC}$ [%]				
	load from start			delayed loading		load from start			delayed loading	
	0%	20%	30%	20%	30%	0%	20%	30%	20%	30%
100	2.3	3.3	3.5	1.7	1.5	-4.5	-5.7	-0.5	-2.0	3.7
200	2.4	4.4	5.1	0.6	1.8	-6.6	-10.3	-2.6	-5.0	6.3
300	1.3	3.7	4.5	-1.1	0.8	-5.4	-10.9	-4.4	-5.8	5.8
400	-0.9	1.0	1.5	-3.3	-1.8	-3.7	-9.4	-5.5	-4.9	3.3
500	-4.1	-3.7	-3.7	-6.1	-5.8	-2.7	-7.7	-6.0	-3.7	0.5

4. CONCLUSIONS

- The specific test conditions have a large influence on the remaining compressive strength. The results presented in this paper are derived from slowly - till uniform temperature - heated (pre-dried) samples under load. No load after cooling.
- A stress-strain model is developed for post-cooling conditions ($T \leq 550°C$).
- With respect to the studied test conditions, heating under load has a positive effect on both post-cooling compressive strength and Young's modulus, although only significant values are found for the latter. On the other hand, a small decrease is found for delayed loading.
- Generally, a faster decrease of Young's modulus is found for HSSC than for TCC. For compressive strength HSSC has less reduction till about 300-400°C.

5. REFERENCES

1. Khoury et al. 2007. *Fib Bulletin 38: Fire Design of Concrete Structures – Materials, Structures and Modelling, State-of-the-art Report*. International Federation for Structural Concrete (fib TG 4.3.1), Lausanne, 106p.
2. Emmanuel Annerel, 2010. Assessment of the Residual Strength of Concrete Structures after Fire Exposure. Ghent University, Ghent, 303p.
3. Tom Van Den Steen, 2012. *Study and modelling of thermos-mechanical behavior of concrete exposed to fire. Master thesis.* Ghent University, 113p. (Dutch)

Experimental Study on Mechanical Properties of Ultra-high Strength Concrete at Elevated Temperatures

MINGXIANG XIONG, J. Y. RICHARD LIEW and YONG DU

Abstract

This paper introduces experimental study on mechanical properties of an ultra-high strength concrete at elevated temperatures. The compressive strength on cylinders and modulus of elasticity of the ultra-high strength concrete (f_c = 166 N/mm^2) were investigated up to 800°C. The temperature dependent mechanical properties were compared with those of normal/high strength concretes provided in Eurocode 2 and ANSI/AISC 360-10, and with those of concretes in literature. The comparisons showed that the compressive strength and elastic modulus of the ultra-high strength concrete were generally reduced less than those of normal/high strength concretes at elevated temperatures, indicating higher fire resistance when it is used in structural load-bearing elements. The temperature-dependent mechanical properties are proposed to evaluate fire resistance of concrete filled tubes using the ultra-high strength concrete in high-rise buildings.

1 Introduction

Ultra-high strength concrete (UHSC) with compressive strength higher than 120MPa has been available with the development of concrete technology and the availability of variety of materials such as silica fume and high-range water-reducing admixtures. It is mainly used in offshore and marine structures and for industrial floors, pavements and security barriers but has not been used in building structures. This may be due to design concerns on its brittleness and fire resistance leading to the situations that the current standards allow the use of

M.X. Xiong[1,2], J.Y. Richard Liew[2,3,*], Y. Du[3]
[1]School of Civil and Transportation Engineering, Guangdong University of Technology, 100 Waihuan Xi Road, GuangZhou, China 510006
[2]Department of Civil Engineering, National University of Singapore, 21 Lower Kent Ridge Road, Singapore 119077
[3]School of Civil Engineering, Nanjing Tech University, NO.30 Puzhu Road(S),Nanjing, China 211816
* Corresponding author: ceeljy@nus.edu.sg

2 Introduction

Ultra-high strength concrete (UHSC) with compressive strength higher than 120MPa has been available with the development of concrete technology and the availability of variety of materials such as silica fume and high-range water-reducing admixtures. It is mainly used in offshore and marine structures and for industrial floors, pavements and security barriers but has not been used in building structures. This may be due to design concerns on its brittleness and fire resistance leading to the situations that the current standards allow the use of concrete only up to C90/105 for concrete structures and C50/C60 for steel-concrete composite structures [1-4]. A concept of steel tubes infilled with the UHSC was proposed by the authors for load-bearing system of high-rise buildings [5; 6]. To evaluate fire resistance of the UHSC infilled tubes, the knowledge of temperature-dependent mechanical properties is required. In literature, the said properties of normal strength concrete (NSC) and high strength concrete (HSC) have been extensively studied, however for the UHSCs, there is still little information, thus research efforts in this domain are needed.

3 Experimental Preparation

3.1 Test Specimens

The basic materials to produce the UHSC were Ducorit® D4 and water. The water/D4 proportion is 0.076 in terms of weight. In other words, 1.9kg water mixed with 25kg D4 makes 9.4 liters UHSC. The Ducorit® D4 is one of the commercial Ducorit® products. It is made from cementitious mineral powder, superplasticizer and fine bauxite aggregates with maximum sizes less than 4.75mm and 49% less than 0.6mm. The slump flow spread was 735mm and the density was 2700 kg/m^3.

Spalling was found for the plain UHSC subject to high temperatures. The spalling is caused by thermal stress due to temperature gradient during heating, and by splitting force due to release of vapor above 100^{o}C. To prevent such spalling, polypropylene (PP) fibers with a dosage of 0.1% in volume has been added [8]. This was lower than that recommended by EC2 where more than 2kg/m^3 (0.25% in volume) of monofilament propylene fiber should be included in the HSC mixtures to prevent spalling [2]. It is worth noting that steel fibers were not effective to prevent spalling. The characteristics of the PP and steel fibers are shown in Table 1. The workability and flowability of the UHSC were not affected by the addition of PP fibers. This is important as the UHSC is mostly pumped into the steel tubes.

For the standard compression tests, cylinder specimens with diameter of 100mm and height of 200mm were prepared. They were cured in lab air where the relative humidity was approximately 85% and the room temperature was around 30^{o}C at daytime and 25^{o}C at night. The test started at 28 days curing.

Table 1. Properties of steel fiber and polypropylene fiber.

Fiber	Code/Type	Diameter (mm)	Length (mm)	Density (kg/m^3)	Tensile Strength (MPa)
Steel	SF13/80	0.16	13	7850	2300
Polypropylene	Monofilament	0.03±0.005	13	910±0.01%	≥450

3.2 Test Setup and Procedure

The compression tests were conducted by means of a servo-hydraulic testing machine with a maximum 300mm stroke displacement and capacity of 10000 kN. The heating system was a split-tube furnace with two-zone configuration and an optional side entry extensometer port. The external dimensions (diameter x height) are 700 x 600mm and internal heating dimensions (diameter x height) are 350 x 400mm. Extensometer was used to measure the thermal/mechanical displacement with a gauge length of 50mm and maximum measurable strain of 20%. The test setup is shown in Figure 1. The concrete specimen was protected by a steel casing in case the crushing debris at failure would damage the furnace. Diameter of 10mm holes were drilled on surface of the steel casing for heat propagation. The rods of the extensometer were attached to the middle 1/4 height of the specimen which was the gauge length.

The test procedure consisted in testing unstressed specimens, which were heated without any pre-loading, and then tested in compression [9]. A small compressive stress of approximately 0.05MPa was applied prior to testing in the direction of the specimen's central axis in order to maintain the specimen at the center of loading machine. Then the specimen was heated up to target temperature with a heating rate of 5^{o}C/min. In addition to ambient temperature which was approximately 30^{o}C, the target temperatures ranged from 100^{o}C to 800^{o}C at an increment of 100^{o}C. As the UHSC is denser and more impermeable than the NSC, a trial test was conducted to investigate the holding time of target temperature during which uniform temperature distributions can be achieved inside both the furnace and the UHSC specimen. Figure 2 shows the recorded temperatures for a 100x200mm cylinder specimen heated up to 800^{o}C in an electrical oven with a heating rate of 5^{o}C /min. It can be seen that the uniform temperature distribution can be achieved in 4 hours. Hence, the holding time at the target temperatures were taken as 4 hours for all specimens.

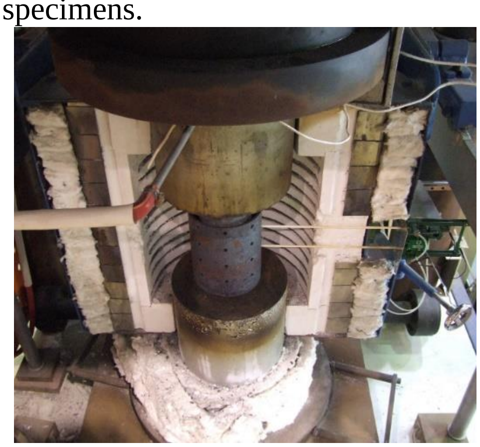

Figure 1. Test setup.

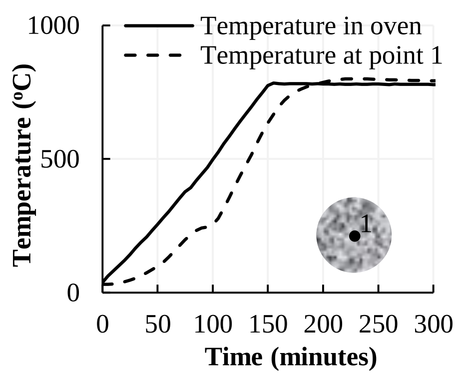

Figure 2. Temperatures in furnace and UHSC specimen.

After holding, the specimen was subjected to three load cycles between 0.05MPa and 15% or between 5% and 15% of the reference strength. The holding time at 5% and 15% load levels was 60s. Then the specimen was loaded to fail. Displacement control was adopted during loading where the displacement rate was 0.4mm/min. It should be mentioned that the full stress-strain curves were not recorded since sudden crush of the UHSC specimen would damage the extensometer. The extensometer was removed when at least 40% of the compressive strength at the target temperature was reached. The 40% compressive strength was measured to calculate the modulus of elasticity. In general, the peak compressive strength and the modulus of elasticity were obtained which are sufficient for fire resistance design of the structural members with the UHSC according to EN 1994-1-2 [4].

4 Test Results

4.1 Compressive Strength

Spalling was not observed during heating of all the UHSC specimens owing to the addition of 0.1% polypropylene fibers. The compressive strength of UHSC at room temperature was 166MPa which was averaged from 6 specimens. 3 specimens were used for the other target temperatures. The compressive strength was taken as the peak stress on the curve of loading head movement versus compressive stress as shown in Figure 3(a). The reduction factor in this paper is defined as the ratio of strength or elastic modulus at target temperature divided by their counterparts at room temperature. The reduction factors of strength are shown in Figure 4. It can be seen that the strength was sharply reduced at 100^{o}C, and then it was partly recovered up to 300^{o}C. It is believed that the chemical composition of the cement paste were not noticeably changed around 100^{o}C. Hence, the sharp reduction of strength at 100^{o}C could be due to the built-up internal pressure by the evaporation of free water. For the recovery of strength up to 300°C, it might be attributed to the general stiffening of the cement gel by shrinkage, in other words, the increase of surface forces (Van der Walls forces) between the gel particles due to the removal of water [10]. The temperature at which water is removed and the strength begins to recover depends on the porosity of the concrete [11]. Beyond 300^{o}C, the strength decreased as the temperature increased. The decrease of strength was attributed to the decomposition of hydration products such as C-S-H and $Ca(OH)_2$, the deterioration of aggregates, and the cracks due to thermal incompatibility between the aggregate and the cement paste which led to stress concentration. At 800^{o}C, the strength was about 30% of that at room temperature.

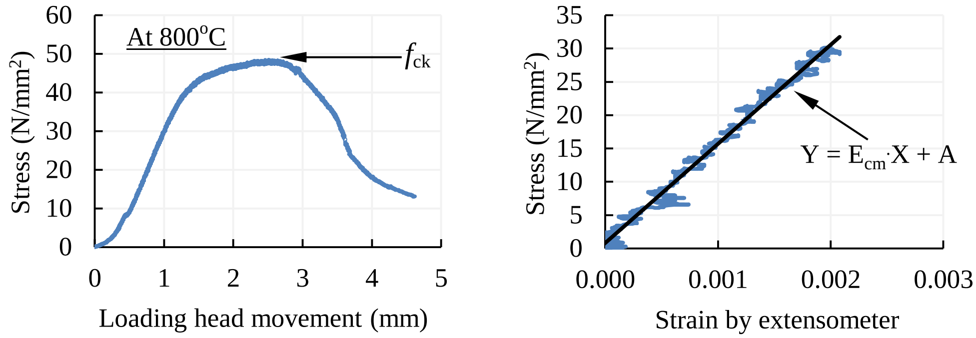

(a) compressive strength (b) modulus of elasticity E_{cm}

Figure 3. Determination of compressive strength and modulus of elasticity.

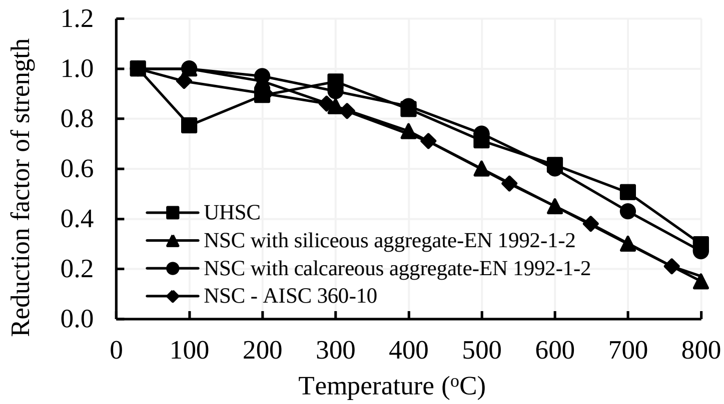

Figure 4. Comparison between strength reduction factors of UHSC and NSC as given in EN 1992-1-2 and AISC 360-10.

The comparisons between the strength reduction factors of UHSC and NSC given in EN 1992-1-2 [2] and AISC 360-10 [12] are also shown in Figure 4. The NSC is implicitly defined as compressive cylinder strength less than 55MPa in EN 1992-1-2, and not greater than 55MPa in AISC 360-10. The reduction factors are applicable to both NSCs with siliceous aggregates and calcareous aggregates in AISC 360-10. It was supposed that the strength of UHSC would reduce greater than that of NSC. However, it can be seen that, beyond 300°C, the reduction factors of UHSC are similar with those of NSC with calcareous aggregates, but higher than those of NSC with siliceous aggregates. The reason was due to the effect of aggregate type. Generally, the aggregates occupy 65% to 75% of the concrete volume. The effect of aggregate mainly depends on thermal stability or integrity of aggregate at high temperatures [13]. Conventional calcareous or siliceous aggregates are thermally stable up to 300°C~350°C. Bauxite aggregates in UHSC are more stable due to high melting point, and thus produced significant improvements in heat resistance of the UHSC. The bauxite aggregates have been used for refractory concretes to achieve super fire performance [14]. The comparison between the strength reduction factors of UHSC and HSC in EN 1992-1-2 are shown in Figure 5. The reduction factors are not provided for HSC in AISC 360-10. It is clear that the strength of UHSC was reduced less than that of HSC due to the effect of aggregate type. The comparisons indicated that, for stub CFST columns with the UHSC governed by compressive resistance, they would withstand longer time when exposed to fire than the CFST columns with the NSC and HSC.

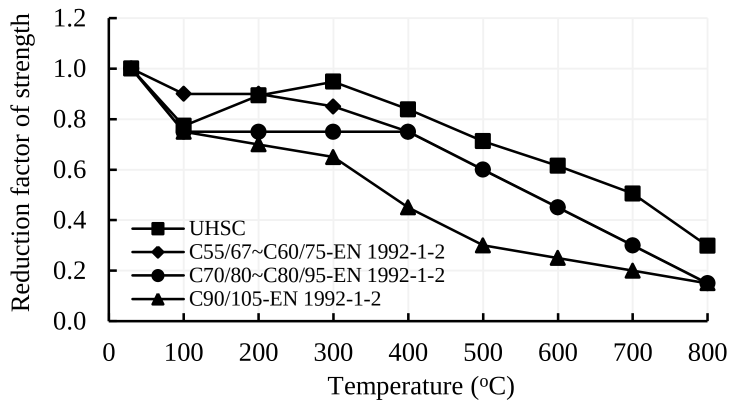

Figure 5. Comparison between strength reduction factors of UHSC and HSC as given in EN 1992-1-2.

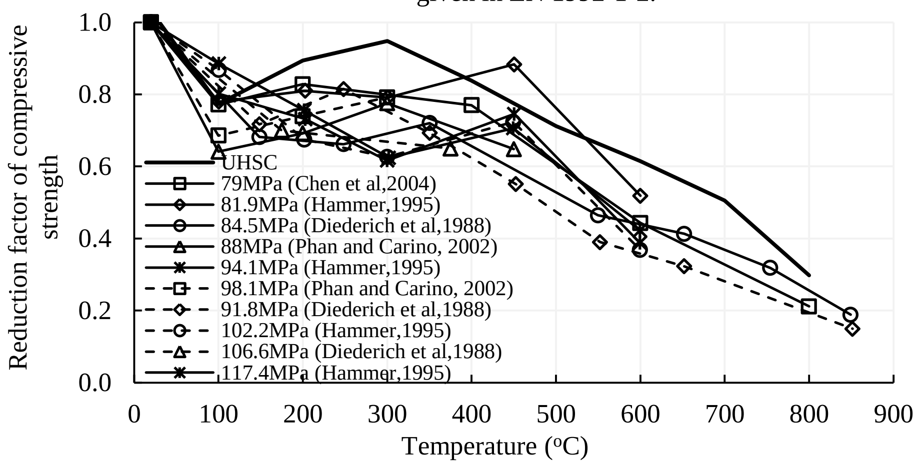

Figure 6. Comparison between strength reduction factors of UHSC and HSC with results from previous researches.

The strength reduction factors of UHSC are compared with those of HSC in the literature as shown in Figure 6 [15-18]. It can be seen that the sharp deterioration at 100°C and the recovery of strength between 100°C~300°C were also captured in previous researches. In general, the strength of UHSC at elevated temperatures were reduced less than those of HSCs in the literature.

4.2 Modulus of Elasticity

The elastic modulus was generally defined as the secant modulus between the stress equal to 40% of peak stress and the stress corresponding to strain of $5x10^{-5}$ in accordance with ASTM C469-02 [19]. For some stress-strain curves with the existence of turbulence, the slope of the regressed linear equation for a straight portion was taken as the modulus of elasticity as shown in Figure 3(b). The reduction factors of elastic modulus at elevated temperatures are shown in Figure 7. Similar to the compressive strength, the sharp reduction and the recovery were also observed for the elastic modulus due to the built-up internal pressure by the evaporation of free water. Figure 7 also gives the comparisons between the modulus reduction factors of UHSC and NSC as given in EN 1992-1-2 and AISC 360-10. The modulus of elasticity of UHSC was less affected than that of NSC.

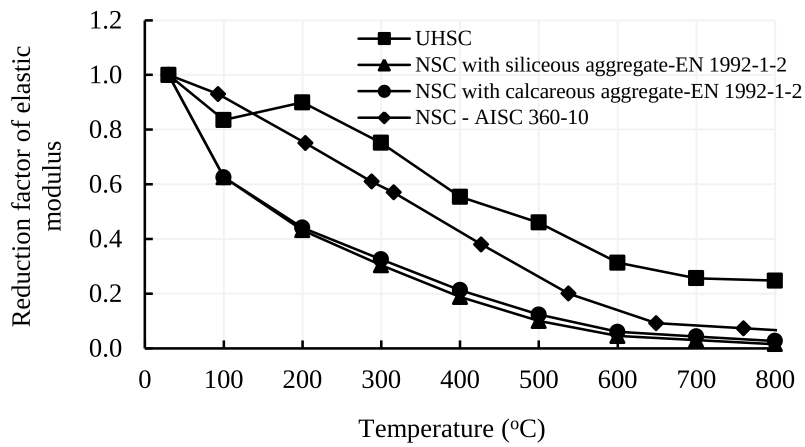

Figure 7. Comparison between elastic modulus reduction factors of UHSC and NSC as given in EN 1992-1-2 and AISC 360-10.

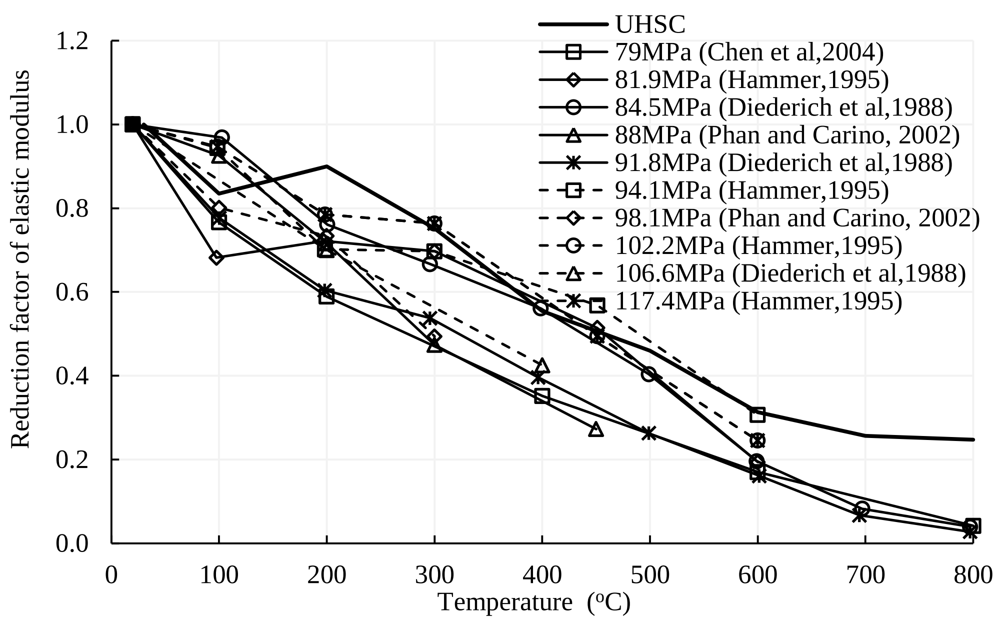

Figure 8. Comparison between reduction factors of elastic modulus of UHSC and HSC as given in previous researches.

The reduced elastic modulus of UHSC are also compared with those of HSC in the literature as shown in Figure 8 [15-18]. The sharp reduction and recovery were also observed in some researches. Overall, the elastic modulus of UHSC was reduced less than most of the HSCs in the literature due to the effect of aggregate. For slender CFST columns with the UHSC governed by buckling resistance, the comparisons indicated that they would withstand longer time when exposed to fire than the CFST columns with the NSC and HSC.

5 Concluding Remarks

Experimental investigation on the mechanical properties of UHSC at elevated temperatures including cylinder compressive strength and modulus of elasticity were presented. The following conclusions can be drawn.

1) Spalling of the UHSC was prevented during heating to 800^{o}C due to the addition of 0.1% polypropylene fibers.
2) Sharp deterioration of strength of the UHSC was observed at 100^{o}C and then it was partly recovered up to 300^{o}C. The deterioration and recovery of strength were induced by the evaporation of free water and the resulted shrinkage. The deterioration around 100°C and recovery of strength up to 300°C were also observed for HSC from previous researches.
3) Strengths of the UHSC at elevated temperatures were reduced less than those of NSC and HSC as introduced in Eurocode 2 and AISC 360, and the HSC reported in the literature. This can be explained through the types of aggregates.
4) Deterioration and recovery of the elastic modulus of the UHSC were observed at the temperature range of 100^{o}C~200^{o}C, similar to HSC from previous researches. The elastic modulus of the UHSC were reduced less than that of NSC in Eurocode 2 and AISC 360.

Acknowledgement

The authors would like to acknowledge the funding support by Singapore A*STAR for research project "Steel-concrete composite systems employing ultra-high strength steel and concrete for sustainable high-rise construction" under SERC Grant No: 092 142 0045.

References

[1] EN 1992-1-1 (2004) “Eurocode 2: Design of concrete structures - Part 1-1: General rules and rules for buildings” European Committee for Standardization.

[2] EN 1992-1-2 (2004) “Eurocode 2: Design of concrete structures - Part 1-2: General rules-structural fire design” European Committee for Standardization.

[3] EN 1994-1-1 (2004) “Eurocode 4: Design of composite steel and concrete structures - Part 1-1: General rules and rules for buildings” European Committee for Standardization.

[4] EN 1994-1-2 (2005) “Eurocode 4: Design of composite steel and concrete structures - Part 1-2: General rules - Structural fire design” European Committee for Standardization.

[5] Liew J.Y.R., Xiong D.X. (2012) “Ultra-high strength concrete filled composite columns for multi-storey building construction” *Adv. Struct. Eng.* 15(9):1487-1503.

[6] Liew J.Y.R., Xiong M.X., Xiong D.X (2014) “Design of high strength concrete filled tubular columns for tall buildings” *Int. J. High Rise Build.* 3(3): 1-7.

[7] Zeiml M., Leithner D., Lackner R. (2006) “How do polypropylene fibers improve the spalling behavior of in-situ concrete?” *Cem. Concr. Res.* 36: 929-942.

[8] Xiong M.X, Liew J.Y.R. (2015) Spalling behavior and residual resistance of fibre reinforced ultra-high performance concrete after elevated temperatures. *Mater. Constr.* 65(320): 1-10.

[9] RILEM Technical Committee (2007) “Recommendation of RILEM TC 200-HTC: mechanical concrete properties at high temperatures – modeling and applications, Part 2: stress-strain relation” *Mater. Struct.* 40:855-864.

[10] Behnood A., Ziari H. (2008) “Effects of silica fume addition and water to cement ratio on the properties of high-strength concrete after exposure to high temperatures” *Cem. Concr. Compos.* 30: 106-112.
[11] Chen B., Liu J.Y. (2004) “Residual strength of hybrid-fiber-reinforced high-strength concrete after exposure to high temperatures” *Cem. Concr. Res.* 34: 1065-1069.
[12] ANSI/AISC 360-10 (2010) “Specification for structural steel buildings” American Institute of Steel Construction, Inc. June 22.
[13] Naus D.J. (2006) “The effect of elevated temperature on concrete material and structures-a literature review” Oak Ridge National Laboratory, U.S. Nuclear Regulatory Commission, Office of Nuclear Regulatory Research, Washington, DC 20555-0001.
[14] Evariste O., Mohsen R., Nicolas P. (2011) “Refractory concretes uniaxial compression behaviour under high temperature testing conditions” *J. Europ. Cera. Soc.* 31: 2763–74.
[15] Hammer T.A. (1995) “High-strength concrete phase 3, compressive strength and elastic modulus at elevated temperatures” SP6 Fire resistance, Report 6.1, SINTEF Structure and concrete, STF70 A95023, February.
[16] Diederichs U., Jumppanen U.M., Penttala V. (1988) “Material properties of highs strength concrete at elevated temperatures”. *IABSE 13th Congress*, Helsinki, June.
[17] Chen B., Liu J.Y. (2004) “Residual strength of hybrid-fiber-reinforced high-strength concrete after exposure to high temperatures” *Cem. Concr. Res.* 34: 1065-1069.
[18] Phan L.T., Carino N.J. (2002) “Effects of test conditions and mixture proportions on behavior of high strength concrete exposed to high temperatures” *ACI Mater. J.* 99(1): 54-66.
[19] ASTM C 469-02 (2002) “Standard test method for static modulus of elasticity and Poisson’s ratio of concrete in compression”.

Assessing Tensile Properties of Fire-Damaged Engineered Cementitious Composites with Hybrid Fibres

JIN-CHENG LIU and K. H. TAN

ABSTRACT

Engineered Cementitious Composite (ECC) is one special type of fibre-reinforced cementitious composite which is well known for its strain hardening behaviour under direct tension. For practical applications of ECC in buildings and infrastructures, performance of ECC under different environments should be evaluated. The fire resistance of ECC is questionable, especially when non-fire-resistant polymer fibres are used. PVA fibres are most widely used polymer fibres in ECC, however, they will melt at temperature around 220 °C leading to disappearance of strain-hardening behaviour. In the study, 0.5% volume of PVA fibres was replaced by steel fibres in ECC so as to alleviate the negative impact of melting of PVA fibres. Tensile stress-strain relationships of this type of ECC with hybrid fibres after 100 °C to 600 °C at an increment of 100 °C were investigated. Digital Image Correlation (DIC) technique was used to capture cracking patterns of fire-damaged ECC. It was found that steel fibres improve tensile behaviour of ECC at 300 °C. After 600 °C, 79% of tensile strength of ECC remained. The results provided useful information of tensile behaviour of ECC with hybrid fibres and yielded promising direction for future improvement of tensile properties of ECC at elevated temperatures.

KEYWORDS

ECC, hybrid fibres, high temperature, tensile behaviour, DIC

INTRODUCTION

Engineered cementitious composite (ECC), first emerged in 1990s [1], is one special type of fibre-reinforced cementitious composite which can be tailored through principle of micromechanics [2-4]. This material is well-known for its strain-hardening behaviour under direct tension with a tensile strain capacity hundred times that of normal concretes. Self-healing capability is another important advantage of ECC owing to its multiple fine cracks with very tight crack widths [5]. It has potential applications in retaining walls, water-retaining structures, repair and retrofitting work, bridges and underground tunnels, etc. (Lepech and Li 2009, Boughanem et al. 2013, Mechtcherine 2013, Rokugo and Kanda 2013). For ECC to bemore widely used in engineering projects, behaviour of ECC under different environments or design situations should be examined as well. ECC has excellent durability at aggressive environments, good seismic, impact and fatigue resistance [2, 6-10]. Fire resistance of ECC is an important aspect, since fire represents one of the most severe environmental conditions to which structures may be subjected during their service life [11]. PVA fibres are the most widely used fibres for the production of ECC and their melting point is around 220 °C. The tensile ductility of ECC relies on PVA fibres, but these fibres will soften, melt and decompose under elevated temperatures. The tensile ductility originally featured by ECC at ambient condition will degrade quickly as temperature rises. Furthermore, whether the voids left by melted PVA fibres will affect the mechanical performance of ECC remains questionable.

Limited work has been conducted on tensile behaviour of ECC under elevated temperatures. Mechtcherine [12] investigated both in-situ and residual tensile behaviour of ECC with 2.2% vol. PVA fibres under different temperatures and strain rates. The selected isothermal temperatures were 22 °C, 60 °C, 100 °C and 150 °C and the selected strain rates were 10^{-5} s^{-1}, 3×10^{-4} s^{-1} and 10^{-2} s^{-1}. When tested under an in-situ temperature of 60 °C, ECC demonstrated an increase in strain and a decrease in strength with a strain rate of 10^{-5} s^{-1}. At 100 °C and 150 °C, ECC demonstrated an increase in both strain and strength with a strain rate of 10^{-5} s^{-1}. While tested under residual state, ECC revealed a decreasing trend in both strain and strength with rise of temperature. Tensile behaviour of ECC beyond 150 °C was not considered in their work. da Silva Magalhães [13] reported residual tensile behaviour of ECC with 2% vol. PVA fibres heated to temperatures ranging from ambient temperature to 250 °C. Strain capacity of this ECC mix after 90 °C remained almost unchanged, but beyond 90 °C it reduced and after 250 °C there was no strain-hardening behaviour. Bhat [14] found that tensile strength and tensile strain in general decreased with increasing temperature from 100 °C to 600 °C. Yu [15] found that tensile strength and strain of ECC containing high volume fly ash increased after 50 °C and 100 °C, but diminished after 200 °C. What was common in previous research works on tensile behaviour of fire-damaged ECCs was that all ECC design mix only contained PVA fibres. Besides, with the exception of Bhat [14], all other researchers only investigated tensile behaviour of ECCs under 250 °C. However, the actual fire temperature is much higher than 250 °C. In this paper, an experimental programme was designed to study tensile behaviour of ECC with hybrid PVA/steel fibres subject to elevated temperatures up to 600 °C. This work will shed more light on tensile behaviour of fire-damaged ECC and study the contribution of steel fibres to residual tensile stress-strain relationship of ECC so as to find a workable mix design to compensate for the complete loss of polymer fibres after attaining their melting temperature.

MATERIALS AND METHODS

Materials

The basic materials used for ECC included CEM I 42.5 N corresponding to EN 197-1, Cass F F40 fly ash conforming to ASTM 618, silica sand, tap water, PVA fibres, steel fibres and superplasticizer. The silica sand has a mean size of 110 μm. The PVA fibre's surface has 1.2% oil coating by weight. Details of the PVA and steel fibres are listed in TABLE I and TABLE II, respectively. Volume of fibres took up 2% of the total volume. A third-generation polycarboxylic type superplasticizer Sika ViscoCrete-2044 was used in preparing the ECC coupons. The adopted ECC mix shown in TABLE III was an optimised mix design in terms of multi-responses of ECC when subject to fire conditions, i.e. compressive strength, tensile strain capacity at ambient and compressive strength of ECC after being exposed to 200 °C, 400 °C, 600 °C and 800 °C.

To prepare the ECC mix, cement, fly ash and sand were mixed for 5 min in a Hobart mixer with a 20 L capacity. Water and superplasticizer were added to the mixer and mixed for another 5 min to allow appropriate workability of the matrix. Lastly, PVA fibres and steel fibres were sequentially added into the fresh matrix in 1-2 min and mixed for another 3 min. Dog-bone specimens were cast to determine residual tensile properties of ECC with hybrid fibres (Figure 1). Specimens were removed from the moulds one day after casting, conditioned inside sealed plastic sheet for 7 days and then conditioned at ambient conditions in the laboratory until 28 days.

TABLE I. Characteristics of PVA fibre.

Fibre	PVA
Tensile strength,	1060
Diameter, μm	39
Length, mm	12
Young's modulus	42.8
Elongation, %	6.0
Density, kg/m^3	1300
Melting	220

TABLE II. Characteristics of steel fibre.

Fibre	Steel
Tensile strength, MPa	2000
Diameter, mm	0.16
Length, mm	13
Young's modulus	200
Shape	Straight
Density, kg/m^3	7800
Aspect ratio	81

TABLE III. ECC mix design.*

Cement	Fly ash	Sand	Water	PVA fibre	Steel fibre	Superplasticizer
1	1.22	1	0.62	1.50%	0.50%	0.011

* Content of fibres is expressed as volume fraction of the mix, while all the other ingredients are expressed as weight proportion of cement content.

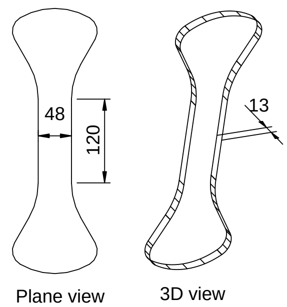

Figure 1. Geometry of tensile specimens.

Experiment design

In this paper, tensile behaviour of ECC with hybrid PVA/steel fibres after exposure to 600 °C were assessed based on unaxial tensile tests. The specimens were heated to target temperature at a heating rate of 10 °C/min and then the temperature was kept constant for 2 hours to allow them to attain isothermal condition. Uniaxial tension tests were conducted after the specimens cooled down naturally to ambient temperature of 30 °C. The specimens were weighed before and after heating to evaluate the mass loss. For each target temperature, three specimens were tested. In this experimental programme, 2D DIC technique was used to confirm the uniaxial tensile test results and to characterise the crack propagation of ECC after exposure to different temperatures. The dog-bone specimen was placed into two wedges fixed at the loading machine. A small tension force (maximum 30N) was applied to avoid any gaps in between the specimen ends and the wedges. Two linear variable differential transformers (LVDTs) were used to measure deformations of the straight segment of the specimen with a gauge length of 100 mm. Load was applied following a displacement-controlled method at a rate of 0.2 mm/min and automatically recorded by an embedded load cell in the Instron machine. A high-resolution digital camera was fixed to a tripod approximately 1 m in front of the specimen. DIC technique was used for one of the three specimens for all target temperatures. During the tests, the digital camera was connected to a control device through the Wi-Fi to facilitate photograph taking without physically touching the camera. Digital images were taken at an interval of 10s in the first 2 min, after that, taken every 30s until softening of specimens occurred.

The working principle of DIC is based on interpreting similarities of subsets (a set of pixels) between subsequent captured images as a grey-scale pattern in light density. To produce the speckle pattern for strain analysis, one surface of a specimen was white-washed using non-sticky white paint. The surface was then sprayed with random small black spots on the region of the white surface within the gauge length of LVDTs.

RESULTS AND DISCUSSIONS

Typical tensile stress-strain curves of the ECC mix with hybrid fibres at ambient condition are given in Figure 2, and the specimens at ambient condition were taken as control samples. Stress-strain curves of ECC mix after exposure to 100 °C, 200 °C, 300 °C, 400 °C, 500 °C and 600 °C are given in Figure 3. The ECC specimens showed tensile strain hardening behaviour up to 200 °C. However, the tensile strain capacity decreased with temperature rise beyond 200 °C. At 300 °C, the ECC specimens lost their strain hardening characteristic, and instead exhibited strain softening behaviour. At target temperature of 400 °C, 500 °C and 600 °C, the specimens completely lost the strain softening behaviour, and behaved like plain concrete. However, with rise of temperature the strain corresponding to the maximum tensile strength increased slightly, possibly due to thermal damage causing degradation of stiffness. That the strain capacities of specimens exposed to temperatures below and above 200 °C were not of the same order of magnitude is due to different failure mechanisms. The specimens exposed to temperature below 200 °C failed by multiple-fine-cracks pattern. It is noteworthy that the strain capacity is closely related to the number of fine cracks developed on the specimen surface. The greater the number of fine cracks, the larger is the strain capacity, and vice versa. However, the specimens exposed to temperature above 300 °C failed in a single-crack mode, i.e. when the tensile stress reached the tensile strength, the capacity sharply reduced to zero. It is noteworthy that although the specimens at 300 °C had the smallest strain capacity, they still can carry certain tensile load after the occurrence of cracks (Figure 3(c)). PVA fibres have already melted at about 220 °C, so when a single crack occurs, they cannot contribute to bridging stress across the crack and steel fibres are the only source of bridging stress. Based on observation of ruptured cross sections, the steel fibres remained intact after failure of tensile specimens. The bridging stress was contributed by bond stress between steel fibres and matrix rather than tensile strength of steel fibres. At 400 °C and above, the specimens lost their capacity completely once a crack occurred (Figure 3(d)-(f)). Although the steel fibres did not melt at these temperatures, the ECC matrix deteriorated due to dehydration, weakening the bond strength between the steel fibres and the matrix. At 400 °C above the resisting stress across the crack was so small that it could be neglected. This explained the quasi-brittle tensile behaviour of ECC specimens above 400 °C. In contrast, ECC with 2% vol. PVA fibres only exhibited a brittle behaviour akin to plain concrete at 300 °C and beyond. The test results showed that steel fibres could improve the tensile performance of ECC to some extent. To further improve the tensile performance of ECC at temperature higher than 300 °C, i.e. to overcome the brittle nature, more steel fibres can be added into the composite. The strain-hardening behaviour of ECC was accompanied by development of multiple fine cracks, reflected by the maximum normal strain contours of ECC specimens at failure as shown in Figure 4(a)-(g). It was consistent that the number of fine cracks reduced with increase of temperature up to 200 °C. At or beyond 300 °C, only one crack appeared on the specimen surface, indicating the loss of tensile strain-hardening characteristic.

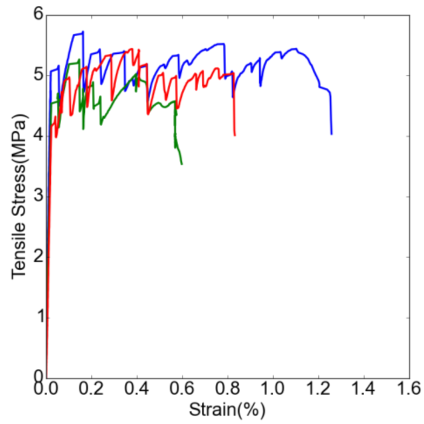

Figure 2. Tensile stress-strain curve of the ECC mix at ambient condition.

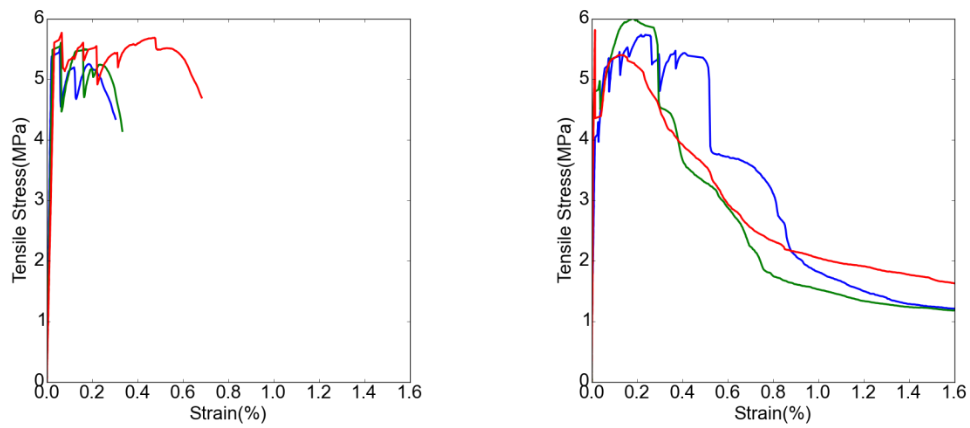

(a) 100 °C (b) 200 °C

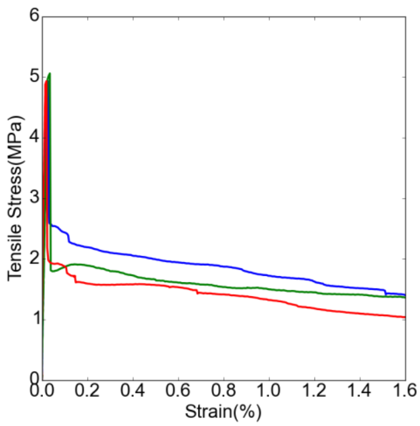

(c) 300 °C

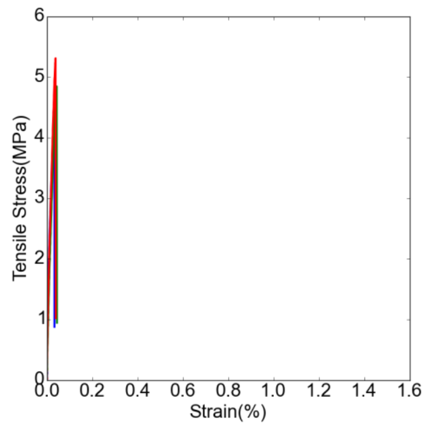

(d) 400 °C

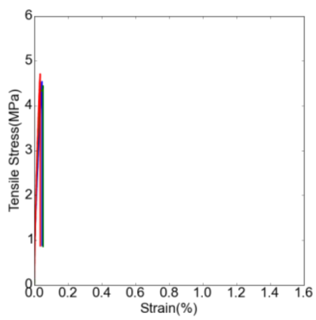

(e) 500 °C

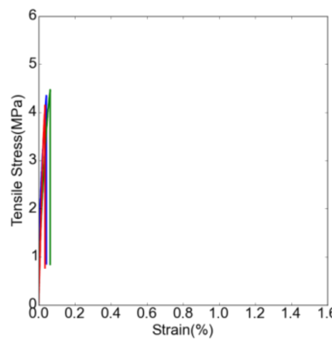

(f) 600 °C

Figure 3. Tensile stress-strain curve of the ECC mix after heating to different temperatures.

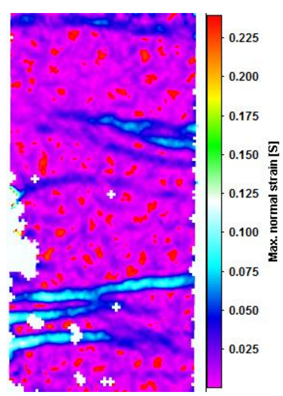

(a) 20 °C

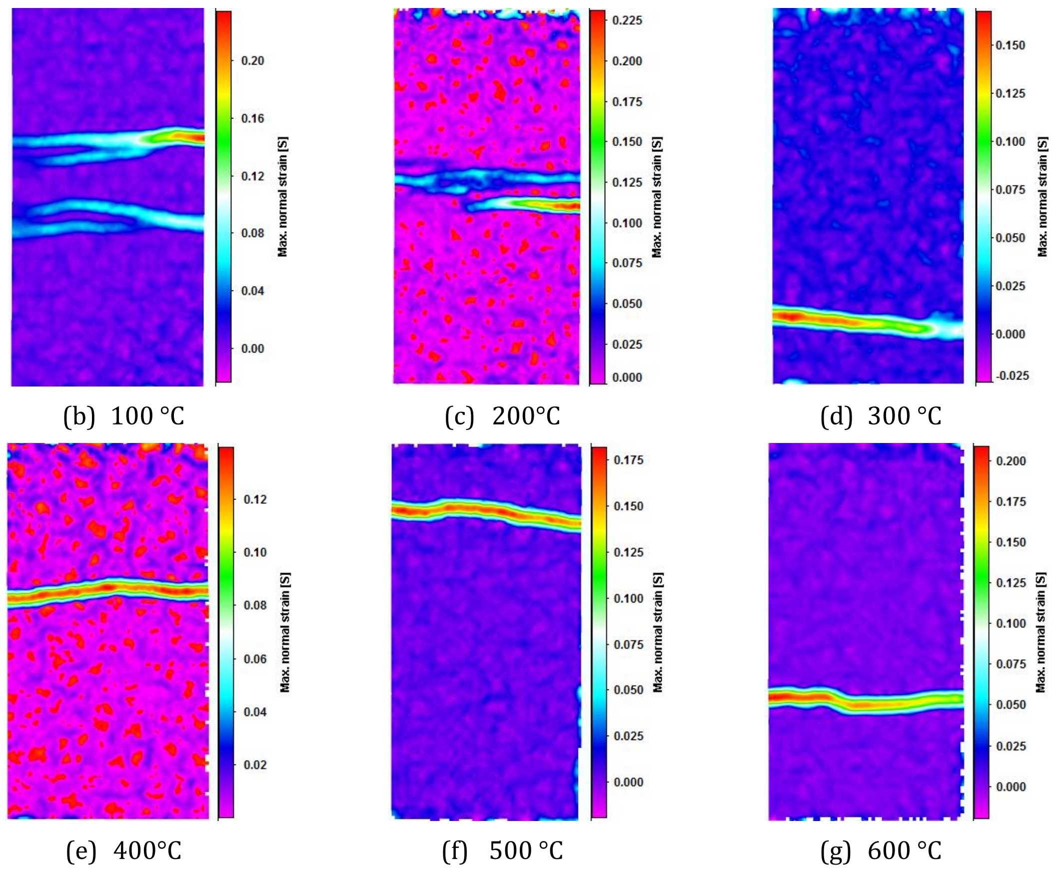

Figure 4. Maximum normal strain fields of ECC specimens at failure at different target temperatures.

Figure 5 shows the mass loss of ECC and that of concrete specified in Eurocode 2 [16] at elevated temperatures. Mass loss is due to moisture loss and loss of dehydrated water. ECC suffers greater mass loss compared to normal concrete at elevated temperatures. At temperature below 200 °C, ECC showed a faster mass loss rate. Beyond 200 °C, the mass loss rate of ECC gradually diminished up to 600 °C.

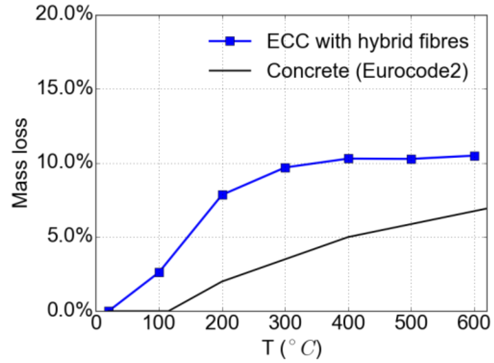

Figure 5. Mass loss at elevated tempeatures.

CONCLUSIONS

ECC outperforms normal concrete due to tensile strain-hardening behaviour at ambient temperature and self-controlled micro-cracks in terms of improved damage tolerance and reduced transport properties. The paper studied conventional ECC mix with 0.5% vol. steel fibres in replacement of equivalent volume of PVA fibres and reported the tensile properties of this type of ECC after heating to temperature up to 600 °C.

This study found that ECC with hybrid fibres exhibited tensile strain-hardening behaviour up to 200 °C. However, its tensile strain capacity decreased significantly with an increase of temperature. At 300 °C, ECC completely lost the strain-hardening characteristic, and instead showed tensile strain-softening behaviour. At temperatures above 300 °C, ECC lost tensile strain softening characteristic, and behaved like normal concrete under tension. Compared with ECC with PVA fibres only, ECC with hybrid steel/PVA fibres can delay brittle failure at high temperatures. Based on crack patterns of ECC from DIC analysis, the number of cracks decreased with temperature rise up to 200 °C. Only one crack was observed on the specimen surface beyond 300 °C.

It is noteworthy that the tensile behaviour of ECC was evaluated under residual conditions. Further work will be conducted to investigate the tensile behaviour under hot conditions.

This study provides a possible mix design to engineer ECC materials with better tensile properties at elevated temperatures, and this type of ECC reinforced with hybrid fibres can be explored for spent nuclear fuel storage applications.

ACKNOWLEDGEMENTS

This material is based on research/work supported by the Singapore Ministry of National Development and National Research Foundation under L2 NIC Award No. L2NICCFP1-2013-4.

DISCLAIMER

Any opinions, findings, and conclusions or recommendations expressed in this material are those of the author(s) and do not necessarily reflect the views of the L2 NIC.

REFERENCES

1. Li, V.C. and Leung, C.K. 1992. "*Steady-state and multiple cracking of short random fiber composites,"* Journal of Engineering Mechanics, 118(11): 2246-2264.
2. Li, V.C. 2003. "*On engineered cementitious composites (ECC),"* Journal of advanced concrete technology, 1(3): 215-230.
3. Li, V.C., Wu, C., Wang, S., Ogawa, A. and Saito, T. 2002. "*Interface tailoring for strain-hardening polyvinyl alcohol-engineered cementitious composite (PVA-ECC),"* ACI Materials Journal-American Concrete Institute, 99(5): 463-472.
4. Kanda, T. and Li, V.C. 2006. "*Practical design criteria for saturated pseudo strain hardening behavior in ECC,"* Journal of advanced concrete technology, 4(1): 59-72.
5. Wu, M., Johannesson, B. and Geiker, M. 2012. "*A review: Self-healing in cementitious materials and engineered cementitious composite as a self-healing material,"* Construction and Building Materials, 28(1): 571-583.
6. Yang, E.-H. and Li, V.C. 2012. "*Tailoring engineered cementitious composites for impact resistance,"* Cement and Concrete Research, 42(8): 1066-1071.
7. Zhang, J., Maalej, M. and Quek, S.T. 2007. "*Performance of hybrid-fiber ECC blast/shelter panels subjected to drop weight impact,"* Journal of Materials in Civil Engineering, 19(10): 855-863.
8. Fischer, G. and Li, V.C. 2002. "*Effect of matrix ductility on deformation behavior of steel-reinforced ECC flexural members under reversed cyclic loading conditions,"* ACI Structural Journal, 99(6): 781-790.
9. Leung, C.K., Cheung, Y.N. and Zhang, J. 2007. "*Fatigue enhancement of concrete beam with ECC layer,"* Cement and concrete research, 37(5): 743-750.

10. Şahmaran, M. and Li, V.C. 2009. "*Durability properties of micro-cracked ECC containing high volumes fly ash,"* Cement and Concrete Research, 39(11): 1033-1043.
11. Kodur, V. and Dwaikat, M. 2008. "*A numerical model for predicting the fire resistance of reinforced concrete beams,"* Cement and Concrete Composites, 30(5): 431-443.
12. Mechtcherine, V., de Andrade Silva, F., Müller, S., Jun, P. and Toledo Filho, R.D. 2012. "*Coupled strain rate and temperature effects on the tensile behavior of strain-hardening cement-based composites (SHCC) with PVA fibers,"* Cement and Concrete Research, 42(11): 1417-1427.
13. da Silva Magalhães, M., Toledo Filho, R.D. and Fairbairn, E.d.M.R. 2015. "*Thermal stability of PVA fiber strain hardening cement-based composites,"* Construction and Building Materials, 94: 437-447.
14. Bhat, P.S., Chang, V. and Li, M. 2014. "*Effect of elevated temperature on strain-hardening engineered cementitious composites,"* Construction and Building Materials, 69: 370-380.
15. Yu, J., Lin, J., Zhang, Z. and Li, V.C. 2015. "*Mechanical performance of ECC with high-volume fly ash after sub-elevated temperatures,"* Construction and Building Materials, 99: 82-89.
16. EN, B. 2004. "*1-2: 2004 Eurocode 2: Design of concrete structures-Part 1-2: General rules-Structural fire design."*.

Experimental Validation of the Damage-Plasticity Modeling Concept for Normal Strength Concrete in Fire

MARTIN NEUENSCHWANDER[1], CLAUDIO SCANDELLA[1], MARKUS KNOBLOCH[2] and MARIO FONTANA[1]

ABSTRACT

The softening behavior of concrete and its elastic stiffness evolution with increasing plastic straining can be investigated experimentally with strain-rate controlled uniaxial cyclic compression tests. Such tests at ambient temperature show that concrete exhibits the phenomenon of elastic stiffness degradation, which can be captured by damage-plasticity models. However, temperature-dependent concrete models implementing this modeling concept are often used today in structural fire engineering, despite the lack of experiment-based validation data. This paper presents the results of a preliminary study on the behavior of normal strength concrete under cyclic compressive loading at elevated temperatures. The experimentally derived evolutions of the elastic stiffness with plastic strain confirm (1) the suitability of the damage-plasticity modeling concept for concrete in compression at elevated temperatures and (2) provide novel calibration data.

INTRODUCTION

Failure analysis of concrete and composite structures in fire that accounts for effects due to load-redistributions and confinement action, is an important task in structural fire engineering. In this framework, advanced generic concrete models, capable of considering these effects have become an important tool for analysis since they are available as temperature-dependent constitutive material models in some finite-element method software packages. However, these models were developed only on the basis of phenomena, observed in the concrete's macroscopic behavior in fracture experiments at ambient temperature.

Plasticity-based concrete models can capture the main macroscopic characteristic of the softening behavior of concrete that consists of a decreasing yield stress upon loading, which is accompanied by irreversible (plastic) strains and inelastic volumetric expansion (depending on the confining pressure). However, plasticity models alone cannot account for the stiffness degradation that has been

1) ETH Zurich, Department of Civil and Environmental Engineering, Institute of Structural Engineering – Steel, Timber and Composite Structures, Stefano-Franscini-Platz 5, 8093 Zurich, Switzerland.
2) Ruhr Universität Bochum, Department of Civil and Environmental Engineering, Institute of Steel, Lightweight and Composite Structures, Universitätsstraße 150, 44801 Bochum, Germany.

repeatedly reported by various researchers from ambient-temperature uniaxial cyclic tests with concrete in compression [1-5] and tension [6]. This shortcoming of simple plasticity models lead to the development of damage-plasticity models that can reproduce the experimentally observed stiffness degradation. A brief overview of this research development is given in ref. [7]. In ABAQUS Standard, a generic damage-plasticity model is implemented that is based on the models of refs. [8,9], which were validated on the level of material property test data with uniaxial monotonic and cyclic tests at ambient temperature in compression [2] and tension [6]. Such a generic model requires hardening, strain-softening and elastic stiffness degradation input data in compression, to fully deploy its features in the inelastic (compressive) regime, and it can account for temperature dependence, when the input data is provided at different temperature levels. More recently, [10] presented a multi-axial temperature-dependent damage-plasticity model that is implemented in the SAFIR software package. This model incorporates (1) temperature-dependent damage evolution relations of exponential form; and (2) temperature-dependent compressive hardening and softening behavior that yields in uniaxial compression similar results as the temperature-dependent Eurocode 2 model [11] for consistency with practical applications [10].

Only recently, [12] could validate experimentally at elevated temperatures the suitability of the damage-plasticity modeling concept for concrete, with a series of strain-rate controlled cyclic compression tests at elevated temperatures with self-compacting concrete (SCC). This paper now presents the results of a subsequent preliminary test program with normal strength concrete (NSC) that confirms the primary findings from the study with SCC also for NSC.

EXPERIMENTAL PROCEDURE

A preliminary test series of strain-rate controlled cyclic compression tests at elevated temperatures of 500, 600 and 700°C (two tests per temperature level) was performed with cylindrical specimens of NSC that featured a diameter, D_0, of 50 mm and a height, h_0, of 100 mm. This section briefly presents the specimen preparation, the test apparatus and the fully automated test sequence used in this preliminary study. A more detailed description of the entire test setup can be found in [12], where the results of an extended cyclic compression test program with SCC specimens are reported that have been obtained using the same test method.

Mixture Proportions and Specimen Properties and Preparation

The mixture proportions of the concrete used to fabricate the specimens are given in Table I. The cement used was an unblended Portland cement (CEM I 42.5) and the aggregates consisted of round siliceous limestone gravel (maximum diameter of 8 mm) and sand. The concrete mixture was prepared in four batches for each of which the wet density, the air content and the spread of the wet concrete from a flow table test were determined according to EN 12350. The mean values of these wet concrete properties are listed in Table I, together with mean values of the compressive strength after 28 and 90 days. The concrete was casted in cylindrical plastic molds with a diameter of 150 mm and a height of 300 mm and then compacted on a laboratory vibration table. After 72 hours storing in a moisture

TABLE I. MIXTURE PROPORTIONS AND PROPERTIES OF CONCRETE

Mixture proportions (kg/m^3)				w/c	Wet density	Flow table test	Air content	Cylinder strength (N/mm^2)	
Cement	Water	Coarse aggregates (4–8 mm)	Fine aggregates (0–4 mm)	(-)	(kg/m^3)	(mm)	(%)	after 28 days	after 90 days
425	234	239	1357	0.55	2297	465	0.75	41.1	46.2

room at 95% relative humidity and 20°C, the cylinders were de-molded and stored furthermore in the moisture room until an age of 28 days. Then the cylinders were halved at mid-height with a diamond saw and four specimen blanks were extracted from each of these halves with a 50 mm diameter core drill. Next the specimen blanks were cut to length (100 mm) and finished on a grinding machine to produce parallel loading faces. Subsequently the specimens were stored for 317 days at 50% relative humidity and 20°C until testing took place. Shortly before testing, the specimens were equipped with two type K thermocouples, as indicated with, $\theta_{\mathrm{Sp,top}}$ and $\theta_{\mathrm{Sp,bot}}$, in the schematic of the test setup in Figure 1.

Test Apparatus

The test apparatus consisted of a combined setup of a universal testing machine (manufacturer Zwick) and a split-tube electric furnace (manufacturer Könn) that features three independently controllable heating zones in vertical direction. Figure 1 shows a schematic of the entire test setup and Figure 2a displays a photograph of the closed furnace mounted within the universal testing machine. The temperature regime of the tests was implemented with a closed-loop control system for the furnace, using the specimen temperature readings, $\theta_{\mathrm{Sp,top}}$ and $\theta_{\mathrm{Sp,bot}}$, as feedback variables. The strain-rate controlled cyclic loading of the specimens at elevated temperatures was realized with a closed-loop control system for the universal testing machine that used the specimen shortening (measured inside the furnace with a high-temperature resisting compressometer) as feedback signal. High-temperature resisting loading rams (Figure 1) allowed loading the specimens at target temperature directly inside the furnace, while the transmitted force was recorded with a load cell that was located outside of the furnace in the upper fixed table of the universal testing machine. The connecting pieces of the loading rams to the universal testing machine were air-cooled with fans during the tests at elevated temperatures.

Test Sequence

A fully automated test sequence was programmed with the general-purpose software provided by the manufacturer of the testing machine. The sequence consisted of three stages: (1) mounting of the specimen in the test apparatus and establishment of the Young's modulus at ambient temperatures with a series of loading-unloading cycles; (2) heating of the specimen to target temperature, T, with a constant heating rate, $\dot{T}$, of 5°C/min of the mean specimen temperature, $\theta_{\mathrm{Sp,top}}$ and $\theta_{\mathrm{Sp,bot}}$, followed by a conditioning time of 60 minutes to reach steady-state conditions, compliant with the RILEM Recommendations [13]; and (3) establishment of the Young's modulus at elevated temperature, E_θ, with a series of loading-unloading cycles and subsequent strain-rate controlled compressive loading of the specimen with a constant rate, $\dot{\varepsilon}$, of 0.1%/min until softening of at

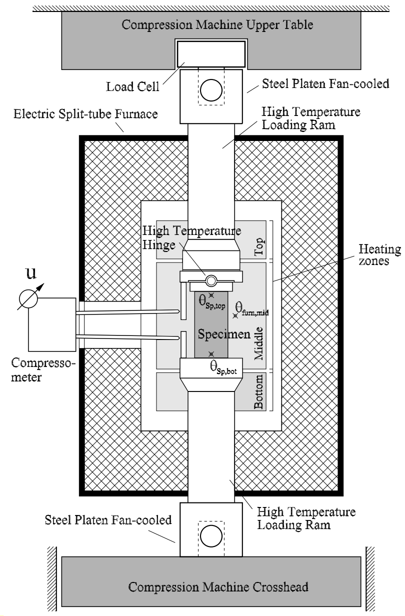

Figure 1. Schematic of the test setup.

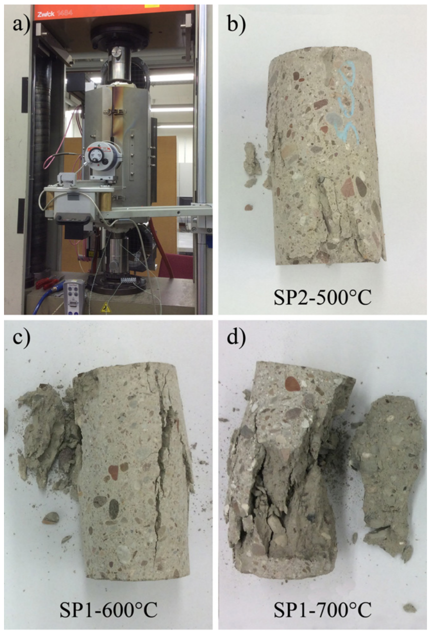

Figure 2. View of test setup (a) and failure modes of specimens (b) through (d).

least, $\sigma_{c,\theta}/f_{c,\theta} = 0.2$, as defined in the RILEM Recommendations [14] and intermediate elastic unloading-reloading cycles in the post-peak regime at pre-defined fractions, $\mu_i = \sigma_{c,\theta}/f_{c,\theta}$, of the compressive strength at elevated temperature, $f_{c,\theta}$.

RESULTS AND DISCUSSION

Data Evaluation within the Framework of Damage-Plasticity

Cyclic compression tests at elevated temperatures allow analyzing experimentally the temperature-dependent elastic stiffness degradation behavior of concrete with increasing plastic straining. This data is needed to properly calibrate state-of-the-art temperature-dependent damage-plasticity models for concrete in compression as e.g. the concrete damage-plasticity model in ABAQUS Standard. This section outlines briefly the evaluation methodology for retrieving from the data of cyclic compression tests at elevated temperatures the temperature-dependent evolution of the elastic stiffness with plastic straining and the damage evolution relations needed as input in the concrete damage-plasticity model in ABAQUS Standard.

ELASTIC STIFFNESS DEGRADATION

Figure 3b shows the raw stress–strain plot of a cyclic compression test performed at 600°C with specimen number 1. The dashed lines approximate the elastic part of the reloading branches and their slopes represent the damaged elastic reloading moduli, $E_{d,\theta}^{(i)}$. The slopes were computed with the points on the stress–strain line that are indicated with rectangular and triangular markers. The results and the respective stress–strain coordinates $(\varepsilon_{c,\theta}^{unl\,(i)}, \sigma_{c,\theta}^{unl\,(i)})$ and $(\varepsilon_{c,\theta}^{rel\,(i)}, \sigma_{c,\theta}^{rel\,(i)})$

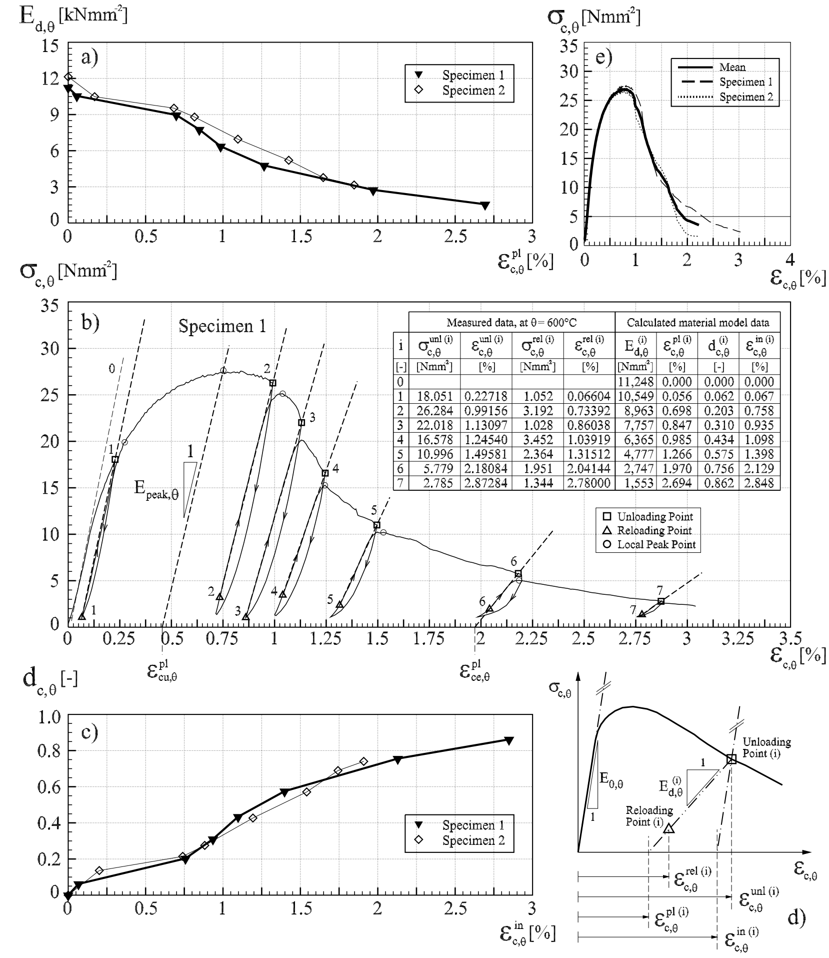

	Measured data, at θ = 600°C				Calculated material model data			
i	$\sigma_{c,\theta}^{unl\ (i)}$	$\varepsilon_{c,\theta}^{unl\ (i)}$	$\sigma_{c,\theta}^{rel\ (i)}$	$\varepsilon_{c,\theta}^{rel\ (i)}$	$E_{d,\theta}^{(i)}$	$\varepsilon_{c,\theta}^{pl\ (i)}$	$d_{c,\theta}^{(i)}$	$\varepsilon_{c,\theta}^{in\ (i)}$
[-]	[Nmm⁻²]	[%]	[Nmm⁻²]	[%]	[Nmm⁻²]	[%]	[-]	[%]
0					11,248	0.000	0.000	0.000
1	18.051	0.22718	1.052	0.06604	10,549	0.056	0.062	0.067
2	26.284	0.99156	3.192	0.73392	8,963	0.698	0.203	0.758
3	22.018	1.13097	1.028	0.86038	7,757	0.847	0.310	0.935
4	16.578	1.24540	3.452	1.03919	6,365	0.985	0.434	1.098
5	10.996	1.49581	2.364	1.31512	4,777	1.266	0.575	1.398
6	5.779	2.18084	1.951	2.04144	2,747	1.970	0.756	2.129
7	2.785	2.87284	1.344	2.78000	1,553	2.694	0.862	2.848

Figure 3. Data evaluation method for cyclic compression tests: Elastic stiffness degradation at 600°C (a), example stress–strain plot at 600°C (b), damage evolution relations at 600°C (c), schematic of the damage-plasticity modeling concept (d) and mean stress–strain curves at 600°C (e).

used in the computation are listed in the inserted table in Figure 3b. The rectangular markers indicate unloading points and triangular markers reloading points, if not shifted upwards on the elastic reloading branch for better approximation of the experimental curve with the straight line. Assuming that the experimentally established elastic reloading modulus is also applicable for unloading (i.e. neglecting the hysteresis loops), the plastic part of the total strain in the unloading points, $\varepsilon_{c,\theta}{}^{pl\ (i)}$, can be computed with the following relation (illustrated in Figure 3d):

$$\varepsilon_{c,\theta}^{pl\ \ (i)} = \varepsilon_{c,\theta}^{unl\ \ (i)} - \sigma_{c,\theta}^{unl\ \ (i)} \Big/ E_{d,\theta}^{(i)} \tag{1}$$

Finally, the evolution of the elastic stiffness with plastic strain at a specific temperature, θ, can be derived, by plotting the damaged elastic moduli, $E_{d,\theta}{}^{(i)}$, against the corresponding plastic strains, $\varepsilon_{c,\theta}{}^{pl\ (i)}$. Figure 3a shows the resulting relations at 600C with triangular and diamond markers for the first and second test respectively. This plot shows that normal strength concrete exhibits also at elevated temperatures the macroscopic behavior of elastic stiffness degradation with increasing plastic straining, which can be captured by damage-plasticity models that have been validated so far only on the basis of cyclic compression tests at ambient temperatures, see e.g. ref. [9]. Evaluation of the entire preliminary test series according to this methodology yielded elastic stiffness degradation plots akin to Figure 3a for the other two temperature levels. This indicates that the damage-plasticity modeling concept is also suitable for normal strength concrete at elevated temperatures.

DAMAGE EVOLUTION RELATIONS

Elastic stiffness degradation relations provide calibration input data for generic temperature-dependent damage-plasticity models, when converted into damage evolution relations. This conversion is presented next for the example of the concrete damage plasticity model in ABAQUS Standard. The damage part (in compression) of this model is implemented by a scalar damage variable, $d_{c,\theta}$, which is equal to zero in the absence of damage and equal to one in the case of complete damage. In a uniaxial setting the undamaged and damaged elastic moduli are related via the scalar damage variable according to the following relation:

$$E_{d,\theta} = \left(1 - d_{c,\theta}\right) E_\theta \tag{2}$$

Rearranging Equation 2, allows to determine the values of the damage variable, prevailing in the state of the material in the unloading points. However, the implementation of the damage part of this model requires the dependence of the damage variable on the inelastic strain, which is defined as (see Figure 3d):

$$\varepsilon_{c,\theta}^{in} = \varepsilon_{c,\theta} - \sigma_{c,\theta} / E_\theta \tag{3}$$

Figure 3c shows the damage evolution relations at 600°C obtained by conversion from the corresponding elastic stiffness degradation relations of Figure 3a. To be usable as input data, a mean damage evolution relation was computed at fixed inelastic strain increments from the single specimen data of Figure 3b. The resulting $d_{c,\theta} - \varepsilon_{c,\theta}^{in}$ input table is given in Table II, together with the mean damage evolution relations of the other two temperature levels that have been evaluated in the same way. This input data set for the damage part in compression of the generic concrete damage-plasticity model in ABAQUS Standard constitutes novel experiment-based temperature-dependent calibration data for NSC.

TABLE II. DAMAGE INPUT DATA

Testing Temperature θ (°C)					
500°C		600°C		700°C	
$d_{c,\theta}$ (−)	$\varepsilon_{c,\theta}^{in}$ (−)				
0.000	0.000	0.000	0.000	0.000	0.000
0.049	0.107	0.080	0.127	0.064	0.216
0.085	0.214	0.122	0.255	0.152	0.863
0.131	0.643	0.216	0.764	0.320	1.295
0.170	0.751	0.282	0.891	0.479	1.726
0.435	1.179	0.430	1.146	0.595	2.158
0.635	1.608	0.586	1.527	0.683	2.589
0.782	2.561	0.721	1.909	0.764	3.236
		0.862	2.848	0.938	4.972

INFLUENCE OF TEMPERATURE ON ELASTIC STIFFNESS DEGRADATION

Figure 4a shows the normalized graphs of the mean elastic stiffness degradation evolutions with different line types for the three temperature levels tested in this preliminary series. These normalized graphs were computed from the normalized elastic stiffness degradation evolutions of the single specimens tested at a specific temperature level, θ, whose data points are indicted also in Figure 4a with different

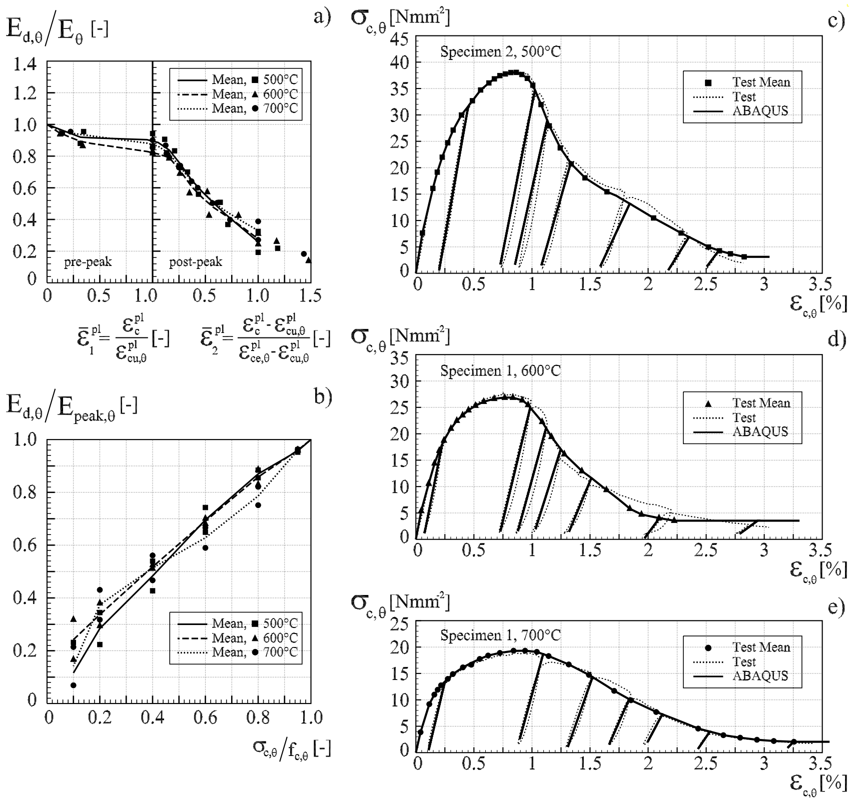

Figure 4. Relative elastic stiffness degradation at elevated temperatures (a), correlation between stiffness and strength degradation in the post-peak regime (b) and simulation results (material point calculations) of the cyclic compression tests (c) through (e).

markers per temperature level. The evolution of the elastic stiffness degradation, $E_{d,\theta}/E_\theta$, of every specimen was assessed with respect to its initial (undamaged) elastic stiffness, E_θ, and the normalization of the plastic strain distinguished between a pre-peak normalized plastic strain, $\bar{\varepsilon}_1^{pl}$, and a post-peak normalized plastic strain, $\bar{\varepsilon}_2^{pl}$, according to the relations given in Figure 4a in comparison with Figure 3b. A detailed description of this normalization method is given in [12]. The normalized graphs in Figure 4a almost overlap in the post-peak regime and do not seem to show a systematic interdependence that could be related to the test temperature. However, a larger data set is required to consolidate this preliminary finding. Furthermore, Figure 4b indicates for the post-peak regime the presence of a temperature-independent linear correlation between the elastic stiffness degradation, $E_{d,\theta}/E_{peak,\theta}$, and the strength degradation, $\sigma_{c,\theta}/f_{c,\theta}$, which was also reported in [12] for an extended test series at elevated temperatures with SCC and in [5] for a test series with NSC at ambient temperature.

Numerical Simulation of the Cyclic Compression Tests

Figures 4c through 4e show the results of verification calculations with the compression damage input data given in Table II, using the concrete-damage plasticity model of ABAQUS Standard. The material model was additionally calibrated in compression hardening and softening with the mean experimental stress–strain lines which are indicated with markers. The simulation responses, given with solid lines, were obtained by subjecting a single 8-node brick element with reduced integration (C3D8R of the ABAQUS element library) to the cyclic loading sequence of the compression tests which are indicated with dashed lines. The close agreement between the simulated elastic unloading-reloading branches with the ascending parts of the experimental reloading branches illustrates the accurate predictive capacity of generic temperature-dependent damage-plasticity models, when used with experiment-based calibration data.

SUMMARY AND CONCLUSION

A preliminary series of strain-rate controlled cyclic compression tests at elevated temperatures of 500, 600 and 700°C has been performed with cylindrical NSC specimens under steady-state conditions. The novel test results (1) confirm the suitability of the damage-plasticity modeling concept also for NSC in compression at elevated temperatures; (2) provide primary NSC calibration data for generic temperature-dependent damage-plasticity models; and (3) indicate good prospects for the development of simplified temperature-dependent generic damage evolution relations.

REFERENCES

1. Sinha, A., K. H. Gerstle, and L. Tulin. 1964. "Stress–strain relations for concrete under cyclic loading," *ACI J. Proc.*, 61: 195-212.
2. Karsan, I. D. and J. O. Jirsa. 1969. "Behaviour of concrete under compressive loadings," *J. Struct. Div.*, 95: 2535-2563.
3. Spooner, D. C. and J. W. Dougill. 1975. "A quantitative assessment of damage sustained in concrete during compressive loading," *Mag. Concr. Res.*, 27: 151-160
4. Bahn, B. Y. and C.-T. T. Hsu. 1998. "Stress–strain behavior of concrete under cyclic loading," *ACI Mater. J.*, 95: 178-193.
5. Lee, Y.-H. and K. J Willam. 1997. "Mechanical properties of concrete in uniaxial compression," *ACI Mater. J.*, 94: 457-467.
6. Gopalaratnam, V. S. and S. P. Shah. 1985. "Softening response of plain concrete in direct tension," ACI J. Proc., 82: 310-323.
7. Grassl, P. and M. Jirásek. 2006. "Damage-plastic model for concrete failure," *Int. J. Solids Struct.*, 43: 7166-7196.
8. Lubliner, J., J. Oliver, S. Oller, and E. Oñate. 1989. "A plastic-damage model for concrete," *Int. J. Solids Struct.*, 25: 299-326.
9. Lee, J. and G. I. Fenves. 1998. "Plastic-damage model for cyclic loading of concrete structures," *J. Eng. Mech.*, 124: 892-900.
10. Gernay, T., A. Millard, and J.-M. Franssen. 2013. "A multiaxial constituive model for concrete in the fire situation: Theoretical formulation," *Int. J. Solids Struct.*, 50: 3659-3673.
11. European Committee for Standardization (CEN). 2004. "Eurocode 2: Design of concrete structures–Part 1–2: General structural rules–Structural fire design," *EN 1992-1-2*, Brussels, Belgium.
12. Neuenschwander, M., M. Knobloch, and M. Fontana. 2016. "Suitability of the damage-plasticity modelling concept for concrete at elevated temperatures: Experimental validation with uniaxial cyclic compression tests," *Cem. and Con. Res.*, 79: 57-75.
13. RILEM Technical Committee 200-HTC. 2007. "Recommendation of RILEM TC 200-HTC: Mechanical concrete properties at high temperatures—Modelling and applications, Part 1: Introduction—General presentation," *Mater. Struct.*, 40: 841-853.
14. RILEM Technical Committee 200-HTC. 2007. "Recommendation of RILEM TC 200-HTC: Mechanical concrete properties at high temperatures—Modelling and applications, Part 2: Stress–strain relation," *Mater. Struct.*, 40: 855-864.

Post-Fire Residual Mechanical Properties of High Strength Concrete (HSC) Made with Basalt Aggregate

MARCELA BARROS DE SOUZA SOLLERO
and ARMANDO LOPES MORENO JR.

ABSTRACT

This paper addresses an investigation of the residual mechanical properties of high strength concrete produced with coarse basalt, limestone and granite aggregate and exposed to temperatures of 200ºC, 400ºC and 600ºC. The paper objectives are: comparatively analyze test results with data from standards and results from other authors, evidencing the influence of coarse aggregate in the material performance; and provide reduction coefficients of mechanical properties of concrete containing basalt aggregate exposed to high temperatures, which is used in many countries and have notable thermal properties, but is not addressed by the structural fire design standards.

INTRODUCTION

It is widely known that, though presenting a good performance when exposed to high temperatures, concrete's mechanical properties are impacted by them.

FIB [1] bulletin nº 38 indicates that concrete behavior during heating and cooling depends on the type of cement paste, type of aggregate, bond region and the interaction between them.

Though changes occur chiefly in the cement paste, the influence of aggregates is very intense, because they usually constitute up to 80% of the concrete volume, and affect the concrete thermal strain and thermal conductivity, restrains creep and shrinkage of the cement paste and may suffer different physical-chemical alterations due to heat, depending on their type.

Norms and bulletins that address concrete in fire situation usually present tables or diagrams relating reduction coefficients of mechanical properties of concrete with normal strength as function of temperature, distinguished by type of course aggregate.

Marcela B. S. Sollero, Faculdade de Engenharia Civil, Arquitetura e Urbanismo, UNICAMP, marcela.barros.souza@gmail.com, Rua Saturnino de Brito, 135, Barão Geraldo, CEP 13083 – 852, Campinas, SP, Brasil.
Armando L. Moreno Júnior, Faculdade de Engenharia Civil, Arquitetura e Urbanismo, UNICAMP, almoreno@fec.unicamp.br, Rua Saturnino de Brito, 135, Barão Geraldo, CEP 13083 – 852, Campinas, SP, Brasil.

Among these documents, Eurocode 2 Part 1-2 presents reduction coefficients of mechanical properties as function of temperature for normal strength concrete made with siliceous and calcareous aggregates and for high strength concrete without specifying the type of aggregate [2]. ACI 216 Report approaches reduction of compressive strength of siliceous aggregate concrete, carbonate aggregate concrete and semi-lightweight concrete exposed to high temperatures and after cooling [3]. Brazilian norm ABNT NBR 15200:2012 presents factors of compressive strength reduction of concrete composed of siliceous aggregate [4].

Among the types of coarse aggregates used to produce concrete addressed by norms and bulletins, however, basalt is missing, a widely used aggregate in many countries.

Another observation is that researches on concrete mechanical properties developed in several countries, including Brazil, often present conflicting results. Such situation can be attributed to the insufficient characterization of the concrete – like the lack of indication of the type of aggregate and the sample humidity in each phase of the experimental program – and the trial regime, like omission of information on cooling conditions and sample loading regime [1].

Hence, the need to study the reduction coefficients of mechanical properties of concrete produced with basalt. The need to research reduction coefficients of mechanical properties of concrete produced with limestone and granite was also observed, using the same trial regime and the same characteristics in samples, in order to make feasible results comparison. Finally, it was observed that high strength concrete is not sufficiently addressed by international norms, in general. As a result, an inedited experimental program was developed in Brazil.

The experimental program was intended to comparatively analyze the reduction coefficient as function of temperature of axial compressive strength and tensile strength of high strength concrete specimen produced with basaltic, granitic and calcareous coarse aggregate.

Influence of aggregate type in concrete subject to high temperatures

Aggregates exert high influence in the behavior of concrete exposed to high temperatures, both for constituting 60 to 80% of the material and for their thermal properties. Furthermore, aggregates restrain creep and shrinkage of the cement paste and influence the concrete risk of explosive spalling [1].

Their influence varies according to the type of aggregate and becomes significant until 600ºC, when aggregates with different thermal expansion coefficients expand in different intensities, creating thermal tensions that tend to disaggregate the concrete – such expansion can be increased by the aggregate type own transformations [12].

Among the transformation suffered by aggregates, the disruption of some types of pebbles at 350ºC, the increase of reduction rate of strength of concrete composed of siliceous aggregates after around 300ºC, the retraction due to dehydration of some siliceous or calcareous aggregates and the volume increase of siliceous aggregates during the transformation from α-quartz to β-quartz at 573ºC, are outstanding [11;13].

The type of concrete aggregate considerably impacts its thermal strain. Figure 1, based on Khoury, Grainger and Sullivan results, shows higher thermal stability of basalt as compared to limestone; in fact, aggregates' thermal stability strongly affects the concrete behavior and increases in the following order: flint, Thames gravel, limestone, basalt, granite, gabbro [11].

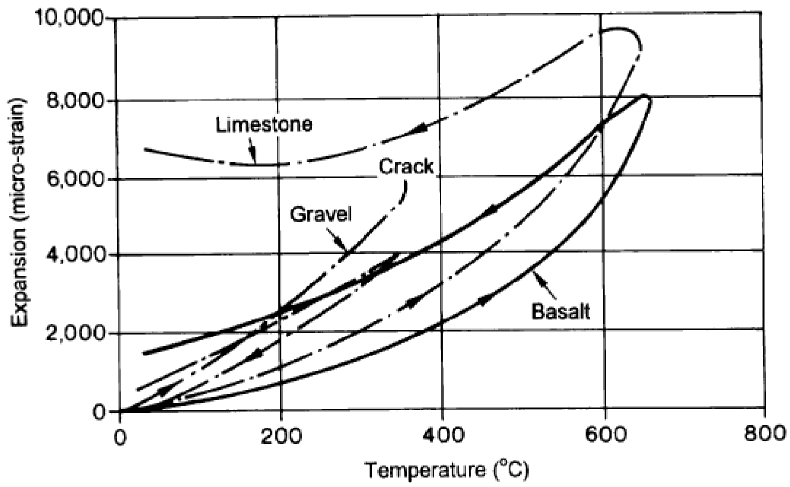

Figure 1. Thermal strain of gravel, limestone and basalt heated at 2°C/min rate [1].

The behavior of some different types of aggregates in terms of stability and processes occurring during their heating is illustrated in Figure 2:

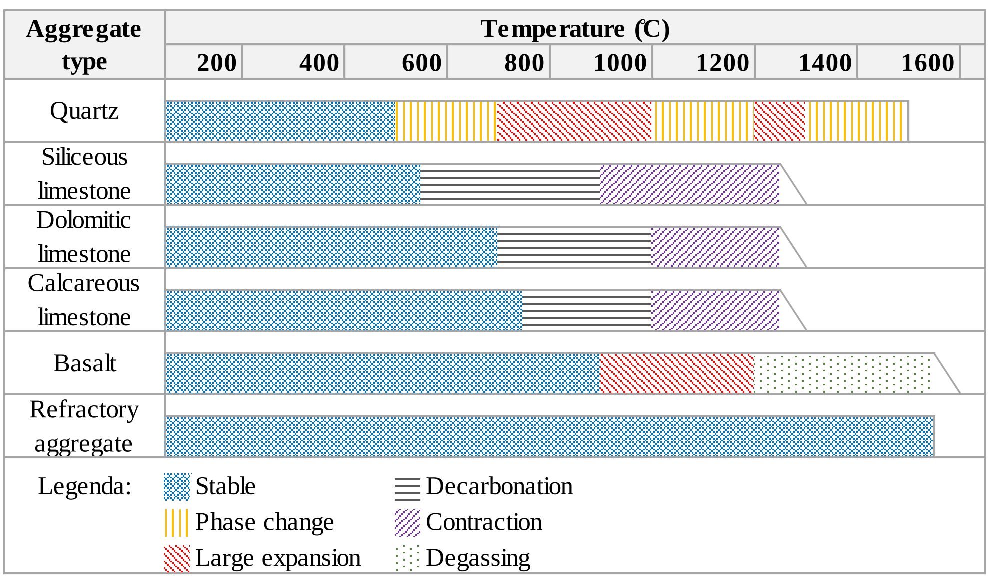

Figure 2. Aggregates' behavior during heating – adapted from [18].

Basaltic aggregate is largely used in several countries. Among its characteristics, its thermal stability reaches around 900 °C, superior to siliceous limestone and calcareous limestone stability, for example, and its reduced mass loss until 1000°C [1], make its use particularly recommended in structures that may be exposed to high temperatures.

EXPERIMENTAL PROGRAM

Preparation of samples

RILEM TC 200 HTC and TC 129 MHT recommendations were adopted to guide the preparation and trial of samples destined to determination of compressive strength, because these recommendations low heating rates make more distinct the effects suffered by the structure and material exposed to high temperatures [1]. RILEM recommendations specify, in addition to the heating rate, the time during which the temperature is kept and samples' cooling rate [5; 6].

The proportions of materials used to produce concrete are: 1:1,5:1,5 (Portland cement produced with blast furnace slag: fine sand: coarse aggregate, with addition of 0.1 of rice husk silica and 0.015 of plasticizing admixture against the cement mass. Water/cement relation was 0.35. Coarse aggregates used were basalt, granite and limestone. Granite and limestone were selected to compare the results obtained with the values found in the technical literature.

Forty 10 x 30 cm cylindrical samples were used in compressive strength tests and 24 10 x 20 cm samples in tensile strength by diametrical compression. Samples were kept sealed for 7 days and stored under "d" (drying concrete) humidity condition until completing at least 2 months. After this period, they were prepared so to have their ends flat and orthogonal to the central axis.

Heating, cooling and trials

Except for the reference samples, the concrete samples with basalt and granite were previously heated in stove at 100ºC for 24h to reduce humidity and the probability of occurrence of explosive spalling in later stages. Up to that temperature, no significant alterations are expected in the concrete mechanical properties, according to data provided by Eurocode 2 [2].

The samples were exposed to 200ºC, 400ºC and 600ºC temperatures, with 1ºC/min heating and cooling rate and for 60 min, under unstressed condition. Heating was carried out in electric vertical furnace and horizontal furnace appropriate for this type of use, belonging to UNICAMP Civil Engineering and Architecture Faculty. After cooling, the samples were kept sealed with plastic film, until the execution of trials.

The limit-temperature of 600ºC was defined in this stage of the study for being the temperature in which the concrete cracking and disaggregation are more outstanding, and for being a temperature in which mechanical properties are already strongly affected – tensile strength starts to be considered null by Eurocode 2 [2] – and for occurring after the α-β inversion of quartz. In later stages of the present study higher temperatures will be studied, reaching up to 900ºC.

The concrete residual compressive strength was determined according to RILEM TC 129-MHT Part 3 recommendation, by applying a uniaxial compressive load towards the central axis at a 0.5 MPa s-1 rate.

The concrete tensile strength by diametrical compression was calculated according to Brazilian norm ABNT NBR 7222 procedures.

This differentiation among norms was chosen due to the testing equipment available. The same reason determined the non-execution of trials to determine elasticity modulus in the current phase of the study.

Results and discussion

Table 1 displays samples average residual compressive strength as well as the average reduction coefficients of compressive strength ($f_{c,\theta}/f_{ck}$) and tensile strength ($k_{c,t}\theta$) obtained.

TABLE I. EXPERIMENTAL AND CALCULATED DATA – CONCRETE COMPRESSIVE STRENGTH AND TENSILE STRENGTH.

Temperature θ (°C)	Type of concrete aggregate								
	Basalt			Granite			Limestone		
	Compressive strength (MPa)	$f_{c,\theta}/f_{ck}$	kc,tθ	Compressive strength (MPa)	$f_{c,\theta}/f_{ck}$	kc,tθ	Compressive strength (MPa)	$f_{c,\theta}/f_{ck}$	kc,tθ
20	79.0 ± 6.3	1.00	1.00	71.8 ± 8.4	1.00	1.00	64.3 ± 8.1	1.00	1.00
200	74.2 ± 3.3	0.94	0.98	71.1 ± 3.0	0.99	1.00	56.6 ± 3.0	0.88	0.96
400	52.8 ± 4.9	0.67	0.88	61.1 ± 2.9	0.85	0.91	45.4 ± 4.5	0.71	0.71
600	37.0 ± 0.7	0.47	0.62	33.7 ± 1.6	0.47	0.55	15.4 ± 1.1	0.24	-

Figure 3 compares compressive strength reduction coefficients obtained in the research developed with HSC (High Strength Concrete) and UHSC (Ultra High Strength Concrete) results from other authors and from Eurocode:

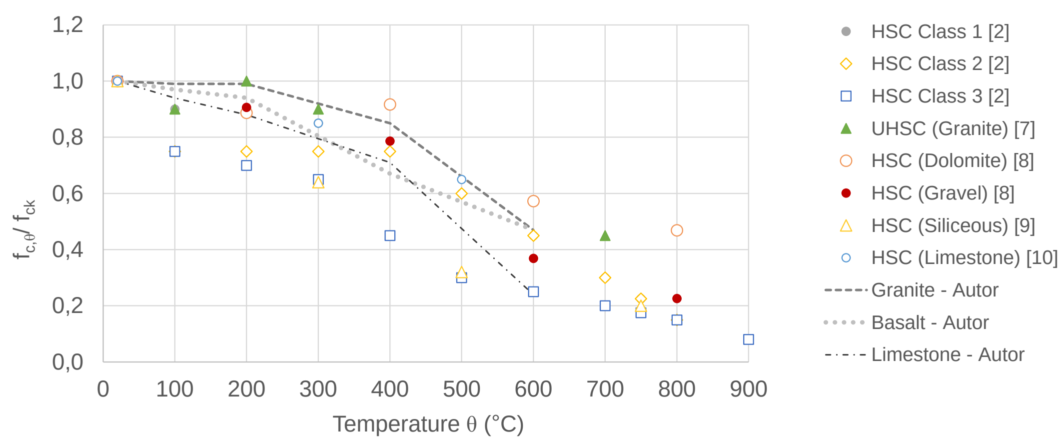

Figure 3. Residual compressive strength of HSC and UHSC at elevated temperature.

It can be observed that the performance of the concrete with basaltic aggregate analyzed in the present study was superior to that of the concrete with calcareous aggregate, as well as to that of siliceous aggregate adopted as reference and, up to 300ºC, to HSC Class 2 of Eurocode 2, a classification in which it would fit. One can also observe that Eurocode does not determine to which type of concrete, as regards coarse aggregate, the reduction factors presented are applicable.

The concrete with granitic aggregate executed with the same proportions as those of the concrete with basaltic aggregate and with calcareous aggregate showed the lower reductions of compressive strength in the temperature range studied.

The results obtained evidence the difference in behavior of concrete produced with different types of aggregates under high temperatures; the main factors contributing to this difference are the lack of standardization of trial regime and characterization of samples and omission of information on these aspects of the studies.

The results show that concrete with basalt, a common aggregate used in several countries, as previously mentioned, presents a good performance under high temperatures. However, it is not addressed by normative codes and its behavior is different from that observed in concretes produced with other aggregates.

Figure 4 compares the results of tensile strength reduction coefficient obtained in the research developed to NSC (Normal Strength Concrete) and HSC results from other authors and from Eurocode:

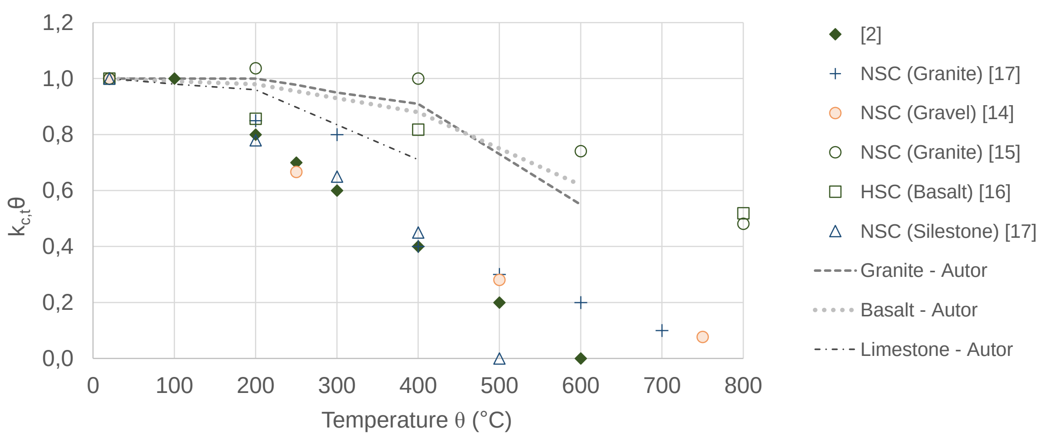

Figure 4. Residual tensile strength of NSC and HSC at elevated temperature.

The concrete tensile strength, a property associated to the material cracking, is more strongly impacted by the rise in temperature than its compressive strength. Figure 4 shows that the performance of concrete with granite and basalt studied is superior to the performance of concrete with limestone, and significantly superior to the performance of the reference presented by Eurocode 2. It is also outstanding the higher variation of tensile strength of the concrete among the several studies, when compared to compressive strength.

CONCLUSIONS

The present study provided data on mechanical properties – compressive strength and tensile strength – of high strength concrete produced with basalt, granite and limestone, and also shown, comparatively, values provided by other studies and by norm EN 1992-1-2:2004, belonging to Eurocode 2.

The results have shown that the concrete suffered a reduction of 1 to 12% in its compressive strength at 200ºC, of 15 to 33% at 400ºC, and of 53 to 76% at 600ºC. Among the tested samples, the concrete with calcareous aggregate was the most affected; the concrete with granite and basalt presented a good performance, equal or superior to that indicated by norm EN 1992-1-2:2004. In the comparison with other authors' results, the values obtained have shown to be consistent, but evidenced the difference of behavior in concretes with different types of aggregates. The larger dispersion of results among the several studies, in the temperature range studied, was observed at temperature of 400ºC.

Thus, it is also concluded that:

- Concrete with basaltic aggregate is widely used and its performance under high temperatures is appropriated, however, different from limestone and granite, it is important to included it in more studies, normative codes and technical recommendations turned to the project and the recovery of structures exposed to high temperatures;
- Since high strength concrete use and study is increasingly more common, the review of reduction curves of mechanical properties specific to this material, intended to include more temperature ranges and information on the type of concrete and the trial method used, as well as the inclusion of these curves in norms that don't address them, is essential to complement normative codes;
- The standardization and statement of parameters used to carry out trials is fundamental to expand the scope of researches on concrete exposed to high temperatures and to reduce disparities among results obtained, optimizing the application of the knowledge generated.

ACKNOWLEDGEMENTS

The authors thank MC-Bauchemie for the supply of additive, and Concremat Engenharia e Tecnologia S.A for the support.

REFERENCES

1. Fédération Internationale du Béton. Fire design of concrete structures - materials, structures and modeling - State-of-art report+ Bulletin d'information 38, Lauseanne, 2007.
2. European Committee for Standardization (CEN). EN 1992-1-2:2004. Eurocode 2: Design of Concrete Structures – Part 1.2: General Rules – Structural Fire Design. CEN, Bruxelas, 2004.
3. American Concrete Institute. ACI 216.1-97.Standard Method for Determining Fire Resistance of Concrete and Masonry Construction Assemblies. Reported by ACI/TMS Committee 216. 1997.
4. Associação Brasileira de Normas Técnicas, NBR 15200. Projeto de Estruturas de Concreto em Situação de Incêndio", Rio de Janeiro, 2012.
5. RILEM TC 129-MHT. Test Methods for Mechanical Properties of Concrete at High Temperatures – Compressive strength for service and accident conditions, V.28, p. 410-414, 1995.

6. RILEM TC 200-HTC. Recommendation of RILEM TC 200-HTC: Mechanical Concrete Properties at High Temperatures - Modelling and Applications. Part 1: Introduction -General Presentation. Materials and Structures, V.40, p. 841-853, 2007.
7. Gyeongcheol, C. et al. Evaluation of the mechanical properties of 200 MPa ultra-high-strength concrete at elevated temperatures and residual strength of column. Construction and Building Materials 86, p. 159-168, 2015.
8. Netinger, I.;Kesegic, I.; Guljas, I. The effect of high temperatures on the mechanical properties of concrete made with different types of aggregates. Fire Safety Journal V.46, Issue 7, p. 425-430, 2011.
9. Heap, M. et al. The influence of thermal-stressing (up to 1000ºC) on the physical, mechanical, and chemical properties of siliceous-aggregate, high-strength concrete. Construction and Building Materials 42, p. 248-265, 2013.
10. Santos, C. C.; Rodrigues, J. P. C.; Coelho, A. P. Resistência à compressão residual de betões calcários após incêndio. Revista Internacional Construlink. ISSN 1645-5576. Vol. 9, nº 27, p. 31-38, 2011.
11. Khoury, A. G. Effect of fire on concrete and concrete structures. Progress in Structural Engineering and Materials, 2000, 2, 429-447.
12. Cánovas, M. F. Patologia e terapia do concreto armado, 1ª Edição, São Paulo, PINI, 1988, pág 173 – 201.
13. Xing, Z. et al. Influence of the nature of aggregates on the behaviour of concrete subjected to elevated temperature. Cement and Concrete Research 41 (2011) 392-402.
14. Sakr, K.; El-Hakim, E. Effect of high temperature or fire on heavy weight concrete properties. Cement and Concrete Research, 35, 2005, p. 590-596.
15. Chen, B., Chen, L.; Li, C. Experimental study of mechanical properties of normal-strength concrete exposed to hight emperatures at na early age. Fire SafetyJournal, 44, 2009, p. 997–1002.
16. Li, M., Xiang, C.; Qian, Sun, W. Mechanical properties of high-strength concrete after fire. Cement and Concrete Research, 34, 2004, p. 1001-1005.
17. Santos, C. C.; Rodrigues, J. P. C. Propriedades mecânicas residuais de betões correntes após incêndio. In: Congresso Ibero-Latino-Americano sobre Segurança contra Incêndio, 2, Coimbra, 29 de Maio a 1 de Junho – CILASCI, 2013, p. 1-12.
18. Khoury, G.A. Effect of heat on concrete material, Imperial College report, 1995, pp. 73 *apud* Fédération Internationale du Béton. Fire design of concrete structures - materials, structures and modeling - State-of-art report+ Bulletin d'information 38, Lauseanne, 2007.

Thermal Properties of Green High-Performance Fiber-Reinforced Cementitious Composites Subjected to High Temperature

XIULING LI, HUINING ZHANG, GENDA CHEN and YI BAO

ABSTRACT

To study the influences of mix proportions and high temperature on the thermal properties of green high-performance fiber reinforced cementitious composites (GHPFRCC), sixteen mix proportions were designed using the Taguchi orthogonal method. Five variables investigated were the water-to-binder ratio (0.24, 0.28, 0.32, and 0.36), sand-to-binder ratio (0.36, 0.46, 0.56, and 0.66), polyvinyl alcohol (PVA) fiber content (1.5%, 1.7%, 2.0%, and 2.2%) by volume, fly ash replacement (60%, 65%, 70%, and 75%) by weight, and the superplasticizer content (0.10%, 0.15%, 0.20%, and 0.25%). Each GHPFRCC specimen was subjected to a target temperature (200 °C, 400 °C, 600 °C, and 800 °C), and then measured for its thermal conductivity using a transient plane source method. The experimental results showed that the thermal conductivity of GHPFRCC decreased dramatically in the initial stage up to 400℃, then slowly decreased with temperature until 800℃. Compared with normal concrete, the GHPFRCC is relatively low in thermal conductivity and, therefore, can be used as a better thermal insulation material for infrastructures.

INTRODUCTION

Concrete is the most widely used building material in the world due to its availability, adaptability, and durability. When reinforced with steel, concrete can act as a heat barrier and provide thermal insulation for steel due to its low thermal conductivity. However, concrete is brittle in nature and prone to cracking under tensile stress. Once cracked, the exposed steel is corroded in an accelerated way, which results in further cracking in concrete [1]. In addition, high energy consumption and greenhouse gas emission during the production of cement have received increasing attention around the world [2].

High performance concrete and ultra-high performance concrete have been developed to

[1]School of Civil Engineering, Shandong Jianzhu University, Jinan, China 250101
[2]School of Engineering & IT, University of Melbourne, Melbourne, Australia 3010
[3]Department of Civil, Architectural, and Environmental Engineering, Missouri University of Science and Technology, Rolla, USA 65409

provide enhanced workability, mechanical strength, and durability of civil infrastructures [3, 4]. At high temperature, however, they may be prone to spalling [5, 6]. On the other hand, engineering cementitious composites (ECC) reinforced with polyvinyl alcohol (PVA) fibers were developed to provide high tensile strength and ductility [7]. In this case, the PVA fibers served as reinforcement to prevent or arrest cracks in ECC. Recently, green high-performance fiber-reinforced cementitious composites (GHPFRCCs) have been proposed [8, 9] with the use of high-volume fly ash. GHPFRCCs had tensile strength and ductility comparable to EEC, but were more eco-efficient and environmental-friendly. Thus, this group of materials is promising in civil infrastructure applications.

Thermal conductivity represents the rate of thermal conduction that can be defined as the quantity of heat (internal energy) transferred in unit time through a unit area every temperature gradient. It plays a vital role in quantification of the fire resistance of a structure [10, 11]. The experimental and analytical studies in the literature indicated that temperature significantly influenced the thermal conductivity [12, 13]. Overall, the thermal conductivity deceased with temperature [12, 13]. However, limited studies have been carried out for fiber-reinforced cementitious composites that are reinforced with PVA fibers and mixed with high-volume fly ash. As temperature increases, PVA fibers melt at about 230℃ and leave sufficient space in the matrix, which leads to alteration of the microstructures. For this reason, the thermal conductivity of GHPFRCC can be significantly different from those of conventional concrete materials. To evaluate the performance of GHPFRCC structures during and after exposure to fire or high temperature, it is essential to gain insight into the thermal conductivity of GHPFRCC subjected to those extreme conditions.

The primary objective of this study is to evaluate the effect of mix proportion on the thermal conductivity of GHPFRCC subjected to the ambient and elevated temperatures. To this end, the GHPFRCC specimens were heated at 200 °C, 400 °C, 600 °C, and 800 °C, and then, the thermal conductivities of the specimens were evaluated using a transient plane source method. Taguchi orthogonal method [14] was employed in the design of 16 mix proportions.

EXPERIMENTAL PROGRAM

Materials and Mix Proportions

The GHPFRCC mixtures included PVA fibers, fine silica sand, ordinary Portland cement, Type F fly ash, water, and superplasticizer. The physical properties and chemical composition of these components are available in Table 1.

Table 1. Chemical composition and physical properties of cement and fly ash.

	OPC	Fly ash
SiO_2	18.9	46.9
Al_2O_3	4.9	28.5
Fe_2O_3	3.6	6.2
CaO	64.1	2.3
MgO	0.8	1.2
SO_3 (%)	1.7	-
Loss of ignition (%)	3.2	2.8

Specific surface area (cm^2/g)	350	460
Specific gravity (g/cm^3)	3.15	2.38

Sixteen mix proportions of GHPFRCC were designed using the Taguchi design method [14], as shown in Table 2, considering different water-to-binder ratio (w/b) at 0.24, 0.28, 0.32, and 0.36, sand-to-binder ratio (s/b) at 0.36, 0.46, 0.56, and 0.66, PVA fiber content at 1.5%, 1.7%, 2.0%, and 2.2%, by volume, fly ash (FA) content at 60%, 65%, 70%, and 75%, by weight, and superplasticizer (SP) content at 0.10%, 0.15%, 0.20%, and 0.25%, by volume.

Table 2. Mix proportions of GHPFRCC.

No.	w/b	s/b	Fiber content (%)	FA content (%)	SP content (%)
1	0.24	0.36	1.5	60	0.10
2	0.24	0.46	1.7	65	0.15
3	0.24	0.56	2.0	70	0.20
4	0.24	0.66	2.2	75	0.25
5	0.28	0.36	1.7	70	0.25
6	0.28	0.46	1.5	75	0.20
7	0.28	0.56	2.2	60	0.15
8	0.28	0.66	2.0	65	0.10
9	0.32	0.36	2.0	75	0.15
10	0.32	0.46	2.2	70	0.10
11	0.32	0.56	1.5	65	0.25
12	0.32	0.66	1.7	60	0.20
13	0.36	0.36	2.2	65	0.20
14	0.36	0.46	2.0	60	0.25
15	0.36	0.56	1.7	75	0.10
16	0.36	0.66	1.5	70	0.15

Treatment and Test of Specimens

Specimens were divided into five groups, including one directly tested and the other four exposed to four target temperatures, which were 200 °C, 400 °C, 600 °C, and 800 °C, respectively, in an electric furnace. Each target temperature was sustained for 2 hours to ensure that the specimens were thermodynamically in equilibrium. Then, the specimens were naturally cooled to room temperature. The thermal conductivities of the specimens were evaluated before and after exposure to high temperatures using a Hot Disk instrument (model: TPS 2500S), as shown in Figs. 1(a)-1(c), based on a transient plane source method. The instrument has a thermal conductivity measurement range of 0.005-1800 W/m/K and can be used to measure various types of materials, such as solids, liquid, paste and thin films. A flat transient plane source sensor was sandwiched between two halves of a sample for the measurement of thermal conductivity. During the measurement, the sensor temperature is increased through electric effects, and heat dissipates into the sample on both sides of the sensor at a rate that depends on the thermal conductivity of the specimen. Then, the thermal properties can be calculated by analyzing the temperature history of the sensor. The surface roughness of the specimen plays an important role in ensuring accurate test results.

(a) (b) (c)

Figure 1. Instrument and test specimen: (a) Hot Disk instrument, (b) Thermal conductivity measurement, and (c) Specimen polishing with sand paper.

EXPERIMENTAL RESULTS

The thermal conductivities of tested specimens are shown in Fig. 2, which reveals a significant reduction of thermal conductivity due to exposure to high temperatures. At low temperature, the thermal conductivity of GHPFRCC was in the range of 1.2-1.5, which was slightly lower than the range of 1.3-2.0 of conventional concrete. At 800 °C, the thermal conductivity ranged from 0.7 to 0.9. Different from plain concrete that does not contain PVA fibers, no spalling happened during exposure to high temperature.

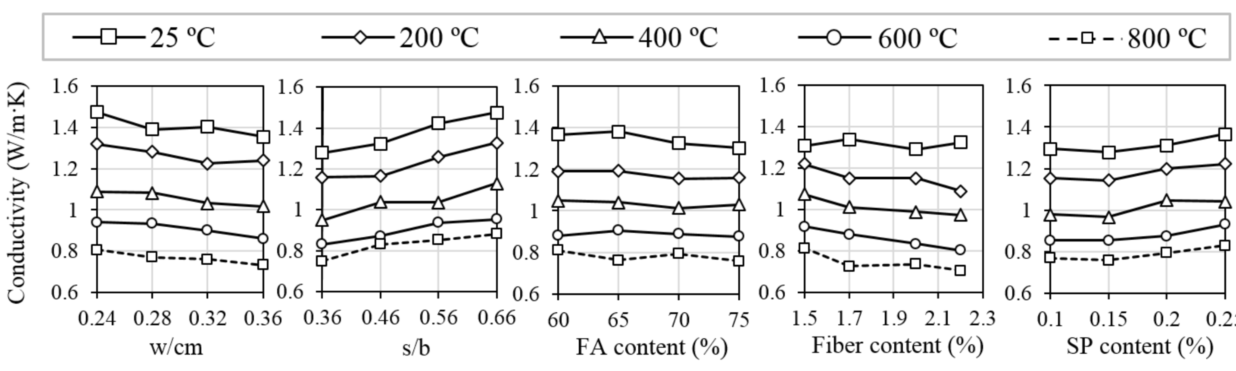

Figure 2. Thermal conductivity.

Among the five influencing factors, the ratio of sand and binder (s/b) dominated the thermal conductivity before and after exposure to high temperatures, which was followed by the water-to-binder (w/b ratio). The thermal conductivity of specimens increased with s/b but decreased with w/b. The fly ash, PVA fiber, and superplasticizer contents appeared to have less impact on the thermal conductivity, compared with s/b and w/b. Overall, increases in flash ash (FA) and fiber contents led to reduction in thermal conductivity, and increase in superplastizer (SP) content increased thermal conductivity.

DISCUSSION

Cement clinker consists of various phases such as C_3S, C_2S, C_3A, C_4AF, gypsum, and a small amount of other phases. When cement grain is mixed with water, those phases react with water and form various hydrates, which include calcium silicate hydrate (C-S-H) gel, calcium hydroxide (CH), ettringite, monosulfoaluminate, and other products in small amounts. In the presence of coarse or fine aggregates containing reactive silica, pozzolanic reaction can occur and form C-S-H gel. Hydration consumed water whose content is typically described by water-to-cement ratio. The water required for full hydration varies with the type of cement, aggregate, supplementary cementitious materials, and admixtures. Unhydrated grains exist when insufficient water is supplied. However, high porosity can be caused when the excessive amount of water is added. The space not occupied by neither unhydrated grains nor hydrates is namely capillary void space, where exists capillary water. Cement hydrates are formed layer by layer with voids in gel, which is namely gel voids. Water can be chemically bound on C-S-H gel, which can be released by heating the C-S-H gel to about 1000 ºC.

When heated up to 200 ºC, ettringite and monosulfoaluminate are decomposed and free water vaporized, resulting in higher porosity. As temperature increased from 200 ºC to 400 ºC, melting and thermal pyrolysis of PVA fibers occur, which leads to more voids in matrix. During the increase of temperature from 400 ºC to 600 ºC, decomposition of calcium hydroxide happens, further increasing the porosity. When temperature is increased from 600 ºC to 800 ºC, dehydration of C-S-H gradually takes place.

The increase in w/b increased the porosity and reduced the volume of solid in specimens. Since air has lower thermal conductivity than that of cementitious hydrates, the increased porosity due to w/b reduced the bulk thermal conductivity of specimens. This mechanism also applies to the PVA fiber content. Increasing the fiber content resulted in high voids, particularly after exposure to high temperatures, thus reducing the thermal conductivity. The increase in quartz sand ratio led to higher thermal conductivity because quartz sands had higher thermal conductivity, which was mainly due to the high crystallinity and low porosity of quartz sands. In addition, quartz sand had relatively higher thermal stability, compared with the cement hydrates. The slight increases in thermal conductivity owing to the SP content was likely due to the enhanced homogeneity of mixtures.

CONCLUSIONS

This paper presents the experimental research undertaken to measure thermal conductivity of GHPFRCC specimens subjected to ambient and four different high temperatures (200 °C, 400 °C, 600 °C, and 800 °C). Sixteen mix proportions were considered with varying water-binder ratio, sand-binder ratio, PVA fiber content by volume, fly ash replacement by weight and the water reducing agent. On the average, the thermal conductivity of GHPFRCC specimens decreased with temperature drastically up to 400 °C and then slowly beyond 400 °C. The thermal conductivity of GHPFRCC is lower than that of normal concrete, which means that GHPFRCC is better than concrete in thermal insulation property.

ACKNOWLEDGEMENT

This study was financially supported by the Natural Science Foundation of China (NSFC) under Grants No. 51278290 and No. 51108253, the Science and Technology Planning Project of Housing and Urban-Rural Development Ministry under Grant No. 2012-K2-11, the Educational Commission of Shandong Province under Grant No. J11LE09, and the Program of Scientific Research Innovation Team in Colleges and Universities of Shandong Province and the Ministry of Education Innovation Team under Grant No. IRT13075.

REFERENCES

[1] Tang, F., Bao, Y., Chen, Y., Tang, Y., Chen, G. “Impact and corrosion resistances of duplex epoxy/enamel coated plates.” Construction and Building Materials, 2016, In Press.

[2] Huntzingera, D.N., Eatmon, D.T. “A life-cycle assessment of Portland cement manufacturing: comparing the traditional process with alternative technologies.” Journal of Cleaner Production, 2009, 17(7): 668-675.

[3] Meng, W., Khayat, K. “Experimental and numerical studies on flexural behavior of ultra-high-performance concrete panels reinforced with embedded glass fiber-reinforced polymer grids.” Journal of Transportation Research Record, 2016, In Press.

[4] Bao, Y., Meng, W., Chen, Y., Chen, G., Khayat, K. “Measuring mortar shrinkage and cracking by pulse pre-pump Brillouin optical time domain analysis with a single optical fiber.” Materials Letters, 2015,145: 344-346.

[5] Kodur, V., Khaliq, W. “Effect of temperature on thermal properties of different types of high-strength concrete.” J. Mater. Civ. Eng., 2011, 23(6): 793-801.

[6] Kodur, V., Shakya, A. “Effect of temperature on thermal properties of spray applied fire resistive materials.” Fire Safety Journal, 2013, 61: 314-323.

[7] Li, V. C., Leung, C. K. “Steady-state and multiple cracking of short random fiber composites.” Journal of Engineering Mechanics, 1992, 118(11): 2246-64.

[8] Li, X., Luo, M., Wang, J. “Experimental research on flexural toughness of green high performance fibre reinforced cementitious composites.” Materials Research Innovations, 2014,18: 43-47.

[9] Li, X., Luo, M., Yan, Q. “Influence of specimen shape and mix proportion on tensile property of Green High Performance Fiber Reinforced Cementitious Composites (GHPFRCC).” Journal of Coastal Research, 2015, 73: 516-520.

[10] Khaliq, W., Kodur, V. “Thermal and mechanical properties of fiber reinforced high performance self-consolidating concrete at elevated temperatures.” Cement and Concrete Research, 2011, 41(11): 1112-1122.

[11] Bao, Y., Chen, Y., Matthew, H., Smith, C., Matthew, B., Chen, G. “Experimental analysis of steel beams

subjected to fire conditions enhanced by Brillouin scattering based fiber optic sensor data." ASCE Journal of Structural Engineering, 2016, under review.
[12] Gandage, A. S., Ram, V. V., Yaswanth, A. B., Thota, K. P., Gupta, S. "Thermal conductivity studies for self-compacting concrete with sand and fly ash variation." ACI Materials Journal, 2015, 112(6): 709-721.
[13] Luccioni, B.M., Figueroa, M.I., Danesi, R.F. "Thermo-mechanic model for concrete exposed to elevated temperatures." Engineering Structures, 2003, 25(6): 729-742.
[14] Tanyildizi, H, Sahin, M. "Application of Taguchi method for optimization of concrete strengthened with polymer after high temperature." Construction and Building Materials 2015,79: 97-103.

Influence of Water on Load Induced Thermal Strain of Concrete

HEISUKE YAMASHITA, TORU YOSHIDA
and TAKEO HIRASHIMA

ABSTRACT

In the present study, the influence of the curing conditions and water cement ratios on the load induced thermal strain (LITS) was considered from the results of the transient tests for measuring the total thermal strain and weight loss of the specimens. The specimens (water/cement ratios were 40-65%) were cured with 3 methods. The results of the tests indicate that the LITS due to dehydration is much larger than that due to water evaporation. Moreover, the numerical model for the modeling of the LITS is proposed as a function of the weight loss of the specimens.

1. INTRODUCTION

When concrete is heated under a sustained load, a large amount of shrinkage occurs to compensate for thermal expansion. This shrinkage was termed the load induced thermal strain (LITS) by Khoury [1], and must be considered when performing a deformation analysis of reinforced concrete structures that are subjected to fire. In the remarkable constitutive strain models used in such analyses like that proposed by Anderberg [2], Schneider [3] or Terro [4], the LITS is a function of the concrete temperature. However, the relationship between the LITS and temperature is influenced by the water of the concrete, making it difficult to apply these models to concrete with different water conditions (i.e. curing conditions, water/cement ratio (W/C)). For example, a pre-heating of specimen alters development of LITS [1,2,5,6] and a lower water/cement ratio causes LITS greater [7]. On the other hand, if the dependence of the LITS on dehydration and decomposition of the cement hydrate could be determined, a comprehensive relationship could be formulated that includes the effects of water, because the LITS is also caused by physical and chemical reactions in the cement hydrate during heating. Although the amount of dehydration and decomposition can be quantified based on weight loss of a specimen measuring

Heisuke Yamashita, Japan Testing Center for Construction Materials, 5-21-20 Inari Soka-shi, Saitama, 340-0003, Japan.
Toru Yoshida, Chiba University, 1-33 Yayoi-cho Inage-ku, Chiba, 263-8522, Japan.
Takeo Hirashima, Chiba University, 1-33 Yayoi-cho Inage-ku, Chiba, 263-8522, Japan

the LITS, there have been no previous reports on the relationship between the LITS and specimen weight loss, except for a study applying a thermos-gravimetric analysis (TGA) [8,9].

In the present study, the influence of the curing conditions (air-dried, oven-dried and sealed curing) and water/cement ratios (40%, 50% and 65%) on the LITS was investigated based on results obtained from the transient tests for measuring total thermal strain of concrete specimens. The relationship between the LITS and specimen weight loss was also evaluated in order to develop a comprehensive model for the LITS that is appreciable to concrete with different curing conditions and water/cement ratios.

2. TEST PROGRAM

2.1 Test Parameter

In this study, 2 kinds of tests were conducted. One of the tests was transient test for measuring total thermal strain of specimens. In this test, a specimen was heated at a constant rate of 1.5°C/min. up to 800°C under constant load, and deformation that occurred in the test was measured. In addition, transient tests under no load were performed in order to measure the free thermal strain. The test parameters are given in Table I. The load levels were given as the ratio of the constant axial load σ to compressive strength of air-dried specimens at room temperature σ_b.

Another test was transient test for measuring weight loss of specimens. In this test, a specimen was heated at same rate as transient test for measuring total thermal strain under no load, and weight loss that occurred in the test was measured.

2.2 Specimen

The specimens were cylinders of 75 mm in diameter and 150 mm in height. The specimen size was determined based on a coarse aggregate size of 25 mm and a uniform temperature distribution. The aggregates were siliceous sand stone.

Table I. PARAMETERS OF TRANSIENT TEST FOR MEASURING TOTAL THERMAL STRAIN

<table>
<tr><th>Name</th><th>W/C</th><th>Curing</th><th>R_{wc}(%)</th><th>Load Level (σ/σ_b)</th><th>Heating Temp.</th></tr>
<tr><td>65A</td><td rowspan="3">65%</td><td>Air-dried</td><td>2.10</td><td rowspan="2">0, 0.1, 0.3, 0.5, 0.7</td><td rowspan="7">R.T.-800°C (1.5°C/min.)</td></tr>
<tr><td>65D</td><td>Oven-dried</td><td>approx.0</td></tr>
<tr><td>65S</td><td>Sealed</td><td>6.08</td><td rowspan="5">(Compressive strength at R.T. σ_b(N/mm^2) = 26.5(W/C=65%) 37.0(W/C=50%) 49.2(W/C=40%))</td></tr>
<tr><td>50A</td><td rowspan="2">50%</td><td>Air-dried</td><td>2.73</td></tr>
<tr><td>50D</td><td>Oven-dried</td><td>approx.0</td></tr>
<tr><td>40A</td><td rowspan="2">40%</td><td>Air-dried</td><td>3.19</td></tr>
<tr><td>40D</td><td>Oven-dried</td><td>approx.0</td></tr>
</table>

*R_{wc} is water content's percentages by weight.

All specimens were cured in water to the age of 28 days. After the water curing, 'air-dried' specimens were cured in an air-exposed state, and 'sealed' specimens were cured in a sealed state in a curing room. Sealed curing was conducted for the specimens of water/cement ratio=65% only. And 'oven-dried' specimens were pre-dried at 105°C for 14 days in a drying oven after the same curing with the air-dried specimens. The testing ages of specimens were 348 to 485 days. The water content's percentages by weight of the specimens (R_{wc}) were indicated in Table 1.

2.3 Testing Equipment

The tests for measuring weight loss were performed using a box type electric furnace shown in Figure 1. In the test, 2 specimens per same kind of specimen were heated at one time, and weight loss and temperature of the specimens were measured by separate specimens. Weight loss of the specimen was measured by a load cell located above the specimen, and temperature of the specimen was measured by thermocouples arranged at depth of 6mm from a surface. All the specimens were heated in the stainless steel mesh cage that was suspended from above.

The tests for measuring total thermal strain were performed using the loading system and an electric furnace shown in Figure 2 [5]. The loading system consisted of steel beams, steel columns, and oil cylinder, which was placed vertically on the lower beam in order to produce the axial force. The relative axial displacement between the top and bottom of the specimen was measured using two transducers. The axial deformation of the specimen was mechanically transferred out of the furnace by a quartz tube. Temperature of the specimen was measured by thermocouples arranged at depth of 6mm from a surface.

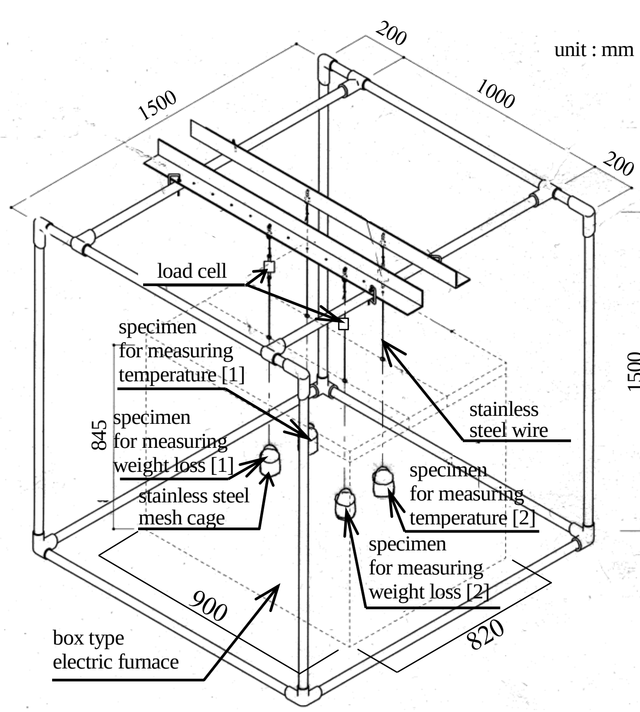

Figure 1. Testing equipment used for measuring weight loss

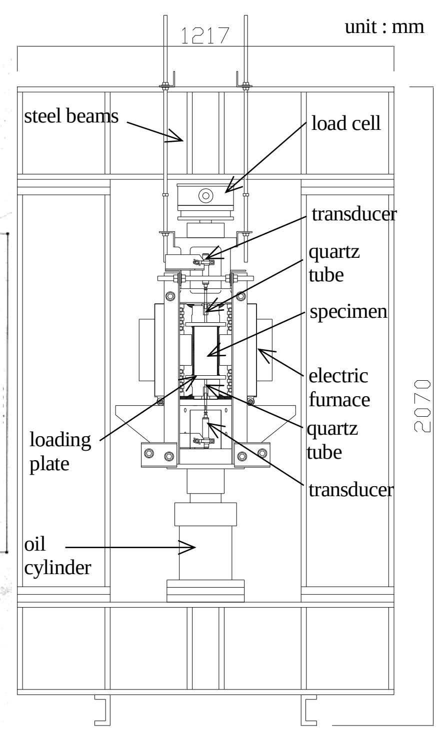

Figure 2. Testing equipment used for measuring LITS

3. RESULTS OF TESTS

3.1 Weight Loss of Specimen

Figure 3 shows the relationship between the weight loss and temperature of specimen. The weight loss is expressed as the percentage (R_{wl}) of the weight loss and the initial weight before the test, and temperature is average of the measuring values.

The weight loss of air-dried specimens and sealed specimens were increased sharply above 100°C due to an evaporation of water in the specimens [2,6,10]. Above 200°C, the weight loss of oven-dried specimens also occurred due to a dehydration of cement hydrate mainly [11]. The slope of relationship between the weight loss and temperature was tends to be steeper for sealed specimens than other curing specimens between 250°C and 500°C. And, in the same temperature range, lower water/cement ratio causes the slope steeper. It is considered that the weight loss of sealed specimens or low water/cement ratio specimens due to a dehydration of cement hydrate were greater because a cement hydrate content of these specimens was relatively high. Above 600°C, while the dehydration of cement hydrate was finished, the decomposition of cement hydrate occurred [11].

3.2 Total thermal strain

Figure 4 shows the relationship between the total thermal strain and temperature of the specimen 65A. In the present study, the total thermal strains were zero at the start of heating, since the initial elastic strains were deduced. And, in the vertical axes of the figures, positive values denote expansion and negative values denote contraction.

When the load level was 0, the free thermal strain reached approximately 15000 ($x10^{-6}$) at 800°C. The total thermal strain decreased with load level because the LITS that was shrinkage increased. Consequently, the total thermal strain became about zero

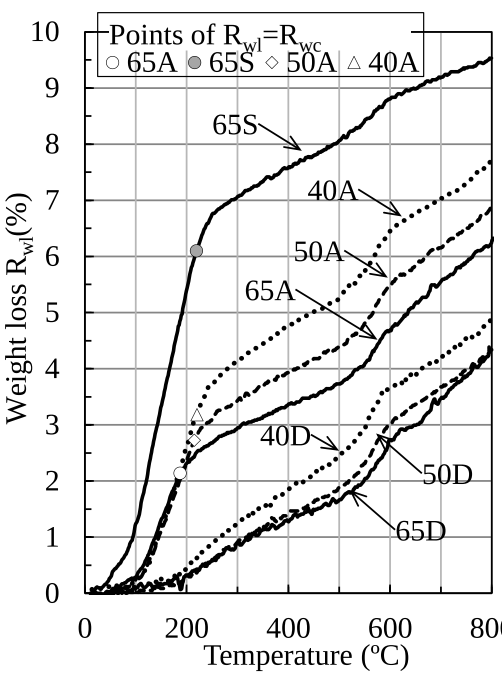

Figure 3. Relationship between the weight loss and temperature

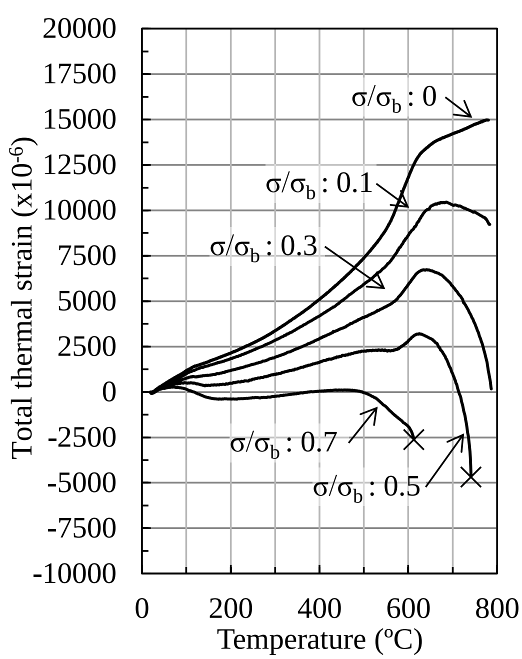

Figure 4. Relationship between the total thermal strain and temperature (Specimen 65A)

when the load level was 0.7. When the load level was more than 0.5, failures of the specimens occurred before temperature reached 800°C.

4. INFLUENCE OF WATER ON LITS

In this section, the influence of water on the LITS is considered. The LITS is calculated by subtracting value of the free thermal strain from the total thermal strain indicated at **3.2**.

4.1 Influence of curing condition

The influence of the curing conditions on the LITS is given in Figure 5. The influence of the water evaporation on the LITS was evident between 100°C and 200°C, and consequently LITS were greater for air-dried specimens than oven-dried specimens. Difference of the LITS between the air-dried specimen and oven-dried specimen reached approximately 2500 ($x10^{-6}$) when the load level was 0.7. It is considered that the cause of the difference between air-dried specimens and oven-dried specimens is drying creep that is generated when the specimen is dried under load [12].

The LITS were greater for the sealed specimens than for the air-dried specimens above 200°C. Difference of the LITS between the specimen 65A and 65S reached approximately 9000 ($x10^{-6}$) when the load level was 0.5. It is considered that the differences of dehydration amount between 250°C and 500°C affected the LITS.

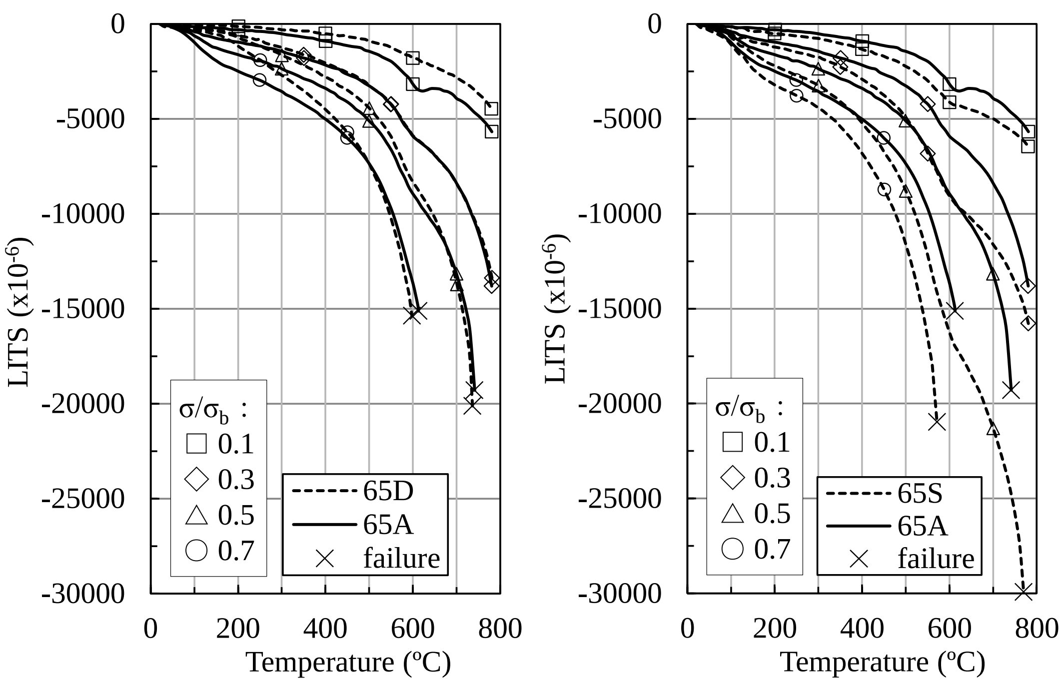

(a) air-dried vs oven-dried specimen (b) air-dried vs sealed specimen

Figure 5. Influence of curing condition

4.2 Influence of water/cement ratio

The influence of water/cement ratio on the LITS is given in Figure 6. The influence of water/cement ratio on the LITS occurred above 200°C. The LITS were greater as the water cement ratio of the specimens was low. Difference of the LITS between the specimen 65A and 40A reached approximately 10000 ($x10^{-6}$) at 800°C when the load level was 0.3. It is considered that the influence was caused by change of effective stress [7] and difference of dehydration amount.

4.3 Influence of load level

The relationship between the LITS and load levels is given in Figure 7. It was observed that the LITS was linearly related to load level up to 0.5 [1,5,6]. In this study, the relationship is seen to be linear up to 0.7 regardless of the curing conditions and water/cement ratios. And the influence of curing conditions and water/cement ratio was increased with load level.

5. RELATIONSHIP BETWEEN LITS AND WEIGHT LOSS

Figure 8 shows the relationship between the LITS and the specimen weight loss at a load level of 0.3. Three types of curve can be seen, depending on the curing conditions used. Figure 9 shows the same data shown in Fig. 8, but divided into two regimes: before and after the weight loss (R_{wl}) was equal to the water content of the specimen (R_{wc}). $LITS_{dh}$ indicates the LITS values after R_{wl} exceeded R_{wc}, and $R_{wl.\mathrm{dh}}$ is calculated by subtracting R_{wc} from R_{wl}. It can be seen that the LITS due to dehydration and decomposition of the cement hydrate (=$LITS_{dh}$) is much larger than that due to

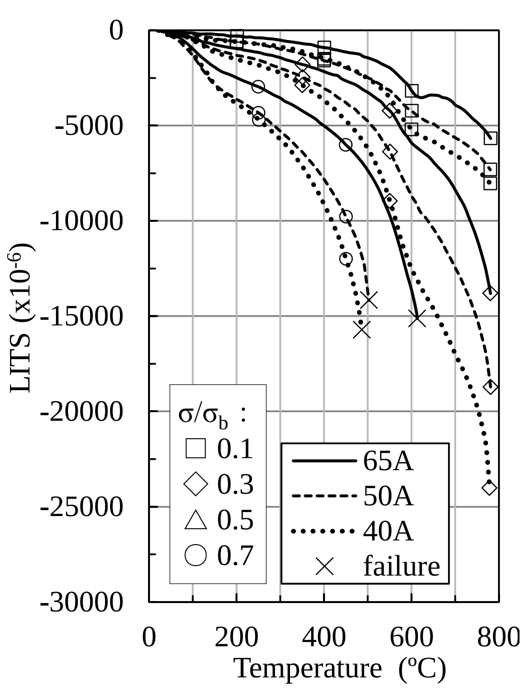

Figure 6. Influence of water/cement ratio

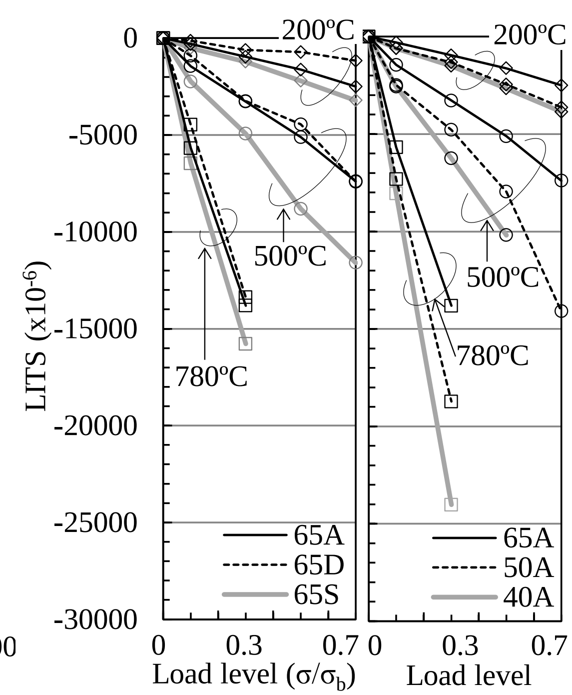

Figure 7. Relationship between the LITS and load levels

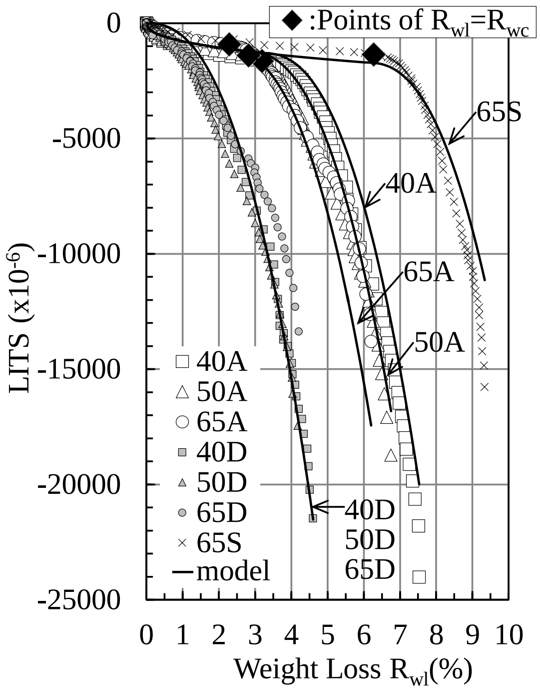

Figure 8. Relationship between the LITS and weight loss at load level of 0.3

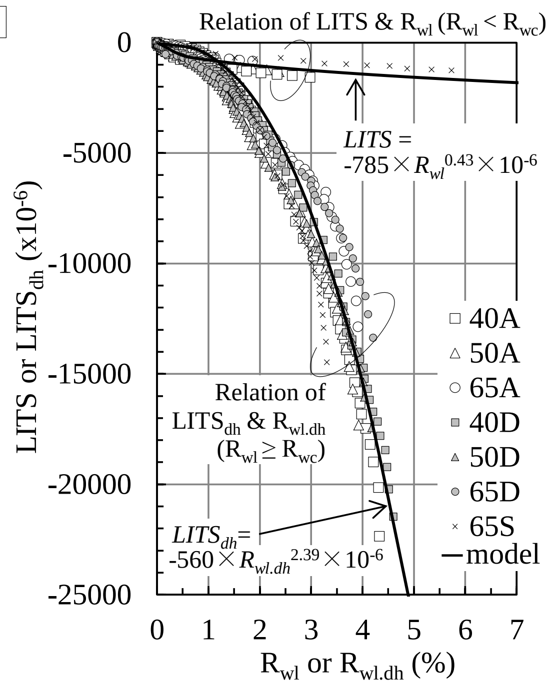

Figure 9. Relationship between LITS and weight loss before and after weight loss is equal to water content

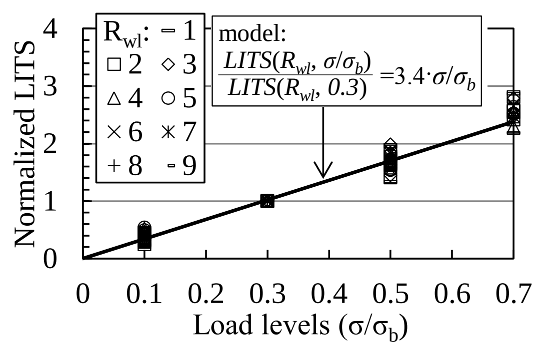

Figure 10. Relationship between normalized LITS and load levels

water evaporation. Furthermore, since all of the data points in Fig. 9 can be reasonably well fitted using just two curves, a comprehensive relationship between the LITS and the weight loss is obtained, which takes into account the influence of curing conditions and water/cement ratio.

The numerical expressions used to fit the data at a load level of 0.3 are shown in the figure 9. And, to expand applicable load levels of the numerical expressions, the relationship between the normalized LITS and the load level was formulated, as shown in Fig. 10. In Fig. 10, the LITS were normalized for values obtained at a load level of 0.3 in accordance with the method that was proposed by Terro [4]. Consequently, the numerical model for the modeling of the LITS is proposed as a function of the weight loss of the specimens as follows.

$$LITS\ (R_{wl}, \sigma/\sigma_b) = 3.4\cdot \sigma/\sigma_b \cdot LITS\ (R_{wl}, 0.3) \tag{1}$$

$$\left.\begin{aligned} &LITS\ (R_{wl}, 0.3) = -785\times R_{wl}^{0.43}\times 10^{-6} && [R_{wl} \leq R_{wc}] \\ &LITS\ (R_{wl}, 0.3) = (-785\times R_{wc}^{0.43} - 560\times(R_{wl} - R_{wc})^{2.39})\times 10^{-6} && [R_{wl} > R_{wc}] \end{aligned}\right\} \tag{2}$$

* application limitation : load level (σ/σ_b) $\leq$ 0.7, specimen temperature $\leq$ 800°C

A comparison between the calculated values using the numerical model and experimental values of LITS is shown in Fig. 8. The calculated values are seen to be in reasonable agreement with the experimental data generally.

6. CONCLUSIONS

In this present study, the following results were obtained from the transient tests of concrete specimens.

(1) The influence of the water evaporation on the LITS was evident between 100°C and 200°C.
(2) The LITS were greater for the sealed specimens than for the air-dried specimens above 200°C.
(3) The influence of water/cement ratio on the LITS occurred from 200°C. The LITS were greater as the water cement ratio of the specimens was low.
(4) The LITS were increased linearly with the load levels between 0.1 and 0.7.
(5) The LITS due to dehydration and decomposition is much larger than that due to water evaporation.
(6) The numerical model for the modeling of the LITS is proposed as a function of the weight loss of the specimens.

7. REFERENCES

1. Gavriel A. Koury, Brian N. Grainger, Patrick J.E. Sullivan: Strain of concrete during first heating to 600°C under load, Magazine of Concrete Research, Vol.37, No.133, pp.195-215, 1985.12
2. Anderberg Y. and Thelendersson S.: Stress and Deformation Characteristics of Concrete at High Temperature 2.Experimental Investigation and Material Behaviour Model, Division of Structural Mechanics and Concrete Construction, Lund Institute of Technology, Bulletin No.54, Lund, Sweden, 1976
3. Schneider U.: Concrete at High Temperatures – A general Review, Fire Safety Journal, 1988, 13, No1, pp.55-68
4. Mohamad J. Terro: Numerical Modeling of the Behavior of Concrete Structures in Fire, ACI Structural Journal, pp.183-193, 1998
5. Heisuke Yamashita, Toru Yoshida, Takeo Hirashima, Influence of Water Content on Total Strain of Super-high-strength Concrete under Elevated Temperature, Proceedings of the 10th Asia-Oceania Symposium on Fire Science and Technology, Tsukuba, 2015.10
6. Jean-Christophe Mindeguia, Izabela Hager, Pierre Pimienta, Helene Carre, Christian La Borderie: Parametrical study of transient thermal strain of ordinary and high performance concrete, Cement and Concrete Research, pp.40-52, 2013
7. Jin Tao, Xian Liu, Yong Yuan, Luc Taerwe: Transient strain of self-compacting concrete loaded in compression heated to 700°C, Materials and Structures, pp.191-201, 2013
8. D. Gawin, F. Pesavento, B.A.Schrefler: Modelling of deformation of high strength concrete at elevated temperatures, Materials and Structures, pp.218-236, 2004
9. Hassen Sabeur, Fekri Meftah: Dehydration creep of concrete at high temperatures, Materials and Structures, pp.17-30, 2008
10. Gavriel A. Koury, Brian N. Grainger, Patrick J.E. Sullivan: Transient thermal strain of concrete: literature review, conditions within specimen and behaviour of individual costituents, Magazine of Concrete Research, Vol.37, No.132, pp.131-144, 1985.9
11. Schneider, U., 1982, Behaviour of Concrete at High Tempera-tures, Vertrieb Durch Verlag Von Wilhelm Ernst & Sohn, Berlin.
12. Z.P. Bazant, J.C. Chern, 1985, Concrete creep at variable humidity: constitutive law and mechanism, Materials and Structures, pp. 1-20.

Elevated Temperature Behavior of Impact-Induced Partially Damaged Concrete

MAHSA MIRMOMENI[1], AMIN HEIDARPOUR[1], XIAO-LING ZHAO[1] and JEFFREY A. PACKER[2]

SUMMARY

Designing protective structures capable of withstanding the combined extreme actions of impact/blast and fire necessitates the accurate prediction of material properties under the coupled effects of high-strain-rate and subsequent elevated temperature loadings. An extensive experimental program was being carried out in the Civil Engineering Laboratories at Monash University to investigate the post-impact fire properties of plain self-compacting concrete (SCC) material and the results are presented in this paper. This will help in evaluating whether partially damaged concrete elements can further sustain additional stresses in case of a subsequent fire outbreak. Specimens have undergone interrupted high-strain-rate compressive loading, controlled locally at defined levels of axial displacement, to account for different deformation states. Results indicate that the mechanical behavior of concrete subject to post-impact fire scenarios is dependent on the rate of loading, the damage history and the fire temperature to which it is subsequently exposed.

INTRODUCTION

Protective concrete structures must be capable of enduring extreme loads such as impact or fire and their combined effects such as post-impact-fire situations. Concrete, as one of the most widely used construction materials, is both rate- and temperature-dependent. A large number of experimental results have been published on the behavior of plain concrete under impact loading [1, 2]. It has been identified that the load-carrying capacity of concrete increases substantially at higher strain rates, which may be due to an inertial effect and resistance to crack opening [1]. Furthermore, studies have shown that the compressive strength enhancement of concrete with strain rate are influenced by many uncertain factors, such as different testing techniques, specimen size effect, material properties (e.g. concrete static compressive strength), aggregate grade, curing and moisture condition, age, boundary effects and specimen

[1]Department of Civil Engineering, Monash University, Melbourne, VIC3800, Australia.
[2]Department of Civil Engineering, University of Toronto, Toronto, Ontario M5S 1A4, Canada.

lateral inertial effect. Recently, Mirmomeni et al. [3] investigated the effect of size, boundary, and curing conditions on the dynamic compressive strength (strain-rates under 5 s^{-1}) of **s**elf-**c**ompacting **c**oncrete (SCC), a high performance concrete developed in Japan in 1988 [4]. Based on experimental results, some typical empirical formulas such as the CEB Model [5] have been developed and used for predicting the dynamic increase factor of concrete material.

A significant amount of research work has been carried out to assess the fire resistance of concrete materials [6, 7]. The mechanical properties of concrete under elevated temperatures depend on the concrete mixture~~s~~ and composition~~s~~. Under elevated temperatures, the behavior of concrete undergoes a detrimental effect and loses a substantial amount of its mechanical strength such as compressive stress. The concrete strength variation with the temperature has been accounted for using reduction factors and design curves in design codes [8].

However, the material tests performed on concrete in recent years do not address the influence of the combined sequential effect of high-strain-rate and temperature on the mechanical properties of concrete. This paper experimentally investigates the mechanical characteristics of high-strain-rate-induced partially damaged unconfined self-compacting concrete meso-scale specimens at elevated temperatures.

EXPERIMENTAL PROGRAM

Test material and specimens

Unconfined self-compacting concrete specimens with nominal dimensions of 40mm diameter and height/diameter ratio of 1, with a target strength grade of C37 (i.e. 37 MPa) have been utilized for the experiments. SCC is well known for its excellent deformability, segregation resistance and consequent vibration-free placing process. The mixture proportion of self-compacting concrete used by Mirmomeni et al. [3] was adopted here and is presented in Table I.

The SCC concrete samples were water-cured for 7 days and subsequently air-cured at room temperature for the remainder of the curing period until tested on the 28th day.

TABLE I. THE MIXTURE PROPORTION OF SELF-COMPACTING CONCRETE.

Ordinary Portland cement (kg/m^3)	Water (kg/m^3)	Class F Fly ash (kg/m^3)	Coarse aggregate (kg/m^3)	Fine aggregate/Sand (kg/m^3)	Superplasticizer (ml)
213.3	112.1	53.3	400.8	434.1	13

For each type test, at least 3 specimens were cast and tested. Where the consistency of the three was not proven to be satisfactory (a deviation of more than 5% from the average strength value of the samples), more tests were carried out till data consistency was achieved. Moreover, samples were chosen from different batches of cast concrete to ensure the accuracy of the results.

Instrumentation, Test Set up and Procedure

The effect of post-impact fire on the residual compressive strength of high-strain-rate partially damaged concrete at elevated temperatures up to 600°C is investigated in this study. The dual-phase experimental set-up simulating the impact and subsequent fire conditions adopted for the tests is presented in Figure 1.

PHASE I: IMPACT SIMULATION

Interrupted high-strain-rate compression tests were conducted at room temperature via an Instron 8802 servo-hydraulic testing machine with a load capacity of 250kN as shown in Figure 1(a). Tests were run in displacement-control mode. Load and position were determined using built-in transducers while direct measurement of strain was achieved using a MTS LX500 non-contact laser extensometer.

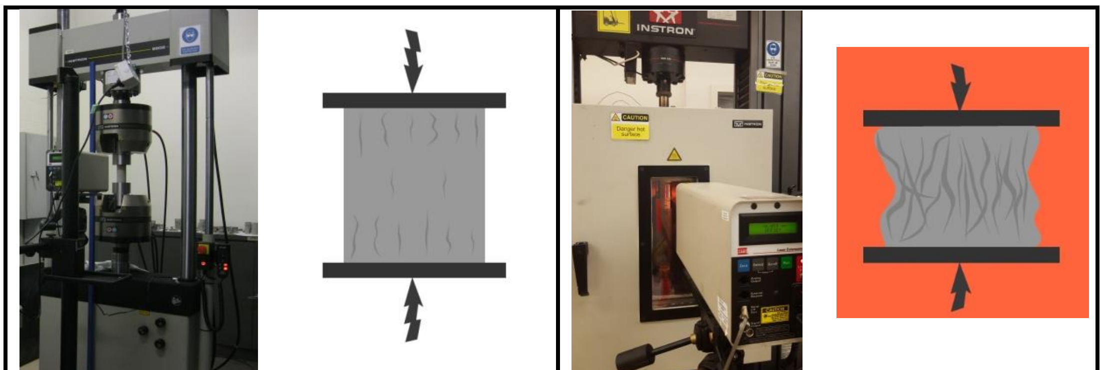

(a) Phase I: Impact Simulation | (b) Phase II: Fire Simulation

Figure 1. Two-phase experimental program setup, (a) Phase I: interrupted high-strain-rate compression test, (b) Phase II: elevated temperature quasi-static compression test.

In order to reduce the effect of the friction between the machine interface and the specimen, a fine layer of high pressure grease was applied to the top and bottom surfaces. Two impact speeds of 150mm/sec and 75mm/sec were chosen to induce the initial partial deformation. The nominal rate of strain was calculated by the ratio of V/L_0, where L_0 is the length of the specimen and V is the crosshead displacement rate. Hence, to achieve a specific nominal strain rate during a test, the machine was operated at a relevant constant crosshead velocity.

Uninterrupted uniaxial **h**igh **s**train **r**ate (HSR) compression tests at aforementioned two different impact speeds were carried out and the obtained load-axial shortening curves were used to define damage levels for each strain rate. For each strain rate regime, two distinct damage levels are defined with respect to the displacement (D_u) corresponding to the ultimate compressive load (P_u) (Figure 2). In the lower damage level, namely 0.5 D_u, high-strain-rate-induced micro-cracks are introduced into the material, however, it is still close to its linear elastic behavior. In the higher damage level, 0.8 D_u, although the material is still fully intact, visible longitudinal micro-cracks appear on the surface of the specimen. Hence the following damage index, defined as the ratio of dissipated energy per unit volume, is indicative of the level of the induced pre-damage to the material:

$$\text{Damage index} = \int_{D=0}^{D=D_i} PdD \Bigg/ \int_{D=0}^{D=D_u} PdD \tag{1}$$

where D_i is the value of axial shortening at the test interruption point and D_u is displacement at which the material is completely damaged, i.e. at the point corresponding to the ultimate compressive load (D_u).

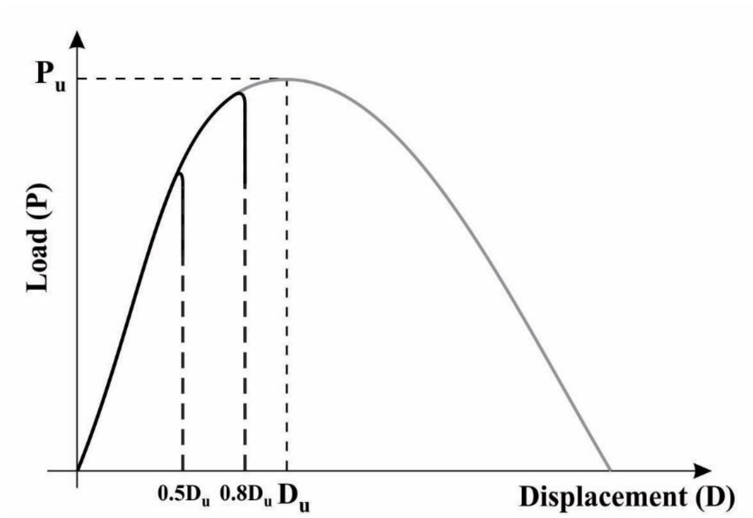

Figure 2. Axial shortening-controlled damage levels.

During phase I tests, specimens underwent interrupted high-strain-rate compressive loading, controlled locally at these defined levels of axial displacement to account for different deformation states. Tests were abruptly terminated by the operating software at the designated shortenings. Subsequently, specimens were taken out of the machine ready for the second Phase.

PHASE II: FIRE SIMULATION

In the second phase, quasi-static compression tests at elevated temperature were carried out on high-strain-rate-induced partially damaged specimens (from Phase I) to understand the influence of elevated temperature on the residual mechanical properties of damaged concrete. Specimens were tested to failure using an Instron environmental chamber mounted onto an Instron 5982 testing machine with a load capacity of 100kN, as shown in Figure 1(b). The partially damaged specimens were tested under target temperatures of ambient, 300°C, 450°C, and 600°C. The surface temperature of the specimen was measured by means of three type *K* thermocouples positioned in intimate contact with the surface of the specimen. A fine hole with the dimensions of the tip of thermocouple have been designated in some of the samples to measure the inside temperature gradient of the samples.

Each specimen was initially heated up to the specified temperature with a heating rate of 10 °C/min and maintained at that constant temperature until the temperature was stabilized, as shown in Figure 3. The data on this figure are based on the readings of the inside sample thermocouples. During the heating process, the load on the specimen was manually maintained at zero. On stabilization of the temperature (at the end point of Figure 3 curves), uniaxial compression load was applied at a displacement rate of 0.1 mm/min until failure.

RESULTS AND DISCUSSION

Figure 4 shows the results of the uninterrupted compressive tests at three loading rates which were performed primarily to indicate the rate dependency characteristics of the test material at room temperature. As anticipated, the behavior of SCC is rate-sensitive.

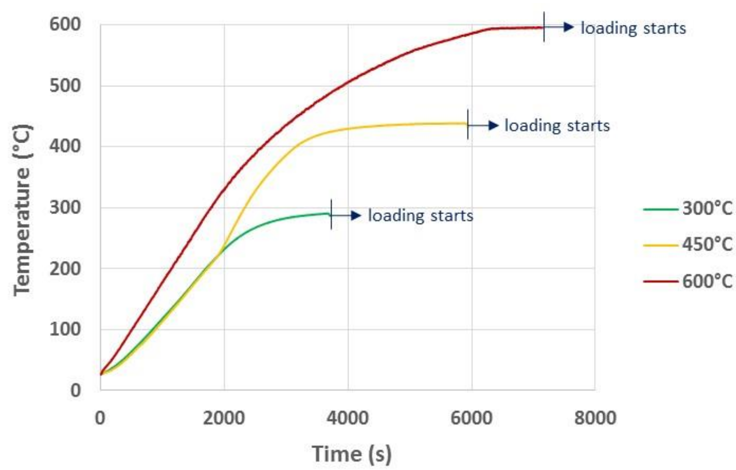

Figure 3. Temperature-time curve for the heat-up process of Phase II tests.

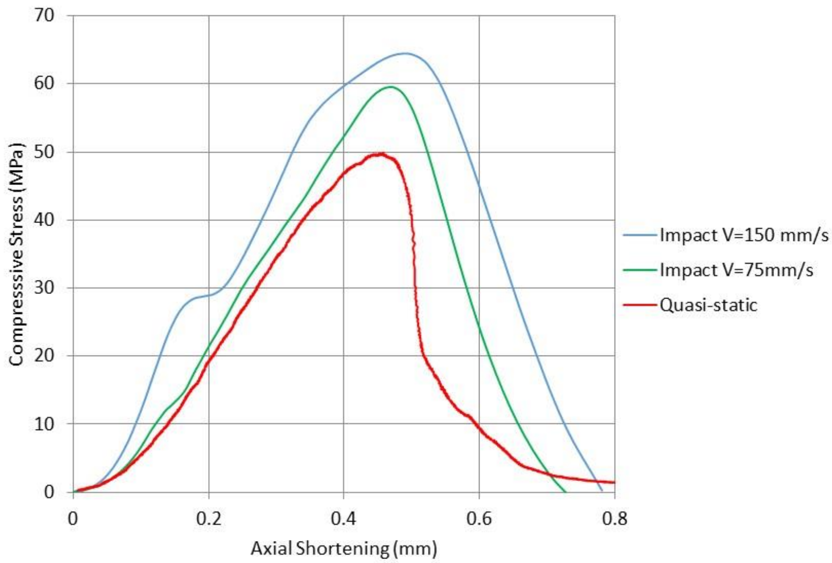

Figure 4. Engineering stress-axial shortening curve of self-compacting concrete for different loading rates at ambient temperature.

The strain-rate induced strength increase model recommended by CEB [5] is one of the most commonly used formulations for concrete in compression which is:

$$DIF_C = \frac{f_{cd}}{f_{cs}} = \left(\frac{\dot{\varepsilon}}{\dot{\varepsilon}_s}\right)^{1.026\alpha_s} \qquad (\dot{\varepsilon} \le 30s^{-1}) \tag{2}$$

where, f_{cs} and f_{cd} are the static and dynamic strength of concrete respectively, in MPa, $\dot{\varepsilon}$ is the dynamic strain rate, $\dot{\varepsilon}_s = 30 \times 10^{-6}\ \mathrm{s}^{-1}$ and the empirical parameters are taken as $\alpha_s = (5 + 9\frac{f_{cs}}{f_0})^{-1}$, and $f_0 = 10$ MPa.

The actual measured strain rates for the high-strain-rate tests with impact velocity of 75 mm/s and 150 mm/s are 1.1 and 2.5 s^{-1}, respectively. The dynamic increase factor (DIF) obtained, based on Figure 4 is approximately 1.18 for the lower strain rate and 1.28 for the higher strain rate. These DIF values calculated via the CEB model for the 75mm/s and 150mm/s loading rates are 1.24 and 1.26, respectively, which shows a small difference to those obtained via test results. This is likely caused by different test conditions between the experiments herein and those used for developing the model, as well as size effects [3]. However, the overall trend of the stress-displacement curve is in agreement with the CEB model, indicating an increase in the compressive stress of the material with an increase of strain rate.

The residual strength of high-strain-rate-induced partially damaged specimens tested in Phase II at different elevated temperatures is presented in Figure 5, for both loading rates.

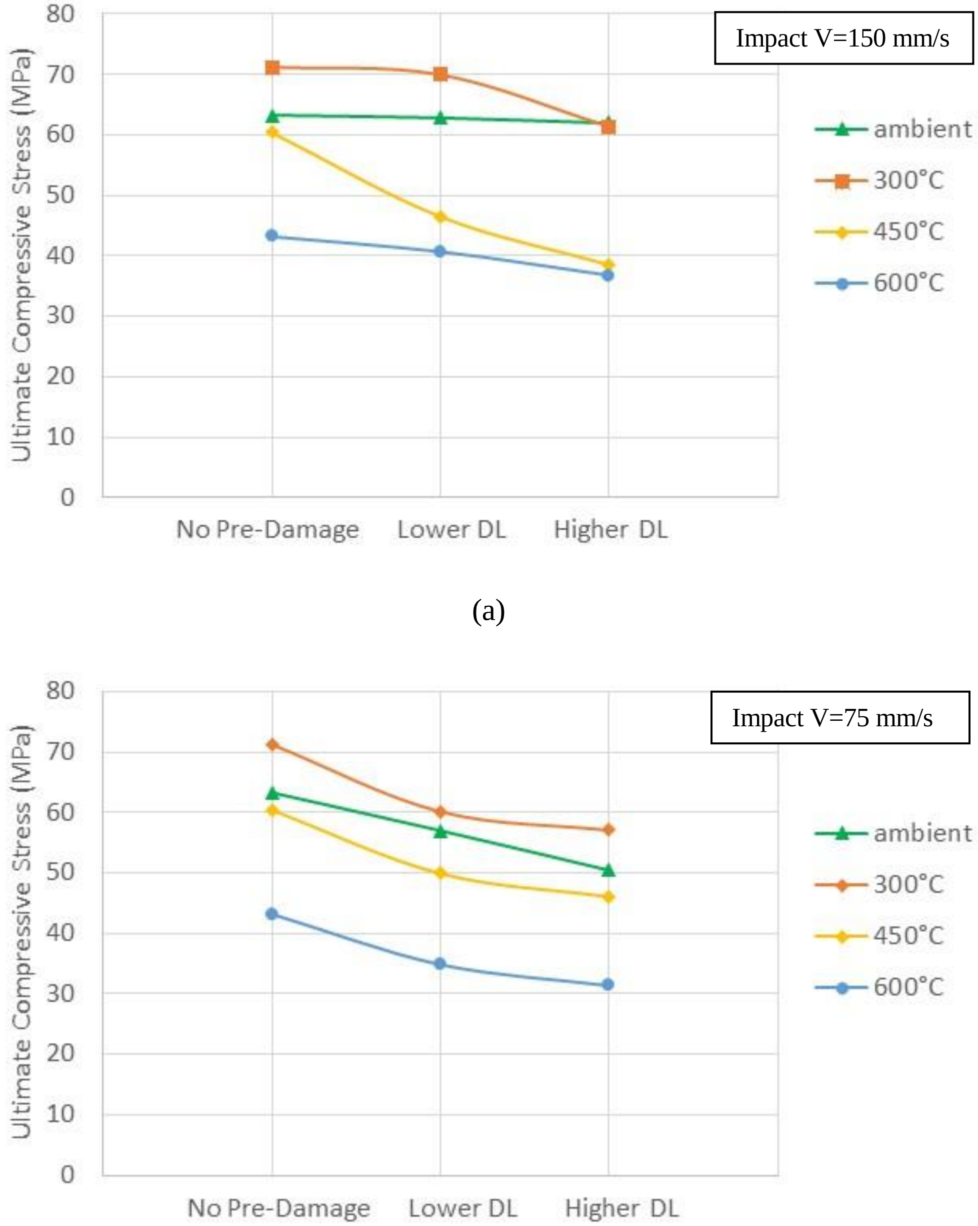

(a)

(b)

Figure 5. Residual strength of high-strain-rate-induced partially damaged SCC at different elevated temperatures for (a) 150mm/s and (b) 75mm/s impact loading rate.

The ultimate compressive strength (UCS) of the SCC has a slight increase up to 300ºC, but decreases dramatically from 300ºC onward. The maximum stress achieved decreases as the temperature increases, such that at 600ºC there is more than 40% reduction in the compressive strength of the material. According to BS 8110 [8], the ratio of material strength at 600°C and 450°C to that at the ambient temperature is 0.5 and 0.8, respectively. As can be seen from Figure 5, the reduced strengths due to temperature-only effects (no induced pre-deformation) are slightly less than those predicted by the aforementioned code for dense concrete, indicating that SC concrete maybe capable of maintaining its properties better than conventional concretes.

With an increase in damage level the material has an increased loss of capacity, hence the residual compressive strength is decreased. This decreasing trend is similar for all temperatures for the tests with the impact velocity of 75mm/s. However, for higher impact rate loading tests, at low temperatures (upto 300°C), the increased amount of micro-cracking introduced into the material and the resultant increase in the damage index enable partial restoration of the material strength. The rational of the strength restoration in higher strain rates is currenly being investigated by the authors through Xray tomography of induced micro-cracks. However, with an increase of temperature to 450°C, temperature is the dominant factor for strength reduction and there is no apparent strength restoration. For tests with pre-deformation at higher impact rate loading and tested at low fire temperatures, the material is capable of maintaining more than 90% of its no-damage strength. This resilience declines with the increase of temperature.

CONCLUSION

The residual elevated temperature compressive strength of self-compacting concrete material, which has been partially damaged under high-strain-rate loading conditions, has been experimentally investigated. The elevated temperature behavior of high-strain-rate-induced pre-damaged concrete was compared to that of each individual loading scenario and to experimental results available in the literature, for high-strain-rate loading and also elevated temperature effects. The stress-strain relationship of concrete under the individual effect of high temperatures was found to be consistent with what has been reported in the literature. The test results demonstrate that the combined effects are different from those in which the material is subject to either high strain rate or thermal loading individually. This is more apparent with an increase in the impact loading rate, where the material is capable of restoring its strength to some extent at low temperatures, whereas at elevated temperatures of 450°C and above, temperature is clearly the dominant factor. This study has thus found that the stress-strain behavior of concrete is dependent on the rate of loading, the damage history and the fire temperature to which it is subsequently exposed.

ACKNOWLEDGMENTS

The work presented in this research is supported by the Australian Research Council through a Discovery Project (DP130100181) and Tsinghua Initiative Scientific Research Program (No.20131089347).

REFERENCES

1. Bischoff, P.H. and Perry, S.H., *Compressive behaviour of concrete at high strain rates.* Materials and structures, 1991. **24**(6): p. 425-450.
2. Arioz, O., *Effects of elevated temperatures on properties of concrete.* Fire Safety Journal, 2007. **42**(8): p. 516-522.
3. Mirmomeni, M., Zhang, S., Heidarpour, A., Zhao, X.L., Al-Mahaidi, R., Packer, J.A. and Wu, C., *Size Dependency and Boundary Effects on the Mechanical Properties of Concrete Filled Steel*

Tubes under Impact Load, in *3rd International Conference on Protective Structures (ICPS3)*. 2015: Newcastle, Australia.

4. Okamura, H. and Ouchi, M., *Self-compacting concrete.* Journal of advanced concrete technology, 2003. **1**(1): p. 5-15.
5. CEB, *Concrete structures under impact and impulsive loading*, in *Bulletin d'Information No. 187*. 1988, Comite Euro-International du Beton: Lausanne, France.
6. Khoury, G.A., *Effect of fire on concrete and concrete structures.* Progress in Structural Engineering and Materials, 2000. **2**(4): p. 429-447.
7. Schneider, U., *Concrete at high temperatures — A general review.* Fire Safety Journal, 1988. **13**(1): p. 55-68.
8. *BS8110*, in *Structural use of concrete. Part I: Code of practice for design and construction*. 1997: British Standards Institution, UK.

METAL STRUCTURES

Beam-columns with Thin Wall Cross-sections in Case of Fire

CARLOS COUTO, ARNAUD SANZEL, PAULO VILA REAL, NUNO LOPES and BIN ZHAO

ABSTRACT

The fire behaviour of class 4 cross-sections beam-columns is investigated in this paper. The local buckling of the cross-sections as well as the global instabilities are evaluated. A numerical parametric study is conducted with the help of different finite element software to analyse the efficiency of current EN 1993-1-2 simple design rules. It is demonstrated that these current simple rules do not allow a cost-effective design of such steel elements. Following the new simple design rules developed in the scope of FIDESC4 project to calculate the effective properties of class 4 cross-sections and the lateral torsional buckling resistance/buckling resistance of corresponding members, a new interaction curve is proposed and the numerical results are now compared with the new obtained resistances. Statistical results are given to approve the new method and show its efficiency in terms of safety level and economic design.

1. INTRODUCTION

At elevated temperatures, the behaviour of steel members with thin wall cross-sections (class 4 steel sections according to Eurocode) subjected to combined compression and bending is not well investigated in existing research projects and the efficiency of current simple design rules of EN 1993-1-2 [1] is not clearly established in terms of both safety level and cost-effective character. In fact, in the scope of the European RFCS project FIDESC4, important research works have been conducted in this field which have provided significant contribution to deep understanding of fire behaviour of such type of steel members under various loading conditions. Several papers were published during lasts years which have covered largely the outcomes of this project with respect to class 4 steel members submitted to single loading condition. For instance, the fire resistance of steel members with class 4 cross-sections submitted to simple bending or axial compression as well as the lateral torsional buckling behaviour of class 4 steel beams in bending and the buckling resistance of class 4 steel columns [2-4]. On the contrary, current paper will be focused on the presentation of the works carried out for the development of new simple design rules dealing with combined compression and bending of steel members with class 4 cross-sections.

2. SIMPLE DESIGN RULES FROM CURRENT EN 1993-1-2

According to EN 1993-1-2, the design buckling resistance $R_{fi,d}$ for a member without lateral restraints and with a Class 4 cross section subject to combined bending and axial compression in fire situation should be verified by satisfying the interaction curve defined by the two following equations for doubly symmetric cross-sections. These are the equations (4.21c) and (4.21d) respectively of EN 1993-1-2 adapted for Class 4, i.e., considering the effective cross-sectional properties:

$$\frac{N_{fi,Ed}}{\chi_{min,fi}A_{eff}k_{0.2p,\theta}\frac{f_y}{\gamma_{M,fi}}}+\frac{k_yM_{y,fi,Ed}}{W_{eff,y,min}k_{0.2p,\theta}\frac{f_y}{\gamma_{M,fi}}}+\frac{k_zM_{z,fi,Ed}}{W_{eff,z,min}k_{0.2p,\theta}\frac{f_y}{\gamma_{M,fi}}}\leq 1 \tag{1}$$

$$\frac{N_{fi,Ed}}{\chi_{z,fi}A_{eff}k_{0.2p,\theta}\frac{f_y}{\gamma_{M,fi}}}+\frac{k_{LT}M_{y,fi,Ed}}{\chi_{LT,fi}W_{eff,y,min}k_{0.2p,\theta}\frac{f_y}{\gamma_{M,fi}}}+\frac{k_zM_{z,fi,Ed}}{W_{eff,z,min}k_{0.2p,\theta}\frac{f_y}{\gamma_{M,fi}}}\leq 1 \tag{2}$$

All symbols are those defined in Eurocode 3. k_y is defined with the following equation:

$$k_y=1-\frac{\mu_yN_{fi,Ed}}{\chi_{y,fi}A_{eff}k_{0.2p,\theta}\frac{f_y}{\gamma_{M,fi}}}\leq 3 \tag{3}$$

And:

$$\mu_y=\left(2\beta_{M,y}-5\right)\bar{\lambda}_{y,\theta}+0.44\beta_{M,y}+0.29\leq 0.8\ but\ \bar{\lambda}_{y,20°C}\leq 1.1 \tag{4}$$

For equation (2), k_{LT} is defined with the following equation:

$$k_{LT}=1-\frac{\mu_{LT}N_{fi,Ed}}{\chi_{z,fi}A_{eff}k_{0.2p,\theta}\frac{f_y}{\gamma_{M,fi}}}\leq 1 \tag{5}$$

And:

$$\mu_{LT}=0.15\bar{\lambda}_{z,\theta}\beta_{M,LT}-0.15\leq 0.9 \tag{6}$$

The equivalent uniform moment factors $\beta_{M,LT}$ and $\beta_{M,y}$ are evaluated using the bending diagram corresponding to the major axis: $M_{y,fi,Ed}$. Only uniaxial bending (about the major axis) was considered in this numerical investigation. Furthermore, in fire situation $\gamma_{M,fi}$ = 1. Then, the terms related to the minor axis (z) are not taken into account. Equations (7) and (8) respectively lead to a value, named κ_{in} for in-plane buckling and κ_{out} for out-of-plane buckling which are compared to 1. $\kappa < 1$ means that the result given by the simple design rules can lead to unsafe design. In fact, when the beam-column reaches its numerical collapse the simple rules would permit a higher load level, which is not safe. On the other side, $\kappa > 1$ means that the numerical results lead to a higher resistance than the one admitted in the simple design rules. Thus, equations (1) and (2) respectively become:

$$\frac{N_{fi,Ed}}{\chi_{min,fi}A_{eff}k_{0.2p,\theta}f_y}+\frac{k_yM_{y,fi,Ed}}{W_{eff,y,min}k_{0.2p,\theta}f_y}\leq \kappa_{in} \tag{7}$$

$$\frac{N_{fi,Ed}}{\chi_{z,fi} A_{eff} k_{0.2p,\theta} f_y} + \frac{k_{LT} M_{y,fi,Ed}}{\chi_{LT,fi} W_{eff,y,min} k_{0.2p,\theta} f_y} \leq \kappa_{out} \tag{8}$$

3. NUMERICAL MODEL AND PARAMETRIC STUDY

In order to develop reliable simple design rules, an important numerical parametric study was conducted in the scope of FIDESC4 project, which has led to the establishment of a consequent database on the fire resistance of steel members with class 4 cross-sections under combined bending and compression. A total of about 6000 advanced simulations based on the GMNIA method have been run with both SAFIR [5] and ANSYS [6] software. In fact, in above GMNIA analysis, not only the geometric and material non-linearities as well as imperfections but also the initial residual stresses were accounted for. With respect to geometrical imperfections, the method of EN 1993-1-5 [7] and the fabrication tolerances provided by EN 1090-2 [8] were adopted. The validity of the numerical models, which are established based on shell finite elements, was checked in advance with the help of fire tests conducted within FIDESC4 project. Numerical failure temperature and buckling mode shape were compared with the ones observed during the fire test and a good correlation was found. In the parametric study, following parameters were investigated: wall slenderness of cross-sections, member lengths, temperature level (350°C, 450°C, 550°C and 700°C), bending moment distribution along member length (uniform, triangular and bi-triangular bending moments as well as distributed load) and load interaction ratio (from pure bending to pure compression). Figure 1 depicts an illustration of a numerical failure of a beam-column.

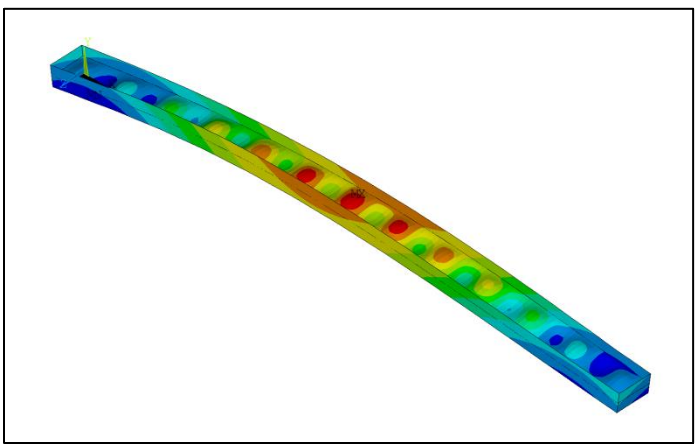

Figure 1. Illustration of the failure mode shape along the minor axis of a beam-column subjected to triangular bending moment.

4. COMPARISON OF CURRENT EN 1993-1-2 DESIGN RULES WITH THE NUMERICAL RESULTS

The coefficient κ_{in} given by equation (7) was then employed considering the ultimate axial force and uniform bending moment given by numerical simulations as the design loads. Buckling reduction factors, effective properties and cross-sectional resistance are determined using EN 1993-1-2 current design rules. Interaction curve is determined following the current EN 1993-1-2 equations too. The values of κ_{in} are plotted in Figure 2 a) against the non-dimensional slenderness $\lambda_{y,\theta}$. The out-of-plane behaviour of beam-columns was also investigated. Coefficient κ_{out} given by equation (8) was used considering ultimate axial load and bending moment provided by the numerical simulations as the design loads. Results are plotted in Figure 2 b) against the non-dimensional slenderness $\lambda_{z,\theta}$. In these figures, the horizontal line at the value 1 in the vertical axis defines the corresponding interaction curve. If the points that represent the numerical results are below the line it means the ultimate loads obtained numerically are below those predicted by equations (7) and (8) for the in-plane and out-of-plane respectively and therefore are unsafe or safe otherwise.

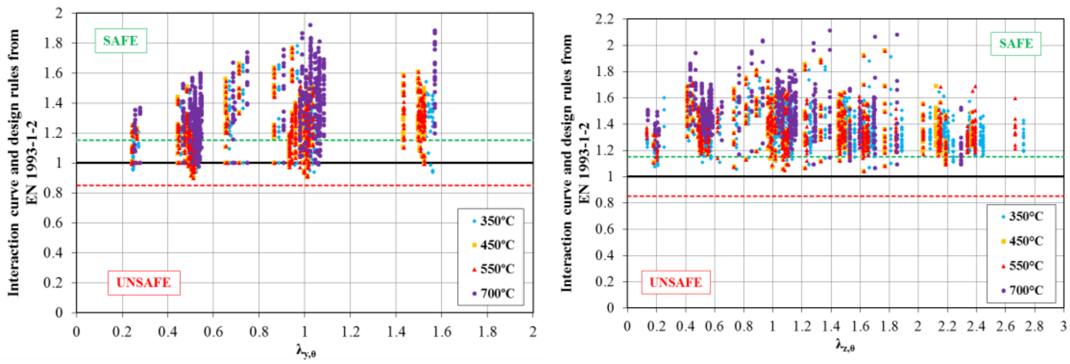

a) b)

Figure 2. Comparison of the numerical analysis results with the design rules of EN 1993-1-2 a) in-plane and b) out-of-plane interaction curve at various temperature levels as a function of the beam-column slenderness.

5. NEW PROPOSAL FOR INTERACTION CURVE AND CORRESPONDING ACCURACY INVESTIGATION

In order to obtain a more economic design, the μ_y and μ_{LT} factor were calibrated following the same methodology adopted by Talamona in [9]. According to this procedure the following expression was used to extract from each numerical simulation the value of μ_y factor, which fulfils equation (3):

$$\mu_y = \frac{M_{y,fi,Rd} \times N_{FEM} - \chi_{y,fi} \times N_{c,fi,Rd} \times M_{y,fi,Rd} + \chi_{y,fi} \times N_{c,fi,Rd} \times M_{FEM}}{N_{FEM} \times M_{FEM}} \tag{9}$$

Moreover, the following equation was used to extract from each numerical simulation the μ_{LT} factor, which fulfils equation (5):

$$\mu_{LT} = \frac{\chi_{LT} \times M_{y,fi,Rd} \times N_{FEM} + \chi_{z,fi} \times N_{c,fi,Rd} \times M_{FEM} - \chi_{z,fi} \times \chi_{LT} \times N_{c,fi,Rd} \times M_{y,fi,Rd}}{N_{FEM} \times M_{FEM}} \tag{10}$$

Where $N_{c,fi,Rd}$ and $M_{y,fi,Rd}$ are respectively the axial and moment cross-sectional resistance obtained with the new design rules proposed in [2,3], χ_{LT} is the reduction factor for LTB proposed in [4] and N_{FEM} and M_{FEM} are the ultimate axial load and bending moment given by finite element analysis.

When in-plane behaviour is concerned, Figure 3 shows the evolution of μ_y factor as a function of the non-dimensional slenderness $\lambda_{y,\theta}$ with the proposed modification given by following equation (11), denoted as "proposal". The "Linear (FEA)" term denotes the linear trend line of the numerical results:

$$\mu_{y,proposal} = (2 \times \beta_{M,y1} - 5) \times \bar{\lambda}_{y,\theta} + 0.44 \times \beta_{M,y2} + 0.7 \leq 0.6 \; but \; \bar{\lambda}_{y,20°C} \leq 1.1 \tag{11}$$

When out-of-plane behaviour is concerned, Figure 4 shows the evolution of μ_{LT} factor as a function of the non-dimensional slenderness $\lambda_{z,\theta}$ with the proposed modification given by following equation (12), denoted as "proposal". The "Linear (FEA)" term denotes the linear trend line of the numerical results:

$$\mu_{LT,proposal} = 0.45 \times \bar{\lambda}_{z,\theta} \times \beta_{M,LT} + 0.2 \leq 0.9 \tag{12}$$

With:

TABLE I. EQUIVALENT UNIFORM MOMENT FACTOR.

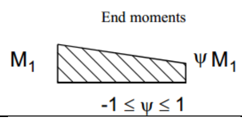	$\beta_{M,y1} = \beta_{M,\psi} = 1.8 - 0.9\psi$ $\beta_{M,y2} = \beta_{M,y1}$ $\beta_{M,LT} = \beta_{M,\psi} = 1.8 - 0.9\,\psi$
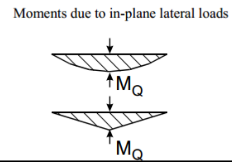	$\beta_{M,y1} = \beta_{M,Q} = 1.6$ $\beta_{M,y2} = 0$ $\beta_{M,LT} = \beta_{M,Q} = 1.6$

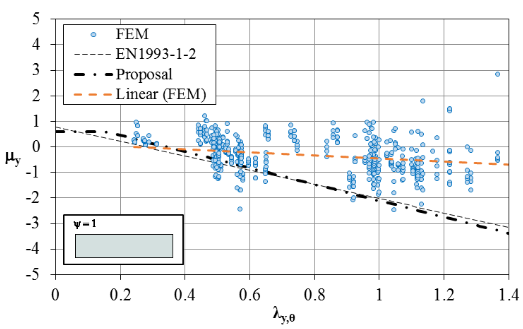

Uniform bending moment

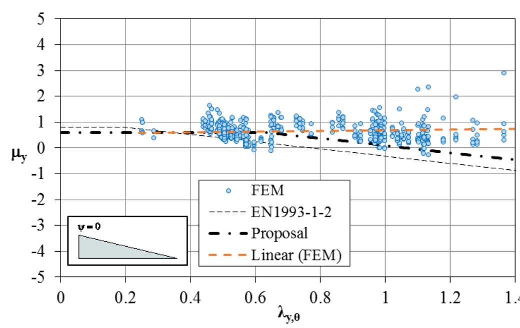

Triangular bending moment

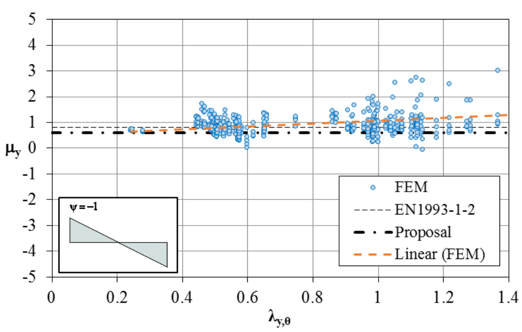

Bi-triangular bending moment

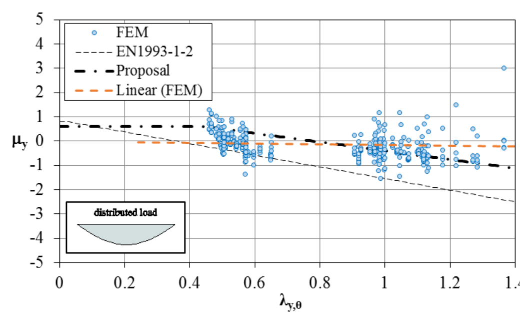

Distributed load

Figure 3. Calibration of μ_y factor for the in-plane behaviour of beam-columns considering different loading cases.

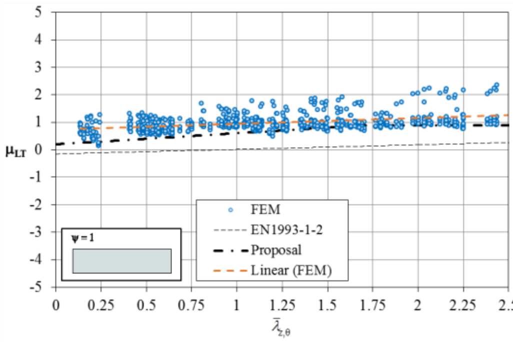

Uniform bending moment

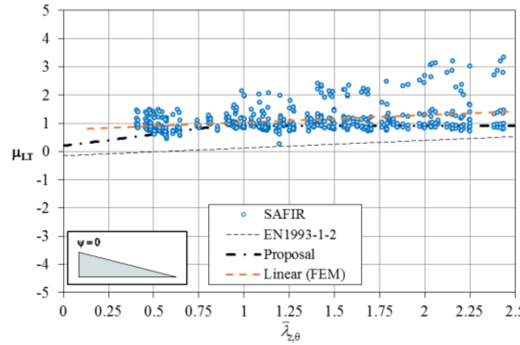

Triangular bending moment

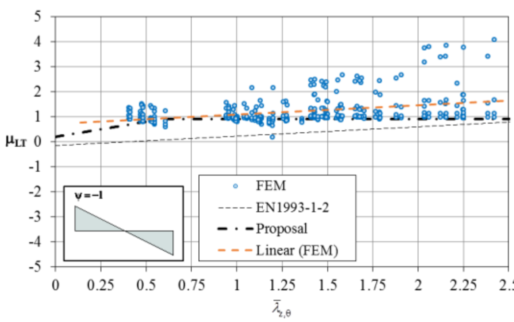

Bi-triangular bending moment

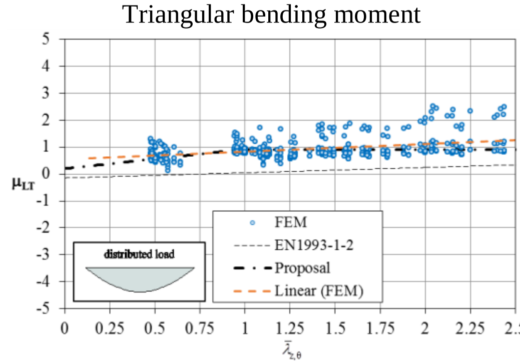

Distributed load

Figure 4. Calibration of μ_{LT} factor for the out-of-plane behaviour of beam-columns considering different loading cases.

The interaction factors $k_{y,new}$ and $k_{LT,new}$ are then calculated with equations (13) and (14).

$$k_{y,new} = 1 - \frac{\mu_{y,proposal} N_{fi,Ed}}{\chi_{y,fi} N_{c,fi,Rd}} \leq 3 \tag{13}$$

$$k_{LT,new} = 1 - \frac{\mu_{LT,proposal} N_{fi,Ed}}{\chi_{z,fi} N_{c,fi,Rd}} \leq 1 \tag{14}$$

Finally, in order to show the accuracy of the new design rules, Figure 5 plots the numerical results and the proposed interaction curves against the non-dimensional slenderness of the beam-column. The values $\kappa_{new,in}$ and $\kappa_{new,out}$ are calculated with equations (15) and (16). In these figures, the horizontal line at the value 1 in the vertical axis defines the new interaction curve.

$$\frac{N_{fi,Ed}}{\chi_{min,fi} N_{c,fi,Rd}} + \frac{k_{y,new} M_{y,fi,Ed}}{M_{y,fi,Rd}} \leq \kappa_{new,in} \tag{15}$$

$$\frac{N_{fi,Ed}}{\chi_{z,fi} N_{c,fi,Rd}} + \frac{k_{LT,new} M_{y,fi,Ed}}{\chi_{LT,fi} M_{y,fi,Rd}} \leq \kappa_{new,out} \tag{16}$$

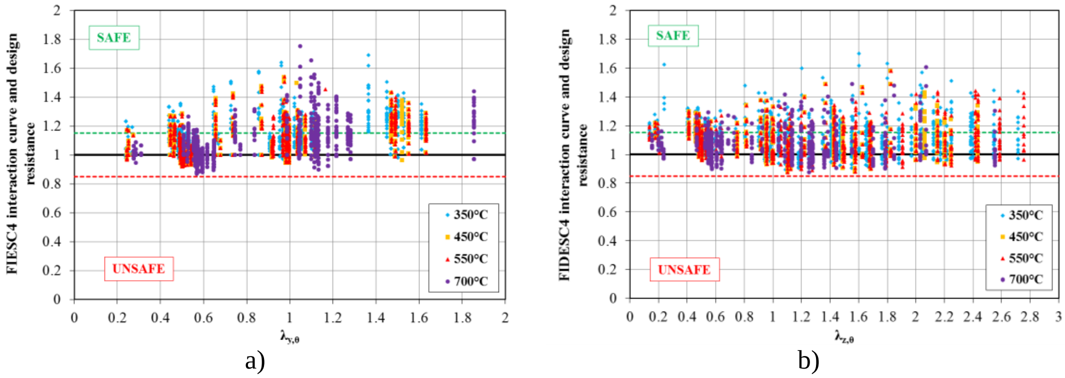

Figure 5. Comparison of the numerical analysis results with the new design rules a) in-plane and b) out-of-plane interaction curve at various temperature levels as a function of the beam-column slenderness.

6. STATISTICAL RESULTS

Table II summarises the statistical data for both in-plane and out-of-plane cases of the conducted simulations compared to EN 1993-1-2 design rules and interaction curve as well as those obtained with the new design rules.

TABLE II. STATISTICAL RESULTS ON TO ABOUT 5900 SIMULATIONS.

	EN 1993-1-2		**New design rules**	
Type of behaviour	**In-plane**	**Out-of-plane**	**In-plane**	**Out-of-plane**
Average ratio (design rule / FEM)	0.81	0.73	0.90	0.91
Percentage of unsafe points (%)	7.42	0	15.29	19.25
Maximum unsafe ratio	1.15	N/A	1.15	1.14
Percentage of safe points by more than 15% (%)	65.94	95.51	32.30	28.75
Standard Deviation	0.18	0.16	0.12	0.11
Coefficient of variation	0.22	0.21	0.13	0.12

When using the full design rules available in EN 1993-1-2 it is noticeable that the design resistance of class 4 cross-sections submitted to combined bending and compression is really not cost-effective. This is the case for both in-plane and out-of-plane behaviours. Furthermore, for beam-columns without lateral restraints, almost all cases (95%) are situated on the safe side by more than 15%.

In what regards the new design rules, it can be found that the new proposed interaction curves now allow a far more cost-effective design of class 4 beam-columns subjected to combined loadings and at different temperature levels for both in-plane and out-of-plane behaviours. Furthermore, the maximum unsafe ratio remains always lower than or equal to 1.15.

7. CONCLUSIONS

It was demonstrated that the current design rules of EN 1993-1-2 are very conservative and not cost-effective at all. Moreover, in case of lateral torsional buckling, this conservative effect becomes even stronger. Then, in order to check the benefits of new design rules proposed in the scope of FIDESC4 project for single loading condition, only the interaction curves for both in-plane and out-of-plane behaviour of current EN 1993-1-2 were kept in the resistance prediction on the basis of simple design rules for the comparison. A substantial gain in accuracy and cost-effective design can be observed except members submitted to lateral torsional buckling of which the resistance is still underestimated leading to an uneconomic design. Finally, new interaction curves for the design of class 4 steel members under combined bending and compression were proposed. These new curves provide not only a more consistent resistance correlation with numerical simulations but lead also to cost-effective design.

ACKNOWLEDGMENTS

The work in this paper was supported by the European Commission, Research Fund for Coal and Steel in the frame of the research project "FIDESC4 - Fire Design of Steel Members with Welded or Hot-rolled Class 4 Cross-sections", Grant Agreement Number RFSR-CT-2011-00030.

REFERENCES

1. CEN, "EN 1993-1-2, Eurocode 3: Design of steel structures - Part 1-2: General rules - Structural fire design." European Committee for Standardisation, Brussels, 2005.
2. Couto C., P. Vila Real, N. Lopes, B. Zhao, "Effective width method to account for the local buckling of steel thin plates at elevated temperatures," Thin-Walled Struct., vol. 84, pp. 134-149, Nov. 2014.
3. Couto C., P. Vila Real, N. Lopes, B. Zhao, "A new design method to take into account the local buckling of steel cross-sections at elevated temperatures," in 8th International Conference on Structures In Fire, 2014.
4. Couto C., P. Vila Real, N. Lopes, B. Zhao, "Numerical investigation of the lateral-torsional buckling of beams with slender cross sections for the case of fire," Eng. Struct., vol. 106, pp. 410-421, 2015.
5. Franssen J.-M., "SAFIR, A Thermal/Structural Program Modelling Structures under Fire," Eng. Journal, A.I.S.C., vol. 42, no. 3, pp. 143-158, 2005.
6. ANSYS, "ANSYS User's Manual for Revision 14.5 - Volume IV – Theory" Swanson Analysis Systems, Inc., Houston U.S.A., 2012.
7. CEN, "EN 1993-1-5, Eurocode 3 - Design of steel structures - Part 1-5: Plated structural elements." European Committee for Standardisation, Brussels, pp. 1-53, 2006.
8. CEN, "EN 1090-2: Execution of steel structures and aluminium structures – Part 2: technical requirement for steel structures." European Committee for Standardisation, Brussels, 2008.
9. Talamona D., "Flambement de poteaux métalliques sous charge excentrée à haute température (in French)," 1995.

Temperature Assessment of a Vertical Steel Member Subjected to Localised Fire: Experimental Tests

FRANCOIS HANUS, OLIVIER VASSART, NICOLA TONDINI, ALI NADJAI and JEAN-MARC FRANSSEN

ABSTRACT

This paper describes the series of pool fire tests performed by the Universities of Liege and Ulster in order to assess the heat fluxes received by vertical members in case of localised fires. All these tests, performed in the scope of the RFCS project LOCAFI, have allowed gathering a large amount of experimental data for calibration and validation of subsequent numerical and analytical models. The influence of several parameters was investigated, such as the type of fuel (heptane, diesel, wood cribs), the dimension of the fire pool (diameter from 0.7 m to 2.2 m), the presence of a column (tubular or I-shape sections) and the presence of a ceiling. Although the wind speed remained limited as these tests have been performed indoor, the inclination of the flames was nevertheless significant and, in many cases, the measurements of gas temperature close to the column showed a quite significant asymmetry.

INTRODUCTION

The most common approach to justify that a structure exhibits a sufficient level of safety in case of fire is the prescriptive approach. This approach assumes that, after occurrence of flashover, the fire is fully developed and the distribution of temperature is uniform in the compartment. In several types of applications (large industrial halls, open car parks, atria, airport terminals…), the occurrence of flashover is unlikely and the use of uniform distributions of temperature in the compartment is unrealistic. In these cases, the impact of localised fires on the bearing capacity of the structure has to be analyzed.

François Hanus, Long Product R&D, Arcelormittal, 66 Rue de Luxembourg, 4009, Esch-sur-Alzette, Luxembourg.
Olivier Vassart, Long Product R&D, Arcelormittal, 66 Rue de Luxembourg, 4009, Esch-sur-Alzette, Luxembourg.
Nicola Tondini, Department of Civil, Environmental and Mechanical Engineering, University of Trento, Via Mesiano 77, 38123, Trento, Italy.
Ali Nadjai, Fire Safety Engineering Research and Technology Centre, University of Ulster, United Kingdom.
Jean-Marc Franssen, Department Architecture, Geology, Environment and Constructions, University of Liege. Belgium.

Investigations on localised fires have mainly focused on impinging fluxes at the ceiling level or temperature evolution along the vertical axis of the fire source. The current Annex C of EN 1991-1-2 [1] is dedicated to localised fire and includes two calculation methods: i) Heskestad's method [2] is applicable when the flame does not impact the ceiling and allows assessing the evolution of gas temperature along the vertical axis of the fire. ii) Hasemi's method is, on the contrary applicable in case of a flame impacting the ceiling. This method, developed on the basis of experimental investigations performed in the 80's and 90's [3,4], defines the flux impinging a horizontal element situated at the ceiling level. The field of application of these two methods is therefore limited and none of these may be used to analyze the following configurations:

- Columns heated by a localized fire but not engulfed in the fire source;
- Effect of the real flame emissivity when the element is engulfed into the localized fire;
- Lower cord and internal bars of deep trusses in large halls;

Three pool fire tests have recently been performed with diesel fuel (Diameter Φ = 1.1 m and 1.9 m) or heptanes pool (Φ = 1.1 m) by Byström et al. [5]. These tests demonstrated that the method described in Eurocode 1 for the calculation of plume temperatures and heat transfer to the column is conservative for the prediction of gas and steel temperatures. Two other pool fire tests (Φ = 0.7 m and 1.1 m) were also performed recently at the University of Coimbra [6]. The influence of ventilation conditions (different openings) and pool distance on measured heat fluxes have been particularly investigated in these tests.

LOCAFI project, funded by the Research Fund for Coal and Steel, was aimed at providing scientific evidence about the thermal attack imposed on a steel column surrounded by a local fire or attacked by a fire situated at a distance from the column and at developing design equations that allow reproducing this thermal attack as well as the temperatures induced in the column. In the scope of this project, two series of experimental tests presented hereafter have been performed at the Universities of Liege and Ulster.

TESTS PERFORMED AT THE UNIVERSITY OF LIEGE

This first series of tests envisaged 24 pool fire tests. 22 of these tests were hydrocarbon pool fires and, in the last 2 tests, the fire load was provided by wood cribs (Table I). In the hydrocarbon pool fires, the fuel flow was controlled (Figure 1a) in order to obtain a heat release rate of about 500 kW/m^2. The principle is to release the controlled flow of fuel in a water filled basin. The flow of fuel was by gravity from a tank to the basin and it was controlled by valves (no pumping device required). The basin serving as a burner was put into a larger basin, which was used to collect the discharged water. Copper pipes were fixed to the bottom of the basin and the combustible liquid was released from the pipes by numerous holes to generate a homogeneous distribution of the combustible liquid in the basin. As the density of the combustible fuels is lower than water density, the liquids rise to the surface. A cooling system was used in order to avoid water boiling (Figure 1b). The influence of several parameters has been investigated: fuel type (diesel, heptane), pool diameter (from Φ = 0.6 m to Φ = 2.2 m) and presence or not of a column engulfed in the pool. The characteristics of the two different types of combustible liquids chosen for these tests, N-heptane and Diesel, are given in Table II.

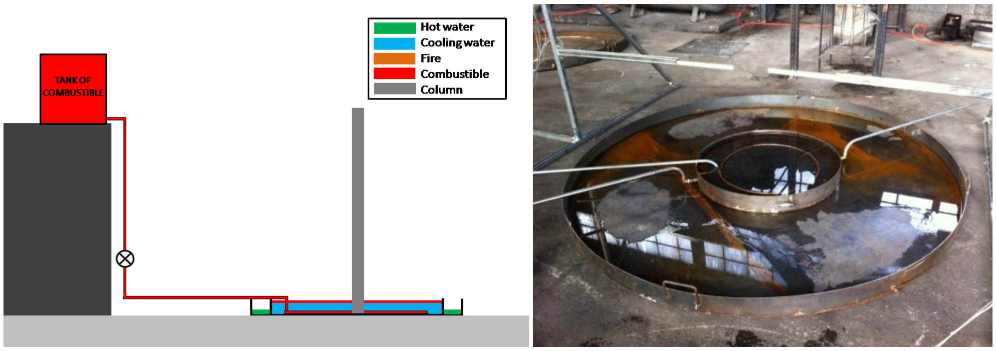

Figure 1. Description of the test set-up (left) and the cooling system of the pan (right).

TABLE I. COMPARISON OF PROPERTIES OF N-HEPTANE AND DIESEL.

Test No.	Diameter [m]	Combustible	Column	Flow q [l/min]
1	0,6	**Diesel**	**NO**	**0.30**
2	0,6	**Heptane**	**NO**	**0.35**
3	0,6	**Diesel**	**Φ203 / L=4m**	**0.25**
4	0,6	**Heptane**	**Φ203 / L=4m**	**0.30**
5	1,0	**Diesel**	**NO**	**0.82**
6	1,0	**Heptane**	**NO**	**0.98**
7	1,0	**Diesel**	**Φ203 / L=4m**	**0.77**
8	1,0	**Heptane**	**Φ203 / L=4m**	**0.92**
9	1,4	**Diesel**	**NO**	**1.59**
10	1,4	**Heptane**	**NO**	**1.92**
11	1,4	**Diesel**	**Φ203 / L=4m**	**1.55**
12	1,4	**Heptane**	**Φ203 / L=4m**	**1.86**
13	1,4	**Diesel**	**HE300A / L=4m**	**1.59**
14	1,4	**Heptane**	**HE300A / L=4m**	**1.92**
15	1,8	**Diesel**	**NO**	**2.63**
16	1,8	**Heptane**	**NO**	**3.17**
17	1,8	**Diesel**	**Φ203 / L=4m**	**2.54**
18	1,8	**Heptane**	**Φ203 / L=4m**	**3.06**
19	2,2	**Diesel**	**NO**	**3.93**
20	2,2	**Heptane**	**NO**	**4.73**
21	2,2	**Diesel**	**Φ203 / L=4m**	**3.84**
22	2,2	**Heptane**	**Φ203 / L=4m**	**4.63**

TABLE II. COMPARISON OF PROPERTIES OF N-HEPTANE AND DIESEL.

Fuel Type	Heat of combustion ΔHc [MJ/kg]	Density [kg/m^3]	Specific Heat [J/kg.K]	Soot Content
N-Heptane	44.64	675	2220	Low (light smoke)
Diesel	43.2	840	1800	High (black smoke)

During all the tests, gas temperature was recorded by two thermocouples trees (Figure 2a). The position of these trees slightly differs with the type of column (if any). Steel temperature was also recorded on the column, when present, at different levels. More details are available in [7]. Pictures were taken with a shooting time interval of 15 seconds in order to determine the height and diameter of the flame and compare those values to the ones predicted by the Eurocode. A 10x10 cm grid was generated numerically and superimposed on the photos to determine the dimensions of the flame. When the flame seemed to tilt, the horizontal air velocity was measured in the direction of the trees and/or in the direction perpendicular to the trees. All the openings of the hall were closed and the values of this velocity remain low. At each recorded time, the flame length was determined by an image processing procedure without accounting detached parts of the flame. The mean flame length is defined as the distance above the fire source where the intermittency has declined to 0.5, where the intermittency I(z) is the fraction of time where the flame height is higher than z [8].


(a) (b)

Figure 2. Thermocouple trees and heat flux gauge (a) and numerically superimposed grid (b).

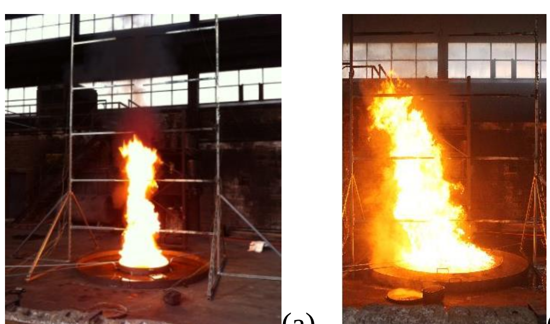
(a) (b)

Figure 3. Illustration of fire tests with different pan diameter.

TESTS PERFORMED AT THE UNIVERSITY OF ULSTER

This second series of tests has also been performed in a controlled environment (inside the laboratory) but the test procedure is different. Instead of using a control system to keep the fire load density constant with time, it was chosen to use the free surface burning in the pan and to measure the rate of heat release by oxygen depletion in a calorimeter hood. An arrangement of columns and beams allowed measuring temperatures in the engulfed column and the neighboring structural elements (Figure 4). The influence of the following parameters on the distributions of temperature was investigated:

- Column cross-section (tubular, I-section or H-section) ;
- Presence of a ceiling or not ;
- Type and quantities of fuel (wooden cribs, kerosene and rubber) ;
- Characteristics of the fire (position of the source, number of sources and delay between their ignitions).

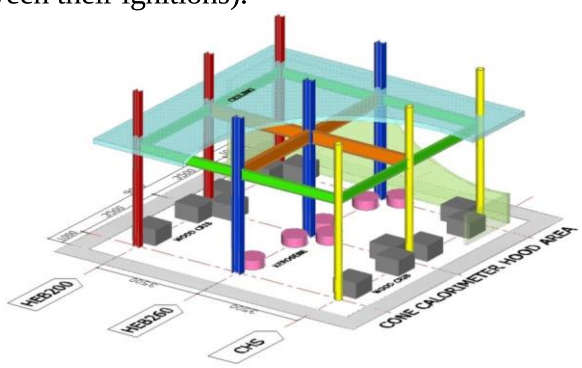

Figure 4. Experimental layout at the University of Ulster.

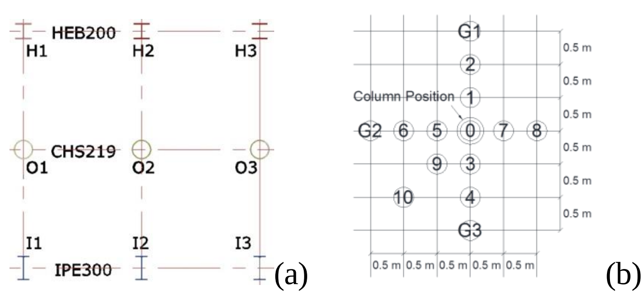

Figure 5. Denomination of the columns (a) and relative position of the fuel pan/gauge (b).

Gas and steel temperatures were measured using 0.25-mm thick thermocouples situated closed to the structure and fixed to the structure (Figure 6), respectively. All the tests performed are listed and described in Table III. This table gives the position and diameter of the fuel pan(s), the quantity and type of fuel and the positions of the gauges. The positions of the gauges are given in Figure 5b. Figures 8 and 9 show some measurements made during test I1 (one pan centered at 0.5m from column axis, Φ = 0.7m, 15 L kerosene). The flame height has also been measured by treatment of data recorded by a camera.

Figure 6. Arrangement of fuel pan, thermocouples and Gordon's gauge for Ulster tests.

TABLE III. LIST AND DESCRIPTION OF THE TESTED CONFIGURATIONS.

Tests without ceiling

Specimen	Test Number	Pan Diameter Position	Fuel Amount	Gauge Position
Column O2	O1	0.7m / (1)	Kerosene/ 15L	G1
	O2	0.7m / (2)	Kerosene/ 15L	G1
	O3	0.7m / (1)	Diesel/ 15L	G1
	O4	0.7m / (2)	Diesel/ 15L	G1
	O5	0.7m / (3)	Diesel/ 15L	G1
	O6	0.7m / (4)	Diesel/ 15L	G1
	O7	0.7m / (5)	Kerosene/ 15L	G1
	O8	1.6m/ (0)	Kerosene/ 60L	G1
	O9	0.7m / (1)(3)(5)(7)	Kerosene/ 60L	G1
	O10	1.6m / (0)	Diesel/ 60L	G1
	O11	0.7m / (1)(3)(5)(7)	Diesel/ 60L	G1
	O12	1.6m/ (0)	Kerosene/ 20L	G1
	O13	0.7m / (1)(3) (5)(7)	Diesel/ 30L Kerosene/ 30L	G1
	O14	Cribs/ (1)(3)(5)(7)	Wood/ 0.5x0.5x0.5m	G1
Column I2	I1	0.7m / (1)	Kerosene/ 15L	G1, G2
	I2	0.7m / (2)	Kerosene/ 15L	G1, G2
	I3	0.7m / (5)	Kerosene/ 15L	G1, G2
	I4	0.7m / (6)	Kerosene/ 15L	G1, G2
	I5	0.7m / (1)	Diesel/ 15L	G1, G2
	I6	0.7m / (2)	Diesel/ 15L	G1, G2
	I7	0.7m / (5)	Diesel/ 15L	G1, G2
	I8	0.7m / (6)	Diesel/ 15L	G1, G2
	I9	1.6m/ (0)	Kerosene/ 60L	G1, G2
	I10	1.6m/ (0)	Kerosene/ 20L	G1, G2
	I11	0.7m / (1)(5)(7)	Kerosene/ 45L	G1, G2
	I12	0.7m / (1)(5)	Kerosene/ 30L	G1, G2
Column I3	I13	0.7m / (1)	Kerosene/ 15L	G2
	I14	0.7m / (2)	Kerosene/ 15L	G2
	I15	0.7m / (6)	Kerosene/ 15L	G2
	I16	0.7m / (1)(5)	Kerosene/ 30L	G2
Column H2	H1	0.7m/ (3)	Kerosene/ 15L	G2, G3
	H2	0.7m/ (4)	Kerosene/ 15L	G2, G3
	H3	0.7m/ (5)	Kerosene/ 15L	G2, G3
	H4	0.7m/ (6)	Kerosene/ 15L	G2, G3
	H5	0.7m/ (3)(5)	Kerosene/ 30L	G2, G3
	H6	0.7m/ (3)(5)(7)	Kerosene/ 45L	G2, G3
	H7	1.6m/ (0)	Kerosene/ 20L	G2, G3

Tests with ceiling

Specimen	Test Number	Pan Diameter Position	Fuel Amount	Gauge Position
Column O2	O21	0.7m / (5)	Kerosene / 15L	G2
	O22	0.7m / (6)	Kerosene / 15L	G2
	O23	0.7m / (3)	Kerosene / 15L	G2
	O24	0.7m / (4)	Kerosene / 15L	G2
	O25	0.7m / (10)	Kerosene / 15L	G2
	O26	1.6m / (0)	Kerosene / 20L	G2
	O27	0.7m / (5)	Diesel / 15L	G2
	O28	0.7m / (6)	Diesel / 15L	G2
	O29	0.7m / (4)	Diesel / 15L	G2
	O30	0.7m / (10)	Diesel / 15L	G2
	O31	0.7m / (6)(8)	Kerosene / 2*8L	G2
	O32	0.7m / (6)(8)	Diesel / 2*8L	G2
	O33	Crib / (5)	Wood / 0.5x0.5x0.5m^3	G2
	O34	Crib / (6)	Wood / 0.5x0.5x0.5m^3	G2
	O35	Crib / (6)(8)	Wood / 2x0.5x0.5x0.5m^3	G2
	O36	Crib / (6)	Wood / 1.0x1.0x0.5m^3	G2
	O37	0.7m / (1)(3)(5)(7)	Kerosene / 4*8L	G2
	O38	Crib / (5)	Wood / 1.0x1.0x0.5m^3	G2
	O39	1.6m / (0)	Diesel / 20L	G2 (+ ceiling)
	O40	0.7m / (7)	Kerosene / 15L	G2 (+ ceiling)
	O41	Crib / (4)	Wood / 1.0x1.0x0.5m^3	G2 (+ ceiling)

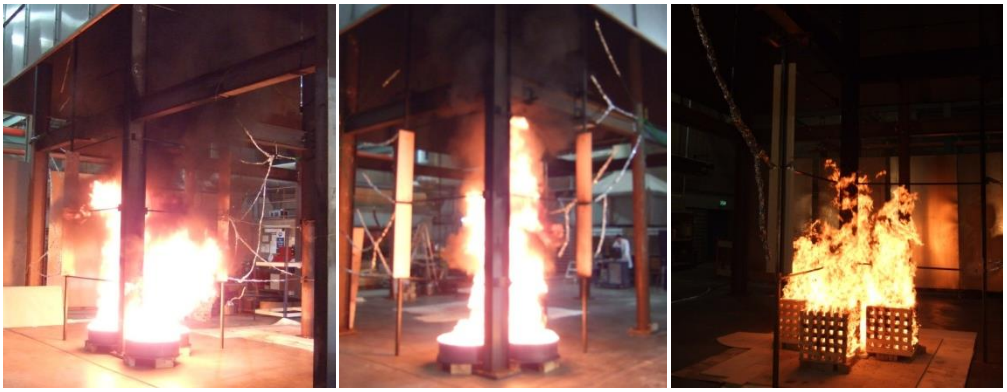

Figure 7. Views of the flames during different fire tests performed at Ulster lab.

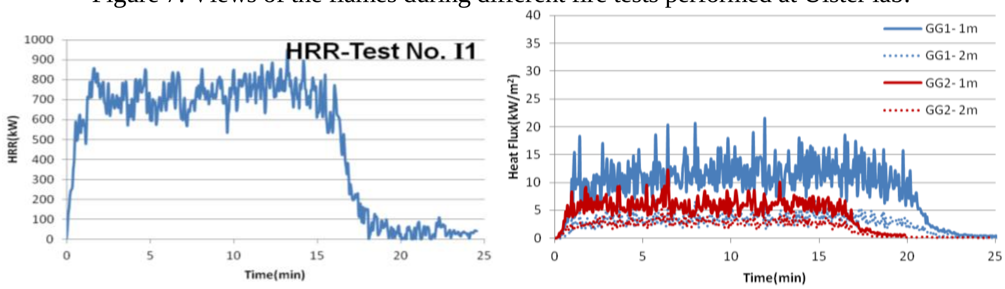

Figure 8. Test I1: HRR measured by calorimeter hood and heat flux received by different GG.

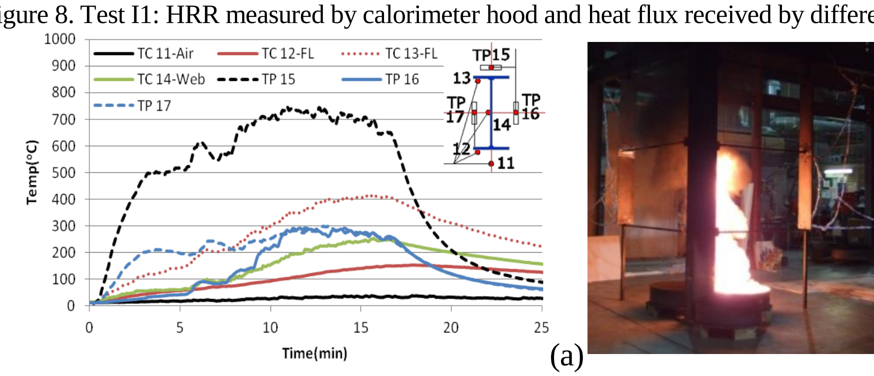

(a) (b)

Figure 9. Test I1: Temperature measurements and view of the flame (b).

COMPARISONS BETWEEN EXPERIMENTAL MEASUREMENTS AND PREDICTIONS BY ANNEX C OF EN 1991-1-2

The measured gas temperatures along the flame axis have been compared to the temperatures predicted by EN 1991-1-2 (Heskestad's model). For both Liege and Ulster tests, it is observed that the Eurocode formula generally overestimates gas temperatures (Figure 10 and TABLE IV).

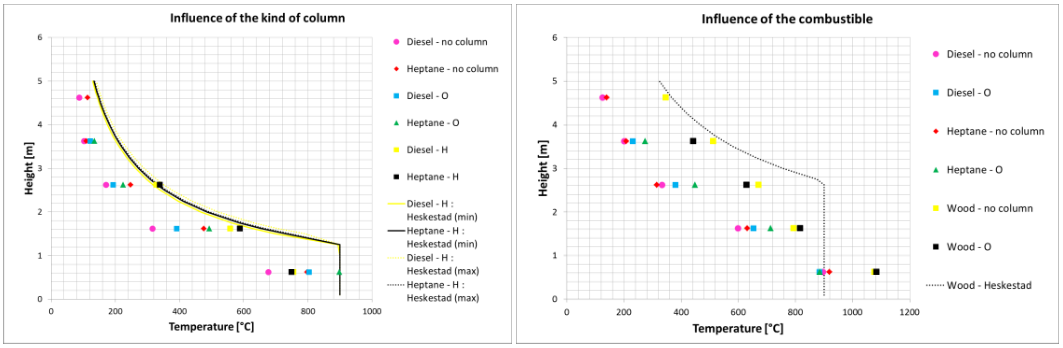

Figure 10. Comparisons between experimental data and Heskestad predictions (Liege Tests).

TABLE IV. COMPARISON BETWEEN GAS TEMPERATURES OBTAINED EXPERIMENTALLY AND BY APPLICATION OF EN1991-1-2 (ULSTER TESTS).

HEIGHT	TEST NO. O8, I9 (KEROSENE, Φ1.6m)		TEST NO. O10 (DIESEL, Φ1.6m)		TEST NO. O1,O2 (KEROSENE, Φ0.7m)		TEST NO. O3,O4 (DIESEL, Φ0.7m)		TEST NO. O14 (WOOD CRIBS)	
	EN	**EXP.**	**EN**	**EXP.**	**EN**	**EXP.**	**EN**	**EXP.**	**EN**	**EXP.**
1m	900	949	900	899	900	686	900	652	900	527
2m	900	810	900	660	845	223	697	208	900	440
3m	900	515	900	339	381	90	325	89	640	317
4m	730	312	663	235	228	-	198	-	391	185
5m	479	179	440	146	157	-	139	-	271	159

CONCLUSIONS

Two series of experimental tests, using different test procedures and set-ups, have been performed in order to provide a large amount of experimental data to characterize the thermal attack imposed by a localized fire.

A general observation is the fact that, despite all the tests were performed inside closed buildings and very low wind speeds were measured, the inclination of the flame may be significant. The measurements of gas temperature close to the engulfed columns show high asymmetry.

The second main observation of these tests is that Heskestad model overestimates gas temperatures for the different types of fuels and columns chosen for these two series of tests.

This large amount of data provides a wide basis for the calibration of numerical and analytical models aimed at representing the thermal attack imposed by localized fires, especially for vertical members that are not engulfed in the fire. The investigations are reported in detail in [7].

ACKNOWLEDGEMENTS

This work was carried out with a financial grant from the Research Fund for Coal and Steel of the European Community, within the LOCAFI project: "Temperature assessment of a vertical steel member subjected to localised fire", Grant N° RFSR-CT-2012-00023.

REFERENCES

1. EN1991-1-2. 2002. "*Eurocode 1: Actions on structures – Part 1-2: General actions – Actions on structures exposed to fire*," CEN, Brussel.
2. Heskestad G. 2002. "Flame height and Air entrainment", *The SPFE Handbook of Fire Protection Engineering*, 3th Edition, National Fire Protection Association, Quincy, MA, USA.
3. Hasemi, Y. and T. Tokunaga. 1984. "Flame Geometry Effects on the Buoyant Plumes from Turbulent Diffusion Flames," *Fire Science and Technology*, Vol. 4, N°1.
4. Pchelintsev A., Y. Hasemi, T. Wakamatsu and Y. Yokobayashi. 1997. "Experimental and numerical study on the behaviour of a steel beam under ceiling exposed to a localized fire," *Fire Safety Science* 5: 1153-1164.
5. Byström A., J. Sjöström, U. Wickström, D. Lange and M. Veljkovic. 2014. "Large Scale Test on a Steel Column Exposed to Localized Fire." *Journal of Structural Fire Engineering* 5-2: 147-160.
6. Ferraz G. 2014. "Thermal analysis of steel columns exposed to localized fires", M. Sc. Thesis, University of Coimbra, Portugal.
7. Vassart, O., M. Brasseur, F. Hanus, J.-M. Franssen, A. Scifo, B. Zhao, C. Thauvoye, R. Zaharia, D. Pintea, A. Nadjai, H. Sanghoon, 2016. "LOCAFI project – Final Report," Research Fund for Steel and Coal.
8. Zukoski E.E., B.M. Cetegen, T. Kubota. 1984. "Visible Structure of Buoyant Diffusion Flames". *Proceedings of the 20th Symposium on Combustion*, 361-366. Combustion Institute, Pittsburgh, PA.

Component-Based Element of Beam Local Buckling Adjacent to Connections in Fire

GUAN QUAN, SHAN-SHAN HUANG and IAN BURGESS

ABSTRACT

An analytical model based on the yield line mechanism [1] has been proposed by the authors to predict the beam-web shear buckling and bottom-flange buckling in fire. This paper described the development of a component-based element considering both buckling phenomena at the beam-ends, based on this analytical model. The component-based buckling element consists of top springs and bottom springs, all of which are capable of dealing with loading-unloading-reloading cycles. This new component-based element has been implemented into the software *Vulcan,* adjacent to the existing component-based connection element. An example case using a single-span beam has been analysed in *Vulcan.* The modelling results have been validated against finite element modelling using *ABAQUS*, indicating that the newly developed component-based buckling element is of good accuracy to reflect the behaviour of local buckling phenomena. Comparison of the structural responses of the beams with and without the buckling element in *Vulcan* has been carried out. This comparison shows that with and without the buckling element does make a difference in the modelling results. This indicates the potential effects of the local buckling at beam ends on the connected joints and columns and on the entire frames at elevated temperatures.

Keywords: Component-based Model, Shear Buckling, Bottom-flange Buckling, Fire

INTRODUCTION

The investigation of the collapse of "7 World Trade" as part of the events of 11 September 2001 in the New York City [2] indicated that the connections are among

Guan Quan, Department of Civil and Structural Engineering, University of Sheffield, Sir Frederick Mappin Building, Mappin Street, Sheffield S1 3JD, United Kingdom.
Shan-shan Huang, Lecturer, Department of Civil and Structural Engineering, University of Sheffield, Sir Frederick Mappin Building, Mappin Street, Sheffield S1 3JD, United Kingdom.
Ian Burgess, Professor, Department of Civil and Structural Engineering, University of Sheffield, Sir Frederick Mappin Building, Mappin Street, Sheffield S1 3JD, United Kingdom.

the most vulnerable elements of steel-framed or composite buildings, and their characteristics can determine the survivability of such buildings in extreme scenarios such as fire. In this case total collapse of the building was triggered by the fracture of beam-to-column connections caused largely by thermal expansion of long-span beams. This emphasized the importance of investigating the complex mechanisms through which forces are transferred from the adjacent parts of a structure to the connections under fire conditions.

The Cardington fire tests in 1995-96 [3] provided ample evidence that both shear buckling of beam webs and beam bottom-flange buckling, near to the ends of steel beams (Figure 1), are very prevalent under fire conditions. Both of these phenomena could affect the force distribution at the adjacent column-face connection bolt rows, and therefore the sequence of fracture of components. However, there is a distinct lack of practical research investigating the post-buckling behaviour of beams of Classes 1 and 2 adjacent to connections at elevated temperatures.

Figure 1. Flange-buckling and beam-web shear buckling in combination [3].

The component-based method is a practical approach to carry out structural performance-based analysis with reasonable simplified assumptions under fire conditions. The finite element software *Vucan* [4] was developed by the Fire Engineering Research Group at the University of Sheffield. The component-based connection element has already been included in this software, which enables *Vulcan* to be time saving, compared with other finite element software such as *ABAQUS* and *DIANA*, *etc*. These features allow engineers to conduct three-dimensional structural robustness assessments under fire conditions.

In this study, the proposed component-based buckling elements have been implemented at both ends of the beam, adjacent to the existing connection elements. The buckling phenomena considered include both the flange-buckling and beam-web shear buckling. Therefore, the buckling element is composed of two parts: flange-buckling element and beam-web shear buckling element. The bottom-flange buckling element is represented by top and bottom components, which will affect the rotation of the whole beam-end. The length of the flange-buckling element is '0'. The shear buckling behaviour has been implemented in the existing beam element adjacent to the flange-buckling element by revising its shear modulus in the post-buckling stage to incorporate the shear buckling behaviour of the beam web, but not changing the original beam curvature. The component-based buckling element is illustrated in Figure 2.

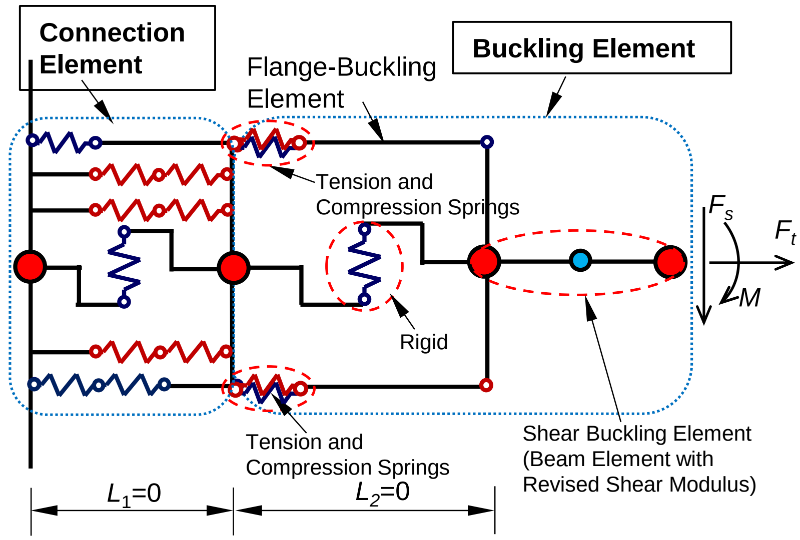

Figure 2. Component-based connections and buckling elements.

The flange-buckling element is composed of four nonlinear horizontal springs at the flange positions. Two springs, one tension and one compression, are located at the same position at each flange, providing the resistance of the flanges. For the two springs at the same location, which spring is activated depends on the direction of the spring force; the tensile spring is activated only when the spring is subject to tension and it is switched off and the compression spring becomes active when the spring force is compressive.

1. DEVELOPMENT OF THE COMPONENT-BASED FLANGE-BUCKLING ELEMENT

During the course of fire, the buckling zones can experience high material nonlinearity, and complex combinations of forces caused by the restraints to thermal expansion and to the beam elongation due to beam deflection. These forces will be resisted by the horizontal springs on the flanges (one at each flange). These springs in the buckling element could be subjecting either compression or tension at different stages of loading/heating. For example, the bottom spring could be in compression during the heating up, and in tension at the catenary-tension stage. Therefore, it is essential to establish a robust loading-unloading-reloading approach to deal with displacement reversal at both constant and changing temperatures.

1.1 Loading and Unloading of the Flange-Buckling Element at Ambient Temperature

According to the analytical model [1], the schematic characteristics of the compression spring on the buckling flange (assuming it is the bottom flange hereafter), is shown in Figure 3 (a). The characteristics of the compression spring can be divided into three stages: pre-buckling, plateau and post-buckling. The pre-buckling stage ends when the compressive force within the spring reaches F_r, which is the axial force when the bottom half of the I-section yields (Figure 3 (b)). The shape of the curved line in the pre-buckling stage is based on the high-temperature constitutive model of steel given in EC3 Part 1-2 [5].

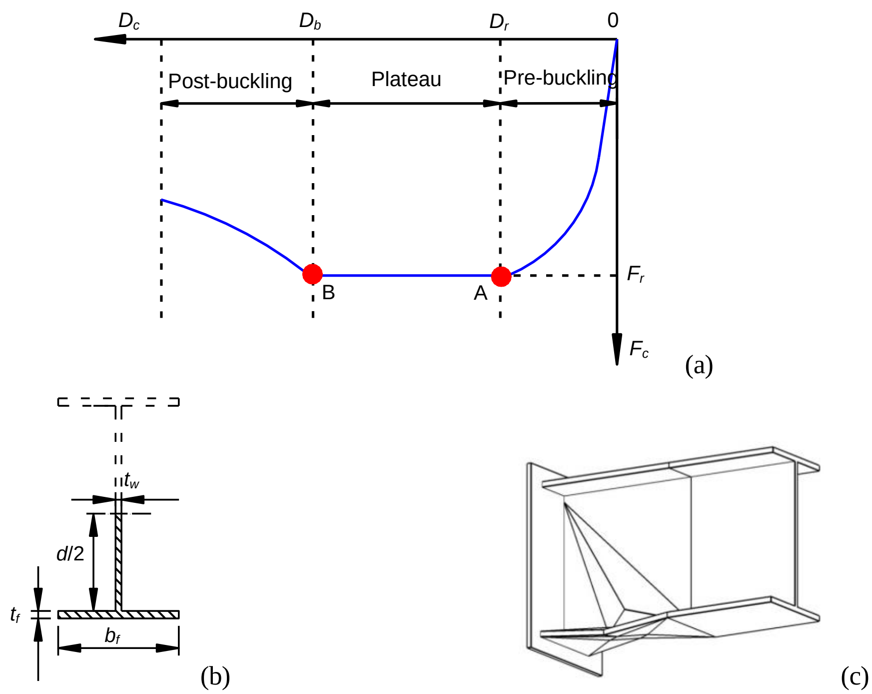

Figure 3. Schematic characteristics of the compression spring on the buckling flange.

In this paper, the Masing Rule [6] was applied to each individual spring, through the whole loading-unloading-reloading procedure (including pre-buckling, plateau and post-buckling stages) subject to both steady-state and transient heating.

At ambient temperature, the component characteristics of a spring can be represented by the combination of a skeleton (loading) curve and a hysteresis (unloading) curve. A schematic illustration of the Masing Rule is shown in Figure 4. The hysteresis curve is the skeleton curve scaled by a factor of two and rotated by 180°.

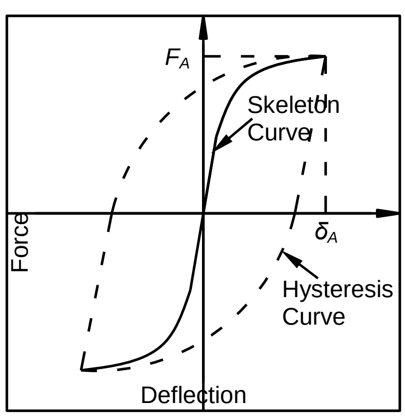

Figure 4. A schematic illustration of the Masing Rule at ambient temperature.

The characteristics of the tension spring for the initial loading are similar to that of the compression spring without the post-buckling phase (Figure 5). The unloading procedure follows the same rules as for the compression spring, as described above.

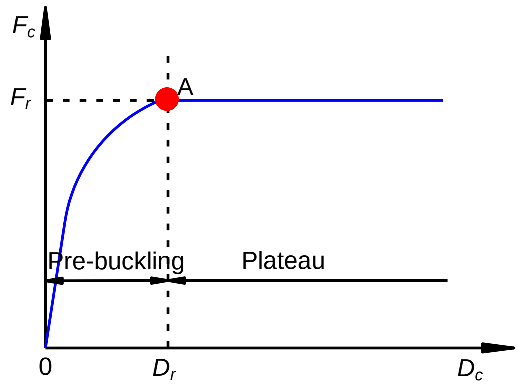

Figure 5. Schematic characteristics of the tension spring.

1.2 Loading and Unloading of the Flange-Buckling Element at Elevated Temperatures

At elevated temperatures, the force-displacement characteristic of the springs is temperature-dependent. When temperature changes, it is assumed that the coordinate of the reference point (the point where the unloading path hit the horizontal axis) remains unchanged. The new unloading path will still be linear and follows the initial slope of the force-displacement relationship of the new temperature and so the intersection point (where unloading initiates) relocates. Taking the compression spring in plateau stage as an example, Figure 6 shows the equilibrium stages when temperature changes on this spring.

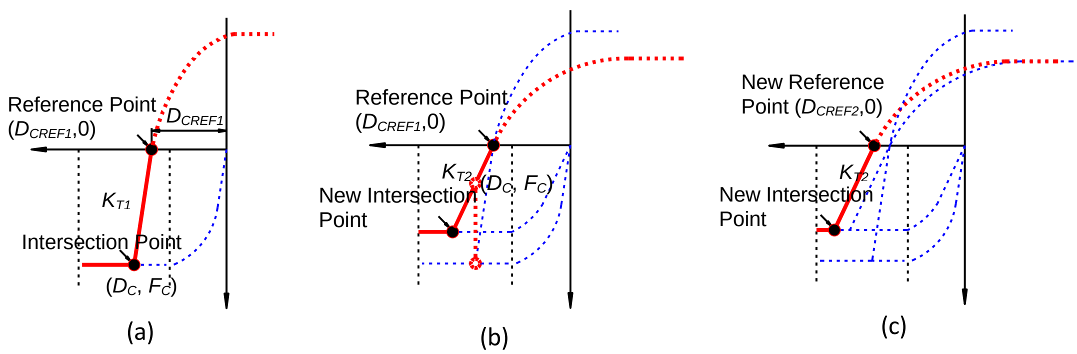

Figure 6. The loading-unloading-reloading loops at different temperatures: (a) at temperature step T_1 (b) during the transition from T_1 to T_2 (c) at temperature step T_2 ($T_2 > T_1$).

The initial stage of the compression spring at temperature T_1 is shown in Figure 6(a). The spring deformation at the reference point can be calculated using,

$$D_{CREF} = D_C - F_C / K_{T1} \tag{1}$$

When temperature elevates to T_2, the reference point remains unmoved, while the new intersection point can be found using the new initial elastic stiffness K_{T2} at T_2. The deflection at the new intersection point is,

$$D_{INTER} = D_{CREF} + F_{r2} / K_{T2} \tag{2}$$

When the spring is further loaded at the same temperature (e.g. T_2), the intersection point will be renewed as the spring displacement increase and the reference point will also be renewed accordingly, as shown in Figure 6(c).

2. RESULTS

2.1 Verification of the *ABAQUS* Model

In order to verify the proposed *Vulcan* buckling element, an example beam was modelled using both *Vulcan* and *ABAQUS*. Vulcan's beam element is actually a wire element and the beam ends are simulated by the new buckling elements. In order to allow comparison, the *ABAQUS* model also consists of three parts: two beam ends modelled by shell elements and the rest of the beam simulated using wire elements, as shown in Figure **7**(a). In order to examine the sensitivity of the modelling results to the element types adopted, another *ABAQUS* model (Figure **7**(b)) with only wire element was built. The two *ABAQUS* models (one using shell elements to model the beam ends and using wire elements to model the rest of the beam; one modelling the entire beam with wire elements) are expected to lead to identical modelling results. The beam section is UB356x171x51 and it is 3 m long. It is short enough to avoid bottom-flange buckling; it is of full axial and out-of-plane restraints, therefore, no beam-web shear buckling is allowed. The beam is loaded with uniformly distributed load 40N/mm, and heated by the ISO834 Standard Fire [7] up to 700°C. The two *ABAQUS* models result in exactly the same deflection and axial force, as expected (Figure **7**(c)).

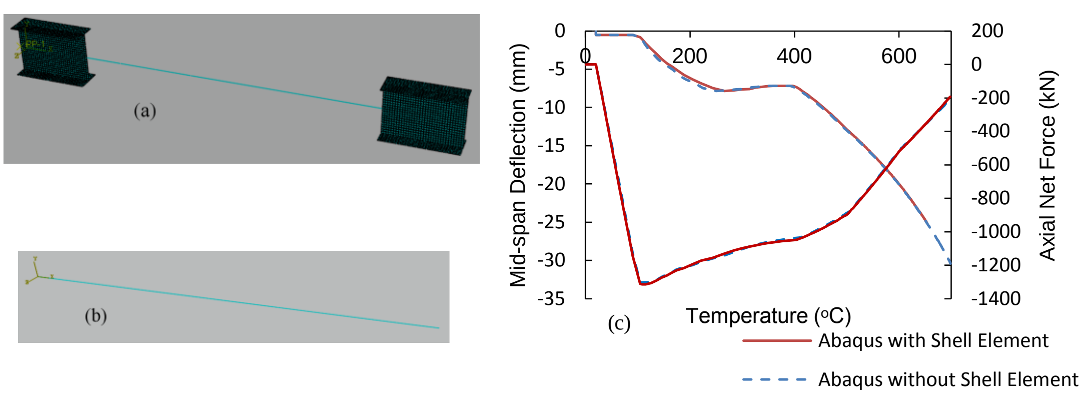

Figure 7. Comparison of *ABAQUS* models: (a) *ABAQUS* image of the 3m beam with shell elements; (b) *ABAQUS* image of the 3m beam with beam elements only; (c) Comparison of the *ABAQUS* results.

2.2 *Vulcan* vs. *ABAQUS*

In order to verify the component-based buckling element, an isolated beam with buckling elements at its ends and wire elements representing the rest of the beam modelled, as shown in Figure 8. The beam section is UB356x171x51. The beam is with full axial and out-of-plane restraints. The beam was initially loaded with uniformly distributed load 40N/mm, and subsequently heated by the ISO834 Standard Fire up to 700°C. The material properties of the steel given in EC3 [5] were adopted.

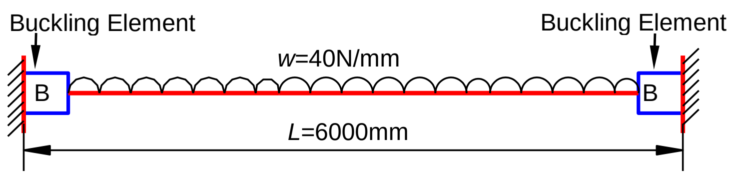

Figure 8. Isolated beam with buckling elements.

Figure 9 plots the development of the mid-span vertical deflection with temperature, given by the *ABAQUS* and *Vulcan* models with and without the beam-end shell or buckling elements. It can been seen that, the deflections of the *ABAQUS* and *Vulcan* models with only beam elements compare well; the discrepancy between the two software is because they use different types of wire elements with different shape functions. The *ABAQUS* model with shell elements, which allows the consideration of buckling at the beam ends, experienced a larger mid-span deflection due to beam-end shear buckling and bottom-flange buckling; the *Vulcan* model with the buckling elements is also able to capture the buckling characteristics, and is able to account for the additional deflection caused by beam-end buckling. Figure 9 shows that the deflections of these two models agree with each other. The *Vulcan* model with the buckling elements failed at around 590°C when both the top and bottom flanges yield without stress hardening, whereas the other three models failed at higher temperatures, because the former uses only two springs to represent the whole beam section which could lead to a slightly early failure compared to the other three models with continuous cross-section at the beam ends.

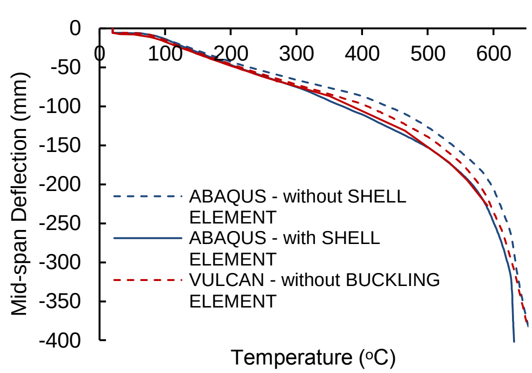

Figure 9. Temperature-Mid-span Deflection Relationship.

CONCLUSION

In this paper, the development of a component-based buckling element, including beam-web shear buckling and bottom-flange buckling has been developed, based on a proposed analytical model. The bottom-flange buckling phenomenon is simulated using two top springs and two bottom springs; each spring is able to deal with loading-unloading-reloading cycles. The beam-web shear buckling phenomenon is considered by modifying the shear modulus of the existing beam element of *Vulcan*. This proposed buckling element has been verified against *ABAQUS* models. A good agreement between the *ABAQUS* and *Vulcan* modelling results indicate that the proposed buckling elements in *Vulcan* are capable of reflecting the influence of the beam-web shear buckling and bottom-flange buckling adjacent to the connections.

REFERENCES

1. Quan G, Huang S-S, Burgess I. 2016. "Component-based model of buckling panels of steel beams at elevated temperatures." *Journal of Constructional Steel Research.*, 118:91-104.
2. Gann RG. 2008. "Final Report on the Collapse of World Trade Center Building 7,Federal Building and Fire Safety Investigation of the World Trade Center Disaster," the National Institute of Standards and Technology (NIST), Gaithersburg, US.
3. Newman G, Robinson JT, Bailey CG. 2001. "Fire safe design: A new approach to multi-storey steel-framed buildings," SCI publication.
4. Huang Z, Burgess IW, Plank RJ. 2003. "Modeling membrane action of concrete slabs in composite buildings in fire. I: Theoretical development." *Journal of Structural Engineering,* 129:1093-102.
5. CEN. 1993. "Eurocode 3: Design of steel structures–Part 1-2: General rules–Structural fire design," European Committee for Standardization, Brussels.
6. Jayakumar P. 1987. "Modeling and identification in structural dynamics," California Institute of Technology.
7. British Standards Institution BS476. 1987. "Fire Tests on Building Materials and Structures, Part 20: Method for Determination of the Fire Resistance of Elements of Construction," London.

Lateral-torsional Buckling of Beams with Corrugated Webs Subjected to Fire

GONCALO CORREIA LOPES, CARLOS COUTO,
PAULO VILA REAL and NUNO LOPES

ABSTRACT

The use of beams with corrugated webs (WCB) has been increasing considerably during the last years due to the high load-carrying capacity in relation to the material usage. The major asset of this structural solution lies in taking advantage of the increase of rigidity provided by the web corrugation leading to better resistance against local buckling and improved shear capacity resulting in higher load bearing capacity combined with significant weight reduction when compared with beams with flat webs.

Despite known benefits of WCB, their behaviour, especially in fire situation, still lacks simplified formulae to enable the designers to exploit better this structural system. Focusing on this aspect, this study aims to develop simplified methods to predict the load bearing capacity, based on numerical simulations with the finite element method, overcoming the limitations encountered in adapting existing design methods of Eurocode 3 to the fire situation.

A proposal is developed in this work which presents a new design philosophy for the fire situation closer to the principles of other structural systems while, at the same time, deliver more accurate solutions for the engineers in practice to use.

1. INTRODUCTION

The advantages in terms of material efficiency and economy are known for I-shaped thin-walled steel beams with flat web. Nevertheless, an alternative that proves to be able to leverage such benefits emerges by replacing the flat web panel by a corrugated one with trapezoidal or sinusoidal shape, with a reduced thickness (in the range of 2-5 mm), in the so-called web corrugated beams (WCB). This solution is particularly appalling for members subjected to in-plane bending moments as the increase of rigidity on the web, due to the corrugation, prevents the local buckling allowing the reduction of thickness without affecting the bending resistance provided by the flanges. On the other hand, WCB have better shear capacity in comparison to the flat-web beams and thus improved load-bearing capacity when subjected to non-uniform bending diagrams.

According to Eurocode 3 (EC3) [1, 2], the load-bearing capacity of WCB can be determined according to the informative Annex D from Part 1-5 [2]. However, the verification of the fire resistance of these elements lacks simplified formulas upholding the benefit provided by this type of solution and no further guidance is given for the use of the Annex D at elevated temperatures. It is unclear if using the reduction factors for the mechanical properties of steel given in Part 1-2 [3] is sufficient to guarantee safety in such conditions and research on this subject is scarce [4, 5].

On the other hand, owing to the high width-to-thickness ratio of the corrugated web, the typical cross-section of these beams is slender and is classified as Class 4 according to EC3 procedure. In terms of the design of slender cross-sections, local buckling prevents the attainment of the yield stress and therefore it needs to be taken into account when calculating the cross-sectional resistance wherein previous investigations [6, 7] have demonstrated that the current procedures underestimate the capacity of slender cross-sections at elevated temperatures.

In this work, a parametric investigation is made to check the accuracy of the design rules of the EC3 adapted to the fire situation of several Class 4 laterally unrestrained beams with corrugated webs subjected to end-moments. Approximately 500 numerical simulations were performed using the finite element software SAFIR [8] to carry out geometrically and materially nonlinear analysis with imperfections (GMNIA) and linear buckling analysis (LBA) in the software Cast3M [9] to obtain the elastic critical moment of the corrugated web beams.

The comparison of the adapted EC3 simple design methods to fire situation demonstrated to be over-conservative thus an improved methodology was developed and it is presented in this study with better correlation with finite element method results.

2. DESIGN PROVISIONS FOR WEB CORRUGATED BEAMS

The informative Annex D of EN1993-1-5 gives design recommendations to check the ultimate limit state of WCB. More particularly, the bending resistance is determined using Eq. (D.1). Accordingly, the bending resistance is obtained by the minimum of the 1) compressed or 2) tensioned flange plastic bending resistance and 3) the out-of-plane buckling resistance of the compressed flange. For the sake of simplicity, these phenomena are treated hereafter as the cross-sectional resistance (1 and 2) and the lateral-torsional buckling (LTB) resistance (3) and equations (1a) and (2a) give, in the traditional notation of the EC3, the bending resistance of WCB adapted to the fire situation. One can notice the use of the reduction factors for the 0.2% steel proof strength in Eq. (1a) because the typical cross-sections of WCB are classified as Class 4. This is in accordance with the rules of the Annex E of EN 1993-1-2, where for members with Class 4 cross-sections it is recommended that the reduced cross-section should be calculated with the effective width method using the steel properties at normal temperature and considering the design value for the steel yield strength as the 0.2% proof strength ($f_{0.2p,\theta} = k_{0.2p,\theta} f_y$). This consideration leads to over conservative results as shown later in Figure 2 a). However, as previously mentioned, Eq. (D.1) from EN1993-1-5 considers the plastic moment of the flanges and therefore the WCB cross-sections are treated as Class 1 or 2, but, if the design value for the steel yield strength correspondent to the stress at 2% total strain had been considered, the results would have been on the unsafe side. In fact, due to the corrugation formats of the webs, the observation of the failure mode of WCB restrained laterally shows that local buckling occurs preferably in the compressed flange, reducing the cross-sectional resistance and preventing the cross-section from reaching its plastic capacity (see Figure 4).

A new proposal is presented in this study, based on a proposal to calculate the resistance of slender cross-section[6, 7] given in Eq. (1b), and on another to calculate the reduction factor for LTB but accounting with the interaction between local and lateral-torsional buckling of beams with slender cross-sections [10], see Eq. (2b). In this work, this methodology is denoted as "New proposal". In Table I, the calculation sequence is given for both methodologies.

TABLE I. CALCULATION SEQUENCE ACCORDING TO BOTH METHODOLOGIES.

Eurocode 3's current methodology for Class 4 cross-sections (EN 1993-1-2 + Annex D of EN 1993-1-5)	**"New proposal" for Class 3 and 4 cross-sections [7, 10]**
Cross-sectional resistance	
	$\bar{\lambda}_p^{new} = \dfrac{c_f/t_f}{28.4\varepsilon\sqrt{k_\sigma}}$
	$\rho_f^{new} = \dfrac{\left(\bar{\lambda}_p^{new} + 1.1 - \frac{0.52}{\varepsilon}\right)^{1.2} - 0.188}{\left(\bar{\lambda}_p^{new} + 1.1 - \frac{0.52}{\varepsilon}\right)^{2.4}} \leq 1$
	$b_{f,eff}^{new} = \left[2\left(\rho_f^{new} c\right) + \left(b_f - 2c\right)\right]$
$A_f = b_f t_f$	$I_{f,eff}^{new} = \dfrac{b_{f,eff}^{new} {t_f}^3}{12} + b_{f,eff}^{new} t_f \times \left(h - z_{CG,eff} - \frac{t_f}{2}\right)^2 + \dfrac{b_f {t_f}^3}{12} + b_f t_f \times \left(z_{CG,eff} - \frac{t_f}{2}\right)^2$
$W_{f,y} = A_f\left(h_w + t_f\right)$	$W_{f,eff,y}^{new} = I_{f,eff}^{new}/z_{CG,eff}$
$M_{fi,\theta,Rd} = W_{f,y} k_{0.2p,\theta} f_y$ (1a)	$M_{fi,\theta,Rd}^{new} = W_{f,eff,y}^{new} k_{y,\theta} f_y$ (1b)
Lateral-torsional buckling (LTB) resistance	
$\bar{\lambda}_{LT,\theta} = \sqrt{\dfrac{M_{fi,\theta,Rd}}{M_{cr}}}\sqrt{\dfrac{k_{0.2p,\theta}}{k_{E,\theta}}}$	$\bar{\lambda}_{LT,\theta}^{new} = \sqrt{\dfrac{M_{fi,\theta,Rd}^{new}}{M_{cr}}}\sqrt{\dfrac{k_{y,\theta}}{k_{E,\theta}}}$
$\alpha = 0.65\varepsilon_\theta$ with $\varepsilon_\theta = 0.85\varepsilon$	$\alpha_{LT}^{new} = \left\{\underbrace{1.25\varepsilon}_{\substack{s>0.9 \\ L1}};\ \underbrace{1.00\varepsilon}_{\substack{0.8<s\leq 0.9 \\ L2}};\ \underbrace{0.75\varepsilon}_{\substack{s\leq 0.8 \\ L3}}\right\}$
$\Phi_{LT,\theta} = \dfrac{1}{2}\left[1 + \alpha\left(\bar{\lambda}_{LT,\theta}\right) + {\bar{\lambda}_{LT,\theta}}^2\right]$	$\Phi_{LT,\theta}^{new} = \dfrac{1}{2}\left[1 + \alpha_{LT}^{new}\left(\bar{\lambda}_{LT,\theta} - 0.2\right) + {\bar{\lambda}_{LT,\theta}}^2\right]$
$\chi_{LT,fi} = \dfrac{1}{\Phi_{LT,\theta} + \sqrt{{\Phi_{LT,\theta}}^2 - {\bar{\lambda}_{LT,\theta}}^2}} \leq 1$	$\chi_{LT,fi}^{new} = \dfrac{1}{\Phi_{LT,\theta}^{new} + \sqrt{{\Phi_{LT,\theta}^{new}}^2 - {\bar{\lambda}_{LT,\theta}^{new}}^2}} \leq 1$
	$\chi_{LT,fi,mod}^{new} = \dfrac{\chi_{LT,fi}^{new}}{f}$
$M_{b,fi,\theta,Rd} = \chi_{LT,fi} M_{fi,\theta,Rd}$ (2a)	$M_{b,fi,\theta,Rd}^{new} = \chi_{LT,fi,mod}^{new} M_{fi,\theta,Rd}^{new}$ (2b)

$\varepsilon = \sqrt{235/f_y}$	$s = \dfrac{W_{f,eff,y}^{new}}{W_{el,y}}$	$f = 0.8 + 0.15\psi + 0.075\psi^2$ $-1 \leq \psi \leq 1$ and $0.8 \leq f \leq 1$

Additionally, as the local plate buckling has a significant role in the case of larger corrugations, namely for the case of trapezoidally corrugated webs, in this study the distance c_f was taken as $b_f/2 + a_3/2$ for beams with the trapezoidal corrugation (see geometry notations in Table II), instead of $b_f/2 - t_w/2$ as for other cases.

3. NUMERICAL MODEL

Geometric and material non-linear analysis of shell element models representing the beams in bending were conducted with the software SAFIR [8]. The members were discretized into several quadrangular shell finite elements with four nodes, each with six degrees of freedom (3 translations and 3 rotations). For the mesh, 10 divisions on the flange, 20 divisions on the web and a variable number of divisions along the length, depending on the web format (16 elements per each trapezoidal corrugation or 8 elements per each sinusoidal corrugation), were considered. The ultimate resistance at elevated temperatures was determined using a transient dynamic analysis, i.e., by first increasing the temperature to the desired value and then applying an increasing load until the collapse occurs. The temperature was considered uniform along the cross-section so that a comparison between the numerical results and the simple design equations could be possible. As for the boundary conditions, the so-called fork supports were considered, and additional restraints to the out-of-plane displacements were imposed at flanges to obtain the cross-sectional resistance, see Figure 1 a).

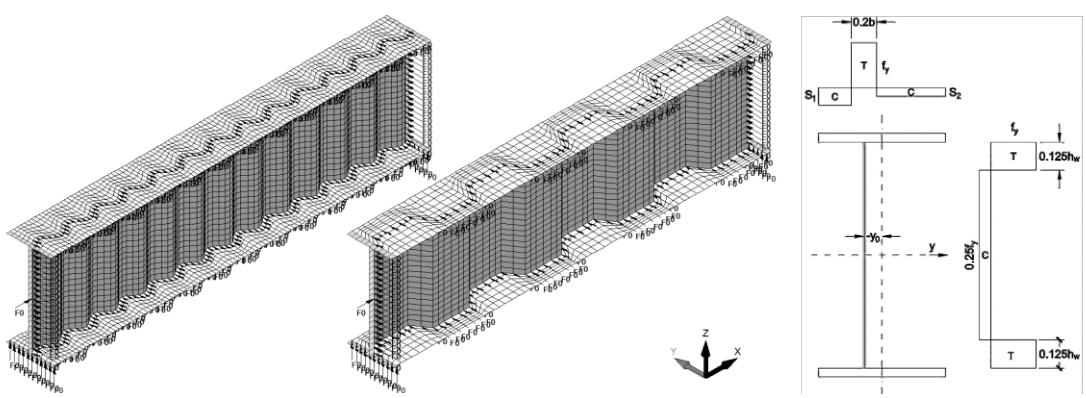

a) boundary conditions of the laterally restrained finite element models with sinusoidal and trapezoidal corrugations

b) distribution of residual stresses adopted in this work

Figure 1. Numerical models.

Geometrical imperfections were introduced in the models by changing the node coordinates affine to the eigenmodes and the amplitudes were scaled to the geometric fabrication tolerances defined in EN 1090-2 [11] in accordance to the recommendations of Part 1-5 of Eurocode 3 [2]. A global imperfection of 80% of L/750, being L the beam length was used, and a local imperfection of 80% of b_f/100 and 80% of $h_w/100$, being b_f the flange width and h_w the web height was considered depending on the most displaced node in the respective local eigenmode.

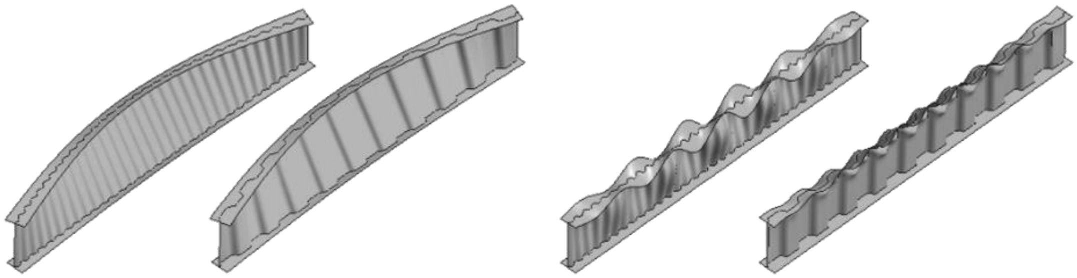

Figure 2. Global and local eigenmodes of WCB.

The residual stress distribution taken in this study is based on the typical distribution of residual stresses used for flat web welded I-beams. Additionally, due to the corrugation of the web, the compressive residual stresses at the flanges were scaled to
$S = b_f f_y/(4b_f \pm 10y_0)$, where y_0 denotes the deviation of the web panel from the beam's centerline on the *y* axis (see Figure 1 b)).

4. RESULTS AND COMPARISON TO SIMPLE DESIGN METHODS

Herein, the results obtained for both cross-sectional and LTB resistance of the beams in bending about the major-axis are shown.

Both laterally restrained and unrestrained cases were considered and a parametric study was carried out at elevated temperatures (400ºC, 500ºC and 600ºC) for beams with three cross-sections and two different web corrugations subjected to uniform ($\psi = 1$) and non-uniform bending moment diagrams ($\psi = 0$ and $\psi = -1$), with spans ranging from 2 m to 17.5 m. Moreover, to access the cross sectional resistance of beams with trapezoidally corrugated webs, seven additional cross-sections were considered (cases marked with * in Table II). The Table II summarizes the different cases that were analysed.

TABLE II. CASES CONSIDERED IN THE NUMERICAL STUDY.

<table>
<tr><th>Case No.</th><th>Cross-section ($h_w \times t_w + b_f \times t_f$)</th><th>Class** web - flange</th><th>Steel grade (MPa)</th><th>Web geometry (mm)</th></tr>
<tr><td>1</td><td>1000×3+280×20</td><td>4 - 1</td><td>S275</td><td rowspan="9">Sinusoidal corrugation
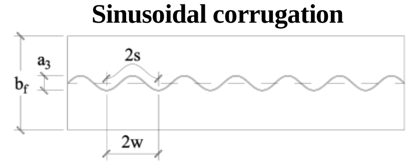

$2w = 155, a_3 = 43, 2s = 181.19$
Trapezoidal corrugation</td></tr>
<tr><td>2</td><td>500×3+240×15</td><td>4 - 3</td><td>S355</td></tr>
<tr><td>3</td><td>750×3+260×20</td><td>4 - 1</td><td>S355</td></tr>
<tr><td>4*</td><td>500×3+200×17</td><td>4 - 1</td><td>S355</td></tr>
<tr><td>5*</td><td>500×3+260×15</td><td>4 - 3</td><td>S355</td></tr>
<tr><td>6*</td><td>500×3+260×17</td><td>4 - 2</td><td>S355</td></tr>
<tr><td>7*</td><td>500×3+260×20</td><td>4 - 1</td><td>S355</td></tr>
<tr><td>8*</td><td>500×3+300×17</td><td>4 - 3</td><td>S355</td></tr>
<tr><td>9*</td><td>500×3+300×20</td><td>4 - 2</td><td>S355</td></tr>
</table>

10*	500×3+300×25	4 - 1	S355	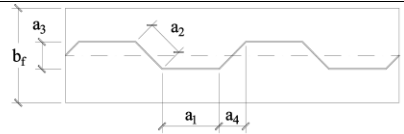 $a_1 = 170, a_2 = 113.14, a_3 = 80, a_4 = 80$
*** To determine the section classes the distance c_f was considered as for flat web beams*				

In Figure 3, the numerical results of the cross-sectional resistance $M_{fi,\theta,Rd}$ obtained with SAFIR for laterally restrained cases are compared with Eurocode 3's simplified design method, using Eq. (1a) in Figure 3 a), and with the methodology proposed in this work, using Eq. (1b) in Figure 3 b).

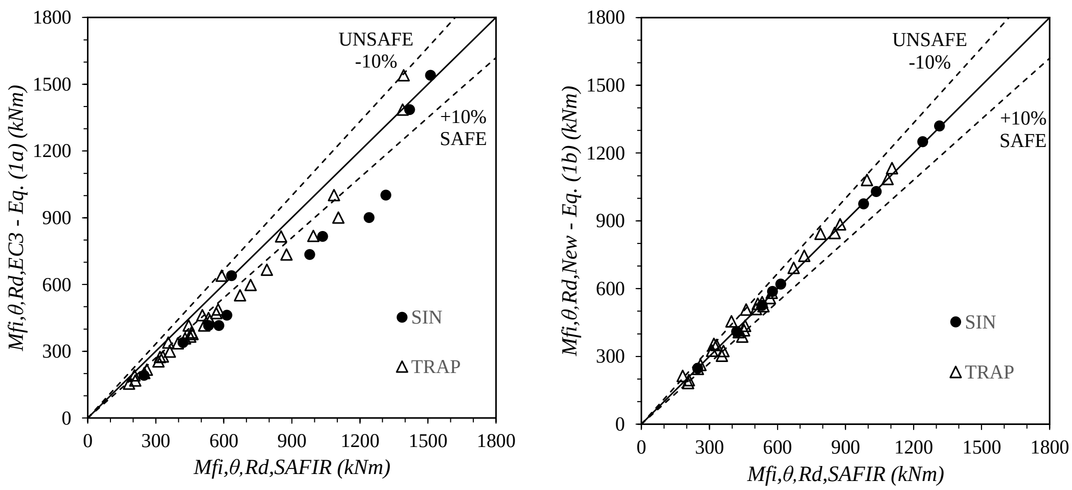

a) Eurocode 3 b) Proposed methodology

Figure 3. Comparison between the cross-sectional resistance obtained with FEA and with Eurocode 3's current methodology and the one proposed in this work.

For the analyzed cases, the Eurocode's current simple design method is too conservative to estimate the cross-sectional resistance. Particularly, if the cross-section is composed by Class 1 or 2 flanges, there is an additional load-carrying capacity provided by those flanges that is taken into account (see § 2). The New Proposal shows better agreement with the results from FEA proving that it is an accurate methodology to estimate the cross-sectional resistance, since a better agreement to the FEA numerical investigation is obtained. In Figure 3, the deformed shape at collapse is shown for two laterally restrained WCB.

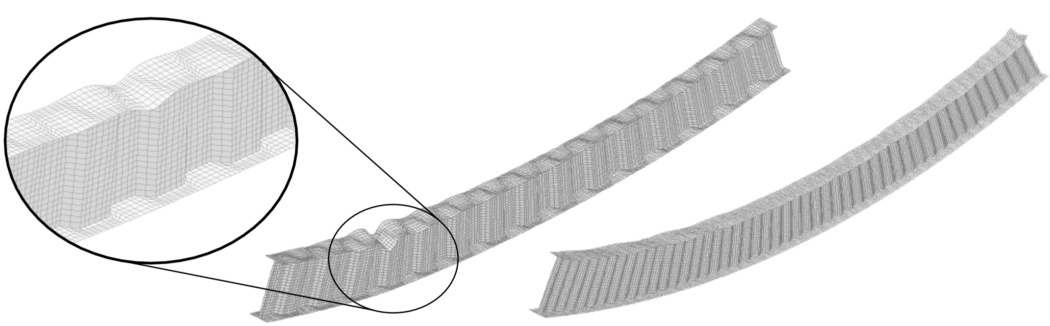

Figure 4. Deformed shape at collapse of two laterally restrained WCB (scale factor = 5).

In Figure 5 the results of the beam's ultimate capacity (i.e., LTB resistance), obtained with SAFIR ($M_{b,SAFIR}$), are shown for one cross-section (case no. 2), considering both corrugation formats at 500°C for three different loading cases. These numerical results are compared to both Eurocode 3's simplified design method using Eq. (2a) – $M_{b,EC3}$ – and with the methodology proposed in this work using Eq. (2b) – $M_{b,New}$ – for each corrugation format.

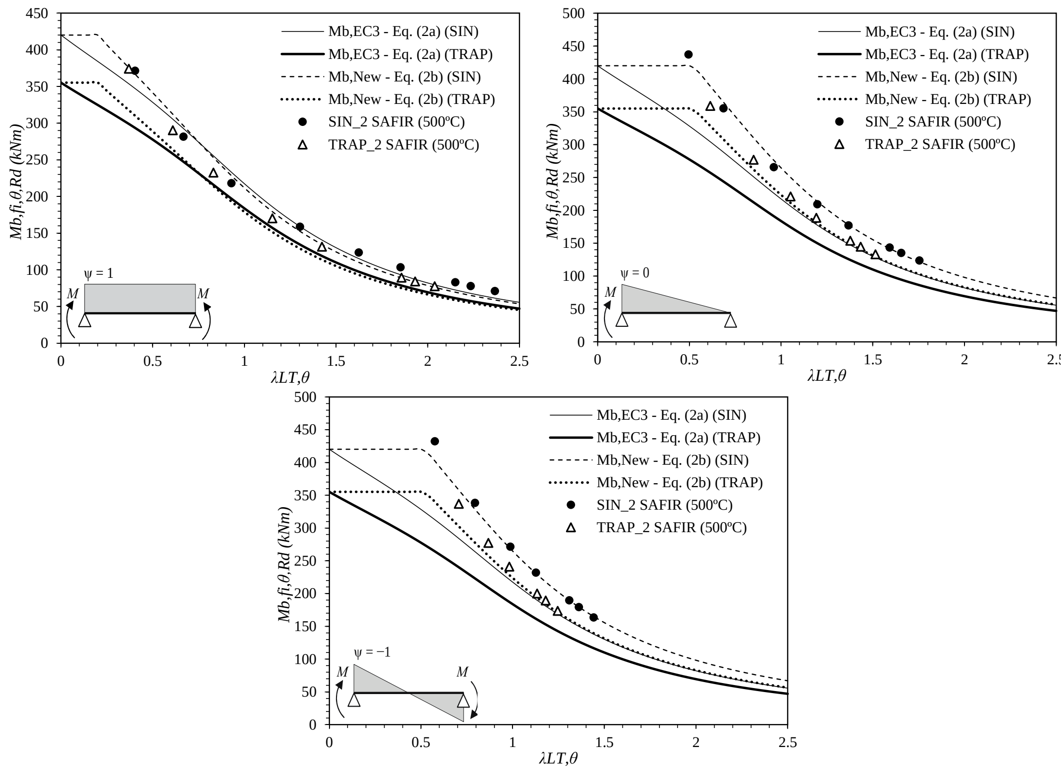

Figure 5. a) Comparison between the numerical results (SAFIR) and the design curves of Eurocode 3 (EC3) and the ones proposed in this work (New) for beams heated at 500°C subjected to different loading conditions.

Although for the cases of uniform moment diagrams the differences to the Eurocode 3 methodology are not much, when in presence of shear loads (i.e., for non-uniform bending diagrams), it is observed that using the New Proposal (with the factor *"f"*), leads to considerable improvements to predict the ultimate capacity of WCB against LTB in case of fire.

In Figure 6, the numerical results of the reduction factor for LTB obtained with SAFIR (χ_{SAFIR}) for laterally restrained cases are compared with Eurocode 3's current methodology, $\chi_{LT,fi}$ (depicted by χ_{EC3}), and with the methodology proposed in this work, $\chi_{LT,fi,mod}^{new}$ (depicted by χ_{New}/f). From that figure, it can be seen that the New Proposal shows a better agreement with the results from the FEA demonstrating that it is an accurate methodology to estimate the LTB resistance of WCB.

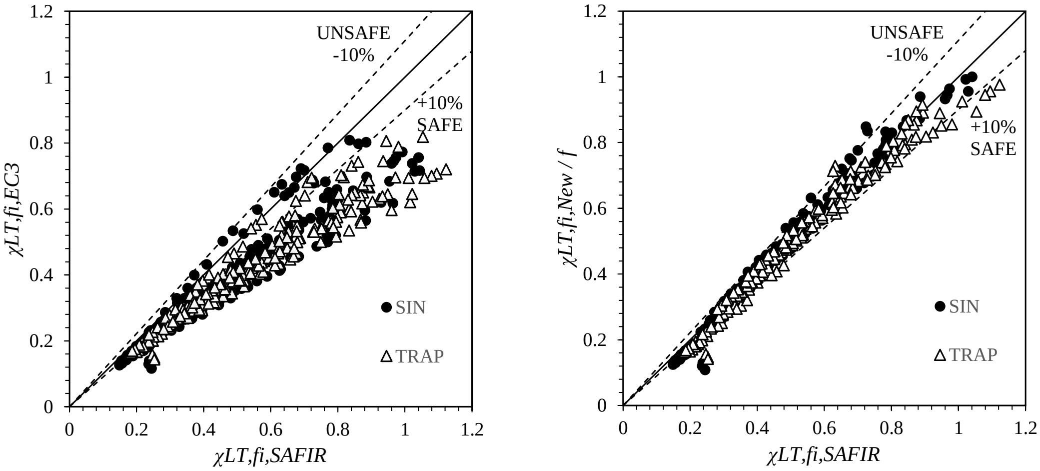

a) Eurocode 3 b) Proposed methodology

Figure 6. Comparison between the LTB resistance obtained with FEA and with both Eurocode 3's current methodology and the one proposed in this work.

5. CONCLUSIONS

It was demonstrated in this study that the current methodology of EC3 to check the ultimate capacity of web corrugated beams subjected to end-moments can be adapted to fire situation. Nonetheless, results are mainly over-conservative.

An improved methodology for the cross-sectional and the LTB resistance was developed and presented in this paper and it was concluded that improved accuracy was obtained when comparing to finite element analysis results.

6. REFERENCES

1. CEN, "EN 1993-1-1, Eurocode 3: Design of steel structures - Part 1-1: General rules and rules for buildings." European Committee for Standardisation, Brussels, 2005.
2. CEN, "EN 1993-1-5, Eurocode 3 - Design of steel structures - Part 1-5: Plated structural elements." European Committee for Standardisation, Brussels, pp. 1–53, 2006.
3. CEN, "EN 1993-1-2, Eurocode 3: Design of steel structures - Part 1-2: General rules - Structural fire design." European Committee for Standardisation, Brussels, 2005.
4. Elamary A. S., "Nonlinear behavior analysis of steel beams with flat or corrugated webs at elevated temperatures," Eng. Sci., vol. 36, no. 3, pp. 657–673, 2008.
5. Vácha J., P. Kyzlík, I. Both, F. Wald, "Beams with corrugated web at elevated temperature, experimental results," Thin-Walled Struct., 2015.
6. Couto C., P. Vila Real, N. Lopes, B. Zhao, "Effective width method to account for the local buckling of steel thin plates at elevated temperatures," Thin-Walled Struct., vol. 84, pp. 134–149, Nov. 2014.
7. Couto C., P. Vila Real, N. Lopes, B. Zhao, "A new design method to take into account the local buckling of steel cross-sections at elevated temperatures," in 8th International Conference on Structures In Fire, 2014.
8. Franssen J.-M., "SAFIR, A Thermal/Structural Program Modelling Structures under Fire," Eng. Journal, A.I.S.C., vol. 42, no. 3, pp. 143–158, 2005.
9. CEA, "CAST 3M is a research FEM environment; its development is sponsored by the French Atomic Energy Commission <http://www-cast3m.cea.fr/>.," 2012.
10. Couto C., P. Vila Real, N. Lopes, B. Zhao, "Numerical investigation of the lateral-torsional buckling of beams with slender cross sections for the case of fire," Eng. Struct., vol. 106, pp. 410–421, 2015.
11. CEN, "EN 1090-2: Execution of steel structures and aluminium structures - Part 2 : Technical requirements for steel structures." European Committee for Standardisation, Brussels, Belgium, 2008.

Fire-induced Progressive Collapse of 3D Steel Frames with Concrete Floors

JIAN JIANG and GUO-QIANG LI

ABSTRACT

This paper investigates the behavior of three-dimensional steel frames with reinforced concrete slabs exposed to localized fire against progressive collapse. The prototype of the model is based on the eight-story building in Cardington tests. The scenario of heating an individual column on the ground floor is adopted. The collapse modes and load redistribution scheme of the frame subjected to different load ratios of columns and fire locations are investigated. The results show that the frame does not collapse in the case of single column heated for a fire design load (load ratio of 0.25), due to the load redistribution to adjacent columns through floors. By increasing the load ratio to 0.5 as for the ambient design, progressive collapse occurs. The collapse modes are dominated by the uneven load redistribution in the two horizontal directions, which cannot be simulated by a 2D model. The loads previously sustained by the buckled heated column are transferred more along the short span than the long span, leading to the advanced buckling of columns along the short span. The critical temperature of a column in a frame is significantly lower (about $200^{o}C$) than that given in EC3, due to the fact that the translational and rotational restraints increase its load ratio and reduce its effective length, respectively.

INTRODUCTION

Since the Broadgate Phase 8 fire in London and the subsequent Cardington fire tests [1] in the 1990s, researchers have begun to investigate and understand the behavior of whole steel-framed structures in fire. It is confirmed that composite floors played a key role in the survival of the frame, through tensile membrane action [2-6]. Especially since the collapse of the Word Trade Tower (WTC) under terrorist attack on September 11, 2001, there has been considerable interest in understanding the progressive collapse of tall buildings in fire, defined as "the spread of an initial local failure from element to element, eventually resulting in the collapse of an entire structure or a disproportionately large part of it" [7].

Most of previous studies focus on two-dimensional planar frames. Although capable of capturing some key issues of the fire-induced collapse mechanisms of

Jian Jiang, College of Civil Engineering, Tongji University, Shanghai 200092, China
Guo-Qiang Li, State Key Laboratory for Disaster Reduction in Civil Engineering, Tongji University, Shanghai 200092, China

structures, they fail to fully consider the load redistribution path in a realistic structure, and especially the tensile membrane action of concrete floors. More recently, there are some research on the three-dimensional steel framed structures [8-10]. However, the conclusions were questionable provided that either all the columns on one floor were heated or the fire occurred on the upper floors (not the severest fire scenario). Therefore, there remains a lack of insight understanding of progressive collapse mechanisms of three-dimensional structures under fire, in which load redistribution path and tensile membrane action of floors can be reasonably considered.

This paper presents numerical analyses of progressive collapse of three-dimensional multi-story steel frames exposed to fire. The modelling of steel columns was first validated against experimental data. An individual column on the ground floor at various locations was heated. The collapse modes and load redistribution scheme of the frames subjected to these fire scenarios are investigated.

NUMERICAL MODEL AND VALIDATION

An explicit dynamic analysis was carried out in LS-DYNA in this study. The three-dimensional Hughes Liu beam element was used to model the steel columns and beams. This element had an integrated cross-section and the command *INTEGRATION_BEAM was used to define an I-shape section. The MAT_24 and MAT_172 were used for beam/column at ambient and elevated temperature, respectively. The flat reinforced concrete slab was modelled instead of composite slabs with profiled decking. This is to consider the effect of concrete floors but prevent the difficulties in using shell element to simulate the ribbed composite slab. The slab was modelled by a layered composite shell formulation (Figure 1), in which a distinct structural material, thermal material, and thickness can be specified for each layer (*PART_COMPOSITE). The primary beam shared the same nodes with the slab and the offset of their reference axis was used for its composite action with the top slab.

The material MAT_172 (MAT_CONCRETE_EC2) was used to model the reinforced concrete slab. This material can be directly used to model plain concrete (FRACR=0), pure steel (FRACR=1), or reinforced concrete with evenly distributed reinforcement (0<FRACR<1). Therefore, separated material IDs (same type of MAT_172) should be assigned for reinforcement (FRACR=1) and concrete (FRACR=1). Each integration point may then be defined as either concrete or steel as appropriate. The stress-strain curves in this material for concrete and reinforcement at ambient and elevated temperature are as specified in EC2 [11]. They will be scaled to the user-defined compressive and tensile strength of concrete, and yield strength of reinforcement. Thermal expansion coefficients as functions of temperature are by default taken from EC2. The advantage of this material is that it only requires the user to input the key mechanical properties of concrete and steel at ambient temperature and their variation with temperature is taken by default from EC2. This simplifies the material definition process and more importantly, avoids mistake resulting from mistyping and lack of knowledge.

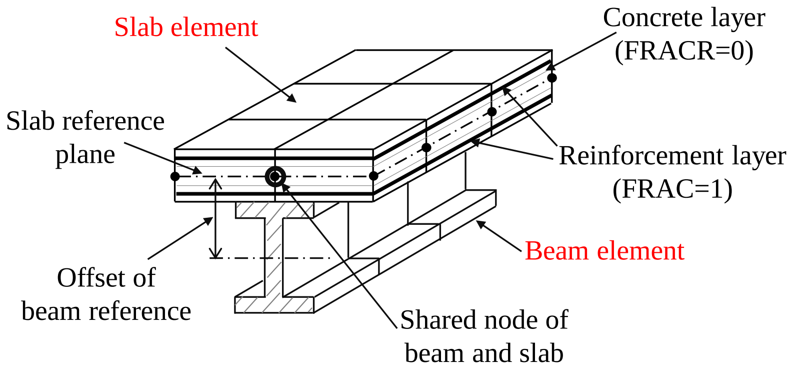

Figure 1. Numerical model of composite slab in LS-DYNA.

The proposed model was validated against a fire test of restrained steel column (denoted as Test02 as shown in Figure 2) by Li et al. [12]. One end of the 3m column was connected to the mid-span of the 3m beam with the other end fixed. The column was heated following the ISO 834 standard fire curve and the beam was kept at ambient temperature to provide constant translational and rotational restraint to the column. An axial load of 100kN was applied to the column at the mid-span of the beam. The fire was stopped once the column temperature reached 800^{o}C (at about 20min). The influence of the mesh size and time scale on the response of the heated column was examined and the results are shown in Figures 3 and 4, respectively. As shown in Figure 3, the mesh size had little effect on the results. The 20-min heating in the test was scaled down to 2s (scale 1min to 0.1s), 4s (1min-0.2s), 10s (1min-0.5s) and 20s (1min-1s) in the explicit dynamic analysis and the results are shown in Figure 4. A time scale ratio of 1 min to 0.2s gives reasonable predictions without causing oscillation. This time scale technique, scaling the heating duration from hours to a level of seconds, significantly save the computing cost of the explicit analysis which requires extremely small time steps (normally in 10^{-6}~10^{-5}s) to ensure a stable and accurate prediction.

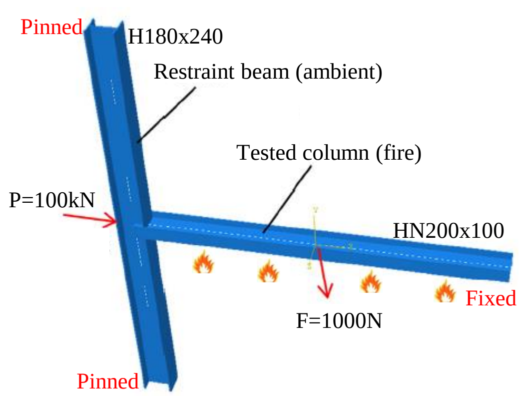

Figure 2. Numerical model of restrained column test at elevated temperature [12].

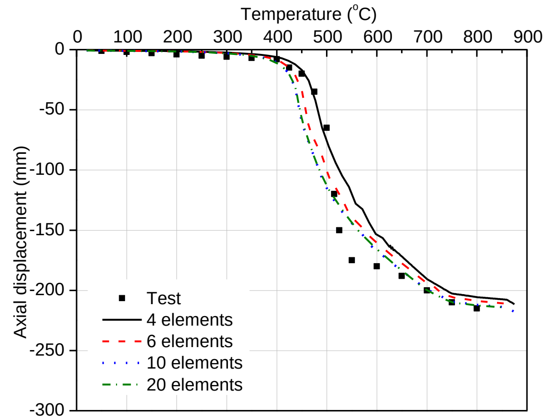

Figure 3. Comparison of column displacements for various mesh sizes.

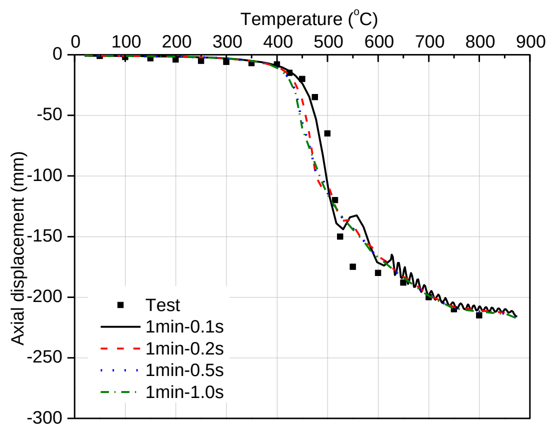

Figure 4. Comparison of column displacements for various time scales.

MODELING OF PROTOTYPE FRAME

A multi-storey moment resisting steel-framed composite frame was modelled in LS-DYNA. The structural layout and member dimensions were based on the prototype building in Cardington tests [1]. The frame had three bays of 6m, five spans of 9m and eight storey of 4m, as shown in Figure 5. All the primary beams and columns were taken as UB 356×171×51 and UC 305×305×198, respectively. No secondary beams were modelled. An initial imperfection of 1mm was imposed on all the columns. The reinforced concrete slab had a thickness of 120mm and reinforcement bars in a diameter of 12mm and spacing of 200mm. The concrete cover of reinforcement bars was 30mm from the bottom of the slab. The Young's modulus and yield strength of steel beams and columns were 200GPa and 355MPa, respectively. The compressive strength of concrete was 35MPa and the yield strength of reinforcements was 500MPa. The properties of the steel material at elevated temperature referred to EC2 [11] and EC3 [13]. A uniformly distributed load q= 6kN/m^2 was imposed on the slab. This applies an axial load of 2.5kN on the internal columns (load ratio of 0.25). The yield strength of reinforcement was 468MPa. In this study rigid connections between beams and columns were assumed, in which their failure and fracture were not considered in the analysis.

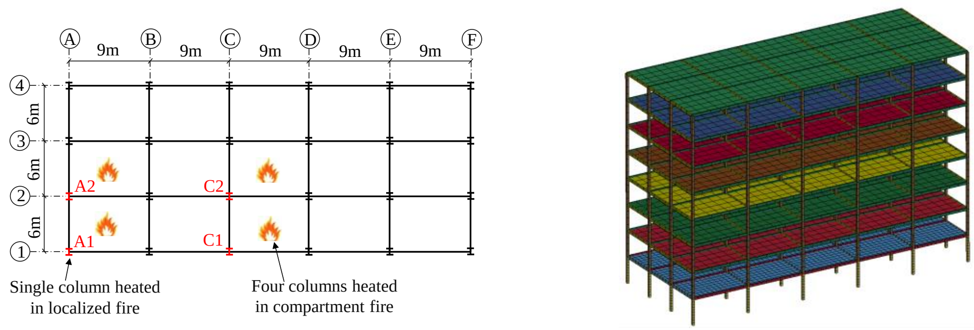

(a) (b)

Figure 5. Model of a multi-story moment resisting frame: (a) plan view; (b) finite element model.

PROGRESSIVE COLLAPSE ANALYSIS OF 3D STEEL FRAME

Effect of location of heated column

According to the design code GSA [14], the columns at the corner, at or near the middle of the short and long side of the building have the highest potential of causing progressive collapse and should be considered in the alternative path method. In this study, these columns as well as the internal column were chosen to be heated. A preliminary study of the frame with only one column heated (Columns A1, A2, C1, C2 as shown in Figure 2a) was first carried out. This applied to a localized fire occurred near a column where the temperature of the beams and floors above the column is assumed low due to the thermal insulation of the ceiling.

There was no collapse for frames subjected to this single column heated scenario. The loads previously sustained by the buckled heated column were redistributed to adjacent columns of which more were transferred along the short span (Figure 6). The internal columns also suffered buckling which was resisted by the perimeter columns. The survival of the frame may be due to its relatively low load ratio of the ground floor columns. In the following section, the uniformly distributed load applied on the floors was increased to a level of ambient temperature design and the resistance of fire-induced progressive collapse of the frame was examined.

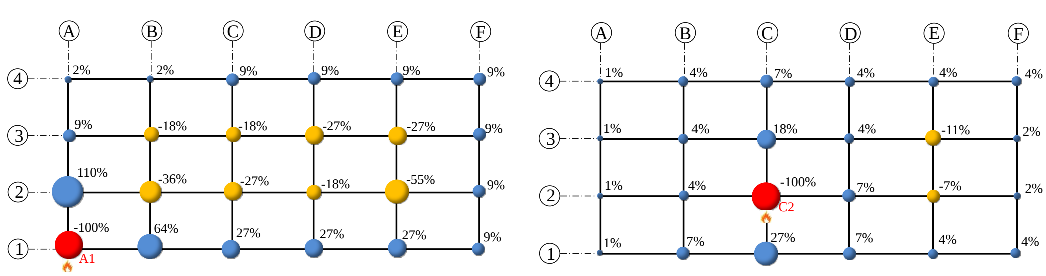

(a) (b)

Figure 6. Load redistribution in ground floor columns after the buckling of heated column: (a) A1; (b) C2.

Effect of load ratios

The uniformly distributed load q=6kN/m^2 on the slab taken in the analysis above was calculated according to the structural fire design using Dead+0.5Live [15]. This led to a load ratio of 0.25 for the internal columns. This seems too small to cause its buckling and subsequent progressive collapse of the whole structure. For an ambient temperature case, the design load is determined by 1.35Dead+1.5Live [16] which always leads to a load ratio of 0.6 for columns. In this section, the uniformly distributed load was increased q=12kN/m^2 for a load ratio of 0.5 in columns. Only the corner column A1 and internal column C2 were heated, respectively.

When the corner column A1 was heated, the buckling of internal columns occurred as early as 300^{o}C, compared to the buckling of the heated column at 470^{o}C. The advanced buckling of columns was definitely due to the increased load ratio of columns which made the columns more sensitive to lateral displacement and disturbance from the thermal expansion of the heated column. The sequence of the failure of columns is shown in Figure 7. The collapse of the structure was triggered by the internal columns E2, E3, B2, B3 located adjacent to the perimeter columns, as shown in Figure 8a. After a further buckling of the internal columns C2, C3, a global downward collapse of the frame occurred (Figure 8b). The perimeter columns along the long span buckled earlier than those along the short span. This was again due to the load redistribution rule that the shorter the span, the more the loads transferred. For a high load ratio, a domino buckling of columns happened the same time as the load redistributed among them.

For the case of heating the internal column C2, the collapse of the frame was triggered by the buckling of the heated column at 320^{o}C, followed by the buckling of other internal columns at about 400^{o}C, almost at the same time, as shown in Figure 9. A similar sequence of buckling of columns to the above corner column heated case formed and the perimeter columns buckled at the same temperature of 470^{o}C. The critical temperatures of internal heated column C2 in a load ratio of 0.25 and 0.5 were 490^{o}C and 325^{o}C, respectively, which were 200^{o}C and 260^{o}C lower than the EC3 results. This is due to the realistic boundary condition of columns in a frame. The translational restraint at the end of the column indirectly increased its compressive force through restrained thermal expansion. The rotational restraint reduced the effective length of columns and thus reduced their buckling resistance. Therefore, the critical temperature of columns should consider the effect the translational and rotational restraint which may increase the load ratio and reduce the effective length, respectively. The load redistribution along the two horizontal directions delays or prevents the collapse of the whole frame. This cannot be simulated by 2D models [17] in which limited alternative loading paths are available and especially unable to model the dependency of load transfer on the path length, i.e. more loads transfer along the short path.

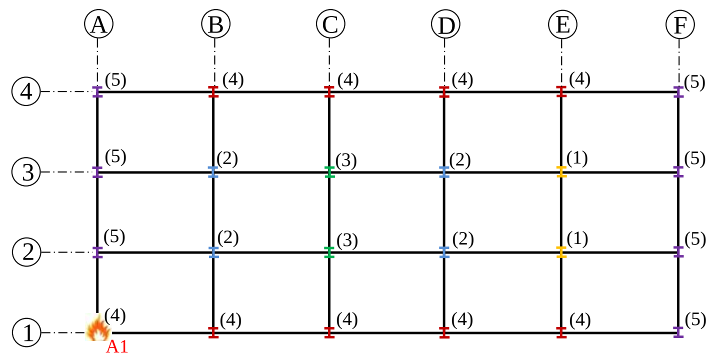

Figure 7. Sequences of buckling of ground floor columns of frames subjected to corner column A1 heated for q=12kN/m^2.

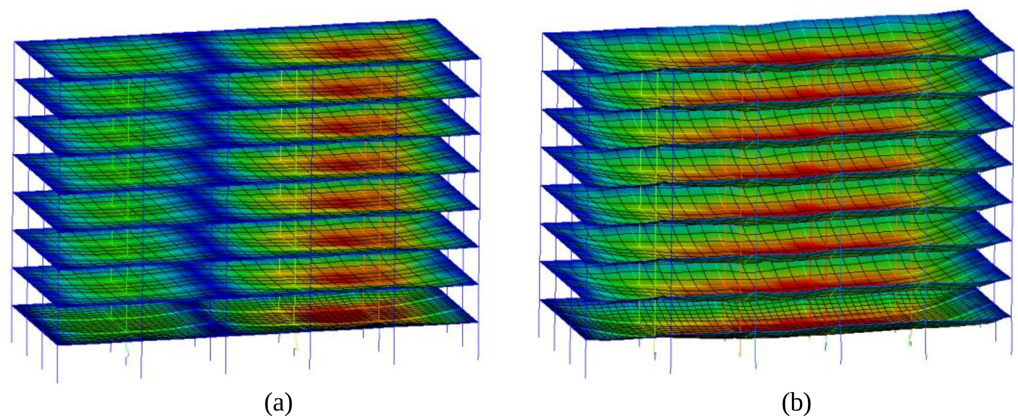

Figure 8. Collapse mode of frames subjected to corner column A1 heated for q=12kN/m^2: (a) local collapse due to buckling of columns B2,B3,E2,E3 at 430^{o}C; (b) global collapse after further buckling of columns C2,C3 at 450^{o}C.

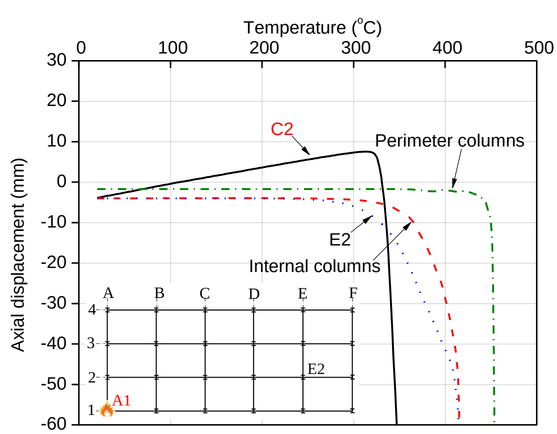

Figure 9. Axial displacements of heated internal column C2 and adjacent columns for q=12kN/m^2.

CONCLUSION

This paper investigated the fire-induced progressive collapse of 3D steel frames subjected to single or four column heated scenarios. An explicit dynamic analysis was performed on a three-bay, five-span and eight-story frame in LS-DYNA. The effect of load ratios and fire locations on the collapse modes and load redistribution scheme were studies. The results show that it is feasible to perform an explicit dynamic analysis for structures in fire by scaling the hour's real fire time to seconds' numerical analysis without causing oscillation. The 3D model shows different collapse modes and load redistribution path from the 2D model. More loads previously sustained by the damaged members were transferred along the short span than the long span. This uneven load transferring plays an important role in the collapse resistance of frames which cannot be considered in a 2D model. The load ratio of columns has significant influence on the collapse resistance of steel frames under fire. A global downward collapse may occur as load ratio increases, no matter the fire locations. The realistic boundary conditions of a column in a frame significantly reduce its critical temperature (more than 200^{o}C). This is due to the fact that the translational and rotational restraint of the column reduce its load ratio and effective length, respectively.

ACKNOWLEDGEMENTS

The work presented in this paper was supported by the National Natural Science Foundation of China with grants 51408418 and 51120185001.

REFERENCES

1. Kirby B. R. 1997. "British steel technical European fire test program design, construction and results. Fire, static and dynamic tests of building structures". Report, London, UK.
2. Bailey C. G., White D. S. and Moore D. B. 2000. "The tensile membrane action of unrestrained composite slabs simulated under fire conditions," *Engineering Structures*, 22: 1583-1595.
3. Huang Z., Burgess I.W., Plank R.J. 2003. "Modelling membrane action of concrete slabs in composite buildings in fire — Part I: Theoretical development," *Journal of Structural Engineering*, 129(8): 1093-1102.
4. Izzuddin B.A., Tao X.Y. and Elghazouli A.Y. 2004. "Realistic modelling of composite and R/C floor slabs under extreme loading-Part I: Analytical method," *Journal of Structural Engineering*, 130(12): 1972-1984.
5. Jiang J., Usmani A.S. 2013. "Modelling of steel frame structures in fire using OpenSees," *Computers & Structures*, 118: 90-99.
6. Jiang J., Usmani A.S., Li G.Q. "Modelling of steel-concrete composite structures in fire using OpenSees," *Advances in Structural Engineering*, 17(2): 249-264.
7. ASCE 7. 2005. American Society of Civil Engineers Standard 7 Minimum Design Loads for Buildings and Other Structures, American Society of Civil Engineers, 2005.
8. Pyl L., Schueremans L., Dierckx W. and Georgieva I. 2012. "Fire safety analysis of a 3D frame structure based on a full-scale fire test," *Thin-Walled Structures*, 61: 204-212.
9. Kilic S.A. and Selamet S. 2013. "Symmetric and asymmetric collapse mechanisms of a multi-story steel structures subjected to gravity and fire," presented at the Structures Congress conference, 2013.
10. Agarwal A. and Varma A.H. 2014. "Fire induced progressive collapse of steel building structures: The role of interior gravity columns," *Engineering Structures*, 58: 129-140.
11. EN 1992-1-2. Design of concrete structures, Part 1.2: General Rules — Structural Fire Design. European Committee for Standardization (CEN), Brussels, 2004.
12. Li G.Q., Wang P.J. and Wang Y.C. 2010. "Behaviour and design of restrained steel column in fire. Part 1: Fire test," *Journal of Constructional Steel Research*, 66: 1138-1147.
13. EN 1993-1-2. 2005. Design of steel structures, Part 1.2: General Rules —— Structural Fire Design. European Committee for Standardization (CEN), Brussels, 2005.
14. GSA. 2003. Progressive Collapse Analysis and Design Guidelines for New Federal Office Buildings and Major Modernization Projects, US General Services Administration (GSA), 2003.

15. EN 1991-1-2.2002. Actions on structures - Part 1-2: General actions-Actions on structures exposed to fire. European Committee for Standardization (CEN), Brussels, 2002.
16. EN 1990. 2002. Basis of structural design. European Committee for Standardization (CEN), Brussels, 2002.
17. Jiang J., Li G.Q. and Usmani A.S. 2014. "Progressive collapse mechanisms of steel frames exposed to fire," *Advances in Structural Engineering*, 17(3): 381-398.

Evaluating Post-fire Mechanical Behavior of Ultra-high Strength (Grade1200) Steel Tubes

FATEMEH AZHARI, AMIN HEIDARPOUR, XIAO-LING ZHAO and CHRISTOPHER R. HUTCHINSON

ABSTRACT

This paper presents an experimental study on the post-fire mechanical behavior of ultra-high strength steel (UHSS) tubes with nominal yield strength of 1200MPa. In order to understand the changes occurring during cooling phase of a fire, the in-fire mechanical behavior of UHSS is also studied experimentally. The temperatures characteristic of fire simulated in this study are within the range of 300ºC to 800ºC. In the experimental tests, standard dog-bone UHSS specimens are subjected to quasi-static tensile tests at fire temperatures and after being cooled to room temperature. The stress-strain curves, strength and ductility of the tested specimens are discussed. To investigate the effect of steel grade on the post-fire mechanical response, the strength deterioration of different grades of steels available in literature including grades of 460, 690, 800 and 960, are compared with those of UHSS (Grade 1200). Finally, the obtained results are explained based on the phase changes occurring in the steel material during fire by calculating the thermodynamic stability of the ferrite and cementite phases in the tested materials.

INTRODUCTION

In recent years, due to the high strength to weight ratio of ultra-high strength structural steels (UHSS), steel manufacturing companies have attempted to offer these material to automotive industries. In civil engineering field, there has also been a growing trend toward using higher strength steels to reduce the structures weight and provide the possibility of producing energy efficient structural members. In this regard, some researchers have recently proposed innovative fabricated columns composed of ultra-high strength steel (UHSS) tubes with nominal yield strength of 1200MPa [1, 2]. The superior performance of these innovative columns indicates the great potential of UHSS to be introduced as a structural material in civil engineering applications. However, there is lack of design equations in civil engineering codes of practice addressing the behavior of this type of steel under extreme structural loadings such as fire.

During the second half of the last century, fire hazards has increased noticeably in many parts of the world [3]. After a structure is cooled from fire, the residual strength of the structural members determines whether or not it is possible to reuse them. In the past decades, there have been great advances in understanding the behavior of steel in fire. However a few researches have focused on the behavior of steels after being cooled from fire [4-8]. In 2015, the authors of this paper performed an experimental study on the UHSS (Grade 1200) tubes subjected to low fire temperatures (up to 600ºC) [9]. The changes occurred in the strength and ductility of UHSS at elevated temperatures and after being cooled to room temperature were discussed.

This paper addresses the post-fire mechanical response of the UHSS (Grade 1200) tube specimens for fire temperature exposures of up to 800ºC. For the purpose of comparison and in order to find a better understanding of the changes occurring during cooling phase of a fire, the in-fire mechanical response of this material is also studied. The stress-strain curves and the changes in the mechanical properties of the material, including strength and ductility are derived from the experimental tests on UHSS test specimens. In order to investigate the effect of steel grade, the results are compared with those of lower grades of steels. Furthermore, by calculating the thermodynamic stability of the ferrite and cementite phases in the tested materials, the obtained results are explained from the micro-structure point of view.

EXPERIMENTAL TESTS

In this research work, two grades of steel tubes are being tested: Grade 1200 (UHSS), which is the main focus of this study; and Grade 800, which is called high strength steel (HSS) and is tested for the purpose of comparison. Using the water-jet cutting technique, standard dog-bone test specimens are sectioned from the two strips located at right angle to the weld line of the HSS and UHSS tubes as shown in Figure 1-a. The geometry and dimensions of the specimens are illustrated in Figure 1-b.

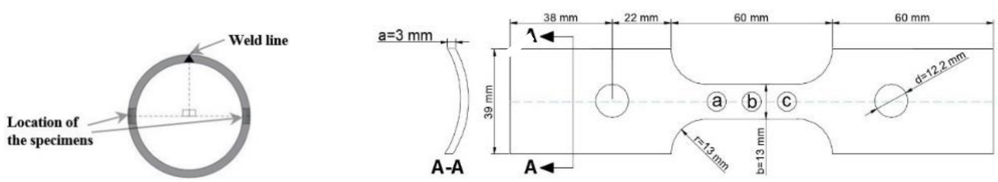

(a) (b)

Figure 1. a) Tube section and b) dimensions of test specimens.

Two sets of experimental tests are carried out in this work. The first set includes heat-up tests where the test specimens are heated up to different fire temperatures (300ºC to 800ºC). Once the temperature is stabilized throughout the specimen, quasi-static tensile test is carried out until failure. This set of tests are performed to investigate the in-fire mechanical behavior of the test materials. The second set includes the cooling tests where the quasi-static tensile test is carried out at room temperature on the test specimens after being air cooled from different fire temperatures (300ºC to 800ºC). These tests are performed to evaluate the post-fire mechanical response of the test materials. The setup of the experimental tests is shown in Figure 2. The device in which the test specimens are heated up to elevated temperatures is a split furnace which works with the combination of convection and radiation heat transfer methods. The tensile load is inserted on the test specimens using the Instron 5982 100kN testing machine with an applied strain rate of

$0.005 \pm 0.002 \text{min}^{-1}$ [10]. In order to measure the strain of the test specimens, a high temperature contact extensometer is inserted to the front cut out of the furnace and is attached to the gauge length of the specimen. As shown in Figure 2-c, for measurement of the temperature of test specimen and assessing the temperature stabilization, 3 thermocouples are attached to 3 points a, b and c (Figure 1-b) on the gauge length of the specimen.

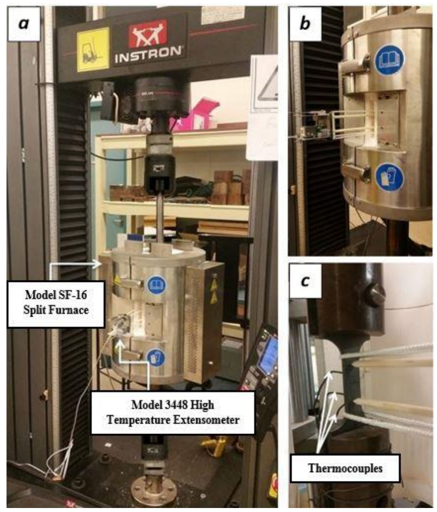

Figure 2. a and b) Test setup from different views, c) inside the furnace.

RESULTS AND DISCUSSION

In order to investigate the in-fire and post-fire mechanical response of the tested materials, in addition to the stress-strain curves, different mechanical parameters including the 0.2% proof stress ($f_{0.2}$), ultimate tensile stress (f_u) and uniform elongation ($\mathcal{E}_u$) are calculated from the experimental tests results. The definition of these parameters is illustrated on a typical stress-strain curve in Figure 3.

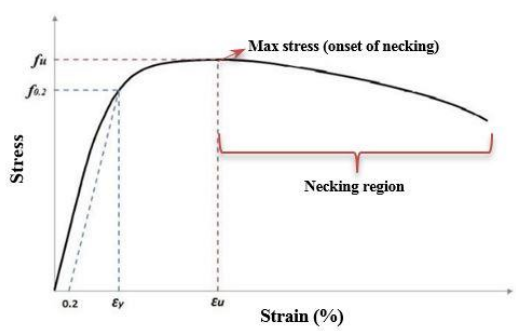

Figure 3. Definition of mechanical properties on a typical stress-strain curve.

Stress-Strain Curves

The stress-strain curves obtained from the heat-up tests and cooling tests are shown in Figures 4 and 5, respectively. Due to the inaccurate strain readings within necking region, the curves are only plotted for the stress and strain values up to the onset of necking (maximum stress). In this paper, the UHSS tube specimen tested at elevated temperature *T* is shown as UHSS-H*T* and that tested after being cooled from temperature *T* to room temperature (*RT*) is labeled as UHSS-C*T*, where H and C represent the heat-up and cooling tests, respectively.

As shown in Figure 4, the UHSS specimens tested at higher fire temperatures experienced more strength reduction. This reduction becomes more significant when the specimens are tested at temperatures above 600ºC and the strength almost disappears when tested at 800ºC.

As can be seen from the curves shown in Figure 5, the specimens cooled from temperatures at or above 470ºC to room temperature did not regain their maximum strength. The most significant reduction in the residual strength can be observed when the UHSS is cooled from fire temperatures above 600ºC. Also, it can be interpreted from the curves shown in Figure 5 that once the UHSS is cooled from fire temperatures above ~750ºC, the strength reduction becomes stabilized such that no more strength reduction is predicted if the specimens are cooled from fire temperatures above 750ºC.

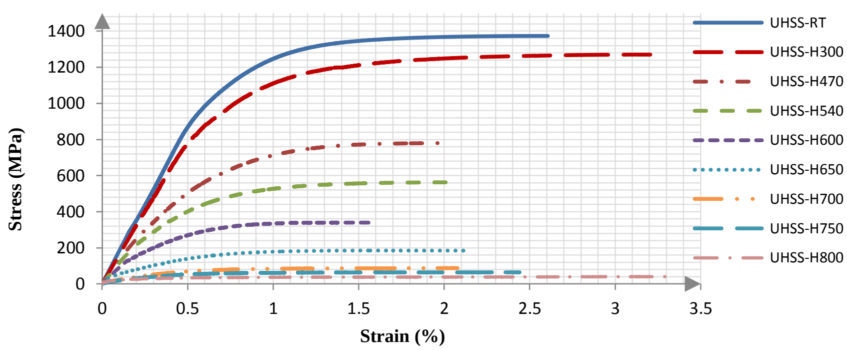

Figure 4. Stress-strain curves of UHSS at elevated temperatures ranging from 300ºC to 800 ºC.

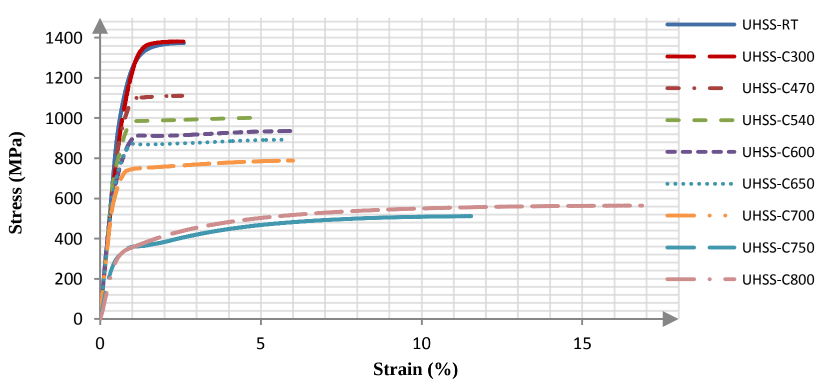

Figure 5. Stress-strain curves of UHSS after cooling from the elevated temperatures ranging from 300ºC to 800ºC.

Proof Stress

In order to study the changes in the proof stress of UHSS under fire conditions, the ratio of the 0.2% proof stress ($f_{0.2}$) of the UHSS specimens obtained from both heat-up and cooling tests to that of the virgin material at room temperature ($f_{0.2,\ RT}$) are calculated. In Figure 6, the variations of $f_{0.2}/f_{0.2,\ RT}$ ratios with respect to the maximum temperature the specimens have experienced are plotted. In this figure, for the purposes of comparison, the values provided by the AS4100 [11] for the 0.2% proof strength reduction factors of mild steel at elevated temperatures are also presented. As can be seen, the strength of the UHSS specimens tested at elevated temperatures reduces more rapidly compared to those tested after being cooled to room temperature. Moreover, the values provided by the AS4100 [11] are in between those obtained for UHSS under heat-up and cooling tests. Thus, using the values of the standard for the prediction of the tensile mechanical behavior of UHSS structural members at elevated temperatures may lead to an unsafe design. On the other hand, there is no design curve in the standards for predicting the behavior of UHSS materials after being cooled from elevated temperatures. This signifies the necessity of proposing a new set of strength design equations for evaluating the tensile mechanical response of UHSS structural members under fire conditions.

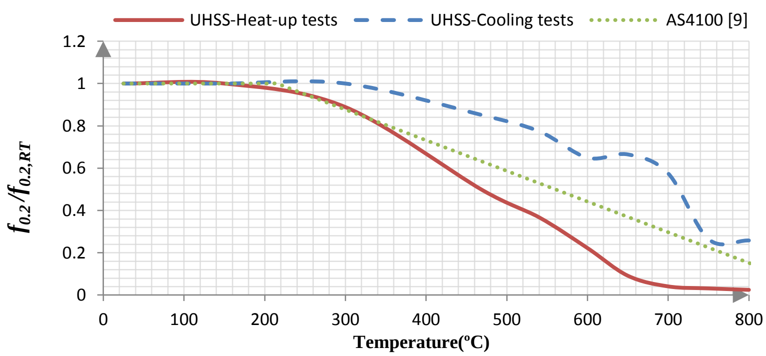

Figure 6. Variation of 0.2% proof stress reduction factor for UHSS under in-fire and post-fire conditions.

Ductility

In order to discuss the ductility of the UHSS under fire conditions, the reduction factors of the uniform elongation ($\varepsilon_u/\varepsilon_{u,RT}$) for both heat-up and cooling tests are plotted in Figure 7 with respect to the maximum temperature the material has experienced. As can be observed, while the maximum $\varepsilon_u/\varepsilon_{u,RT}$ value for the UHSS specimens under heat-up tests is only 1.27, the values of $\varepsilon_u/\varepsilon_{u,RT}$ ratio for the UHSS specimens under cooling tests increase up to 6.5 as the maximum temperature reaches 800ºC. Moreover, since the elongation of a material is strongly governed by the strain hardening capacity of its structure, the significant increase in the elongation of the specimens tested after being cooled from temperatures above 700ºC indicates a major change in the micro-structure of these steels.

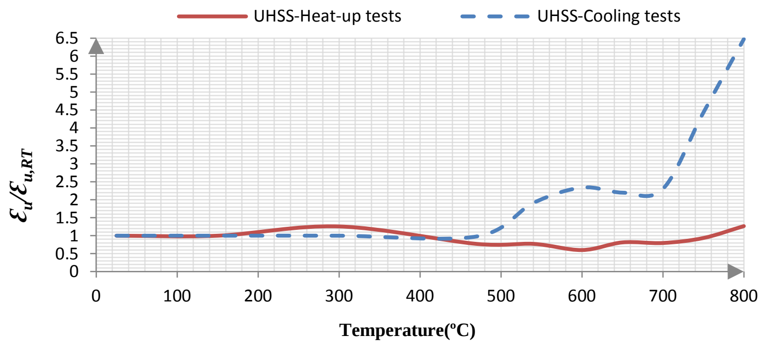

Figure 7. Variation of uniform elongation reduction factors for UHSS under in-fire and post-fire conditions.

Effect of Steel Grade

In order to investigate the effect of steel grade on the post-fire mechanical properties of steel, the heat-up and cooling tests are also conducted on specimens taken from high strength steel (HSS) tubes with nominal yield strength of 800MPa. The reduction in the ultimate tensile strength after being cooled from different fire temperatures with respect to that of the virgin material at room temperature ($f_u/f_{u,\ RT}$) are compared for five different grades of steel including the UHSS-Grade 1200 and HSS-Grade 800 tested in this study, and the HSS-Grade 960, HSS-Grade 690, and HSS-Grade 460 studied by other researchers [4, 5, 8] (Figure 8). It can be seen from Figure 8 that while the strengths of all the HSS materials are almost fully regained when cooled from temperatures below 600ºC to room temperature, the UHSS loses 32% of its strength. Also, while the ultimate strength of the HSS specimens cooled from 800ºC to room temperature is reduced to less than 65% of that of the virgin HSS specimen at room temperature, the corresponding reduction factor for the UHSS (Grade 1200) is 40%. These results indicate the higher sensitivity of the UHSS to the temperature history of the material.

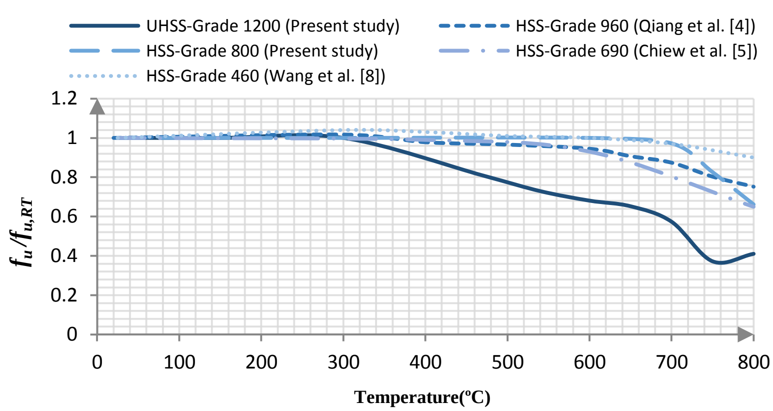

Figure 8. Variation of the ultimate tensile strength reduction factors for different grades of steels after cooling from various fire temperatures.

Microstructural Evaluation

In this study, in order to better explain the changes occurring in the mechanical response of the tested materials under fire conditions, a rational microstructural evaluation is performed. To this end, plots of the thermodynamic stability of the phases present in the microstructure of UHSS (Grade 1200) are calculated using the Thermo-Calc program [12] and the most up to date steel database, TCFe7 (Figure 9).

The UHSS considered in this study derives its strength from a tempered martensitic microstructure [13]. Based on the phase diagrams obtained for the UHSS (Figure 9), after the UHSS is subjected to temperatures below 650ºC, its microstructure remains a tempered martensite/ferrite and the identity of the phases present (ferrite/martensite and cementite) remains unchanged and only their sizes change. For these temperatures, i.e. low fire temperatures, the residual strength after cooling is controlled by the maximum temperature and the time the material is exposed to that temperature which is ~20 mins for the cooling tests performed in this study. However, as can be seen from Figure 9, when the UHSS is subjected to temperatures above 650ºC (high fire temperatures), the green curve appears which represents the formation of a new phase called austenite. Depending on the rate of cooling from these high temperatures, different percentage of austenite is converted to ferrite or pearlite phases. The original martensite microstructure may be re-created in case of very high cooling rates such as quenching the steel in water and the strength may not be reduced. After the exposure of the UHSS to temperatures above ~770ºC, since the steel phase is almost 100% austenite, the residual mechanical properties of the UHSS cooled from temperatures above this would be basically the same. This explains the reason behind the overlapping of the stress-strain curves obtained for the UHSS specimens cooled from 750ºC and 800ºC to room temperature (Figure 5).

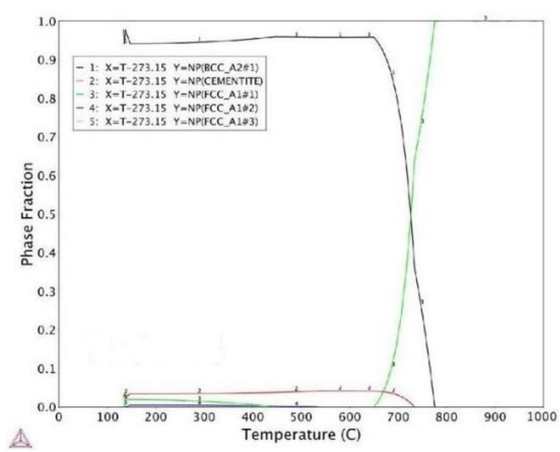

Figure 9. Calculated plots of the thermal stability of ferrite (BCC), cementite and austenite (FCC) in UHSS as a function of temperature using the software package, Thermo-Calc [12].

CONCLUSION

In this research, the in-fire and post-fire mechanical response of ultra-high strength steel (UHSS) tubes are studied. Strain-controlled tensile tests are conducted on the UHSS tube specimens at elevated temperatures of up to 800ºC and after being cooled to room temperature. The results showed that the strength of the specimens tested at fire temperatures above 300ºC is considerably reduced, such that at 800ºC, most of the material's strength is deteriorated. Also, the post-fire residual strength of the UHSS tube starts to deteriorate after being cooled from temperatures above 470ºC. However, the major reduction in the residual strength is occurred when the material is cooled from fire temperatures above 600ºC. To evaluate the effect of steel grade on the post-fire mechanical response, the strength deterioration of UHSS is compared with that of different grades of steels available in literature. The results obtained from the experimental tests are rationalized by calculating the thermodynamic stability of the phases present in the microstructure of the UHSS.

ACKNOWLEDGEMENT

This research work was supported by the Australian Government-Department of Education and also by Australian Research Council through a Discovery Project (DP130100181) awarded to the second and third authors. The authors thank SSAB Corporation for providing ultra-high strength and high strength steel tubes.

REFERENCES

[1] Javidan F, Heidarpour A, Zhao X-L, Minkkinen J. Performance of innovative fabricated long hollow columns under axial compression. Journal of Constructional Steel Research. 2015;106:99-109.

[2] Nassirnia M, Heidarpour A, Zhao XL, Minkkinen J. Innovative hollow columns comprising corrugated plates and ultra high-strength steel tubes. Thin-Walled Structures. 2016;101:14-25.

[3] Viedma O, Moity N, Moreno JM. Changes in landscape fire-hazard during the second half of the 20th century: Agriculture abandonment and the changing role of driving factors. Agriculture, Ecosystems & Environment. 2015;207:126-40.

[4] Qiang X, Bijlaard FSK, Kolstein H. Post-fire performance of very high strength steel S960. Journal of Constructional Steel Research. 2013;80:235-42.

[5] Chiew SP, Zhao MS, Lee CK. Mechanical properties of heat-treated high strength steel under fire/post-fire conditions. Journal of Constructional Steel Research. 2014;98:12-9.

[6] Qiang X, Jiang X, Bijlaard FSK, Kolstein H, Luo Y. Post-fire behaviour of high strength steel endplate connections — Part 1: Experimental study. Journal of Constructional Steel Research. 2015;108:82-93.

[7] Qiang X, Bijlaard FSK, Kolstein H, Xia R. Experimental study on high strength structural steel S460 in fire and after cooling down. IES Journal Part A: Civil and Structural Engineering. 2013;6:104-11.

[8] Wang W, Liu T, Liu J. Experimental study on post-fire mechanical properties of high strength Q460 steel. Journal of Constructional Steel Research. 2015;114:100-9.

[9] Azhari F, Heidarpour A, Zhao X-L, Hutchinson CR. Mechanical properties of ultra-high strength (Grade 1200) steel tubes under cooling phase of a fire: An experimental investigation. Construction and Building Materials. 2015;93:841-50.

[10] ASTM Standard E8/E8M. Standard Test Methods for Tension Testing of Methallic Materials: ASTM International, West Conshohocken, PA: USA; 2011.

[11] Australia Standards AS4100, Steel structures. Sydney, Australia1998.

[12] Sinaie S, Heidarpour A, Zhao XL. Stress-strain-temperature relation for cyclically-damaged structural mild steel. Engineering Structures. 2014;77:84-94.

[13] Bhadeshia HKDH, Honeycombe SR. Chapter 5 - Formation of Martensite. In: Honeycombe HKDHBR, editor. Steels (Third Edition)-Microstructure and Properties. Oxford: Butterworth-Heinemann; 2006. p. 95-128.

Effect of Initial Geometric Imperfection on the Performance of Single-Layer Reticulated Shells at Elevated Temperatures

YE-HUA WANG[1,2], ZU-YAN SHEN[1,2] and YUAN-QI LI[1,2]

ABSTRACT

Single-layer reticulated shells are belong to the structures sensitive to initial geometric imperfections, however in the study of the behavior of single-layer reticulated shells under fire conditions, the effect of initial geometric imperfections was rarely considered. This paper presents a numerical study investigating the effect of initial geometric imperfections on the performance of single-layer reticulated shells at elevated temperatures using the finite element software ANSYS. The results of the stability analysis at different temperature points show that the buckling load of the structure with initial geometrical imperfections is less than that of the ideal structure, and the results of the analysis under condition of increasing temperatures at different loads indicate that the critical temperature of the structure with initial geometrical imperfections is less than that of the ideal structure.

Ye-hua Wang. [1]State Key Laboratory of Disaster Reduction in Civil Engineering, [2]Department of Building Engineering, Tongji University, No.1239 Siping Road, Shanghai, P.R.China
Zu-yan Shen. [1]State Key Laboratory of Disaster Reduction in Civil Engineering, [2]Department of Building Engineering, Tongji University, No.1239 Siping Road, Shanghai, P.R.China
Yuan-qi Li. [1]State Key Laboratory of Disaster Reduction in Civil Engineering, [2]Department of Building Engineering, Tongji University, No.1239 Siping Road, Shanghai, P.R.China

INTRODUCTION

Single-layer reticulated shells are extensively used in China with the advantage of light weight, covering large areas, various attractive geometrical surface, simple production and fast assembly and so on. Recently the fire resistance of the structures has gradually become more and more attractive to researchers, however in these studies [1-6], initial geometric imperfections on the performance of single-layer reticulated shells at elevated temperatures was rarely considered. A lot of experimental and theoretical researches on the behavior of single-layer reticulated shells at normal temperature and some engineering accidents show that many single-layer reticulated shells are belong to the structures sensitive to initial geometric imperfections, and the initial geometric imperfections have significant effect on the stability of single-layer reticulated shells at normal temperature. Meanwhile stability analysis is a principal problem for the design of the single-layer reticulated shell structures. So in this paper effect of initial geometric imperfections on the performance of single-layer reticulated shells at elevated temperatures are investigated through numerical simulations based on the finite element package ANSYS.

THE FININT ELEMENT MODEL

The analytical model of the single-layer reticulated shell is the Kiewitt-6 single-layer reticulated shell, as shown in Fig.1, which is designed in the common way. The structure has a span of 30m and a rise of 5m. Steel tubes of Φ114 mm×4 mm are used as the members of the structure with a yield strength is 345Mpa and Young's modulus E is 2.06×10^5Mpa at ambient temperature.

The modeling of the single-layer reticulated shell is conducted by means of the finite-element package ANSYS10.0. For the FE model, the beam188 element, a 3-D linear finite strain beam element based on Timoshenko beam theory [7], is selected to simulate the members of the structure. The constitutive model of the steel at elevated temperature is based on Eurocode 3[8]. Connections between the members at the node are assumed to be rigidly, as it is always the case with analysis of single-layer reticulated shells. The boundaries along the base are fixed. The uniformly distributed vertical load is applied. Also, Forde method (arc-length method) [9] is used to trace nonlinear equilibrium paths in the stability analysis.

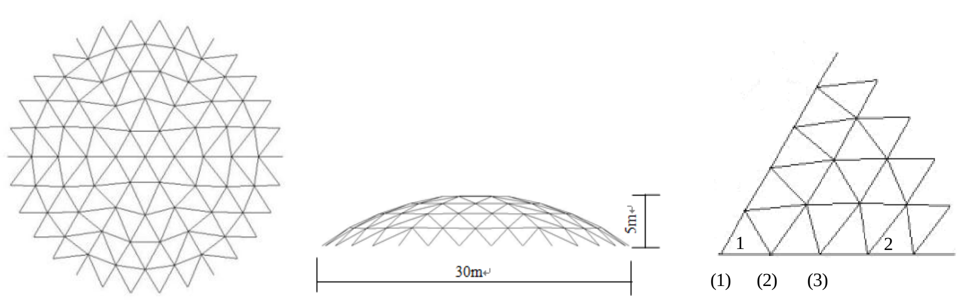

(a) plane graph (b) elevation graph (c) the number of node and element

Fig.1 Analysis mode of Kiewitt-6 shell

INITIAL GEOMETRICAL IMPERFECTIONS

Two ways have generally been developed to introduce the initial geometrical imperfections into a reticulated shell in conducting the nonlinear analysis, i.e. the random imperfection mode method [10], the consistent imperfection mode method [11]. Generally, as for the random imperfection method prediction, many random imperfection cases are needed to cover the lowest buckling load. While as for consistent imperfection mode method, the lowest buckling load can be predicted with satisfactory accuracy with only one case of imperfection. The imperfection mode is easier to obtain by conducting a linear-elastic eigenvalue buckling analysis, which is also the method recommended in Technical Specification for Space Frame Structures of China [12]. This method is thus employed in all the following analysis.

The initial geometrical imperfections in the analysis were assumed to be distributed following the first eigenvalue buckling mode of the respective structure, i.e. the lowest buckling mode. The magnitude of the initial geometrical imperfections is L/300 according to Technical Specification for Space Frame Structures of China. L is the span of the structure. The lowest buckling mode of the structure is shown in Fig.2.

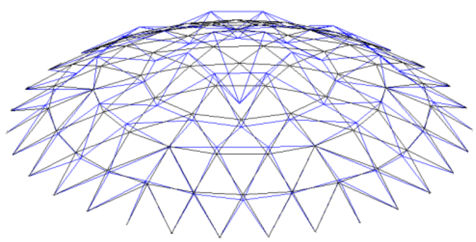

Fig.2 The distribution of initial geometrical imperfections (deflection enlarged 5 times)

ANALYSIS AND DISCUSSION OF RESULTS

In this paper two kinds of analysis were conducted. One case study is the geometrically and materially nonlinear stability analysis of the structures at different temperature points. And the other is the nonlinear analysis of the performance of the structures under condition of increasing temperature at different loads. These topics are discussed next.

Effect of Initial Geometrical Imperfections on the Bulking Load

The geometrically and materially nonlinear stability analysis of the ideal structure and that of the structure with initial geometrical imperfections are respectively conducted at the temperature of 20℃, 200℃, 300℃, 400℃, 500℃, 600℃, 700℃ and 800℃.

Fig.3 shows the load-deflection curves of the ideal structure obtained from the stability analysis at different temperature points, in which the deflection represents the maximum vertical displacement occurring at No.3 node (as shown in Fig.1) of the ideal structure. Fig.4 shows the load-deflection curves of the structure with initial geometrical imperfections, in which the deflection represents the maximum vertical displacement occurring at No.1 node (as shown in Fig.1) of the structure with initial geometrical imperfections. From Fig.3 and Fig.4, it can be seen that the buckling load of the structure with initial geometrical imperfections at each temperature point is less than that of the ideal structure, and the maximum vertical displacement of the structure with initial geometrical imperfections at each temperature point is more than that of the ideal structure.

The buckling loads of the two kinds structures at different temperatures are also listed in Table I. It can be seen that at ambient temperature the buckling load of the ideal structure is 1.55 times of the bulking load of the structure with initial geometrical imperfections. So the single-layer reticulated shell is the structure sensitive to initial geometrical imperfections. It is also noticeable that the buckling load of the structure with initial geometrical imperfections at each temperature point is less than that of the ideal structure, and the reduction rate of buckling load due to initial geometrical imperfections is reduced slightly, not distinctly with the increase of temperature, and the value keeps up at level of 30% or so in.

These results indicate that at ambient temperature the single-layer reticulated shell is sensitive to the initial geometrical imperfections, and then at elevated temperatures it is also sensitive to the initial geometrical imperfections. The reduction of buckling load due to the initial geometrical imperfections is reduced slightly with the increase of temperature. The maximum vertical displacement of the node of the structure with initial geometrical imperfection at the ultimate limit state is larger than that of the ideal structure.

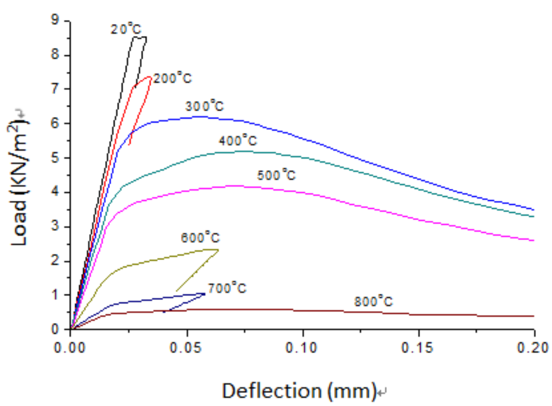

Fig.3 Load-deflection curves of the ideal structure

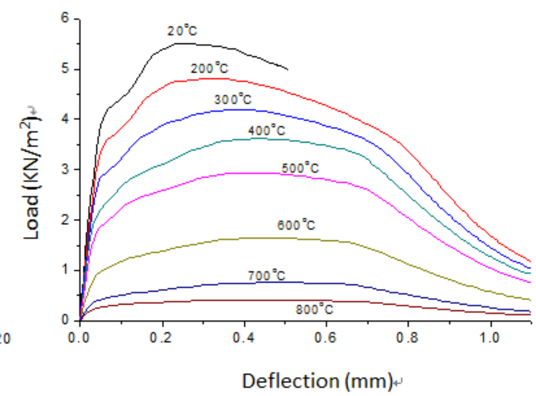

Fig.4 Load-deflection curves of the structure with initial geometrical imperfections

TABLE I EFFECT OF INITIAL GEOMETRICAL IMPERFECTIONS ON THE BUCKLING LOAD OF THE STRUCTURES AT DIFFERENT TEMPERATURE POINTS

Temperature (℃)	Buckling load of ideal structure (KN/m^2)	Buckling load of structure with initial geometrical imperfections(KN/m^2)	Reduction rate of buckling load due to initial geometrical imperfections
20	8.531	5.515	35.4%
200	7.371	4.817	34.7%
300	6.187	4.193	32.2%
400	5.203	3.619	30.5%
500	4.194	2.942	29.9%
600	2.341	1.644	29.8%
700	1.046	0.757	27.6%
800	0.593	0.416	29.9%

Effect of Initial Geometrical Imperfections on Performance of Structures in Fire Condition

The nonlinear finite element analysis of the ideal structure and that of the structure with initial geometrical imperfections under conditions of the International Standardization ISO834 temperature curve simulating fire conditions are respectively conducted at the load of 0.5 KN/m^2, 0.8 KN/m^2, 1.0 KN/m^2, 1.3 KN/m^2, 1.5 KN/m^2, 2.0 KN/m^2 and 2.5 KN/m^2. The performance of the structures such as the deformation, the axial stresses and the critical temperature are discussed as follows.

DEFORMATION OF THE STRUCTURES

Fig.5 shows that the vertical displacements of the same nodes of the ideal structure and the structure with initial geometrical imperfections obtained from the analysis at the load of 1.3 KN/m^2. It is clearly observed that the deflection of the structure with initial geometrical imperfections has the characteristic of expand-to-fall. It can be also seen that the structure with initial geometrical imperfections enters into the stage of ultimate limit state earlier than the ideal structure, and the vertical displacement of the structure with initial geometrical imperfections at the ultimate limit state is becoming larger and larger.

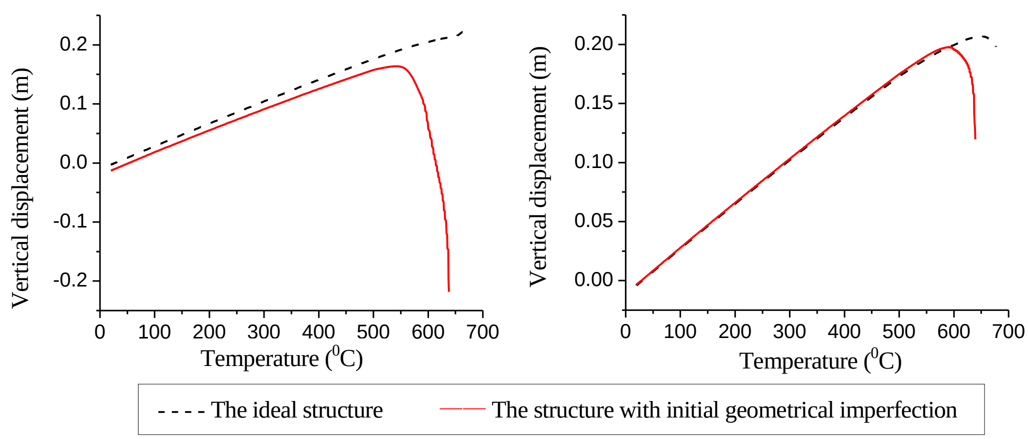

(a) No.1 node (b) No.2 node

Fig.5 Vertical displacement of nodes

AXIAL STRESSES IN THE STRUCTURES

Fig.6 shows that the axial stresses of the representative member in the central zone and the representative member in the edge zone of the two kind structures obtained from the analysis at the load of 1.3 KN/m^2. It is noticeable that with the increase of temperature, the axial stresses of the central member of the structures with initial geometrical imperfections are different from that of the ideal structure, while the axial stresses of the edge member of the two kind structures are similar. The main reason for this difference is that the buckling starts from joints at the central zone and then grows slightly based on the distribution of initial geometrical imperfection as shown in Fig.2.

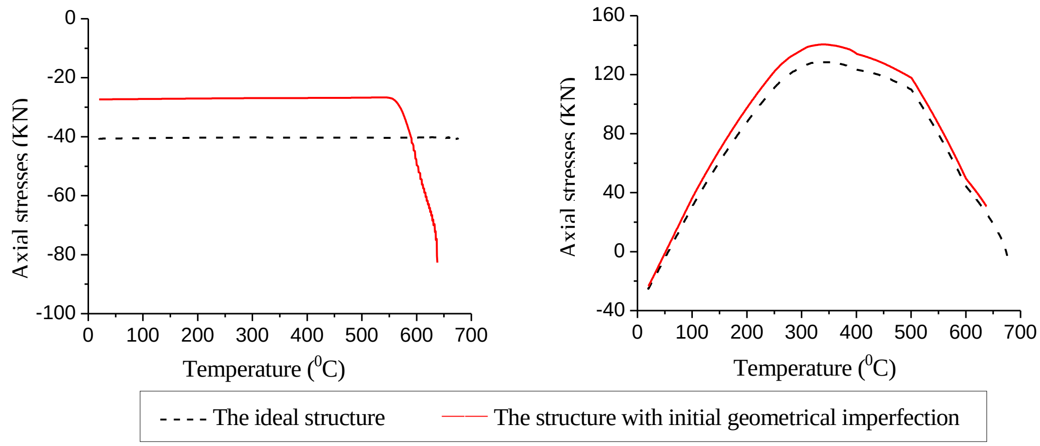

(a) the central member (No.1) (b) the edge member(No.2)

Fig.6 Axial stress in structures

CRITICAL TEMPERATURE OF THE STRUCTURES

The critical temperatures obtained from the nonlinear analysis under condition of increasing temperatures at different loads are listed in Table II. It can be seen that at the same load condition the critical temperature of the structure with initial geometrical imperfections is less than that of the ideal structure. And with the increase of the load, the difference of the critical temperature between the ideal structure and the structure with initial geometrical imperfections is becoming lager and lager.

These results show that initial geometrical imperfections have significant effect on the deflection, axial stresses and the critical temperature of the single-layer reticulated shell under the condition of increasing temperatures. The performance of the structure with initial geometrical imperfections is different from that of the ideal structure.

TABLE II FEEECT OF INITIAL GEOMETRICAL IMPERFECTION ON THE CRITICAL TEMPREATURE OF THE STRUCTURES AT CONDITION OF ISO834 INCREASING TEMPERATURE

Load (KN/m^2)	**Critical temperature of ideal structure (℃)**	**Critical temperature of structure with initial geometrical imperfections (℃)**	**Difference of critical temperature due to initial geometrical imperfections (℃)**
0.5	800.8	754.2	46.6
0.8	738.1	689.0	49.1
1.0	699.0	667.8	31.2
1.3	676.8	635.8	41.0
1.5	661.5	614.3	47.2
2.0	624.4	573.8	50.6
2.5	591.1	538.5	52.6

CONCLUSIONS

The effect of initial geometric imperfections on the performance of single-layer reticulated shell at elevated temperatures is studies in this paper.

The results of geometrically and material nonlinear stability analysis show that the buckling load of the structure with initial geometric imperfections is smaller than that of the ideal structure at different temperature points, and the deflection of the structure with initial geometric imperfections is larger than that of the ideal structure when the structure is reaching the ultimate limit state.

The nonlinear finite element analysis simulating fire condition shows that the reflection and the axial stresses of the structure with initial geometric imperfections are different from those of the ideal structure, which is caused by the distribution of initial geometrical imperfections. The critical temperature of the structure with initial geometric imperfections under fire condition is in general smaller than that of the ideal structure.

Initial geometric imperfections have significant effect on the performance of the single-layer reticulated shells, so initial geometric imperfections should be taken into account in the nonlinear finite analysis at elevated temperatures.

ACKNOWLEDGMENTS

The authors acknowledge the financial support of the National Natural Science Foundation of China (Grant No.51478332).

REFERENCES

1. Wang Xin-mei, Dong Ji-bin. 2008. “Identification and repairing of the steel reticulated shell after the fire”. *Shan-xi Architecture*, 34(31):73-74.
2. Yin-Yue1, YuanTie-zhu, Chen Zhi-hua. 2010. “Numerical study on the behavior of a lattice shell structure under fire and damage estimation,” *China Civil Engineering Journal, 43(8):*51-56.
3. Chen Bo, Zhang Jin, Yue Lei. 2007. “Nonlinear Finite Element Analysis of a Reticulated Shell Subjected to a Fire, ” *Journal of Wuhan University of Technology*, 29(6):69-84.
4. Liu Ming-you, Wang Hai-zhong. 2009. “Study on fire resistance performance of single layer spherical reticulated shell structure,” *Engineering construction,*41(1):10-17.
5. Xue Su-duo, Qiu Lin-bo, Li Xiong-yan. 2012. “Overall performance analysis of single layer reticulated dome under fire,” *Journal of Beijing University of Technology*, 38(4):. 488-491.
6. Qiao Da.2013.”Fire resisting performance Analysis of Single layer spherical reticulated shells. MS thesis,” Harbin Engineering University, Harbin.
7. ANSYS, Inc. 2009. Theory Manual. 001369. Twelfth Edition. SAS IP, Inc.
8. European Committee for Standardization. 2005. Eurocode 3-Design of steel structures-Part 1-2:General rules-Structural fire design, Brussels.
9. Forde WRB, Stiemer SF. 1987. “Improved arc length orthogonality methods for nonlinear finite element analysis,” *Comput Struct*, 27(5):625-630.
10. Yamada S, Takeuchi A. Tada Y, Tsutsumi K. 2001. “Imperfection-sensitive overall buckling of single-layer lattice domes,” *J Eng Mech*,4:382–396.
11. Chen X, Shen SZ. 1993. “Complete load–deflection response and initial imperfection analysis of single-layer lattice dome,” *Int J Space Struct*,8(4):271–8.
12. Ministry of Housing and Urban-Rural Development of the People’s Republic of China. 2010.Technical specification for space frame structures. Beijing: The Industry Standard Press of the People’s Republic of China.

The Performance of Structural Steel Beams Subject to a Localized Fire

LISA CHOE, SELVARAJAH RAMESH, CHAO ZHANG
and JOHN GROSS

ABSTRACT

This paper presents the results from the open flame, localized fire tests conducted on 6.17 m long, simply supported W16×26 beam specimens. The cross sections at midspan (i.e., expected plastic hinge zone) of the beam specimen were directly exposed to the natural gas fire. Two different tests were conducted: (1) fire-thermal tests to evaluate the effects of the prescribed heat release rates (HRR), provided by the 1 m^2 natural gas burner, on the thermal responses of the specimen and (2) structural-fire test to evaluate the fire effects on the overall behavior and the load-bearing capacity of the specimen. The test results indicated that the prescribed heat release rates from the burner affected the heating rate of the specimen. When the HRR-time relationship of the burner followed a step function, the fire-exposed region of the beam specimen was heated essentially linearly with increasing time of fire exposure. When the HRR was set to a target magnitude of 400 kW throughout the test, the fire-exposed region was heated nonlinearly until it reached a steady-state temperature condition. When the beam specimen was subjected to linearly increasing flexural loads at a maintained HRR of 700 kW, combined flexural and lateral torsional failure of the specimen was exhibited. The lateral deformations in the compression flange at the fire-exposed critical sections initiated at 124 ± 5 kN-m, which is 39% of the plastic moment capacity at room temperature. The peak moment capacity was 171 ± 9 kN-m (54 % of the plastic moment capacity at room temperature), while the maximum temperature was 642 ± 28 ˚C at the HRR of 700 kW. The test results from the present study can be used for developing or calibrating analytical models, which can be eventually used for evaluating the performance of structural members subjected to a localized fire.

INTRODUCTION

The 6.17 m long W16×26 beam specimens subjected to a localized fire were tested at the National Fire Research Laboratory (NFRL) [1] of the National Institute of Standards and Technology (NIST). The main objective of these tests was to commission the structural fire experimental measurement capabilities of the newly constructed laboratory. A secondary objective was to generate data set for validation of analytical models. The experimental tests were divided into two parts: the fire-

National Institute of Standards and Technology, 100 Bureau Dr, Gaithersburg, Maryland 20899, USA
lisa.choe@nist.gov, selvarajah.ramesh@nist.gov, chao.zhang@nist.gov, john.gross@nist.gov

thermal tests and the structural-fire test. The fire-thermal tests were intended to evaluate temperature-time responses of the steel beam specimen exposed to an open flame, localized fire with controlled heat release rates (HRR). No structural load was applied except the self-weight of the beam specimen. The structural-fire test was conducted such that the flexural loads and the open flame fire were applied to the critical sections (i.e., expected plastic hinge zone) of the specimen to evaluate the behavior and the flexural strength of the simply supported steel beam specimen.

FIRE-THERMAL TEST

Test setup, test protocol, and instrumentation layout

Figure 1 shows the test setup under the exhaust hood (13.7 m ×15.2 m) in the NFRL structural fire test bay. The W16×26 beam specimen of ASTM A992 steel [2] was placed on seated connections which were bolted to the W12×106 reaction column assemblies. Nominal dimensions of the W16×26 and W12×106 shapes are provided in ANSI/AISC 360-10 [3]. The fuel delivery system consisted of two natural gas burners with a nominal flame zone of one square meter to provide heat release rate (HRR) up to 1.5 MW. The uncertainty in the HRR measurements with a natural gas burner is presented in Bryant et al. [4] and not presented here for brevity. The distance from the lower flange of the beam specimen to the strong floor was 1.6 m. The assembled burner was placed 1 m below the lower flange of the specimen.

To evaluate the thermal behavior of the beam specimen and the reproducibility of the fire test in the NFRL, five individual tests were conducted on the same specimen under two different fire conditions provided by the natural gas burner. The first series of the tests was conducted by increasing the heat release rate in 100 kW increments approximately every 5 min (Tests 1 and 2); the second series of the tests utilized the heat release rate fixed at 400 kW throughout the test period (Tests 3, 4, and 5). All of the five tests were terminated when any one of the thermocouples installed at the specimen indicated about 500 °C.

Test data included the heat release rate of the burner, temperatures, adiabatic surface temperatures (to characterize thermal exposure), and displacements of the beam specimen. For temperature measurements, a total of fifty-three, type-K, 24 gauge thermocouples (tc) were installed at eleven different cross sections along the specimen length as shown in Figure 1. Four 25 mm linear position sensors were installed at 0.29 m from the beam ends to measure the axial displacements (thermal elongation). Two 50 mm linear position transducers were used to measure the vertical displacement induced by thermal bowing effects. For tests 3 through 5, four plate thermometers were installed to measure the adiabatic surface temperature at midspan of the beam specimen. A thermal imaging camera was used to record the spatial temperature distribution in the fire-exposed portion of the beam specimen.

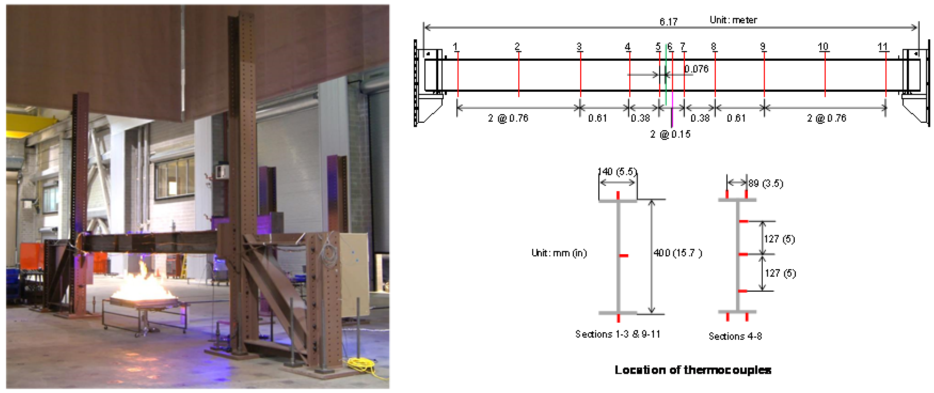

Figure 1. Fire-thermal test setup and thermocouple layout

Test results

Figure 2 shows the heat release rate output from the burner for each test and the corresponding temperature changes at the fire-exposed zone of the specimen. Temperatures shown herein are the average values tc readings across sections 5, 6, and 7 at five different locations through the section depth. Six thermocouple readings were used to obtain the average temperature of the upper and lower flange and three thermocouple readings were used for each web temperature in Figure 2. No permanent deformation of the beam specimen was observed in the heating or cooling phase of the fire.

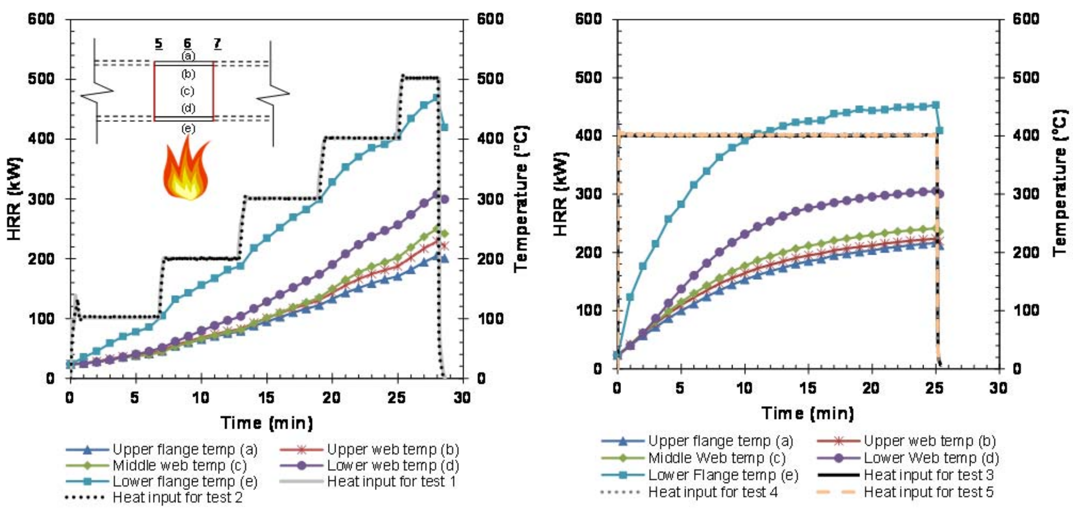

Figure 2. Heat input from the burner and steel temperatures at midspan†

When a step function was used to increase the heat source (i.e., HRR from the burner), it took approximately 28 min after ignition to reach the maximum discrete temperature of 500 °C at the lower flange of the specimen at midspan. The coefficient

† The estimated expanded uncertainty (U) of the temperature data is 20 °C (confidence interval of 95%) with U determined from a combined standard uncertainty (u_c = 10 °C) in the repeated temperature measurements at sections 5, 6, and 7 and the assumption that the possible estimated values of the standard are normally distributed with u_c.

of variation (COV) in the measured HRR from the two repeated tests (Tests 1 and 2) was 0.3%. The temperatures at the fire-exposed midspan of the beam specimen increased almost linearly until the fire was extinguished. A thermal gradient through the section depth was also exhibited. The temperature difference between the lower flange and the lower web (i.e., tc locations e and d, respectively, as shown in Figure 2) increased with increasing time of fire exposure, and reached 160 °C at 28 min. However, the maximum difference in temperatures at the upper portion of the cross section (along the tc locations a through c) remained below 25 °C.

When the burner was set to generate the constant HRR of 400 kW, it took approximately 25 min after ignition to reach the maximum discrete temperature of 500 °C at the lower flange of the specimen at midspan. The COV of the heat input from the three repeated tests (Tests 3, 4, and 5) was 0.2%. Unlike the previous tests, the temperatures at the exposed midspan of the specimen increased nonlinearly. The temperatures of the specimen increased rapidly following ignition, and then the rate of the temperature change decreased to slowly reach the steady-state regime. Thermal gradient through the section depth was also developed in a way that severe temperature gradients (as large as 150 °C) were observed in the lower portion of the exposed cross section, while small differences (≤ 17 °C) were exhibited in the temperatures of the upper portion.

Figure 3 shows the temperature distribution (at 11 different sections shown in Figure 1) along the specimen length before the fire was extinguished. Temperatures in this figure were the average values of tc readings from the repeated tests, with the expanded uncertainty (± *U*) indicated as error bars. *U* was estimated based on the estimated values of the standard‡ (u_c) with a coverage factor of 2 (95% confidence interval). As shown in the figure, the thermal gradient along the beam length developed under two different fire conditions were similar. The constant HRR tests (Tests 3 through 5) showed a better representation of the symmetric thermal gradient with respect to the centerline of the beam specimen than the other tests (Tests 1 and 2).

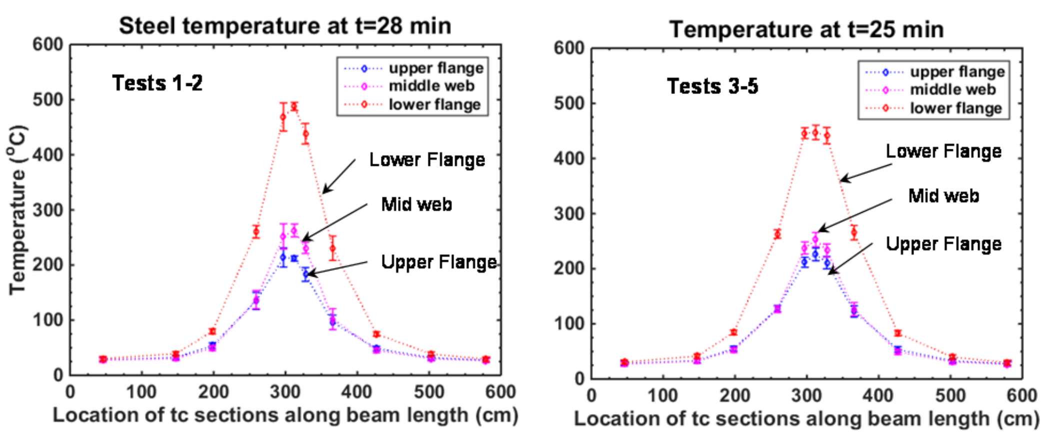

Figure 3. Thermal gradient along the beam length

‡ The components of standard uncertainty (u_c) included test repeatability estimated using uniform distribution and manufactures' specifications on thermocouple error (± 0.4%) and digitization error (± 3.2 ˚C) with 95 % confidence interval. Test repeatability was estimated using individual data points at specific tc locations (Figure 1) at a specific time of occurrence (t) after ignition. For sections 4 through 8 (Figure 1), there were two thermocouples at the upper and lower flanges each. These two tc readings were averaged to represent the upper and lower flange temperate at the specific location of the section.

STRUCTURAL FIRE TEST

Test setup, test protocol, and instrumentation layout

The W16×26 steel beam specimen was tested under combined flexural loading and a localized fire condition. Figure 4 shows the structural fire test setup. The same natural gas burner used in the fire-thermal tests was used to create a localized, open flame fire exposure directly to the critical sections (i.e., expected plastic hinge zone) of the specimen. For the structural loading, two hollow steel section (HSS) loading beams (placed on the top of the specimen) served as two point loads to produce a uniform bending moment across the fire-exposed critical sections of the beam specimen. The distance between the two loading points was 2.44 m (8 ft). The ends of the two HSS loading beams were connected to four 235 kN (53 kip) actuators via four 34.9 mm (1.38 inch) diameter high-strength steel rods. The high-strength steel rods had no rotational restraints at the ends. The actuators were mounted to the underside of the strong floor to protect them from fire. The HSS loading beams were water-cooled during the fire exposure.

The beam specimen was simply supported such that both end rotations about the principal axes and the axial (longitudinal) displacements were not restrained, whereas the beam ends were laterally restrained. The bearing-to-bearing length of the specimen was 5.87 m (19.25 ft). The room-temperature yield and ultimate strengths of the specimen were 440 ± 1.15 MPa and 530 ± 1.73 MPa, respectively[§].

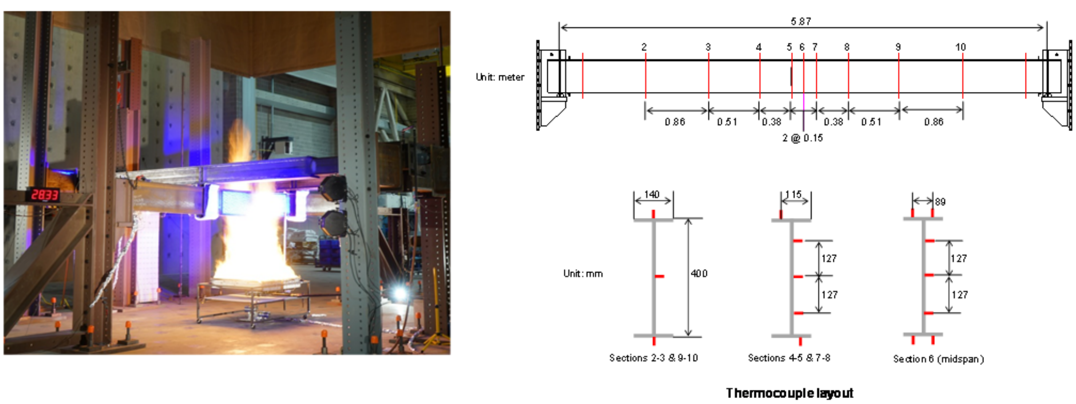

Figure 4. Structural fire test setup and thermocouple layout

The test was conducted in two steps as follows: (i) The HRR of the burner was increased to a target magnitude of 700 kW and maintained constant throughout the test. (ii) After the maximum temperature at the fire-exposed cross sections reached the steady-state condition, two point loads were programed to increase at a rate of 2 kip/min (8.90 kN/min) simultaneously until the failure occurred.

For temperature measurements, a total of thirty nine, type-K, 24 gauge thermocouples were installed at nine different cross sections along the beam length as shown in Figure 4. Four plate thermometers and a thermal imaging camera were installed to supplement the temperature data of the specimen. The vertical and lateral

[§] The standard uncertainty (u_c) is estimated based on the certified material test report provided by steel fabricator and the assumption of uniform distribution. The numbers following the symbol ± are the expanded uncertainty (U) with a level of confidence of approximately 95%.

displacements of the beam specimen in the fire-exposed zone were measured using specially designed potentiometers with temperature compensation. Two rotational transducers were installed at the specimen ends to measure the rotations about the principal axes of the beam cross section. The digital image correlation method was also used to measure the three-dimensional strains in the fire-exposed zone of the specimen. Technical details of the high-temperature displacement and strain measurements were not presented in this paper for brevity and because they are still under development. In addition to four actuators to apply and measure the structural loads, a 222 kN (50 kip) load cell were installed at each end of the beam specimen to measure the reaction forces during the test.

Test results

Figure 5 shows the test results including (i) the HRR data from the burner, (ii) the temperature data at the critical section (i.e., expected plastic hinge zone) of the specimen, (iii) the applied bending moment data, and (iv) the vertical displacement data at the fire-exposed midspan of the specimen. Note that the temperature data in Figure 5 are the average values of thermocouple readings of sections 5 and 6 only (Figure 4) and those of section 7 are not included as a result of flame lean during the test. The failed section was also located between the sections 5 and 6.

With the HRR-time relationship shown in Figure 5, the lower flange temperature reached steady-state at approximately 21 min. While the HRR of the burner was increased to 700 kW, no structural load was applied other than the self-weight of the specimen and the two water-filled HSS loading beam assemblies 16.7 ± 0.4 kN. The thermal gradient was developed through the cross sections, which resulted the thermal bowing about the strong axis.

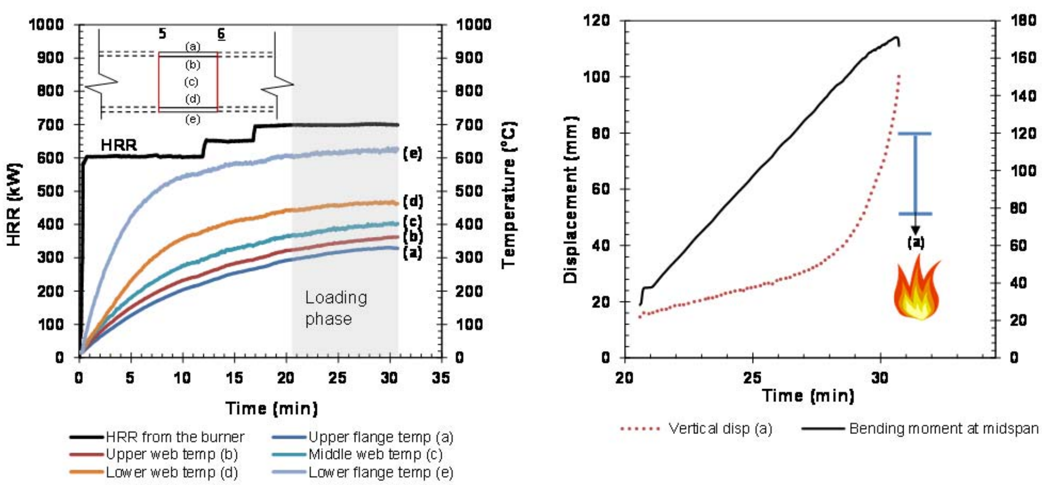

Figure 5. Fire-temperature and structural behavior of the beam specimen.**

** The temperature data has a maximum expanded uncertainty (U) of 34.0 ˚C calculated from a combined standard uncertainty (u_c) of 17.0 ˚C and a coverage factor of 2 (95 % confidence interval); The bending moment has U of 10.4 kN-m calculated from u_c of 5.2 kN-m and a coverage factor of 2. The vertical displacement data has U of 0.3 mm with a coverage factor of 2.

Under the loading phase where the HRR from the burner was maintained at a set point of 700 kW, the bending moment was applied at a rate of 14.7 ± 0.3 kN-m/min until failure occurred at approximately 31 min. The maximum temperature (at the lower flange at midspan) was 642 ± 28 ˚C, while the HRR was maintained at 700 kW. As shown in Figure 5, the vertical (downward) displacement of the beam specimen linearly increased with linearly increasing bending moments until the moment reached 124 kN-m (39 % of the plastic moment capacity at ambient temperature calculated using the plastic modulus in the steel manual [3]), then the nonlinear behavior was followed until failure. The increase in lateral displacements at midspan was also initiated at 124 kN-m. The measured peak moment capacity was 171 kN-m (54 % of the plastic moment capacity at ambient temperature) followed by runaway displacements. The failure was indicated by a sudden drop of the reaction force accompanied with rapidly increasing (runaway) displacements. As soon as the applied load and fire was removed, the beam specimen slightly bounced upward.

Figure 6 shows the photographs of the specimen at failure and the deformed shape of the specimen after cooling. Overall, when subjected to increasing flexural loads and the 700 kW fire, the beam specimen behaved in a complicated way that flexural bending and lateral torsional behavior were exhibited simultaneously.

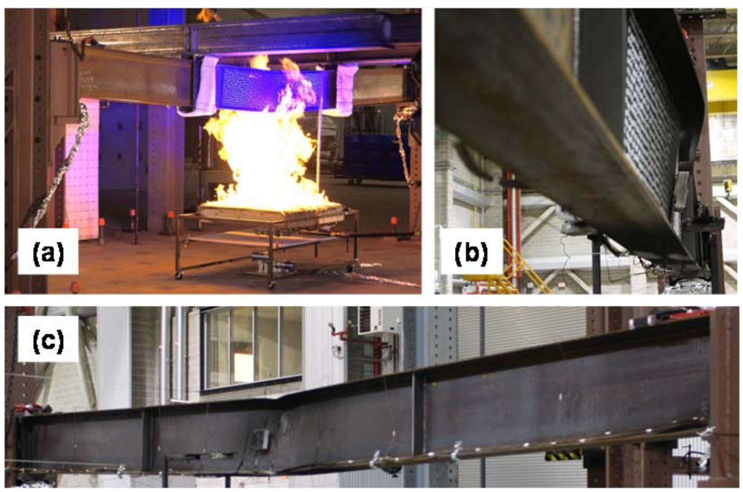

Figure 6. Photographs of (a) the beam specimen at failure, (b) the lateral-torsional deformation at the fire-exposed region, and (c) the beam specimen after cooling down.

SUMMARY

The open flame, localized fire tests were conducted on 6.17 m long W16×26 beams with simply supported boundary conditions. The experimental tests consisted of two parts: (1) fire-thermal tests to evaluate the effects of the prescribed heat release rates (HRR), provided by the 1 m × 1 m natural gas burner, on the thermal responses of the steel beam specimen and (2) structural-fire test to evaluate the effects of the localized fire on the behavior and the load-bearing capacity of the steel beam specimen. The cross sections at midspan (i.e., expected plastic hinge zone) of the beam specimen were directly exposed to a natural gas fire.

The test results indicated that the prescribed heat release rates from the burner affected the heating rate of the steel beam specimen. When the HRR-time relationship of the burner followed the step function with 100 kW increments approximately every 5 minutes, the temperatures at the fire-exposed region of the beam specimen increased linearly with increasing fire exposure time. When the HRR was set to a constant target magnitude of 400 kW, the specimen temperature indicated nonlinear heating to reach the steady-state condition. When the beam specimen was subjected to linearly increasing flexural loads at maintained HRR of 700 kW, combined flexural and lateral torsional failure of the specimen was exhibited. The peak moment capacity was achieved at 171 kN-m, which is 54 % of the plastic moment capacity at room temperature.

The test results from the present study can be used for developing or calibrating analytical models, which can be eventually used for evaluating the performance of structural members subjected to a localized fire. The findings from this study are limited to the range of parameters included in the tests. Further evaluation on the effects of various boundary conditions (axial and rotational restraints) and heating rates on the fire performance of the beam specimens are currently on going.

ACKNOWEDGEMENT

The research presented in this paper was carried out under the NFRL Infrastructure and Commissioning project which seeks to deliver a fully operational NFRL, including outfitting of laboratory infrastructure and verifying operation and calibration of individual and combined fire and structural systems. We thank our colleagues Matthew Bundy, Anthony Chakalis, Artur Chernovsky, Leaurean DeLauter, Matthew Hoehler, Doris Rinehart, Brian Story, Christopher Smith, Nelson Bryner, and Jian Jiang who provided insight and expertise that greatly assisted the experimental research at NFRL or helped to improve the paper.

REFERENCES

1. Bundy, M., Hamins, A., Gross, J., Grosshandler W., Choe, L. 2016. "Structural Fire Experimental Capabilities at the NIST National Fire Research Laboratory," *Fire Technology.,* pp. 1-8, doi:10.1007/s10694-015-0544-4.
2. ASTM International. 2015. "Standard Specification for Structural Shapes," Standard A992, ASTM International, W. Conshohocken, Pa.
3. AISC. 2010. Steel Construction Manual, 14th edition, American Institute of Steel Construction (AISC), Table 1-1, Chicago, IL
4. Bryant, R., Bundy, M., Zong, R. 2015. "Evaluating Measurements of Carbon Dioxide Emissions Using a Precision Source—A Natural Gas Burner," *J. the Air & Waste Management Association*, 65(7), pp, 863-870. doi: 10.1080/10962247.2015.1031294.

3D FEA of Load-bearing Cold-formed Steel Wall Systems with Web-perforated Studs Subjected to Standard Fire

SHIJUN YANG and LEI XU

ABSTRACT

Presented in this paper is a study using finite element (FE) analysis to investigate the thermal and structural performance of CFS load-bearing walls with C-shape studs with web perforations subjected to standard fire. Sequentially coupled 3D FE thermal-stress analysis is carried out in which the heat transfer analysis is conducted to obtain the temperature distribution of an entire CFS wall. In the subsequent structural analysis, a CFS wall frame rather than a single stud is modeled to achieve system-level structural responses. The axial force at the bottom end of the stud is used to predict the failure of the wall. The finite element analysis (FEA) results are compared with that from two full-scale fire tests.

INTRODUCTION

Load-bearing cold-formed steel (CFS) wall systems are commonly constructed with CFS C-shape studs with one or two layers of fire-rated sheathing attached to both sides. In practice, perforations are placed in stud web to accommodate the passage of utilities or to install intermediate braces. Full-scale standard fire tests on laterally braced load-bearing CFS walls found that local buckling occurred at web perforations, together with global buckling of the stud [1]. Local buckling was also observed at web-perforated regions by other tests [2, 3]. In a standard fire test, the wall studs are subjected to non-uniform temperature distribution which results in both axial and bending stresses. The presence of web perforations may be detrimental to the structural stability of the studs and consequently to the integrity of the walls. As full-scale fire tests can be expensive and time-consuming, employing advanced numerical tools such as FEA is a viable alternative to investigate the performance of CFS load-bearing walls subjected to standard fire.

Shijun Yang, Research Assistant (corresponding author), University of Waterloo, ON, N2L 3G1, Canada; s82yang@uwaterloo.ca
Lei Xu, Professor, Canadian Cold-Formed Steel Group, University of Waterloo, ON, N2L 3G1, Canada; lxu@uwaterloo.ca

For CFS load-bearing walls with non-web perforated C-shape studs, the acceptability of using finite element modeling to characterize the structural responses has been validated by full-scale fire tests [4, 5]. In these studies, the CFS walls were simplified using a single stud model for stress analysis and temperature distributions used in the analysis were obtained from tests. Although the structural responses obtained from the single stud model were appeared to be acceptable, the system effect, such as the possible redistribution of load between studs was not considered. It is also noted that the abovementioned investigations assumed that temperature distributions to be bilinear or linear along the web depth as shown in Figure 1. For CFS walls with web-perforated studs, the validity of such simplification is yet to be investigated. Presented in this paper is a sequentially coupled 3D FE thermal-stress analysis for evaluating the performance of CFS load-bearing walls with web-perforated CFS C-shape studs subjected to standard fire.

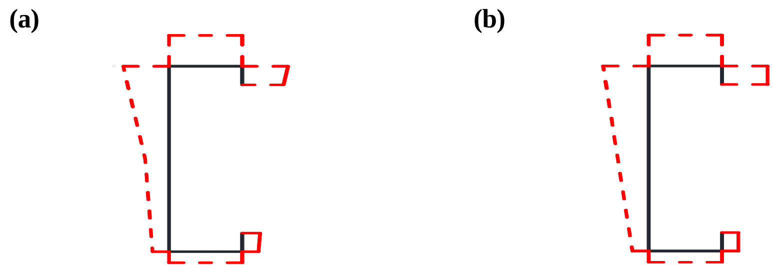

Figure 1. Temperature distribution in non-web perforated CFS studs: (a) simplification [4], (b) simplification [5].

FINITE ELEMENT MODELING

In this study, FEA is carried out using software ABAQUS [6]. Sequential coupled thermal-stress analysis, that is, a thermal analysis followed by a stress analysis is employed. Nodal temperatures from the thermal analysis are used as a predefined boundary condition on the structural model. The stress analysis is carried out by first applying axial target loads and then exposing the wall to the standard fire. Material properties at elevated temperature are used. The axial force at the bottom end of studs is used to determine the failure time. Results from FEA are compared with results of two full-scale load-bearing CFS wall tests [1].

Description of experiments

Shown in Figure 2 are the configuration details of the two test specimens [1]. The overall dimension of the specimens is 3550 mm by 3200 mm. The specimen LBW-2 is sheathed with a double layer of 12 mm thick Type X gypsum board on both sides and the other LBW-3 with a double layer of 12 mm Type C gypsum board on both sides. The 150 mm deep wall cavities are filled with 90 mm thick glass fibre on the fire side. Seven C-shape CFS studs (150 mm×40 mm×15 mm×1.5 mm) are evenly spaced 600 mm o.c., except for the rightmost stud which is spaced 550 o.c. Five slotted web perforations (38 mm×130 mm) along the length of each stud are evenly spaced 640 mm o.c. An additional CFS stud is placed on each end of the CFS frame to eliminate the gap between the specimen and the test frame in which the specimen is mounted so as to prevent lateral sway. The top and bottom ends of these studs are connected with U-shape CFS track (150 mm×50 mm×1.5 mm). The CFS frames are laterally braced with a horizontal bridge at mid-height. The CFS studs, tracks and bridging are fabricated from Z345 cold-formed galvanized steel sheets.

Shown in Figure 3 is the experimental setup. The target load was applied first and maintained throughout the fire test. The target load of 26.5 kN/m was applied axially to the specimens through ten jacks and maintained throughout the test. These jacks were connected to the same hydraulic pump and were spaced 310 mm along a 3470 mm long loading beam. A propane fired gas furnace was used to expose one side of the wall to the ISO 834 time-temperature fire curve [7]. Eight type K thermocouples were installed to measure the temperature development of the gypsum board surface on the ambient side.

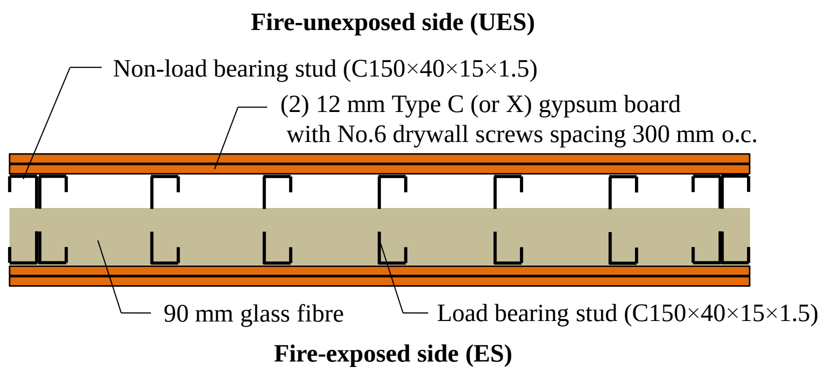

Figure 2. Configuration of load-bearing CFS wall specimens.

Figure 3. Experimental setup.

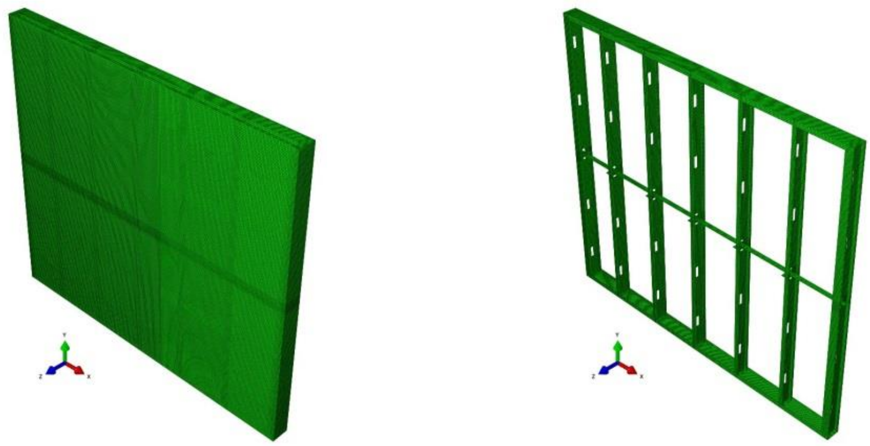

Figure 4. Finite Element Mesh: (a) gypsum board and glass fibre, (b) CFS frame.

Finite element thermal analysis

The gypsum boards and glass fibre are modeled using 8-node continuum solid elements (DC3D8). The steel studs, bottom and top tracks, and mid-height bridging are simulated with 4-node shell elements (DS4). The DC3D8 and DS4 are elements that have only temperature degrees of freedom. For the reasons of simplification of FE mesh, the thickness of glass fibre used in this analysis is taken as 94 mm, rather than 90 mm in the test; and rectangular web perforations (38 mm×150 mm) are adopted to simulate the slotted perforations in the specimens. No thermal contact resistance between adjacent elements is assumed [8]. Double layers of gypsum boards on both sides and glass fibre within the cavity are merged into one instance, whereas the intersecting boundaries are retained. By doing this, tie constraints between contact surfaces can be reduced so as to improve computational efficiency; also, material properties can be assigned to gypsum board and glass fibre individually due to the existence of intersecting boundaries. The temperature degree of freedom between all the contact surfaces between elements is tied. Shown in Figure 4 are the FE meshes of the test specimens. A global mesh size of 15 mm is used, and local seeds are assigned. As a result, the meshes between different elements are compatible with one another. Heat transfer through solid materials is considered as conduction, and on the fire-exposed and unexposed sides and within a cavity is described as a combined radiation and convection. The convection in the cavity is neglected at elevated temperatures. A convection coefficient of h = 25 W/m^{2}K and 10 W/m^{2}K is used on the fire-exposed side and the unexposed side, respectively. Relative emissivity is taken as 0.9 for gypsum board surfaces and 0.6 for steel stud surfaces within the cavity. The CFS walls are exposed to the standard fire curve defined by ISO 834 for up to 240 minutes. The measured thermal properties of glass fibre reported by [9] and for Type C and Type X gypsum board and steel reported by [10] are used. The parameters, including thermal conductivity, specific heat, and density, vary as functions of temperature are defined.

Finite element structural analysis

Unlike the FE models from [5], which simulated CFS walls using a single simple-supported stud, the 3D FE model developed in this study includes all the steel components of CFS frame except for the bottom track. In such way, stress redistribution within the members can be simulated. In addition, it is important to consider the restraining effect associated with the gypsum to against possible lateral torsional buckling and distortional buckling of CFS wall studs. Due to lack of the material properties of gypsum board at elevated temperature over 800 ^{o}C, similar to that reported in [5], the FE model does not include gypsum board sheathing in this study. However, the restraints associated with gypsum board are modeled by restraining the horizontal displacement (UX) at the locations of screws. As to glass fibre filling, its contribution of delay to the temperature rise is modeled in the thermal analysis, but the effect of glass fibre swelling is disregarded in the stress analysis. In this study, swelling of glass fibre may not have much effect on CFS studs as there is about 50 mm space in the wall cavities since the stud depth is 150 mm but the thickness of glass fibre is only 90 mm.

To incorporate nodal temperatures into sequential stress analysis, the location of each node in the FE mesh should be consistent with that of the thermal analysis. The finite element meshes of the structural model are the same as those of the heat transfer model, for which correlation is required to import the heat transfer results. The time period of the step specified is 14400 (240 minutes). The maximum number of increments is 200. The initial increment size is 30, whereas the minimum and maximum increment size is 1×10^{-9} and 300, respectively. The stress analysis is carried out subsequently to investigate fire resistance of CFS walls. The CFS frame is also modeled with a 4-node shell element with reduced integration (S4R) in structural analysis. The contact interaction between the webs of the two studs on each end of the CFS frame is hypothesized to be frictionless and the hard contact is selected for the normal direction behavior. The tie interaction is defined to model the contacted surfaces between the loading beam and top track of the CFS frame, and the locations of nodes are where screws placed. The spring/dashpots are defined to simulate the contact relationship between the track web and stud ends. All the three translational displacements associated with the bottom end of the stud, i.e. UX, UY and UZ, are restrained. The horizontal displacements of the web of the top track, UZ, are restrained. The lateral restraint provided by the test frame is simulated by restraining the corresponding lateral displacement (UX) of the bracing stud on each end of the CFS frame. The axial loads are applied evenly to eight nodes at the locations of the ten jacks to prevent the composed loading beam from local failure. The material properties including thermal expansion of cold-formed steel at elevated temperature are assumed to follow as those specified in EC3 part 1.2 [11].

COMPARISON WITH TEST RESULTS

Shown in Figure 5 is the temperature contour of specimen LBW-3 obtained from FEA. The higher temperature is represented by red color whereas the lower temperature is depicted by blue one. The temperature difference between the top and bottom of the frame is not observed since the convection in the height direction, namely, hot air rises and cold air sinks, is not considered in this study. Thermal bridge occurs since cold-formed steel has significantly higher heat conductivity than the surrounding materials. Due to the presence of perforations in the stud web, the heat transfer around perforations is interrupted. As a result, the temperature of the cross-section at the location of web perforation is higher on the hot side and lower on the cold side compared with that at the location there is no web perforation as shown in Figure 5(b).

Illustrated in Figure 6 is a comparison of the temperature profiles of gypsum board surfaces on the unexposed side obtained from the FEA results and the tests [1]. Good agreement is achieved between the results of the FEA and tests. The maximum temperature on gypsum board surfaces on the unexposed side at failure is less than 100 ^{o}C, which indicates that the specimens fail by structural instability as reported in [1].

Shown in Figure 7 is the structural response of specimen LBW-2 obtained from FEA. Presented in Figure 7(a) is the predicted failure mode of specimen LBW-2. It demonstrates that the wall fails by a significant lateral movement towards the furnace, and meanwhile local buckling at the bottom web perforation is also observed. The detail views are the stress contour in the circled region of Figure 7(a) at different fire-exposure time. At ambient temperature (0 minute's exposure to fire), the full section of the stud is under compression resulted from the applied load, and higher stress is observed at the location of the web perforation. As fire-exposure time increases, the temperature in studs rises accordingly so that the stiffness and strength of the studs reduce. At elevated temperature, non-uniform temperature distributions vary through the cross sections, inducing bending in the studs due to effects of neutral axis shifting and thermal bowing. At the web perforation, the stress on the hot side reaches the yield stress first. Local failure occurs on the hot side at about 34 minute's exposure to fire. Soon after that, the stress on the cold side reaches yield stress at about 37 minute's exposure to fire. As temperature further increases, the specimen fails at about 82 minutes. Additionally, no in-plane lateral sway of the whole specimen is observed due to sufficient restraints provided by gypsum board and the non-load-bearing stud at each end of the frame. Illustrated in Figure 7(b) is the average axial displacement of all the loaded nodes of top track plotted as a function of fire exposure time. It indicates that the frame is shortened at ambient temperature when the load is applied but subsequently elongated at elevated temperature due to thermal expansion.

At the end of the analysis, the axial reaction forces, RF2, at the bottom ends of the second stud on the left drop rapidly, indicating the frame can no longer sustain the applied load at this time. The ratios of the failure time from FEA over that of the tested

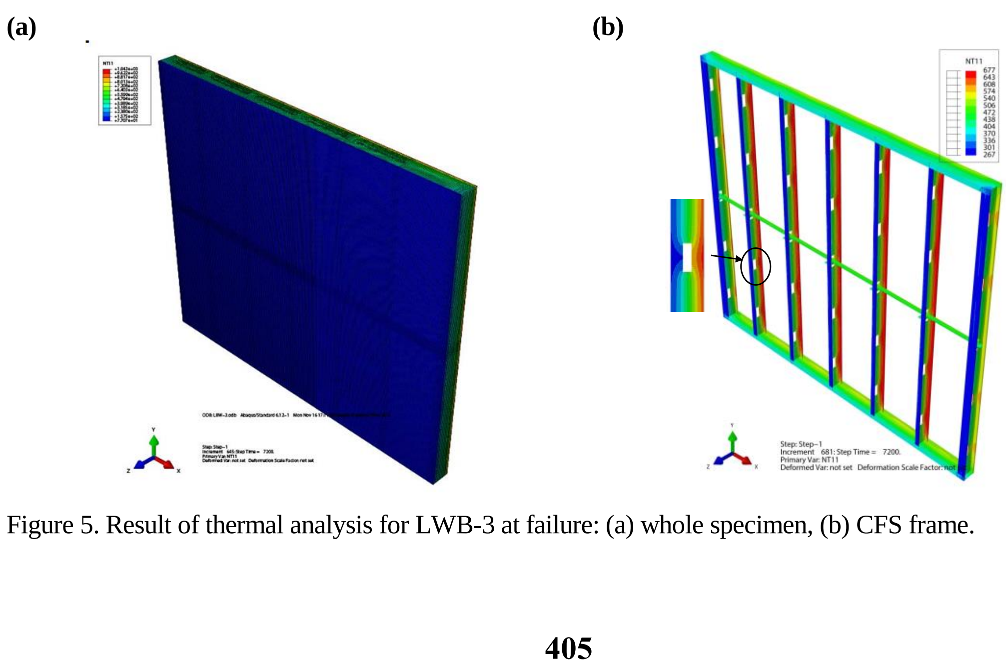

Figure 5. Result of thermal analysis for LWB-3 at failure: (a) whole specimen, (b) CFS frame.

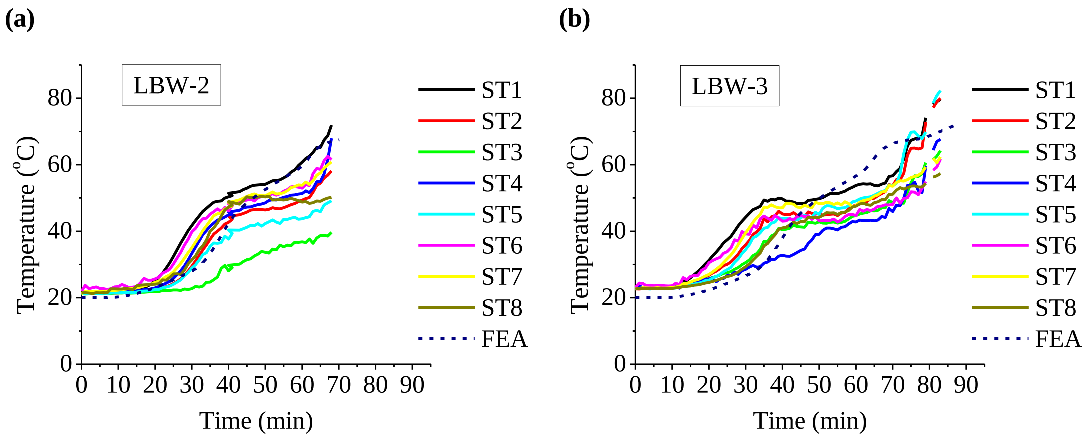

Figure 6. Comparison of temperature on fire-unexposed side: (a) LBW-2, (b) LBW-3.

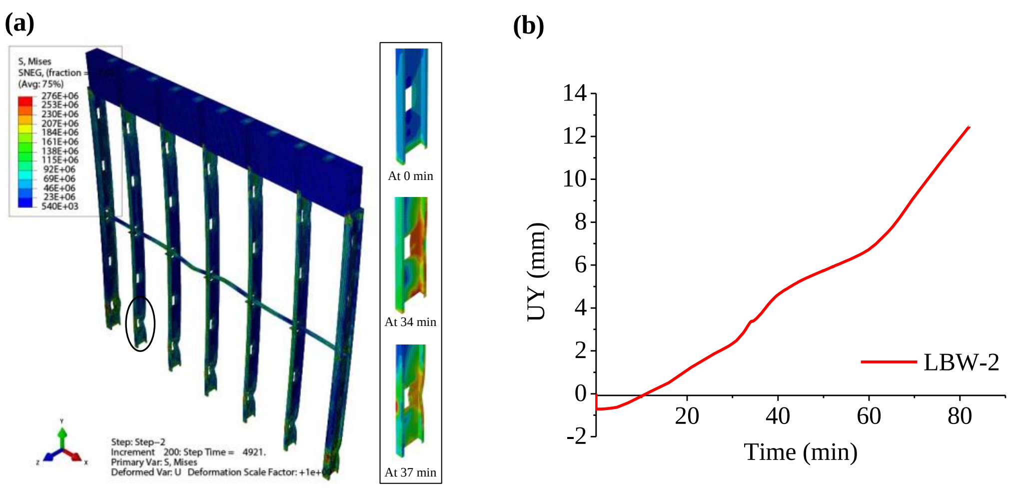

Figure 7. Result of structural analysis of LBW-2: (a) failure Mode, (b) axial displacement versus fire expose time.

specimens LBW-2 and LBW-3 are 1.13 and 1.10, respectively. In general, the results obtained from the 3D FE model developed in this study match well with that of the tests. But it is noted that the failure time predicted FEA is highly depended on the nodal temperatures incorporated from the heat transfer analysis; therefore, the accuracy of the nodal temperature is crucial for the evaluation of the performance of CFS load-bearing wall subjected to elevated temperature.

CONCLUSIONS

A sequentially coupled 3D FE thermal-stress analysis is proposed for evaluating the performance of load-bearing CFS walls with C-shape web-perforated studs subjected to the standard fire. The predicted temperature profiles and the failure time are compared with the tests. It is concluded that the models developed in this study are valid and can be applied to investigate the behavior of CFS walls subjected to elevated temperature. The nodal temperature obtained from the heat transfer analysis is critical to the accuracy of the structural response of CFS load-bearing walls; therefore, wall assembly details, such as cavity insulation, web perforation and bridging, which may influence the temperature distributions of CFS C-shape studs, should be accounted for in the modeling.

REFERENCES

1. Xu, L. 2011. Internal report of W-IBS system load bearing wall fire test, Worthington Construction Group.
2. Alfawakhiri, F. 2002. "Behaviour of cold-formed steel framed walls and floors in standard fire resistance tests", PhD thesis, Carleton University, Ottawa, Ontario, Canada.
3. Feng, M., & Wang, Y. C. 2005. "An experimental study of loaded full-scale cold-formed thin-walled steel structural panels under fire conditions," *Fire safety journal*, 40(1), 43-63.
4. Zhao, B., Kruppa, J., Renaud, C., O'Connor, M., Mecozzi, E., Apiazu, W., Salmi, P. 2005. "Calculation rules of lightweight steel sections in fire situations," France: European Communities.
5. Gunalan, S., & Mahendran, M. 2013. "Finite element modelling of load bearing cold-formed steel wall systems under fire conditions," *Engineering Structures*, 56, 1007-1027.
6. HKS, ABAQUS Standard User's Manual Version 6.12, Hibbit, Karlsson & Sorensen Inc., USA, 2012.
7. ISO 834-1 1999. "Fire resistance tests – elements of building construction - Part 1: general requirements," International Organization for Standardization, Geneva, Switzerland.
8. Feng, M., Wang, Y. C., & Davies, J. M. 2003. "Thermal performance of cold-formed thin-walled steel panel systems in fire," *Fire safety journal*, 38(4), 365-394.
9. Keerthan, P., & Mahendran, M. 2012. "Numerical modelling of non-load-bearing light gauge cold-formed steel frame walls under fire conditions," *Journal of Fire Sciences*, 0(0) 1-29.
10. Mehaffey, J. R., Cuerrier, P., & Carisse, G. 1994. "A model for predicting heat transfer through gypsum-board/wood-stud walls exposed to fire," *Fire and Materials*, 18(5), 297-305.
11. Eurocode 3. 2005. "EN1993-1-2: The European Standard; Part 1-2: General rules - Structural fire design," European Committee for Standardization, Brussels, Belgium.

Experimental and Numerical Analysis of Cold-Formed Steel Columns at Both Ambient Temperature and Simulated Fire Conditions

HELDER D. CRAVEIRO, JOÃO PAULO C. RODRIGUES and LUIS M. LAIM

ABSTRACT

Cold-formed steel profiles with a wide range of cross-section shapes are commonly used in building construction as structural elements. Also the use of built-up members has increased significantly, however, so far, its design is only briefly addressed in the current design codes, such as EN 1993-1-3 [1]. Regarding fire behavior of built-up structural members the research is still scarce, especially if the influence of restraining to thermal elongation provided by the surrounding structure is considered. Taking into account the current limitations it was intended to conduct a large experimental campaign in order to assess the behavior of single and built-up cold-formed steel columns at both ambient temperature and simulated fire conditions with restraint to thermal elongation. In this paper some of the most relevant results as well as the finite element models developed to accurately reproduce the behavior of cold-formed steel columns are presented.

INTRODUCTION

Nowadays, built-up cold-formed steel (CFS) structural members are widely used in building construction. A built-up structural member can span more distance, present higher load bearing capacity and higher torsional stiffness. Moreover, usually built-up members are symmetric, eliminating eccentricities between shear and gravity centers, leading to higher member stability. Compound cross-sections are built using self-drilling screws or by seam weld [2, 3, 4]. At ambient temperature some studies concerning the assessment of the ultimate load carrying capacity were already conducted [2, 3, 4].

Design guidelines in the EN 1993-1-3 [1] for built-up members are still vague. For instance the EN 1993-1-3 [1] only predicts that the buckling resistance of closed built-up members should be determined using the buckling curve *b* in association with the basic yield strength f_{yb}, and buckling curve c in association with the average yield strength f_{ya} provided that $A_{eff} = A_g$. In fire situation the design methods presented in the EN 1993-1-2:2005 [5] for hot-rolled steel members are also applicable to cold-formed steel members with class 4 cross-sections. Also the EN 1993-1-2:2005 [5] for class 4 cross-sections limits the critical temperature to 350ºC. Moreover, there are no specific design guidelines regarding the influence of restrained thermal elongation in the overall behavior of CFS columns in fire. Several studies on this matter were already conducted but for heavy hot-rolled steel columns [6, 7]. However, regarding built-up CFS columns in fire, considering the influence of restrained thermal elongation, research is still very scarce. In this paper the most relevant results on the behavior of CFS columns at both ambient and simulated fire conditions are presented. Based on the experimental results, finite element models were developed in order to accurately reproduce the behavior of CFS columns at both ambient and fire conditions with restrained thermal elongation.

EXPERIMENTAL TESTS AND PROCEDURE

The designed and built experimental test set-ups, for both ambient temperature and fire tests with restrained thermal elongation are briefly described in this chapter.

In this experimental campaign fire resistance tests and buckling tests at ambient temperature on four cross-section shapes were tested, namely single (C), open built-up (I) and two closed built-up cross-section (R and 2R) (L=2.95 m) (Figure 1).

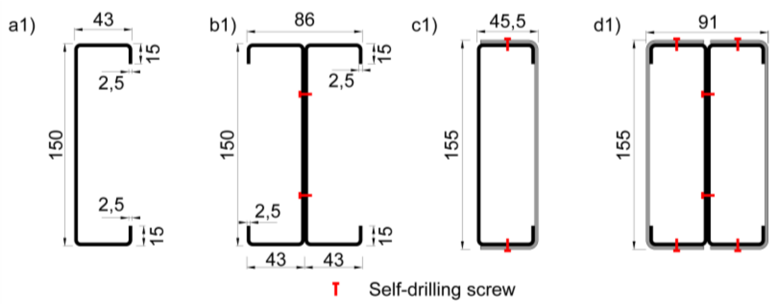

Figure 1. Tested cross-sections. a1) C. b1) I. c1) R. d1) 2R.

For the buckling tests at ambient temperature, the experimental test set-up comprised a 2D reaction steel frame (1), a concrete footing (2), the designed end-support devices (3), load cell used to measure the applied load (4), the hydraulic jack (5) used to apply the load to the CFS column and a data acquisition system (Figure 2a)). The concrete footing was specifically designed and fabricated for this experimental campaign. To the concrete footing two steel plates were fixed. The hydraulic jack was connected to the top steel plate of the concrete footing. To the piston of the hydraulic jack a new set of steel plates were fixed, and to these steel plates the end-support devices were connected. Additional steel plates were placed around the loading system in order to prevent any type of rotations during loading. In these tests both pinned and fixed end-support conditions were tested, in order to assess lower and upper bounds of the buckling load of the tested columns. The loading was applied under displacement control. Twenty four tests were conducted (3 repetitions for each test condition).

For the fire tests with restraint to thermal elongation (Figure 2b)) the test set-up comprised a two dimensional reaction steel frame (1) and a three dimensional restraining steel frame consisting of four columns, two top and two bottom beams (2) placed orthogonally, used to simulate the stiffness of a surrounding structure to the CFS column subjected to fire. In these experimental tests two restraining frames were used in order to study the influence of different values of stiffness of the surrounding structure to the CFS column (axial stiffness of 3 and 13 kN/mm). The compressive load, was applied using the hydraulic jack (3). The constant compressive load corresponded to the serviceability load (30 and 50% of the design buckling load, $N_{b,Rd}$) applied to the CFS column with the hydraulic jack (3) fixed to the reaction frame (1) and with the nuts of the threaded rods loosened (free body vertical movement of the top beams of the restraining frame) guaranteeing that the compressive load was totally transferred to the CFS column.

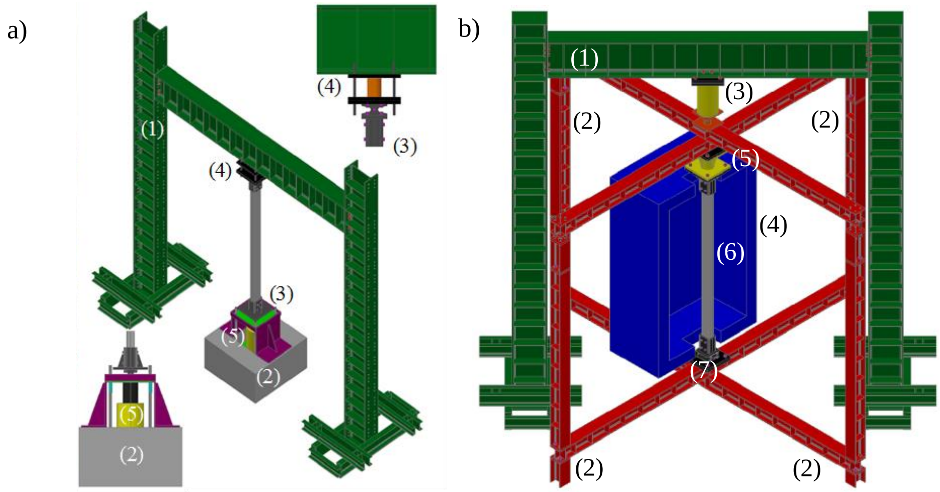

Figure 2. Schematic view of the experimental test set-ups. a) Test set-up for buckling tests at ambient temperature. b) Test set-up for fire tests with restraint to thermal elongation.

The applied service load was controlled by a load cell placed between the top beams of the restraining frame and the hydraulic jack. Reaching the serviceability load defined, the nuts of the threaded rods were tightened (vertical rigid body movement of the top beams was blocked) and from that moment the restraining frame started to exert axial and rotational restraint to the CFS column being tested in fire (6). To measure the restraining forces generated on the testing column during the heating process a special device was built ((5) in Figure 2 b)), consisting of a hollow steel cylinder where a stiff steel cylinder Teflon (PTFE) lined slides through it. On the top of the stiff steel cylinder a 500 kN load cell was placed and compressed against the top end plate of the hollow steel cylinder. In these tests, temperature evolution in different points of the cross-section and along the length of the column were monitored, as well as loads and axial and lateral displacements. Ninety-six tests were conducted. Four different cross-section shapes (C, I, R and 2R), two end-support conditions (pinned and semi-rigid) and two levels of restraint to thermal elongation (3 and 13 kN/mm; K1 and K2 for pinned conditions, K3 and K4 for semi-rigid conditions) provided by the surrounding structure. For each one of the defined test conditions, three repetitions were performed.

NUMERICAL ANALYSIS

Based on the observed behavior and obtained results, finite element models were developed in order to accurately reproduce the behavior of CFS columns at both ambient temperature and simulated fire conditions with restraint to thermal elongation.

In this chapter a brief description of the finite element models, developed using the commercial software package *Abaqus* [8], is presented.

Shell elements are commonly used to model thin-walled structural elements. The S4R element was used to model the steel profiles. Regarding the self-drilling screws, the finite element chosen was the C3D8R.

The material modelling was based on the mechanical and thermal properties of the S280GD+Z steel determined on the experimental tests conducted in the scope of this research. Yield strength, elastic modulus and the stress-strain curves that were determined at both ambient temperature and elevated temperatures up to 800ºC. The stress-strain curves used as input were converted to true stress and logarithmic plastic strain. In Figure 4 the stress and logarithmic plastic strain curves used as input in the finite element model is presented, as well as the relative thermal elongation determined in experimental tests conducted in the scope of this research [9]. Thermal properties were also determined experimentally using the Transient Plane Source Technique [9]. Residual stresses were not included in the developed finite element models.

The accuracy of the finite element model is governed by the mesh size. Hence a sufficiently fine mesh shall be used. However, computational resources are limited and it is often necessary to assess the adequate mesh size in order to obtain accurate results with adequate computational times. A mesh size of 5 mm × 5 mm was adopted.

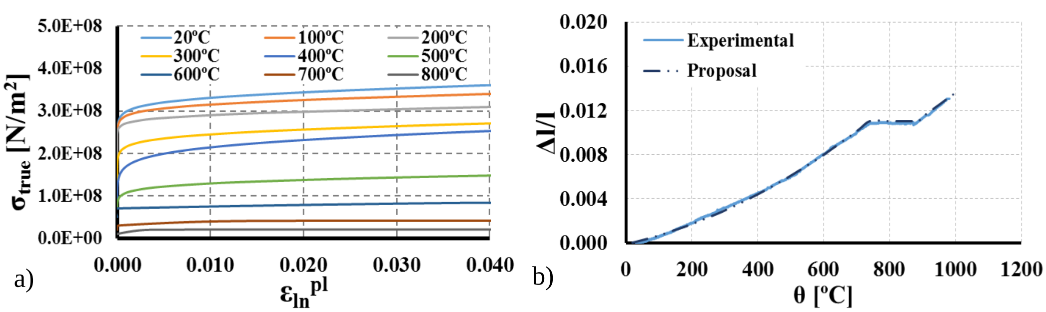

Figure 4. a) Logarithmic plastic strain curves for the S280GD+Z. b) Relative thermal elongation.

In order to reproduce accurately the behaviour of CFS columns observed in the experimental tests appropriate boundary, loading and contact conditions, for single and built-up cross-sections, must be defined in the finite element model. Using the capabilities of the software Abaqus, hinges, acting as rotational springs, were considered in the boundary conditions of the finite element model. The surrounding structures used in the experimental tests replaced by linear springs (3 and 13 kN/mm) connected to the centroid of the column to be simulated.

Contact between the CFS profiles and between profiles and self-drilling screws was modelled assuming a tangential friction coefficient of 0.2 for the contact behaviour in tangential direction and a hard contact for the contact behaviour in normal direction between the profile surfaces. The *surface-to-surface* contact was used considering the *finite-sliding* tracking method to model the interaction between the surfaces of the individual profiles. For the contact between CFS profiles and self-drilling screws a *rough and hard contact* was also used.

To simulate ambient temperature tests displacement loading control was used in the numerical simulations. For the fire tests load control was used to apply the serviceability load defined for each column. The monitored temperatures in the cross-section and along the length of the column were used as input in the validation process of the finite element model. Influence areas were defined for each thermocouple and its temperature evolution, as a function of time, was allocated to the defined influence area.

Two different types of analysis were conducted by using the developed finite element model, namely elastic buckling analysis, to determine critical buckling loads and the associated buckling modes, and then a nonlinear static analysis. The buckling modes are then used to input the geometric imperfections in the nonlinear analysis. The adopted maximum value for global imperfections was *L/1000*, for distortional imperfections a value of *t*, and finally for local imperfections *h/200*. Finally, a structural analysis was undertaken in order to simulate the behaviour of CFS columns. In all structural simulations the nonlinear geometric parameter (*NLGEOM=ON) was active in order to deal with the geometric nonlinear analysis.

RESULTS

Buckling Tests at Ambient Temperature

Regarding the buckling tests at ambient temperature it was observed that the use of built-up cross-sections will ensure significantly higher values of buckling loads. As an example, the obtained results for fixed columns are presented and compared with the numerical results (*j*_FF_FEA) based on the developed finite element model. A very good agreement was obtained both in terms of the buckling load and vertical axial displacement. These results are depicted in Figure 6.

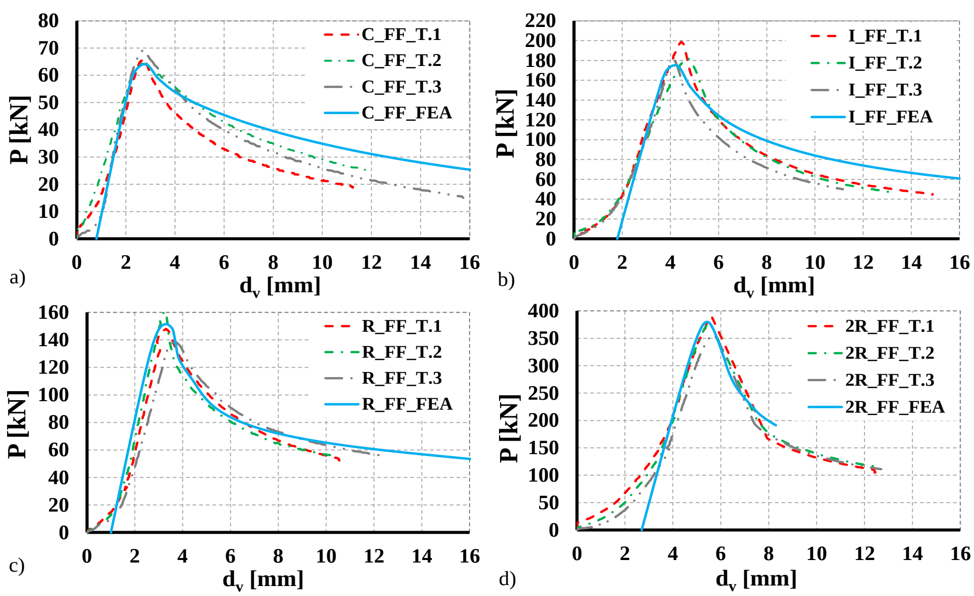

Figure 6. Comparison of FEA and experimental axial load vs axial shortening curves for all tested cross-sections and fixed-ended supports. a) C. b) I. c) R. d) 2R cross-section.

For instance, for fixed-end support condition, the buckling load of columns with 2R cross-section was 5.6 times higher than the buckling load of columns with lipped channels, 2.01 times higher than the buckling load of columns with open built-up I cross-section and 2.51 times higher than the buckling load of columns with closed built-up R cross-section. Comparing the buckling loads obtained in the experimental tests with the design predictions, based on the Eurocode, it was found that the design predictions were conservative for columns with a single lipped channel profile and generally unsafe for columns with built-up cross-sections (2 or more profiles). Increasing the number of profiles lead to unsafe predictions. The unsafe design predictions for built-up members may be due to inadequacy of the Effective Width Method to deal with built-up members. Also spacing of fasteners can influence the failure load. Additional experimental and numerical studies are needed and will be undertaken in order to address this topic. In Table 1 the mean values of the buckling load, obtained in the experimental tests, are compared with the design predictions, based on the EN 1993-1-3 [1]

TABLE I. MEAN EXPERIMENTAL VALUES AND COMPARISON WITH THE DESIGN BUCKLING LOAD DETERMINED ACCORDING TO THE EN 1993-1-3.

Test	$\bar{P}_{max}$ [kN]	$N_{b.Rd}$ [kN]	Test	$\bar{P}_{max}$ [kN]	$N_{b.Rd}$ [kN]	Test	$\bar{P}_{max}$ [kN]	$N_{b.Rd}$ [kN]	Test	$\bar{P}_{max}$ [kN]	$N_{b.Rd}$ [kN]
C_PP	26.9	24.8	I_PP	75.6	85.51	R_PP	70.0	76.55	2R_PP	253.88	379.07
C_FF	66.4	41.8	I_FF	187.0	187.7	R_FF	149.0	151.1	2R_FF	374.38	443.42

Fire Tests with Restraint to Thermal Elongation

The evolution of restraining forces is presented as a non-dimensional P/P_0 ratio in function of the mean temperature of the column ($\bar{\theta}_C$). In these graphs (Figure 7) it is possible to observe the expected behaviour of a column in a real structure as the effect of a surrounding structure was simulated with the 3D restraining frames. Due to the thermal action and since the column was axially restrained the restraining forces on the column started to increase whereas the mechanical properties of CFS degraded with the temperature increase. After reaching a maximum (P_{max}) the restraining forces (P) started to decrease reaching the initial service load applied (P_0) to the CFS column. This point defines the critical temperature (θ_{cr}) as the failure criteria in these experimental tests. In Figure 7 some test results are presented, specifically for the closed built-up R cross-section. The presented results are representative of the remaining tested conditions. Observing the obtained results the influence of the initial applied load is clear. Increasing the serviceability load from 30 to 50% $N_{b,Rd}$ critical temperatures and critical times decreased for all tested cross-sections. In terms of the imposed levels of restraint to thermal elongation to the CFS column it was found that increasing the level of the imposed restraint to thermal elongation the critical times and temperatures decreased.

It was clearly observed for every tested conditions that increasing the level of axial restraint to thermal elongation from 3 to 13 kN/mm the generated restraining forces increase significantly and the maximum value was reached for much lower mean temperatures. Also, it was observed that the magnitude of the generated restraining forces was higher for the lower initial load level. For instance, the average magnitude of the generated restraining forces ($P-P_0$) obtained for the R_SR_30LL_K3 tests was about 32.78 kN whereas for the R_SR_50LL_K3 tests was 25.33 kN.

All experimental results are presented in Figure 8. The critical temperature monitored for all tests is presented as a function of the ratio ($\alpha_k = K_{a.s}/K_{a.c}$ – non-dimensional axial restraint ratio) between the axial stiffness of the surrounding structure to the CFS column ($K_{a.s}$) and the axial stiffness of the CFS column ($K_{a.c}$). For isolated columns under fire conditions subjected to a low level of restraint to thermal elongation its failure is clearly controlled by temperature increase and by consequent degradation of mechanical properties of the S280GD+Z steel.

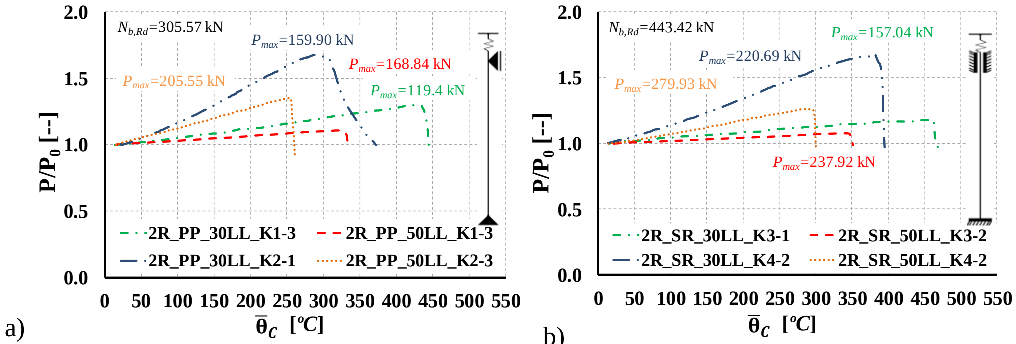

Figure 7. Comparison of FEA and experimental axial load vs axial shortening curves for all tested cross-sections and fixed-ended supports. a) C. b) I. c) R. d) 2R cross-section.

However, if an isolated column under fire conditions is subjected to high or very high levels of restraint to thermal elongation its failure may be controlled by the severity of the generated restraining forces during the heating phase. Consequently, buckling loads may be reached for lower temperatures. Moreover, assuming that the highest critical temperature occurs if the column can freely expand, it seems that critical temperature reduction is more significant for lower values of the ratio α_k. For higher values of α_k ratio the temperature decrease becomes smaller.

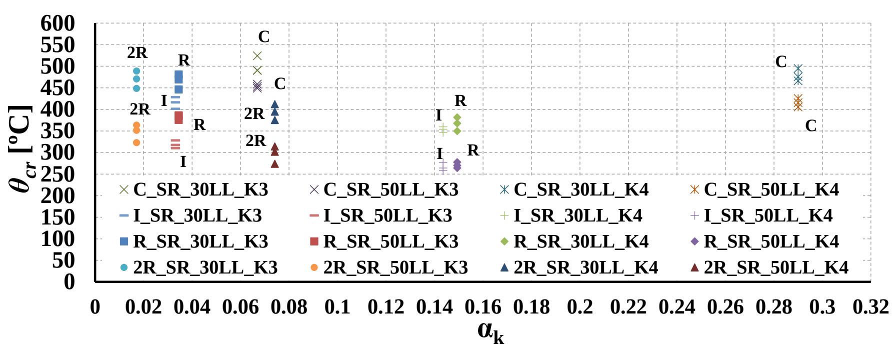

Figure 8. Variation of critical temperature (θ_{cr}) as a function of the non-dimensional restraint ratio (α_k) for columns with semi-rigid end-support condition.

In terms of the developed finite element model it was found that the numerical model is able to accurately reproduce the behavior of CFS columns in fire with restrained thermal elongation, provided that the mechanical and thermal properties determined in the scope of this investigation at both ambient and elevated temperatures are used as input. In Figure 9 some results, for columns with closed built-up R cross-section are presented. It is clear that the finite element model is in very good agreement with the obtained experimental results.

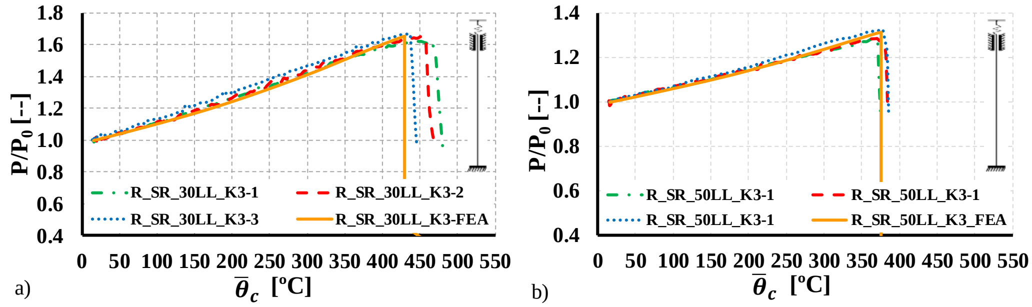

Figure 9. Comparison between experimental and FEA results for semi-rigid columns with closed built-up R cross-section.

CONCLUSIONS

In this paper a large experimental campaign on CFS columns at both ambient temperature and simulated fire conditions with restrained thermal elongation is reported. The developed finite element model is also described and the final results regarding the calibration process are presented.

In the buckling tests at ambient temperature the advantage of using built-up members was clear, since the increase in the buckling load was significant. In terms of the design predictions it was observed that increasing the number of profiles leads to unsafe results.

In the fire tests it was found that the interaction between the initial applied load and the imposed level of restraint to thermal elongation significantly influence the behavior of isolated CFS columns under fire conditions. When some level of restraint exists additional forces are generated, which may lead to premature collapse and consequently to lower critical temperatures. It seems that increasing the level of thermal restraint the failure of the columns may be controlled by the generated axial restraining forces whereas for lower levels of thermal restraint the failure is controlled by temperature increase and consequent degradation of the mechanical properties of the S280GD+Z steel. It seems that the higher temperature reductions, due to restraint, occur for lower values of α_k.

The developed finite element models are able to accurately reproduce the behaviour of CFS columns at both ambient and fire conditions with restrained thermal elongation provided that the mechanical and thermal properties determined in the scope of this research are used as input. Based on the developed and calibrated finite element models parametric studies shall be undertaken in order to propose new/improved design methodologies for CFS columns at both ambient temperature and simulated fire conditions, taking into consideration the influence of restrained thermal elongation.

REFERENCES

1. EN 1993-1-3:2004, Eurocode 3: Design of steel structures, Part 1-3: General rules, Supplementary rules for cold-formed members and sheeting, European Committee for Standardization, Brussels, Belgium, 2004.
2. Stone TA, Laboube RA. Behavior of cold-formed steel built-up I-sections. Thin-Walled Structures, 2005; 43 (12):1805-17.

3. Li, Y, Li, Y, Wang S, Shen Z. Ultimate load-carrying capacity of cold-formed thin-walled columns with built-up box and I section under axial compression. Thin-Walled Structures, 2014; 79: 202-217.
4. Wilson, R, Guzmán, A. Evaluation of the slenderness ratio in built-up cold-formed box sections. Journal of Constructional Steel Research, 2011; 67: 929-935.
5. EN 1993-1.2:2005 Design of steel structures. General rules. Structural fire design. European Committee for Standardization, Brussels, Belgium, 2005.
6. Franssen JM. Failure temperature of a system comprising a restrained column submitted to fire. Fire Safety Journal, 2000; 34: 19-207.
7. Ali, F., O'Connor, D. Structural performance of rotationally restrained steel columns in fire. Fire Safety Journal, 2001; 36: pp.:679-91.
8. Simulia. ABAQUS/CAE. v. 6.10-1. USA; 2010.
9. Craveiro, H.D., Rodrigues, J.P., Santiago, A., Laím, L., Review of the high temperature mechanical and thermal properties of the steels used in cold-formed steel structures – the case of the S280GD+Z steel, Thin-Walled Structures, 2016, Volume 98 Part A, pp.: 154-168.

Modeling Fire Induced Burnthrough Rupture of Marine Grade Aluminum Panels

CHRISTIAN RIPPE, BRIAN LATTIMER and SCOTT CASE

ABSTRACT

Burnthrough of aluminum plates subjected fire was experimentally and numerically explored. Experimental burnthrough was observed to occur below the material melting temperature and during thermal steady state leading to the development of a new creep rupture based burnthrough model. To characterize this behavior, a series of uniaxial, isothermal creep experiments were used in combination with published data. The creep rupture based burnthrough model was implemented in finite element models of the burnthrough experiments. Simulated burnthrough times were generally within 50% of experimental values. Much of this difference is attributed to the repeatability of the diffusion flame exposures which resulted in variations in experimental and simulated burnthrough times of up to 50%.

INTRODUCTION

The use of aluminum alloys is becoming more common in marine structure applications in both structural and nonstructural capacities. While aluminum alloys offer many advantages over traditional steel, including reduced weight and increased corrosion resistance, one drawback is aluminum's high temperature performance. The ramifications of this performance extends beyond a structure's ability to carry necessary loads. This performance also affects a structure's ability to contain localized fires and prevent fire propagation. One of the primary mechanisms of fire propagation through an aluminum structure is through fire induced burnthrough of overheads, bulkhead panels, and ventilation ducting.

Most existing fire induced burnthrough research has been limited to experimental observation and focused on the burnthrough performance of particular materials or assemblies [1]–[4]. While useful for evaluating the fire safety response of these assemblies, these do not aim to explore the burnthrough mechanism. Current software packages such as Fire Dynamics Simulator use simple temperature

Christian Rippe[1], Brian Lattimer[1], Scott Case[2]
[1]Jensen Hughes, Inc., 2270 Kraft Dr. Suite 1260, Blacksburg, VA 24060, U.S.A.
[2]Virginia Tech, 495 Old Turner St., Blacksburg, VA 24061, U.S.A.

thresholds to predict burnthrough but admit that these are not good predictors of fire induced burnthrough for varying exposure scenarios [5].

Much of the current research in burnthrough of metals is being conducted by the pipeline industry to predict welding induced pipeline burnthrough. Initial empirical rules based on temperature thresholds have been replaced in recent years by deflection, and then strain based burnthrough models [6]–[8]. These models are designed for a limited range of materials under short exposure durations (<10 s), thus creep strain effects of longer exposures has been neglected [8]. This research experimentally and numerically explores the mechanisms for fire induced burnthrough of aluminum plates. To do this, the rupture strain based models developed for weld induced burnthrough were adapted for used in fire exposure scenarios.

BURNTHROUGH EXPERIMENTS

Burnthrough tests were performed on horizontally oriented, 0.61 m by 0.61 m AA6061-T651 rolled plates exposed to a diffusion flame from a 0.3 m by 0.3 m propane sand burner. Plate thicknesses ranged from 0.79 to 6.35 mm. In this test apparatus, seen in Figure 1, plates were exposed to the flames from the burner directly beneath while thermography measurements were taken from the top of the plate. Plates were supported on screw tips along the perimeter of the plate with a 102 mm spacing. Walls 254 mm deep were placed along three sides of the plate to maximize the heat flux into the test plate.

On the exposed side, plates were coated with several optically thick layers of Rust-Oleum® flat black spray paint. This provided a high surface absorptivity (0.95) which maximized the energy flow into the plate. During initial experiments, the unexposed side of the plate was also coated. However, the increased radiation losses were preventing sufficient temperatures to initiate burnthrough using the burner and fire heat release rates possible in the lab. Subsequently, a pattern of squares was painted on the unexposed side to allow for non-contact infrared (IR)

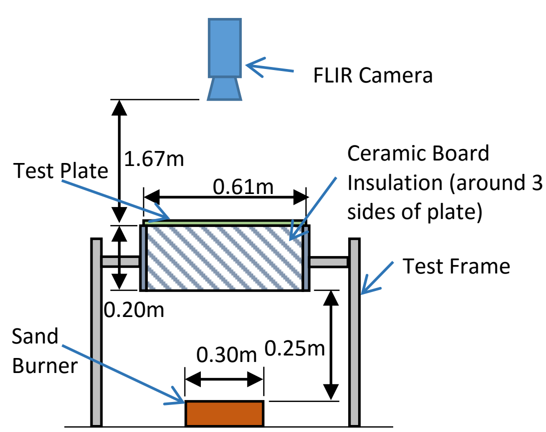

Figure 1. Experimental setup for burnthrough of AA6061 plates exposed to diffusion flame.

temperature measurement at select locations. These painted sections were large enough to obtain accurate surface temperature measurements, but small enough to minimize the additional radiative losses caused by the high emissivity of the paint.

A FLIR SC655 IR camera was used with the software package ExaminIR to conduct the thermography measurements on the unexposed side of the plate. The SC655 uses uncooled microbolometer type sensors with a wavelength measurement range of 7.5 to 14 μm. Environmental losses between the measurement surface and camera were approximated and accounted for within the ExaminIR software for the given ambient conditions at the time of testing. Thermographs were generated at frequencies between 0.5 and 5 Hz depending on the expected duration of the particular experiment.

Fire exposures were varied by changing the heat release rate of the fire. Tests were conducted at fire sizes ranging from 30 to 100 kW. Propane flow into the burner was measured and controlled using an Alicat MC-100 mass flow controller operated through a LabView interface. The flow controller has an accuracy of 0.20 slpm which corresponds to a heat release rate accuracy of 0.29 kW.

BURNTHROUGH MODEL

Experimentally observed burnthrough occurred at temperatures below the measured melting temperature (632°C) and even occurred at temperatures below the measured solidus temperature (600°C) for this alloy. Additionally, burnthrough was observed with the material at its steady-state temperature for a long period. This suggests that it cannot be captured using a solely thermally based mechanism, such as a melting temperature. The thermo-mechanical rupture mechanism was observed to be a function of both exposure time and exposure temperature which led to the application of a creep based rupture mechanism as seen in Figure 2.

Several different approaches have been developed for modeling the relationships between the creep rupture time, applied stress, and temperature of materials. Larson and Miller [9] developed a material specific relationship for predicting rupture of metallic materials. Similar relationships were also developed by Manson and Haferd [10] as well as Sherby and Dorn [11] using different basic assumptions. In this research, the Larson-Miller relationship was used to predict creep rupture. The Larson-Miller relationship involves the calculation of a temperature independent Larson-Miller parameter (LMP). The LMP is derived from

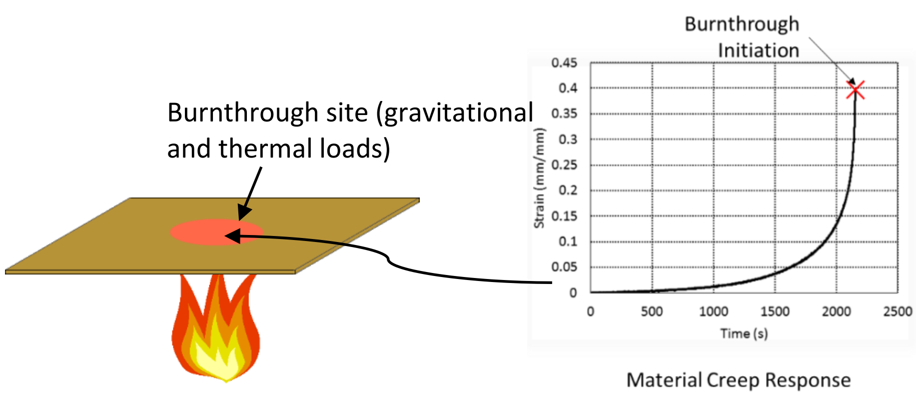

Figure 2. Proposed thermo-mechanical rupture mechanism for horizontally oriented (overhead) plate exposed to fire from underneath.

the integral of the steady state creep rate equation evaluated at rupture to obtain

$$LMP = T[log_{10}(t_r) + C]$$
where
$$LMP = Qlog_{\ 10}(e)/R \qquad (1)$$
$$C = log_{10}(\theta_r)$$

where T is the temperature, t_r is the creep rupture time, Q is the activation energy for the particular creep mechanism, R is the universal gas constant, and Θ_r is the temperature compensated rupture time. Additionally, it is assumed that the LMP is only a function of applied stress state. Using data from a series of uniaxial tensile creep tests, a LMP curve was generated for AA6061.

The Larson-Miller parameter relationship only exists for constant temperature and stress conditions. During a realistic thermal exposure, spatial and temporal temperature gradients within plates generate similar spatial and temporal stress gradients. To account for these variations, a Palmgren-Miner damage accumulation model was implemented to monitor the progress of a particular location to a burnthrough state through the use of a life fraction variable. This approach naturally leads to use in a time-discretized numerical model of the creep rupture mechanism. In this type of analysis, the life fraction evolution is calculated on a discrete time step assuming constant temperature stress conditions as

$$\Delta f = {}^{\Delta t}/_{t_r(\sigma,T)} \qquad (2)$$

where failure is defined when $f \geq 1$.

Finite Element Models

The creep rupture based burnthrough model was implemented into the commercial finite element (FE) code Abaqus 6.10 EF through use of user-subroutines. The FE models were then used to simulate the burnthrough experiments. The thermal and mechanical FE analyses was performed in a sequential approach assuming the thermal response is not dependent on the mechanical response, which is aligned with experimental observations prior to the onset of burnthrough.

Thermal models were developed using solid quadratic heat transfer elements (DC3D20). For all thicknesses, thermal models were conducted with in-plane meshes seeded at 30 mm and a single element through the thickness as this was found to accurately capture the spatial thermal gradients. Temperature dependent thermal properties were used in all analyses.

Spatially and temporally varying full-field discrete heat flux maps were generated for each of the exposures used in the burnthrough experiments using the IR thermography method from Rippe and Lattimer [12]. These heat flux maps were applied to the thermal models through a user heat flux subroutine. Natural convection heat transfer coefficient correlations by Sparrow *et al.* [13] were used during the generation of the heat flux map the calculation of the thermal response.

A surface emissivity of 0.95 was used for surfaces coated with high temperature paint while an emissivity of 0.5 was used for bare aluminum surfaces.

Once plate temperature predictions were generated using the thermal models, these were inserted into mechanical models to predict the stress response and burnthrough behavior of the plate. For all of the mechanical models, temperature dependent mechanical properties were used including thermal expansion, elasticity, plasticity with hardening, and creep. The creep model used in the analysis captured the material secondary and tertiary creep behavior [14].

All of the mechanical models were meshed using fully integrated solid quadratic elements (C3D20). Initial models used 5 elements through the plate thickness to capture the propagation of the burnthrough state. This was reduced the 3 elements through thickness as the burnthrough time was found to converge at this mesh density. In-plane meshes densities were biased towards the center of the plate such that an element aspect ratio of 1:1 between the in-plane and through thickness directions at the plate center existed and ratios of 1:10 existed at the corners. The models were found to be converged at these mesh densities.

Mechanical boundary conditions were applied to the model to mimic experimental conditions. Point boundary conditions were used to mimic the screw tips used to support the test articles during experiments. For all mechanical models, gravitational forces were prescribed on the plate via volumetric loads.

CREEP RUPTURE BEHAVIOR

Near melting creep rupture properties of AA6061-T651 plate were obtained from experimental uniaxial tensile creep test data by Rippe [15]. These tests were performed at temperatures between 500°C and 580°C and at stresses from 0.5 MPa to 5.0 MPa. This experimental data was combined with data from Kaufman [16] and Allen [17] to characterize the creep rupture behavior of the alloy over a large range of stresses and temperatures. Creep rupture time results are seen in Figure 3 in the form of the Larson-Miller parameter as calculated by Eq. (1). In order to calculate LMPs from the experimental rupture data, material activation energy and the value of the constant C are needed. Activation energy was calculated using a multi-variable, non-linear regression analysis of steady-state strain rate data from these experiments and experiments by Allen [17]. Activation energy for this alloy and creep mechanism was found to be 205 kJ/mol which is within 5% of values

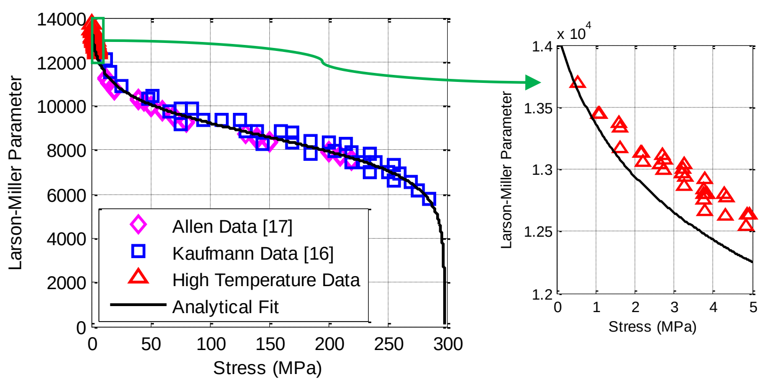

Figure 3. Analytical fit of experimentally measured creep rupture times combined with values from literature.

reported by Maljaars [18] for a similar alloy (T6060-T66).

Once the stress dependent LMP is calculated for a given material, the rupture time can be calculated by rearranging Eq. (1) as

$$t_r = 10^{\frac{LMP}{T} - C} \tag{3}$$

for any particular temperature and stress combination. Using existing high temperature data from Allen [17], the lower temperature data from Kaufman [16], combined with the low stress, high temperature data obtained here, a Larson-Miller curve was generated for AA6061. Non-linear regression was used to produce an analytical fit of the data in the form

$$LMP = C_1 \tanh^{-1}\left[\frac{2}{\sigma_{ul} - \sigma_{ll}}\left(\sigma - \frac{\sigma_{ul} + \sigma_{ll}}{2}\right)\right] + C_2 \tag{4}$$

where C_1=-1853, C_2=8611, σ_{ul}=298 MPa, and σ_{ll}=-0.76 MPa as seen in Figure 3.

RESULTS AND DISCUSSION

Figure 4 contains the typical observed experimental burnthrough site evolution. For all of the experiments, the appearance of visual surface damage occurred over 200 s before burnthrough initiation. Additionally, no evidence of molten material was observed for any tests. Temperature measurements in the vicinity of the burnthrough site are seen in Figure 5 along with model predictions. A comparison of experimentally measured and modeled burnthrough times is seen in Figure 6. Predicted and observed burnthrough times were higher for thicker plates due to the increased thermal mass as well as an increase in the lateral diffusion of thermal energy from the burnthrough site via conduction. Additionally, burnthrough times were reduced with increasing fire heat release rates and subsequent peak exposure heat flux.

Using the FE model results, the evolution of the life fraction, temperature, and

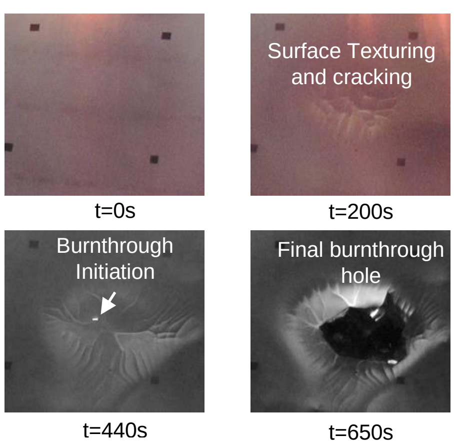

Figure 5. Burnthrough site evolution for horizontally oriented 3.18 mm thick plate exposed to 70 kW fire from sand burner.

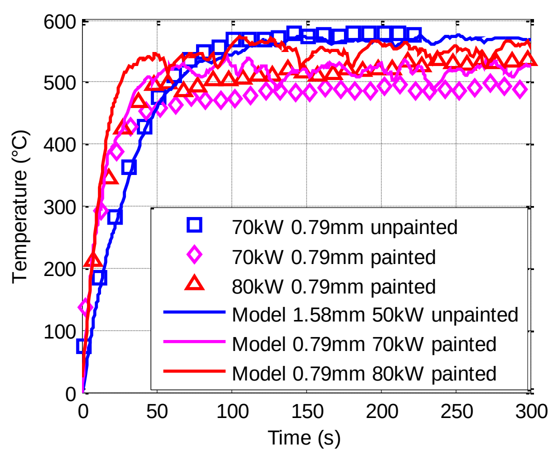

Figure 5. Measured burnthrough site temperature response for horizontal plates exposed to diffusion flame.

stress response of the burnthrough location was studied to gain a better understanding of the creep rupture burnthrough phenomenon. Figure 7 contains overlaid responses of each of these three variables. Before the start of exposure, plate stresses are approximately 0.5 MPa to 2 MPa depending on the plate thickness. Once heating begins, a temporary increase in stress due to thermal gradients occurs reaching values between 20 MPa and 80 MPa. During this time, plate temperatures are not high enough to cause significant life fraction evolution. Once the burnthrough site reaches high enough temperatures for life fraction evolution, the high stresses are relaxed due to increasing amounts of creep strain.

To investigate the effects of fire repeatability on the numerical solution, multiple FE models were conducted for a 1.58 mm thick horizontally oriented plate exposed to a 60 kW fire. Identical parameters were used for all of the models except for three different measured time varying heat flux maps measured from three separate 60 kW fires and a time-averaged heat flux map. While each heat flux map was generated from a nominally identical fire, fire dynamic repeatability resulted in local heat fluxes that vary up to 15%. The thermal response for each of these models was within the variation seen in the experimentally observed steady state temperatures. However, the average temperature differentials of 10-15°C between tests resulted in burnthrough times that varied by up to 50% as seen by the life fraction evolutions in Figure 8.

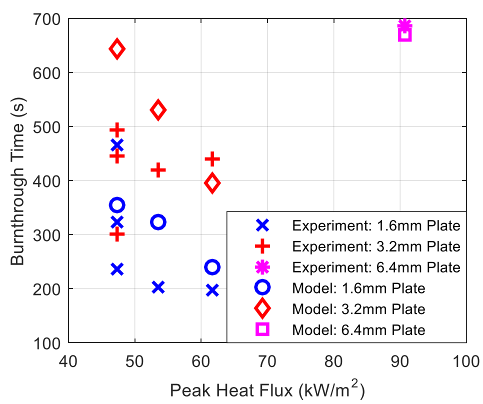

Figure 6. Comparison of experimentally measured burnthrough times and predicted burnthrough times from FE models.

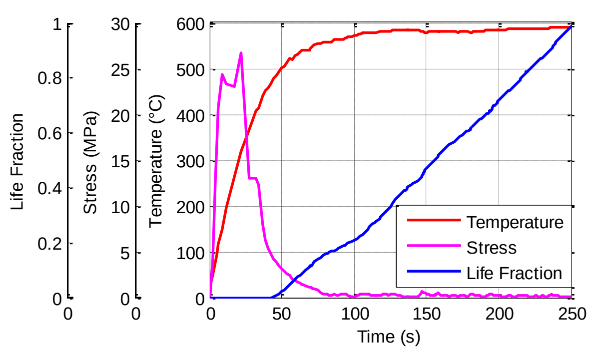

Figure 7. Burnthrough site temperature, stress, and life fraction evolution of a 1.58mm thick plate

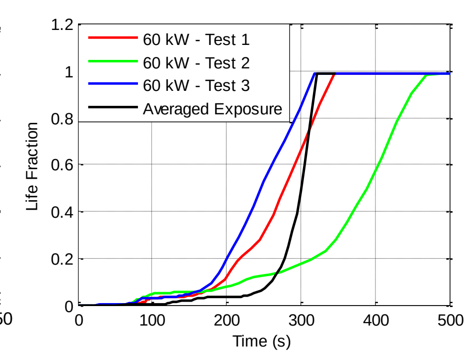

Figure 8. Life fraction evolution for 3 FE models of nominally identical exposures.

CONCLUSIONS

This research experimentally and numerically investigated the mechanisms of fire induced burnthrough of marine grade aluminum plates. A creep rupture based burnthrough model was developed to capture experimentally observed burnthrough at temperatures of 550-580°C. The creep rupture behavior was characterized using a Larson-Miller approach and implemented in finite element models of the burnthrough experiments. Model burnthrough times were within 50% of experimental values. Repeatability of fire dynamics and sensitivity of burnthrough time to plate temperature caused experimental and numerical repeatability of 50%.

REFERENCES

[1] I. D. Bennetts and K. M. Moinuddin, "Aspects of the Design of Fire-Resistant Plasterboard Walls in Fire," *Electron. J. Struct. Eng.*, vol. 6, pp. 39-48, 2006.

[2] H. Webster, G. Geyer, D. Do, J. Wright, and J. Collins, "Full-Scale Air Transport Category Fuelage Burnthrough Tests," Washington, DC, 1990.

[3] E. Johnsson and J. C. Yang, "Experimental study on tire fire penetration into a motorcoach," *Fire Mater.*, vol. 38, pp. 63-76, 2014.

[4] F. Takahashi, A. Abbot, T. Murray, J. T'ien, and S. Olson, "Thermal Response Characteristics of Fire Blanket Materials," *Fire Mater.*, vol. 38, pp. 609–638, 2014.

[5] K. Mcgrattan and H. Baum, "NIST Special Publication 1018-5 Fire Dynamics Simulator (Version 5) Technical Reference Guide," no. Version 5.

[6] R. D. Felix, W. A. Bruce, and P. L. Threadgill, "Development of Procedures for Hot Tap Welding ont Sour Service Pipelines," in *Proceedings from the International Arctic Technology Conference*, 1991.

[7] P. N. Sabapathy, M. A. Wahab, and M. J. Painter, "Numerical Methods to Predict Failure During the In-Service Welding of Gas Pipelines," *J. Strain Anal. Eng. Des.*, vol. 36, no. 6, pp. 611-619, 2001.

[8] M. A. Boring, W. Zhang, and W. A. Bruce, "Improved Burnthrough Prediction Model for In-service Welding Applications," in *Proceedings of International Pipeline Conference*, 2008, pp. 1–11.

[9] F. R. Larson and J. Miller, "A Time-Temperature Relationship for Rupture and Creep Stresses," *Trans. ASME*, vol. 74, pp. 765-771, 1952.

[10] S. S. Manson and A. M. Haferd, "A Linear Time-Temperature Relationship for Extrapolation of Creep and Stress-Rupture Data," 1953.

[11] O. D. Sherby and J. E. Dorn, "Creep Correlations in Alpha Solid Solutions of Aluminum," *Trans. ASME*, vol. 194, 1952.

[12] C. M. Rippe and B. Y. Lattimer, "Full-field surface heat flux measurement using non-intrusive infrared thermography," *Fire Saf. J.*, vol. 78, pp. 238-250, 2015.

[13] E. M. Sparrow, R. J. Goldstein, and D. C. Jones, "Natural Convection Mass Transfer Adjacent to Horizontal Plates," *Int. J. Heat Mass Transf.*, vol. 16, pp. 1025-1035, 1973.

[14] I. Rabotnov, *Creep Problems in Structural Members*. Amsterdam, Holland: North-Holland Publishing Company, 1969.

[15] C. M. Rippe, "Burnthrough Modeling of Marine Grade Aluminum Alloy Structural Plates Exposed to Fire," Virginia Tech, 2015.

[16] J. G. Kaufman, *Properties of Aluminum Alloys*. Materials Park, OH, USA: ASM International, 1999.

[17] B. Allen, "Creep and Elevated Temperature Mechanical Properties of 5083 and 6061 Aluminum," Virginia Polytechnic Institute and State University, 2012.

[18] J. Maljaars, F. Soetens, and L. Katgerman, "Constitutive Model for Aluminum Alloys Exposed to Fire Conditions," *Metall. Mater. Trans. A*, vol. 39, no. 4, pp. 778-789, 2008.

Buckling Analysis of Rack Uprights Exposed to Localised Fires

SHUBIN HE, CHONG REN, XIANZHONG ZHAO
and CHUNXIANG LI

ABSTRACT

This paper describes a numerical investigation into buckling behaviour of bare cold-formed steel uprights subjected to compression when exposed to a localised fire in a large open-plan compartment (i.e. storage warehouse). Two positions of fire sources, at the bottom and at the mid-span of uprights, are considered in the study. Heat transfer analysis for both fire sources are initially studied to consider the temperature gradients along the length of upright. According to EN 1991-1-2, a subroutine is compiled to simulate the non-uniform temperature distributions of member exposed to a localised fire and the subroutine is implanted into ABAQUS. Steel rack uprights with various boundary conditions are investigated to determine the critical buckling loads of uprights. The developed finite element model is carefully validated against experimental data. The results reveal that the variations of temperature along the length of member have some influences on the buckling performance. Moreover, the boundary restraint appears to be a significant influence on the buckling performance when the members experience different fire sources.

INTRODUCTION

In storage rack systems, cold-formed steel uprights are commonly used as main structural members to take compression load. The characteristics of cold-formed steel upright are about complicated cross-sections and continuous perforations along the length. Recently, the rising demand of storage racks attracts researchers to study its structural behaviour and the stability of member is considered preferentially. However, the lack of fire design guidelines lead to that the cold-formed steel uprights for fire design have been facing challenges in storage rack systems. EN1993-1-2 provides design specifications for cold-formed steel at elevated temperatures, but it is based on simple modifications of hot-rolled steels, which use the same material properties and theory of hot-rolled steel. In the former, the significant differences of material properties between cold-formed steel and hot-rolled steel are found and addressed into current design codes. In the latter, compared with hot-rolled steel, cold-formed steel members are susceptible to

Shubin He, Xianzhong Zhao, College of Civil Engineering, Tongji University, 1239 Siping Road, Yangpu District, Shanghai, 200092, China.
Chong Ren, Chunxiang Li, Department of Civil Engineering, Shanghai University, 99 Shangda Road, Baoshan District, Shanghai,200444, China.

bucklings, such as local, distortional, global buckling and buckling interactions, which dominate the ultimate failure and are thus necessarily concerned to be the priority of cold-formed steel design [1].

Previous studies on the cold-formed steel members in fire have focused one valuating the response of members heated while considering the structural behaviour of members subjected to a uniform thermal situation [2]. However, the thermal performances are totally different in a large open-plan compartment, in which the members are in a non-uniform thermal condition [3-5]. Existing structural fire design guidelines do not consider the temperature gradients along a length of member, and the assumption adopted in the design codes is based on the bare steel members subjected to a uniform temperature circumstance. Alternatively, non-uniform temperature distribution along a length of member caused by localised fire may accord with the situation of real fire. In recent investigations, some researchers [6-8] have studied the response of steel members under non-uniform temperatures, and the comparative results reveal considerable differences between uniform and non-uniform heating distributions. Most researches on fire design solely focus on the constant fire source, which is at the bottom of steel column. However, different positions of fire source are responsible for the variability of mechanical properties and thermal strains of the member. For example, the stored goods may have flame and become as a fire source at any height within the rack systems, and the thermal distributions of cold-formed steel upright are therefore substantially different from the fire source located at the bottom of member. Consequently, localised fires with different fire sources throughout a member are considered to be sufficiently important to warrant further investigation for cold-formed steel upright of storage rack systems.

This paper describes a numerical investigation into buckling behaviour of cold-formed steel uprights with localised fire subjected to compression. The temperature within the member varies with both time and position. Two positions of fire sources are considered in the study, which are at bottom and at middle of upright. Heat transfer analyses for both fire sources are conducted initially to consider the temperature distributions within rack upright. According to EN 1991-1-2, a subroutine is compiled to simulate the non-uniform temperature distributions in member exposed to a localised fire and is implanted into ABAQUS. Steel rack uprights under non-uniform temperatures are carried out using finite element analysis, which is to determine the critical buckling loads of uprights. The developed finite element model is carefully validated against experimental data, and the validations include both thermal and buckling analyses. Good agreements of the present model with the experimental data demonstrate that using the buckling analysis model and taking into account the thermal influences can provide a good prediction of the elastic buckling load of cold-formed steel uprights with non-uniform temperature distributions under compression.

FINITE ELEMENT ANALYSIS MODELS AND VALIDATIONS

The analysis of critical buckling load of cold-formed steel upright with non-uniform temperature distribution involves the use of linear finite element analysis. Consider a cold-formed steel member of length L=3000 mm, having a complex cross section of web depth d=90 mm, flange width b=66 mm, lip length c=7 mm and thickness t=1.8 mm (see Figure 1). The mechanical properties of the member at ambient temperature are assumed as: Young's modulus, E=206 GPa, Poisson's ratio, v=0.3 and density, ρ=7850 Kg/m^3. However, due to the elevated temperature, the mechanical properties and thermal properties are evaluated, in which the properties of young's modulus, thermal conductivity and specific heat in accordance with EN1993-1-2 [9] are adopted.

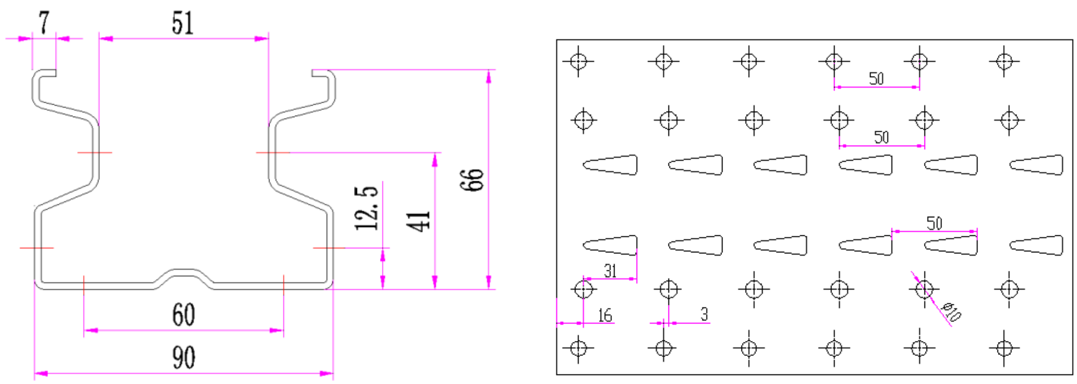

Figure 1. Dimensions of cross-section and perforations.

In order to simulate two different situations, two positions of fire sources, at the bottom and at the mid-span of uprights, are considered in the study and are shown in Figure 2. Two steps of analyses are performed. One is heat transfer analysis, which is to obtain the temperature distributions along the length of member. The other is the elastic, linear buckling analysis, which is to determine the critical buckling load for structural analysis of members. In the heat transfer analysis, the height of flame described in the Annex C of EN1993-1-2 is employed and the maximum rate of heat release (RHR_f) is assumed to be the ratio of shopping centre (RHR_f=250 kW/m^2), which has similarity to the storage warehouse. Additionally, a subroutine is compiled and implanted into ABAQUS to simulate the non-uniform temperature distributions along the length of member, and both convection and radiation of heat transfer on the surface of member are concerned in the subroutine.

For the structural analysis, two boundary conditions are considered here for simulating simply supported and fixed boundary conditions. The former is where the lateral and vertical displacements of the cross-section at the both end of the member are zero, and the rotation about the longitudinal direction is assumed to be zero (U1=U2=UR3=0). The latter is where the lateral and vertical displacements of the cross-section at the both end of the member are zero, and the rotations about the lateral, vertical and longitudinal directions are assumed to be zero (U1=U2=UR1=UR2=UR3=0). In either case, the coordinate point at the mid-span is restrained in the longitudinal axis of the member in order to eliminate the axial rigid displacement. Figure 3 provides the details of boundary conditions of upright. The member is assumed to be subjected to unit compression loads at cross-section edges of both ends. The option for analysis in ABAQUS buckling is chosen as the eigen-value analysis for linear analysis to determine the critical load at which the member has a bifurcation buckling. The four-node shell element of reduced integration scheme built into ABAQUS is employed to carry out the analyses. The element used is a thin, shear flexible, isometric quadrilateral shell element.

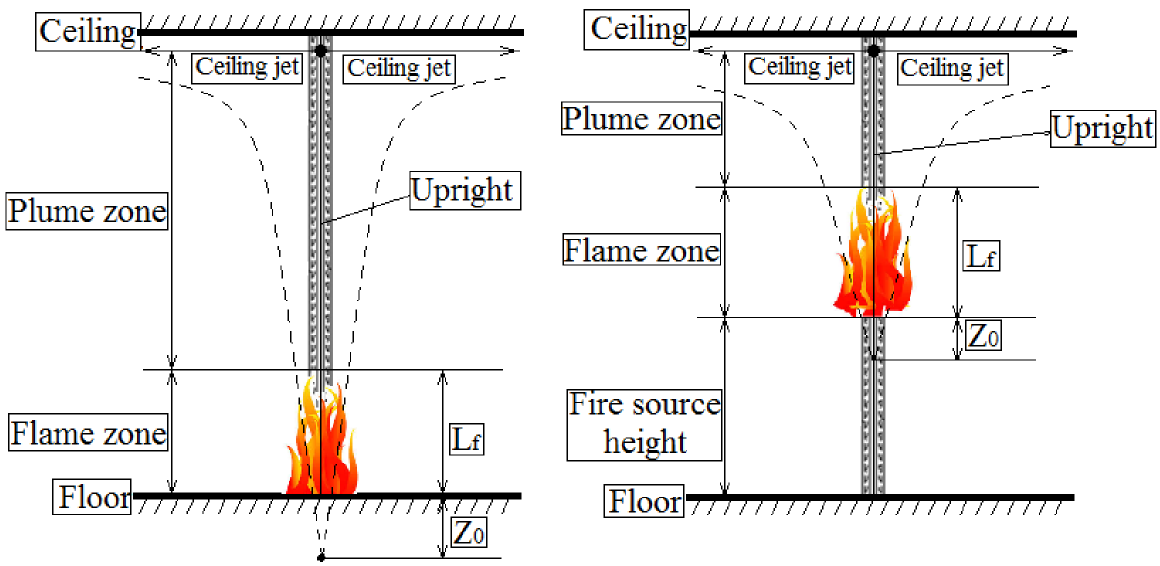

(a) Fire source at bottom of upright (b) Fire source at middle of upright
Figure 2. Rack uprights subjected to localised fire.

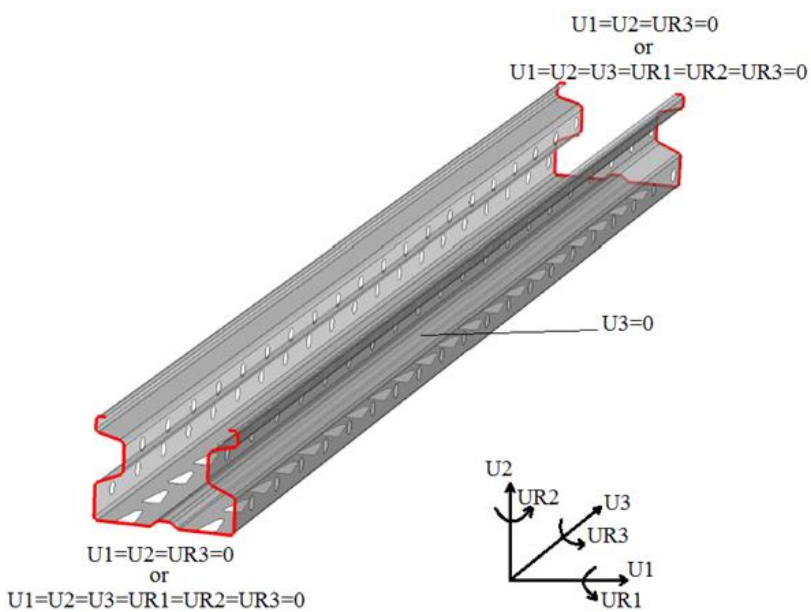

Figure 3. Boundary conditions of finite element model.

Available experimental results are used to validate the accuracy of the present finite element model. It should be mentioned that the present numerical modelling strategy does not match any available tests, the validations are thus subdivided into two parts, the thermal analysis validation and buckling analysis validation respectively. Craveiro et al. conducted an experimental investigation into the fire behaviour of cold-formed steel lipped channel with restrained thermal elongation [2].

Figure 4 presents the standard fire curve (ISO834), furnace mean temperature curve and temperature curves obtained from the experimental and FEA. It can be seen in the figure that the temperatures obtained from the experiment and FEA are lower than the furnace mean temperature. This is because the influence of the emissivity of fire on a specimen is negligible when a member exceeds a certain distance from fire source. In this case, a slender specimen is in a large furnace chamber (the size of furnace in the test is 2.5 m x 1.5 m x 1.5 m), and the heating wires in the furnace chamber are far away from the specimen. However, for bare steel member in a fire, the surface emissivity is necessary to consider, and the ratio of the surface of the fire, $\varepsilon_f = 0.8$ is employed in the finite element model. Experimental results of Kwon and Hancock [10] are used to verify the finite element model of buckling analyses. Table I provides a detailed comparison of the critical buckling stresses and buckling modes obtained from the experimental method and the present finite element analysis model. In General, good agreements of the present finite element models with the experimental data demonstrate that using the buckling analysis model and taking into account the thermal influences can provide a good prediction of the elastic buckling load of cold-formed steel uprights with non-uniform temperature distributions.

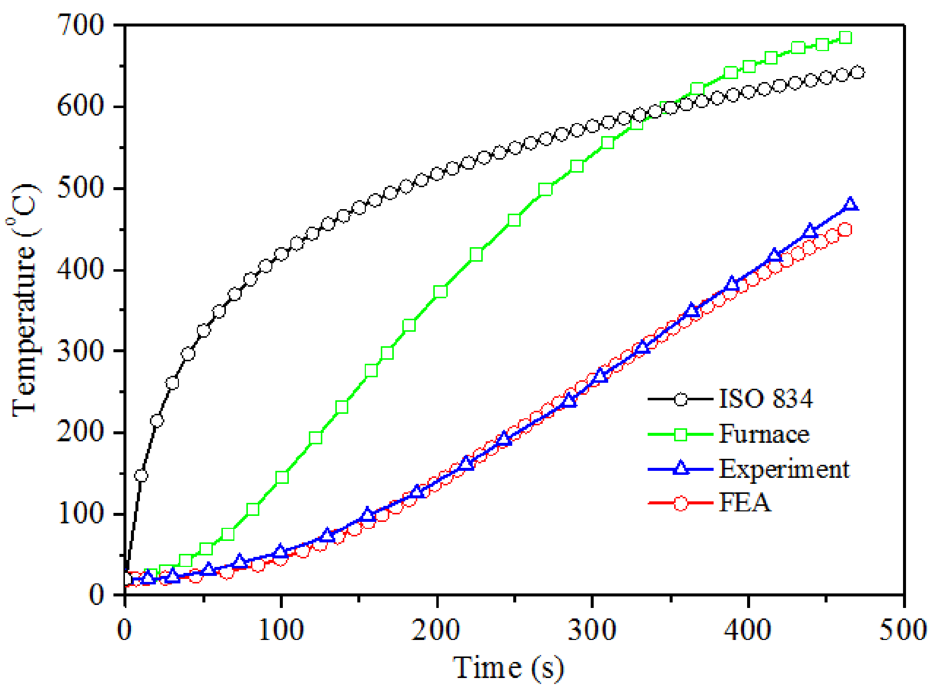

Figure 4. Comparison of FEA results with experimental data.

TABLE I. COMPARISON OF BUCKLING STRESS AND BUCKLING MODE OF SIMPLE LIPPED CHANNEL BETWEEN EXPERIMENT AND FINITE ELEMENT ANALYSIS.

Specimens	**Buckling stress**		**Buckling mode**	
	Test (MPa)	FEA (MPa)	Test	FEA
CH1-5-800	45.0	43.5	D(2)	D(2)
CH1-6-800	55.5	52.8	D(2)	D(2)
CH1-7-800	68.6	62.1	D(2)	D(2)
CH1-7-600	75.8	63.8	D(1)	D(1)
CH1-7-400	88.8	75.4	D(1)	D(1)

Note: D = Distortional buckling mode; ( ) = numbers of buckle half-wavelength.

HEAT TRANSFER AND BUCKLING ANALYSIS

By conducting heat transfer analysis using the FEA, the developments of temperature distribution along the length of uprights are performed. Figure 5 shows the temperature distributions along the length of uprights at five different times for both fire sources. It can be found from the figure that the variations of temperature along the length of uprights are significant for both fire sources, indicating that the temperature is not uniformly distributed in the uprights. The temperature at top of upright keeps low even after about 22 minutes of the fire exposure for both fire sources. Note that the temperature at the top for the middle fire source is higher than the temperature at the top for the bottom fire source, and also for the fire source at the middle of upright the temperature at the bottom is about ambient temperature. These findings imply that the different fire sources have significant influences on the temperature distributions along the length of uprights. For example, after about 22 minutes of the fire exposure, for the fire source at the bottom of upright, the temperature at the top is about 170 ^{o}C, while the temperature at the bottom is about 900 ^{o}C. It also can be seen in the figure that the temperature does not increase rapidly in the fire unexposed part of upright where is vertically below the fire source. This is due to the thermal action and the heat flux of a localised fire have insignificant influences on the ineffective zone of structural member.

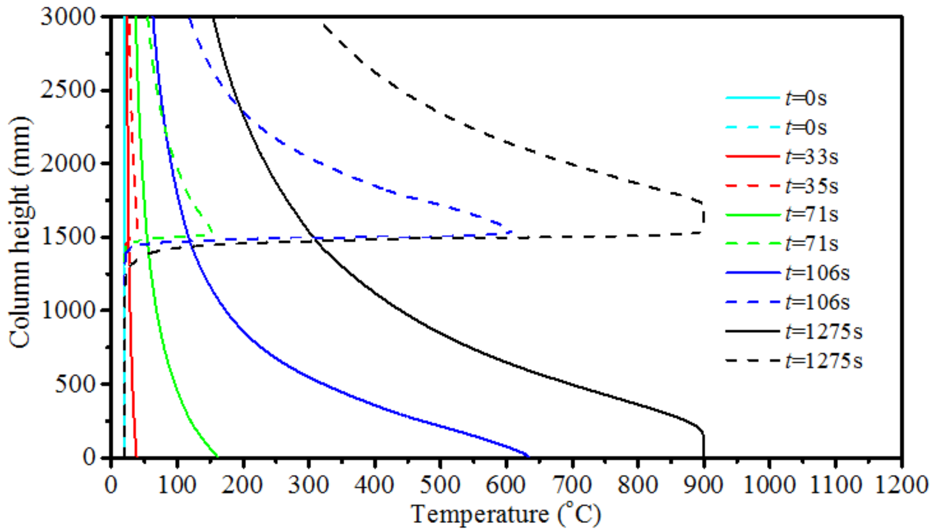

Figure 5. Temperature distributions along the length of upright for two fire sources.

Following the heat transfer analysis, a numerical study was carried out. The goal of the finite element analysis is to provide a better understanding of the buckling behaviour of bare cold-formed steel uprights subjected to compression when exposed to a localised fire in a large open-plan compartment. For a given member length (L=3000 mm), a linear finite element analysis is performed, from which the critical buckling load of bifurcation buckling are obtained. Figure 6 shows the critical buckling loads of a member exposed to a localised fire. Figure

6(a) is for the member with both simply supported ends and Figure 6(b) is for the member with both fixed ends. It is seen from the figure that, the tendency for both fire sources and for both end support conditions is identical, the critical buckling load decreases with time until it reaches a certain time, and then it remains the same with further increased time. As expected, the buckling load obtained from the member with simply supported boundary condition is lower than that provided by the member with fixed boundary condition. It also can be found in the case of simply supported boundary condition that, the critical buckling loads of fire source at the bottom are slightly greater, while diametrically opposite results are obtained in the case of fixed boundary condition. This can be explained by in the case of fixed boundary condition, the restraints at the bottom of upright are significantly eroded by the elevated temperature, the critical buckling load are thus relatively lower. Figure 7 presents some typical buckling modes of uprights of two fire sources, with fixed boundary condition at the two ends. The non-uniform temperature distributions have some influences on its length of the half-wavelength of flexural-torsional buckling.

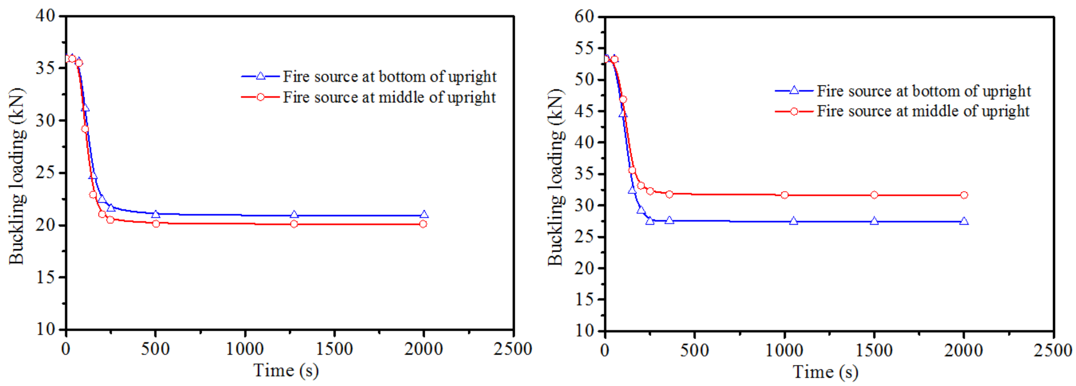

(a) Simply supported (b) Fixed

Figure 6. Critical buckling loads of cold-formed steel member exposed to a localised fire.

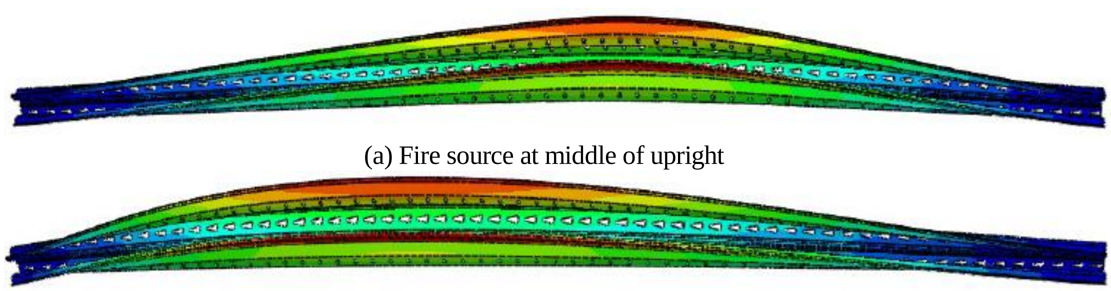
(a) Fire source at middle of upright

(b) Fire source at bottom of upright

Figure 7. Buckling modes of cold-formed steel uprights under compression (Fixed).

CONCLUSIONS

This paper has presented a numerical investigation into buckling behaviour of bare cold-formed steel uprights subjected to compression when exposed to a localised fire. Some important conclusions drawn from the present study are summarised. The finite element model used in the study can properly represent the buckling behaviour of cold-formed steel uprights subjected to compression when exposed to a localised fire in a large open-plan compartment. The significant different distributions of non-uniform temperature for members under two fire sources have been provided. Apparent variances in buckling behaviour of cold-formed steel uprights exposed to localised fires have been highlighted. Furthermore, the crucial influences of different support conditions have been presented.

ACKNOWLEDGEMENTS

The authors would like to acknowledge the financial supports received from the National Natural Science Foundation of China (51508402).

REFERENCES

[1] Shahbazian, A. and Wang, Y.C. 2012. "Direct Strength Method for calculating distortional buckling capacity of cold-formed thin-walled steel columns with uniform and non-uniform elevated temperatures". *Thin-Walled Structures*, 53, 188-199.
[2] Craveiro, H. D., Rodrigues J. P. C. and Laím, L. 2014. "Cold-formed steel columns made with open cross-sections subjected to fire". *Thin-Walled Structures*, 85, 1-14.
[3] Zhang, C. and Usmani, A. Heat transfer principles in thermal calculation of structures in fire. *Fire Safety Journal*, Volume 78, Pages 85-95.
[4] Lange, D. and Sjöström, J. 2014. Mechanical response of a partially restrained column exposed to localised fires. Fire Safety Journal, Volume 67, Pages 82-95.
[5] Zhang, G.W., Zhu, G.Q. and Huang, L.L. 2014. Temperature development in steel members exposed to localized fire in large enclosure. Safety Science, Volume 62, Pages 319-325.
[6] Cheng, S., Li, L.Y. and Kim, B. 2015. "Buckling analysis of partially protected cold-formed steel channel-section columns at elevated temperatures". *Fire Safety Journal*, 72, 7-15.
[7] Lange, D. and Sjostrom, J. 2014. "Mechanical response of a partially restrained column exposed to localised fires". *Fire Safety Journal*, 67, 82-95.
[8] Zhang, C., Gross, J., McAllister, T. and Li, G.Q. 2014. "Behavior of unrestrained and restrained bare steel columns subjected to localized fire". *Journal of Structural Engineering*. Volume 141, Issue 10.
[9] EN. 1991-1-2. 2002: "General actions — Actions on structures exposed to fire". Brussels, Belgium: European Committee for Standardization (CEN).
[10] Young, B., Kwon, B. and Hancock, G. J. 1992. "Tests of cold-formed channels with local and distortional buckling". *Journal of structural engineering*, 117 (7), 1786-1803.

METAL STRUCTURES: CONNECTIONS AND COMPOSITE FLOORS

Creep Behavior of Flush Endplate Connections at Elevated Temperatures Due to Fire

AHMAD H. EL GHOR[1], ELIE G. HANTOUCHE[2],
MOHAMMED ALI MOROVAT[3] and MICHAEL D. ENGELHARDT[4]

ABSTRACT

This paper highlights some preliminary results of a computational study investigating the effect of thermal creep of structural steel on the behavior of steel beam-column connections subjected to elevated temperatures due to fire. Through a series of finite element simulations that were partly verified against experimental data, a practical methodology was developed to investigate the time-dependent nature of the behavior of flush endplate beam-column connections at elevated temperatures. In this methodology, time effects on the strength and rotational capacity of flush endplate connections are explicitly presented in the form of isochronous force-rotation curves. The isochronous representation provides a possible framework for including creep effects in predicting the response of structural steel connections to fire.

INTRODUCTION

Flush endplate connections are one of the extensively used moment-resistant connections in steel buildings and steel portal frames due to economy and ease of construction. During a fire event, different components of the flush endplate connections can undergo significant loss of strength and stiffness. Large axial forces are also developed in these connections and the connecting beams as a result of restraints to thermal displacements [1]. These axial forces are initially compressive when beams expand during the initial heating stage of a fire. With increasing temperatures, these axial forces can become tensile as beams begin to sag and catenary action develops. Additional axial tensile forces are further developed as deflected beams contract during the cooling stage of a fire [2, 3].

[1]Graduate Student, Department of Civil and Environmental Engineering, American University of Beirut, Riad El-Solh 1107 2020, Beirut, Lebanon, Email: ahe26@mail.aub.edu
[2]Assistant Professor, Department of Civil and Environmental Engineering, American University of Beirut, PO Box 11-0236, Riad El-Solh 1107 2020, Beirut, Lebanon, Email: eh12@aub.edu.lb
[3]Research Scientist Associate, Department of Civil, Architectural and Environmental Engineering, Ferguson Structural Engineering Laboratory, The University of Texas at Austin, Austin, Texas 78758, Email: morovatma@utexas.edu
[4]Professor, Department of Civil, Architectural and Environmental Engineering, Cockrell School of Engineering, The University of Texas at Austin, Austin, Texas 78758, Email: mde@mail.utexas.edu

Moreover, steel flush endplate connections in fire are subjected to significant rotation demands. These large deformation and force demands combined with loss of strength can potentially result in the failure of flush endplate connections during and after a fire [1, 2, 3, 4].

There have been a number of attempts in the past to investigate the combined effects of shear and axial forces on the strength and rotational capacity of flush endplate connections subjected to fire [1, 2, 3, 4]. In these studies, both isolated connections under steady-state temperature conditions and connection sub-assemblies under transient-state temperature conditions were examined. A major observation from these studies was that the strength, rotational capacity, and failure modes of the flush endplate connections were significantly affected by temperature-dependent behavior of their components, mainly the endplate and the bolts [1, 2, 3, 4]. It is clear from these past observations that good understanding of mechanical properties of steel plates and bolts at elevated temperatures is crucial in accurately predicting the response of the flush endplate connections to fire.

The stress-strain behavior of structural steel at elevated temperatures has been shown to be highly time dependent for some ranges of stresses and temperatures expected during a building fire [5, 6]. Nonetheless, research on the effect of creep on the behavior of steel connections is quite meager [7].

In an effort to address this shortcoming, this paper proposes a methodology to characterize the time-dependent strength and deformation capacity of flush endplate connections when subjected to fire. It will be further shown how this methodology can be used in a performance-based framework to evaluate the performance of steel connections in fire.

THERMAL CREEP OF STRUCTURAL STEEL

Creep Phenomenon

Creep is defined as the time-dependent plastic strain under constant stress and temperature conditions. It is often stated that steel creep occurs when temperature of steel exceeds one-third to half of the steel melting temperature. The creep of steel is a complex phenomenon that depends on steel material type, applied stress, temperature, time duration, and stress and temperature histories. Creep curves, defined as strain versus time curves, are typically divided into the three phases of primary, secondary, and tertiary. In the primary stage, the curve is non-linear and exhibits a decreasing creep strain rate. In the secondary stage, the creep strain is almost constant. In the tertiary stage, the creep strain rate increases with time. For steel, the shape of the creep curve, the magnitude of the creep strain and the time scale are highly dependent on both the temperature and the stress levels [5, 6].

Creep of ASTM A36 Steel at Elevated Temperatures

Experimental and empirical models have been developed to predict creep strain of ASTM A36 steel at elevated temperatures [8, 9]. One of the widely used creep models in structural-fire engineering applications proposed by Fields and Fields [9] incorporates a power law creep and represents creep strain, ε_c, in the form of a Norton-Bailey equation as follows:

$$\varepsilon_c = a\,t^b\,\sigma^c \tag{1}$$

In this equation, t is time and σ is stress. The parameters a, b and c are temperature-dependent material properties. Fields and Fields [9] derived equations for these temperature-dependent material properties for ASTM A36 steel. The model developed by Fields and Fields [9] is capable of predicting creep in the temperature range of 350 °C to 600 °C and for creep strains up to 6-percent. The creep model by Fields and Fields [9] was used in the studies presented in this paper on the time-dependent response of steel flush endplate connections to fire.

TIME-DEPENDENT BEHAVIOR OF FLUSH ENDPLATE CONNECTIONS IN FIRE – DEVELOPMENT OF METHODOLOGY

In this section, a practical methodology developed to assess the time-dependent nature of the behavior of flush endplate beam-column connections in fire will be presented and explained. In this methodology, time effects on the strength and rotational capacity of flush endplate connections are explicitly presented in the form of isochronous force-rotation curves.

Flush Endplate Connection Prototype

The connection prototype selected for analysis followed the flush endplate connection details incorporated in the experiments conducted at University of Sheffield [10]. More specifically, as shown in Figure 1, the Flush endplate connection specimen used in the analysis consisted of a PL13×8×0.4 in. (PL332.4×200×10 mm) endplate, a W12×26 (UB305×165×40) beam, and a W10×60 (UC 254×254×89) column. Further, six grade 8.8 M20 bolts were used to connect the endplate to the column. Details of the connection configuration can be found in different publications from researchers at the University of Sheffield [1, 3, 10].

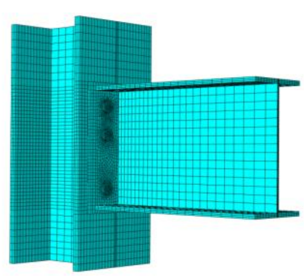

Figure 1. Flush endplate connection configuration used in simulations in Abaqus.

Important Modeling Considerations

An idealized bilinear stress-strain relation with isotropic hardening was used to model the mechanical behavior of both structural bolts and structural steel. The ambient temperature properties incorporated in connection simulations were based on the reported values in the experimental work at University of Sheffield [1, 3, 10]. Retention factors proposed by researchers from the University of Texas at Austin [11] and University of Sheffield [12] were used to respectively model stress-strain characteristics of structural steel and structural bolts at elevated temperatures. To account for the time-dependent behavior of structural steel at elevated temperatures, a power law creep model proposed by Fields and Fields [9] was included in mechanical properties of structural steel used to model both the beam and the endplate. Thermal creep of structural bolts was ignored in connection simulations.

Development of Methodology

To develop the methodology, two series of finite element analyses were performed. In the first series, steady-state temperature analyses were conducted to characterize the strength of flush endplate connections under combined shear and tension forces at elevated temperatures. At each specific temperature (450 °C, 550 °C, and 650 °C), an inclined concentrated force (with the initial angle of 35°) was monotonically applied to the beam end with an angle varying throughout the loading step in accordance with the experimental protocol at University of Sheffield [10]. Figure 2 shows sample results of such analyses where experimental and finite element predictions of the strength of flush endplate connections are compared at various temperatures. As seen in Figure 2 and as shown in previous studies [1, 2, 3], finite element simulations are capable of predicting the experimental observations with reasonable accuracy. Note that due to the rapid loading protocol adopted in connection experiments at University of Sheffield [10], the strengths obtained in the first series of simulations were assumed to be time-independent and therefore thermal creep of steel was ignored in these simulations.

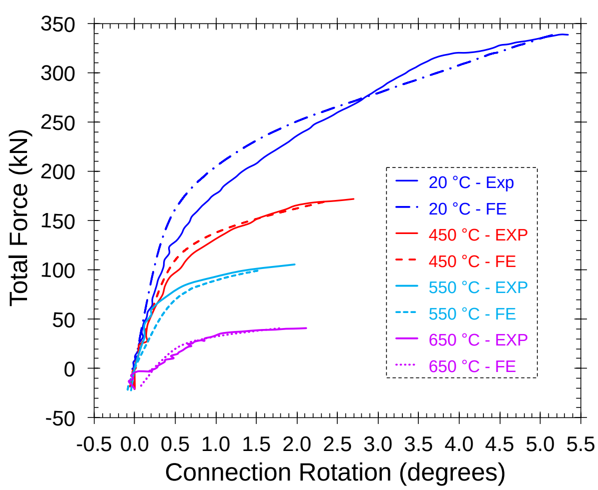

Figure 2. Time-independent strength of flush endplate connections at ambient and elevated temperatures.

In the second series, steady-state temperature creep tests were performed to investigate the creep response of flush endplate connections under combined shear and tension forces at elevated temperatures. More specifically, at each specific temperature (450 °C, 550 °C, and 650 °C), an inclined force, equal to a fraction of the ultimate load predicted in the first series of analyses, was applied and kept constant throughout the test. Simulations were conducted for 240 minutes or until the connection failed. Representative results of creep tests at 550 °C and under various applied loads are depicted in Figure 3. As seen in Figure 3, connection rotations increased with time as a result of explicit consideration of thermal creep of structural steel in simulations. Further, the rate of increase in connection rotations was higher for larger applied loads.

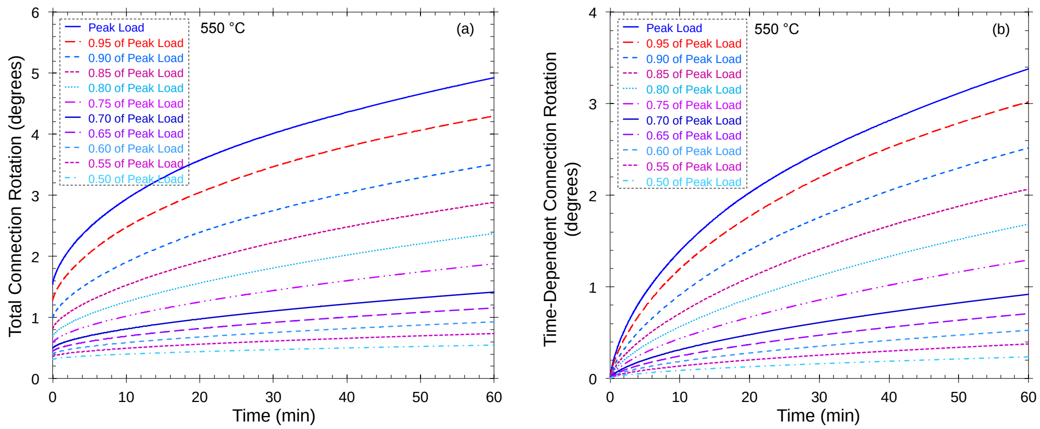

Figure 3. Effect of creep on the connection rotation at 550 °C.

Results obtained from steady-state temperature creep tests in the form of rotation versus time, like those shown in Figure 3, can alternatively be presented in the form of isochronous force-rotation curves. Figure 4 shows a sample of isochronous force-rotation curves corresponding to the creep test results shown in Figure 3. As can be seen in Figure 4, for any specific temperature like 550 °C, isochronous force-rotation curves are force-rotation curves at different time. In other words, they represent the time-dependent force-rotation response of the connection at any specific temperature. As further observed in Figure 4, compared to a single curve from connection experiments, isochronous force-rotation curves provide much richer insight into the connection behavior at elevated temperatures. It can be seen that at a specific time, larger connection rotation can be obtained for larger applied load.

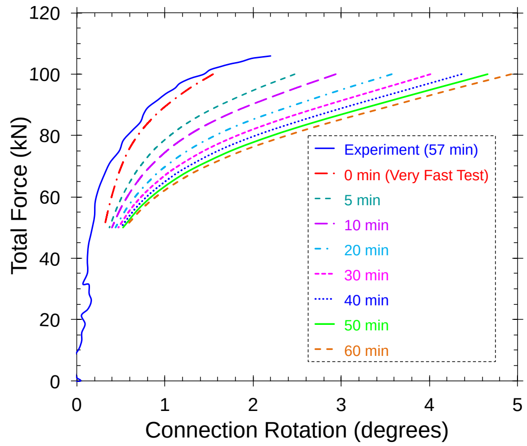

Figure 4. Isochronous force-rotation curves for the flush endplate connection in consideration at 550 °C.

TIME-DEPENDENT BEHAVIOR OF FLUSH ENDPLATE CONNECTIONS IN FIRE – APPLICATION OF METHODOLOGY

The methodology presented in the previous section to assess the time-dependent behavior of flush endplate connections subjected to fire temperatures can be used to study the behavior of flush endplate connections under more general conditions characteristics of the building fires such as variable temperatures.

Steady-state temperature creep tests, as explained previously, can be performed on the isolated flush endplate connection model in Abaqus under a constant applied load at different temperatures. If the results from these connection creep tests are combined in such a way that rotation-temperature points relating to the same time are connected to each other, the isochronous rotation-temperature curves will be constructed. A representative of these isochronous rotation-temperature curves for a constant load of 76 kN is depicted in Figure 5. Isochronous rotation-temperature curves such as the ones shown in Figure 5 simply indicate the time-dependent behavior of the flush endplate connections under transient-state temperature conditions characteristics of structural fires.

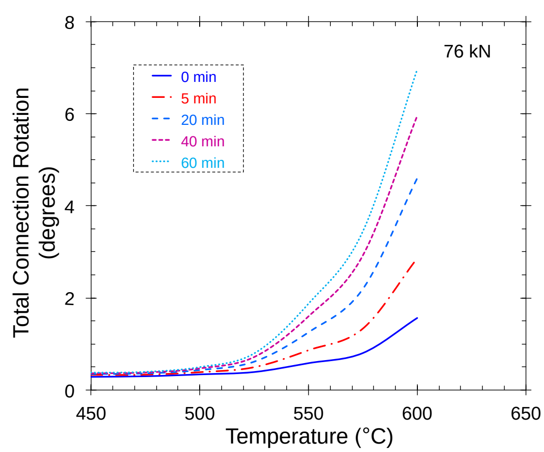

Figure 5. Isochronous rotation-temperature curves corresponding to the constant load of 76 kN.

The graphs shown in Figure 5 can further be represented in more general forms where the time-dependent behavior of flush endplate connections is presented under the conditions of variable loads and temperatures. Samples of such general isochronous rotation-temperature curves are shown in Figure 6. Note that eventhough curves in Figures 6(a) and 6(b) correspond to the ultimate loads and half of ultimate loads at each temperature, respectively, the actual loads are diferent from one temperature to the other (ultimate loads are the peak loads predicted in the first series of analyses where the creep effects are ignored).

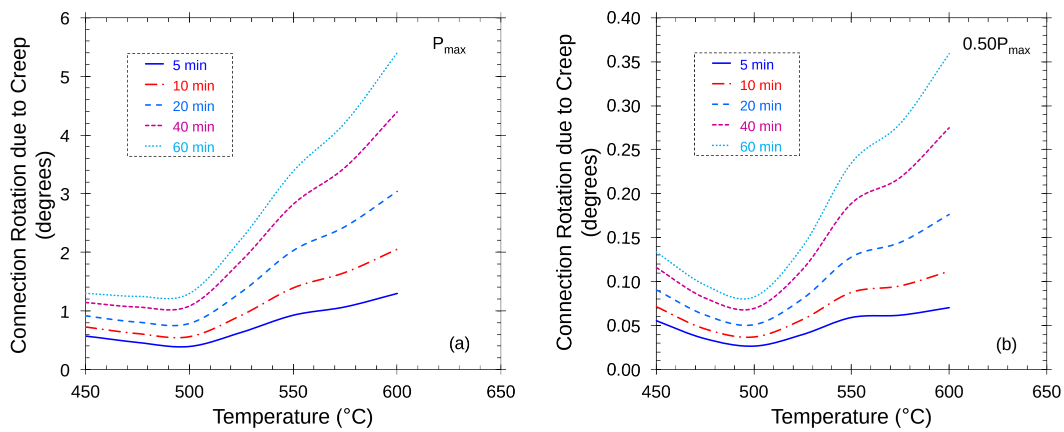

Figure 6. Isochronous rotation-temperature curves under variable loads.

An important observation from Figures 5 and 6 is that, according to the adopted creep model by Fields and Fields [9], the behvior of the selected flush endplate connection becomes highly time dependent for temperatures above about 500 °C. Figure 6 further shows that creep effect on the connection response to fire becomes more significant at higher applied loads.

Any time and temperature point on the isochronous rotation-temperature curves in Figures 5 and 6 can be related to a corresponding point on the design fire curve. This correspondence allows a designer to define the desirable performance levels for steel connections in terms of specific times or temperatures. In other words, the isochronous representations shown in Figures 5 and 6 can be utilized to define critical times and temperatures for designing connections in fire. This utilization can further provide a smooth transition from the current prescriptive-based approaches to the performance-based ones.

CONCLUDING REMARKS

Through a series of finite element simulations that were partly verified against experimental data, a practical methodology was developed to investigate the time-dependent nature of the behavior of flush endplate beam-column connections at elevated temperatures due to fire. In this methodology, time effects on the strength and rotational capacity of flush endplate connections are explicitly presented in the form of isochronous force-rotation curves. An example was provided of how the isochronous representation can be used to aid in the design of steel connections in fire. The accuracy of the suggested methodology can be enhanced by considering more reliable creep models for structural steel at elevated temperatures, by including the thermal creep models for structural bolts, and by considering the constraints to thermal expansion and resulting stress relaxations.

ACKNOWLEDGMENTS

The authors gratefully acknowledge the financial support provided by the American University of Beirut Research Board under grant No.21113-102726, and by the Lebanese National Council for Scientific Research (LNCSR) under grant No. 103091-22968. The authors further would like to thank researchers at the University of Sheffield for making the connection test results publicly available.

REFERENCES

1. Yu, H., I. Burgess, J. Davison and R. Plank. 2011. "Experimental and Numerical Investigations of the Behavior of Flush End Plate Connections at Elevated Temperatures," *J. Struct. Eng.*, pp. 80-87.
2. Li, J.-T., G.-Q. Li, G.B. Lou and L.-Z. Chen. 2012. "Experimental Investigation on Flush End-plate Bolted Composite Connection in Fire," *J. Constr. Steel Res.*, pp. 121-132.
3. Al-Jabri, K .S., A. Seibib, and A. Karrech. 2008. "Modelling of Unstiffened Flush End-Plate Bolted Connections in fire," *J. Constr. Steel Res*., 62, pp. 151-159.
4. Li, G.-Q. and S.-X. Guo. 2008. "Experiment on Restrained Steel Beams Subjected to Heating and Cooling," *J. Constr. Steel Res.*, 64, pp. 268-274.
5. Morovat M.A., Lee J., Engelhardt M.D., Taleff E.M., Helwig T.A. and Segrest V.A. 2012. "Creep Properties of ASTM A992 Steel at Elevated Temperatures", *Advanced Materials Research*, 446-449, 786-792.
6. Morovat, M. A., J. Lee, M. D. Engelhardt, T. A. Helwig and E. M. Taleff. 2011. "Analysis of Creep Buckling of Steel Columns Subjected to Fire," *Structures Congress, ASCE,* pp. 2929-2940.
7. Kdour, V. K. R. and M. M. S. Dwaikat. 2010. "Effect of High Temperature Creep on the Fire Response of Restrained Steel Beams" *Materials and Structures*, 43, pp. 1327-1341.
8. Harmathy, T. Z.1967. "A Comprehensive Creep Model" *J. of Basic Eng., Trans. ASME*, 89(3), pp. 496-502.
9. Fields, B. A. and R. J. Fields. 1989. "Elevated Temperature Deformation of Structural Steel," *Report NISTIR 88-3899,* NIST, Gaithersburg, MD.
10. http://fire-research.group.shef.ac.uk/downloads.html, November, 2007.
11. Lee J., M .A. Morovat, G. Hu, M. Engelhardt, and E. Taleff. "Experimental investigation of mechanical properties of ASTM A992 steel at elevated temperatures," *Eng. J.*, 50(4), pp. 249-272.
12. Hu, Y., J. B. Davison, I. W. Burgess, and R.J. Plank. 2007. "Comparative Study of the behaviour of BS 4190 and BS EN ISO 4014 bolts in fire," *Proc., ICSCS* , Taylor & Francis, London, pp. 587-592.

Experimental and Numerical Study on High Strength Steel Endplate Connections after Fire

XUHONG QIANG[1,2], XU JIANG[1], FRANS S. K. BIJLAARD[2] and HENK KOLSTEIN[2]

ABSTRACT

In order to reveal more information and understanding on performance and failure mechanisms of high strength steel endplate connections after fire, an experimental and numerical study has been carried out. Firstly, full-scale tests on seven endplate connections were carried out after cooling down from fire temperature 550°C. The moment resistance, rotation capacity and failure mode of high strength steel endplate connections after fire were obtained and compared with those of mild steel endplate connections, as well as with their performance at ambient temperature without fire exposure. Moreover, the provisions of Eurocode 3, which were mainly obtained based on the mild steel structures, were validated with the test results of high strength steel endplate connections. Furthermore, a numerical study via ABAQUS is reported and validated against the experimental results. It has been demonstrated that this finite element analysis gives reasonable accuracy compared with the experimental results, providing an efficient, economical, and accurate tool to assess the post-fire performance of high strength steel endplate connections.

1. INTRODUCTION

For the time being, high strength steels (HSS) are more and more popular in mechanical engineering, ship engineering, offshore structures and civil engineering. In practice, high strength steels have been employed in some significant structures and landmark constructions. However, in current literature of civil engineering there is very limited report on the performance of high strength steel structures. It will retard the application of these high strength materials in civil engineering, or leads to an uneconomical design of high strength steel structures.

Since 9.11 Tragedy, structural fire safety has been a worldwide key consideration in the design of building structures. Provided that collapse does not occur when a steel structure is exposed to fire, the steel members will begin to cool once the fire starts to decay and the air temperature begins to decrease. Residual forces and deformations redevelop in steel structures during the cooling phase due to the shrinkage of the steel

---

[1]College of Civil Engineering, Tongji University, 200092 Shanghai, China.
[2]Department of Structural Engineering, Faculty of Civil Engineering, Delft University of Technology, P.O.BOX 5048, 2600GA Delft, the Netherlands.
Authors' emails: Qiangxuhong@tongji.edu.cn, jiangxu@tongji.edu.cn, F.S.K.Bijlaard@tudelft.nl, M.H.Kolstein@tudelft.nl.

members, which might be more dangerous conditions than in fire. If all the structures exposed to fire are dismantled and then new alternates are built, it is wasteful and time-consuming; whereas if the post-fire structures are reused directly or simply reinforced, it may be safety-compromised, which makes people feel unsafe when they step into the structures. Whether the structures exposed to fire should be demolished, repaired or reused directly, a reliable assessment is needed.

In Europe, endplate connections are typical beam-to-column connections for steel structures produced by welding at workshops and erected by bolting in situ. The simplicity and economy associated with its fabrication make this type of connection popular in steel structures. Hence, the post-fire performance of high strength steel endplate connections is assessed herein to reveal their residual performance after fire.

Firstly, full-scale tests on seven endplate connections were carried out after cooling down from fire temperature 550°C to evaluate their post-fire performance. The moment resistance, rotation capacity and failure mode of high strength steel endplate connections after fire were obtained via tests and compared with those of mild steel endplate connections, as well as with their original performance at ambient temperature without fire exposure. Moreover, the provisions of European design standard for steel structures Eurocode 3, which were mainly obtained based on the mild steel structures, were validated with test results of high strength steel endplate connections. Furthermore, a numerical study on high strength steel endplate connections after fire conducted via ABAQUS was carried out and validated against the experimental results.

2. EXPERIMENTAL STUDY

2.1 Test Specimen

The endplate connections were designed according to Eurocode 3: Part 1:8 [1]. In the high strength steel endplate connections, the endplates are made of high strength steels (S690 and S960) while the beam and column are made of Q345 (similar to S355). For comparison, the connections with endplates made of mild steels Q235 (similar to S235) and Q345 (similar to S355) are also included herein. In order to compare the performance of endplate connections after fire with that without exposure to fire, the tests at ambient temperature without fire exposure on each concerned endplate connection were carried out as well. The detailed drawing of endplate connection test specimen is shown in Figure 1, while the characteristics and test conditions of the specimens are shown in Table I.

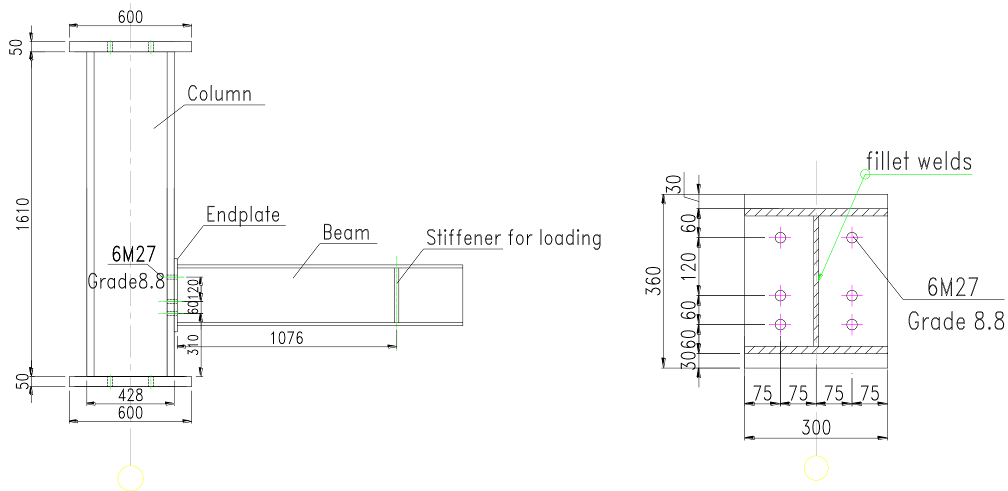

(a) Endplate connection (b) Endplate

Figure 1. Endplate connection specimen.

Table I. Test specimens and test conditions.

Test ID	Endplate material	Endplate thickness (mm)	Weld type	Highest fire temperature (°C) in post-fire tests	Temperature(°C) of specimens in ambient tests without fire exposure
1-1 P	Q235	20	overmatched	550	-
1-2 P	S690	12	matched	550	-
1-3 P	S960	10	under matched	550	-
2-1 P	Q235	25	overmatched	550	-
2-2 P	Q345	20	overmatched	550	-
2-3 P	S690	15	matched	550	-
2-4 P	S960	12	under matched	550	-
1-1 A	Q235	20	overmatched	-	20
1-2 A	S690	12	matched	-	20
1-3 A	S960	10	under matched	-	20
2-1 A	Q235	25	overmatched	-	20
2-2 A	Q345	20	overmatched	-	20
2-3 A	S690	15	matched	-	20
2-4 A	S960	12	under matched	-	20

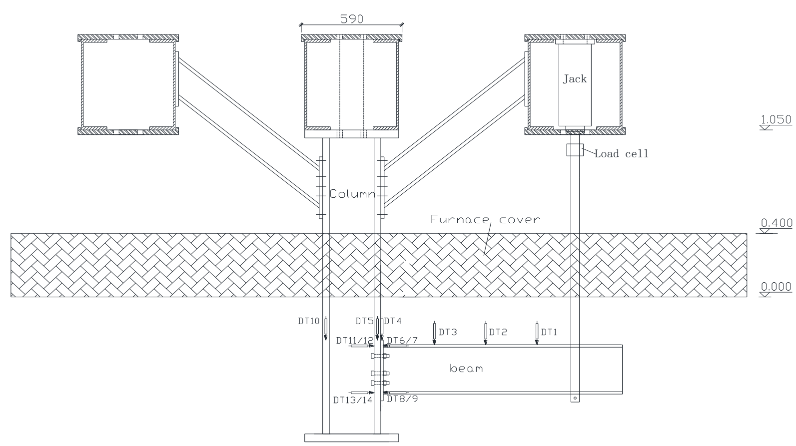

Figure 2. Fire test set-up.

2.2 Test set-up and Procedure

The heating process was conducted in a gas furnace (4.5m×3.0m×1.7m). Since applying a tensile load under fire conditions is more stable than applying a compressive load, the connection specimens were designed to be located upside down in order to easily apply the tensile load from the outside of the furnace, see Figure 2.

The specimen was firstly heated to 550°C at a constant heating rate 10°C/min (which corresponds to normally protected steel members in fire [2]), after the temperature of connection components achieved 550°C and being stable, the heating was stopped and the specimens began to cool down to ambient temperature. After cooling down, the post-fire connection specimens were loaded at ambient temperature until failure to evaluate the residual load bearing capacity, displacement, rotation, and failure modes of HSS endplate connections after cooling down from fire.

2.3 Displacement Measurement

In the fire tests, 3 vertical displacement sensors (DT1-DT3) were used to obtain the vertical displacement of the beam, as shown in Figure 2. According to the vertical displacements of beam, the rotation of beam can be calculated. In order to record the displacement of column, 2 vertical displacement sensors (DT5 and DT10) were arranged. According to the displacement of column, the rotation of column can be calculated. In order to measure the displacement of endplate, one vertical displacement sensor (DT4) and 4 horizontal displacement sensors (DT6-DT9) were placed, as shown in Figure 2. According to the displacement of endplate, the rotation of endplate can be calculated. Based on the displacements of the aforementioned components, the rotation of endplate connection in tests can be obtained.

2.4 Test Results

2.4.1 Deformation at the end of tests

An overall description on components of all connections at the end of the tests is listed in Table II, including post-fire tests and ambient tests.

Table II. Description of components at the end of tests.

Test ID	Endplate yielding	Fracture of bolts in top tensile row	Nuts in top tensile row stripped off	Weld failure in heat affected zone	Bolts in compression almost straight
1-1 P	Yes	No	No	No	Yes
1-2 P	Yes	No	Yes	No	Yes
1-3 P	Yes	No	No	Yes	Yes
2-1 P	Yes	Yes	No	No	Yes
2-2 P	Yes	Yes	No	No	Yes
2-3 P	Yes	Yes	No	No	Yes
2-4 P	Yes	No	Yes	No	Yes
1-1 A	Yes	No	No	No	Yes
1-2 A	Yes	No	Yes	No	Yes
1-3 A	Yes	No	No	Yes	Yes
2-1 A	Yes	Yes	No	No	Yes
2-2 A	Yes	Yes	No	No	Yes
2-3 A	Yes	Yes	No	No	Yes
2-4 A	Yes	Yes	No	No	Yes

Table III. Characteristics of connections after cooling down from fire temperature 550°C.

Test ID	Endplate		Peak load		Connection rotation
	Material	Thickness (mm)	Moment (kN·m)	Force (kN)	ϕ_C (mrad)
1-1 P	Q235	20	255.56	237.51	249
1-2 P	S690	12	226.67	210.66	397
1-3 P	S960	10	230.80	214.50	147
2-1 P	Q235	25	272.59	253.34	150
2-2 P	Q345	20	272.35	253.11	139
2-3 P	S690	15	261.79	243.30	141
2-4 P	S960	12	252.85	234.99	238

2.4.2 Moment-rotation relationship of endplate connections

The tested characteristics of moment-rotation relationship for all endplate connections after cooling down from elevated temperature 550°C are presented in Table III.

3. NUMERICAL STUDY

3.1 Finite Element Model

The geometric details of all connections' components modelled in FEM are the same as those of the test specimens. Because the geometric details, load, temperature distribution and boundary conditions of the beam-to-column endplate connection are symmetric, half of the endplate connection was modelled, to reduce computer costs. There are 7 surface-to-surface contact interactions and 7 tie interactions in this FE model, and the materials are endowed with non-linear properties. The whole connection was modelled using C3D8I elements.

3.2 Contact Interaction

The contact pairs in this numerical model comprise the bolts-to-column flange, column flange-to-endplate, endplate-to-nuts and bolt shanks-to-bolt holes. The nuts were tied to the corresponding bolt shanks. Surface-to-surface contact, with a small sliding option, was employed for all contact surfaces to fully transfer load. The penalty friction was employed in the contact interaction property. The failure criterion employed herein is based on deformation by assuming that cracking occurs when the ultimate strain ε_u of the material (either endplate or bolt) is reached, as proposed by Girao Coelho et al. [3, 4].

3.3 Material Properties

In this FE modelling, the material properties of mild steels (including Q235 and Q345) after cooling down from fire temperature 550°C are 90% of their original mechanical properties at ambient temperature without fire exposure, according to the recommendation on post-fire remaining factor of S235 and S275 from British Standard 5950: Part 8 [5]. The material properties of Grade 8.8 bolt assembly at ambient temperature without fire exposure input herein are in accordance with those reported by the University of Sheffield in literature [6-9], and the remaining factors of mechanical properties of Grade 8.8 bolt assembly after fire reported by Guobiao Lou et al. [10] are employed herein. The material properties of high strength steels S690 and S960 after cooling down from fire input in this FE model are obtained by the experimental study presented in references [11-12].

4. DISCUSSIONS

4.1 Validation of Numerical Modelling against Experimental Results

4.1.1 Deformation at the end of test

The numerically simulated final deformation states of all endplate connections were compared with those obtained from the experimental study. Figure 3 and Figure 4 present the comparisons on the connection 2-3 P (S690 15mm) and its components after failure at ambient temperature after 550°C, as an example. It can be seen that good agreements exist on the final deformation of connection 2-3 P after fire. Although the current numerical model cannot simulate the fracture of the bolts, it is able to reveal the location where the fracture initiates and evolves, see Figure 4 (c). Similar conclusions can be drawn for all 7 connection specimens after fire.

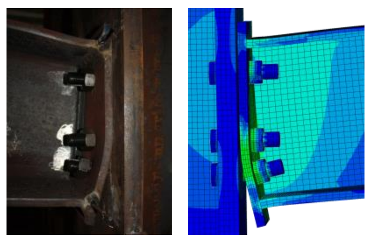

Figure 3. Comparison on final deformation state of connection 2-3 P (S690 15mm) after 550°C.

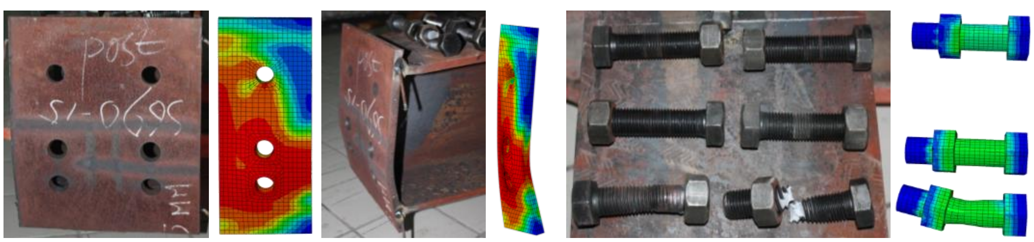

(a) Endplate front view (b) Endplate side view (c) Bolts

Figure 4. Comparison on post-fire components of connection 2-3 P (S690 15mm) after failure.

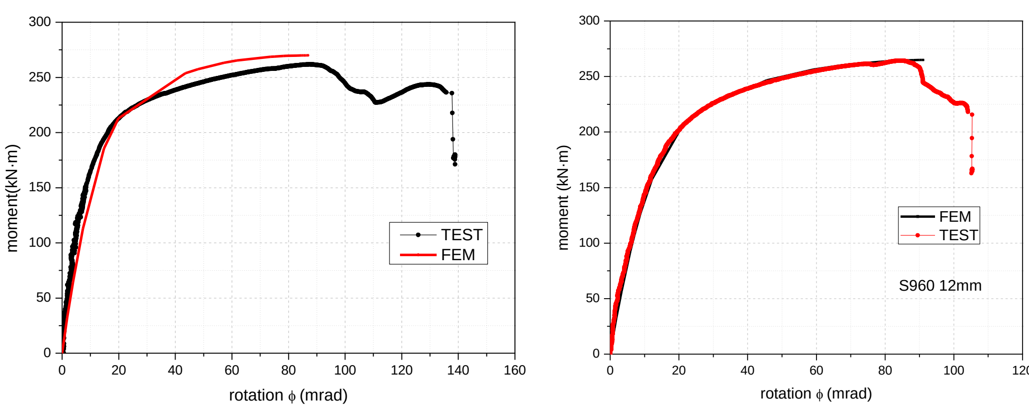

(a) 2-3 P (S69015mm) (b) 2-4 A (S960 12mm)

Figure 5. Moment-rotation comparison of endplate connections.

4.1.2 Moment-rotation characteristic

The comparisons of numerical modelling and experimental study on the moment-rotation relationship of various endplate connections (both high strength steel endplate connections and mild steel endplate connections) after cooling down from elevated temperature 550°C as well as at ambient temperature were carried out, where good agreements exist in general on initial stiffness, load bearing capacity and the connection rotation at the maximum load level $\phi_{M\max}$. For example, Figure 5 illustrates the moment-rotation comparison of two connections 2-3 P and 2-4 A.

4.2 Verification against Eurocode 3

4.2.1 Failure modes

According to Eurocode 3 Part:1-8 [1], there are 3 failure modes for endplate connections. Mode 1 is complete yielding of endplate or column flange, Mode 2 is bolt failure with yielding of endplate or column flange, while Mode 3 is bolt failure. Mode 3 is considered to be brittle and should be avoided in practical design. The failure modes of all endplate connections after fire obtained via theoretical analysis based on the rules of Eurocode 3 were validated against those from post-fire tests, as shown in Table IV. It can be observed that the predictions of Eurocode 3 agree very well with the test results.

Table IV. Failure modes of endplate connections after cooling down from 550°C.

Test ID	Endplate		Failure mode	
	Material	Thickness (mm)	EC3	Test
1-1 P	Q235	20	Mode 1	Mode 1
1-2 P	S690	12	Mode 1	Mode 1
1-3 P	S960	10	Mode 1	Mode 1
2-1 P	Q235	25	Mode 2	Mode 2
2-2 P	Q345	20	Mode 2	Mode 2
2-3 P	S690	15	Mode 2	Mode 2
2-4 P	S960	12	Mode 2	Mode 2

4.2.2 Plastic flexural resistance

The plastic flexural resistances of all endplate connections at elevated temperature 550°C are compared with the theoretical predictions of Eurocode 3 [1], as listed in Table V. It can be observed that good agreements exist between the theoretical predictions and experimental results. Via Ratio3 presented in Table V, it can be found that $M_{j,Rd,test,1}$, obtained based on Zanon and Zandonini's definition [13], is generally smaller than $M_{j,Rd,test,2}$, which is defined according to Weynand's proposal [14] and the simplified method recommended by Eurocode 3. The comparison of $M_{j,Rd,test,2}$ with the predicted plastic flexural resistance according to Eurocode 3 shows that the predictions of Eurocode 3 are generally at the conservative side when the test result is obtained based on Weynand's method. However, when the test obtained plastic flexural resistance is defined according to Zanon and Zandonini's method, the predictions of Eurocode 3 are not as conservative as the former, but still on the conservative side in general. This validates that the accuracy of Eurocode 3 is acceptable to predict the plastic flexural resistance of endplate connections after fire, no matter the endplate is made of mild steels or high strength structural steels.

Table V. Evaluation of plastic flexural resistance after cooling down from 550°C.

Test ID	$M_{j,Rd,EC3}$ (kN·m)	$M_{j,Rd,test,1}$ (kN·m)	$M_{j,Rd,test,2}$ (kN·m)	$\text{Ratio}_1=\frac{M_{j,Rd,EC3}}{M_{j,Rd,test,1}}$	$\text{Ratio}_2=\frac{M_{j,Rd,EC3}}{M_{j,Rd,test,2}}$	$\text{Ratio}_3=\frac{M_{j,Rd,test,1}}{M_{j,Rd,test,2}}$
1-1 P	150.36	164.98	161.21	0.911	0.933	1.023
1-2 P	158.93	190.17	205.88	0.836	0.772	0.924
1-3 P	153.56	175.67	194.24	0.874	0.791	0.904
2-1 P	223.06	227.59	233.18	0.980	0.957	0.976
2-2 P	211.12	232.07	238.41	0.910	0.886	0.973
2-3 P	228.32	216.43	227.73	1.055	1.003	0.950
2-4 P	222.11	215.80	228.26	1.029	0.973	0.945

Note:

$M_{j,Rd,EC3}$ is the predicted plastic flexural resistance according to Eurocode 3;

$M_{j,Rd,test,1}$ is the test obtained plastic flexural resistance according to Zanon and Zandonini's evaluation method;

$M_{j,Rd,test,2}$ is the test obtained plastic flexural resistance according to Weynand's evaluation method.

5. CONCLUSIONS

The following conclusions can be drawn from this experimental and numerical study:

1. The post-fire load bearing capacity as well as rotation capacity of endplate connections is dependent on the combination of endplate material and endplate thickness.
2. In endplate connections, a proper design using a thinner high strength steel endplate can achieve the same failure mode, similar residual load bearing capacity and comparable or even higher rotation capacity after cooling down from fire, in comparison with a connection with thicker mild steel endplate.
3. It is found that high strength steel endplate connection can regain more than 90% of its original load bearing capacity after cooling down from fire temperature 550°C. This important finding is very promising for the reuse of steel structures with high strength steel endplate connections after fire.
4. The accuracy of Eurocode 3 for plastic flexural resistance of endplate connections is validated to be acceptable to predict post-fire performance, no matter the endplate is made of mild steels or high strength structural steels.

REFERENCES

[1] CEN.2005. Eurocode 3: Design of steel structures, Part 1-8: Design of joints. Brussels.

[2] J. Witteveen, L. Twilt, F.S.K. Bijlaard. 1976. Theoretical and experimental analysis of steel structures at elevated temperatures, in: *International association for bridge and structural engineering*, Tokyo.

[3] A.M.G. Coelho, F.S.K. Bijlaard, L.S.D. Silva. 2002. On the deformation capacity of beam-to-column bolted connections, in, European Convention for Constructional Steelwork – Technical Committee 10: Structural connections (ECCS-TC10).

[4] A.M.G. Coelho. 2004. Characterization of the ductility of bolted end plate beam-to-column steel connections, PhD thesis, University of Coimbra, Coimbra, Portugal.

[5] B.S. Institution. 1998. Structural use of steelwork in building, in: Part 8: Code of practice for fire resistant design, London.

[6] Y. Hu, J.B. Davison, I.W. Burgess, R.J. Plank. 2007. Comparative Study of the Behaviour of BS 4190 and BS EN ISO 4014 Bolts in Fire, in: *ICSCS 2007*, Manchester, UK, 587-592.

[7] Y. Hu, J.B. Davison, I.W. Burgess, R.J. Plank. 2008. Experimental Study on Flexible End Plate Connections in Fire, in: *5th European Conference on Steel and Composite Structures*, Graz, Austria, 1007-1012.

[8] Y. Hu. 2009. Robustness of flexible endplate connections under Fire Conditions, PhD thesis, University of Sheffield, Sheffield, UK.

[9] Y. Theodorou. 2003. Mechanical properties of grade 8.8 bolts at elevated temperatures, Master's dissertation, University of Sheffield, Sheffield, UK.

[10] G.B. Lou, S. Yu, R. Wang. 2010. Experimental Study of Mechanical Properties of High-Strength Bolts After Fire, *Structures in Fire: Proceedings of the 6th International Conference*, 679-686.

[11] X. Qiang, F.S.K. Bijlaard, H. Kolstein. 2012. Post-fire mechanical properties of high strength structural steels S460 and S690, *Eng Struct*, 35:1-10.

[12] X. Qiang, F.S.K. Bijlaard, H. Kolstein. 2013. Post-fire performance of very high strength steel S960, *J Constr Steel Res*, 80: 235-242.

[13] P. Zanon, R. Zandonini. 1988. Experimental analysis of end plate connections, in: *Proceedings of the state of the art workshop on connections and the behaviour of strength and design of steel structures*, Cachan, 41-51.

[14] K. Weynand. 1997. Sicherheits- und Wirtschaftlichkeitsuntersuchungen zur Anwendung nachgiebiger Anschlüsse im Stahlbau. Heft 35, Shaker Verlag, Aachen.

Experimental Study of High-Strength Bolts under Combined Tension and Shear During and After Fire

ANNE K. KAWOHL and JORG LANGE

ABSTRACT

Experimental studies on high-strength bolts which included both tests under tension and shear show deviating reduction of strength with rising temperatures depending on whether the bolts were loaded by tension or shear. In this paper an experimental study on high-strength bolts of the property class 10.9 under a combination of both tension and shear will be presented. Tests were carried out both under fire conditions and at ambient temperature on bolts first heated to a specified temperature and then cooled slowly to establish the post-fire performance.

INTRODUCTION

Connections are essential to the stability of a steel structure. The connections not only transfer load from one bearing member to another but, through their rigidity they also influence internal forces. During a fire the connections are exposed not only to thermal strain in addition to the internal forces at ambient temperatures; in the heating phase of a fire a connection which usually is designed to bear moment and shear receives compression from the thermal expansion of the connected member. In a later phase of the fire the strain changes to shear and tension as the connected beam hangs more or less in catenary. For the load case fire, connections therefore must have sufficient ductility. The rotational capacity depends on the different elements that form a connection, e.g. the bolts used. In addition to the load bearing capacity the load-deflection behavior is of interest.

The behavior of high-strength bolts in fire is of special interest as they obtain their enhanced strength through different heat treatments which are partially reversed in fire. Several studies on the load bearing behavior of high-strength bolts under fire have been carried out in recent years. Most of these studies, however, focus either on pure tension or pure shear tests. Those studies, which included both tests (tension and shear) show deviating reduction factors for bolt strength depending on whether the bolts were loaded by tension or shear. One of these studies is the extensive test series done by Kirby [1] on different bolts of the property class 8.8 (f_u = 800 N/mm²). At

Institute for Steel Structures and Materials Mechanics, Technische Universität Darmstadt, Franziska-Braun-Straße 3, 64287 Darmstadt, Germany

very high temperatures (above 600°C) the reduction of load bearing capacity was less for the bolts tested under shear than for the bolts tested under tension. The reduction factors for bolt strength given in Appendix D of the Eurocode 3 part 1-2 [2] are based on the test results by Kirby. As stated in the ECCS Model Code on Fire Engineering [3] the test results of the tension tests were used as these lead to more conservative values. An experimental study done by Kodur et al. [4] on A325 and A490 bolts (f_u = 830 N/mm² and f_u = 1,030 N/mm²) also includes both tension and shear tests. Similar to the tests done by Kirby, the test results show a deviating reduction of strength depending on the strain to the bolts and the temperature. For the A325 bolts the absolute value of shear strength lies above the absolute value of the ultimate tensile strength in the temperature range between 450°C and 550°C. For the A490 bolts the absolute values of shear strength are above the absolute values of the ultimate tensile strength beginning at a temperature of approximately 550°C. This effect of differing strength reduction depending on the strain was also observed by González [5] in his test series on bolts of the property class 10.9 (f_u = 1,000 N/mm²). The strength reduction of the bolts strained by shear is in general less than for the bolts strained by tension. The difference between the reductions becomes larger with rising temperature from 450°C onwards.

A test series was outlined to examine whether a combination of tension and shear has an influence on the load bearing behavior of high-strength bolts during fire. Within the test series, bolts were tested both during fire and also with reference to their post-fire performance. This article presents the test layout, test results and initial conclusions from the experimental investigation.

EXPERIMENTAL SET-UP

A special test rig was designed which allows a bolt to be strained both by tension and shear at the same time by applying pressure to the test rig, Figure 1. NIMONIC 80A, a nickel-based high-temperature alloy, was chosen as material for the rest rig to eliminate unwanted deformation or even failure of the test rig. Two different angles were chosen to investigate different shear-to-tension combinations, 30° and 45°. In addition, the angle of 0°, which leads to pure tension in the bolts, is also investigated as reference.

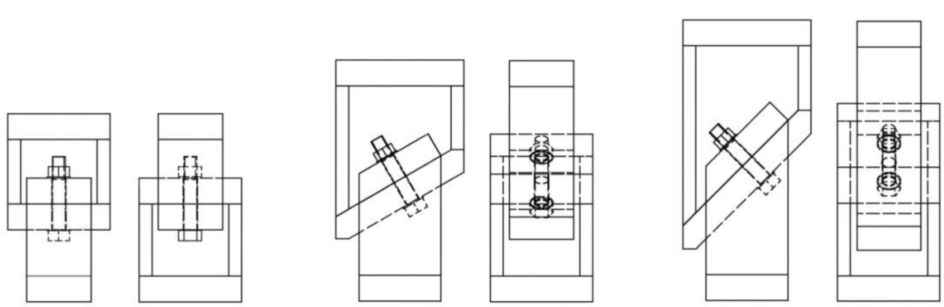

Figure 1. Test rigs for an angle of 0° (left), 30° (center) and 45° (right).

The tests at elevated temperatures were conducted as steady-state tests with the temperature rising until the exposed bolt reached the specified temperature. A 4 zone electric furnace with a maximum temperature of 1,000°C was used. The furnace used is fitted with a 3 MN compression machine. The furnace has a heating rate of approximately 10 K/min. A heating rate of 5 K/min was chosen for the tests to ensure a stable heating process. The initial plan was to conduct three tests each for every combination of temperature and angle. But after the first three tests (45° angle and 500°C) showed very good compliance, it was decided to conduct only two tests for each combination.

For the tests of post-fire performance the bolts and nuts were heated without additional mechanical loading to the specified temperature in an electrical furnace. The heating rate was approximately 10 K/min. The bolts and nuts were then cooled slowly to ambient temperature. The testing was carried out at ambient temperature with a testing machine with a maximum load of 1 MN. 5 tests were done for each combination of angle and temperature.

The strain rate for both tests – at elevated temperatures and post-fire performance tests – was chosen according to DIN EN ISO 6892-1 [7] or DIN EN ISO 6892-2 [8] respectively to 0,015 min^{-1}. As recommended the testing was carried out at constant velocity until failure.

EXAMINED BOLTS

Whole bolt sets according to DIN EN 14399-1 [6] of the property class 10.9 were used in the study. The bolts are shank bolts. All elements of the bolt sets (bolts, nuts and washers) were hot-dip galvanized. These bolt sets were chosen as they are commonly used in German steel structures. All tested bolts were from a German manufacturer and from the same batch. The bolts were made of 36CrB4; the chemical composition is stated in Table I. The bolts were manufactured by cold forming of wire rod and thread rolling. Equivalent to the forming of the bolts, the quenching and tempering of the bolts occurs in flow production. In the final step the bolts and nuts were hot-dip galvanized.

EXAMINED TEMPERATURES

As experimental studies at elevated temperatures are both expensive and time-consuming only two temperatures are specified at approximately 500°C and 700°C. 500°C was chosen as the difference between the load bearing capacity under shear and under tension becomes significant for 10.9 bolts beginning at temperatures around 450°C as mentioned above. Three additional thermocouples of the type K were installed in the testing furnace to monitor the temperature. One thermocouple was fixed to the surface of the testing rig. Another thermocouple was fed through a channel to the outer surface of the bolt in the shear plane where the surrounding mass of the test rig is highest to ensure that the bolt is uniformly heated. As the temperature of the

TABLE I. CHEMICAL COMPOSITION OF TESTED BOLTS.

chemical composition in wt%					
C	**Si**	**Mn**	**P**	**S**	**Al**
0.367	0.095	0.715	0.013	0.002	0.022
Cr	**Ni**	**Mo**	**B**	**Ti**	**Cu**
1.050	0.036	0.005	0.0024	0.040	0.009

test rig and therefore also that of the bolt is not the same as the air temperature in the furnace, it is very difficult to meet the specified temperature exactly; it can only be reached approximately. The test was not started before a significant stabilising time had passed during which the temperature was held constant and the temperature readings of the thermocouples showed constant temperatures.

As the post-fire performance tests are less time-consuming a larger number of temperatures were tested. The specified temperatures are 500°C, 600°C, 700°C, 800°C and 900°C. González [5] showed in his experimental study that temperatures below 500°C have no influence on the post-fire bearing capacity of bolts of the property class 10.9. Once the bolts had reached the target temperature, it was kept constant for 30 min to ensure that the temperature had been reached throughout the bolt section. In addition, bolts without further heat treatment were tested as reference. The results of these tests are marked with 20°C.

RESULTS

TEST RESULTS AT ELEVATED TEMPERATURES

As is shown in Figure 2, the load-deflection curves of the bolts tested at approximately 500°C differ significantly according to the angle at which the bolt was tested. While the bolts tested at an angle of 45° show large deflection even after the maximum load is reached this is not true for the bolts tested at an angle of 30° and 0° (pure tension). The difference is also visible in the failure mode of the bolts. The bolts

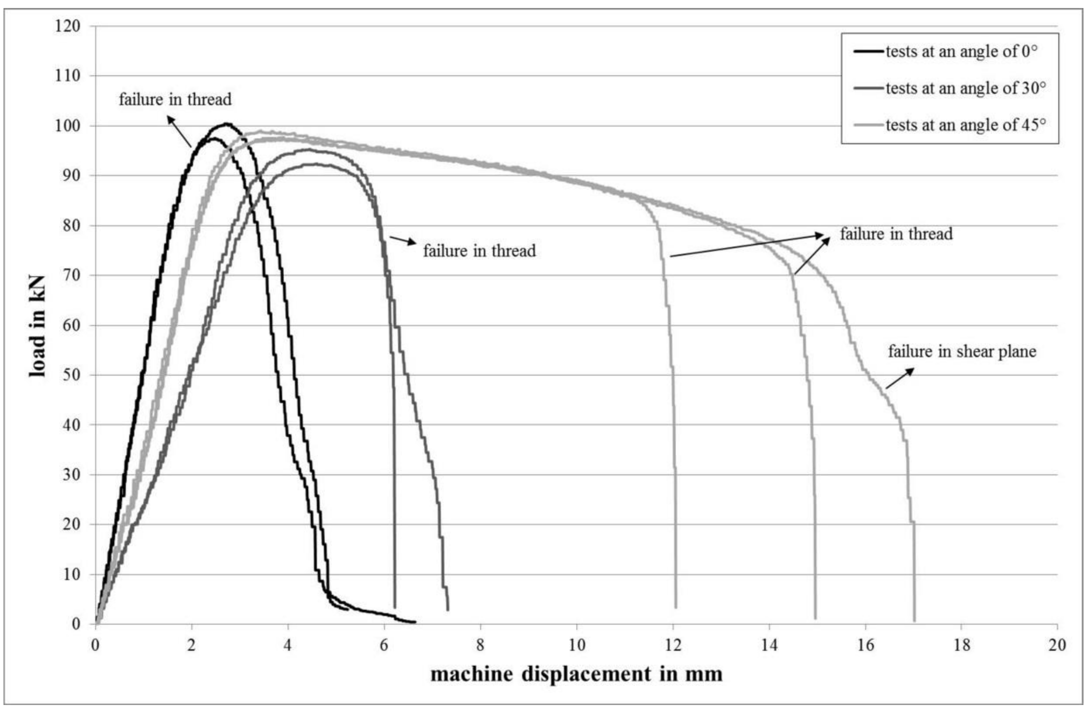

Figure 2. Load-deflection diagram of the tests at approximately 500°C.

tested at an angle of 0° and 30° all failed in the thread. Of the bolts tested at an angle of 45° one bolt failed in the shear plane as was anticipated from the tests at ambient temperature; the other two bolts failed also in thread but failure in the shear plane was imminent. In comparison to the tests at ambient temperature also the bolts tested at an angle of 30° were expected to fail in the shear plane. The failure in the thread points to a failure due to LME (liquid metal induced embrittlement), where the liquid zinc of the coating flows into the micro cracks along the grain boundaries due to tensile stresses and consequently leads to brittle failure of the microstructure. The temperature of approximately 500°C is within the temperature range which was to found to be the critical temperature range for LME for hot-dip galvanized bolts of the property class 10.9 by González [9]. This assumption was verified by an EDX-analysis in which zinc was found on the entire fracture surface.

The other investigated temperature was approximately 700°C. This temperature is outside of the critical temperature range for LME of galvanized 10.9 bolts. For the bolts tested at an angle of 30° and 45° the failure occurred in the shear plane with a large necking of the cross section. The bolts tested at an angle of 0° failed through stripping of the thread, see Figure 3. The furnace used for the testing offers no possibility of visual monitoring of the tests. Some of the tests were therefore stopped before rupture of the bolts but well after the maximum load had been reached. The maximum load reached at this temperature is only about a fifth of the maximum load reached at a temperature of approximately 500°C. However the bolts show a very large deflection at 700°C.

In Figure 4 the results of the current tests are put into the context of the reduction factors for bolt strength at elevated temperatures for all property classes as stated in Appendix D of Eurocode 3, the reduction factors given by Kirby [1] from his tests on 8.8 bolts and the reduction factors given by Lange and González [9] for bolts of the property class 10.9. In addition, the test results of the tension and shear tests on

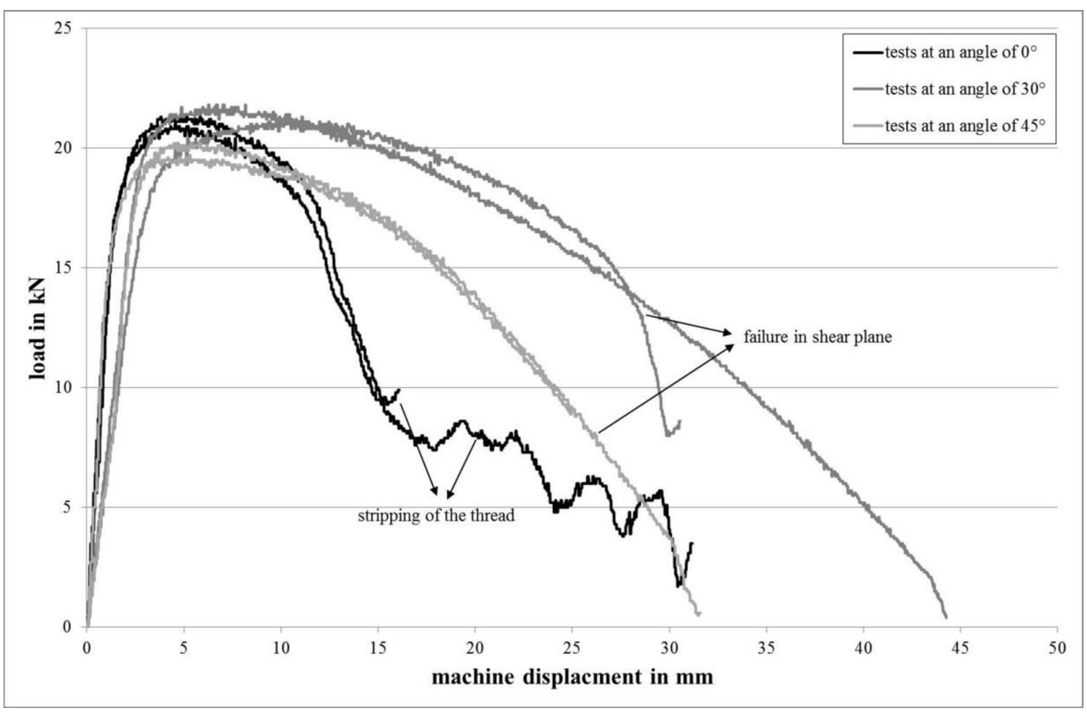

Figure 3. Load-deflection diagram of the tests at approximately 700°C.

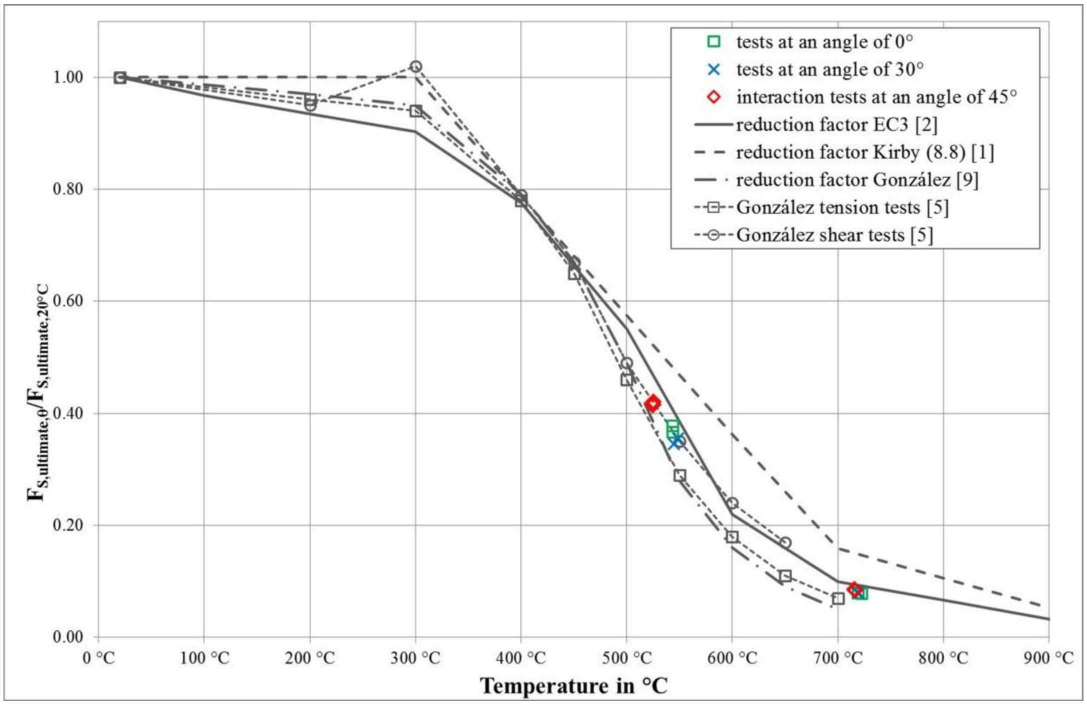

Figure 4. Test results compared to the reduction factors from EC 3 [2], Kirby [1] and Lange and González [9] as well as the test results from González [5].

10.9 bolts conducted by González [5] are plotted. As in the tests results from González [5], the maximum load of the current tests lie below the reduction factor given by the Eurocode, but well above the reduction factors given by Lange and González [9] for bolts of the property class 10.9. In comparing the values of the tests by González and the current tests one must take into consideration that the strain rate of the current tests (of 0.015 min^{-1}) is faster than the strain rate used by González [5]. Due to high-temperature creep the strain rate has a significant influence on the tensile strength as shown, among others, by Bull et al. [10].

RESULTS OF THE POST-FIRE PERFORMANCE TESTS

High-strength bolts obtain their enhanced strength through a carefully controlled heat treatment (quenching and tempering). The uncontrolled heating and cooling in the event of fire can therefore lead to a complete change of the material properties as the microstructure is changed. In his dissertation [5] González states two reduction factors for evaluating the post-fire strength of bolts of the property class 10.9. The maximum reduction factor $k_{Red,max}$ is based on pure tension tests on specimens and bolts that where both heated and at the same time mechanically loaded. The minimum reduction factor is based on pure tension tests on specimens and bolts that were heated without additional mechanical load. The post-fire reduction of the strength of a 10.9 bolt should generally lie between equation (1) and (2).

$$k_{Red,min} = \begin{cases} 1.0 & 20°C \leq T \leq 500°C \\ -1.434 \cdot 10^{-3} \cdot T + 1.717 & 500°C \leq T \leq 800°C \end{cases} \tag{1}$$

$$k_{Red,max} = \begin{cases} 1.0 & 20°C \leq T \leq 450°C \\ -2.0 \cdot 10^{-3} \cdot T + 1.9 & 450°C \leq T \leq 800°C \end{cases} \tag{2}$$

As mentioned above, in the current study bolts are tested which had been heated without additional mechanical load. Therefore, the values lie nearer to the reduction factor $k_{Red,min}$, see Figure 5. In Figure 5 the test results are plotted as loss of strength against temperature, where the loss of strength is the quotient of the failure load of the bolt preheated to the specific temperature and the average of the failure loads of the tests of the untreated bolts (20°C). The reduction factors stated by González [5] are also applicable for the tested batch of 10.9 bolts and the combination of tension and shear. In addition, the test results show that the combination of shear and tension has a positive effect on the post-fire load-bearing capacity of the tested bolts. With rising shear component (angle) the load bearing capacity is also increased. Independent of the temperatures to which the bolts were heated, the failure occurred for an angle of 0° in the thread and for the angles of 30° and 45° in the shear plane.

Noticeable is the increase of load-bearing capacity of the bolts heated to 900°C in comparison to the bolts heated to 800°C. In addition, specimens turned from the bolts were tested to obtain the stress-strain relations. Up to 600°C the stress-strain relations show no yielding, which is typical for quenched and tempered steels. The specimens taken from the bolts heated to 700°C, 800°C and 900°C all show a yield plateau. Even though the specimens from the 900°C bolts show a further decrease of the proportional limit in comparison to the 800°C bolts, the strain hardening is increased which leads to higher ultimate stress values. Micrographs of the bolts of both temperatures show that in both cases only pearlite and ferrite remains, but in addition the microstructure of the bolts heated to 900°C is coarser.

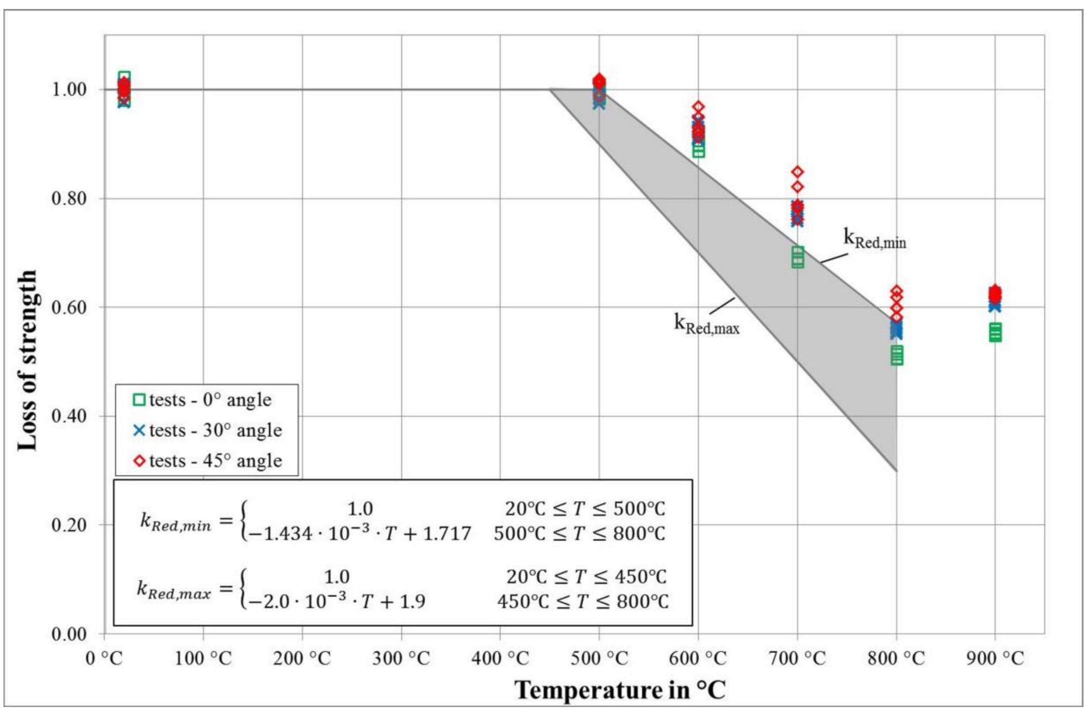

Figure 5. Test results of post-fire tests in comparison to the reduction factors stated by González [5].

CONCLUSIONS

In this experimental study the load bearing behavior of high-strength bolts of the property class 10.9 under a combination of tension and shear was investigated to contribute to the understanding of the load bearing behavior of these bolts during and after fire. From the fire tests it can be concluded that the sudden failure due to LME in the critical temperature range depends on the amount of shear – the higher the shear component the lower the risk of failure due to LME. At a temperature of approximately 500°C the bearable deflection of the system is increased with the increase of the shear component. However, this is not true for the temperature of approximately 700°C. Here, the bearable deflection seems to decrease. The results from the post-fire tests show a positive influence of increase of shear component on the load-bearing capacity of the bolts. The reduction factors for the post-fire performance as stated by González [5] can also be used for bolts under combined strain. Up to a temperature of around 500°C the bolts regain their original load-bearing capacity after cooling.

ACKNOWLEDGEMENTS

The authors thank Prof. Dr. Mario Fontana, ETH Zürich, and his staff for the most helpful support during the fire tests.

REFERENCES

1. Kirby, B.R. 1995. "The Behaviour of High-strength Grade 8.8 Bolts," *J. Construct. Steel Research,* 33(1995): 3-38.
2. DIN EN 1993-1-2: Eurocode 3: Design of steel structures, Part 1-2: General rules – Structural Fire Design, German Version: EN 1993-1-2:2:2005 + AC:2009.
3. European Convention for Constructional Steelwork / Technical Committee Fire Safety of Steel Structures ECCS. 2001. "Model Code on Fire Engineering," Brussels, Belgium.
4. Kodur, V., Kand, S. and W. Khaliq. 2012. "Effect of Temperature on Thermal and Mechanical Properties of Steel Bolts," *J. Mater. Civ. Eng.*, 24 (2012):765-774.
5. González Orta, F. 2011. "Untersuchungen zum Material- und Tragverhalten von Schrauben der Festigkeitsklasse 10.9 während und nach einem Brand", Technische Universität Darmstadt. Darmstadt.
6. DIN EN 14399-1: High-strength structural bolting assemblies for preloading – Part 1: General requirements, German Version: EN 14399-1:2015.
7. DIN EN ISO 6892-1: Metallic materials – Tensile testing – Part 1: Method of test at room temperature, German Version EN ISO 6892-1:2009.
8. DIN EN ISO 6892-2: Metallic materials – Tensile testing – Part 2: Method of test at elevated temperature, German Version EN ISO 6892-2:2011
9. Lange, J. and F. González. 2012."Behavior of High-Strength Grade 10.9 Bolts under Fire Conditions," *Structural Engineering International,* 4(2012). 470-475
10. Bull, L., Palmiere E.J., Thackray, R.P., Burgess, I.W. and B. Davison. 2015. "Tensile Behaviour of Galvanised Grade 8.8 Bolt Assemblies in Fire," *Journal of Structural Fire Engineering* 6(3): 197-212

Post-Fire Mechanical Properties of High Strength Grade 8.8 Steel Bolts

MAHMOOD YAHYAI[1], ABBAS REZAEIAN[2],
VENKATESH KODUR[3], MOHAMMADREZA ESLAMI[3]
and ALIREZA POORMOHAMADI[1]

ABSTRACT

In order to understand the post-fire performance of bolted connections, it is essential to have a deep knowledge of the material behavior of all the components, including bolts, after fire conditions. Very limited research has been carried out on the behavior of high-strength steel bolts during and after fire conditions. This paper presents experimental investigations of the residual mechanical properties of Grade 8.8 bolts after exposed to elevated temperatures up to 900°C. The post-fire stress-strain curves, residual elastic modulus, yield and ultimate strengths as well as tensile failure modes of bolts were investigated. Also, the effect of factors including target temperature level, chemical composition of feedstock steels (SAE 10B21 and 10B38) and heat treatment characteristics in production process of Grade 8.8 bolts were studied. It was observed that, the bolts exhibited drastic reduction in strength after cooling down from temperatures beyond 400°C, as they lost about 50% of their ultimate strength after experiencing 800°C. Furthermore, a set of predictive equations are proposed for evaluating the residual mechanical properties of Grade 8.8 bolts after fire.

Keywords: Steel bolt, Mechanical properties, Post-fire, Residual factor, Tensile fracture, Temperature

1. INTRODUCTION

Connections in a structural system play a critical role in transferring loads from one member to the other. The integrity of a structural system may be compromised in the event of connections failure, leading to damage or even collapse of the structure. The role of bolted connections is much more crucial under fire condition; as significant fire-induced forces have to be withstood (Rezaeian and Yahyai 2015; Yahyai and Rezaeian 2015; Saedi and Yahyai 2009) [1-3]. As the critical basis of

[1] Department of Civil Engineering, K.N. Toosi University of Technology, Iran,
E-mail: yahyai@kntu.ac.ir
[2] Department of Civil Engineering, Shahid Chamran University of Ahwaz, Iran,
E-mail: rezaeian_a@scu.ac.ir
[3] Department of Civil and Environmental Engineering, Michigan State University, USA,
E-mail: kodur@r.msu.edu; eslami@msu.edu

evaluating the performance of steel structures after fire, the post-fire material properties of all components including bolts are essential.

The mechanical behavior of bolts at elevated temperatures differs considerably from that of structural (carbon) steel due to difference in manufacturing process used in bolts, where is based on quenching and tempering processes. Eurocode3: Part 1.2 [4] proposes strength reduction factors as a function of the temperature for evaluating strength requirements in bolts under fire conditions. These factors have been proposed on the basis of limited experimental work by Kirby [5] (1995) on grade 8.8 hexagonal head bolts, at temperatures up to 800°C. Also, Kodur et al [6] (2012) proposed relations for variation of thermal and mechanical properties of Grade A325 and A490 steel bolts at temperatures up to 800°C**.** These, mechanical models for bolts are developed by considering heating conditions only and without due consideration to the cooling phase [7,8].

Grade 8.8 bolts are produced by quenching and tempering carbon or alloy steels that contain more carbon, molybdenum and chromium than conventional steels. The different chemical composition of high-strength steels influence the high-temperature and post-fire mechanical properties of Grade 8.8 bolts. Few research studies are reported on behavior of these bolts in fire conditions [5]. There is no available data on post-fire mechanical properties of Grade 8.8 bolts.

To overcome these limitations, an experimental study is carried out on Grade 8.8 bolts, made with different chemical compositions and heat treatments, to evaluate residual mechanical properties after exposed to temperatures up to 900°C and then cooled down. The post-fire residual stress-strain response, elastic modulus, yield and ultimate strength are presented in this paper. Furthermore, a set of predictive equations are proposed for expressing residual mechanical properties of bolts as a function of temperature.

2. EXPERIMENTAL PROGRAM

2.1 Test methodology

In this research, two types of tests have been performed on full size bolts: (a) Room temperature tensile strength tests, performed in order to get the reference strength of unheated bolts; and (b) Post-fire tensile strength tests, in which the bolts were heated up to a pre-specified temperature cooled down to ambient temperature, and then tested for tensile strength. The tensile test was carried out in each case by subjecting the bolts to failure.

2.2 Test specimens

High-strength Grade 8.8 bolts are manufactured through either hot or cold forging followed by a quench and temper heat treatment to achieve the required mechanical properties. The bolts should not only meet the specification for the intended use at ambient temperature, but also their performance is important during and after fire.

In present test program three sets of bolts were used (Table I). Two sets of bolts were selected from cold forging SAE 10B38 steel bar, followed by quenching from an austenitising temperature of 870°C and subsequently tempering at 530°C. The third set of bolts was taken through cold forging SAE 10B21 steel bar, quenched from 870°C and tempered at 475°C. To provide a consistent basis for comparing their behavior after fire exposure, the bolts within each set were taken from a single production botch, using the same bar feedstock, forging operation and subsequent heat treatment conditions. In total, tests on 99 bolts were carried out. All specimens were Hexagon cap screws partly threaded bolts produced by ITC Company in compliance with DIN 931 standard [9].

The chemical compositions of bolts were acquired using FOUNDRY-MASTER UV metal analyzer (Figure 1). Obtained chemical compositions of both sets of grade 8.8 bolts are given in Table II.

TABLE I. CHARACTERISTICS OF TEST SPECIMENS.

Bolt set ID	**Bolt grade**	**Bolt size**	**Material**	**Yield strength F_y (MPa)**	**Ultimate strength F_u (MPa)**	**Elasticity Modulus E (GPa)**	**Rockwell Hardness (HRC)**	**Number of tests**
M16(10B38)	8.8	M16	SAE 10B38	834	951	210	29	33
M18(10B38)	8.8	M18	SAE 10B38	831	945	211	29	33
M22(10B21)	8.8	M22	SAE 10B21	986	1079	202	30	33

TABLE II. CHEMICAL COMPOSITION OF FEEDSTOCK STEELS FOR GRADE 8.8 BOLTS.

	Chemical composition (%)											
Material	**Fe**	**C**	**Si**	**Mn**	**P**	**S**	**Cr**	**Mo**	**Ni**	**Al**	**Co**	**Cu**
SAE10B38	98.3	0.399	0.270	0.736	0.0117	0.0047	0.0733	<0.005	0.0085	0.0267	0.0094	0.0779
SAE10B21	98.3	0.223	0.253	0.851	0.0132	0.0070	0.1415	<0.005	0.0171	0.0184	0.0092	0.0893
	Nb	**Ti**	**V**	**W**	**Pb**	**Sn**	**B**	**Ca**	**Zr**	**As**	**Bi**	
SAE10B38	0.0023	0.0365	<0.002	<0.015	<0.025	0.0046	0.0015	0.0007	<0.002	0.0089	<0.030	
SAE10B21	<0.002	0.0354	<0.002	<0.015	<0.025	0.0049	<0.001	<0.001	<0.002	0.0075	<0.030	

Figure 1. FOUNDRY-MASTER UV metal analyzer.

Figure 2. Electrical testing furnace.

2.3 Test Procedure

An electric furnace, with manual adjustment of power, was used for heating the bolts (Figure 2). Two K-type thermocouples, mounted on the specimen and furnace, recorded the temperature of the specimen and the furnace. As shown in Figure 3, the bolts were heated from ambient temperature to specific target temperatures at a rate of 10°C/min. Ten target temperatures (T_u), of 300, 400, 500, 600, 650, 700, 750, 800, 850 and 900°C were selected. Once the specimen was heated to the target temperature, it was stabilized for a period of 15 min to ensure uniform temperature distribution throughout the bolt. In the cooling phase, the furnace was switched off and the bolt specimen was allowed to come down (cool) to room temperature naturally. The cooling rate was approximately in the range of 10-20°C/min, and thereafter tensile strength tests was performed on bolt specimens at ambient temperature. The tensile strength tests were conducted using SANTAM universal test machine. All the tensile tests were conducted at room temperature according to the ASTM E8 (2009) [10] test procedure. Three repeating tests were conducted for each bolt under the same conditions to ensure the reproducibility of results. A displacement-controlled quasi-static load, with a displacement rate of 0.02 mm/s, was applied on the specimens until failure. A high resolution axial extensometer gauge was used to measure the strain in the central region of the bolt. Obtained data were recorded by a computer and visual observation were also taken during the tests.

3. EXPERIMENTAL RESULTS

Stress-strain curves are obtained from universal machine in order to understand the general material behavior. The test results are presented in the form of post fire residual factor for yield and ultimate strength.

3.1 Post fire stress-strain curves

Figure 4 illustrates the stress-strain relationship from residual strength tests performed after cool down of specimens from target temperature T_u. Each curve represents response averaged from date on three tests. Bolts show linear-elastic response up to yield, followed by nonlinear behavior. Once ultimate stress is reached, both types of steels undergo plastic deformation and then fracture. The bolts exhibit higher ductile behavior when they are heated above 750°C. Since the results of both M16 and M18 bolts follow the same pattern, the results of M18 are only presented. As shown in Figure 4a, when the heating is below 500°C, the peak stress of M18(10B38) bolts is negligibly lower (around 2%) and there is no clear

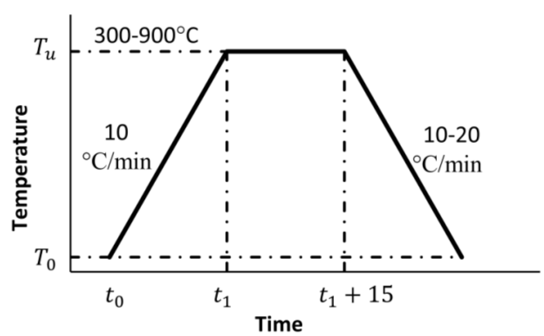

Figure 3. Heating and cooling procedures for test specimens.

demarcated yield plateau in the stress-strain diagrams. The bolts experience significant reduction in strength and increase in failure strain after being exposed to target temperatures of 600°C. On the other hand, a gradual change is observed in M22(10B21) bolts when heated to more than 400°C, as shown in Figure 4b. The effect of temperature on ductility of M22(10B21) bolts is not significant up to 500°C. When heated beyond 500°C and cooled down, bolts possess significant ductility.

3.2 Post fire ultimate strength

Tensile strength property varies not only with chemical composition and type of heat treatment of bolts but also with level of heating (temperature) of the bolts. In present study, the tensile tests were carried out until failure of specimens. Obtained residual factors for ultimate strength of M18(10B38) and M22(10B21) bolts are given and compared in Figure 5a in terms of heating temperature (T_u) up to 900°C.

The results show that when M18(10B38) bolts are exposed to elevated temperatures up to 500°C, they could regain their nominal ultimate strength after cooling down. If T_u is more than 500°C they lose their ultimate strength quickly, so that the residual ultimate strength is only about 0.55 after cooling down from 800°C. On the other hand, the ultimate strength of M22(10B21) bolts exhibit no change up to 300°C, but strength reduction starts at 400°C and degradation is significant up to 800°C, as residual factors almost reach 0.46. This trend in strength degradation can be attributed to the fact that grade 8.8 bolts are made of 10B21 and 10B38 steels with carbon content ranging from 0.22% to 0.40% and produced by quenching followed by tempering at appropriate temperatures, to achieve higher strength.

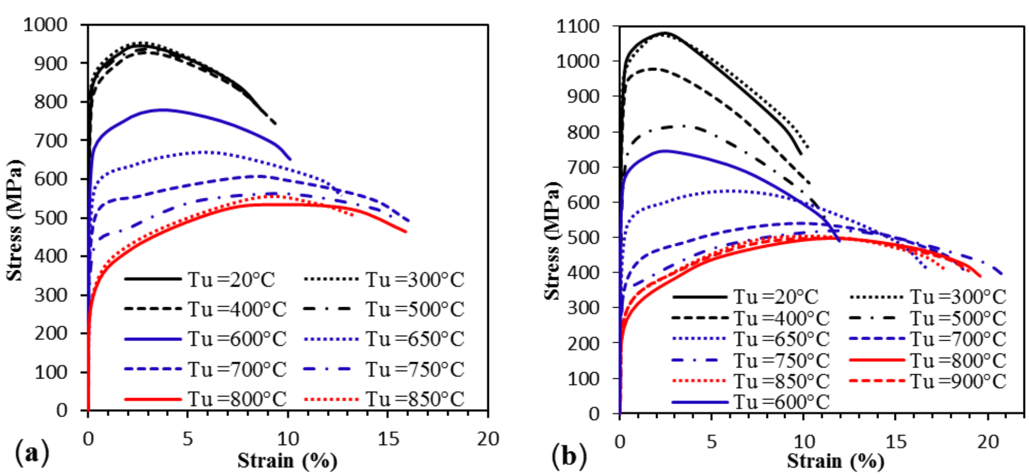

Figure 4. Post-fire stress-strain diagram: a) M18(10B38), b) M22(10B21) bolts.

During heat treatment of grade 8.8 bolts, steel is heated to approximately 870°C, where it transforms into the γ-austenite crystalline structure. Rapid cooling (quenching) of steel leads to transformation of austenite into a finer-grain body-centered tetragonal crystalline structure called martensite. Martensite contains a considerable number of carbon atoms. These trapped carbon atoms in iron crystal impart high strength to steel as a result of quenching. This martensite crystalline structure is the hardest form of steel microstructure, but is brittle and is in a metastable phase of steel, which is susceptible to changes with varying temperature. To restore ductility, the steel is reheated to temperatures above 400°C, allowing diffusion of carbon atoms into martensite steel [11]. In fire conditions, when the temperature of steel exceeds tempering temperature, strength imparting microstructure (carbon rich martensite) loses its hardness due to diffusion of carbon atoms. This causes rapid loss of strength in grade 8.8 bolts after being exposed to the fire, beyond tempering temperature.

3.3 Post fire yield strength

The post-fire yield strength of bolts at ambient temperature is determined by the 0.2% proof stress method, which uses the intersection point of the stress-strain curve and the proportional line offset by 0.2% strain. The results obtained from tensile tests of bolts at room temperature after cooling down from various target temperatures (T_u) are presented in Figure 5b.

The results demonstrate that when the target temperature increases, the residual yield strength of bolts decreases. As shown in Figure 5b, for M18(10B38) bolts when T_u is below 500°C, the yield strength exhibits no obvious change, i.e. reduction by about 5%. As T_u continued to increase, the residual yield strength decreased and the elongation increased significantly. For 800°C, the residual yield strength is about 35% of that of bolts without being exposed to fire. On the other hand, different results are obtained from M22(10B21) bolts test. When T_u is below 400°C, residual yield strength showed slight change (by about 5%). For bolts experienced target temperatures more than 400°C, the yield strength decreased rapidly and the elongation increased considerably. For 800°C, the residual yield strength was about 26% of that of bolts without being exposed to fire.

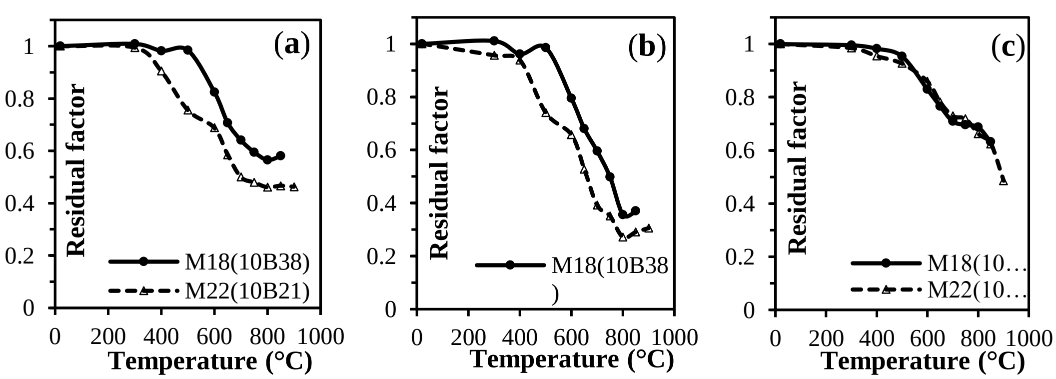

Figure 5. Residual factor for mechanical properties of bolts: a) Ultimate tensile strength, b) Yield strength, c) Elastic modulus.

3.4 Post fire elastic modulus

The post-fire elastic modulus of bolts is determined from the stress-strain curves, on the basis of the tangent modulus of the initial elastic linear curve. The post-fire material properties of steel bolts are representative by residual factors. The residual factors are calculated as the ratio of the mechanical property after cooling down from elevated temperature to that of ambient temperature without being exposed to fire.

Residual factors for elastic modulus of M18(10B38) and M22(10B21) bolts are given and compared in Figure 5c after cooling down from various target temperatures (T_u). As can be seen, when T_u is below 500°C, the bolts can approximately regain their elastic modulus. Beyond 600°C there is a considerable degradation of elastic modulus for both groups of bolts. Different quenching and tempering conditions used in manufacturing process of grade 8.8 bolts from 10B38 and 10B21 steels cause such difference in residual elastic modulus. It is notable that at least 75% of elastic modulus is recovered after cooling at 650°C and lower temperatures for both groups of bolts.

4. POST-FIRE MECHANICAL PROPERTY RELATIONS

Post-fire mechanical properties of high-strength Grade 8.8 steel bolts have significant influence on the performance of steel-framed structures after exposed to fire. For realistic performance assessment of bolted connections, reliable post-fire properties of steel bolts are to be utilized. Results from tests performed on Grade 8.8 bolts clearly show that their post-fire properties differ significantly from those of conventional steel. Using the data generated from these tests, a series of simplified expressions are proposed for evaluating post-fire elastic modulus; yield strength and ultimate strength degradation of Grade 8.8 bolts. These relationships are derived as a function of target temperature (T_u) by regression analysis of measured properties and summarized in Table III.

The variation of elastic modulus (E_{pf}), yield strength ($F_{y,pf}$) and ultimate strength ($F_{u,pf}$) after exposed to elevated temperatures can be represented through residual coefficients $R_{E,pf}$, $R_{y,pf}$ and $R_{u,pf}$, respectively. These residual coefficients represent the ratio of elastic modulus, yield and ultimate strength of steel after cooling down from target temperature (T_u) to those at ambient temperature as defined below:

TABLE III. POST-FIRE MECHANICAL PROPERTY RELATIONSHIPS FOR GRADE 8.8 BOLTS.

Mechanical property	**Relationship**	**Target temp. (°C)**
Elasticity modulus	$R_{E,pf} = -1.74(10^{-9})T_u^3 + 8.33(10^{-7})T_u^2 - 1.57(10^{-5})T_u + 1$	$20 \leq T_u \leq 700$
	$R_{E,pf} = -5.32(10^{-8})T_u^3 + 1.20(10^{-4})T_u^2 - 9.10(10^{-2})T_u + 23.70$	$700 < T_u \leq 900$
Yield strength	$R_{y,pf} = 1$	$20 \leq T_u \leq 300$
	$R_{y,pf} = 1.50(10^{-6})T_u^2 + 6.10(10^{-4})T_u + 0.954$	$300 < T_u \leq 600$
	$R_{y,pf} = 7.92(10^{-6})T_u^2 - 1.33(10^{-2})T_u + 5.90$	$600 < T_u \leq 900$
Ultimate strength	$R_{u,pf} = 1$	$20 \leq T_u \leq 300$
	$R_{u,pf} = 2.26(10^{-8})T_u^3 - 3.18(10^{-5})T_u^2 + 1.36(10^{-2})T_u + 0.825$	$300 < T_u \leq 600$
	$R_{u,pf} = -1.72(10^{-8})T_u^3 + 4.38(10^{-5})T_u^2 - 3.72(10^{-2})T_u + 11.06$	$600 < T_u \leq 900$

$$R_{E,pf} = E_{pf} / E \quad (1)$$

$$R_{y,pf} = F_{y,pf} / F_y \quad (2)$$

$$R_{u,pf} = F_{u,pf} / F_u \quad (3)$$

Where, E, F_y and F_u are elastic modulus, yield and ultimate strength at ambient temperature without being exposed to fire, respectively. The use of these material properties will lead to a safer prediction for fire-damaged steel structures.

5. CONCLUSIONS

Fire has significant influence on residual mechanical properties of high-strength grade 8.8 bolts. The experimental investigations on post-fire mechanical properties of Grade 8.8 bolts revealed that the bolts tend to turn back to the softer but more ductile parent steel after heating beyond tempering temperature used in bolt production. 400°C is observed as critical temperature above which significant reduction in strength occurs. Minor loss of strength is detected between 300°C and 400°C. Between 400 to 600°C residual factors for ultimate tensile strength is considerable. Beyond this temperature residual factors would be around 0.30. Proposed equations were proposed to determine the residual mechanical properties of grade 8.8 bolts.

Results also demonstrated that residual mechanical properties of Grade 8.8 bolts are sensitive to chemical composition and heat treatment characteristics of their manufacturing process. Therefore, the use of alloy steel (such as SAE 10B38) containing higher levels of carbon than SAE 10B21 carbon steel, along with higher tempering temperature in bolt production process can significantly enhance the post-fire mechanical properties of Grade 8.8 bolts.

REFERENCES

1. Rezaeian A, Yahyai M (2015) Fire response of steel column-tree moment resisting frames. Mater Struct 48:1771–1784. doi: 10.1617/s11527-014-0271-1
2. Yahyai M, Rezaeian A (2015) Behavior of beams in bolted column-tree frames at elevated temperature. Fire Mater. doi: 10.1002/fam.2305
3. Saedi Daryan A, Yahyai M (2009) Behavior of bolted top-seat angle connections in fire. J Constr Steel Res 65:531-541. doi:10.1016/j.jcsr.2008.07.021
4. CEN. EN 1993-1-2:2005/AC:2009, Eurocode 3: Design of steel structures - Part 1-2: General rules - Structural fire design. Brussels: European committee for standardization; 2009.
5. Kirby BR. The behaviour of high-strength grade 8.8 bolts in fire. J Constr Steel Res 1995;33:3-38.
6. Kodur V, Kand S, Khaliq W. Effect of temperature on thermal and mechanical properties of steel bolts. J Mater Civil Eng 2012;24:765-774. doi:10.1061/(ASCE)MT.1943-5533.0000445.
7. Yang KC, Hsu RJ, Chen YJ. Shear strength of high-strength bolts at elevated temperature. Constr Build Mater 2011;25:3656-3660. doi: 10.1016/j.conbuildmat.2011.03.003.
8. Gonzalez F, Lange J. Behavior of high strength grade 10.9 bolts under fire conditions. Struct Eng Inter 2012;4:470-475. doi: 10.2749/101686612X13363929517451.
9. DIN. DIN 931-1: M1.6 to M39 Hexagon cap screws partially threaded. Berlin: Deutsches Institut für Normung; 1986.
10. ASTM. ASTM E8: Standard test methods for tension testing of metallic materials. West Conshohocken: American Society for Testing and Materials; 2009.
11. Meyers M, Chawla K (2009) Mechanical behavior of materials. Cambridge University Press. New York.

Analytical Study on Critical Temperature of Bolted Splice Connections

ROBERT DWIPUTRA, SHUHEI ANDO and TAKEO HIRASHIMA

ABSTRACT

The resistance of bolted splice connections is calculated on the basis of tensile strength obtained from high temperature tensile tests (coupon tests) of steel plates and bolt materials. The strengths of both steel plates and bolt materials over 500℃ are greatly affected by the strain rate applied in the high temperature coupon test. This paper investigates the effect of strain rate applied in high temperature coupon tests on the ultimate tensile strength of steel plates and bolt materials by comparing the test and analysis results of 20 cases. These strain rates eventually have a remarkable relation to the behaviour of the connections in elevated temperatures. Numerical analysis results on the basis of a component-based model using the strengths from high temperature coupon tests under high-strain-rate approximately agreed with the critical temperatures of bolted splice connections obtained from elevated temperature tests.

1 INTRODUCTION

The resistance of bolted splice connections (BSC) is calculated on the basis of tensile strength obtained from high temperature tensile tests (coupon tests) of steel plates and bolt materials. For fire engineering design of steel structures, the design tensile resistance of the connections should be determined carefully because the tensile strength of steels at elevated temperature depends on the strain rate applied in the high temperature coupon tests. In Japan, strain rates in high temperature coupon tests were designated 0.3%/min in elastic region and 7.5%/min in plastic region in accordance with JIS G 0567 [1].

The previous study [2] indicated that the strength of steel plates and bolt materials is greatly influenced by the strain rate. Generally, in order to obtain the strength of steel materials in high temperature, coupon tests are usually conducted at a constant strain rate as well as temperature. However, in real fire conditions, structures are supporting constant loads while the temperature is increasing. Considering that, the elevated temperature tests were conducted in order to investigate the behaviour of BSC. This paper discusses the effect of strain rate applied in high temperature coupon tests on the ultimate tensile strength of steel plates and bolt materials, which eventually had a remarkable relation to the behaviour (strength and critical

Chiba University, Graduated School of Eng., Division of Architecture and Urban Science, 1-33, Yayoi-cho, Inage-ku, Chiba 263-8522, Japan

temperature) of BSC in elevated temperatures, by comparing the test and analysis results under 20 cases and also analysis results using Eurocode values [3] as standard.

2 ANALYSIS OUTLINE

Numerical analyses were conducted on the basis of a component-based model in which each connection component (beam, splice plate and bolt) was defined independently and its characteristics (stiffness and strength) were determined by means of nonlinear load deformation curves. The component-based model of BSC is shown in Figure 1. In this model, the main equations of each BSC component are described in Table I [4]~[8]. As defined in the table, the ultimate tensile strengths of both steel plate and bolt material are closely related to the maximum strength of each BSC component at elevated temperatures. At the same time, the load-deformation relationships of BSC itself will also be influenced greatly by those strengths.

TABLE I. THE MAIN EQUATIONS OF EACH BOLTED SPLICE CONNECTION COMPONENT.

	Load-deformation relationship [N]	Maximum strength [N]
Steel plate (beam and splice plate)	$F = \left\{ \dfrac{\psi}{\left(1+\sqrt{\dfrac{\delta \times K}{F_{b,t,Rd}}}\right)^2} - \phi \right\} \times K \cdot \delta$ [4],[5]	$F_{b,t,Rd} = e \times t_p \times f_{u,\theta}$ [6],[7]
Bolt in shear	$F = \left\{ 1 - 16\left(\dfrac{\delta}{d_b} - \dfrac{1}{4}\right)^2 \right\} \times F_{v,t,Rd}$ [8]	$F_{v,t,Rd} = 0.6 \times A_{bs} \times f_{bu,\theta}$ [6],[7]

* Notations;
ψ, ϕ : Curve fitting parameters in accordance with steel temperature θ
δ : Deformation [mm]
K : Stiffness [N/mm]
e : End distance [mm]
t_p : Thickness of the plate [mm]
$f_{u,\theta}$: Ultimate tensile strength of the steel plate at temperature θ [N/mm^2]
d_b : Nominal diameter of the bolt shank [mm]
A_{bs} : Shear stress area of the bolt [mm^2]
$f_{bu,\theta}$: Ultimate tensile strength of the bolt material at temperature θ [N/mm^2]

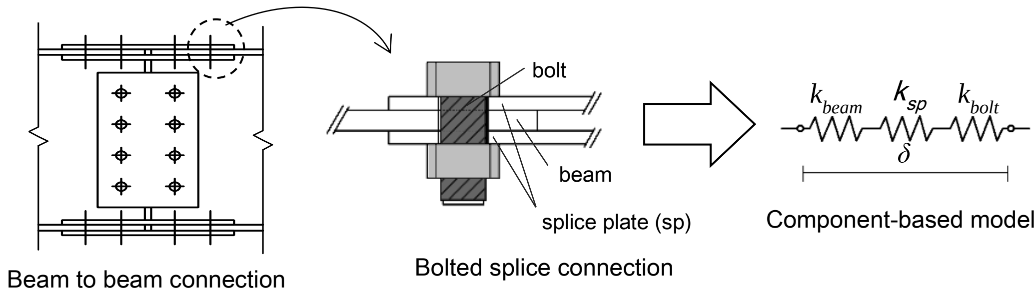

Figure 1. Component-based model of bolted splice connection.

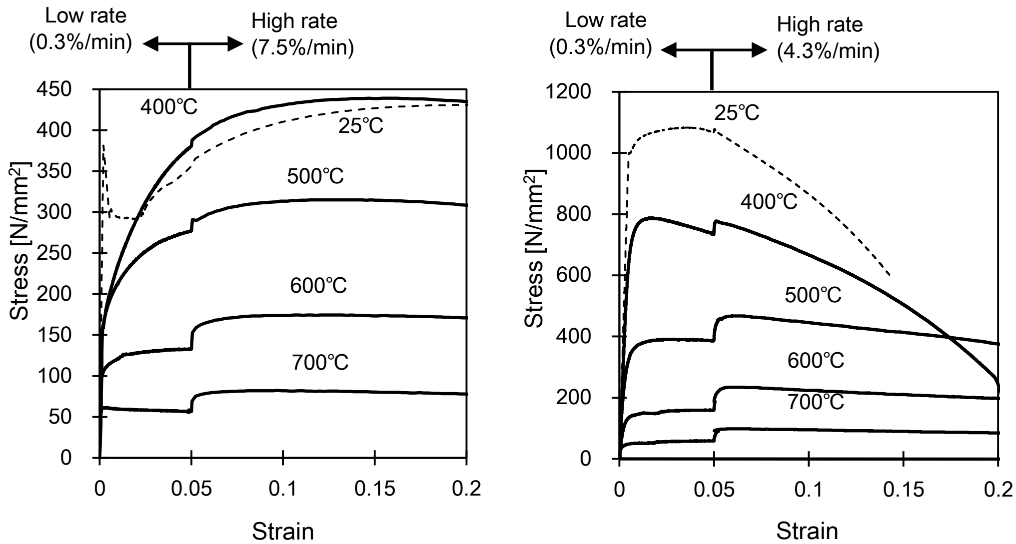

(a) Steel plate's behaviour (SN400B) (b) Bolt's behaviour (F10T)

Figure 2. Stress-strain relationships of steel plate and bolt in high temperature.

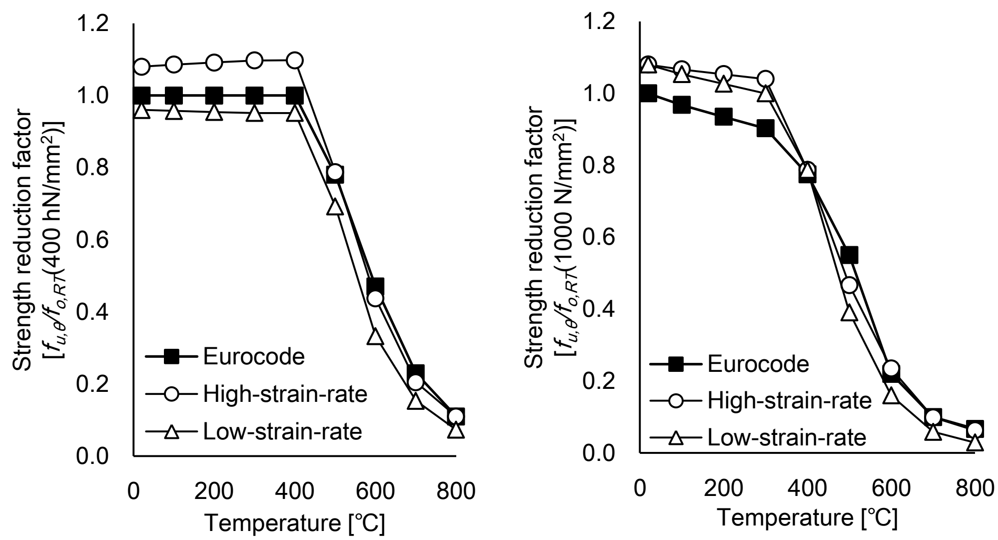

(a) Steel material (SN400B) (b) Bolt material (F10T)

Figure 3. The comparison of strength reduction factor of steel and bolt material.

The previous study [2] showed that the strength of steel plates and bolt materials is greatly influenced by the strain rate. The stress-strain relationships of the employed steels were shown in Figs. 2 (a) and (b). The stress increased instantly at 5% strain due to the change in the strain rate, and this was remarkable above 500°C.

Figure 3 shows the comparison of steel material's (SN400B) and bolt material's (F10T) strength reduction factors in high temperature according to Eurocode, high-strain-rate coupon tests, and low-strain-rate coupon tests. The strength reduction factors determined by dividing the ultimate tensile strength of the material obtained from the tests to the nominal ultimate tensile strength of each material in room temperature.

In the case of steel material, Eurocode strength reduction factors indicated lower values than high-strain-rate coupon tests' at low temperature (under 500℃). But, in

TABLE II. ANALYSIS CASES AND RESULTS.

Test type	Specimen				Type	Applied temp. or load	Test results**		Analysis results**					
	Bolt	Plate							Eurocode model		High-strain-rate model		Low-strain-rate model	
CT test*	F10T-M22	SN400B	t_p=9mm	e=33mm	Plate failure	20℃	156 kN	P	176 kN	P	156 kN	P	153 kN	P
						500℃	105 kN	P	113 kN	P	116 kN	P	115 kN	P
						600℃	56 kN	P	68 kN	P	64 kN	P	55 kN	P
						700℃	23 kN	P	33 kN	P	30 kN	P	25 kN	P
				e=55mm	Plate → Bolt failure	20℃	237 kN	P	268 kN	P	239 kN	P	239 kN	P
						500℃	152 kN	P	170 kN	P	175 kN	P	173 kN	P
						600℃	77 kN	B	101 kN	B	97 kN	P	74 kN	B
						700℃	34 kN	B	46 kN	B	45 kN	P	28 kN	B
	F10T-M20	SN490	t_p=19mm	e=50mm	Bolt failure	20℃	421 kN	B	374 kN	B	406 kN	B	374 kN	B
						500℃	169 kN	B	206 kN	B	175 kN	B	147 kN	B
						700℃	36 kN	B	38 kN	B	34 kN	B	23 kN	B
ET test*	F10T-M22	SN400B	t_p=9mm	e=33mm	Plate failure	105 kN	525℃	P	489℃	P	525℃	P	507℃	P
						56 kN	627℃	P	621℃	P	631℃	P	600℃	P
						23 kN	744℃	P	770℃	P	747℃	P	717℃	P
				e=55mm	Plate → Bolt failure	152 kN	532℃	P	523℃	P	469℃	P	469℃	P
						77 kN	651℃	B	637℃	B	627℃	P	597℃	B
						34 kN	757℃	B	758℃	B	753℃	P	715℃	B
	F10T-M20	SN490	t_p=19mm	e=50mm	Bolt failure	176 kN	527℃	B	547℃	B	568℃	B	547℃	B
						89 kN	629℃	B	645℃	B	637℃	B	613℃	B
						37 kN	749℃	B	758℃	B	760℃	B	715℃	B

*CT test: Constant Temperature test, ET test: Elevated Temperature test
**Results: maximum strength [kN] or critical temperature [℃]
P: Plate failure, B: Bolt in shear failure

high temperature, Eurocode and high-strain-rate coupon test results showed the similar value of strength reduction factor over 500℃. In addition, it also shows that the low-strain-rate coupon test results indicated lower values compared to Eurocode and high-strain-rate coupon tests at every temperature condition

In the case of bolt material, Eurocode and high-strain-rate coupon tests showed the same relationship as those in steel material, but the switching temperature was 400℃. On the other hand, unlike the steel material, in the case of bolt material, the low-strain-rate coupon test results showed higher values than Eurocode at low temperature, but reversed and decreased greatly after 400℃.

The cases of analysis models in this study are shown in Table II. Each model was analysed under 3 conditions－Eurocode, high-strain-rate and low-strain-rate.

3 ANALYTICAL RESULTS AND DISCUSSIONS

3.1 Resistance of Bolted Splice Connection under Constant High Temperature

Figure 4 shows the load - deformation relationships of test results and analysis results in the case of constant temperature tests. Figure 4 (a), (b) and (c) show the test results and analysis results of plate-failure type specimens, plate-and-bolt-intermediate failure type specimens, and bolt-failure type specimens. The plot indicates experimental results and the line indicates analytical results (dashed line: using Eurocode value; solid thick line: using the value from high-strain-rate coupon test; solid thin line: using the value from low-strain-rate coupon test). The temperatures written in the figure are the constant temperature applied to each specimen. Referring to Sarraj's formula [4], the author determined the strength adjustment factor and the curve fit coefficients according to the load-deformation relationship obtained from constant temperature tests in the previous report [5].

In the case of plate-failure type specimens, as well as plate-and-bolt-intermediate failure type specimens, the numerical analysis models, which applied low-strain-rate strength reduction factors, could predict the maximum strength reasonably close to the test results since these tests were conducted under a low deformation rate of 0.6 mm/min. The analysis results using Eurocode values showed similar behaviour to the numerical analysis models which applied high-strain-rate strength reduction factor.

On the other hand, in the case of bolt-failure type specimens, the numerical analysis models which applied high-strain-rate strength reduction factors showed the closest results to the test results compared to those which applied low-strain-rate strength reduction factors and those which used Eurocode values.

3.2 Critical Temperature of Bolted Splice Connection under Constant Load

Figure 5 shows the deformation – temperature relationships of test results and analysis results in the case of elevated temperature tests. Figure 5 (a), (b) and (c) show the test results and analysis results of plate-failure type specimens, plate-and-bolt-intermediate failure type specimens and bolt-failure type specimens. The plot indicates experimental results and the line indicates analytical results (dashed line: using Eurocode values; solid thick line: using the value from high-strain-rate coupon test; solid thin line: using the value from low-strain-rate coupon test). The loads written in the figure are the constant load applied to each specimen, which is the maximum load obtained from the test under constant temperature. (See Figure 4)

All of the analysis results showed similar deformation behaviour to the test results. The test results, as well as the analysis models, showed that the deformation rate of specimens increased to about 5 mm/min as they got closer to their failure stage and this behaviour was also considered to be remarkably related to the critical temperature or the resistance of BSC.

In the case of plate-failure type specimens, the analytical results using either the high-strain-rate value or the low-strain-rate value showed similar behaviour to the experiment results, from the beginning up to about 100℃ before the critical temperature, due to the thermal expansion. However, after that, the numerical analysis models which applied low-strain-rate strength reduction factors started to deform earlier than test results, and failed at lower critical temperature than the test results. On the other hand, the numerical analysis models which applied high-strain-rate strength reduction factors, as well as those which used Eurocode values, showed the approximate behaviour and obtained close critical temperature to the test results. The plate-and-bolt-intermediate failure type specimens showed the same behaviour as the plate-failure type specimens, as well as that of bolt-failure type specimens.

Therefore, it was indicated that using the ultimate tensile strength in accordance with the high-strain-rate coupon test, or Eurocode values, is appropriate for approximation of the critical temperature because the BSC rapidly deforms at the ultimate state stage in real fire conditions.

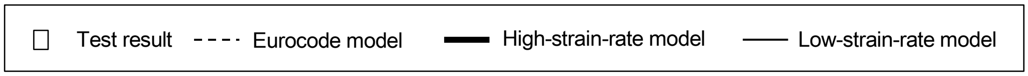

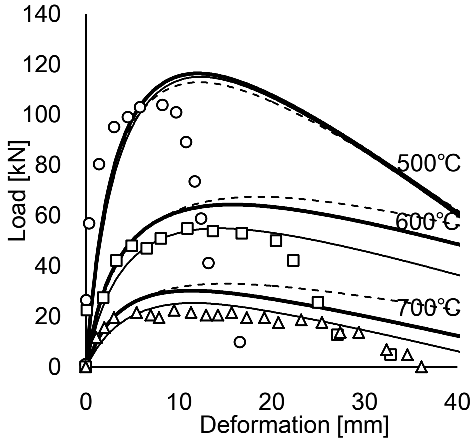

(a) Plate-failure type
(t_p = 9 mm, e = 33 mm)

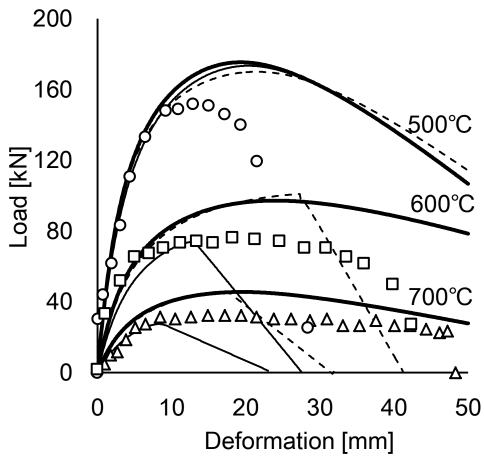

(b) Plate-bolt-failure intermediate type
(t_p = 9 mm, e = 55 mm)

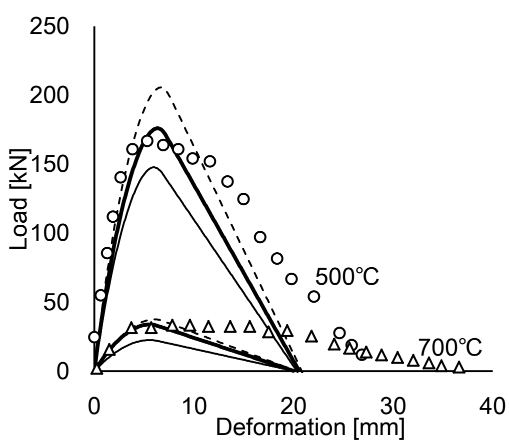

(c) Bolt in shear failure type
(t_p = 19 mm, e = 50 mm)

Figure 4. Load-deformation relationships from constant temperature tests.

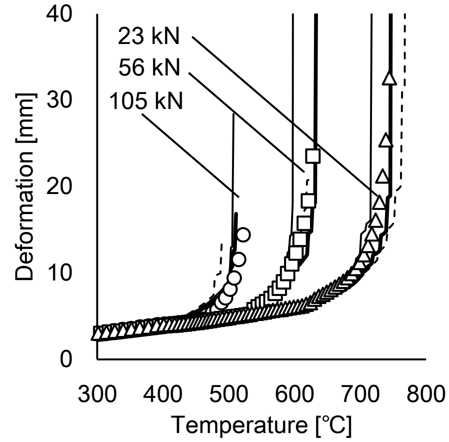

(a) Plate-failure type
(t_p = 9 mm, e = 33 mm)

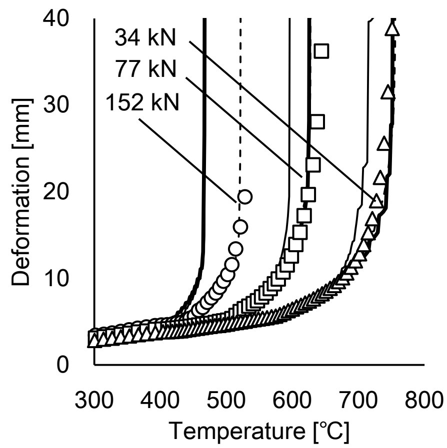

(b) Plate-bolt-failure intermediate type
(t_p = 9 mm, e = 55 mm)

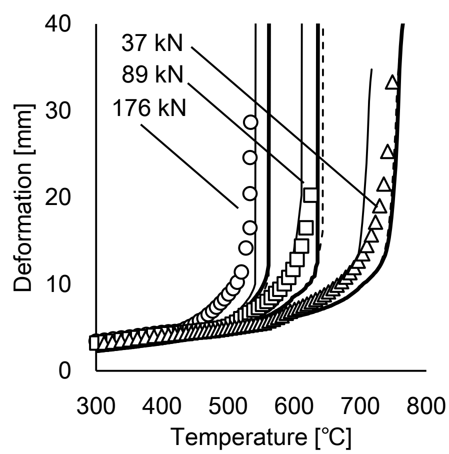

(c) Bolt in shear failure type
(t_p = 19 mm, e = 50 mm)

Figure 5. Deformation-temperature relationships from elevated temperature tests.

3.3 Deformation Detail of Each Component in Bolted Splice Connection

Figure 6 shows the deformation detail of each component. The deformations showed in this figure were obtained from the deformation of each component after the experiments finished, and those after the analysis was conducted. Figure 6 (a), (b) and (c) show the test results and analysis results of plate-failure type specimens, plate-and-bolt-intermediate failure type specimens and bolt-failure type specimens. This paper only discusses the component's deformations obtained from the tests and the numerical analysis which applied high-strain-rate strength reduction factors.

As shown in Figure. 6 (a), in the case of plate-failure type specimens, it is obvious that the deformation was concentrated at the beam component in the analytical results, as well as the test results. On the other hand, as shown in Figure. 6 (c), in the case of bolt-failure type specimens, the deformation was concentrated at the bolt component in the analytical results, as well as the test results. And, as shown in Figure 6 (b), in the case of plate-and-bolt-intermediate failure type specimens, especially for ET-77kN and ET-34kN where the beam and bolt failed simultaneously, the analytical results, as well as the test results, showed that the deformation was distributed at the beam component and bolt component.

Therefore, it is indicated that using this analysis method could predict the distribution of the deformation in bolted splice connections in real fire conditions.

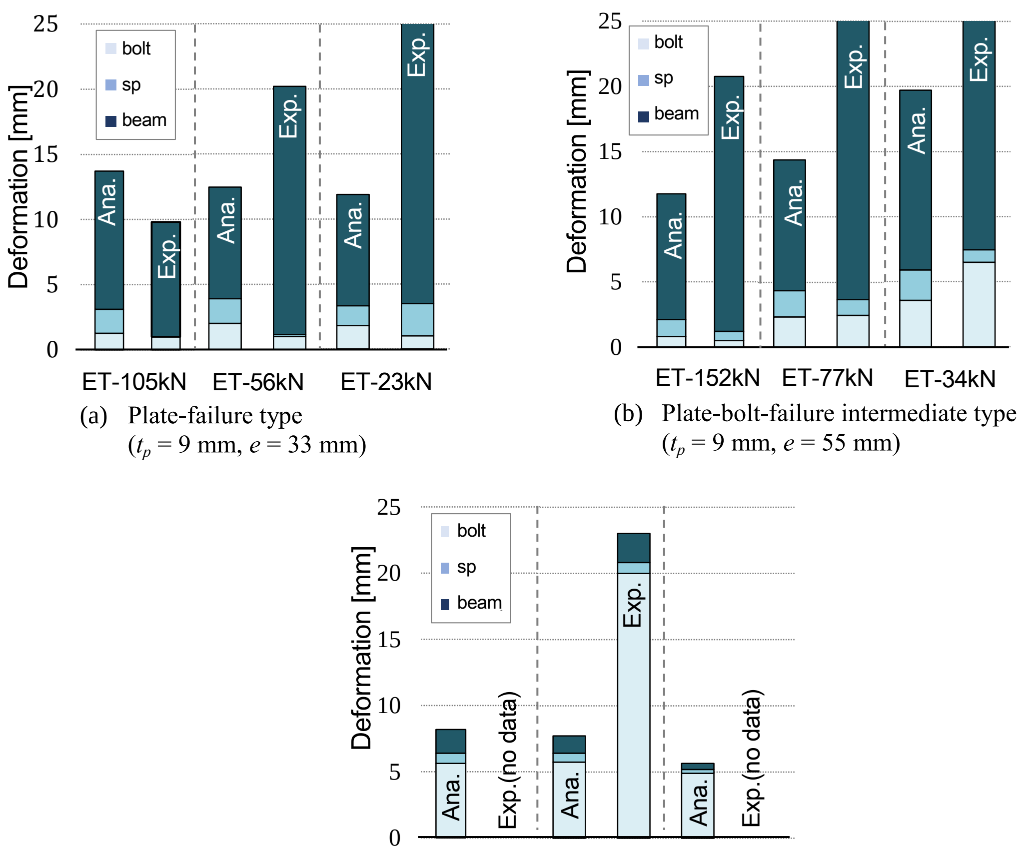

(a) Plate-failure type (t_p = 9 mm, e = 33 mm)

(b) Plate-bolt-failure intermediate type (t_p = 9 mm, e = 55 mm)

(c) Bolt in shear failure type (t_p = 19 mm, e = 50 mm)

Figure 6. Deformation detail of each component in bolted splice connection.

4 CONCLUSIONS

The following conclusions can be drawn from this study:

(1) The numerical analysis model of bolted splice connections on the basis of a component-based model showed similar behaviour to the results of both constant temperature tests and elevated temperature tests.

(2) In the case of constant temperature tests, all numerical analysis models could show similar load-deformation relationships to the test results. In this paper, numerical analysis models which applied low-strain-rate strength reduction factors could predict the maximum strength reasonably close to the test results since these tests were also conducted under a low deformation rate.

(3) In the case of elevated temperature tests, numerical analysis results using the strengths from high temperature coupon tests under high-strain-rate approximately agreed with the critical temperatures of the test results.

(4) This analysis method could predict the damage level and the failure type of bolted splice connections in fire conditions to a reasonable extent.

ACKNOWLEDGMENT

The author would like to thank to Japan Society for the Promotion of Science Research expenses 24560677 - base (C) "Strength – Deformation – Failure Behaviour of Friction Type High Strength Bolted Joints at High Temperature and Cooling Process" due to financial to the research.

REFERENCES

1. Japanese Industrial Standards Committee, 1998, "Method of elevated temperature tensile test for steels and heat resisting-alloys," JIS G 0567.
2. S. Ando, R. Dwiputra, and T. Hirashima, October 2015, "Tensile Resistance of Splice Connections with High Strength Bolts in Fire," *The 10th Asia-Oceania Symposium on Fire Science and Technology*.
3. CEN, prEN 1993-1-8. Eurocode 3: Design of steel structures, Part 1-8: Design of joints, 2005
4. Marwan Sarraj, July 2007, "The Behaviour of Steel Fin Plate Connections in Fire," Ph.D. Thesis, University of Sheffield.
5. R. Dwiputra, S. Ando, T. Hirashima, September 2015, "Load-Deformation Relationship of Friction Type High Strength Bolted Joints at Elevated Temperature (Part 4. Numerical Analysis Modeling)," *Summaries of Technical Papers of Annual Meeting Architectural Institute of Japan 2015*, AIJ, pp.21-22 (In Japanese).
6. Architectural Institute of Japan, March 2008, "Recommendation for Design of Connections in Steel Structures" (In Japanese).
7. S. Ando, T. Hirashima, June 2015, "Tensile Resistance of Friction Type High Strength Bolted Joints in Fire," J. *Struct. Constr. Eng.*, AIJ, No. 712, pp.961-970 (In Japanese).
8. T. Hirashima, N. Hamada, F. Ozaki, T. Ave, H. Uesugi, November 2007, "Experimental Study on Shear Deformation Behaviour of High Strength Bolts at Elevated Temperature," *J. Struct. Constr. Eng.*, AIJ, No. 621, pp.175-180 (In Japanese).

Fire Performance of Hybrid Stainless-carbon Steel Composite Beam-column Joints with Blind-bolted Connections

TIAN-YI SONG, ZHONG TAO, ALI RAZZAZZADEH
and LIN-HAI HAN

ABSTRACT

This paper presents the fire resistance and post-fire test results of eight full-scale concrete filled stainless steel tubular (CFSST) column to steel beam joints with blind-bolted connections. The investigated parameters included whether applying fire protection to the steel beam or not, beam load ratio (0.25 and 0.5), steel tube type (stainless and carbon steel tubes) and presence of binding bars or not. The test results show that the joint failure was mainly dominated by flexural failure of the steel beams near the panel zone despite the variation of parameters. But when the beam load ratio was 0.25, the joint specimen with a circular column failed due to axial crushing of the column. In general, the blind-bolted connections demonstrated good workability in fire, and no bolt shank fracture or bolt pull-out failure was observed in any joint test.

INTRODUCTION

In recent years, bolted joints have been widely used in frame structures because of their advantages such as high reliability and ease of construction [1]. By using Hollo-bolts developed by Lindapter [2], a type of hybrid stainless-carbon steel composite beam-column joint was proposed by the authors to connect steel beams to concrete-filled stainless steel tubular (CFSST) columns as shown in Figure 1. So far, the research on fire performance of blind-bolted CFSST joints is very limited. Pascual et al. [3] measured the temperature distribution of small size specimens consisting of a blind bolt that clamped an endplate and a concrete filled steel tubular (CFST) column, and Pascual et al. [4] established structural numerical models to predict the fire resistance of blind-bolted CFST joints using Hollo-bolts. The results indicate that the column section size affects the temperature field of Hollo-bolts slightly, and the dominated joint failure is the bolt shark fracture of Hollo-bolts when tensile force is applied.

Tian-Yi Song, Zhong Tao, Ali Razzazzadeh, Institute for Infrastructure Engineering, Western Sydney University, Penrith, NSW 2751, Australia.
Lin-Hai Han, Department of Civil Engineering, Tsinghua University, Beijing 100084, China.

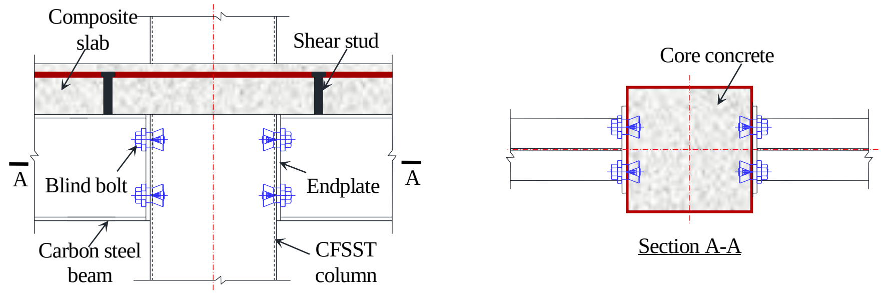

Figure 1. Typical CFSST column to steel beam joint with blind-bolted connection.

To further investigate the fire performance of CFSST column to steel beam joints with blind-bolted connections, a series of full-size blind-bolted CFSST joint specimens subjected to ISO 834 standard fire [5] were tested, and the test results of temperature distribution, failure mode and joint deformation were reported and discussed in this paper.

TEST PROGRAM

A total of eight CFSST column to steel beam joints with blind-bolted connections, including six joints with square columns and two joints with circular columns, were designed based on Eurocode 4 [6] and Eurocode 3 [7]. Details are introduced as below.

Specimen details and material properties

Each joint consisted of a square or circular CFSST column, two H-shaped carbon steel beams and a composite slab with profile steel sheeting. A flush end plate with a thickness of 10 mm was welded to one end of the H-shaped steel beam, and four blind bolts (Lindapter HB20-1 Hollo-bolts) were used to connect the steel tube and H-shaped steel beam through the end plate. One row of shear studs with a diameter of 19 mm were welded on the top flange of the H-shaped steel beam, and embedded into the composite slab. The total height of a CFSST column with two 20 mm thick endplates was 3800 mm; the length of the steel beam was 3900 mm; and the thickness of the composite slab with 1 mm thick BONDEKII profile steel sheet was 120 mm. More information of the eight joint specimens is given in Table. I, in which D is the width or diameter of the square or circular column cross-section; t_s is the steel tube thickness; b_f and h are the width and height of the H-shaped steel beam, respectively; t_w and t_f are the web and flange thicknesses of the H-shaped steel beam, respectively; n is the column load ratio; m is the beam load ratio; N_F is the axial load applied to the column; P_F is the vertical load applied to the beam; t_R is the measured fire resistance; and t_h and P_{up} are the heating time and residual ultimate strength of a post-fire test specimen.

The testing parameters for the fire resistance tests included whether applying fire protection to the steel beam or not, beam load ratio (0.25 and 0.5), steel tube type (stainless and carbon steel tubes) and presence of binding bars or not. For specimen SB0-1, two layers of 30 mm thick LYGX-312 ceramic fibre blanket were used to protect the upper column, upper and side surfaces of the composite slab. Except for these components being protected, the H-shaped steel beam in all other specimens was also protected using one layer of ceramic fibre blanket. For specimen SB1-2, two binding bars with a diameter of 20 mm were used to improve the robustness of the joint in fire.

TABLE I. DETAILS OF CFSST JOINT SPECIMENS.

Specimen label	Column		Beam	Binding bar	n	N_F (kN)	m	P_F (kN)	t_R or t_h (min)	P_{up} (kN)	Test type
	$D \times t_s$ (mm)	Steel type	$h \times b_f \times t_w \times t_f$ (mm)								
SB0-1	□-300×5	Stainless	252×146×6×8	No	0.3	1812	0.5	64	22	-	Fire resistance
SB0-2	□-300×5	Stainless	252×146×6×8	No	0.3	1812	0.5	64	72	-	
SB0-3	□-300×5	Stainless	252×146×6×8	No	0.3	1812	0.5	64	36	71	Post-fire
SB1-1	□-300×5	Stainless	252×146×6×8	No	0.3	1812	0.25	32	90	-	Fire resistance
SB1-2	□-300×5	Stainless	252×146×6×8	Yes	0.3	1812	0.25	32	90	-	
SB1-3	□-300×5	Carbon	252×146×6×8	No	0.3	1760	0.25	32	90	-	
CB2-1	○-300×5	Stainless	252×146×6×8	No	0.3	1860	0.5	41	74	-	Fire resistance
CB2-2	○-300×5	Stainless	252×146×6×8	No	0.3	1860	0.25	20.5	82	-	

Two types of commercial concrete were used to fabricate the composite slabs and fill the tubes, respectively. At the time of testing, concrete cube compressive strengths for composite slabs and columns were 49.4 and 58.2 MPa, respectively. For the steel properties, the measured modulus of elasticity (E_s), yield strength (f_y), tensile strength (f_u), and Poisson's ratio (μ) corresponding to different steel types are presented in Table II.

TABLE II. SUMMARY OF STEEL PROPERTIES.

Steel type	E_s (MPa)	f_y (MPa)	f_u (MPa)	μ
Circular stainless steel tube (Thickness: 5 mm)	200,310	315.1	698.4	0.296
Square stainless steel tube (Thickness: 5 mm)	200,700	292.3	702.5	0.270
Square carbon steel tube (Thickness: 5 mm)	187,770	371.6	478.3	0.268
Web of H-shaped steel beam (Thickness: 6 mm)	188,350	330.4	478.0	0.268
Flange of H-shaped steel beam (Thickness: 8 mm)	190,100	368.4	500.0	0.272
Beam flush endplate (Thickness: 10 mm)	215,400	383.7	521.0	0.259
BONDEKII profile steel sheet (Thickness: 1 mm)	202,730	566.7	577.5	0.261
Binding bar (Diameter: 20 mm)	203,570	454.7	608.3	0.260
Shear stud (Diameter: 19 mm)	202,410	468.3	412.4	-

Test setup and procedures

The test setup is shown in Figure 2. A gas furnace with an internal dimension of 2,500×2,500×3,000 mm^3 (length × width × height) was used. Two exhaust fans, eight gas burners, and eight thermocouples at different positions of the furnace chamber were used to control the furnace temperature to follow the ISO 834 standard fire. As shown in Figure 2(a), the bottom end of the column was fixed with twelve high strength bolts, the top end of the column was restrained against horizontal displacement and rotation, and the two beam ends were free. A hydraulic jack with a capacity of 5000 kN was used to apply axial load N_F to the column, and two jacks with a capacity of 300 kN were used to apply P_F at the beam ends. As mentioned before, some joint components were protected by ceramic fibre blankets, which could minimise the heat transfer from the environment to these parts during fire exposure.

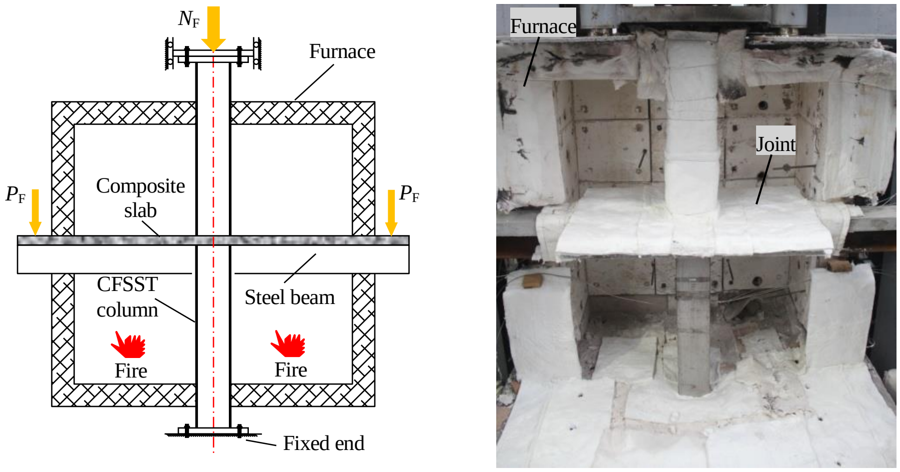

(a) Schematic of test setup (b) A CFSST joint specimen in the furnace

Figure 2. Test setup.

Fire resistance tests were conducted for all the specimens except for the specimen SB0-3. At ambient temperature, the predetermined column load N_F and beam load P_F were applied on the joint specimen first, and then the external loads were kept constant, and the joint specimen was exposed to ISO 834 standard fire [5] until the joint failure. For the post-fire test specimen SB0-3, N_F and P_F were applied first at ambient temperature, and then the joint was exposed to ISO 834 standard fire. When the predetermined heating time (t_h) was reached, the furnace was switched off to allow the joint specimen to cool down to ambient temperature with the furnace door opened. In the post-fire stage, the column load was kept constant, and the beam loads were increased until the joint failed to support the loads. The ultimate beam load obtained in the post-fire phase is defined as the residual ultimate strength (P_{up}) of the joint.

During the test, the axial deformation of the column and vertical deflections of the beam ends were measured by displacement transducers. The temperature developments of joint specimens during the fire exposure were measured by thermocouples embedded in the beams, columns, as well as panel zones.

TEST RESULTS AND DISCUSSION

The measured temperature distributions, joint failure modes and deformation developments are presented and discussed in this section.

Temperature distributions

In general, all the eight joint specimens demonstrated a similar temperature variation tendency. For a same specimen, when comparing the temperatures of the beam section near the panel zone and those of the beam section far from the panel zone, the difference between the peak temperatures in the two beam sections at the same points is generally less than 100°C because of the good thermal conductivity of steel. But the peak temperature of a point in the column section near the panel zone is significant lower than that of the same point in the column section far from the panel zone. This is because of the significant heat sink effect of the panel zone.

During the test, the temperatures of the external surface of the stainless steel tube and the surface of core concrete were measured. Taking specimen SB0-3 as an example, the peak temperature of the external surface of the steel tube is 331°C higher than that of the surface of core concrete. The results indicate the significant influence of the thermal contact resistance between the steel tube and core concrete. In addition, the comparison between specimens SB0-1 (unprotected steel beam) and SB0-3 (protected steel beam) indicates that the beam's temperature can be reduced to about 50% by wrapping the steel beam with one layer of ceramic fibre blanket, but the protection of the beam has no influence on the column's temperature development.

Failure modes

Two types of global failure modes, including beam failure mode and column failure mode, were observed for the test specimens. For the fire resistance tests, all the specimens with square columns (SB0-1, SB0-2, and SB1-1 to SB1-3) and specimen CB2-1 with a circular column show a similar beam failure mode. Taking specimen SB1-1 as an example, a typical beam failure mode is shown in Figure 3(a). With the increase of the temperature, the left beam of joint SB1-1 could not support the applied beam loads due to the local buckling occurred at the bottom flange and web of the steel beam near the panel zone, and a significant beam bending deformation was observed. Thus, this type of failure is called beam failure. For the post-fire test specimen SB0-3, a similar beam failure mode was observed. For specimen CB2-2, because of the lower beam load ratio (m = 0.25), the beam did not develop significant deflection. Instead, this specimen failed due to the excessive column contraction, as shown in Figure 3(b). The steel tube developed significant outward local buckling in the lower column after reaching the ultimate stage.

(a) Beam failure mode (SB1-1) (b) Column failure mode (CB2-2)

Figure 3. Typical failure modes of CFSST joints.

The test results indicate that the Hollo-bolts show excellent workability in fire. No bolt shank fracture was observed in all specimens. It should be noted that the current joints were only tested in an isolated condition, which could not reflect the influence of structural continuity on the behaviour of realistic joints. At the presence of structural continuity, tension force will be developed in the steel beam after catenary action has been initiated. This may pose significant risk to the Hollo-bolts. Further experimental and theoretical studies should be conducted in the future to clarify this.

Joint deformation

When joint specimens demonstrated a beam failure mode, they had a similar deformation tend. Therefore specimen CB2-1 is chosen as a typical example. Figure 4 shows the measured column axial deformation ($\varDelta_c$) versus time (t) and beam vertical deformation ($\varDelta_b$) versus t curves for specimens CB2-1 (beam failure) and CB2-2 (column failure).

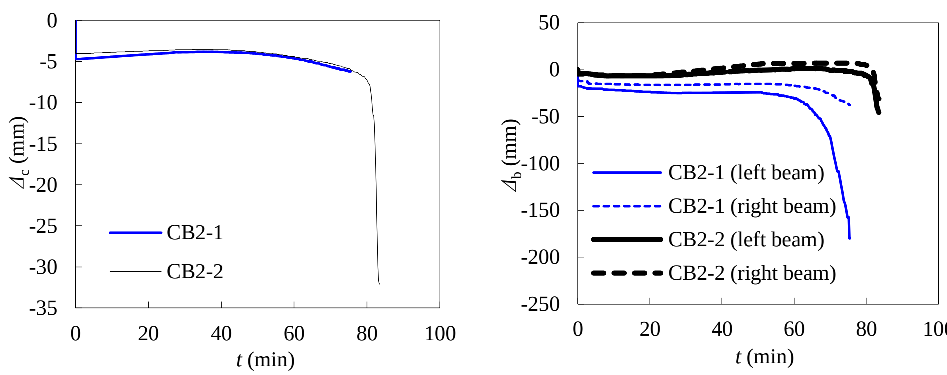

(a) $\varDelta_c$ - t curve (b) $\varDelta_b$ - t curve

Figure 4. Deformation developments of specimens CB2-1(beam failure) and CB2-2 (column failure).

In general, the $\varDelta_c$-t curve can be divided into three or four stages:

(1) Initial contractive stage under external loads. In this stage, external beam and column loads were applied to the joint prior to the fire exposure (t = 0). Because of the same column load ratio (n = 0.3), both joint specimens developed a close $\varDelta_c$-value of around 5 mm;

(2) Fire-induced expansion stage. At the beginning of fire exposure, the column started to expand due to the thermal expansion of steel tube and core concrete in the column;

(3) Fire-induced contractive stage. As the further increase of joint temperature, the fire-induced strength degradation of stainless steel and concrete in the column counteracted the influence of thermal expansion, and the contraction deformation of the column started to increase again;

(4) Failure stage in fire. Specimen CB2-1 with a beam failure did not have this stage. But specimen CB2-2 demonstrated a column failure, the axial deformation of the column increased sharply in this stage.

For specimen CB2-1 with a higher beam load ratio (m = 0.5), the beam vertical deformation kept increasing during the fire exposure stage. But for specimen CB2-2 with a lower beam load ratio (m = 0.25), the beam vertical deformation increased first, and then decreased due to the longitudinal thermal expansion of the steel beam. When reaching the ultimate state, there was a sudden increase in the beam vertical deformation. This was not caused by the failure of the beam; it simply reflected the sudden increase of the column axial deformation.

For the post-fire test specimen SB0-3, the measured residual ultimate strength is 71 kN as shown in Table I. By using finite element analysis, the predicted ultimate strength for this joint at ambient temperature is 128 kN. Therefore, the ratio of measured residual ultimate strength to ultimate strength at ambient temperature is 0.55. This result highlights the significant influence of fire exposure on the joint performance, which needs further experimental and theoretical studies.

INFLUENCE OF DIFFERENT PARAMETERS

The measured fire resistance (t_R) is given in Table I and Figure 5 for each specimen. It can be seen that, by protecting the steel beam, the fire resistance of the joint can be improved 2.2 times compared with the joint without fire protection for the steel beam. As expected, the fire resistance of the joint decreases with increasing beam load ratio. When the beam load ratio is doubled, the fire resistance of SB0-2 with an *m*-value of 0.5 is 80% that of SB1-1 with an *m*-value of 0.25.

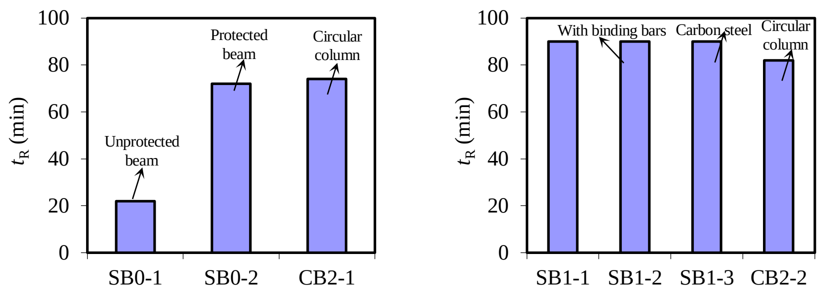

(a) Specimens with m = 0.5 (b) Specimens with m = 0.25

Figure 5. Fire resistance of joint specimens.

The influence of binding bars and steel tube type on the joint fire resistance is negligible. The fire resistances of SB1-2 with binding bars and SB1-3 with carbon steel tube are 90 min, which is equal to that of the reference specimen SB1-1. The use of the binding bars aimed to improve the integrity of the panel zone with Hollo-bolts. Since the failure of SB1-2 was its beam rather than the connection, it is understandable that the binding bars had no influence on the joint fire resistance. Similar reason can be used to explain the negligible effect of steel tube type on the joint fire resistance.

CONCLUSIONS

The following conclusions can be drawn based on the experimental research:

(1) There is significant thermal contact resistance between the steel tube and core concrete, which leads to higher surface temperature for the steel tube than that for the core concrete. This effect should be considered in future numerical analysis.

(2) The joint failure was mainly dominated by flexural failure of the steel beams near the panel zone despite the variation of parameters. But when the beam load ratio was 0.25, the joint specimen with a circular column failed due to axial crushing of the column. In general, the blind-bolted connections demonstrated good

workability in fire, and no bolt shank fracture or bolt pull-out failure was observed in any joint test.

(3) The fire protection method affects the fire resistance of joints significantly. The fire resistance of the joint specimen with a protected steel beam is 3.2 times that of the joint specimen without fire protection for the steel beam. The joint fire resistance decreases with increasing beam load ratio, but the influence of binding bars and steel tube type on the joint fire resistance is negligible.

(4) Since the current joints were only tested in an isolated condition, further experimental and theoretical studies should be conducted on beam-column assemblies to consider the influence of structural continuity and interaction.

ACKNOWLEDGEMENTS

This work is supported by the Australian Research Council (ARC) under its Discovery scheme (Grant No: DP120100971) and China National Key Basic Research Special Funds project (Grant No: 2012CB719700). The financial support is gratefully acknowledged.

REFERENCES

1. Liang, Q.Q. 2014. "Analysis and Design of Steel and Composite Structures," CRC Press.
2. Lindapter. 2011. "Type HB Installation Card," http://www.lindapter.com/Products/ Cavity_Fixings/ 2/Type_HB_Hollo-bolt.
3. Pascual, M.A., M.L. Romero, and W. Tizani. 2015. "Thermal Behavior of Blind-Bolted Connections to Hollow and Concrete-Filled Steel Tubular Columns," *J. Constr. Steel. Res.*, 107: 137-149.
4. Pascual, M.A., M.L. Romero, and W. Tizani. 2015. "Fire Performance of Blind-Bolted Connections to Concrete Filled Tubular Columns in Tension," *Eng. Struct.*, 96: 111-125.
5. ISO-834-1. 1999. "Fire-Resistance Tests-Elements of Building Construction—Part 1: General Requirements," International Standard ISO 834, Geneva.
6. European Committee for Standardization. 2004. "Design of Composite Steel and Concrete Structures – Part 1–8: General Rules and Rules for Buildings," EN 1994-1-1:2004, Eurocode 4, Brussels, Belgium.
7. European Committee for Standardization. 2005. "Design of Steel Structures – Part 1–8: Design of Joints," EN 1993-1-8:2005, Eurocode 3, Brussels, Belgium.

The Effects of Load Intensity and Restraint on the Fire Resistance of Steel and Composite Beams

FARID ALFAWAKHIRI[1], CHARLES J. CARTER[2], ROBERT M. BERHINIG[3], PATRICK ZEEVELD[4], FREDERICK E. HERVEY[4] and LUKE C. WOODS[4]

SUMMARY

The paper presents the results of sixteen fire resistance tests (in accordance with ASTM E119 and ANSI/UL 263 standards) on structural steel beams and composite steel/concrete beams conducted by the authors in 2015 at the Underwriters Laboratories facility in Northbrook, Illinois. The described experimental program was designed to investigate the effects of load intensity and restraint on the fire resistance of steel and composite beams in the context of contemporary construction materials and structural design standards. In terms of the scope and the range of investigated parameters, such experimental study was carried-out in North America for the first time. The test results confirmed the beneficial effects of reduced loads and restraint on the performance of beams in standard fire resistance tests and quantified these beneficial effects in terms of critical (failure) temperatures. The tests results also confirmed and quantified the long existing knowledge about non-composite structural steel beams performing much better than comparable composite steel/concrete beams in fire resistance tests. The generated experimental data will be used to validate numerical models, conduct parametric studies and develop simplified correlations for load intensity versus fire resistance time (and/or protection thickness). It will be of interest to certification laboratories, product developers and the broader structural fire protection design community.

INTRODUCTION

Fire resistance tests of loaded beam specimens, with a representative section of floor or roof construction not exceeding 7 ft (2.1 m) in width, were first adopted in North America in the early 1970s [1]. Earlier, standardized testing of loaded beams

[1]American Iron and Steel Institute, 25 Massachusetts Avenue, NW, Suite 800, Washington, District of Columbia 20001, U.S.A.
[2]American Institute of Steel Construction, One East Wacker Drive, Suite 700, Chicago, Illinois 60601-1802, U.S.A.
[3]Berhinig Services LLC, 1310 Chestnut Avenue, Arlington Heights, Illinois 60004, U.S.A.
[4]Underwriters Laboratories LLC, 333 Pfingsten Road, Northbrook, Illinois 60062, U.S.A.

was only carried-out within larger, usually 14 ft x17 ft (4.3 m x 5.2 m), floor or roof assembly specimens. Over the subsequent four decades, the loaded beam specimens were specified to be tested only in the restrained condition - until in 2011, both ASTM E119 [2] and ANSI/UL 263 [3] standards adopted an additional test for loaded unrestrained beams. The historical background and motives for the adoption of the new standard test were described elsewhere [4].

In the context of ASTM E119 [2] and ANSI/UL 263 [3] loaded beam tests, "a restrained condition is one in which expansion and rotation at the ends and supports of a load carrying test specimen resulting from the effects of the fire are resisted by forces external to the test specimen exposed to fire". "An unrestrained condition is one in which the load carrying test specimen exposed to fire is free to expand and rotate at its supports". The restrained conditions do not create the condition of rotational restraint, or rotational fixity, for beam ends under normal room temperatures because the test frame offers vertical (gravity) support only. However, the restrained conditions generate horizontal reactions of the test frame in response to the thermal expansion of fire-exposed beam specimens. Because the resultants of these horizontal frame reactions do not necessarily coincide with the specimen sections' centroids (that is, frame reactions apply eccentrically to the specimen for extended periods during the test), rotational restraints are also generated. This partially replicates similar conditions found in building floors and roofs in terms of multi-directional resistance to expansion (restraint) that occurs under real fire conditions. However, this similarity is not complete as, for instance, the test frame does not replicate structural continuity, it does not offer anchorage to specimens sagging in the tensile membrane action mode (that is, the test frame does not resist the horizontal contraction of the specimen), and the stiffness of restraints in real construction does not necessarily match the test conditions.

Although some limited comparative testing of restrained vs. unrestrained steel beam specimens was carried-out in the past [5], the topic of restraint in loaded beam tests continued to generate substantial confusion and intense debates over several decades, caused primarily by the lack of convincing experimental evidence. The test program described in this paper was intended in part to address the knowledge gap for this topic. However the primary motivation for this study was to investigate the effects of load intensity on the performance of steel and composite steel/concrete beams in fire resistance tests.

In the context of ASTM E119 [2] and ANSI/UL 263 [3], the standards require to "apply a superimposed load to the test specimen to simulate a maximum-load condition. This load shall be the maximum load condition allowed under nationally recognized structural design criteria unless limited design criteria are specified and a corresponding reduced load is applied". So, technically, the standards allow the application of a reduced load in a fire resistance test, however, the reduced load condition has to be specified in the certification listing. Therefore, product developers usually tested their specimens under the "maximum" load in order to achieve an "unrestricted" certification.

Over the years, however, the evolution of structural design standards, in some cases allowing higher design loads, resulted in changes to the "maximum" load condition in fire resistance tests. So, many certified designs developed originally as "unrestricted" are now often forced to undergo certification revisions, in the context of more recent structural design standards, specifying load "restrictions" to the application of the certified designs. These developments generated substantial demand for improved knowledge on the effects of load intensity on the performance of loaded beams in fire resistance tests. Such improved knowledge would allow the adjustment of fire protection thickness based on the expected load intensity. Given that many beams in real buildings are over-designed for gravity loads, such thickness adjustments could also lead to more rational fire protection design practices in North America. Adjustments of fire protection for the expected load intensity level have been a routine practice in the United Kingdom [6] and other counties [7] for many decades.

LOADED BEAM TESTS

Sixteen beams were tested in standard floor furnace setups, with each setup consisting of 4 similar beams tested concurrently at different load intensity levels of 100%, 80%, 60% and 40% of the maximum design load (in the context of most recent structural design criteria). Figure 1 illustrates the typical 4-beam test setup. The program involved tests of

- Four unrestrained structural steel beam specimens,
- Four restrained structural steel beam specimens,
- Four unrestrained composite steel-concrete beam specimens, and
- Four restrained composite steel-concrete beam specimens.

Beam Specimens

In order to facilitate direct comparisons of test results, all the beam specimens were designed having similar dimensional configurations, built of similar materials, and protected with the same sprayed fire resistive material (SFRM) of the same thickness.

The beam specimens consisted of lightly reinforced lightweight concrete slabs, 2.5 inches (64 mm) thick, 47 inches (1190 mm) wide, over composite galvanized fluted steel deck units, 0.037 inches (0.94 mm) thick, 2 inches (51 mm) deep, supported by W8x28 (grade A992) structural steel beams.

The minimum specified strength of structural steel beams was 50 ksi (345 MPa). All steel beams were cut to the length of 163 inches (4140 mm). The beams were seated on 6 inches x 6 inches x 1 inch steel angles, secured to the test frame and positioned at a clear span of 155 inches (3937 mm). Steel plates, 12 inches (305 mm) long, 8 inches (203 mm) high and 0.38 inches (thick were welded to the ends of the steel beams, as shown Figure 2(a). These end plates served as the points of lateral and torsional restraint for the steel beams. After the positioning of the steel beams within the test frame, a clear space of about 1.6 inches (41 mm) wide was left between the end plates of the steel beams and the test frame.

The steel deck units were oriented perpendicular to the supporting steel beams. Each of the units was nominally 36 inches (914 mm) wide and cut to the length of approximately 46.75 inches (1187 mm). In cross-section, the ribs (valleys) of the steel deck units formed trapezoidal shapes, nominally 5 inches (127 mm) wide at the bottom, and 7 inches (178 mm) wide at the top, of the steel deck. The nominal

Figure 1. Unrestrained non-composite steel beams before and after the test (top and bottom views).

center-to-center spacing of the ribs was 12 inches (305 mm). The steel units were centered over the supporting steel beams and attached to the beams by means of puddle welds, 0.75 inches (19 mm) in diameter, at each joint of adjacent units. Additionally, the joints of adjacent units were secured together with #10 screws, 0.75 inches (19 mm) long, at the distance of 18 inches (457 mm) from the centerline of the supporting steel beam. To form the end closure to the ribs (valleys) of the steel deck units, 2 inches x 0.75 inches (51 mm x 19 mm) angles, formed of galvanized steel sheet, were attached (welded) to the ends of the floor units, as shown in Figure 2(b).

In all specimens, uncoated steel welded wire reinforcement mesh, designated as "6 x 6 - W1.4 x W1.4" - i.e. consisting of 0.014 in^2 (9 mm^2) wires spaced at 6 inches (152 mm) in both the longitudinal and transverse directions, was placed on top of the steel deck. During concrete placement, the wire mesh was lifted to about the mid-depth of the concrete topping thickness, i.e. to the depth of about 1.25 inches (32 mm) from the top concrete surface.

The lightweight concrete had a nominal dry density of 115 pcf (1840 kg/m^3) and the minimum specified strength of 3 ksi (20.7 MPa). During placement, the concrete was wood-floated and rough troweled to a flat surface. Numerous concrete thickness measurements were carried-out during concrete placement for each beam specimen to ensure accurate "as designed" and uniform slab thickness. The curing of the concrete after placement followed the following procedures in accordance with ASTM E119 [2] and ANSI/UL 263 [3]. Initially, the beam specimens were

(a) Steel beam end support configuration (view from top).

(b) The end closure to the ribs (valleys) of the galvanized steel deck units.

Figure 2. Construction Details of the Beam Specimens.

stored at normal room conditions for about a month. Afterwards, the specimens were stored in special curing cells for several months until the relative humidity of concrete was reduced below 70%. After that, the beam specimens were again stored at normal room conditions for about two months, while undergoing the application and conditioning of SFRM protection. The relative humidity of concrete was also checked to stay below 70% on the day of the fire resistance test. The age of concrete in the beam specimens, from the date of placement to the date to the fire resistance test, ranged between 234 and 293 days.

Each of the eight composite beam specimens was also provided with 56 shear connector studs, 0.75 inches (19 mm) in diameter, 3.5 inches (90 mm) long, welded to the top flange of the steel beam through the steel deck – these shear connectors were sufficient to ensure the full composite action of the composite steel-concrete section in accordance with ANSI/AISC-360-10 [8].

Restraint Conditions

For the eight restrained beam specimens, the space between the steel beam end plates and the test frame were filled with concrete. Also, in accordance with ASTM E119 [2] and ANSI/UL 263 [3], for the four restrained composite steel-concrete beam specimens, only the 39.7-inch (1010-mm) effective design width of the concrete slab, per ANSI/AISC-360-10 [8] was extended to the test frame – for the remaining 8.25 (210-mm) width of the concrete slab, a clear space of about 2 inches (51 mm) wide was left between the concrete and the test frame. For the four restrained non-composite steel beam specimens, a similar clear space, about 2 inches (51 mm) wide, was left between the concrete slab and the test frame.

For the eight unrestrained beam specimens, the spaces between the steel beam end plates and thee test frame were left clear of any obstructions, ensuring the free expansion and rotation of the beam specimens. Clear spaces, about 2 inches (51 mm) wide, were also left between the ends of the concrete slabs and the test frame.

SFRM Protection

For all beam specimens, the SFRM was applied to the steel beams to a uniform thickness of 1 inch (25 mm) verified by 90 thickness measurements for each beam specimen. The deck flutes above the steel beams were filled with SFRM. The choice of the SFRM product and thickness was intended to target fire test durations of around 2 hours. During SFRM applications, additional samples of SFRM (applied to separate steel plates) were prepared – these samples were used to verify the dry density of SFRM over time with purpose to ensure adequate conditioning of SFRM.

Instrumentation

The furnace and the beam specimens were instrumented in accordance with ASTM E119 [2] and ANSI UL 263 [3]. Each beam specimen was instrumented with 16 thermocouples to measure and record steel beam temperatures at 4 specified locations at each of the 4 specified beam sections. The beam specimens were also instrumented to measure and record mid-span deflections. Additionally, a few thermocouples were placed at various depths in concrete slabs.

Test Loads

All the beam specimens were loaded in a similar manner with three equal concentrated loads, as shown in Figure 1. For each specimen, one concentrated load

TABLE I. CONCENTRATED LOADS IN LOADED BEAM TESTS.

Load Intensity, %	For Non-Composite Steel Beam Specimens, kips (kN)	For Composite Steel-Concrete Beam Specimens, kips (kN)
100	8.75 (38.9)	17.8 (79.2)
80	6.90 (30.7)	14.1 (62.7)
60	5.05 (22.5)	10.5 (46.7)
40	3.20 (14.2)	6.82 (30.3)

was centered at the mid-span, and the other two concentrated loads were centered at 36 inches (914 mm) from the mid-span, on both sides of the mid-span. These concentrated loads, listed in Table I, in addition to the self-weight of the beam specimens, were intended to impose the respective percentage of the maximum design bending moment at the mid-spans of the beam specimens.

In accordance with ANSI/AISC-360-10 [8], the design span for all beam specimens was estimated equal to 159 inches (4040 mm), and the maximum design bending moment capacities were estimated at 769 kips-inches (86.9 kN-m) and 1521 kips-inches (171.8 kN-m) for non-composite and composite beam specimens, respectively. It should also be noted here that these maximum design bending moment capacities correspond to 60% of the nominal bending moment capacities of the beam specimens, in accordance with ANSI/AISC-360-10 [8].

The concentrated loads above were gradually applied through hydraulic jacks to reach the intended test load level for each beam specimen approximately 30 minutes before the furnace ignition. The measured hydraulic system pressures were used to control the concentrated loads. The test loads were then maintained constant throughout the duration of the fire resistance test for each beam specimen until the specimen was deemed no longer capable to sustain the applied loads.

Test Results

For unrestrained non-composite steel beam specimens, the deflection criterion was estimated at 7.51 inches (191 mm), and the rate of deflection criterion was estimated at 0.334 inches/minute (8.48 mm/minute.).

For unrestrained composite steel-concrete beam specimens, the deflection criterion was estimated at 4.81 inches (122 mm), and the rate of deflection criterion was estimated at 0.214 inches/minute (5.44 mm/minute).

The unrestrained beam specimens were deemed failed when both of the respective deflection and rate of deflection criteria were reached. For all tested unrestrained beam specimens, the deflection criterion was reached before the rate of deflection criterion was reached. The restrained beam specimens were deemed failed based on the judgement of the laboratory staff, however, the deflections and

TABLE II. MEASURED CRITICAL (FAILURE) TEMPERATURES.

Load Intensity, %	For Restrained Non-Composite Beams, ˚F (˚C)	For Unrestrained Non-Composite Beams, ˚F (˚C)	For Restrained Composite Beams, ˚F (˚C)	For Unrestrained Composite Beams, ˚F (˚C)
100	1263 (684)	1220 (660)	1132 (611)	1056 (569)
80	1293 (701)	1274 (690)	1166 (630)	1113 (601)
60	1348 (731)	1379 (748)	1271 (688)	1255 (679)
40	1447 (786)	1488 (809)	1448 (787)	1438 (781)

rates of deflection recorded at the time of the deemed failure were reaching values close to the comparable criteria used for unrestrained beam specimens.

For all specimens, the heating of the steel beams proceeded in a relatively uniform (along the beam) manner, with limited scatter of recorded temperatures at comparable measurement locations and with limited scatter in the recorded average section temperatures. Neither any significant SFRM fall-off nor any explosive spalling of concrete was observed.

The maximum average steel section temperatures, in the context of ASTM E119 [2] and ANSI/UL 263 [3] tests, for all tested beam specimens at the time of the deemed failure are listed in Table II as the critical (failure) temperatures.

CONCLUSIONS

The tests described in this paper confirmed the beneficial effects of reduced loads and restraint on the performance of beams in standard fire resistance tests and quantified these beneficial effects in terms of critical (failure) temperatures. The beneficial effects of restraint, however, seem to diminish at reduced loads.

The tests results also confirmed and quantified the long held notion about non-composite structural steel beams performing substantially better than comparable composite steel/concrete beams in fire resistance tests.

The generated experimental data will be used to validate numerical models, conduct parametric studies and develop simplified correlations for load intensity versus fire resistance time and/or protection thickness.

REFERENCES

1. Bono, J.A. 1970. "New Criteria for Fire Endurance Tests", *Fire Test Performance, ASTM STP 464*, ASTM International, West Conshohocken, PA, pp. 106-126.
2. ASTM E119-14. 2014. “Standard Test Methods for Fire Tests of Building Construction and Materials”, ASTM International, West Conshohocken, PA, United States.
3. ANSI/UL 263-14. 2014. “Standard for Fire Tests of Building Construction and Materials”, Underwriters Laboratories Inc., Northbrook, IL, United States.
4. Berhinig, R. M. and F. Alfawakhiri. 2014, “New Fire Resistance Test for Loaded Unrestrained Beams”, *Proceedings of the 2014 Structures Congress, April 3-5, Boston, Massachusetts*, American Society of Civil Engineers, Reston, VA, pp. 1175-1184.
5. Bletzacker, R. W. September 1966. “Effect of Structural Restraint on the Fire Resistance of Protected Steel Beam Floor and Roof Assemblies,” Final Report EES 246/266, Building Research Laboratory, Engineering Experiment Station, The Ohio State University, Columbus.
6. Lawson, R. M. and G. M. Newman. 1990. “Fire Resistant Design of Steel Structures — A Handbook to BS5950: Part 8”, *SCI Publication 080*, The Steel Construction Institute, UK.
7. Lawson, R. M. and G. M. Newman, G. M. 1996. “Structural Fire Resistant Design to EC3 & EC4, and Comparison with BS 5950”, *SCI Publication 159*, The Steel Construction Institute, UK.
8. ANSI/AISC-360-10. 2010. “Specification for Structural Steel Buildings”, American Institute of Steel Construction, Chicago, IL.

Numerical Modeling of Heat Transfer in Steel-concrete Composite Slabs

JIAN JIANG, JOSEPH A. MAIN, JONATHAN M. WEIGAND and FAHIM SADEK

ABSTRACT

This paper presents detailed and reduced-order numerical modeling of heat transfer in composite floor slabs with profiled steel decking for analysis and design of structures exposed to fire. The detailed modeling approach represents the concrete slab with solid elements and the steel decking with shell elements. The reduced-order modeling approach represents the thick and thin parts of a composite slab with alternating strips of layered shell elements. The detailed modeling approach was validated against experimental results available in the literature, and the reduced-order modeling approach was calibrated and verified against the detailed model results. A parametric study using the detailed modeling approach was conducted to investigate the influence of slab geometry on the temperature distribution within composite slabs. The results show that the rib height of the decking and the width at the top of the rib are key factors governing the temperature distribution in the rib. The paper also presents comparisons with Eurocode 4 calculations of fire resistance of composite slabs. The comparisons indicate that the Eurocode 4 overestimates the fire resistance compared to the numerical results by up to 12 %.

INTRODUCTION

Typical steel/concrete composite floor slab construction consists of a concrete topping on profiled steel decking, typically reinforced with welded wire mesh. The decking acts as reinforcement and permanent formwork, reducing materials and construction time. One of the advantages of this type of construction when exposed to fire is the shielding effect provided by the ribs, which limits the temperature rise in the reinforcement. However, the presence of the ribs creates an orthotropic profile, which results in thermal and structural responses that are more complex than those for flat slabs, presenting challenges in numerical analysis and practical design.

The objective of this study is to develop a reduced-order modeling approach for heat transfer analysis of composite slabs that is also suitable for structural analysis, so that the same model can be used for thermal and structural analysis. Previous heat transfer analyses have generally used a detailed finite-element modeling approach, with solid elements for the concrete slab and shell elements for the steel decking [1-3].

National Institute of Standards and Technology (NIST), 100 Bureau Drive, Stop 8611, Gaithersburg, MD, 20899, U.S.A.

In considering the suitability for heat transfer analysis of reduced-order modeling approaches previously used for structural analysis, the grillage approach with beam elements [4] has significant limitations, because of the inadequacy of the 1D elements to represent in-plane and through-thickness heat transfer in the slab. Modeling approaches that use a constant shell thickness [5] also have limitations for thermal analysis because they fail to capture the shielding effect of the ribs, which results in curved isotherms in the floor slab, significantly affecting both the structural response and the thermal insulation provided by the slab. The modeling approach that uses alternating strips of shell elements in structural analyses [6], however, has the potential to capture both in-plane and through-thickness heat transfer in composite slabs.

In this study, a detailed finite-element model was first developed and validated for heat transfer analysis in composite floor slabs. This approach was then used to conduct a parametric study by varying the geometric parameters of the slab to examine their influence on the slab's thermal response. The numerical results were compared against calculations based on Eurocode 4 (EC4) [7]. A reduced-order modeling approach consisting of layered shell elements was then proposed and verified against the detailed model.

DETAILED NUMERICAL MODELING

The heat transfer analysis of composite slabs was performed using the finite element software LS-DYNA[1] [8]. Noting the periodicity of the composite slab profile, only one half-strip of the composite slab was modeled, with adiabatic boundary conditions at the right and left boundaries, as shown in Figure 1. The concrete slab was modeled with solid elements and the steel decking was modeled with shell elements. The concrete slab and steel decking had a consistent mesh at their interface and shared common nodes. The model used temperature-dependent thermal properties of concrete and steel based on EC4 [7].

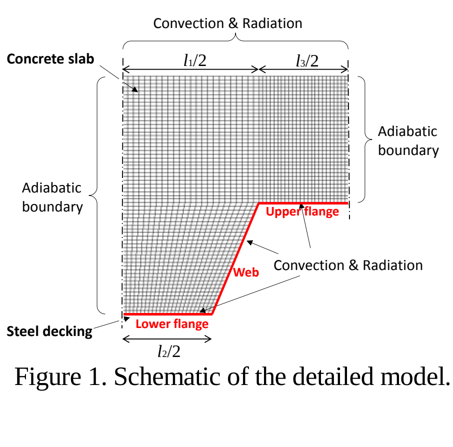

Figure 1. Schematic of the detailed model.

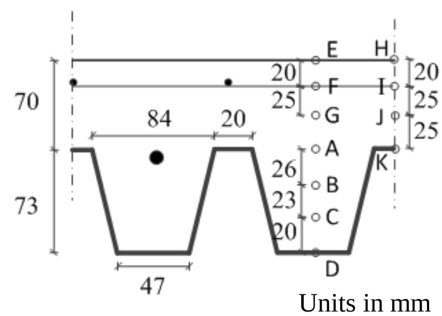

Figure 2. Geometry of the tested slab [1].

The detailed modeling approach was validated against a standard fire test denoted as Test 2 in [1]. The tested slab had 6 ribs and used Prins PSV73[1] steel decking and

[1] Certain commercial entities, equipment, products, or materials are identified in this document in order to describe a procedure or concept adequately. Such identification is not intended to imply

normal weight concrete with a measured moisture content of 3.4 %. The effect of moisture content is accounted for in the temperature-dependent specific heat model from EC4. The geometry of the tested slab is shown in Figure 2. Thermal boundary conditions at the top and bottom of the slab were taken from [1], and gas temperatures applied to the bottom surfaces were based on ISO 834 [9]. Numerical and experimental results for several points shown in Figure 2 are compared in Figure 3. The difference between the measured and computed temperatures did not exceed 15 % (Point B at time 80 minutes).

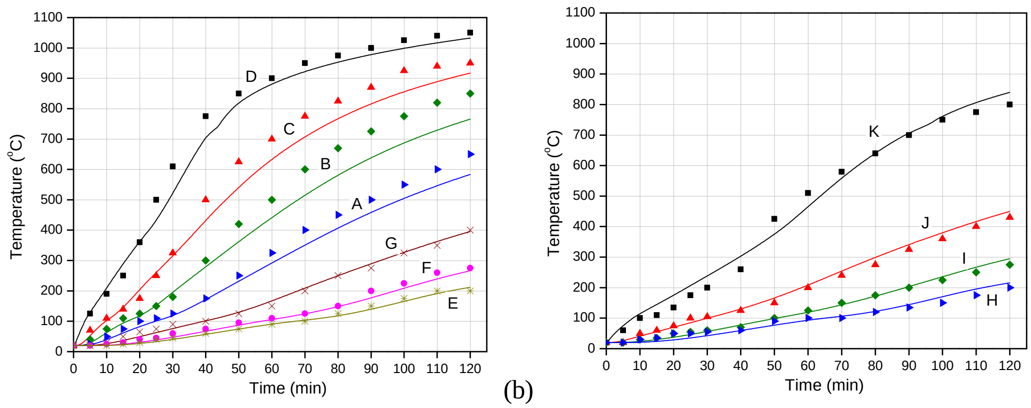

Figure 3. Comparison of calculated (solid curves) and measured[2] (discrete symbols) temperatures: (a) in the thick part; (b) in the thin part.

PARAMETRIC STUDY

The detailed modeling approach was used to perform a parametric study on the thermal behavior of composite slabs. Vulcraft 3VLI[1] decking, commonly used in North America, was selected as the baseline configuration for the parametric study. The selected geometry is depicted in Figure 4. The thickness of the steel decking was 0.9 mm and lightweight concrete was used. The same modeling approach and thermal loading as in the previous section was used in the parametric study. Figure 5 shows the predicted temperature distribution in the slab for the baseline configuration after three hours. Inclined temperature contours indicate non-uniform heat transfer through the composite slab, resulting from the profiled shape of the steel decking.

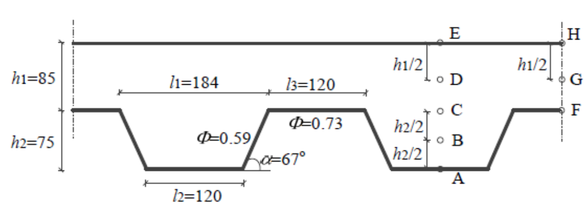

Figure 4. Configuration of the slab Vulcraft 3VLI (all dimensions are in mm).

---

recommendation, endorsement, or implication that the entities, products, materials, or equipment are necessarily the best available for the purpose.

[2] The policy of the National Institute of Standards and Technology is to include statements of uncertainty with all NIST measurements. In this document, however, measurements of authors outside of NIST are presented, for which uncertainties are not reported and are unknown.

Considering the practical ranges of geometric parameters (h_1, h_2, l_1, l_2, and l_3), the parametric study used values of h_1 = (50 mm, 85 mm, 125 mm), h_2 = (50 mm, 75 mm, 100 mm), l_1 = (130 mm, 184 mm, 250 mm), l_2 = (80 mm, 120 mm, 160 mm), and l_3 = (80 mm, 120 mm, 160 mm). Only one geometric parameter was changed at a time, with all other parameters having the values shown in Figure 4. The results are shown in Figure 6. The parameter h_1 had a significant influence on the temperature of the unexposed surface of the slab (Point E) as shown in Figure 6a. The height of the rib, h_2, and the width at the top of the rib, l_1, affected the temperature in the rib (Point C) more significantly than they affected the temperature at the unexposed surface (Point E), as shown in Figures 6b and 6c. The temperature in the slab increased as h_2 and l_1 decreased, due to the reduced amount of concrete in the rib. Compared to h_2 and l_1, the dimensions l_2 and l_3 had a less significant effect on the temperature at point C (Figures 6d and 6e). However, the width of the upper flange of the deck, l_3, along with the height of the concrete topping, h_1, governed the heat transfer through the thin part of the slab, where the maximum temperature at the unexposed side occurred (Point H).

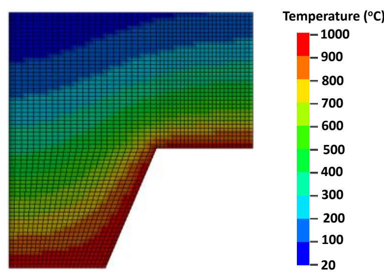

Figure 5. Temperature contours in the baseline slab configuration after three hours.

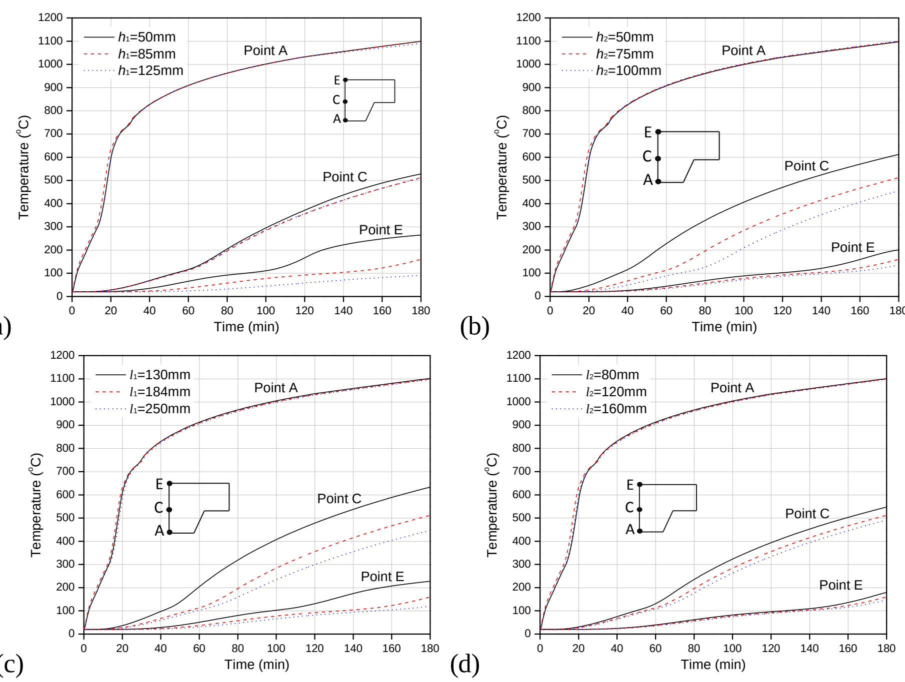

(a) (b) (c) (d)

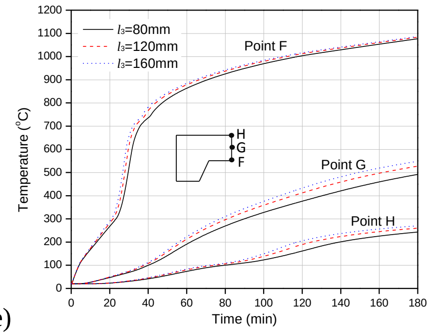

(e)

Figure 6. Variation of temperature within the slab against: (a) h_1; (b) h_2; (c) l_1; (d) l_2; (e) l_3.

Table 1 presents a comparison of fire resistances for composite slabs estimated from Annex D in EC4 calculations [7] and from numerical analyses. The fire resistance in EC4, expressed in minutes, is based on the fire duration until a maximum temperature of 180 °C or an average temperature of 140 °C, whichever governs, is achieved at the unexposed surface of the slab. As shown in Table 1, the fire resistance of the composite slabs, based on the numerical results, was governed by the maximum temperature (Max) occurring at the unexposed surface of the slab, rather than by the average temperature (Ave). The table indicates that the EC4 calculation overestimates the fire resistance compared with the numerical results by up to 12.3 %. The overestimation of fire resistance would be even greater in comparison with the experimental data because, as shown Fig. 3, the numerical results underestimate the temperatures by as much as 15 %. This overestimation of fire resistance in the EC4 calculation may be is likely due to an underestimation of the effect of the upper flange width, l_3, which was a key factor influencing the maximum temperature at the top surface of the thin part of the slab.

TABLE 1. COMPARISON OF FIRE RESISTANCE BETWEEN EC4 CALCULATIONS AND NUMERICAL PREDICTIONS.

Varied parameters		Fire resistance (min)				
		EC4 Annex D	Detailed Numerical			
			Max	Difference (%)	Ave	Difference (%)
h_1	50 mm	64	55	14	60	6.25
	85mm	140	124	11.4	136	2.9
	125 mm	227	247	8.8	249	9.7
h_2	50 mm	131	121	7.6	124	5.3
	75 mm	140	124	11.4	136	2.9
	100 mm	146	128	12.3	136	6.8
l_1	130 mm	135	128	5.2	130	3.7
	184 mm*	N/A	124	–	136	–
	250 mm*	N/A	121	–	130	–
l_2	80 mm	137	122	10.9	127	7.3
	120 mm	140	124	11.4	136	2.9
	160 mm*	N/A	128	–	135	–
l_3	80 mm	147	139	5.4	143	2.7
	120 mm	140	124	11.4	136	2.9
	160 mm*	N/A	117	–	123	–

*Asterisk indicates parameters are beyond range of EC4 calculation method.

REDUCED-ORDER NUMERICAL MODELING

The reduced-order modeling approach was developed using a layered composite shell formulation, in which a distinct structural material, thermal material, and thickness can be specified for each layer, including layers to represent fireproofing, if needed. The proposed approach uses alternating strips of shell elements to represent the thick and thin parts of composite slabs, as illustrated in Figure 7. For the half-strip configuration in Figure 1, only two shell elements were used, with the width of the thick and thin parts each being spanned by a single shell element. The tapered profile of the slab rib was accounted for in Shell A by reducing the density of concrete in the rib to ensure accurate representation of the mass of concrete in each layer (i.e., $\rho_1, \rho_2, \ldots$ in Figure 7), since the shell formulation assumes constant width of all layers. The reduced concrete density in the ith layer of the rib, ρ_i, was calculated based on the ratio of the average rib width for that layer, d_i, to the total width at the top of the rib, l_1 (i.e., $\rho_i = \rho_0 \times d_i / l_1$).

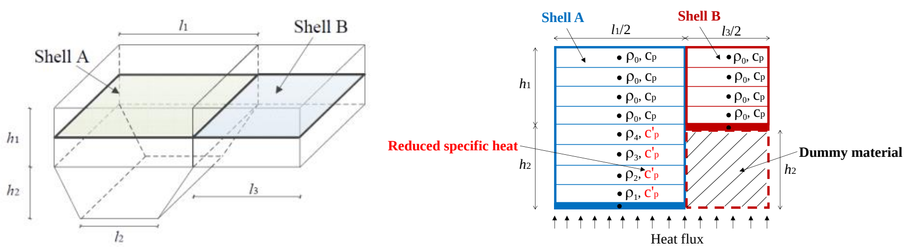

Figure 7. Schematics illustrating reduced-order modeling of composite slabs.

In modeling the thin part of the slab (Shell B), a "dummy material" with high thermal conductivity and negligible specific heat was used to represent the absence of material below the steel decking. The use of the dummy material allowed Shell A and Shell B to be modeled with the same thickness, so that in-plane heat conduction between corresponding layers of adjoining shell elements could be properly accounted for. Thermal boundary conditions were applied at the fictitious bottom surface of Shell A, and the high thermal conductivity of the dummy material ensured an essentially equivalent temperature at the top of the dummy material, thus providing appropriate thermal boundary conditions for the steel decking. The essentially uniform temperature through the depth of the dummy material also provided thermal loading to the adjoining layers in the rib of Shell A, thus partially accounting for heat input through the web of the decking. Analysis of the reduced-order model was carried out with the same material characterization and thermal loading as the detailed model in the previous section. Figure 8 shows a comparison of the calculated temperature histories from the detailed and reduced-order models for the composite slab. The largest difference between the results of the two models is at point M, where the temperatures differed by about 16 % at the end of the analyses. This difference was found to be much larger when the dummy material was not used, and the remaining difference (16 %) resulted from not completely accounting for the heat input through the web of the decking within the layered shell formulation.

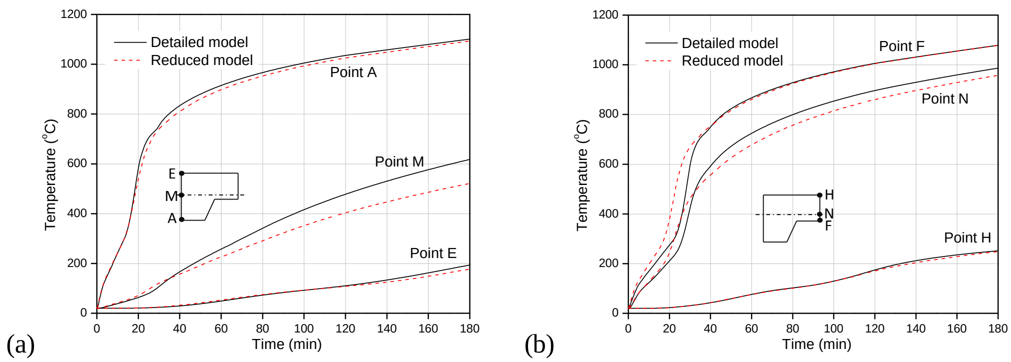

Figure 8. Comparison of average temperature histories for detailed and reduced models: (a) in the thick part; (b) in the thin part.

To improve the accuracy of the reduced-order model, the specific heat of concrete in the rib, c'_p (see Figure 7), was reduced to compensate for the delayed heating observed above the rib in Shell A (point M in Figure 8). The optimum value of c'_p was determined by minimizing the differences in the calculated temperatures at point M between the detailed and reduced-order models. Figure 9 shows the overall difference in temperature, T_{gap}, between the detailed model and the reduced-order models with different values of c'_p, calculated as follows:

$$T_{gap} = \sqrt{\frac{\sum_{i=1}^{n}(T_{reduced} - T_{detailed})^2}{n}}, \tag{1}$$

where n is the number of time samples. The minimum value of T_{gap} = 14 °C corresponded to $c'_p = 0.7c_p$, and Figure 10 shows the resulting temperature distribution for this optimum value. The computed temperatures from the detailed and reduced-order models differed by 5 % or less. The influence of the slab geometry on the optimal value of c'_p has been investigated and will be presented in a future publication.

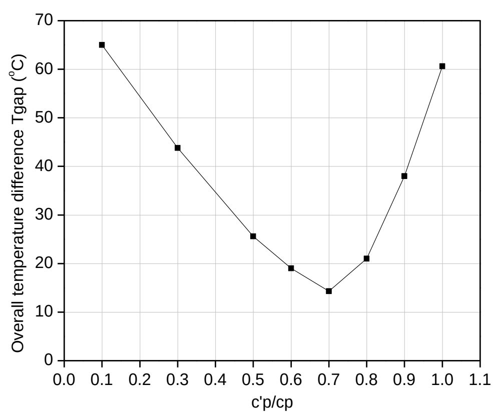

Figure 9. Overall temperature difference at the middle surface of Shell A (Point M) against various values of reduced specific heat.

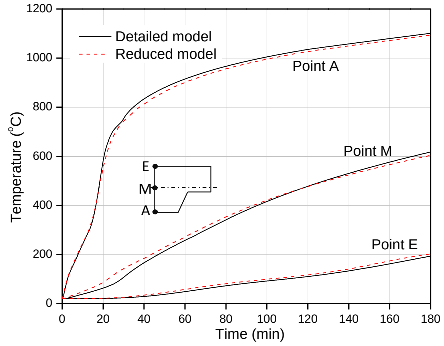

(a)

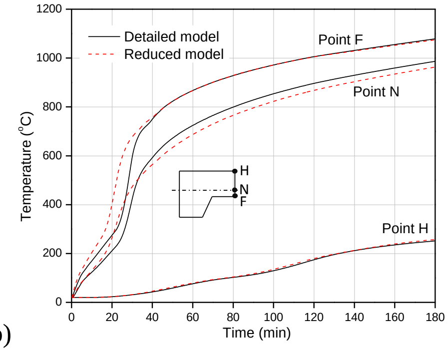

(b)

Figure 10. Comparison of temperature histories for detailed and reduced models with reduced specific heat of $c'_p=0.7c_p$: (a) in the thick part; (b) in the thin part

SUMMARY AND CONCLUSIONS

This paper presented detailed and reduced-order finite element models for heat transfer in composite floor slabs with profiled steel decking. The detailed modeling approach represented the concrete slab with solid elements and the steel decking with shell elements. The reduced-order modeling approach represented the thick and thin parts of a composite slab with alternating strips of layered shell elements. The detailed modeling approach was validated against experimental results available in the literature, and the reduced-order modeling approach was verified and calibrated against the detailed model results. A parametric study using the detailed modeling approach was conducted to investigate the influence of slab geometry on the temperature distribution within composite slabs. The results showed that the rib height of the steel decking and the width at the top of the rib are key factors affecting the temperature distribution in the rib. The heat input through the web of the steel decking also plays a key role in the non-uniform temperature distributions in the horizontal plane of slabs. It is possible to account for this web heat input in reduced-order models (shell elements) by reducing the specific heat of concrete in the rib and adding dummy material with low specific heat and high thermal conductivity in the thin part of the slab. The paper also presented comparisons with Eurocode 4 calculations of fire resistance of composite slabs. The results showed that the fire resistance of composite slabs, based on the thermal insulation criterion, was governed by the maximum temperature at the unexposed surface, rather than the average temperature. The comparison indicated that the Eurocode 4 overestimates the fire resistance compared to the numerical results by up to 12 %.

REFERENCES

1. Hamerlinck R., Twilt L. and Stark J. 1990. "A Numerical Model for Fire-exposed Composite Steel/concrete Slabs," presented at the 10th International Specialty Conference on Cold-formed Steel Structures, USA, 1996.
2. Guo S. 2012. "Experimental and Numerical Study on Restrained Composite Slab during Heating and Cooling," *Journal of Constructional Steel Research*, 69: 95-105.
3. Pantousa D. and Mistakidis E. 2013. "Advanced Modelling of Composite Slabs with Thin-walled Steel Sheeting submitted to Fire," *Fire Technology*, 49: 293-327.
4. Elghazouli A. Y., Izzuddin B. A., and Richardson A. J. 2000. "Numerical Modelling of the Structural Fire Behaviour of Composite Buildings," *Fire Safety Journal*, 35: 279-297.

5. Huang Z., Burgess I. W. and Plank R. J. 2000. "Effective Stiffness Modelling of Composite Concrete Slabs in Fire," *Engineering Structures*, 22(9): 1133-1144.
6. Main J.A. and Sadek F. 2012. "Robustness of Steel Gravity Frame Systems with Single-Plate Shear Connections," *NIST TN-1749*, National Institute of Standards and Technology, Gaithersburg, MD.
7. European Committee for Standardization (CEN). 2005. Eurocode 4 Design of composite steel and concrete structures: Part 1.2: General rules, Structural fire design, EN 1994-1-2, Brussels.
8. Livermore Software Technology Corporation (LSTC). (2012), LS-DYNA Keyword User's Manual, Version 971, Livermore, CA.
9. International Organization for Standardization (ISO). 2014. *Fire-resistance tests – Elements of building construction, ISO 834-11*, Geneva, Switzerland.

Evaluation of Composite Steel-Concrete Slab Performance Subjected to Travelling Fire: A Case Study

RUI R. SUN and BERNICE V. Y. WONG

ABSTRACT

This paper presents a case study which aims to contribute a better understanding of the fire performance of composite slab panel structural under non-uniform fire. A travelling fire which simulates the procedure of fire spread over a large office compartment is introduced. The coupled CFD modelling and heat transfer model is used for the fire and thermal analysis. The elevated composite slab temperatures are applied to finite element model for structural fire analysis by using ABAQUS. The phenomenon of tensile membrane action in partially fire protected composite slab when subjected to travelling fire is presented. It has been observed that the predicted office compartment fire has slower temperature growth rate than that of the ISO 834 standard fire as well as the parametric fire. The study has found out that the traditional structural fire engineering design may lead to over-conservative prediction with respect to composite slabs structural fire performance under travelling fire.

INTRODUCTION

Design fire for the elevation of structural performance in case of fire has been outlined in Eurocodes, assuming a homogeneous temperature distribution throughout the entire fire compartment, regardless of its size. However in reality, fire do not burn simultaneously but spread across floor plates, from its ignition source travel to adjacent combustible surfaces by direct flame contact. There are a number of investigations concerning tensile membrane action in composite floor when under homogeneous compartment fire. The composite slab behavior under travelling fire however has not been extensively studied. In this paper, a case study has been carried out to examine the behavior of this form of structural action under the exposure of travelling fire and whether the current design method to this situation gives a more-conservative assumption.

Rui R. Sun, MMI Engineering, KMD Media Centre, Wellington Circle, Aberdeen, AB12 3JG, UK.
Bernice V. Y. Wong, Ramboll Fire, 240 Blackfriars Road, London SE1 8NW, UK.

CFD FIRE MODELLING

Design fire scenario

The current structural fire engineering practice adopts standard fire and/or natural fire curves assuming a homogenous temperature throughout a compartment. This assumption may be justified in small and medium compartments; however, several tests and observation in large compartment fire have revealed that this assumption is not precise since the fire in the compartment does not burn simultaneously throughout the enclosure leading to a non-uniform temperature in the compartment [1]. A theoretical travelling fire model has been proposed by Gottfried et al. [2], where the compartment is divided into two relative regions: near filed and far field. It provides the practical engineer a simplified model to estimate the effect of travelling fire to the structural resistance. However, in this study, sophisticated CFD modelling is employed to simulate the travelling fire scenario, which is then fed into structural fire analysis to assess the structural behavior of the composite slab. This study focuses on illustrating the structural behavior of composite slab subjected to travelling fire and importance of advance numerical modelling when taking into account such scenarios, rather than the accuracy and conservatism of different approaches (simplified or sophisticated) to simulate the travelling fire scenarios.

Fire Dynamics Simulator [3], CFD code has been widely used by fire engineers around the world. In CFD code, the radially spreading fire has been adopted to evaluate a fire accident in a large compartment, where fire starts from a source of ignition and spreads out across the floor area. Fire is directed to start at the point of ignition and spread outwards, growing in size and assuming elliptical shape with a spreading rate, S (m/s). A ramp function has been introduced into the CFD model, to turn the burning on and off to simulate the consumption of fuel as the fire spreads radially. The ramp-up begins at the time when fire arrives at a given point. Each surface cell burns for a specified period of time at a steady state as the fire spreads outward, creating a widening ring of fire, fire in the burning cells enter the decay stage as the available fuel is consumed. The burning time is determined as a function of the heat release rate and fire load density per unit area.

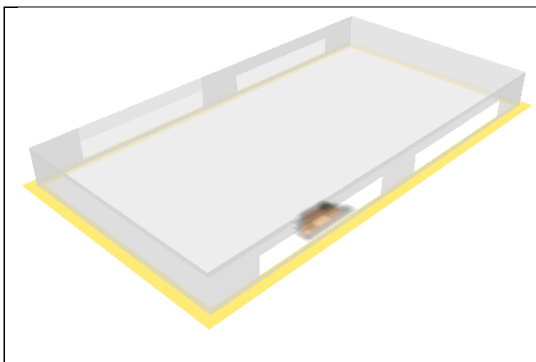

Figure 1. Fire compartment isometric.

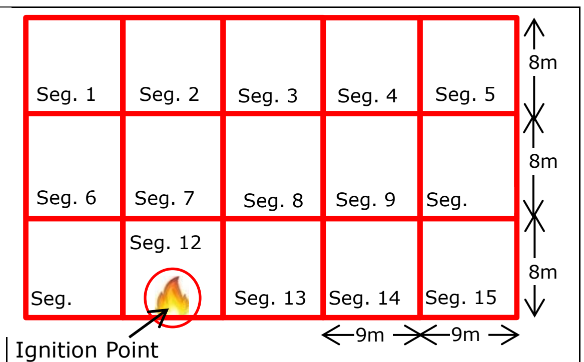

Figure 2. Plan of fire compartment.

Fire cases have been considered in this study where fire is originating adjacent to the long wall. The geometry of the fire compartment used in this study was a one storey open plan building. The overall enclosure was rectangular having 45m length by 24m width and a height of 3.5m, ventilated through four openings (15m by 2m), as shown in Figure 1. The compartment floor plan is divided into 12 segments, each having a dimension of 9m by 8m. Figure 2 illustrates the segment locations and ignition location of the fire case that has been considered in the study. The compartment walls and ceiling were made of 200mm thick gypsum plasterboard, the thermal properties is obtained from EN 12514 [4] with density 900kg/m^3, thermal conductivity 0.25 W/m/K and specific heat ranged 1000J/kg/K. In CFD, the concept of Adiabatic Surface Temperature (AST) is introduced as a practical means to express the thermal exposure of a surface. The concept has proved particularly useful when calculating temperatures in fire exposed structures [5]. In this study, FDS computed the gas phase temperatures, produced as output quantities of the AST, which were then input into ABAQUS to determine the heat transfer to structural elements.

Compartment temperatures

Given a fire originating adjacent to the long wall in Segment 12, the recorded AST as fire spread from south to the north wall at ceiling level are shown in Figure 3. Figure 3a illustrates temperature-time history as fire spread horizontally towards the east and west wall, whereas Figure 3b shown temperatures in Segments 2, 7 and 12 as fire spread vertically towards the north wall. Parametric fire based on the fire compartment condition as described above is also shown alongside the Standard fire curve. It has been observed that higher temperatures occur at Segment 11 adjacent to the short wall with highest compartment temperature of 891°C was recorded at time around 59 minutes. These temperatures – time plots were input into ABAQUS to evaluate the heat transfer to structural elements, which steel beam and concrete slab temperatures were used for structural fire analysis.

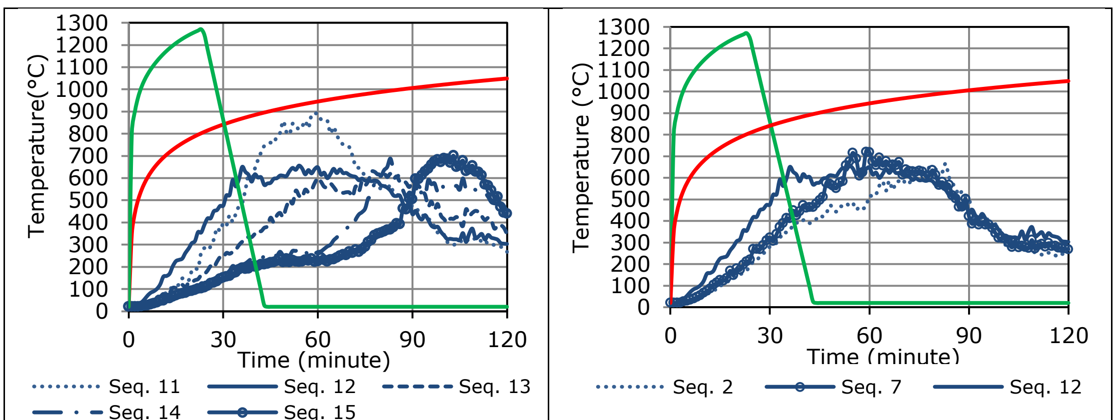

(a) Temperatures for segments 11 to 15

(b) Temperature for segments 2, 7 and 12

Figure 3. Temperature – Time plots.

STRUCTURAL MODELLING

Structural arrangement

The geometry of the structure floor plan was relatively simple, a single storey, composite floor construction formed by concrete floor slab supporting by down-stand steel beams, designed in accordance with the Eurocodes [6]. A plan of the structure is shown in Figure 4. The composite floor slabs are made of a 140mm thick Grade 35 normal weight concrete on trapezoidal profiled deck spanning on steel beams. Using Eurocodes, the beams were designed for full composite action, with 0.7 degree of utilization factor. Considered the loading condition as listed in Table I, the dimensions of the steel beams have been selected and slab panel design requirements for 120 minute fire resistance is given in Table II.

Finite Element Model

Both the thermal and structural respond of the composite slab in the fire scenario is simulated using the commercial finite element software package ABAQUS. The composite slabs are modelled by shell elements and the primary frame is modelled by beam-column elements. Fully interaction between steel supporting beams and composite slab is assumed. Typical fire protection scheme is applied to the slab systems, where the primary supporting beams are protected and the secondary beams are exposed to fire directly. This scheme allows large deflections developing in the slab and thus utilizes the tensile membrane action of the slab to enhance the ultimate capacity of slab in fire. Figure 5 shows the ABAQUS finite element model.

The ASTs derived from FDS are applied as flame temperatures impinging on the underside of the slab and the top surface of the slab is assumed to be exposed to ambient temperature. The thermal properties of the concrete and rebar steel follow these defined in Eurocodes 4. The transient temperature profiles of the slab, beam and columns are mapped into the structural model as temperature loads to capture the structural responds under the temporary and spatial varying temperatures.

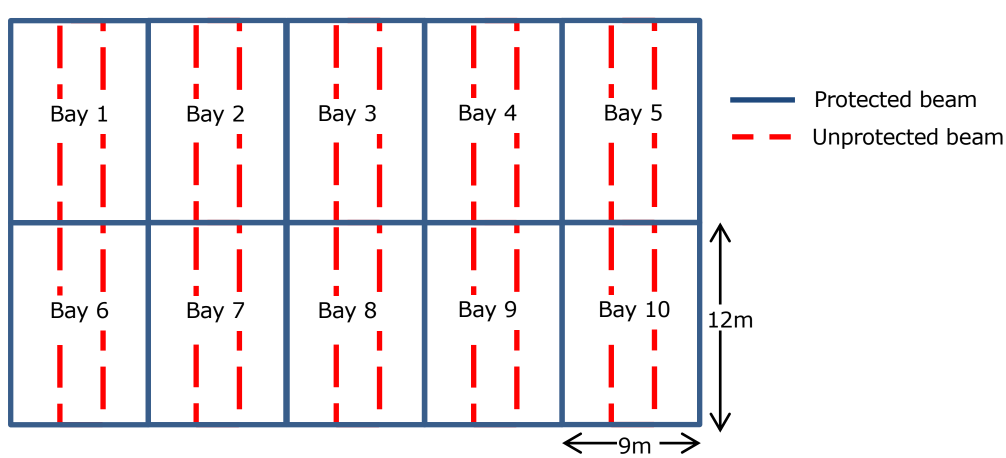

Figure 4. Structure plan – divided into 10 bays for structural fire analysis

TABLE I. STRUCTURE DESIGN – APPLIED LOADINGS.

Description	Loading	Safety factor At ULT	Safety factor At FLT
Live loads comprise:			
Office floor	2.50 kN/m^2	1.5	0.5
Partition (Permanent)	1.00 kN/m^2	1.5	1.0
Dead loads comprise:			
Slab self weight inc. finishes & ponding (140mm thick)	3.48 kN/m^2	1.35	1.0
Steelwork self-weight	1.00 kN/m^2	1.35	1.0
Superimposed dead loads	0.90 kN/m^2	1.35	1.0
Hence, the factored applied area load to the office floor:			
At ULT = 12.513kN/m^2			
At FLT = 7.63kN/m^2			

TABLE II. STEEL BEAMS DESIGN DATA.

Beam Type	Beam section	Load Ratio	Critical Temperature	Temperature at 120 minutes
Secondary beam	UB457 X 152X60	0.416	622.5	550
Primary beam	UB610 X 229X113	0.46	604.4	550

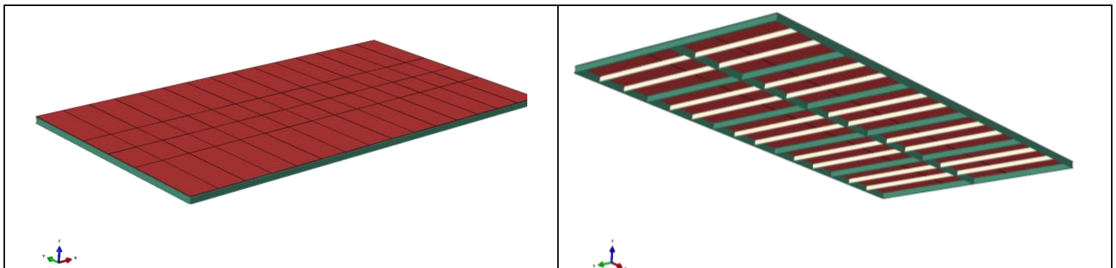

Figure 5. Finite element model for thermal-stress analysis.

Thermal and Structural Analysis Results

As mentioned previously, the compartment was divided into 15 segments to capture the temperature development in different part of the compartment. It should be noted that a finer division or a fully coupled CFD-FEA analysis would allow the temperature mapping in a more accurate way. However, they are considerably more computationally expensive. In each structural bay, gas temperatures obtained from the FDS analysis have been fed into the numerical model for thermal analysis. The slab sections in each segment are subjected to the same fire temperature. Heat transfer analysis is performed to capture the temperature gradient across the thickness of the slab. The temperature development in the structural model is captured as shown in Figure 6. It can be seen that travelling fire within the fire compartmentation has caused temporal and spatial varying temperature in the slab as the fire spreads. The thermal analysis also captured the thermal gradient across the slab thickness. Figure 7 shows the temperatures at top and bottom layers of the slab in different bays. The largest temperature gradient and highest temperature are observed in bay 6, adjacent to the west wall that without opening on it. The temperature increases is due to less heat from the plume can be absorbed by the wall as the compartment temperature rises, and hot air is being contained as no ventilation to outside through the west wall.

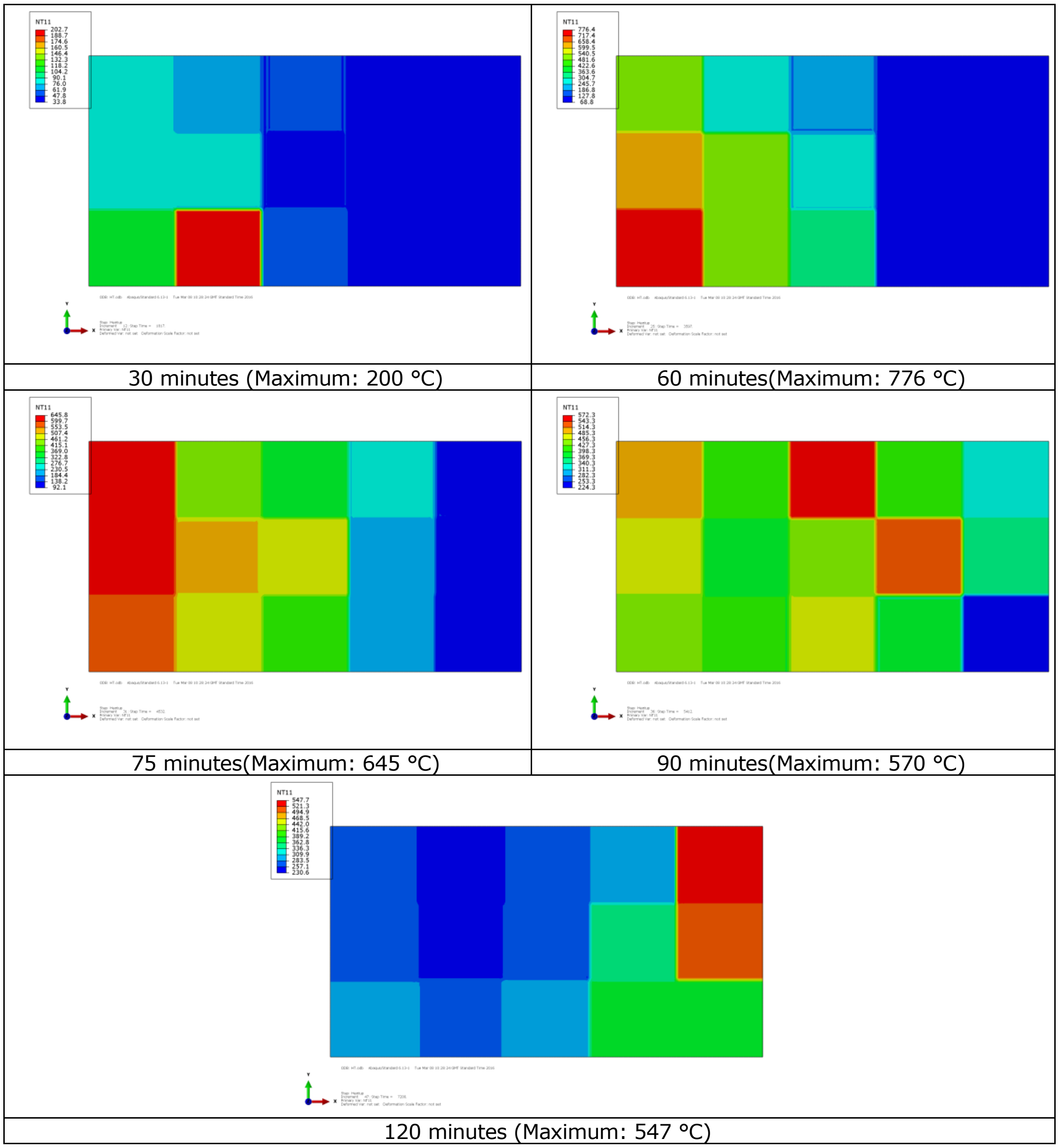

Figure 6. Temperature developments in the structural model.

Figure 8 shows the deflections of the slab in different bays. It can be seen that the largest deflection occurred in Bay 6 due to the high temperature induced significant thermal gradient within the slab. The deflection contours in Figure 8 at different time point demonstrated that as fire travels horizontally within the compartment, large sagging deflections appear in different area of the slab system. As fire travels towards east to the far end along the long wall, the deflection in the slab decreases as fire gradually spreads out and impinges smaller area.

The oscillations in the deflection curves of the slabs are observed in deflections-time curves as presented in Figure 8. The chaotic behaviour of the unprotected slab is due to the non-uniform temperature distribution in the compartment and different transient fire developments in different areas.

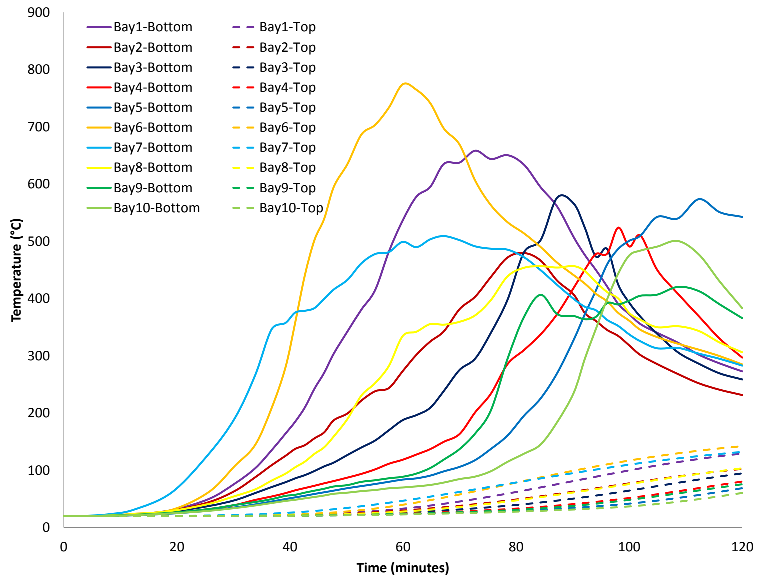

Figure 7. Temperature difference between the top and bottom layer of the slab in different bays.

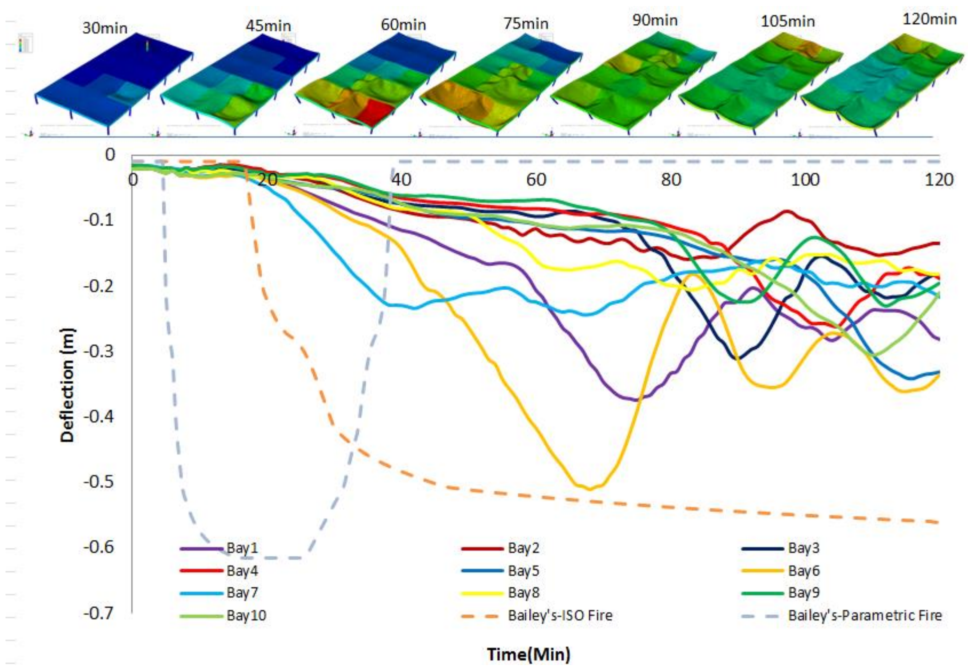

Figure 8. Deflection developments within the compartment.

COMPARISON WITH STANDARD FIRE DESIGN

The traditional structural fire engineering design of composite slab system follows Bailey's method [7] to predict the maximum deflection in the slab under either standard or natural fire. They are lack of research and design guidance has been proposed to predict the structural behavior of composite slab under travelling fire, considering the non-uniform temperature distribution and cooling effects. Comparison has been made between the traditional structural fire engineering design and numerical prediction of the slab behavior is presented in Figure 8. It can be seen that when subjected to travelling fire, Bailey's method gives over-conservative prediction of the unprotected composite slab fire behavior. The non-uniform temperature of the compartment fire has induced different slab deflections pattern in each bays and more importantly, the oscillative deflection caused by the travelling flames may imply recurrently changing in the direction of forces to the connections, which may vulnerable to failure under fire exposure.

CONCLUSION

A case study on the behavior of composite slab in large compartment under travelling fire is performed with the aim to reveal the key response of the composite slab. It has been observed that:

1. Advanced computational analysis is essential for the structural fire engineering design of composite slab when considering travelling fire in a large compartment;
2. Spatial and temporary varying in temperature caused by the travelling flame has induced different slab deflections pattern in each bays within the compartment;
3. Traditional structural fire engineering design method may lead to over-conservative estimation of composite slab fire response under travelling fire. Employing advanced computational analysis may produce more cost-effective structural fire engineering design for such scenario;
4. Oscillative deflection in the composite slab may induce unexpected changes of the forces in the connections. This area requires further research.

REFERENCES

1. Stern-Gottfried, J, Rein, G. 2012b. "Travelling fires for structural design–Part I: Literature review". *Fire Safety Journal* 54(0):74-85.
2. Gottfried, S. J., A. Law, G. Rein, M. Gillie & J. L. Torero 2010 "A Performance Based Methodology Using Travelling Fires for Structural Analysis" *In Proceedings of Fire Protection Engineering*.
3. McGrattan, K., Klein, B., Hostikka, S., Floyd, J., "Fire Dynamics Simulator (Version 5) User's Guide," National Institute of Standards and Technology Special Publication 1019-5, U.S. Printing Office Washington, 2007, 200 p.
4. BS EN 12524:2000, Building materials and products. Hygrothermal properties. Tabulated design values. *British Standard, 2000.*
5. Wickström U, Duthinh D, McGrattan K. Adiabatic surface temperature for calculating heat transfer to fire exposed structures. *In: The 11th international conference on fire science and engineering, Interflam 2007*, London, UK, 3–5 September 2007.
6. Eurocode 4: Design of composite steel and concrete structures – Part 1-2: General rules - Structural fire design, *European Committee for Standardisation, 2005.*
7. Bailey, C. G., 2000. "Design of Steel Structures with Composite Slabs at the Fire Limit State", Final Report No. 81415, prepared for DETR and SCI, The Building Research Establishment, Garston, UK.

Development and Modification of Yield Line Patterns in Thin Slabs Subjected to Tensile Membrane Action

FABIEN QUICHAUD, IAN BURGESS and SHAN-SHAN HUANG

ABSTRACT

It is widely recognized that composite floor slabs experiencing large displacement develop a central zone of hydrostatic membrane tension, surrounded and equilibrated by a ring of membrane compression around the periphery. This mechanism, known as tensile membrane action, can greatly enhance the load-bearing capacity of a slab compared with that defined by yield line analysis. This is a very useful effect in cases where large deflections can be accepted, particularly in fire-resistance design of composite slabs, since the strength enhancement permits some beams to be left unprotected. Studies of tensile membrane action in the 1960s led to the development of several methods to define slab load capacity under large displacement. The method due to Hayes [5] has become the most widely accepted, and was adopted by Bailey [1, 2] in developing the BRE method for fire-safe design of composite floors. Based on observations from the Cardington fire tests and on assumptions concerning yield line patterns and membrane stresses, it calculates the load-carrying enhancement of a slab as a function of its deflection [2]. It also postulates a deflection limit at which the maximum acceptable strain in the rebar is reached. On close examination, however, several hypotheses, such as the assumed failure mechanisms, seem illogical.

The BRE method assumes that a common observation, of a through-depth crack forming across the central short-span of the slab, represents the limit state for such slabs. However, it has been observed that similar cracks can also appear at the intersections of the yield lines, or even not appear at all [3]. This paper proposes a simple way to define the deflection at which the through-depth crack forms, and where on the slab it appears. Based on consistent kinematic assumptions, it calculates the tensile stresses at key points of the slab [4], and predicts the position and displacement at which through-depth cracking occurs.

INTRODUCTION

The Cardington Fire tests on a full-scale composite building in 1995-96 clearly showed composite floor slabs resisting much higher temperatures than those for which they had been designed [1]. This enhancement was recognized as being due to tensile membrane action (TMA); at large displacement, the slabs experienced high double

University of Sheffield, Department of Civil & Structural Engineering, Sir Frederick Mappin Building, Mappin Street, Sheffield, S1 3JD, United Kingdom.

curvatures which led to the development of internal membrane stress fields. In TMA a zone of hydrostatic tension is created in the central region of the slab, equilibrated by a ring of compression around its periphery. For normal service conditions this phenomenon cannot be used in design since it requires unacceptably large deflections. However, it becomes a useful tool in fire engineering, since no limitation of displacement is imposed. Therefore, in building design, some beams can be left unprotected due to the beneficial effect of TMA, and this has considerable economic advantages.

Since these tests, several methods have been developed to try to predict a slab's behavior in fire scenarios. The BRE method [1, 2] has been used widely, and is likely to be introduced into Eurocodes, despite its reliance on some illogical assumptions. This simple design method is largely based on Hayes's work [5] in the 1960s. It assumes the shape of the membrane stress distributions along yield lines for the plastic action of the slab. It also assumes that rebars act at 110% of their yield stress across a through-depth crack located centrally across the short span. It then calculates two 'enhancements' of yield-line capacity; the first for moment capacity across yield lines (which may be less than 1) and the second for enhancement by membrane action. Both of these enhancement factors are found for each slab facet. These are then compounded in an unexplained way to give an overall enhancement of the load capacity of the slab. This enhancement evolves linearly with deflection, up to a maximum deflection at which rebars across the short span crack fracture. This limiting deflection is found by superposing two displacements; firstly a 'thermal' deflection, calculated using a simple beam model which allows horizontal movement of one support, and secondly a 'mechanical' deflection at which rebars reach half of their maximum elastic strain at ambient temperature, based on a beam which has both ends fixed. These cases, based on different boundary conditions, should clearly not be superposed. The method allows failure to occur either by fracture of rebars across the short-span crack or by crushing of concrete at the slab's corners. Some small-scale tests by Foster *et al* [3] showed that failure mechanism can differ. In this paper a new method is proposed to address TMA in lightly-reinforced composite slabs.

KINEMATIC PATHS

As loading increases, a slab starts by developing a yield line mechanism in the sequence shown in Figure 1(a, b). As the deflection of the mechanism increases, it increasingly activates TMA. At this stage the slab is then acting in "Mechanism B" (Figure 1 (c)), dissipating energy along its yield lines as deflections increase. On further increase of the deflection, a through-depth crack usually appears across the centre of the slab, giving rise to "Mechanism A" (Figure 1(d)). In some cases the failure mechanism can differ; the through-depth crack may appear at the intersections of the yield lines or, rarely, not appear at all (Figure 1(e, f)).

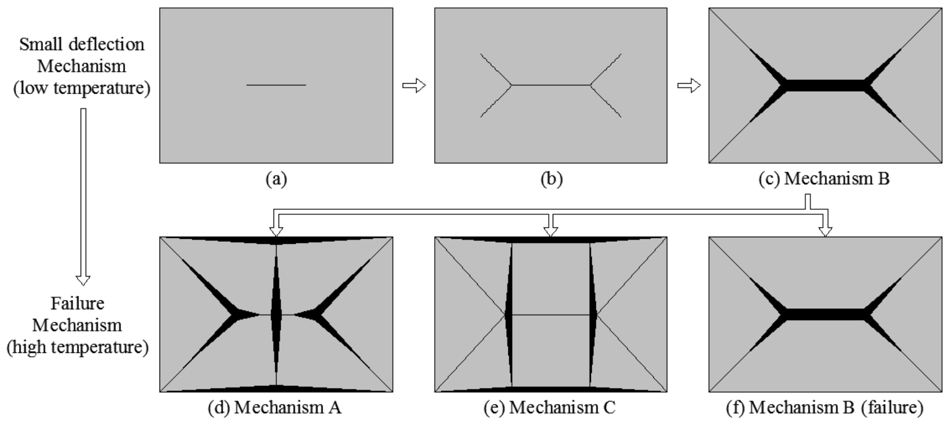

Figure 1. Yield line pattern development (a & b) and possible failure mechanisms (d, e & f).

It is obviously essential to be able to identify the correct failure mechanism, and to apply a consistent and accurate method to define membrane forces and the load-capacity of the slab.

NEW KINEMATICALLY CONSISTENT METHOD

A new kinematically consistent treatment of TMA has been developed to attempt to clarify the issues of the existing methods. Based on a plastic analysis and on an optimized small-deflection yield line mechanism, it relates the displacements and rotations of the slab facets on the basis of the in-plane equilibrium conditions. Once the yield line pattern has formed, facets rotate freely about their respective supported edges and also experience in-plane movements, with concrete acting at its compressive strength where facets overlap. Rebars are assumed to act at their tensile yield strength where they are subject to tension across yield lines [4]. At any deflection the displacements along yield lines, and hence the neutral axis alignments, are determined from horizontal equilibrium of the facets. Two different mechanisms (B and A from Figure 1) are investigated in this paper. The former has already been the source of several publications and will be quickly summarized. Mechanism A will be explained in greater depth, since its development is new.

Mechanism B

In this mechanism the triangular and trapezoidal facets remain parallel to their respective edges. Compatible rotations of the two facets about their respective edges, together with the movements derived from horizontal equilibrium, creates regions where crack-faces remain in contact and concrete is then being compressed at its yield stress, and regions where rebars are being stretched since the crack-faces have separated [4]. At any given deflection, all the in-plane force resultants along the yield lines are found, together with their corresponding displacements. The work done through rebar extension and concrete compression is equated to the loss of potential energy of the external load to find the enhancement factor of the slab's capacity.

As deflection increases, crack widths increase and the shapes of the compression stress blocks along yield lines change as the neutral axis alignments change. At a critical maximum crack-width at the level of the rebar, the steel reaches its maximum extension and fractures. Since no reliable principles exist to calculate the free length of a rebar across a discrete crack, it is assumed that the length of rebar which can extend freely is the distance between its positive anchor points at which transverse (orthogonal) bars are welded to it. All this extension is assumed to be plastic, leading to a limiting crack-width for bar fracture:

$$\Delta lim = \varepsilon_u . d \tag{1}$$

in which ε_u is the ductility (fracture strain) of the mesh and d the space between bars in the orthogonal direction.

Mechanism A

As has previously been mentioned, Mechanism A is the failure mechanism in which a through-depth crack is assumed to have formed across the centre of the slab. Similarly to mechanism B [4], it defines the shape of the compression stress blocks along the yield lines as shown in Figure 2 (c). Mechanism A introduces an in-plane rotation β and an inward movement Δ_{xy} of the trapezoidal facet (Figure 2 (b)), which create a compression stress block and a through-depth crack across the central short span (Figure 2 (a)). Since the edges of the slab do not experience any deflection the two trapezoidal facets stay in the same plane, which creates a rectangular compression stress block with a vertical neutral axis (Figure 2 (a-i)). Inward movements Δ_x and Δ_y still exist as in mechanism B. Displacement of any point of yield lines can be expressed as a function of Δ_x, Δ_y and Δ_{xy}, the out of plane compatible rotations (θ and ϕ) and the in-plane rotation (β). Examples of the x & y-movements along the diagonal yield line of the trapezoidal Facet 2 are given, respectively in Equations (1) and (2).

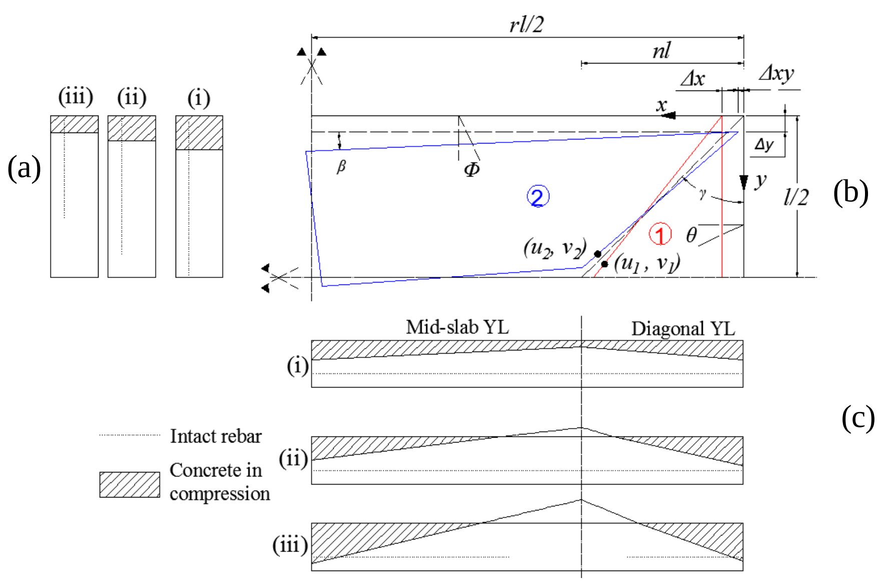

Figure 2. Views of (a) through-depth crack evolution. (b) facet in-plane movements. (c) central and diagonal yield line compression stress blocks and rebar state.

$$u_2 = \Delta_{xy} - \beta . y \tag{2}$$

$$v_2 = \Delta_y + \beta.x - \emptyset.z - \frac{\emptyset^2.y}{2} \quad (3)$$

As for Mechanism B, several cases need to be investigated for different compression stress block types and rebar states along the yield lines. For infinitesimal deflection, an isotropic slab has a uniform-depth layer of compressed concrete, along all its yield lines. On increasing the central displacement, the neutral axis tilts so that the compression block thickness reduces at the intersection of the yield lines and increases at both the centre and the corners of the slab (Figure 2(c-i)). On further deflection, the neutral axis may rise out of the slab at the yield line intersection, which creates a partial through-depth crack along both yield lines (Figure 2(c-ii)), whilst the through-depth crack across the short span widens.

At some point the through-depth crack width reaches a value at which x-direction bars crossing it start to fracture (Figure 2(a-ii)). Beyond this point, the crack width at mesh level may also reach the bar fracture value in either the x- or y-direction at the yield-line intersection, causing a progressive "unzipping" of bars along either or both of the diagonal and central yield lines (Figure 2(c-iii)) while the bars crossing the short-span crack continue to "unzip" towards the slab edge (Figure 2(a-iii)). Equating the displacements, such as those in Equations (1) and (2), to zero and extracting z gives the position of the neutral axis at any coordinates (x, y) considered, depending on the displacement Δ_x, the in-plane rotation β and the rotation θ. It is then possible to express the geometry of the compression stress blocks and the length of intact rebar. This can be done for every combination of rebar position relative to the neutral axis, the positions of the neutral axes at yield line extremities and the state of the rebar (intact or broken). In-plane force equilibrium (eliminating the shear force S) and moment equilibrium about point O (Figure 3) are respectively given by:

$$T_{x1}.\cos(\gamma) + (T_{y1} + T_{y4}).\sin(\gamma) = C_1 + C_4.\sin(\gamma) \quad (4)$$

$$X_{c4}.C_4 + X_{ca1}.C_1.\sin(\gamma) + Y_{ca1}.C_1.\cos(\gamma) + Y_{tx3}.T_{x3} - X_{Ty4}.T_{y4} - X_{Ty1}.T_y - Y_{ca3}.C_3 - Y_{tx1}.T_{x1} = 0 \quad (5)$$

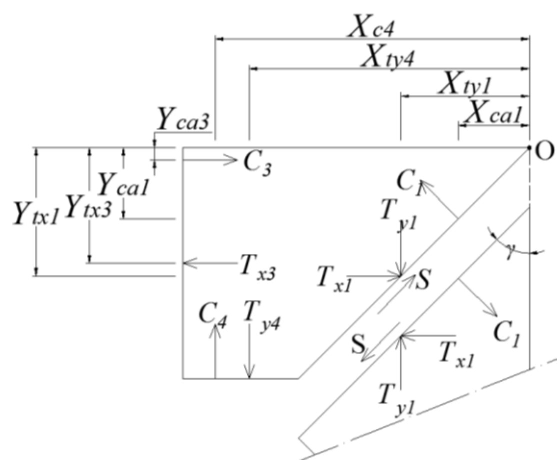

Figure 3. Internal forces and lever arms of Mechanism A.

Solving these equations gives the lateral displacement Δ_x and the in-plane rotation β at any deflection. Then, every force and movement is known, which allows the enhancement of the slab capacity to be calculated as for Mechanism B. Similarly to Mechanism B, only one case of geometric conditions gives an exact solution. Comparing results and geometric assumptions, this case can be identified.

Through-depth crack opening criterion

The next step of this approach is to identify in which mechanism the slab is behaving at any deflection, and hence when and where a through-depth crack appears. A simple way to achieve this objective is to monitor concrete tension stresses at key slab cross-sections. A calculation of tensile stresses across the facets is done for Mechanism B, for which no through-depth crack is present. Moments are calculated at points N and Q (Figure **4**), according to the following equations:

$$M_Q = [C_1 \sin(\gamma) - S\cos(\gamma)].(n.l - x_{ca1}) - [C_1\cos(\gamma) + S\sin(\gamma)].y_{ca1} + T_{x1}.y_{tx1} - T_{y1}.\left(n.l - x_{ty1}\right) \tag{6}$$

$$M_N = [C_1 \sin(\gamma) - S\cos(\gamma)].\left(\frac{r.l}{2} - x_{ca1}\right) - [C_1\cos(\gamma) + S\sin(\gamma)].y_{ca1} + T_{x1}.y_{tx1} - T_{y1}.\left(\frac{r.l}{2} - x_{ty1}\right) \tag{7}$$

The maximum tensile stresses are then found at points N' and Q':

$$\sigma_{Q'} = \frac{M_{Q'}}{I_{eq}} \text{ and } \sigma_{N'} = \frac{M_{N'}}{I_{eq}} \tag{8}$$

Where I_{eq} is the inertia of cross sections NN' and QQ' assuming equivalent concrete sections only.

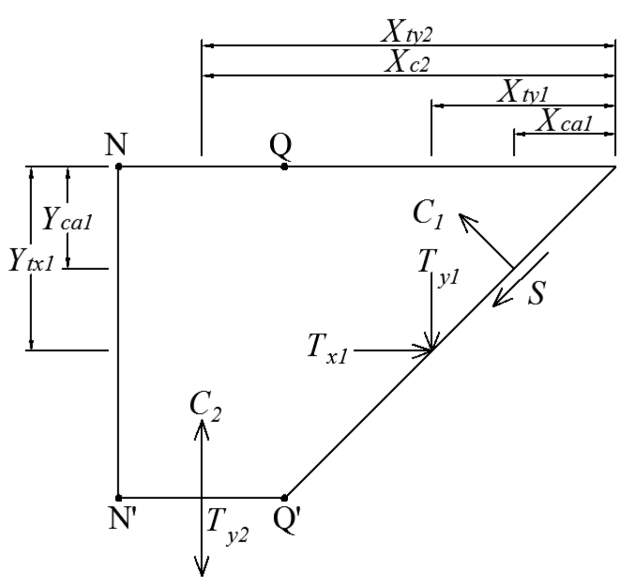

Figure 4. Internal forces and lever arms of Mechanism B.

At very small displacement, both moments are very small and the concrete tensile strength is high enough not to experience any cracking. On increasing the deflection, resultant compression forces and lever arms change, as do moments M_Q and M_N. At a certain deflection, one of these moments may engender stresses higher than the concrete tensile strength (f_{ct} in the Eurocode). At this point a through-depth crack starts to form across the short span, at the intersection of yield lines if $\sigma_{Q'} > f_{ct}$ or at the centre of the slab if $\sigma_{N'} > f_{ct}$. From that point forward, the appropriate mechanism should be used to define the enhancement.

RESULTS

Examples of the new method's results will be shown in this section. The slab, with an aspect ratio r=1.5 (9m x 6m), is 130mm deep, fitted with an isotropic A142 mesh of 5% ductility, positioned 50mm below the top surface. Tensile yield strengths of the rebar and concrete are 500MPa and 3MPa respectively, for rebars and concrete; the concrete compression yield strength is 30MPa.

Figure **5**(a) shows the evolution of load capacity enhancement of 4 slabs of aspect ratios from 1 to 1.5, while Figure **5**(b) plots the evolution of maximum tensile stress for the same 4 slabs. For aspect ratios 1.25 and 1.50, the slab starts to deflect in Mechanism B, but the tensile stress in the concrete at the middle of the slab rapidly increases until it reaches its tensile strength. From this point, a through-depth crack exists across the short span and Mechanism A applies. For aspect ratio 1.1, tensile stresses increase more slowly, implying that the through-depth crack appears later. In this case the peak in the enhanced load capacity is actually reached in Mechanism B. Finally, for a square slab, the maximum tensile stress never reaches concrete strength, therefore, the failure mechanism is B without a mid-span through-depth crack appearing.

In Figure **6**(a), the rebar temperature leading to slab failure has been plotted for 6 loadings on the slab of aspect ratio r=1.5 and yield line failure load of 1.63kN/m^2. Maximum tensile stresses are also plotted in Figure **6**(b). For applied loadings of 1.40 and 1.63kN/m^2, the peak in the temperature enhancement is reached within Mechanism A, when rebars start to break across the through-depth crack. Indeed, in-plane forces engender high enough tension stress at the middle of the slab to open the through-depth crack at fairly small deflection.

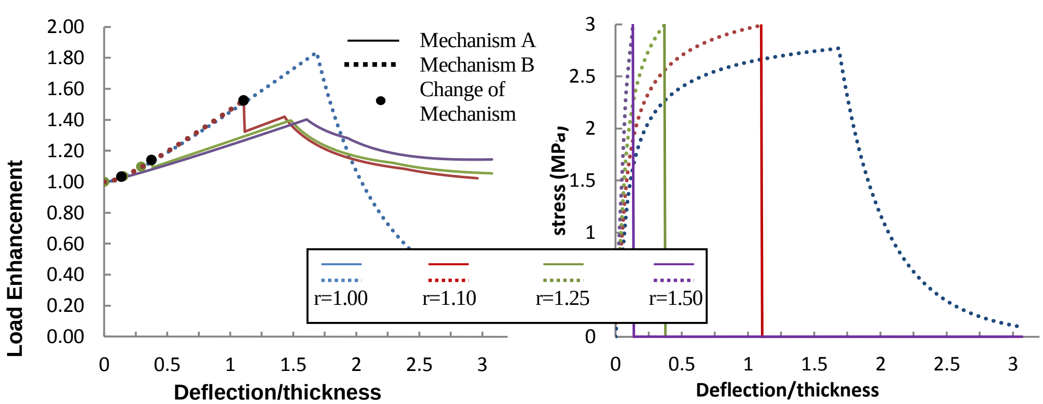

Figure 5. (a) Load enhancement for different aspect ratios (ambient temperature).
(b) Tensile stress at point N' for different aspect ratios (ambient temperature).

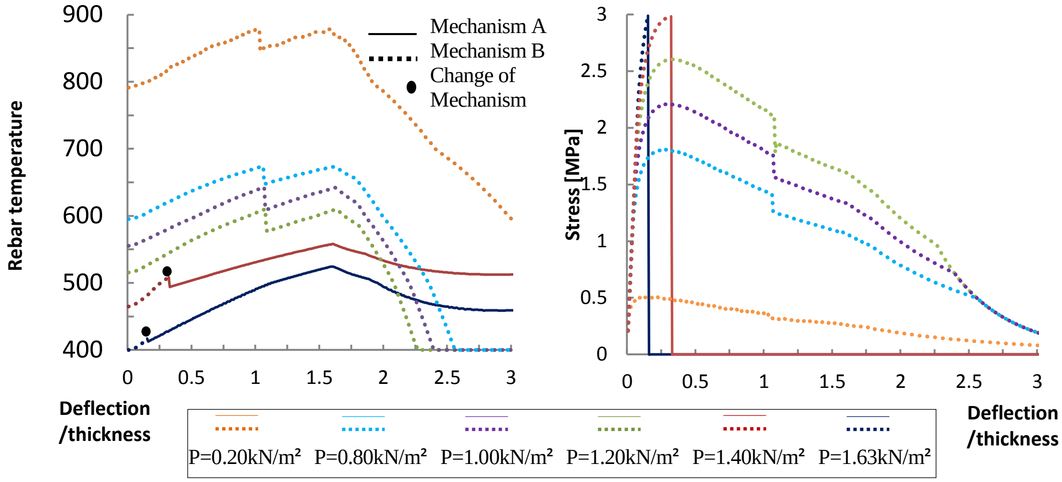

Figure 6. (a) Rebar yield temperature for different transverse loadings. (b) Tensile stress at point N' for different loadings at yield temperature.

In contrast, for lower loading intensities, at any deflection the yield temperature leads to a failure of the slab in Mechanism B, since the concrete tensile strength is never reached at the centre of the slab.

CONCLUSION

This paper has presented a method which permits the prediction of when a thin slab changes its tensile membrane action mechanism from one with no through-depth crack to one in which a pure tension crack appears either at the middle of the slab or at the intersection of its yield lines. The method is founded on consistent kinematics and assumes only that plastic behaviour follows from the optimum small-deflection yield-line mechanism, denoted here as Mechanism B. Although Mechanism A seems the more conservative of the two, the sequence of events always begins with Mechanism B, and Mechanism A may not necessarily be generated. In high-temperature cases the results from examples also tend to show that, if rebars are heated beyond 500°C under low loadings, or if the slab is square, the through-depth tensile crack is less likely to occur. Some aspects which are necessary for practical use of the method need further study; in particular the crack-opening at which rebar crossing it fractures, and the maximum concrete tensile stress at which the through-depth crack is initiated.

REFERENCES

[1]. Newman G. M., Robinson J. T., Bailey C. G. “Fire Safe Design: A New Approach to Multi-Storey Steel-Framed Buildings.” Second Edition, SCI Publication P288.

[2]. Bailey C. G. “Membrane action of unrestrained lightly reinforced concrete slabs at large displacements.” Engineering Structures 23 (2001), pp470-483.

[3]. Foster S. J., Bailey, C. G., Burgess, I. W. and Plank, R. J. “Experimental Behaviour of Concrete Floor Slabs at Large Displacements.” Engineering Structures 26 (2004), pp1231-1247.

[4]. Burgess I. W., Huang S-S., Staikova S. “A Re-Examination of the Mechanics of Tensile Membrane Action in Composite Floor Slabs in Fire.” Proc. Structures in Fire, Shanghai, (2014) pp209-218.

[5]. Hayes B., “Allowing for membrane action in the plastic analysis of rectangular reinforced concrete slabs”, Magazine of Concrete Research, 20 (65), (1968) pp205-212.

Advanced Analysis of the Membrane Action of Composite Slabs under Natural Fire Scenarios: a Case Study of the New JTI Headquarters

LORENZO LELLI and JONAS LOUTAN

ABSTRACT

The paper details the advanced natural fire simulations that were carried out for the composite steel-reinforced concrete structure of the JTI Building in Geneva. Such analyses led to a significant reduction of the fireproofing of the steel floor framing. Several scenarios were studied considering different thermal behaviours of the peripheral cladding. Despite the small thickness of the resisting slabs, the analyses carried out with SAFIR showed that the typical storey bay (12 m x 15.86 m) could resist to the design fire temperatures without the protection of the main and secondary beams while the spandrels remain protected. For study completeness, the composite frame-membrane model was also simulated with Hasemi localized fire routines on SAFIR. The results are here exposed and commented.

INTRODUCTION

The new JTI Headquarters in Geneva is a model of modern engineering in Switzerland. Shaped as a triangular spiral, the building is a composition of three-dimensional steel-framed tubes that outstands for its fully clad façades. The building consists of two levels of concrete frame below ground and a steel structure of nine levels above ground. The headquarters will provide open space offices and other amenities. The underground construction is dedicated to the car park and technical rooms. The building is lifted off the ground on two of the three corners, creating a public pedestrian passage at ground floor and an impressive 60 metres span cantilever on the northeast corner.

The main frame is composed of six sloped façade trusses, braced at the upper and lower chords forming three rigid structural tubes (see Figure 1). The superstructure rests only on 11 supports. The control of the deformations, in particular those at the cantilever tip, was the main feature of the design of the structure. Specific procedures, namely, controlled unpropping, jacking and temporary tie-down of the structure,

INGENI SA, Rue du Pont-Neuf 12, 1227 Carouge, Switzerland

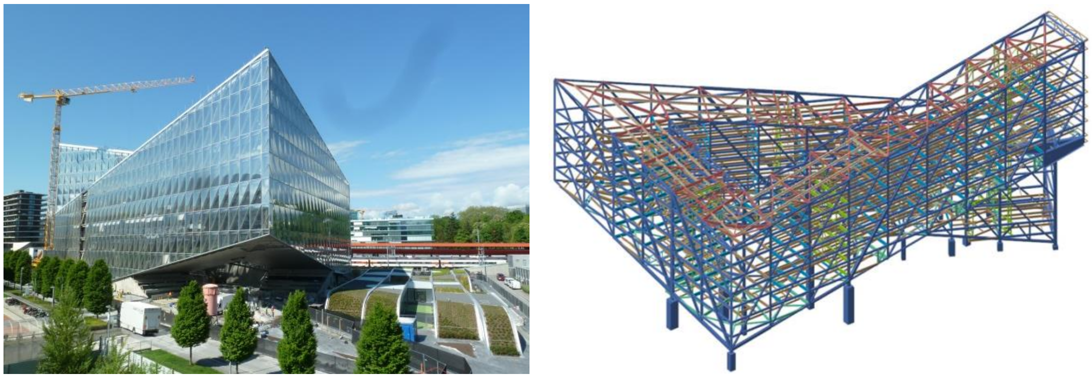

Figure 1. View of the building (left) and 3D structural model rendering (right).

allowed for safe cladding installation and control of the building deformations.

According to the Swiss regulations at the time of the construction, the building is classified, for fire safety purposes, as a “high building” since the highest point of the building is located at more than 30 metres from ground. This limit is related to the maximum height that can be reached from the road with the telescopic stair of a fire truck. According to this category, the structure must be R90 (i.e. it should resist up to 90 minutes under ISO834 fire conditions) and the sprinkler installation cannot be taken into account to reduce the fire resistance scale.

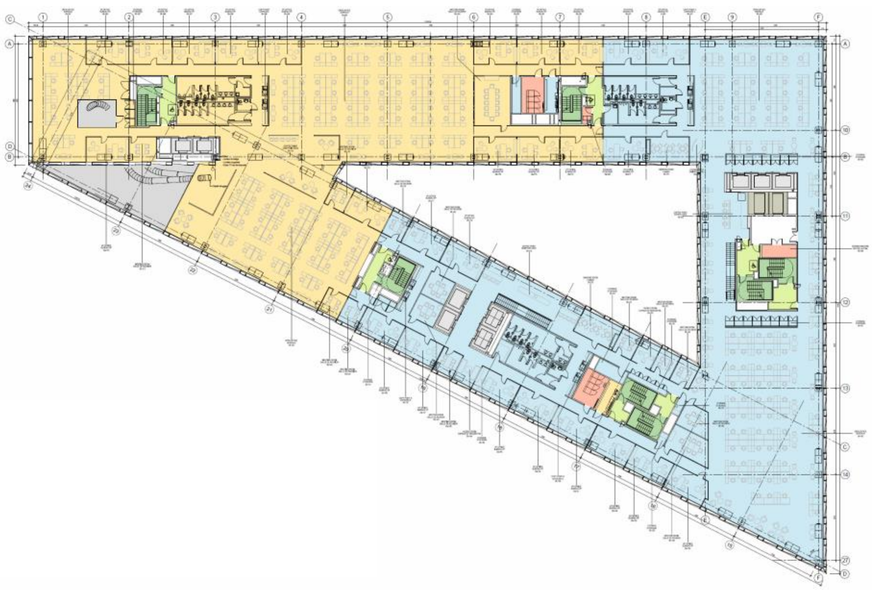

Figure 2. Fire compartmentalization of a typical floor of the superstructure.

STRUCTURE DESCRIPTION

The superstructure can be thought of as three interconnecting tubular steel frames or bars, where each bar has two full depth trusses with fully cross-braced top and bottom chords. The façade structures support the floors and constitute the main structural frame. Each façade is made of a double Pratt truss with top and bottom chords defining the sloped profile of the building; a virtual middle chord is formed of spandrel beams that are rigidly connected to the main columns and diagonals at different levels (see Figure 1, right).

The composite steel-concrete structure of the floors rests on the lateral trusses without any intermediate support. In order to limit the dead load, a V60 metal deck with an 80mm-thick lightweight concrete topping composes the slab. The primary storey beams are built-up I-section 900mm-deep and rest over the 12m-spacing vertical bars of the façade trusses. IPE600 beams with 3.94 m spacing compose the secondary beams gridline. The typical bay results in 12x15.76 m.

FIRE SAFETY CONCEPT

The architecture of the building is based on a continuous landscape concept, creating a "promenade" with non-compartmentalized staircases and eliminating the partitions between the floors. In case of fire, the separation between the levels is ensured by automated fire protection closures falling from the false ceiling and closing the stair shafts. With these devices, under fire conditions, each compartment corresponds to an entire floor or half of it depending on the regulation surface limits (see Figure 2). This applies to the major office compartments, while plant room and security staircase shafts are separated by fixed R90 partitions.

The fire compartments in the basement levels are defined by fixed partitions and do not follow the continuous landscape concept. The sprinkler installation covers the entire surface of the basement and over ground levels. The office compartments are mainly set up in open space.

In Switzerland the Fire Insurance Institutions Association issued the guideline 155-03 that contains several ranges of values for thermal loads depending on the occupancy [1]. In case of office occupancy, the range varies from 300 MJ/m² to 900 MJ/m². The higher values are related to partitioned offices with shelves and wooden furniture. The value of 600 MJ/m² was chosen as more suitable for open office spaces. It should be noted that Eurocode 1991-1-2 gives the close value of 511 MJ/m² for the 80% fractile of the same occupancy [2].

PERFORMANCE-BASED APPROACH

The ISO fire approach remains quite conservative and overestimates the effects of a fire. A natural fire study was conducted in order to reduce the amount of the necessary fire coating of the steel elements of the superstructure. As a matter of fact, the fire compartments of the superstructure are extremely wide (up to 2'000 m²) and glazed along the perimeter. When the façade collapses, the incoming of cold air drastically reduces the room temperature.

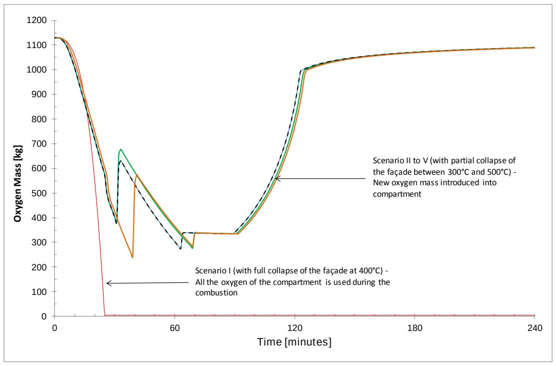

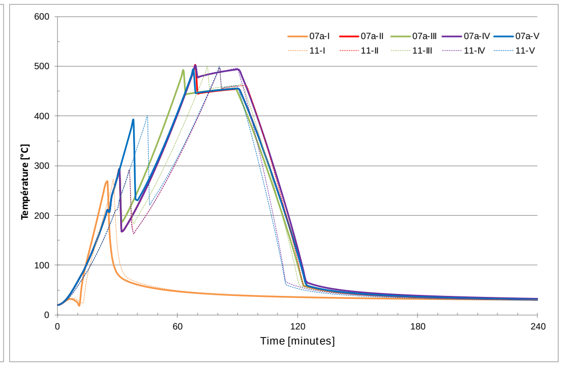

Figure 3. Oxygen mass comparison between the scenarios.
Figure 4. Comparison of the temperature curves between the smallest (11) and the biggest (07) office compartment in the five scenarios

On the contrary, the prescriptive-based approach was maintained for the concrete as well as the composite structure of the underground structure. The absence of openings combined with the high thermal load result in a more critical natural fire scenario compared to the standard curve.

The software OZone was used for the fire simulations, using the following parameters as proposed by [2]:

- RHR_f = 250 kW/m²
- Fire Growth Rate = 300
- $q_{f,k}$ = 600 MJ/m² (80% fractile)

Even if Eurocode considers the combination of several parameters to reduce the thermal load, the local fire authority accepted only one single reducing factor that corresponds to the one related to the sprinkler installation ($\delta_{n,1}$=0.61) [2].

Different scenarios were considered to describe the façade behaviour under fire. The guideline for performance-based analyses issued by the Luxembourg fire authority suggests that a glazed façade cannot resist to more than 500°C [3]. The scenarios consider different percentage of collapsing façade between 400°C and 500°C, but, with the exception of scenario I, 10% of the façade surface is open from the beginning to sustain the fire during the initial phase.

- Scenario I – 100% of the glazed façade collapses at 400°C
- Scenario II – 50% of the glazed façade collapses at 300°C / 90% at 500°C
- Scenario III – 40% of the glazed façade collapses at 300°C / 100% at 500°C
- Scenario IV – 50% of the glazed façade collapses at 300°C / 80% at 500°C
- Scenario V – 50% of the glazed façade collapses at 400°C / 100% at 500°C

A comparison of the fire curves related to each scenario is shown on Figure 4 for the smallest and the biggest compartment. The main difference is represented by the fire duration. In the first scenario the oxygen is consumed before reaching the temperature for the façade collapse and, consequently, the incoming of new air.

For the other scenarios, the chosen percentage of the collapsing façade slightly changes the curves but the temperature peak remains close to 500°C. Due to the large amount of glazed surface for all compartments, when the critical temperature for the façade is reached, a great amount of cold air is introduced in the model. The consequence is on one hand an increase of oxygen mass which sustains the fire, but on the other hand the gas temperatures do not rise beyond 500°C.

STRUCTURAL MODELLING

The typical framing of the floor has been modelled with SAFIR software [4]. The composite slab is modelled by beam and shell finite elements connected together. For each composite section of the framing, a 2D thermal analysis was carried out to determine the temperature distribution over the section at each time step (see Figure 5, left). In this case, the slab is modelled as a thick element since the influence of the real geometry of the slab is negligible for the thermal distribution. On the contrary, for the modelling of the 2D thermal shell elements, the mean thickness (which takes into account the ribbed geometry of the metal deck) defines the depth of the finite element (see Figure 5, right).

Finally, the 3D static model combines the beams and shell elements for the time-dependent analysis. Given that in the static analysis the slab is represented by the shell finite elements, the mechanical properties of the concrete in the composite beam are set to zero. In addition, in order to limit the membrane thickness to the full section of the slab (8 cm in this case), the shell elements depth is also reduced (see Figure 5, right). With this setting, the membrane has the same depth in both orthogonal directions and only the upper layer of bars in the two directions is taken into account for the development of the membrane forces.

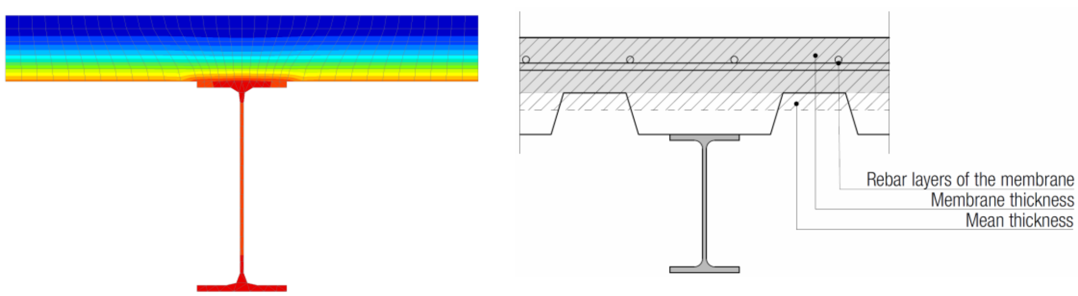

Figure 5. Typical section (left) and thermal 2D analysis (right) of a composite beam.

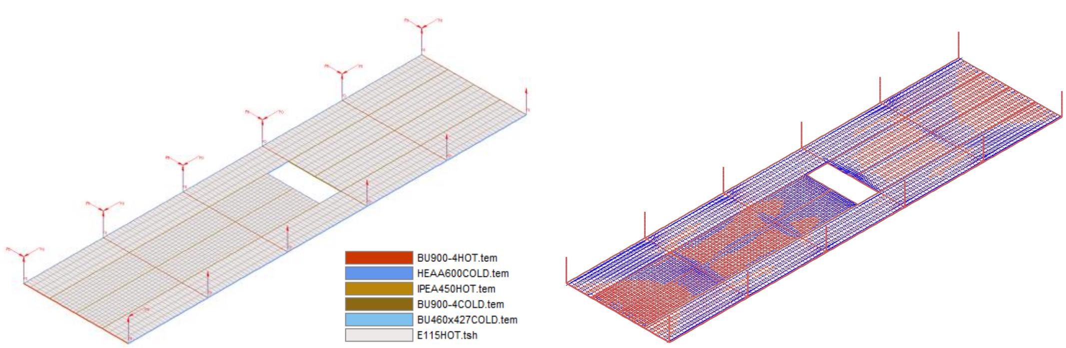

Figure 6. Regular bay model meshing (left) and membrane forces (right) at temperature peak (68m).

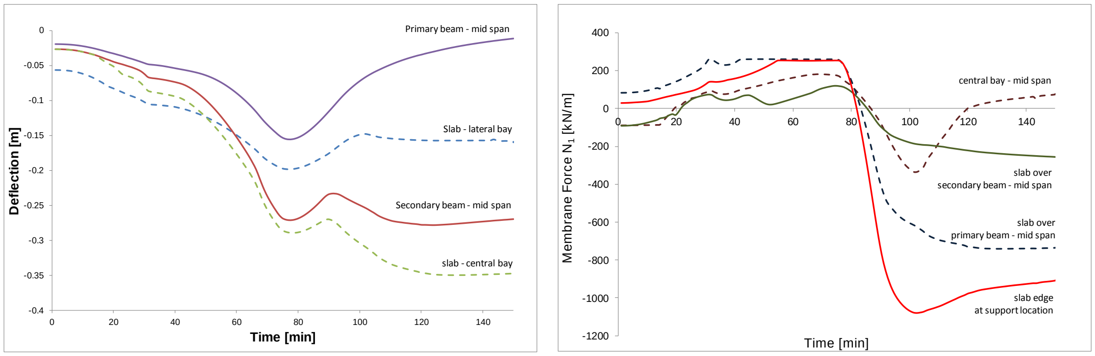

Figure 7. Regular bay– Deflections (left) and membrane forces (right) in the transversal direction.

For most of the truss elements the protection was maintained. This choice was justified by the fact that a local failure of a main diagonal or vertical bar (that could have happened in case of a localized fire close to the element) would have resulted in a non-recoverable deflection at the cantilever. The jacking forces that were developed during the steel frame installation were far lower than those that would have been necessary to uplift the building once the fit-out was completed (the superimposed dead load correspond to 69% of the dead load).

Figure 6 (left) shows the typical model used for regular bays. The spandrels are protected to ensure the membrane edge support. As mentioned before, the columns are protected and the diagonals (that are also fireproofed) are removed from the model. The model is laterally restrained from one side to take into account the rigidity of the protected façade truss.

Generalized fire analysis

In the generalized fire analyses the temperatures curves calculated with Ozone are applied to all elements. Due to the large slenderness of the floors, the contribution of the concrete membrane was significant even if the gas temperatures were not drastically affecting the steel properties (see Figure 4).

The primary built-up beams result in a very low heated perimeter/cross sectional area ratio so the temperatures in the section are lower compared to the other elements. With a peak temperature of 495°C the stiffness is reduced by 40%. With these conditions, the membrane mechanism is developed over a full 15.76 x 12m bay since the deflection at the primary beams support is limited and mostly recoverable (see Figure 7, left). To avoid the collapse of the membrane, the reinforcement ratio has been increased to 10 kg/m² (524 mm²/m in both directions) instead of 8.4 kg/m², which corresponded to the “cold” design ratio.

While the primary beams mostly recover their deflection during the cooling, the residual deformation of the slab reaches 35 cm.

Due to the triangular geometry of the building, a non-orthogonal meshing was carried out for the simulations of the corner area of the floors (see Figure 8, left). The peripheral bars of the model are protected in order to ensure the vertical support of the membrane during fire. Local distortions in the membrane forces path are detected due to the non-orthotropic mesh. In fact, in the SAFIR version used at the time of the study, the reinforcement orientation was directly related to the shell local axes orientation. However, the impact on the overall behaviour of the membrane, in terms of deviating tensions appears to be negligible (see Figure 8, right).

Localized fire analysis

The models implemented for the generalized fire were also used for the localized fire analysis to cover this kind of critical scenarios. The Hasemi fire model was chosen since it considers the case of the flame touching the ceiling. The critical Hasemi fire curve was determined between different suitable scenarios for open office compartments. Table I summarizes the parameters applied to each scenario:

Table I. Scenarios parameters for localized fire.

Scenario	**Mass** kg	**RHR_{fi}** kW/m²	**Flame surface** $A_{fi,0}$ m²	**Fire surface** $A_{fi,dev}$ m²	**Q_{max}** $RHR_f \cdot A_{fi}$ kW	**Flame position** m
Paper Palette	250	500	1.00	5.8	2900	0.6
Paper Shelf	720	250	1.44	15.8	3960	1.0
Isolated fire	500	500	0.79	2.7	1340	0.3

Even if in the shelf scenario the peak temperature is not reached (900°C), the fire duration remains more severe for the steel beams, in particular the primary beam whose lower flange is the closest to the fire. A specific routine on SAFIR evaluates the temperature distribution at each time step for all shell and beam finite elements depending on the position of the fire source in the model.

The result is that each finite element is defined by a specific temperatures distributions set. The fire has been placed at different locations in order to define the critical configuration for the primary and secondary beam or the slab mid-span.

Figure 9 shows the typical two-bay model (left) used for the localized fire analysis of the standard bay compartments in case of a centred fire. The graph (right) shows the temperature of the primary beam and of a close slab element in the centre of the model. Even if the steel temperature is locally higher compared to those reached in the generalized fire (800°C versus 495°C, see Figure 9, right), the local weakness of the system does not cause the collapse of the floors due to the stiffness of the composite system.

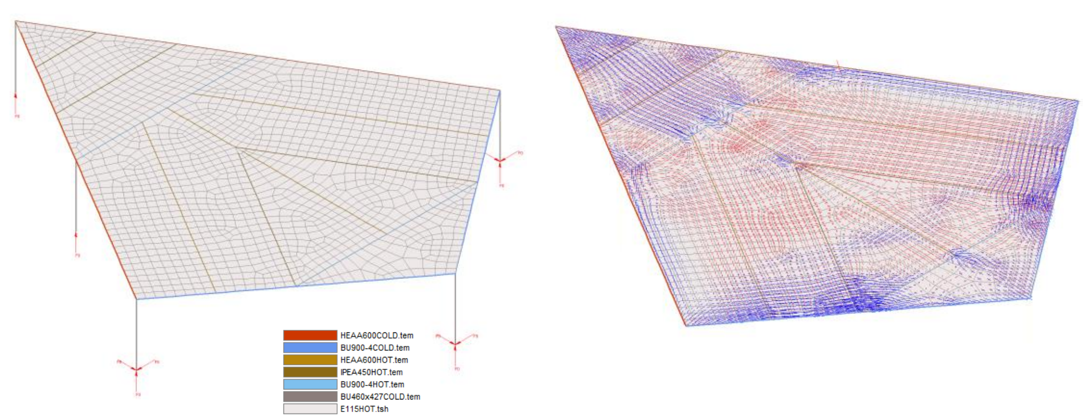

Figure 8. Corner area model meshing (left) and membrane forces (right) at temperature peak (68m).

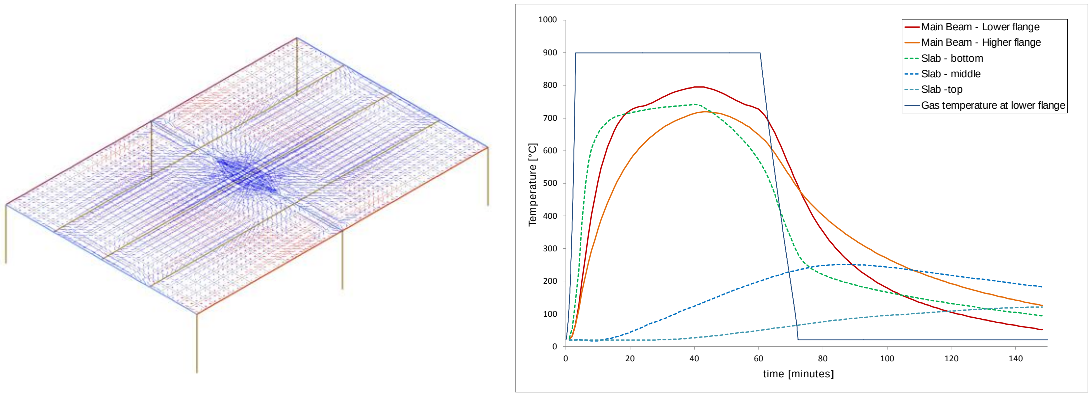

Figure 9. Localized fire – membrane forces for the two-bay model (left) and temperatures plot (right) for central beam and slab (fire placed at centre of model) compared with the gas temperature.

With regards to the generalized fire analyses, the calculated forces and deflections for the localized fire scenarios are more severe close to fire location (beam and shell deflection equals to 23 cm after 40 minutes) but generally lower in the surrounding area.

CONCLUSIONS

The analyses have shown that the membrane behaviour of composite slabs under fire allows a significant reduction of the fire protection even in case of small thickness of the concrete topping. The increase of the reinforcement ratio to sustain the membrane forces is widely compensated by the savings related to the fireproofing of the steel framing.

A natural fire approach is particularly worthwhile in case of fully glazed buildings, since the incoming of a great amount of cold air when the façade collapses limits the increase of the gas temperature inside the compartment.

In addition to the generalized fire analysis, automated routines can also perform localized fire analysis using the Hasemi fire model. The composite floors are sufficiently stiff to resist to these scenarios even if higher gas and steel temperatures are expected locally .

REFERENCES

1. Association des Etablissement cantonaux d'Assurance Incendie (VKF-AEAI). 2007. *Note Explicative de protection incendie 4415-03f – Evaluation en vue de la determination de la grandeur des compartiments coupe-feu*. Bern, pp. 25-37.
2. CEN, European Committee for Standardization. 2002. *EN 1991 Eurocode 1 Part 1-2 Actions on structures exposed to fire*. Brussels, pp. 43-56.
3. Inspection du Travail et des Mines. 2012. *1551.1 Instruction Technique – Etude de stabilité au feu à l'aide d'une approche performancielle*. Luxembourg, pp. 8-9.
4. Franssen, J-M. 205. "SAFIR. A Thermal/Structural Program Modelling Structures under Fire", *Engineering Journal*, AISC, 42(3):143-158.

COMPOSITE COLUMNS

Stability Behavior of Concrete-Filled Steel Tube Columns in Real Fire Conditions

SHASHANK TADDHANPALLY and ANIL AGARWAL

ABSTRACT

Finite element based method is used to simulate the fire behavior of CFT columns at elevated temperatures. The proposed technique is calibrated to against experimental data to find the values of several input parameters such as the post-crack tension behavior of concrete and the normal and tangential behavior of the interface between the steel and the concrete components. The preliminary results indicate that the interface model and the tension properties of concrete play a very critical role in determining the load capacity of CFT columns at elevated temperatures.

INTRODUCTION

Concrete Filled Steel Tube (CFT) columns are popular because they are faster to build in comparison to reinforced concrete and the formwork is also not required. Under fire conditions, CFT columns exhibit better fire resistance than bare-steel columns as they have more thermal inertia. The failure behavior of CFT columns at elevated temperatures, however, is more complicated than the steel columns. Some of the primary reasons are as follows: (1) Temperatures and the corresponding thermal strains in the cross-section are non-uniformly distributed. This leads to high variability in the levels of longitudinal and hoop stresses at different locations in the cross-section. (2) The steel-concrete interface behavior at elevated temperatures is not very well established. The interface has been found to introduce discontinuity both in terms of temperatures and strains [1].

A large number of full-scale fire tests of CFT columns are available in the literature. These tests, along with various numerical methods proposed by various researchers have led to a better understanding of the fundamental behavior of the CFT columns at elevated temperatures. Lie & Chabot [2], Kodur & Lie [3], Han et al. [4,5], Han & Huo [6] and Romero et al. [7] are some of the studies that have contributed significantly to this field. Some of the common observations of various studies are summarized here. At ambient temperatures the applied compressive load is carried by both the steel tube and the concrete core. As temperatures rise, the steel tube expands faster than the concrete core. This leads to an increase in the share of compressive force carried by the steel tube and a reduction in the force carried by the concrete core. As steel temperatures keep rising, the steel tube either yields or buckles locally. This is often reflected in the bulged shape of the column. At this point, the load is transferred back to the concrete core. Slender members are more likely to fail in flexural bucking mode, whereas stockier members tend to fail in squash mode. It is often found that the steel tube's contribution to the total load resistance is negligible in comparison to the contribution from the concrete core in columns that fail in the quash mode.

A number of equations/guidelines have also been proposed to calculate the fire resistance of CFT columns. Two of the popular guidelines are listed here.

Kodur [8, 9] proposed a simplified equation based on the results of parametric studies supported by an experimental program carried out in NRCC, Canada [2], on square and circular CFT columns under fire. The fire resistance of CFT column is evaluated from the given equation:

$$R= f\left(\frac{f_c+20}{KL-1000}\right) D^2\sqrt{\frac{D}{N}}$$

Where, R is the Fire resistance in minutes, f_c is the concrete strength at the age of 28 days in MPa, D is the outside diameter/width of the column, N is the applied load in kN, KL is the effective length of the column and f is the coefficient which includes the effect of rest of the parameters given by Kodur [10].

Han et al [5] proposed a formulation to determine the strength index of circular CFT columns filled with plain concrete.

The Strength Index is defined as:

$$SI=\frac{\mathrm{Nu(t)}}{\mathrm{Nu}}=\begin{cases}\dfrac{1}{1+a.to\text{^}2.5}, & t_o\leq t_1\\[2ex] \dfrac{1}{b.\mathrm{to}+\mathrm{c}}, & t_1< t_o\leq t_2\\[2ex] k.t_o+d, & t_o>t_2\end{cases}$$

Where, $N_u(t)$ is the ultimate strength of the column corresponding to the fire resistance time (t) and N_u is the ultimate strength of the column at room temperature, $t_o = t/100$, t_1 and t_2 are the transition times depending on the value of $D_o = D/600$ and $\lambda_o = \lambda/40$. a, b, c, d, k are the regression coefficients which also depend on D_o, λ_o, and t_1, t_2. The definitions of different coefficients are not presented here for brevity.

Both these guidelines predict the fire resistance of CFT columns that are directly exposed to standard fire loading. If a column is exposed to a long duration fire with slow rising temperatures or if it is covered with appropriate fire-protection, the temperature in the column cross-section is likely to be more uniformly distributed, thereby affecting the load carrying capacity of the column. It is important to account for the rate of heating along with other structural parameters, such as member dimension and material properties, etc.

This paper presents a numerical approach to study the failure behavior of CFT columns exposed to fire conditions. The objective of this study is to identify the various modes of failure of CFT columns at elevated temperatures and to develop a design methodology to predict the fire resistance of such columns. The specific goals of this study are to understand the following: (1) does the confinement provided by the steel tube affect the load bearing capacity of the concrete core, (2) does the structural bond between the steel tube and the concrete core break during the heating of the column and how it affects the column response, (3) how local buckling of the steel tube affects the column behavior, and (4) how the rate of heating affects the temperature distribution inside the concrete core and the structural response of the column.

MODELING TECHNIQUE AND VALIDATION

Finite element based numerical simulations are used to model the behavior of CFT columns. Sequentially coupled thermal-stress analysis on 3-D models of CFT columns is performed to estimate (1) the temperature field and (2) the pre and post-failure structural behavior of CFT columns. If structural and thermal properties of steel and concrete are reported in the studies that report the CFT column tests, these values are used. Otherwise, the values provided by the Eurocode are used.

For heat transfer analysis, only conduction part of the heat transfer was modeled. Steel temperatures as reported in the experimental studies were directly assigned to the outer surface of the steel tube in the numerical models. Steel tube was modeled using heat transfer plate elements with 5 or more temperature degrees of freedom along the thickness of the plate. The concrete core was modeled using 3-D linear heat transfer elements. For some the tests simulated in this study, measured thermal and structural properties of steel and concrete were reported. For other tests, the properties available in the Eurocode [11] were used. The interface between steel and concrete parts is assumed to offer no thermal inertia or resistance to the heat flow. This is a simplifying assumption. This will be rectified in the subsequent iterations.

For the purpose of the stress analysis, steel tube is modeled using 4-noded shell elements and concrete core is modeled using 8-noded solid elements. Material properties (i.e., temperature dependent stress-strain curves and thermal expansion coefficients) for steel and concrete are taken from the Eurocode if the measured values are not available. Nodes at each column-end are rigidly connected to a representative point so that overall movement and rotation of the cross-section is allowed but relative displacements in the out-of-plane direction are prohibited. The interface between the concrete and steel parts was modeled as a hard contact with zero bond strength.

Several column tests, both at ambient and elevated temperatures were simulated using the methodology explained above. A comparison of the simulated and tested compressive load capacities at ambient temperature [12] of seven columns has been presented in Table 1. The comparison shows that the column capacities predicted by the FEM based simulations are in good agreement with the test values. However, the in most cases, simulations predict marginally higher capacity than the test values.

TABLE 1. COMPARISON BETWEEN THE CALCULATED AND TEST COLUMN CAPACITIES AT AMBIENT TEMPERATURE.

Specimen	Diameter (mm)	thickness (mm)	length (mm)	eccentricity (mm)	f_y (MPa)	f_{ck} (MPa)	$N_{u,exp}$ (kN)	$N_{u,FEM}$ (kN)	Error (%)
1	100	3	2135	20	322	32.7	181.6	198	8.3
2	100	3	2135	50	322	34.5	117.5	128	8.2
3	100	3	2135	50	322	71.6	151.6	157	3.4
4	100	3	2135	50	322	93.0	154.2	165	6.5
5	125	5	3135	20	322	88.0	474.2	492	3.6
6	125	5	3135	50	322	96.7	317.9	331	4.0
7	125	5	3135	20	322	107.3	489.5	530	7.6

A number of fire tests on CFT columns were also simulated to validate the FEM model. Time vs. axial deformation curve for one of the columns (SQ17) tested by Lie and Chabot [2] has been compared with the time-displacement plot predicted by the numerical models in Figure 1. The plot show that the modeling technique presented in this section simulates the failure behavior reasonably well as ambient as well as at elevated temperatures.

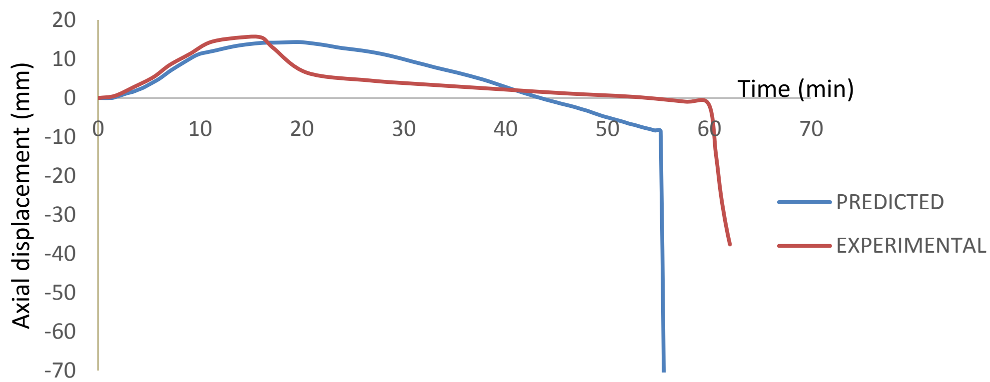

Figure 1. Validation of the presented technique: comparison between the tested and the simulated axial displacement vs time curve for a CFT column.

SENSITIVITY STUDY

It is important to understand how certain parameters, especially the ones about which there may be uncertainty while developing the numerical models, affect the overall structural behavior of the columns. This exercise gives us more confidence in our choice of input parameters. Two parameters – namely structural properties of the steel-concrete interface and concrete post-crack tension properties – were found to be of high importance to accurately model the compression failure behavior of CFT columns at elevated temperatures. Post-cracking behavior of concrete in tension is found to have a significant amount of influence on the behavior of CFT columns at elevated temperatures. A simply supported circular CFT column (length =2135 mm, outer diameter = 100 mm, and steel tube thickness = 4 mm) was simulated to study the effects of change in post-crack behavior of concrete. These simulations were conducted in three different conditions, namely (i) ambient temperature, (ii) uniform temperature of 600 ^{o}C, and (iii) simulated thermal loading where steel temperature rises to 600 ^{o}C in approximately 20 minutes. Concrete tension strength at a given temperature was taken as 9% of compressive strength at the respective temperature. Two different post-cracking tension properties were considered. (i) Post cracking strength is reduced to 20% of the maximum tensile strength after a plastic tensile strain of 0.01 and (ii) concrete retains its full tensile strength for very large plastic strain. It was observed that for columns at ambient temperature, the two types of post-crack concrete behaviors leads to a very small difference (0.3%) in the column capacities. In the case where the column is at a uniform temperature of 600 ^{o}C, the difference between the column axial load capacities estimated using the two types of post-crack concrete behaviors was approximately 9.2%. However, for the column subjected to a non-uniform temperature distribution, the difference between the axial load capacities estimated using the two post-crack concrete behaviors was approximately 13.2%. This clearly indicates that at ambient temperature, concrete is hardly subjected to tension cracking; therefore, post-crack tension property of concrete does not have a significant effect on the column capacity. However, as the temperatures rise, due to uneven expansion of different elements, some portions of concrete may be subjected to tensile stresses. Therefore, accurate modeling of post-crack tension behavior of concrete behavior becomes very important.

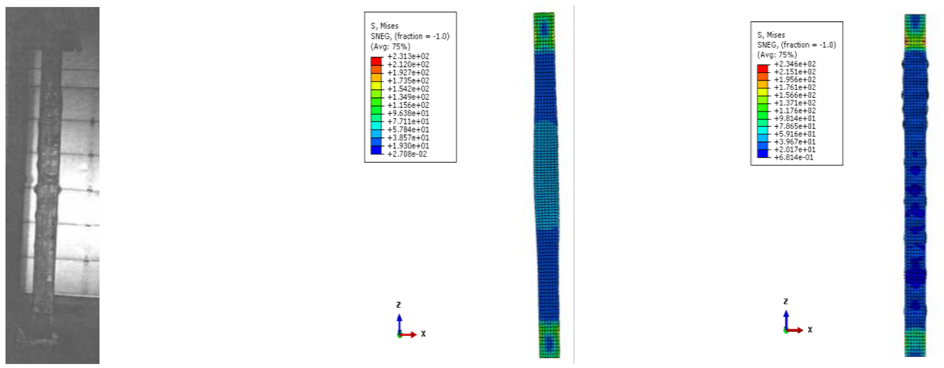

(a) Experimental (b) Perfect bond (c) hard contact

Figure 2. Deformed shapes of a column (a) observed during the test and predicted with the assumption of (b) a perfect bond and (c) zero bond strength.

Several options are tried for modeling the mechanical interface between the steel and concrete parts. It was observed that the overall strength of these columns are sensitive to the change in the interface behavior. Two extreme cases namely (1) perfect bond and (2) hard contact with zero bond strength are considered in FEM simulations and the results are compared with the behavior of the tested columns. It is observed that a perfect bond does not allow the steel tube to buckle locally. Figure 2 compares the simulated deformed shapes of column SQ17 tested by Lie and Chabot [5] under the two interface assumptions with the deformed shape observed during the test. The test specimen had undergone significant amount of local buckling, which is captured well by the simulation where the interface is assumed to have zero bond strength. On comparing the simulated duration of fire sustained by the column, it is observed that the model with contact interface that has zero bond strength predicts higher fire resistance than the model where a perfect bond is assumed between the steel tube and the concrete core. For example, column SQ17 is predicted to have a fire resistance of only 46 minutes if the interface is modeled as perfectly bonded. However, the predicted fire resistance increases to 55 minutes if the interface is modeled to have zero bond strength. This is counter-intuitive because the column capacity seems to be decreasing as the bond strength is increasing. Further investigation into this behavior indicates that there is a hoop stress introduced by uneven thermal expansion of different elements in the column cross-section. Portions of the cross-section closer to the center are at a lower temperature than the surface. Therefore, internal elements (i.e., concrete core) expand less than the outer elements (i.e., steel tube). If the interface is modeled as perfect bond, this differential expansion leads to a tensile hoop-stress in the peripheral elements of the concrete and a compression hoop-stress arises in the steel tube. As concrete has very low strength in tension, this leads to cracking of the concrete core, which, in turn, leads to a reduction in the overall column capacity. If concrete is modeled so that concrete retains most of its tension strength after cracking in tension, the perfect bond between the steel tube and the concrete core leads to a very high fire resistance (101 minutes). This establishes that both the interface properties and the concrete tension properties significantly affect the column fire resistance prediction. Moreover, the effect of the post-crack tension strength of concrete is coupled with the effect of the interface model.

PARAMETRIC STUDY

A detailed parametric study is conducted on a number of different column geometries, load levels, and two fire loading situations. In first condition, unprotected CFT columns are subjected to the ASTM standard fire and in the second condition, the columns are assumed to be protected for 1 hour of fire resistant rating. The first case leads to a rapid rise in the steel temperature while the concrete core remains at a much lower temperature. The temperature of steel rises relatively slowly in the second case, thereby allowing for the concrete core temperatures to rise significantly. For example, the steel tube in the unprotected column reaches the temperature of approximately 900 ^{o}C and the center of the concrete core reaches 275 ^{o}C after an unprotected column is exposed to one hour of fire. When a protected column is exposed to fire, the respective temperatures are 536 ^{o}C and 155 ^{o}C.

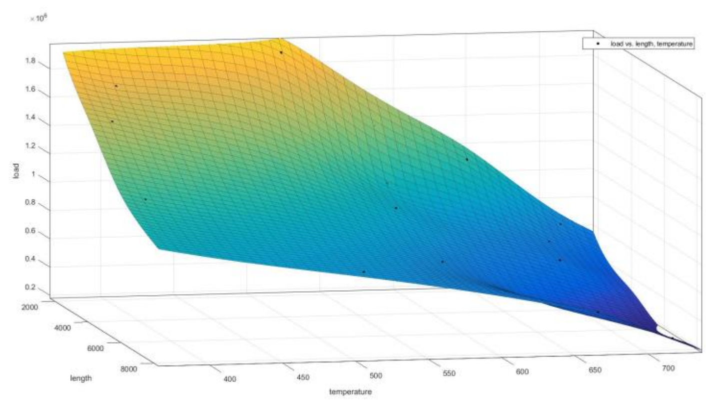

Figure 3. Column failure surface developed using the simulation results.

All the simulations in the parametric study are conducted using the numerical model developed and validated in the above section. The interface is modeled as contact with zero bond strength.

The CFT columns are of square cross-section with outer dimension as 250x250mm. Concrete of compressive strength is assumed to be 40 MPa and steel yield strength is assumed to be 350 MPa. The length of the CFT columns that are used are 2000 mm, 3000 mm, 4000 mm, 6000 mm, and 8000mm and three different steel tube thickness values (4 mm, 6 mm, and 9 mm) are taken for each of the lengths and fire loading conditions. The loads applied on the columns are 20%, 35%, and 60% of the axial load carrying capacity of the respective column at ambient temperature. For simulating the behavior of the columns in combined axial compression and fire conditions, first the designated amount of load is applied on a numerical model of a column and then the fire loading is applied till the column fails. The results from the parametric study offer an insight into the interplay of various parameters that influence the fire resistance of a CFT column. The objective of this parametric study is to eventually develop a column design equation to predict the fire resistance that a column. Databases listing the values of column length, steel temperature, and failure load for all the column geometries are developed. Regression analysis on this data for a particular column allows us to develop a failure surface for a column. Column curves (load vs. slenderness) for a given steel temperature can be developed by taking a section of this surface. Figure 3 shows the column capacity surface for an unprotected column with 4 mm thick steel tube. The vertical axis in this surface plot is the maximum load carried by the column; one of the horizontal axes is the length of the simply-supported column; the other horizontal axis represents the steel temperature at the time of failure. It is clearly evident from the figure that as the slenderness of the column or the steel temperature increases, the column load capacity decreases. Black dots on this surface represent the simulation results.

SUMMARY AND CONCLUSION

A finite element based numerical approach to model the failure behavior of CFT columns under fire loading conditions was presented in the paper. It was observed that the temperature variation across the cross-section plays a very important role in determining the fire resistance of a CFT column. Due to this temperature variation in the radial direction, CFT columns are found to be subjected to the hoop stresses, which are not observed in typical steel columns at elevated temperatures. These stresses make the overall compressive load carrying capacity of the column at elevated temperature depend on the tensile strength of concrete. Also, it was found that the column capacity and the deformed shape depend significantly on the interface properties. A parametric study was conducted. The parametric study will be used to develop a guideline to assess the fire resistance of a CFT column.

REFERENCES

1. Ana Espinos capilla (2012), *"Numerical analysis of the fire resistance of Circular and Elliptical Slender Concrete filled Tubular Columns"*, PhD Dissertation, Department of Construction Engineering and Civil Engineering Projects, University at politecnica De Valencia, Spain.
2. Lie, T.T and Chabot, M., *"Experimental studies on the Fire Resistance of Hollow Steel Columns filled with Plain Concrete"*, IRC Internal Report NO. 611, National Research Council of Canada, Institute for Research in Construction, Ottawa, Ontario, 1992.
3. Lie T. T. Kodur VK, (1994), *"Fire resistance of circular steel columns filled with bar-reinforced concrete"*. J. Struct. Engg. ASCE, 120(5), 1489-1509.
4. Han LH, Yang YF, Xu L. *"An experimental study and calculation on the fire resistance of concrete filled SHS columns"*. Journal of Constructional Steel Research 2003; 59(4):427-452.
5. Han LH, Zhao XL, Yang YF, Feng JB. "*Experimental study and calculation of concrete-filled hollow steel columns"*. Journal of Structural Engineering, ASCE 2003; 129(3):346-356.
6. Han, L. and Huo, J. (2003). *"Concrete-Filled Hollow Structural Steel Columns after Exposure to ISO-834 Fire Standard". J. Struct. Eng.*, 10.1061/(ASCE)0733-9445(2003)129:1(68), 68-78.
7. Romero ML, Moliner V, Espinos A, Ibanez C, Hospitaler A. *"Fire behavior of axially loaded slender high strength concrete-filled tubular columns"*. Journal of Constructional Steel Research 2011: 67(12): 1953-1965.
8. Kodur VK. "*Design equations for evaluating the fire resistance of SFRC-filled HSSS columns*". Journal of Structural Engineering 1998: 124(6): 671-7.
9. Kodur, V. K. R (1996b). *"Factors affecting the fire resistance of square hollow steel columns filled with steel fibre-reinforced concrete".* IRC Internal Rep. No. 590, National Research Council of Canada, Institute for Research in Construction, Ottawa, Ontario, Canada.
10. Lie, T. T., and Kodur, V. K. R. (1996). *"Fire resistance of steel columns filled with bar-reinforced concrete."* J. Struct. Engrg., ASCE, 122(1), 30-36.

11. CEN. EN 1994-1-2, Eurocode 4: Design of composite steel and concrete structures. Part 1-2: General rules – Structural fire design. Brussels, Belgium: Comite Europeen de Normalisation; 2005.
12. J.M. Portoles, M.L. Romero, J.L. Bonet, F.C. Filippou, *"Experimental Study of High Strength Concrete Filled Tubular Columns under Eccentric Loading."* J Constr Steel Res 2011;67:623-633.

Development of a Calculation Method for the Fire Design of Concrete-Filled Steel Tubular Columns

ANA ESPINOS[a], MANUEL L. ROMERO[a], VICENTE ALBERT[a], ANTONIO HOSPITALER[a], GISELS BIHINA[b] and CHRISTOPHE RENAUD[b]

ABSTRACT

This paper presents a method for evaluating the fire resistance of concrete-filled steel tubular columns (CFST), developed in the framework of the European Project FRISCC. The aim of this project is to develop a full methodology that solves the shortcomings of the current design rules in EN 1994-1-2, proved unsafe for slender columns. For that purpose, two numerical models are developed and validated against the results of an extensive experimental programme. The numerical models are subsequently used for conducting a comprehensive parametric study. Based on the results of the parametric study, design rules for the evaluation of the fire resistance of CFST columns of different cross-section shape are developed, extending the applicability of the current code provisions. Innovative sections, such as elliptical hollow sections (EHS) are accounted for in the method. The design proposal is divided into two parts: a simplified cross-sectional temperature field assessment and a method for evaluating the ultimate buckling load in the fire situation, using the equivalent temperatures obtained from the previous step. The effect of eccentricity is evaluated through a modification in the method, which accounts for eccentricities on both minor and major axis, reaching large eccentricities of $e/D = 1$.

1. INTRODUCTION

Previous investigations have revealed that the current calculation method for CFST columns in Eurocode 4 Part 1.2 [1] produces unsafe results for slender columns [2,3], which has led to the approval of an addenda to Eurocode 4 by the committee CEN/TC250/SC4 limiting the applicability of Annex H to a maximum relative slenderness of 0.5 [4]. With this motivation, an extensive fire testing program on slender CFST columns of different geometries was recently carried out by the authors in the framework of the European Project FRISCC [5,6], in order to provide a full range of experimental evidence on the fire behaviour of CFST columns, a necessary basis for the development of numerical models and simple calculation rules. In this work, a new simplified design method is developed, which solves the limitations of the current calculation method in Eurocode 4 and extends the range of

[a]Concrete Science and Technology Institute (ICITECH), Universitat Politècnica de València, Valencia, Spain
[b]Centre Technique Industriel de la Construction Métallique (CTICM), Saint Aubin, France

application to all the cross-section geometries available in the market and large load eccentricities.

2. DEVELOPMENT AND VALIDATION OF THE NUMERICAL MODELS

Two different numerical models were developed by two of the partners involved in the Project, Universitat Politècnica de València (UPV) and Centre Technique Industriel de la Construction Métallique (CTICM), to simulate the fire behaviour of concrete-filled steel tubular columns with different cross-section shape (CHS, SHS, EHS and RHS). The model by UPV was a three-dimensional finite element model (Figure 1a), while the model from CTICM was a fiber-based model (Figure 1b), which, although more simplified, allowed for a reduction in the computational cost of the numerical simulations. A detailed description of the finite element model from UPV can be obtained from [7], while the fiber model from CTICM is fully described in [8]. The numerical models were validated against the extensive database of test results available from the experimental program of the European project FRISCC [5,6].

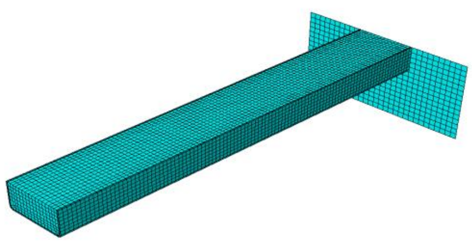
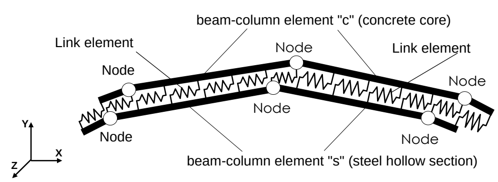

a) 3D finite element model from UPV b) Specific beam element from CTICM 2D model

Figure 1. Numerical models used for conducting the parametric study.

Once the numerical models were validated, they were used for conducting a parametric study. After having proved that the response of the 2D model was consistent with that of the 3D model, the first model was used to perform the numerical simulations in the parametric studies, since it allowed for a significant reduction of the computational cost without loss of accuracy.

2. PARAMETRIC STUDIES

An extensive programme of numerical simulations was designed, in order to investigate the behaviour of CFST columns at elevated temperatures considering different cross-section shapes (CHS, SHS, EHS and RHS). The parameters studied were the outer diameter (D) or larger and smaller outer dimension (H - B) in the case of RHS and EHS columns, the thickness of the steel tube wall (t), the relative slenderness at room temperature ($0.2 \leq \bar{\lambda} \leq 2$), the percentage of reinforcement ($0\ \% \leq \rho \leq 5\ \%$), the concrete cover ($u_s$), the load level ($0\ \% \leq \mu \leq 70\ \%$) and the relative eccentricity ($0 \leq e/D \leq 1$). In all, 4400 circular, 4400 square, 8136 rectangular and 3600 elliptical column specimens were analysed, amounting a total of **20536** numerical simulations. All the specimens were designed to meet the criteria of non-slender sections ($D/t \leq 90\varepsilon^2$), having a steel contribution ratio between $0.2 \leq \delta \leq 0.9$, in order to accomplish with the limitations in EN 1994-1-1 [9].

The numerical fire buckling resistance of the columns ($N_{fi,Rd}$) was obtained from the results of all simulations performed in the parametric studies. From this buckling resistance, the normalized buckling load (χ) is obtained by dividing its value by the cross-sectional plastic resistance in the fire situation ($N_{fi,pl,Rd}$) and plotted against the relative slenderness at elevated temperature (λ_θ) in Figure 2. This figure only shows the results for axially loaded columns, 3000 specimens approximately from all sections shapes, superimposed with buckling curve "c", which is used in Clause 4.3.5.1(2) of EN 1994-1-2 [1] for the fire design of composite columns.

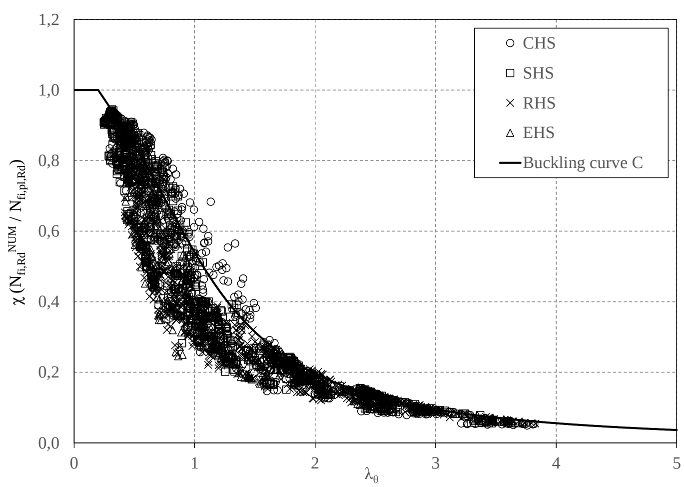

Figure 2. Results of the numerical simulations from the parametric studies (concentrically loaded columns).

3. DEVELOPMENT OF A NEW SIMPLIFIED DESIGN METHOD

In order to solve the shortcomings of the current calculation method in EN 1994-1-2 [1] and extend its applicability limits to other cross-section geometries, a new proposal is developed. The new simplified design method is based in the general method from Clause 4.3.5.1(2) of EN 1994-1-2, which is grounded on the elastic buckling theory, as an extension of the method for room temperature design.

3.1. Simplified cross-sectional temperature field

In order to be able to calculate the buckling load of a CSFT column in the fire situation by means of the simple calculation model in Clause 4.3.5.1(2) of EN 1994-1-2 [1], the cross-sectional temperature field at elevated temperature is previously required. However, the code does not provide any simplified method to obtain this temperature field. Therefore, in order to help designers in this task, a simple method to is proposed here. This proposal is valid for CHS, SHS, RHS and EHS columns and fire exposure times ranging from 30 to 240 minutes.

In the proposed method, a single equivalent temperature is provided for each part of the cross-section (see Figure 3): an equivalent temperature for the whole concrete core ($\theta_{c,eq}$), another one for the steel tube ($\theta_{a,eq}$) and finally one for the reinforcement ($\theta_{s,eq}$). This approach is already used in Annex G of EN 1994-1-2 [1] for composite columns with partially encased steel sections, being its main benefit that designer can evaluate the fire resistance of the column by using a single strength and stiffness value for each component of the composite cross-section corresponding to its equivalent temperature.

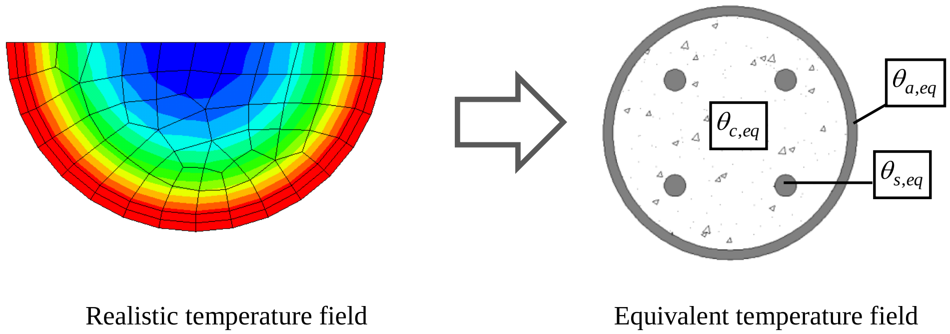

Figure 3. Scheme for the simplified temperature field proposal.

In order to obtain these equivalent temperatures, the calculation procedure described by Espinos et al. [2] has been followed in this work. For the ease of presentation, this procedure is not described here, but the reader can refer to the aforementioned paper.

Once the equivalent temperatures were calculated for all the case specimens, a generalized approach was developed to merge all section shapes in a single and compact formulation. In order to do so, a non-linear regression analysis was applied to all the numerical data from the parametric studies.

For the concrete core, the equation for evaluating the equivalent temperature ($\theta_{c,eq}$) is as follows:

$$\theta_{c,eq} = 81.801 - 5.046R + 0.003R^2 - 15.07A_m/V + 0.331(A_m/V)^2 - 0.875R \cdot A_m/V + \\ +7.428R^{0.842} \cdot (A_m/V)^{0.714} \quad (1)$$

In turn, the equation which provides the equivalent temperature of the steel tube ($\theta_{a,eq}$) is given below:

$$\theta_{a,eq} = -824.667 - 5.579R + 0.007R^2 - 0.009R \cdot A_m/V + 645.076R^{0.269} \cdot (A_m/V)^{0.017} \quad (2)$$

For the reinforcing bars ($\theta_{s,eq}$), an expression based in Wickström [10] was developed, depending on the factor t/u_s^2 (min/mm^2) with the following shape:

$$\theta_{s,eq} = \chi_3 \cdot (t/u_s^2)^3 + \chi_2 \cdot (t/u_s^2)^2 + \chi_1 \cdot (t/u_s^2) + \chi_0 \quad (3)$$

where the χ coefficients depend on the section shape and concrete cover, and are not provided here for simplicity.

3.2. Proposal for concentrically loaded columns

In previous work, the applicability of the general principles in Clause 4.3.5.1 of EN 1994-1-2 [1] was studied by the authors. It was revealed that the predicted buckling load result in most cases unsafe when the flexural stiffness reduction coefficients are neglected [2, 4]. Through the results of the parametric studies presented in this paper, the values of these coefficients were derived for the standard fire exposure times. The value of the concrete flexural stiffness coefficient was fixed to $\varphi_{c,\theta} = 0.8$. Regarding the flexural stiffness reduction coefficient for the steel tube, the procedure described in Espinos et al. [2,3] was applied. Again, for the sake of brevity, this procedure is omitted here, but the reader can refer to the aforementioned papers.

In the present work, buckling curves "a" and "b" were used for unreinforced and reinforced columns respectively, instead of curve "c", which is prescribed in Clause 4.3.5.1 of EN 1994-1-2 [1]. This assumption is in line with the recommended buckling curves in EN 1994-1-1 [9] for CFST columns at room temperature.

A statistical analysis was applied to the parametric studies results, in order to obtain the correlations of the different variables and the shape of the functions. Through a multiple nonlinear regression analysis, the following equation was proposed for the steel tube reduction coefficient:

$$\varphi_{a,\theta} = \varphi_{a,\theta,1}\left(A_m/V\right)\cdot\varphi_{a,\theta,2}\left(l_\theta/D\right)\cdot\varphi_{a,\theta,3}\left(D/t\right)\cdot\varphi_{a,\theta,4}\left(R\right) \qquad (4)$$

As an example, the proposed functions for CHS columns are shown in Table I. For the sake of brevity, the formulation of the rest of geometries is not included in this paper.

TABLE I. REDUCTION COEFFICIENTS FOR THE STEEL TUBE (CHS COLUMNS).

$l_\theta / D \leq 12$	$l_\theta / D > 12$
$\varphi_{a,\theta,1} = 6.05 - 1.16\cdot(A_m / V)^{0.417}$	$\varphi_{a,\theta,1} = 0.2$
$\varphi_{a,\theta,2} = 0.55 + 0.082\cdot(l_\theta / D)^{0.979}$	$\varphi_{a,\theta,2} = -4262 + 4253\cdot(l_\theta / D)^{9.03\cdot10^{-4}}$
$\varphi_{a,\theta,3} = 566.37 - 565.25\cdot(D / t)^{2.21\cdot10^{-4}}$	$\varphi_{a,\theta,3} = 0.5375 + 7.5\cdot10^{-3}\cdot(D / t)$
$\varphi_{a,\theta,4} = 0.116 + 8.84\cdot10^{-12}\cdot(R)^{4.285}$	$\varphi_{a,\theta,4} = 2.66 - 0.44\cdot(R)^{0.28}$

Regarding the flexural stiffness reduction coefficient for the reinforcement, different functions were adjusted for the various reinforcement levels studied. As an example, these expressions can be seen in Table II for CHS columns.

$$\varphi_{s,\theta} = \varphi_{s,\theta,1}\left(A_m / V\right)\cdot\varphi_{s,\theta,2}\left(R\right) \qquad (5)$$

TABLE II. REDUCTION COEFFICIENTS FOR THE REINFORCEMENT (CHS COLUMNS).

$\rho \leq 2.5\%$	$\rho \leq 5\%$
$\varphi_{s,\theta,1} = 0.23 + 0.018\cdot(A_m / V)$	$\varphi_{s,\theta,1} = 0.57 + 0.017\left(A_m / V\right)$
$\varphi_{s,\theta,2} = 0.8 - 0.001\cdot(R)$	$\varphi_{s,\theta,2} = 0.83 - 0.001\cdot(R)$

Finally, the results shown in Figure 4 were obtained by applying the proposed flexural stiffness reduction coefficients to all the concentrically loaded cases from the parametric studies (about 3000 specimens in total). Once all the calculation points had been obtained, the accuracy of the proposal was assessed.

The criteria used in this work for verifying the accuracy of the developed simplified design method was that approved by CEN/TC250/SC4 Horizontal Group Fire [11], which prescribes that three criteria should be met for a calculation method to be considered accurate. Firstly, the calculation result shall not be on the unsafe side by more than 15% of the reference result, secondly a maximum of 20% of individual calculation results shall be on the unsafe side and thirdly the mean value of all percentage differences between calculation results and reference results shall be on the safe side. Taking all the calculation points from the parametric studies results, the average error lies on the safe side with a value of 1.203 and a standard deviation of 0.164. A maximum deviation on the unsafe side of 14.91% (<15%) is observed and only 8.02% (<20%) of the cases lie on the unsafe side. Therefore, all the prescribed criteria are met.

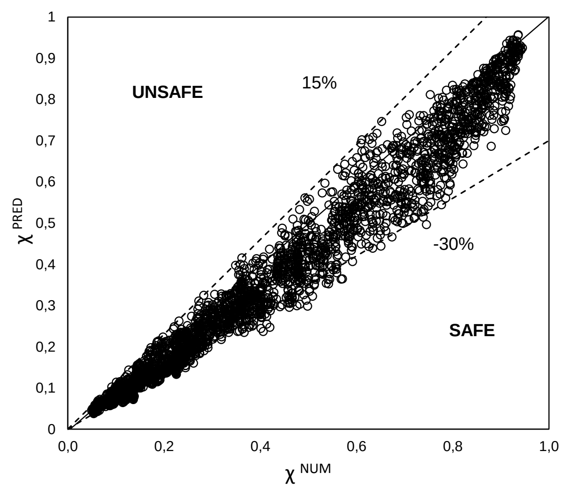

Figure 4. Comparison between the proposed simplified design method predictions and parametric studies results (concentrically loaded columns).

3.3. Proposal for eccentrically loaded columns

A proposal to account for eccentricity was developed through the parametric studies results. Based on the approach from Annex G of EN 1994-1-2 [1] for partially encased steel sections, the following equation was proposed:

$$N_{fi,Rd,\delta} = \alpha \cdot \left(\frac{N_{Rd,\delta}}{N_{Rd}} \right)_{room} \cdot N_{fi,Rd} \tag{6}$$

This formulation assumes that the relation between concentric and eccentric ultimate load in the fire situation ($N_{fi,Rd,\delta}$ / $N_{fi,Rd}$) and at room temperature ($N_{Rd,\delta}$ / N_{Rd}) are similar. Note that the concentric and eccentric ultimate loads of the column at room temperature should be computed following the design rules in EN 1994-1-1 [9].

This relation was adjusted for the different geometries through the coefficient α, for which a formulation was developed as a combination of the contribution of the different parameters. As an example, the proposed functions for CHS and SHS sections are given next. For the sake of brevity, the formulation for EHS and RHS sections is not included in this paper.

$$\alpha = \alpha_{A_m/V} \cdot \alpha_{D/t} \cdot \alpha_R \cdot \alpha_s \tag{7}$$

where:

$$
\left.\begin{aligned}
\alpha_{A_m/V} &= 0.0089\cdot(A_m / V) + 0.443 \\
\alpha_{D/t} &= -0.0049\cdot(D / t) + 0.5426 \\
\alpha_R &= 6.9598\cdot R^{-0.221}
\end{aligned}\right| \quad (l_\theta / \mathrm{D} \le 15)
$$

$$
\left.\begin{aligned}
\alpha_{A_m/V} &= 1 \\
\alpha_{D/t} &= 1 \\
\alpha_R &= 0.92
\end{aligned}\right| \quad (l_\theta / \mathrm{D} > 15)
$$

and

$$
\begin{aligned}
\alpha_s &= 0.8 && (\rho = 0\%) \\
\alpha_s &= -6.44\cdot 10^{-4}(l_\theta / D)^2 + 4.17\cdot 10^{-2}(l_\theta / D) + 0.553 && (0\% < \rho \le 2.5\%) \\
\alpha_s &= -7\cdot 10^{-4}(l_\theta / D)^2 + 4.54\cdot 10^{-2}(l_\theta / D) + 0.601 && (2.5\% < \rho \le 5\%)
\end{aligned}
$$

Additionally, it should be noticed that for reinforced CHS and SHS columns and fire exposure times over 60 minutes ($R \ge 60$), this coefficient to account for eccentricity should be simplified to $\alpha = 0.92\,\alpha_s$, instead of using the partial coefficients.

The results of the proposal for eccentrically loaded columns, applied to all the analysis cases from the parametric studies (about 17500 eccentrically loaded specimens) are presented in Figure 5, showing accurate predictions with the average error lying on the safe side. The accuracy parameters for the prediction of this proposed method against the parametric studies results are shown in Table III, meeting the CEN/TC250/SC4 criteria [11] for both minor and major axis eccentricity.

a) b)

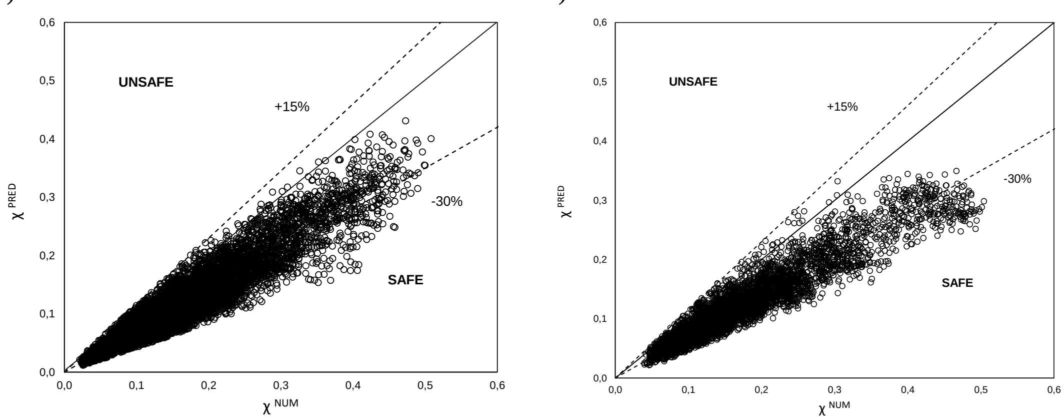

Figure 5. Comparison between the predictions of the proposed simplified design method and the parametric studies results (eccentrically loaded columns). a) Minor axis. b) Major axis.

TABLE III. ASSESSMENT OF THE ACCURACY OF THE SIMPLIFIED DESIGN METHOD.

Accuracy parameters	**Axially loaded**	**Eccentrically loaded**		**HGF [11]**
		minor axis	major axis	
Avg. error	1.2	1.45	1.42	> 1
Std. dev.	0.16	0.27	0.24	-
Max. unsafe dev.	14.9 %	14.7 %	14.5 %	< 15%
Num. unsafe results	8.0 %	2.4 %	3.1 %	< 20 %

4. SUMMARY AND CONCLUSIONS

In this work, a new simplified design method for evaluating the fire resistance of CFST columns of different cross-section shapes has been presented.

Two numerical models were set up and validated against an extensive experimental database from the European Project FRISCC: a 3D model (UPV) and a 2D model (CTICM), which allowed for a significant reduction of computational time without loss of accuracy. By means of these numerical models, parametric studies were conducted in order to develop a full method which solves the shortcomings of the current design rules in EN 1994-1-2 [1], proved to be unsafe for slender columns.

Through the parametric studies results, expressions for obtaining the equivalent temperatures of the different components of the composite cross-section were developed. Design equations were also proposed for defining the appropriate values of the flexural stiffness reduction coefficients. A proposal for eccentric load was included, extending the current applicability limits of the method to large eccentricities. A good agreement was found between the proposed method predictions and the numerical simulations, meeting the criteria for accuracy from CEN/TC250/SC4 [11] and significantly improving the current provisions of Eurocode 4 Part 1.2.

ACKNOWLEDGEMENTS

The authors would like to express their sincere gratitude to the European Union for the help provided through the Project RFSR-CT-2012-00025, carried out with a financial grant of the Research Programme of the Research Fund for Coal and Steel.

REFERENCES

1. CEN. 2005. “EN 1994-1-2, Eurocode 4: Design of composite steel and concrete structures. Part 1-2: General rules - Structural fire design”, Brussels, Belgium: Comité Européen de Normalisation.
2. Espinos, A., Romero, M.L. and Hospitaler, A. 2012. “Simple calculation model for evaluating the fire resistance of unreinforced concrete filled tubular columns”, *Engineering Structures*, 42:231-44.
3. Espinos, A., Romero, M.L. and Hospitaler, A. 2013. “Fire design method for bar-reinforced circular and elliptical concrete filled tubular columns”, *Engineering Structures*, 56:384-95.
4. CEN. 2011. “CEN/TC250/SC4–N358. Resolutions agreed by unanimity at the CEN/TC 250/SC4 meeting in Vienna on the 14th April 2011”, Comité Européen de Normalisation.
5. Espinos, A., Romero, M.L., Serra, E. and Hospitaler, A. 2015. Circular and square slender concrete-filled tubular columns under large eccentricities and fire. J Constr Steel Res. 110:90-100.
6. Espinos, A., Romero, M.L., Serra, E. & Hospitaler, A. 2015b. “Experimental investigation on the fire behaviour of rectangular and elliptical slender concrete-filled tubular columns”, *Thin-Walled Structures*, 93:137-48.
7. Espinos, A., Romero, M.L. and Hospitaler, A. 2010. “Advanced model for predicting the fire response of concrete filled tubular columns”, *Journal of Constructional Steel Research*, 66:1030-46.
8. Renaud, C., Aribert, J.M. and Zhao, B. 2003. “Advanced numerical model for the fire behaviour of composite columns with hollow steel section”, *Steel and Composite Structures*, 3:75-95.
9. CEN. 2004. “EN 1994-1-1, Eurocode 4: Design of composite steel and concrete structures. Part 1-1: General rules and rules for buildings”, Brussels, Belgium: Comité Européen de Normalisation.
10. Wickström, U. 1987. “A very simple method for estimating temperature in fire exposed concrete structures. Fire Technology. Technical Report. SP-RAPP 1986:46”, Borås, Sweden: Swedish National Testing Institute.

11. Kruppa, J. 1999. "Document n. 99/130 CEN/TC250/SC4 Horizontal Group Fire. Eurocodes – Fire parts. Proposal for a methodology to check the accuracy of assessment methods", Saint-Rémy-lès-Chevreuse, France: Centre Technique Industriel de la Contruction Métallique (CTICM).

Experimental and Numerical Investigations on the Composite Behavior of Concrete-Filled Tubular Columns with Massive Steel Core at High Temperatures

PETER SCHAUMANN and INKA KLEIBOEMER

ABSTRACT

This paper deals with experimental and numerical investigations on concrete-filled tubular columns with embedded massive steel core (CFTES columns) aiming at justified design recommendations on reliable shear stresses.. Push-out tests at room temperature and high temperatures are described in detail and analyzed in terms of ultimate shear strength, bond strength and shear strength-displacement-curve shape. The test data reveal a distinctive reduction in both ultimate shear and bond strength for high temperatures, whereas the strength-displacement-curve shape is in general similar for all investigated temperature levels.

The numerical implementation of the performed tests reproduces the experimentally observed shear strength-displacement-behavior in very good accordance. Using a three-dimensional volume model in Abaqus and applying temperature-dependent joint stiffness, maximum shear stress criterion and damage evolution, the composite behavior is described in a realistic manner.

INTRODUCTION

CFTES columns represent an attractive constructional option to design slender columns providing both high load-bearing capacity and high fire resistance. The structural detailing, particularly in the load introduction zone, thereby depends on the designated loading and required load transfer between the cross-sectional parts. Certainly, it is preferable to transfer the load via composite action instead of applying shear connectors to the steel core. However, the amount of shear stresses that can be transferred along the interface between steel core and concrete in CFTES columns is unexplored up to now. Furthermore, considering the design in fire situations, no database is available yet. In particular, EN 1994-1-2 does not provide any design values of shear stresses for composite columns at elevated temperatures. EN 1994-1-1 contains values for a limited number of cross-sections, but does not address CFTES.

Peter Schaumann and Inka Kleiboemer, Institute for Steel Construction, Leibniz Universitaet Hannover, Appelstrasse 9A, 30167 Hannover, Germany.

Literature, e.g. [1] - [4], provides experimental data on standard concrete-filled tubular (CFT) columns that focus mainly on the effect of different types and amounts of shear connectors or lubrication. None of the literature implies any investigations at elevated temperatures - neither experimentally nor numerically. Therefore, a test program has been accomplished that enables the quantification of shear stresses for CFSTES columns both at room temperature and high temperatures. Furthermore, a numerical model has been setup, which implies the observed composite behavior.

EXPERIMENTAL INVESTIGATIONS

Test specimens, test procedure and data measurement

The aim of the experimental campaign was the identification of transferable shear stresses along the interface between steel core and concrete in CFTES columns at different temperature levels. Therefore, an innovative test setup was designed that allows the performance of push-out tests combined with a heating of the specimens.

Three test series that differ in terms of their geometrical dimensions have been conducted (series I, II and III, see Table I). Besides three tests at room temperature (RT), two tests each at three high temperature (HT) levels - namely 300 °C, 400 °C and 500 °C - have been performed for each series. The cross-section of series I served as a reference configuration with a core diameter of 140 mm and an outer dimension of 219 mm. Keeping the outer dimension constant, the specimens of series II had a smaller steel core (80 mm diameter) and consequently a thicker concrete cover and a smaller composite surface. The specimens of series III had the same concrete cover as the reference configuration, but a larger steel tube and steel core diameter (273 and 190 mm, respectively). All tested specimens consisted of an outer steel tube of grade S235, normal strength concrete ($f_{c,cube}$ = 44 N/mm²) and a circular steel core of grade S355. The axial joint length between steel core and concrete was 500 mm (see Fig. 1).

The test procedure implied a dynamical pre-loading with 1000 load cycles at 3 Hz, ensuring the detachment of the adhesion between steel core and concrete. The pre-loading resulted in shear stresses oscillating between 0.25 N/mm² $\leq \tau \leq$ 0.5 N/mm². Subsequently, the specimens of the HT-series were heated in an electric furnace. Aiming in reproducible test conditions and excluding non-linear effects due to temperature gradients, a homogenous temperature within the specimen was aspired. The last step of the test procedure implied the push-out test and thus a displacement-controlled compression, aiming in a relative displacement of 15 mm. For this purpose, the load P was applied on top of the steel core, whereas only the concrete and outer steel tube were supported at the bottom (see Fig. 1). In doing so, the entire load was transferred

TABLE I. EXPERIMENTAL TEST PROGRAM OF PUSH-OUT TESTS.

Series	No. of tests	D (mm)	t (mm)	d_{core} (mm)	c (mm)	d_{core}/D	θ_{joint} (°C)
RT I	3	219.1	4.5	140	35.05	0.64	20
RT II	3	219.1	4.5	80	65.05	0.37	20
RT III	3	273.0	5.6	190	35.90	0.70	20
HT I	6	219.1	4.5	140	35.05	0.64	300 / 400 / 500
HT II	6	219.1	4.5	80	65.05	0.37	300 / 400 / 500
HT III	6	273.0	5.6	190	35.90	0.70	300 / 400 / 500

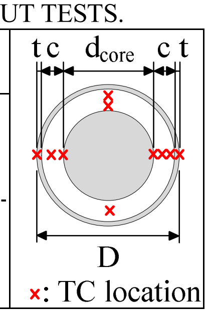

Series HT I Series RT II Series HT III x: TC loaction

Figure 1. Test specimens and geometrical dimensions.

through the interface between steel core and concrete. Supposing that the shear stress τ is uniformly distributed across the interface of the stub column, the shear stress can be recalculated from the applied load by $\tau = P/(L \cdot \pi \cdot d_{core})$.

The relative displacement u between steel core and concrete was measured by lasers and revised in terms of elastic deformations of the specimen and test frame. 14 thermocouples (TC) were used to record and control the temperature increase within the specimens both through the cross-section and along the specimen's height.

Results

From the recorded load and displacement data, shear stress-displacement-curves (τ-u-curves) were recalculated, which serve as the basis for the analysis of the composite behavior. The τ-u-curves are analyzed in terms of the ultimate shear strength τ_u, the bond strength τ_r and the curve shape.

The maximum recorded load F_{max} that was recognized during the entire test procedure was employed to recalculate the ultimate shear strength τ_u. The bond strength τ_r is defined in accordance with Roik [1] as the mean value of the capable shear stresses at 5 mm and 7.5 mm displacement. The mean values of both τ_u and τ_r, for each series and temperature level separately, are listed in Table II. Furthermore, the corresponding reduction coefficients defined as the ratio of the shear strength at high temperature to the shear strength at room temperature are also given in Table II.

First of all, the results at room temperature reveal that the measured bond stresses (1.84 - 2.27 N/mm²) are much higher than the design value of 0.55 N/mm² given by EN 1994-1-1 for concrete-filled circular hollow sections. Furthermore, a comparison with elderly tests on CFT specimens at room temperature [1] - where τ_r-values between 0.48 and 0.72 N/mm² were obtained - identifies distinctively higher bond strength for the here investigated CFTES specimens.

Comparing the ultimate shear strength τ_u at room temperature in relation to the corresponding composite surface for each series, it can be concluded that for smaller composite surfaces, τ_u is higher. In contrast, the bond strength τ_r reveals the lowest value for series II with the smallest composite surface.

The τ-u-curves show significantly different characteristics for the three series (see Fig. 2-4). In doing so, the curve shape is in general similar at room temperature and at high temperature for each series. The curves of series I show a slight decrease or even a plateau after reaching the maximum load. In contrast, the specimens of series II reveal a noticeable drop after the ultimate shear strength is exceeded and for further displacements considerably lower load is necessary. The τ-u-curves recorded for series III show a similar behavior to those of series I.

The test data clearly identify a significant reduction of the transferable shear stresses for high temperatures. In doing so, those specimens at 300 °C (blue curves) resisted higher loads than those at 400 °C (green curves) and 500 °C (red curves). Using mean values for τ_u and τ_r for room temperature and each high temperature level separately, Table II reveals that both τ_u and τ_r show similar reduction coefficients for the investigated temperature levels. It is remarkable that those coefficients are in a range between 0.12 and 0.37, thus indicating a significant reduction of shear and bond strength for high temperatures (63 - 88 % reduction related to room temperature). This reduction certainly needs to be considered in the design of CFTES columns.

The specimens of series HT II (and thus an increased concrete cover) reach the highest ultimate shear stresses for 20 °C and 300 °C. Concurrently, the specimens of series II reveal the lowest bond strength compared to the other two series (see Table II). Furthermore, series HT II shows strictly decreasing τ_u and τ_r with increasing temperature. Obviously, the struts that arise within the concrete due to the three-dimensional stress states are more distinctive for a higher concrete cover. Once the

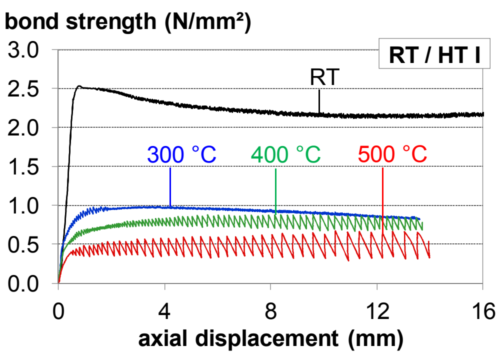

Figure 2. Bond strength-displacement-curve of push-out tests of series I.

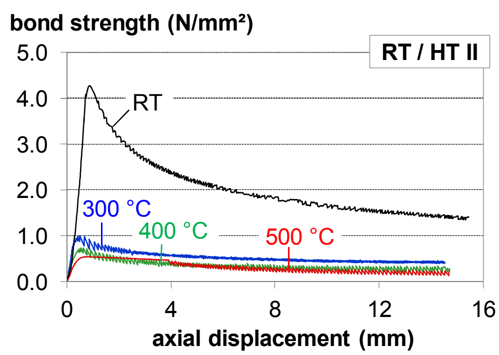

Figure 3. Bond strength-displacement-curve of push-out tests of series II.

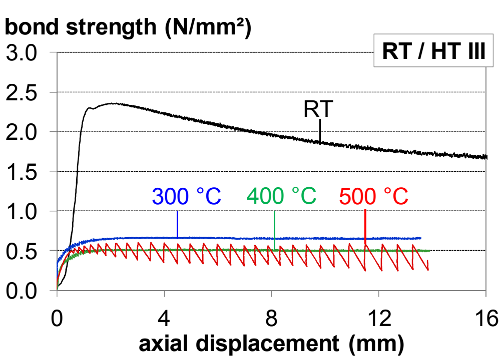

Figure 4. Bond strength-displacement-curve of push-out tests of series III.

TABLE II. MEAN ULTIMATE SHEAR AND BOND STRENGTH.

	Temp (°C)	$\tau_{u,mean}$ (N/mm²)	$\tau_{r,mean}$ (N/mm²)	$\tau_{u,HT}/\tau_{u,RT}$	$\tau_{r,HT}/\tau_{r,RT}$
I	20	2.58	2.27	-	-
	300	0.90	0.80	0.35	0.35
	400	0.74	0.63	0.29	0.28
	500	0.71	0.64	0.28	0.28
II	20	4.00	1.84	-	-
	300	1.23	0.61	0.31	0.33
	400	0.62	0.36	0.16	0.20
	500	0.49	0.35	0.12	0.19
III	20	2.31	1.98	-	-
	300	0.61	0.56	0.26	0.28
	400	0.62	0.61	0.27	0.31
	500	0.78	0.74	0.34	0.37

ultimate load is exceeded, this effect becomes less dominant and other effects mainly influence the composite behavior for greater displacements.

The phenomenon of decreasing τ_u and τ_r with rising temperature - but less distinctive - is also found for series HT I. Only for series HT III there is no obvious dependency of τ_u and τ_r on the cross-sectional temperature.

Furthermore, it is conspicuous that for both series I and III (having the same concrete cover) the displacement behavior of the steel core along the concrete changes at higher temperatures. At room temperature as well as at 300 °C, the steel core undergoes a steady displacement through the concrete, whereas for higher temperatures such as 400 °C and especially 500 °C the core moves unsteadily and erratically. This effect arises due to the different thermal elongations of concrete and steel. For 300 °C, the thermal elongation of steel is larger than the one of concrete. Consequently, the steel core widens radially more than the concrete ring. Thus, pressure arises in the inner interface and the load transfer is supported by the higher thermal strain of steel. This effect reduces with increasing temperature. In a temperature range around 450 °C the effect reverses so that the thermal elongation of concrete becomes larger than the one of steel. Hence, the concrete ring gradually separates from the steel core and the normal pressure disappears. As a consequence, the displacement behavior of the steel core is more dependent on macrolocking-effects - such as unroundness or conical shape. This dependency results in erratic τ-u-curves for the push-out tests. In contrast, microlocking-effects, which mainly depend on the roughness of the two adjacent surfaces, are of minor interest for temperatures higher than 400 °C.

NUMERICAL INVESTIGATIONS

A three-dimensional model of the specimens has been set up in Abaqus using C3D8RT volume elements. The analysis comprised of a heating step (for HT-series only) and sequentially a linearly imposed displacement of the steel core. For the simulation of the HT-tests, a homogenous temperature of 300 °C, 400 °C and 500 °C respectively, was specified through the specimen. Boundary conditions were applied to the bottom of the steel tube and concrete, reproducing the bearing in the test setup. The thermal material properties and constitutive models were adopted from EN 1994-1-2, applying the measured steel and concrete strength.

Previous investigations as well as the presented tests reveal, that the usually observed composite behavior of CFT and CFTES columns can properly be defined by three parameters (see Fig. 5, left): First, the joint stiffness K of the ascending branch characterizes the elastic behavior before plastic displacements are imposed between the two adjacent surfaces. Second, the maximum shear stress criterion τ_{max} identifies the damage initiation within the joint and defines the change between elastic behavior and residual deformations. Third, the damage evolution D defines the frictional behavior of the two surfaces sliding along each other. The implementation of the mechanical interaction between steel and concrete in Abaqus was realized defining *cohesive behavior* for the elastic branch as well as a *damage* formulation implying an initiation criterion based on *maximum nominal stresses*.

The numerical definition of interaction between two surfaces is a simplified reproduction of the real effects - implicitly including the effects of micro- and macro-scale imperfections. Furthermore, a criterion defining that interaction is active for two adjacent surfaces, is necessary in numerical models. Due to the different thermal elongation of steel and concrete, it is therefore necessary to either permit a certain gap between the two surfaces without influencing the imposed composite behavior or to suppress the radial thermal elongation to keep the surfaces in contact during the entire analysis. Avoiding both possibilities would result in a separation of the cross-sectional parts during the analysis and thus no mechanical interaction would be active.

The measured data of the τ-u-curves and thus the basis for the parameters K, τ_{max} and D, already imply all effects that arise due to the different thermal elongations of the two materials. Hence, they imply the actual normal stresses or even detachment of the surfaces. Consequently, the radial component of the thermal elongation can be neglected as all effects are included in the temperature-dependent formulation of K, τ_{max} and D, provided that the surfaces are in contact.

The mean values of K and τ_{max} derived from the test data are summarized in Table III separately for each temperature level. It is obvious, that the stiffness at room temperature exceeds the stiffness at high temperatures in all test series. For the majority of the tests, the stiffness steadily decreases with increasing temperature. The influence of temperature on the joint stiffness is thereby higher for smaller composite surfaces. In addition, the values indicate that the major reduction in stiffness occurs up to 300 °C, whereas for higher temperatures the reduction is less distinctive.

The recalculated values of the damage initiation criterion of maximum shear strength τ_{max} reveal the same scatter as the joint stiffness in terms of high temperatures and joint surface. At that, the definition of τ_{max} differs for some tests from the ultimate shear strength τ_u of the experimental data. In contrast to the usual shape of τ–u-curves as shown in Fig. 5 (left), some of the tests exhibit a curve shape with continuously rising shear strength for increasing displacements. Thus, τ_u corresponds to large displacements for those tests. Since the parameter τ_{max} defines the end of the elastic behavior, it is nevertheless necessary to define the damage initiation in a range of small displacements. It was decided that the maximum measured shear strength up to 1 mm displacement is taken as the damage initiation criterion. For most tests, τ_u is reached for displacements smaller than 1 mm anyway and thus is equal to τ_{max}. Only for those tests with rising τ-u-curves, the maximum measured shear strength below 1 mm is applied as the initiation criterion τ_{max} for the numerical analysis.

The reproduction of higher shear strength for greater displacements is nevertheless possible by adjusting the damage evolution for those tests. In Abaqus, the damage

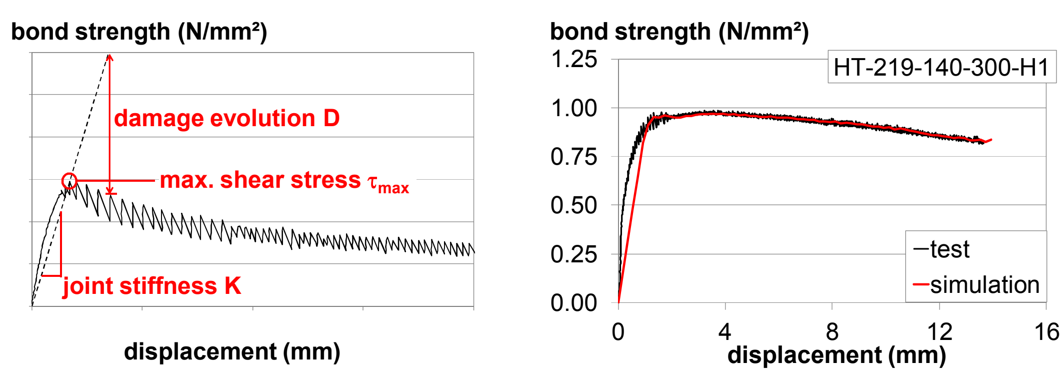

Figure 5. Parameter definition for numerical interaction formulation (left), test data and numerical simulation of push-out-test HT-219-140-300-H1 (right).

TABLE III. MEAN VALUES OF MAXIMUM SHEAR STRENGTH τ_{max} AND JOINT STIFFNESS K FOR DEFINITION OF INTERACTION IN NUMERICAL ANALYSIS.

Series	Maximum shear strength τ_{max} (N/mm²)				Joint stiffness K (N/mm²/mm)			
	20 °C	300 °C	400 °C	500 °C	20 °C	300 °C	400 °C	500 °C
RT/HT I	2.49	0.70	0.50	0.50	3.19	0.75	0.52	0.55
RT/HT II	4.00	1.23	0.62	0.49	6.13	2.48	0.97	0.72
RT/HT III	2.21	0.51	0.51	0.70	2.24	0.56	0.54	0.78

evolution D is defined as a reduction of the shear strength, referred to an idealized elastic behavior within the joint (compare definition in Fig. 5, left). Hence, all values for D are in a range between 0 (elastic behavior) and 1 (no shear strength).

To validate the numerical model and the applied material and interaction properties, several tests have been recalculated based on their specific K, τ_{max} and D values. Exemplarily, one sample of the validation is shown in Fig. 5, right. Since the stiffness is a constant value, the elastic branch is linear and marginally overestimates the displacement until damage is initiated. The following branch is in very good accordance with the measured τ-u-data. Eventually, the model is able to reproduce the real composite behavior in very good consistence.

Applying the mean values for K and τ_{max} as specified in Table III as well as a corresponding damage evolution that is based on the performed tests and related to the mean value of K, all test series have been analyzed for each temperature level (see Fig. 6). Especially for the test series at room temperature the simulations show a good accordance. As the scatter of the τ-u-curves of the high temperature tests is a bit wider, the numerically calculated curves identify an intermediate behavior. However, the calculations also reveal the temperature-dependency of the composite behavior in terms of stiffness, maximum shear strength and slope. Applying the recalculated K, τ_{max} and D to the numerical model, it is possible to reproduce the composite behavior and thus the performed push-out tests in a realistic manner.

CONCLUSION AND OUTLOOK

The presented experimental and numerical investigations quantify transferable shear stresses in concrete-filled tubular columns with embedded massive steel core (CFTES columns). Applying an innovative test setup, shear stresses are measured at different temperature levels for the first time. The recorded τ-u-curves reveal significantly reduced ultimate shear strength and bond strength for high temperatures (reduction of 63-88 %). Nevertheless, the curve shape remains similar for each test series separately, whereby significant dependencies are identified in terms of composite surface and concrete cover. Using the presented numerical model, it is possible to reproduce the experimentally observed τ-u-behavior in a realistic manner.

The presented results have been achieved for homogenous temperatures through the specimen. However, in case of a real fire, this state is not existing. It is reasonable that transient temperature fields with higher outer and lower inner temperatures support the separation of concrete and steel core due to different thermal elongations of the cross-sectional parts. In this case, it becomes more realistic that no contact

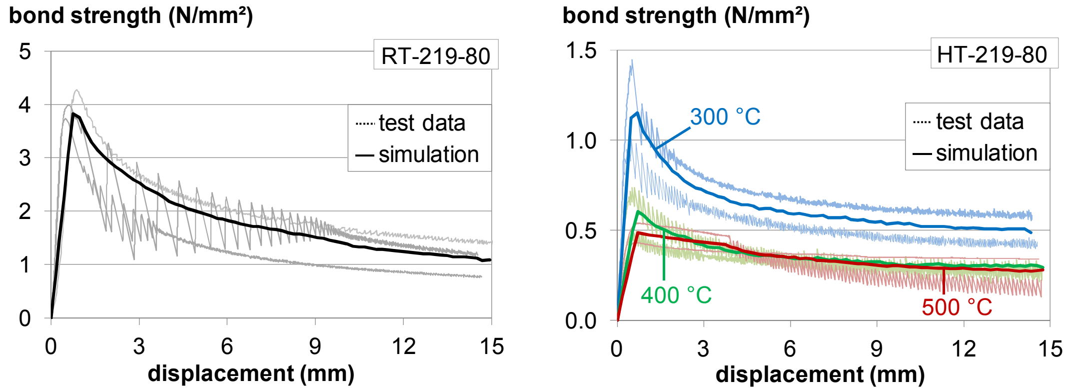

Figure 6. Measured and simulated τ-u-curves of push-out tests of series II at room temperature (left) and high temperature (right).

pressure is active between concrete and steel core. Considering that, it is expected that the bond strength is lower for CFTES columns subjected to a transient temperature field than for homogenous temperatures. The phenomenon of changing composite behavior in CFTES columns subjected to transient heating is objective of current research studies at the Institute for Steel Construction. Preliminary studies identified a distinctive reduction of ultimate shear and bond strength for stub columns with a transient temperature field and therefore support the theoretical approach.

Since the derivation of design recommendations was the aim of the research project, the experimental data have been appropriately processed. The test data at room temperature reveal significantly higher shear strength of CFTES columns than the established value for CFT columns of 0.55 N/mm² given by EN 1994-1-1. Applying the procedure given in EN 1990 for the determination of design values, the design value for CFTES columns would amount to 0.90 N/mm² and could be considered in further evolutions of the code. Due to the significant reduction in shear strength in the experimental campaign, it is however recommended to neglect shear stresses in simplified methods for high temperature design. If advanced methods implying three-dimensional stress states are applied, the temperature-dependent shear stresses can be adopted similar to the present paper, considering that they are only valid for homogenous temperatures.

REFERENCES

1. Roik, K.H. 1984. "Investigations on the composite action between steel profile and concrete in columns of residential constructions," Final Report (in German), Institute for Structural Engineering, Ruhr-Universitaet Bochum, Bochum.
2. Shakir-Khalil H. 1993. "Resistance of concrete-filled steel tubes to pushout forces," *The Structural Engineer*, 71(13): 234-243.
3. Roeder C.W., Cameron B. and Brown C.B. 1999. "Composite action in concrete filled tubes," *Journal of Structural Engineering*, 125(5): 477-484.
4. Qu X., Chen Z., Nethercot D.A., Gardner L., Theofanous M. 2015. "Push-out tests and bond strength of rectangular CFST columns," *Steel and Composite Structures*, 19(1): 21-41.

ACKNOWLEDGEMENTS

The presented work is part of the European RFCS-research project FRISCC ("Fire resistance of innovative and slender concrete filled tubular composite columns") and was kindly funded by the European Commission (Grant No. RFSR-CT-2012-00025).

Numerical Analysis of the Fire Performance of Innovative Steel-Concrete Composite Columns

ANA ESPINOS[a], MANUEL L. ROMERO[a] and DENNIS LAM[b]

ABSTRACT

Previous investigations have revealed the limited fire resistance of concrete-filled steel tubular (CFST) columns in applications where the slenderness is important. Innovative solutions are therefore sought to help improving the performance of this typology of composite columns in the fire situation. This paper aims at designing strategies for maximizing the fire resistance of CFST columns using innovative solutions such as double-tube sections, embedded HEB profiles or embedded steel cores. Additionally, the fire performance of such columns may be enhanced by using high strength steels (HSS). In this paper, a numerical model is developed and, after being validated against experimental results available in the literature, it is used for conducting a parametric study. Different steel grades are considered for the inner profiles, in order to investigate the influence of HSS. Through the results of the parametric study, the fire performance of the different cross-sectional geometries is compared, and recommendations are given for enhancing the fire resistance of CFST columns.

1. INTRODUCTION

The premature failure of slender CFST columns when exposed to fire has been highlighted in previous investigations by the authors [1, 2]. Therefore, solutions are needed for improving the fire performance of this typology of composite columns.

In this paper, different innovative sections are studied, which may solve the limitations of traditional CFST columns, such as double-tube columns (CFDST), embedded HEB profiles (CFST-HEB) or embedded massive steel cores (CFSTES), where the inner profiles are protected from the direct exposure to the fire by the outer concrete ring.

Additionally, high strength steels (HSS) – with yield strength over 460 MPa – are acquiring an increasing popularity in the construction industry, owing to their excellent mechanical properties. The advantages of HSS opens a new range of possibilities regarding their application in CFST columns, where they can result of great utility to solve the problem of the limited fire resistance of slender members. The enhancement in fire resistance obtained by using HSS is also investigated in this paper.

[a]Concrete Science and Technology Institute (ICITECH), Universitat Politècnica de València, Valencia, Spain

[b]Faculty of Engineering & Informatics, University of Bradford, Bradford, United Kingdom

2. DESCRIPTION AND VALIDATION OF THE NUMERICAL MODEL

2.1. General description of the numerical model

A three-dimensional numerical model (Figure 1) is developed in this work by means of the general purpose nonlinear finite element analysis package ABAQUS [3]. This numerical model had been previously used by the authors with satisfactory results for simulating the fire behaviour of CFST columns [4], having been validated against an extensive series of experimental results. The main features of the numerical model can be found in the referred work. The numerical model is additionally validated in this paper for CFDST, CFST-HEB and CFSTES sections, by comparison with experimental results from the literature.

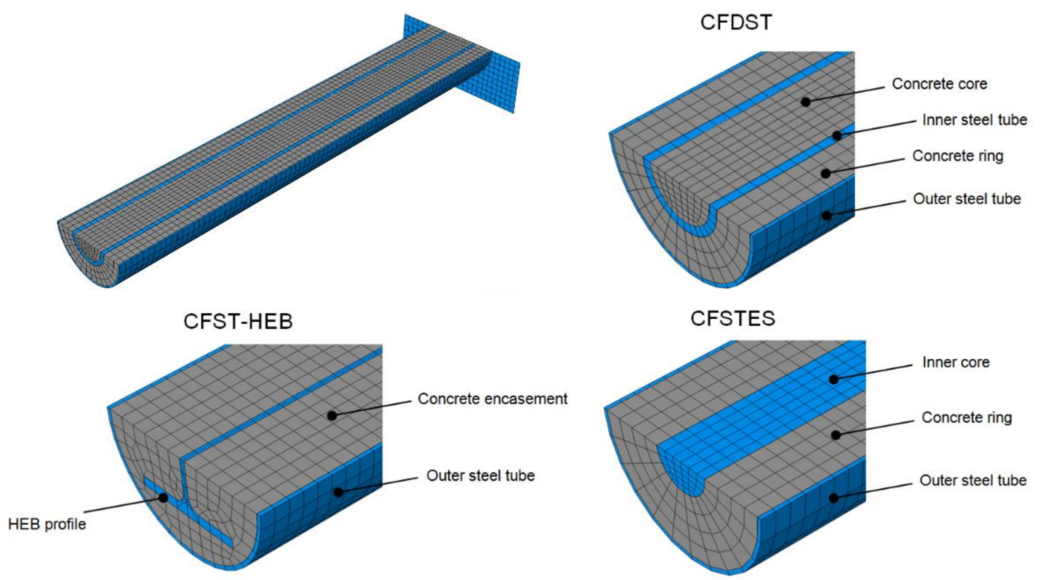

Figure 1. Finite element mesh for the different type of columns analysed.

2.2. Validation of the numerical model for normal strength steel

In this section, the described numerical model is validated against experimental tests on the three types of sections studied: double-tube columns (CFDST), CFST columns with embedded HEB profiles (CFST-HEB) and CFST columns with embedded steel core (CFSTES). The columns used for the comparison are summarized in Table I.

In the first instance, the numerical model is validated for concrete-filled double-skin and double-tube columns (CFDST).

TABLE I. INPUT DATA OF THE COLUMN SPECIMENS USED FOR VALIDATION.

a) CFDST								
Specimen	D_o **(mm)**	t_o **(mm)**	f_{yo} **(MPa)**	f_{co} **(MPa)**	D_i **(mm)**	t_i **(mm)**	f_{yi} **(MPa)**	f_{ci} **(MPa)**
C200-3-30-C114-8-00 [5]	200	3	300	46	114.3	8	377	-
C200-3-30-C114-8-30 [5]	200	3	332	46	114.3	8	403	45
C200-6-30-C114-3-00 [5]	200	6	407	43	114.3	3	343	-
C200-6-30-C114-3-30 [5]	200	6	377	44	114.3	3	329	42
CC2 [6]	300	5	320	$38^{(2)}$	125	5	320	-
CC3 [6]	300	5	320	$38^{(2)}$	225	5	320	-

b) CFST-HEB						
Specimen	**D_o (mm)**	**t_o (mm)**	**f_{yo} (MPa)**	**Inner profile**	**f_{yi} (MPa)**	**f_c (MPa)**
3A [7]	219.1	5	420	HEB120	375	35
4A [7]	200	5	510	HEB120	375	35
c) CFSTES						
Specimen	**D_o (mm)**	**t_o (mm)**	**f_{yo} (MPa)**	**D_{core} (mm)**	**$f_{y,core}$ (MPa)**	**f_c (MPa)**
SP1 [8]	133	4	$235^{(1)}$	60	$355^{(1)}$	$25^{(2)}$
SP2 [8]	219.1	4.5	$235^{(1)}$	110	$355^{(1)}$	$25^{(2)}$
SP3 [8]	219.1	4.5	$235^{(1)}$	110	$355^{(1)}$	$25^{(2)}$
SP4 [8]	219.1	4.5	$235^{(1)}$	150	$355^{(1)}$	$25^{(2)}$
CFSTES [9]	219.1	4.5	308.2	140	349	27.5
d) CFST-HSS						
Specimen	**D_o (mm)**	**t_o (mm)**	**Rebars**	**f_y (MPa)**	**f_s (MPa)**	**f_c (MPa)**
C4 [10]	355.6	12	8ϕ18	822	546	55.1

(1) nominal values, (2) cube strength

Experimental results are available from previous investigations by the authors [5], as well as from a previous research from Lu et al. [6], see Table Ia. For the case of CFST columns with embedded HEB profile (CFST-HEB), the experimental results from Dotreppe et al. [7] are used for validation, see Table Ib. The numerical model for sections with embedded steel core (CFSTES) is validated against the experimental results reported by Neuenschwander et al. [8] and Schaumann and Kleiboemer [9], see Table Ic. Figure 2 shows a comparison between the numerical and experimental axial displacement curves for some of the column specimens used for validation. It can be seen that there was a good agreement for both the own tests [5] and those from the literature [6-9]. The failure time was well captured, although the numerical model predicted a higher axial displacement than that measured in the test in the experiments from Dotreppe et al. [7] and Neuenschwander et al. [8]. This difference in axial displacement may be attributed to the impossibility to reproduce with precision the different test setups, given the various uncertainties within the reported test data – i.e. heating condition along the length of the column, degree of axial and rotational restraint at the column ends, deviation of the nominal value of the load eccentricity, etc.

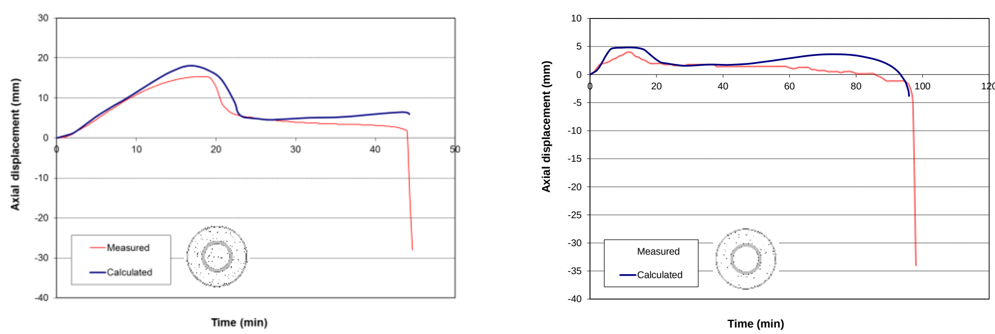

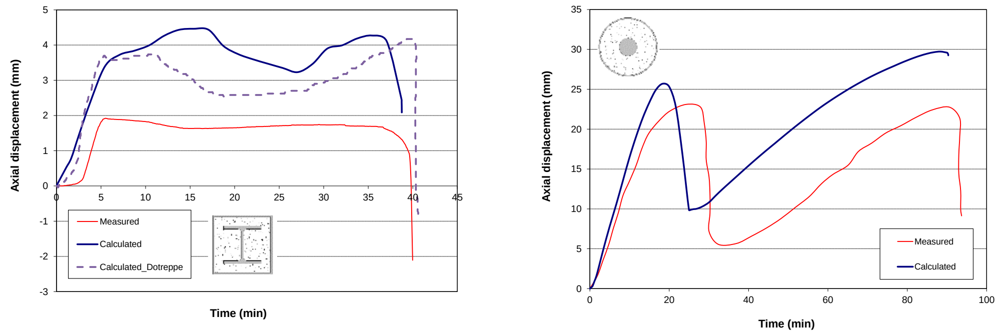

Figure 2. Comparison between numerical simulations and experimental axial displacement curves: a) C200-6-30_C114-3-30 [5], b) CC2 [6], c) 4A [7], d) SP1 [8].

2.3. Validation of the numerical model for high strength steel

After an extensive literature review on composite sections using high strength steel (HSS), only one fire test was found, performed by Tondini et al. [10] on a CFST column where the hollow steel section was made of HSS. That test specimen is used in this research for validating the numerical model for its use with HSS. The measured properties of the materials, as well as the rest of input data, are given in Table Id. For modelling the behaviour of HSS at elevated temperatures, the shape of the constitutive laws given in EN1993-1-2 [11] was used, together with the reduction factors proposed by Qiang et al. [12] for HSS. It can be seen in Figure 3 that the numerical model predicts well the fire behaviour of CFST columns with HSS, with a good estimation of the axial displacement along the fire exposure time, capturing well the elongation of the outer steel tube and its subsequent yielding and shortening due to thermal degradation.

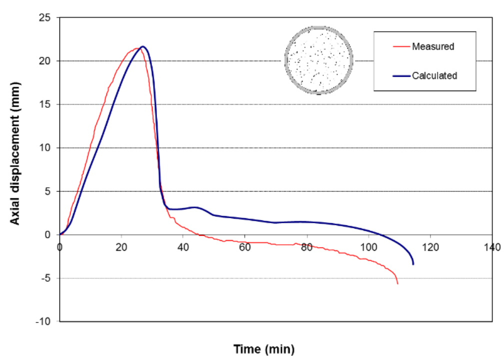

Figure 3. Validation of the numerical model for HSS, specimen C4 from Tondini et al. [10].

3. PARAMETRIC STUDY

A parametric study was carried out in order to analyse the interest of using the innovative sections proposed in this paper for improving the fire performance of CFST columns. An initial CFST section of 273×12.5 mm was chosen as a reference, and the amount of steel employed by that section was used to generate other three innovative sections with inner profiles (CFDST, CFST-HEB and CFSTES). The different sections studied in the parametric study can be seen in Figure 4, while their geometrical and mechanical features are summarized in Table II. The column specimens were chosen to have exactly the same quantity of steel split into the two profiles (inner + outer) – i.e. same total steel cross-sectional area –.

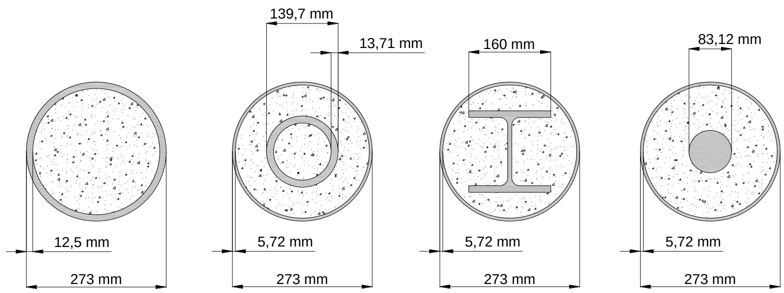

Figure 4. Cross-sectional dimensions used in the parametric studies: a) CFST; b) CFDST; c) CFST-HEB; d) CFSTES.

The length of the columns was 3240 mm and pinned-pinned boundary conditions were used in all the numerical simulations, resulting in a relative slenderness of 0.5 in the case of the reference CFST column. The steel grade of all the outer tubes was S355, while C30 concrete was used for the encasement. A concentric axial load of 1408.80 kN was applied to all the columns, corresponding to a 30% of the maximum capacity of the CFST column at room temperature.

TABLE II. DETAILS OF THE COLUMNS ANALYSED IN THE PARAMETRIC STUDY.

Specimen	**Outer profile**	**Inner profile**	f_{yo} **(MPa)**	f_{yi} **(MPa)**	$\bar{\lambda}$	$N_{b,Rd}$ / $N_{b,Rd}$**(CFST)**	μ **(%)**	**Time (min)**
CFST	273x12.5	-	355	-	0.50	1	0.30	28
CFDST-01	273x5.72	139.7x13.71	355	355	0.59	0.97	0.31	77
CFDST-02	273x5.72	139.7x13.71	355	460	0.63	1.06	0.28	94
CFDST-03	273x5.72	139.7x13.71	355	690	0.69	1.25	0.24	120
CFDST-04	273x5.72	139.7x13.71	355	960	0.76	1.45	0.21	141
CFST-HEB-01	273x5.72	HEB160	355	355	0.60	0.96	0.31	47
CFST-HEB-02	273x5.72	HEB160	355	460	0.63	1.05	0.28	57
CFST-HEB-03	273x5.72	HEB160	355	690	0.70	1.24	0.24	71
CFST-HEB-04	273x5.72	HEB160	355	960	0.77	1.44	0.21	86
CFSTES-01	273x5.72	ϕ83.12	355	355	0.63	0.95	0.32	36
CFSTES-02	273x5.72	ϕ83.12	355	460	0.66	1.04	0.29	37
CFSTES-03	273x5.72	ϕ83.12	355	690	0.73	1.22	0.25	37
CFSTES-04	273x5.72	ϕ83.12	355	960	0.81	1.41	0.21	37

3.1. Influence of the cross-sectional geometry

In the first instance, only columns using normal strength steel S355 at the inner profiles were compared, in order to study the effect of the geometry alone.

The four columns were analysed by means of the previously described numerical model. The results of the simulations are shown in Figure 5 in the form of axial displacement versus time curves, measured at the top end of the columns. Besides, the values of the different failure times are given in Table II. As it can be seen, the reference CFST column presented a very limited fire resistance of only 28 minutes. The CFSTES solution lengthened the failure time slightly, up to 36 minutes (CFSTES-

01). In turn, with the CFST-HEB solution, using an inner HEB160 profile, the fire resistance of the column was increased up to 47 minutes (CFST-HEB-01).

Finally, if the steel tube was split into two tubes, generating the CFDST column with the ticker tube in the inner part of the section, the fire resistance was significantly improved to 77 minutes (CFDST-01). Therefore, it is proved that a good strategy for enhancing the fire resistance of traditional CFST columns is to split the outer steel tube into two tubes, using most of the steel in the inner profile, which is thermally protected by the concrete encasement, delaying its degradation at elevated temperatures. Note that these solutions make use of the same amount of steel and concrete, whilst maintaining the same external dimensions of the columns.

This strategy for enhancing the fire resistance of CFST columns can be thought as an alternative to applying external protection with intumescent coatings or paintings. By splitting the outer tube into two profiles, moving most of the amount of steel to the inner part of the section, the resisting profile results "internally" protected by the surrounding concrete and, what is more, its capacity at elevated temperature can be improved by increasing the inner steel grade, without changing the external appearance of the column as well as being maintenance free.

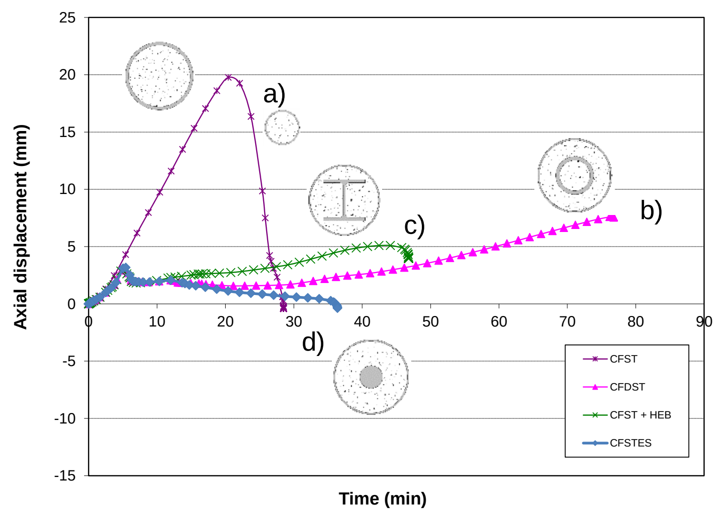

Figure 5. Comparison between the fire response of the different cross-section configurations studied, using S355 steel: a) CFST; b) CFDST; c) CFST-HEB; d) CFSTES.

3.2. Influence of the steel grade of the inner profiles

The fire resistance of these innovative solutions can be further increased by using high strength steels (HSS) for the inner profiles. In order to investigate the effect of using HSS, the yield strength of the inner profiles was varied for each of the cross-sections studied, using steel grades S460, S690 and S960, alongside the already used S355. The results obtained by upgrading the steel grade of the inner profiles to S460, compared to the previous simulations using S355 steel, can be seen in Table II for all the geometries studied. For the CFSTES column, only a marginal increment was found. However, in the case of the CFST-HEB, the fire resistance increased from 47 to 57 minutes (CFST-HEB-02 vs CFST-HEB-01). Finally, for the CFDST column, a noticeable increase from 77 to 94 minutes (CFDST-02 vs CFDST-01) was obtained.

If the grade of the inner steel tubes is further increased to S690 or S960, the increase in the fire resistance is more noticeable, reaching fire resistance times of 120 and 141 minutes (CFDST-03 and CFDST-04) for the case of the CFDST column, or 71 and 86 (CFST-HEB-03 and CFST-HEB-04) for the CFST-HEB column. A general comparison is shown in Figure 6 for S960 steel in the inner profiles, superimposed with the reference of the results for S355. It can be seen that a significant enhancement is obtained for the CFDST column. However, in the case of the CFSTES column, no benefit is observed by increasing the strength of the embedded steel core, as due to its reduced diameter, its slenderness is too high and hence it is unable to sustain the load on its own after the rest of the section has degraded.

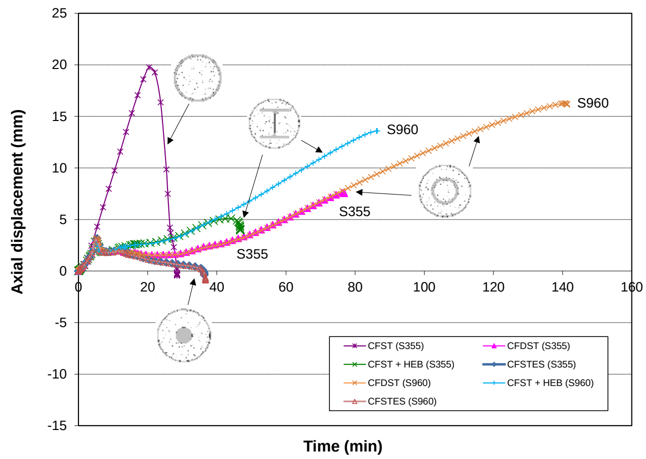

Figure 6. Comparison between the fire behaviour of the cross-section configurations studied, using different steel grades and equal steel area (S355 vs S960).

4. SUMMARY AND CONCLUSIONS

This paper presented a numerical study for investigating the fire behaviour of innovative steel-concrete composite columns using inner steel profiles, in order to propose strategies for enhancing the fire resistance of traditional CFST columns. A finite element model was developed and validated for the different types of sections studied. The influence of the cross-sectional geometry and the use of HSS at the inner profiles over the fire endurance of the columns was assessed through a parametric study.

It was proved that a good strategy for enhancing the fire resistance of traditional CFST columns is to split the outer steel tube into two profiles using most of the steel in the inner profile, which is thermally protected by the concrete encasement.

If the steel grade of the inner profiles is increased by using HSS, for the same steel usage, both the load-bearing capacity of the columns at room temperature and their fire resistance are enhanced, although it must be taken into account that this comparison was performed under constant applied axial load and therefore the utilization level decreases for increasing steel grades. Moreover, the differences in cost related to using HSS at the inner profiles should be evaluated.

ACKNOWLEDGEMENTS

The authors gratefully acknowledge the financial support given by Universitat Politècnica de València for providing the funding for the first author's stay as a visiting fellow at the School of Engineering of the University of Bradford.

The authors would also like to express their sincere gratitude to the Spanish "Ministerio de Economía y Competitividad" for the help provided through the Project BIA2012-33144, from which some of the experimental results have been used in this work for validation of the numerical model.

REFERENCES

1. Espinos, A., Romero, M.L., Serra, E. and Hospitaler, A. 2015. "Circular and square slender concrete-filled tubular columns under large eccentricities and fire", *Journal of Constructional Steel Research*, 110:90-100.
2. Espinos, A., Romero, M.L., Serra, E., Hospitaler, A. 2015. "Experimental investigation on the fire behaviour of rectangular and elliptical slender concrete-filled tubular columns", *Thin-Walled Structures*, 93:137-48.
3. ABAQUS. 2014. "Abaqus/ Standard version 6.14 user's manual, vols. I – III", Pawtucket, Rhode Island: Hibbit, Karlsson & Sorenson, Inc.
4. Espinos, A., Romero, M.L., Hospitaler, A. 2010. "Advanced model for predicting the fire response of concrete filled tubular columns", *Journal of Constructional Steel Research* 66(8–9):1030-1046.
5. Romero, M.L., Espinos, A., Portoles, J.M., Hospitaler, A., Ibañez, C. 2015. "Slender double-tube ultra-high strength concrete-filled tubular columns under ambient temperature and fire", *Engineering Structures*, 99:536-45.
6. Lu, H., Han, L., Zhao, X. 2010. "Fire performance of self-consolidating concrete filled double skin steel tubular columns: Experiments", *Fire Safety Journal*, 45(2):106-115.
7. Dotreppe, J.C., Chu, T.B., Franssen, J.M. 2010. "Steel hollow columns filled with self-compacting concrete under fire conditions" in *Proceedings of the 3rd Congress of the International Federation for Structural Concrete (FIB) and PCI Conference*, Washington DC, USA.
8. Neuenschwander, M., Knobloch, M., Fontana, M. 2013. "Fire tests of concrete-filled circular hollow section columns with solid steel core" in *Proceedings of the VII International Composite Construction*, Palm Cove Cairns, Queensland, Australia.
9. Schaumann, P., Kleiboemer, I. 2015. "Experimental investigations on the thermal and mechanical behaviour of composite columns with massive steel core in fire" in *Proceedings of the 1st International Fire Safety Symposium (IFireSS)*, Coimbra, Portugal.
10. Tondini, N., Hoang, V.L., Demonceau, J.F., Franssen, J.M. 2013. "Experimental and numerical investigation of high-strength steel circular columns subjected to fire", *Journal of Constructional Steel Research*, 80:57-81.
11. CEN. 2005. "EN 1993-1-2, Eurocode 3: Design of steel structures, Part 1.2: General rules – Structural fire design", Brussels, Belgium: Comité Européen de Normalisation.
12. Qiang, X. 2013. "Behaviour of high strength steel endplate connections in fire and after fire. Doctoral thesis", Delft, Netherlands: Delft Academic Press.

Experimental Investigation on Axially and Rotationally Restrained Circular and Elliptical Concrete-Filled Hollow Columns Subjected to Fire

JOAO PAULO C. RODRIGUES and LUIS LAIM

ABSTRACT

This paper presents the outcomes of an experimental investigation on the performance of axially and rotationally restrained concrete-filled hollow columns subjected to fire. The specimens were uniformly exposed to a standard fire curve and the critical time (fire resistance), the failure temperature and the respective failure modes were assessed. The paper also includes a comparison of the behavior of these columns under both axial and rotational restraint with identical columns under axial restraint only. The primary test parameters take into account in this research work were the column slenderness, the type of cross-section (circular and elliptical) and the restraint level imposed by a surrounding steel frame to the column in test. Finally, the results of this research study showed mainly that the fire resistance of identical columns under low load levels may be not significantly affected by the stiffness of the surrounding structure, except for low rotational restraint levels and high slenderness values.

Keywords: fire resistance, concrete-filled, hollow columns, axial restraint, rotational restraint.

1. INTRODUCTION

Concrete-filled steel tubular (CFST) columns are gaining increasing usage in practice owing to their excellent structural performance and ease of construction. Extensive research has been conducted on the behavior of CFST columns at ambient temperature [1-4]. Several observations can be made from these investigations. For instance, as the concrete strength increases the effects of the bond of the concrete and the steel tube may become more critical. In other words, for normal concrete strength, the reduction on the axial capacity of a CFST column due to bonding may be negligible, but for high-strength concrete, the variation between CFST columns with

ISISE – Institute Sustainability and Innovation on Structural Engineering, University of Coimbra, Portugal.
jpaulocr@dec.uc.pt, phone:+ 351 239797237; fax:+ 351 239797123

the inner surface of the steel tube non-greased and greased may be 17% [1]. Other interesting point to note is that EN 1994-1.1:2004 [5] predictions for circular axially and eccentrically loaded CFST columns with single curvature bending may be on the safe side, whereas for columns in double curvature bending those predictions may be on the unsafe side [2]. In addition, in columns which fail essentially by local buckling, when the concrete strength increases the confinement effect of the concrete core decreases, as well as when the tube diameter to wall thickness ratio increases [3]. Note that, the diameter of the steel tube has the most significant effect on both the ultimate axial load and the corresponding axial shortening of the circular CFST columns [4].

Since fire safety is also one of the key aspects of structural design, it is essential to develop a full understanding of the fire performance of CFST columns. Some experimental and numerical research has been carrying out to investigate the fire performance of these columns in the last years. Examples of this are the research works of Espinos et al. (2010) [6], Moliner et al. (2013) [7] and Pagoulatou et al. (2014) [8]. The most important outcome to be stressed from the literature is that the EN 1994-1.2:2005 [9] simple calculation model may lead to unsafe results for pinned-pinned columns under concentric axial loads and to highly conservative results for eccentric loads [6 and 7]. This simple calculation model may produce high errors for columns which do not make use of reinforcing bars, but it may give accurate predictions for bar-reinforced columns [7]. Note that the concrete filling offers an attractive practical solution for providing fire protection to steel hollow columns without any external protection, since the fire resistance of this type of columns may be between 30 and 60 minutes when the load level is 20% of the respective design value of the buckling load at room temperature [10] in contrast to the bare steel hollow columns where their fire resistance is commonly less than 30 minutes [11].

On the other hand, most of the studies did not take into account the interaction between the column and the surrounding building structure. The response of these columns when inserted in a building structure is different than when isolated [12]. Therefore, this paper will present and discuss the results of nine fire resistance tests on axially loaded CFST columns with restrained thermal elongation. The testing column was placed in the center of a three-dimensional frame in order to investigate the separate and combined effects of the axial and rotational stiffness imposed by the surrounding structure to the column. Lastly, other important goals of this research work were also to evaluate the influence of the cross-sections (circular and elliptical sections) and the slenderness of this kind of columns on their fire resistance.

2. EXPERIMENTAL TESTS

2.1. Test Specimens

Two different types of composite columns were selected for this study: circular and elliptical columns (Fig. 1). All columns were made of hollow steel profiles completely filled with reinforced concrete. All reinforcing bars used in the test specimens were made of B500 structural steel and all specimens present a similar concrete composition with calcareous aggregate and C25/30 class. All steel profiles were 3.15 m tall and made of S355 structural steel. Prior to concrete casting, the longitudinal steel reinforcement bars and a steel hook were welded at a steel plate, measuring 450 mm x 450mm x 30 mm, which was then welded to the section extremity of the steel tube as well. After concrete curing, it was checked that the concrete surface was level with the steel tube at the top. Note that the longitudinal steel reinforcement bars were a little bit longer than the steel tube so that both ends of these bars were welded to the steel end plates of the columns. Hence, some holes in the top end plate of the columns had to be made.

For each specimen the transversal reinforcement was performed by 8 mm diameter stirrups with a spacing of 150 mm until about 800 mm from the supports, and with a spacing of 200 mm in the central part. The concrete covering related to the stirrups for all test columns was about 25 mm. For each type of column, two different cross-sections were used for the circular columns (two different slenderness) and one for the elliptical columns. Therefore, the circular hollow steel sections were 193.7 mm (CC194) and 273.0 mm (CC273) in diameter and the elliptical ones were 320 mm long and 160 mm wide (EC320). The widest circular specimens had eight longitudinal steel reinforcing bars, four of which were 16 mm in diameter and the others were 10 mm, and the respective steel tube had a 10 mm wall thickness; whereas the narrowest specimens had four longitudinal steel reinforcing bars with 12 mm in diameter and a steel tube with a 8 mm wall thickness. On the other hand, the elliptical specimens had four longitudinal steel reinforcing bars with 20 mm in diameter and a steel tube with a 12.5 mm wall thickness.

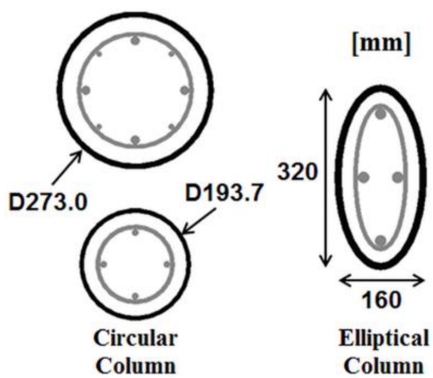

Figure 1. Scheme of the cross-sections of the tested columns.

2.2. Test Set-up

Figure 2 illustrates some views of the experimental system used in the fire resistance tests of CFST columns, in which all the components are labelled. The experimental set-up comprised a two dimensional (2D) reaction steel frame (1) and a three dimensional (3D) restraining steel frame (2) adaptable for different levels of stiffness in order to simulate the axial and rotational restraint provided by a surrounding structure to a CFST column in fire. The 2D reaction frame was composed by two HEB500 columns with 6.6m in height and by one HEB600 beam with 4.5m in length using M24 steel grade 8.8 bolts in the connections. To achieve the desired levels of stiffness of the surrounding structure with the purpose of imposing axial and rotational restraint to the thermal elongation of the CFST columns, a 3D restraining frame with four HEB300 columns and four HEB400 beams (2 on the top and 2 on the bottom, arranged orthogonally) was assembled. Note that the stiffness could be modified every time the position of the columns or the height of the beams cross-section was changed. During these experimental tests, only the position of the columns was different. For this case study, three different restraint levels of the surrounding structure were imposed to the columns: i) a 30 kN/mm axial restraint to their thermal elongation; ii) a 30 kN/mm axial restraint and a 94615 kN.m/rad rotational restraint; iii) a 110 kN/mm axial restraint and a 131340 kN.m/rad rotational restraint, corresponding the two last ones to a 6 and 3m span of the 3D restraining frame's beams, respectively. This restraining system intended to reproduce the actual boundary conditions of a CFST column when inserted in a real building structure. The connections between the peripheral columns and the upper beams of the restraining frame were performed with M27 grade 8.8 threaded rods. A hydraulic jack of 3MN capacity in compression (3) was hung on the 2D reaction frame (1) and controlled by a servo hydraulic central unit W+B NSPA700/DIG3000 (4) and, beneath this one, a load cell of 2 MN capacity in compression was mounted in order to monitor the applied load during all tests. The tested columns (5) were placed in the center of the 3D restraining frame and properly fitted to it (at each end plate) with four M24 steel grade 8.8 bolts, simulating semi-rigid end support conditions. Only axial restraint was also imposed by this surrounding structure to the columns by means of pin-ended supports. Hence, steel semi-spheres covered with a layer of Teflon (in order to reduce friction) were placed between the 3D restraining frame and the specimens. Note that this type of connection only works in compression, so this is why a huge steel safety box was built (6). Additionally, above the specimen a 3MN compression load cell was mounted (7) to monitor the axial restraining forces generated in the CFST columns during the whole test. Regarding the thermal action, the specimens were heated by means of a vertical modular electric furnace (8) which was programmed to reproduce the standard fire curve ISO 834 [13].

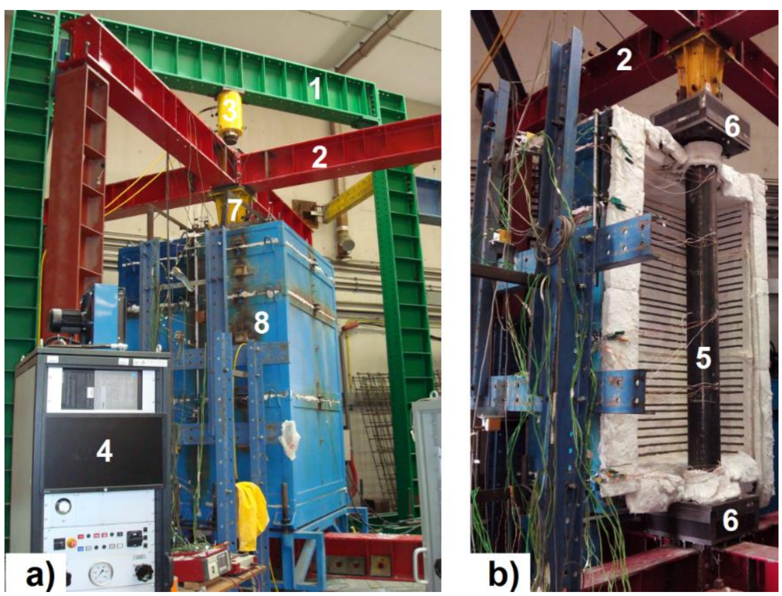

Figure 2. General (a) and detailed (b) view of the experimental set-up.

2.3. Test Procedure

Nine full-scale fire tests on CFST columns were conducted under transient state fire conditions. Three of which were performed on columns under a 30 kN/mm axial restraint to their thermal elongation and without rotational restraint (CC194-30ka-PP, CC273-30ka-PP and EC320-30ka-PP), three others under both a 30 kN/mm axial restraint and a 94615 kN.m/rad rotational restraint (CC194-30ka-SR, CC273-30ka-SR and EC320-30ka-SR), and the others under both a 110 kN/mm axial restraint and a 131340 kN.m/rad rotational restraint (CC194-110ka-SR, CC273-110ka-SR and EC320-110ka-SR). Hence, to achieve the goals of this investigation, these experimental tests were basically performed in two stages: loading and heating stage. The specimens were first axially loaded up to the target force under load control at a rate of 2.5 kN/s. The load level applied on the columns, P_0, was 30% of the design value of the loadbearing capacity of the columns at ambient temperature, calculated in accordance with the methods proposed in EN 1994-1.1:2004 [5]. This loading intended to simulate a common serviceability load of a CFST column inserted in a real building structure. Finally, the heating stage was started after the desired load was reached. Thus, the specimens were uniformly heated up in such a way that the average temperature in the furnace followed as closely as possible the ISO 834 standard fire curve [13]. During the heating period, the load was kept constant until the specimen failed. The failure criterion adopted in this paper was based on the load-bearing capacity of the columns, in other words, a column was considered to have failed when it could no longer support the initial applied load. Therefore, the critical time (fire resistance) in these tests corresponded to the time when the axial restraining forces in the column returned to the value of the initial applied load ($P / P_0 = 1$).

2.4. Results and Discussion

In Figure 3 it is presented, for instance, the evolution of temperatures in a circular cross-section at mid-height of the tested column CC273-110ka-SR, as well as the respective furnace temperature. Although the furnace temperature was higher than 700ºC for over 30 minutes, the temperature in the column core (T_C1) and on the longitudinal steel reinforcing bars (T_S1) did not exceed 150 and 200ºC, respectively. This means that the loadbearing capacity loss of the CFST columns was essentially due to deterioration of mechanical properties of the steel from the tubular profile and of concrete between the tube and the rebars. From 30 minutes of test run, the temperature in steel tube followed nearly the furnace temperature, with the difference between them being greater than 10% but less than 20%. A large thermal gradient was then observed from the surface to the core center of the CFST column (from T_S2 to T_C1), reaching temperature differences around 700ºC. Note that great part of this gradient was concentrated near the surface of the column, where the difference between the thermocouples T_S2 and T_S1 at mid-height was as an example about 618ºC for the circular column (CC273-110ka-SR) at the ending of the test.

The curves shown in Figures 4 and 5 are typical of the relative axial restraining force (P / P_0) vs time curves for columns subjected to fire. As it can be seen, these curves had nearly the same trend but they may differ in the values and their rates depending on the studied parameters, especially on the slenderness, axial restraining level and boundary conditions. These curves show clearly that the higher the stiffness of the surrounding structure, the higher the maximum axial restraining forces generated in the columns was. For instance, when the minimum axial restraint was used, the maximum axial compression force, P_{max}, in the circular columns increased approximately 34% of the applied load, and 72% for the maximum axial restraint (fig. 4a). It is quite interesting to observe that the failure in the circular columns appeared earlier than the elliptical columns. The fire resistance of the column CC194-110ka-SR (relative slenderness equal to 0.58) was about 31 minutes (fig. 4a), whereas it was about 40 minutes for the column EC320-110ka-SR (relative slenderness equal to 0.69) (fig. 4b), corresponding to an increase of 28%, in spite of their similar section factors (about $20m^{-1}$) and of the great difference in their relative slenderness, i.e., a higher difference is expected for those columns with identical slenderness. In addition, it seems that the fire resistance of the CFST columns did not change significantly with the stiffness of the surrounding structure. In the worst case study, the fire resistance of the column CC194-30ka-SR (relative stiffness equal to 0.05) was about 35 minutes, whereas it was about 31 minutes for the column CC194-110ka-SR (relative stiffness equal to 0.17) (fig. 4b), corresponding to a slight decrease of about 10%.

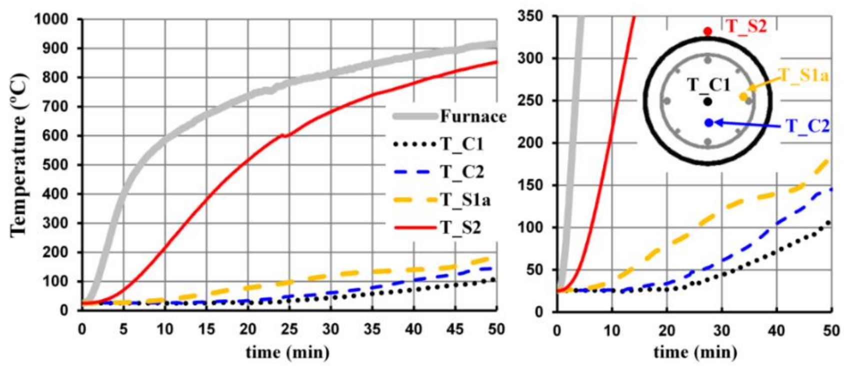

Figure 3. Evolution of temperature at mid-height of the tested column CC273-110ka-SR.

Still note that the order of magnitude of restraint in real buildings is usually of the order of magnitude of 2-3% [13] and it is expected that the fire resistance of the columns remains constant for any degree of restraint higher than 17% [14]. Anyway, this may be possible at the expense of the rotational restraint, as it can be seen in Figure 5. This one shows that the fire resistance of the column EC320-30ka-SR (relative slenderness equal to 0.69) was 42.5 minutes, whereas it was 33.4 minutes for the column EC320-30ka-PP (relative slenderness equal to 0.85) (fig. 5b), corresponding to a decrease of 22%. However, this beneficial effect of the rotational restraint may depend on the column slenderness. In fact, for a relative slenderness less than 0.7 (column CC194-30ka-PP) the effect of the rotational restraint was neglected (fig. 5a), except for the maximum axial restraining force generated in the columns during the heating where it presented a lower value in the pin-ended columns.

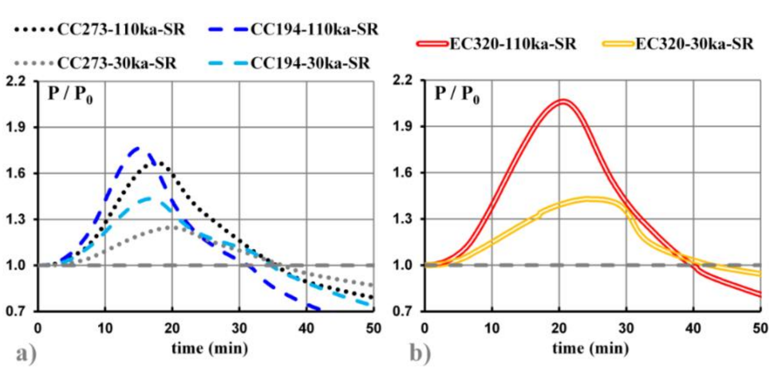

Figure 4. Evolution of the relative axial restraining forces generated in semi-rigid end columns with circular (a) and elliptical-shaped (b) sections.

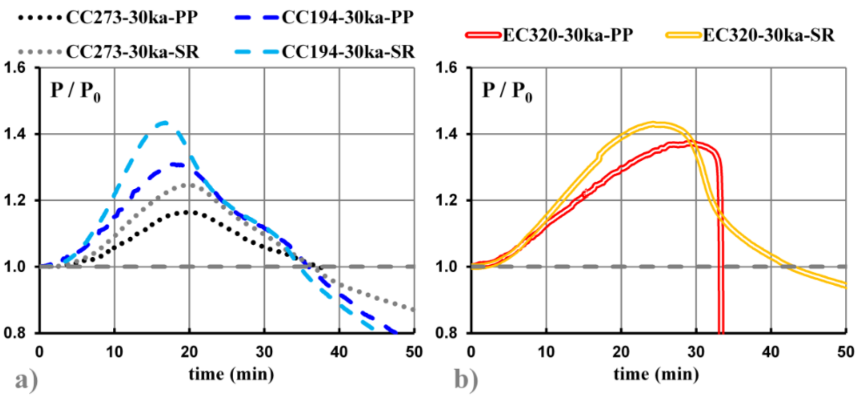

Figure 5. Evolution of the relative axial restraining forces generated in columns with circular (a) and elliptical-shaped (b) sections and with different boundary conditions.

2.5. Columns after Test

Figure 6 shows, for instance, the main views of the failure modes of the tested columns EC320-110ka (a) and EC320-30ka-PP (b). It was observed that the tested specimens all failed by compression or global flexural buckling (fig. 6). The absence of local buckling in the tested columns can be explained by the fact that the steel tubes were filled with concrete. This concrete is therefore beneficial as it not only provides thermal insulation but also prevents local buckling of the steel tube.

Figure 6. Deformed semi-rigid ended (a) and pin-ended (b) columns with elliptical-shaped section after fire test.

3. CONCLUSIONS

This paper presented and discussed the results of an experimental investigation into the behavior of concrete-filled hollow columns under fire conditions and with different restraining conditions to their thermal elongation, including axial restraint only and combined axial and rotational restraint. The results of this research study showed mainly that the fire resistance of identical semi-rigid ended columns may be not significantly affected by the stiffness of the surrounding structure. When the axial and rotational restraint increased respectively from 30 to 110 kN/mm and from 94615 to 131340 kN.m/rad, the fire resistance of the CFST columns decreased 10% in the maximum. On the other hand, because of the rotational restraint and the concrete filling, the tested columns under standard fire behaved in a relatively ductile manner and tests proceeded in a smooth and controlled way until failure. However, columns under axial restraint only may exhibit sudden instability depending on their slenderness at least.

REFERENCES

1. Giakoumelis, G., and D. Lam. 2004. "Axial capacity of circular concrete-filled tube columns", *Journal of Constructional Steel Research,* 60: 1049-1068.
2. Zeghiche, J., and K. Chaoui. 2005. "An experimental behaviour of concrete-filled steel tubular columns", *Journal of Constructional Steel Research*, 61: 53-66.
3. Gupta, P.K., S.M. Sarda, and M.S. Kumar. 2007. "Experimental and computational study of concrete filled steel tubular columns under axial loads", *Journal of Constructional Steel Research*, 63: 182-193.
4. Chitawadagi, M.V., M.C. Narasimhan, and S.M. Kulkarni. 2010. "Axial strength of circular concrete-filled steel tube columns - DOE approach", *Journal of Constructional Steel Research*, 66: 1248-1260.
5. EN 1994-1.1:2004, Eurocode 4 - Design of composite steel and concrete structures - Part 1-1: General rules and rules for buildings, CEN, Brussels.
6. Espinos, A., M.L. Romero, and A. Hospitaler. 2010. "Advanced model for predicting the fire response of concrete filled tubular columns", *Journal of Constructional Steel Research*, 66: 1030-1046.
7. Moliner, V., A. Espinos, M.L. Romero, and A. Hospitaler. 2013. "Fire behavior of eccentrically loaded slender high strength concrete-filled tubular columns", *Journal of Constructional Steel Research,* 83: 137-146.
8. Pagoulatou, M., T. Sheehan, X.H. Dai, and D. Lam. 2014. "Finite element analysis on the capacity of circular concrete-filled double-skin steel tubular (CFDST) stub columns", *Engineering Structures*, 72: 102-112.
9. EN 1994-1.2:2005, Eurocode 4 - Design of composite steel and concrete structures - Part 1-2: General rules - Structural fire design, CEN, Brussels.
10. Romero, M.L., V. Moliner, A. Espinos, C. Ibanez, and A. Hospitaler. 2011. "Fire behavior of axially loaded slender high strength concrete-filled tubular columns", *Journal of Constructional Steel Research*, 67: 1953-1965.
11. Oliveira, T.A.C.P. 2013. "Fire resistance of composite columns made of concrete filled circular hollow sections and with restrained thermal elongation", Ph.D. thesis, Faculty of Sciences and Technology of University of Coimbra, Coimbra, Portugal, p. 207.
12. Pires, T.A.C., J.P.C. Rodrigues, and J.J.R. Silva. 2012. "Fire resistance of concrete filled circular hollow columns with restrained thermal elongation", *Journal of Constructional Steel Research*, 77: 82-94.
13. Wang, Y.C., D.B. Moore. 1994. "Effect of thermal restraint on column behavior in a frame". In: Moore DB, editor, *4th International Symposium on Fire Safety Science*, Ottawa, IAFSS, Kashiwagi T, editor, p. 1055-66.
14. Franssen, J.-M. 2000. "Failure temperature of a system comprising a restrained column submitted to fire", *Fire Safety Journal,* 34: 191-207.

Flexural Behaviours of Reinforced Concrete Columns Confined by Circular Steel Tubes after Fire Exposure

FAQI LIU, HUA YANG and SUMEI ZHANG

ABSTRACT

The post-fire flexural behaviours of steel tube confined reinforced concrete (STCRC) columns (also known as reinforced concrete columns confined by circular steel tubes), were investigated in this paper. A 3D finite element (FE) model was developed with the program ABAQUS, using the sequentially coupled thermal-stress analysis method. A set of test data was used to verify the FE model and good agreement was achieved. The moment versus curvature curves were analysed and discussed. After that, parametric studies were performed to investigate influences of some key parameters on the flexural capacity and flexural stiffness of STCRC columns, including heating time, cross-sectional dimension, material strength, steel tube to concrete area ratio and reinforcement ratio. Simplified design methods were proposed for predicting flexural capacity and flexural stiffness of STCRC columns after exposure to ISO-834 standard fire condition.

KEY WORDS: bending; flexural capacity; flexural stiffness; post-fire; reinforced concrete columns confined by circular steel tubes; STCRC column

1. INTRODUCTION

The steel tube confined reinforced concrete (STCRC) columns, also referred as reinforced concrete columns confined by steel tubes, are a kind of composite member with outer steel tubes terminated at beam to column connections. Therefore the steel tube in STCRC columns mainly works as hoop reinforcement, maximising its confinement to the concrete and reducing the possibility of local buckling, compared with concrete-filled steel tubular (CFST) columns. Besides, the reinforced concrete beam to STCRC column connections can be designed and constructed following methods for conventional reinforced concrete structures, which overcomes the complexities of design and construction of the reinforced concrete beam to CFST column connections [1,2].

Previous studies, conducted by Tommi et al. [3-5], Aboutaha et al. [6,7], Han et al. [8,9], Liu et al. [10-12] and Yu et al. [13], all focus on the axial compression behaviour or seismic performance of steel tube confined reinforced concrete or plain concrete (STCRC or STCPC) columns at ambient temperature. Yu et al. [14] studied the pure bending behaviour of STCPC columns. Sun et al. [15,16] studied the flexural behaviour of circular and square STCRC columns. The authors are conducting a research project focusing on the post-fire behaviour of STCRC columns. As the first two parts, the post-fire behaviours of STCRC stub columns and STCRC slender columns have been studied and presented in [1] and [2], respectively. To date, no research has been reported on the post-fire flexural behaviour of the STCRC columns. Hence, it's essential to study the flexural behaviour of the STCRC column after fire exposure to provide insight of its flexural capacity and flexural stiffness.

A 3D finite element (FE) model was developed with the program ABAQUS, adopting the sequentially coupled thermal-stress analysis method. The moment versus curvature curves were analysed and discussed. After that, parametric studies were performed to identify the influences of key parameters on the flexural capacity and flexural stiffness, including heating time, cross-sectional dimension, strengths of materials, steel tube to concrete area ratio and reinforcement ratio. Then simplified design methods were proposed for predicting the flexural capacity and flexural stiffness of STCRC columns, after the ISO-834 standard fire exposure.

2. NUMERICAL MODELLING

A 3D finite element (FE) model was developed using the program ABAQUS, to investigate the flexural behaviour of STCRC columns. The most important advantage of the FE model is that the confinement effect can be modelled explicitly by defining interactive behaviour of the steel tube and concrete. Besides, the global buckling and local buckling of steel tube also can be modelled directly. The pure heat transfer analysis was conducted firstly to identify the thermal distributions of STCRC columns subjected to ISO-834 standard fire condition including the heating and cooling phases [17]. After that, the thermal analytical results were imported into the subsequent mechanical analysis to study the flexural performance of those STCRC columns. The STCRC columns were heated in an unstressed condition, which is more conservative to evaluate residual properties of concrete [18-22]. The details of the FE model can be referred in [1,2]. The 4-point loading method was employed to generate a zone of constant moment and zero shear in the FE simulation (Fig.1).

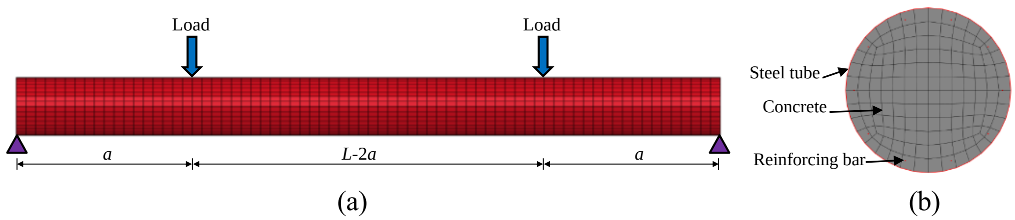

Figure 1. Finite element model of the STCRC column subjected to bending: (1) Schematic view; and (b) Cross-section.

3. VERIFICATION OF THE FE MODEL

The heat transfer model has been validated by tests of STCRC stub columns [1], STCRC slender columns [2] and square and rectangular CFST columns [23,24] subjected to ISO-834 standard fire condition. Therefore the aim of this part is to test the robustness of the FE model to analyse flexural behaviour of STCRC columns. The tests of circular steel tube confined plain concrete (STCPC) beams conducted by Yu et al. [14] were predicted with the FE model (Fig.2(a)). Besides, the CFST beams tested after fire exposure [25] were employed to test the FE model. The predictions agrees well with test results and original authors' predictions (Fig.2(b)).

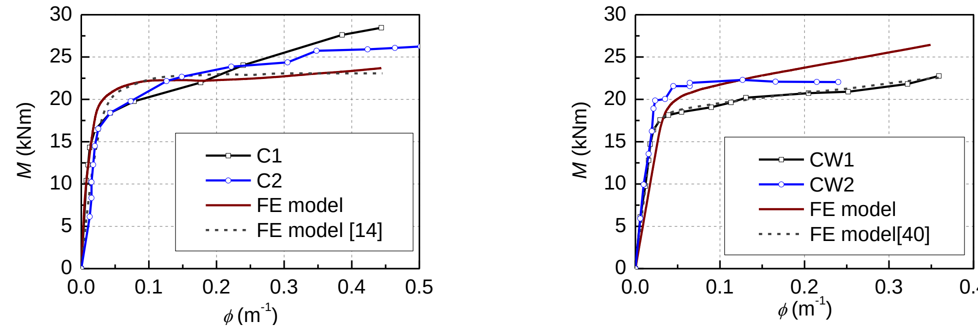

(a) (b)

Figure 2. Comparisons between predicted and tested results of: (a) STCPC beam at ambient temperature [14]; and (b) CFST beam after exposure [25].

The CFST beams tested by Wheeler and Bridge [26], Elchalakani et al. [27] and Lu et al. [28] were also employed to validate the FE model. The predicted and tested flexural capacities of those specimens are depicted in Fig.3.

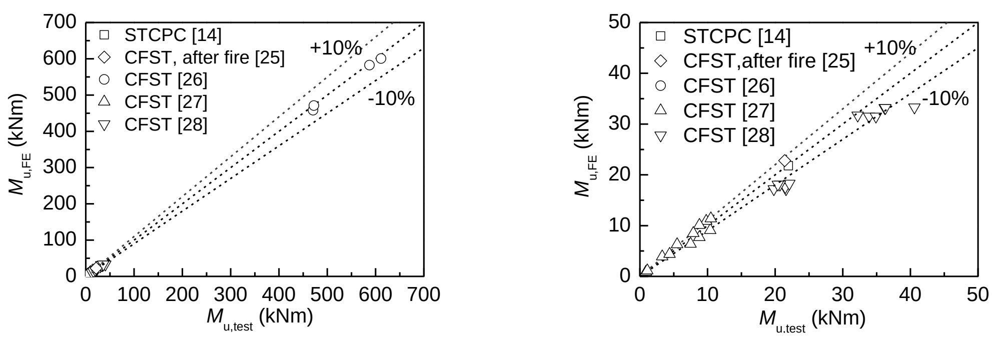

(a) (b)

Figure 3. Comparisons between FE model and test results of flexural capacities: (a) FE model and test results; and (b) partial enlargement of (a).

4. TYPICAL MOMENT VERSUS CURVATURE CURVE

The typical moment versus curvature curve is presented in Fig.4, in which point A corresponds to the initial crack of concrete, points B and C correspond to the initial yield of steel tube in the tensile and compression zone, points D and E correspond to the initial yield of reinforcement in the tensile and compression zone, and points F and G correspond to the maximum tensile fibre strain of 0.01 and 0.02. Obviously, the moment versus curvature curve can be divided into three stages: (i) elastic (OA), (ii) elastic-plastic (AF) and (iii) plastic (FG). In the elastic stage (OA), the moment increases linearly with the curvature. The elastic stage ends at point A due to the onset of the crack of the concrete, which degrades the stiffness of the STCRC column. However, the degradation of flexural stiffness is not obvious before the initial yield of steel tube in tension happens at point B. This can be attributed to the interactive behaviour between the steel tube and concrete. Since the bond and friction stress at the interactive face delay the development of crack of concrete. And the reduction of stress caused by the crack of concrete would be compensated by the increase of stress in steel tube, until the steel tube yields at point B. The decrease of flexural stiffness accelerates from the yield of steel tube in tension (point B). At point E, both the extreme fibres of steel tube in tension and compression and the extreme fibres of reinforcement in tension and compression have yielded, resulting in the dramatic reduction of flexural stiffness. When the extreme fibre tensile strain reaches 0.01 (point F), the moment tends to be stable and the curvature increases dramatically (plastic stage (FG)). The moment corresponding to the maximum fibre strain of 0.01 was defined as the flexural capacity of the STCRC column, consistent with that of the CFST columns[25,29].

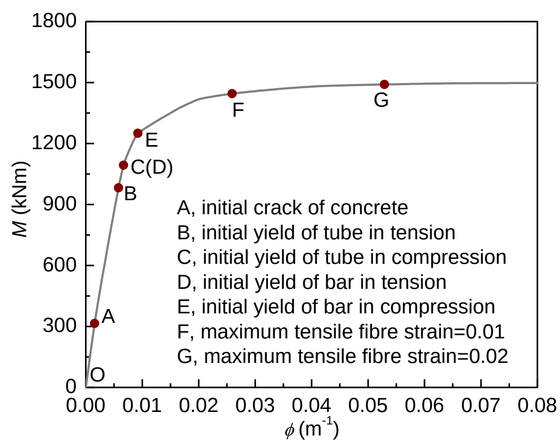

Figure 4. A typical moment versus curvature curve (t_h=60 min).

5. PARAMETRIC STUDIES AND DESIGN METHOD

Parametric studies were further conducted to investigate the influences of key parameters on the residual flexural capacities and flexural stiffness of STCRC columns after fire exposure, including the heating time, cross-sectional dimension, concrete compressive strength, yield strength of steel, yield strength of reinforcement, steel tube to concrete area ratio and reinforcement ratio. The ranges of the studied parameters are as following: D=200 - 1500 mm, t_h=0 - 180 min, f_c'=24 - 50 N/mm^2, f_y=235 - 420 N/mm^2, f_b=335 - 500 N/mm^2, α_s=2.0% - 4.0%, α_b=2.0% - 6.0%. Previous studies reveal that the shear span to depth ratio has negligible influence on the flexural behaviours of CFST columns [29], different from its influences on the conventional reinforced concrete beams. Because the outer steel tube works as continuous stirrup to resist the shear force in the shear span, resulting in less possibility of shear failure. It can be predicted that the shear span to depth ratio also has negligible influence on the flexural behaviours of STCRC columns. The shear span to depth ratio was defined to be 3.0 in the parametric study, which would be large enough to achieve the composite action.

The influences of these parameters on the residual flexural capacities of STCRC columns are depicted in Fig.5. It can be found that the residual flexural capacity decreases with increase of heating time, and increases with the increase of the cross-sectional dimension. The effect of temperature on the deterioration of flexural capacities reduces with the increase of cross-sectional dimension, because the lower temperatures would be achieved for larger cross-sectional columns, corresponding to the same heating time. The flexural capacities tend to increase approximately linearly with increase of material strength, steel tube to concrete area ratio and reinforcement ratio. These figures were not presented due to the limited space.

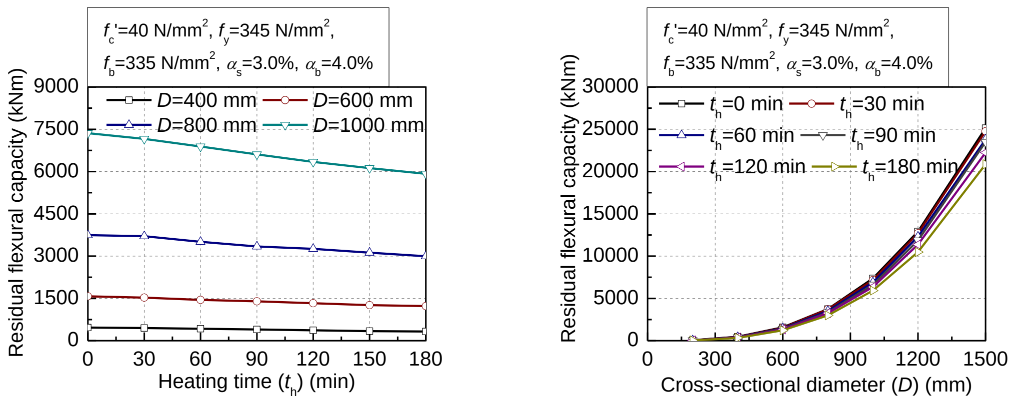

(a) (b)

Figure 5. Influences of key parameters on the residual flexural capacities of STCRC columns: (a) heating time; and (b) cross-sectional diameter.

The influences of those parameters on the flexural stiffness of STCRC columns are presented in Fig.6. As can be seen, the flexural stiffness gradually decreases with increase of heating time, while it increases significantly with the increase of cross-sectional diameter. Besides, the flexural stiffness increases approximately linearly with the increase of concrete strength, steel tube to concrete area ratio and reinforcement ratio. And these figures were not presented due to the limited space.

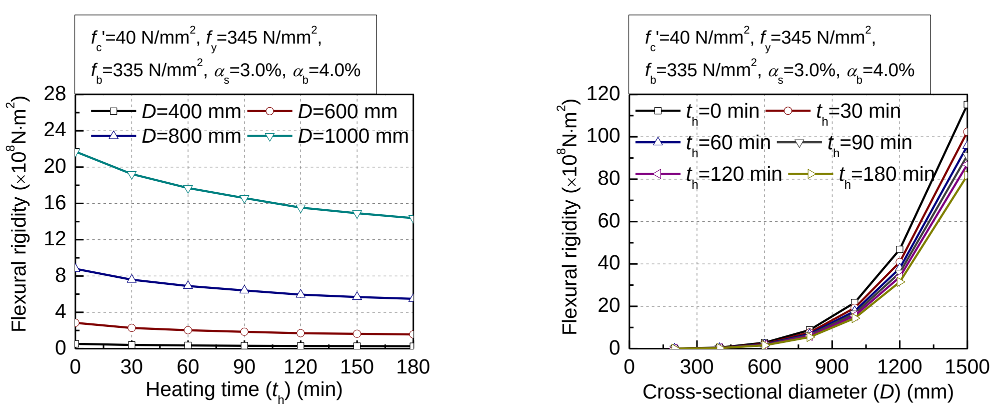

(a) (b)

Figure 6. Influences of key parameters on the flexural stiffness of STCRC columns: (a) heating time; and (b) cross-sectional diameter.

Sun et al. [15,16] proposed an equivalent stress block method to calculate the flexural capacity of STCRC columns, which utilises the stress-strain model of confined concrete to take into account the confinement effect of steel tube, and yield good predictions. In this study, the confinement effect of steel tube is also incorporated into the concrete by using confined concrete strength, consistent with the authors' previous studies on STCRC stub columns [1] and STCRC slender columns [2].

A simplified design method was proposed for predicting flexural capacities of STCRC columns, presented as follows:

$$\mathbf{M_u} = 0.7 f_{\mathbf{cc}} \mathbf{W_c} + f_{\mathbf{b}} \mathbf{W_b} \tag{1}$$

where W_c and W_b are the section modulus of concrete and reinforcement, respectively, f_b is the yield strength of reinforcement and f_{cc} is the compressive strength of confined concrete, which can be determined as follows [30]:

$$f_{cc} = \left(-1.254 + 2.254\sqrt{1 + 7.94\frac{f_r}{f_c^{'}}} - 2\frac{f_r}{f_c^{'}} \right) f_c^{'} \tag{2}$$

where the f_c' is the concrete cylinder strength, f_r is the confining stress that can be calculated as follows:

$$f_r = \frac{2t_s f_y}{D - 2t_s} \tag{3}$$

where D is the outer diameter of the cross-section, f_y and is the yield strength of steel tube and t_s is the thickness of steel tube.

The post-fire flexural capacities of STCRC columns can be determined by inducing the effect of temperature, given as follows:

$$M_{\mathbf{uT}} = \beta_{\mathbf{T}} M_{\mathbf{u}} \tag{4}$$

$$\beta_T = 1.0 - (\frac{0.025}{D} + 0.038)t_h \tag{5}$$

where β_T is a reduction factor accounting for the effect of temperature, M_u is the flexural capacity at ambient temperature and can be determined by Eq.(1), D is the cross-sectional diameter in meters and t_h is the heating time in hours.

A design method for predicting the flexural stiffness of STCRC columns after fire exposure was proposed, maintaining the same form as the formula for CFST columns given in EC4, presented as follows:

$$EI = E_{sT}I_s + E_{bT}I_b + 0.6E_{eq,cT}I_c \tag{6}$$

where

$$E_{sT} = (0.008t_h^2 - 0.05t_h + 1.0)E_s \tag{7}$$

$$E_{eq,cT} = k \times [1 - (0.42 - 0.01\frac{t_h}{D})\sqrt{\frac{t_h}{D}}]E_c \tag{8}$$

$$E_c = 4700\sqrt{f_c^{'}} \text{ N/mm}^2 \tag{9}$$

$$E_{bT} = \begin{cases} E_b & t_h \le 1.0 \\ (1.015 - 0.015t_h)E_b & 1.0 < t_h \le 3.0 \end{cases} \tag{10}$$

where I_s, I_b and I_c are the second moment of area for the steel tube, reinforcing bars and concrete, respectively; E_s and E_{sT} are the elastic modulus of steel tube before and after fire exposure, respectively; E_b and E_{bT} are the elastic modulus of reinforcing bars before and after fire exposure, respectively; E_c is the elastic modulus of concrete and $E_{eq,cT}$ is the equivalent elastic modulus of concrete after fire exposure, respectively;

k is a factor to consider the influence of delay of temperature rise, taken to be 1.0 and 0.98 for unexposed and exposed condition, respectively; D is the cross-sectional diameter in meters and t_h is the heating time in hours.

The limits of validity of the design method are: D =0.2 – 1.5 m, t_h=0 – 3 h, f_c'=24 N/mm^2 - 50 N/mm^2, f_y=235 N/mm^2 - 420 N/mm^2, f_b=335 N/mm^2 - 500 N/mm^2, α_s=2.0% - 4.0%, α_b=2.0% - 6.0%.

6. CONCLUSIONS

A FE model was developed with the program ABAQUS to investigate the flexural behaviour of STCRC columns after fire exposure. Upon validation of the FE model, parametric studies were conducted to assess the influences of some key parameters on the flexural capacity and flexural stiffness of STCRC columns. Simplified design methods were proposed for predicting residual flexural capacity and flexural stiffness of STCRC columns after ISO-834 standard fire exposure. The following conclusions can be drawn from this study:

(1) The moment versus curvature curve can be divided into three stages, elastic, elastic-plastic, and plastic. When the extreme fibre tensile strain reaches 0.01, the moment tends to be stable and the curvature increases dramatically, therefore the moment corresponding to maximum fibre strain of 0.01 can be defined as the flexural capacity of the STCRC column.

(2) The flexural capacity and flexural stiffness of STCRC columns decrease with increase of heating time, but increase with increase of cross-sectional dimension, material strength, steel tube to concrete area ratio and reinforcement ratio. The flexural capacity is more sensitive to the elevated temperature than the flexural stiffness.

(3) The proposed design methods for predicting residual flexural capacity and flexural stiffness can yield acceptable predictions for STCRC columns before and after fire exposure.

7. ACKNOWLEDGEMENT

The research presented in this paper was sponsored by the National Natural Science Foundation (NO. 51508131), Excellent Young Talents Program of Harbin Institute of Technology and Hei Long Jiang Postdoctoral Foundation; their financial support is highly appreciated.

8. REFERENCES

1. Liu, F., Gardner, L. and Yang, H., 2014. "Post-fire behaviour of reinforced concrete stub columns confined by circular steel tubes," *J CONSTR STEEL RES*, 102: 82-103.
2. Yang, H., Liu, F. and Gardner, L., 2015. "Post-fire behaviour of slender reinforced concrete columns confined by circular steel tubes," *THIN WALL STRUCT*, 87: 12-29.
3. Tomii, M., Sakino, K., Watanabe, K., Xiao, Y., 1985. "Lateral Load Capacity of Reinforced Concrete Short Columns Confined by Steel Tube," in *Proceedings of the International Speciality Conference on Concrete Filled Steel Tubular Structures*, Harbin, China, pp. 19-26.
4. Tomii, M., Sakino, K., Xiao, Y., Watanabe, K., 1985. "Earthquake Resisting Hysteretic Behavior of Reinforced Concrete Short Columns Confined by Steel Tube," in *Proceedings of the International Speciality Conference on Concrete Filled Steel Tubular Structures*, Harbin, China, pp. 119-125.

5. Sakino, K., Tomii, M., Watanabe, K., 1985. "Sustaining Load Capacity of Plain Concrete Stub Columns Confined by Circular Steel Tube," in *Proceeding of the International Speciality Conference on Concrete Filled Steel Tubular Structures*, Harbin, China, pp. 112-118.
6. Aboutaha, R.S. and Machado, R., 1998. "Seismic resistance of steel confined reinforced concrete (SCRC) columns," *STRUCT DES TALL BUIL*, 7(3): 251-260.
7. Aboutaha, R.S. and Machado, R., 1999. "Seismic resistance of steel-tubed high-strength reinforced-concrete columns," *J STRUCT ENG-ASCE*, 125(5): 485-494.
8. Han, L.H., Yao, G.H., Chen, Z.B. and Yu, Q., 2005. "Experimental behaviours of steel tube confined concrete (STCC) columns," *STEEL COMPOS STRUCT*, 5(6): 459-484.
9. Han, L.H., Qu, H., Tao, Z. and Wang, Z.F., 2009. "Experimental behaviour of thin-walled steel tube confined concrete column to RC beam joints under cyclic loading," *THIN WALL STRUCT*, 47: 847-857.
10. Liu, J. and Zhou, X., 2010. "Behavior and strength of tubed RC stub columns under axial compression," *J CONSTR STEEL RES*, 66: 28-36.
11. Zhou, X. and Liu, J., 2010. "Seismic behavior and shear strength of tubed RC short columns," *J CONSTR STEEL RES*, 66: 385-397.
12. Liu, J., Abdullah, J.A. and Zhang, S., 2011. "Hysteretic behavior and design of square tubed reinforced and steel reinforced concrete (STRC and/or STSRC) short columns," *THIN WALL STRUCT*, 49(7): 874-888.
13. Yu, Q., Tao, Z., Liu, W. and Chen, Z.B., 2010. "Analysis and calculations of steel tube confined concrete (STCC) stub columns," *J CONSTR STEEL RES*, 66: 53-64.
14. Yu, Q., Tao, Z., Chen, Z.B., Wu, Y.X., 2008. "Flexural behaviour of steel tube confined concrete members under pure bending," *ENG MECH*, 25(3): 187-193. (in Chinese)
15. Sun, Y.P., Sakino, K., 2000. "Simplified design method for ultimate capacities of circularly confined high-strength concrete columns," ACI Special Publication; 193: 571-586.
16. Sun, Y., 2008. "Proposal and application of stress-strain model for concrete confined by steel tubes," in *Proceedings of the 14th World Conference on Earthquake Engineering*, Beijing, China.
17. ISO-834, 1975. "Fire resistance tests - elements of building construction," *Switzerland: International Organization for Standardization*.
18. Abrams, M.S., 1971. "Compressive strength of concrete at temperatures to 1600 F," *ACI Special Publication*, 25: 33-58.
19. Phan, L.T., Carino, N.J., 1998. "Review of mechanical properties of HSC at elevated temperature," *J Mater Civ Eng-ASCE*, 10(1): 58-64.
20. Hertz, K.D., 2005. "Concrete strength for fire safety design," *MAG CONCRETE RES*, 57(8): 445-453.
21. Tao, J., Yuan, Y., Taerwe, L., 2010. "Compressive strength of self-compacting concrete during high-temperature exposure," *J Mater Civ Eng-ASCE*, 22(10): 1005-1011.
22. Huo, J.S., Huang, G.W., Xiao, Y., 2009. "Effects of sustained axial load and cooling phase on post-fire behaviour of concrete-filled steel tubular stub columns," *J CONSTR STEEL RES*, 65: 1664-1676.
23. Yang, H., Liu, F.Q., Zhang, S.M., Lv, X.T., 2013. "Experimental investigation of concrete-filled square hollow section columns subjected to non-uniform exposure," *ENG STRUCT*, 48: 292-312.
24. Yang, H., Liu, F.Q., Gardner, L., 2013. "Performance of concrete-filled RHS columns exposed to fire on 3 sides," *ENG STRUCT*, 56: 1986-2004.
25. Han, L.H., Huo, J.S. and Wang, Y.C., 2005. "Compressive and flexural behaviour of concrete filled steel tubes after exposure to standard fire," *J CONSTR STEEL RES*, 61(7): 882-901.
26. Wheeler, A., Bridge, R., 2006. "The behaviour of circular concrete-filled thin-walled steel tubes in flexure," in *Proceedings of the 5th International Conference on Composite Construction in Steel and Concrete V*, ASCE, Reston, Virginia, pp. 413-423.
27. Elchalakani, M., Zhao, X.L. and Grzebieta, R.H., 2001. "Concrete-filled circular steel tubes subjected to pure bending," *J CONSTR STEEL RES*, 57: 1141-1168.
28. Lu, H., Han, L.H. and Zhao, X.L., 2009. "Analytical behavior of circular concrete-filled thin-walled steel tubes subjected to bending," *THIN WALL STRUCT*, 47(3): 346-358.
29. Han, L.H., Lu, H., Yao, G.H. and Liao, F.Y., 2006. "Further study on the flexural behaviour of concrete-filled steel tubes," *J CONSTR STEEL RES*, 62(6): 554-565.
30. Mander, J.B., Priestley, M.J. and Park, R., 1988. "Theoretical stress-strain model for confined concrete," *J STRUCT ENG-ASCE*, 114(8): 1804-1826.

Experimental Study on Bond-slip between Shaped Steel and Concrete under High Temperature

YUZHUO WANG, DEJIAN XU, CHUNYANG LIU
and CHUANGUO FU

ABSTRACT

This paper presents results from an experimental study on the effect of temperature on bond strength between steel and concrete. 11 steel reinforced concrete (SRC) specimens were tested by home-made fire test furnace to evaluate bond strength under different constant high temperatures (20-600°C). Results from these tests indicate that the ultimate bond strength and the residual load decrease significantly in 20-250°C temperature range, the ultimate bond strength is much lower at high temperature and just retain 20-30% of its original property at 250°C. It is well established that the quantity of extreme slip (the slip at the ultimate bond load) at evaluate temperature is larger than that at room temperature, and fluctuate with the temperature from 1mm to 8mm. Data from tests also proves that the variation trend of bond-slip curve in 20-250°C temperature range is similar to that at room temperature, and the descending stages of bond-slip curves disappear from 300°C to 600°C. Data from the test is utilized to propose the empirical relations of bond strength and temperature.
Keywords: high temperature; steel reinforced concrete; push-out test; bond slip; steel and concrete;

INTRODUCTION

For its excellent mechanical properties, steel reinforced concrete (SRC) has been widely used in high-rise buildings. Meanwhile, fire often occurs in this kind of construction. How to improve fire resistance has received a great deal of attention since provision of appropriate fire resistance to structural members is a major design requirement.

The theoretical calculation for bearing capacity of SRC is based on the properties

Yuzhuo Wang, College of Civil Engineering, Shandong Jianzhu University, No.1000, Fengming Street, Licheng District, Jinan, 250101, China .
Dejian Xu, College of Civil Engineering, Shandong Jianzhu University, No.1000, Fengming Street, Licheng District, Jinan, 250101, China .
Chunyang Liu, College of Civil Engineering, Shandong Jianzhu University, No.1000, Fengming Street, Licheng District, Jinan, 250101, China .
Chuanguo Fu, College of Civil Engineering, Shandong Jianzhu University, No.1000, Fengming Street, Licheng District, Jinan, 250101, China .

of bond-slip between steel and concrete. Numerous studies on bond properties of steel reinforced concrete has proven that the bond-slip performance of SRC at room temperature depends on a number of parameters such as concrete strength, surface condition of steel and cross-sectional shape.

There are limited researches in the literature on the performance of bond strength both at room temperature and high temperature [1-9]. Some of notable studies are reviewed here.

By conducting 28 push-out tests on the bond of steel and concrete at room temperature, Xue Jianyang and Zhao Hongtie[1] drew the load-displacement curve based on parameters of concrete strength, surface condition of steel and cross-sectional shape. And the simplified formula was attained. Xu Youlin and Jin Weiliang established the five-part bond-slip constitutive relation as well as the bond-displacement formula of rebar and concrete by conducting 6 push-out tests[3].

B. Yu and V.K.R. Kodur[5] tested 36 NSM FRP specimens, fabricated using different types of epoxy adhesive and FRP reinforcements under the temperature of 20-400°C. Results from these tests reveal that bond strength and modulus degrades significantly in 20-200°C, only retain 20-30% of their original values at 200°C, and NSM FRP strips and rods possess negligible bond strength beyond 400°C.

Royles and P.D. Morley[6][7] carried out bond-slip test on deformed rebar and concrete at high temperatures (20°C to 750°C). Then conclusions about the performance of bond-slip were drawn, with different temperatures and different cover thicknesses under and after the elevated temperature.

In order to study the bond strength and slip behavior of SRC members after being exposed to high temperature, the statically push-out test for 18 SRC short columns after being exposed to high temperature and 3 other comparative short columns at room temperature were carried out by Li Junhua and Qiu Dongliang[8]. Based on test results, a bond-slip constitutive model for SRC member sunder this condition was proposed, and the calculating methods to ultimate bond strength, residual bond strength and their corresponding slip in this model were also put forward.

The literature review above indicates that there is limited information on the bond-slip performance of steel reinforcement concrete member at high temperature. To develop additional data on bond strength of SRC member at high temperature, a series of push-out tests were carried out. Data from these tests is utilized to develop empirical relations on variation of bond strength between steel and concrete over a wide temperature range.

PREPARATION OF TEST SPECIMENS

The experimental program consisted of 11 push-out tests on short SRC columns at various temperatures, the specimens were heated to 20°C, 50°C, 100°C, 150°C, 200°C, 250°C, 350°C, 400°C, 500°C and 600°C respectively and maintained at these temperatures until the end of the experiment.

The temperature fields of specimens are measured by built-in thermocouples. For the temperature fields uniformly distribute along the axial direction, the thermocouples were arranged only on the midsection. The locations of six measuring points and section dimension of the column and steel are provided, as shown in Figure 1. Parameters of specimens and mechanical properties of rebar and steel are tabulated in Table I and Table II.

A number of concrete blocks, of 100mm×100mm×100mm size, with short SRC columns, were all cast from one bath of concrete. They were allowed to cure under the same conditions as the short SRC columns for at least 28 days, and then taken strength tests a day before the push-out test. The modulus and compressive strength of concrete blocks are tabulated in Table III.

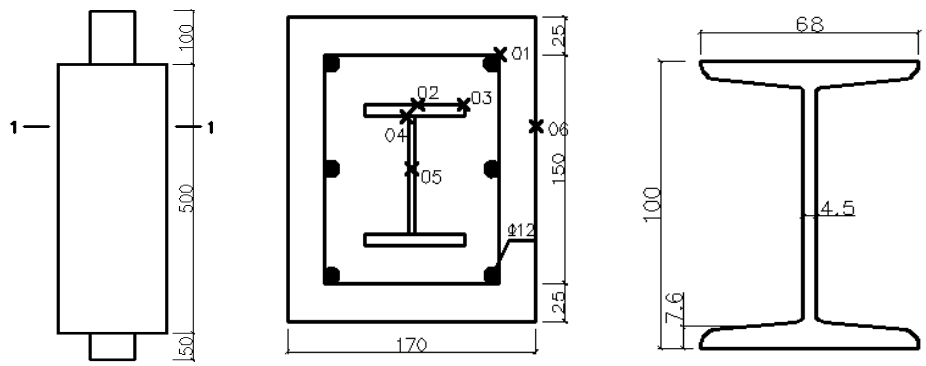

a. Specimen shape b. Section dimension and thermocouple layout c. I-steel
Figure 1. Specimen dimension, I-steel size and thermocouple layout.

TABLE I. Parameters of specimens.

Specimen	Design concrete strength f_{cu} (MPa)	Concrete cover (mm)	Anchorage length of steel (mm)	Stirrup ratio (%)	Arrangement of stirrup	Steel ratio (%)	Size b×h (mm×mm)
SRC-1~11	C40	50	500	0.22	A6@150(4)	4.2	170×200

TABLE II. The mechanical properties of steel.

Steel type	Elasticity modulus(MPa)	Strength of steel(MPa)	
		Yield strength f_y	Tensile strength f_u
A 6 HPB300 rebar	2.04×10^5	490	605
B12 HRB335 rebar	1.97×10^5	450	635
I-steel(100×68×4.5×7.6)	2.10×10^5	275	390

TABLE III. The mechanical properties of concrete.

Specimen	Elasticity modulus (MPa)	Measured strength of concrete (MPa)
SRC- 1~11	3.11×10^4	33.5

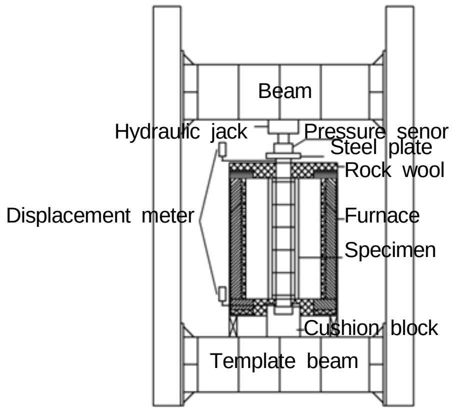

Figure 2. The loading device.

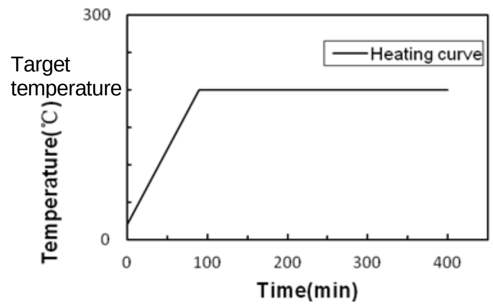

Figure 3. Heating curve.

TEST SET-UP

To undertake high temperature bond tests, a special set-up was designed and the facility is shown in Figure 2. The test equipment comprises loading machine and an electric furnace to generate high temperature. At the preparation stage of the test, the specimens were fixed as shown in Figure 2. The upper end of the short SRC column is taken as load end and the lower end, supported by U-shaped cushion block is free end. The column should always be maintained in a perfectly horizontal position to minimize onset of eccentric loading during the movement. The thermocouples in specimen are connected with the data acquisition instrument by wire covered with special insulation materials. To protect the pressure senor from high temperature and make sure the load be evenly applied, a piece of steel plate were placed between specimen and pressure senor.

During the heating test, specimen was heated to a target temperature with heating rate of 2°C/min, and then the temperature was maintained until the end of the test. The furnace temperature and temperature inside the specimen were measured by thermocouple automatically. The heating curve is shown in Figure 3.

Following the specimen attaining a target temperature, a load test was carried out through the application of load using hydraulic jack. At first, the load was applied at 1.9kN per level, then loading rate was changed to 0.98kN per level when the slip between steel and concrete occurred. To measure slip that occurred during the push-out test, two displacement meters were attached to the upper end and lower end of the specimen as indicated in Figure 2. The loading test was ended when push-out length of shaped steel exceeded 50 mm.

EXPERIMENT PHENOMENA

The specimen was heated when it was mounted and properly fixed. It can be seen that after heating for 80 min, vapor appeared from above the furnace which lasted for about 90 min. Then, following the specimen attaining a target temperature, the load was applied. At the beginning of loading stage, there was no slip between steel and concrete at both ends of specimen. With the increasing of load, the top of the steel started to slip. A few moments later, cracks appeared on the upper end of specimen near the acropodium of steel at a 45-degree angle and extended to four corners of the specimen. In the meantime, micro-cracks perpendicular to the steel flange appeared on some of the specimens. And as slip of upper end increased gradually, the steel at lower end started slipping too.

When reached ultimate load(P_u), a noise appeared and lasted to the end of test. Then the load value decreased significantly to 60%-80% of its peak value and became stable, in this condition the cracks on the both ends of specimen extended rapidly in a wider range both in width and depth. As the displacement increased, concrete spalling occurred and some of them even cracked massively, as shown in Figure 4.

Through the test, all the steels were not deformed. The color of concrete turned gray white because of high temperature, and when temperature raised continuously, it changed to light red (see Figure 5.a). The steel flange which was pushed out has a smooth surface without obvious marks of rubbing against concrete (see Figure 5.b). By contrast, there were obvious gray white abrasion marks on the web surface which were very close to the color of concrete (see Figure 5.c).

a. The lower end of SRC-1   b. The lower end of SRC-2

Figure 4. Concrete falling off.

a. The surface of SRC-7 and SRC-8   b. The flanges of steel at lower end of SRC-3 and SRC-6

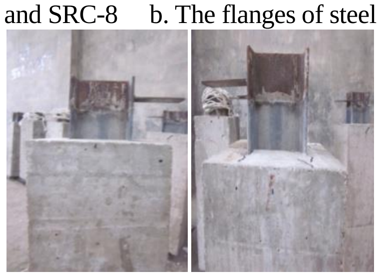

c. The webs of shaped steel at lower end of SRC-6 and SRC-7

Figure 5. Steel push-out.

Figure 6. Cracks at upper end of SRC-8 and SRC-10.

Figure 7. Cracks at lower end of SRC-2 and SRC-7.

a. Lower end of SRC-3 b. Lower end of SRC-4

Figure 8. The lower end without any cracks.

RESULTS AND DISCUSSION

Crack Patterns and Analysis

The patterns of cracks on steel reinforced concrete specimens at high temperatures are shown in Figure 6, which demonstrates the distribution of cracks on the top of the concrete. Distribution of cracks on the lower end is shown in Figure 7, but it can be seen that there is no crack on the lower end of some specimens in Figure 8.

By observing crack patterns on all the specimens, the ultimate failure mode can be classified into two forms: cracked and crack-free. The cracked form can be further divided into two patterns, as shown in Figure 9.

The first crack pattern: The cracks appear on the tip of steel flange at a 45-degree angle when the load reaches a certain level. Such cracks are found on both ends of some specimens. And cracks begin to extend to the flank of specimen gradually as the temperature increases.

The second crack patterns: This kind of crack appears on the upper end of specimens when the temperature goes beyond 250°C. But they appear randomly only on one side near the steel web at 250°C and 300°C. The cracks gradually extend to the flank of specimen beyond 300°C.

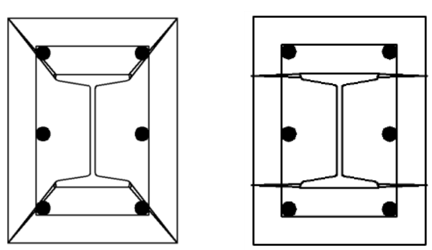

a. The first crack pattern b. The second crack pattern

Figure 9. The simplified diagram of the main components of fracture morphology.

The formation of crack on the specimens can be summarized based on their patterns:

(1) The first kind of crack appears both at room temperature and high temperature. The bond stress near the upper end gradually disappears as load applied. When relative bond-slip appears on the interface, the cement crystals are sheared off or crushed; cracks emerge on the steel tip and become more apparent with the rise of temperature.

(2) The second kind of crack often appears simultaneously with the first kind. Cracks on some specimens extend to the flank of the specimen.

(3) The cracks (shown in Figure 7) are found only on one side, mainly attribute to the uneven concrete quality. In addition, effects of the high temperature on the concrete properties also account for the irregular occurrence of cracks.

The Bond-Slip Curves of the Upper End Steel at Different High Temperatures

The load-slip curve of upper end of steel was drawn by conducting tests at different high temperatures. The record data are plotted in Figure 10.

Data plotted in Figure 10 clearly indicates the load-slip curve of the upper end of steel, it can be seen that the variation trend of the *P-S* curve of SRC at high temperature is much similar to that at room temperature and it can be roughly divided into three stages: the ascending stage, the descending stage and the residual stage.

The curves of bond-slip between steel and concrete at different temperature indicate that: (1) The variation trend of curve at high temperature is identical to that at room temperature. However, the ultimate bond load and residual bond load degrade sharply and the descending stage becomes less apparent with the rise of temperature. (2) The descending stage fades away gradually when the temperature goes beyond 250°C. (3) The extreme slip of specimen at high temperature is larger than that at room temperature, and fluctuates from 1mm to 8mm following the change of temperature.

According to previous studies, the bond strength on the contact surface of shaped steel and concrete consists of chemical cementation stress, mechanical interaction force and friction resistance, and among the three constituent parts of bond strength, chemical cementation stress accounts for a significant proportion of the bond strength. However, the cement gel in the concrete is damaged seriously due to the effect of elevated temperature that causes the loss of chemical cementation stress and ultimately led to the rapid degradation of bond strength and the increase of the extreme slippage.

The Formulas of the Tests at High Temperatures

By analyzing experimental data in Figure 10, the distribution diagram of relations between temperature and the ultimate bond load (see Figure 11) as well as that of temperature and extreme slip (see Figure 12) can be derived. In addition, the relevant calculation formulas are attainted by numerical fitting, showing the specific change rules of bond load and extreme slip between steel and concrete with the increase of temperature.

Figure 11 shows the distribution diagram of relations between temperature and the ultimate bond load. It can be seen that the ultimate bond load drops significantly in 20-250°C temperature range, and this degradation trend slows down beyond 300°C.

Based on data above, the calculation formula of ultimate bond load at high temperature is obtained through regression fitting (see 2.1):

$$P_u(t) = -31\ln(t) + 202,\ 20°C \le t \le 600°C \tag{2.1}$$

where

P_u(t), the ultimate bond load between steel and concrete when the temperature is t, kN;
t, the temperature at the contact surface between steel and concrete, °C.

Figure 12 shows the distribution diagram of relation between temperature and the quantity of extreme slip (i.e. the slip at the ultimate bond load). It can be observed that the extreme slip increases gradually and the data exhibits discrete properties with the change of temperature. Regression fitting is contributed to the calculation formula(see 2.2):

$$S_e(t) = 0.008t + 1.749,\ 20°C \le t \le 600°C \tag{2.2}$$

where

$S_e(t)$, the extreme slip when the temperature is t; mm;
t , the temperature at contact surface between steel and concrete; °C.

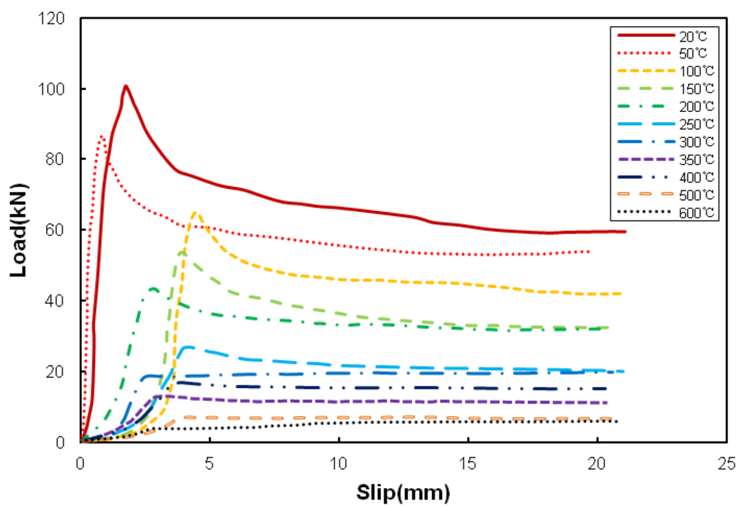

Figure 10. The *P-S* curves of tested specimens at different high temperatures.

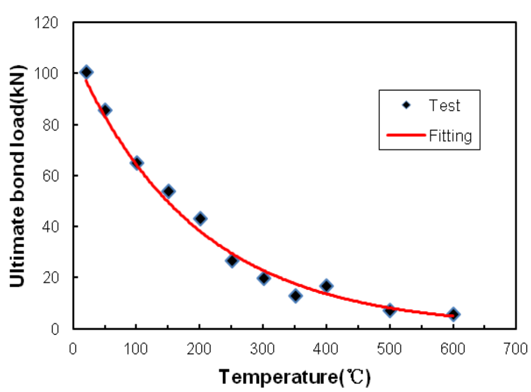

Figure 11. Relationship between temperature and ultimate bond load.

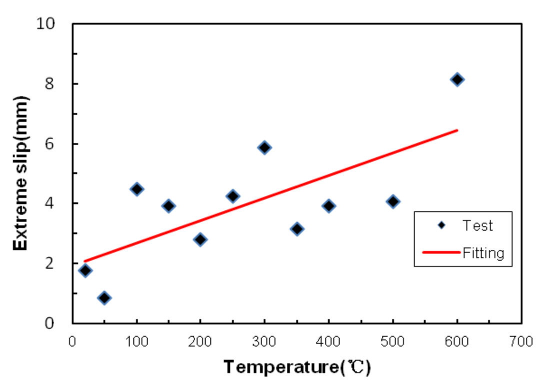

Figure 12. Relationship between temperature and extreme slip.

CONCLUSIONS

Based on the results presented in this paper, the following conclusions can be drawn:

(1) It can be seen that both ultimate bond load and the residual bond load degrade rapidly with the increase of temperature, and the degradation can be grouped into two stages. In 20-250°C temperature range, the rate of degradation reaches its peak. In 300-600°C temperature range, the rate of degradation becomes slower, and the ultimate bond load further deteriorates, only retains 6% of that at room temperature when the temperature reaches 600°C. In addition, the descending stage of the bond-slip curve disappears gradually in 300-600°C temperature range.

(2) The extreme slip of specimen at high temperature is larger than that at room temperature, and fluctuates from 1mm to 8mm along with temperature increasing.

(3) More and longer cracks appear on the specimens as the temperature increases.

(4) Due to the influence of high temperature on the material, displacement difference between lower and upper end of steel is further decreased. When the temperature of SRC specimen exceeds 250°C, the descending of bond load becomes negligible after the bond strength has already reached its peak value.

(5) The calculation formulas of relations between ultimate bond load and quantities of extreme slip at different temperatures are put forward based on the test data.

(6) The cement gel in the concrete is damaged seriously due to the effect of elevated temperature that causes the loss of chemical cementation stress and ultimately led to the rapid degradation of bond strength and the increase of the extreme slippage.

ACKNOWLEDGMENTS

The authors would like to acknowledge the National Science Foundation of China (Grant No: 51378302), the Science and Technology Development of Shandong Province, China (Grant No: 2013GSF12005), the Science and Technology Development Plan of Jinan city, China (the Innovation Plan of Universities and research institutes. Grant No: 201303085), the Research and development program of Shandong Province's university (Grant No: J11LE06), the Science and Technology project of Housing and Urban Construction Ministry (Grant No: 2013-K2-39) and Michigan State University. The authors are also grateful to the graduate students and the staff of SDJZU for their assistance in the experimental work.

REFERENCES

1. Xue Jianyang, Yang Yong and Zhao Hongtie, "Study on Push-out Test and Bond Strength of Steel Reinforced Concrete," J. Steel Structures, 2006, 21(6): 28-32.
2. Yang Yong, Xue Jianyang and Zhao Hongtie, "Analysis of Bond Strength of Steel Reinforced Concrete Structure," J. Building Structures, 2001, 31(7): 31-34.
3. Xu Youlin, Shen Wendu and Wang Hong, "Experimental Study on the Bond-Anchorage Properties of Reinforced Concrete ,"J. Journal of Building Structures,1994,15(3): 26-36.
4. Jin Weiliang and Zhao Xiyu, "Bond Constitutive Relation between Rebar and Concrete at Different Positions," J. Journal of Zhejiang University,2002, 36(1): 1-6.
5. B. Yu, V.K.R. Kodur, "Effect of High Temperature on Bond Strength of Near-surface Mounted FRP Reinforcement," J. Composite Structures, 110(2014) 88-97.

6. R. Royles and P.D. Morley, "Further Responses of the Bond in Reinforced Concrete to High Temperatures," J. Magazine of Concrete Research: Vol.35, No.124: September 1983.
7. P.D. Morleyand, R. Royles, "Responses of the Bond in Reinforced Concrete to High Temperatures," J. Magazine of Concrete Research: Vol.35, No.123: June 1983.
8. Li Junhua, QIU Dongliang and Yukai, et al, "Study on Bond-Slip Properties of Post-high-temperature Steel Reinforced Concrete," J. Engineering Mechanics, 2015, 32(2):190-200.
9. Sun Guoliang and Wang Yingjie, "Experimental Study on Axial Force Transmission on the Ends of the Rigid Concrete Column and Calculation Method," J. Journal of Building Structures,1989 (6):40-49.

METAL STRUCTURES: MATERIAL BEHAVIOR

S500M and Grade 70 Steel Grades—Material Properties Assessed through Full Scale Tests

FRANCOIS HANUS, OLIVIER VASSART, NICOLAS CAILLET and JEAN-MARC FRANSSEN

ABSTRACT

This paper presents two experimental fire tests performed at the University of Liege in the scope of an internal project supported by ArcelorMittal Global R&D and focused on the fire resistance of S460M and S500M steel grades at high temperatures. Two similar beams have respectively been subjected to fast (standard ISO curve) and slow (fixed 5°C/min heating rate) elevations of temperature under a mechanical loading kept constant. The objective of these fire tests is to provide data on the resistance of S460M and S500M steel grades in the critical temperature range [500 °C; 700 °C] through full scale tests. A comparison between the reduction factors obtained from experimental tests and those defined in European and American standards [1,2] will allow confirming that reduction factors defined in these standards also apply to S500M and Grade 70 steel grades.

INTRODUCTION

The use of high-strength steels is more and more widely used in steel and steel-concrete composite structures throughout the world. In many countries like UK, USA, Canada and in Scandinavia, the use of S355 steel grade (or Grade 50) represents more than 90% of the steel consumption in structural applications where S235 and S275 were the most commonly-used steel grades earlier. The extra cost of high-strength steels compared to normal steel grades is largely counter-balanced by design optimization (lighter sections), reduction of welding time and work on site (reduced number of welding passes), and reduction of beam and column bulk.

The S500M steel grade will be integrated into the future versions of the EN 10025-4 [2] and EN 1993-1-1 European standards [3] and the Grade 70 (yield point $\geq$

François Hanus, Long Product R&D, Arcelormittal, 66 Rue de Luxembourg, 4009, Esch-sur-Alzette, Luxembourg.
Olivier Vassart, Long Product R&D, Arcelormittal, 66 Rue de Luxembourg, 4009, Esch-sur-Alzette, Luxembourg.
Nicolas Caillet, Long Product R&D, Arcelormittal, 66 Rue de Luxembourg, 4009, Esch-sur-Alzette, Luxembourg.
Jean-Marc Franssen, Department Architecture, Geology, Environment and Constructions, University of Liege, Belgium.

485 MPa) has already been included into the A193/A193M – 15 American standard [4]. However, the use of the reduction factors for yield strength $k_{y,\theta}$ and for the slope of the linear elastic range $k_{E,\theta}$ currently defined in the EN 1993-1-2 (Table I) are limited to steel grades classified between the S235 and S460 boundaries. Similarly, the AISC code defines mechanical properties of steels at elevated temperatures only for grades up to Grade 65 [5]. These AISC laws are the same as those defined in the Eurocodes.

The EN 1993-1-2 reduction factors have been defined on the basis of experimental tests performed predominantly on mild steels (S235 steel grade) at constant elevated temperatures during the 80's and reported in [6] (steady-state tests). During the last two decades, several authors have published results of experimental tests performed on coupon tests following another testing procedure (transient tests). Schneider and Lange observed from transient tests performed on steel coupons in tension that the reduction of mechanical properties was more important for normalized rolled steels S460N than for thermomechanical rolled steels S460M [7]. Their results show that, for numerous cases, the reduction factors obtained from tests are below the recommended values of EN 1993-1-2. Qiang et al. performed investigations on the mechanical properties of S460N steels at elevated temperatures [8]. They also stated that the current EN 1993-1-2 reduction factors on yield strength could not be applied to S460N and proposed new predictive equations. Recent investigations by Knobloch also underlined that the loading rate in steady-state tests has a significant impact on the stress-strain relationships of carbon steels at elevated temperatures [9].

TABLE I. REDUCTION FACTORS FOR STRESS-STRAIN RELATIONSHIP OF CARBON STEEL AT ELEVATED TEMPERATURES [1].

T°	k_y	k_p	k_E
20°C	1.000	1.000	1.000
100°C	1.000	1.000	1.000
200°C	1.000	0.807	0.900
300°C	1.000	0.613	0.800
400°C	1.000	0.420	0.700
500°C	0.780	0.360	0.600
600°C	0.470	0.180	0.310
700°C	0.230	0.075	0.130
800°C	0.110	0.050	0.090
900°C	0.060	0.0375	0.0675
1000°C	0.040	0.0250	0.0450
1100°C	0.020	0.0125	0.0225
1200°C	0.000	0.0000	0.0000

The aim of the two tests presented in this paper is to assess the capability of stress-strain relationships presented in EN 1993-1-2 to represent at the structural level the behavior of steel beams made of high strength steel.

EXPERIMENTAL TESTS

Two experimental tests have been performed. The first one with an unprotected steel beam subjected to standard ISO-834 fire curve [10] in a gas furnace. In the second one, the steel profile was heated by electric resistances and covered by insulating blanket so that the temperature in the central part of the beam was increased with a constant rate of 5°C/min. This very low heating rate is representative of fire-protected steel beams that must satisfy to R120 requirement (increase of temperature after 2 hours close to 600°C).

Whereas the first test is representative of a qualification test performed on a loaded beam and covered by the accreditation under ISO17025 of the laboratory, the second one is closer to the better controlled conditions of a scientific experiment. The use of a controlled heating in the second test was driven by the desire to ensure a temperature distribution that is as much uniform as possible in the critical sections of the beam. In particular, the temperature differences that are observed between the upper flange and the lower flange in the gas furnace should be reduced. The behavior of the beam at any time is then influenced only by the steel properties at one temperature.

The length and the cross-section designation of the two tested specimens are respectively 4.4 m and HEB 300. The two specimens have not been extracted from the same batch and therefore exhibit different chemical and mechanical properties. During the fire tests, specimens have been heated on their 4 sides. The tested beams are simply-supported with one fixed support and one rolling support, allowing thermal elongations and longitudinal displacements induced by the beam deflections to develop. The distance between the supports is 4.2 m.

TABLE II. RESULTS OF FLANGE COUPON TEST PERFORMED AT ROOM TEMPERATURE ON SPECIMEN N°1.

REFERENCE	R_m [MPa]	R_{eH} [MPa]	A% ($5.65\sqrt{S_0}$)
NC 1327-4A	603	528	27.5

Test n°1

The mechanical loading was kept constant during the whole test and applied in the two sections situated at L/3 from each support, so that the central zone is subjected to a uniform bending moment. The total load applied to the specimen is 2 x 307 kN = 614 kN. The load ratio, defined as the ratio between the applied bending moment at mid-span and the plastic bending moment of the section, was expected to be 0.5 with yield strength equal to 460 N/mm^2. The coupon tests performed at room temperature after fire tests demonstrated that the yield strength was much higher and that the load ratio was actually equal to 0.5 x 460/528 = 0.435.

The evolution of temperature with time in the steel profile has been measured in the three sections (Figure 1). Figure 3 shows respectively temperatures measured in the web and the bottom flange.

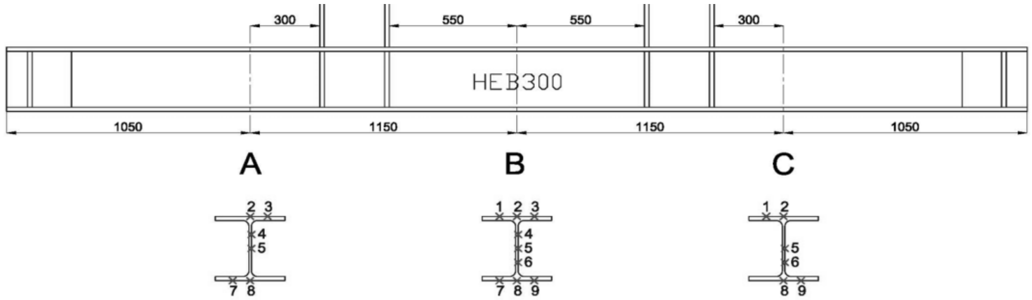

Figure 1. Position of the thermocouples during Test n°1.

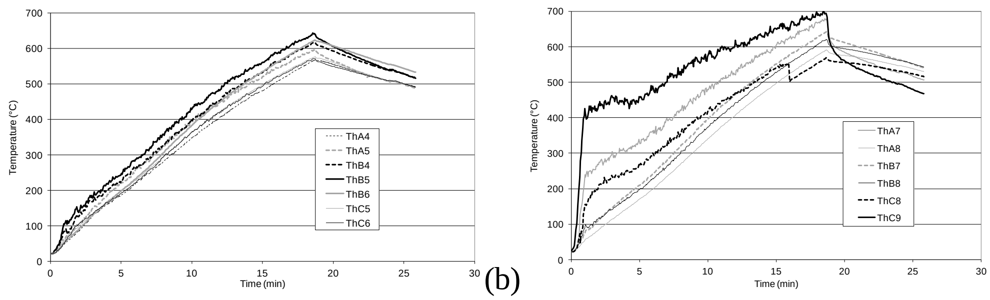

(a) (b)

Figure 3. Evolution of temperature measured in the web (a) and bottom top flange (b) during Test n°1.

The deflections of Test n°1 beam are plotted in Figure 4. The deflection of the beam after application of the mechanical loading at room temperature is 22.5 mm. NBN EN 1365-3 [10] defines two criteria for the end of the stability of the beam subjected to fire that are function of the profile height d:

- A vertical deflection of the mid-span section equal to $L^2/400$ = 147 mm. This corresponds here to a total deflection equal to 169.5 mm.
- A speed of deflection equal to $L^2/9000d$ = 6.53 mm/min.

In the present test, the two criteria have respectively been reached after 19 and 14 minutes.

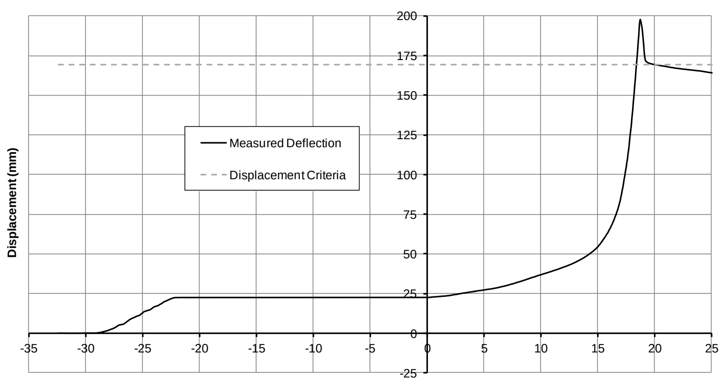

Figure 4. Evolution of vertical deflections in the beam mid-span section (Test n°1).

Test n°2

The tensile yield strength of the steel profile has been measured by 5 specific coupon tests (2 on upper flange, 2 on bottom flange and 1 in the web). The results of one coupon test performed on the upper flange are presented in Table III.

TABLE III. RESULTS OF COUPON TEST PERFORMED AT ROOM TEMPERATURE ON SPECIMEN N°2.

REFERENCE		**R_m [MPa]**	**R_{eH} [MPa]**	**A% (5.65 $\sqrt{S_0}$)**
NC 1501-4A	UF-1	639	556	24.0

The mechanical loading is kept constant during the whole test and applied in the two sections situated at L/4 from each support, so that the central zone is subjected to a uniform bending moment. The total load applied to the specimen is 2 x 409 kN = 818 kN. The load ratio, defined as the ratio between the applied bending moment at mid-span and the plastic bending moment of the section, was expected to be 0.5 if the yield strength of steel was 460 N/mm^2. The coupon tests performed at room temperature demonstrated that the yield strength of steel was much higher and that the load ratio was actually equal to 0.42.

The evolution of temperature with time in the steel profile has been measured in 6 sections (Figure 5). On this figure, the zone of electric resistances and the insulated zone are respectively in dark grey and light grey. Figure 6 shows the temperatures measured in the top flange and the web. The evolution of temperature is quite similar in the two flanges. As expected, temperature decreases with distance from mid-span section.

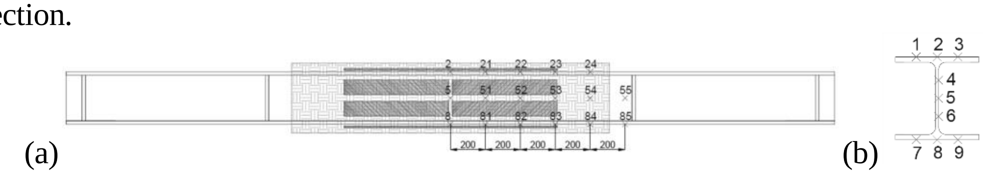

Figure 5. Position of thermocouples during Test n°2. Longitudinal (a) and transversal (b) sections.

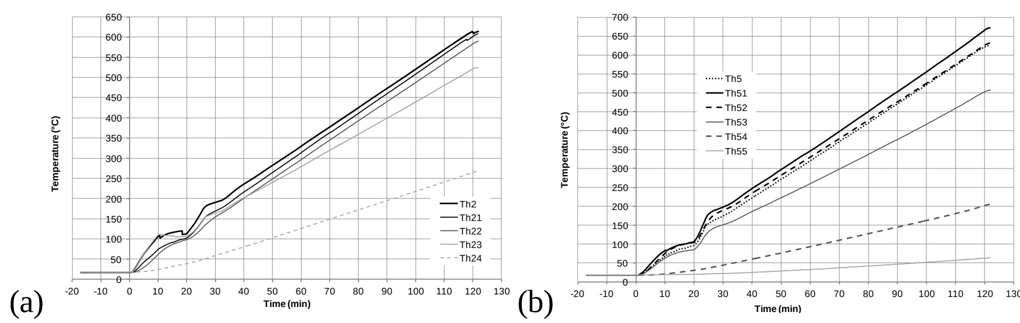

Figure 6. Evolution of temperature measured in the top flange (a) and the web (b) during Test n°2.

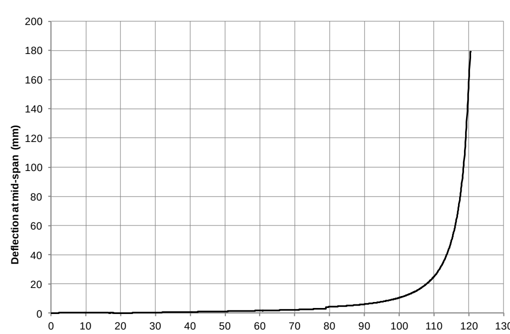

Figure 7. Evolution of vertical deflections in beam mid-span section (Test n°2).

The measured values of experimental deflections have been compared to the deflections obtained by use of a F.E.M. using the reduction factors recommended by the EN 1993-1-2 [1]. SAFIR® software is developed at the University of Liege and dedicated to the thermo-mechanical analyses of structures subjected to fire [11]. In SAFIR, thermal and mechanical calculations are performed separately. In the present case, the evolutions of temperature in the different parts of the profiles have directly been imposed based on the measurements of the tests.

The first test has been reproduced numerically using shell finite elements (Figure 8) and considering three values of the steel yield strength: the nominal values (460 MPa and 500 MPa) and the value obtained from coupon tests (528 MPa). The applied evolutions of temperature in the top flange, the web and the bottom flange are the average values between all the measurements made on each parts of the beam. The constitutive model for steel is a plane stress associated plasticity model, with a Von Mises yield surface, the evolution of which follows the evolution of the limit of proportionality of EN 1993-1-2 with the strain hardening driven for the stress-strain relationship of this standard until the effective yield strength. The Young's modulus evolution and the thermal elongation are also taken from Eurocode 3. Figure 8 shows the numerical model of the beam, including the two short columns used to report the loading jack outside the heated zone, the web stiffeners under the loads and on the supports and the flange stiffeners provided to restrain warping and reduce than likelihood of lateral torsional buckling.

The correlation between the F.E.M. curve obtained with the real yield strength and the experimental one is very good (Figure 9). At the end of the test, the burners have been stopped and the deflection reduced. The runaway failure is observed in the F.E.M. analysis because no strain hardening is considered beyond the effective yield strength in the material law of steel. The failure mode observed during the test and in the model is a bending failure in the central zone, without any local buckling or lateral torsional buckling (Figure 10), as foreseen.

The second test has also been reproduced numerically with the nominal strengths (460 MPa and 500 MPa) and the yield strength measured experimentally. Three different values have been considered for the top flange, the web and the bottom flange (Figure 11). For flanges, the yield strength is the average between the two R_{eH} values obtained from two coupon tests. The distribution of temperature has been considered as symmetric (temperature measurement were focused on one side) and applied by zones, on the basis of the measurements made during the tests.

Again, the deflections predicted by the F.E.M. correlate very well with the measured deflections, with very slight differences at the end of the test where the prediction of the model is on the safe side (Figures 12 and 13). The temperature in the top and bottom flanges at failure is around 590°C.

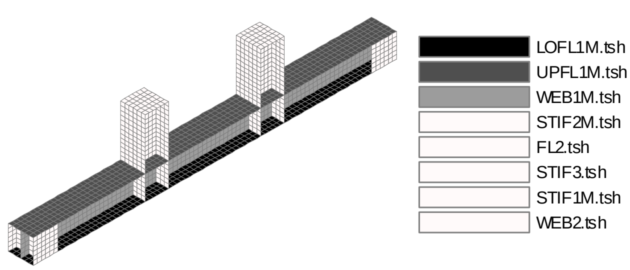

Figure 8. Finite element model of Test n°1.

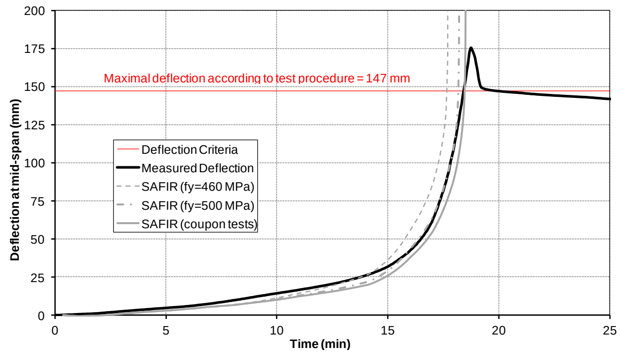

Figure 9. Comparison between experimental and numerical deflections of the beam (Test n°1).

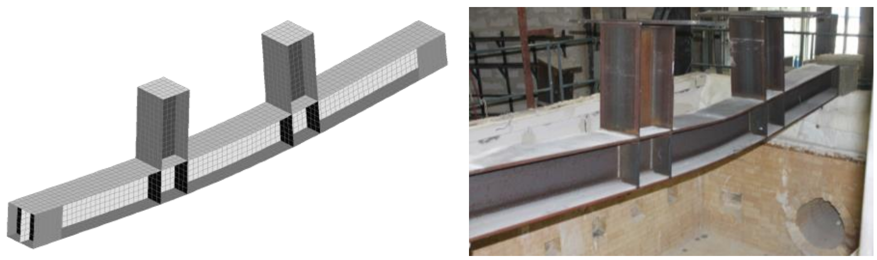
Figure 10. Comparison between F.E.M. and observed deformations at the end of Test n°1.

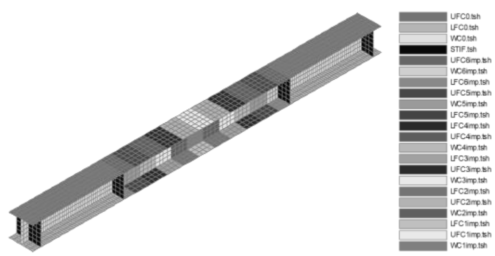
Figure 11. Finite element model of Test n°2.


Figure 12. Comparison between F.E.M. and observed deformations at the end of Test n°2.

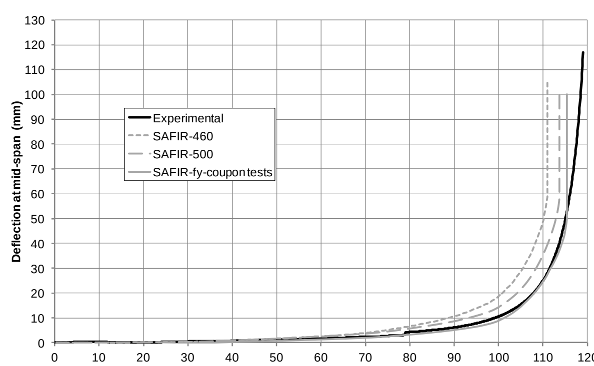

Figure 13. Comparison between experimental and numerical deflections of the beam (Test n°2).

CONCLUSIONS

The reduction factors for yield strength of carbon steel at elevated temperatures defined in the EN 1993-1-2 are the output of series of experimental investigations consisting in steady-state and transient-state steel coupons or reduced-scale specimen tests as well as in full-scale tests performed on beams and columns subjected to ISO fire. Several authors have underlined the significant influence of testing procedures on the reduction of steel resistance at elevated temperatures. The choice of the test procedure has therefore a considerable effect on the conclusions made about the material properties of steel at elevated temperatures.

In recent publications, the results of coupon tests performed on high-strength steel have been presented. Some of these tests led to ratios between the coupon resistances at elevated temperatures and at room temperature lower than Eurocode reduction factors. The authors have consequently questioned the validity of these factors for these steel grades, without referring to any full-scale fire tests.

The present paper describes two experimental tests performed tests performed on high-strength steel beams under fast and slow elevations of temperature in the range from 550°C to 650°C. The material properties of the tested profiles at ambient temperature allow the designation of the profiles by both S460M and S500M steel grades. The comparisons between experimental measurements and results of SAFIR simulations performed using Eurocode 3 material laws show very good correlations. This confirms the applicability of the existing reduction factors for S460 steel grades and even opens the door to the extension of the field of application of these rules to S500 steel grades.

REFERENCES

1. EN1993-1-2. 2005. "*Eurocode 3: Design of steel structures – Part 1-2: General rules – Structural fire design*", CEN, Brussels.
2. prEN10025-4. 2011. "*Hot rolled products of structural steels – Part 4: Technical delivery conditions for thermomechanical rolled weldable fine grain structural steels*", CEN, Brussels.
3. EN1993-1-1. 2005. "*Eurocode 3: Design of steel structures – Part 1-1: General rules and rules for buildings*", CEN, Brussels.
4. A913/A913M. 2015. "Standard Specification for High-Strength Low-Alloy Steel Shapes of Structural Quality Produced by Quenching and Self-Tempering Process (QST)", ASTM Int., West Conshohocken, PA, USA.
5. Specification for Structural Steel Buildings. Public Review Draft dated March 2. 2015, American Institute of Steel Construction, Chicago, IL, USA.
6. Arbed-Recherches. 1993. "Practical design tools for unprotected steel columns submitted to ISO-Fire", REFAO III, Contract No 7210-SA/505, Final Report.
7. Schneider R. and J. Lange. 2009. "Constitutive equations of structural steel S460 at high temperatures", Nordic Steel Construction Conference, Sweden, 204-211.
8. Qiang X., F. Bijlaard and K. Kolstein. 2013. "Elevated-temperature mechanical properties of high strength structural steel S460N: Experimental study and recommendations for fire-resistance design", *Fire Safety Journal*, 55:15-21.
9. Knobloch M., J. Pauli and M. Fontana. 2013. "Influence of the strain-rate on the mechanical properties of mild carbon steel at elevated", *Materials and Design*, 49:533-565.
10. NBN EN1365-3. 2000. "*Essais de résistance au feu des éléments porteurs – Partie 3 :Poutres*", NBN, Brussels.
11. Franssen J.-M.. 2005. "SAFIR: A thermal/structural program for modeling structures under fire", *Engineering Journal*, American Institute of Steel Construction Inc, 42(3): 143-158.

Development of True Stress-Strain Curves of Structural Steel for Fracture Simulations

WENYU CAI and MICHAEL D. ENGELHARDT

ABSTRACT

True stress-strain curves are needed for fracture simulation of structural steel using the finite element analysis method. This paper summarizes recent research on development of true stress-strain curves for ASTM A992 structural steel at ambient temperature and at elevated temperatures up to 1000°C. Calibration of true stress-strain curves was based on measured engineering stress-strain curves of ASTM A992 steel obtained from isothermal tests for tension coupons at both ambient and elevated temperatures. Prior to necking, the true stress-strain curve was derived directly from the engineering stress-strain curves using well established equations. After the onset of necking, due to the non-uniform deformation and complex stress state in the necked region, the established equations are no longer valid. Thus, in this research, true stress-strain curves for the post-necking region were developed by calibrating detailed finite element models of the tested tension coupons to match measured engineering stress-strain curves. Comparisons are presented between measured engineering stress-strain curves and simulated results to examine the accuracy of the calibrated true stress-strain curves. Furthermore, generalized true stress-strain curves based on the derived curves are proposed for fracture simulations for ASTM A992 steel.

INTRODUCTION

The ultimate failure of connections in steel buildings, either at ambient temperature or at elevated temperatures, often involves fracture. The ability to accurately simulate fracture behavior of steel connections provides a powerful tool to better understand the response of steel structure under extreme loading condition, such as fire. An example of a computational fracture simulation is shown in Figure 1 for a simple bolted connection. To accurately simulate fracture of steel using the finite element approach requires an accurate description of true stress-strain response beyond necking and up to fracture strain levels. However, beyond necking, due to the non-uniform deformation and the non-uniform stress state along the gage length of the tested steel coupon, obtaining a true stress-strain curve from a measured engineering

[1]Ferguson Structural Engineering Laboratory, University of Texas at Austin, 10100 Burnet Road, Austin, Texas 78759 USA

stress-strain data becomes difficult. This difficulty can be overcome by calibrating detailed finite element models of tested tension coupons to match measured and predicted engineering stress-strain data.

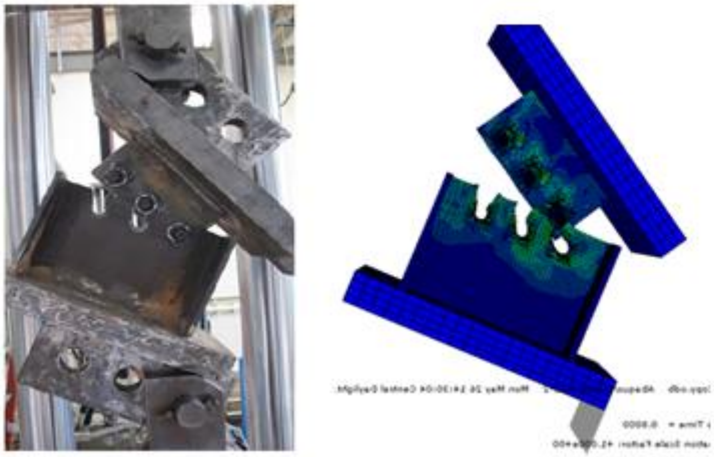

Figure 1. Simulation of fracture for a connection test specimen.

TENSION COUPON MODELS IN TESTS AND SIMULATIONS

The engineering stress-strain data of ASTM A992 steel used in the analysis of true stress-strain curves were reported by Lee et al. [1]. This was among the few test data found in the literature for ASTM A992 steel at elevated temperature, reporting the full measured engineering stress-strain curves from the beginning of loading up to fracture. The ASTM A992 material used for the test coupons were designated as MA, MB and MC, which were cut from wide-flange sections of ASTM A992 steel from three different production heats (see Figure 2). The tension tests were conducted as steady-state temperature tests. The measured engineering stress-strain curves for material MC were shown in Figure 3. The curves for materials MA and MB are reported by Lee et al [1].

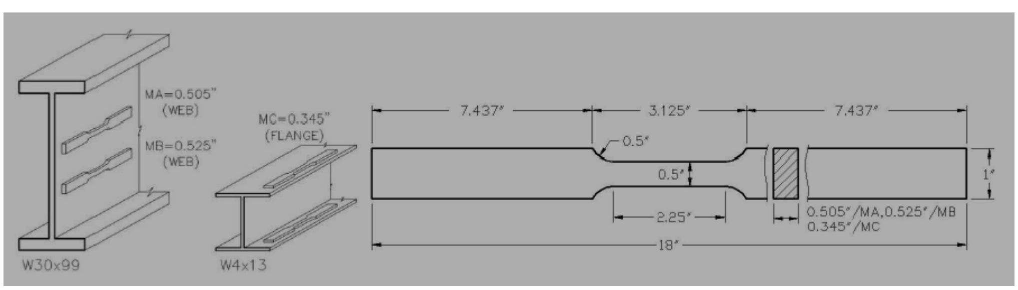

Figure 2. Coupon specimens from Lee et al.'s tests [1].

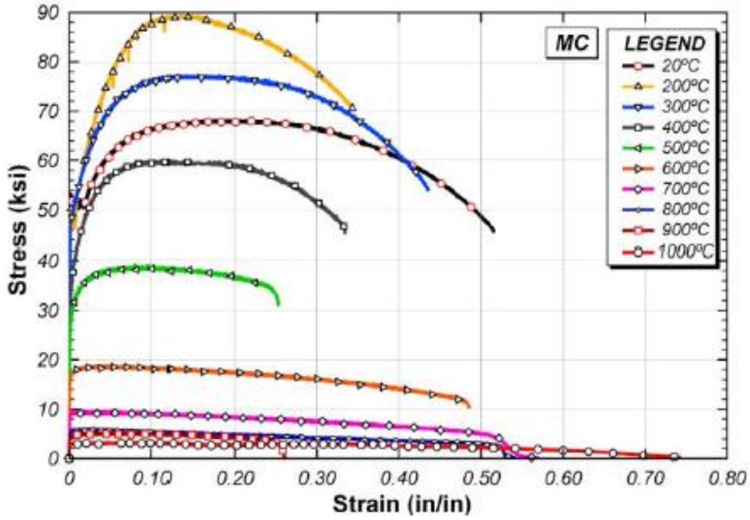

Figure 3. Engineering stress-strain curves for material MC at elevated temperature from Lee et al.'s tests [1]

Detailed models of the tested coupons were developed in the finite element computer program ABAQUS (Version 6.12) [2]. The material input to the model was in the form of a true stress-strain curve. Axial displacement was applied to the model to simulate the displacement controlled tensile coupon test. The model used at this stage simulated necking as shown in Figure 4, but did not simulate fracture. An engineering stress-strain curve was then computed from the simulation results. Engineering stress was computed by taking the load on the coupon and dividing by the initial cross-sectional area. Engineering strain was computed by taking the relative displacement of two nodes along the coupon that were originally 1-inch apart and then dividing by this 1-inch length. This gage distance was chosen to match the gage length of the extensometer used in the tests. Thus, the engineering stress-strain curves in the simulations were computed in the same manner as in the tests.

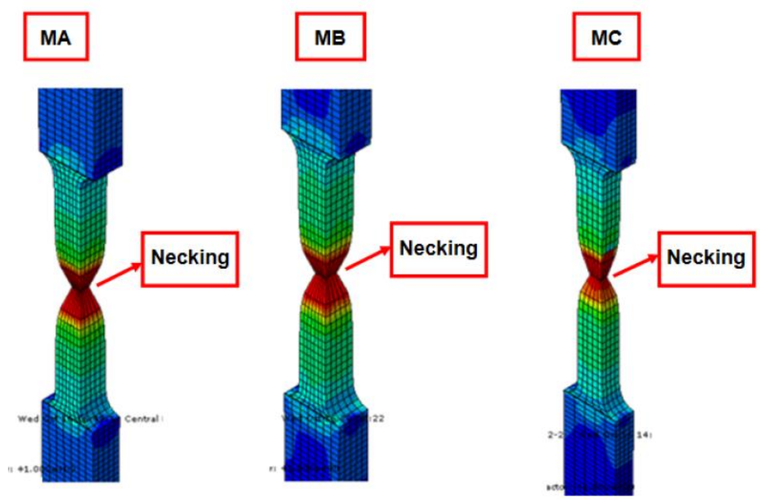

Figure 4. Coupons simulated in ABAQUS from Lee's tests with formation of necking.

CALIBRATION OF TRUE STRESS-STRAIN CURVES BEFORE AND AFTER ONSET OF NECKING

True stress-strain response prior to necking can be computed from measured engineering stress-strain data using well-established equations. The true strain prior to necking can be computed from Equation 1. In the elastic region, true stress can be computed from engineering stress, engineering strain and Poisson's ratio using Equation 2. In the plastic region from the initiation of yielding up to initiation of necking, true stress can be computed from engineering stress and strain using Equation 3 based on the assumption that post-yielding deformation occurs largely at constant volume [3]. According to the derived true stress-strain response in the elastic region, the relationship between true stress and true strain is linear and the value of slope is quite close to the Young's modulus in the engineering stress-strain curve. In the plastic region, the true stress-strain relationship can be expressed using a follows power law function as shown in Equation 4.

$$\varepsilon_t = \ln(1 + \varepsilon_e) \qquad (1)$$

$$\sigma_t = \frac{\sigma_e}{(1 - \nu \varepsilon_e)^2} \qquad (2)$$

$$\sigma_t = \sigma_e(1 + \varepsilon_e) \qquad (3)$$

$$\sigma_t = K\,\varepsilon_t^n \qquad (4)$$

In the equations above, σ_t and ε_t are true stress and true strain respectively; σ_e and ε_e are engineering stress and engineering strain respectively; ν is Poisson's ratio of steel; K and n are parameters for the power law function.

After necking is initiated, due to the non-uniform deformation and state of stress in the necked region, Equations 1 to 3 are no longer valid. To develop true stress-strain response after the onset of necking, finite element simulations of tension coupon tests were utilized. Tested coupons were simulated in the finite element computer program ABAQUS using various true stress-strain curves input for the post-necking region, until the simulated results agreed reasonably well with the measured experimental data. By trial and error, it was observed that a bilinear curve can be utilized to represent the relationship of true stress and strain after the onset of necking. The first linear segment has a positive slope and the second linear segment has a zero slope. The slope of the first linear segment is listed in Table I. Note that this slope is identical for the tested materials MA, MB and MC and it decreases with increasing temperature. It was also found that the end of this first linear segment, when the maximum true stress is achieved, can be taken as the value of true strain which is equal to engineering strain at fracture. The true strain corresponding to the maximum true stress at elevated temperatures are listed in Table II.

TABLE I. SLOPE OF TRUE STRESS-STRAIN CURVES AFTER ONSET OF NECKING.

Slope of Linear Part after Onset of Necking	Temperature (°C)									
	20 °C	200 °C	300 °C	400 °C	500 °C	600 °C	700 °C	800 °C	900 °C	1000 °C
MA (ksi)	60	60	60	50	40	20	5	2	2	1
MB (ksi)	60	60	60	50	40	20	5	2	2	1
MC (ksi)	60	60	60	50	40	20	5	2	2	1
Average (ksi)	60	60	60	50	40	20	5	2	2	1

TABLE II. TRUE STRAIN CORRESPONDING TO MAXIMUM TRUE STRESS.

True Strain at Maximum True Stress	Temperature (°C)									
	20 °C	200 °C	300 °C	400 °C	500 °C	600 °C	700 °C	800 °C	900 °C	1000 °C
MA	0.55	0.47	0.48	0.50	0.45	0.57	0.74	1.28	0.59	0.43
MB	0.44	0.45	0.52	0.46	0.43	0.57	0.61	1.10	0.49	0.40
MC	0.52	0.34	0.44	0.33	0.25	0.49	0.57	0.54	0.26	0.74
Average	0.50	0.42	0.48	0.43	0.38	0.54	0.64	0.97	0.45	0.52

Results of material MC are taken as an example to show the comparison of the simulated experimental engineering stress-strain response. Since fracture simulation was not included in the model at this stage, the engineering stress-strain curves from the simulations extend beyond the point of fracture observed in the tests. However, as illustrated in Figure 5, the simulated curves matched the measured curves quite well up to the fracture strain level for each temperature case.

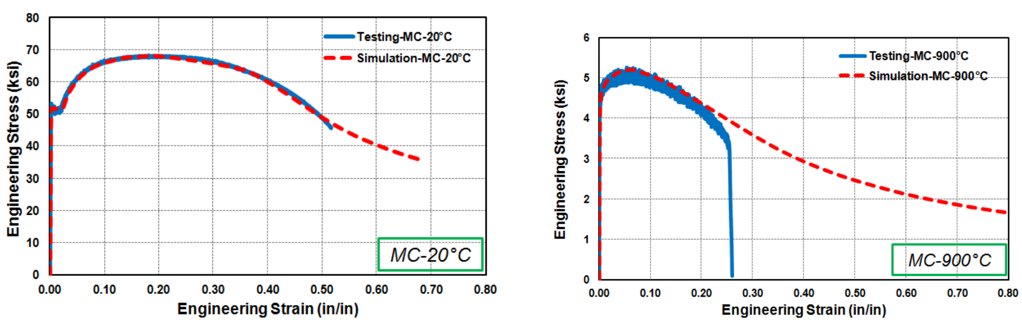

Figure 5. Comparison of simulations and testing results for ASTM A992 specimens at 20°C and 900°C.

Using the average results of the derived true stress-strain data for material MA, MB and MC, generalized true stress-strain curves are proposed for fracture simulation of ASTM A992 steel at elevated temperatures as shown in Table III. The derived true stress-strain curves at ambient and elevated temperatures are illustrated in Figure 6. As shown in Figure 6, the true stress-strain curves are extended to very large strains, which is required for fracture simulations.

TABLE III. GENERALIZED TRUE STRESS-STRAIN PARAMETERS FOR ASTM A992 STEEL.

Temperature	Elastic Region			Strain Hardening to Necking				After Necking	
	ε_{ty} (in/in)	Reduction Factor of E_t	E_t (ksi)	ε_{tsh} (in/in)	K (ksi)	n	$\varepsilon_{t\text{-}necking}$ (in/In)	Slope (S) (ksi)	ε_{tu} (in/in)
20°C	0.002	1	29000	0.02	110	0.15	0.15	60	0.45
200°C	0.002	0.9	26100	0.01	110	0.15	0.15	60	0.45
300°C	0.002	0.8	23200	0.002	115	0.15	0.15	60	0.45
400°C	0.002	0.7	20300	0.002	110	0.15	0.15	50	0.45
500°C	0.002	0.6	17400	0.002	65	0.1	0.1	40	0.4
600°C	0.001	0.31	8990	0.001	55	0.25	0.05	20	0.55
700°C	0.001	0.13	3770	0.001	65	0.4	0.01	5	0.55
800°C	0.001	0.09	2610	0.001	10	0.2	0.02	2	1
900°C	0.0005	0.0675	1958	0.0005	7	0.2	0.05	2	0.45
1000°C	0.0003	0.045	1305	0.0003	11	0.4	0.1	1	0.5

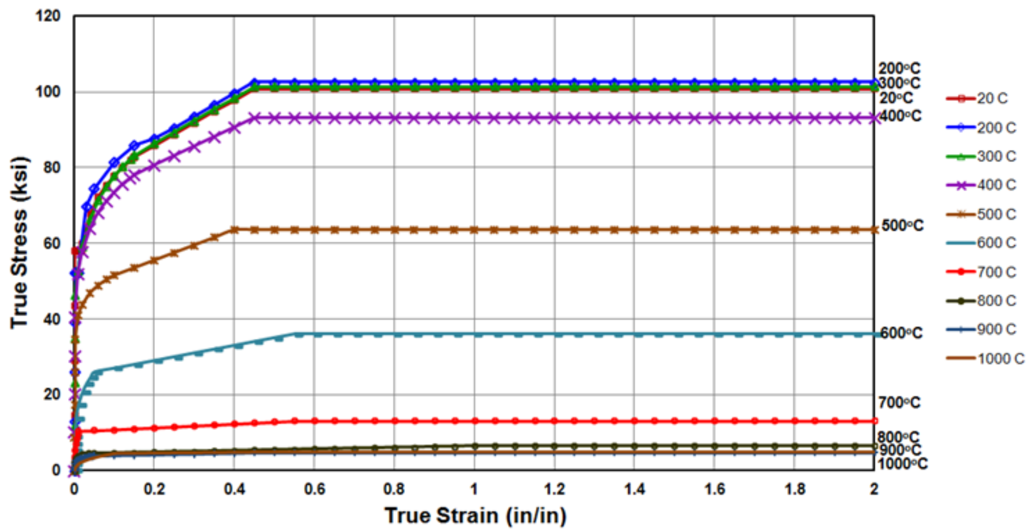

Figure 6. Preliminary Generalized True Stress-Strain Curves for ASTM A992 Steel at Ambient Temperature and Elevated Temperatures up to 1000°C.

CONCLUSIONS AND FUTURE RESEARCH NEEDS

This paper has described recent research on development of true stress-strain curves for ASTM A992 steel at elevated temperatures up to 1000°C. The true stress-strain curves derived in the study describe the behavior both before and after necking. While the research described herein is preliminary in nature and limited in scope, it has demonstrated the potential for reasonable computational simulation for tensile test coupons at elevated temperatures.

Further research is needed to validate and improve the developed true stress-strain curves at elevated temperatures. The simulated tension coupon tests used to calibrate the post-necking true stress-strain response are affected by modeling techniques including mesh density, element type, model geometry, etc., and the influence of these finite element modeling issues on the derived true stress-strain curves deserves further study. Additional work is also needed to assess the effect of strain rate, loading rate and load duration, as well as material variability on the true stress-strain response.

REFERENCES

1. Lee, J., Morovat, M., Hu, G., Engelhardt, M., and Taleff, E. 2013, “Experimental Investigation of Mechanical Properties of ASTM A992 Steel at Elevated Temperatures.” *Engineering Journal, American Institute of Steel Construction, Vol 50, No. 4, Fourth Quarter 2013, p 249-272.*
2. ABAQUS Version 6.12 User’s Manual. (2012). Hibbitt, Karlsson, & Sorensen, Inc., Pawtucket, RI.
3. Boresi, Arthur Peter, Richard Joseph Schmidt, and Omar M. Sidebottom. Advanced mechanics of materials. Vol. 6. New York: Wiley, 1993.

Constitutive Modelling of Ductile Metals at High Temperature

PAWEL WOELKE, RYAN ANDERSON, BADRI HIRIYUR and NAJIB ABBOUD

Constitutive behaviour of ductile metals subjected to thermo-mechanical loads associated with a fire condition as well as small-to-medium rate mechanical loads is discussed in this paper. Effective analysis and design of structures in fire require material models that are valid over a wide range of stresses, strain rates, loading and unloading cycles and temperatures. Thermal loading of metals results in a slow, creep-dominated behaviour, which can lead to local or global component failures and progressive collapse. The collapse mechanism for structures and their components, once initiated, occurs at much higher strain rates than creep. A comprehensive modelling framework that allows simulation of large-scale metal structures subjected to a wide range of stresses, strain rates and temperatures is presented. An advanced viscoplastic constitutive model is developed based on micromechanical material failure mechanisms and experimentally observed time- and temperature-dependent material behaviour. This model (*WAifire*) allows bridging the time-scale gap between creep-dominated behaviour and resulting thermo-mechanical stiffness and strength degradation on the one hand, and the high strain rate deformation and fracture caused by structural collapse on the other hand.

Keywords: Fire, Constitutive modelling, Thermo-mechanical coupling, Structural Collapse

1 Introduction

This paper gives a brief summary of the new thermo-mechanical constitutive model for ductile metals subjected to mechanical stresses and transient temperature condition caused by fire. The model takes into account the influence of stress triaxiality, normalized Lode angle and thermal material softening caused by the fire condition. The material model itself is applicable to any ductile metal with failure governed by nucleation, growth and coalescence of voids.

The theoretical development and implementation of the model into dynamic explicit finite element codes NLFlex and EPSA [8, 9] has been completed by Thornton Tomasetti - Weidlinger Applied Science (TT-WAS).

2 Material constitutive model

The new material constitutive model [1, 2, 9, 10] covers a wide range of stresses, strain rates and temperatures. One of the key advantages of the proposed model is its applicability and accuracy of the solution with different levels of strain rates ranging from thermally activated creep-dominated behaviour ($\dot{\varepsilon} = 10^{-6}/s$) to high strain rate response of the material subjected to dynamic loads ($\dot{\varepsilon} = 10^{1}/s$). Applicability to such a wide range of strain rates offers a significant advantage for

Thornton Tomasetti - Weidlinger Applied Science, 40 Wall Street New York, NY 10005-1304, USA
PWoelke@ThorntonTomasetti.com, RAnderson@ThorntonTomasetti.com,
BHiriyur@ThorntonTomasetti.com, NAbboud@ThorntonTomasetti.com

considerations of structural response to fire. The progressive collapse process, which can be caused by fire, is associated with impulsive dynamic response of the structure and its components. The ability of the proposed model to address both slow rate of deformation induced by fire, as well as impulsive loading conditions, is a unique capability which distinguishes it from existing approaches addressing a specific ranges of behaviour.

3 Abaqus implementation, verification and validation

The model implementation into the explicit dynamic code Abaqus has been accomplished through the user subroutine VUMAT. The verification and validation of model is based on the tests carried out by Maljaars [3-6], who investigated behavior of aluminium through a wide range of laboratory tests for different load and thermal conditions. In presented paper the following validation cases are used: (1) steady-state uniaxial tensile test at ambient and elevated temperatures; (2) creep test of specimen subjected to uniaxial tension and constant heating rates; (3) steady-state buckling tests of aluminium columns in room and elevated temperatures.

3.1 Uniaxial tensile test

A series of uniaxial tensile tests was carried out using a tensile coupon with dimensions 80x50x5 mm. A single shell finite element was used to represent each test, with the same dimensions as the specimen. The analysis results show very close agreement with the experimental test results (Fig.1). This agreement validates the model assumptions as well as the implementation process. The comparison between the experimental test data and analysis results is given in Fig.1.

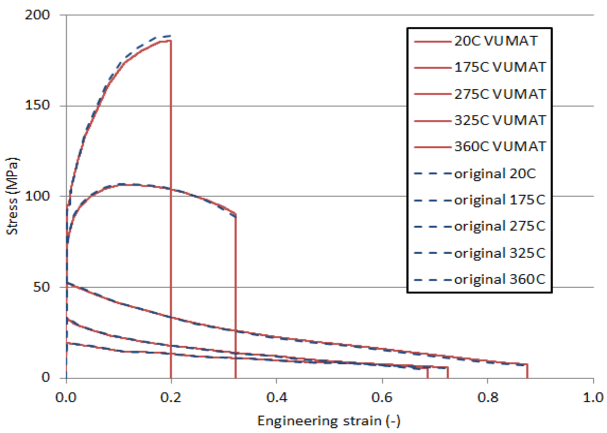

Figure 1. Steady state uniaxial tensile test.

3.2 Creep test

Creep test was conducted using similar tensile specimens with the dimensions 75x12, 5x5 mm. As previously, the tests were represented using a single shell element. A constant tensile stress of 70 MPa was applied to the specimen with a transient temperature rising at the rate of 9,0^{0}C/min. The analysis results are shown in Fig.2. All creep phases, including the tertiary stage have been well represented by the model. As in the previous case, very close correlation with the test data has been achieved.

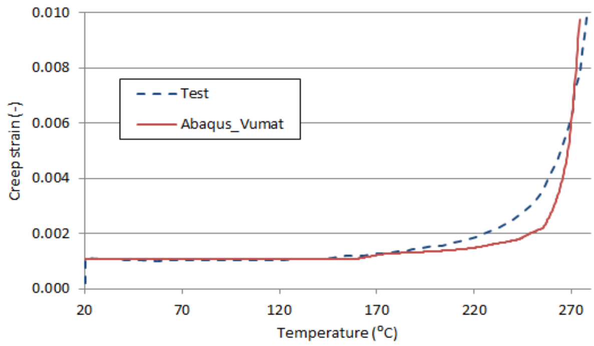

Figure 2. Transient creep test.

3.3 *Buckling test*

Buckling tests were conducted on tubular columns with dimensions of 60.0x5.0x0.1 cm. Taking into account significant imperfections sensitivity of shell structures in compression, special considerations must be given to initial column imperfections in the undeformed state. Following the documentation of the measured specimen imperfections [4, 5] a fundamental buckling mode was determined by solving the eigenvalue problem. The determined initial shape of the specimen, with imperfections was used to define the geometry of the finite element model with a maximum imperfection level equal to the measured value (0,25-6,0 mm depending on the test case).

In addition to the column imperfection, the load was applied non-symmetrically due to lack of symmetry in the supports. A one-sided gap between the top support (load application cell) and the column edge was observed during testing [4,5]. This lack of symmetry was also accounted for in the model.

The analysis results revealed that the initial column imperfections and lack of symmetry in the load application had a significant effect on the location of buckling along the height of the column. This had however a minor influence on the general force-displacement response. The measured and calculated buckling shapes of the columns are shown in Fig. 3.

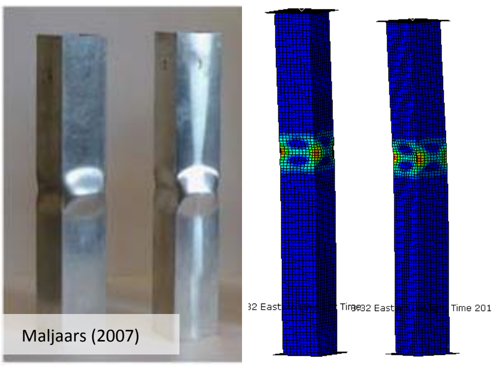

Figure 3. Shape comparison between Maljaars test and obtained numerical results.

4 Summary

The thermo-mechanical structural response to fire and impulsive dynamic loads is complex and involves multiple physical phenomena. Reliable representation of these phenomena on a structural scale requires development of new approaches. This paper presented the new advanced thermo-mechanical constitutive damage model, developed by TT-WAS (*WAifire*) for ductile metals subjected to fire and blast conditions. The main emphasis of this summary has on validation against the experimental test data for the range of deformation dominated by high temperature creep and softening.

Model validation was performed for both transient and steady-state temperature behaviour. All the presented analysis results are in good agreement with the experimental data, which validates the model and its implementation.

References

[1] Woelke, P., Abboud, N., Modeling Fracture in Large Scale Shell Structures, *J. Mech. Phys. Sds.* 60, 2044-2063, 2012.

[2] Woelke, P., Voyiadjis, G.Z. and Perzyna, P., Elasto-plastic Finite Element Analysis of Shells with Damage due to Microvoids, *Int. J. for Num. Meth. Eng.* 68, 338-380, 2006.

[3] Maljaars, J., Local buckling of slender aluminium sections exposed to fire. Mechanical properties at elevated temperature. *TNO, Eindhoven University of Techn.* 2007.

[4] Maljaars, J. Soetens, F. and Snijder, H.H. Local Buckling of Aluminium Structures Exposed to Fire. Part 1: Tests, *Thin-Walled Struct.,* 47, pp. 1404-1417, 2009.

[5] Maljaars, J. Soetens, F. and Snijder, H.H. Local Buckling of Aluminium Structures Exposed to Fire. Part 2: Finite Element Models, *Thin-Walled Struct.,* 47, 1418-1428, 2009.

[6] Atkatsh, R.S., Bieniek, M.P., Baron, M.L., Dynamic elasto-plastic response of shells in an acoustic medium—EPSA code. *Int. J. Num. Methods Eng.* 19 (6), 811–824, 1983.

[7] Vaughan, D.K., FLEX User's Guide – Report UG8298, Weidlinger Associates Inc., Mountain View, CA, 2006.

[8] Woelke, P.B., Shields, M.D., Hutchinson, J.W. (2015) "Cohesive Zone Modeling and Calibration for Mode I Tearing of Large Ductile Plates"; *Eng. Fr. Mech.*; 147, 293-305.

[9] Woelke, P., Shields, M.D., Abboud, N.N. and Hutchinson, J.W. (2013) "Simulations of Ductile Fracture in an Idealized Ship Grounding Scenario using Phenomenological Damage and Cohesive Zone Models"; *Comp. Mat. Sci*., 80, 79-95.

[10]Voyiadjis, G.Z. and Woelke, P. (2008) "Elasto-Plastic and Damage Analysis of Plates and Shells" 2008 Springer-Verlag Berlin Heidelberg. ISBN-13: 978-3540793502.

Constitutive Modeling for Fire Engineering Purposes—The Challenge of Modeling Creep in an Appropriate Way

MANFRED KORZEN

ABSTRACT

The phenomenon of creep of structural steel in fire engineering is gaining more and more interest. Due to shortcomings of the EC3 constitutive model and other approaches based on classical creep theory an alternative approach mainly based on the ideas of Krempl [3] is proposed. Due to this so-called operator approach the material as well as the constitutive model is looked upon as an operator. The application of this view serves as a guide through the analysis of the relationship between experimental facts and constitutive theory especially in the context of transient creep.

1 INTRODUCTION

Looking back in *Structures in Fire* conferences history you will see that the phenomenon of creep of structural steel is gaining more and more interest. One of the reasons for this development is that creep is only represented *implicitly* (according to a wording in [1]) in the constitutive model of Eurocode 3 [2] (EC3).

The EC3 stress-strain relationship represents a non-linear rate-independent relationship between stress σ, mechanical strain ε^{me} and temperature θ. The experimentally observed phenomenon of creep at constant stress but linear time varying temperature (*transient creep*) is represented only through the temperature dependence of the material parameters characterizing the EC3 constitutive model. As a consequence, some important phenomena cannot properly be described: e.g., creep or relaxation at constant temperature or sensitivity of the transient creep process on the temperature rate.

Historically, due to the advancement of power generation technology into the high temperature regime in the early 1930's creep became an engineering concern [3]. The subject of creep entered the fire engineering scene through the work of Hamarthy [4] based on ideas of Dorn [5]. Although working in different time scales (power plants: years, fire: hours) both areas worked with the same type of approach: To look upon the protocol of creep experiments as constitutive equations.

But creep is not a material property it is a time driven process, i.e. the change in

---

Manfred Korzen, Bundesanstalt für Materialforschung und -prüfung (BAM),
Unter den Eichen 87, 12205 Berlin, Germany

in strain (or mechanical deformation) as a function of time at a constant stress. It is a response to a specific time-dependent stimulus (simulated via a testing machine to the specimen), combined with a variety of other possible input constraints such as the environment.

2 THE OPERATOR POINT OF VIEW

In order to overcome the problems mentioned in the introduction the material behavior in general and the phenomenon of creep in particular will be viewed according to [3] from the standpoint of the experimenter using a servo-controlled thermo-mechanical testing system.

A phenomenological, continuum approach is applied throughout our analysis since it is assumed that only such an approach can be developed sufficiently for fire engineering applications. We limit our attention to uniaxial stress cases with macroscopically homogeneous states of stress σ and infinitesimal strain ε. Any heating due to dissipation is neglected.

The capability of imposing almost any time variation of the stress or the displacement/ strain boundary condition has not existed prior to the advent of servo-controlled testing [6]. Due to considerable advances in electronics and electro-hydraulics especially this innovative feature, gives us the possibility to look upon the material as well as the constitutive model as an operator [2] (see Figure 1). This operator maps time-dependent inputs (loading function) into corresponding time-dependent outputs (response function). According to [7] the experimental input-output relationship, which is realized through the servo-controlled testing system including the device for heating of the specimen, corresponds to a mathematical operator $\mathfrak{F}$, i.e.

$$\sigma(t) = \underset{0 \le \tau \le t}{\mathfrak{F}} \left(\varepsilon(\tau), \theta(\tau) \right) \tag{1}$$

which assigns with every strain and temperature history $\varepsilon(\tau)$ and $\theta(\tau)$ on [0, t] an actual stress $\sigma(t)$, respectively.

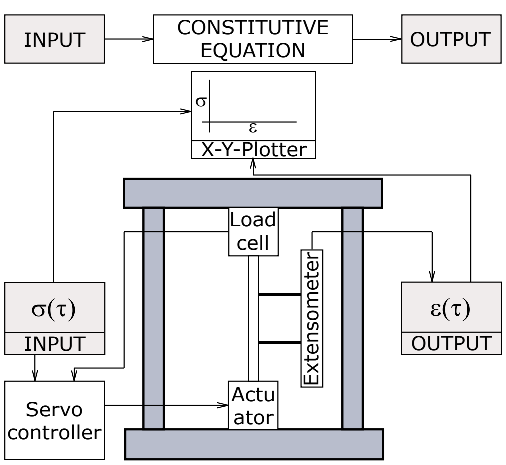

Figure 1. Constitutive equation and testing system as an operator in force/stress control.

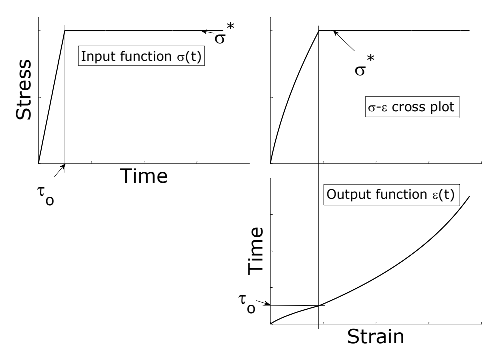

Figure 2. Classical creep test, input and output function plus cross-plot.

Classical representations of (1) are constitutive equations within the theories of elasticity [8], viscoelasticity [9] and plasticity [10]. All of them satisfy basic axioms of continuum mechanics and are capable to be adjusted to a variety of input functions to get proper material response functions. They have to be strictly distinguished from the constitutive equations itself [2]. Nevertheless they play an important role as part of the identification process of the operator $\mathfrak{F}$ on the basis of a finite number of input-output-function pairs.

3 CLASSICAL CREEP MODELS AS RESPONSE FUNCTIONS

If during monotonic loading at constant temperature $\theta = \theta^*$ and stress rate $\dot{\sigma} = \dot{\sigma}^*$ the stress σ is kept constant at value σ^* from a certain time instant, say τ_0, on and the specimen elongates freely we say that the material creeps [2]. A superposed dot denotes material time derivative. The corresponding experimental situation is briefly depicted in Figure 2.

According to the terminology introduced in chapter 2 this test is defined by two loading/input functions for stress and temperature:

i) L_σ :
$$\sigma(\tau) = \dot{\sigma}^* \tau, \sigma < \sigma_0, \tau < \tau_0 \tag{2}$$
$$\sigma(\tau) = \sigma^* = const., \tau \geq \tau_0 \tag{3}$$
ii) L_θ :
$$\theta(\tau) = \theta^* = const., \tag{4}$$

respectively, and one response/output function $\varepsilon(t)$ (cf. [11]).

Against the background of such type of tests with different values of stress σ^* and temperature θ^* at the same stress rate $\dot{\sigma}^*$ one modeling approach with an additive decomposition of the total strain ε into three parts is very often found in the engineering creep theory literature [12], i.e.

$$\varepsilon = \varepsilon^{th} + \varepsilon^{el} + \varepsilon^{cr} \tag{5}$$

defining the thermal strain
$$\varepsilon^{th} := \alpha[\theta - \theta_0] \tag{6}$$

with a reference temperature θ_0 and the thermal expansion coefficient α, the elastic strain

$$\varepsilon^{el} := \frac{\sigma}{E_0} \tag{7}$$

with Young's modulus E_0 and the so called creep strain usually assumed in the form

$$\varepsilon^{cr} := f_1(\sigma) f_2(t), \sigma = const. \tag{8}$$

with nonlinear temperature dependent functions f_1 and f_2.

Please note that (8) is valid only for constant stresses. As long as all material points of a structure under fire load stay at constant stress the simulation of the corresponding deformation behaviour via (5) to (8) is fully appropriate. Obviously, the assumed scenario is completely unrealistic. At least due to restrained thermal elongation generated by non-uniform temperature fields there will be changes in stress. That's why some rules, so-called time- and strain-hardening rules, apparently introduced by [13] according to [2], have been developed to handle the situation for time varying stresses even though they have been proposed for non-smooth variations of stress. Unfortunately, the derivation of such procedures is mathematically inconsistent. The main reason of inconsistency is that a response-function is used as a constitutive equation inherently combined with the fact that the stress, introduced as a parameter, is used as a variable [2].

4 MODIFIED 3-PARAMETER MODEL VIA OPERATOR APPROACH

It is well known that the phenomenon of creep can be predicted from viscoelasticity theory [9]. Therefore, we start with one of the simplest models within that class, the 3-parameter solid (3PS) [9, Table 2.2], which is briefly illustrated in Figure 3. This model is the basis of most of the constitutive equations within the class of so-called unified theories. Assuming

$$\sigma = E\varepsilon \tag{9}$$

$$\sigma = \eta\dot{\varepsilon} \tag{10}$$

as the constitutive equations of the springs and dashpot with viscosity η, respectively, and defining

$$E_\infty := \frac{1}{\frac{1}{E_0} + \frac{1}{E_2}} \tag{11}$$

as the *equilibrium Young's modulus* and

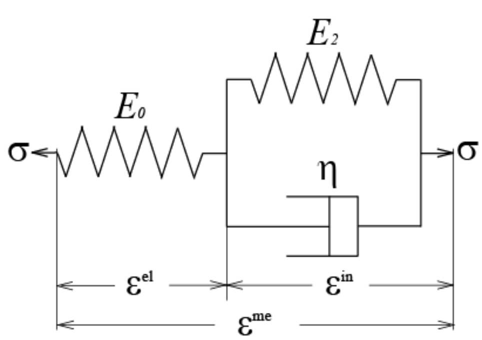

Figure 3. 3-Parameter solid (3PS).

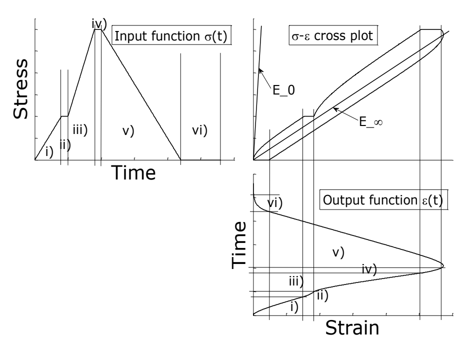

Figure 4. Material response of 3PS to special 6 segment input.

$$\varepsilon^{me} := \varepsilon - \varepsilon^{th} \tag{12}$$

as the *mechanical strain* it can be shown that the model of Figure 3 corresponds to the following ordinary differential equation (ODE) for ε^{me} with given initial condition ε_0^{me} and input function $\sigma(t)$:

$$\dot{\varepsilon}^{me}(t) = \frac{\dot{\sigma}(t)}{E_0} + \frac{1}{E_0 \dfrac{\eta}{E_0 - E_\infty}} \left[\sigma(t) - E_\infty \varepsilon^{me}(t) \right], \varepsilon^{me}(0) = \varepsilon_0^{me} \tag{13}$$

Defining

$$\varepsilon^{in} := \varepsilon^{me} - \varepsilon^{el} \tag{14}$$

as the *inelastic strain* (13) can be written as

$$\dot{\varepsilon}^{me} = \dot{\varepsilon}^{el} + \dot{\varepsilon}^{in} \tag{15}$$

with

$$\dot{\varepsilon}^{in} = \frac{1}{E_0 \lambda} \left[\sigma - \sigma^\infty \right] \tag{16}$$

as the *inelastic strain rate* with the *relaxation time* $\lambda := \eta / [E_0 - E_\infty]$ and the *equilibrium stress* $\sigma^\infty := E_\infty \varepsilon^{me}$ and therefore directly associated with the additive decomposition of ε^{me} in Figure 3. The term *inelastic* is used (i) to indicate that there is no difference between so-called plastic (i.e. rate-independent inelastic) strain and creep strain in the sense of so-called unified constitutive equations and (ii) to demonstrate a certain wording neutrality in the sense that ε^{in} may be active also in non-creep processes like isothermal relaxation, i.e. at $\varepsilon^{me} = const$.

It can be shown for constant temperature via rescaling [14] of (13) that the material response for fast loadings, i.e. $\dot{\varepsilon}^*, \dot{\sigma}^* \to \infty$, and slow loadings, i.e. $\dot{\varepsilon}^*, \dot{\sigma}^* \to 0$, is $\dot{\sigma} = E_0 \dot{\varepsilon}$ and $\sigma = E_\infty \varepsilon$, respectively (see Figure 4).

Eq. (13) represents an operator as introduced in chapter 2 with the difference that input and output functions are interchanged. We have especially chosen this form in order to study creep processes. To this end we analyse a special input function composed of six so-called segments (i-vi) at constant temperature - due to lack of space only graphically depicted in Figure 4 - and remark the following features:

(a) During the loading segments (i, iii) the $\sigma - \varepsilon$ curves go asymptotically parallel to the σ^∞-curve so that the so-called *overstress* $\sigma^{ov} := \sigma - \sigma^\infty$ becomes stationary
(b) The dependence of the stationary overstress on the loading rate is linear
(c) During the creep segments (ii, iv) σ^{ov} is decreasing to zero for $t \to \infty$
(d) During the recovery segment (vi) the strain goes back to zero for $t \to \infty$
(e) Due to the ODE representation including initial conditions of the constitutive equation no special procedures have to be established for changing stresses, even if

the stress rates are not smooth.

Particularly, observations (b) and (d) are in variance with the behavior of structural steel at room and elevated temperatures. In order to adjust (13) for structural steel we assume (i) that the relaxation time is function of the overstress to model nonlinear rate sensitivity and (ii) that the equilibrium stress is nonlinear including a hysteresis property to model non-zero recovery strain. To this end λ is replaced by

$$\bar{\lambda}(\sigma^{ov}) = \lambda M(\sigma^{ov}) \tag{17}$$

with e.g.

$$M(\sigma^{ov}) = \left[1 + \left[\frac{|\sigma^{ov}|}{m_1}\right]^{m_2}\right]^{-1}. \tag{18}$$

Eq. (18) represents a non-dimensional monotonic decreasing and temperature dependent scale function of the absolute value of the overstress, i.e. it diminishes λ with increasing σ^{ov}. The algebraic equation of the equilibrium stress (11) will be replaced by the ODE

$$\dot{\sigma}^{\infty}(t) = -\frac{|\dot{\varepsilon}^{me}(t)|}{\beta}\left[\sigma^{\infty}(t) - E_p\varepsilon^{me}(t)\right] + E_e\dot{\varepsilon}^{me}(t), \sigma^{\infty}(0) = \sigma_0^{\infty}. \tag{19}$$

The structure of (19) together with its three temperature dependent parameters β, E_e and E_p is very similar to (13) except for the term $|\dot{\varepsilon}^{me}|$, which guarantees rate independence with respect to ε^{me}. The behaviour of the modified 3-parameter model (M3PS) represented by (13) together with (17) to (19) at constant temperature is depicted in Figure 5 for identical input functions as in Figure 4 to demonstrate nonlinear rate dependence and non-zero recovery strain according to our modifications through (17) to (19). Eqs. (12) to (19), especially with the overstress format for $\dot{\varepsilon}^{in}$ together with a rate-independent ODE for σ^{∞}, are with minor differences according to different individual tastes of the authors and the standard structure for the majority of unified constitutive equations (see [15] [16]).

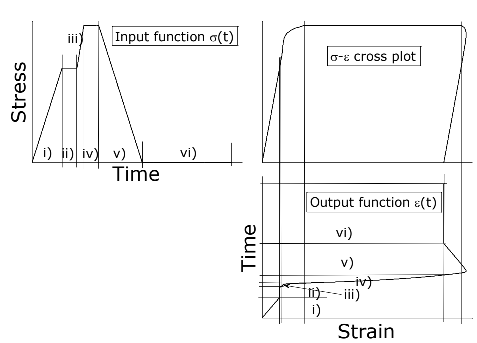

Figure 5. Material response of M3PS to special 6 segment input.

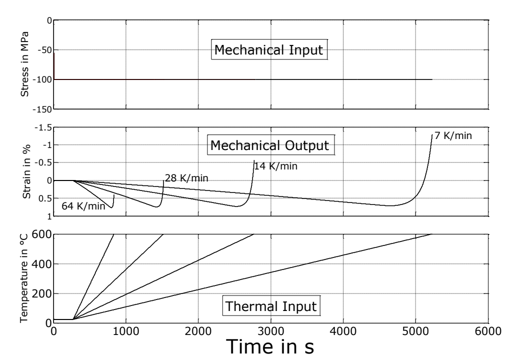

Figure 6. Transient creep as material response of M3PS for different heating rates.

5 TRANSIENT CREEP

Finally, we will discuss the behavior of our model for the situation of transient creep, i.e. for the input functions L_σ : $\sigma(t)=\sigma^*=const.$ and L_θ : $\theta(\tau)=\dot{\theta}^*\tau$, $\dot{\theta}^*=const.$ in comparison to two other approaches, i.e. (i) creep theory and (ii) EC3 model.

In the first case the corresponding equation according to (5) to (9) is

$$\varepsilon^{me}(t)=\frac{\sigma^*}{E_0(\theta)}+f_1\left(\theta(t),\sigma^*\right)f_2\left(\theta(t),t\right), \tag{20}$$

where functions f_1 and f_2 are augmented for temperature dependence. Eq. (20) is a response function in the sense of this article and not a constitutive equation and therefore not capable to describe the realistic overall material behavior. Nevertheless ε^{me} varies for varying and constant temperature but does not take into account loading history.

The corresponding equation of EC3 is given by

$$\varepsilon^{me}(t)=h\left(\theta(t),\sigma^*\right), \tag{21}$$

where h is some inverse function of the original EC3 equation. According to (21) ε^{me} varies with varying temperature but stays constant at constant temperature without any consideration of loading history. Both models cannot take into account the influence of temperature rate.

To analyze the behavior of our approach we apply the input functions L_σ and L_θ to the right hand side of (13), i.e.

$$\dot{\varepsilon}^{me}(t)=\frac{1}{E_0\left(\theta(t)\right)\bar{\lambda}\left(\theta(t),\sigma^*-\sigma^\infty(t)\right)}\left[\sigma^*-\sigma^\infty(t)\right], \tag{22}$$

put this equation into (18) in order to get the evolution of σ^∞ and arrive finally at the following set of two ODEs:

$$\dot{\varepsilon}^{me}(t)=g_1\left(\sigma^*,\sigma^\infty(t);\theta(t)\right),\varepsilon^{me}(0)=\varepsilon_0^{me} \tag{23}$$

$$\dot{\sigma}^\infty(t)=g_2\left(\varepsilon^{me}(t),\sigma^*,\sigma^\infty(t);\theta(t)\right),\sigma^\infty(0)=\sigma_0^\infty \tag{24}$$

In contrast to both other approaches according to the ODE system structure the behaviour of the M3PS is sensitive to loading history and especially to its rate. The behaviour of the M3PS for different heating rates at constant stress is depicted in Figure 6.

6 CONCLUSION

After discussion of the shortcomings of the traditional modelling approaches via creep theory and EC3 stress-strain-temperature relationship an alternative method has been proposed. Following the ideas of Krempl [3] due to this method material behaviour in general and the phenomenon of creep in particular will be viewed from the standpoint of the experimenter using a servo-controlled thermo-mechanical testing system. Based on this approach as an example of a unified constitutive equation a simple modified 3-parameter solid is proposed to model transient creep as a phenomenon which depends on the mechanical and thermal loading history.

ACKNOWLEDGEMENTS

The author is very grateful to Le Trung Nguyen for the development of the GEMS software to analyse experiment and constitutive equation via the operator concept.

REFERENCES

1. Toric, N. et al. . 2014. "Testing the Acceptability of Different Creep Strain Calculation Models in Structural Fire Analysis", in 8^{th} *International Conference on Structures in Fire*, G.-Q. Li et al., eds. Shanghai, China: Tongji University Press, pp. 895-902.
2. EN 1993-1-2, Eurocode 3: Design of steel structures - Part 1.2: General rules - fire design, CEN, 2010.
3. Krempl, E. 1974. "Cyclic Creep – An Interpretive Literature Survey", in *Welding Research Council Bulletin No. 195*, New York, NY, pp. 63-123.
4. Hamarthy, T.Z. 1967. "A Comprehensive Creep Model", *Journal of Basic Engineering*, 9(4):214-217.
5. Dorn, J.E. 1955. "Some Fundamental Experiments on High Temperature Creep", *Journal of the Mechanics and Physics of Solids*, 3(2):85-116.
6. Krempl, E. 1984. "Viscoplasticity Based on Overstress. Experiment and Theory", in *Mechanics of Engineering Materials*, C. S. Desai et al., eds., New York, NY, Wiley, pp. 369-384.
7. Onat, E.T. et al. 1972. "Representation of Creep of Metals", Oak Ridge National Laboratory, Oak Ridge, TN, Report ORNL-4783.
8. Love, A.E. 1944. *A Treatise on the Mathematical Theory of Elasticity*. New York, Dover.
9. Flügge, W. 1967. Viscoelasticity.Waltham et al.: Blaisdell.
10. Lubliner, J. 2008. *Plasticity Theory*. New York, Dover.
11. Anderberg, Y. 2008. "The Impact of Various Material Models on Structural Fire Behaviour Prediction", in 5^{th} *International Conference on Structures in Fire*, K. H. Tan et al., eds., Singapore: Research Publishing Services, pp. 253-265.
12. Boyle, J.T. et al. 1983. *Stress Analysis for Creep*. London. Butterworth.
13. Davenport, C.C. 1938. "Correlation of Creep and Relaxation Properties of Copper", *Trans. ASME, Journal of Applied Mechanics*, June 1938, A-55-A-60.
14. Gurtin, M.E., I. Herrera. 1965. "On Dissipation Inequalities and Linear Viscoelasticity", *Quarterly of Applied Mathematics*, 23: 235-245.
15. Krempl, E. 1987. "Models of Viscoplasticity. Some Comments on Equilibrium (Back) Stress and Drag Stress", *Acta Mechanica*, 69: 25-42.
16. Chaboche, J.L. 2008. "A Review of some Plasticity and Viscoplasticity Theories", *International Journal of Plasticity*, 24: 1642-1693.

High-temperature Material Constitutive Models for Structural-Fire Analysis

CHAO ZHANG, LISA CHOE and JOHN GROSS

ABSTRACT

The applicability of three steel constitutive models was evaluated using finite-element analyses and various member capacity equations. Three different high-temperature stress-strain models were compared: the model recently developed by the National Institute of Standards and Technology (NIST) [1], the Eurocode 3 model [2] and the model developed by Lie [3]. The testbed used in the analyses included twenty steel column tests and two restrained steel beam tests reported in the technical literature. The selected column tests reported buckling temperatures ranging from 500 ^{o}C to 700 ^{o}C and applied axial load ranging from 20 % to 65 % of the axial-load capacity at ambient temperature. Each reported test was analyzed in two different ways: (1) finite-element model was developed to predict the buckling temperature of the steel columns and response of the restrained steel beams in fire condition. (2) member capacity equations prescribed in Eurocode 3 and ANSI/AISC-360-10 [4] were used to compute the buckling temperature of the steel columns. Overall, the results indicate that all investigated material models give acceptable prediction of the buckling temperature of the steel columns and the behavior of restrained beams. The finite-element model with the NIST and the Lie material models predict the buckling temperature more accurately than that with the EC 3 material model. When the Eurocode column capacity equations were used, the buckling temperatures calculated using the NIST and the EC 3 models are more comparable with test results than those using the Lie model. It was also found that the current ANSI/AISC 360-10 Appendix 4 equation conservatively estimate the buckling temperature of the tested column specimens with difference of 20% on average. When the standard column equation in the Chapter E of ANSI/AISC 360-10 was used, both the EC 3 and the NIST models accurately predict the buckling temperature of the tested column specimen with difference less than 5% on average.

INTRODUCTION

Calculation methods are often adopted to determine the fire protection for steel structures as opposed to conducing costly experiments. Accurate high temperature constitutive models are required to reasonably predict the structural performance

chao.zhang@nist.gov; lisa.choe@nist.gov; john.gross@nist.gov
Engineering Laboratory, National Institute of Standards and Technology, Gaithersburg, MD 20899, U.S.A

under fire conditions. As part of the investigation on the collapse of the World Trade Center, the National Institute of Standards and Technology (NIST) characterized the steels recovered from the collapse site to analyze the failure induced by the air-craft impact and fire. In the investigation [5], the high-temperature tensile testing was conducted following ASTM E21 [6]. With the test data in the investigation and the data found in the technical literature, a new constitutive model, referred to as the NIST steel stress-strain model or NIST model in this paper, was developed to predict the high-temperature behavior of structural steels [1,7]. This paper compares the NIST model with the two widely used constitutive models, the Eurocode 3 model [2] and the TTLie model [3], for predicting the behavior of steel components under fire conditions. The constitutive models are used to predict the buckling temperature of steel columns and the response of restrained steel beams under uniform fire condition. In this paper, buckling temperature is defined as the steel temperature at the onset of buckling.

STEEL STRESS-STRAIN MODELS

Mathematical formulation

Detailed description of the NIST model can be found in Ref.[8]. The stress-strain expressions for the NIST model is given in Eq.1,

$$\sigma = \begin{cases} \varepsilon E_T \quad (\varepsilon \le \dfrac{f_{yT}}{E_T}) \\ f_{yT} + (k_3 - k_4 f_{y20}) \exp[(\dfrac{T}{k_2})^{k_1}](\varepsilon - \dfrac{f_{yT}}{E_T})^n \quad (\varepsilon > \dfrac{f_{yT}}{E_T}) \end{cases} \tag{1}$$

where k_1=7.82, k_2=540°C, k_3=1006 MPa, k_4=0.759, and n=0.503. The elastic modulus and yield strength at elevated temperature are calculated by

$$\frac{E_T}{E_{20}} = \exp[-\frac{1}{2}(\frac{T-20}{639})^{3.768} - \frac{1}{2}(\frac{T-20}{1650})] \tag{2}$$

and

$$\frac{f_{yT}}{f_{y20}} = \exp[-\frac{1}{2}(\frac{T-20}{590})^{5.7} - \frac{1}{2}(\frac{T-20}{919})] \tag{3}$$

where E_{20}, E_T are elastic modulus of steel at ambient and elevated temperatures, respectively; and f_{y20}, f_{yT} are yield strength of steel at ambient and elevated temperatures, respectively.

The expressions for the Eurocode 3 model and the TTLie model can be found in Refs.[2] and [3], respectively.

Compare with material test data

Figure 1 compares the calculated reduction factors for elastic modulus and yield strength with the test data collected by Luecke et al. [1]. The NIST model shows good agreement with the test data.

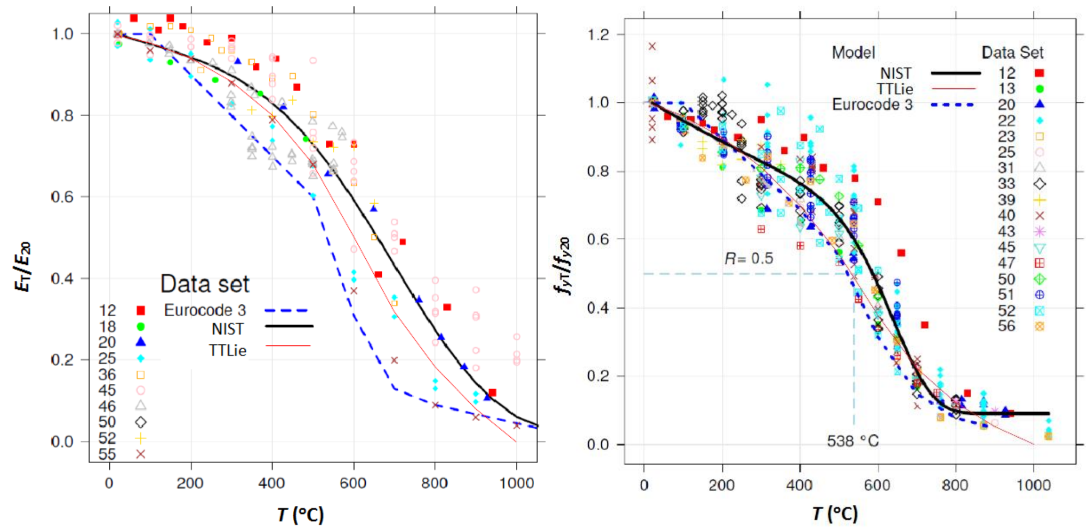

Figure 1. Calculated reduction factors for elastic modulus and yield strength against the test data collected by Luecke et al. [1]. The test labels are the same as in Ref. [1].[1]

CALCULATION APPROACHES

Eurocode 3 design approach

Simple analytical approaches given in the design codes are mostly used in daily design work. The simple approach developed by Franssen et al. [9] is recommended in the Eurocode 3 [2] for calculating the buckling resistance of axially loaded steel columns in fire, which is given by

$$N_{b,T} = \chi_T A f_{yT} \tag{4}$$

with

$$\chi_T = \frac{1}{\varphi_T + \sqrt{\varphi_T^2 - \bar{\lambda}_T^2}} \tag{5}$$

$$\varphi_T = \frac{1}{2}[1 + \alpha \bar{\lambda}_T + \bar{\lambda}_T^2] \tag{6}$$

where $\alpha = 0.65\sqrt{235/f_{y20}}$, $\bar{\lambda}_T = \sqrt{Af_{yT}/P_{ET}}$. A is the steel cross section area and P_{ET} is Euler bucking load at elevated temperature. By solving $P_T = N_{b,T}$, we obtain the column buckling temperature. Here P_T is the column service load under fire condition.

ANSI/AISC design approach

The 2005 and 2010 editions of the ANSI/AISC-360 Appendix 4 [4] specify to use the Eurocode 3 temperature-dependent mechanical properties for design of steel

[1] The Eurocode 3 yield strength plotted here is determined at the 0.2 % offset for comparison purposes, while the high-temperature yield strength in the Eurocode 3 is defined at 2% strain.

members at elevated temperatures. According to the 2005 edition, the critical buckling stress, $F_{cr}(T)$, for steel column for fire conditions can be computed using the standard design equations (i.e., in Chapter E of the ANSI/AISC-360), as expressed in Eqs [7] through [9], with the temperature-dependent values of elastic modulus, $E(T)$, and yield strength, $F_y(T)$. On the other hand, the 2010 edition prescribes Eq [10] to compute flexural buckling strength of columns at elevated temperatures. The Eq [10] is valid only when Eurocode 3 mechanical properties are considered for design. Both versions of the equations use the effective column slenderness ratio, KL/r, which is independent of temperatures, to compute the temperature-dependent elastic buckling stress $F_e(T)$ (given in Eq [9]).

$$F_{cr}(T) = \left[0.658^{\frac{F_y(T)}{F_e(T)}} \right] \cdot F_y(T) \quad \text{for } F_e(T) \geq 0.44 F_y(T) \tag{7}$$

$$F_{cr}(T) = 0.877 \cdot F_e(T) \quad \text{for } F_e(T) < 0.44 F_y(T) \tag{8}$$

$$F_e(T) = \frac{\pi^2 E(T)}{\left(\frac{KL}{r} \right)^2} \tag{9}$$

$$F_{cr}(T) = F_y(T) \cdot 0.42^{\left(F_y(T)/F_e(T)\right)^{0.5}} \tag{10}$$

FE approach

COLUMN MODEL

The three-dimensional shell element, SHELL181, implemented in ANSYS 14.0.0 [10] was used since this element is suitable for analyzing thin to moderately thick shell structures. The column cross sections were discretized into twenty elements based on mesh optimization study. The shape of initial column crookedness was defined as the first mode obtained from elastic buckling analysis. The initial deflection amplitude at mid-height, if not specified, was taken as $L/1000$. Neither the effect of residual stress due to cooling of the hot-rolled shape nor the thermal gradient from fire was modeled explicitly. The buckling temperature of columns was computed from the point at which the force equilibrium could not be achieved.

RESTRAINED BEAM MODEL

Figure 2 shows a FE structural model for a restrained steel I-shaped beam. The steel beam was modeled using SHELL181, and the restraints at the beam ends were modeled using spring-damper element COMBIN14. As shown at the right corner in Figure 2, an axial spring and a rotational spring located at mid-height of the beam end section were used to provide axial and rotational restraints, respectively. This approach can be used to model various end conditions.

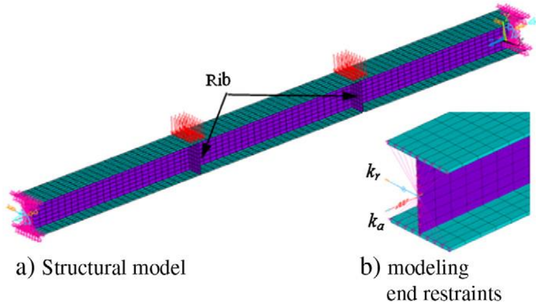

Figure 2. FE model of a restrained steel I beam.

TEST DATA

Steel columns

The five column data sets, which were selected from Zhang et al. [11], were used for FE simulations and design calculations, Table II shows a total of twenty individual column specimens along with the reported failure temperatures ($T_{b,meas}$) and other test parameters, such as the ambient temperature yield strength (f_{y20}), column length (L),slenderness ratio ($\lambda = L/r$, where r is the radius of gyration), the applied axial load(P_T), the boundary conditions (ends, where P-P is pinned-pinned; F-F is fixed-fixed; and P-R is pinned-rotationally restrained), and the initial eccentricity (e).

TABLE II. STEEL COLUMN TEST DATA.

Data	Test	Shape	f_{y20} (MPa	L (mm)	λ	P_T (kN)	e (m	Ends	$T_{b,mea}$ (°C)
Ali [12]	Ali1	UC152×152×23	320	1800	47	186	0	P-P	701
	Ali2	UC152×152×23	320	1800	47	373	0	P-P	626
	Ali3	UC152×152×23	320	1800	47	559	0	P-P	557
	Ali4	UB178×102×19	320	1800	75	202	0	P-P	629
	Ali5	UB178×102×19	320	1801	75	303	0	P-P	539
	Ali6	UB178×102×19	320	1802	75	101	0	P-P	644
	Ali7	UB127×76×13	320	1803	97	50	0	P-P	717
	Ali8	UB127×76×13	320	1804	97	101	0	P-P	658
	Ali9	UB127×76×13	320	1805	97	151	0	P-P	567
Choe[13]	1	W8×35	413	3500	67.	1134	0	P-P	500
	2	W8×35	413	3500	67.	800	0	P-P	600
	3	W14×53	406	3450	70.	1435	0	P-P	500
	4	W14×53	406	3450	70.	1070	0	P-P	600
	Lie1	W10×60	300	3810	34	1760	0	F-F	565
Lie [2]	Lie2	W10×49	300	3810	34	1424	0	F-F	586
	Lie3	W10×49	300	3810	34	1424	0	F-F	584
	RS45	UC152×152×37	326	1500	38	708.5	1.74	P-P	647
Tan [14]	RS55	UB203×133×25	357	1500	47	444.3	3.19	P-P	571
	RS81	UB152×89×16	312	1500	70	260.6	2.38	P-P	499
	RS97	UB127×76×13	320	1500	83	134	4.08	P-P	606

*Note: Ali, Lie, and Tan - transient tests; Choe - steady state tests.

Restrained steel beams

Two tests were considered to evaluate the response of restrained beams in fire. Test on specimen 1 in Li and Guo [15] and test on "FUR15" in Liu et al.[16] were considered. In [15], the tested beam had a cross section H250×250×8×12 and a clear span length of 4500 mm. Two concentrated loads were applied symmetrically on the restrained beam by two jacks. The space between these two point loads was 1500 mm. The load ratio of the restrained beam was 0.7. The axial stiffness provided by the restrained frame was k_a=39.54 kN/mm and the rotational stiffness was k_r=1.09×10^8 Nm/rad. In [16], the tested beam had a cross section 178×102×19UB and a clear span length of 2000 mm. Two symmetrical concentrated loads were applied. The space between these two point loads was 800 mm. The load ratio of the restrained beam was 0.5. End-plate beam-to-column connections were used. The axial stiffness provided was k_a=8 kN/mm and the rotational stiffness was k_r=1.4×10^5 Nm/rad.

RESULTS

Buckling temperatures

Figure 3 shows comparisons among the predicted and measured values for column buckling temperature by using different material models. Table III shows the statistics of the ratios of the difference among the analytical results and measured data for different material models. The mean and standard deviation (Std) are presented in the table. For FE approach, all three models give acceptable predictions, and NIST and TT Lie models give better prediction than the EC3 model. For Eurocode 3 approach, all three models give under-predictions, and NIST and EC3 models give better prediction than the TT Lie model.

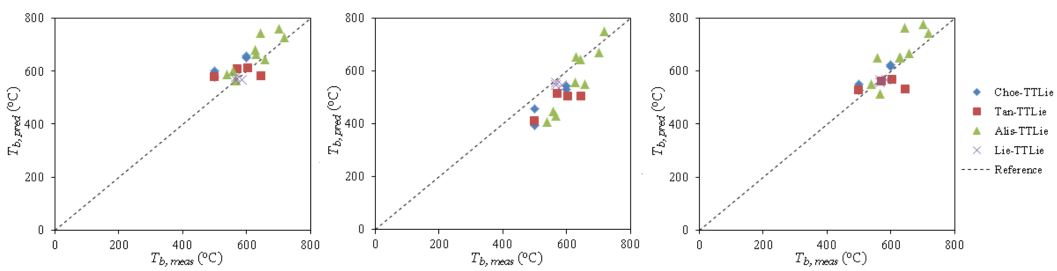

(a) FEM

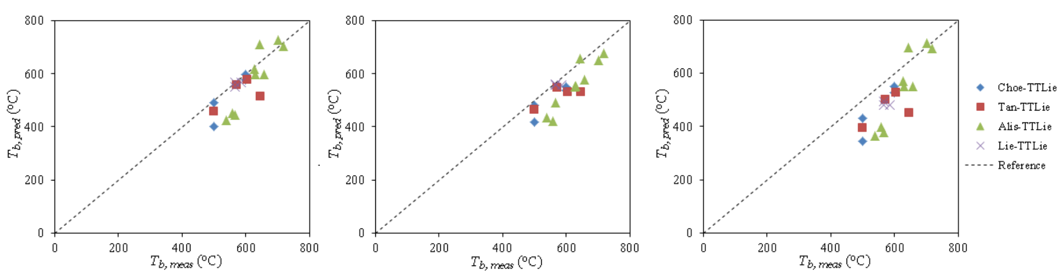

(b) Eurocode 3 method

Figure 3. Column buckling temperatures predicted using FEM (a) and Eurocode 3 method (b).

TABLE III. STATISTICS OF THE RATIOS OF THE DIFFERENCE AMONG THE ANALYTICAL RESULTS AND MEASURED DATA*.

Statistics	***NIST***	***EC3***	***TT Lie***
FEM: mean	0.060	0.110	0.024
FEM: standard Std	0.075	0.091	0.084
Eurocode 3: mean	-0.066	-0.096	-0.156
Eurocode 3: standard Std	0.091	0.068	0.113

*Note: the ratio is defined as $(T_{b,pred} - T_{b,meas})/T_{b,meas}$.

Figure 4 shows that the current ANSI/AISC 360-10 Appendix 4 equation conservatively estimate the buckling temperature of the tested column specimens with difference of 20% on average (Figure 4a). When the standard column equation in the Chapter E of ANSI/AISC 360 was used, both the EC 3 and the NIST models accurately predict the buckling temperature of the tested column specimen with the difference less than 5% on average (Figure 4b).

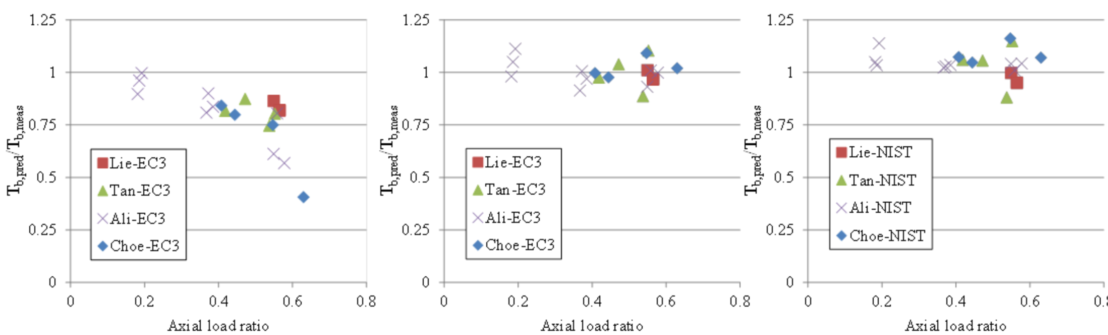

(a) Appendix 4 (b) Chapter E

Figure 4. Column buckling temperature predicted using ANSI/AISC-360 (a) Appendix 4 (b) Chapter E.

Response of restrained beam

Figure 5 show the FE predicted results for the restrained steel beam. All three material models give good prediction of the response of the restrained beams.

CONCLUSIONS

A comparative study of three high temperature steel constitutive models for structural fire analyses was presented. All investigated material models give acceptable prediction of the buckling temperature of steel columns. For the FE approach, using NIST and TTLie models give better prediction than the EC3 model; and for the Eurocode analytical approach, NIST and EC3 models give better prediction than the TTLie model. All three models give good prediction of the response of restrained steel beams subjected to fire.

DISCLAIMER Certain commercial entities, equipment, or materials may be identified in this document in order to describe an experimental procedure or concept adequately. Such identification is not intended to imply recommendation or endorsement by the National Institute of Standards and Technology (NIST), nor is it intended to imply that the entities, materials, or equipment are necessarily the best available for the purpose.

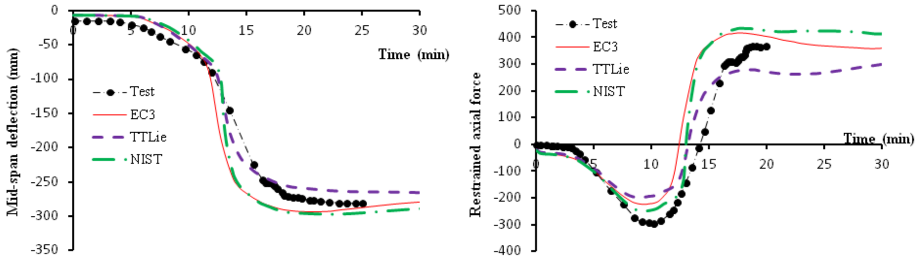

(a) Li & Guo [15]

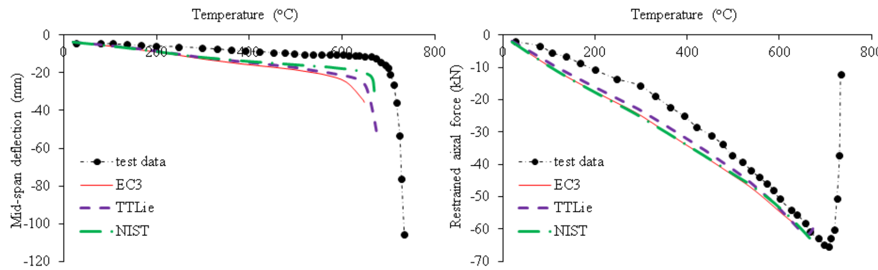

(b) Liu et al. [16]

Figure 5. FE results for restrained force and mid-span deflection for restrained steel beam.

REFERENCES

1. Luecke W E, Banovic SW, McColskey JD (2011). “High-temperature tensile constitutive data and models for structural steels in fire,” NIST Technical Note 1714.
2. ECS (2005). Eurocode 3. "Design of steel structures. General rules. Structural fire design," Standard EN 1993-1-2, European Committee for Standardization.
3. Lie TT, Macaulay JD (1989). “Evaluation of the fire resistance of protected steel columns,” Internal Report No. 583, National Research Council Canada.
4. AISC (2005, 2010). “Specification for structural steel buildings,” Specification ANSI/AISC 360-10, American Institute of Steel Construction (AISC).
5. NIST (2005). "Federal building and fire safety investigation of the World Trade Center disaster: Mechanical properties of structural steel," Technical Report NCSTAR 1-3D.
6. ASTM International (2009). “Standard test methods for elevated temperature tension tests of metallic materials.” Standard E21-09, ASTM International, W. Conshohocken, Pa.
7. Choe L, Zhang C, Luecke WE, Gross JL, Varma AH (2016). “Influence of material models on predicting the fire behavior of steel columns,” *Fire Technol.*, DOI: 10.1007/s10694-016-0568-4.
8. NIST (2016) “Temperature-dependent material modeling for structural steels: formulation and application.” NIST Technical Note 1907.Doi: 10.6028/NIST.TN.1907
9. Franssen JM, Schleich JB, Cajot LG, Azpiazu W (1996). "A simple model for the fire resistance of axially-loaded members - comparison with experimental results," *J. Constr. Steel. Res*., 37:175-204.
10. ANSYS (2012) ANSYS User Manual Version 14.0.
11. Zhang C, Li GQ, Wang YC (2012). "Predictability of buckling temperature of axially loaded steel columns in fire," *J. Constr. Steel. Res*., 75:32-7.
12. Ali FA, Shepherd P, Randall M, Simms IW, O’Connor DJ, Burgess I (1998). "Effect of axial restraint on the fire resistance of steel columns," *J. Constr. Steel. Res*., 46:305-6.
13. Choe L, Varma AH, Agarwal A, Syrovek A (2011). "Fundamental behavior of steel beam-columns and columns under fire loading: experimental evaluation," *J. Struct. Eng.-ASCE*, 137:954-66.
14. Tan KH, Toh WS, Huang ZF, Phng GH (2007). "Structural responses of restrained steel columns at elevated temperatures. Part 1: Experiments," *Eng. Struct.*, 29:1641-52.
15. Li GQ, Guo SX (2008). "Experiment on restrained steel beams subjected to heating and cooling," *J. Constr. Steel. Res*., 64:268-74.
16. Liu TCH, Fahad MK, Davies JM (2002). "Experimental investigation of behavior of axially restrained steel beams in fire," *J. Constr. Steel. Res*., 58:1211-30.

Behaviour of High Strength Steel under Fire Conditions

DOROTHY A. WINFUL[a,b,c], KATHERINE A. CASHELL[b], ADRIENE M. BARNES[c] and RICHARD J. PARGETER[c]

ABSTRACT

This paper is concerned with the material characteristics of various commercial high strength structural steels (yield strengths between 460 and 700 N/mm^2) at elevated temperatures. These steels vary in chemical composition and production route but have similar tensile properties at ambient temperature. Preliminary data of the following: proportional limit ($f_{p,\theta}$), elastic modulus ($E_{a,\theta}$), effective yield strength ($f_{y,\theta}$) based on the total strain level at 2% (in accordance with the Eurocode approach) obtained from isothermal tests are presented as reduction factors and compared with literature and the Eurocode (EN 1993-1-2). The consequences for material selection and design are also discussed.

1. INTRODUCTION

During the conceptual design stage of a project, the selection of materials and structural schemes are often governed by the requirement for solutions to be economically viable whilst equally providing a positive contribution towards the environment and society. High strength steels (HSS, defined here as materials with yield strength between 460 and 700 N/mm^2 in accordance with the Eurocode Part 1-12 [1]) have the potential to make a positive contribution towards these demands by reducing the material usage and hence weight of structural elements when employed in appropriate applications. Lighter structures lead to smaller foundations, reduced transportation costs and potentially reduced construction times and costs, as well as lower CO_2 emissions and energy use during construction.

One of the issues preventing more widespread use of HSS in structures is the lack of reliable information relating to the response of these materials at elevated temperature. Although the Eurocode does include a section for HSS [1], the guidance for fire design is based on experiments on steel with yield strengths below 460 N/mm^2. For HSS, there are limited data in the literature (e.g. [2, 3]) that present the effects of

[a]National Structural Integrity Research Centre (NSIRC), Great Abington, Cambridge, CB21 6AL UK
[b]Department of Civil Engineering, Brunel University London, Kingston Lane, UB8 3PH, UK
[c]TWI Ltd, Great Abington, Cambridge, CB21 6AL, UK

© Copyright in this article remains with TWI Ltd as TWI is a not-for-profit organisation

temperature on the mechanical properties in terms of reduction factors. Whilst the loss of strength and stiffness during a fire is inevitable, a recent review highlighted that the strength and stiffness of HSS at elevated temperature are directly related to the alloying elements and processing route employed [4]. This implies that by choosing particular alloying elements and processing routes, possible metallurgical effects such as secondary (or precipitation) hardening could potentially be utilised to retard the loss of strength and stiffness of HSS during a fire, therefore buying valuable evacuation time. However, because limited metallurgical analysis was presented in the literature, the influence of strengthening mechanisms such as precipitation hardening on the performance of HSS at elevated temperature is not clear. In this context a primary aim of this work is to provide engineers and designers with essential and reliable information to support the safe design of fire resistant structures made from high strength steels (HSS). A further aim of the work is to develop a detailed understanding of the effects of steel alloying and processing routes on the structural response of HSS in fire as these are likely to have a strong influence on the degradation of mechanical properties.

In this paper, a series of isothermal elevated temperature tests on commercially-available HSS grades is described. Based on the findings of this study, preliminary data of the following mechanical properties are presented: proportional limit ($f_{p,\theta}$), elastic modulus ($E_{a,\theta}$) and effective yield strength ($f_{y,\theta}$) based on the total strain level at 2% (in accordance with the Eurocode approach). The results are compared with available results in the literature and also the Eurocode values [5]. The tests described herein are part of a larger programme which includes anisothermal testing as well as detailed metallurgical studies.

1 EXPERIMENTAL INVESTIGATION

Ambient and elevated tensile tests were conducted on an electromechanical testing machine, which has a maximum displacement rate capacity of 100 mm/min. The machine consists of a load frame with a maximum capacity of 100 kN, a three-zone furnace with a temperature controller that has a maximum temperature capability of 1200^{0}C, and testXpert II software that monitors and controls the mechanical and thermal variables of the system through a digital closed loop control. A total of three thermocouples were used to monitor the top, middle and bottom temperature of the tensile specimen and an axial contact extensometer, compliant with ISO 9513 Class 1 [6], was used to measure the strain up to 4% before switching to crosshead displacement to estimate the strain for the remainder of the test.

1.1 TEST MATERIAL AND SPECIMENS

Table I presents the HSS grades which are included in the experimental investigation, covering a range of nominal yield strengths (σ_y) between

TABLE I. GRADES OF COMMERCIAL HSS INCLUDED IN THE PROGRAM.

	Grade	**σ_y (N/mm^2)**	**Plate thickness (mm)**	**Tensile specimen**	**Manufacturing process**
Steel A	S690QL	690	16	M12	Quenched and tempered
Steel B	S700MC	700	12	M10	TMCP + cold-formed
Steel C	S690QL	690	15	M12	Quenched and tempered

TABLE II. CHEMICAL COMPOSITION OF THE HSS INCLUDED IN THE PROGRAMME.

	Chemical composition (wt %)											
	C	**Mn**	**Cr**	**Si**	**Ni**	**Cu**	**Mo**	**Al**	**Ti**	**Nb**	**V**	**B**
Steel A	0.17	1.29	0.56	0.29	0.46	0.18	0.21	0.037	0.002	-	0.003	0.003
Steel B	0.12	1.98	0.26	0.15	0.033	0.019	0.004	0.046	0.12	0.09	0.2	-
Steel C	0.2	1.44	0.015	0.17	0.17	0.015	-	0.062	0.004	0.06	0.06	0.004

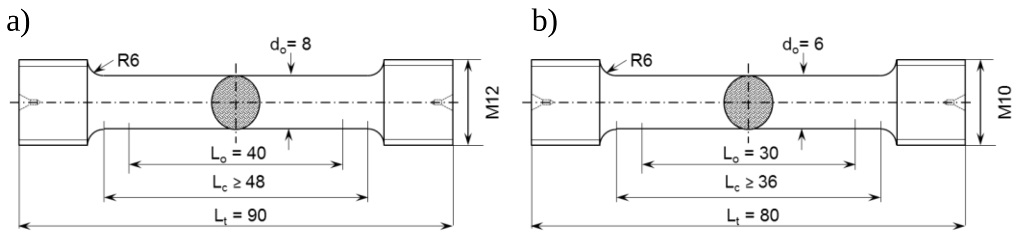

Figure 1. Dimension of a) M12 and b) M10 tensile specimen in mm.

690 and 700 N/mm^2 at ambient temperature (note that σ_y is used to describe the nominal yield strength whilst f_y, is used later to represent the effective yield strength defined in section 3.2). The designations for structural steel grades within EN 10025 [7] and EN 10149 [8] are denoted by an S at the beginning followed by the nominal yield strength (σ_y) at ambient temperature and then the production route/delivery condition. Q in the designation S690QL refers to the quench and tempered production process whilst L indicates that the material meets the minimum impact energy requirement at -40^{0}C [7]. Likewise M and C in S700MC indicate thermo-mechanical control processed (M or TMCP) and cold-formed (C) materials, respectively [8]. It is noteworthy that although steels A and C have the same designation, analysis by optical emission spectrometry revealed that these steels varied in chemical composition. The results from the analyses are presented in Table II. As shown in this table, both steel A and C were alloyed with chromium (Cr), nickel (Ni) and boron (B), however steel C contained no molybdenum (Mo) and had a slightly higher carbon content (0.20% vs 0.17%) but lower nickel content (0.17% vs 0.46%) and was also microalloyed with equal amounts of niobium (Nb) and vanadium (V). The TMCP steel B, had a lower carbon content than the quenched and tempered steels, a lower chromium addition and combined microalloying with titanium, niobium and vanadium, at higher levels than recorded for steels A and C.

Round M10 and M12 tensile specimens were machined parallel to the rolling direction from each of the plates detailed in Table I. The dimensions of the specimens which follow ISO 6892-1/2 [9, 10] are shown in Figure 1. The total length L_t, parallel length L_c, and the diameter at three positions along the gauge length L_o were measured for each tensile specimen using a digitised travelling light microscope. The average diameter d_o was then calculated and used to determine the cross-sectional area for each tensile specimen. The standard gauge length was calculated using the following formula for proportional tensile specimens (Eq. 1)

$$L_o = 5.65\sqrt{A_c} \tag{1}$$

where A_c is the cross-sectional area of the tensile specimen. L_o was rounded to nearest multiple of 5 mm, as recommended in ISO 6892-1 [9]. Such approximation is only valid if the difference between the calculated gauge length and approximate gauge length is less than 10%. In total, 27 specimens (9 for each steel type) were tested in the current study.

1.2 ELEVATED TEMPERATURE TESTS

Tensile testing at elevated temperature may be conducted isothermally or anisothermally, also known as steady-state and transient testing, respectively. In an isothermal test, the specimen temperature is equilibrated at the target temperature before straining to failure at a controlled rate. In an anisothermeal test, the specimen is held at a target load and then the temperature is increased at a controlled rate until failure occurs, the strain is recorded to generate a set of load-strain curves for different temperatures. Researchers have compared data taken from isothermal and aniosthermal tests for mild steels at 0.2% and 1.0% proof strength [11]. The results for the 0.2% proof strength from transient-state tests were found to be at least 10% below the minimum steady-state range between 400 and 800^{0}C due to the increasing influence of creep strains above 400^{0}C [12]. However, for the 1.0% proof stress there was good agreement between the two test methods. Moreover, Kirby and Preston concluded that for large strains (i.e. 2% and above), data derived from either test method can be used to predict the behaviour of steel components in a fire [13]. This paper will present data from isothermal tests.

1.2.1 STRAIN RATE

Knobloch *et al.* investigated the influence of strain rate on the stress-strain response of mild steel at 400, 550 and 700^{0}C under isothermal conditions [14]. The strain rates adopted were 0.0002/min, 0.001/min and 0.005/min, which are representative of the range of long to short fire durations. It was found that as the strain rate decreased, a lower effective yield strength ($f_{y,\theta}$) was observed, so the reduction factors from the experimental data did not correlate well with the European and American fire design guidelines when the strain rate was 0.0002/min or 0.001/min. However, there was good agreement between the experimental data and the reduction factors when the strain rate was 0.005/min. Thus a strain rate of 0.005± 0.002/min was used throughout the current investigation, which is also in agreement with the American standards [15]. The strain rate was indirectly controlled by specifying a crosshead displacement rate (mm/min) v_c, based on Eq. 2:

$$v_c = \dot{\varepsilon}_{L_c} \times L_c \tag{2}$$

where $\dot{\varepsilon}_{L_c}$ and L_c are the target strain rate and parallel length of the tensile specimen, respectively. This method gave strain rates that were compliant with ASTM E21-09.

1.2.2 HEATING RATE

In structural fire design, heating rates for steel should be within the range of 2 to 50^{0}C/min as specified in EN 1993-1-2 [5] in order to reflect real fire behaviour. In this study the temperature was increased at a steady rate of 10°C/min, which represents a fire resistance time of 1 hour based on the standard ISO 834 fire curve [13]. This heating rate has also been consistently used in literature (e.g [13, 16]). To avoid any temperature overshoot and to reach the prescribed temperature within the limits of $\pm 3^{o}C$, the heating rate decreased steadily to $3^{o}C$/min when the temperature reached 80% of the target temperature. This ensured that the entire parallel length of the specimen reached thermal equilibrium by the time the target temperature was reached. Two tensile specimens were tested at each of 400, 500 and $600^{o}C$.

2 RESULTS AND DISCUSSION

In this subsection, the main parameters related to strength and stiffness (i.e. $f_{p,\theta}$, $f_{y,\theta}$ and $E_{a,\theta}$) are assigned reduction factors, which is the ratio between the property at elevated temperature and the corresponding term at ambient temperature. The results presented in Table III are compared with literature where tests were conducted under isothermal conditions [2, 3, 16] and the Eurocode [15].

2.1 PROPORTIONAL LIMIT

The proportional limit ($f_{p,\theta}$) is defined as the point where the stress-strain curve changes from linear to non-linear. As this is difficult to identify in materials with no distinctive yield point such as high strength steel or stainless steel, the 0.2% offset value is widely used. This is the point where the proportional line offset at 0.2% strain intersects the stress strain curve and is also known as the 0.2% proof stress or the 0.2% offset yield strength. In Figure 3, the reduction values for the 0.2% proof strength at elevated temperatures ($f_{p,0.2,\theta}/f_y$) are presented along with data from literature [2, 3, 16] and the reduction factors for the proportional ($f_{p,\theta}/f_y$) and effective yield strength ($f_{y,\theta}/f_y$) from EN 1993-1-2 [5]. From Figure 3 it can be seen that in many cases the $f_{y,\theta}/f_y$ reduction factors are unconservative, except for steel B (S700MC) at all temperatures tested, HSA800 (S650M) tested by Choi *et al* [16] between 20 – $300^{o}C$ and BISPLATE 80 tested by Chen *et al* [2] between 500 – $700^{o}C$. Hence $f_{p,\theta}$ is more appropriate, although it is noteworthy that at temperatures below $200^{o}C$ even $f_{p,\theta}$ reduction factors are slightly unconservative and do not depict the loss in strength accurately.

2.2 EFFECTIVE YIELD STRENGTH

In the Eurocode EN 1993-1-2, the effective yield strength ($f_{y,\theta}$) is based on the total strain level at 2.0% [11] (depicted in Figure 2) . In Figure 4 the reduction values for the effective yield strength at elevated temperatures ($f_{y,\theta}/f_y$) are presented along with data from literature [2, 3, 16] and the reduction curve taken from the Eurocode. Generally it is observed that the Eurocode is conservative at predicting the effective yield strength for all three steels, with the exception of steel A (S690QL) and

TABLE III. REDUCTION FACTORS OF YIELD STRENGTHS AND ELASTIC MODULUS.

θ, Temperature (^{0}C)	Steel A			Steel B			Steel C		
	$f_{p0.2,\theta}/f_y$	$f_{y,\theta}/f_y$	$E_{a,\theta}/E_a$	$f_{p0.2,\theta}/f_y$	$f_{y,\theta}/f_y$	$E_{a,\theta}/E_a$	$f_{p0.2,\theta}/f_y$	$f_{y,\theta}/f_y$	$E_{a,\theta}/E_a$
20	0.96	1.00	1.00	0.98	1.00	1.00	0.99	1.00	1.00
400	0.80	0.86	0.72	0.91	0.99	0.81	0.84	0.93	0.85
500	0.78	0.84	0.70	0.83	0.87	0.82	0.74	0.80	0.83
600	0.57	0.66	0.73	0.62	0.69	0.40	0.51	0.54	0.60

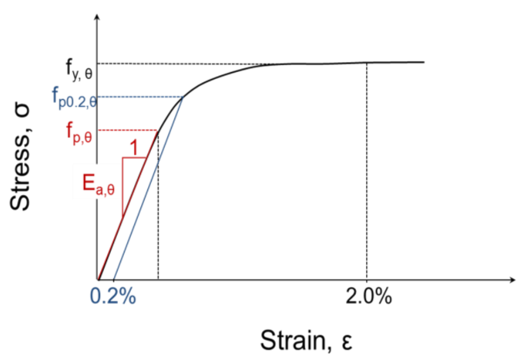

Figure 2. Stress-strain curve at elevated temperature.

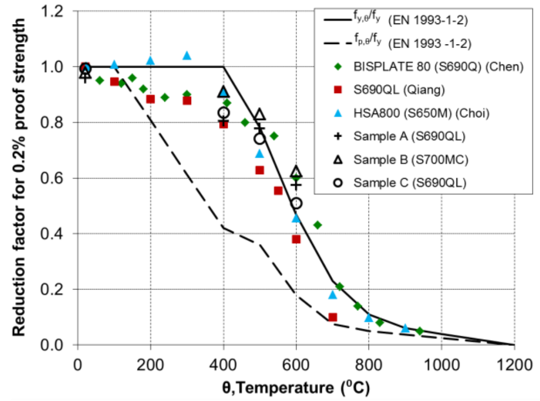

Figure 3. Reduction factors for the 0.2% proof strength.

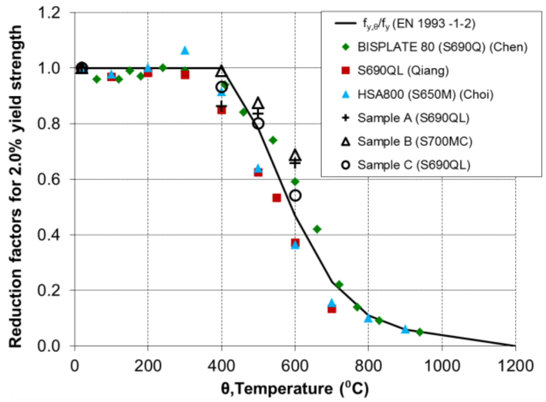

Figure 4. Reduction factors for the 2% yield strength.

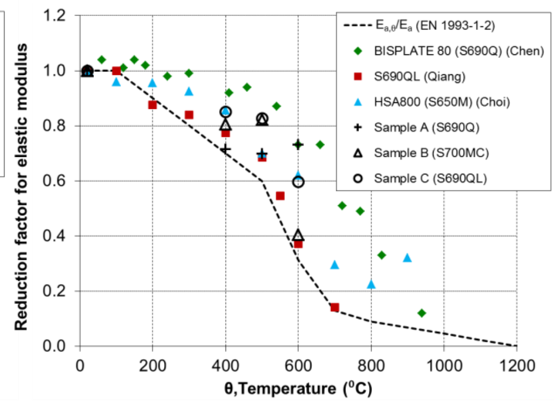

Figure 5. Reduction factors for the elastic modulus.

C (S690QL) at 400^{0}C. In comparison the Eurocode is not conservative at predicting the reduction factors of the effective yield strength for the steels in literature, with the exception of HSA800 tested by Choi *et al.* [16] at 300^{0}C and BISPLALTE 80 (S690Q) tested by Chen *et al.* [2] between 500 and 700^{0}C. Steel B, a thermomechanical control processed and cold formed material had the best strength reduction properties compared to all other steels at the tested temperatures. This steel contains niobium and titanium and also had the highest reported vanadium content of the tested steels (see Table II) which suggests that this steel may contain stable precipitates of niobium or vanadium carbonitrides. Such precipitates play a crucial role in retention of steel strength at temperatures up to 650^{0}C [17]. Steels A and C are both quenched and tempered materials that vary in chemical composition. Steel A contains molybdenum and substantially more chromium than steel C, which could be linked to its better strength retention properties by comparison with steel C but further research is needed to confirm this.

2.3 ELASTIC MODULUS

The elastic modulus, E_a is used to determine the stiffness of a structural element and hence its load bearing capacity [3]. E_a and $E_{a,\theta}$ (i.e. the elastic modulus at a temperature θ) were determined based on the tangent modulus of the initial linear elastic region of the stress-strain curve (Figure 2). Figure 5 illustrates the reduction factors for the elastic modulus ($E_{a,\theta}/E_a$) from the experimental study compared with literature [2, 3, 16] and the Eurocode (EN 1993-1-2) [5]. From the results it can be seen that the elastic modulus follows a similar trend to the other steels tested in literature and the reduction factors are generally conservative. Some of the results should be treated with caution, particularly the elastic modulus for steel A which will require further testing to ensure consistent results.

3 CONCLUSIONSAND FUTURE WORK

This paper has presented preliminary results as part of an experimental study on the material properties of three commercial HSS at elevated temperatures. The 0.2% proof strength ($f_{p0.2,\theta}$), effective yield strength ($f_{y,\theta}$) and elastic modulus ($E_{a,\theta}$) were obtained from ambient and isothermal tests at 400, 500 and 600^{o}C. The results were presented as reduction factors and compared to literature [2, 3, 16] and EN 1993-1-2 [5]. The results suggest that the Eurocode provides conservative predictions for the proportional limit at temperatures greater than 200^{o}C and the elastic modulus at all temperatures for the steels tested. Steel B had the best strength reduction factors compared with steels A and C. On the other hand, steel C had the poorest strength retention properties. It is clear from the results presented in Figure 3 and Table II that there are significant differences in the performances of high strength steels from different sources and it is likely that the chemical composition and production route are influential on the material performance at elevated temperatures. A previous study supports the view that elements such as niobium, and molybdenum have a positive influence on the strength retention properties at temperatures as high as 650^{o}C [17] but further research is required to find out, for instance the metallurgical influences that result in steel B having better strength retention properties than steel A or C. Hence future plans for this wider research project will include a detailed metallurgical investigation with the aim of characterising the microstructural changes in terms of time and temperature. In particular, the influence of grain size and precipitates on the mechanical properties at elevated temperature will be studied.

The HSS presented in Table I will be heat treated to replicate isothermal tensile tests. Thereafter, a technique called electron backscatter diffraction (EBSD) will be used to characterise the grain size of the heat treated samples and compared with the sample at ambient temperature. Future work will include transmission electron microscope (TEM) studies to characterise precipitates and microstructure. Such information will support further material developments to optimise the ambient and elevated temperature properties by providing steel producers with preliminary guidance on the effects that chemical composition and processing routes have on the elevated temperature performance. The steels will also be tested to get a full temperature profile from 20-900^{0}C under isothermal and anisothermal conditions. The data from this project will be incorporated into ABAQUS models to evaluate the behaviour of HSS structural members during a fire.

ACKNOWLEDGEMENTS

The authors would like to acknowledge the EPSRC and TWI Ltd. for the financial support provided for this work through an Industrial CASE award scheme.

REFERENCES

1. EN 1993-1-12. 2007. "Eurocode 3 Design of Steel Structures - Part 1-12: Additional Rules for the Extension of EN 1993 up to Steel Grades S700," *CEN*.
2. Chen, J., Young, B. and Uy, B. 2006. "Behaviour of High Strength Structural Steel at Elevated Temperatures," *J. Struct. Eng.*, 132(12):1948-1954.
3. Xiang, Q., Biljaard, F. and Kolstein, H. 2012. "Dependence of Mechanical Properties of High Strength Steel S690 on Elevated Temperatures," *Constr. Build. Mater.*, 30: 73-79.
4. Winful, D. A., Cashell, K. A., Barnes, A. M. and Pargeter, R. J. 2015. "High Strength Steel in Fire" Proceedings of CONFAB, the first International Conference on Structural Safety under Fire & Blast, Glasgow, Scotland. ASRANet Ltd, pp. 105-114.
5. EN 1993-1-2. 2005. "Eurocode 3. Design of Steel Structures – Part 1 - 2: General Rules - Structural Fire Design," *CEN*.
6. EN ISO 9513. 2012. "Metallic Materials – Calibration of Extensometer Systems used in Uniaxial Testing," *CEN*
7. EN 10025-6. 2004. "Hot Rolled Products of Structural Steels – Part 6: Technical Delivery of Flat Products of High Yield Strength Structural Steels in Quenched and Tempered Conditions," *CEN*
8. EN 10149-2. 2013. "Hot Rolled Flat Products made of High Yield Strength Steels for Cold Forming – Part 2: Technical Delivery Conditions for Thermomechanically Rolled Steels," *CEN*.
9. EN ISO 6892-1. 2009. "Metallic Materials – Tensile Testing. Part 1: Method of Testing at Ambient Temperature," *CEN*.
10. EN ISO 6892-2. 2011. "Metallic Materials – Tensile Testing. Part 2: Method of Test at Elevated Temperature," *CEN*.
11. Wang, Y., Burgess, I., Wald, F. and Gillie, M. 2012. *Performance-Based Fire Engineering of Structures*. CRC Press, pp. 98-99.
12. Gardner, L., Insausti, I., Ng, K. T. and Ashraf, M. 2010. "Elevated Temperature Material Properties of Stainless Steel Alloys," *J. Constr. Steel. Res.*, 66(5): 634-647.
13. Kirby, B. R. and Preston, R. R. 1988. "High Temperature Properties of Hot Rolled Structural Steels for use in Fire Engineering Design Studies," *Fire. Saf. J.*, 1: 27-37.
14. Knobloch, M., Pauli, J. and Fontana, M. 2013. "Influence of the Strain-Rate on the Mechanical Properties of Mild Carbon Steel at Elevated Temperatures," *Mater. Des.*, 49: 553-565.
15. ASTM International. 2009. "ASTM E21-09 Standard Test Methods for Elevated Temperature Tension Tests of Metallic Materials."
16. Choi, I.-R., Chung, K.-S. and Kim, D.-H. 2014. "Thermal and Mechanical Properties of High-Strength Structural Steel HSA800 at Elevated Temperatures," *Mater. Des.*, 63: 544-551.
17. Sha, W., Kelly, F. S. and Guo, Z.X. 1999. "Microstructure and Properties of Nippon Fire-Resistant Steels," *J. Mater. Eng. Perform.*, 8(5): 606-612

TIMBER STRUCTURES

Development of Wood Structural Elements for Fire Resistant Buildings

HIROKAZU OHASHI, SHINYA IGARASHI
and TSUTOMU NAGAOKA

ABSTRACT

As forestry contributes to the reduction of greenhouse gases by CO_2 fixation, in recent years, use of wood in buildings has attracted all over the world more attention. However construction of large wood structures is almost inexistent within urban areas in Japan. This is due to the Japanese law on fire protection of wood buildings in cities, which is considered very strict with severe requirements.

This paper presents a research work relative to the development of fire resistant wood structural elements for buildings in cities. These wood structural elements, made of glued laminated timber with self-charring-stop, have sufficient fire resistance during and after a fire, and comply with the strict Japanese standard for wood structural elements, which stipulates that such elements have to withstand the whole dead-load of concerned buildings after fire. To comply with such requirements, new elements of glued laminated timber with self-charring-stop layer were developed and their performance was confirmed. Several fire resistant tests conducted on columns, beams, column-beam joints, connections between beams and walls, and beams with holes were carried out. All tests proved that the elements have sufficient fire resistance. No damage was found out at the load-bearing part of the elements after testing. These wood structural elements have already been applied in six projects, where large-size wooden buildings were constructed in urban areas in Japan.

INTRODUCTION

As the major portion of constructions built in Japan was made principally of wood, the domestic forest resource was heavily drained, especially after the war. Furthermore, Japanese cities had experienced many disasters where wooden structures collapsed or underwent severe damages due to devastating typhoons, or were destroyed by large fires like the one that occurred during the Great Kanto Earthquake. For that reasons, the Building Standard Law enacted in 1950 had forbidden the generalization of wooden buildings that exceed a certain size in urban areas.

Hirokazu Ohashi, Research & Development Institute, Takenaka Corporation, 1-5-1, Ohtsuka, Inzai-shi, Chiba 270-1395, JAPAN
Shinya Igarashi, Takenaka Corporation, 1-1-1, Shinsuna, Koto-ku, Tokyo 136-0075, JAPAN
Tsutomu Nagaoka, Takenaka Corporation, 1-5-1, Ohtsuka, Inzai-shi, Chiba 270-1395, JAPAN

However, in recent years, the use of wood received a great deal of attention with a growing environmental awareness. To meet the diverse requirements and continuous development within the country, the Building Standard Law was revised in 2000 towards performance-based regulations, and since then it has become possible to deal with wooden structures as fire resistant buildings by satisfying a predetermined fire resistant performance level.

While use of wood as a structural element in relatively tall and/or large buildings has attracted all over the world more attention, in Japan, to enhance the use of wood in the construction of buildings, the "Act for Promotion of Use of Wood in Public Buildings" was established in 2010 [1]. The act was enacted in order to contribute to the reduction of greenhouse gases by CO_2 fixation. Despite the fact that wooden elements should be protected, mainly from fire, use of wood has been increasing due to various developments in fire protection [2].

Most simple and easy solutions to cover the surface of wooden members by nonflammable material sheets have been reported by N. Yasui et al.[3] However, in this case, fine characteristics of wooden material, such as softness, warmth etc., are completely lost. Other methods, based on the theory of self-charring-stopping, or installing a steel frame in the wooden member, were described by M. Tokoyoda et al.[4] or injecting an incombustible material in the wooden member to form fire protect layer, has been studied by T. Harada et al.[5] As for the method of installing steel frame, wooden materials cannot be used effectively as structural members. Moreover, the method of injecting an incombustible material needs some special and/or large facilities to produce the members. The outlines of these methods are shown in Figure 1.

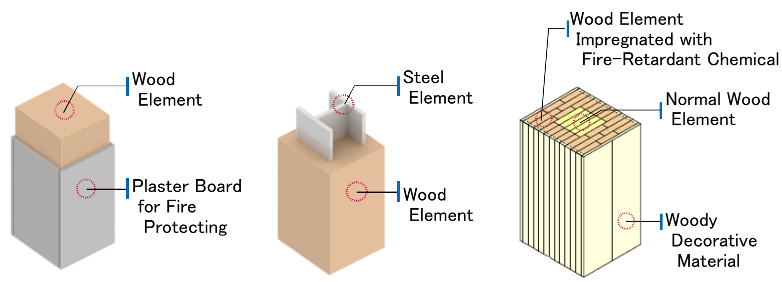

Membrane Type [3] Steel Hybrid Type [4] Fire-Retardant Wood Type [5]

Figure 1. Previously proposed fire resistant wooden column members.

This paper presents a novel technique by which wooden load-bearing elements, made of glued laminated timber, can resist fire and comply with the Japanese law on fire protection of wood buildings in cities. Besides the sacrificial (surface) layer of the wooden elements, the authors introduced an intermediary layer that improved considerably the performance of these elements. At the early stage, the development of the glued laminated timber with self-charring-stop performance had been carried out until 2008 [6], [7], [8], [9]. The adequacy of the developed technique has been confirmed through laboratory tests, conducted on columns, beams, column-beam joints, connections between beams and walls, and beams with holes. Wood structural elements using this technique have already been applied in six projects, where large-size wooden buildings were constructed in urban areas in Japan [10], [11], [12], [13].

TECHNOLOGY DEVELOPMENT

Concept

To be implemented in buildings within urban areas, the developed wood elements should have a self-charring-stop characteristic after a fire without need for water. The original cross-section of the developed structural element is composed of three layers made of glued laminated timber: an outer "surface layer" known as "sacrificial layer", a middle "self-charring-stop layer" and an inner "load-bearing part" (see Figures 2, 4). The outer "sacrificial layer" is a layer that can be carbonized during fire. It exhibits a thermal barrier effect and reduces the flow of thermal energy to the interior of the section. The middle "self-charring-stop layer" stops the combustion propagation by absorbing the thermal energy of the "sacrificial layer" which continues its self-combustion after the end of fire. A material that has a large heat capacity, or can efficiently insulate invasion of heat to the "load-bearing part" is used for this middle layer. The role of the inner "load-bearing part" is to support safely the load on the element after a fire.

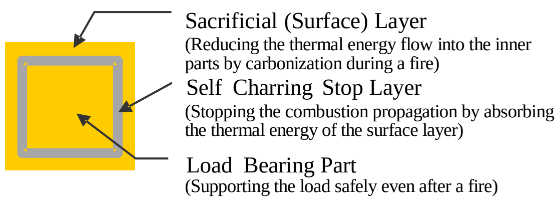

Figure 2. Concept of Cross-sectional Division.

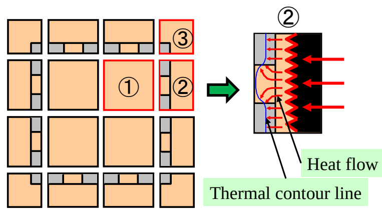

Figure 3. Thermal equivalent condition model.

Figure 3 illustrates the thermal equivalent condition parts in the section of a column member. The section is divided to three elements, that are “the load-bearing part ①, the plane region ② of the outer layer, and the corner part ③ of the outer layer”. Plane region ② is divided to smaller parts that are the sacrificial layer and the self-charring-stop layer. The self-charring stop layer consists of wood pieces and mortar pieces arranged mutually. Since the mortar pieces, which have a high heat capacity compared to the wooden materials, are placed on both sides of the wood, they can absorb heat from the sacrificial layer and restrain the temperature rise in the load-bearing part ①. As for the corner parts ③, mortar pieces are placed by all means, because this part tends to become a weak point by receiving heat from two directions.

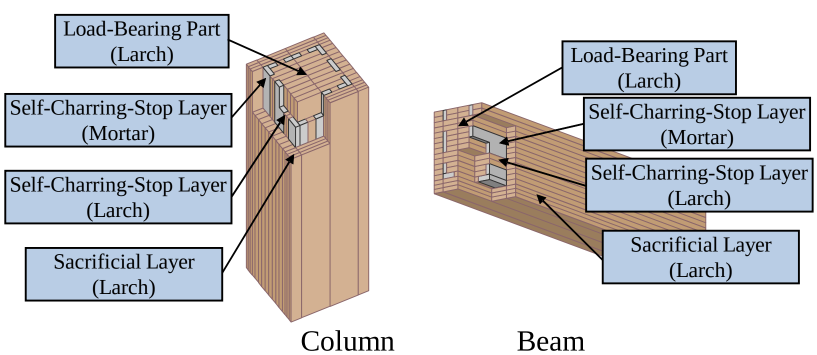

Figure 4. Illustration of Column and Beam Elements.

Performance Testing Process

Testing process of the proposed technique has known various stages. At first, the fire resistance of a beam and a column was investigated (see PHOTOGRAPH 1, Figures 5, 6). Then, more details were explored for the development of fire resistant connections and penetrations. Particular attention was considered for column-beam joints (see Figures 7, 8), partition walls and beams with holes (see PHOTOGRAPHS 2, 3, Figures 9). These investigations were approved by authorized institutions, where these wood structural elements were granted a one-hour fire resistant certification. Furthermore, during the service life of buildings, as cracking of the newly developed fire resistant wood elements is a problem that cannot be avoided due to the nature of wood, an allowable crack value (width: 5mm, depth: 60mm) was specified based on the combustion test of a full scale column specimen.

ONE HOUR FIRE RESISTANT CERTIFICATION

In order to ensure a good structural performance and a sufficient fire resistance, and improve the fire performance of glued laminated timber, various ways and materials' combinations have been studied. Thickness of the outer layer was made into a minimum size that allows a certain carbonization area to fully burn at the time of the end of heating, without reaching to the self-charring-stop layer. Finally, in addition to this result and taking into account some other conditions such as productivity, quality control and cost of the wooden elements, the alternate arrangement of wood and mortar test was selected as the suitable arrangement for the newly developed element. Then, the one-hour fire resistant certification of structural elements (column and beam) was obtained for the case of larch (see PHOTOGRAPH 1, Figures 5, 6).

Limit Level:
Temperature (℃) ≦260
Deformation (mm): h / 100
Deformation Speed (mm/min.): 3h / 1000

h: Height of Column (mm) 2670


Before Test　During Test　After Test

PHOTOGRAPH 1. Fire Resistant Certification Test.

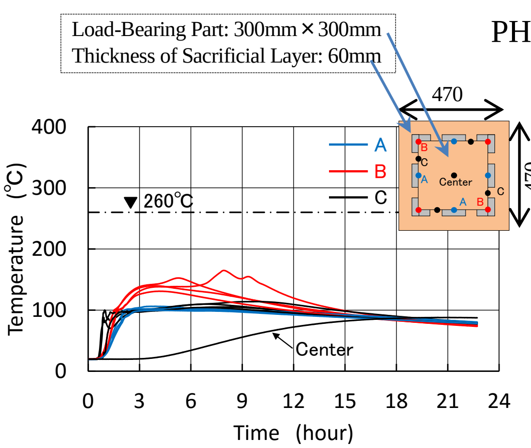

Figure 5. Temperature Variation of Column.

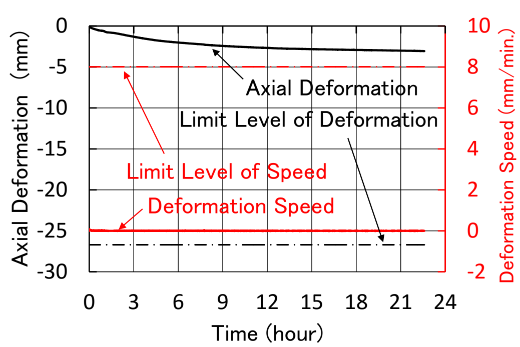

Figure 6. Axial Deformation and its Speed Variation of Column.

COLUMN-BEAM JOINTS

Development of column-beam joints was performed by setting, first, the structural type of the planed building. Frames of the building to be handled were of mixed types. A combination of steel or reinforced concrete frames and fire resistant glued laminated timber frames was considered. The steel or reinforced concrete frames were assigned all the horizontal forces (such as seismic forces) while the glued laminated timber frames would bear only their corresponding vertical loads. While metal joints such as drift pins or bolts with specific data records were adapted to joint the wooden elements, the heat transfer to the load-bearing part via such joints was of great concern when the metal joint would be exposed to the flame during fire, as the fire could enter from the gap of columns and beams. Therefore, it was decided to secure the one hour fire resistance for the beam-column joints, insure compatibility of deformations within the joint as well as the stress transfer between the columns and beams.

In order to satisfy these performance requirements, the beam end was provided with a drift-pin type joint to fix a gusset steel plate inserted into a slit within the load-bearing part of the beam, while another steel plate (end plate) welded transverse to the beam's gusset plate was provided with long through bolts to be screwed into the load-bearing part of the column. In order to ensure the required fire resistance and suppress any heat bridge coming from the metal plate during fire, the end plate was installed inside the charring-stop-layer of the column. Finally, the holes and gaps of the beam-column joints were, respectively, finished with wooden taps and filled with rock-wool of excellent fire resistance (see Figure 7).

The column-beam joints showed also a one hour fire resistance during an experiment of a vertically loaded and heated full scale specimen in the presence of representatives of a public organization of performance evaluation that affirmed the results (see Figure 8).

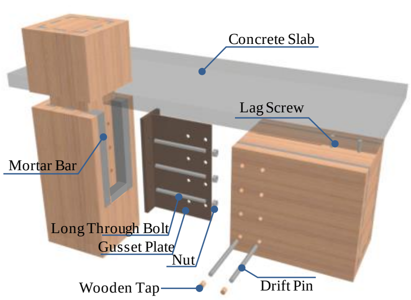

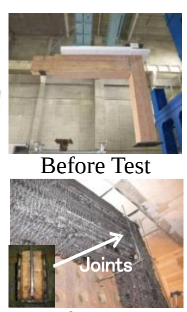

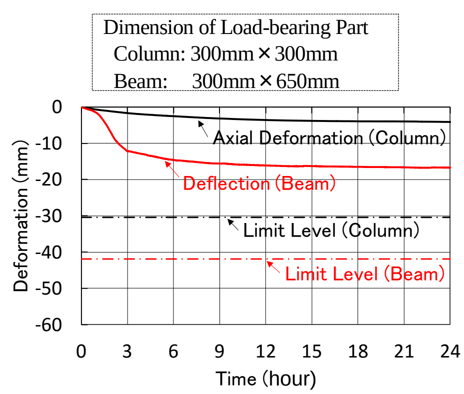

Figure 7. Column- Beam Joints.

Figure 8. Deformation of Column and Deflection of Beam.

FIRE RESISTANT PARTITION WALLS AND BEAMS WITH HOLES

In order to increase the flexibility of both equipments and building planning, beams with holes as well as partition walls had to be secured as to fire. Therefore, full scale combustion experiments were performed, where it was comfirmed that such elements had a fire resistance of one hour (see PHOTOGRAPH 2). In the experiment of the fire resistant partition wall, the wall resisted well and did not let fire cross to the opposite side of the wall.

In the experiment of the beam with holes, it was confirmed that the inside of the member did not burn along the holes (see Figure 9), as heat insulating material and heat capacity material (mortar) were provided around the hole (see PHOTOGRAPH 3).

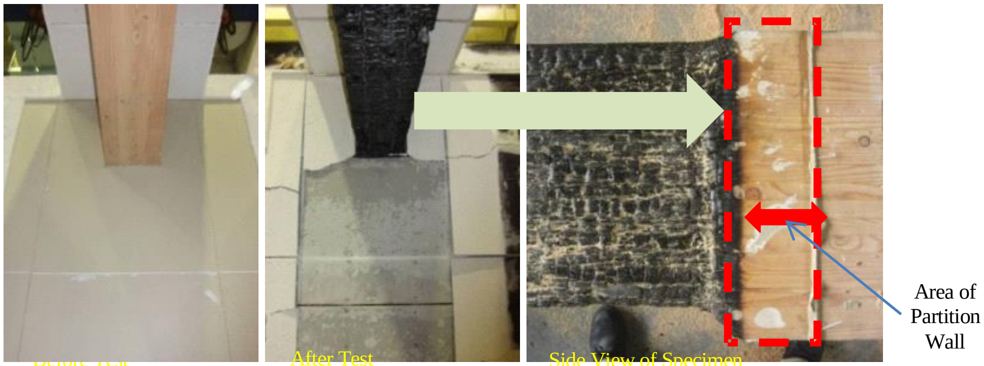

PHOTOGRAPH 2. Burning Test of Connections between Beam and Fire Resistant Partition Wall.

Before Test | During Test | After Test | Load-bearing part After Test

PHOTOGRAPH 3. Burning Test of a Beam with holes.

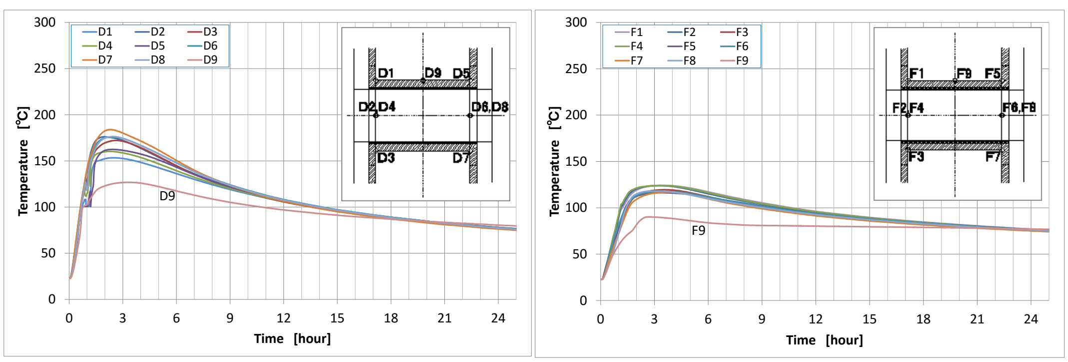

Figure 9. Temperature Variation around Holes.

EFFECT OF CRACK IN SACRIFICIAL LAYER

An investigation by combustion test on the presence of cracks in the newly developed wooden elements was carried out. While several cases with cracks of different widths and depths were investigated, no problem has been found as to the fire

TABLE 1. Range of cracks in tested specimens.

Width(mm)	Depth(mm)	Location Surface/Back
3	35	Back
	50	Surface
	60	Surface
5	30	Surface
	35	Back
	50	Surface
	60	Surface

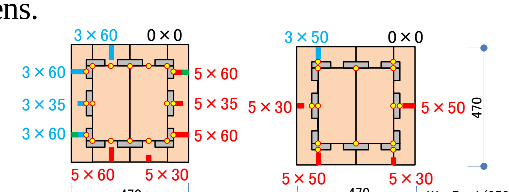

Figure 10. Cracks illustration in specimens.

resistance of the tested wooden elements with thin cracks on their sacrificial layer. The tested crack parameters are shown in TABLE 1 and Figure 10. The cracks were located on the surface and on the backside of the sacrificial layer. After the test, no effect was found on the load-bearing part's surface between the simulated cracks, where no charring and no change of color were observed.

APPLICATION OF TECHNOLOGY

The technology has already been applied in six buildings (office, commercial facilities, clinic, school and showroom) (see PHOTOGRAPH 4, 5, 6, 7). In 2016, it will be applied to a large school building in Tokyo.

PHOTOGRAPH 4. Office building in Osaka.

PHOTOGRAPH 5. Clinic in Chiba.

PHOTOGRAPH 6. School building in Yokohama.

PHOTOGRAPH 7. Showroom in Nagoya.

Commendations

The new product by its environmental contributions has received three ministerial awards (see Figure 11).

Minister of Agriculture, Forestry and Fisheries Award (2012)

Minister of Land, Infrastructure and Transportation Award (2013)

Minister of the Environment Award (2013)

Figure 11. Ministerial Awards.

CONCLUSION

To construct large wooden buildings in cities, research on fire resistant wood structural elements has been carried out and a novel technique has been developed. Every wooden element is composed of three layers made of glued laminated timber. The elements have a typical performance of self-charring-stop after fire without need for water of firefighters. More technologies related to these elements, including column-beam joints, beams with holes and effect of crack, were also developed to design and construct the safe wooden buildings. The newly developed structural elements have already been applied in six projects, where large-size wooden buildings were constructed in urban areas in Japan.

ACKNOWLEDGMENT

This study has been funded by NEDO (New Energy and Industrial Technology Development Organization), MLIT (Ministry of Land, Infrastructure and Transport and MAFF (Ministry of Agriculture, Forestry and Fisheries).

REFERENCES

1. "Act for Promotion of Use of Wood in Public Buildings", Japan, 2010 May.
2. "Develop guidelines for wooden fire resistant buildings in government buildings", Government Buildings Department, Ministry of Land, Infrastructure, Transport and Tourism, Japan, 2013 March.
3. N. Yasui, M. Koshihara, E. Kosugi, A. Utsumi, T. Sato, Y. Hirano, Y. Ohashi, "Development of Wooden Fireproof Building Made of Japanese Cedar", *<GBRC> General Building Research Corporation*, Vol.31, No.3, 2006 July, pp. 6-16.
4. M. Tokoyoda, Y. Fukuda, M. Sudou, T. Yoshikawa, H. Kinjo, T. Hirashima, K. Harada, S. Yusa, K. Saito, "Fire Resistance on Hybrid Wooden Structure (Part 21: Prediction of Internal Temperature Profile on H Shaped Steel Columns Protected by Wood during Fire Resistance Test)", *Summaries of Technical Papers of Annual Meeting - Architectural Institute of Japan*, 2005 September, pp. 133-134.
5. T. Harada, N. Hattori, K. Ando, Y. Nishioka, M. Miyabayashi, M. Shiozaki, "Development of Fire preventive Glued Laminated Lumber, (Part 1) Flaming Die Out of Fire-retardant Glued Laminated Lumber", *Summaries of Technical Papers of Annual Meeting - Architectural Institute of Japan*, 2006 September, pp. 85-86.
6. Hori N., Niwa H., Ohashi H., Oka H., Yamaguchi J., et al., "A Study on Fire Resistance Wooden Structure (Part 1-8)", *Summaries of Technical Papers of Annual Meeting - Architectural Institute of Japan* (2004, 2006, 2007, 2008).
7. Abe H., Ohashi H., Oka H., "Development of Wooden Structural Members with Fire Resistance", *Takenaka Technical Research Report*, No.62, 2006, pp. 1-8.
8. Oka H., Ohashi H., Yamaguchi J., Hori N., "A Study on Self-charring-stop of Glued Laminate Timber Made of Japanese Cedar Installing Mortar", *WCTE2008-10th World Conference on Timber Engineering-Miyazaki, JAPAN*, 2008 June.
9. Oka H., Ohashi H., Yamaguchi J., Hori N., "Development of Fire Resistant Glued Laminate Timber Made of Japanese Cedar", *Quality Forum 2008 Union of Japanese Scientists and Engineers,* 2008, pp. 189-194.
10. Ohashi H., Igarashi S., Nagamori H., Kinjyo H., et al., "A Study on Self-Charring-Stop of Wooden Structure (Part 1-5)", *Summaries of Technical Papers of Annual Meeting - Architectural Institute of Japan* (2012, 2013).
11. Ohashi H., Igarashi S., "Development of Fire-resisting Wood Structural Elements for Buildings", ICQ'14-Tokyo-*International Conference on Quality, Poster Session, P6*, Japan, 2014 October.
12. Ohashi H. , Nagaoka T. , Nagamori H, et al., "Influence of Wood Density to Fire Resistance of the Load-Bearing Part", *Journal of Technology and Design - Architectural Institute of Japan*, Vol.21, No.47, Japan, 2015, pp. 151-156.
13. Oka H., Igarashi S., Ohashi H., et al., "Large-Scale Fireproof Wooden Buildings in the Urban Areas of Japan", *SEFC 2015 PROCEEDINGS Structural Engineering Frontier Conference*, Japan, 2015 March.

Changing Failure Modes of Cross-Laminated Timber

RICHARD EMBERLEY, ALEXANDER NICOLAIDIS,
DILUM FERNANDO and JOSE L. TORERO

ABSTRACT

Cross-laminated timber relies on the adhesive layer between adjacent timber plies to provide composite action between the lamella for increased member strength and stiffness. Previous research has shown that adhesive loses normal and shear stiffness at elevated temperatures increasing the slip between adjacent timber plies. Slip in the bond layer results in reduced composite action increased deflections and a potential loss in ultimate strength in the CLT member. In order to study the effects of temperature on the flexural behavior of CLT, two series of tests were conducted. The first series focused on identifying the changing failure modes while the second series established conditions that led to those failure modes in large CLT beams. The results clearly showed the failure mode of CLT changes from timber failure to failure in the adhesive as a function of the in-depth temperatures. The adhesive failure yielded larger deflections and a loss in stiffness and ultimate strength.

INTRODUCTION

Cross-laminated timber (CLT) is an engineered mass timber product which relies on an adhesive layer between two adjacent timber plies to provide composite action of the plies for increased section strength. The crosswise layering homogenizes the timber properties in both the longitudinal and transverse directions. The adhesive layer in CLT provides composite action between timber plies while being subjected to both interfacial normal and shear forces. At ambient temperatures, the adhesive layer is typically strong enough to delay interfacial failures until the occurring of timber failures such as rolling shear or tensile failure in timber. Any loss of bond strength affecting the stiffness and strength of the adhesive could yield increases in deflection and decreases in ultimate strength due to loss of composite action due to increased slip or debonding of the bonded interface. Slip is the relative movement of two adjacent lamella apart from a complete rigid bond.

Very little research has been conducted on the relationship between adhesive behavior and the timber at elevated temperatures. Of the few studies conducted all have found that adhesive stiffness, strength, and slip are dependent primarily on the

The University of Queensland, School of Civil Engineering, Staff House Road, St. Lucia, QLD, 4072, Australia

temperature of the adhesive and independent of the heating of the timber. Frangi et al. [1] conducted shear tests on glued timber blocks (40mm bond line) at temperatures ranging from 20 to 170°C. Resorcinol-formaldehyde, one-component polyurethane, and epoxy were used to bond the timber joints. The study concluded that the only failure mode present above 70°C was cohesion failure of the adhesive. The results showed that the performance of the glue was highly dependent on the chemical composition of the adhesive. Clauß et al. [2] performed single-lap shear tests on a 10mm bond line at temperatures ranging from ambient to 220°C. The results were similar to the results in [1] in that the performance of the joint was dependent on the temperature of the adhesive. The chemical composition also varied the performance between adhesives.

Adhesive failure in CLT has clearly not been studied in depth and systematic research needs to be conducted to further understand elevated temperature effects on adhesive performance in CLT.

METHODOLOGY

Two series of tests were conducted in order to study failure mode changes in CLT at elevated temperatures. The first series of tests was structured to focus directly on the bond-line failure mode at elevated temperatures. The bond-line length was designed an order of magnitude greater than previous research in order to study the effect bond length has on the overall performance of the joint. This was based on the well demonstrated effects of bond length on the load carrying capacity of different bonded joints [3]. The second series of tests was designed to study whether the failure mode changes appeared in large CLT samples, the conditions inducing these failure modes and the structural consequences which occurred as a result. Specifics of the first test series can found in [4]. Since the first and second series were done in conjunction with one another, a general description of the methodology is summarized and the two series of tests are compared to show similarities in the bond failure.

The first series of tests consisted of a single lap shear test where the samples were subjected to temperatures ranging from ambient (25°C) to 150°C. Radiata pine timber samples with a 600mm bond length were glued together using a structural adhesive. Each sample was placed inside an MTS Series 651 Environmental Chamber and allowed to reach steady-state temperature. The force applied and the overall displacement of the sample were measured during each test. Observational data was collected as to the failure mode of each specimen [4].

The second series of tests focused on overall CLT beam performance when the first adhesive bond line separating the first and second timber plies was elevated to temperatures above ambient. Five-layer (145mm height) European spruce CLT beams of 1.5 meter length were exposed to a uniform 6 kW/m^2 heat flux from a natural gas powered radiant panel for two hours (Figure 1). The structural adhesive used in the CLT beams was a one-component polyurethane adhesive. The thermal load increased the bond line to temperatures between 65-80°C. Immediately, the samples were subjected to a three-point bend test until failure (Figure 1). Observational data on the

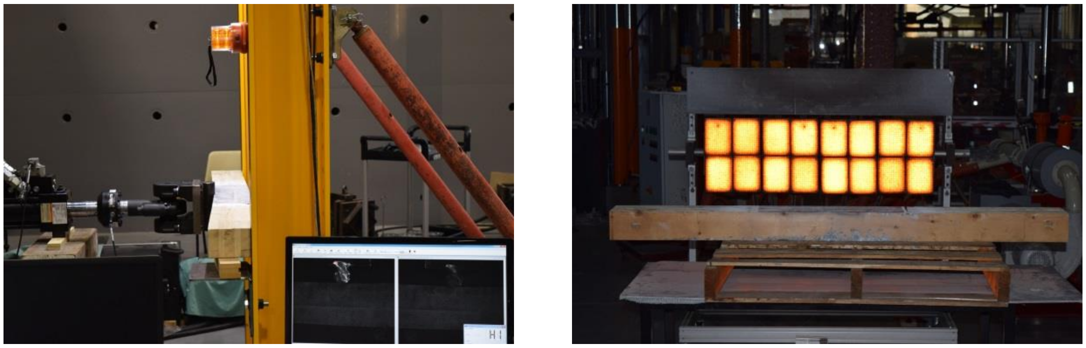

Figure 1. Three-point bend test of CLT beam (Left). Sample heated with 6kW/m^2 heat flux from radiant panel array (Right).

failure modes was collected. To guarantee that a failure mode would occur over the entire width of the beam, the samples were cut to a width of 100mm. The relatively slender nature of the beam also ensured the bond line temperature was uniform over the entire area. A 300x145mm area was captured using Digital Image Correlation (DIC) cameras to record strains, displacements and deflections in three dimensions at the mid-span of the beam. The images collected also showed the initiation and propagation of failure mechanisms in the CLT beams. An ambient temperature test was conducted as well as a control and means of comparison for the test at elevated temperatures.

RESULTS

In the first series of tests, single-lap shear tests were conducted with the bond-lines at elevated temperatures. While further detailed in [4], one of the main conclusions of the test was that as the temperature of the bond-line increased then the likelihood of a failure within the glue increased as well. For this type of glue, the temperature point was between 80-110°C (Figure 2). Below the threshold, the timber is the weakest portion of the beam and failure progresses through the timber. Above the threshold, the glue strength is weakest resulting in a failure through the bond-line.

Ambient Temperature Test

As in the first test series, clear timber failures were observed at ambient temperature (Figure 3). Failure initiation of the CLT beam initiated due to shear failure in the transverse lamellas. Rolling shear failure was observed in ply four. Ply four is the transverse lamella in the tensile region of the bending beam. The occurrence of rolling shear was due to the thin nature of the beam and the weak shear modulus of timber perpendicular to the grain. The grain structure of plies two and four was perpendicular to the load. Slight rolling shear occurred in ply two but the failure quickly propagated through the timber. Each of the main failure cracks continued to open with one of the cracks passing through several bond lines. Any crack at the bonded interface, whether in the compressive or tensile region of the cross section, will generate high interfacial shear and normal stresses. Nevertheless, bond strength was strong enough to diverge the failure to occur within timber substrate. The final failure of the beam was when the beam fractured through to the end as shown in figure 3 (left).

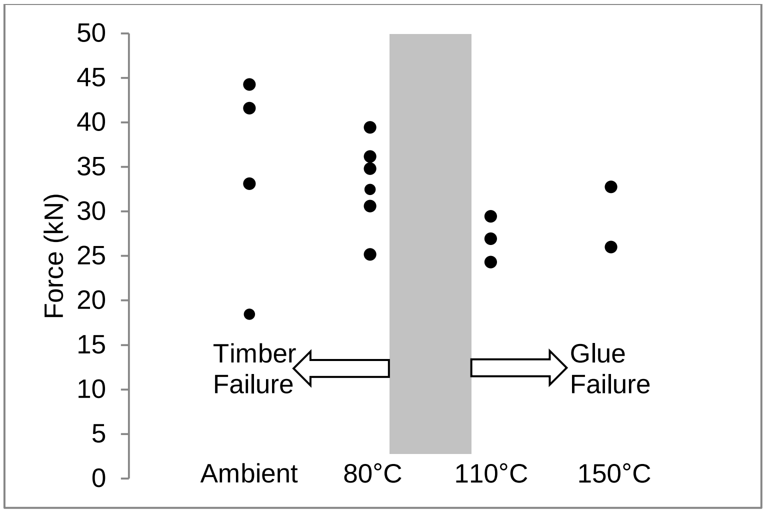

Figure 2. Elevated temperature single-lap shear test failure loads and failure types [4].

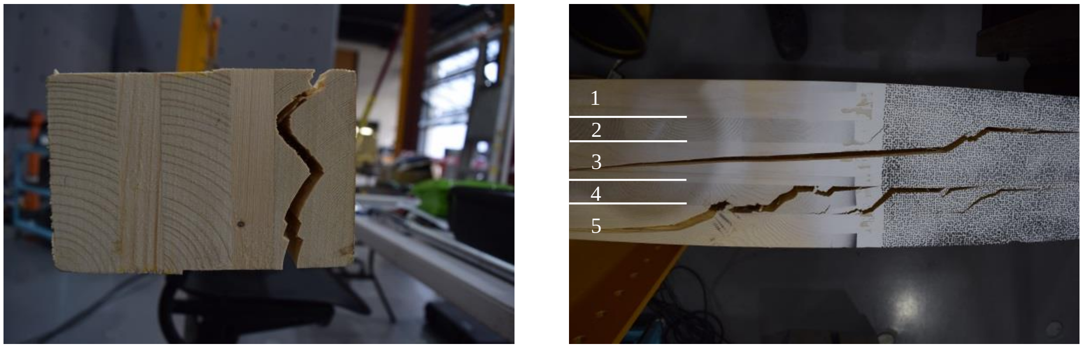

Figure 3. Ambient temperature test. Beam failure at end support (Left). Beam failures near mid-span (Right).

Elevated Temperature Test

In the elevated temperature tests, failure initiation was due to shear failure in the transverse lamellas, while debonding between ply four and five was the predominant failure mode (Figure 4). Rolling shear occurred this time in ply two. As the shear crack of ply four (i.e. transverse lamella) approached the bonded interface, debonding of the lamella four and five occurred and propagated towards the end of the beam. A tensile failure was also observed in the ply five but was not the main failure mode as the rolling shear and debonding were more extensive. In the portions of the beam farthest away from heated region, namely plies one and two, the failure modes did not go through the adhesive but cracks travelled through the timber to the end of the beam.

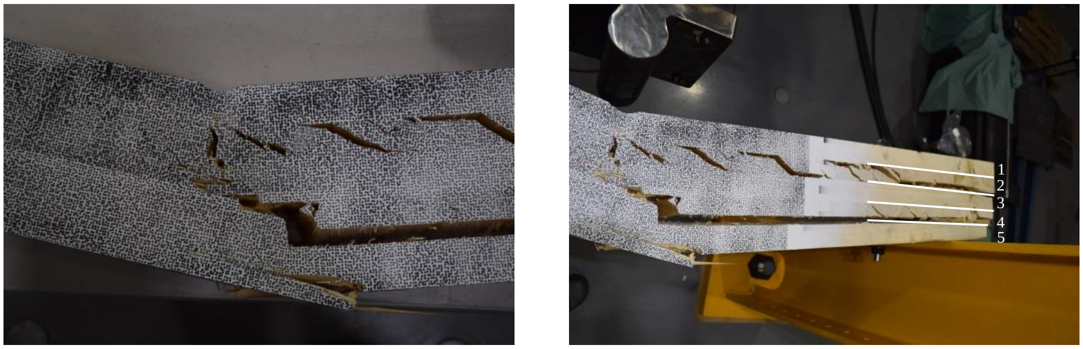

Figure 4. Elevated temperature test. Center of beam and failure initiation location (Left). Beam after failure (Right).

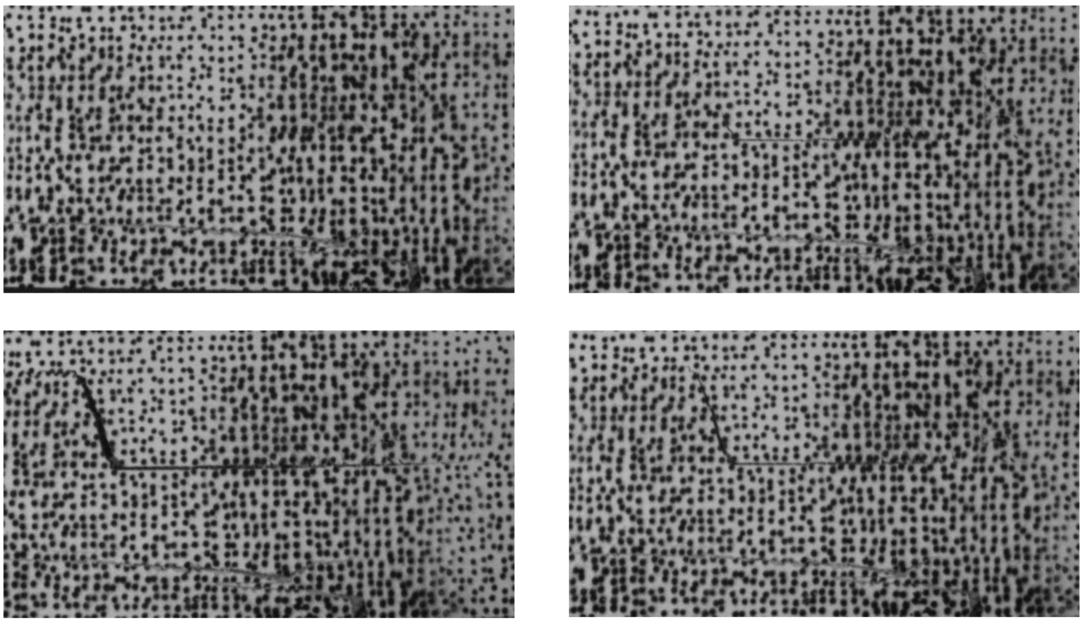

Figure 5. Delamination failure sequence (clockwise from top left) between lamella four and five.

Debonding Initiation and Propagation

Debonding of the bonded interfaces is mainly due to high interfacial stresses, i.e. shear and/or normal. In laminated beams subjected to flexure, high interfacial shear and normal stresses may arise due to discontinuities (e.g. a crack or a gap in the interface) in the high moment region. Debonding of plated beams due to high interfacial shear and normal stresses has been studied extensively [5, 6]. High interfacial shear and normal stresses near the immediate area of the crack may cause debonding of the interface. The normal stresses act to pull apart the two lamella and are commonly referred to as peeling forces.

Figure 5 shows the delamination failure sequence during the elevated temperature test. The first failure observed was a shear crack formed in ply four. Once the crack occurred, the increased stresses around the area of discontinuity directed the crack along the bonded interface which was the weakest portion in this test. Once in the interface, the crack continued through the interface down the length of the beam.

Debonding will continue until the crack reaches the end of the beam or reaches an area where the glue is stronger than the surrounding timber. At this point, the crack will then move into the timber. The top left picture in Figure 5 highlights the first instance of a visible crack. The top and bottom right pictures show the initial stages of debonding, and the bottom left picture shows a large portion of the bond-line has separated. This debonding, as can be seen in Figure 3, continued to almost the end of the beam. In the same beam however, the failure in the low temperature region (i.e. lamella one and two) did not occur within the interface but occurred within the timber similar to the specimen in the first test at ambient temperature. This clearly showed the effects of temperature in changing the failure modes (i.e. from failure within the timber to failure within the bonded interface) of CLT under flexural loading.

The results from both test series showed that as the temperature in the bond layers of CLT increases the failure mode changes from failure solely in the timber to cohesion failure in the adhesive. Both series also showed decreases in ultimate strength and increases in overall deflection of both the CLT beams and single joints. Figure 6 shows the changes in deflection and the ultimate strength failure of the CLT beams. Displacement was measured by the travel distance of the actuator. The CLT beam at ambient temperatures completely failed in the timber at approximately 35mm of deflection whereas the beam at elevated temperatures continued deflecting until complete failure around 100mm of deflection. The ultimate strength of the elevated temperature test was about 10 kN less than the ultimate strength of the ambient test. One reason for this could be due to the decrease in strength properties of the timber at elevated temperatures. Another reason could be due to the loss of composite action between the layers potentially due to the deterioration of the bond stiffness. Visible debonding occurred just after the peak load in the elevated temperature test.

The two CLT beams were identical samples with the only difference between them being one sample was heated with a 6kW/m^2 heat flux for two hours and the other one was at ambient temperature. All the failures in the ambient test were timber failures whereas debonding failure occurred in the heated sample. The occurrence of debonding in the elevated temperature test instead of timber failure indicates the strength deterioration of the bond between lamella four and five ahead of the strength reduction of the timber.

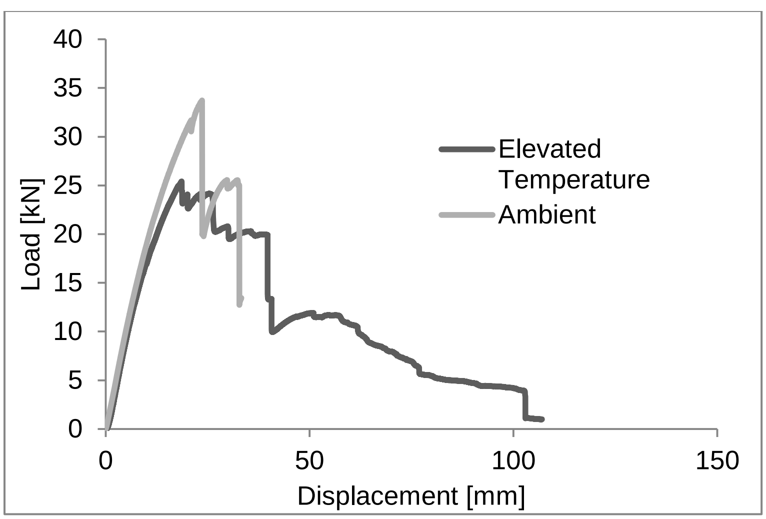

Figure 6: Load-displacement curve representative of the CLT beam tests.

CONCLUSIONS

The combined results from both series of tests clearly show the increased potential for bond-lines in CLT and glued joints to shift from a timber failure mode to a failure mode dominated by the decrease in residual strength of the adhesive when increased in temperature. Increases in deflection and a loss in ultimate strength are all potentially results from the adhesive losing its ability to transfer stresses between the timber plies without slip.

Even with reductions in the timber strength properties, the failure mode in the elevated temperature tests still occurred in the bond-line. If the bond had held, timber failures would have been expected at lower ultimate strength values due to timber strength reductions. Bond-line failures are not accounted for in current design practice of CLT. The only failure modes accounted for are timber failures and the loss of cross-section due to charring. Even in the charring failure mode, the structural failure is due to timber failure. With CLT relying heavily on composite action, any bond-line failure is unacceptable and is currently unaccounted [7].

Local discontinuities play a critical role in the initiation of debonding due to the high concentration of shear and normal forces. In these series of tests, cracks and the end of the single-lap shear bond were the discontinuities lead to debonding. However, other discontinuities occur in engineered timber. Due to the nature of CLT, discontinuities occur between the cross-layered boards throughout the entire member. Knots in the wood and manufacturing errors could also result in gaps. Each of these areas of discontinuity in the bond-lines has the potential to be an area of high stresses for the bond.

The work in this paper adds to the research conducted by [1, 2] and provides an explanation for increases in deflections in CLT members at elevated temperatures and reductions in ultimate strength. This work also highlights delamination and the mitigating factors for it. Continued research and tests need to be conducted to further understand bond-line slippage and failure in CLT beams.

REFERENCES

1. Frangi, A., M. Fontana, and A. Mischler, *Shear behaviour of bond lines in glued laminated timber beams at high temperatures.* Wood Science and Technology, 2004. **38**(2): p. 119-126.
2. Clauß, S., M. Joscak, and P. Niemz, *Thermal stability of glued wood joints measured by shear tests.* European Journal of Wood and Wood Products, 2011. **69**(1): p. 101-111.
3. Fernando, D., T. Yu, and J.G. Teng, *Behavior of CFRP Laminates Bonded to a Steel Substrate Using a Ductile Adhesive.* Journal of Composites for Construction, 2014. **18**(2): p. 04013040.
4. Nicolaidis, A., et al. *Thermally Driven Failure Mode Changes in Bonded Timber Joints*. in *World Conference on Timber Engineering* 2016. Vienna, Austria.
5. De Lorenzis, L., D. Fernando, and J.-G. Teng, *Coupled mixed-mode cohesive zone modeling of interfacial debonding in simply supported plated beams.* International Journal of Solids and Structures, 2013. **50**(14–15): p. 2477-2494.
6. Smith, S.T. and J.G. Teng, *Interfacial stress in plated beams.* Engineering Structures, 2001. **23**: p. 857-871.
7. Emberley, R. and J.L. Torero. *Cross-Laminated Timber Failure Modes for Fire Conditions*. in *Second International Conference on Performance-based and Life-cycle Structural Engineering*. 2015. Brisbane, Australia.

External an Internal Factors Influencing the Charring of Timber – an Experimental Study with Respect to natural Fires and Moisture Conditions

NORMAN WERTHER

ABSTRACT

The following publication summarizes the experimental work of fire tests as well as the accompanied analytical studies conducted by the author in order to assess the influence of the initial moisture content as well as varying temperature time scenarios, including the heating- and cooling phase of a fire on the charring of timber and on the temperature profiles within timber cross sections. The outcome of this research is a simplified design approach for calculating the charring depth, and an improved material model that can be used in numerical simulations.

INTRODUCTION

In recent years, an increased interest in using timber as a construction material has been noted all over the world, driven by a discussion of energy- and resource efficiency in the building sector. Despite political initiatives, which support the use of timber, concerns and gaps of knowledge still exist, particularly related to fire safety and the performance based design process. In case of a fire, failure of loadbearing elements may cause significant human and economic losses that are not tolerated by society. Considering these aspects, several design standards such as EN 1995-1-2 [1] have been developed to assess the fire safety of timber elements and structures. In general, the basic concept of these methods is the determination of the charring depth, followed by an assessment of the structural performance of the residual cross section. For unprotected timber elements exposed to standard fire, the reduction of the original cross section by charring has a larger influence on the load-bearing capacity as the thermal softening within the remaining cross section [2]. Considering this fact, the determination of the char depth is the key to a reliable structural fire design with timber. However, several experimental studies have shown that external and internal parameters influence the charring of timber and indicate for largely scattered results.
With respect to performance based design, it becomes ever more important to better understand how the charring of timber is influenced by specific parameters such as

Norman Werther, Technical University Munich, Chair for Timber Structures and Building Construction, Arcisstraße 21, 80333 Munich, Germany.

moisture content, permeability, incident heat fluxes or oxygen concentration in the fire compartment.

The following article comprises mainly the investigations and results of the conducted fire tests with varying temperature time scenarios and summarizes the general setup and results of the additional tests with varying initial moisture content. The numerical investigations including the derived material models, as well as detailed information of the test results for the charring behaviour of timber with individual initial moisture content, will be subject of additional articles by the author and will be published in due course.

EXPERIMENTAL INVESTIGATIONS

The following paragraphs provide details about the design of the fire tests. The tests were carried out at the fire testing facilities of the Leipzig Institute of Material Research and Testing (MFPA Leipzig).

Specimens

All specimens in the conducted fire tests were made out of glulam (strength class GL24) with lamellas that were graded visually prior to the examination. In all tests the specimen were 422 x 422 mm in size and exposed to fire from one side. The depth of all specimens was 140 mm. To avoid thermal exposure from the narrow sides, the specimens were lined sidewise with gypsum boards. The investigated glulam beams were composed of three individual beams (I – III) which were prepared in advance. To ensure similar quality and boundary conditions for the timber elements, all specimens were obtained from the same individual cross sections (lower part always from beam I, middle part always from beam II and upper part always from beam III). Hence, comparable lamellas of the test specimens originated always from the same beam. This procedure also ensured no branches being located in the area where the in-depth temperature measurement took place. The three parts of each specimen were glued with a melamine-urea-resin. All glulam specimens for the tests with varying temperature time scenarios consisted of spruce with a bulk density of 462 kg/m³ $\pm$ 10 and a moisture content of 12.5 M-% $\pm$ 0.2.

Instrumentation and Testing Facilities

In all specimens, Type K thermocouples (2 x 0.5) were installed at four positions (A – D) to continuously measure the temperature rise in steps of 6 mm throughout the thickness of the timber specimens during the fire tests, as shown in figure 1. In each specimen, 44 thermocouples were installed. The thermocouples were placed in 25 mm deep holes with a diameter of 2 mm, drilled-in from the top and bottom lamella of the middle section (II) of each specimen. To provide an even surface for proper gluing the thermocouples were fed in groves to the unexposed side. This procedure ensured that the thermocouples were aligned parallel to the isotherms under one dimensional fire exposure. The obtained measurements of these thermocouples were used to give an indication about the charring rate and thermal influenced area behind the char front during the fire exposure.

The specimens were placed in a diesel fired furnace as shown in figure 2 (left), and exposed from one side with varying temperature time scenarios, depicted in figure 2 (right). To control the furnace temperature, a plate thermocouple was installed in accordance with EN 1363-1 [3]. In addition, a 3 mm thick sheathed type K thermocouple was mounted besides the plate thermocouple in order to show the difference between the measurement systems for the gas furnace temperature. Furthermore, a sheathed thermocouple with 1 mm diameter was used to measure temperatures at the fire exposed surface of each specimen. Besides the temperatures, the atmospheric conditions were recorded during the tests.

Thermal Exposure

The temperature-time curves utilized in these fire tests represent a spectrum of heating- and decay phases of potential compartment fires, derived from a literature review and zone model simulations. These results cover opening factors varying from 0.04 $m^{1/2}$ to 0.12 $m^{1/2}$ in combination with a fuel load density of 500 MJ/m² and 1000 MJ/m² and a thermal inertia of well insulating enclosure materials (750 $J/(m^2Ks^{1/2})$). To allow a better comparison of the results, the maximum temperatures for all fire scenarios were assumed to occur after 30 and 60 minutes respectively, followed by three different types of decay phases (fast, medium, slow). Therefore the timber elements were ether exposed to low or high heating rates for a short and long period of time, combined with slow, medium and fast decay rates, in order to investigate resultant influences on the charring rate and the course of temperatures in the wooden cross sections. The chosen temperature time scenarios were intended to represent an upper and lower limit including a level of exposure similar to the standard fire. The resulting temperature time curves are shown in figure 2. In this context, it must be noted that a certain temperature time scenario is not solely defined by the three input parameters (opening factor, fuel load density and thermal inertia of the compartment) but is also influenced by the employed assessment method or simulation tool [5, 6, 7].

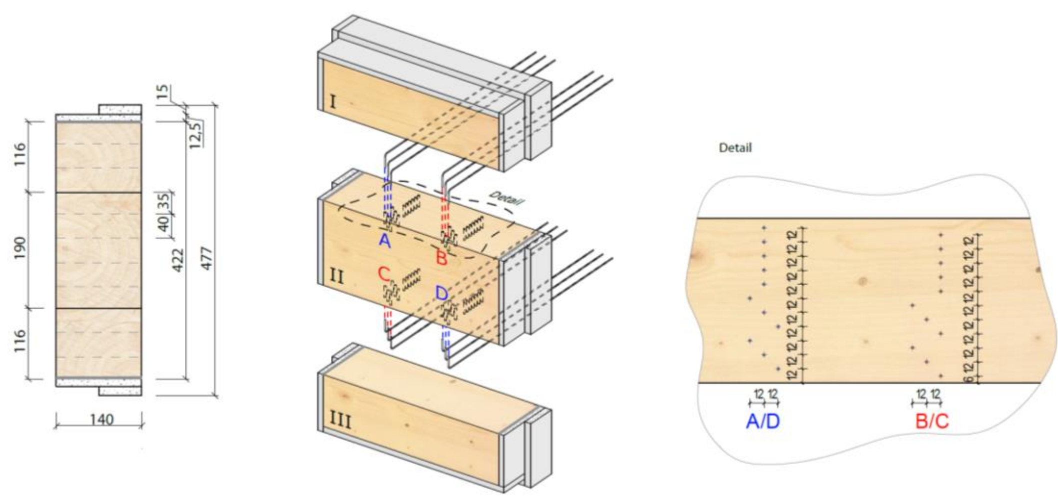

Figure 1. Setup of the specimens.

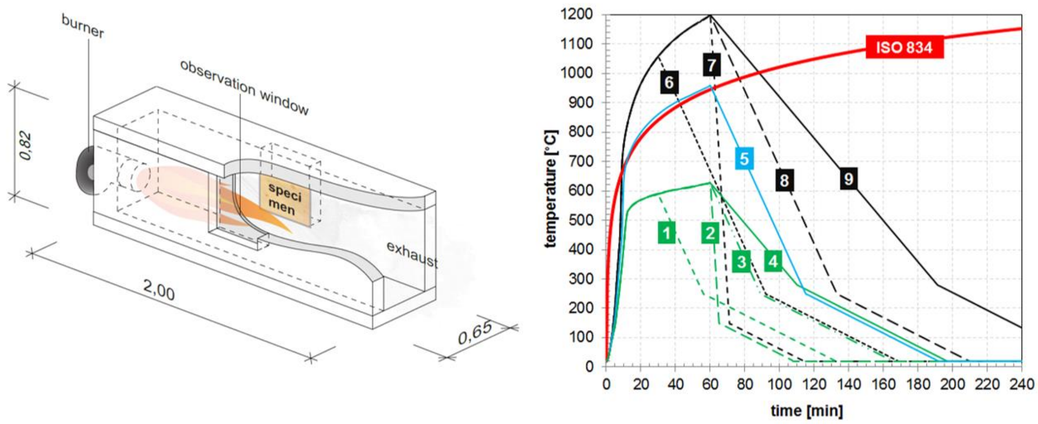

Figure 2. Test arrangement (left) and summary of temperature time scenarios (right).

Deviating from the specimens used in the tests to assess the influence of varying temperature time scenarios, the specimens for investigating the moisture influence were exposed to the standard fire curve in accordance with EN 1363 [3]. These specimens were conditioned in four different climates to reach constant moisture contents of 0 M-%, 6 M-%, 12 M-% and 18 M-%. The specimens were of the same size like the previous ones but with only a depth of 100 mm.

EXPERIMENTAL RESULTS

Temperature Time Scenarios

The comparison of the investigated temperature time scenarios showed significant differences between resulting charring and heating up behavior of the specimens. The magnitude and wide scatter of results is not known when examine other influencing factors under standard fire exposure. The tests suggested to distinguish between the heating and decay phase for assessing the data, due to the differences of the boundary conditions. An important aspect became evident from the comparison of temperature measurements at the surface of the timber elements with the plate thermocouple temperatures. During heating phases with low heating rates, temperatures up to 100°C above the furnace gas temperature were recorded on the surface. This was attributed to flaming combustion and exothermal reactions in the char layer. For a heating phase with heating rates similar to the standard fire and above, this difference became less evident and negligible. However, this phenomenon became more dominant for the decay phase particularly in combination with slow cooling rates. Figure 3 depicts an exemplary comparison of the temperatures measured during the tests No. 3 (low heating rate) and No. 8 (high heating rate) in combination with a medium duration of the cooling phase. The conducted tests show that exothermal reactions can significantly contribute to the charring process at the surface and must be taken into account in the heating- and most notably in a long cooling phase of the fire, when exothermal reaction in the char layer increases the affecting temperature. Within the cooling process an increase in oxygen concentration was recorded, which supports the exothermal reactions.

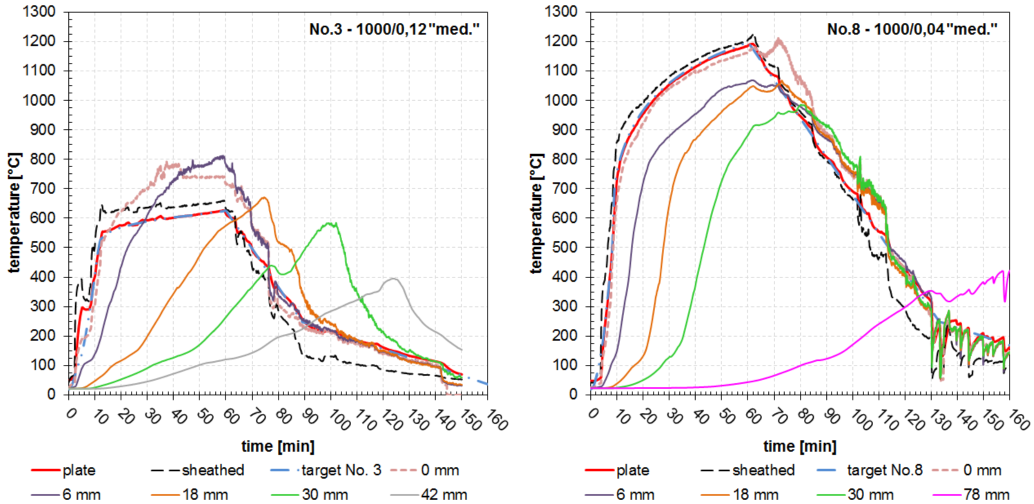

Figure 3. Comparison of surface temperature in tests No. 3 and No. 8.

The test results show that an increased heating rate results in an increased charring depth as well as an increased charring rate. The determination of the charring depth was based on the in-depth temperature measurements. The position of the char line was taken as the position of the 300°C isotherm, according to EN 1995-1-2. A comparison of the remaining cross sections with the temperature measurements confirmed that this assumption is also acceptable for the conducted series of fire tests. The examined "hot" fires (test No. 7, No. 8, No. 9) led, in the heating phase, to a charring rate almost twice as high as for the "cool" fire scenarios (test No. 2, No. 3, No. 4), see figure 4. Concurrently the temperature time scenario was not only influencing the charring rate but also had a significant impact on thermal affected region behind the char line. In this study, the depth between the 300°C and 60°C isotherm was estimated to be the thermally affected region behind the char line. Therefore, "hot" fire scenarios resulted in slender thermal affected zones as "cooler" fire scenarios as shown in figure 4.

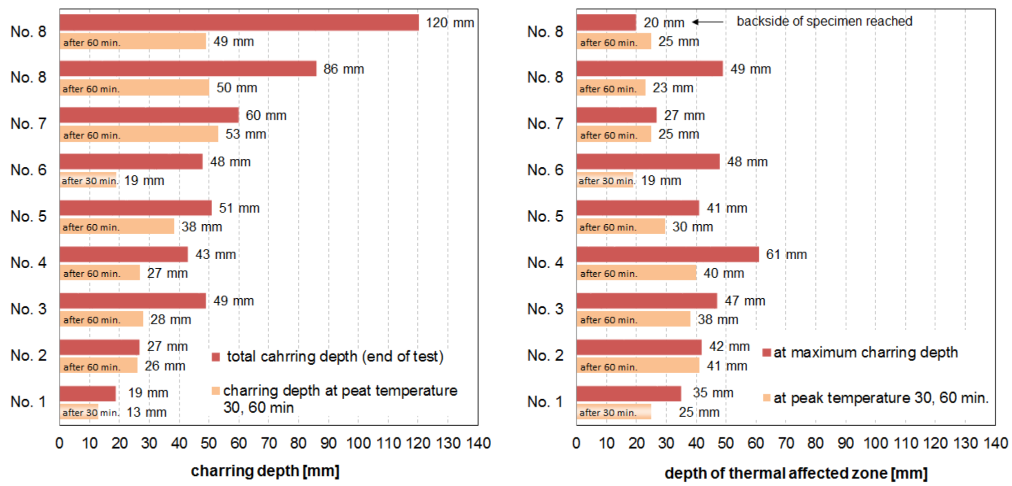

Figure 4. Comparison of the size of the charring depth and thermal affected zone.

These findings are attributed to two circumstances. On the one hand, a high exposure level leads to steeper temperature gradients behind the char line due to the increased charring rate. On the other hand, an additional mass transport into the cross section contributes to the heating up process, which is less distinct for a high exposure level compared to a lower one. After the maximum furnace temperature during the fire exposure was reached, previously described results begin also to be influenced by the duration and thermal exposure level of the cooling phase. As expected, the lowest increase in charring depth and thermal affected zone was realized for a rapid temperature decrease (test No. 2 and No. 7). In contrast, charring depths almost twice as high were recorded at the end of the fire exposure compared to the depth at the occurrence of the maximum furnace temperature for long decay phases. The additional influence of the cooling phase was also noticeable within the assessments of the size of the thermal affected zone. With an increased duration of the cooling phase, the depth of the thermal affected zone increased too. On note is the influence of the fire scenario on the cracking pattern within the formation of charcoal in the heating phase of the examined fire curves. “Hot” fires scenarios always led to deeper cracking and smaller sizes of the char blisters compared to “cooler” fire scenarios, see figure 5. However, these differences disappeared with an increase of the decay phase duration due to the surface oxidation and regression of the char coal.

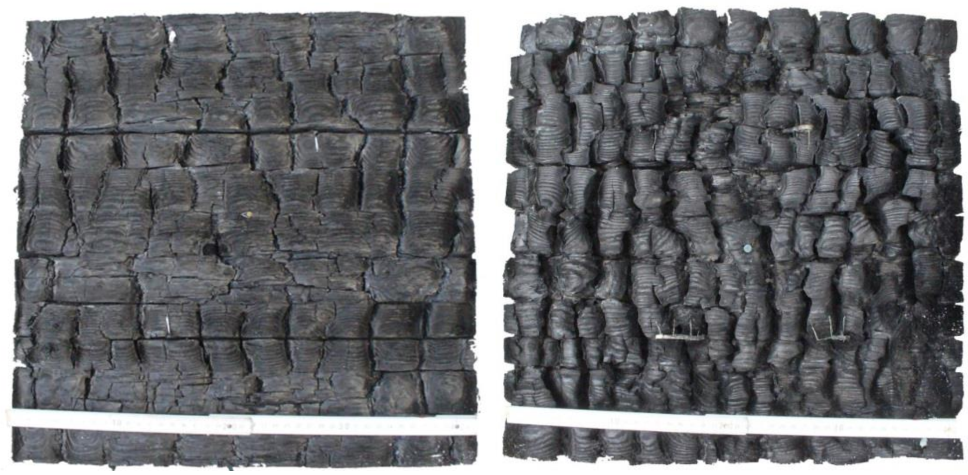

Figure 5. Char pattern after 60 minutes fire exposure (left - lower exposure level test No. 2; right – hot exposure level of test No. 7).

Moisture Influence

The results of the fire tests with different initial moisture contents showed that an increase in moisture content of about 1 M-% led to a decrease in the charring rate of 1 %. Mass transport processes with accumulation of liquids in the cross section and at the unexposed side of the specimens became evident during the tests. In the latter fact, this became particularly obvious at the end of the experiments. This effect became obvious from the in-depth temperature measurements too. Furthermore a reduction in the charring rate connected with an increased region affected by temperatures behind the char-line was observed in the specimens with increasing initial moisture content.

ANALYTICAL RESULTS

Based on the experimental examinations further analytical and numerical studies were conducted. The numerical investigations of the influence of moisture as well as fire scenarios are beyond of the scope of this article and will be subject of future publications by the author. An analysis of the data gained from the tests with different fire scenarios showed that the current design approach of EN 1995-1-2 Annex A [1] is not able to accurately predict the gained results, especially when the cooling phase was taken into account. However, a strong correlation between the charring depth and the received cumulative thermal exposure within all fire tests was established, in particular for the heating phase of a fire, as depicted in figure 6, The same correlation has been found for test results taken from literature.

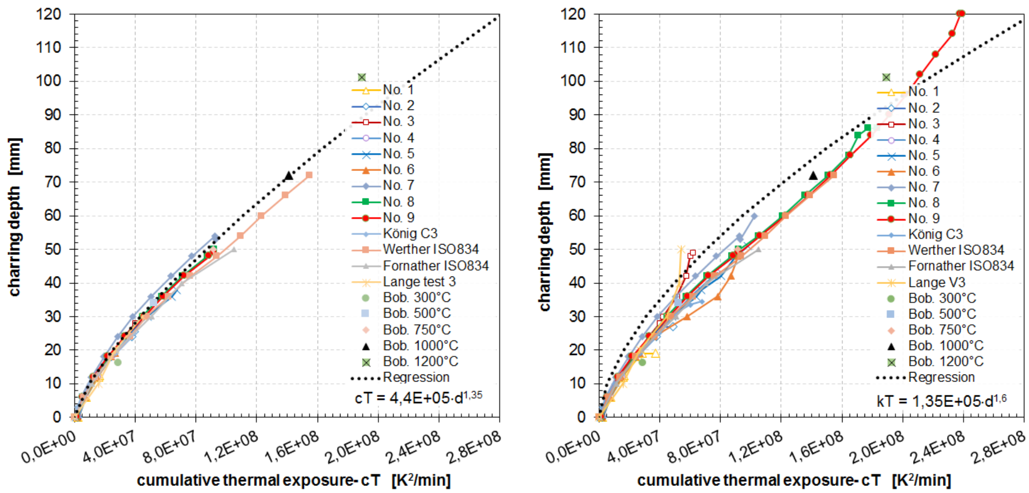

Figure 6. Charring depth vs. received cumulative thermal exposure for the heating phase (left) and for the entire fire duration (right). With König [8], Werther [9], Fornather [10], Lange [11], Bobacz [12].

Analyzing the results gained from the fire tests with varying initial moisture contents suggested the following equation (1) to describe the time dependent charring depth and the temperature distribution behind the char line, considering that an increase in moisture content of about 1 M-% led to a decrease in the charring rate of 1 % for β_u.

$$\vartheta_x = 20 + 280 \cdot \left(\frac{\beta_u \cdot t}{x}\right)^{\alpha} \tag{1}$$

with: $\alpha_t = 0.038 \cdot t + 1{,}22$

x – depth from original surface in mm

t – time in minutes

CONCLUSION

This article provides an overview of a series of fire tests with respect to the influence of different fire scenarios and the initial moisture content on charring and temperature development in timber elements exposed to fire from one side.

The tests and the accompanied analysis showed that temperature time scenarios above the standard fire curve led to an increased charring rate but at the same time to a slender thermal affected zone behind the char-line compared to the standard fire. Examining temperature time scenarios below the level of the standard fire led to opposite results. Both findings are relevant for the structural assessment of timber elements.

The tests also showed that mass transport processes contribute to an increase of temperatures within the cross section under fire exposure. In contrast, an increased moisture content reduces the charring rate. However the investigation revealed that for practical applications, the moisture influence on charring can be neglected compared to the influence of the potential fire scenario.

REFERENCES

1. EN 1995-1-2. 2004. “Design of timber structures – Part 1-2 General – Structural fire design” European Standard. CEN, European Committee for Standardization, Brussels.
2. Just, A., Schmid, J, Werther, N. and Frangi, A. 2014 “ire protection of timber members – Determination of the fire protection system characteristics for the verification of the load-bearing resistance by means of calculation models”, Proceedings, 8th International Conference on Structures in Fire - SiF'2014.
3. EN 1363-1. 2012. “Fire resistance tests - Part 1: General Requirements”, European Standard. CEN, European Committee for Standardization, Brussels.
4. Werther, N. 2016. “Factors influencing the fire performance of timber elements and their consideration in the empirical and numerical evaluation method” PhD thesis, Technical University Munich. in German language (submitted)
5. Mayer, C. 2012. „Ingenieurmethoden im Brandschutz – Möglichkeiten zur Beschreibung der Brandentstehungs- und Vollbrandphase bei Raumbränden“ Masterarbeit, TU München, Lehrstuhl für Holzbau und Baukonstruktion.
6. Ruck, V. 2011. Ingenieurmethoden im Brandschutz – Verifizierung versuchsbasierender Raumbrandtemperaturen mittels empirischer Ansätze und numerischer Simulation. Masterarbeit, TU München, Lehrstuhl für Holzbau und Baukonstruktion.
7. Rein, G., et al. 2009. “Round-robin study of a priori modelling predictions of the Dalmarnock Fire Test One”, Fire Safety Journal, Volume 44, Issue 4, page 590-602, Elsevier Ltd.
8. König, J. and Walleij, L. 1999 “One dimensional charring of timber exposed to standard and parametric fires in initially unprotected and postprotection situation”, SP Trätek Rapport I 9908029, Stockholm.
9. Werther, N. and Margesin, M. 2013 „Untersuchungsbericht Nr. 01-06-13, Versuche zum Einfluss der Holzfeuchte auf das Abbrandverhalten von Nadelholz“, TU-München, Lehrstuhl für Holzbau und Baukonstruktion.
10. Fornather J. H. 2003 „Brandverhalten von Holz unter besonderer Berücksichtigung stiftförmiger Verbindungsmittel – experimentelle und numerische Untersuchungen“, Dissertation, Universität für Bodenkultur Wien.
11. Lange, D., Boström, L., Schmid, J. and Albrektsson, J. 2014 “The influence of parametric fire scenarios on structural timber performance and reliability”, Project 303-121, Fire Research SP Report 2014:35, Boras, Sweden.
12. Bobacz, D 2006 “Behavior of Wood in Case of Fire - Proposal for a Stochastic Dimensioning of Structural Elements”, Doctoral Thesis, University of Natural Resources and Applied Life Sciences, Vienna.

Parameters Influencing the Behaviour of Timber Frame Assemblies Exposed to Fire, Development of New Design Criteria for Insulation Materials

MATTIA TISO and ALAR JUST

ABSTRACT

Insulation materials may give a different contribution to the fire resistance of timber frame assemblies. At present, Eurocode 5 Part 1-2 [1] provides a model for fire design of the load bearing function of timber frame assemblies with cavities completely filled with stone wool. The extension of this model for glass wool for post protection phase has been published in the European technical guideline Fire Safety in Timber Buildings [2]. Very little is known about the protection of other insulation materials. This paper attempts to analyze the most sensitive parameters that describe in a universal way the protection against the charring given by different insulations not included in Eurocode 5 part 1-2. A series of model scale furnace tests of floor specimens for three different insulation materials was carried out. An analysis on the resistance of the residual cross sections was conducted by means of a resistograph device. The study offers some important insights into the concept of a new design model.

INTRODUCTION

The behavior of timber frame assemblies in fire is influenced by the protective properties of cladding and insulation materials. The primary protection for a timber member is given by the cladding. The charring of a timber member protected by cladding is considered the protection phase. After the fall off of the cladding, the secondary protection might be provided by insulation materials. The charring of a timber member after the fall off of the cladding is considered the post-protection phase.

While the cavities of timber frame assemblies are completely filled with insulation materials in addition to the (protective) effect of cladding, the charring of a timber member (clearly) depends on the type of insulation used.

Annex C of the current Eurocode 5 Part 1-2 [1] presents a design model that

Mattia Tiso, Tallinn University of Technology, Ehitajate tee 5, 19086 Tallinn, Estonia
Alar Just, Tallinn University of Technology

considers the contribution of stone wool. The model is extended to assemblies filled with glass wool until the failure of the claddings. The European guideline Fire Safety in Timber Buildings (FSITB) [2] includes a design model that considers the contribution of glass wool to the fire resistance during the post protection phase. All the other insulation materials are excluded in the models described above.

The EN-standards dealing with thermal insulations for building are only referring to the performance in reaction to fire and do, therefore, not provide information on fire resistance performance; see, for example, the standard for factory made mineral wool product [3].

The model presented in Eurocode 5 Part 1-2 was developed by König and Walleij [4]. It considers a one-dimensional heat transfer, simplifying the residual cross section into a rectangular one, and introduces coefficients that correct the nominal charring rate to take into account the corner roundings. The greater charring depth for narrow elements is considered through the coefficient k_s, which depends on the width of the original cross section. To transform the real cross section into a rectangular one, the coefficient k_n is used, based on the ratio of section modulus of the real and simplified cross-sections. The protection coefficients describe the different charring rates in the protection and post-protection phase. The coefficient k_2 considers the protection of gypsum plasterboard, while k_3 considers a greater charring rate during the post protection phase and it depends on the failure time of the fire protection.

The design model for glass wool protected timber frame assemblies inserted in FSITB was proposed by Just [5]. It considers also charring from the lateral sides, with different starting times for the top and the bottom of the side; giving the residual cross section a trapezoidal shape. This introduction was made due to a faster recession of the glass wool in respect of the stone wool in the fire condition.

METHODOLOGY

The protection on the fire resistance of three different insulations was studied by means of model scale furnace tests. The specimens consisted of timber beams and the insulation materials applied. The insulation materials involved in this investigation are glass wool (GW), high temperature extruded mineral wool (HTE) and cellulose fiber in loose fill type (CF).

Furthermore, a series of resistograph measurements were carried out on the timber beams which were tested in furnace. This investigation was conducted to define the border where the residual cross section loses its load bearing capacity.

Model scale furnace tests

Fourteen specimens of timber frame assemblies were tested in horizontal position in a cubic meter furnace following the standard fire curve according to ISO 834 [6] (Table I). The specimens consisted of timber beam with sides protected by insulation as a portion of floor (Figure 1). The external dimensions of the specimens were 80 x 100 cm. To investigate the influence of beam width on the charring rate at the middle of the section, different widths were chosen.

TABLE I. OVERVIEW OF MODEL SCALE FURNACE TESTS PERFORMED.

Test number	Insulation material	Fire protection	Beam width (mm)	Fall-off of fire protection (min)	Duration of test (min)
1	HTE	GtF, 15 mm	45	45	60
2	HTE	GtF, 15 mm	45	45	60
3	HTE	GtF, 15 mm	45	30	60
4	HTE	GtF, 15 mm	45	45	60
5	HTE	NO	45	N.A.	60
6	HTE	GtF, 15 mm	75	45	60
7	GW	GtF, 15 mm	45	45	54,5
8	GW	NO	45	N.A.	21
9	GW	GtF, 15 mm	45	30	41
10	GW	GtF, 15 mm	75	45	60
11	CF	GtF, 15 mm	45	45	60
12	CF	GtA, 12.5 mm	45	NO	60
13	CF	GtF, 15 mm	45	NO	60
14	CF	NO	45	N.A.	23

The timber beam cross sections chosen were 45 x 145 mm and 75 x 145 mm for specimens insulated with GW and HTE; specimens insulated with CF were tested only with 45 x 145 mm timber beams. The fire side of the tested assembly was protected by 15 mm thick gypsum plasterboard Type F from different providers. A specimen insulated by cellulose fiber and protected by 12,5 mm thick gypsum plasterboard was also tested. Three specimens, one for each insulation material, were tested without cladding.

(a)

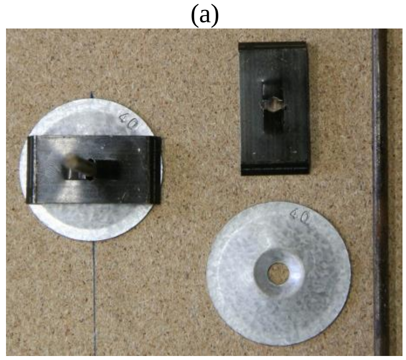

(b)

Figure 1. Example of specimen tested in furnace and clips used to hold the fire protection.

On the unexposed side the particle board with the thickness of 19 mm was used in all the tests. Different techniques were adopted to prevent the fall off of the insulation materials after the failure of the cladding. GW and HTE were glued on the particle board by means of fluid sodium silicate based glue. The CF insulation was held in place by a chicken net. Thermocouples were embedded on the timber beam and insulation material at different depths to follow the charring scenario. In order to obtain comparable results for the post-protection phase among the insulation materials, the fall off of the gypsum plasterboard was imposed. This was done by releasing the special fastening system (Figure 1). To identify the influence of the different charring phases, the following fall-off times of the fire protection were used.

The expected duration of the tests was 60 minutes; in some tests the specimen was removed earlier due to the start of charring of the particle board.

Resistograph measurements

At the end of the tests the char layer was removed from the beams with a metal brush. For each beam the instrumented and the minimum residual cross sections were collected. The residual cross-sections were analyzed with the resistograph drilling along the height from the side unexposed to the side exposed to fire. The resistograph gives the resistance to the penetration versus the drilling depth.

The profiles obtained were compared overlapped to the negative pictures of the residual cross section. This comparison should show if there is a decrease of resistance in pyrolysis zone of the wood. This method was adopted to obtain further in-depth information on properties of the residual cross-section.

RESULTS

The comparison of resistance profiles with the negative pictures of residual cross section reveals that a resistance to the penetration in pyrolysis zone exists (Figure 2). These findings suggest that even the white zone visualized in a negative picture should be considered when the geometrical properties of the residual cross sections have to be recorded.

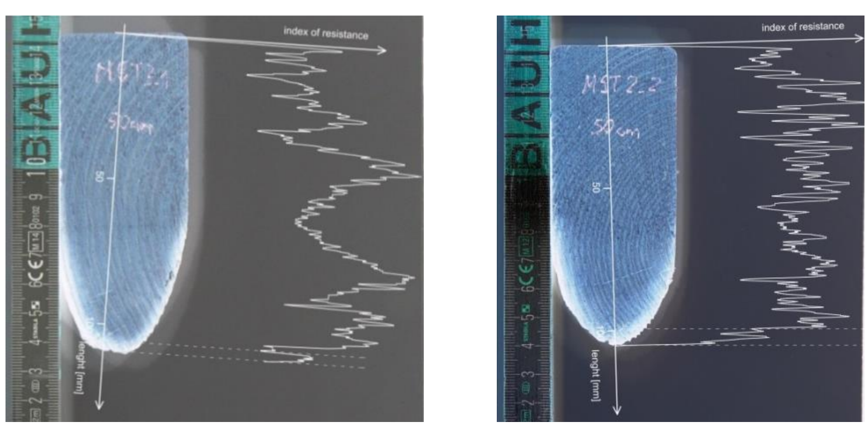

(a) (b)

Figure 2. Resistance profile in the middle of the beam for Test 2 and Test 3.

The results obtained from model scale furnace tests are shown below, gathered by insulation material. The geometric properties of the residual cross sections were obtained by means of AutoCAD. The residual moment of inertia ratio is plotted against the charring depth ratio (Figure 3).

König defines the coefficient k_s on unprotected members [4]. In this study three unprotected specimen are present, one for each insulation material studied (see Table I). The coefficient k_s was calculated as

$$k_s = \beta_m / \beta_0 \tag{1}$$

where β_m is the charring rate in the middle of the narrow side, β_0 is the charring rate for one-dimensional charring of initially unprotected wood according to Eurocode 5 [1]. The three specimens that were tested unprotected had a beam width of 45 mm. The k_s factors resulted for GW and CF are respectively 1,51 and 1,49. For the specimen tested with HTE mineral wool, the k_s resulted 1,32.

Post protection factors (k_3) are compared with fall-off times of claddings (Figure 3d).

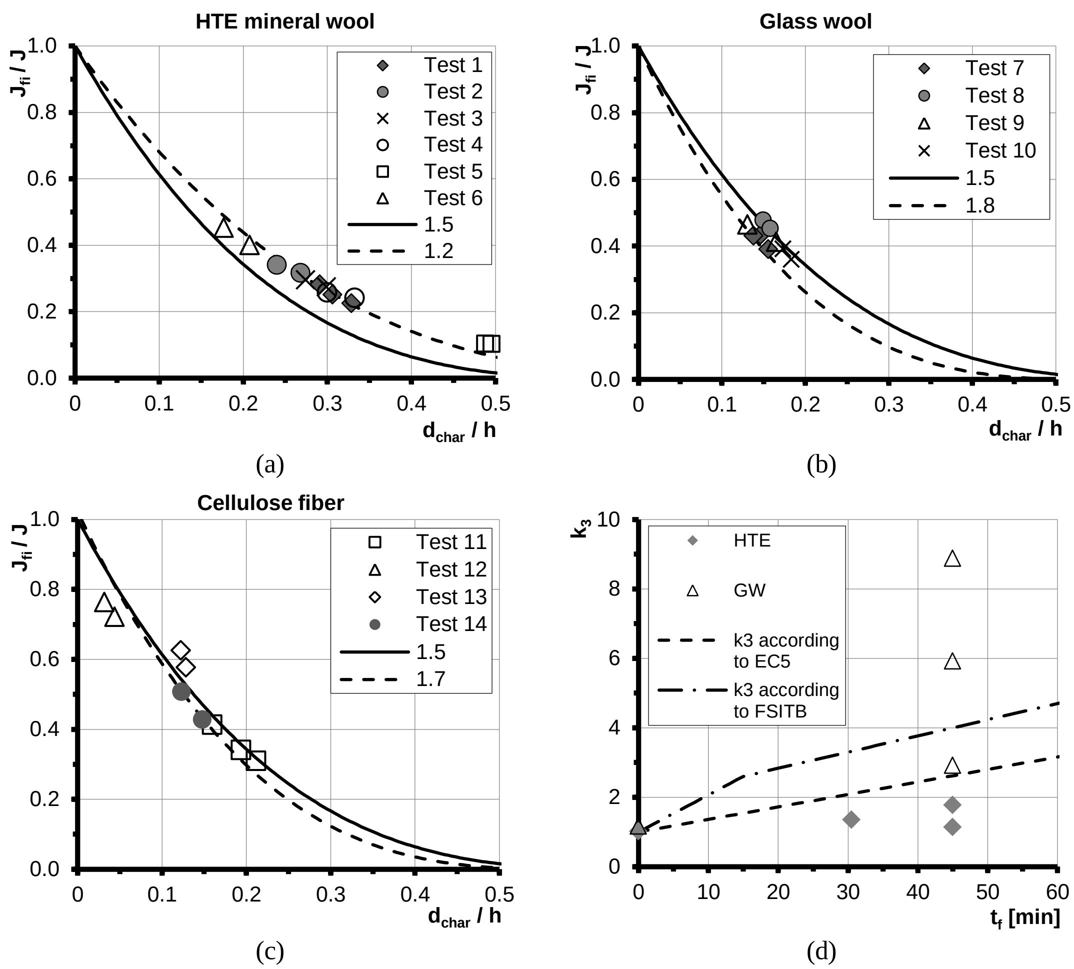

Figure 3. Reduction of moment of inertia versus charring depth ratio and k_3 factors.

The coefficients k_3 were calculated by dividing the charring rate in post protection phase (k_3) by the one dimensional charring rate (β_0) for the cross-section factor according to Eurocode 5 ($k_{s,EC5}$) as

$$k_3 = \beta_3 / k_{s,EC5} \cdot \beta_0 \tag{2}$$

It is shown on Figure 3a that the relation between d_{char}/h and J_{fi}/J for HTE follows the line of $k_n = 1{,}2$. Observing this relation for glass wool and cellulose fiber it can be seen that the data are more spread. The k_s factor obtained for HTE mineral wool is approximately the same as proposed in the Eurocode 5. On the other hand, the same coefficient calculated in GW and CF protected samples slightly differ from the value proposed in the Eurocode 5.

DISCUSSIONS

The results of this study indicate that the protection given by HTE mineral wool can be calculated using the design model present in Eurocode 5. These results are in agreement with Just, Schmid and König's findings [7]. Furthermore, coefficients can be improved to not underestimate the performance of this insulation material.

The spread observed for the reduction of moment of inertia in the specimen insulated with cellulose fiber and glass wool is caused by a two-dimensional charring behavior.

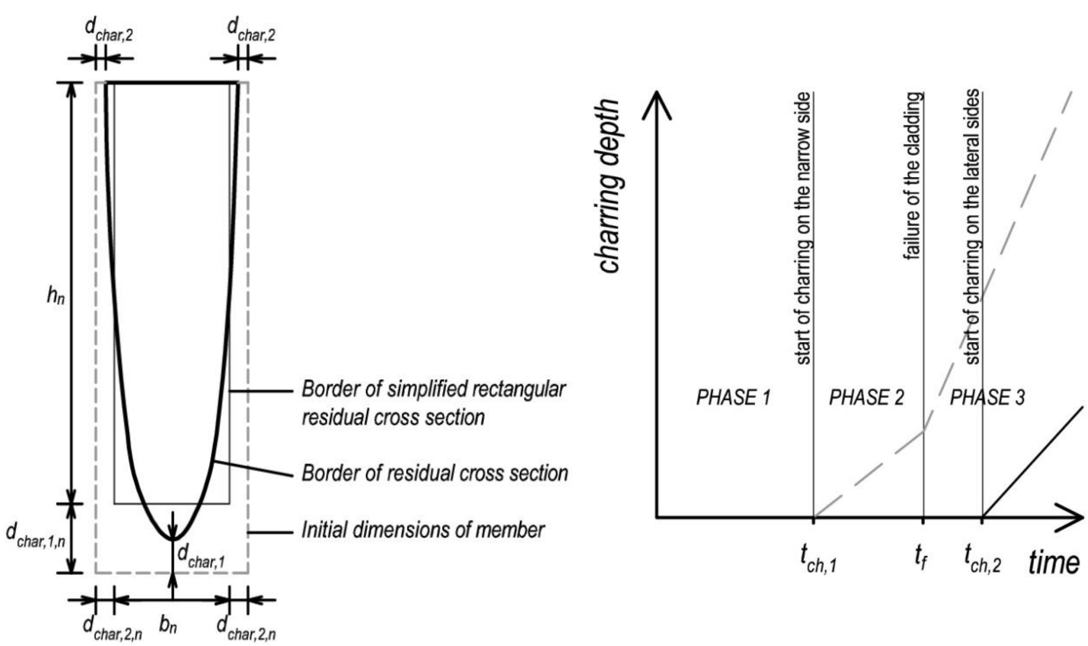

(a) (b)

Figure 4. Concept of the new universal design model proposed.

In fact, it can be observed that the same charring depth on the narrow side can give two different moment of inertia, for example in the tests 7 and 8 or in the tests 13 and 14. This result can be explained by the fact that the unprotected tests (8 and 13) were stopped quite early, before the lateral sides had completely charred. In the longer tests, at a certain point, these insulation materials lost their ability to protect the lateral sides of the beam from charring. At that point the start of charring on the lateral sides takes place with a different charring rate compared to the narrow side. For that reason the k_n factor applied on the narrow side may not be capable to correlate the charring depth with the residual section modulus. This observation may support the idea to introduce a design model that considers charring from three sides.

CONCLUSIONS

For timber frame assemblies with cavities completely filled with HTE mineral wool, the charring occurs mainly on the fire-exposed side of the member, while the lateral sides are protected by the insulation. For timber frame assemblies with cavities completely filled glass wool, due to the degradation or recession of the insulation material, the influence of the rounding of the char line can be noticed and from a certain point the cross section is charred even from the sides. It was already proved that the charring rates in the protection and post-protection phases are different. From a designer´s point of view it would be helpful to simplify the irregular cross section into a rectangular shape of the residual cross section without neglecting the effect of the corner roundings. The main advantage of this simplification is that it enables a simpler determination of the properties for design residual cross-section.

Overall, this study strengthens the idea that a universal design method to calculate the contribution in fire resistance of timber frame assemblies given by different insulation materials is needed. A reasonable approach to take into account the effect of the corner roundings suggests bypassing the k_n factor. While the charring does not start for the lateral sides, this effect could be taken into account by a modified k_s factor applied on the narrow side. After that, the charring rate of the lateral sides could consider the effect of the corner roundings.

More research is required to define the criteria to determine the start of charring from the lateral sides, moreover how to determine the charring rate of the lateral sides.

Beside the design model, further research is concentrate on a qualification methodology to describe the contribution of different insulation materials to the fire resistance of timber frame assemblies.

REFERENCES

1. EN 1995-1-2:2004, "Design of timber structures – Part 1-2: General – Structural fire design," European Committee for Standardization.
2. Östman, B., et al. 2010. "Fire safety in timber buildings. Technical Guideline for Europe," SP Technical Research Institute of Sweden, SP Report 2010:19, Stockholm, Sweden.
3. EN 13162:2012, "Thermal insulation products for building – Factory made mineral wool (MW) products – Specification," European Committee for Standardization.
4. König, J., & Walleij, L. 2000. "Timber frame assemblies exposed to standard and parametric fires: part 2: a design model for standard fire exposure," Rapport-Institutet för Träteknisk Forskning, (0001001), Sweden.

5. Just, A. 2010. "Post protection behaviour of wooden wall and floor structures completely filled with glass wool," *Structures in Fire: Proceeding of the 6th international conference*. East Lansing, USA. June 2nd to 4th 2010, pp 584-592.
6. ISO 834-1:1999, "Fire-resistance test – Elements of building construction – Part 1: General requirements," International Organization for Standardization.
7. Just, A., Schmid, J., König, J. 2012. "Post-protection effect of heat-resistant insulations on timber-frame members exposed to fire," *Fire and Materials,* 36.2: 153-163.

Deflection Behavior and Load-Bearing-Period of Structural Glued Laminated Timber Beams in Fire Including Cooling Phase

YUSUKE KATAKURA[1], HITOSHI KINJO[2], TAKEO HIRASHIMA[1], SHUITSU YUSA[3] and KIYOSHI SAITO[4]

ABSTRACT

This paper reports on the behavior of structural glued laminated (glulam) timber beams under the constant load during and after fire conditions. Previous tests have indicated that the resistance of a beam exposed to standard fire for one hour declined by approximately 30% compared to that of a beam in ambient conditions. Additionally, it was reported that the strength of a beam exposed to heat in a furnace for one hour, followed by three hours of natural cooling, declined by approximately 14%. In this report, the fire performance of glulam timber beams is discussed based on their deflection behavior and load-bearing-period, which were obtained from load-bearing fire tests under constant load conditions.

1 INTRODUCTION

Unlike other elements, a characteristic problem of timber elements is that their load bearing capacity decreases as they are consumed in a fire, and their bearing capacities may continue to degrade even after the fuel in the room has been exhausted. Therefore, the structural fire performance of timber elements should be clarified not only during the heating phase, but also during the subsequent cooling phase.

In the case of fire safety engineering designs for timber structures, the effective section method is generally used and timber charring rates are considered significant factors. However, according to the previous investigation [1], it is difficult for the effective section method to approximate accurately the fire resistance of timber beams including cooling phase, because the strength at the section. Furthermore, in addition to the reduction of section caused by charring, strength reduction was considered to be an important factor when attempting to approximate the fire performance of timber beams. In this report, the fire performance, primarily deflection

1 Chiba University, Dept. of Architecture and Urban Science, Japan1-33, Yayoi-cho, Inage-ku, Chiba Pref, 263-8552, Japan
2 Centre for Better Living, Tsukuba Building Research & Testing Laboratory, Japan
3 Waseda University
4 Saito Wood Industry CO., LTD, Japan

behavior and load-bearing-period, of glued laminated (glulam) timber beams will be discussed from the standpoint of load-bearing fire tests conducted during the cooling phase under constant load conditions. Then, based on the charring depth and the per section temperature transformation obtained from loading test results, the load-bearing capacity of the glulam timber beams will be discussed using the effective section method and the strength reduction factor, which will be calculated in accordance with the European standards for the design of timber structures (Eurocode 5) [2].

2 TEST PROGRAM

The tree species selected for testing was Japanese larch. Each laminar specimen was 210 mm wide, 420 mm high, and 6000 mm long, and 30 mm thick. The finger-joints of all laminas were located to the outside of the constant-bending-moment zone. The 14 laminas used in our study were bonded by a resorcinol-phenol resin adhesive and the top surface of each specimen was coated with calcium silicate plate.

The strength grade of the glulam utilized fully complied with the standards of same-grade composition structural members stipulated in the Japan Agricultural Standard (JAS) E95-F315 standard. The average density of the specimens was 0.53 g/cm^3, and moisture content was 10.4 mass%.

TABLE I shows the test program. First, a loading test for one specimen (L-RT) was conducted at ambient temperature conditions in order to obtain the resistance and rigidity of the glulam timber beams used. The other specimens (LF-0.2 to 1.0) were subjected to load-bearing fire tests where the main test parameter was the applied constant load.

The constant load ratios were based on the permanent allowable design load of the specimen at ambient temperature. These tests were carried out in order to obtain the deflection behavior and the load-bearing-period of the beams during the cooling phase while under constant loads. All tests were carried out using the furnace for horizontal elements at the Tsukuba Building Research & Testing Laboratory Center for Better Living.

TABLE I. TEST PROGRAM.

Specimens	Test terms	Applied load	Load ratio according to permanent allowable design load
L-RT	loading test	20.0 kN/min	-
LF-1.0	load-bearing fire test	79.2 kN	1.0
LF-0.8		63.4 kN	0.8
LF-0.6		47.5 kN	0.6
LF-0.4(1)		31.7 kN	0.4
LF-0.4(2)			
LF-0.2		15.8 kN	0.2

The tests in this study were conducted under the same conditions as shown in our previous work [1]. The distance between supports was 5,400 mm, and heated length was 4,000 mm. The two-point loading method was used to apply loading to the beam, and the distance between two points was set at 1,800 mm. The vertical displacements through the length of the beam were measured by wire-type transducers and the section temperature of the LF-0.4 specimen was measured by thermocouples installed in the section at 1000 mm outside the loading point.

During the load-bearing fire tests, the beams were subjected to one hour of standard fire heating and then allowed to cool naturally until failure occurred. The furnace temperature was followed the International Organization of Standardization (ISO) 834 fire standard. During the post-heat cooling phase, the furnace cover was left in place and air was supplied to facilitate smoke extraction.

3 RESULTS AND DISCUSSION

3.1 Cross Section State

Measurements of the charring progress were obtained from the beam section after the tests were complete. Figure 1 shows the cross-section of some beams after testing. In comparison to the section reported in our previous heating tests [1], the bottom of the non-charred section was narrow and the top was wide owing to bending moment. In case of the beam, charring behavior was influenced by the applied load.

TABLE II shows the effective cross-section decline. The measurement points were set 500 mm off from the center of the beam length. In LF-0.8, the decreasing section rate was relatively large because of the specimen failed due to self-burning. The charring in the height direction for both LF-0.4(1) and LF-0.4(2) showed approximately the same ratio, despite the fact that there were given more than five hours of cooling time. This outcome was consistent with our previous report, which showed the charring rate was near zero in the cooling phase.

Figure 2 shows cross-section temperatures on the lines of height direction at 45 mm inside from side face (a) and the center width (b). In Figure 2(a), the temperature at a depth of over 90 mm had reached about 150°C at the one hour mark, and rose to 200°C by the second hour. Subsequently, the temperature dropped steadily until reaching 100°C after eight hours. At the 60 mm depth point, the temperature exceeded 260°C and the nearby area was carbonized.

In Figure 2(b), it can be seen that the temperatures at depths over 90 mm from the initial bottom surface reached approximately 30°C at the first hour mark, and then gradually increased until reaching 100°C between two or three hours into the cooling phase. The mean temperature of the un-charred section reached approximately 150°C between the fourth and fifth hour, yet remained at 100°C and above after seven hours of natural cooling.

LF-1.0

LF-0.8

LF-0.4(1)

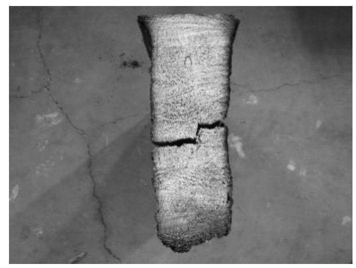

LF-0.2

Figure 1. Charring condition.

TABLE II. SPECIMEN DETAILS AFTER TESTS.

Specimen	LR-T	LF-0.8	LF-0.6	LF-0.4(1)	LF-0.4(2)	LF-0.2
Time [hour]	-	1.32	1.27	2.65	8.00	25.00
Section area [mm^2]	88,200	40,085	48,460	45,779	45,808	38,696
Height* [mm]	420	361	370	370	370	325
Width* [mm]	210	52.2	42.8	45.5	45.7	46.1

* Height, Width: measured at center of the effective section

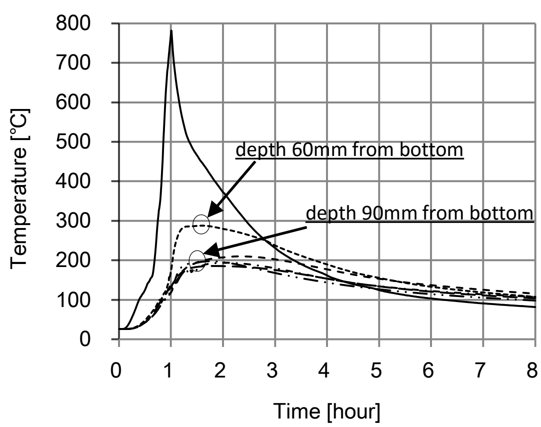

(b) Depth 45mm from side surface

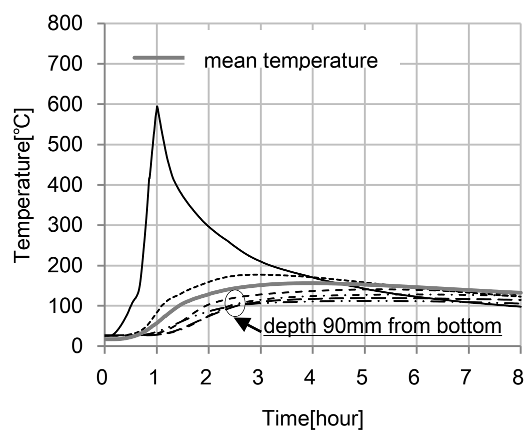

(a) Center width

Figure 2. Cross-section temperature.

3.2 Beam Deflection Behavior

Figure 3 shows the deflection behavior of a beam under constant load exposed to one hour of standard fire heating. As the constant applied loads increased, the deflection became larger. Not all of the specimens broke during the heating phase, and the deflection increased considerably from the start of the cooling phase. It could be considered that the reason was because the cross-section's mean temperature started rising.

LF-1.0 and LF-0.8 showed the same deflection behavior and displayed no differences in load-bearing period. Judging from the section at breaking point, this result was caused by rapid charring owing to lamina exfoliation (Figure 4(a)). The deflection curve for LF-0.4(2) resembled that for LF-0.4(1) for about two hours, after which the deflection for LF-0.4(2) considerably increased and failure occurred. The failure mode for LF-0.4 was determined from the condition of disrepair in the form of a deep horizontal crack at the middle height of the specimen, as shown in Figure 4(b).

As a result, the load-bearing periods of the two abovementioned specimens were significantly different in spite of being subjected to the same load ratio. Therefore, it can be said that the load-bearing capacity of timber beams varies widely depending on whether or not shear failure occurs. The deflection increase for LF-0.4(1) and LF-0.2 showed a slowing trend after approximately three hours, when the section temperature stabilized at 100°C. Subsequently, the deflection became constant. The decrease in deflection behavior changes was proportional to the mean temperature distribution (Figure 2(b)).

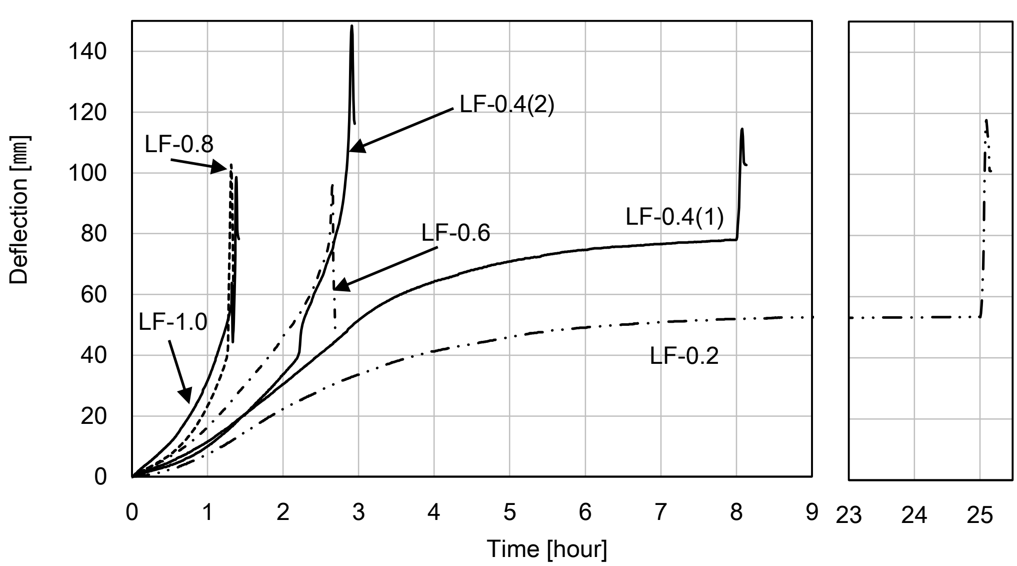

Figure 3. Deflection behavior.

(a) LF-0.8

(b) LF-0.4(2)

Figure 4. Failure stages of specimens.

3.3 Lowering Resistance with Time

TABLE III shows the load-bearing periods and failure modes, while Figure 5 shows the resistance reduction ratios for each test. The solid line in Figure 5 represents the value of the bending resistance calculated based on previous studies produced by using the reduction factor [2] [3] .

The permanent allowable design load was 23% of the resistance at ambient temperature. The resistance decreased substantially from ambient temperature levels after one hour of heating and continued to decrease gradually after the subsequent cooling phase.

TABLE III. TEST RESULTS.

Specimen	LR-T	LF-1.0	LF-0.8	LF-0.6	LF-0.4(1)	LF-0.4(2)	LF-0.2
Constant load (failure) [kN]	(350.0)	79.2	63.4	47.5	31.7 (42.8)	31.7	15.8 (32.8)
Load-bearing period	-	79 min	76 min	159 min	480 min	165 min	25 hour
Failure mode	Bending	Bending	Bending	Shear	Bending	Shear	Bending

From an examination of these results, it can be seen that (with the exception of LF-0.4(2)) the reduction ratio for each specimen shows a tendency to decline with the passage of time. The fire load-bearing period for LF-1.0, which had been subjected to the allowable load, exceeded one hour. There was also a significant difference in bearing period between LF-0.4(1): bending failure, and the LF-0.4(2): shear failure.

In order to obtain resistance values, the extra loads were applied to LF-0.4(1) after eight hours and to LF-0.2 after 25 hours. In case of LF-0.2 test, the section temperature was expected to have declined to ambient levels after 24 hours of natural cooling in the furnace. According to the reduction factor, the timber elements in ambient states have strength levels four times those measured at 100°C with respect to compression, and double the level in terms of tensile strength. The failure load could not reach that of the specimen with same section in ambient state. Even though the specimen was naturally cooling down up to ambient state, the strength did not recover in this test.

TABLE IV shows the values used for our calculations. These values were calculated based on the charring depth and the mean temperature of the effective cross-section obtained from the test results. The temperatures written in the table are the highest achieving temperature of each specimen. Strengths and Young's modulus were determined from the calculations based on the reduction factor from Eurocode 5 [2]. The material strength of a timber element under ambient conditions was the adopted value obtained from the LR-T test. The data on effective section for one to four hours applied load were obtained from previous heating tests [1]. As shown in Figure 5, the calculated value approximately traced the test results above for approximately three hours. Our timber beam resistance decrease predictions generally conformed to the reduction factor provided in Eurocode 5, not only in the process of fire heating, but also during natural cooling.

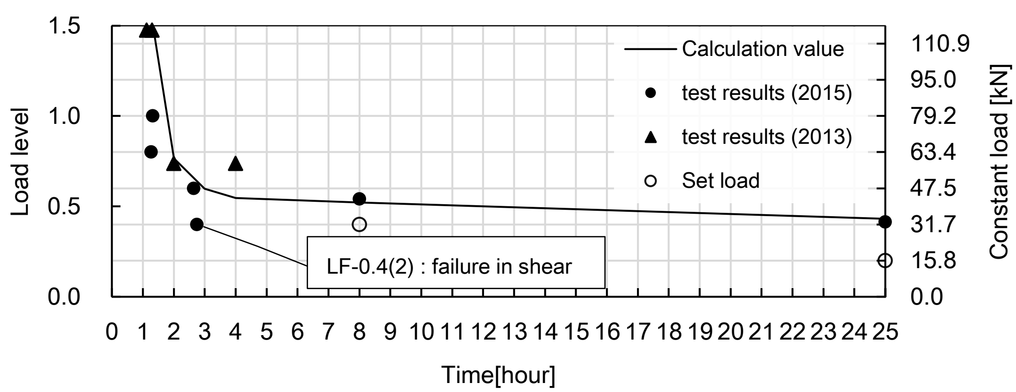

Figure 5. Resistance reduction.

TABLE IV. VALUE USED IN CALCULATION.

TIME [hour] (Heating + Cooling)		0+0	1+0	1+1	1+2	1+3	1+7	1+24
Height [mm]		420	355.8	345.6	342.6	343.9	340	322
Width [mm]		210	122.8	115.2	117.6	114.4	119.3	103.3
Temperature [°C]		20	22	106	144	155	156	156
Tensile	Strength [N/mm^2]	51.02	51.02	33.16	26.02	23.98	23.98	23.98
	Young's modulus [N/mm^2]	9500	9500	4560	3610	3420	3420	3420
Compress	Strength [N/mm^2]	51.02	51.02	12.76	9.69	9.18	9.18	9.18
	Young's modulus [N/mm^2]	9500	9500	3230	2565	2375	2375	2375

4 CONCLUSIONS

This paper described the fire performance, including the cooling phase, of larch glulam timber beams exposed to a one hour standard fire test. The main conclusions are as follows:

- The resistance decreased considerably from ambient temperature values during the one hour heating period. However, the fire resistive period of LF-1.0 exceeded one hour.
- The load bearing period of a beam under shear loading decreased considerably in comparison with one under a bending load. Therefore, sections should be emplaced correctly to prevent shear failure during a fire.
- The glued laminated timber beam maintained a load bearing capacity of less than 40% of the allowable load after the one hour heating period, except in the case of the specimen that suffered a shear failure.
- The resistance of a beam that had been subjected to a high temperature did not recover with cooling.
- An effective section method that considers the strength reduction factor could be used to approximate the load-bearing-periods of the beams.

REFERENCES

[1] H. Kinjo, S. Yusa, T. Horio, T. Hirashima and T. Matsumoto, K. Saito, Fire performance, including the cooling phase, of structural glued laminated timber beams, 8th International Conference on Structures in fire, pp.593-600, 2014.

[2] Eurocode 5 Design of timber structures, Part 1-2: General-Structural fire design. BS EN1995-1-2: 2004.

[3] H. Kinjo, S. Yusa , T. Horio, T. Hirashima and T. Matsumoto, K. Saito, Behaviours of lurch glued laminated timber beams exposed to standard fire heating during the cooling phase-Part 1, J. Struct. Constr. Eng., AIJ, Vol. 80 No. 711, pp. 831-840, 2015. (in Japanese)

Simulation of Charring Depth of Wooden-based Products when Exposed to Non-standardized Fire Curves

JEAN-CHRISTOPHE MINDEGUIA, GUILLAUME CUEFF, VIRGINIE DREAN and GILDAS AUGUIN

ABSTRACT

Fire resistance of wooden structures is based on the calculation of the charring depth. Analytical models for charring are given in regulations, e.g. the European Eurocodes, only for standard fire curves and for parametrical fires. This paper presents a numerical model for heat diffusion in wooden products and the induced charring. After calibration of the model it is used to analyze the fire resistance of a wooden beam under different fire models, including a non-standard fire curve.

INTRODUCTION

Justification by calculation of the fire resistance of structures made of wooden-based products is mainly based on the determination of the thickness of char that is formed at the surface exposed to fire. For example, the Eurocode 5 [1] proposes a method entitled "reduced cross-section" which is based on analytical models of charring versus time. Charring models are given for unprotected and protected structures (by wooden-based panels or plasterboard). This method is today the most used in engineering to verify or to design timber structures when exposed to fire.

The Eurocode charring models have been validated on the basis of tests carried out with the standard fire curve [2]. This method is therefore limited to a prescriptive calculation, which is generally very conservative for the structure. In order to approach a performance-based design, the Eurocode 5 also offers analytical charring models for wooden elements exposed to "parametric" fires. These so-called "natural fires", unlike the standard fire, allow taking into account the geometry of the local (constitution of the walls, dimensions of the room, presence of openings) as well as the nature of fire (fire surface, fuel characteristics…). For a purely performance-based design, advanced fire models are needed. For example, compartment fire models or CFD software can be used.

Jean-Christophe Mindeguia, Univ. Bordeaux, I2M, UMR 5295, Talence, France, jean-christophe.mindeguia@u-bordeaux.fr
Guillaume Cueff, Virginie Dréan, Gildas Auguin, Efectis France, Bordeaux, France

When using advanced fire models, there is no analytical model for corresponding charring. In that case, the use of a numerical charring model, coupled to the fire calculation, is therefore necessary. Some approaches of this kind have been experienced for steel constructions [3, 4] and very close studies also exist on wooden-based products [5, 6, 7, 8].

In this paper, the coupling between different types of fire models (standard, parametric and 2 zones model) and a numerical model for charring of wooden-based products is presented. After calibration of the model based on experimental results, a case study is presented. The influence of the type of fire curve on wood charring is then discussed.

NUMERICAL MODEL FOR HEAT TRANSFER AND CHARRING

Heat conduction

The Fourier law (1), in which energy sources Q_i are added in order to take in account the thermal impact of water vaporization and pyrolysis (cellulose, hemicellulose and lignin), is resolved by finite elements. The code Cast3M [9] has been used for this study.

$$\rho_{sol}.Cp_{sol}.{}^{\partial T}/_{\partial t} = \nabla(\lambda_{sol}.\nabla T) + Q_i \tag{1}$$

Simplified pyrolysis model

Many authors propose to describe pyrolysis by using more or less complex degradation schemes [10, 11]. In this study, a simplified first order degradation model has been used (Arrhenius laws). It is composed of six independent reactions respectively for the vaporization of water and the separated pyrolysis of wood components: cellulose (3 sub-reactions), hemicellulose and lignin. The kinetic of each reaction k_i is calculated by the Arrhenius law in equation (2). In equations (2), (3) and (4), i can be: w for water vaporization, c for the first cellulose degradation, a and b for the two degradations of β-cellulose, h for the hemicellulose degradation and l for the lignin degradation.

$$k_i = A_i \, exp(-E_i/RT) \tag{2}$$

For each reaction i, the degree of reaction χ_i and the reaction rate $d\chi_i/dt$ are calculated according to the differential equation (3).

$$d\chi_i/dt = k_i \, (1 - \chi_i) \tag{3}$$

Energy sources Q_i associated with the water vaporization (endothermic) and wood pyrolysis (exothermic) are calculated by the use of equation (4) where ρ_i is the volumic mass of the component (water or dry wood) and Hr_i the energy associated to the reaction i.

$$Q_i = d\chi_i/dt * \rho_i * Hr_i \tag{4}$$

Thermal properties

At each time step of the calculation, and at each node of the finite element geometry, the thermal conductivity λ_{sol} and the density ρ_{sol} of the solid are calculated as functions of mass fractions of the three following phases: dry wood (*s*), water (*w*) and charcoal (*char*) according to equations (5) and (6). The variation of the specific heat Cp_{sol} is depending on the volume fraction of the three phases according to equation (7). The mass and volume fractions of each phase are calculated thanks to equation (3).

The charcoal production is here driven by χ_l the degree of reaction of lignin pyrolysis (that gives the better results when comparing calculations to experiments). The production rate of charcoal is defined as γ (given as a mass fraction of initial dry wood). The coefficient β stands for the initial water content of wood.

$$\lambda_{sol} = \left(1 - \chi_l\right).\lambda_s + \frac{\rho_s}{\rho_{char}}.\gamma.\chi_l.\lambda_{char} + \frac{\rho_s}{\rho_w}.\beta.\left(1 - \chi_l\right).\lambda_w \qquad (5)$$

$$\rho_{sol} = \rho_s.\left[1 + \chi_l.\left(\gamma - 1\right) + \beta.\left(1 - \chi_w\right)\right] \qquad (6)$$

$$Cp_{sol} = \frac{\left(1-\chi_l\right).Cp_s + \gamma.\chi_l.Cp_{char} + \beta.\left(1-\chi_w\right).Cp_w}{\left[1+\chi_l.\left(\gamma-1\right)+\beta.\left(1-\chi_w\right)\right]} \qquad (7)$$

MODEL CALIBRATION

Experimental data

The parameters of the model were calibrated from the works of König [2]. During these tests, sections of softwood (spruce) were submitted to standard fires (ISO 834-1) and two types of parametric fires. In addition, the influence of thermal protection (plywood panels and plasterboards) on the temperature field and charring has been studied. For each test, the author gives the temperature at different depths of the timber section as well as an estimation of the charring depth. The latter is considered by the author as being the position of the 300 °C isotherm. The model parameters were calibrated so as to reproduce as well as possible the temperature field and the charring depth for the different fire curves.

Simulations details

Calibration simulations were performed on a 2D geometry (9.5 x 1 cm) representative of a slice of the wood sections tested by König. The thermal load is applied on one side of the geometry in order to recreate a uniaxial thermal diffusion. The experiments show that the temperature measured on the surface of the wood sections is very close to the temperature measured in the hot gas. We therefore applied a mix boundary (convection and radiation) with an infinite coefficient of convection H_c and a surface emissivity $\varepsilon = 0.8$. The model was confronted with tests on unprotected wood sections subjected to standard fire curve (5 tests), with tests on protected wood sections (two 15 mm thick plasterboards) subjected to standard fire (2 tests) and unprotected wood sections subjected to 2 parametric fires (3 tests by parametric fire). The fitted parameters of the model are given in Table I.

TABLE I. CALIBRATED MODEL PARAMETERS.

A_w (s^{-1})	A_c (s^{-1})	A_a (s^{-1})	A_b (s^{-1})	A_h (s^{-1})	A_l (s^{-1})	E_w (J/mol)	E_c (J/mol)
$1.00\ 10^{20}$	$4.71\ 10^{31}$	$4.71\ 10^{31}$	$1.96\ 10^{5}$	$5.78\ 10^{13}$	$5.09\ 10^{5}$	$1.62\ 10^{5}$	$3.33\ 10^{5}$
E_a (J/mol)	**E_b (J/mol)**	**E_h (J/mol)**	**E_l (J/mol)**	**Hr_w (J/m^3)**	**Hr_c (J/m^3)**	**Hr_a (J/m^3)**	**Hr_b (J/m^3)**
$1.51\ 10^{5}$	$1.96\ 10^{5}$	$1.04\ 10^{5}$	$1.64\ 10^{5}$	$-7.00\ 10^{6}$	0.00	$418.0\ 10^{3}$	$418.0\ 10^{3}$
Hr_h (J/m^3)	**Hr_l (J/m^3)**	**γ (%)**	**β (%)**	**ρ_s (kg/m^3)**	**Cp_s (J/kgK)**	**λ_s (W/mK)**	**ρ_w (kg/m^3)**
0.0	$79.0\ 10^{3}$	20	12	425	1636	0.123	1000
Cp_w (J/kgK)	**λ_w (W/mK)**	**ρ_{char} (kg/m^3)**	**Cp_{char} (J/kgK)**	**λ_{char} (W/mK)**	**R (J/molK)**	**Hc (W/m²K)**	**ε (-)**
4286	0.658	85	1100	0.6	8.314	∞	0.8

Results

Measured and calculated temperatures at different depths in the wood and the charring depth evolution are presented in Figures 1 to 3. In the model, the front of charring corresponds to the position where the reaction rate associated with β-cellulose pyrolysis is maximum. Globally the model overestimates the temperature. Therefore, calculated charring is slightly higher than the measures.

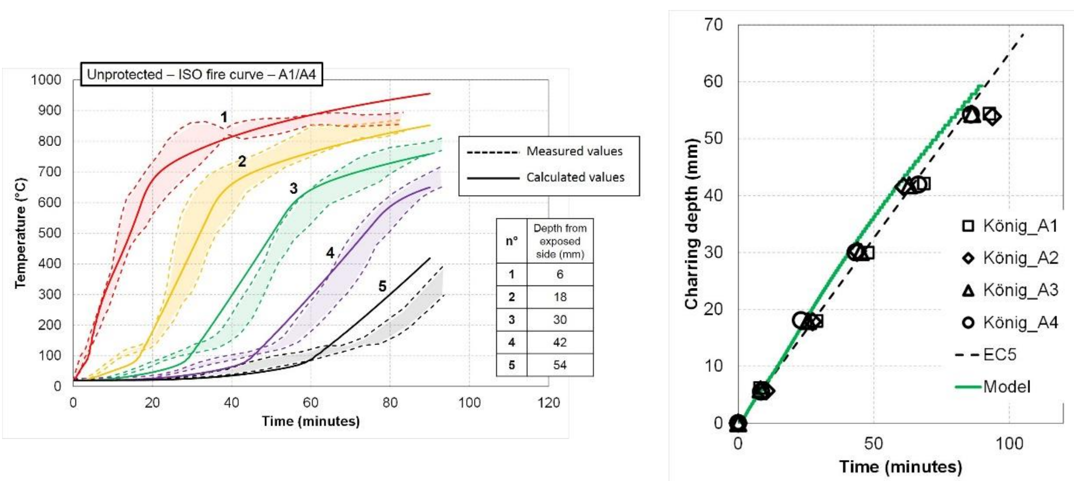

Figure 1. Results for unprotected sections exposed to ISO fire curve. On the left, evolution of the temperature in the wood section. Solid lines are for calculations, dotted lines are for experimental values (the colored area is the dispersion of 4 tests). On the right, evolution of the charring depth. Dotted line is for the charring model given by the Eurocode 5 for unprotected section exposed to ISO fire curve.

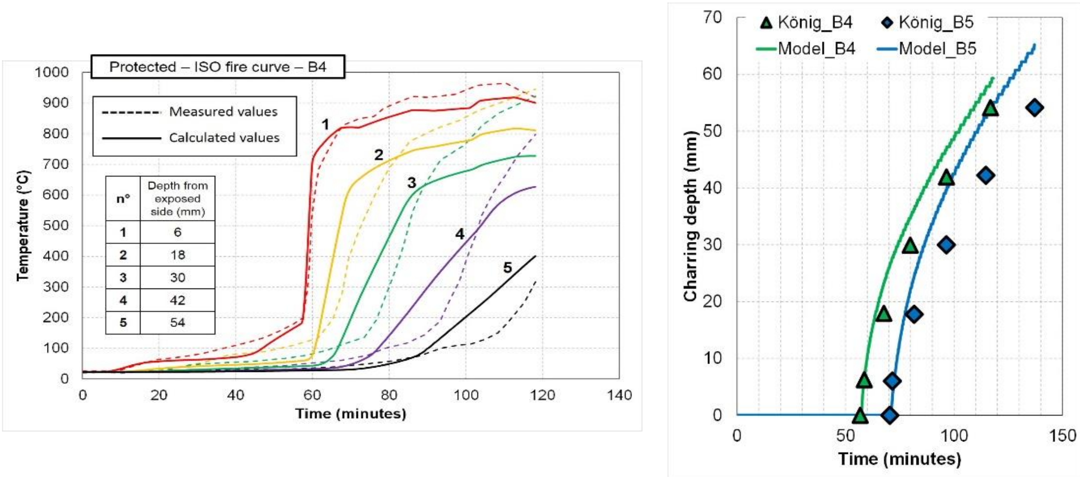

Figure 2. Results for protected sections exposed to ISO fire curve. On the left, evolution of the temperature in the wood section. Solid lines are for calculations, dotted lines are for experimental values (only one test is presented here). On the right, evolution of the charring depth of the two tests.

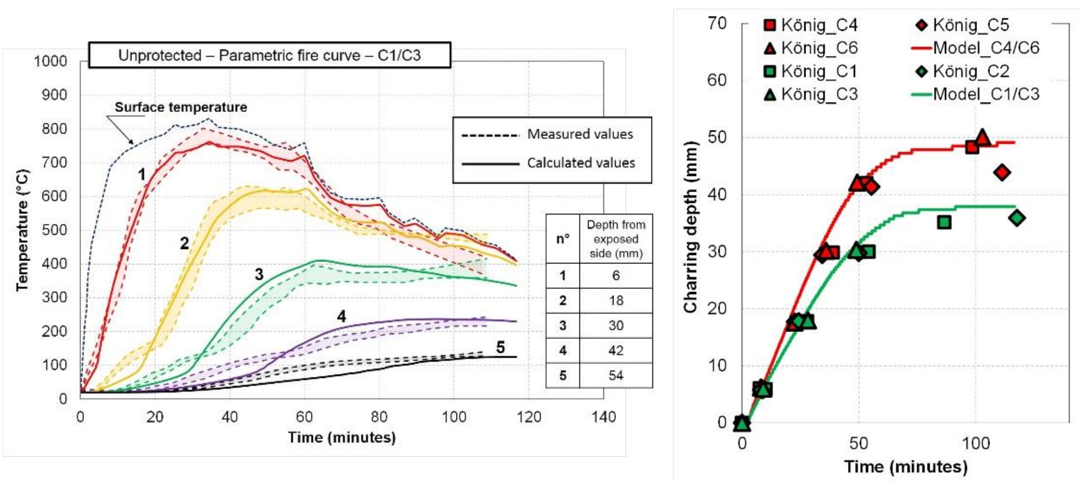

Figure 3. Results for unprotected sections exposed to parametric fires. On the left, evolution of the temperature in the wood section. Solid lines are for calculations, dotted lines are for experimental values (the colored area is the dispersion of 3 tests). On the right, evolution of the charring depth for the two series of parametric fires.

CASE STUDY

The wooden structure

A wooden floor in an office building is studied. The floor is made up of main unprotected beams made of glued laminated wood (GL24h according to the EN 338 norm) of dimensions 24 (width) x 54 (height) cm. Beams have a span of 8 m and are simply supported by 2 columns. The distance between main beams is 4 m. The main beams support a wooden CLT floor (20 cm thick), which receives a finish wooden flooring (2 cm thick). Design of beams was conducted according to the Eurocode 5

(Work ratio at 20 °C: 90 %). The compartment has a surface area of 64 m² (8 m x 8 m) and a ceiling height of 3 m. The 4 walls respectively have a surface area of openings of 4.8 m², 1.44 m², 4.45 m² and 2 m². The walls are composed of 20 cm thickness bricks, protected by plasterboards. The purpose of the study is to calculate the fire resistance of main beams, depending on the type of fire model.

Fire curves and simulation details

In accordance with the possibilities offered by the Eurocode 5, three models of fire are used: (i) the standard fire curve, (ii) a parametric fire and (iii) a 2-zones fire model. The parametric fire is calculated according to the Annex A of the Eurocode 1 [12]. For the 2-zones fire model, the Ozone software [13] is used. Ozone is a compartment fire model which includes a two-zone (localized fire) and a one-zone model (fully engulfed fire) with a possible switch from two to one zone if some criteria are encountered. The parameters used for the parametric fire and the 2-zones model are presented in Table II. The simulations were conducted on a 2D geometry of a main beam. Fire is applied on 3 sides of the beam through a mix boundary with a surface emissivity of 0.8 and a coefficient of convection of 25 W/m²K for the standard fire and 35 w/m²K for the parametric fire and the 2-zones fire. The model parameters are those obtained after the calibration study (Table I).

TABLE II. PARAMETERS FOR THE PARAMETRIC AND 2 ZONES FIRES.

Occupancy / Opening factor ($m^{1/2}$)	**Fire growth rate**	**Max. quantity of energy released by unit area of fire RHRf (kW/m²)**	**Combustion efficiency**	**Fire load density $q_{f,k}$ (MJ/m²)**	**Combustion heat of fuel (MJ/kg)**
Office / 0.05	Medium	250	0.8	511	17.5

Numerical results

Figure 4-a presents the evolution of the temperature in the hot gases, depending on the fire model. Figure 4-b presents the evolution of the temperature inside the beam at 6, 30 and 42 mm from the exposed surface. At the beginning of fire, parametric fire is the fastest. For the 2-zones fire, heating at the beginning is slower because fire remains localized for 10 min (two zones model), until it becomes fully engulfed in the compartment (one zone model. Prior to cooling, the temperature in the 2-zones model is the highest (1094° C). Unlike natural fires (fire parametric and 2-zones fire), the standard fire curve does not have a cooling phase. For both of the natural fires, the cooling phase starts almost simultaneously (34 min for the 2-zones model, 36 min for the parametric fire). On the other hand, the kinetics of cooling are different between these 2 fires. Finally, it is worth noting that the 3 fire curves have clearly different behaviour, leading to a different temperature field within the beam. It is important to remember that the Eurocode 5 makes possible the use of these 3 types fire modelling. The fire resistance of a structure will therefore strongly depend on the choice of the fire model.

The Figure 5-a presents the evolution of charring depth, depending on the fire model. Charring under ISO fire curve is almost linear, with a rate of 0.7 mm/min, i.e. similar to the Eurocode 5 model. Under parametric fire, charring is faster because of the rapid heating at the beginning of the fire. Regarding the 2-zones model, charring is delayed because the fire remains localized for 10 minutes. After 20 min, charring in the beam is close to that of the parametric fire. After 40 min of fire, charring is stabilized for both natural fires because of the cooling phase. The figure 5-b shows the change of the moment resistance of the beam depending on the fire model. The resistance of the beam is calculated from the residual cross-section of the beam. The resistant moment is compared at the design bending moment under fire (105 kNm, calculated according to Eurocode 5). Because of the very different kinetics of fire models, it is difficult to determine which is the more prescriptive or the more optimized: the beam is more resistant at the beginning of fire (0-18 min) when the 2-zones model is used (because the fire remains localized). Between 18 and 60 min, the standard curve gives better resistance because fire is slower and reaches lower temperatures. Finally, after 60 min, and due to the extinction of fire, the beam is more resistant for both natural fires. In the end, the fire resistance of the beam is 100 min under standard fire curve. The beam remains resistant during all the 2 natural fires.

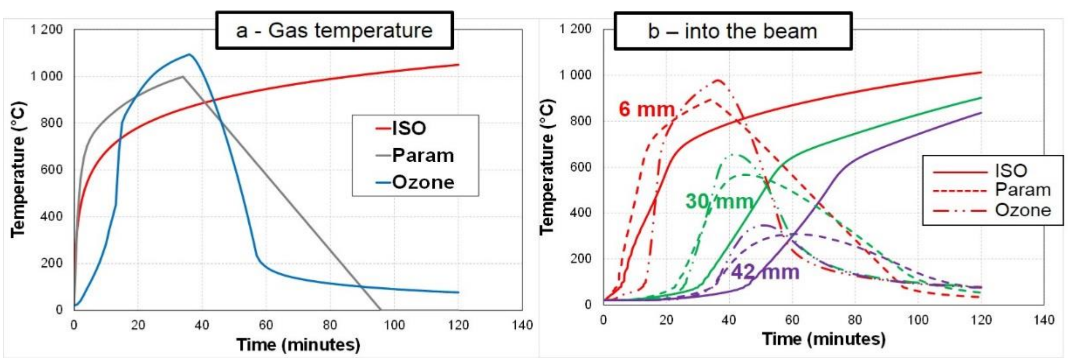

Figure 4. a – evolution of the gas temperature depending on the fire model. b – evolution of the temperature in the beam at 3 different depths from the exposed surface.

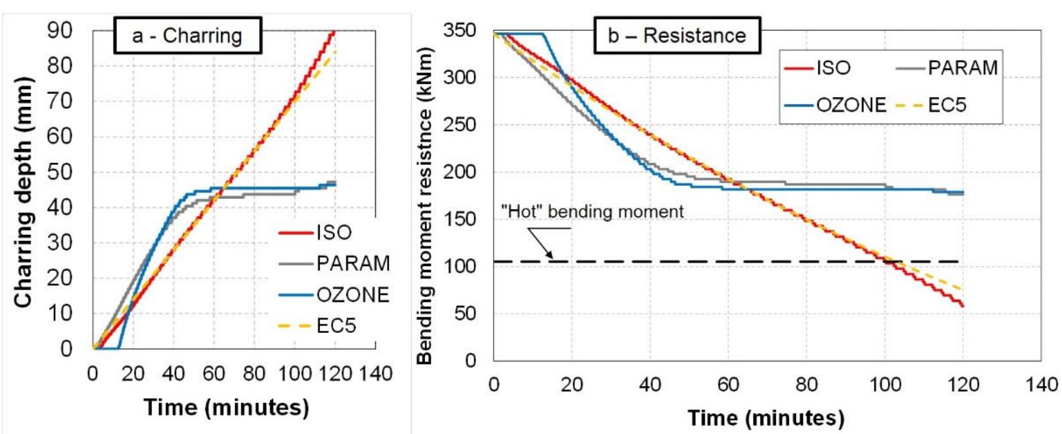

Figure 5. a – evolution of the charring depth depending on the fire model. b – evolution of the bending moment resistance of the beam. Dotted line is the design bending moment at high temperature.

CONCLUSIONS

A numerical model for calculation of heat diffusion and charring depth in wooden structures has been developed and calibrated based on experimental results. This model is able to assess the charring depth, and so the fire resistance of a structure element (unprotected or protected), whatever the applied heating. In particular, it allows using different types of fire models: from the standard fire curve to more advanced models (2-zones model for instance). A numerical study was carried out on a 2D geometry of a wooden beam exposed to three types of heating: the standard fire cure, a parametrical fire and a 2-zones fire. We clearly showed that for the same compartment, the way the fire is simulated can lead to quite different heating. Charring depth, and so the fire resistance, is dependent on the fire model. At certain times of the fire, the standard fire curve leads to oversized design of the structure (at the very beginning and at the end of the fire in our case study) but can also leads to optimized design compared to more advanced fire models (in the intermediate phase of the fire in our case study). Parametrical numerical studies and more experimental data are needed in order to give guidelines to engineers when designing wooden structures exposed to fire. It can help to promote the use of wooden in civil structures, tall buildings for instance.

REFERENCES

1. EN 1995-1-2. 2004. Eurocode 5: Design of timber structures - Part 1-2: General - Structural fire design, European Committee for Standardization.
2. König J. and L. Walleij. 1999. "One-Dimensional Charring of Timber Exposed to Standard and Parametric Fires in Initially unprotected and Postprotection Situations". SP Technical Research Institute of Sweden, Wood Technology, Stockholm, Sweden.
3. Tonicello E., O. Vassart, R. Zanon and J.M. Franssen. 2012. "Structural Fire Design and Optimization of a Building", *Structural Engineering International*, 22(4):541-544.
4. Rackauskaite E., C. Hamel, A. Law and G. Rein. 2015. "Improved Formulation of Travelling Fires and Application to Concrete and Steel Structures", *Structures*, 3:250-260.
5. Bartlett, A., R. Hadden, L. Bisby, and A. Law. 2015. "Analysis of Cross-Laminated Timber Charring Rates upon Exposure to Non-standard Heating Condition" presented at the 14th International Conference on Fire and Materials, San Francisco USA, February 2-4 2015, 667-681.
6. Richter F. and G. Rein. 2015. "Numerical simulation of the charring of timber structures under non-uniform fires", presented at the 1st European Workshop Fire Safety of Green Buildings, Berlin, Germany, October 6-7 2015, pp. 91-92.
7. Hopkin D. 2012. "The adaptation of DIANA for simulating fire exposed timber structures in natural fire conditions", presented at the 7th International conference on Structures and Fire, Zurich, Switzerland, June 6-8 2012, pp. 377-386.
8. Lange D., L. Boström, J. Schmid and J. Albrektsson. 2014. "Charring rate of timber in natural fires", presented at the 8th International conference on Structures and Fire, Shanghai, China, June 11-123 2014, pp. 521:528.
9. CAST3M-2014. 2014. Finite element software, CEA, www-cast3m.cea.fr
10. Di Blasi C. 1998. "Comparison of semi-global mechanisms for primary pyrolysis of lignocellulosic fuels", *Journal of Analytical and Applied Pyrolysis*, 47(1):43-64.
11. Bal N. 2012. "Uncertainty and complexity in pyrolysis modelling", PhD thesis, University of Edinburgh.
12. EN 1991-1-2. 2002. Eurocode 1: Actions on structures – Part 1-2: General actions – Actions on structures exposed to fire, European Committee for Standardization.

13. Cadorin J.F. and J-M. Franssen. 2003. "A tool to design steel elements submitted to compartment fires—OZone V2. Part 1: pre- and post-flashover compartment fire model", *Fire Safety Journal*, 38(5):395-427.

Sectional Analysis of Cross-Laminated Timber as a Design for Fire Methodology

ALASTAIR BARTLETT, RORY HADDEN, LUKE BISBY
and BARBARA LANE

ABSTRACT

Current European structural fire design methodology for cross-laminated timber (CLT) elements predominantly uses a reduced cross-section method, which fails to realistically capture the variation of mechanical properties of timber at elevated temperature or with variable grain directions. A thermomechanical sectional analysis, compared against fire tests on CLT slab strips is presented herein, using two different sets of temperature-dependent mechanical properties available in the literature. This is investigated as an alternative, more rational design approach for CLT flexural elements exposed to fire. Initial results show reasonable correlation with experimentally observed failure times (i.e. fire resistances). Both failure time and deflection response are shown to depend on the temperature-dependent mechanical properties of timber used as modelling inputs, and the recommended properties presented in the Eurocode may not be suitable on the basis of the testing and analysis presented. Further research is needed to corroborate this conclusion.

INTRODUCTION & BACKGROUND

Cross-laminated timber (CLT) is one of several engineered timber products gaining popularity in the construction industry due to its attractive aesthetic, structural, and sustainability credentials. One significant factor preventing its widespread application in high-rise buildings is uncertainty around its performance in fire when used as the main structural frame. The majority of available research on timber's structural performance in fire focuses on determining the effective charring rates under standard fire testing furnace exposures, with consequent limited understanding of its behaviour in real fire scenarios. For the architectural aspirations of unprotected CLT structural members to be fully achieved, the fire behaviour and real structural response of CLT buildings in such scenarios must be properly understood.

CLT is formed from several lamellae of timber with adjacent lamellae arranged with perpendicular grain directions. This gives strength and stiffness in both directions, allowing CLT to be used as two-way spanning slabs, load-bearing and shear walls, and diaphragms. Existing structural fire design guidance for solid or glued laminated timber assumes axial/flexural strength in the grain direction only, and thus may be unsuitable for CLT elements. This paper examines an alternative method that accounts for the cross-wise laminations of CLT, and compares response predictions made using the more advanced analysis against experimental data from a recent set of flexural fire tests on softwood CLT beams.

EXISTING METHODOLOGY

The current design methodology recommended by Eurocode 5 [1] offers two approaches to determine the fire resistance of a solid or engineered timber element. The first of these is a 'reduced properties' method in which the residual section below the char line is analysed accounting for reduced overall mechanical properties, which are determined as functions of the element's heated perimeter and exposed area. This method is intended for beams, and is unsuitable for application to slabs [1]. The second method, which is the preferred method currently used in design is the 'reduced cross-section' method, in which a char layer is determined and is assumed to have zero strength, as is an additional "zero-strength layer" (typically 7mm) below the char, which is subtracted to account for the reduced mechanical properties of a certain depth (about 35-45mm) of heated timber below the char. This approach was originally developed by Schaffer et al. [2] using tests and modelling of glued-laminated beams tested in standard fire testing furnaces. Schaffer et al. [2] proposed that the reductions in mechanical properties over the (approximately) 40mm heated zone beneath the char layer could be accounted for by assuming that an additional 7.6mm of timber had zero-strength, with the remainder having full ambient strength. This method was not intended for application to CLT without further validation [3]. Due to the cross-wise layup of CLT, perpendicular lamellae have negligible strength. Thus, depending on the location of the char layer, the Eurocode's "zero-strength layer" could simply eliminate 7mm of strength from a weak lamella that contributes very little to the element's strength anyway, whilst neglecting the reduced mechanical properties of a heated strong layer underneath. This is illustrated in Figure 1 and is unconservative in terms of structural fire resistance predictions.

EXPERIMENTAL WORK

In order to verify (or otherwise) the existing approach and the more rational approach examined herein, CLT slab strips with a length of 2000mm, width of 300mm, and depth of 100mm were prepared with lay-ups of either of three or five lamellae of uniform thickness. In a series of ambient temperature control tests (performed in duplicate on each lay up) load was applied using a hydraulic actuator at 2mm/min in 4-point bending until failure. The 3-layer beams failed at an average load of 52.6±0.2kN by a 'rolling shear' failure mode, and the 5-layer beams failed at an average load of 40.4±2.3kN in a flexural (tension) mode.

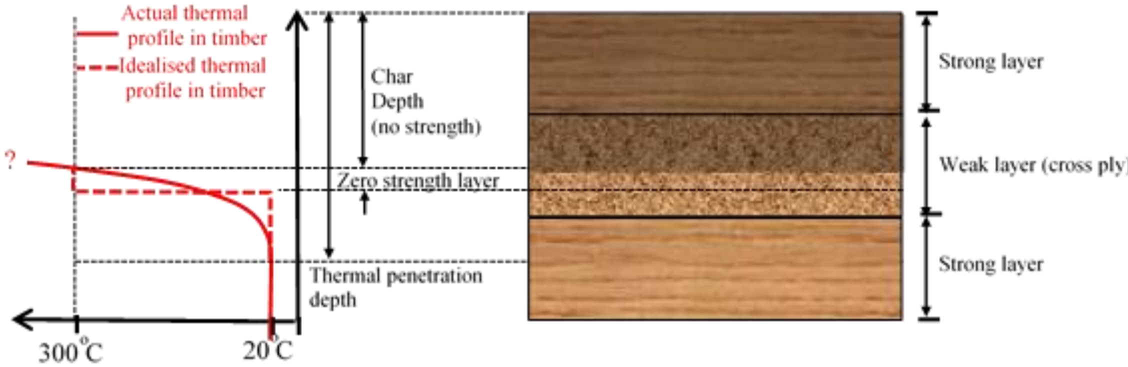

Figure 1. Charring of a CLT element highlighting strong and weak layers and extent of the heated region.

Eight further tests (again in duplicate) were performed under sustained load and mid-span radiant heating, on samples loaded to 10 or 20% of their ultimate ambient strength found from the ambient temperature tests. Only the constant moment region of the beams was heated (from below) with a radiant panel; the remainder of the cross-section was insulated with mineral wool to promote one-dimensional heat transfer. The incident radiant heat flux was 25 to 30kW/m^2. These tests were intended to investigate the effects of loss of section on structural capacity and failure mode. The Eurocode's methods were initially used to predict the charring and residual cross-section, from which reductions in structural capacity during heating were predicted.

Whilst it was observed that failures were predicted reasonably accurately using the Eurocode approach, the observed charring rate from the tests did not agree well with those predicted by the Eurocode's notional charring rate of 0.65mm/min. Experimental charring rates of about 0.5mm/min were observed based on in-depth temperature measurements; these resulted in experimental char depths of only 20mm and 35mm at failure for the 3- and 5-lamellae samples at 20% loading respectively, rather than the 26mm and 49mm that would be expected on the basis of the Eurocode. This means that zero-strength layer depths of 13mm or 21mm would be required to corroborate the Eurocode's effective cross-section approach for the 3- and 5-lamellae samples respectively, thus clearly demonstrating the inadequacy of this approach, both for standard and non-standard heating regimes [4]. It was also noted that the charring was not perfectly one-dimensional; some charring occurred outside the heated region.

Predictive models developed to predict the beams' time-deflection response also showed that the zero-strength layer approach failed to capture the physics of the problem, and that the concept of a zero-strength layer applied to CLT is fundamentally flawed due in part to grain-dependent strength parameters [4]. The possibility of applying a thermomechanical sectional analysis approach is now being explored, in which temperature-dependent mechanical properties are mapped onto the known temperature profile within the heated CLT elements to give a physically based representation of the strength over the cross-section. Such a method has the additional advantage that it can be applied to any heating scenario where the temperatures are known or can be calculated.

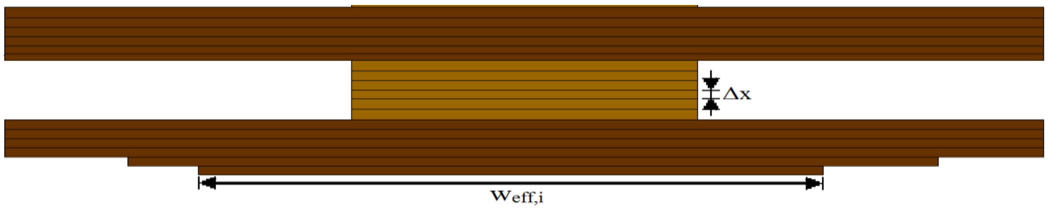

Figure 2. Transformed CLT cross-section showing element discretisation and effective widths.

SECTIONAL ANALYSIS METHODOLOGY

Analysis Approach

To account for the different orientations of lamellae present in CLT, a more rational sectional analysis method is proposed. CLT cross-sections are divided into elemental thicknesses of depth Δx. The temperature of each element is determined for each time step, based initially on experimental data obtained during testing in the current study [4]. Factors for reduction of elastic modulus with temperature, such as those in Eurocode 5 [1] are applied over the cross-section, and a new "transformed width" is determined for each elemental layer using Equation 1:

$$w_{eff,i} = E_i/E_0\, w \tag{1}$$

where $\boldsymbol{E_i}$ and $\boldsymbol{E_0}$ are the elastic moduli of each element and the original cross-section respectively (a similar method is typically used for ambient design of CLT, wherein a transformed cross-section is developed by reducing the effective widths of the perpendicular layers). An example of a transformed section during heating is shown in Figure 2, where both the weak and heated strong sections have been transformed.

The elastic section modulus is then calculated using a MATLAB script, and the tensile stress in each of the fibres is calculated. This is compared against temperature-dependent tensile strengths, again calculated based on Eurocode 5 reduction factors (although for tensile strength in this case) and any elements in which stress exceeds strength are ignored. The elastic section modulus is then recalculated, and the elastic section modulus for failure (S_f) is given by Equation 2 [6]:

$$S_f/S_0 = P_a/P_f \tag{2}$$

where $\boldsymbol{P_a}$ and $\boldsymbol{P_f}$ are the sustained applied and ambient ultimate failure loads, respectively. It is noteworthy that the experimental thermal profiles used in the analysis were derived by fitting a polynomial curve to the in-depth temperatures measured in the tests [4], since a smooth thermal profile was needed to implement the analysis calculations described.

The beams' deflection responses can also be predicted from the transformed section and the applied load. This analysis requires the heated and unheated portions of the beams to be considered independently. The support conditions were assumed as pinned, with deflection and rotation continuity at the interface between the heated and unheated portions of the beam. Flexural stiffness matrices for both regions were then calculated, and the resulting mid-span deflection determined for each time step.

Material Input Parameters

A central consideration challenge in accurately predicting the in-depth flexural elastic modulus of the samples arises in determining the temperature-dependent mechanical properties for heated timber, both along and perpendicular to the grain direction. Figure 3 shows various data sets and proposals from the literature. Considerable variation in the data is evident.

The variation in elastic modulus with temperature proposed by König and Walleij [7] is based on bending tests [18] and are used by Eurocode 5. The König [18] samples were heated on one side only, and the strength and flexural stiffness reductions were back-calculated based on the observed element response. Since these are not direct measurements, the results are *effective* parameters specific to the test setup used, rather than directly measured material properties. Since the cross-section used by König [18] was significantly different (145mm deep x 45mm wide) to that used herein, the resulting mechanical properties may not be suitable. Indeed, Table I shows that use of the König and Walleij [7] results in consistent under-prediction of the fire resistance.

Other data sets in Figure 3 are based on tests under different conditions; e.g. the results from Östman [13], Young [11], and Schaffer [17] are all derived from small-scale tensile tests. Tests in pure tension, whilst giving actual properties rather than effective properties, may not be the most suitable for application to bending tests due to the differences in mechanical response in tensile and bending tests.

To investigate the effect(s) of the assumed variation in elastic modulus with temperature on the model predictions, the model was re-run using Thomas' [8] tensile elastic modulus data, with all elements at temperatures above 300°C assumed to have zero strength and stiffness. Thomas' model is based on the same principles as König and Walleij [7] and used the test results from König [18], but only calculated the elastic modulus at failure, whereas König and Walleij calculated the values at each instant in time throughout the tests based on the time-history of mid-span deflection, also using the results from König [18] supplemented with additional tests [7]. Whilst the two methods give similar results for the compressive elastic modulus, as shown in Figure 3, for tensile elastic modulus the methods give different results. As with König and Walleij's model, Thomas' model only gives *effective* parameters, and may not be appropriate for the current tests; however they are used herein for comparison and the results are given in Table I.

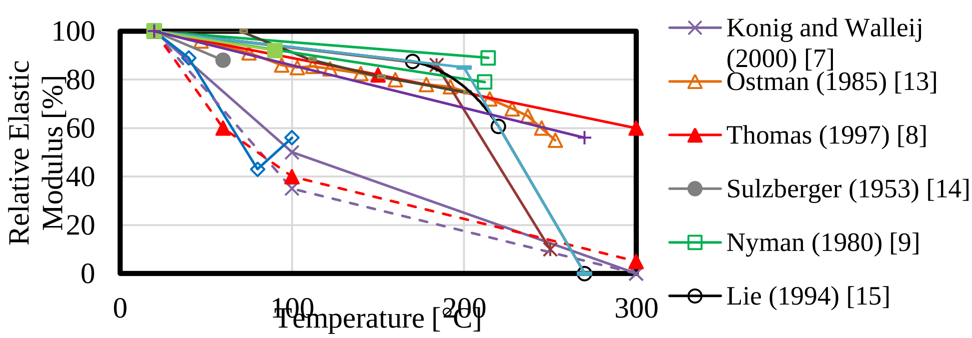

Figure 3. Elastic modulus of softwood timber, parallel to grain, as a function of temperature from the available literature; compressive elastic modulus is shown by dashed lines.

RESULTS AND DISCUSSION

The observed and predicted failure times from each of the eight fire tests are given in Table I, where the clear underestimation of failure times by the model using Eurocode 5 property variation is clear. It is evident that, using property variations according to Thomas [8] gives better predictions for most tests, with an average prediction error of +6%, compared with +30% for the Eurocode 5 properties.

The first of the 5-lamellae tests, which failed after 86 minutes, was predicted not to fail using Thomas' properties; temperature measurements were taken up to 104 minutes, at which point the Thomas' properties model predicted a load-bearing capacity greater than the applied load of 10% of the ambient capacity. Examining the predicted and measured deflection responses for this test, shown in Figure 4, it can be seen that the response closely resembles the Eurocode model predictions. In some other tests, the deflection response more closely resembled the Thomas' model, whereas in others it did not show a particularly strong correlation to either model. Four typical time-deflection responses for different beams, along with their model predictions are shown in Figure 4.

The generally poor correlation is likely primarily due to incorrect mechanical property relationship parameters being used. Two sets of properties from opposite ends of the spectrum of available data in Figure 3 were selected and used to study their influences on the predictions. Figure 4 shows that the majority of experimental results lie somewhere in between these two models. It is therefore likely that the "true" variation of mechanical properties with increasing temperature lies somewhere in between these two extremes. Therefore, understanding and characterising suitable material properties for timber at elevated temperature is vital for implementation of this (and similar) model. Furthermore, due to some slight two-dimensional charring effects outside the heated zone in the tests presented herein, mechanical properties in the "non-heated" region would also be slightly reduced, resulting in an over-prediction of the beam's strength and stiffness using the proposed model.

TABLE I. MODEL-PREDICTED AND EXPERIMENTALLY OBSERVED FAILURE TIMES FOR CROSS-LAMINATED TIMBER BEAMS UNDER SUSTAINED LOAD DURING HEATING.

Test	Sustained load/ ambient ult. load [%]	Actual failure [min]	Predicted failure (EC5 properties) [min]	Under-prediction (EC5 properties) [%]	Predicted failure (Thomas' properties) [min]	Under-prediction (Thomas' properties) [%]
3-lamellae						
1†	10	60*	58	3	67	-11
2†	10	89	54	39	60	32
3	20	38	29	23	42	-10
4	20	39	27	31	40	-3
5-lamellae						
5	10	86	69	20	None	n/a
6†	10	85	73	15	89	-5
7	20	74	32	57	42	43
8†	20	76	61	20	79	-4

*test erroneously halted prior to failure due to a sudden (but not catastrophic) deflection

†particularly poor fit to thermocouple data

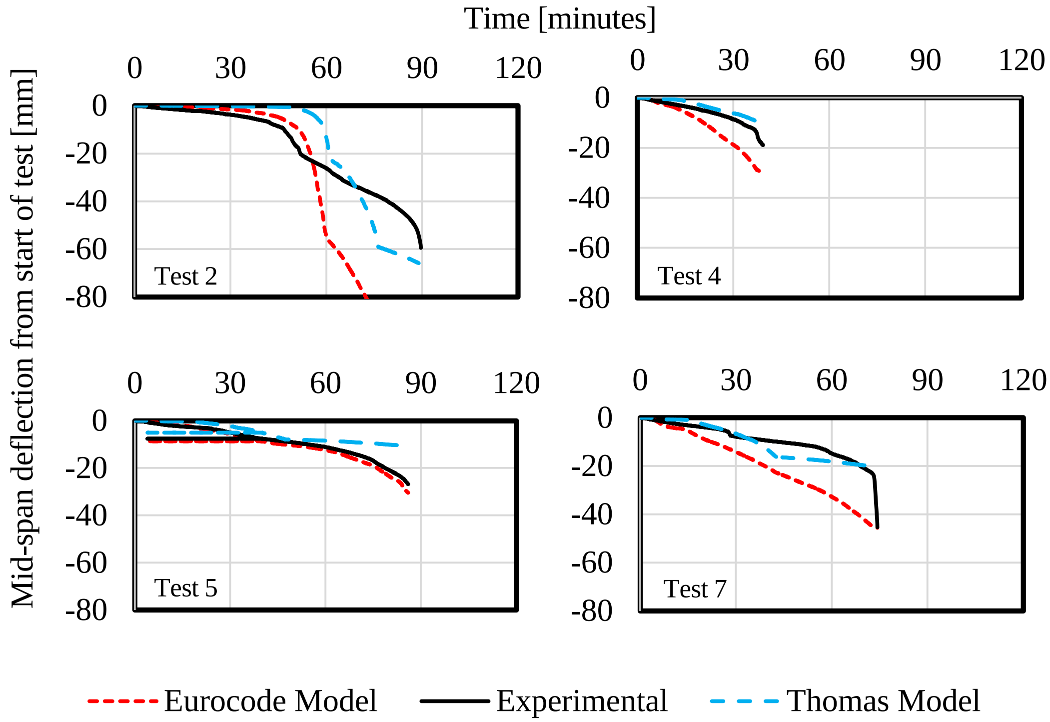

Figure 4. Predicted and experimental deflection responses for tests 2, 4, 5, and 7.

CONCLUSIONS AND FURTHER WORK

A thermomechanical sectional analysis has been applied in an attempt to undertake a rational analysis to predict the structural response (i.e. deformation response and fire resistance) of CLT flexural elements. The initial results show a reasonable ability to predict failure times (i.e. fire resistances) given a known (measured) time-history of internal temperature profiles.

For the majority of samples tested, Thomas' [8] properties provide a better estimate of failure time than the Eurocode 5 [1] suggested properties, with an average prediction error of 6% compared with 30%. The predicted deflection responses in Figure 4 show that both sets of properties give poor predictions of the response. It can be observed, however, that the predicted deflection response depends heavily on the assumed variation of mechanical properties of timber with temperature – it is therefore vital to better understand and obtain more realistic properties for various configurations and conditions of timber under elevated temperature exposures.

Once these material properties are known with confidence, they should be validated across multiple scales and structural and loading configurations, including beams, columns, and slabs to allow use for predicting CLT mechanical response during heating. Methods for predicting the temperature profiles in heated CLT, rather than using the experimental data or notional charring rates, should also be explored in future work, to allow a fully predictive model for CLT structural elements in fire. This will require a detailed heat transfer analysis, and depending on the orientation, one-dimensional heat transfer analysis may be insufficient.

REFERENCES

1. CEN 2004. Eurocode 5. Design of timber structures. *Part 1-2: General. Structural fire design*, Brussels: European Committee for Standardisation.
2. Schaffer, E. L., Marx, C. M., Bender, D. A. and Woeste, F. E. 1986. Strength validation and fire endurance of glued-laminated timber beams.
3. Schmid, J., König, J. and Köhler, J. 2010. Fire-exposed cross-laminated timber-modelling and tests. in World *Conference on Timber Engineering*.
4. Lineham, S., Thomson, D., Bartlett, A., Bisby, L. and Hadden, R. (in Press) Structural Response of Fire-Exposed Cross-Laminated Timber Beams under Sustained Loads. *Fire Safety Journal*.
5. Schmid, J., Just, A., Klippel, M. and Fragiacomo, M. 2014. The Reduced Cross-Section Method for Evaluation of the Fire Resistance of Timber Members: Discussion and Determination of the Zero-Strength Layer. *Fire Technology*, pp. 1-25.
6. Janssens, M. 1997. A Method for Calculating the Fire Resistance of Exposed Timber Decks. in *5th International Symposium on Fire Safety Science*, Melbourne, Australia.
7. König, J. and Walleij, L. 2000. Timber frame assemblies exposed to standard and parametric fires: part 2: a design model for standard fire exposure. *Rapport-Institutet för Träteknisk Forskning*, (0001001), pp. 1-76.
8. Thomas, G. C. 1997. *Fire Resistance of Light Timber Framed Walls and Floors*. PhD Thesis, University of Canterbury.
9. Nyman, C. 1980. The effect of temperature and moisture on the strength of wood and glue joists. *Technical Research Centre of Finland (VTT). Report Forest Products Lab,* (6).
10. Kollmann, F. 1951. Über das mechanische Verhalten von Kiefernholz bei Biegung und Temperaturen zwischen 20 und 100 C. *Svenska Träforskningsinstitutet, Trätekniska Avdelningen, Meddelande, 22*.
11. Young, S. 2000. *Structural Modelling of Plasterboard-Clad, Light Timber*. Unpublished, Victoria University of Technology.
12. James, W. L. 1961. Effect of temperature and moisture content on: Internal friction and speed of sound in Douglas-fir. *Forest Prod. J, 11*(9), pp. 383-390.
13. Östman, B.-L. 1985. Wood tensile strength at temperatures and moisture contents simulating fire conditions. *Wood science and technology, 19*(2), pp. 103-116.
14. Sulzberger, P. H. 1953. The effect of temperature on the strength of wood, plywood and glued joints.
15. Lie, T. 1994. Structural fire protection, manuals and reports on engineering practice, No. 78. *ASCE, New York, NY*.
16. Preusser, R. 1968. Plastic and elastic behaviour of wood affected by heat in open systems. *Holz-technologie*, *9*(4), pp. 229-231.
17. Schaffer, E. 1973. Effect of pyrolytic temperatures on longitudinal strength of dry Douglas-fir. *Journal of Testing and Evaluation, 1*(4), pp. 319-329.
18. Konig, J. 1991. Modelling the Effective Cross-Section of Timber Frame Members Exposed to Fire. International Council for Building Research Studies and Documentation. Working Commission W18A - Timber Structures Meeting 24. Oxford, United Kingdom. September 1991.

Timber under Real Fire Conditions – the Influence of Oxygen Content and Gas Velocity on the Charring Behavior

JOACHIM SCHMID, DANIEL BRANDON, ALESSANDRO SANTOMASO, ULF WICKSTROM and ANDREA FRANGI

ABSTRACT

As for any building material, verification of fire resistance is mandatory for separating and loadbearing timber members. While non-standard fire design for steel members has long tradition, the corresponding possibilities for timber members are limited. Reasons for this can be found in the degree of complexity of the material and the limited research done in the field. This paper summarizes selected outcomes of tests investigating the influences on the charring behavior varying the oxygen content and the gas velocity. Besides the charring rate the char layer depth was the focus of this study to investigate char contraction (consumption of the char layer). In general, measurements are in line with previous results reported in literature. Results show that charring is predominantly depending on the fire compartment temperature.

Results show further that for gas oxygen contents below 15 percent the gas velocity has no influence on the charring. However, at higher oxygen rates char contraction was observed affecting the protective function of the char layer. Thus, the charring and the temperature distribution was affected and the residual cross-section was decreased. In fully developed fires increased charring due to char contraction may not be observed due to the low oxygen contents. Contrary, in travelling fires or in the decay phase char contraction may be considered. This may have significant impact to Performance Based Design using non-standard temperature fire curves where the complete fire duration has to be taken into account.

The work was performed within a FORMAS project “Natural fire design of timber structures” and the test series presented here were conducted within a Master Thesis in collaboration with the University of Trieste by A. Santomaso.

Schmid J., ETH Zurich, Institute of Structural Engineering, Chair Timber Structures, schmid@ibk.baug.ethz.ch
Brandon D., SP Wood Building Technology, Sustainable Built Environment, Sweden
Santomaso A., University of Trieste, Italy
Wickström U., LTU Lulea University of Technology, Sweden
Frangi A., ETH Zurich, Institute of Structural Engineering, Chair Timber Structures, Switzerland

INTRODUCTION AND BACKGROUND

Fire design of structural timber members is done in Europe according to rules given in the fire part of Eurocode 5 [1]. Design models are usually developed for standard fire exposure [2]. Very limited models are available for non-standard fires. In general, design of timber members considers the reduction of the cross-section by char as well as the reduction of strength and stiffness of the residual cross-section. While the charring rate in standard fires is normally observed to be constant [3], charring rate for non-standard fires varies and existing rules may be questioned.

The origin of this study is based on observations in fire resistance tests following the standard fire exposure (defined time-temperature and pressure curves as well as minimum oxygen content of 4% [2]) in different furnaces where different charring rates were observed for the same product. A further motivation can be found in observations of fire accidents where different residual cross-section of solid timber members inside a fire compartment depending on the air flow [4].

TEST PROGRAM

In total 12 tests with various test conditions were performed in a custom made gas fired furnace; the tests lasted 60 minutes after ignition. After each test the specimen was removed from the furnace and any burning was extinguished with water; this procedure took less than 30 seconds to allow for accurate evaluation of the residual cross-section and the char layer depth.

Material

Tests were performed with CLT (Cross Laminated Timber) beams (150 mm x 150 mm x 1730 mm, C24 European wood grade) with 12% ±1% equilibrium moisture content. The five layer product (top layer 42 mm) is glued with PUR (Polyurethane) adhesive and all specimens were stored in a conditioning room before testing. CLT was used to have a homogeneous material with limited number of defects. The timber members with a width of 150 mm were insulated on both sides with stone wool (thickness 45 mm; 35 kg/m^3). In four cross sections (A to D) the progression of char, temperatures and the oxygen content were recorded during the tests.

Test Equipment

The equipment used in the tests consisted of: (i) a gas supply unit in which a defined gas volume and the oxygen content of the supplied gas were controlled by means of mixing ambient air with nitrogen or oxygen; (ii) a heating device where the supply air was mixed with burning Gasol (95 % Propane and 5 % Butane); (iii) a fire compartment (insulated steel channel 200 mm x 160 mm x 2000 mm) and; (iv) an exhaust unit (part of the fire lab).

Three sides of the fire compartment were designed to function as a large plate thermometer (PT) [2] comprising a steel plate at the exposed side and ceramic fiber insulation at the unexposed side. Temperatures were measured at sections A to D. Tests were performed in low under-pressure (ca. 10 Pa) to provide a good working environment in the laboratory. The air velocity was controlled in the inlet (cold condition) as well as in the fire compartment. Both measurements were in a good agreement. The oxygen content of the air was measured with a paramagnetic and an electrochemical method in five cross sections; at the beginning of the fire compartment (cross section zero) and sections A to D.

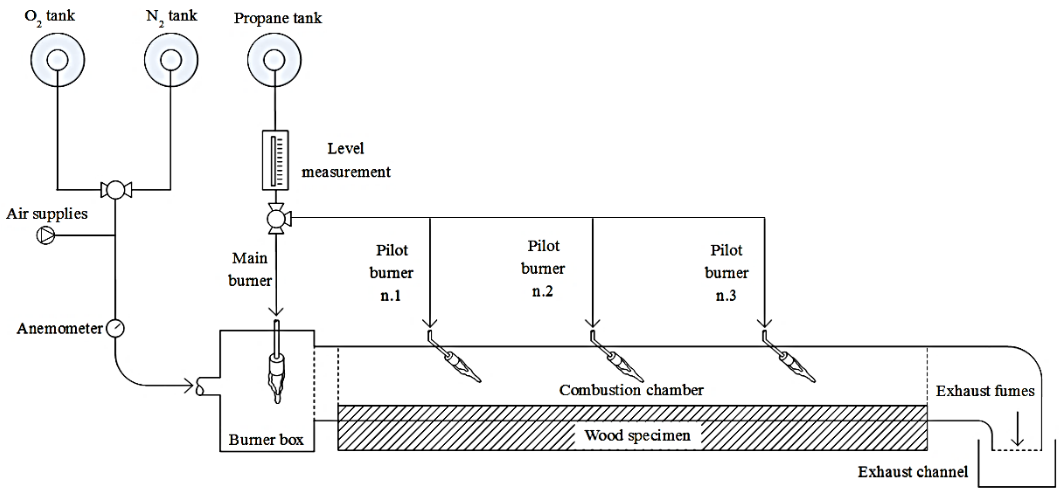

Figure 1. Schematic cross-section view of the test set-up.

Test Conditions

All fire tests aimed for a quick initial fire compartment temperature rise and a constant temperature during the test. During the early testing phases different temperatures of the cross-sections A to D were measured (compartment PT temperatures). Additionally to the PT temperature the gas temperature inside the fire compartment was measured using small thermocouples; the gas temperature was further used to determine the gas velocity in the fire condition in combination with a Pitot tube [5]. The temperatures (PT and gas) in the end of the tests varied between about 700°C and 900°C.

Air velocities were varied between about 1 m/s and 15 m/s in the fire compartment. The oxygen content was varied from 5% up to 15% (percentage by volume).

RESULTS

The documentation comprises the recordings gas concentrations, pressure, gas velocity, temperature and residual cross-section and char-layer after the tests. For the evaluation of variations of charring depth in longitudinal direction, residual longitudinal-sections at the center lines of the timber specimens were documented; an example is shown in Figure 2.

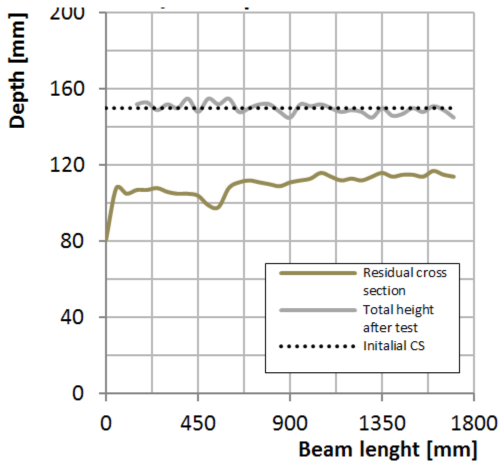

Figure 2. Residual cross-section (length profile), and total depth after the fire test 8 (1m/s gas velocity, 5% O_2)

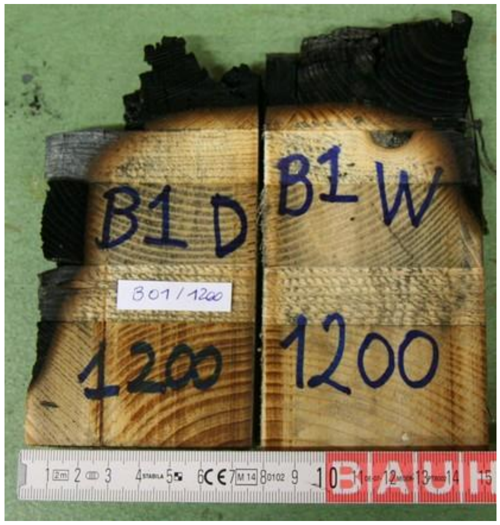

Figure 3. Residual cross-section, and total depth after the fire test 8 (1m/s gas velocity, 5% O2).

To evaluate the residual cross-section at the corresponding temperature measurement stations (cross-sections A to D), as well as effects of the limited cross-section width of the beams, images of the residual cross-section were taken; an example is shown in Figure 3.

ANALYSIS BY SIMULATIONS

The aim of the simulations was to estimate the effect of the gas velocity in comparison to temperature on the specimen. Thus, in the following, two tests (test 09 and test 14) are compared where equal temperature time curves were achieved. The oxygen content was set to 15% and the gas velocity was 3 m/s and 15 m/s respectively. The temperature exposure showed a logarithmic temperature rise (ca 30 min) up to a plateau with about 800°C; the test lasted 60 min. Fire exposures are specified Figure 4. Results show different cross-section depths for both tests with respect to the remaining cross-section (total depth including the char layer) and the residual cross-section. The length profile was observed to be most steady in cross-section B at about 700 mm length position, see Figure 4. In the following, the residual cross-sections and temperature measurements in cross-section B (see Figure 5), about 400 mm in length, are further analyzed. The cross-sections after fire exposure of tests 9 and 14 are shown in Figure 6.

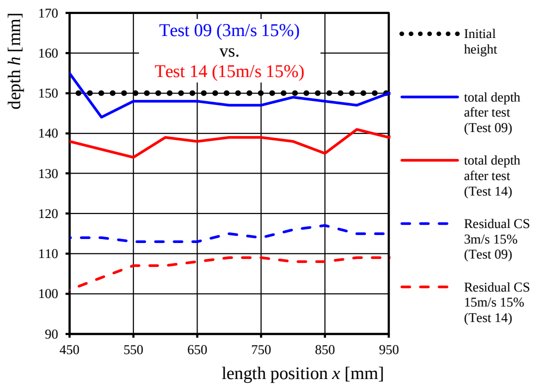

Figure 4. Remaining cross-section (including the char layer) and residual cross-section in the length profile allocated to cross-section B (position 700 mm) thermal exposure.

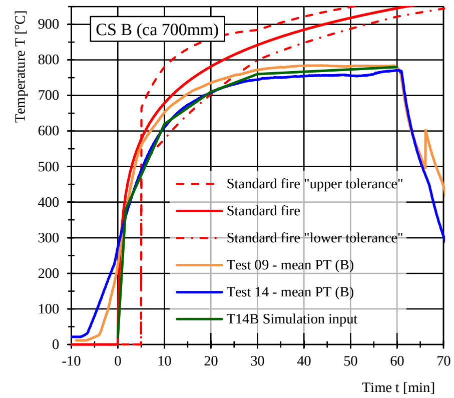

Figure 5. Temperature in tests no. 09 and 14 and the standard fire exposure.

(A) (B)

Figure 6. Cross-section at 700 mm length (cross-section B) after test 9 (A) and after test 14 (B).

Simulation of Char Contraction

One dimensional thermal simulations were performed with elements of 1 mm depth. Simulations used the effective material properties available in Eurocode for fire design of timber structures [1] for standard fire exposure as deviations are limited, see Figure 5.

At standard fire exposure, charring depth after one hour can be expected to about 40 mm according to the simplified, linear charring rules in [1] and literature. In the following, the temperature rise in 40 mm depth is analyzed with respect to different conditions investigating char contraction. Char contraction was observed to be 10 mm after 60 min in the fire test 14. Char contraction was assumed to occur linearly which was realized in the simulations by deleting elements in equal steps of 6 min; every 6 min simulations were stopped, one element deleted and simulations continued using the before obtained temperature field. The following cases were investigated:

(i) Standard fire exposure and no char contraction as basis for the following comparison.

(ii) Standard fire exposure and char contraction to document the importance of the char layer as insulating layer.

(iii) Actual fire exposure and char contraction

Simulation Results and Conclusions

Results show that case (i) would lead charring of 40 mm at about 63 min which is slightly later than the conservative rules of Eurocode. In corresponding fire tests performed in this study the corresponding charring depth was 35 to 38 mm.

Results for case (ii) show that the temperature increase in 40 mm deviates significantly after 30 min resulting in charring at this depth about 8 min earlier than in case (i). This shows that the char layer provides significant protection of the virgin wood in the inner part of cross section. The significance of the char layer has been investigated in many tests with cross-laminated timber where char ablation (e.g. for Cross-Laminated Timber) lead to a significantly increased charring rate.

Results for case (iii) show that considering the slightly lower fire exposure measured in test 14 charring would not reach 40 mm depth. This is in contradiction to the observations where the residual cross-section was significantly below 110 mm (corresponding 40 mm charring depth) which would be more appropriate for standard fire exposure.

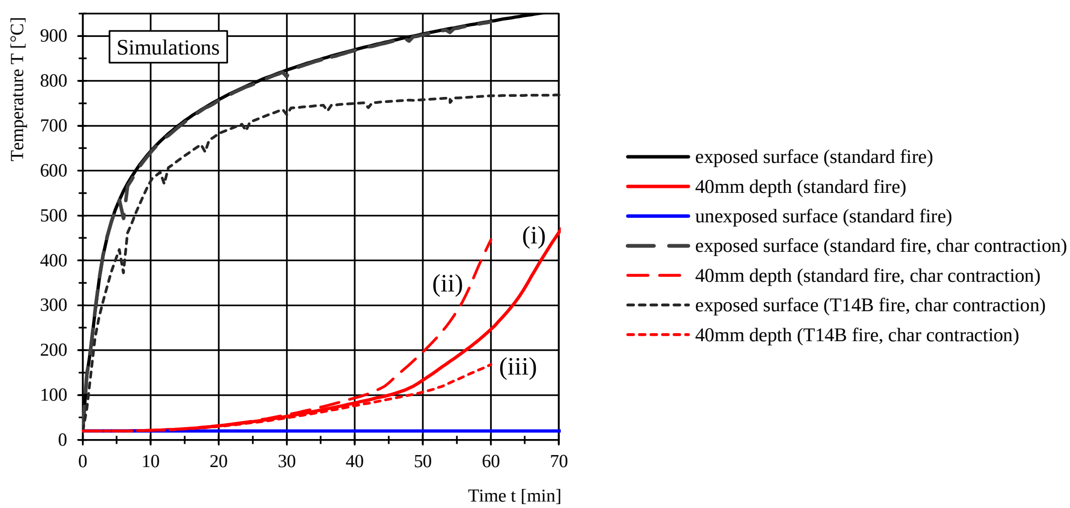

Figure 6. Simulated surface temperatures and temperature in 40 mm depth for different fire exposures with and without char contraction.

Considering the actual difference of the char layer depth (10 mm) and of the charring depth (42 and 35 mm) it can be assumed that the only varying parameter, the gas velocity is responsible for the char oxidation and subsequently the smaller residual cross-section. It is assumed that the actual gas velocity in combination with the oxygen content leads to glowing combustion which causes char contraction. This effect may be considered as an increased fire compartment temperature of about 200°C.

ESTIMATION OF THE HEAT RELEASE BY THE TEST SPECIMEN

To estimate the fire development in a fire compartment the fire load from the construction has moved into the focus of many authorities and researchers especially since solid timber products, e.g. CLT appeared on the market. With the actual test set-up it was possible to estimate the contribution of the test specimen by two alternative methods. Firstly, (a) based on the charring rate, and secondly, (b) by means of the oxygen consumption.

(a) Cone calorimeter tests have previously been conducted to determine the heat release rate of different materials under certain exposures of constant incident heat flux. In this test, a specimen is exposed to a homogeneous incident heat flux. It can be concluded that the following ratio is valid:

Heat Release Rate: Charring Rate = Heat Release: Char Depth (1)

As a basis for a compartment fire model, a relationship between the charring rate and the heat release rate was determined from cone calorimeter test results. Investigations of heat release rates and corresponding charring were investigated in [6]. At 75 kW/m^2 incident radiant heat flux, a heat release of 5385 kJ/m^2 per millimeter of charring depth, for charring depths exceeding 10mm was determined. For simplicity, the heat release rate is taken as constant for the whole period of the fire.

(b) The heat release rate can be performed from the oxygen consumption using calorimetry [7]; it can be assumed that the heat release per consumed mass of oxygen is 13.1 MJ/kg for most bio-based materials. This has been used as a basis for calorimetry in previous test setups, such as the cone calorimeter [7].

In the test setup the oxygen concentration was measured in section 0, A, B, C and D, further the gas velocity of the air was determined. The mass of oxygen passing each section can be determined in a similar way as is done using a cone calorimeter. For this study, the heat release rate was estimated is determined using the volume percentage of oxygen in dry air and the estimated volume flow of air excluding water vapor.

Results of the Heat Release Estimation Results using the two methods are in rough agreement. However, the results are not accurate enough to determine the difference in heat release rates between tests, as indicated in Table I. In the ongoing study the methods will be revised in order to improve the estimations of the heat release rate. The following improvements are planned for further tests: (I) A method should be developed to increase the frequency and the reliability of the oxygen measurements. (II) The water that is extracted from the sample gas prior to the gas analysis will be quantified in order to confirm the quantity of water vapor in the fire compartment.

TABLE I. ESTIMATED HEAT RELEASE.

	Heat release rate (kW/m^2)		
	Method 1		Method 2
	Section B	Section C	Between section B and C
Test 14	55.9	48.7	48.5
Test 9	44.5	52.7	61.7

METHODS FOR SAMPLE GAS AND GAS VELOCITY ANALYSIS

The study used redundant systems to estimate the (i) gas velocity in the fire compartment and the (ii) oxygen content at the inlet (0) as well as positions A, B, C and D.

(i) The gas velocity was estimated using a Pitot tube [5] combined with a small thermocouple wire to measure the gas temperature. This is needed in order to take into account the correct volume of the heated gas. Further, the gas velocity was determined using anemometer measurements considering combustion reactions of Propane. The propane flow was measured with a flow meter in order to determine the amount of gas used. Assumptions executing the chemical reaction with respect to the incomplete combustion of propane at different available oxygen contents as well as some uncertainties regarding the maximum flow delivered by the gas vaporizer used lead to the evaluation that this procedure is less accurate. Differences of about 30% in gas velocity were determined. It was concluded that the Pitot tube measurements are more reliable.

(ii) The gas analysis was performed with an electrochemical gas analysis device and paramagnetic analysis. In earlier studies [8] it was found that the electrochemical method is not as accurate as short peaks are not covered using this method. However, in this study it was found that the electrochemical electrodes provide sufficiently accurate results for the test set-up presented here.

REFERENCES

1. EN 1995-1-2: Design of timber structures – Part 1-2: General – Structural fire design, CEN, European Committee for Standardization, Brussels, 2004.
2. EN 1363-1: Fire resistance tests - Part 1: General requirements, CEN, European Committee for Standardization, Brussels, 2012.
3. Frangi, Andrea, and Mario Fontana. "Charring rates and temperature profiles of wood sections." Fire and Materials 27.2, 2003.
4. Babrauskas, V., "Charring rate of wood as a tool for fire investigations." Fire safety journal 40.6. 2005.
5. Heskestad, G. Bidirectional Flow Tube for Fire Induced Vent Flows, Appendix K in PA. Croce, and H. W. Emmons, eds. The Large-Scale Bed-Room Fire Tests, Factory Mutual Research, FMRC S/N 21011.4 (July 1974).
6. Crielaard, R. Self-extinguishment of cross-Laminated timber. Diss. TU Delft, Delft University of Technology, 2015.
7. Hugget, Clayton. Estimation of rate of heat release by means of oxygen consumption measurements. Fire and Materials. 4(2), pp.61-65. (1980)
8. Nussbaum, R., "Oxygen Consumption Measurements in Cone Calorimeter", Fire and Materials. 11, 201-203 (1987).

Full-scale Fire Test of a Laterally Loaded Light Timber-framed Compartment

DANIEL JESSOP, ANTHONY ABU, COLLEEN WADE,
MICHAEL SPEARPOIONT, HANS GERLICH
and ANDY BUCHANAN

ABSTRACT

The lateral stability of buildings during and after fire is of interest to fire-fighters, for protection of other property, and for post-fire investigators who may access buildings after a fire has occurred. A common approach for designing for lateral stability in New Zealand (NZ) is to provide sufficient resistance to ensure that a fire-rated structure does not collapse when subjected to a uniformly distributed horizontal face load and vertical loading. For residential buildings their external fire-rated walls are required to resist a lateral load of 0.5 kPa. This requirement results in the need for thicker walls, as these walls are assessed as isolated elements exposed to the standard fire. It is thought that by the consideration of the support the adjacent structure could provide to these walls, the requirement can be met with reductions in construction costs. This paper reports on the fire performance of a laterally loaded light timber-framed wall by a full-scale furnace experiment as part of a research project that investigates the lateral stability of buildings during and after fire.

INTRODUCTION

The New Zealand Building Code (NZBC) deemed to satisfy solution for houses and small multi-unit dwellings requires external walls within 1 m of and at angles less than 90° to a property boundary to be fire-rated to a minimum 30-min fire resistance rating (FRR) [1]. The NZBC also requires structural building systems to remain stable during and after fire [2]. The associated NZ design standards have various provisions for strength and stability assessment of structures. For post-fire structural stability the NZBC B1/VM1 [2] simplifies this requirement to the provision of sufficient resistance to ensure that a structure does not collapse when subjected to a uniformly distributed horizontal face load of 0.5 kPa. For residential buildings this load is typically applied to fire-rated external walls only.

Daniel Jessop, Cosgroves Ltd., Christchurch, New Zealand
Anthony Abu, University of Canterbury, Christchurch, New Zealand
Colleen Wade, BRANZ Ltd, Porirua, New Zealand
Michael Spearpoint, University of Canterbury, Christchurch, New Zealand
Hans Gerlich, Fi-St Consulting Ltd, Paraparaumu Beach, New Zealand
Andy Buchanan, University of Canterbury, Christchurch, New Zealand

Common design methods assume that non-fire-rated elements of buildings do not provide support to fire-rated elements at the fire limit state. As such, the fire-rated external walls of residential buildings are designed to be self-supporting with full fixity at their bases. In simple single-story buildings, the support provided by non-fire-rated roof truss systems and non-fire-rated walls may be able to provide sufficient restraint for the lateral load resistance required by the NZBC.

EXPERIMENT DESIGN

The building design was based on common NZ residential building construction practice to NZS 3604:2011 [3]. The compartment dimensions were 4.33 m × 3.35 m with stud height of 2.4 m as shown in Figure 1. One of the 4.33 m walls was 30-min fire-rated, while all other building elements were of typical non-fire-rated residential construction. The roof trusses provided lateral support to the fire-rated wall and were constructed with a splice in the centre of the bottom chord, connected by toothed metal connector plates. The fire-rated wall was fixed to one of the end walls only, to simulate the effect of a wall twice as long as the tested configuration.

The four walls of the compartment were constructed with 90 mm × 45 mm timber for the studs, dwangs, top plate and bottom plate. The top and bottom plates were continuous along the length of each wall. Studs were spaced nominally at 600 mm centres and were fixed to the bottom and top plates with two nails at each end. The timber used was kiln dried structural framing grade radiata pine. The roof pitched approximately 15° and spanned 3.35 m between the 4.33 m long walls. Internal wall and ceiling linings were 10 mm thick standard grade plasterboard, except for the fire-rated wall which had 10 mm fibre reinforced plasterboard on both sides of the timber framing.

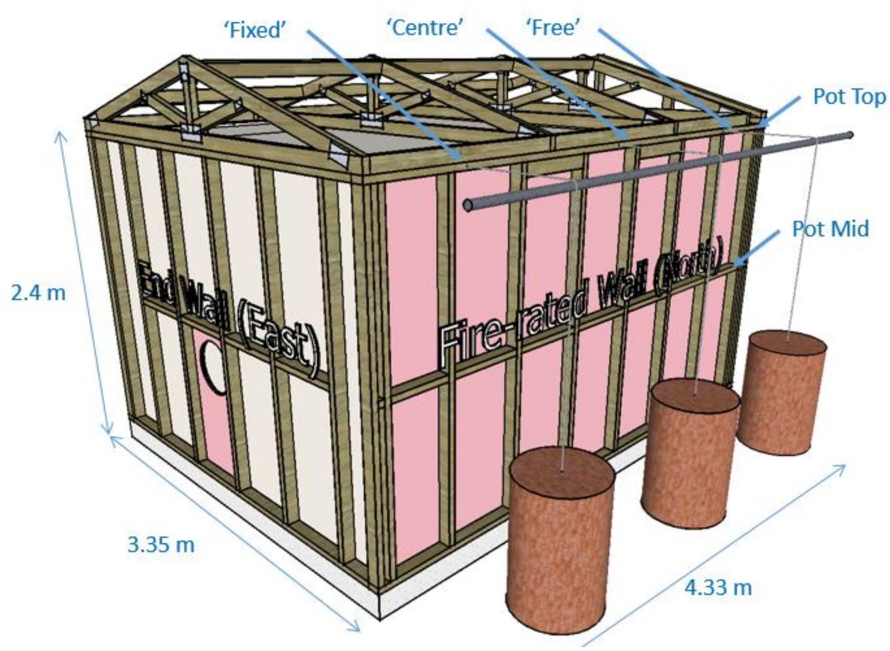

Figure 1. Representation of compartment and lateral loading arrangement used for experiment.

The ceiling systems consisted of sheets of 10 mm standard plasterboard fixed to metal ceiling battens. The fire-rated wall had no additional covering on the exterior side. The non-fire-rated long wall was clad externally with three different light-weight systems: 10 mm standard plasterboard, 7 mm plywood and 6 mm fibre cement board to assist with additional research on cladding systems. The short end walls were clad with 0.35 gauge profiled mild steel. The roofing was constructed of 0.35 gauge profiled mild steel sheets.

Figure 2 shows the roof truss layout for the experiment, with the fire-rated wall at the bottom of the image. Five roof trusses spanned between the fire-rated wall and the opposite non-rated 4.33 m wall. Four of these trusses were physically connected to the top plate of the fire-rated wall (T1 – T4), with the fifth resting on top of the wall at the 'free' end (T5).

The four fixed roof trusses were of timber construction and consisted of a bottom chord, top chord, and three diagonal members. A splice and truss connector plate connection located at the mid-span of the bottom chord was included in the experimental setup to assess the performance of such connections, as would commonly be found in trusses spanning greater than 6 m. The truss connector plates were manufactured from 1.0 mm thick steel with teeth punched out to a depth of approximately 8 mm. Timber members of the roof truss are held together with wire dogs prior to having the connector plates pressed in and these remained embedded in the timber. The trusses were fixed to the top plate of the walls using two 1.55 mm thick steel right angle brackets.

A lateral load was designed for the fire-rated wall based on B1/VM1 [2] requirements for a 0.5 kPa face load. This translated to a 0.6 kN/m line load at the top of the wall. The load was applied as an 'outward' pulling load on the fire-rated wall rather than a push as this was considered to be the more onerous scenario and was also more practical to achieve. The lateral load was applied at three points along the top edge of the fire-rated wall. The magnitude of the load at each of the three points was 88.3 kg. This lateral load was achieved by suspending three water-filled steel drums suspended via a pulley system fixed at 0.72 m from each end, and one at the centre of the wall.

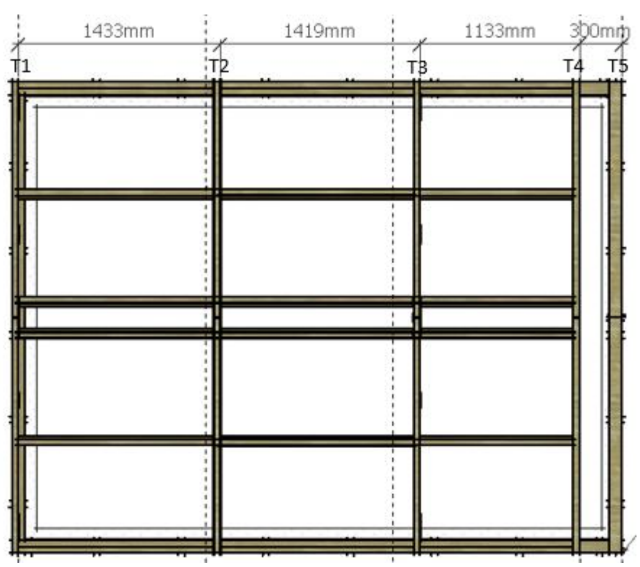

Figure 2. Roof truss layout.

INSTRUMENTATION

A dummy chord with an array of twelve thermocouples was installed in the roof space of the compartment, at the same height and similar location to the bottom chords of the roof trusses. A nail plate was fixed to one side of the dummy chord, so that the difference in char rates on timber with and without a nail plate could be compared.

Surface temperatures and adiabatic surface temperature measurements were recorded at a number of locations on the internal walls, cladding and at the ceiling. Copper disc thermocouples constructed in accordance with AS 1530 Part 4 [4] were used to measure cavity and unexposed lining surface temperatures. Thin steel plate with affixed thermocouple and ceramic fibre insulation backing, compressed thickness approximately 10 mm, were used to measure adiabatic surface temperature on the exposed ceiling lining. These had wires suspended from the purlins that provided support after the ceiling failed. Plate thermometers constructed in accordance with ISO 834-1 [5] and EN1363-1 [6] were used to measure adiabatic surface temperature on walls.

The deflection of the laterally loaded fire-rated wall was measured using two methods. One was a manual measurement of the fall in height of the drums which were suspended from the wall. At the free end of the wall, along the end stud-line, three linear potentiometers were fixed on a frame to measure deflection at the bottom plate, dwangs and top plate heights.

FURNACE AND EXPERIMENT PROCEDURE

The intent was to carry out the experiment in accordance with AS 1530 Part 4 [4] as closely as possible. The gas-fired furnace's twelve chromel-alumel thermocouples were used to drive the furnace to follow the standard time-temperature curve. These thermocouples were at approximately 100 mm below the notional floor level which in a standard furnace test would be located 100 mm from the face of a ceiling test specimen.

AS 1530 Part 4 [4] specifies that a furnace pressure of zero is established at a height of 500 mm above the notional floor level for the specimen for vertical elements. During the experiment, the laboratory became smoke-logged and the furnace negative pressure was increased in an attempt to reduce the volume of combustion products escaping from the compartment into the laboratory space. The negative pressure would have slightly reduced the fire severity experienced by construction elements during the experiment compared to a standard fire resistance test.

RESULTS

Dummy Chord and Fire-rated Wall Deflection

The dummy chord was directly exposed to the furnace fire when the ceiling failed after 16 min. Figure 3 shows temperature measurements from the dummy chord. Charring is considered to have occurred when the wood reaches a temperature of 300°C [7]. An analysis of the results of the dummy chord temperatures determined an average charring rate of 1.2 mm/min for timber behind the nail-plate, and 1.1 mm/min for timber

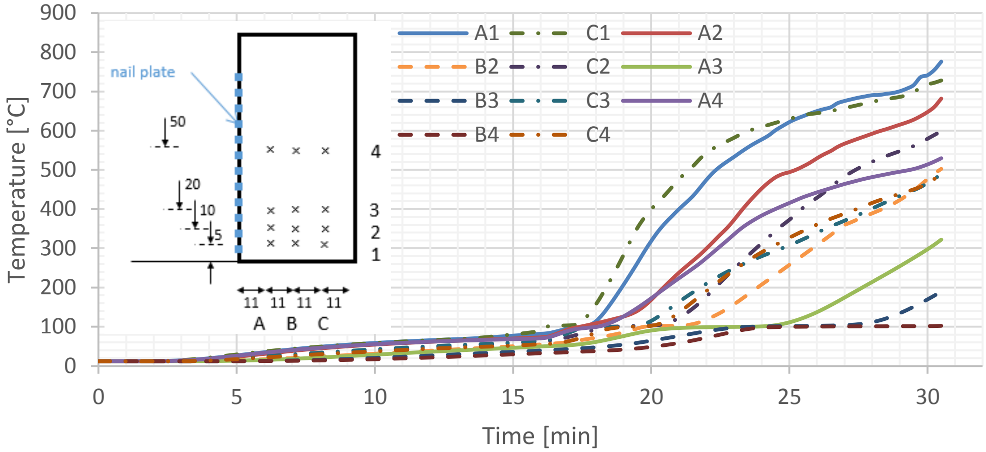

Figure 3. Experiment #1 dummy chord thermocouple temperature measurements.

not behind a nail plate. These were used to determine residual cross-section areas for the bottom chord of the trusses, and compared to cuts taken from samples of bottom chords after the experiment. Figure 4 shows the deflection measurements for the fire-rated wall taken during the experiment. At 30 min there is a notable increase in displacement measured at the drums, the fixed, centre and free end increased to 17 mm, 28 mm and 38 mm respectively. The wall lost its structural stability at 30.5 min, as shown in the deflection measurements. The experiment was designed such that the weighted drums would rest on the ground thereby relieving the wall of any lateral load after failure.

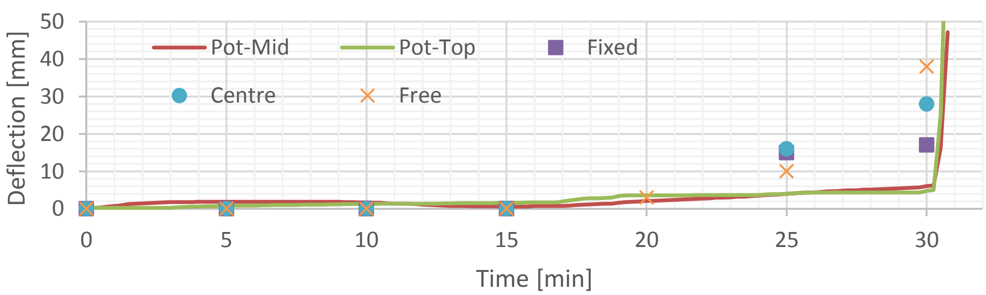

Figure 4. Deflection measurements for fire-rated wall.


(a) T3

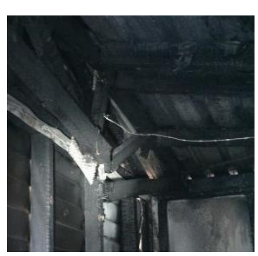
(b) T4


(c) T2

Figure 5. Failure of trusses after experiment.

Inspection of the compartment after the experiment indicated that the main mechanism of failure was the failure of the splice in the bottom chord of each of the intermediate (load-carrying) roof trusses, as shown in Figure 5.

Compartment Temperature Distribution

Figure 6 shows a comparison of the adiabatic surface temperature measured for the walls and at the ceiling with the temperature measured by the furnace thermocouples, and the standard time-temperature curve. It can be seen that the furnace temperature closely follows the standard time-temperature curve and is within AS 1530 Part 4 [4] tolerance. The adiabatic wall and ceiling temperatures follow a similar path to each other, and are less than the standard curve throughout the experiment. Figure 6 also shows the cavity temperature which clearly indicates the failure of the ceiling lining at around 16 min.

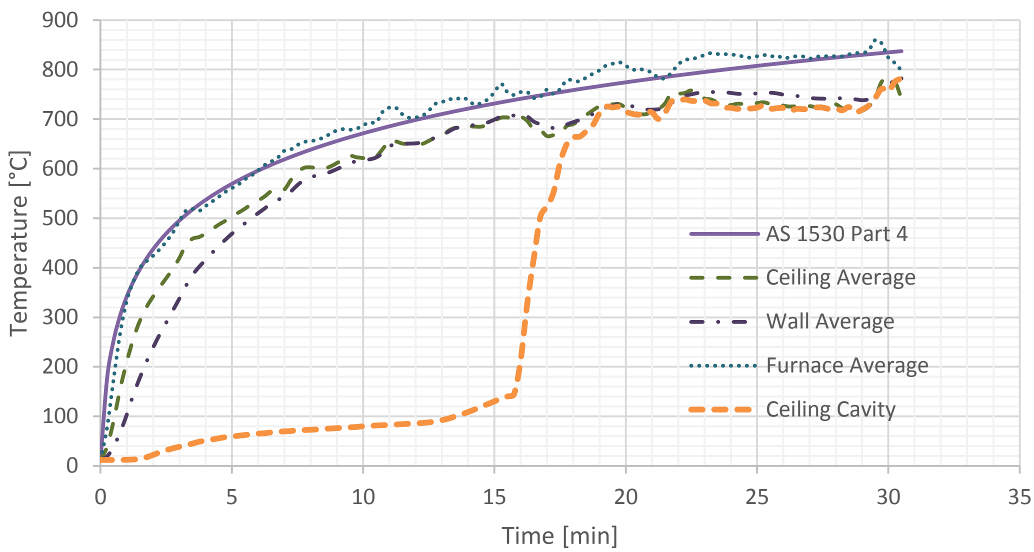

Figure 6. Furnace and compartment temperatures.

ANALYSIS

AS 1530 Part 4 [4] has failure criteria for axially loaded elements and laterally loaded elements. It is recognised that this failure criteria is not intended to test for a horizontally loaded vertical element, i.e. a fire-rated wall. However, it can provide one way of establishing a failure criteria definition for the experiment. It may be reasonable to allow an external fire-rated wall to deflect further than the failure criteria of AS 1530 Part 4.

The fire-rated wall framing was 90 mm deep and 2400 mm high. Using Equation 2.12(4) from AS 1530 Part 4 [4] the limiting rate of deflection is 7 mm/min. The limiting rate of deflection measured over 1 min intervals was exceeded at 30.5 min, with the wall deflecting at an average rate of 21 mm/min between 29.5 and 30.5 min. This calculated failure time is consistent with the observed failure time.

An analysis of the results of the dummy chord temperatures determined an effective charring rate of 1.2 mm/min for timber behind the nail-plate, and 1.1 mm/min for timber not behind a nail plate. These charring rates are based on the time of exposure from when the ceiling failed to the end of the experiment. The charring rates were used to determine residual cross-section areas for the bottom chord of the trusses, and compared to cuts taken from samples of bottom chords after the experiment. This comparison is shown in Table I. It can be seen the calculated char rate based on dummy chord temperature measurements tends to over-predict the reduction in section area when compared to experiment results. This could be due to charring rates being faster in the early stages and more thermocouples may have been required to better capture the char profile in the timber.

Table II shows the elongation of each truss for the cold condition and elongation based on the residual cross-section areas at the end of the experiment, measured from cuts taken and calculated from the dummy chord charring rates. Note that the 'averaged' char rate value based on the dummy chord temperature readings at the end of the experiment was used, i.e. 1.1 mm/min. The table also shows the minimum cross-sectional area required to carry the load, based on the design characteristics of the truss. These calculations do not take into account the nail plate connection in the bottom chord of the truss, which governed failure in the experiment, but allow an assessment to be made of performance without a nail plate connection.

The results show that there was sufficient cross-sectional area of unaffected timber to support the lateral load being applied to the fire-rated wall and the predicted elongation of the trusses remains negligible. It is not unreasonable that the nail plate failed much earlier than the timber member would have expected to fail. Without the splice in the roof truss system, it is expected that for this experiment the wall would have been sufficiently restrained for an estimated additional 4 min based on the minimum required cross section area and char rates. An adequately protected splice could also be designed to achieve sufficient restraint for this additional time, such that the failure occurs due to charring of timber away from the splice.

TABLE I. COMPARISON OF MEASURED AND ESTIMATED CHAR DEPTHS.

	T4	T3	T2	Calculated (with nail plate)	Calculated (non-nail plate)
Depth remaining [mm]	52.5	55	60	55.2	58.0
Width remaining [mm]	22.5	20	22.5	10.2	13.0
Cross section area remaining [mm^2]	1181	1100	1350	498	706
Eff. charring rate (depth) [mm/min]	1.3	1.2	1.1	1.2	1.1
Eff. charring rate (width) [mm/min]	0.8	0.9	0.8	1.2	1.1

TABLE II. SUMMARY OF TRUSS PERFORMANCE.

<table>
<tr><th></th><th colspan="3">Cross section area [mm²]</th><th colspan="3">Elongation [mm]</th></tr>
<tr><th>Truss</th><th>Minimum to carry load</th><th>Measured from cuts taken after experiment</th><th>Calculated from char rate in dummy chord (non-nail-plate)</th><th>Cold</th><th>Calculated using measured residual cross-section area</th><th>Calculated based on char rate in dummy chord</th></tr>
<tr><td>T2</td><td>143</td><td>1350</td><td rowspan="3">708</td><td>0.09</td><td>0.27</td><td rowspan="3">0.51</td></tr>
<tr><td>T3</td><td>123</td><td>1100</td><td>0.08</td><td>0.28</td></tr>
<tr><td>T4</td><td>94</td><td>1181</td><td>0.06</td><td>0.20</td></tr>
</table>

The toothed nail plate connection performed better than would be expected or predicted if it is assumed there is no residual strength in the connection once charring of the timber exceeds the depth that the nails penetrate the timber. There may have been contribution from other construction elements which provided sufficient residual capacity to withstand the applied load, after the truss connector plate would have otherwise failed. There is likely to be a contribution of strength to the connection from the wire dogs connecting the spliced bottom chord and this was not quantified. Similarly, the effect of the roof bracing has not been quantified although it is considered less likely this contributed significantly to the strength of the system in fire.

CONCLUSION

An experimental investigation of the fire performance of a laterally loaded light timber-framed compartment was carried out. Performance has been assessed for a roof truss system spanning between a fire-rated wall and non-rated wall, with a lateral load applied parallel to the direction of the bottom chord members of the roof truss. The bottom chord of the roof truss failed at the spliced connection in tension after 30.5 min in the experiment, this was 14.5 min after the ceiling failed. An analysis of the observed failure time applying the criteria specified in AS 1530 Part 4 for limiting rate of deflection is consistent with the observed failure time. The results show there was a non-uniform temperature distribution in the compartment.

Based on the experimental results, a small timber-framed compartment with 10 mm standard plasterboard linings and a suitable roof truss structure providing lateral support to a fire-rated wall could be designed to achieve stability for a 30-min FRR equivalent duration. This can be achieved without the need for providing moment-resisting fixity at the connection between the studs and bottom plate of the fire-rated wall.

ACKNOWLEDGEMENTS

The work reported here was funded by BRANZ from the Building Research Levy. Support and resources were provided by University of Canterbury, Versatile Homes & Buildings and Winstone Wallboards.

REFERENCES

1. MBIE. 2014. *C/AS1 Acceptable Solution for Buildings with Sleeping (residential) and Outbuildings (Risk Group SH)*. New Zealand Government, Wellington, New Zealand.
2. MBIE. 2014. *Acceptable Solutions and Verification Methods for New Zealand Building Code Clause B1 Structure*. New Zealand Government, Wellington, New Zealand.
3. SNZ. 2011. *NZS 3604:2011 Timber-framed buildings*. Wellington, New Zealand.
4. SAA. 2005. *AS 1530: Part 4: Fire Resistance Tests of Elements of Construction*. Standards Association of Australia, NSW, Australia.
5. ISO. 1999. *ISO 834-1 Fire-resistance tests — Elements of building construction — Part 1: General requirements*. International Organization for Standardization.
6. BSI. 2012. *BS EN 1363 Fire resistance tests. General requirements.* British Standards Institution, United Kingdom.
7. Buchanan, A. H. 2001. *Structural design for fire safety*. Wiley, Chichester, England; New York.

A Framework for Finite Element Modelling of Timber Connections in Fire

PEDRO PALMA and ANDREA FRANGI

ABSTRACT

This paper presents a framework to model timber connections exposed to fire, using the Python [1] interface of Abaqus FEA [2] software suite for FE analysis, currently being developed at ETH Zurich. Models of three-member connections can be easily generated (with any arrangement of fasteners, member geometry, and material properties), submitted to the solver, and the results post-processed. The framework has been used to perform stress and uncoupled heat transfer analyses and is being extended to perform sequentially coupled thermal-stress analyses.

1 INTRODUCTON

1.1 Background

The behaviour of connections is paramount to the performance of timber structures at normal temperature and even more so in fire. Dowel-type connections with metal fasteners are the most common connection typology. However, because of the strong anisotropic nature of wood, the different possible failure modes, and the high localized stresses close to the fasteners, the development of analytical and numerical models can become very complex, even for simple situations. Therefore, only few numerical models have been developed to study the fire behaviour of timber connections, even though experimental studies are also difficult to perform. Two main approaches have been followed in the development of numerical models for timber connections in fire: thermal-mechanical finite element (FE) models; and thermal FE models combined with modified Johansen's models. The first approach is based on a sequentially coupled thermal-stress analysis and requires not only temperature-dependent thermal properties, to obtain the temperature profiles, but also temperature-dependent constitutive laws and failure criteria, to simulate the mechanical behaviour [3, 4]. The second approach, besides the same temperature-dependent thermal properties, requires only a temperature-dependent embedment strength, to be used in the classical Johansen's yield model [5–7].

Pedro Palma, ETH Zurich, Institute of Structural Engineering (IBK), Stefano-Franscini-Platz 5, 8093 Zurich, Switzerland.
Andrea Frangi, ETH Zurich, Institute of Structural Engineering (IBK), Stefano-Franscini-Platz 5, 8093 Zurich, Switzerland.

1.2 Objectives and scope

This paper presents a framework to model timber connections exposed to fire, using the Python [1] interface of Abaqus FEA [2] software suite for FE analysis, currently being developed at ETH Zurich. This framework is particularly suited to perform parametric studies, as models of three-member connections can be easily generated (with any arrangement of fasteners, member geometry, and material properties), submitted to the solver, and the results post-processed. The framework has been successfully used to perform stress and uncoupled heat transfer analyses of steel-to-timber dowelled connections, the latter combined with a modified Johansen's model, and is being extended to perform sequentially coupled thermal-stress analyses.

2 MODELLING TECHNIQUES FOR TIMBER CONNECTIONS

2.1 Models for connections at normal temperature

There are several modelling techniques available to simulate the behaviour of timber connections at normal temperature, namely empirical, analytical (based on a mechanics approach), and numerical models (usually based on the FE method).

Empirical models are based on observed relations between relevant parameters. They are mostly used to model systems for which a mechanics-based approach would be too complex, but their use is limited by the scope of the underlying data (e.g. the slip modulus of connections with dowel-type fasteners [8], the load-carrying capacity of connections loaded perpendicularly to the grain [9]).

Analytical models based on a mechanics approach allow for a better understanding of the factors influencing the connection behaviour. Their scope is not limited by the available data, but by the simplifications assumed in the mechanical models. A well-known analytical model is the Johansen model [10], also known as *European yield model*, which is widely used to estimate the load-carrying capacity of connections with dowel-type fasteners. Other analytical models are, e.g., *beam on elastic foundation* for a single dowels or *component models* for whole connections [11].

Numerical models based on the FE method have also been used to model timber connections and have shown to be able to provide approximate solutions for complex problems. The accuracy of FE simulations depends on the complexity of the model (e.g. directional dependency of material properties, constitutive models, failure criteria), which in turn is dependent on available data. Most recent FE models take into account the different mechanical behaviours in the various anatomical directions mostly by adopting two main constitutive laws: ductile elastic-plastic behaviour in compression and brittle elastic in tension and shear. In compression, some authors assume a linear-elastic perfectly-plastic behaviour, while others consider additional softening and hardening (in the directions parallel and perpendicular to the grain, respectively). In tension and shear, failure is usually addressed by imposing a severe softening of the material once given failure criteria have been reached, to allow for some damage evolution. Given that, in wood, stress interactions in three-dimensional models may influence the failure mode, using appropriate failure criteria is paramount. More or less sophisticated failure criteria have been adopted, from single-surface failure criteria [12, 13] to separate criteria per failure mode [14].

2.1 Models for connections exposed to fire

The transient nature of the behaviour of timber connections exposed to fire makes the development of exclusively analytical models very difficult. Therefore, the most common approaches are to use empirical or numerical models, the latter sometimes combined with analytical models.

Empirical models, such as the *reduced load method* in EN 1995-1-2 [15], provide an easy way to estimate the load-carrying capacity after a given exposure R_{fi}, or the fire resistance for a given load level, using a single parameter k that accounts for the connection typology ($R_{\mathrm{fi}} = \mathrm{e}^{-k \cdot t_{\mathrm{fi}}} \cdot R_{20°\mathrm{C}}$). As at normal temperature, the accuracy of these models depends on the quality and quantity of the available data, which for connections exposed to fire is scarce in comparison with the various geometrical, physical, thermal, and mechanical parameters that define each connection.

FE simulations of timber connections in fire can be divided in two main groups: uncoupled heat-transfer analyses and sequentially coupled thermal-stress analyses.

Uncoupled heat-transfer analyses are conducted to assess temperature profiles in the connection and are used alongside with analytical models with temperature-dependent parameters [5, 16, 17], which provide an estimate of the load-carrying capacity after a given exposure period. An uncoupled heat-transfer FE analysis requires the temperature-dependent physical and thermal properties of the connection components (timber and steel), and the associated analytical model requires temperature-dependent embedment properties (either strength or stiffness, for Johansen's or component models, respectively). One of the advantages of this approach is that, since the analytical models are usually based on a single fastener, the thermal model can be simplified due to symmetry and, therefore, the heat-transfer analysis will be faster. In addition, since no FE stress analysis is to be performed, there is no need to define mechanical and thermal contact interactions between the different components of the connection (fasteners, steel plates, and timber members) and a simpler single-part model can be used. The main shortcoming of this modelling approach is that aspects related to the behaviour of the connection as a whole (e.g. load distribution between fasteners, splitting failure modes) are not considered, because of the single-fastener nature of the analytical models.

Sequentially coupled thermal-stress analyses comprise an uncoupled heat-transfer analysis followed by a series of sequential stress analyses, in which the temperature-dependent mechanical properties are reduced according to the temperature field [3, 4]. It is assumed that the stress analysis is dependent on the temperature field but not the other way round (this simplification implies that increased deformations and displacements will not exposed further surfaces to high temperatures). The initial heat-

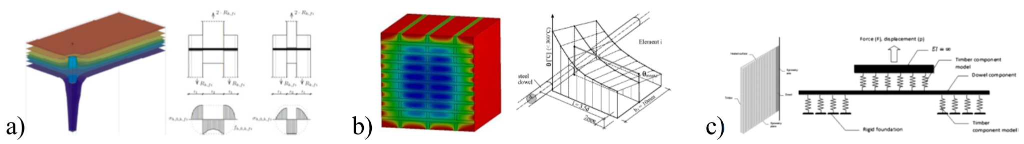

Figure 1. Uncoupled heat transfer analyses combined with analytical models: a) heat-transfer FE model combined with Johansen's model [16]; b) heat-transfer FE model combined with Johansen's model (only embedment failure mode) [5]; c) heat-transfer FE model combined with a component model [17].

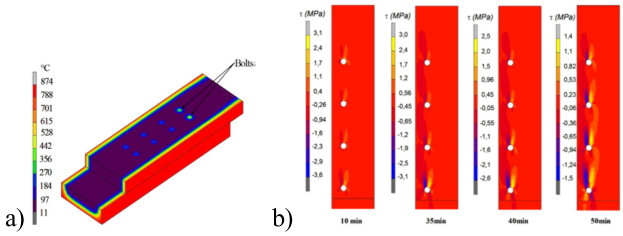

Figure 2. Sequentially coupled thermal-stress analyses performed by Laplanche [3]: a) temperature field; b) shear stresses at 10, 35, 40, and 50 minutes.

transfer analysis requires temperature-dependent physical and thermal properties of the connection components (timber and steel) and provides the temperature field at requested time steps. Since stress analyses are to be performed, models have to be created as an assembly of multiple parts (fasteners, steel plates, and timber members), for which thermal contact interactions (i.e. conductive and radiative heat transfer between parts) have to be defined. The ensuing stress analyses require temperature-dependent elastic and strength properties and are sequentially performed at each of the previous time steps, with the temperature-dependent mechanical properties adjusted according to the corresponding temperature field (Figure 2). In addition, the stress analyses require adequate constitutive models and failure criteria to be defined, and also mechanical contact interactions between the different components of the connection need to be defined. The main advantage of this modelling approach is that the behaviour of the whole connection is considered and load redistribution between fasteners can be assessed. Also time-displacement curves can be easily obtained and the post-processing of simulation results is reduced in comparison with uncoupled heat-transfer analyses used alongside with analytical models. The main shortcomings of this approach are the significant amount of input parameters it requires, namely temperature-dependent mechanical and strength properties (which are not always easily available), and the very long simulation times required.

3 DEVELOPED MODELLING FRAMEWORK

3.1 Computational framework

The modelling framework for timber connections, currently being developed at ETH Zurich, is able to generate FE models of three-member steel-to-timber dowelled connections for uncoupled heat-transfer analyses (combined with an analytical modified Johansen's model), stress analyses, and sequentially coupled thermal-stress analyses.

The framework was developed using the Python [1] scripting interface of Abaqus Unified FEA [2] software suite for FE analysis. Python is a high-level, general-purpose, programming language that, through the scripting interface, can access the models and data used by Abaqus, e.g. create and modify models and analyses, submit simulations, and access the results' output databases. Models of connections can be easily and rapidly generated, with any number and layout of fasteners, member geometry, and material properties, and the simulations' results can be quickly post-processed. The simulation jobs are submitted to the central high-performance cluster of ETH Zurich, which allows multiple simulations to run simultaneously and faster, due to the possibility of using multiple processors to parallelize the calculations. These characteristics make the modelling framework particularly suited for parametric studies and sensitivity analyses.

3.2 Model characteristics

The used temperature-dependent physical and thermal properties of timber are those prescribed in Annex B of EN 1995-1-2 [15] and by Cachim and Franssen [18], to account for the orthotropic thermal behaviour, conductivity in the direction parallel to the grain (Figure 3). The elastic and strength properties at normal temperature are based on different sources [8, 19–23] and their reduction with temperature is mostly based on EN 1995-1-2 [15], but also other sources [21, 22] (Figure 4).

The physical, thermal and mechanical properties assumed for the steel components are those prescribed by EN 1993-1-2 [24].

Thermal actions on the fire exposed surfaces follow EN 1991-1-2 [25], for a gas temperature according to the standard temperature-time curve, a coefficient of heat transfer by convection $\alpha_c = 25\ \mathrm{kW{\cdot}m^{-2}{\cdot}K}$, and surface emissivities $\varepsilon_{m,timber} = 0.8$ for timber and $\varepsilon_{m,steel} = 0.7$ for steel (EN 1993-1-2 [24]).

Contact properties are defined for both thermal and mechanical interactions. Thermal contact interactions between the different parts are modelled by defining a thermal contact conductance as a function of the gap clearance. A very high gap conductance coefficient is used if the parts are in contact and there is no heat transfer

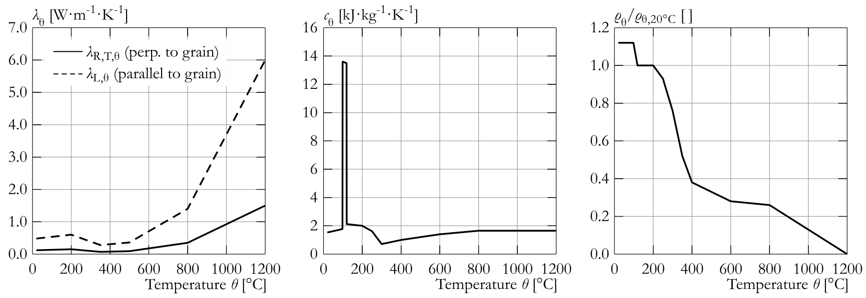

Figure 3. Temperature-dependent physical and mechanical properties of timber: thermal conductivity, specific heat, and density (from left to right).

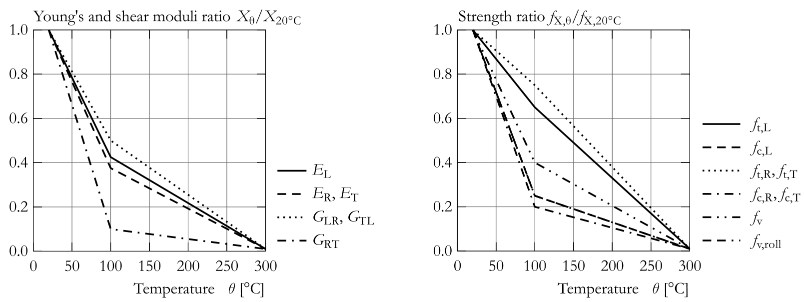

Figure 4. Temperature-dependent elastic and strength ratios: Young's and shear moduli (left); strengths (right).

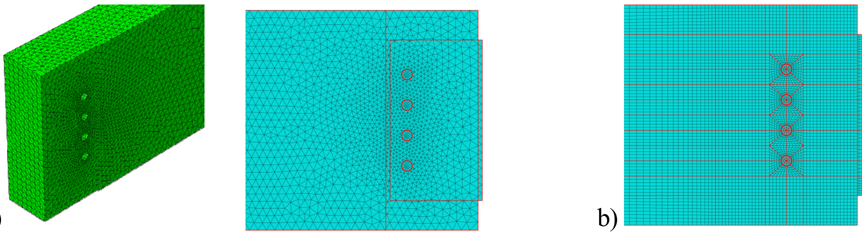

a) b)

Figure 5. Meshing techniques applied to the same connection geometry: a) free mesh with tetrahedral-shaped elements; b) structured mesh with hexahedral elements.

by conduction if the surfaces are more than 2 mm apart (heat transfer by radiation in). Mechanical contact in the direction perpendicular to the contacting surfaces is modelled as "hard" contact (no contact pressure when the clearance between the surfaces greater than zero; no limit on the contact pressure once the clearance between them reduces to zero.) and for the tangential behaviour a "penalty" friction formulation is used, with friction coefficients $\mu = 0.4$ between timber and steel and $\mu = 0.7$ between steel parts.

The variety of geometries that can be generated can make automatic meshing very complex and, therefore, a "free" meshing technique with tetrahedral-shaped elements is preferably used. This approach is more flexible and allows to automatically mesh regions with complex geometries. The mesh size is controlled by assigning global and local mesh constraints for each part of the model. Element sizes vary throughout the different regions of each part of the model (fasteners, steel plate, and timber member) and are controlled by setting global element sizes for the different parts (based on the overall dimensions of each part) and imposing mesh size constraints along the edges of the different regions of each part (based on relevance of each edge, i.e. edges where high stress or temperature gradients are expected will be assigned finer meshes). The size of the interior elements is controlled by a mesh growth rate parameter, which allows to increase the element size in regions that are not so relevant for the analyses and increase computational efficiency. Structured meshes can also be generated, but are not so easily adapted to different geometries (Figure 5). Comparison analyses were performed and, in the relevant model regions, no significant temperature or stress differences were observed between the two meshing techniques.

4 EXAMPLES

Based on a previous experimental study conducted by the authors [26], on the fire resistance of beam-to-column connections loaded in shear, several FE analyses have been performed. As it was found that the minimum spacing between fasteners in the direction perpendicular to the grain was compromising the fire resistance in some situations, a parametric study performed with the presented framework allowed to run hundreds of simulations to assess the influence of dowel spacing in the charred depth, showing that for longer exposures, wider spacings are necessary (Figure 6). An example of uncoupled heat transfer analyses is shown is Figure 7, in which the temperature fields of single and multiple-part models are compared. The latter model was then used to perform a stress analysis (Figure 8).

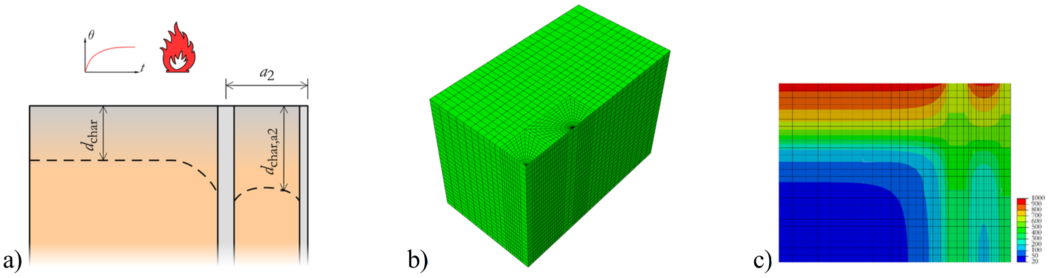

Figure 6. Influence of dowel spacing in the charred depth: a) charring between and away from the dowels; b) FE mesh; c) temperature profile.

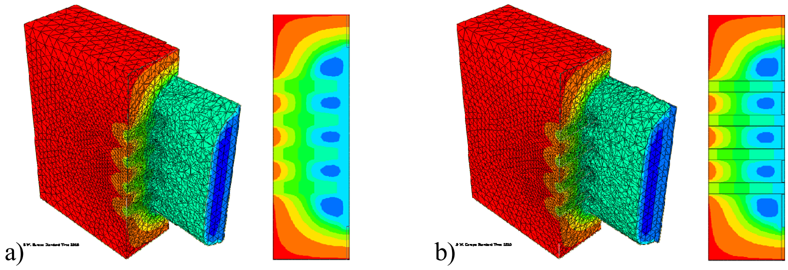

Figure 7: Uncoupled heat transfer analyses – temperatures after 50 min of fire exposure: a) model with a single part; b) model with multiple parts. The three-dimensional views show a cut with only the elements with temperatures below 300 °C.

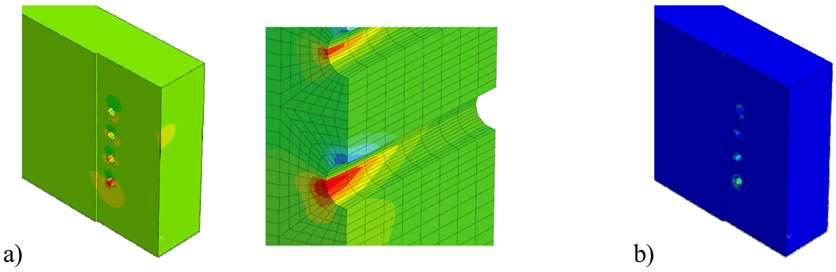

Figure 8: Stress analysis at normal temperature: a) stresses in the direction perpendicular to the grain; b) Hoffman failure criteria.

5 CONCLUSIONS

The presented modelling framework is able to quickly generate FE models of three-member steel-to-timber dowelled connections, submit the analyses to the solver, and the post-process the results. The framework was successfully used to perform uncoupled heat transfer analyses (combined with analytical models), and stress analyses. It is currently being extended to perform sequentially coupled thermal-stress analyses.

REFERENCES

1. Python Software Foundation (2015) Python (version 2.7.11) [programming language]. Python Software Foundation
2. Dassault Systemes (2013) Abaqus FEA (version 6.13-2) [computer program]. Dassault Systemes
3. Laplanche K (2006) Étude du comportement au feu des assemblages de structures bois: approche expérimentale et modélisation. PhD Thesis, University Blaise Pascal (Clermont-Ferrand)
4. Racher P, Laplanche K, Dhima D, Bouchaïr A (2010) Thermo-mechanical analysis of the fire performance of dowelled timber connection. Engineering Structures 32:1148–1157. doi: 10.1016/j.engstruct.2009.12.041
5. Erchinger C (2009) Zum Verhalten von mehrschnittigen Stahl-Holz-Stabdübelverbindungen im Brandfall (On the behavior of multiple shear steel-to-timber dowel connections in fire). Doctoral thesis, ETH Zürich
6. Moss P, Buchanan A, Fragiacomo M, Austruy C (2010) Experimental testing and analytical prediction of the behaviour of timber bolted connections subjected to fire. Fire Technol 46:129–148. doi: 10.1007/s10694-009-0096-6
7. Peng L, Hadjisophocleous G, Mehaffey J, Mohammad M (2012) Fire performance of timber connections, Part 2: Thermal and structural modelling. Journal of Structural Fire Engineering 3:133–154. doi: 10.1260/2040-2317.3.2.133
8. EN 1995-1-1:2004. Eurocode 5: Design of timber structures – Part 1-1: General – Common rules and rules for buildings. 123.
9. DIN 1052:2004-08. Entwurf, Berechnung und Bemessung von Holzbauwerken. Allgemeine Bemessungsregeln und Bemessungsregeln für den Hochbau. 235.
10. Johansen KW (1949) Theory of timber connections. IABSE Publications 9:249–262. doi: http://dx.doi.org/10.5169/seals-9703
11. Ly D (2006) Développement de modèles analytiques pour la prédiction du comportement élastique des assemblages mécaniques à broches dans la construction en bois. PhD Thesis, Université de Liège
12. Xu B (2009) Modélisation du comportement mécanique d'assemblages bois avec prise en compte de critères de rupture (Modelling the mechanical behaviour of timber connections considering the failure criteria). PhD Thesis, University Blaise Pascal (Clermont-Ferrand)
13. Dorn M (2012) Investigations on the serviceability limit state of dowel-type timber connections. PhD Thesis, Technische Universität Wien (TU Wien)
14. Sandhaas C (2012) Mechanical behaviour of timber joints with slotted-in steel plates. Doctoral thesis, Delft University of Technology (TU Delft)
15. EN 1995-1-2:2004 Eurocode 5: Design of timber structures – Part 1-1: General – Structural fire design. 69.
16. Scheer C, Povel D (2002) Stabförmige Verbindungsmittel im Brandfall – Grundlagenuntersuchungen (Dowel-type fasteners in fire – Fundamental research). 206.
17. Cachim P, Franssen J-M (2009) Numerical modelling of timber connections under fire loading using a component model. Fire Safety Journal 44:840–853. doi: 10.1016/j.firesaf.2009.03.013
18. Cachim P, Franssen J-M (2009) Comparison between the charring rate model and the conductive model of Eurocode 5. Fire and Materials 33:129–143. doi: 10.1002/fam.985
19. EN 14080:2013. Timber structures – Glued laminated timber and solid timber – Requirements. 106.
20. (2006) JCSS Probabilistic Model Code. Joint Committee on Structural Safety
21. Gerhards C (1982) Effect of moisture content and temperature on the mechanical properties of wood: an analysis of immediate effects. Wood and Fiber Science 14:4–36.
22. Youngs RL (1957) The perpendicular-to-grain mechanical properties of red oak as related to temperature, moisture content, and time. 122.
23. Bodig J, Jayne B (1993) Mechanics of wood and wood composites. Krieger Publishing Company
24. EN 1993-1-2:2002. Eurocode 3: Design of steel structures– Part 1-2: General rules – Actions on structures exposed to fire. 78.
25. EN 1991-1-2:2002. Eurocode 1: Actions on structures – Part 1-2: General actions – Actions on structures exposed to fire. 59.
26. Palma P, Frangi A, Hugi E, et al (nd) Fire resistance tests on beam-to-column shear connections. Journal of Structural Fire Engineering (accepted for publication)

BRIDGES AND NON-BUILDING STRUCTURES

Comparative Behavior of Fire-Exposed Composite Girders Subjected to Flexural and Shear Loading

M. Z. NASER and V. K. R. KODUR

ABSTRACT

This paper presents results from experimental studies on the comparative behavior of fire exposed composite steel girders subjected to flexural and shear loading. Three composite girders, comprising of steel girders and concrete slab, were tested under simultaneous structural loading and fire exposure. The main test variables are type and magnitude of loading, as well as level of composite action. The composite girder, mainly subjected to flexural loading, failed through flexural yielding of steel girder without any signs of shear failure. On the other hand, girders with shear loading failed in shear through shear web buckling early into fire exposure. A comparative performance evaluation of response parameters clearly shows that shear limit state should be considered when evaluating behavior of fire exposed composite girders.

INTRODUCTION

Steel structural members, when exposed to fire, experience loss of sectional capacity and stiffness due to temperature-induced degradation in strength and modulus properties of steel. Thus, these members become vulnerable to different failure modes such as runaway deflections, lateral torsional buckling, out-of-plane buckling and web local buckling. Recent studies have indicated that steel girders are highly susceptible to shear web buckling failure mode under high temperature exposure [1-3]. However, despite experimental and numerical evidence, current fire design provisions only account for flexural limit state in evaluating failure and do not specifically consider the effect of shear limit state. This approach of deriving failure in fire-exposed steel girders based on flexural limit state only is valid for most loading scenarios, but may not be representative in certain situations where shear forces are dominant, or shear capacity degrades at a rapid pace with fire exposure time.

Department of Civil and Environmental Engineering, Michigan State University, East Lansing, MI, 48824, USA. Email: kodur@egr.msu.edu, nasermoh@msu.edu

One of the main factors that influences shear response of steel structures is instability (local buckling) arising due to slenderness. As part of stability based design specifications, steel girders at ambient conditions are classified as compact, non-compact or slender (or as Class 1, 2, 3 and 4) depending on slenderness of the flange and web plates. This classification defines the stability state of a steel girder to account for buckling in evaluating sectional capacity at room temperature [4, 5]. For instance, a compact section does not exhibit any local buckling and can attain full sectional plastic capacity (flexure and shear), thus eliminating any localized failure. A non-compact or slender section exhibit either inelastic or elastic buckling behavior, respectively, and fail pre-maturely through a localized failure in web or flanges, before attaining full plastic capacity.

A review of relevant literature indicates that majority of previous experimental and numerical studies focused on flexural response of steel girders at ambient and fire conditions [6-8]. However, the effect of high shear loading or sectional instability was not considered in evaluating degrading shear capacity of fire exposed steel girders.

Limited studies carried out recently have pointed out that fire-exposed steel girders are highly susceptible to shear failure mode since webs in these girders are much more slender than that in flanges. However, despite these experimental and numerical findings, the current fire design provisions continue to derive failure in fire-exposed steel girders based on flexural limit state. To illustrate the importance of shear loading on fire exposed composite girders, results from experimental studies on the response of fire exposed composite girders subjected to high flexural and shear loading is compared here.

FIRE RESISTANCE EXPERIMENTS

To develop data on comparative performance of fire exposed composite girders subjected to shear loading, three composite girders were tested by subjecting them to combined effects of structural loading and fire exposure.

Test Specimens

Each composite girder comprised of a steel girder supporting a reinforced concrete slab. The three steel girders, designated as CB1, CB2, and CB3, were designed according to AISC specifications [5]. The steel girders made of W24x62 standard hot rolled section, were fabricated using A572 Grade 345 steel. The concrete slab, cast along the full length of the steel girder, has a depth and width of 140 and 815 mm, respectively and was made of compressive strength of 45 MPa. Details of tested composite girder is shown in Fig. 1.

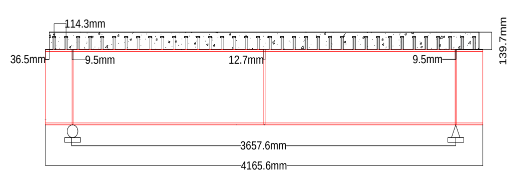

(a) Composite girders CB1 and CB2

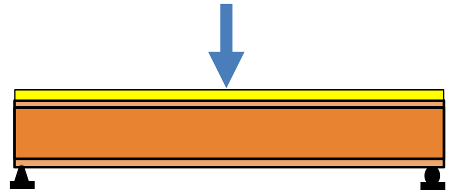

(b) Loading on CB1

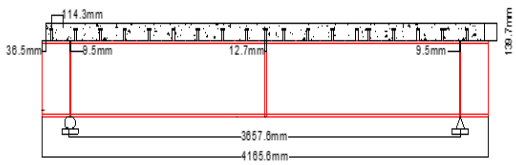

(c) Composite girders CB3

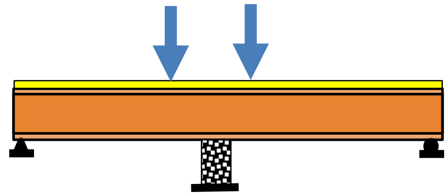

(d) Loading on CB2 and CB3

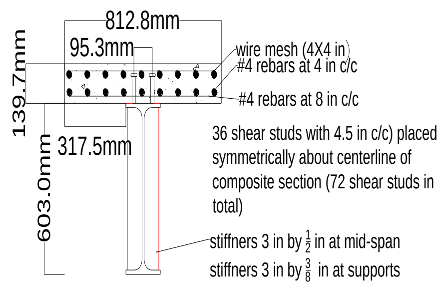

(e) Cross section of composite girders

Fig. 1 Longitudinal and traverse sections for composite girders

The main test variables are loading type and level of composite action. Composite girder CB1, tested to evaluate benchmark response, was subjected to flexural loading, while the other two composite girders, CB2, and CB3 were subjected to high shear loading as shown in Fig. 1. In addition, composite girders CB1 and CB2 were designed to ensure full composite action between the steel girder and the concrete slab, while composite girders CB3 was provided with two rows of 19 mm diameter shear studs placed at 230 mm to achieve partial (50%) composite action. The different shear stud arrangements in these girders is shown in Fig. 1. The concrete slab is reinforced with two layers of No. 4 rebars placed at 25 mm (at the top and bottom) as shown in Fig. 1e.

Test Set-up

The fire resistance tests were carried out at the structural fire testing facility at Michigan State University. In order to simulate high shear forces on composite girders CB2 and CB3 during fire exposure, a new loading set-up was specially designed for the current test program. The new loading set-up required addition of an intermediate support to be placed at the mid-span of a composite girder, such that high shear loading can be applied on the composite girder using two hydraulic actuators placed on the sides of the intermediate support. This intermediate support was designed to be a reinforced concrete (RC) column of a square cross section (204x204 mm) and was casted with high strength concrete reinforced with polypropylene fibers. During fire tests, this RC column was insulated with 50 mm thick fire insulation to limit temperature rise in concrete column and to minimize possible elongation of column.

Test Conditions and Procedure

Prior to fire tests, a predefined vertical load was applied using hydraulic actuators and this load was kept constant throughout the fire test. This predefined load was 33-40% of flexural and shear capacity of the tested girders and was limited by the capacity of the different hydraulic actuator systems used. For instance, in the first test, composite girder CB1 was subject to a single point load equivalent to 40% of its room temperature flexural capacity, which translates to 27% of its shear capacity. However, composite girders CB2, and CB3 were subjected to two point loads placed at 430 mm from mid-span of the girder utilizing a different set of actuators (smaller than the one used in testing CB1). To simulate high shear forces in girders CB2 and CB3, full capacity of these smaller actuators was utilized. The applied loading on composite girders CB2, and CB3 was equivalent to 5% of flexural capacity and 33% of shear capacity of these girders. In all three fire tests, a fire exposure following the ASTM E119 time-temperature curve was simulated and the tests were terminated when the girders could no longer carry the applied loading.

RESULTS AND DISCUSSION

Data generated from the above fire tests is utilized to trace the response of fire-exposed composite girders. Relative thermal and structural response, as well as failure modes, are compared to evaluate the effect of loading, and level of composite action on the fire response of composite girders.

Thermal Response

Figure 2 shows measured temperatures in steel girder CB1 as a function of fire exposure time. Since all three composite girders have similar cross-sectional geometry, material properties, and fire exposure, they experienced similar temperature rise. Hence, thermal response is presented for girder CB1 only. In general, temperatures in steel girders rise in a steady and rapid pattern. It can be seen that the top flange of the steel girder experienced much lower temperatures as compared to that at bottom flange and this is mainly due to the heat-sink effect from concrete slab. Throughput the fire test, the temperature in concrete, at mid-depth of slab, remained low, below 150°C, till failure of the girder.

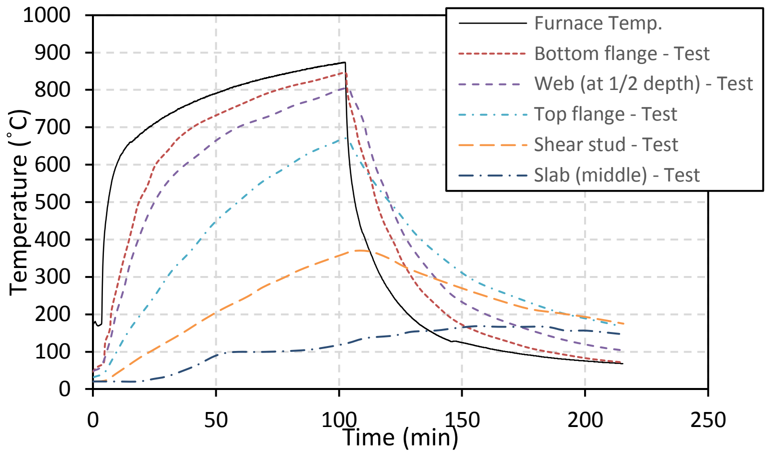

Fig. 2 Measured temperature profiles in girder CB1 as a function of fire exposure time

Structural Response

Predicted and measured mid-span deflections for the tested composite girders are shown in Figs. 3a, and 3b, to illustrate comparative structural response under fire exposure. It can be seen that the mid-span deflection in all girders gradually increase with fire exposure time especially in early stage of fire exposure. The initial deflection in these girders are mainly due to high temperatures developing in steel girders and associated reduction in elastic modulus and strength of steel. In general, response of girders, under flexural (CB1) and shear (CB2, and CB3) loading, varied significantly as shown in Figs. 3a and b, respectively. For instance, composite girder CB1 experience large mid-span deflections after 20 min of fire exposure. On the other hand, deflections in girders CB2, and CB3, measured below load points actuators (see Fig. 1d), remained much lower (12% of that in CB1) till failure of the girder.

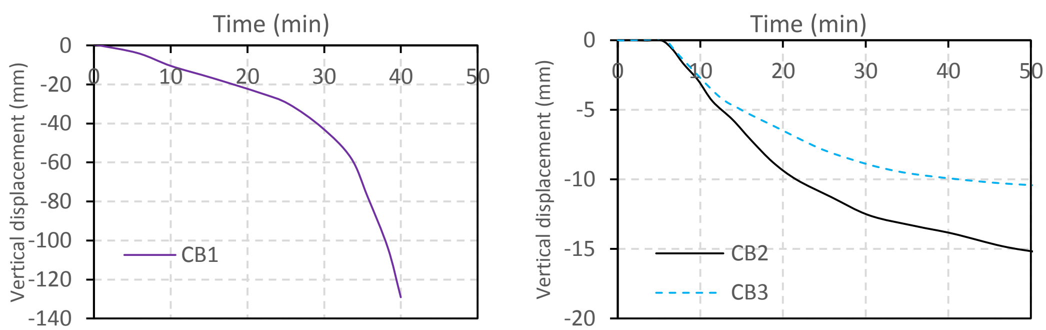

(a) CB1 (b) CB2 and CB3

Fig. 3 Comparison of measured vertical deflections in tested girders

The structural response of tested composite girders CB1, CB2, and CB3 with fire exposure time is further illustrated in Fig. 4, where progression of out-of-plane web displacement is plotted. The measured out-of-plane displacement shown in Fig. 4 is at a point located at the mid-height of the web and 430 mm away from mid-span (below the load point – see Fig. 1d). Girder CB1, tested under predominant flexural loading, did not experience any web lateral displacement as shown in Fig. 4. However, in steel girders CB2, and CB3, tested under predominant shear loading, out-of-plane web displacement varied significantly. In the case of composite girder CB2, the out-of-plane web displacement steadily increased to 5 mm at 22 min into fire exposure, when average web temperature reached 460˚C. After that, the web displacement rapidly increased to 25.4 mm at 30 min of fire exposure, when average web temperature is 500˚C. At this point, out-of-plane web displacement increased at a higher pace to 35.6 mm (which corresponds to average web temperature of 590˚C) at which point failure occurred in the girder.

The out-of-plane web displacement in girder CB3 was similar to that observed in girder CB2, but the extent of displacement was higher due to lesser composite action (50%) that develop in girder CB3. The out-of-plane web displacement in girder CB3 starts to increase linearly until it reaches 20.3 mm, then suddenly jumps to 31 mm at about 30 min into fire exposure when average web temperature is 500˚C. Table 1 summaries details on comparative thermal and structural response parameters of girders CB1, CB2 and CB3.

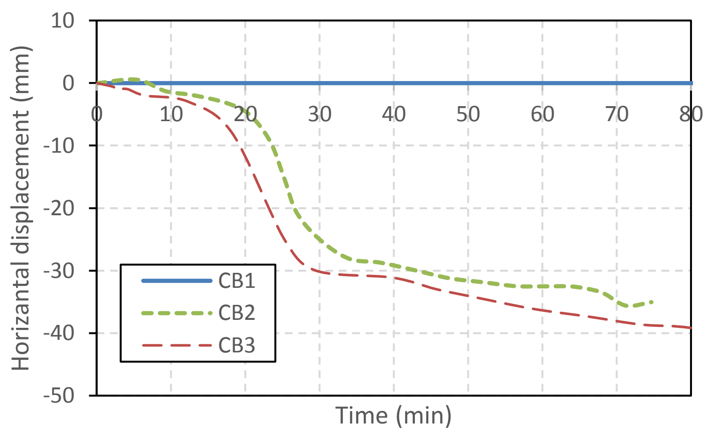

Fig. 4 Variation of web out-of-plane displacement as a function of fire exposure time in composite girders

Table 1 Varied parameters in fire resistance tests

Specimen	Level of composite action	Load mechanism	Time at initiation of web bucking (min)	Temp. at initiation of web bucking (˚C)	Max. out-of-plane displacement (mm)	Temp. at max. out-of-plane displacement (˚C)
CB1	100%	Flexural	-	-	-	-
CB2	100%	Shear	9	220	35.6	590
CB3	50%	Shear	5	153	36	620

Failure Modes

Visual observations were made during and at the end of fire tests to capture response patterns and failure mechanisms in tested composite girders. Observations recorded in tested girder CB1 indicate that flexural behavior dominated response till failure of girder. This girder experienced significant degradation in flexural capacity and thus failed through yielding at the bottom flange, and through large rotations at supports with no signs of web buckling as shown in Fig. 5a. Figure 5 also shows failure mode and magnitude of deformation in composite girders CB2, and CB3. Both girders CB2 and CB3 failed early into fire exposure at 55 and 50 min, respectively. The failure of girders CB2 and CB3 was in shear mode in which web buckling was dominant. These results infer that shear action dominated structural response of these girders due to occurrence of large web shear buckling and lack of any significant mid-span deflection or rotation at the end supports. Composite girder CB3 experienced larger torsional effects and cracking of slab than that observed in girder CB2. This is due to the fact that there was less interaction between the concrete slab and steel girder as girder CB3 had half the number of shear studs (designed for 50% composite action) as that in girder CB2.

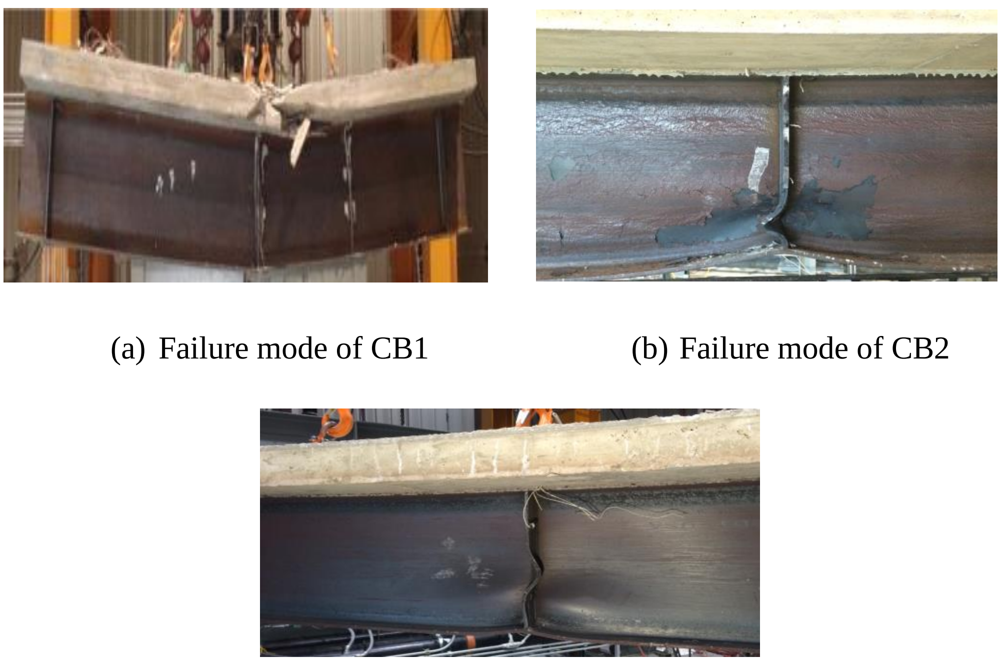

(a) Failure mode of CB1 (b) Failure mode of CB2

(c) Failure mode of CB3

Fig. 5 Illustration of failure pattern in steel girders CB1, CB2, and CB3 after exposure to fire

CONCLUSIONS

Based on the results of the analysis presented herein, the following conclusions can be drawn:

1. Steel girders exposed to fire can experience failure under flexural, shear or local instability failure limit state, or due to combination of different failure modes. The current philosophy of evaluating failure of fire-exposed girders

solely based on flexural limit state may not be conservative in situations where girders are subjected to high shear forces.

2. Steel girders designed for full composite action with concrete slab, can effectively transfer some level of stresses to slabs under fire conditions and hence achieve better fire resistance than steel girders designed for 50% composite action.
3. Composite girders loaded with high shear forces, and exposed to fire do not undergo large deflections or rotations at end supports and thus, deflection limiting criteria cannot be valid in defining failure. These girders fail due to temperature-induced web shear buckling and related degradation of shear capacity.

ACKNOWLEDGMENT

This material is based upon the work supported by the National Science Foundation under Grant number CMMI-1068621 to Michigan State University. Any opinions, findings, and conclusions or recommendations expressed in this paper are those of the authors and do not necessarily reflect the views of the sponsors.

REFERENCES

[1] Naser M.Z., Kodur V.K.R. Factors Governing onset of Local Instabilities in Fire Exposed Steel Beams. Journal of Thin-Walled Structures 2014. In press.

[2] Kodur V.K.R., Naser M.Z. Effect of Local Instability on Capacity of Steel Beams Exposed to Fire. Journal of Constructional Steel Research 2014;111: 31–42.

[3] Kodur VKR, Naser MZ. Effect of Shear on Fire Response of Steel Beams. Journal of Constructional Steel Research 2013;97:48-58 .

[4] Eurocode 3. Design of steel structures, Part1-2: General rules-structural fire design, Document CEN, European Committee for Standardization, UK in, 2005.

[5] AISC. Specification for structural steel buildings 360–11. American Institute of Steel Construction Inc.; Chicago, IL 2011.

[6] Basler K, Yen B, Mueller J, Thürlimann B. Web Buckling Tests on Welded Plate Girders. Welding Research Council Bulletin 1960;64.

[7] Vasdravellis G, Uy B. Shear Strength and Moment-Shear Interaction in Steel-Concrete Composite Beams. J. Struct. Eng. ASCE 2014;140(11).

[8] Aziz E, Kodur V, Glassman J, Garlock M. Behavior of steel bridge girders under fire conditions, Journal of Constructional Steel Research 2015;106: 11-22

Factors Governing Response of Steel Bridge Girders under Fire Conditions

ESAM M. AZIZ and VENKATESH K. KODUR

ABSTRACT

This paper presents results from numerical studies on the response of fire exposed steel bridge girders. A finite element model is applied to quantify critical factors influencing the fire resistance of steel girders in bridges. The varied parameters include: fire intensity, exposure scenario, web slenderness, and span length. Results from numerical studies indicate that fire resistance and failure mode in steel bridge girders is highly influenced by fire intensity, exposure scenario, and web slenderness. A typical steel girder can experience failure in less than 20 minutes under hydrocarbon fires. Failure through web shear buckling is the most dominant failure limit state, when web slenderness of the girder exceeds 50.

INTRODUCTION

Fire is one of the most severe environmental hazards to which structures may be subjected during their lifetime. In recent decades, due to rapid development of urban ground-transportation system, as well as increasing transportation of hazardous materials, bridge fires have become a growing problem [1, 2]. Damage or collapse of bridges arising from such fires can lead to significant economic and public losses. However, at present there are no specific fire resistance provisions in bridge design codes and standards to enhance structural fire safety of bridges [3, 4]. This is in contrast to buildings where building codes and standards specify fire resistance provisions to structural members to maintain structural stability and integrity in the event of a fire.

The most common cause of bridge fires is due to crashing of fuel transporting trucks and burning of gasoline, in the vicinity of the bridge. These hydrocarbon fires are much more intense, as compared to building fires, and grow at a rapid heating pace and produce very high peak temperature within first few minutes. In

Esam M. Aziz: Department of Architectural Engineering, University of Sulaimani, Kurdistan Region, Iraq. Email: esam.azez@univsul.edu.iq
Venkatesh K. Kodur: Department of Civil and Environmental Engineering, Michigan State University, East Lansing, MI, 48824,USA. Email: kodur@egr.msu.edu

some cases, such intense fires can pose a severe stress to stability of structural members and can lead to collapse of structural members in bridges. Stability of a bridge under such fire exposure depends on key factors, namely; fire intensity, material type, and characteristics of structural members [2].

The response of structural members in bridges under fire conditions can be significantly different than those in buildings due to differences in fire scenarios, load level, support conditions, and sectional characteristics of structural members. The effect of these factors on fire resistance has been well established for building elements [5, 6]. However, there is limited information on the effect of these factors in bridges. Also, the information that is specially established for structural members in buildings might not be directly applicable to bridge structural members. There is only limited research that has been carried out on fire resistance of structural members of bridges [1, 7, 8, 9, 10]. This paper discusses results from numerical studies on the critical factors influencing the response of steel bridge girders exposed to fire.

NUMERICAL MODELING

A numerical model is developed in ANSYS software for tracing the response of fire exposed steel bridge girders [11]. Uncoupled thermo-mechanical analysis was undertaken for tracing thermal and structural response of a bridge girder. Different structural components of the composite girder (shown in Figure 1(a)), namely steel girder, reinforced concrete slab, shear studs and stiffeners, were discretized with different elements available in ANSYS.

The heat transfer analysis of the composite steel-concrete girder is carried out using two types of elements available in ANSYS, namely SOLID70 and SURF152. For the discretization of girder, slab, and the stiffeners, SOLID70 elements are used. SOLID70 is a 3-D element with three-dimensional thermal conduction capability. SURF152 element is utilized for simulating various surface effects such as thermal radiation and heat convection. The discretization adopted for modeling temperature progression in cross-section of a segment of the steel bridge girder is shown in Figure 1(b). For thermal analysis, temperature dependent thermal properties for steel and concrete; namely thermal conductivity, specific heat and thermal expansion, were provided as input into ANSYS and these properties are assumed to follow relations specified in Eurocodes 1, 2, and 3 [12, 13, 14].

For structural analysis, the bottom flange, web, top flange and stiffeners of the steel girder were modeled with SHELL181 elements, and the concrete slab was modeled with SOLID185 elements. These elements are capable of accounting for plasticity, stress stiffening, and large strain effects. To account for composite action between the concrete slab and the top flange of the steel girder, 3-D nonlinear surface-to-surface fully bonded contact elements (CONTA174 and TARGE170) are used. Temperatures generated from thermal analysis were applied as a thermal-body-load on the structural elements to simulate conditions of fire exposure on steel bridge girder. The temperature dependent mechanical properties (stress-strain relationships) of steel and concrete are assumed to follow as that of Eurocode 2 and Eurocode 3 provisions and these relations are provided as input into ANSYS [13, 14]. The 3-D structural model and the meshing used for structural analysis is illustrated in Figure 1(c).

Under fire exposure, steel bridge girders experience high temperatures and thus web shear buckling might dominate the failure limit state due to higher slenderness of the web as compared to the flanges. Also, significant deflections can occur under fire conditions due to development of high thermal gradients along the girder cross-section, and due to rapid degradation of strength and stiffness of steel. Therefore, web shear buckling (instability) and deflection limit states were also applied in evaluating failure. The failure is said to occur when the mid-span deflection of the girder exceeds (L/30) or when web out-of-plane displacement leads to runaway displacement [15].

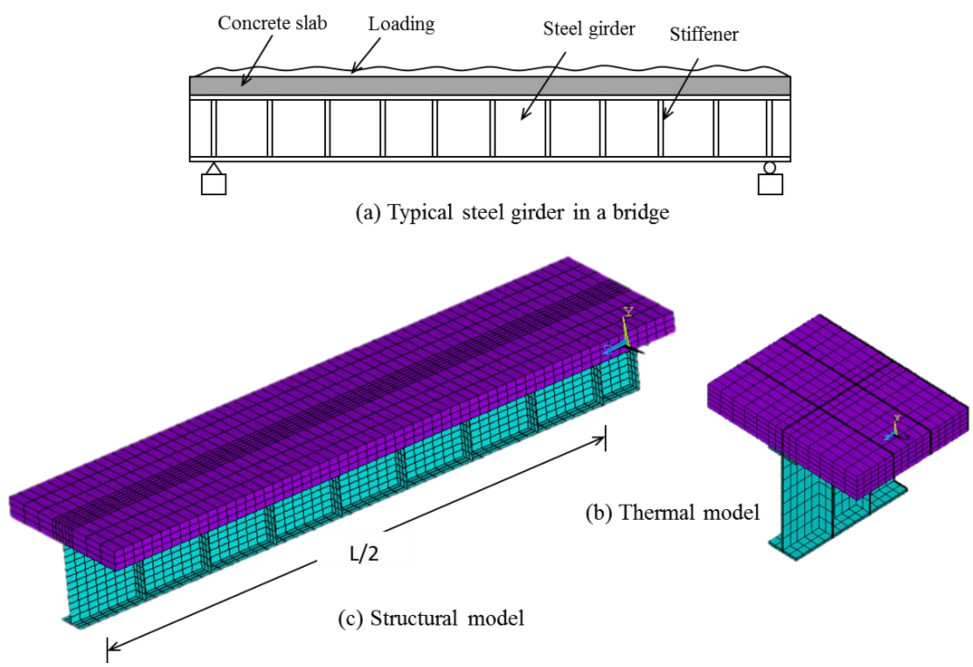

Figure 1. 3-D discretization of the typical steel girder used in numerical analysis.

MODEL VALIDATION

The developed numerical model was validated against data generated from fire resistance tests on typical steel bridge girders (designated as G2 and G3) carried out at Michigan State University [10]. Steel girders G2 and G3 are built-up plate girders with web slenderness (D/t_w) of 123. These girders were tested under ASTM E119 fire exposure and subjected to applied loading of 40% and 33% of their flexural capacity, respectively, which equates to 56% of their shear capacity. The validation process included comparison of both thermal and structural response predictions from the analysis with that measured during fire tests.

As part of thermal response validation, predicted steel and concrete temperatures are compared against corresponding temperatures measured in fire tests as shown in Figure 2(a). Predicted temperatures from the analysis compare well with measured data from fire tests throughout the fire exposure duration, with slight differences. This is due to variation of heat transfer parameters used in the analysis as compared to actual conditions present in the furnace conditions. As part of structural response validation, mid-span deflections predicted by numerical model are compared with those measured in fire tests (see Figure 2(b)). Mid-span deflections from ANSYS compare well with those measured during fire tests. Also, failure time predicted from analysis compare well with failure time observed during fire test with slight variation in case of girder G3.

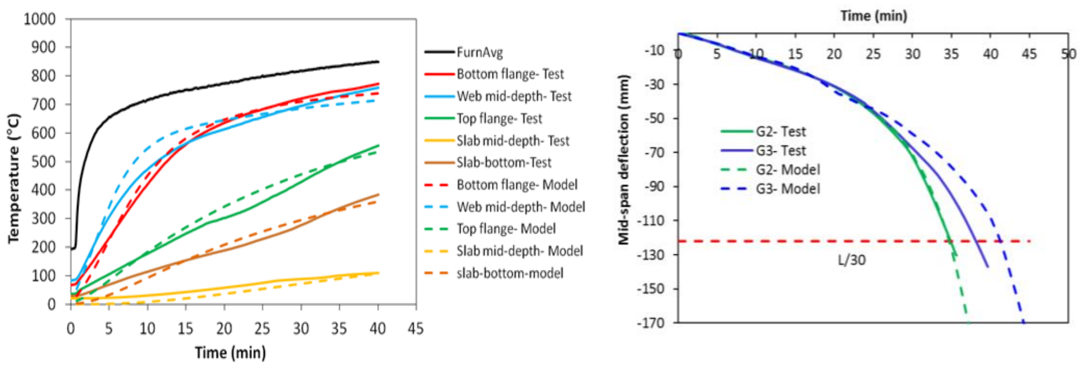

(a) Thermal response (b) Structural response

Figure 2. Comparison of predicted and measured thermal and structural response in steel girders G2, and G3

PARAMETRIC STUDIES

The validated numerical model is applied to trace the fire response of a typical steel bridge girder. In the analysis, the selected girder shown in Figure 3 is subjected to a given fire scenario and load level of 30% of the flexural capacity of the girder at room temperature. Results from structural analysis are evaluated in terms of mid-span deflection as a function of fire exposure time to quantify the effect of various factors on fire resistance of steel girders.

Varied Parameters

The factors that varied in the parametric studies are; fire severity, exposure scenario, web slenderness, and span length. The range of these factors was selected based on common scenarios encountered in practice. Fire intensity is varied from severe to low intensity fires, namely hydrocarbon fire, design fire, ISO 834 fire, and external fire. The time-temperature curves correspond to these fire scenarios are illustrated in Figure 4. Also, three fire exposure scenarios on girders, namely entire span exposure, mid-span zone exposure, and support zone exposure are considered in the analysis. Web slenderness (D/t_w) in girder is varied from 30 to 100, while span length of 12.2 m, 17 m, and 22 m representing short (up to 15 m), medium (15- 50 m) span bridges is considered.

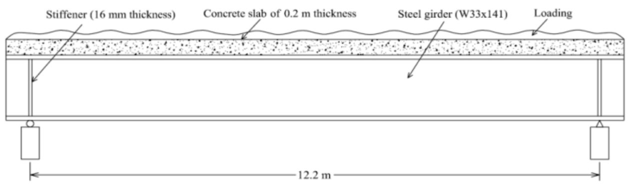

(a) Longitudinal section

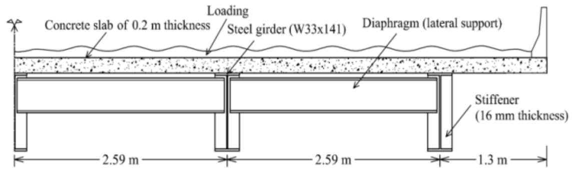

(b) Traverse section near supports

Figure 3. Typical steel bridge girder used in analysis.

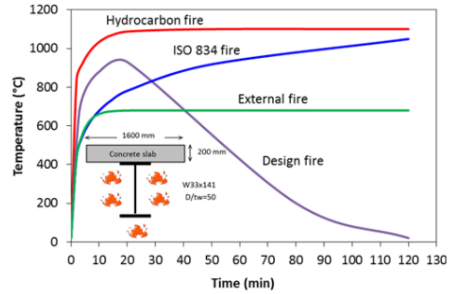

Figure 4. Fire scenarios used for numerical analysis.

Effect of Fire Severity

The effect of fire severity on structural response of steel bridge girder is shown in Figure 5 in which the mid-span deflection is plotted as a function of fire exposure under hydrocarbon fire, design fire, ISO 834 fire and external fire exposure. It can be seen that the fire resistance (failure time) of the steel girder is highly influenced by the extent of fire severity. The steel girder exposed to hydrocarbon fire failed in 14 minutes, while the steel girder exposed to external fire survived (no failure) 120 minutes of fire exposure. This can be attributed to fire intensity that is much higher in the case of hydrocarbon fire as compared to that of external fire. In the case of design and ISO 834 fires, steel girder exhibits higher fire resistance as compared to case of hydrocarbon fire and failure occurs at 22 and 33 minutes respectively. The low fire resistance of steel bridge girder under hydrocarbon fire, typical of fires resulting from crashing of gasoline tankers, indicates that firefighters have very little time to respond to such fire incidents. Under such scenario steel girder are highly vulnerable to collapse.

Effect of Exposure Scenario

To study, the effect of exposure scenario on the fire response of steel bridge girders, the selected girder is analyzed under hydrocarbon fire using three exposure scenarios, namely entire span exposure, mid-span zone exposure, and support zone exposure. In the first case, the entire span of the girder (12.2 m) is exposed to fire, while only 4.2 m of the mid-zone of the span of 12.2 m is exposed to fire in second case. For third case, 4 m length of the span from one side of end support is exposed to fire. The mid-span deflection under these three cases is plotted in Figure 6 as a function of time exposure.

It can be seen that extent of mid-span deflection varies depending on the exposure scenario. The mid-span deflection in first case (entire span exposure) is higher than the other two cases and this is due to degradation of shear and flexural capacity simultaneously due to fire exposure on the entire span. However, in other two cases (support zone or mid-span zone exposure); either the shear or the flexural capacity degrades due to fire exposure depends on the exposure zone. Therefore, the mid-span deflection is higher in case of mid-span zone exposure as compared to support zone exposure case. Results in Figure 6 also indicate that progression of mid-span deflections prior to failure occur in a rapid pace when web shear buckling is attained. This results in lower fire resistance (14 minutes) in the case of entire span and support zone exposure as compared to the case of mid-span zone exposure, where failure time is about 19 minutes.

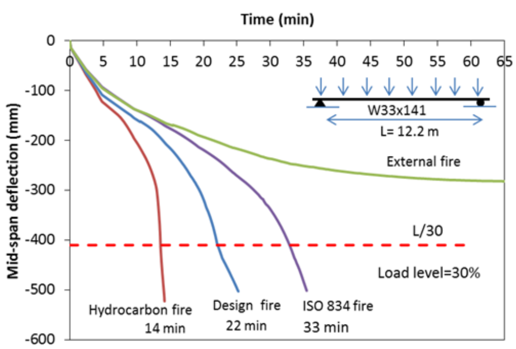

Figure 5. Effect of fire scenario on the fire performance of steel bridge girders.

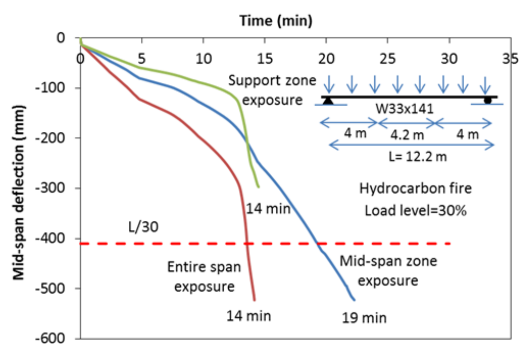

Figure 6. Effect of exposure scenario on the fire performance of steel bridge girders.

Effect of Web Slenderness

Rolled steel sections typically used in buildings have web slenderness (D/t_w) in the range of 30 to 50. However, typical steel girders used in bridges have web slenderness in the range of 75 to 150. This makes fire exposed steel girders in bridges to be highly vulnerable to fail under web shear buckling mode rather than flexural (bending) mode of failure. To study the effect of slenderness on the fire response of steel bridge girder, five different values of web slenderness (D/t_w = 30, 40, 50, 70, and 100) are considered. The web slenderness of the girder is varied by changing the thickness of the web, while the depth of the section is kept constant.

The effect of web slenderness on fire response of steel bridge girder is illustrated in Figure 7, in which progression of mid-span deflection is plotted with fire exposure time for different web slenderness values. It can be seen that decreasing web slenderness from 50 to 30 resulted in an increase in fire resistance from 14 to 26 minutes. This is due to the fact that increasing web thickness enhances the shear capacity of the girder and also result in slower temperature rise in the web. Increasing web slenderness from 50 to 100 leads to decrease in fire resistance of the steel girder from 14 to 7 minutes. This is due to lower web thickness that results in rapid rise in temperature in the slender web as compared to the flanges. As a result, web buckles rapidly leading to lower shear capacity and higher deflection in the girder.

Effect of Span Length

To investigate the effect of span length on fire response of steel bridge girders, the numerical analysis is carried considering different spans length of girders, namely 12.2 m, 17 m, and 22 m. Figure 8 shows the effect of span length on the response of the selected steel bridge girder under hydrocarbon fire scenario. It can be seen from Figure 8 that the mid-span deflection increases with increasing span length of the girder. This is due to the fact that longer span length produces higher shear force and bending moment resulting in higher stresses developed in the girder. This causes earlier spread of plasticity in the girder as compared to the cases with shorter span, resulting in earlier occurrence of web buckling. Therefore, fire resistance decreases with increasing span length. For example, fire resistance decreased from 14 to 11 minutes with increasing girder span from 12.2 m to 22 m.

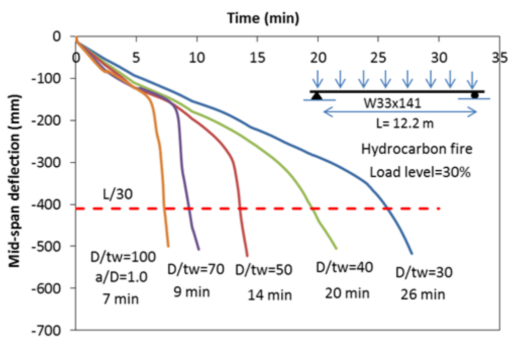

Figure 7. Effect of web slenderness on the fire resistance of steel bridge girders.

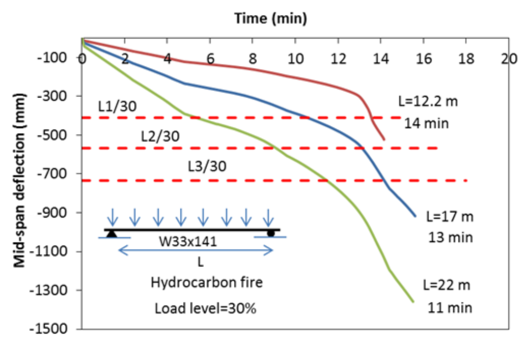

Figure 8. Effect of span length on the fire resistance of steel bridge girders.

CONCLUSIONS

Based on the results of numerical studies the following conclusions can be drawn:

1. Steel bridge girders can experience failure in less than 20 minutes under hydrocarbon fire exposure. The failure time and mode of failure is influenced by fire severity, exposure scenario and web slenderness.
2. Fire exposed steel girders are susceptible to failure through web shear buckling when web slenderness (ratio of depth to thickness of web) exceeds 50.
3. Increasing web thickness enhances fire resistance of steel bridge girder to some extent and alters the failure mode from web shear buckling to flexural bending mode.

4. Failure through web shear buckling in steel bridge girders result in lower fire resistance as compared to situation where flexural response is the dominate failure limit state. Therefore, fire exposure in the vicinity of support zone of steel girders leads to much lower fire resistance than the case of fire exposure close to the mid-span zone.
5. Increasing girder span result in lower fire resistance.

ACKNOWLEDGEMENTS

This material is based upon work supported by the National Science Foundation under Grant No. CMMI-1068621 and the authors wish to acknowledge NSF's support. Any opinions, findings, conclusions, or recommendations expressed in this paper are those of the authors and do not necessarily reflect the views of the NSF. The support from University of Sulaimani in the form of a scholarship to the first author is also acknowledged.

REFERENCES

1. Kodur V.K.R., Gu L., Garlock M.E.M. 2010. "Review and Assessment of Fire Hazard in Bridges". Transportation Research Board, 2172: 23-29.
2. Kodur V.K.R., Aziz E.M., Dwaikat M.M.S. 2013. "Evaluating Fire Resistance of Steel Girders in Bridges". ASCE Journal of Bridge Engineering, 18: 633-643.
3. AASHTO. 2007. "AASHTO LRFD Bridge Design Specifications". Edition 4, American Association of State Highway and Transportation Officials, Washington DC, USA.
4. NFPA 502. 2011. "Standards for Road Tunnels, Bridges, and other Limited Access Highways". Edition 2011.
5. Kodur V.K.R. and Dwaikat M.M.S. 2009. "Response of Steel Beam–Columns Exposed to Fire". Engineering Structures Journal, 31: 369-379.
6. Dwaikat, M.M.S, and Kodur V.K.R. 2010. "Effect of Location of Restraint on Fire Response of Steel Beams". Journal of Fire Technology, 46(1): 109-128.
7. Aziz E.M., Kodur V.K.R. 2013. "An Approach for Evaluating the Residual Strength of Fire Exposed Bridge Girders". Journal of Constructional Steel Research, 88: 34-42.
8. Payá-Zaforteza I., Garlock M.E.M. 2012. "A Numerical Investigation on the Fire Response of a Steel Girder Bridge". Journal of Constructional Steel Research, 75: 93-103.
9. Vimonsatit V., Tan K., Qian Z. 2007. "Testing of Plate Girder Web Panel Loaded in Shear at Elevated Temperature". Journal of Structural Engineering, 133(6): 815-824.
10. Aziz E. M., Kodur V.K.R., Glassman J. D., Garlock M. E. 2015. "Behavior of Steel Bridge Girders under Fire Conditions. Journal of Constructional Steel Research, 106: 11-22.
11. ANSYS. 2013. ANSYS metaphysics. Version 14.5 ANSYS Inc. Canonsburg, PA, USA.
12. European Committee for Standardization (CEN). EN 1991-1-2: 2002. Eurocode 1: Actions on Structures. Part 1.2 General Action-Action on Structures Exposed to Fire. CEN, Brussels, Belgium.
13. European Committee for Standardization (CEN). EN 1992-1-2: 2004 Eurocode 2: Design of Concrete Structures. Part 1.2 General Rules-Structural Fire Design. CEN, Brussels, Belgium.
14. European Committee for Standardization (CEN). EN 1993-1-2: 2005 Eurocode 3: "Design of Steel Structures. Part 1.2 General Rules-Structural Fire Design. CEN, Brussels, Belgium.
15. Wainman D.E., Kirby B.R. 1989. "Compendium of UK Standard Fire Test Data for Unprotected Steel-1". Published by British Steel Technical and Swinden Laboratories, Rotherham, UK.

Postbuckling Shear Strength at Elevated Temperatures using a Compression-based Approach

JONATHAN A. GLASSMAN
and MARIA E. MOREYRA GARLOCK

ABSTRACT

Steel plate girders are susceptible to web shear buckling at elevated temperatures; however, the underlying mechanics governing this buckling behavior have eluded understanding despite decades of research. Tension field theory, which assumes that postbuckling shear strength is derived from the formation of diagonal tensile stresses after elastic buckling, has traditionally served as the basis for web shear buckling models. While grounded in extensive experimental work conducted at ambient temperatures, tension field theory has been shown to become inaccurate over a range of plate geometries, steel yield strengths, and temperatures from 20^{o}C to 1100^{o}C. Given these limitations, the authors have previously proposed a compression-based approach that characterizes a web plate's ability to develop postbuckling shear strength based on an interaction of diagonal compressive and tensile stresses. This paper presents the derivation of this compression-based approach for steel temperatures of 20^{o}C up to 1100^{o}C. It is shown that correlation to experimental results is within 13%.

INTRODUCTION

The primary motivation for studying web shear buckling at elevated temperatures is the observation of diagonal buckles in fire-damaged steel plate girder bridges. A notable example is the "Malfunction Junction" fire in Birmingham, Alabama in January 2002 (Figure 1) [1, 2]. Despite the intense tanker truck fire, the bridge girders remained standing, albeit with significant deformation. The most overt damage is the residual vertical deflection of the girder that bore the brunt of the fire loading; a close-up of this girder's web panels shows additional deformations in the form of diagonal buckles. This observation of web shear buckling has since prompted deeper experimental and numerical research to understand the contribution of web shear buckling to the fire performance of steel plate girders.

Jonathan D. Glassman, Exponent, Inc., 5401 McConnell Avenue, Los Angeles, CA 90066
Maria E. Moreyra Garlock, Princeton University, Princeton, NJ 08544

Figure 1. Damaged steel plate girders of the Malfunction Junction fire in Birmingham, Alabama in January 2002. The right image shows evidence of web shear buckling (courtesy of Alabama DOT).

Any research involving web shear buckling will invariably encounter tension field theory. This theory has been employed since the early 1960s to characterize the ability of steel plates subjected to pure shear loads to develop significant postbuckling shear strength beyond elastic shear buckling. To this day, tension field theory is the basis for the design code equations in both the United States and Europe that address web shear buckling [3]. Numerous researchers, however, have consistently challenged the underlying assumptions of tension field theory. Most notable of these challenges involves the fundamental assumption that once elastic shear buckling has occurred, compressive stresses do not increase in the web plate and any postbuckling shear strength is derived solely from the diagonal tensile stresses. Extensive numerical analyses have found that this assumption is not applicable [3, 4, 5, 6, 7, 8, 9].

The compression-based approach addresses this problem with tension field theory's fundamental assumption by proposing that postbuckling shear strength is derived from an interaction of diagonal tensile and compressive stresses. Buckling is inherently a compression problem; therefore, the compression-based approach assumes that compressive stresses, with support from the diagonal tension field, work together to develop the postbuckling shear strength. Ultimate postbuckling shear strength predictions from the compression-based approach have validated well with published experimental results at ambient temperature [9].

The objective of this paper is to build on the compression-based approach, which was derived at ambient temperature, and apply it to elevated temperatures. Over five-hundred finite element models are used to develop a proposed formulation that is then compared to published experimental results [10, 11]. An equation is proposed to predict the postbuckling shear strength of steel plates up to a temperature of 1100^{o}C, thus illustrating that the compression-based approach is a viable alternative to traditional tension field theory models.

BACKGROUND

Figure 2 illustrates how the compression-based approach relies on an interaction of diagonal compressive and tensile stresses to develop the postbuckling shear capacity. For $\tau \leq \tau_{cr}$, the applied pure shear load is equivalent to an axial load applied along the diagonal compression element shaded in blue in Figure 2(a). This compression element has a moment of inertia (named the "equivalent moment of inertia," I_{eq}), which allows for the externally applied pure shear loading, τ, to be translated into an equivalent axial force, P, acting along the diagonal compression element (Figure 2(b) and 2(c)).

When $\tau > \tau_{cr}$, the web plate enters the postbuckling range during which a diagonal tension field forms (Figure 2(d)). This tension field provides additional stability to the diagonal compression element that has buckled due to the applied load, $P > P_{cr}$. The diagonal tension field (in red shading) crosses the diagonal compression element over a width, w (Figure 2(e)). This diagonal tension field is assumed to be sufficiently tensioned such that the length of the equivalent column reduces to an effective length, L_e, with a length of $L_e/2$ on each side of w (Figure 2(f)).

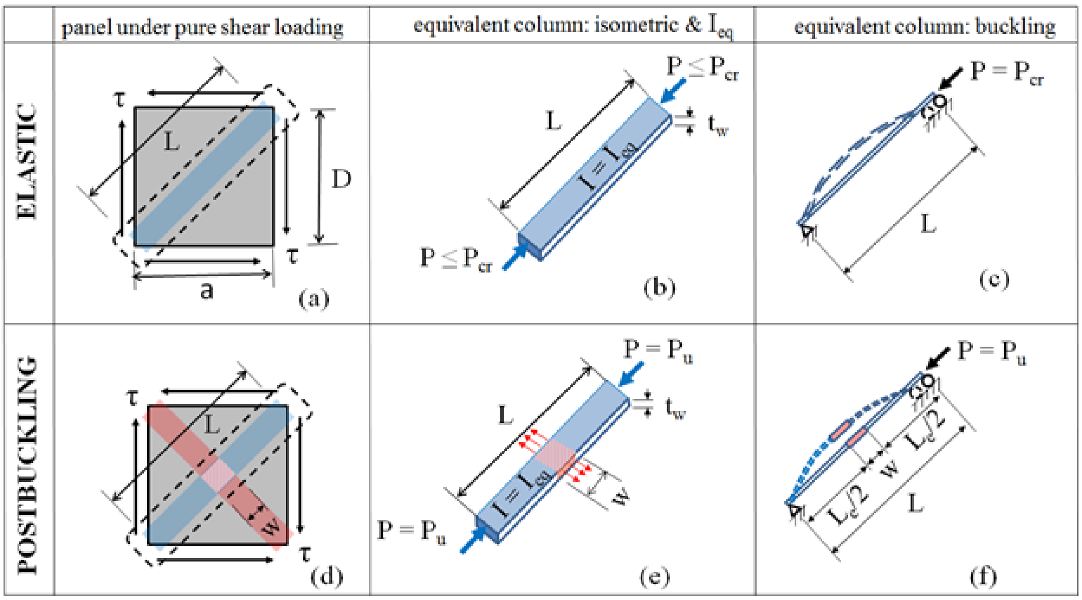

Figure 2. The compression-based approach for web shear buckling (reproduced from [9]).

Based on the model presented in Figure 2 and the extensive derivation provided in [9], the ultimate postbuckling shear load, V_u, can be calculated from the following equation:

$$V_u = V_{cr}\left(\frac{L}{L_e}\right)^2 \cdot Q_v \qquad (1)$$

From Eqn. (1), L is the length of the diagonal compression element, V_{cr} is the elastic shear buckling load that can be calculated using the classical solution presented in [12, 13], $L_e = L - w$, and Q_v is a function of the distribution of compressive stresses that act along the tension field. From [9], Q_v can be assumed to equal unity. The only unknown in Eqn. (1), therefore, is w, which is needed to calculate the L_e value. The value of w is a function of a/D (the span-to-depth ratio), D/t_w (the slenderness ratio, where t_w is the thickness of the web plate), D (the depth of the web plate), and σ_y (the steel yield strength). Results from numerous analyses involving experimentally-validated finite element models were used to derive the following equations for w at ambient temperature [9]. Eqn. (2) is for σ_y of 250 MPa (36 ksi), while Eqn. (3) is for σ_y of 345 MPa (50 ksi), both of which represent common yield strengths used for steel plate girders.

$$w = \left(\left(0.315\ln\left(\frac{D}{t_w}\right) - 1.306\right)\left(\frac{a}{D}\right) + 0.647\ln\left(\frac{D}{t_w}\right) - 3.209\right) \times D \quad D/t_w \leq 164 \quad \text{(2a)}$$

$$= \left(\left(0.278\ln\left(\frac{D}{t_w}\right) - 1.124\right)\left(\frac{a}{D}\right) + 0.376\ln\left(\frac{D}{t_w}\right) - 1.792\right) \times D \quad 164 < D/t_w \quad \text{(2b)}$$

$$w = \left(\left(0.278\ln\left(\frac{D}{t_w}\right) - 1.072\right)\left(\frac{a}{D}\right) + 0.622\ln\left(\frac{D}{t_w}\right) - 2.99\right) \times D \quad D/t_w \leq 164 \quad \text{(3a)}$$

$$= \left(\left(0.31\ln\left(\frac{D}{t_w}\right) - 1.249\right)\left(\frac{a}{D}\right) + 0.238\ln\left(\frac{D}{t_w}\right) - 0.992\right) \times D \quad 164 < D/t_w \quad \text{(3b)}$$

Eqn. (1) was extensively validated with published experimental test data at ambient temperature. For experiments using web plates with typical geometries and material parameters, such as $1.0 \leq a/D \leq 3.0$, $D/t_w < 300$, and 180 MPa $\leq \sigma_y \leq$ 420 MPa, Eqn. (1) predicted V_u values that more closely aligned with experimental V_u values compared to the Basler-Thürlimann equation that is the basis for the bridge design code used in the United States [3, 14]. To extend the applicability of the compression-based approach for temperatures up to 1100°C, however, more extensive finite element modeling and additional experimental validations were necessary.

FINITE ELEMENT MODELS

Figure 3 shows mesh densities for the finite element models used to extend the compression-based approach for steel temperatures up to 1100°C. The three web plates shown have a/D values of 1.0, 2.0, and 3.0. Each model was analyzed with 13 different D/t_w values and 11 different temperatures (20°C, 200°C, 300°C, and 100°C increments up to 1100°C). Over 500 finite element models were used to extend the range of Eqn. (1) for elevated temperatures. The web plates were assumed to have simply supported boundary conditions shown in Figure 4 and were previously validated with published experimental data [8, 9].

The Eurocode material model was assumed for the changes in steel material properties of σ_y, σ_p (the proportional limit stress), and E (Young's modulus) at elevated temperatures [15]. The Eurocode uses temperature-dependent reduction factors to reduce the ambient temperature material properties to their correspondingly high temperature values; these reduction factors are plotted in Figure 5.

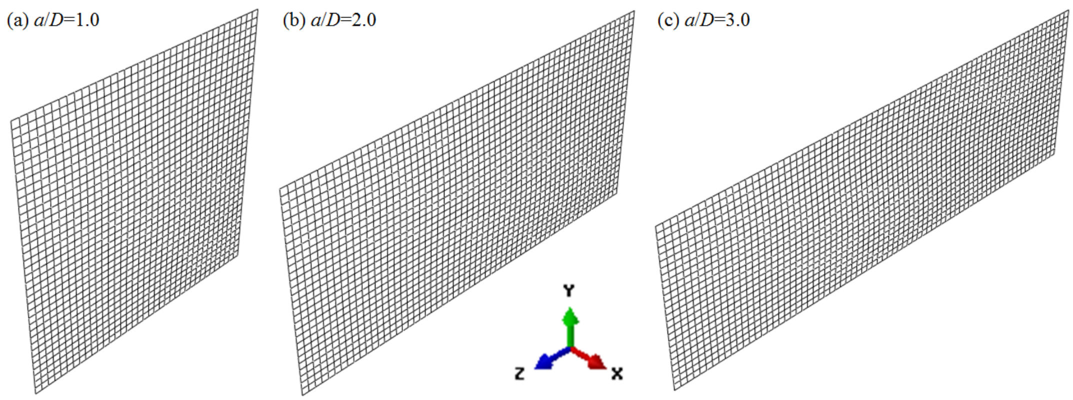

Figure 3. Mesh densities for the finite element models with a/D values of 1.0, 2.0, and 3.0.

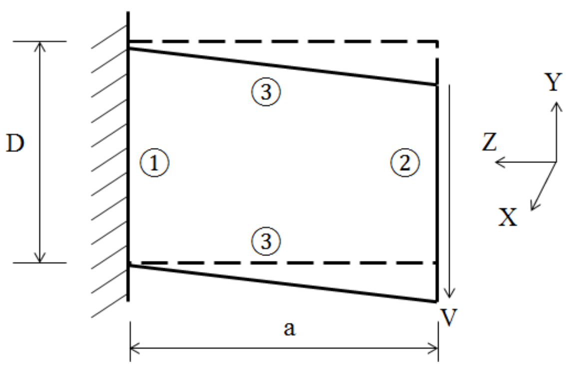

	U_X	U_Y	U_Z	UR_X	UR_Y	UR_Z
①	•	•	•	•		•
②	•		•	•		•
③	•		•	•	•	

Figure 4. Simply supported boundary conditions assumed for the finite element models that ensured pure shear deformations. A "•" indicates a restrained degree of freedom.

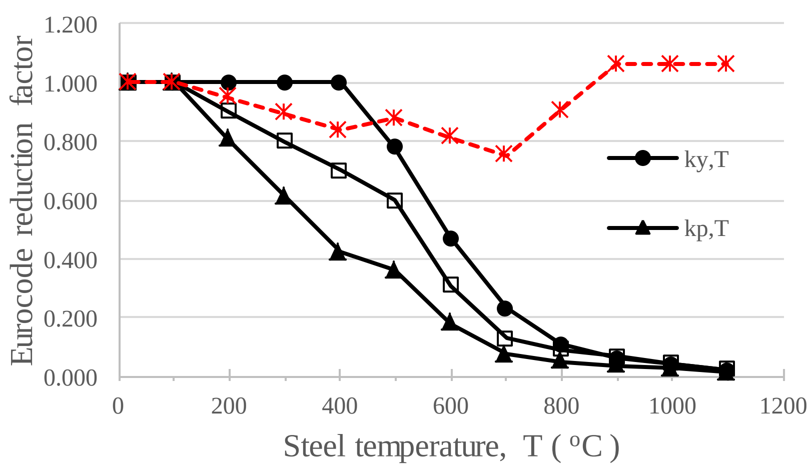

Figure 5. Plot of Eurocode reduction factors for σ_y, σ_p, and E ($k_{y,T}$, $k_{p,T}$, and $k_{E,T}$, respectively). Also plotted are the values of $\sqrt{(k_{E,T}/k_{y,T})}$.

COMPRESSION-BASED APPROACH AT ELEVATED TEMPERATURES

The two terms in Eqn. (1) that are a function of temperature are V_{cr} and L_e. Since V_{cr} is a function of E, high temperature values for V_{cr} can be accurately calculated by multiplying E by $k_{E,T}$ [8]. A temperature-dependent L_e term (L_e^T) was developed by first solving for values of L_e^T such that the V_u value from Eqn. (1) equals the V_u value determined from the experimentally-validated finite element models (V_u^{FE}). Figure 6 plots values of L_e^T* (the L_e^T value calculated by replacing V_u in Eqn. (1) with V_u^{FE}) for web plates with σ_y of 250 MPa at ambient temperature.

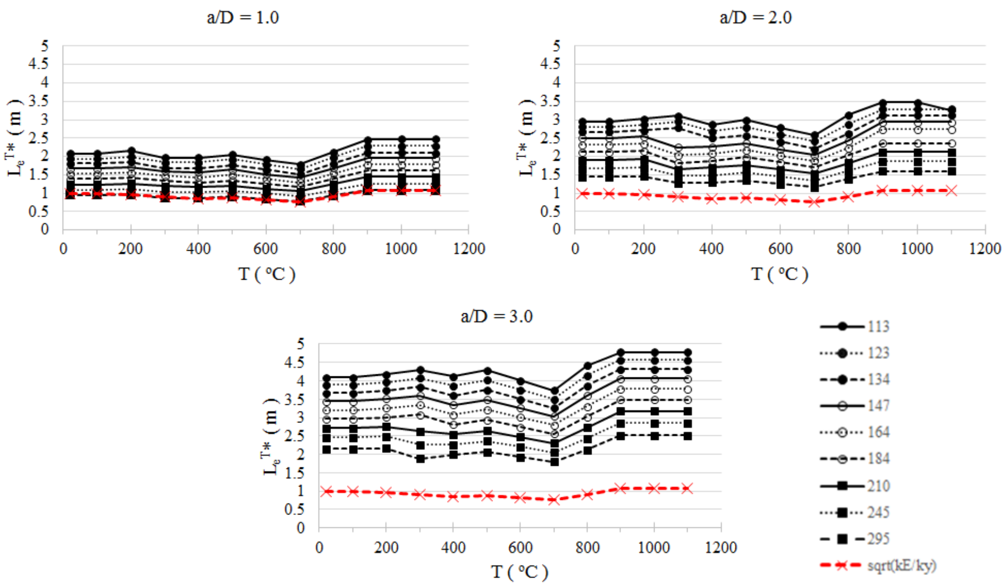

Figure 6. L_e^T* versus temperature for web plates with a/D = 1.0, 2.0, and 3.0 and σ_y = 250 MPa. The red line is a plot of the $\sqrt{(k_{E,T}/k_{y,T})}$ values from Figure 5. Similar behavior is observed for σ_y = 345 MPa.

The plots in Figure 6 show that the L_e^T* values follow a very similar trend to the plot of $\sqrt{(k_{E,T}/k_{y,T})}$ from 20°C to 1100°C, albeit with a vertical shift in the data points. Based on these observations, the original L_e term in Eqn. (1) can be replaced with the following equation:

$$L_e^T = (L - w)(\beta)\left(\sqrt{\frac{k_{E,T}}{k_{y,T}}}\right) \tag{4}$$

The β term in Eqn. (4) is a multiplier that, referring to Figure 6, moves the plot of $\sqrt{(k_{E,T}/k_{y,T})}$ vertically to account for various geometric and material property parameters. Since the $(L - w)$ term in Eqn. (4) is the L_e value that has already been determined at ambient temperature [9], the only unknown in Eqn. (4) is β. By setting L_e^T equal to L_e^T* from Figure 6, the corresponding β values can be determined that are necessary to preserve the equality from Figure 6.

The black dashed line in Figure 7 indicates a β value of 1.20, which approximately represents the average of the β values for the data sets in Figure 7 plus one standard deviation. Selecting a higher β value drives more conservatism into the prediction of V_u. For σ_y = 345 MPa, a slightly lower β value of 1.15 was determined.

Replacing the L_e term in Eqn. (1) with L_e^T from Eqn. (4) results in the temperature-dependent form of Eqn. (1):

$$V_u = V_{cr} \bullet \frac{L}{(L-w)(\beta)\left(\sqrt{k_{E,T}/k_{y,T}}\right)} \bullet Q_v \qquad (5)$$

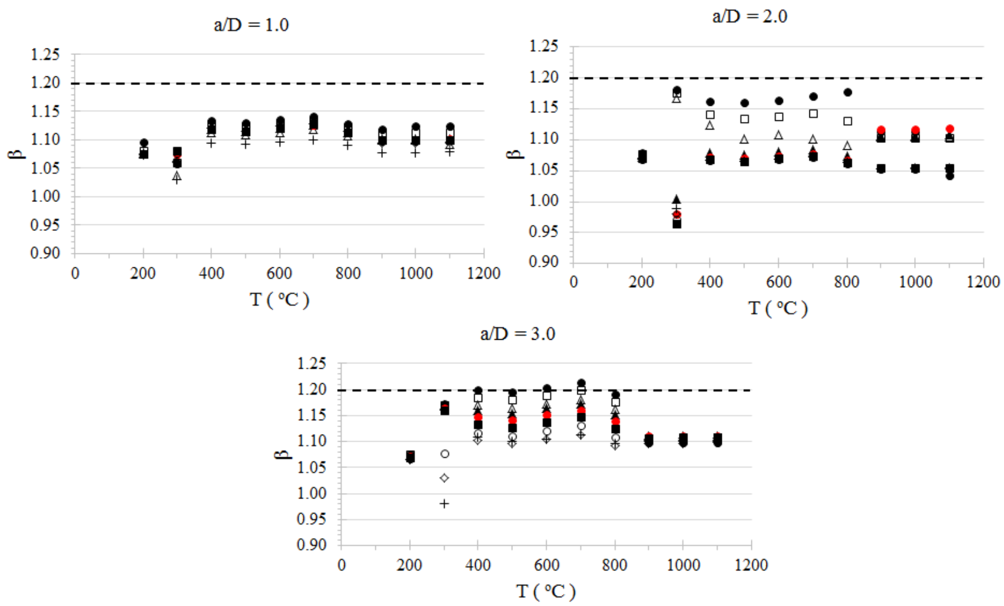

Figure 7. Plot of β versus temperature for web plates with a/D = 1.0, 2.0, and 3.0 and σ_y of 250 MPa.

Table 1 compares ultimate postbuckling shear load values calculated from FE models and Eqn. (5) with published experimental data [10, 11] (V_u^{FE}, V_u, and V_u^{Exp}, respectively). The V_u^{FE}/V_u^{Exp} and V_u/V_u^{Exp} performance ratios show how well V_u^{FE} and V_u compare with experimental data. V_u values in particular are observed to come within 13% of the V_u^{Exp} values. The V_u value for specimen TG3 at 700°C produced a slightly more conservative prediction, however this is a reasonable expectation given the variations in material properties at higher steel temperatures [8]. Linear interpolation and extrapolation were used to calculate w for the TG3 and TG4 models since their σ_y values at 20°C were not precisely 250 MPa.

Table 1. Comparison of ultimate postbuckling shear load values.

Specimen	a/D	D/t_w	D (m)	T (°C)	σ_y (MPa)	V_u^{FE} (kN)	V_u (kN)	V_u^{Exp} (kN)	V_u^{FE}/V_u^{Exp}	V_u/V_u^{Exp}
TG3	1.0	153	0.305	20	288	82.4	82.4	79.85	1.03	1.03
				400	288	69.4	59.2	67.63	1.03	0.87
				565	166	40.2	34.2	34.34	1.17	0.99
				700	66	15.7	13.6	17.15	0.92	0.79
TG4	1.0	113	0.305	20	233	102.9	109.4	111.8	0.92	0.98
				400	233	82.9	74.8	77.1	1.08	0.97
				700	54	18.9	17.2	15.94	1.18	1.08

CONCLUSION

This paper presented an extension of the compression-based approach for predictions of ultimate postbucking shear strength in steel plate girder web plates at elevated temperatures. Through the study of numerous experimentally-validated finite element models, two temperature-dependent parameters (β and $\sqrt{(k_{E,T}/k_{y,T})}$) were proposed that allow the compression model to be used for steel temperatures of 20^{o}C to 1100^{o}C. This is a significant advancement for the design and analysis of steel plate girders because it shows that a web shear buckling model based on compression (which is a more representative portrayal of the web shear buckling mechanism) can accurately predict ultimate postbuckling shear load values across a wide range of geometric, material, and temperature parameters.

REFERENCES

[1] M. Garlock, I. Payá-Zaforteza, V. Kodur and L. Gu, "Fire Hazard in Bridges: Review, Assessment, and Repair Strategies," *Engineering Structures*, vol. 35, pp. 89-98, 2011.

[2] I. Payá-Zaforteza and M. Garlock, "A numerical investigation on the fire response of a steel girder bridge," *Journal of Constructional Steel Research, Elvesier, V.75*, pp. 93-103, 2012.

[3] D. W. White and M. G. Barker, "Shear Resistance of Transversely Stiffened Steel I-Girders," *Journal of Structural Engineering*, vol. 134, no. 9, pp. 1425-1436, 2008.

[4] C. H. Yoo and S. C. Lee, "Mechanics of Web Panel Postbuckling Behavior in Shear," *Journal of Structural Engineering*, vol. 132, no. 1, pp. 1580-1589, 2006.

[5] K. N. Rahal and J. E. Harding, "Transversely stiffened girder webs subjected to shear loading - part 1: behaviour," *Proceedings of the Institution of Civil Engineers*, vol. 89, no. 2, pp. 47-65, 1990.

[6] K. N. Rahal and J. E. Harding, "Transversely stiffened girder webs subjected to shear loading - part 2: stiffener design," *Proceedings of the Institution of Civil Engineers*, vol. 89, no. 2, pp. 67-87, 1990.

[7] C. Marsh, W. Ajam and H.-K. Ha, "Finite Element Analysis of Postbuckled Shear Webs," *Journal of Structural Engineering*, vol. 114, no. 7, pp. 1571-1587, 1988.

[8] M. E. M. Garlock and J. D. Glassman, "Elevated temperature evaluation of an existing analytical model for steel web shear buckling," *Journal of Constructional Steel Research*, vol. 101, pp. 395-406, 2014.

[9] J. D. Glassman and M. E. M. Garlock, "A compression model for ultimate postbuckling shear strength," *Thin-Walled Structures*, vol. 102, pp. 258-272, 2016.

[10] V. Vimonsatit, K.-H. Tan and S.-K. Ting, "Shear strength of plate girder web panel at elevated temperature," *Journal of Constructional Steel Research*, vol. 63, pp. 1442-1451, 2007.

[11] V. Vimonsatit, K.-H. Tan and Z.-H. Qian, "Testing of Plate Girder Web Panel Loaded in Shear at Elevated Temperature," *Journal of Structural Engineering*, vol. 133, no. 6, pp. 815-824, 2007.

[12] S. P. Timoshenko and J. M. Gere, Theory of Elastic Stability, Second Edition, New York: McGraw-Hill Book Company, Inc., 1961.

[13] R. D. Ziemian, Guide to Stability Design Criteria for Metal Structures, 6th ed., Hoboken: John Wiley & Sons, 2010.

[14] American Association of State Highway and Transportation Officials, "AASHTO LRFD Bridge Design Specifications (6th Edition)," 2012. [Online]. Available: http://www.knovel.com/knovel2/Toc.jsp?BookID=4852. [Accessed 13 February 2013].

[15] European Committee for Standardization (CEN), "Eurocode 1: Actions on Structures - Part 1-2: General Actions - Actions on Structures Exposed to Fire," CEN, Brussels, 2002.

Analysis of the Factors that Influence the Maximum Adiabatic Temperatures in I-girder Bridges

GUILLEM PERIS-SAYOL[1,2], IGNACIO PAYA-ZAFORTEZA[2], SEBASTIA BALASCH-PARISI[3] and JOSE ALOS-MOYA[2]

ABSTRACT

Bridges are a critical element of the transportation system of a country. To ensure bridge safety and functionality, bridge design is guided by bridge standards which prescribe the loads to be considered when designing a bridge or when assessing its structural performance. However, bridge standards do not make any reference to fire, despite the fact that bridge fires are a real threat and a major concern nowadays. This paper uses Computational Fluid Dynamics simulations to study the parameters influencing the temperatures in the gas surrounding I girder bridges during a fire, since this is a critical parameter governing the response of the bridge. More specifically, the study considers four geometric parameters (vertical clearance, bridge substructure configuration, span length and bridge width) and two fire scenario parameters (position of the fire load and type of fuel). Results show that vertical clearance, type of fuel and position of the fire load are the most influential parameters for the flange temperatures and that web temperatures are also influenced by the bridge substructure configuration.

1. INTRODUCTION

Bridges are a critical element of the transportation system of a country whose loss can have important consequences. To ensure bridge safety and functionality, bridge design is guided by bridge standards which prescribe the loads to be considered when designing a bridge or when assessing its structural performance. These standards detail dead and live loads as well as accidental loads due to earthquakes or vehicle impacts among others. However, they do not make any reference to fire. The only standard containing information on how to deal with bridge fires is the National Fire Protection Association's NFPA 502 "Standard for road tunnels, bridges and other limited access highways" [1]. This standard contains some guidelines that apply to bridges over 300

[1]Euroestudios, Ingenieros de Consulta. c/ Castelló 128, 28006 Madrid, Spain.
[2]ICITECH, Departamento de Ingeniería de la Construcción. Universitat Politècnica de València. Camino de Vera S/N, 46071 Spain.
[3]Dpto. de Estadística e Investigación Operativa Aplicadas y Calidad, Universitat Politècnica de València. Camino de Vera s/n, 46071 Valencia, Spain.

m long, but the guidelines are along general lines and do not explain how to analyze a bridge under fire loads or how to protect bridges against fires. This lack of guidelines is a problem because bridge fires are a real threat and a major concern nowadays as pointed out by Garlock et al. [2] and Peris-Sayol et al. [3].

The temperature in the gas surrounding a specific bridge deck is a critical parameter governing the response of the bridge to a fire due to its influence on the mechanical properties of the bridge construction materials. High temperatures can cause the collapse of the bridge due to loss of resistance of the materials as it happened in the MacArthur Maze in Oakland in 2007 or in a bridge near Hazel Park in Detroit in 2009. In both cases a tanker truck carrying gasoline crashed under the bridge and caught fire, provoking temperatures higher than 900 ºC and decreasing the mechanical resistance of the bridge in a relatively short time. Both bridges collapsed around 20 minutes after the tanker caught fire.

Temperatures in the gas surrounding the bridge deck can be obtained using Computational Fluid Dynamics (CFDs) models [4-8]. However, building and running a CFD analysis is a task that requires a considerable amount of time and a very skilled team. In this context, the aim of this paper is to analyze the factors that influence the maximum temperatures in the gas surrounding I-girder bridges such as those of Figure 1 as previous research by Peris-Sayol et al. [3] has shown that this type of bridge is very vulnerable to fires. More specifically, this paper studies the influence of four geometric parameters (vertical clearance, bridge substructure configuration, span length and bridge width) and two parameters related to the fire scenario (position of the fire load and type of fuel) on the maximum temperatures in the gas surrounding the bridge deck. A tanker truck fire has been chosen because previous research [3] has shown that this is the most critical case. To reach this goal 32 CFD simulations of different fire scenarios and bridge configurations have been carried out. The fire scenarios were not chosen randomly, they were selected with a 2^{6-1} Taguchi design of experiments technique [9] and the influence of every parameter on the bridge temperatures was obtained with an ANOVA statistical analysis of the CFD results.

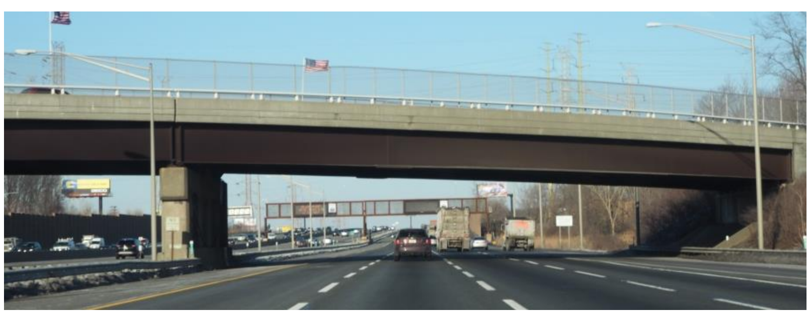

Figure 1. Typical I-girder bridge similar to the bridges analyzed in the paper.

3. METHODS

This section explains the parameters analyzed, the methodology used and the CFD models design.

3.1 Parameters Studied

This study considers six parameters: four of them describe the geometry of the bridge (vertical clearance, bridge substructure configuration, span length and bridge width) and two of them (position of the fire load and type of fuel) are related to the fire scenario. Other parameters such as the soot yield or the position of bridge transverse diaphragms have not been included to avoid running an extremely high number of computer simulations (considering 8 parameters and two possible values for each parameter would have required 128 simulations instead of the 32 simulations done for the present study). Table I and Figure 2 describe the parameters considered and the possible values for each parameter. These values were chosen based on the results of previous studies [3, 5, 7 and 8]. It must be noted that, for all the bridges studied in this paper, the distance between two adjacent girders was taken as 2.6 m and the girder depth as 0.8 m. All the bridges also had a concrete slab 0.2 m thick on top of the I-girders.

TABLE I. PARAMETERS STUDIED.

Vertical Clearance	Bridge Substructure Configuration	Span	Heat Release Rate	Position	Width
6 m	Piers	16 m	1800 kW/m^2 (diesel)	Center-Span	13 m
9 m	Abutment	24 m	2400 kW/m^2 (gasoline)	Abutment	23.4 m

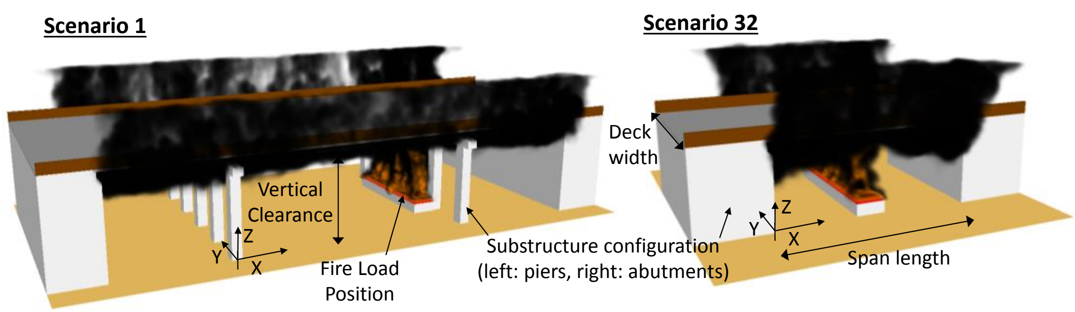

Figure 2. Parameters studied in the analysis. 3D view of two CFD models.

3.2 Computational Fluid Dynamics Models (CFDs).

FDS Software 6.1.1 [11] has been chosen to obtain gas temperatures around the structure. FDS was developed at the National Institute of Standards and Technology (NIST) and applies computational fluid dynamics (CFD) techniques to fire engineering. FDS has been successfully used to study real bridge fires (see e.g. [4-6]). Building the FDS model requires defining: (1) a control volume with its boundary conditions representing the volume in which the entire analysis is carried out, (2) a geometry included in the control volume which represents the geometry of the case study, (3) a mesh or discretization of the control volume, (4) material properties, (5) fire sources, (6) a combustion model, and (7) sensors or elements of the model where the outputs (e.g. temperatures) are recorded.

3.2.1 CONTROL VOLUME AND MESH

The control volume used in this study includes the bridge as well as part of its approaches. The model varies according to the scenario from 28 to 58 m in the x-direction, 27 to 30 meters in the y-direction and 12 to 15 meters in the z-direction (see Figure 2 bottom). The variations depend on the span length, vertical clearance, span width and abutment configuration considered. In FDS the domain is made up of rectilinear volumes called meshes and each mesh is divided into rectangular cells. All the FDS models have cells with dimensions of 0.20 m x 0.20 m x 0.20 m. The total amount of cells in the model ranges from 1,134,000 to 3,262,500. This is a coarse mesh according to FDS guidelines, but the sensitivity analyses conducted showed that it is fine enough for the goals of the present study.

3.2.2 FIRE LOAD AND COMBUSTION MODEL

The FDS model includes the tanker of the tanker truck modeled as a horizontal surface of 30 m^2 (12 x 2.5 m) at one meter above the road level. The CO and soot yields have been chosen according to the recommendations of the SFPE Handbook manual [10] for hydrocarbon liquids and have values of 0.019 and 0.059 respectively. It has been assumed that diesel and gasoline have the same yields.

3.2.3 ADIABATIC TEMPERATURES

The adiabatic surface temperature developed by Wickström et al. [12] is used to transfer the information obtained by the fire model to the thermal model. This adiabatic surface temperature is a fictitious temperature obtained by FDS assuming that the structural element is a perfect insulator and is commonly used for calculating both convective and radiative heat transfer. The use in this paper of adiabatic temperatures is justified because it is a value that does not depend on the material of the bridge and can be used as an input in the thermo-mechanical models.

Adiabatic temperatures are measured in FDS with sensors defined by the user. The model includes sensors only in the central girder, as the fire is centered under it, and therefore, it is the most heated girder. Sensors have been placed in cross sections spaced 20 cm. Each monitored has three sensors located in: the bottom flange (sensor 0), the south face (sensor 1), and the north face (sensor 2). The total number of sensors varies according to the span length.

3.3 Design of Experiments

Running one of the FDS models built for this paper could take up to one week. Therefore, running the 64 fire scenarios resulting from the combination of all the parameters considered in this study was undesirable and a design of experiments using Taguchi’s method [9] has been carried out to select which fire scenarios should be modeled to extract the maximum of information and to know which parameter interactions are important. The resulting scenarios that had to be run are shown in Table II.

TABLE II. EXPERIMENTAL DESIGN OF THE SIMULATIONS.

Nº Case	Parameters					
	Vertical Clearance	**Bridge Substructure Configuration**	**Span**	**Heat Release Rate**	**Position**	**Width**
	9m/6m	**Abutment/Piers**	**16m/24m**	**1800-2400 kW/m^2**	**Central/ Abutment**	**13 m**
1	9m	Piers	24m	2400 kW/m^2	Abutment	23.4m
2	6m	Piers	24m	2400 kW/m^2	Abutment	13m
3	9m	Abutment	24m	2400 kW/m^2	Abutment	13m
4	6m	Abutment	24m	2400 kW/m^2	Abutment	23.4m
5	9m	Piers	16m	2400 kW/m^2	Abutment	13m
6	6m	Piers	16m	2400 kW/m^2	Abutment	23.4m
7	9m	Abutment	16m	2400 kW/m^2	Abutment	23.4m
8	6m	Abutment	16m	2400 kW/m^2	Abutment	13m
9	9m	Piers	24m	1600 kW/m^2	Abutment	13m
10	6m	Piers	24m	1600 kW/m^2	Abutment	23.4m
11	9m	Abutment	24m	1600 kW/m^2	Abutment	23.4m
12	6m	Abutment	24m	1600 kW/m^2	Abutment	13m
13	9m	Piers	16m	1600 kW/m^2	Abutment	23.4m
14	6m	Piers	16m	1600 kW/m^2	Abutment	13m
15	9m	Abutment	16m	1600 kW/m^2	Abutment	13m
16	6m	Abutment	16m	1600 kW/m^2	Abutment	23.4m
17	9m	Piers	24m	2400 kW/m^2	Center-Span	13m
18	6m	Piers	24m	2400 kW/m^2	Center-Span	23.4m
19	9m	Abutment	24m	2400 kW/m^2	Center-Span	23.4m
20	6m	Abutment	24m	2400 kW/m^2	Center-Span	13m
21	9m	Piers	16m	2400 kW/m^2	Center-Span	23.4m
22	6m	Piers	16m	2400 kW/m^2	Center-Span	13m
23	9m	Abutment	16m	2400 kW/m^2	Center-Span	13m
24	6m	Abutment	16m	2400 kW/m^2	Center-Span	23.4m
25	9m	Piers	24m	1600 kW/m^2	Center-Span	23.4m
26	6m	Piers	24m	1600 kW/m^2	Center-Span	13m
27	9m	Abutment	24m	1600 kW/m^2	Center-Span	13m
28	6m	Abutment	24m	1600 kW/m^2	Center-Span	23.4m
29	9m	Piers	16m	1600 kW/m^2	Center-Span	13m
30	6m	Piers	16m	1600 kW/m^2	Center-Span	23.4m
31	9m	Abutment	16m	1600 kW/m^2	Center-Span	23.4m
32	6m	Abutment	16m	1600 kW/m^2	Center-Span	13m

4. RESULTS AND DISCUSSION

Table III shows the maximum web and flange adiabatic temperatures reached on the structure. Web temperatures are the average of the temperatures in the two web faces.

TABLE III. MAXIMUM TEMPERATURES REACHED OVER THE STRUCTURE.

Maximum Temperatures			**Maximum Temperatures**			**Maximum Temperatures**		
Case	**Flange**	**Web**	**Case**	**Flange**	**Web**	**Case**	**Flange**	**Web**
1	1126	1014	12	1114	1160	23	909	886
2	1323	1294	13	990	820	24	1073	1166
3	1301	1340	14	1253	1157	25	694	629
4	1248	1312	15	1178	1215	26	1043	1038
5	1170	1064	16	1225	1290	27	711	650
6	1288	1278	17	905	877	28	1022	1028
7	1170	1226	18	1162	1208	29	702	646
8	1081	1133	19	902	871	30	1037	1044
9	990	821	20	1158	1208	31	696	641
10	1246	1173	21	704	646	32	973	1000
11	1188	1216	22	1157	1204			

To assess the significance of the parameters in the maximum adiabatic temperatures reached over the structure an analysis of variance (ANOVA) using the Statgraphics software [13] was carried out. An ANOVA statistical test compares the means of three or more groups in response to one or several variables and is used to determine the impact of independent variables (e.g. the parameters studied) on the dependent variables (temperatures reached by the structure) in a regression analysis. This impact is given by a coefficient known as the p-value. Low p-values indicate a significant influence (Values below of 0.05). Table IV and V show the ANOVA results. These results show that:

1) The bridge span and bridge width do not influence the maximum adiabatic temperatures of the bridge (p-values of 0.10 and 0.52 for the bottom flange temperatures and 0.35 and 0.77 for web temperatures respectively), although they do have a significant influence on the distribution of temperatures along the longitudinal axis of the bridge.
2) The bottom flange adiabatic temperatures are influenced mainly by the vertical clearance, the fuel type and the position of the fire load (p-values below 0.05 and close to 0). Web temperatures are influenced by the parameters mentioned before, but also by the bridge substructure configuration (p-value of 0.0074) due to the effect that the presence/absence of abutments has on the accumulation of smoke between two consecutive girders.
3) A tanker fire with the tanker close to the abutments is the fire load position that provokes the maximum adiabatic temperatures (values between 1100 and 1300 ºC). This is due to the Coandă effect that makes the fire flames adhere to the walls of the abutments. This effect can make the fire cause problems even in bridges with high vertical clearance.
4) The location of the maximum temperatures depends on the bridge substructure configuration and the position of the fire. If the fire happens under an intermediate span, then the maximum temperatures are usually in the bottom flange, because there is less accumulation of smoke within the girders. If the fire is close to the abutments, then the smoke accumulates within the girders and the maximum temperatures are located in the web.

TABLE IV. RESULTS OF THE ANOVA ANALYSIS FOR FLANGE TEMPERATURE.

Flange Temperatures	**Sum of squares**	**Degrees of freedom**	**Mean Square**	**F-ratio**	**p-value**
Principal Effects					
A: Vertical Clearance	294352	1	294352	107,77	**0,0000**
B: Bridge Substructure	782,497	1	782,497	0,29	0,6042
C: Span Length	8739,08	1	8739,08	3,20	0,1039
D: Heat Release Rate	81466,7	1	81466,7	29,83	**0,0003**
E: Position of the Fire Load	511435	1	511435	187,25	**0,0000**
F: Bridge Width	1214,01	1	1214,01	0,44	0,5201
Interactions					
AB: Clearance-Bridge Sub.	60498,1	1	60498,1	22,15	**0,0008**
AC	145,181	1	145,181	0,05	0,8223
AD	6628,03	1	6628,03	2,43	0,1503
AE: Clearance-Position	93893,9	1	93893,9	34,38	**0,0002**
AF	11044	1	11044	4,04	0,0721
BC	723,521	1	723,521	0,26	0,6180
BD	655,039	1	655,039	0,24	0,6349
BE	193,75	1	193,75	0,07	0,7954
BF	4865,91	1	4865,91	1,78	0,2116
CD	11939,8	1	11939,8	4,37	0,0630
CE	856,566	1	856,566	0,31	0,5878
CF	2484,07	1	2484,07	0,91	0,3627
DE	10028,8	1	10028,8	3,67	0,0843
DF	6704,82	1	6704,82	2,45	0,1482
EF	3587,89	1	3587,89	1,31	0,2784
Residuals	27313,2	10	2731,32		
Total	1,14E+06	31			

TABLE V. RESULTS OF THE ANOVA ANALYSIS FOR WEB TEMPERATURE.

Web Temperatures	**Sum of squares**	**Degrees of freedom**	**Mean Square**	**F-ratio**	**p-value**
Principal Effects					
A: Vertical Clearance	533413	1	533413	93,80	**0,0000**
B: Bridge Substructure	63857,6	1	63857,6	11,23	**0,0074**
C: Span Length	5517,49	1	5517,49	0,97	0,3479
D: Heat Release Rate	151161	1	151161	26,58	**0,0004**
E: Position of the Fire Load	444768	1	444768	78,21	**0,0000**
F: Bridge Width	532,277	1	532,277	0,09	0,7659
Interactions					
AB: Clearance-Bridge Sub.	83045,4	1	83045,4	14,60	**0,0034**
AC	509,683	1	509,683	0,09	0,7708
AD	4304,76	1	4304,76	0,76	0,4047
AE: Clearance-Position	121255	1	121255	21,32	**0,0010**
AF	17145,4	1	17145,4	3,01	0,1131
BC	33,3949	1	33,3949	0,01	0,9404
BD	3086,43	1	3086,43	0,54	0,4782
BE: Bridge Sub.-Position	38680,2	1	38680,2	6,80	**0,0261**
BF	6239,28	1	6239,28	1,10	0,3195
CD	12050,9	1	12050,9	2,12	0,1761
CE	523,18	1	523,18	0,09	0,7679
CF	2075,77	1	2075,77	0,37	0,5592
DE	10552,8	1	10552,8	1,86	0,2030
DF	6036,53	1	6036,53	1,06	0,3271
EF	5513,29	1	5513,29	0,97	0,3480
Residuals	56866,8	10	5686,68		
Total	1,57E+06	31			

5. CONCLUSIONS

This paper studies the factors that influence the maximum temperatures in the gas surrounding I-girder bridges. To reach this goal a combination of CFD models and statistical analyses (design of experiments, ANOVA) have been used. Results show that vertical clearance, type of fuel and position of the fire load are the most influential parameters for the flange temperatures. Web temperatures are also influenced by the bridge substructure configuration. This type of analysis is very relevant as it constitutes the basis for the development of parametric temperature curves specific for bridges.

REFERENCES

1. NFPA (National Fire Protection Association). 2014. "NFPA 502: Standard for Road Tunnels, Bridges, and Other Limited Highways." Quincy, MA, USA.
2. Garlock, M.E., Paya-Zaforteza, I., Gu, L., Kodur, V. 2012. "Fire Hazard in Bridges: Review, Assesment and Repair Strategies." Engineering Structures, 35, pp. 89-98.
3. Peris-Sayol G., Payá-Zaforteza I., Balasch-Parisi S., Alós-Moya J. 2016. "Detailed Analysis of the causes of bridge fires and their associated damage levels." Submitted to the ASCE Journal of Performance of Constructed Facilities.
4. Wright, W., Lattimer, B., Woodworth, M., Nahid, M., Sotelino, E. 2013. "Highway Bridge Fire Assesment Draft Final Report." Prepared for the NCHRP Program Transportation Research Board of the National Academies, Virginia Polytechnic Institute and State University.
5. Alos-Moya J., Paya-Zaforteza I., Garlock, M.E., Loma-Ossorio E., Schiffner D., Hospitaler A. 2014. "Analysis of a Bridge Failure due to fire using Computational Fluid Dynamics and Finite Element Models." Engineering Structures, 68, pp. 96-110.
6. Gong X., Agrawal A.K. 2015. "Numerical Simulation of fire damage to a long-span truss bridge". Journal of bridge Engineering, 20 (10).
7. Peris-Sayol G., Payá-Zaforteza I., Alós-Moya, J., Hospitaler, A. 2014. "A parametric study on the thermos-mechanical response of a multi-girder steel bridge submitted to real fires" [Estudio paramétrico de la respuesta termo-estructural de un puente metálico multijácena sometido a incendios reales]. Informes de la Construcción, 66, Special Issue 1, pp. 1-11. DOI: 10.3989/ic.13.077 . In Spanish.
8. Peris-Sayol G., Payá-Zaforteza I., Alós-Moya, J., Hospitaler, A. 2015. "Analysis of the influence of geometric, modeling and environmental parameters on the fire response of Steel bridges subjected to realistic fire scenarios." Computers and Structures, 158, pp. 333-345.
9. Taguchi, G., Chowdhury, S., Wu, Y. 2005. "Taguchi's Quality Engineering Handbook." Wiley. Hoboken, New Jersey. ISBN 0-471-41334-8.
10. SFPE (Society of Fire Protection Engineering). 2002. "Handbook of Fire Protection Engineering" 3th Edition. NFPA, USA, ISBN 087765-451-4.
11. Mc Grattan K, Hostikka S, Floyd J, Baum H,Rehm R, Mell W, McDermott. 2010. *Fire Dynamics Simulator User's Guide.* NIST Special Publication 1019 Sixth Edition, Gaithersburg, MD.
12. Wickstrom U, Dat Duthinh D, McGrattan K. 2007. "Adiabatic Surface Temperature for Calculating Heat Transfer to Fire Exposed Structures". Interflam. September 2007, Vol. 2: 943-953.
13. StatPoint technologies, Inc. 2010. "STATGRAPHICS®: Centurion XVI User Manual".

Resilient Bridge Design Framework to Extreme Fire Loading

KEVIN MUELLER[1], SHALVA MARJANISHVILI[1]
and SPENCER QUIEL[2]

ABSTRACT

Several recent fire-induced bridge failures have highlighted the need for improved simplified tools to evaluate the response of bridges to fire. A streamlined design framework has been previously developed [1] for efficient calculation of a steel-supported bridge's response to an open-air hydrocarbon pool fire resulting from a tanker truck crash and subsequent fuel spill. The framework consists of four steps: (1) calculate the fire's characteristics; (2) calculate the heat transfer from the fire to the structural elements; (3) calculate the temperature increase of the structural elements; and (4) calculate the resulting material and mechanical response of the structural elements. The approach synthesizes calculation techniques based on both first principles and empirical data to quantify the extent of damage caused by the fire hazard. Due to its efficiency, this approach can be used to calculate an envelope of effects for a wide range of fire parameters. This paper proposes a new framework that uses the point source fire model for quantitative measure and mathematically reproducible definitions of structural resiliency as it pertains to a bridge's ability to minimize the potential for undesirable consequences. The resiliency assessment and design process follows logical progression of steps, starting with the characterization of fire hazards, continuing through analysis simulations. The outcomes of each process are articulated through a series of generalized variables, termed as topology, geometry, damage, and hazard intensity measures. A rigorous probabilistic framework permits consistent characterization of the inherent uncertainties through the process. The proposed framework is well suited for design process through stochastic characterization of assessment measures. Through stepwise approach, the framework facilitates a system wide approach to multi-fire hazard threats by establishing functional relationships between the development of appropriate models, design methods, damage acceptance criteria and tools necessary for implementation. The proposed methodology can be implemented directly for performance assessment, or can be used to as a basis for establishing simpler performance criteria and provisions to achieve resilient structural solutions.

[1]Kevin Mueller & Shalva Marjanishvili, Hinman Consulting Engineers, Inc., One Bush Street, Suite 510, San Francisco, CA 94104, U.S.A.
[2]Spencer Quiel, Lehigh University, Department of Civil & Environmental Engineering, 117 ATLSS Drive, IMBT Lab, Bethlehem, PA 18015, U.S.A.

INTRODUCTION

On April 29, 2007 around 3am, a gasoline tanker truck overturned while traveling through the MacArthur Maze in Oakland, California. This type of accident routinely occurs throughout the United States, typically on rural highways with limited surrounding infrastructure. However, when an accident occurs under a bridge or highway span, the large pool fire can have devastating effects on the structural performance under fire [2]. These low-probability-high-consequence events highlight the significant threat to our built environment and how our current "collapse proof" design methods are not sufficient [3]. The design team selects specific threats and analyzes the structure to resist these threats to a certain performance level. The resulting design may be unable to handle even a small increase in threat, which leads to an inefficient design and large vulnerabilities to the public.

This paper will introduce the framework to design structures to resist the effects of fire using a resiliency approach. Namely, the structure should be able to resist, adapt to, and recover from exposure to a wide range of threats [4,5]. Resiliency can be applied at all levels of our built environment, from component behavior to system interaction. The framework presented herein focuses on a single structure (cable-stay bridge) exposed to a high-intensity hydrocarbon pool fire.

ROBUSTNESS AND RESILIENCY

When dealing with accidental threats (i.e., tanker truck crash) it is impossible to know exactly where and at what magnitude it will occur. To determine how a structure will respond, it is useful to incorporate the concept of robustness into the resilience model. A system with high robustness is able to maintain stability under a wide range of credible threats, while a system with a low robustness is not able to maintain stability. There are two ways to handle the concept of robustness in design:

Method 1) Traditional "Collapse-Proof" Design

- Step 1. Determine structural geometry
- Step 2. Determine threat magnitude and locations
- Step 3. Analyze structure to threats
- Step 4. Calculate response parameters of structural components
- Step 5. Provide local strengthening, if necessary
- Step 6. Structural system is robust up to maximum threat considered

Method 2) Proposed "Resilient" Design

- Step 1. Determine structural geometry
- Step 2. Determine threat magnitude and locations
- Step 3. Determine acceptable consequences
- Step 4. Analyze structure to threats
- Step 5. Determine acceptable extent of damage and compare to Step 4
- Step 6. Improve design if damage level is not acceptable
    - i. Revise structural geometry for same extent of damage
    - ii. Allow increased damage for same geometry
- Step 7. Structural system is robust within appropriate damage level

The proposed resilient design framework is based on the assumption that robustness is a fixed property of the system and is uniquely tied to the structural configuration as shown in Equation 1:

$$Robustness = f(topology, geometry) \quad (1)$$

Topology in Equation 1 refers to the structural configuration relative to the site. Considering that the threat locations are relative to the same site as the structure, topology essentially relates the structural configuration to the threats. Similarly, the geometry term in Equation 1 refers to the layout of the structural load bearing elements. Both of these term are absolute properties and cannot be changed without modification to the site or structural system. This way, when the site location and structural system is selected, so is the inherent robustness.

Now that the robustness of the system is fixed to the structural system and site location, resilience can represent a variable property that fluctuates with design decisions, as reflected in Equation 2:

$$Resilience = f(resistance, adaptation, recovery) \quad (2)$$

Resistance in Equation 2 refers to the structural system's ability to withstand a prescribed hazard (i.e., the system's robustness against the prescribed hazard). A higher level of resistance allows the structure to rapidly recover from a wide range of threats without damage. However, even robust systems may experience damage when subjected to extreme loads. Allowing damage during an extreme event is already commonplace in the blast, earthquake, and fire communities. Therefore, enough resistance should be provide so that the allowable damage is limited to minimize casualties and reduce the likelihood of catastrophic structural failure. The adaptation and recovery components of Equation 2 are understood and formulated at higher-level emergency planning efforts. These terms are also not well suited for incorporation into design parameters that relate to the structural system behavior. Modifying Equation 2 to relate resistance in terms of robustness and hazard is reflected in Equation 3:

$$Resilience = f(robustness, hazard) = f(topology, geometry, hazard) \quad (3)$$

In Equation 3, resilience is now directly correlated to the topology (structural configuration to hazard), geometry (configuration of structural elements), and hazard (threats considered). The contribution of component strengthening necessary to achieve the desired performance level under the threat is no longer in the resilience formulation. The hazard magnitude is carried by the inherent properties of the structural system under an allowable level of damage. This allows engineers to quantify resilience with an assigned robustness continually throughout the project.

PROPOSED FRAMEWORK

The proposed framework, as described previously, is shown as a flowchart in Figure 1. It is centered on a performance-based calculation of the consequences due to fire-induced local damage. As a starting point, a risk-based integral is constructed to calculate the likely magnitude of consequences in terms of system topology and geometry. The methodology is based on the total probability theorem, similar to that used by several performance-based approaches [6, 7]:

$$C(T) = \iint G(DM \mid IM) \cdot DM(IM) \cdot dDM \cdot dIM \tag{4}$$

DM(IM) is the cumulative probability of damage *DM*, given the intensity measure *IM* and represents the topology function for the system. The topology function informs about expected damage due to the certain event. Multiple events can be included using numerical simulation techniques [8].

G(DM|IM) is the cumulative probability of consequences (total collapse) given the damage *DM* and represents the geometry function. The geometry function informs about the structure's ability to absorb localized damages as identified in the topology function.

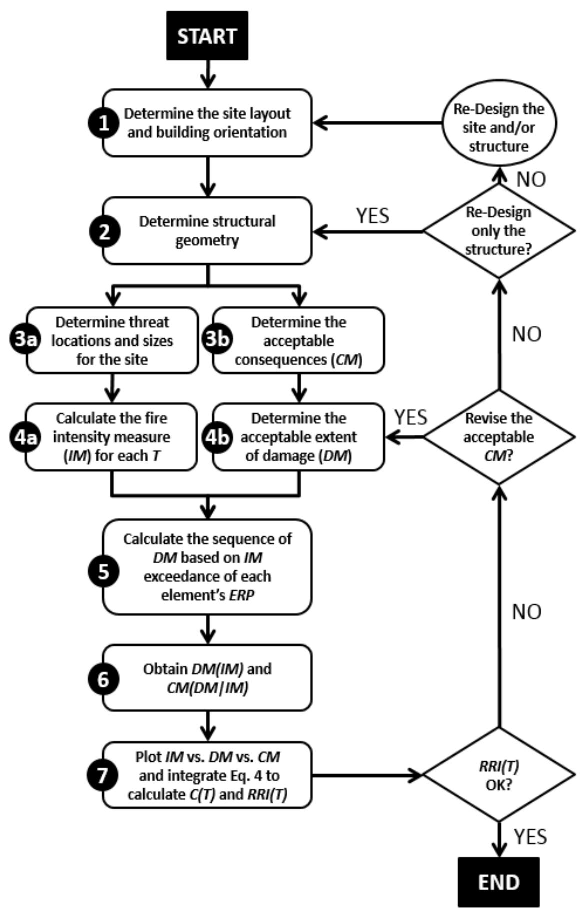

Figure 1. Flowchart Illustrating the Proposed Framework (adopted from [3]).

CASE STUDY

A simple cable-stayed bridge is used to illustrate the proposed framework as shown in Figure 2. Only the cables are analyzed, the tower and bridge deck are not part of this study but the same framework could be applied to these systems.

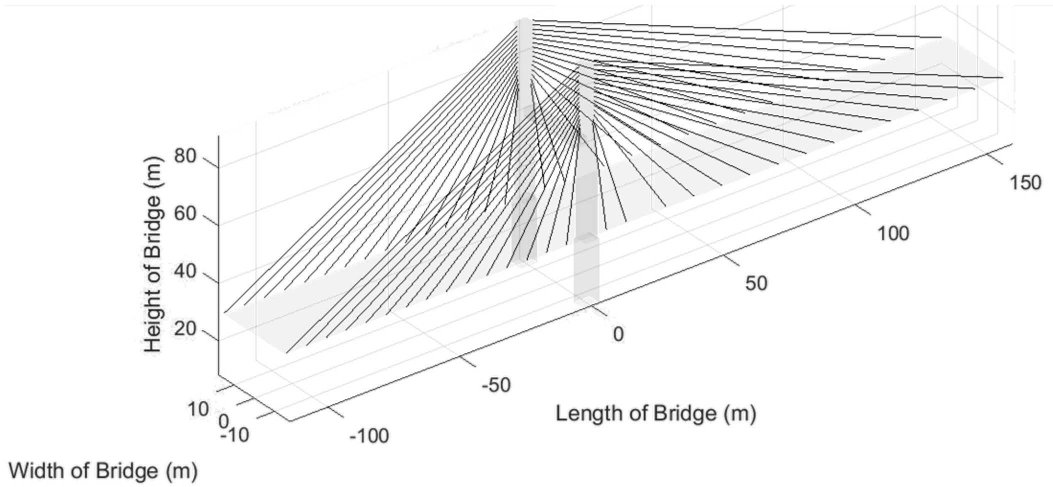

Figure 2. 3D Model of the Case Study Bridge.

The hazard is a pool fire represented as a radiative point source. The convection contribution for a pool fire on the deck of a bridge is minimal, so only the radiation component is considered. The total radiative energy contained in the pool fire radiates out from this point source to the structure. Details on the heat transfer methodology of the point source fire can be found in the literature [9]. Equation 5 shows the incident radiative heat flux, q, on each cable segment as a function of Q, the total heat release rate of the fire; θ, the angle between the cable segment and fire point source; and R, the straight-line distance between the cable segment and fire point source:

$$q = \frac{Q\cos\theta}{4\pi R^2} \tag{5}$$

It is clear the primary driving force that determines the incident radiative heat flux on each cable segment is the distance and angle from the fire location, considering that the total heat release rate has a discrete time-history and remains at a constant position relative to the bridge. For the purposes of this resiliency framework, the relationship between the structure and hazard is the most critical, which can be initially determined without knowing the size or magnitude of the fire. The heat release rate modifier, H (shown in Equation 6) can be used to develop the intensity measure:

$$H = \frac{\cos\theta}{4\pi R^2} \tag{6}$$

After the heat release rate modifier is calculated, the critical fire locations can be easily determined that drive the protection requirements for any magnitude threat. To illustrate this, Figure 3 shows 200 fire threats randomly placed on the bridge deck along the length of the bridge. All of the fire threats are at the same height, representing the mid-height of a typical pool fire created from a 9000 gallon hydrocarbon tanker truck. Figures 4 and 5 show a scatter of the heat release rate modifier of each cable segment for all 200 fire threats. The cable height and distance from the fire is plotted as a percentage, so 1 = highest segment/longest distance from fire and 0 = lowest segment/shortest distance from fire. There is a clear critical relationship between the cable height (Figure 4) and straight-line cable distance from fire (Figure 5) to the heat release rate modifier.

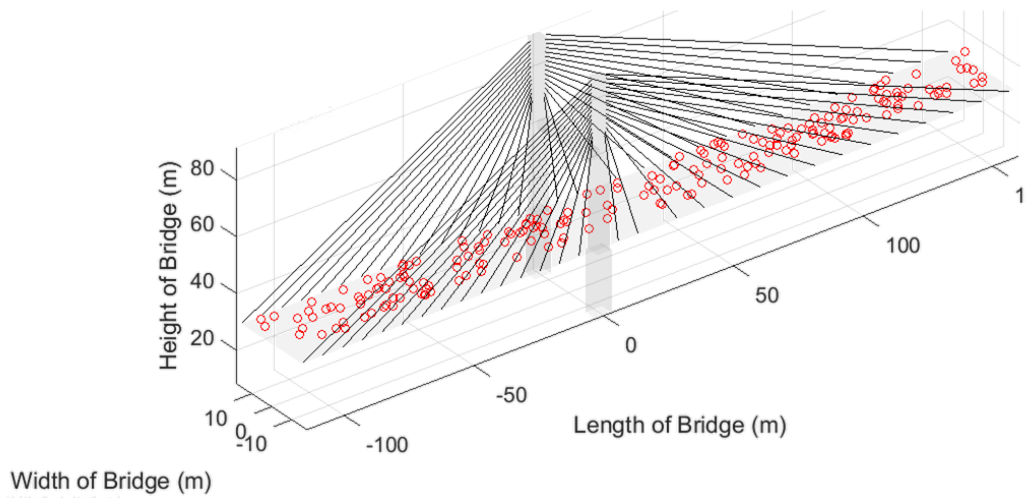

Figure 3. Location of 200 Random Fire Threats on Bridge Deck.

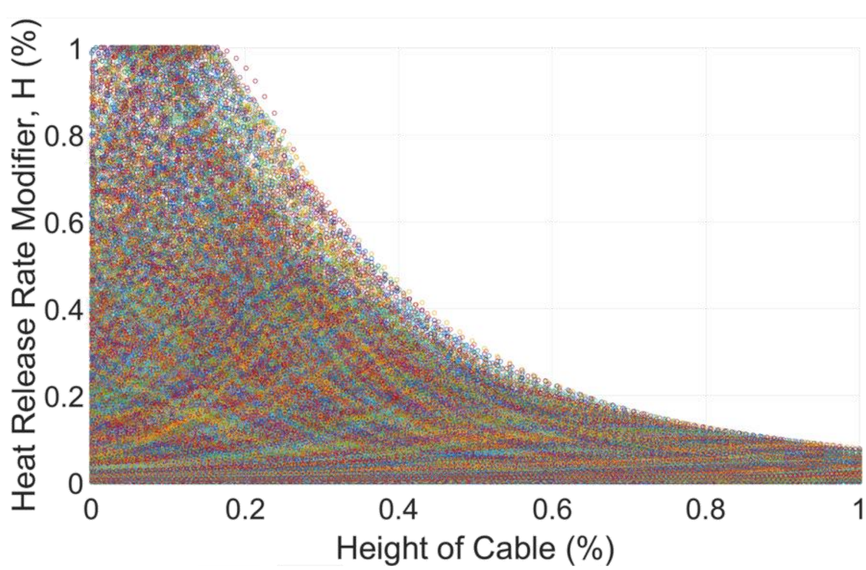

Figure 4. Heat Release Rate Modifier (H) along Cable Height.

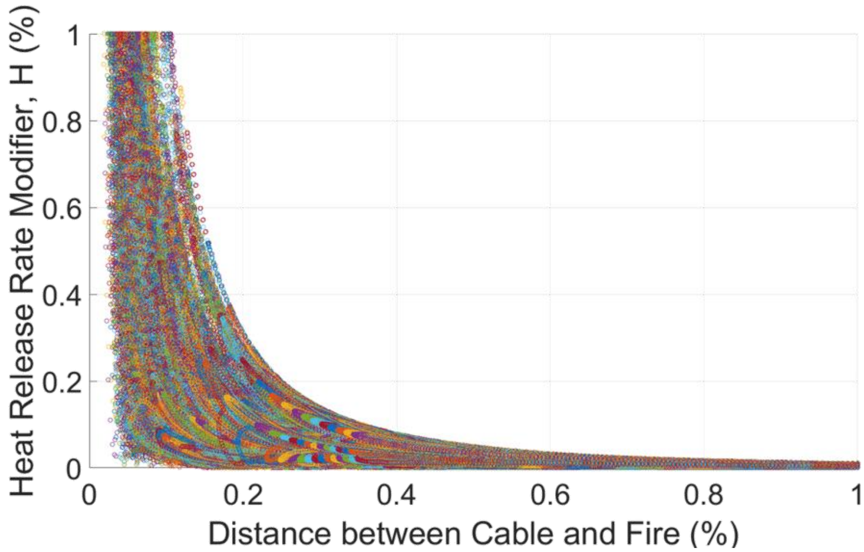

Figure 5. Heat Release Rate Modifier (H) with Cable Distance from Fire.

Upon further analysis, the fire threat that produces the maximum heat release rate modifier at each cable segment can be extracted from Figure 4 to determine the worse-case scenario. Figure 6 shows the maximum heat release rate modifier along the height of the bridge. The noise in the data is due to the relatively large discretization of segments along the length of the cables. However, there is a clear profile of the maximum heat intensity along the height of any cable at any point along the length of the bridge.

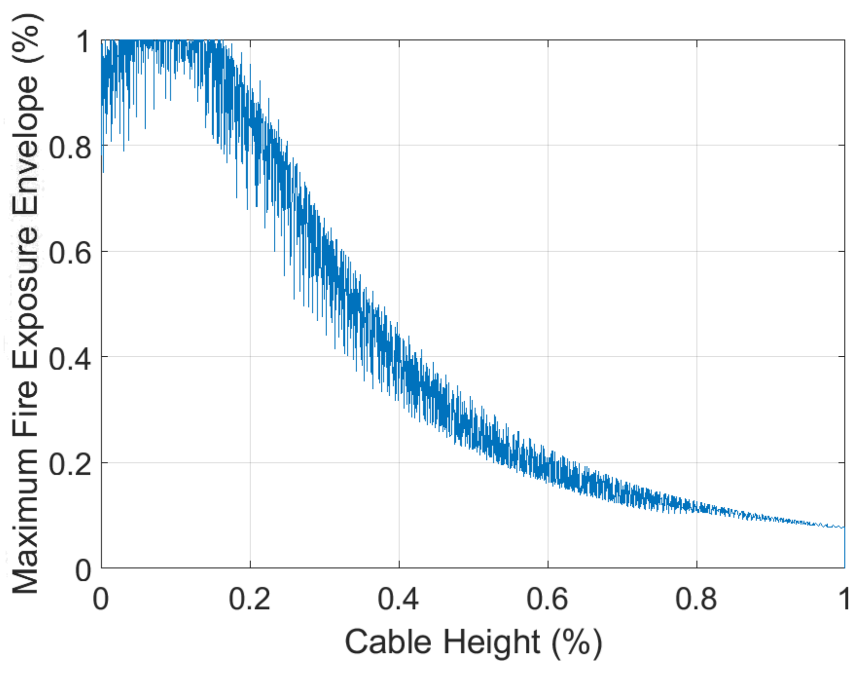

Figure 6. Maximum Fire Exposure Envelope along Cable Height.

After the maximum fire exposure envelope is established for the bridge design, various mitigation options can be employed. Additional analysis needs to be done for the critical fire locations to establish the total energy applied to the critical cable segments (Figure 6). However, instead of having to consider 200 fire threat locations, only those that create the maximum fire exposure envelope need to be analyzed, saving valuable design and allowing this process to be implemented at multiple stages in the project.

CONCLUSIONS

A resiliency and robustness based framework was developed to address common shortcomings of traditional "collapse-proof" design methods. The process created a relationship between the structural system and the fire threat that results in a maximum fire exposure envelope. This framework was applied to an example cable-stay bridge. After implementing this method, various mitigation options would be available to protect the bridge, including:

1) Apply intumescent paint to the cables. This can be optimized by only applying the paint up to the critical cable height as shown in Figure 6. The critical height is defined as the point where the maximum fire exposure levels off (i.e., point where additional damage starts to increase rapidly). For the bridge studied in this paper, the critical height is around 60% from the bridge deck.
2) Change bridge cable design to create a more favorable maximum fire exposure level. Considering the simplicity of this method and ability to easily implement at all stages of design, modification of the bridge layout relative to the site (and subsequently to the threat) could be done to reduce the maximum fire exposure.

REFERENCES

1. Quiel, S., Yokoyama, T., Bregman, L., Mueller, K., Marjanishvili, S. 2015. "A streamlined framework and case study for calculating the response of bridges to open-air tanker truck fires." *Fire Safety Journal*, 73:63-75.
2. Garlock, M., Paya-Zaforteza, I., Kodur, V., Gu, L. 2012. "Fire hazard in bridges: Review, assessment, and repair strategies." *Engineering Structures*, 35:89-98.
3. Marjanishvili, S., Fayad, F., 2015. "Resilient Bridge Design to Extreme Loads." *Proceedings of the 8th New York City Bridge Conference*.
4. Baker J.W., Schubert, M., Faber, M. 2008. "On the assessment of robustness." *Structural Safety*, 30:253-267.
5. Bocchini, P., Frangopol, D.M. 2012. "Optimal resilience- and cost-based post disaster intervention prioritization for bridges along a highway segment," *Journal of Bridge Engineering*, 17:117-129.
6. Barbato M., Petrini, F., Unnikrishman, V.U., Ciampoli, M. 2013. "Performance-based hurricane engineering (PBHE) framework," *Structural Safety*, 45:24-35.
7. FEMA, 2012. "FEMA P-58: Seismic Performance Assessment of Buildings," *Federal Emergency Management Agency (FEMA)*.
8. DoD 2008. "UFC 3-340-02: Structures to Resist the Effects of Accidental Explosions," *Unified Facilities Criteria (UFC)*, Department of Defence (DoD), Washington, DC (superseded TM5-1300).
9. Heskestad, G., 2008. "Fire Plume, Flame Height, and Air Entrainment," *SFPE Handbook on Fire Protection Engineering*, 4th edition,. National Fire Protection Association, Quincy, MA, (Chapter 2-2).

Assessing the Fires on the Deck of Cable Stayed Bridges

PANAGIOTIS KOTSOVINOS, GARY WALKER,
GRAEME FLINT and BARBARA LANE

ABSTRACT

Bridges are community critical infrastructure and, therefore, the consequences arising from extensive structural damage due to a fire on the bridge could be significant. This paper presents the process for the characterisation of the design fires on a bridge deck utilised to assess the thermal and mechanical response of a cable-stayed bridge structure. Future research requirements are also identified.

1 INTRODUCTION/KNOWLEDGE GAP

Bridges are community critical infrastructure and, therefore, the consequences arising from extensive structural damage due to a fire on the bridge could be significant. However, the fire resistance requirements for civil structures such as bridges are not explicitly covered by national building regulations or, typically, by specific owner/operator requirements and would need to be assessed from first principles.

A limited number of studies have been carried out on the assessment of cable stayed bridges from fires on their deck [1, 2, 3]. The majority of previous research is based primarily on steel girder bridges [4, 5, 6] as a response to the MacArthur Maze bridge collapse in Oakland. However, a number of incidents involving fires in cable stayed bridges have occurred in the past such as the ones on the Mezcala and Rio-Antirio bridges that resulted in failure of a stay cable although fortunately without collapse.

This paper will present the first principles approach that was adopted by Arup as part of a recent commercial cable stayed bridge project in the UK.

2 ROBUSTNESS ASSESSMENT PROCESS

Cable stayed bridges typically are formed with large spans (hundreds of meters) and rely on complex load paths to support the bridge structure over areas where piers cannot be provided. The robustness of a cable stayed bridge under fire conditions can be influenced by the type of deck (box girder, ladder deck, etc.) and the arrangement of the steel stay cables (spacing, located on the edges or the middle of the deck, etc.). Cable loss from a fire on the bridge deck could be important given that cable stayed bridges are not typically designed for the potential loss of multiple cables.

In order to carry out an assessment of the robustness of a cable stayed bridge in fire it is proposed to follow the process identified in Figure 1. Such an assessment needs to satisfy the stated fire safety goals and the owner's/operator's requirements for property protection and business continuity. This typically involves understanding potential fire events on the deck, and in the surrounding area leading to and under the bridge.

Figure 2 describes the number of steps that the assessment needs to follow.

This paper will concentrate on the part of the process for the identification of fire hazards where and the resulting design fire characterization for a cable-stayed bridge structure. This is a critical step in the design process since it affects the input to the thermo-mechanical assessment of the bridge structure. Such as an assessment is required so that the fire resistance requirements of bridges are determined.

Note that this paper only considers the potential fire scenarios on the deck. Any fires below the deck or around the site are not presented here.

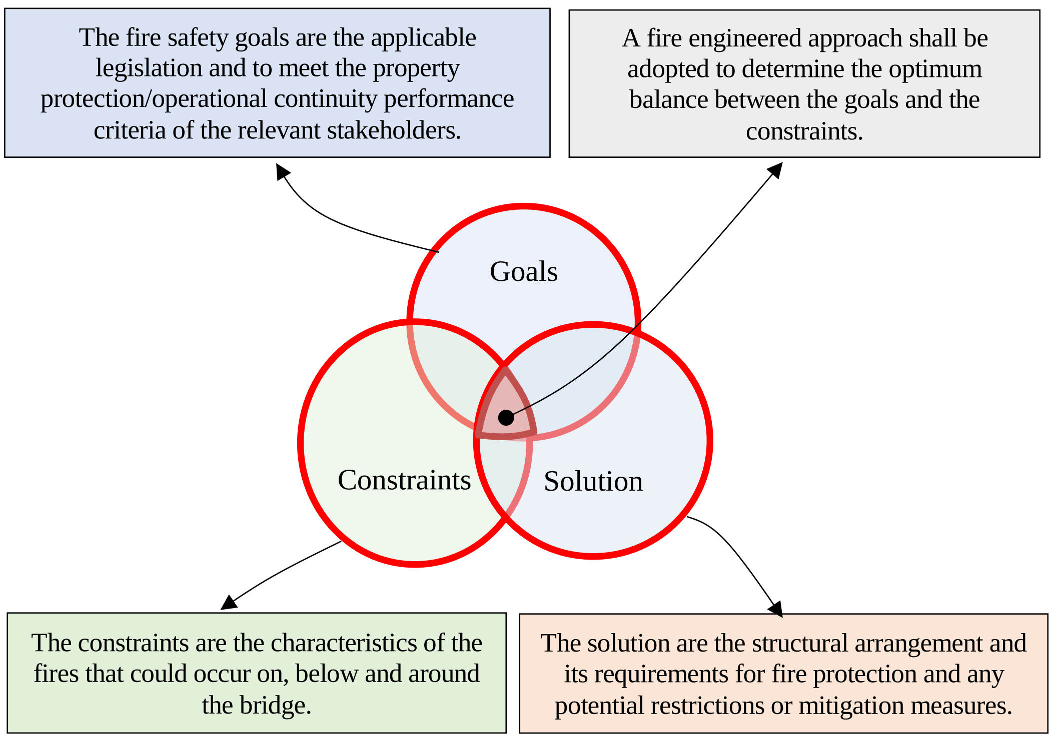

Figure 1. Project goals, constraints and solution of the design process.

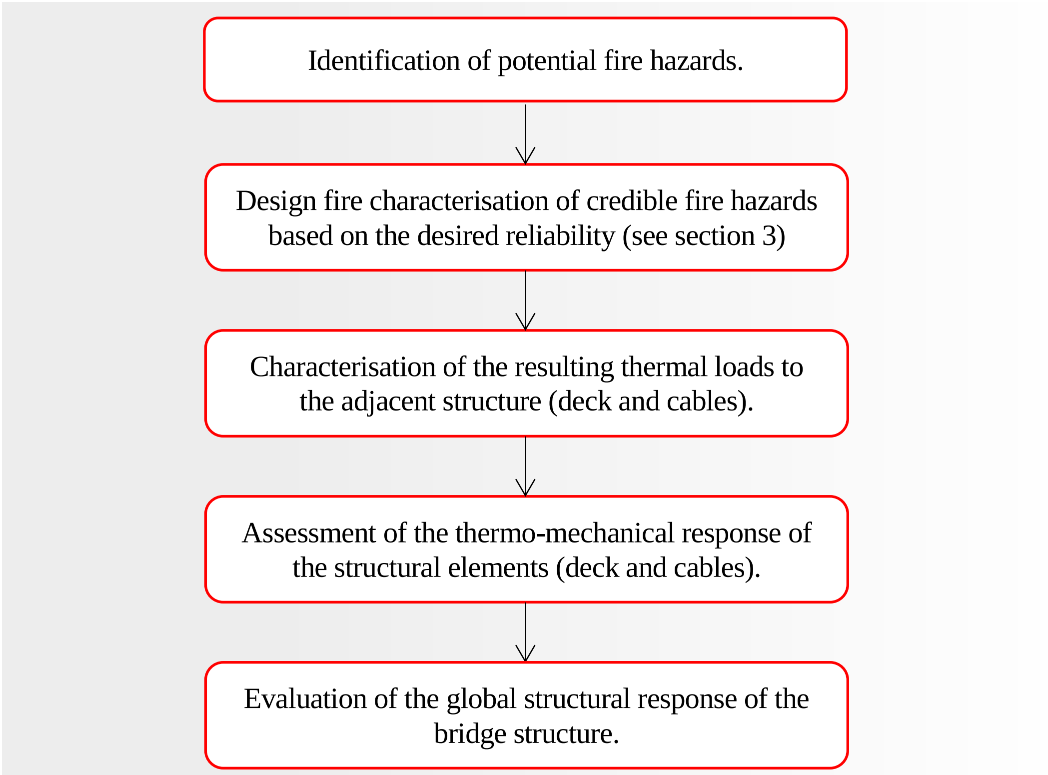

Figure 2. Structural Fire Assessment Process.

3 GOALS (RELIABILITY OF THE BRIDGE)

The required reliability for a bridge project is dependent on the fire safety and property protection/business continuity goals. Depending on the size, use and location of the bridge (and therefore if other alternatives exist in case of an accident) there may be different reliability requirements.

The fire safety goals for the project regarding life safety of s users and staff and fire-fighter life safety will be depended upon local legislation. Note that for critical infrastructure it is likely that the property protection/business continuity goals will drive the required reliability for the project.

To determine the property protection/business continuity goals of the project, the following need to be discussed/agreed with the Owner/Operator of the project.

- Whether damage to the structure from a low likelihood fire scenario leading to local/global collapse is acceptable.
- An acceptable probability of occurrence of a fire scenario
- Specific business continuity requirements (acceptable level of disruption/downtime in case of an accident). This will impact the acceptable damage to the structure requiring significant time and/or resources to repair.
- Willingness to provide restrictions on the traffic of the bridge e.g. HGVs and petrol tankers to be restricted from using the bridge or to be escorted

- Willingness to provide an emergency response plan on the control of the traffic after a fire accident (good management can limit the potential for fire spread between vehicles).
- Whether fires originating due to arson/terrorism need to be considered (and therefore fires potentially igniting in more than one location).
- Whether the bridge needs to be designed for multihazard actions such as fire followed by explosion

4 CONSTRAINTS (POTENTIAL FIRE SCENARIOS ON THE DECK)

In order to determine the potential fire scenarios on the bridge deck the fire consultant, in conjunction with the security consultant of the project carrying out a threat and risk assessment, needs to review the following:

- A traffic study indicating also any future demands of the bridge
- The anticipated traffic speeds and density on the bridge
- Statistics relating to the occurrence of traffic accidents and occurrence of fires in roads in the nearby area and in bridges in general.
- The anticipated types of vehicles crossing the bridge
- The anticipated contents that will be transported by the vehicles crossing the bridge
- Whether suppressions systems and supplies/hydrants will be provided.
- Meeting with the local fire service to understand the capability of the local fire crews to engage and suppress the identified fires and the proximity of the nearby station to the bridge
- Crossfall of the deck and the deck drainage provided to the bridge and the associated drainage rates
- The wind conditions in the area
- The potential for alternative vehicles such as CNG and LNG to cross the bridge now or in the future
- Any heavy industry sites (DSEAR zones or COMAH zones) that would require road transport to use the bridge.
- The potential for ammunition or explosives being transported over or under the bridge for nearby military bases or ammunition factories

In addition to the above, in order to identify the potential fire hazards and their severity, previous notable incidents on road bridges were reviewed [7]. In most of the reported cases, the fire was triggered by an accident (collision, impact etc.) involving a truck transporting flammable material such as gasoline or heating oil. Additionally, the design fires used in tunnels were reviewed [8].

The following four fire scenarios have been identified for a commercial project in the UK:

- a Heavy Goods Vehicle (HGV) fire;
- a petrol tanker fire arising from the early ignition of the fuel at the release location following puncture of the tank containing the fuel;
- a pool fire on the deck of the bridge arising from the delayed ignition of the fuel spilled from the location of the localised failure / puncture of the envelope of the tank of a petrol tanker;
- a tanker transporting Liquefied Natural Gas resulting in pool/jet fires.

Bridges are typically designed to sustain the loss of at least a single cable. As a result, car and van fires, though the most likely to occur, are not considered to lead to failure of more than one stay cable and, therefore, are not considered further.

The consequence of the potentially structurally significant fires need to be considered for all possible fire scenarios in order to assess the risk to the structure (and determine whether such a risk is acceptable to the owners/operators of the bridge).

All available experimental data of HGVs and petrol tankers are from a tunnel environment. Experiments conducted to 'replicate' the environment in a tunnel are unlikely to be representative of the condition for open air fires on the bridge deck due to the enhanced radiative feedback in the enclosed geometry of a tunnel and the forced ventilation applied in the experiments (typical of a tunnel ventilation / smoke extract system) [9]. Therefore, it is anticipated that the peak heat release rate expected from a fire on the deck of a bridge would be of lower severity than that of a comparative tunnel fire. The fire severity of the potential fire scenarios has been assessed from first principles.

4.1 Heavy Goods Vehicle (HGV)

Table A.11.4.1 of NFPA 502 [10] notes experimental data indicating that the peak heat release rate varies from 20MW to 200MW for vehicles in tunnels.

Recent incidents involving HGVs in the UK are summarized below:

- A Co-op delivery lorry fire on the A9 on the 13th July 2012. The content of the lorry was not reported. Photographs taken at the scene (see Figure 3a) suggest persistent flame heights of up to 10m observed at the scene.
- A lorry fire on the M1 on the 19th June 2014. The reported cargo was mattresses. Photographic evidence (see Figure 3b) indicates flames reaching heights of up to 10m from ground surface.
- A lorry loaded with plastics caught fire on the M20 on the 29th November 2012. Photographic evidence (see Figure 3c) suggests flame heights of up to 12-15m from the road surface.

a)


Figure 3. Previous incidents of HGV fires in the UK.

It is assumed that an HGV fire on the bridge deck will be limited by the geometry and nature of the fuel that the vehicle is transporting, i.e. that it is the transported goods that provide the bulk of the combustible fuel for the fire. Experimental measurements of heat release rate per unit area (at various incident heat flux) for a range of plastic and wood materials are provided in Babrauskas and Grayson [12] and therefore the mean heat release rate taken can be determined.

The dimensions of a HGV vary and, therefore, so does the quantity of combustible material transported. For the purpose of this assessment, the maximum permissible dimensions of a HGV in the UK were taken. The fire is assumed to be restricted to the five sides of the trailer. The maximum heat release area can be determined based on the HRRUA of a material type and by considering all 5 sides of the trailer.

The assessment presented, demonstrates that onerous fire heat release rates are 185MW for polypropylene, 130MW for polyethylene and 95MW for polyurethane based on the maximum dimensions of a HGV in the UK.

Based on the above and the peak heat release rate data for tunnels presented, it is considered that a 150MW (corresponding to a heat release rate of 1130kW/m2) fire is representative of a very low likelihood HGV fire event. In addition, for the majority of the cases where the fire size would be around 150MW, the weight of the transported material would be higher than the maximum allowed in the UK which is 44 tonnes.

A 100MW fire might be described by the following.

- A fully developed fire having a heat release rate of 755kW/m2 on the five sides (excluding the base) of the HGV trailer identified in Appendix A1 (i.e. 13.6m x 2.6m x 3.0m (L x W x H)). Such a fire emphasises the length over which the fire base is distributed.
- A higher release rate (1350kW/m2) fire distributed over a smaller area of a non-articulated lorry (i.e. four sides, excluding the base and the side adjacent to the cab, of 8.9m x 2.6m x 2.5m (L x W x H)). Such a fire emphasises the fire intensity and flame height (though it should be noted that this will be affected by the wind).

The anticipated duration of steady-state burning of a 100MW fire is calculated to be approximately 4hours. The thermal load incident on the structural cables should be determined both in the absence and presence of wind. The location of the fire, plus the magnitude and direction of the wind (with reference to the local wind rose) should be selected to maximise the exposure of the structural cables to the thermal load from the fire.

4.2 Petrol Tankers

A peak heat release rate in excess of 200MW was reported in Ingason [8] for a petrol tanker in a tunnel. As noted before, experiments conducted to 'replicate' the environment in a tunnel are unlikely to be representative of the condition for open air fires on the bridge deck.

4.2.1 PUNCTURE – IGNITION – RUPTURE

The scenario assumes that rupture occurs along the entire length of the tank and close to its top. The burning takes place at the subsequent rupture location. Such a scenario was experienced in 2011, when a petrol tanker caught fire under the Paramount Boulevard bridge, Montabello, CA, USA (Figure 4).

For the purposes of this assessment it was assumed that the area of the tanker is 11.7m x 2.5m and the height of the fuel is 2.5m (dimensions selected such as the fire area is maximised). An assessment in accordance to [13] suggests that:

a) the heat release rate is approximately 70MW;
b) the duration of a steady-state fire is approximately 5hours;
c) the visible flame height is approximately 17.8m (measured from the elevated base in the absence of wind).

Figure 4. Petrol Tanker Fire at Paramount Boulevard Bridge, Montabello, CA, USA, 2011.

4.2.2 FUEL SPILL – POOL FIRE

The scenario considers a localised failure / puncture of the envelope of the tank leading to sustained release of fuel onto the deck of the bridge. Subsequent ignition of the fuel leads to a pool fire.

The spill rate (of fuel from the tanker) is a function of the tanker geometry and the hole size and hole location. Petrol tankers vary in capacity (and, therefore, dimension). The maximum capacity of a petrol tanker in the UK is $38m^3$. It is assumed that the tanker is not pressurised. To maximise the spill rate, the height of the free surface of the fuel is taken to be 2.0m initially (and, the cross-section of the tank is adjusted to ensure that the maximum initial volume of the fuel is $38m^3$).

The hole is assumed to develop as a result of a failure of the supply / discharge valve during the initiating event. A review of typical valve sizes has indicated that the diameter of the valve could vary from 80mm to 100mm. The hole is assumed to be located at the bottom of the tanker.

Bridge decks typically have a gradient through the width of the deck (crossfall) and are provided with drainage units (based on the expected rainfall). The deck drainage rate is a function of the downpipe diameter and the lateral (across deck) gradient. For a gradient, that the drainage rate exceeds the maximum spill rate it is unlikely that a non-instantaneous spillage will lead to a significant pool of flammable fuel.

Assuming a low lateral gradient and a drainage rate of $0.018m^3/s$, taking the mean volumetric spill rate during which it exceeds the drainage rate, the steady-state area of the ignited fuel spill is estimated [13] to be $80m^2$. The heat release rate is estimated to be 190MW. The duration of the fire should not exceed 30 minutes.

It should be noted that no assessment of the likelihood of the diameter of the hole (leading to the loss of fuel) has been undertaken. The assessment indicates that a hole size less than 80mm diameter is unlikely to provide a significant pool fire sufficient to be a direct threat to the structural cables. (Though it could lead to a Boiling Liquid Expanding Vapor Explosion also known as BLEVE.)

Figure 5. Spill from a petrol tanker.

4.3 LNG VEHICLES

In some countries such as the UK the transport of LNG through road tankers is allowed (other countries restrict this transportation). LNG tankers transport Liquefied Natural Gas over long distances where pipelines do not exist.

One of the threats of vehicles transporting LNG is fire. Fires resulting from LNG tankers are not frequent but have occurred in the past (in 2002 there was the first incident involving a LNG tanker that resulted in a fire). Some of these fires have led also to an explosion (see Figure 6). A LNG tanker fire specifically on a bridge structure has not been reported in the past. However, where LNG terminal operators have facilities around the bridge, such a scenario needs to be considered.

Figure 6. LNG Tanker Fire on the A-91 motorway in Spain (2002) before an explosion occurred after 20-25 minutes of burning.

An LNG tanker fire could result in the following type of events:

- Pool fire
- Jet fire producing a long/narrow turbulent jet
- Flash fire where the flame front moves through vapour cloud
- BLEVE - Note that BLEVEs are currently outside the scope of this report

The exposure of a flash fire normally lasts no more than a few seconds. After a flash fire burns back to the LNG pool, or if ignition begins at the pool, the result could be a pool fire. Based on the data available in SFPE Handbook [13], LNG has a higher mass burning rate compared to gasoline and therefore a higher heat release rate could be expected for the same amount of fuel.

To characterise an LNG fire, CFD and non-CFD (e.g. PHAST) methodologies can be used. A single peak heat release rate of the LNG fire scenario as for the rest of the proposed design fires cannot be determined. The type and geometry of fire and the fire duration are dependent on the release rate from the vehicle following the rupture of the tank. Assuming a catastrophic tank failure (i.e. a high release rate) would lead to an intense but short duration fire and therefore it would not necessarily represent a conservative thermal exposure for a protected structure. A number of release rates need to be examined to determine the LNG fire scenario that would result in the most onerous thermal load to the structure.

5 CONCLUSIONS AND NEXT STEPS

This paper presents a framework for assessing the robustness of cable stayed bridges from fires in their deck. The potential fire scenarios on a bridge deck that could affect the thermal and structural response of the bridge have been determined.

The following areas of future research have been identified:

- Experimental data on open air fires of HGVs and petrol tankers are required.
- A probabilistic framework that relates the likelihood of a fire and its consequence (i.e. structural damage) is needed. This could allow for the project stakeholders to define their desired level of reliability/resilience depending on their specific property protection and business continuity criteria.

8 REFERENCES

1. Bennetts, I., & Moinuddin, K. (2009). Evaluation of the impact of potential fire scenarios on structural elements of a cable-stayed bridge. Journal of Fire Protection Engineering, 19(2), 85-106.
2. Quiel, S., Yokoyama, T., Mueller, K., Bregman, L., Marjanishvili S. (2015). Mitigating the effects of a tanker truck fire on a cable-stayed bridge, 2nd International Conference on Performance-based and Lifecycle Structural Engineering, Queensland, Australia.
3. Woodworth, M., Hansen, E., McArthur, C., and Abboud, N. (2015) Protection of Cable-Stay Bridges from Accidental and Man-Made Fire Hazards: A Rational Physics-Based Approach to Analyzing Vulnerabilities and Mitigations. Structures Congress 2015: pp. 24-37.
4. Aziz, E. M., Kodur, V. K., Glassman, J. D., & Garlock, M. E. M. (2015). Behavior of steel bridge girders under fire conditions. Journal of Constructional Steel Research, 106, 11-22.
5. Alos-Moya, J., Paya-Zaforteza, I., Garlock, M. E. M., Loma-Ossorio, E., Schiffner, D., & Hospitaler, A. (2014). Analysis of a bridge failure due to fire using computational fluid dynamics and finite element models. Engineering Structures, 68, 96-110.
6. Quiel, S., Yokoyama, T., Bregman, L., Mueller, K., Marjanishvili, S. (2015). "A streamlined framework and case study for calculating the response of bridges to open-air tanker truck fires." Fire Safety Journal, 73, 63-75.
7. Garlock, M., Paya-Zaforteza, I., Kodur, V., & Gu, L. (2012). Fire hazard in bridges: Review, assessment and repair strategies. Engineering Structures, 35, 89-98.
8. Ingason, H. (2006). "Design fires in tunnels," in Safe and Reliable Tunnels, Innovative European Achievements, Lausanne, Switzerland.
9. Carvel, R, Beard, A., Jowitt P., & Drysdale, D. (2004). The influence of tunnel geometry and ventilation on the heat release rate of a fire," Fire Technology, vol. 40, pp. 5-26.
10. NFPA 502, (2014) Standard for Road Tunnels, Bridges, and Other Limited Access Highways.
12. Babrauskas V., & Grayson, S. (1992) Heat Release In Fires, Taylor & Francis.
13. SFPE (2002). Handbook of Fire Protection Engineering, Third Edition, NFPA.

New Design Fires for Performance Based Engineering of Highway Bridges

JIAYU HU[1], RICKY CARVEL[1], ABDEL SANAD[3] and ASIF USMANI[2]

ABSTRACT

This paper presents new design fires resulting from vehicle accidents applied to a commonly found highway bridge in the U.K. The new design fires have been derived by modifying localized fires corresponding to the size of vehicles, in which smoke layer and decay with respect to the distance form fire origin is modelled. Four scenarios including four standard vehicle types are investigated associated with a different mean heat release rate (HRR). The measured mean HRR from burning vehicle tests are used to determine a distribution of heat flux along the bridge span. A performance-based approach proposed, in which the bridge fire and its resistance to fire are determined. This methodology can be used by authorities, which responsible for managing a bridge network to assess its vulnerability to a vehicle fire incident.

NOMENCLATURE

Dof - Degree of freedom
FEM - Finite element method
H_B - Distance between the fire source and the bottom of the beam (m)
HGV - Heavy goods vehicles
L_B - Flame tip length flowing along the lower surface of the beam (m)
LGV - Large goods vehicles
q'' - Heat flux (kW/m^2)
r - Radial distance from the fire plume centreline to measurement location (m)
z' - Virtual position of heat resource (m)

[1]School of Engineering, The University of Edinburgh, King's Buildings, Edinburgh EH9 3JL, U.K.
[2]Department of Mechanical, Aerospace and Civil Engineering, Brunel University London, Middlesex UB8 3PH, Uxbridge, U.K.
[3]Department of Physics, Faculty of Science, Al-Azhar University, Nasr City, 11884 Cairo, Egypt.

INTRODUCTION

Highway bridge fires have a low-probability of occurrence but with potential severe consequences on structural damage and business disruption, leading to very high direct and indirect economic losses. In 2007, a gasoline tanker overturned within the MacArthur Maze freeway interchange in Oakland, California resulting in $6 million a day economic loss during the 26 days closure [1]. In 2004, another tanker truck fire accident occurred on the Wiehlthal Bridge in Germany, which resulted in a total loss of $400 million [2]. In July 2009, a speeding driver hit a fuel tanker with 13,000 gallons of fuel, causing the tanker to impact into a column supporting the 9 Mile Road Bridge in the city of Hazel Park, Michigan bursting into flames under the bridge and resulting in a loss of many millions of dollars [3]. The potential of such a high magnitude of adverse impact requires an intelligent approach to the allocation of limited resource so that the risk of such losses in a bridge network is most optimally mitigated.

There is currently very limited test data available for vehicle fires and most available data is in the context of tunnels, therefore unlikely to provide a realistic representation of bridge fires. As a result of most investigations of bridge performance rely upon code-based on prescriptive fire curves such as standard or hydrocarbon fires which have inherent limitations as discussed by J.Alos-Moay *et al.*[4]. In 2008, C.R. Nobel *et al.* [5] carried out a case study of the MacArthur Maze freeway interchange in which flame temperatures were estimated to be around 3000°F (1649°C). In this study [5], the thermo-mechanical analysis is based on a moving box region with a fixed temperature of 1200°C. In 2012, another study carried out for a simply supported steel highway overpass bridge considering both the hydrocarbon fire and a real tanker fire (referred to as Stoddard's fire, reaching flame temperature of 3000°F) [6]. The study showed that despite the high maximum temperature (assumed in the paper as 1500°C), the simulated bridge survives longer due to significantly lower temperatures at the early stages when compared to the hydrocarbon fire.

NEW DESIGN FIRES

In most previous research, uniform heating along the entire bridge span is commonly assumed [1,7,8]. In order to perform a more realistic representation of a bridge fire, the design fires presented in this paper introduce the possibility of decay along the bridge span. It is expected that a bridge can be subjected to a variety of fires depending upon the size of the vehicle involved in an incident. Further uncertainties arise from the unknown magnitude of combustibles in the burning vehicle and the resulting heat release rate (HRR). To develop a robust methodology for characterising the fire hazard to a bridge, a probabilistic approach should ideally be developed. However in this paper we will restrict our discussion to a deterministic approach, albeit distinction will be made between the sizes of vehicles involved in order to be able to assign different levels of expected performance under fires of different magnitude.

Four types of vehicles including cars, light goods vehicles (LGV), heavy goods vehicles (HGV) and buses or coaches are selected to represent the hazard. "Standard trucks" are commonly used for gravity load characterization on bridges which makes this idea of representing the fire hazard the extension of a familiar notion for structural engineers. Specific vehicle models for each category are sourced from the database in the UK government website (GOV.UK). The area of the localized fire source is assumed to be half the footprint of the four standard vehicles. Measured HRR of burning vehicles in a fuel-controlled regime is obtained from surveys of vehicles fires with the assumption of standard vehicle shapes and sizes. For the purposes of this paper we will restrict the discussion to steel frame composite grillage type bridge structures, which is a very common motorway bridge design in the UK.

When the localized vehicle fire impinges upon a structural steel I-beam, the heat flux incident on the steel beams composite with the concrete deck must be defined. A framework for determining heat fluxes to different parts of the I-beam proposed by Wakamatsu *et al*. [9] and adopted by the SFPE handbook [10] is used. A combined model consisting of a smoke layer away from the fire and the localized Wakamatsu fire is developed in this study, consisting of 4 scenarios as shown in **Figure 1**. In scenario 1 (low intensity fire), the bridge structure is exposed only to heat flux from the smoke with an assumption that only car fires would produce this scenario. Scenario 2 (moderate fire) is considered to be the lower limit of an intermediate fire, in which the flame directly impinges upon the soffit of the bridge deck at a single point. Such a scenario may also exist in a larger car fire. Scenario 3 (severe fire) is considered to be the upper limit of an intermediate fire and is defined by assuming that the whole bridge span is exposed to flame. Scenario 4 is considered for depicting large fire, with whole span exposed to fire and part of heat leak from two sides.

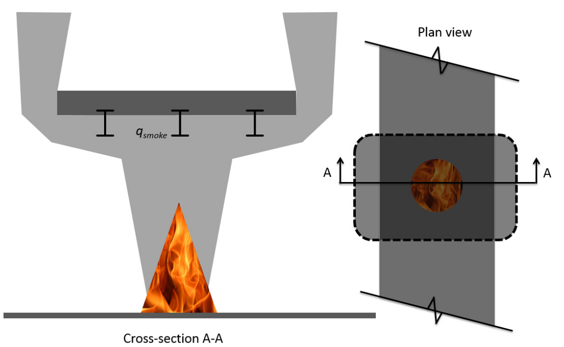

a) Scenario 1: Low intensity fire (0~7.42MW in car fire)

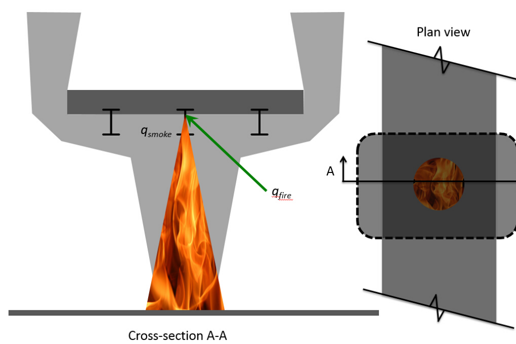

b) Scenario 2: Moderate fire (7.42MW in car fire)

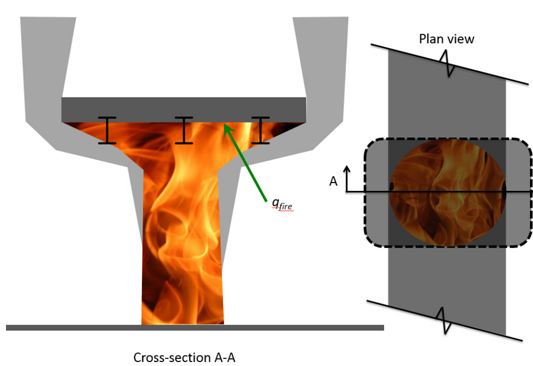

c) Scenario 3: Severe fire

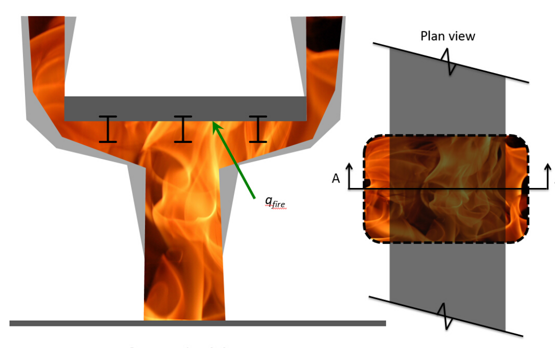

d) Scenario 4: Extreme fire (>=30MW)

Figure 1. Above figures show four different scenarios in vehicle fire (not to scale)

A deep beam may result in a shielding effect of beam flanges, which may lead to a different value of heat flux can measured across the beam section. However, Myllymaki and Kokkala [11] found that for large fires over 2MW, the correlations suggested by Wakamatsu *et al.* [9] for the upward face of the lower flange, web and downward face of the upper flange underestimate the heat flux to these areas on the I-beam as the I-beams are completely engulfed in fire. Hence, a uniform heat flux is used in this project for all the parts of the I-section based on the highest measured value. The heat flux variation is shown as below, which is formulated as a function of flame tip length against the distance from fire origin. In this project, the correction part based on virtual source is ignored.

$$q^{"} = 682e^{-3.4w} \tag{1}$$

Where $w = (r + H_B + z')/(L_B + H_B + z')$

The magnitude of heat flux received over two spans of bridge for different scenarios can be seen in **Figure 2**. In the accident, vehicle fire is assumed to occur at mid-position of the right span and the left span is considered to be engulfed in smoke (trapped in the space between the I-beams). Scenario 1 assumed that the whole span is exposed to heat flux from accumulated smoke. An intermediate fire scenario (between the Scenario 2 and Scenario 3) is illustrated based on an HGV fire and considering a transition period with a smooth exponential decay between the fire-exposed and smoke-exposed part.

HEAT TRANSFER

Both heat transfer and structural analysis are carried out using the commercial finite element software ABAQUS. The steel beams and the transverse diaphragm components are assumed to suffer fire exposure on three faces from the localized heat flux, while concrete deck experiences one-sided heat exposure. A 2D transient heat transfer analysis is performed using the element DC2D4. The bottom surfaces of beams are assumed to receive incident heat fluxes through the mechanisms of convection and radiation, while top of the slab is allowed radiative and conductive

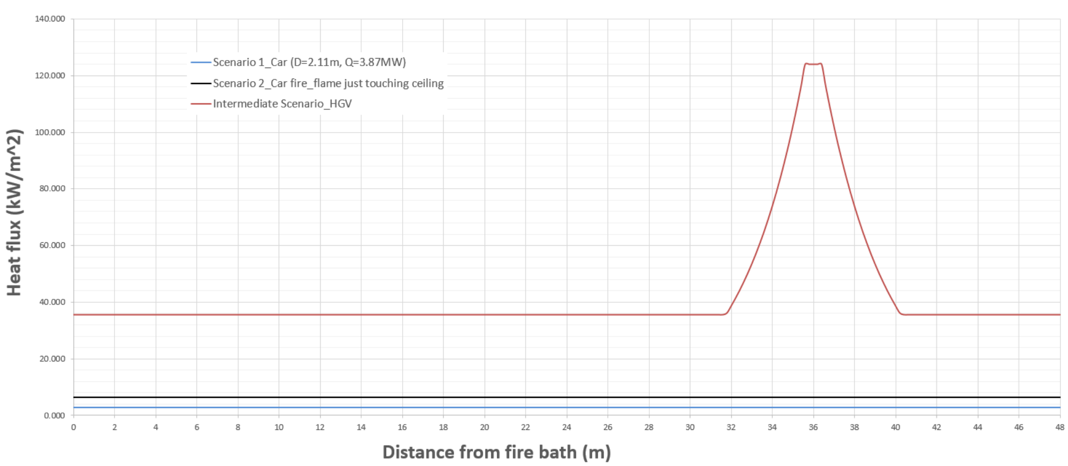

Figure 2 Heat flux variation for different scenarios along the bridge

losses to ambient. Material properties used including temperature-dependent conductivity and specific heat are specified based on Eurocode [12][13]. The boundary conditions of radiation and convection are defined for all heated and non-heated surfaces. The temperature variation along the composite section as a function of heat flux exposure time is shown in the **Figure 3**.

THERMO-MECHANICAL ANALYSIS

BRIDGE BACKGROUND

Transport Scotland is currently using a risk assessment for bridges in two parts: ranking the risks and scoring potential hazards using forms developed by the Department for Transportation; and assessing the risk reduction costs. Based on the discussion with Network Bridges Manager from Transport Scotland, a generic composite steel and concrete highway bridge typically found on the UK motorway network is investigated. The Stirlingshire Link Motorway Bridge (**Figure 4**) located in the rural area of Greater Glasgow, U.K., which is a skew two-span, simply supported bridge of steel concrete composite construction.

LAYOUT AND BOUNDARY CONDITION

In order to simplify the model and enable a more generic investigation, the actual bridge dimensions are regularized making five primary beams parallel to each other with identical overall lengths of 57.6m over the two spans. Two grillage models using beam elements are developed in both the original skew configuration and an adapted rectangular configuration in order to investigate the effect of skewness on the bridge thermo-mechanical response. Two further models using shell elements for concrete slab and beam elements for the I-beams are created for a more realistic structural representation of the structural system with the composite action modelled using multi-freedom constraints.

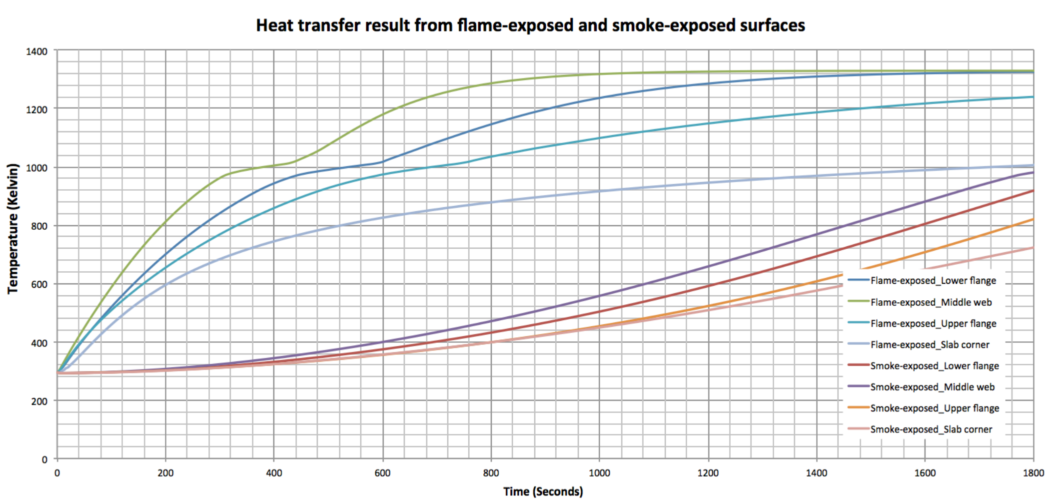

Figure 3. Temperature evolution with time along the composite section

For both primary beams, the middle support above the central pier is set to be fully fixed in 5 dofs other than rotation about the horizontal axis perpendicular to the longitudinal beam axis. At the two end supports above abutments, the horizontal displacement and rotations in the same sense are free while all other dofs are restrained. Identical boundary conditions at both ends of each span are used for the elements representing the concrete deck (rotations free in the same sense as the beams and translations along the beam axes directions also free).

RESULTS

Half of the bridge is assumed to be heated assuming an HGV accident and the other span is considered to be engulfed by smoke. Instead of using a uniform heating along the whole length, a series of new design fires are considered corresponding to different scenarios along the span. In this paper, only a moderate fire is assumed based on choosing parameters (HRR and dimensions) corresponding to an HGV. The thermo-mechanical response can be seen from the **Figure 5**, showing that the bridge experiences thermal bowing ([14]) due to a high thermal gradient in the composite deck structure. The calculation aborted at 556s, when flame-exposed surfaces in primary beam reached 731°C and smoke-exposed part reached 90°C.

RESILIENCE OF BRIDGES IN FIRE

Currently there is no national code having specific requirements about bridge fire resistance. This project aims to create provisions to ensure that bridge structures can adequately resist vehicle fires. The project as a whole is intended to study the thermo-mechanical behaviour of bridge under fire; carrying out risk and vulnerability assessment for existing bridges; and creating an integrated computational tool for rapid modelling and thermo-mechanical analysis. The risk assessment will be designed to help bridge network managers to understand the magnitude of potential fire risk of in their network and identity the most vulnerable bridge where, in order to mitigate this risk, fire passive protection could be used and therefore resources may be targeted more efficiently within the regional transport network and improve the overall resilience of the network.

Figure 4 General view below span

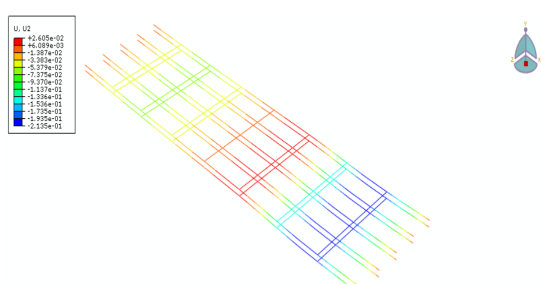

Figure 5 Deformed shape of rectangular grillage

CONCLUSION

As found in the previous study [7], skew bridge seem to possess greater resistance to fire as compared to rectangular bridges. A class of bridge design fires has been developed for a more realistic estimation of bridge performance in fire. The nonlinear FEM analysis was applied to evaluate structural response of a highway bridge under non-uniform heat flux. Comparing with the previous analysis of using uniform heating with hydrocarbon fire, the type of fire exposure have significant influence on fire resistance.

FUTHUR STUDY

Considering the complexity of using FEM and CFD modelling (used in [4]) to analyze the post-fire behaviour of bridges, an integrated computational tool named SIFBuilder (proposed in 2015 [15]), based on the OpenSees software framework will be implemented. This tool couples the design fire loads, the heat transfer and thermal-mechanical analysis in OpenSees, allowing engineers to easily use it without requiring too much fire science knowledge.

The final goal is to create a comprehensive bridge assessment methodology including whole network risk assessment. This could provide useful advice to bridge network managers to consider tailored fire protection for bridges, which can improve the efficiency of limited financial resources. This would ideally be done in multiple phases, beginning with a desk study based on a raking of bridges in terms of risk (through analysis or traffic flows and estimating the consequences of a fire). This should be followed by drawing up a short list for investigating the most vulnerable bridges using the aforementioned tool. Finally retrofit passive fire protection recommendations should be developed based on the resourced available for an even smaller subset of bridges that would minimise the overall network risk.

ACKNOWLEDGEMENTS

The authors would like to thank Wayne Hindshaw from Transport Scotland for sharing information about a real bridge and providing relevant drawings. We would also like to thank Hazel McDonald and Nick Conroy for the opportunity to present the current work to them and for providing valuable advice.

Table 1 Definitions of structural performance due to fire exposure

Fire Intensity	Performance Category	Damage level
Low	Operational	Superficial damage
Moderate	Usable during repair	Significant damage
Severe	Usable after repair	Extensive damage/stable structure
Extreme	Not repairable	Catastrophic damage/unstable (Partial or complete collapse)

REFERENCES

[1] M. Garlock, I. Paya-Zaforteza, V. Kodur, L. Gu, Fire hazard in bridges: Review, assessment and repair strategies, Eng. Struct. 35 (2012) 89–98. doi:10.1016/j.engstruct.2011.11.002.

[2] W. Wright, NCHRP 12-85 Final Report: Highway Bridge Fire Hazard Assessment, (n.d.).

[3] J. Hedden, M. Quagliata, T. Wandzilak, Emergency Renovation, Natl. Steel Bridg. Alliance. (2010).

[4] J. Alos-Moya, I. Paya-Zaforteza, M.E.M. Garlock, E. Loma-Ossorio, D. Schiffner, A. Hospitaler, Analysis of a bridge failure due to fire using computational fluid dynamics and finite element models, Eng. Struct. 68 (2014) 96–110.

[5] C.R. Noble, A.P. Wemhoff, L.D. McMichael, Thermal-structural analysis of the MacArthur Maze Freeway collapse, in: ASME 2008 Heat Transf. Summer Conf. Collocated with Fluids Eng. Energy Sustain. 3rd Energy Nanotechnol. Conf., American Society of Mechanical Engineers, 2008: pp. 511–519.

[6] I. Payá-Zaforteza, M.E.M. Garlock, A numerical investigation on the fire response of a steel girder bridge, J. Constr. Steel Res. 75 (2012) 93–103.

[7] J. Hu, A. Usmani, A. Sanad, Structural response analysis of a highway bridge subjected to accidental vehicle fires, in: A. Usmani, Y. Lu, P. Das (Eds.), First Int. Conf. Struct. Saf. under Fire Blast CONFAB 2015, 2015: pp. 465–474.

[8] V. Kodur, E. Aziz, M. Dwaikat, Evaluating Fire Resistance of Steel Girders in Bridges, J. Bridg. Eng. (2012) 293. doi:10.1061/(ASCE)BE.1943-5592.0000412.

[9] A. Pchelintsev, Y. Hasemi, T. Wakamatsu, Y. Yokobayashi, Experimental and numerical study on the behaviour of a steel beam under ceiling exposed to a localized fire, Fire Saf. Sci. 5 (1997) 1153–1164.

[10] H.T.Z. Kodur V. K. R., SFPE Handbook of Fire Protection Engineering Fifth Edition, 2016. doi:10.1080/10543400701199486.

[11] J. Myllymaki, M. Kokkala, Thermal exposure to a high welded I-beam above a pool fire, in: Struct. Fire Proc. First Int. Work. Copenhagen, Denmark, 19th 20th June, 2000: pp. 211–224.

[12] BSI, Eurocode 2: Design of concrete structures - Part 1-2: General rules - Structural fire design, BS EN 1992 (2004) 97.

[13] B.S. Institution, Eurocode 3: Design of Steel Structures - Part 1.2: General Rules - Structural Fire Design BS EN 1993-1-2: 2005, (2005).

[14] A.S. Usmani, J.M. Rotter, S. Lamont, A.M. Sanad, M. Gillie, Fundamental principles of structural behaviour under thermal effects, Fire Saf. J. 36 (2001) 721–744.

[15] L. Jiang, X. Dai, K. Praveen, A. Usmani, OpenSees-based integrated tool for modelling structures in fire, in: A. Usmani, Y. Lu, P. Das (Eds.), First Int. Conf. Struct. Saf. under Fire Blast CONFAB 2015, 2015: pp. 556–565.

Performance-Based Prioritization of Fire Mitigation for Highway Bridges

SPENCER QUIEL[1], ZHEDA ZHU[1], KEVIN MUELLER[2], AERIK CARLTON[2] and SHALVA MARJANISHVILI[2]

ABSTRACT

The authors have recently developed a 3D Matlab-based modeling tool that links the actual geometry of a bridge structure with the realistic exposure to an open-air hydrocarbon fire caused by a tanker truck accident. The streamlined framework at the core of this tool synthesizes numerous calculation techniques based on both first principles and empirical data to quantify the extent of damage caused by a specified fire hazard. Due to its computational efficiency, this framework can be used to develop an envelope of performance for a range of fire hazard scenarios. In this study, 2,500 analyses are performed using fire hazard parameters that are selected via weighted random sampling from fields of probable inputs. The results of these analyses provide hazard-based consequence maps which can then be used to determine fire protection prioritization among a collection of overpass bridges in an interchange.

INTRODUCTION

Tanker trucks ferrying hydrocarbon fuels, which are common and necessary to meet our society's current transportation demands, have provided the fuel for most of the recent severe fire events involving bridge structures. These events include but are certainly not limited to the collapse of the MacArthur Maze I-80//I-580/I-880 interchange overpass in Oakland, CA, USA in 2007; the near-collapse of the I-65 overpass near Birmingham, AL, USA in 2002; and the severe damage leading to demolition of the Route 22 overpass at I-81 near Harrisburg, PA, USA in 2013. To date, most bridge collapses due to tanker truck fires have involved common highway overpasses (typically supported by steel girders), which represent a large segment of the existing bridge inventory [1].

---

[1]Spencer Quiel, Zheda Zhu, Lehigh University, 117 ATLSS Drive, Bethlehem, PA 18015, USA
[2]Kevin Mueller, Aerik Carlton, Shalva Marjanishvili, Hinman Consulting Engineers, Inc., One Bush Street, Suite 510, San Francisco, CA 94104, USA.

Researchers at Lehigh University and Hinman Consulting Engineers, Inc. have collaboratively developed FLaME (Fire Loading and Mitigation Evaluator), a 3D Matlab-based modeling tool that links the actual geometry of a bridge structure with the realistic exposure to a tanker truck fire. FLaME has been previously used to successfully model the mode and time to failure of the MacArthur Maze overpass in response to the 2007 fire event [2]. The streamlined framework at FLaME's core synthesizes numerous calculation techniques based on both first principles and empirical data to quantify the extent of damage caused by a specified fire hazard. Due to its computational efficiency, this framework can be used to develop an envelope of performance for a series of fire hazard scenarios. These results can then be used to evaluate the risk of damage and the effectiveness of potential fire protection strategies.

New research by the authors has incorporated a more performance-based approach into this framework by accounting for realistic variation in the fire hazard, including its combustion parameters, spill footprint, and location. For a network or grouping of bridge assets (such as the MacArthur Maze interchange), the authors have also begun to incorporate traffic information to determine which bridges may be most susceptible to fire and which pose the greatest loss if they fail. By considering the likelihood and severity of a fire event, the prioritization of fire protection among a group of bridges in a network, interchange, or inventory can be developed.

The MacArthur Maze will be used as an example to demonstrate this hazard-based approach using FLaME. Variation of the fire hazard parameters are performed via weighted random sampling from fields of probable inputs. The results of this example will provide hazard-based consequence maps which can then be used to determine fire protection prioritization among the overpasses in the interchange. This example illustrates how the proposed approach can be used as a decision making tool to strategically protect our highway bridge infrastructure from tanker truck fires.

METHODOLOGY

Fire models of varying complexity have been previously implemented by other researchers and practitioners to calculate the response of bridges to tanker truck pool fires. The majority of these efforts have used models at either the very simple (i.e. standard fire curves) or very complex (i.e. computational fluid dynamics) ends of the spectrum for fire and heat transfer modeling. Most previous efforts have been deterministic (using a worst case fire hazard scenario) or multi-deterministic (using a collection of worst case scenarios to develop an envelope of response) in their approach, due to either the simplistic nature of the fire load calculation or the significant computational resources required for a single analysis. An engineering tool such as FLaME provides a so-called "intermediate" modeling approach, which is capable of conservatively calculating the spatial distribution of structural exposure to a tanker truck fire at computational efficiencies greater than that of CFD models [2].

To date, FLaME has typically been used for multi-deterministic evaluations of a pre-defined series of fire hazards and locations for a long-span bridge or collection of neighboring bridges. The results of these analyses have been used to determine the extent of fire protection or fire avoidance needed to withstand a worst case scenario while minimizing the additional cost of the mitigation (which can be significant). Though the multi-deterministic approach can be effective in many cases, the hazard due to a hydrocarbon fire from a tanker truck is more appropriately represented as a stochastic problem due to high levels of uncertainty associated with the potential location of a tanker truck crash (and the resulting fire) along a roadway, the amount and type of fuel that burns, the fuel spill geometry, and other environmental conditions. Though these fire events are rare and localized, the loss of a bridge due to fire can have an enormous economic impact to the areas it serves and pose a grave threat to user life safety. However, it is often not fiscally feasible to apply fire mitigation to all components and spans in a network of bridges.

The methodology proposed in this paper leverages the FLaME software to provide a decision making tool for prioritizing the amount and extent of fire mitigation against tanker truck fires for steel-supported bridges. The authors are proposing a new framework in which multiple input parameters for the fire hazard analysis in FLaME are selected from weighted random fields. The results of a large series of FLaME analyses (i.e. several thousand) for these scenarios are then mapped over a long-span bridge or a collection of neighboring bridges in order to determine the extent and severity of fire-induced damage. Fire mitigation can then be prioritized and designed using these damage maps according to a given level of risk tolerance.

Calculating the Effects of a Single Fire Hazard

This study focuses on open-air hydrocarbon pool fires resulting from a tanker truck crash or sabotage since the quantity and flammability of its contents poses one of the worst-case hazards to the bridge components. First, the hydrocarbon pool fire is modeled using analytical calculations of the fire characteristics (e.g. flame height, heat release rate, duration, and radiative intensity) based on idealized semi-empirical combustion models. The results of these models can then be used to calculate radiation heat transfer from the fire to the structural elements. For open-air pool fires this size (with footprint dimensions ranging from 4 m to 20 m), radiation is the dominant heat transfer mode and the effects of convection can therefore be neglected [3].

Once the heat release rate and height of the fire are calculated for the given fuel type, fuel quantity, and spill size, the fire can be represented with a solid flame model (i.e. a radiation-emitting 3D object) which can be used to calculate heat transfer to structural elements as shown in Figure 1. The solid flame surfaces are discretized into rectangular elements, each of which emits radiation toward potential targets. For the fire footprint sizes considered for this study, preliminary analyses has indicated that a maximum discretized edge dimension of 1 meter produced an acceptable resolution of resulting radiation heat flux contours. Each surface *i* is assigned an emissive power based on its location in either the luminous zone or the smoke layer. The luminous zone is conservatively modeled as the lower half of the solid flame model, which is consistent with experimental results from Munoz et al. [4]. For this study, values of E_{flame} are calculated according to the empirical expressions developed by Shokri and Beyler [5], and E_{smoke} = 40 kW/m^2 in accordance with the

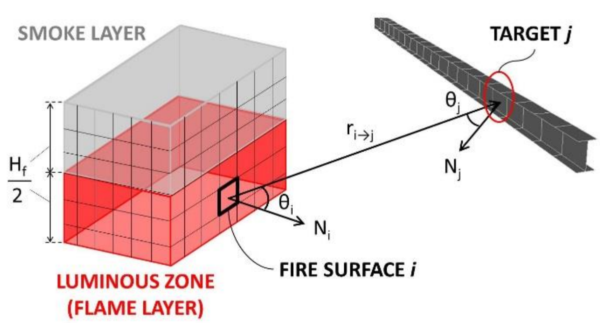

Figure 1. Heat transfer from the MDSF model of a hydrocarbon pool fire to a discretized steel beam.

experimental study of Munoz et al. [4]. The fire representation shown in shown in Figure 1 is referred to as a modified discretized solid flame (MDSF) model, where "modified" refers to the use of layered model with a luminous zone and a smoke layer.

Calculating the summation of radiation heat flux from the discretized fire surface elements allows the user to choose varying fire footprint sizes and shapes, as well as assign varying distributions of thermal emissivity to each vertical zone of the fire. Girders that are shielded from fire exposure by a bridge deck receive no heat flux. Targets engulfed by the solid flame model are directly subjected to an in-fire heat flux [2]. The engulfed heat flux values conservatively combine direct flame radiation and convective heat transfer into a single heat flux that is based on experimental measurements on objects engulfed in a hydrocarbon fire.

Having obtained the radiation heat flux for each target, the increase in the target's temperature can be calculated using a lumped thermal mass approach. Steel girders are represented as line elements that are discretized along their lengths into multiple targets for which lumped mass heat transfer is calculated. For this study, each girder is uniformly discretized such that each lumped mass element j has length L_j (m), and each girder is assumed to have a uniform cross-sectional area, A_j, for all discretized elements along its length. The temperature time history of each target can be used to calculate the corresponding decrease in material strength and stiffness as well as the element's thermal expansion. Time histories of these responses can then be used to evaluate structural behavior either via simple demand-to-capacity calculations or by mapping the results to a structural finite element model. In this paper, the calculated decrease of yield strength is used as a simplified indicator of potential damage.

Calculating a Damage Envelope via a Randomized Parametric Fire Hazards

The authors have developed a procedure for selecting input parameters for a larger series of FLaME analyses from weighted random fields. With this approach, the user can develop an envelope of fire-induced effects which better reflects the uncertainty associated with the characteristics of the fire hazard. This study will focus on a highway interchange which includes several overpass bridges that are in close proximity and cross over one another in several locations. Though many other parameters could also be randomly selected, the following six parameters are considered for random selection from weighted fields or, where appropriate, a probabilistic distribution as a demonstration for this study:

(1) Selection of an overpass in the interchange based on traffic data
(2) Selection of a fire location along the length of that overpass
(3) Selection of a lane location for the tanker truck which catches fire
(4) Selection of a fuel spill footprint based on the lane location
(5) Selection of a volume of fuel for combustion (to account for drainage or runoff)
(6) Selection of a fuel type among those that are likely to be carried by a tanker truck

In practice, the parameters designated for random selection as well as the data needed to drive the random selection process would be determinerd in consultation with a bridge owner such as a state department of transportation or port authority. In this study, publicly available data has been used where possible to develop the weighted random fields. For other parameters for which there is little available data, assumptions have been made to demonstrate the procedure. The focus of this study is to demonstrate the capabilities of the proposed procedure rather than to definitively determine the required fire mitigation of the prototype overpass bridges. The parameters and the weighting functions that have been implemented here could easily be augmented in accordance with the objectives and data for a specific bridge or collection of bridges.

CASE STUDY: THE MACARTHUR MAZE

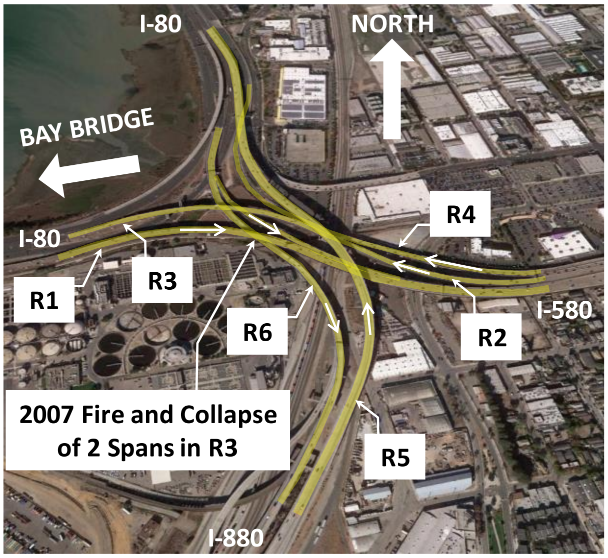

Figure 2. Aerial diagram of the MacArthur Maze interchange

The proposed approach is demonstrated using the MacArthur Maze as a prototype highway interchange comprised of several overpass bridges that are in close proximity. The geometry of the MacArthur Maze, including elevations, is modeled based on digitized satellite images from Google Earth [6]. Figure 2 shows an aerial diagram of the interchange – the critical overpasses that are considered for this analysis are labeled as R1 through R6. The girder dimensions are based on a 2008 Caltrans report which followed the 2007 fire and collapse at this interchange [7]. Per Figure 1, each girder is discretized into 1-m lengths that are each modeled as lumped thermal masses. Similar discretization was used to for the FLaME analyses which successfully calculated the time to failure for the girders in R3 due to the 2007 fire, which was located on the R6 road surface below (see Figure 2) [2]. Heat transfer is not calculated for the bridge decks in this study since the steel girders are much more susceptible to fire effects.

Kodur and Naser [8] recently developed an importance factor calculation which can be used to quantify the vulnerability of bridges to fire hazards. Using that approach, class coefficients ranging from 0.65 to 0.68 were calculated for overpasses R1 through R6 of the MacArthur Maze (neglecting the added historical event weighting due to the 2007 fire). These coefficient values indicate that these bridges have a high risk grade for fire exposure, which suggests that the MacArthur Maze would reasonably warrant an evaluation for fire hazards even without prior knowledge of the 2007 event. FLaME analyses were performed for a total of 2,500 tanker truck fire scenarios in which the six aforementioned input parameters were randomly selected based on user-defined weighted or distributed fields. The selection procedure for the six aforementioned parameters for the MacArthur Maze interchange is demonstrated below.

PARAMETER 1: OVERPASS SELECTION

For each analysis, the overpass on which a tanker truck fire would be located was selected among R1 through R6. The selection was based on a weighted random field that was developed using the annual average daily traffic (*AADT*), the truck traffic percentage (*TTP*), and the average accident rate (*AAR*) for each overpass. Traffic data for each overpass was obtained from the Caltrans traffic volume database [9] for the time period of July 2013 to July 2014. The truck traffic percentage from this data set is for trucks with 5+ axles, which would be typical of a tanker truck. The average accident rate was obtained from a NYDOT database for *AAR* on state highways [10] for the time period of August 2012 through July 2014. The relevant data for each overpass R1 through R6 is shown in Table I. The likelihood of a tanker truck accident on overpass *i* is weighted relative to the other overpasses using Eq. (1).

TABLE I. TRAFFIC DATA USED FOR OVERPASS SELECTION

Overpass No.	AADT (No. vehicles per day)	No. of Lanes	AAR (ACC/MVM)	Road Length (miles)	TTP (%)	Truck ACC	Weighing Value
R1	45953	3	2.53	0.764	0.378	336	0.29
R2	39828	2	2.30	0.691	0.378	239	0.21
R3	40416	3	2.53	0.700	0.378	271	0.24
R4	39828	2	2.30	0.476	0.378	165	0.14
R5	31313	3	2.53	0.988	0.103	81	0.07
R6	31557	2	2.30	0.715	0.103	53	0.05

$$Relative\ Frequency\ of\ Truck\ Accident\ \approx \frac{AADT_i * AAR_i * L_i * TTP_i}{\sum_{j=1}^{n}\left(AADT_j * AAR_j * L_j * TTP_j\right)} \qquad (1)$$

AADT is the total number of vehicles on each overpass for a year divided by 365 days, *AAR* is number of accidents per million vehicle miles, *L* is the total length of the overpass that is considered for this study, and *TTP* is the percentage of overall *AADT* that is comprised of 5+ axle trucks. The overpass location for each FLaME analysis is randomly selected from this weighted field, whose sum is unity.

PARAMETER 2: LOCATION ALONG THE OVERPASS

Once an overpass is selected, the location of the tanker truck fire along the length of that overpass is randomly selected. In practice, the user could assign greater weighting to road segments whose characteristics increased the likelihood for a truck accident. Parameters could include the curvature, cross-slope, or grade of the road as well as historical data of localized traffic buildup or accident rates. Such data was unavailable for this study, and all locations along the overpass lengths in Figure 2 are therefore assigned equal probability for occurrence of a tanker truck accident and resulting fire.

PARAMETER 3: LANE LOCATION

A lane location is selected based on a weighted field which assumes that truck traffic will be heavily biased toward the right-hand lanes in the direction of traffic flow. In practice, a state DOT or other client organization may have data that quantifies the relative frequency of lane locations for truck travel. For this study, the relative weighting of lanes for the presence of a tanker truck is 0.6, 0.3, and 0.1 for the right, middle, and left lanes, respectively, of a 3-lane highway. Weighting values of 0.7 and

0.3 are assigned to the right and left lanes for a 2-lane highway. These values are implemented uniformly across the entire length of all relevant overpass segments in the MacArthur Maze. These values are generally representative of common truck highway traffic and could be easily augmented and tailored in response to more specific data.

PARAMETER 4: SIZE OF FUEL SPILL FOOTPRINT

For simplicity, the footprint of all fuel spills is assumed to be rectangular. The dimensions of the spill footprint are determined according to the selected lane location as shown in Figure 3. Tanker truck fire locations in the outermost right or left lanes are assumed to have a footprint with a width of one lane and a length of 12.2 meters (40 feet). For a truck location in the middle lane, it is assumed that the spill will spread laterally across two lanes (the middle lane and an adjacent lane) due to the cross-slope. For this study, the lateral direction of this two-lane spill (right or left) is randomly selected with equal weighting to each direction. Future studies will account for the cross-slope direction of the each overpass when determining the dimensions of the spill footprint.

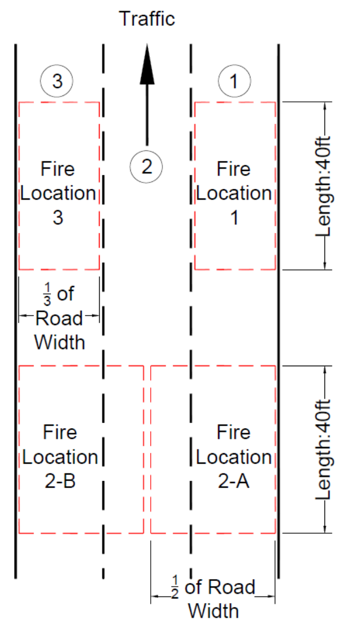

Figure 3. Fire footprint dimensions

PARAMETER 5: FUEL VOLUME

For this study, the total fuel volume of a typical tanker truck is considered to be 34 cubic meters (9,000 gallons). It is realistically assumed that the fuel leakage flow rate from a crashed tanker truck will be larger than the fire's fuel consumption rate such that some of the total fuel volume will drain away or run off from the spill area before it can be consumed. To characterize this loss, the fuel volume for each FLaME analysis is randomly sampled from a normal distribution centered at 75% of total fuel with a standard deviation of 10%. The tail ends of this distribution are capped at 100% and 50%. This random sampling approach could be augmented or replaced with other assumptions or models in practice as needed.

PARAMETER 6: FUEL TYPE

Tanker trucks realistically transport a variety of flammable hydrocarbon liquids and gases, each of which have different combustion characteristics that could influence the heat release and duration of an open-air fire. For this study, three liquid fuels that are commonly transported via tanker truck are considered as a demonstration: gasoline, diesel, and ethanol. The relative weighting for random sampling among these three fuel options is assumed to be 0.5, 0.3, and 0.2 respectively.

RESULTS AND CONCLUSION

For this study, it is assumed that a steel bridge girder will be at risk of incurring damage once its fire-induced temperatures exceed 400°C, beyond which the yield strength decreases per Eurocode 3 [11] and permanent deformations will become more pronounced due to increasing nonlinearity and weakening in the steel's material stiffness. Of the 2,500 FLaME analyses that were performed for the MacArthur Maze interchange using the random weighted selection of fire parameters, 992 (~40%) of the fire hazard cases induced temperatures greater than 400ºC in at least one girder segment. Figure 4 shows an intensity map of girders that experienced damage per this definition. These results show that the most intense concentration of damage occurrence was located in the R6 overpass (which collapsed during the 2007 fire event) where it crosses over R1 and R3 (where R6 has a maximum of 43 cases or ~2% of the 2,500 total exceeding 400ºC). Maps like Figure 4 can be developed from the results of the proposed procedure to address a range of performance metrics and identify the locations and amounts of fire mitigation that would be most effective in reducing the risk of damage due to tanker truck fires.

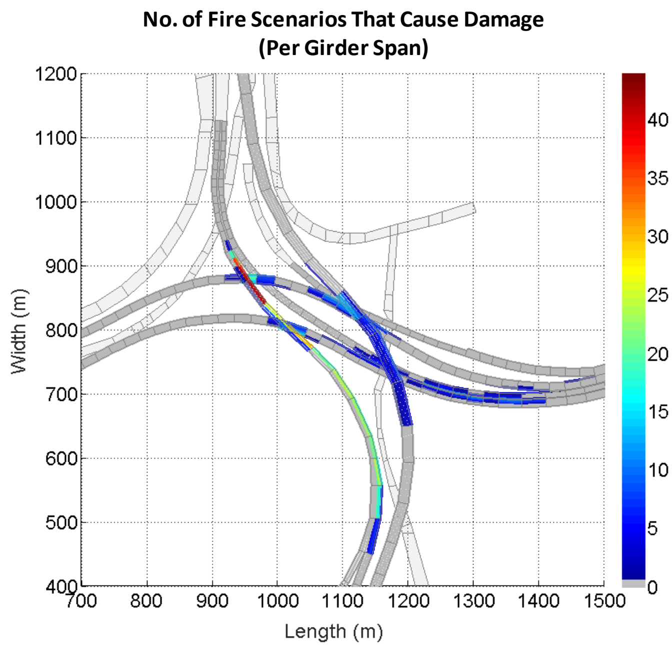

Figure 4. Map of damage frequency results

REFERENCES

1. Garlock, M., Paya-Zaforteza, I., Kodur, V., Gu, L. 2012. "Fire hazard in bridges: Review, assessment, and repair strategies." *Engineering Structures*, 35:89-98.
2. Quiel, S., Yokoyama, T., Bregman, L., Mueller, K., Marjanishvili, S. 2015. "A streamlined framework and case study for calculating the response of bridges to open-air tanker truck fires." *Fire Safety Journal*, 73:63-75.
3. Babrauskas, V. 1983. "Estimating large pool fire burning rates." *Fire Technology*, 19:251-261.
4. Munoz, M., Planas, E., Ferrero, F., Casal, J. 2007. "Predicting the emissive power of hydrocarbon pool fires." *Journal of Hazardous Materials*, 144:725-729.
5. Shokri, M., Beyler, C.L. 1989. "Radiation from large pool fires." *Journal of Fire Protection Engineering*, 4:141-150.
6. Google Earth. MacArthur Maze. 37°49'39" N 122°17'32" W. Accessed March 15, 2016.
7. Caltrans 2008. *Accelerated Bridge Construction Applications in California: A Lessons Learned Report (Version 1.1)*. California Department of Transportation Engineering Services.
8. Kodur, V.K.R., Naser, M.Z. 2013. "Importance factor for design of bridges against fire hazard." *Engineering Structures*, 54:207-220.
9. Caltrans. *Traffic Census Program: Traffic Counts* (http://traffic-counts.dot.ca.gov/). California Department of Transportation. Accessed February 1, 2016.
10. NYDOT. *Average Accident Rates for State Highways by Facility Type (August 1, 2012 to July 31, 2014)* (https://www.dot.ny.gov/divisions/operating/osss/highway-repository/Table2_2014.pdf). New York State Department of Transportation. Accessed February 1, 2016.
11. CEN 2001. *Eurocode 3: Design of Steel Structures, Part 1.2: General Rules – Structural Fire Design*. European Committee for Standardization, Brussels, Belgium.

Fire Test of FRP Members Applied to Railway Bridge

KAMILA CABOVA, PAVEL RYJACEK, ONDREJ HRASKY, LUDVIK KOLPASKY, JAN VUJTECH and FRANTISEK WALD

ABSTRACT

The research reported in this paper is focused on the application of FRP (fibre-reinforced polymers) for the equipment of railway bridges. After investigation of the FRP manufacturer possibilities, several systems were proposed to be applied on railway bridges. As the FRP is a fire sensitive material, systems mounted on a test bridge were exposed to in-situ fire tests in order to verify human safety and possible environmental impact. Based on results of the fire test, FRP solutions for floor on sleepers, floor on consoles and railing were proposed for railway bridge reconstructions.

INTRODUCTION

The steel bridges form large and important part in the large amount of bridges in the Czech Republic. There are totally 2609 steel and composite bridges in the railway network. Their average age of 73 years is getting closer to the end of their assumed life-end. The state of the bridges is generally not very good. The corrosion is still the most common problem, especially on the railing, where the profiles are in some cases missing. Steel profiles on railing and the deck are also popular subject for the thieves.

Recently, FRP materials for reconstructions of railway bridges which may prevent thefts of steel parts, increase the durability and decrease finance spend on maintenance have been promoted. However, specific material parameters, such as low modulus of elasticity, orthotropic material properties and sensitivity to elevated temperatures should be verified before large applications on the railway infrastructure will be enabled. The paper describes in-situ fire tests carried out to verify resistance of bridge floors and railing during fire which is essential for escaping people and fire-fighters, addition of FRP material to fire spread and development of smoke and burning droplets which may pollute surrounding environment.

Kamila Cabova, Pavel Ryjacek, Ondrej Hrasky, Ludvik Kolpasky, Jan Vujtech, Frantisek Wald, Department of Steel and Timber Structures, Faculty of Civil Engineering, Czech Technical University in Prague, Thakurova 7, 166 29 Prague 6, Czech Republic

FRP MEMBERS APPLIED TO STEEL BRIDGE

Several solutions of FRP systems were applied on a typical steel bridge in Hostivice, close to Prague. The bridge consists of two main steel girders with timber bridge sleepers, see Fig. 1. The steel consoles with timber floor and steel railing are mounted to the main girders. The bridge is currently out of order and therefore the floor and railing are heavily damaged. However, it creates the perfect opportunity for the test application of the elements.

The bridge was mounted with FRP floor panels on sleepers, consoles and with the railing systems. Commonly, the floor on the open deck is made from steel plates. For the purpose of experimental investigation, several FRP systems were mounted to the bridge, as shown in Fig. 1 and 2. In each field of the bridge applied systems were different. The panels varied in the surface finishing, see Fig. 3 to Fig. 5, classification of resistance to fire and also way of mounting to sleepers and superstructure. The matrix material was polyester and in one case fire resistant phenol resin. The floor panels on the sleepers were bolted using both special railway bolts S1 and regular bolts of different size (Ryjacek et al, 2015).

The floor on consoles was made from the same decking, but it was placed and bolted on the longitudinal FRP U profiles, attached to the steel cross beams, except the field 2. A bridge deck panel Fiberline FBD 300 was used here instead of a FRP grid. This panel can span the 2.5 m itself.

Railing consists of a pair of U profiles which were attached by combined bonded and bolted connection in order to increase the initial stiffness of the connection, the square tube was used for the handrail due to its high stiffness in torsion, and bottom rails were made from circular tubes, see Fig. 1.

Figure 1. The view on the test bridge before FRP application (left), mounted FRP members on the bridge (right).

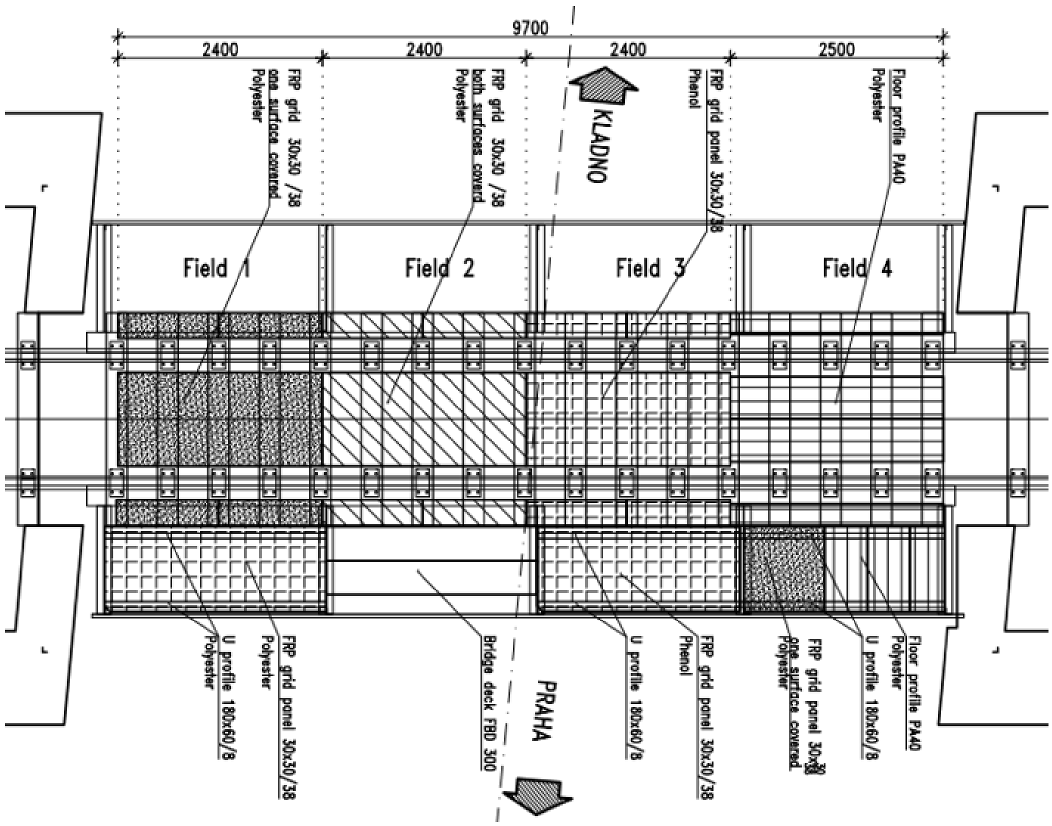

Figure 2. Floor panels mounted on the bridge in Hostivice.

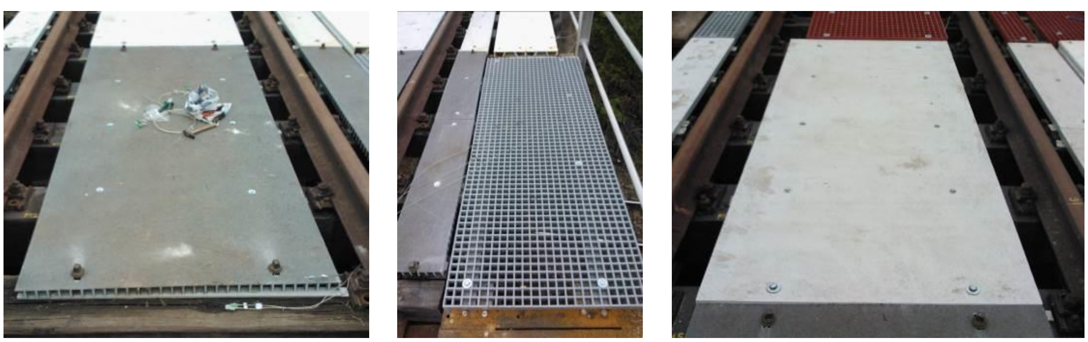

Figure 3. Field 1 - FRP grid on sleepers with laminate deck on the top surface (left), FRP grid on consoles (centre), Field 2 - FRP grid on sleepers with laminate deck on both surfaces (right).

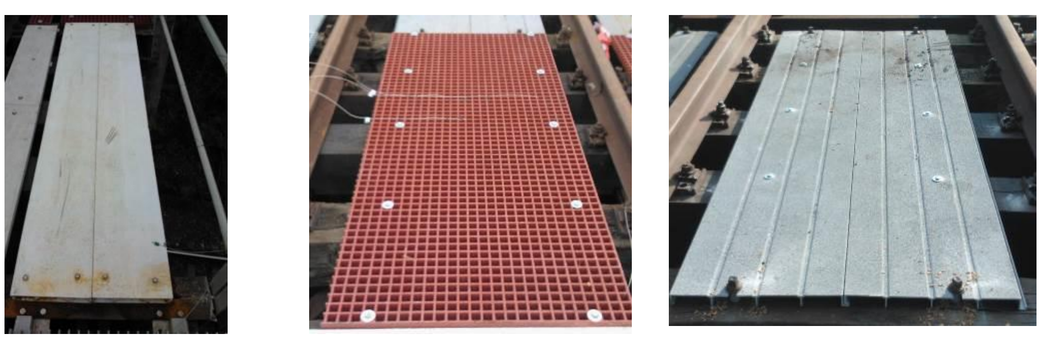

Figure 4. Field 2 - FBD 300 Bridge deck on consoles (left), Field 3 - FRP grid on sleepers (centre), Field 4 –FRP system PA 40 plank on sleepers (right).

FIRE TESTS

Fire scenarios and measurement

For testing of FRP members mounted on the bridge two fire scenarios were chosen. Statistically the most often burning of rubbish and dry leaves between timber sleepers (simulated by 500 g of paper uniformly distributed between sleepers, on area of 0.800 m x 0.355 m) and burning of the electric cables placed in a U profile on the steel consoles (Hrasky, 2016). Both fire loads are illustrated on Fig. 5. Two cables TCEKPFLEZE 7P1,0 D of 1.25 m length which are commonly used on bridges were ignited. Both simultaneously running scenarios were repeated in four fields corresponding to four types of FRP floor and railing systems indicated on Fig. 2.

Resistance of FRP may be evaluated by temperature of the glass transition (T_g) of the matrix resin. This temperature ranges from 90°C to 200°C depending on the type of resin (Bisby, 2012). To evaluate a possible degradation of FRP properties, gas temperature in the vicinity of FRP members was measured by total number of 29 coated thermocouples of diameter 3 mm. 3 thermocouples were located on the floor deck in each field, from 1 to 2 on the consoles floor deck in each field, 3 in different vertical levels of railing and 2 on bearing U profiles of console decks. Structural surface temperature was scanned by thermo-camera. Mechanical loading of 1 kN in the mid-span of FRP console panels which should simulate presence of a fire-fighter was formed by 100 kg of bricks. The vertical deformation of console panels was monitored during the fire test.

Behavior of FRP floor systems on sleepers during fire

Fire scenario between sleepers may be characterized by fast and intensive burning with high temperatures. In comparison burning of cables below consoles was very slow reaching low temperatures. The severity of fire was highly influenced by shape of mounted FRP profiles. The worst fire case was observed in field 4 where the profile PA40 was mounted. At the bottom side of the panel longitudinal ribs along the whole panel length may be found.

Figure 5. Fire load between sleepers, picture from bottom side (left), Burning of two electric cables below console deck (right).

These ribs protected the fire and it could not be cooled down by surrounding gas convection. The gas temperature accumulated under the FRP deck (maximal temperature of 700°C was reached at thermocouple TC10, see Fig. 6) and supported by burning of an impregnation oil of timber sleepers ignited the floor panel, see Fig. 7. Through ribs fire spread quickly from the place of ignition along the whole profile length. The fire, which went beyond the control, was distinguished by fire fighters. As illustrated on Fig. 7 considerable destruction of floor deck PA40 was observed after the fire test.

FRP floor panels made of inner grid which is covered from upper surface by flat deck or covered from both sides with the flat deck were mounted on fields 1 and 2. Due to full upper surface which did not allow gas ventilation, burning was controlled by fire load. However, the temperature below the full floor panel rose up to 350°C (recorded by thermo camera, Fig. 8), the fire burned out quickly. During both fire cases flames were visible along sides of panels. As illustrated on Fig. 8 FRP floor decks were affected only in edge regions and the total resistance was not influenced. The shape of the panel which closely lied on the surface of sleepers did not allow any fire spread.

In field 3 FRP grid panel with fire resistant phenol resin was used. However, gas temperatures below the floor grid reached more than 500°C, see Fig. 9, the duration of temperatures above 150°C which may influence FRP properties did not last longer than 2 min. Thanks to grid shape gas temperature was cooled down by wind flow which ranged from 1.0 to 2.3 m/s. The fire load burnt out quickly, therefore the test was repeated (the second peak on diagram on Fig. 9). After the fire test the FRP products changed the colour only. The load bearing capacity was not influenced.

Behavior of FRP floor and rail systems on consoles during fire

FRP panels and rail members located on steel consoles were influenced by burning of electric cables. Considering slow burning, a distance between FRP members and position of fire and wind flow, measured temperature did not reach high values. In general, gas temperature measured below FRP floor panels with laminated deck on both sides (field 4 and 2) ranged between 100°C and 150°C.

Grid panels with and without fire resistant phenol resin were applied on consoles in field 3 and 1. The maximal measured temperature in the middle of the grid span which was caused by burning of electric cables reached 120°C. This temperature is considered as safe for FRP materials. The maximal vertical deformation measured in mid-span of console deck reached 2.6 mm (field 1).

On railing members, temperature was measured in the middle of span of each rail and handrail. Recorded temperature increase was negligible. The maximal temperature measured during tests was 40°C.

During all fire tests burning droplets which may cause ignition of combustible materials located below the bridge and pollute the environment were not observed.

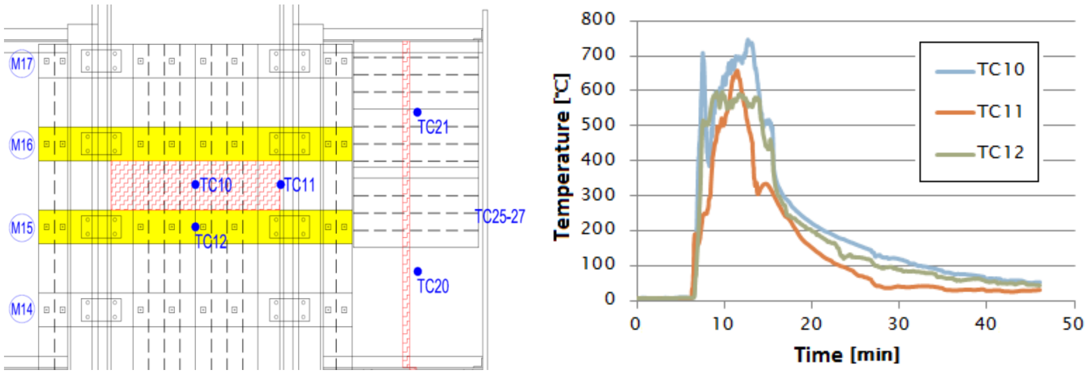

Figure 6. Location of thermocouples in field 4 (left); Measured gas temperature below FRP floor panel PA40 during fire test in field 4 (right).

Figure 7. FRP floor deck PA40 ignited by burning of papers placed between two sleepers (left); Destruction of floor deck PA40 after the fire test (right).

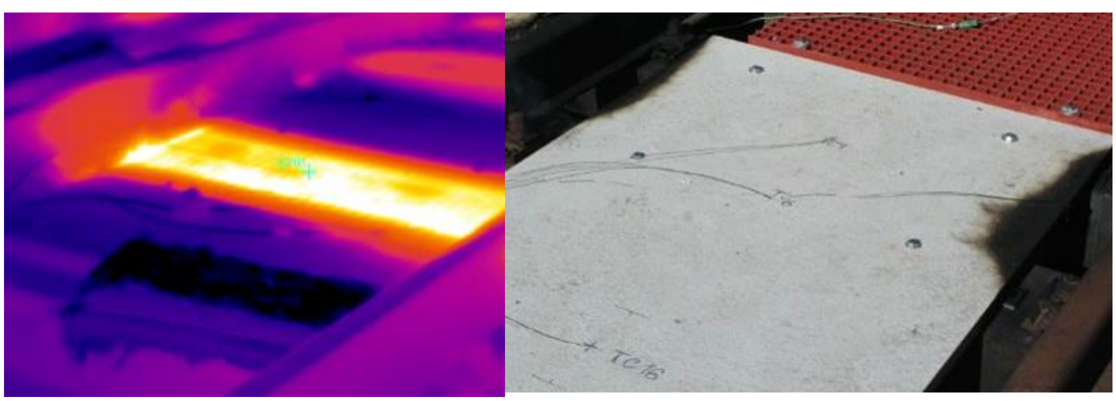

Figure 8. FRP floor deck with laminate deck on the top surface in field 1 controlled by thermo-camera (left); FRP floor deck with laminated decks on both sides in field 2 after the fire test (right).

CONCLUSION

The research described in this paper is focused to verification of new solutions, in order to apply them in large scale on railway bridges. Based on above described fire tests suitable FRP profiles, which may be used on bridges from the view of fire safety, were evaluated. Results of the research may be concluded as follows:

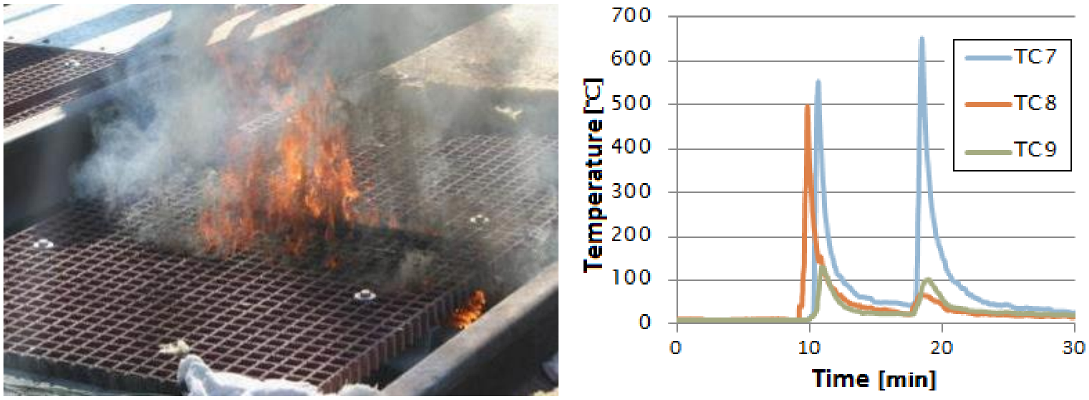

Figure 9. FRP grid floor in field 3 during the fire test (left); Measured gas temperature below FRP grid in field 3 during fire test – TC7 located in the center of gap between sleepers, TC8 close to rail, TC9 between FRP grid and wooden sleeper (right).

- The fire tests on the consoles showed that the effect of burning of electric cables is negligible
- The fire tests on the floor on sleepers showed that except floor panel PA40 with longitudinal ribs at the bottom side all FRP systems – grids with or without laminated decks was able after the fire and some damage to carry the live load.
- Good fire behaviour was achieved even with the profiles of reaction to fire class C to F, so it is not necessary to use more fire resistant gratings with phenol resin. Looking at price of profile of reaction to fire class B which was used in field 3, it is from 2 to 3 times higher comparing to normal grid profile.
- After evaluation of the experiments, the application of the FRP systems was proposed on the old steel bridge. Before public using the bridge will be monitored in order to verify the impact of traffic on the used connections and the reduction of the noise, in comparison with steel floor.

Finally, the FRP equipment showed to be suitable, durable and competitive solution to the traditional steel materials, even for the very traditional railway bridge management.

Research presented in this paper was supported by SŽDC internal grants and project n. 16-18448S in the frame of Czech science foundation (GA CR).

REFERENCES

1. Bisby L. and T. Stratford. 2012. “Opportunities for performance-based fire resistance design of FRP reinforced concrete slabs,” in *Proceedings of conference on FRP Composites in Construction*, Italy.
2. Ryjacek P. et al. 2015. “Aplikace polymerních FRP materiálů na železničních mostech a tunelech”, Reseach report, Czech Technical University in Prague.
3. Hrasky O. 2016. “Vlákny vyztužené polymery za zvýšené teploty”, Diploma thesis, Czech Technical University in Prague.

Behavior of Structural Tunnel Elements Exposed to Fire and Mechanical Loading

MATTHIAS SIEMON and JOCHEN ZEHFUß

ABSTRACT

Incidents like the fire in the Channel Tunnel [1], where concrete spalling with a depth of 30 cm over a length of 500 m was determined, have led to requirements in limiting the spalling depth and involved zone to local and compatible magnitudes. To account for the high heating rate of tunnel fires, the fire resistance of railway tunnel structures was investigated using the German EBA tunnel fire curve [2], which was derived from large-scale fire tests on railway cars [3].

The behavior of structural tunnel elements exposed to fire and mechanical loads have been investigated in several research programs during the last years [4],[5], [6].

In this paper, the results of an extensive research program investigating the fire behavior of two concrete mixtures four small- and two large-scale tests are presented. The small-scale tests prior to the main tests were conducted to determine an appropriate concrete mixture for the large-scale tests. For those tests, real-scale tunnel segments representing a design-relevant sector of an existing railway tunnel were used.

During the large-scale tests, the tunnel segment is loaded with horizontal and vertical loads derived from a calculation taking into account the ground pressure, water pressure and dead loads corresponding to the situation of the existing railway tunnel. Additionally, the resulting restraint forces were calculated using the soil stiffness and the EBA tunnel fire curve [2] as fire scenario and induced via hydraulic jacks (force controlled). In order to avoid additional restraint forces during the experiment, thermal strains due to fire exposure were allowed by the statically determined boundary conditions.

INTRODUCTION

In line with the restoration of parts of the railway tunnel “Schlüchterner Tunnel” in Hesse (Germany), a new reinforced concrete tunnel lining was planned. In a survey assessing the mechanical behavior for two load cases “fire” and “after fire exposure”, the tunnel shell stiffness, restraint forces and moments during and after fire exposure were calculated. The material properties of the reinforced concrete under fire exposure were assumed according to Eurocode 2 1-2 [7], the heat transfer properties according

TU Braunschweig, Institute of Building Materials, Concrete Construction and Fire Protection (iBMB), 38106 Braunschweig, Germany

to Eurocode 1 1-2 [8]. Because the EBA tunnel fire curve leads to a transient calculation, the maximum restraint forces determining the controlling, fire induced load case, were considered in the following calculation of the complete tunnel cross-section to prove the load carrying capacity.

Both calculations, the determination of the tunnel shell stiffness and restraint forces as well as the calculation to determine the cross-sectional load carrying capacity were based on the fact that no spalling would occur over the time of fire exposure. To ensure this, an amount of 2.0 kg/m³ polypropylene fibres were considered in the concrete mixture. This value is listed in Eurocode 2 1-2 [7] as suitable for high strength concrete exposed with the standard ISO 834 fire curve to avoid concrete spalling.

Because the prevention of critical concrete spalling was significant for the validity of the load carrying capacity calculation, it was decided to investigate the spalling behavior of two contemplable concrete mixtures for the later scheduled construction of the tunnel shell. The large-scale tests should show the load carrying capacity over the whole duration of the fire exposure respecting all thermal and mechanical loads considered in the calculations. The tests should also prove the efficiency of the PP fibres to prevent or at least reduce the concrete spalling to an acceptable level.

CONCRETE MIXTURES AND TEST SPECIMENS

Both concrete mixtures can be classified as C25/30 regarding EN 206 [9]. As shown in Table I, the main difference is the cement with the CEM I consisting completely (95-100 %) of clinker and the CEM II with 6-20 % slag sand fraction.

TABLE I. CONCRETE MIXTURES ANALYZED IN THIS PROJECT.

Mixture	**M1**	**M2**
Cement	CEM I 42.5 R	CEM II/A-S 52.5 R
Amount of Cement	330 kg/m³	310 kg/m³
Fly ash	80 kg/m³ Kreament H7 k=0.40	
Water	181 kg/m³	171 kg/m³
Sand 0/2	44 %	
Gravel 2/8	17 %	
Gravel 8/16	39 %	
Organic fibres	2.0 kg/m³ polypropylene fibres	
Plasticizer	4.29 kg	3.72 kg
Consistency	F 4 > 5	
W / C ratio	0.50 (max. 0.55)	0.50 (max. 0.50)
Volumetric air content	1.8 vol.-%	2.8 vol.-%
Class (EN 206)	**C25/30**	**C25/30**

TABLE II. LARGE SCALE TEST SPECIMENS.

	Specimen 1	**Specimen 2**
Date of production	15.03.2012	26.03.2012
Date of test	12.12.2012	19.12.2012
Age	272 days	268 days
Concrete mixture	M2 (CEM II)	M1 (CEM I)

Table II lists the age of the two large-scale specimens and the concrete mixture. For both large-scale test specimens, a number of accompanying cylinders for the determination of the moisture content were produced. They were kept in the same location as the large-scale test specimens and consists of a concrete filled tube with a diameter of 15 cm and a length of 40 cm, matching the thickness of the tunnel shell.

SMALL-SCALE TESTS

In the small-scale tests, a total of four unloaded concrete specimens (*S1* – *S4*) with two specimens for each concrete mixture were analyzed. The specimens had a length of 1 m and a cross-section of 0.4 m x 0.4 m. They were exposed to the EBA tunnel fire curve on the surfaces left and right, where the other surfaces were insulated using mineral wool and insulation plates. The tests were conducted in a small furnace with a top-view cross-section of 1.5 m x 1 m and a height of 1.25 m. Two oil burners were mounted at the front section to heat up the volume. The temperature was controlled using two mantle thermocouples in 10 cm distance to the fire exposed surfaces [10].

All test specimens were 96 days old when a small sample was taken to measure the moisture content by drying the samples at 105 °C and recording the mass loss. The results on the spalling area and depth compared to various older data is shown in Figure 1.

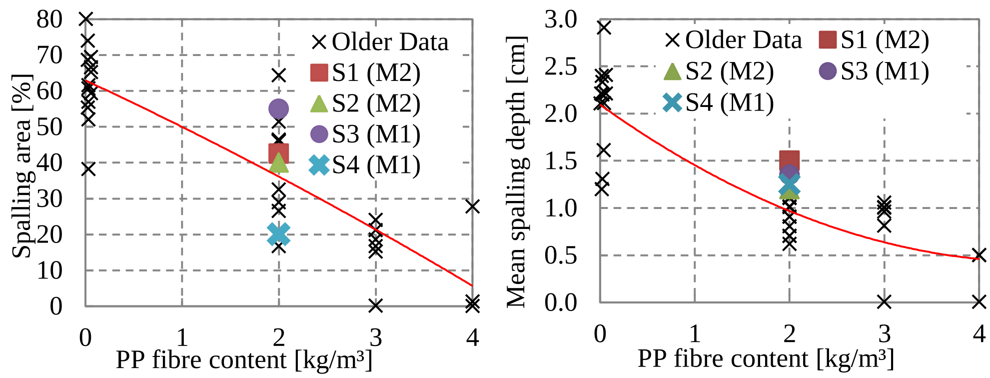

Figure 1. Spalling area and mean depth of the four small-scale test specimens after fire exposure.

LARGE-SCALE TESTS AND TEST SETUP

An overview of the test setup is shown in Figure 3. The location of the oil burners (total amount of six) are marked with yellow lines. Due to the large volume of the furnace, the walls of the chamber were bricked up using gas concrete bricks. Without this, the high heating rate of the EBA tunnel fire curve (see Figure 2) of 240 K/min in the first 5 minutes of fire exposure cannot be ensured for a large chamber volume. The gas concrete walls were dried before the installation of the tunnel shell to prevent the introduction of moisture.

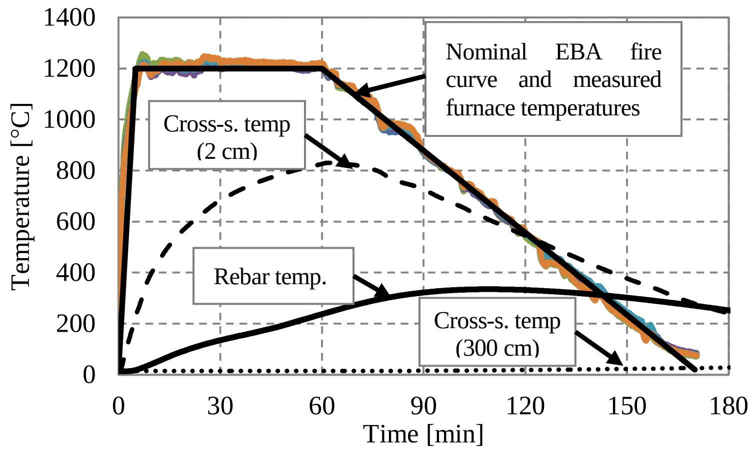

Figure 2. EBA tunnel fire curve, furnace temperature and cross-section temperatures during test (S1).

As shown in Figure 2, the measured furnace temperature near the lower surface show a good agreement with the nominal EBA tunnel fire curve. Additionally, the cross-section temperatures during fire exposure are shown. During fire exposure, in a depth of 2 cm the maximum value about 820 °C is reached in minute 70, whereas the maximum reinforcement temperature (~350 °C) in a depth of 6 cm is reached at minute 110.

The position of the mantle thermocouple for control and measurement of the nearby surface gas temperature were mounted in about 10 cm distance to the lower tunnel shell surface. Overall, six elements were installed (two in a line).

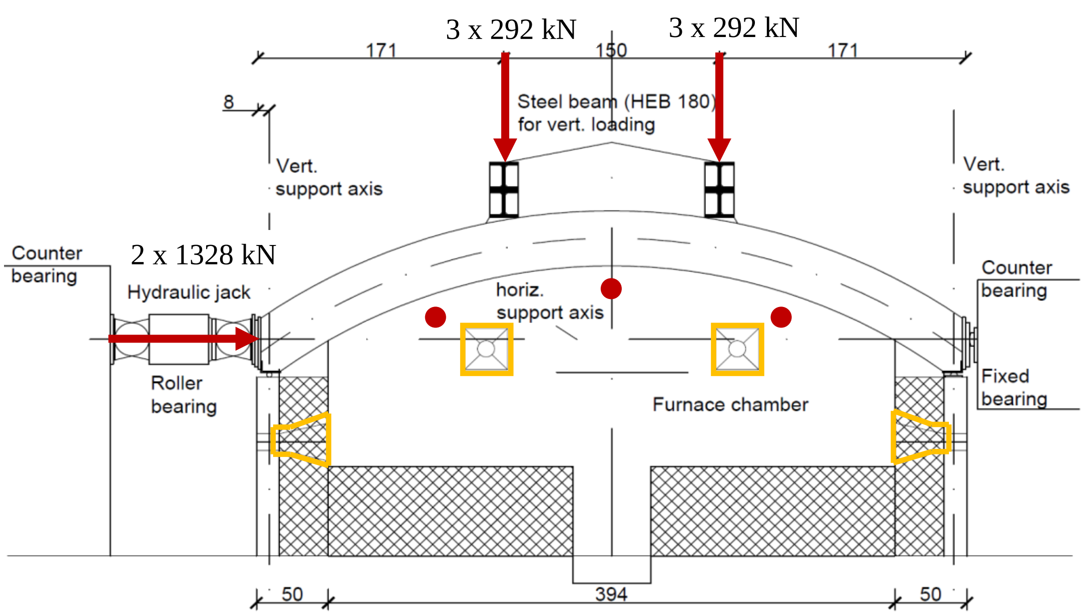

Figure 3. Overview of the test setup.

The vertical loads were induced via steel beams that were mounted in a horizontal distance of 1.50 m on a mortar bed. To avoid shearing of the steel beams on the curved surface of the tunnel shell specimen, the area was roughened and the steel frames connected with threaded bars. Additionally, the lower steel beams were connected to the tunnel shell specimen using steel bolts. The vertical forces are induced using three hydraulic jacks with a force of 292 kN for each steel beam. The total vertical force was 1752 kN.

The horizontal forces were established using two hydraulic jacks mounted between the counter bearing point of the test facility and the tunnel shell specimen, connected with steel plates to ensure a homogeneous stress distribution as well as to account for minor inaccuracies of the test specimen. The horizontal forces applied were 2656 kN in total.

Both vertical and horizontal loads were determined considering the controlling in-situ situation of the tunnel shell. They account for the ground and water pressure, the dead loads and the restraint forces occurring in the event of a fire, considering the stiffness of the environmental soil. Because the resulting bending moments were larger than possibly generated via all vertical hydraulic jacks, an eccentricity of the horizontal fixed bearing and the horizontal forces of +5 cm regarding the midpoint of the front surface of the tunnel shell element was provided. The mechanical loading was applied in 20 substeps with a loading velocity of <= 30 kN/min to avoid failure in the loading phase. After reaching both vertical and horizontal maximum values and a duration of about 5 min, the fire exposure was started [10].

Both vertical and horizontal jacks were force controlled. The initial forces were kept constant during the whole fire exposure.

Temperature and displacement measurements

Cross-sectional temperatures were recorded using thermocouples which were mounted at the casing of the lower surface during the production of the tunnel shell elements. The first thermocouple was than located in a depth of 20 mm, the next four with a plus of 20 mm, others following in different distances, taking into account the expected thermal gradient inside the cross-section during fire exposure. Three ladders with a total of 24 thermocouples were placed in the tunnel shell element, one at the section at key and two at the each thirds of the element. Details and the results of the cross-section temperatures are shown in [10].

The deflection measurement was done using six rotary potentiometers with a maximum recordable distance of 400 mm. They were attached at the points depicted in Figure 5 using steel strings. The labels *V_X* stand for vertical deflections, measured for two points in the section at key and at the thirds on both sides with a distance of 10 cm to the edge. The horizontal deflections *H_X* were also measured using rotary potentiometers and were connected with the steel plate which connects the hydraulic jacks and with the front surface of the tunnel shell specimen.

RESULTS AND CONCLUSIONS

The two large-scale tests showed different results regarding the spalling behavior. Over the whole duration of fire exposure, the first test specimen (*S1*) remains nearly undamaged with only minor spots on the fire exposed surface. During the test of *S2*, spalling started about 3 min after burner activation. The last spalling event was recorded at minute 18.

The spalling led to the introduction of a significant amount of water into the fire chamber during the test of S2. Due to the evaporation and cooling effect, all oil burners operated at full power over a long duration to ensure the heating rate and maximum temperature of 1200 °C inside the fire chamber, which succeeded (see Technical Report [10]). Unfortunately, this led to the failure of a horizontal ceiling element made of porous concrete which was located directly above two oil burners. At this point, the test was stopped (minute 45).

The fire exposed surface of the test specimen *S1* and *S2* after the test is shown in Figure 4. The effect of the concrete spalling, leading to a reduction of the concrete cross-section and a locally bounded direct fire exposure of the reinforcement can be seen in the measured vertical displacements shown in Figure 5.

Figure 4. Fire exposed surfaces of S1 (left) and S2 (right) after the tests.

The displacements in Figure 5 are shown without the fractions due to mechanical loading before the start of the fire exposure. The diagram begins with start of the fire exposure, with the deflection values set to zero. On the other hand, the absolute values are low and did not reach more than 5 mm for the first 160 minutes. In contrast to *S1*, the spalling of S2 which was not equally distributed led to the torsion of the cross-section at key. In contrast to the vertical displacements are the horizontal displacements which are quite similar for both tests for the first 45 minutes. Due to the thermal expansion of the specimen in combination with the force controlled hydraulic jacks, the specimen elongates until the cross-section is heated up, leading to a lower load carrying capacity and a horizontal contraction after minute 85 for *S1*.

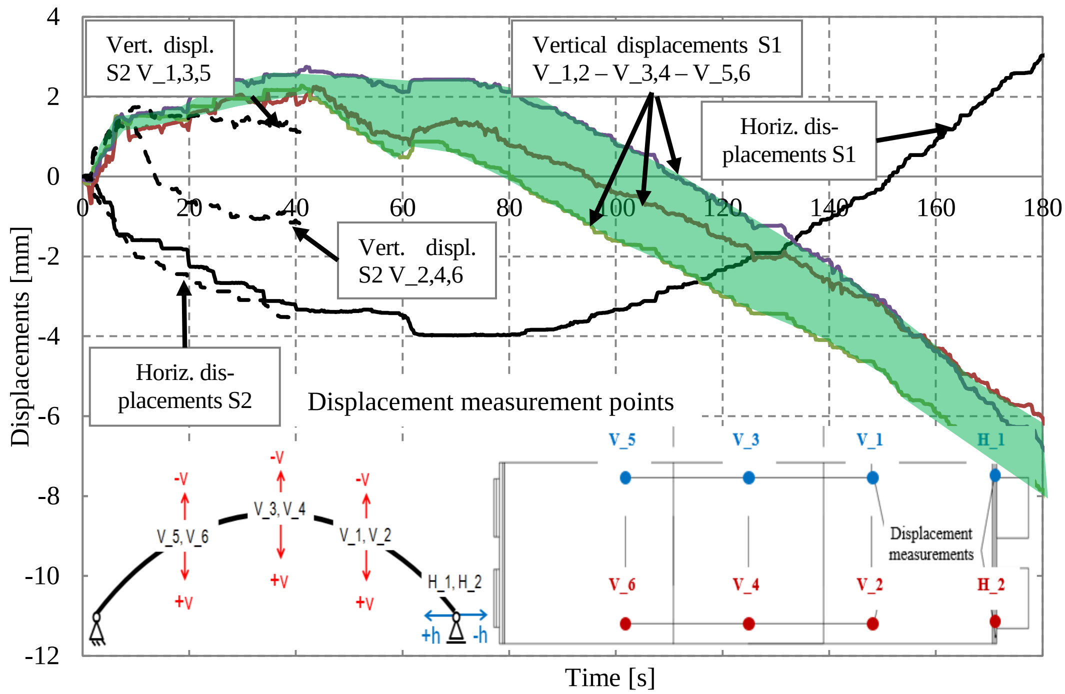

Figure 5. Displacement during both tests.

The temperature development in the cross-section showed that the lower reinforcement bars reached maximum values of about 325 °C after 100 minutes of fire exposure. This is slightly above a value of 300 °C which is recommended for road tunnels as maximum temperature criteria at the reinforcement bar [11]. The test results taking into account the missing concrete spalling and low displacements show that the specimen *S1* is capable of withstanding the severe fire exposure under mechanical loading without any problems.

To make a statement regarding the second test *S2*, the spalling depth and area was determined with a grid resolution of 20 cm (5 and 10 cm at the edges in width direction). The results are shown in Figure 6 as a contour plot, giving the arc length of the specimen surface at the x-axis and the width of the specimen at y-axis. Figure 6 allows a good overview of the areas where the reinforcement bars are directly exposed to the fire (>= 6 cm). The colored area is the fire exposed surface, the white parts are the areas which were protected by mineral wool. A total spalling area of 70.1 % of the fire exposed surface was measured with a mean value of the spalling depth of 2.43 cm (only regarding values > 0). Most values were lower than 2 cm which results in a median of 1.5 cm spalling depth.

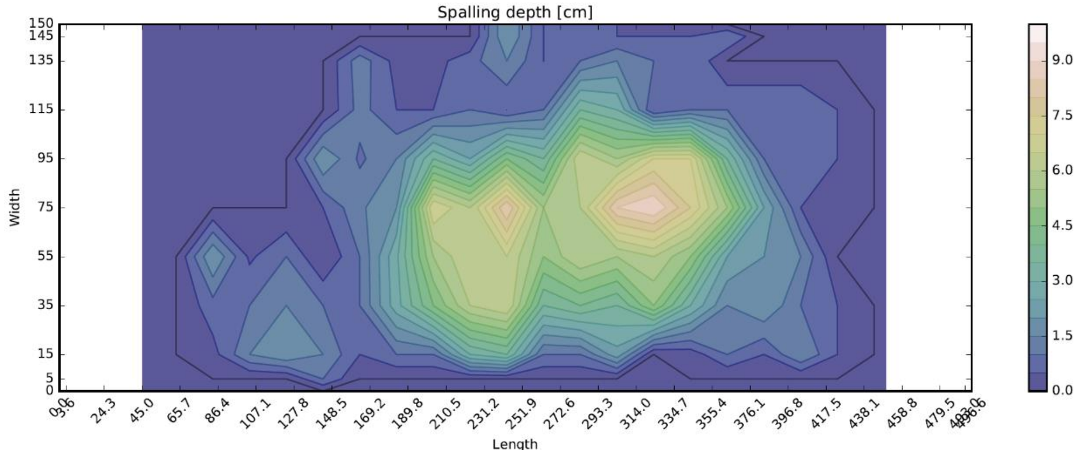

Figure 6. Spalling depth of S2 measured after the test.

In order to evaluate the results, they were compared with similar results obtained at other testing facilities and in a past research project assessing comparable specimens in geometry, concrete mixture, mechanical and thermal loading [12], [13]. Without polypropylene fibres, a maximum spalling depth of more than 30 cm for a thickness of 35 cm was measured, other results considering an amount of 2 – 4 kg/m³ PP fibres range from 4 to 6 cm. As mentioned by [14], [15], concrete spalling is a complex phenomenon depending on a large amount of influence parameters.

An important influence factor is the moisture content of the concrete, which was determined using the accompanying specimens. Each cylinder was sliced in four samples to widen the sample number and then dried at 105 °C, beginning with the day of the large-scale test. The mass loss obtained was 4.6 % for *S1* and 5.3 % for *S2* with both specimens having a comparatively high moisture content. The slightly different moisture content alone cannot be responsible for the large differences in spalling behavior. Comparing the mixture *M1* used for specimen *S2* with *M2* used for specimen *S1*, the volumetric air content is higher for *M2* (*S1*). A higher air content leads to a larger pore volume and permeability and consequently to a lower risk of spalling.

The third property is the cement type which differs from a pure Portland cement for mixture *M1* resp. specimen *S2*, to a cement with up to 20 % slag sand for mixture *M2* resp *S1*, yielding in a different hardening behavior.

The results of the small-scale tests did not allow for a clear statement whether one concrete mixture would perform better regarding the spalling behavior, but as shown in Figure 1, the variance for the specimen out of mixture *M1* is large compared to *M2*. Considering this, the large difference in the large-scale tests might also be caused by a bad sample of *M1* in comparance with a good sample of *M2*. Because the development of a specifically optimized fire protection concrete was not the goal of the project, investigations for further reasons explaining the spalling behavior of mixture M1 were not considered.

As a result of the project, a clear suggestion for the concrete mixture (*M2*) of the first test was made, and this mixture was then used for the redevelopment of the existing railway tunnel. By considering the test results, it was possible to avoid additional expensive and time-consuming fire protection measures like the installation of thermal insulation boards.

REFERENCES

1. Ingason, H., Li, Y. Z., Lönnermark, A. 2015. *Tunnel Fire Dynamics*. Springer, New York Heidelberg Dordrecht London.
2. Richtlinie Anforderungen des Brand- und Katastrophenschutzes an den Bau und den Betrieb von Eisenbahntunneln. 2008. Eisenbahn-Bundesamt (The Federal Railway Authority).
3. "Fires in Transport Tunnels: Report on Full-Scale Tests", Studiensgesellschaft Stahlanwendung e. V. 1995. EUREKA-Project EU499:FIRETUN, Düsseldorf, Germany.
4. Richter, E. 2005. "Fire tests on single-shell tunnel segments made of a new high-performance fireproof concrete", in *Fire design of concrete structures: what now? What next?; proceedings of the workshop*, Brescia: Starrylink Editrice Brescia, pp. 261-268.
5. Richter, E., Paliga, K. 2000. "Tunnel shells and fire protection – tests and analysis", in *Abnormal loading on structures: experimental and numerical modelling*. London: Spon, pp. 115-124.
6. Paliga, K., Hosser, D. 2002. "Theoretical and experimental study on concrete spalling in tunnel fires", in *Concrete structures in the 21st century: proceedings of the first fib congress*, Osaka condensed papers. Vol. 2. Tokio: Japan Prestressed Concrete Engineereing Association, pp. 11, 29-30.
7. Eurocode 2: Design of concrete structures – Part 1-2: General rules – Structural fire design; German version EN 1992-1-2:2004 + AC:2008.
8. Eurocode 1: Actions on structures – Part 1-2: General actions – Actions on structures exposed to fire; German version EN 1991-1-2:2002 + AC:2009.
9. Concrete - Part 1: Specification, performance, production and conformity; German version EN 206-1:2000/A2:2005.
10. Hosser, D., Siemon, M., Kampmeier, B. 2013. „Versuche zum Brandverhalten von Tunnelinnenschalen aus Ortbeton", Technical Report, Institute of Building Materials, Concrete Construction and Fire protection, Technische Universität Braunschweig, Braunschweig.
11. Zusätzliche Tecnische Vertragsbedingungen und Richtlinien für Ingenieurbauten ZTV-ING, part 5, Tunnelbau, Section 1, Geschlossene Bauweise. 2007.
12. Dehn, F., Hauswaldt, S., Juknat, M. 2009. "Grundsätzliche Überlegungen zur Brandprüfung von Tunnelbauteilen", *Beton- und Stahlbetonbau*, 104(12): 869-875.
13. Hosser, D., Richter, E., Schnetgöke, R. 2003. „Brandversuche an belasteten Tübbings, Referenzbalken und Tübbingfugen", Technical Report, Institute of Building Materials, Concrete Construction and Fire protection, Technische Universität Braunschweig, Braunschweig.
14. Khoury, G. A. 2008. "Polypropylene fibres in heated concrete. Part 2: Pressure relief mechanism and modeling criteria", *Magazine of Concrete Research*, 60(2):189-204.
15. Bentz, D. P. 2000. "Percolation and Spalling of High-Performance-Concrete", *ACI Materials Journal*, 97(2):351-359.

EXPERIMENTAL METHODS

Temperature and Strain Measurements with Fiber Optic Sensors for Steel Beams Subjected to Fire

YI BAO[1], YIZHENG CHEN[1], MATTHEW S. HOEHLER[2], CHRISTOPHER M. SMITH[2], MATTHEW BUNDY[2] and GENDA CHEN[1,*]

ABSTRACT

This paper presents measurements of high temperatures using a Brillouin scattering based fiber optic sensor and large strains using an extrinsic Fabry-Perot interferometric sensor for assessing the thermo-mechanical behaviors of simply-supported steel beams subjected to combined thermal and mechanical loading. The distributed fiber optic sensor captures detailed, non-uniform temperature distributions that are compared with thermocouple measurements resulting in an average relative difference of less than 5 % at 95 % confidence level. The extrinsic Fabry-Perot interferometric sensor captures large strains at temperatures above 1000 °C. The strain results measured from the distributed fiber optic sensors and extrinsic Fabry-Perot interferometric sensors were compared, and the average relative difference was less than 10 % at 95 % confidence level.

INTRODUCTION

During a fire, the load capacity and stability of steel structures can significantly degrade due to adverse temperature-induced deformations and reduced material properties [1]. To assess the thermo-mechanical conditions of a structure, both temperatures and strains must be known. The current state of practice in experimental fire testing is to measure the temperature and global deformation of specimens and to use analytical models to understand the behavior of the member. Effective tools are lacking to directly measure strains in steel members subjected to fire, reliably and accurately.

Fiber optic sensors have drawn intense research interest in the past decade due to their unique advantages, such as immunity to electromagnetic interference, small size, light weight, and excellent durability and resistance to harsh environments. However, their application to structures in fire has not yet been fully explored. Conventional grating-based fiber optic sensors degrade significantly when heated over 300 °C and typically fail around 600 °C [2], which limits their application in fire. Although their temperature operation range can be increased to 1000 °C through means such as the regenerated fiber Bragg grating technique [2], the grating sensors do not provide spatially distributed measurements, but rather a point

Department of Civil, Architectural, and Environmental Engineering, Missouri University of Science and Technology, 1870 Miner Circle, Rolla, MO 65409, USA
National Fire Research Laboratory, National Institute of Standards and Technology, 100 Bureau Drive, Stop 8666, Gaithersburg, MD 20899, USA
*Corresponding to Dr. Genda Chen. Email: gchen@mst.edu, Phone: (573)341-4462

measurement at the grating location. In contrast, fully-distributed fiber optic sensors provide a more detailed picture of the structural thermal field. Based on Brillouin scatterings in optical fiber, Brillouin Optical Time Domain Analysis and Brillouin Optical Time Domain Reflectometry technologies have been developed to measure strain and temperature distributions [3]. However, their spatial resolutions were typically limited to half a meter or larger, which is not precise enough in many applications. Recently, a pulse pre-pump Brillouin Optical Time Domain Analysis (PPP-BODTA) technology was developed with a 2 cm spatial resolution [4].

In this study, distributed fiber optic sensors with PPP-BODTA [5] and extrinsic Fabry-Perot interferometric (EFPI) sensors [6] are employed to measure temperatures and strains in steel beams exposed to fire. The sensors' accuracies and precisions for temperature and strain measurements are compared and evaluated.

WORKING PRINCIPLES

The working principles of the distributed fiber optic sensor and extrinsic Fabry-Perot interferometric sensor are briefly introduced in this section. In this study, all fiber optic sensors were fabricated using telecommunication-grade fused silica single-mode fibers. The fiber cross section consisted of an 8.2 μm glass core and a 125 μm glass cladding [7]. Typically, optical fibers are coated with protective polymer coatings outside of cladding to enhance the mechanical performance [8]. In this study, for strain measurement, the coatings were removed before the fibers were installed on the test specimens. However, for temperature measurement, the coatings could be left and burned off at about 300 °C to 400 °C [9].b

Distributed Fiber Optic Sensor

In this study, PPP-BOTDA based on stimulated Brillouin scatterings in optical fiber was employed. Stimulated Brillouin scatterings result from the interactions between light waves and acoustic waves in optical fiber [2]. PPP-BOTDA measures the Brillouin frequency shift along the optical fiber, which is related to the strain and temperature changes of the optical fiber. For light signals with wavelengths of 1.3 μm to 1.6 μm in single mode fibers, the Brillouin frequency shift is about 9 GHz to 13 GHz. The Brillouin frequency shift increases approximately linearly with increasing tensile strain or temperature when the temperature is not very high (< 400 °C). However, after the optical fiber is exposed to high temperatures, the linear relationships are not satisfied and must be modified [7].

Extrinsic Fabry-Perot Interferometric Sensor

An EFPI sensor typically consists of two parallel reflecting surfaces, which are separated by a cavity, as illustrated in Figure 1. Interference occurs between the multiple reflections of light between the two reflecting surfaces. The reflection spectrum of an EFPI can be described as the wavelength dependent intensity modulation of the input light spectrum [6], which is mainly caused by the optical phase difference between two reflected light beams. Constructive interference occurs if the reflected beams are in phase, and this corresponds to a high-transmission peak. If the reflected beams are out-of-phase, destructive interference occurs and this corresponds to a reflection minimum. Whether the multiply reflected beams are in phase or not depends on the wavelength (λ) of the incident light (in vacuum), the angle with which the incident light travels through the reflecting surfaces (θ), the physical length of the cavity (L) and the refractive index of the material between the reflecting surfaces (n).

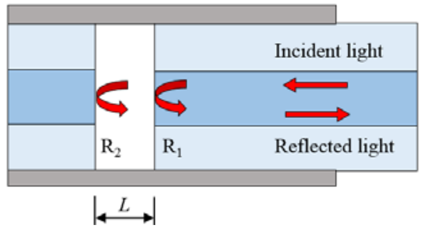

Figure 1. Illustration of a typical EFPI.

The phase difference between each reflected pair of the EFPI is given as:

$$\phi = \frac{2\pi}{\lambda} 2nL\cos(\theta) \tag{1}$$

When perturbation is introduced to the EFPI, the phase difference is influenced with the variation in the optical path length difference of the interferometer. Applying longitudinal strain to the EFPI sensor, for instance, changes the physical length of the cavity, which results in phase variation. By measuring the shift of the wavelength spectrum, the applied strain can be quantified.

EXPERIMENTAL PROGRAM

Test Specimens and Setup

Three S3×5.7 "I-shaped" steel beams were tested with a three-point bending setup in a compartment fire ('flame channel') as shown in Figure 2. Combined temperature and mechanical loading was applied. The three test beams were designated Beam #1, Beam #2, and Beam #3. Each of the beams had a 76 mm depth, 59 mm width, and 1420 mm length. The cross sectional area was 1077 mm^2.

A flame channel, which consisted of a burner rack, an enclosure, and a specimen loading system, was located under a 6 m × 6 m (plan) exhaust hood. The burner rack had four natural gas diffusion burners made of sheet metal, and each of the burners was 300 mm × 300 mm × 140 mm (length × width × height) in dimension. Natural gas entered a burner from the bottom, filled the burner cavity, and then, passed through a ceramic fiber blanket to distribute the gas. The burners were manually regulated by the energy content of the supplied gas, which was measured with an expanded uncertainty of less than 2.4 % [10]. An enclosure constructed of square tube steel, cold-formed steel C-profiles and gypsum board lined with thermal ceramic fiber enclosed the space above the burner rack. The enclosure was open at three faces: the bottom and the two ends in longitudinal direction of the beam, creating the compartment flame dynamics. The heated "compartment" created by the enclosure was approximately 380 mm × 400 mm × 1830 mm (height × width × length) in dimension. Each test beam was simply supported on two supports constructed of 1-1/2” Schedule 40 pipe, at a 1250 mm clear span. The specimen was loaded by a U-shape 1/2” Schedule 40 pipe (outer diameter: 21 mm) “loading yoke” at the mid-span. The supporting pipes and loading yoke were cooled with the exiting water temperature controlled to less than 50 °C. Load was transferred to the loading yoke with a pulley system.

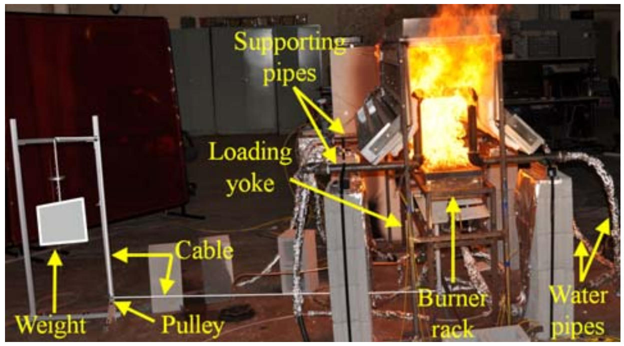

Figure 2. Experimental setup.

Instrumentation of Test Beams

Each beam was instrumented with four glass-sheathed, K-type, bare-bead thermocouples peened into small (diameter < 2 mm) holes, which were drilled into the bottom and top flanges as indicated in Figure 3: TC1 and TC3 at mid-span, and TC2 and TC4 at quarter-span. The thermocouples had a manufacturer-specified temperature standard limit of error of 2.2 °C or 0.75 % (whichever value is greater) over a measurement range of 0 °C to 1250 °C. A calibrated load transducer by Omegadyn was installed on a spanning bar at the bottom of the loading yoke and used to measure the applied load. The linearity and repeatability of the load transducer were ±0.03 % and ±0.01 %, respectively. Each beam was instrumented with one distributed fiber optic sensor (DFO-T) to measure temperature distributions, three distributed fiber optic sensors (DFO-ST1, DFO-ST2, and DFO-ST3) and three EFPI sensors (EFPI1, EFPI2, and EFPI3) to measure strains. The sensors EFPI1, EFPI2, and EFPI3 were closely deployed to DFO-ST1, DFO-ST2, and DFO-ST3, respectively.

Data from the fuel delivery system, thermocouples, displacement sensors and a load transducer were measured continuously using a National Instruments data acquisition system (NI PXIe-1082). Thermocouple data were recorded using 24-bit Thermocouple Input Modules (NI PXIe-4353), and load and displacement data were recorded using a high-speed, 16-bit multifunction module (NI PXIe-6363). Data were sampled at 90 Hz with average values and standard deviations recorded in the output file at a rate of 1 Hz.

A Neubrescope data acquisition system (NBX-7020) for the distributed fiber optic sensors was used to perform PPP-BOTDA measurements with 2 cm spatial resolution and accuracies of 0.75 °C and 15 με for temperature and strain, respectively. In this test, the spatial resolution was 2 cm, meaning that the Brillouin frequency shifts of two points spaced at no less than 2 cm could be distinguished. An optical spectrum analyzer (Yokogawa AQ6370C) was used to acquire data from the extrinsic Fabry-Perot interferometers with a broadband (1470 nm to 1630 nm) light source (Keysight 83437A). The operation wavelength ranged from 1500 nm to 1600 nm. The sampling frequency ranged from 0.2 Hz to 1 Hz.

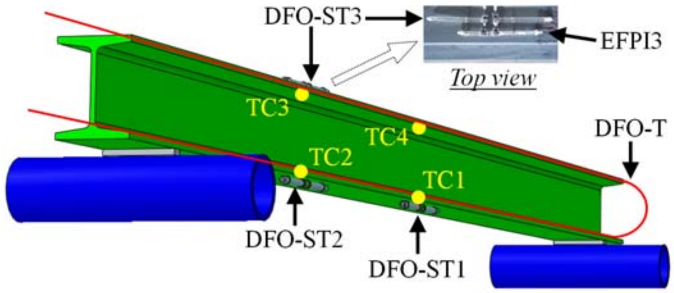

Figure 3. Instrumentation of test beams.

Test Protocol

Each beam was subjected to both fire and mechanical loading. Figure 4 illustrates the fire test protocol.

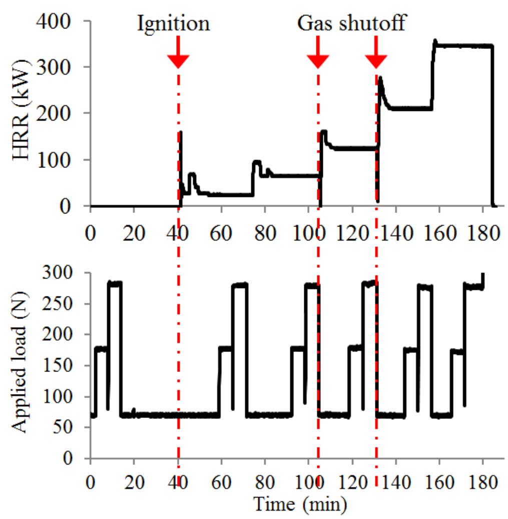

Figure 4. Test protocol.

The heat release rate (HRR) was held approximately constant at five target levels: 25 kW, 65 kW, 120 kW, 195 kW, and 350 kW, which corresponded to beam temperatures at TC1 of approximately 200 °C, 400 °C, 600 °C, 850 °C, and 1050 °C, respectively. During the test of Beam #2, the gas was turned off for about 20 seconds before the HRR was increased to 120 kW and 195 kW, respectively, to allow for visual observation. When the HRR was increased to a higher level, the target value was overshot and then quickly regulated down to the expected value. At each HRR level, in addition to the self-weight, the beam was subjected to three levels of loads at the mid-span. For Beam #1, the three loads were approximately 68 N, 98 N, and 126 N, and sustained for 7 minutes, 4 minutes, and 4 minutes, respectively. For Beams #2 and #3, the three loads were approximately 68 N, 176 N, and 285 N, each sustained for 6 minutes.

EXPERIMENTAL RESULTS AND DISCUSSION

Temperature Measurements

At each sustained HRR level, the beam temperature gradually stabilized to a temperature with some variation. To quantify the temperature variations, the mean values and standard deviations were calculated over 15 minutes for Beam #1, and 18 minutes for Beams #2 and #3 when the mechanical loads were applied at each temperature level. The coefficient of variation for all the thermocouple readings is less than 4 %. Similarly, to average out the effects of temperature fluctuation, five measurements were made using the DFO-T at each sustained temperature level. Each measurement was an implicit average over a time between 15 seconds and 40 seconds. The DFO-T readings have a maximum coefficient of variation of 4 %, which was similar to that of the thermocouples. The relative difference between the mean temperatures from the DFO-T and the thermocouple ranges from -10 % to 8 %. To understand the statistical significance of the measurement differences, the average of mean temperature differences (four for Beam #1, three for Beam #2, four for Beam #3) was calculated at each HRR level and presented in Figure 5 as an average temperature difference. In addition, the range of mean differences at 95 % confidence level is represented by the error bar.

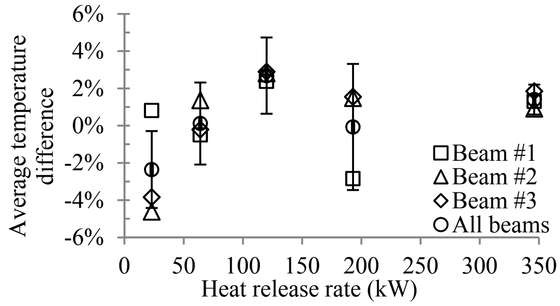

Figure 5. Difference between the fiber optic sensor and thermocouple temperature readings (error bars at 95% confidence).

It can be observed from Figure 5 that the mean difference at 95 % confidence level is less than 5 %, which is acceptable in many engineering applications. The discrepancies may be attributed to several factors. First, the DFO-T sensor was installed in a slightly different location than the thermocouples. Second, the thermocouple beads were located slightly below the surface of the beam and the DFO-T slightly above the surface, and thus, the influence of gas temperature variation on the measurements varied. Additionally, the thermocouples were not corrected for radiation losses.

Strain Measurements

The strain results measured from the EFPI sensors are plotted in Figure 6. As the HRR increases, the strain values approximately linearly increase. When the HRR was no more than 120 kW, the strain results from different sensors attached on different test beams agreed well. At the HRR equal to 120 kW, the strain values were approximately 8000 με to 9000 με. When the HRR became larger than 120 kW, greater variation of the strain results was observed from different sensors deployed at different locations. At the HRR equal to 350 kW, up to 35,300 με (3.53 %) strain was measured by the EFPI sensors.

Similar to the temperature measurements, multiple strain measurements were made from the distributed fiber optic sensors and EFPI sensors at each HRR level. The mean values for the two measurement methods were compared statistically for the conditions when the HRR was no larger than 120 kW, as shown in Figure 7. The mean strain difference at 95 % confidence level is less than 10 %. There are several reasons for the discrepancy between strain measurements from different sensors. First, the two sensors were deployed at slightly different locations that were subjected to different strains. Second, the data used to calculate the mean values of the two independent sensing systems were not selected at exactly the same moment. Although the two data acquisition systems were synchronized, they had different measurement (reading) durations, and thus, the measurement results were not achieved simultaneously. Third, each instrument has its own accuracy and repeatability at a level, and the measurement results contain error.

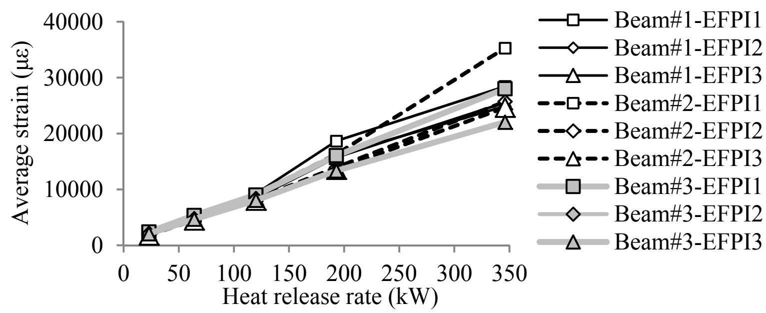

Figure 6. Average strain results measured from EFPI sensors.

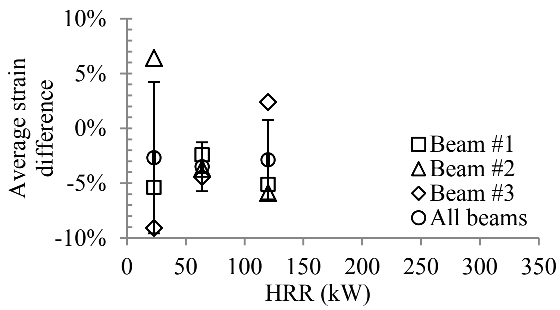

Figure 7. Difference between the distributed fiber optic sensor and EFPI sensor strain readings (error bars at 95% confidence).

CONCLUSIONS

Pulse pre-pump Brillouin Optical Time Domain Analysis distributed fiber optic temperature sensors have been demonstrated at temperatures up to 1050 °C in fire with adequate sensitivity and accuracy for typical structural engineering applications. These measurements add significant value over traditional thermocouples by providing distributed measurements over the length of the optical fiber with a spatial resolution of 2 cm. The measured temperatures were validated by thermocouples resulting in an average relative difference of less than 5 % at 95 % confidence level.

Extrinsic Fabry-Perot interferometric strain sensors have been demonstrated to operate up to 1050 °C in fire and measure at least 35,300 με (3.53 %) strains. The thermal strain predicted from the distributed fiber optic sensor and the extrinsic Farby-Perot interferometric sensor strain results were compared. The mean strain difference at 95 % confidence level was less than 10 %.

These results demonstrate the potential application of fiber optic temperature and strain sensors in structural fire testing. The investigated sensors provide increased temperature resistance, strain capacity, and spatial resolution when compared to traditional methods. Further development of the sensors is required to improve the robustness of the sensors and the speed of installation and measurement.

ACKNOWLEDGEMENT

This work was funded by the National Institute of Standards and Technology (NIST) under Award No. 70NANB13H183. The contents of this paper reflect the views of the authors, and do not necessarily reflect the official views or policies of NIST. Certain commercial equipment, instruments, or materials are identified in this paper to specify the experimental procedure. Such identification is not intended to imply recommendation or endorsement by NIST, nor to imply the materials or equipment are necessarily the best available for the purpose.

REFERENCES

1. Kodur, V., M. Dwaikat, and N. Raut. 2009. "Macroscopic FE model for tracing the fire response of reinforced concrete structures," Eng. Struct., 31 (10), 2368-2379.
2. Rinaudo, P., B. Torres, I. Paya-Zaforteza, P.A. Calderón, and S. Sales. 2015. "Evaluation of new regenerated fiber Bragg grating high-temperature sensors in an ISO834 fire test," Fire Safety J., 71, 332-339.
3. Bao, X., and L. Chen. 2011. "Recent progress in Brillouin scattering based fiber sensors." Sens., 11, 4152-4187.
4. Kishida, K., and C.H. Li. 2006. "Pulse pre-pump-BOTDA technology for new generation of distributed strain measuring system." Proc. Struct. Health Monit of Intel. Infrastruct., 471-477.
5. Bao, Y., and G. Chen. 2015. "Fully-distributed fiber optic sensor for strain measurement at high temperature." Proc. 10th Int. Workshop Struct. Health. Monit., Stanford, CA.
6. Rao, Y. J. 2006. "Recent progress in fiber-optic extrinsic Fabry-Perot interferometric sensors," Opt. Fiber Technol. 12, 227-237.
7. Bao, Y., W. Meng, Y. Chen, G. Chen, K.H. Khayat. 2015. "Measuring mortar shrinkage and cracking by pulse pre-pump Brillouin optical time domain analysis with a single optical fiber," Mater. Lett. 145, 344-346.
8. Bao Y, G Chen. 2016. "Strain distribution and crack detection in thin unbonded concrete pavement overlays with fully distributed fiber optic sensors." Opt. Eng. 55(1), 011008.
9. Bao, Y., and G. Chen. 2016. "Temperature-dependent strain and temperature sensitivities of fused silica single mode fiber sensors with pulse pre-pump Brillouin optical time domain analysis," Mes. Sci. Tech., under review.
10. Bundy, M., A. Hamins, E.L. Johnsson, S.C. Kim, G.H. Ko, and D.B. Lenhert. 2007. "Measurements of heat and combustion products in reduced-scale ventilation-limited compartment fires," NIST Technical Note 1483.

Thermographic Digital Image Correlation (TDIC) Measurements of Mechanically-Loaded Structures

JONATHAN L. HODGES, CHRISTIAN RIPPE, SCOTT W. CASE and BRIAN Y. LATTIMER

ABSTRACT

This research examined the use of Thermographic Digital Image Correlation (TDIC) in fire testing with flames in the field of view. The error and uncertainty in the deformation measurements obtained via TDIC with fire in the field of view were reduced by ensuring the grayscale histogram of the CCD images was neither under-saturated nor oversaturated once fire was present. Quantitatively, this corresponded to the greyscale histogram having a mean value between 13-91 out of 255 and a kurtosis between 2.7-10.7 without the fire present. Results obtained from testing using this setup were found to reduce data loss due to overexposure when compared to results obtained using arbitrary light conditions. Thus, future investigators may reduce the error in the system for live fire testing before exposing the sample to fire by setting up lighting and camera settings to obtain histograms in this range.

INTRODUCTION

In structural experiments involving fire it is often desirable to measure both deformation and temperature fields of load-carrying members being tested. Traditionally these measurements are obtained using physical methods such as string potentiometers and thermocouples. Obtaining full field measurements requires an array of these devices along the specimen. Unfortunately it can be difficult to attach these devices without affecting the physical system. In addition, it is often difficult to determine where failure may occur so that instrumentation can be appropriately positioned. Non-contact measurement methods are desirable to reduce setup issues and ensure the appropriate data is captured.

Numerous non-contact measurement methods have been proposed for obtaining either deformation or temperature field measurements; however, few have been proposed which simultaneously measure both quantities. Thermographic Digital

Jonathan L. Hodges, Virginia Tech, 635 Prices Fork Road, Blacksburg, VA 24061
Christian Rippe, Jensen Hughes, Inc., Blacksburg, VA 24061
Scott W. Case, Virginia Tech, 635 Prices Fork Road, Blacksburg, VA 24061
Brian Y. Lattimer, Jensen Hughes, Inc., Blacksburg, VA 24061

Image Correlation (TDIC) is an optical method for measuring full field 3-D deformation and temperature on surfaces by mapping simultaneously captured CCD and IR images to a common coordinate system and tracking anisotropic speckle patterns [1]. The fusion of the DIC and thermography measurements through the calibration process allows temperature and deflections to be aligned and tracked, even in cases with large deflections.

Traditionally DIC has been limited to laboratory conditions since the DIC algorithms depend on consistent lighting [2], which has limited the use of this method in fire testing to measurements without fire in the field of view (FOV) of the cameras [1,3]. Recent studies have been performed testing this limitation. Yoneyama et al. [4] used DIC to measure the deformation of an in-service bridge where ambient conditions may change. Pan et al. [5] investigated the potential use of bandpass filters and monochromatic lighting to minimize the effects of ambient lighting on DIC, and this system has been tested in high temperature applications [5-7]. However, the effects of active flames in the FOV (which will affect the sample and sensor in different ways over time) have not been quantified. The purpose of this study was to determine ideal camera settings to minimize the error and uncertainty in TDIC measurements of displacement for structural elements exposed to diffusion flames that are in the FOV of the measurement cameras.

TDIC SETUP

The TDIC system used in this testing consists of two CCD cameras and one IR camera. The CCD cameras used were Allied Vision Technologies Prosilica GE 4000 CCD cameras (12-bit, 4008 x 2672 pixels, up to 10 Hz). Nikon AF Nikkor lenses with a focal length of 28mm were used with various f-stop values. The IR camera used was a FLIR A655sc (16-bit, 640 x 480 pixels, up to 100 Hz). Simultaneous imaging was achieved by using a hardware trigger to synchronize capture. The calibration procedure presented by Cholewa et al. [1] was used. The TDIC setup is shown in Fig. 1. Images were sampled at 2 Hz, and deformation measurements were obtained using Vic-3D [8].

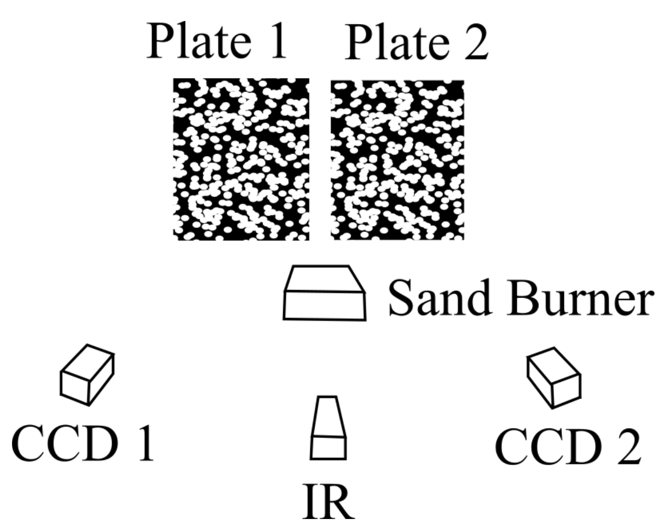

Figure 1. Schematic of fire in FOV experiment.

FIRE IN FIELD OF VIEW TESTING

Aluminum 6061-T6 samples were exposed to 20 kW fires produced by a 0.3 m square sand burner. Two 0.60 m x 0.80 m plates were located 0.7 m behind the sand burner, and uniformly lit with 2 Hilio LED light panels, each providing a luminous output equivalent to a 1000W traditional light, set to maximum, as shown in Fig. 2a. When a fire is in the FOV as in Fig. 2b, the samples were occluded by overexposure from the flame, the overall intensity of the lighting on the plate increased, and the lighting was no longer consistent across the plate. An example of the change in contrast on the sample due to fire in the FOV is shown in Fig. 2c which contains the grayscale histogram of the sample images shown in Fig. 2a-b. Figure 2c shows the percentage of oversaturated pixels (i.e., values at 255) increases drastically when the fire is in the FOV. Additionally, if all overexposed pixels are ignored in Fig. 2c, the mean and standard deviation grayscale intensity on the samples increases from 91 to 108 and 61 to 68, respectively. Because a fire in the FOV will typically be transient, the effect on the intensity of reflected light at an individual location will change over time.

Because the contrast on the sample depends on aperature, exposure time, and fire size, a parametric study was performed to determine the optimum camera settings for TDIC testing with fire in the FOV. The metrics used to compare settings were projection error, uncertainty, and percentage of data loss. Projection error is defined as the root mean square euclidean distance in pixels of each point viewed from one CCD camera to the epipolar line of the point viewed from the other CCD camera. The uncertainty results from the DIC algorithm matching of speckle subsets. The percentage data loss is defined as the percentage of pixels which had data available at the start of the test from which measurements of deformation could not be obtained.

The results of testing with and without fire in the FOV for an f-stop (the ratio of focal length of the lens to the diameter of the entrance pupil) of 11 are shown in Fig. 3. As expected, each metric is worse in fire testing than the corresponding baseline due to the transient pixel intensities caused by the fire exposure. Considering Fig. 3 as a whole, exposure times in the range of 7.5-30 ms were found to correspond to the ideal contrast levels for testing with a 20 kW fire in the FOV with an f-stop of 11. Grayscale histograms of images taken at the lower and upper contrast levels identified as ideal (7.5ms and 30ms exposure time for this test) are shown with and without fire in the FOV in Fig. 4a-b, respectively. No significant variation was observed for various f-stop values with similar histograms.

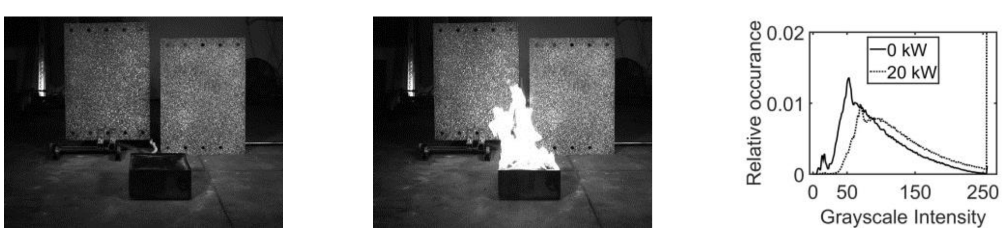

(a) (b) (c)

Figure 2. Sample images and grayscale histograms with and without fire exposure (a) Sample without fire. (b) Sample with fire. (c) Grayscale histograms of a-b where the relative occurrence is the percentage each intensity value occurs on the sample.

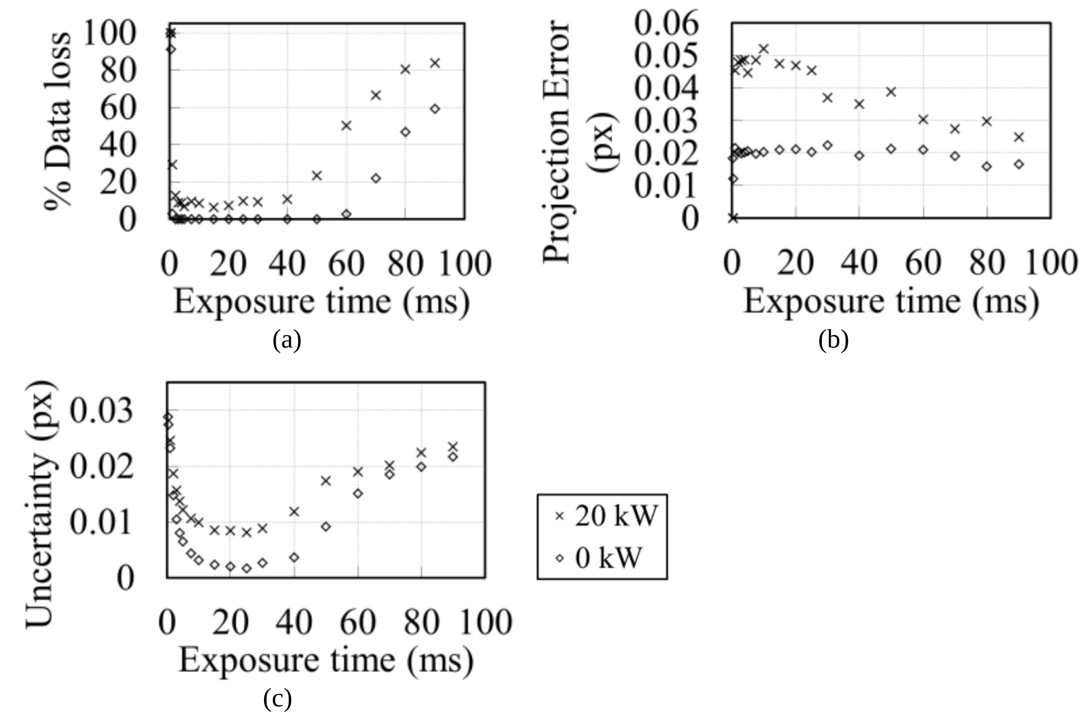

Figure 3. Performance metrics of measurement from sample under various contrast levels with and without fire exposure. (a) Percentage of data loss. (b) Projection error. (c) Uncertainty.

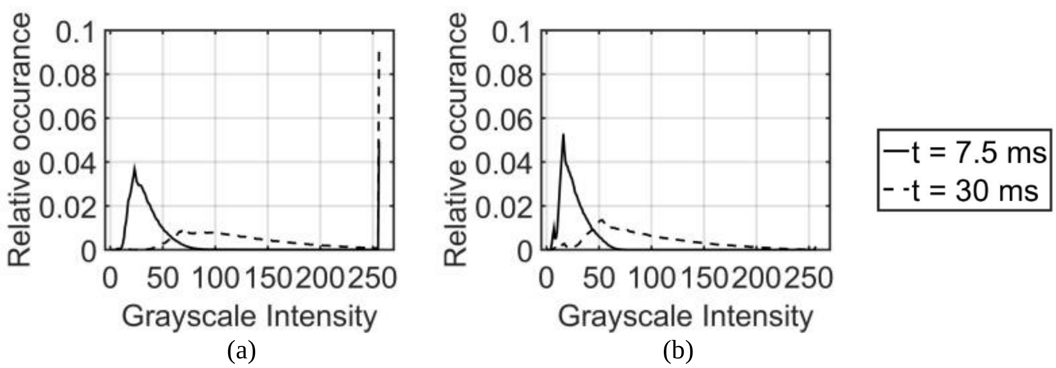

Figure 4. Boundary sample grayscale histograms showing viable contrast levels for TDIC measurements with fire in the FOV from exposure times identified in Fig. 3. (a) Grayscale histograms with fire in the FOV (b) Grayscale histograms with the same camera settings as previous with no fire in the FOV.

As the exposure time is increased the mean value of the histogram increases and the histogram becomes more flat. It was found that the ideal measurement regions had a mean grayscale intensity between 13-91 out of 256 and a kurtosis (sharpness of peaks) between 2.7-10.7 without fire in the FOV. Additionally, less than 10% of the total pixels on the sample were overexposed once the fire was present. Thus, when initially calibrating the system, it is a best practice to sample an initial data set with varying contrast levels and comparing the grayscale histograms of the samples at each level. Choosing an exposure time such that the grayscale histogram of the sample in the CCD images falls within the limits shown in Fig. 4b before taking measurements with fire will result in lower error and less pixels overexposed by the fire.

To examine the effects of using these camera settings on deformation measurements, TDIC measurements were taken as Plate 1 in Fig. 1 was moved a known distance on a stage with 0.1 mm resolution. Between each movement, images were sampled with no fire, 20kW, 50kW, and 100kW fires, sampled at both 7.5ms and 30ms exposure times using the method presented herein. While better results could have been achieved by matching the histogram of the sample to that shown in Fig. 3a with each fire size, the tests were conducted with the same settings across multiple fire sizes to test the method presented in this work. As shown for each camera setup in Fig. 5 with different fire sizes, the most significant difference in performance is in the percentage of data loss. The average data loss increases as the fire size increases due to an increase in the percentage of oversaturated pixels on the sample. Additionally, better results for larger fire sizes are obtained when the grayscle histograms of the sampled images are closer to the lower end of the range. This is due to the larger fire sizes shifting the higher end grayscale histogram out of the ideal range. Using the camera setup presented herein improves performance by reducing the percentage of neighboring pixels oversaturated by the fire.

I-BEAM TESTING USING IDEAL GRAYSCALE HISTOGRAM

To examine the utility of this method in structural testing, the camera settings identified above were used for testing of Aluminum 6061-T6 structural I-beams subjected to four point bending. The samples were supported 0.3 m from each end of the beam and loaded with 500 pounds split evenly between two points 0.25 m from the center of the beam. Baseline measurements were taken prior to mechanical loading; however, the system was allowed to rest with the static load for 15 minutes before fire testing began. Timestamps were taken to be zero at the start of fire testing.

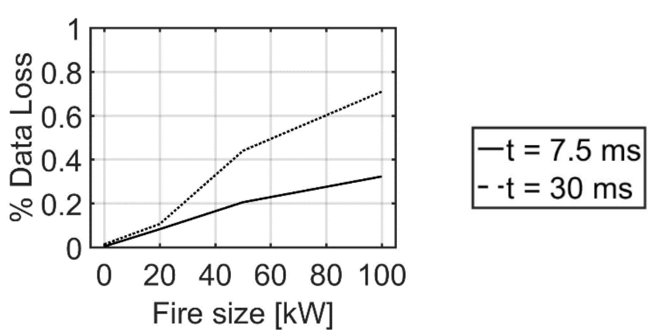

Figure 5. Percentage of data loss with fire in the FOV using typical TDIC setup and the recommendations presented in this work for various fire sizes.

An example image of an unloaded beam from a CCD camera is shown in Fig. 6a, and an example of the beam exposed to fire viewed from the IR camera is shown in Fig. 6b. The deformation and temperature of the beam along the line shown in Fig. 6a throughout testing is shown in Fig. 7. The empty points in Fig. 7 correspond to times when the flame occluded the beam. The last point in Fig.7 shows a loss of correlation on the right side of the beam. This occurred due to the beam yielding into the fire and the CCD camera being unable to track the anisotropic speckle pattern.

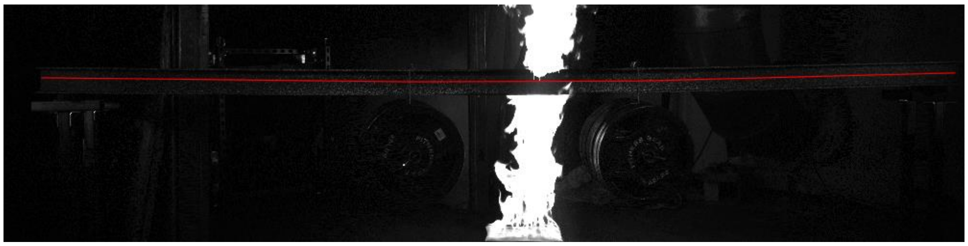

(a)

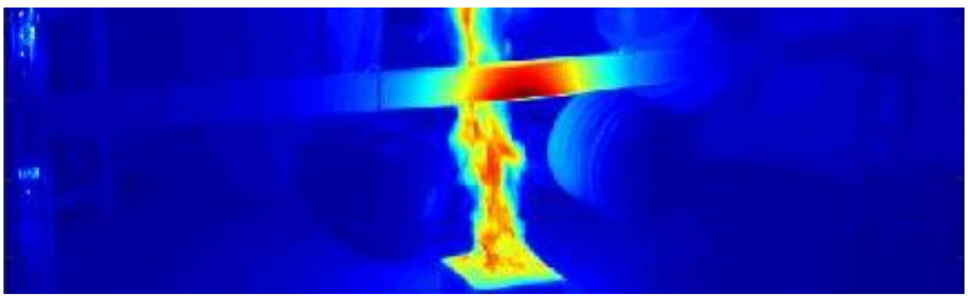

(b)

Figure 6. Example images of a structural I-beam test from (a) CCD camera. (b) IR camera.

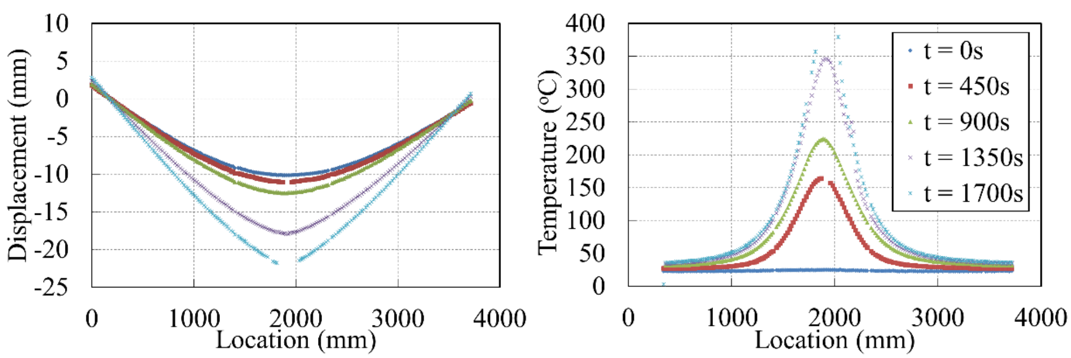

Figure 7. Example of deformation and temperature data fusion from a structural I-beam testing for the red line slice shown in Fig. 6a at various times throughout testing. (a) Deformation. (b) Temperature.

A baseline I-beam test was performed with traditional TDIC setup parameters and the results compared to testing with adjusted contrast levels. An example image from each test is shown in Fig. 8. The overlaid contour map corresponds to the deformation measurements from the TDIC system. Figure 8a shows the pixels near the center of the beam lose correlation when the fire is present. This is due to the speckle pattern becoming oversaturated. In contrast, Fig. 8b shows the pixels near the flame maintain correlation and provide deformation measurements in the reduced contrast case. Thus, additional measurements of deformation are obtained using the adjusted contrast settings which otherwise would have been unavailable.

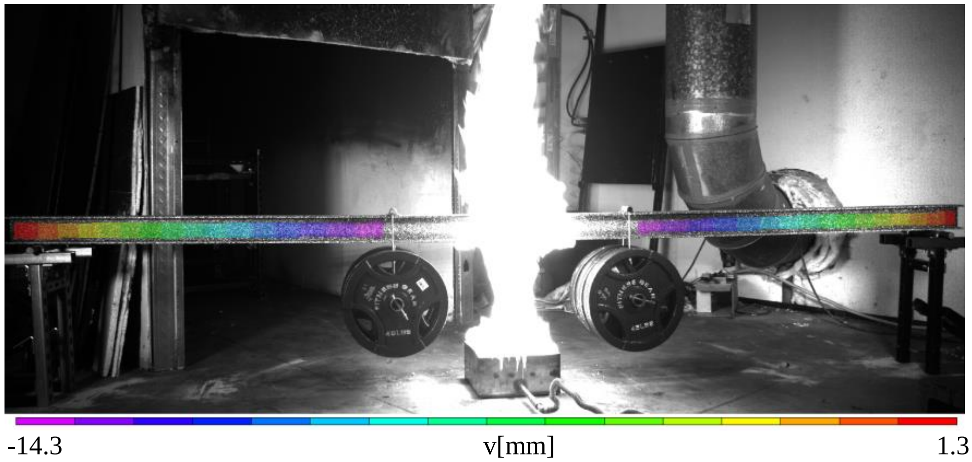

(a)

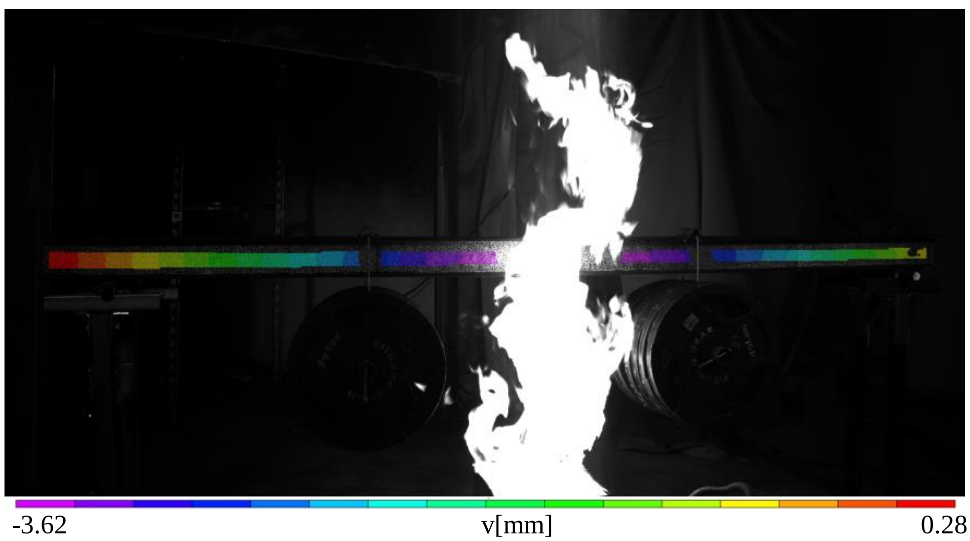

(b)

Figure 8. Example of deformation measurements of structural I-beams exposed to 100 kW fire imaged with (a) traditional TDIC settings, and (b) modified settings based on grayscale histogram.

CONCLUSION

The application of TDIC measurement to open fire testing of structural members was examined. Initial results show that it is most important to ensure the grayscale histogram of the speckling on the sample have as little as possible pixels over or under saturated. The mean and kurtosis of the grayscale histogram were identified as two important parameters which can be used to quantify the contrast on a sample prior to fire testing. Calibrating the system without fire in the FOV such that the mean grayscale intensity falls within 13-91 out of 255 and the kurtosis between

2.7-10.7 yielded improved results for a 20 kW fire in the field of view. Testing of additional fire sizes showed staying closer to the lower end of this range is beneficial as the presence of larger fires will result in the histogram on the sample shifting outside the identified ideal contrast range. Setting the cameras using this method, full field deformation measurements were obtained through a variety of intensity changes due to fire in the FOV.

ACKNOWLEDGEMENTS

The authors appreciate the sponsorship related to this work from N00014-13-1-0894 DURIP for the IR camera and DIC equipment. The work in this paper was supported by the Department of the Navy, contract N65540-10-C-0003.

REFERENCES

1. Cholewa, N., Summers, P. T., Feih, S., Mouritz, A. P., Lattimer, B. Y., & Case, S. W. 2015. "A Technique for Coupled Thermomechanical Response Measurement Using Infrared Thermography and Digital Image Correlation (TDIC)," *Experimental Mechanics*, 1-20.
2. Schreier, H., Orteu, J. J., & Sutton, M. A. 2009. *Image correlation for shape, motion and deformation measurements*. Springer US.
3. Rippe, C., 2015. "Burnthrough Modeling of Marine Grade Aluminum Alloy Structural Plates Exposed to Fire," *Virginia Tech*.
4. Yoneyama, S., Kitagawa, A., Iwata, S., Tani, K., & Kikuta, H. 2007. "Bridge deflection measurement using digital image correlation," *Experimental Techniques*, *31*(1), 34-40.
5. Pan, B., Wu, D., & Xia, Y. 2012. "An active imaging digital image correlation method for deformation measurement insensitive to ambient light," *Optics & Laser Technology*, *44*(1), 204-209.
6. Pan, B., Wu, D., & Yu, L. 2012. "Optimization of a three-dimensional digital image correlation system for deformation measurements in extreme environments," *Applied optics*, *51*(19), 4409-4419.
7. Berke, R. B., & Lambros, J. 2014." Ultraviolet digital image correlation (UV-DIC) for high temperature applications," *Review of Scientific Instruments*, *85*(4), 045121.
8. Solutions, Correlated. 2005. "VIC-3D user manual." *Correlated Solutions*.

Consolidated Fire Analysis—Coupled Thermo-mechanical Modelling for Global Structural Fire Analysis

PATRICK SCHULTHESS[1], MARTIN NEUENSCHWANDER[1], MARKUS KNOBLOCH[2] and MARIO FONTANA[1]

ABSTRACT

Consolidated fire analysis (CFA) consolidates numerical simulation and physical element testing in order to analyze the global structural behavior of structures in fire. As the testing technique facilitates the investigation of **the global behavior of structures in fire** while only physically testing a substructure, it might become increasingly important in fire safety engineering. In order to develop an analysis procedure that meets the requirements arising from fire engineering, a benchmark problem has been elaborated and is presented in this paper. This methodological problem can be solved by both, consolidated fire analysis and pure physical testing. This approach allows verifying the results obtained using the consolidated fire analysis technique by pure physical testing. In this paper, the benchmark problem is explained in detail and results from two consolidated fire tests at high temperatures are presented.

INTRODUCTION

Fire resistance is usually assessed based on the structural fire behavior of isolated load-bearing members and connections under natural fire or standard fire exposure. However, global fire tests [1] and experience from real building fires have shown that in case of fire entire structures usually perform better, than predicted on the basis of their single components' performance [4]. Global structural effects often prevent the failure of entire structures, even after failure of single elements, due to load redistribution or a change in the structural behavior or in the statical system. Therefore, experimental and numerical analysis of the global structural behavior is crucial for a realistic performance assessment and optimized structural fire design. However, global fire testing is very expensive and rare and purely numerical simulations require assumptions and are confronted with uncertainties. Consolidated Fire Analysis (CFA) methodically merges physical testing and numerical structural

[1] ETH Zurich, Department of Civil and Environmental Engineering, Institute of Structural Engineering – Steel, Timber and Composite Structures, Stefano-Franscini-Platz 5, 8093 Zurich, Switzerland.
[2] Ruhr Universität Bochum, Department of Civil and Environmental Engineering, Institute of Steel, Lightweight and Composite Structures, Universitätsstraße 150, 44801 Bochum, Germany.

simulation and facilitates the investigation of the global structural fire behaviour [2]. In a consolidated (coupled experimental and numerical) assessment method for thermo-mechanical problems only isolated members or parts of structural systems are tested while the remaining structures are considered in the numerical simulation. The interactions of members and parts of structures respectively with the entire structures during a CFA are achieved by consecutively updating the numerical model using data measured in the experiment and simultaneously control the loading of the test specimen based on the results of the numerical simulation. CFA therefore allows incorporating effects like stiffness- and strength degradation, thermal expansion and creep of structural members and the redistribution of loads on the global structural level. As the consolidated fire analysis technique is capable of accounting for the global structural behaviour, without the need for fire tests on entire structures, it promises to be a valuable tool and may become increasingly important in structural fire engineering. The concept of combined numerical simulation and physical testing is known for a long time. The first application of this technique, back then refered to as "online testing", was in the 1970s by Takanashi et al. [8] who used combined experimental and physical testing in order to evaluate the seismic behavior of structures. Since then many researchers have continued to work on the development of the analyzing technique, nowadays often denoted by hybrid testing [6]. However, as the requirements and challenges in fire engineering are different from seismic engineering, a fundamental adjustment to the testing procedure is necessary in order to allow for the successful conduction of consolidated fire tests. This is due to effects like strength and stiffness degradation, load redistributions, thermal expansion and creep phenomena that may significantly influence the response of a structure in fire. Even though CFA bears an enormous potential for applications in fire safety engineering, there are only very few theoretical and experimental investigations covering this topic. One of the first applications of hybrid testing in fire engineering was by Mostafei [5] who manually combined a numerical simulation of a six storey reinforced concrete building and a physical test of a single column in order to analyse the global structural fire behaviour.

It is the objective of ongoing research at ETH Zürich and Ruhr-Universität Bochum to develop an analysis procedure that meets the requirements from fire engineering and facilitates the conduction of fully automated consolidated fire analyses.

BENCHMARK PROBLEM

The CFA method combines physical testing and global structural numerical simulation. Considerable complexity is added to the part of the physical component testing by temperature-dependent aspects of material behavior, e.g. stiffness and strength degradation, thermal expansion, high-temperature creep phenomena and strain rate effects. Therefore, a suitable benchmark problem for consolidated thermo-mechanical modelling was developed to comprehensively study basic methodological problems and to verify the methods solely by physical testing. Figure 1 overviews the concept of the benchmark problem studied. Figure 1a shows the static system consisting of a simply supported beam that is connected to a truss element at midspan. While the beam remains at ambient temperature throughout the

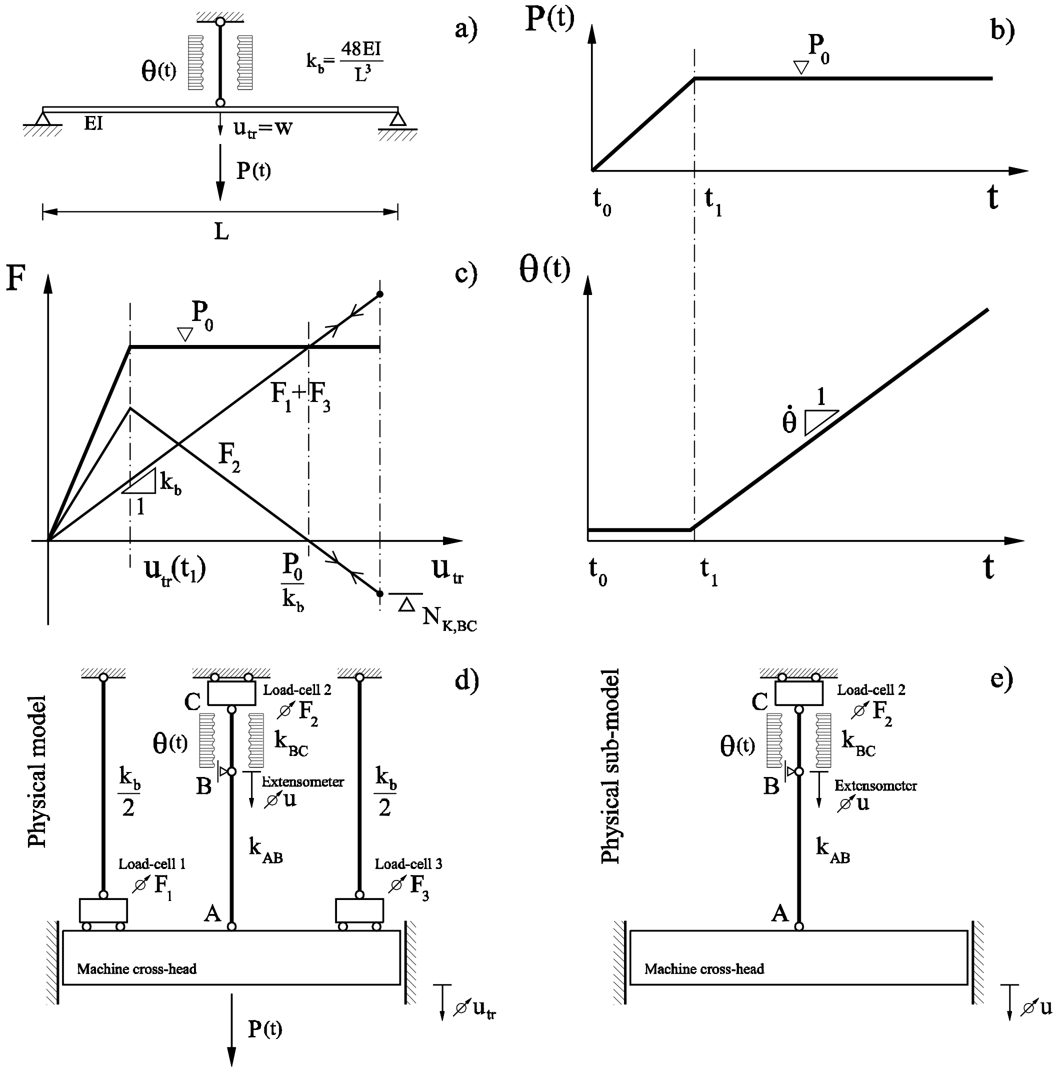

Figure 1. Benchmark test for combined thermo-mechanical consolidated fire testing. a) Static system b) time history of thermal and mechanical load application c) Expected structural response of the benchmarkproblem d) Test setup for sole physical testing e) Physical sub-model for consolidated fire test setup

full course of the CFA procedure, the truss element is additionally exposed to thermal loads. Figure 1b illustrates the sequence of mechanical and thermal load application. In the beginning of the test at time t_0, up to time, t_1, the external load P_0 is applied to the structural system. Thereafter the magnitude of the external force remains constant and the gas temperature is increased at a constant heating rate, $\dot{\theta}$, until the target temperature, $\theta_{target,}$ is reached. The global behavior of this benchmark problem can be analyzed by both CFA and sole physical testing. This approach facilitates the verification of the results obtained by CFA and ensures that important effects that may influence the structural response during a fire event like strength- and stiffness degradation, thermal expansion and creep effects are considered in the testing procedure. Figure 1d schematically illustrates the configuration for the pure physical test. The truss element extending from B to C represents the steel coupon specimen that is mounted into the universal testing machine (UTM) inside the electric furnace. The change in specimen length is denoted by, $u_{specimen}$,and measured using a high temperature resisting extensometer. The truss element extending from point A to B represents the connecting rods and attachments between the specimen and the UTM crosshead. These two serially connected elements represent the truss element of the benchmark problem. In order to model the beam in the sole physical test, two tension rods of an elastic stiffness equivalent to the beam stiffness $k_B=48EI/L^3$ are installed inside the UTM. During the pure physical test, the beam force F_1+F_3 and the force in the truss element F_2 are continuously recorded. Figure 1e shows the setup used for the analysis of the global structural behavior using the consolidated fire analysis technique. In the physical sub-model only the truss element is considered and physically tested, while the beam is numerically modelled. As can be seen from Figure 1e, the representation of the truss element in the CFA setup is identical to the physical test setup mentioned before.

Figure 1c illustrates the expected behavior of the benchmark problem. In the beginning of the test the total external load, P_0, is applied. The load distribution between the truss element and the beam after this step is dependent on the stiffness ratio between the two elements. During the heating phase, a load redistribution from the truss to the beam element is expected due to thermal expansion and thermally induced stiffness degradation of the truss element.

EXPERIMENTAL SETUP FOR CONSOLIDATED FIRE ANALYSIS

The experimental setup is illustrated in Figure 2. Its main components are the numerical and the physical sub-model that are coupled through a server. In the physcial sub-model only the truss element is considered and physically tested. The combined setup of a universal testing machine (UTM) and a split-tube furnace facilitates the application of both thermal and mechanical loads. Dog-bone shaped steel coupon specimens of steel grade S355 (mild steel) were used to represent the truss element in the physical model. These specimen were cut from an SHS 160·160·8 section and originate from the same batch of steel, that was used for the material tests at elevated temperatures presented in Knobloch et. al 2013 [2]. A high temperature resisting extensometer is used to measure the specimen longitudinal displacement, $u_{specimen}$, during a CFA. Furthermore the crosshead displacement, $u_{crosshead}$, the specimen force, F_{truss}, as well as the gas and the specimen temperature are constantly recorded. The numerical model was implemented in ABAQUS Standard and involves the entire structure of the benchmark problem (beam and truss element). The thermal and mechanical load application is conducted using a static solution procedure in the FEM-model. The necessary communication between the numerical model and the server is accomplished by making use of user defined elements for the modelling of the truss element in the FEM-model. This feature of ABAQUS allows its user to define the element's behavior in a user subroutine (UEL). This subroutine is called in every Newton-Raphson-iteration. During such a subroutine call, the elemental calculations have to be performed and the nodal forces and the element stiffness have to be updated. As the numerical model is put on hold until completion of a subroutine call, it is possible to update the numerical model with data acquired in the physical part of the CFA [6]. The server is connected to the

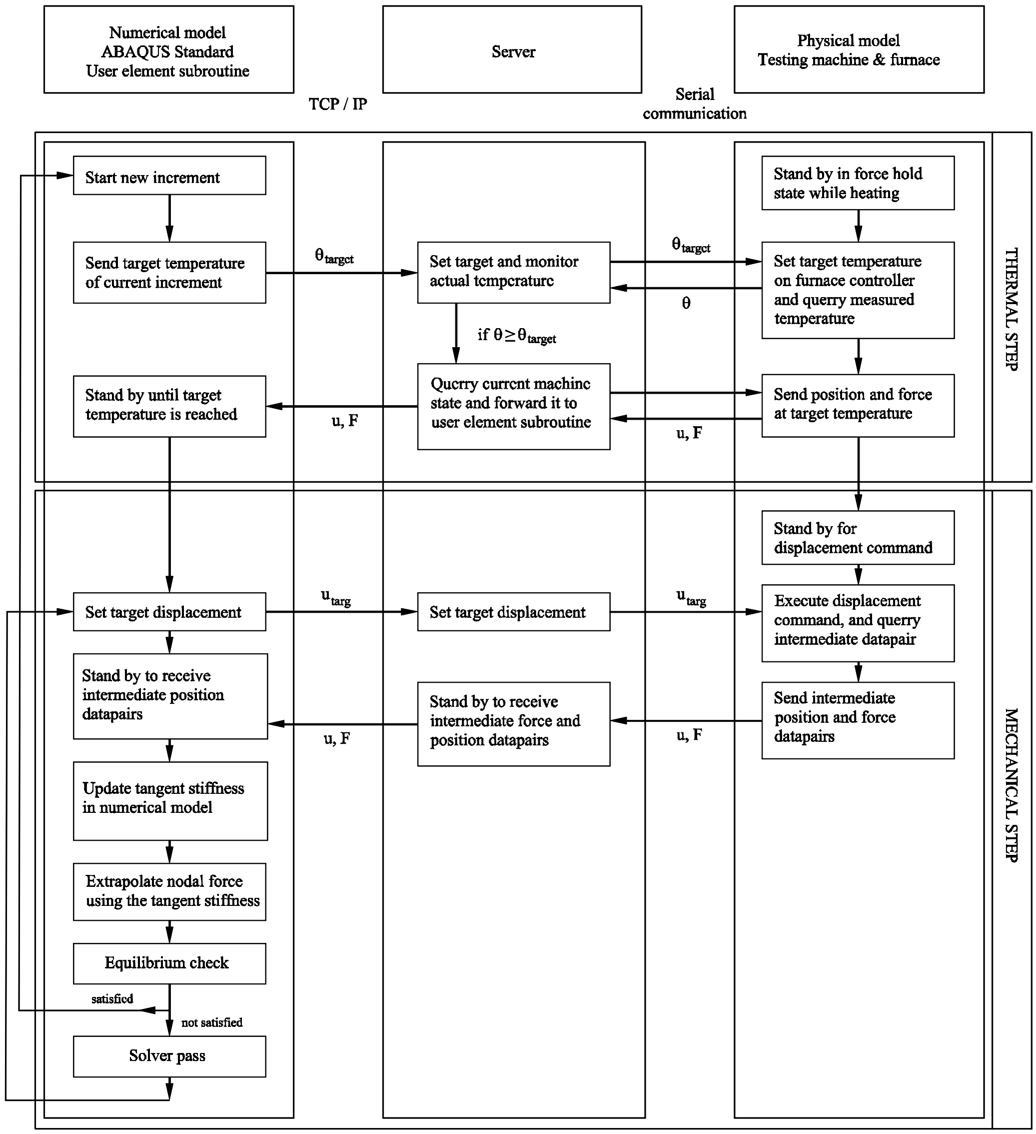

Figure 2. Testing procedure

numerical model by a TCP/IP connection while the furnace and the UTM in the physcial model are individually connected to the server using serial communication. The main tasks of the server are to ensure synchronicity and provide the CFA procedure with the capability of data exchange between the numerical and the physical model. A simplified illustration of the testing procedure is shown in Figure 2.

TEST RESULTS

Figure 3 shows consolidated fire test results from two different tests that were performed at the Structures Laboratory at ETH Zurich. Figure 3a and 3b show in a sequence as a function of the crosshead displacement, $u_{crosshead}$, the externally applied load, P, the truss element force recorded during the CFA in the physical model, F_{truss}, and the force in the beam in the numerical model, $F_{beam,ABAQUS}$. Figure 3c and 3d show the evolution of the gas and the specimen temperature in relation to both the crosshead displacement, $u_{crosshead}$, and the specimen displacement, $u_{specimen}$..

Given the elastic stiffness of the truss element in relation to the crosshead displacement, the elastic beam stiffness was determined in order to achieve the desired initial load shares of 10% in the beam and 90% in the truss element after the application of the total external load, P_0. As the steel coupon specimens used in the two CFAs were derived from the same batch of steel as those tested by Knobloch et. al 2013 [2], the material behaviour at elevated temperatures and various strain rates is known a priori. This approach facilitated the construction of the temperature and strain rate dependent 0.2% proof strength line, designated by $F_{p,0.2,\theta,\dot{\varepsilon}}$ in Figure 3a, b, e and f. The results of [2] showed that the material strength at high temperatures was almost reached at 0.2% plastic strain and thus the 0.2% proof strength line can be used for determining the truss element strength.

The difference between the two consolidated fire tests presented in this paper is the beam behaviour in the numerical model. The beam stiffness of test A remained constant throughout the full course of the CFA resulting in a linear relation between, $F_{beam,ABAQUS}$, and the crosshead displacement, $u_{crosshead}$. In test B, the beam stiffness gradually decreases once a crosshead displacement of 1 mm is exceeded.

After the application of the total load, P_0, the externally applied load is held constant and the heating phase commences. At this stage, a state of equilibrium can only be achieved if an increase in load share of the beam is accompanied by an equally large decrease in the truss element. This behaviour can be observed e.g. in the CFA results from test A. The internal forces of the two load carrying components balance the externally applied load at all times and the truss element force decreases linearly. Furthermore it can be noted, that the solution obtained by CFA yields internal forces below the elastic limit.

Figure 3b shows the beam force – midspan deflection behavior of the CFA where a bilinear stress relationship was used for the modelling of the material behavior of the beam in the numerical model. It can be noted, that this change in the numerical model had a significant influence on the test results. The truss element force recorded during test B follows a different path than in test A and is not linear anymore. As the beam stiffness starts decreasing once a displacement of 1 mm is exceeded, the truss element load share in Point, M, has to be larger in test B than in test A. However, due to the temperature induced strength degradation, the force required to reach a state of equilibrium cannot be taken anymore by the steel coupon specimen for displacements larger than u_M. It can be seen from Figure 3b that point M marks the intersection of the F_{truss} line with the 0.2% proof strength line. As the numerical model is continuously updated with the current specimen force and stiffness measured in the physcial sub-model, this transition is recognized by the numerical model. Further, it can be seen from the analysis results that for the maximum displacement fixed in the test, no equilibrium could have been achieved and consequently the analysis was aborted by ABAQUS. The abort of the CFA is a consequence of the setting used for the maximum displacement. This could be avoided if this number was increased.

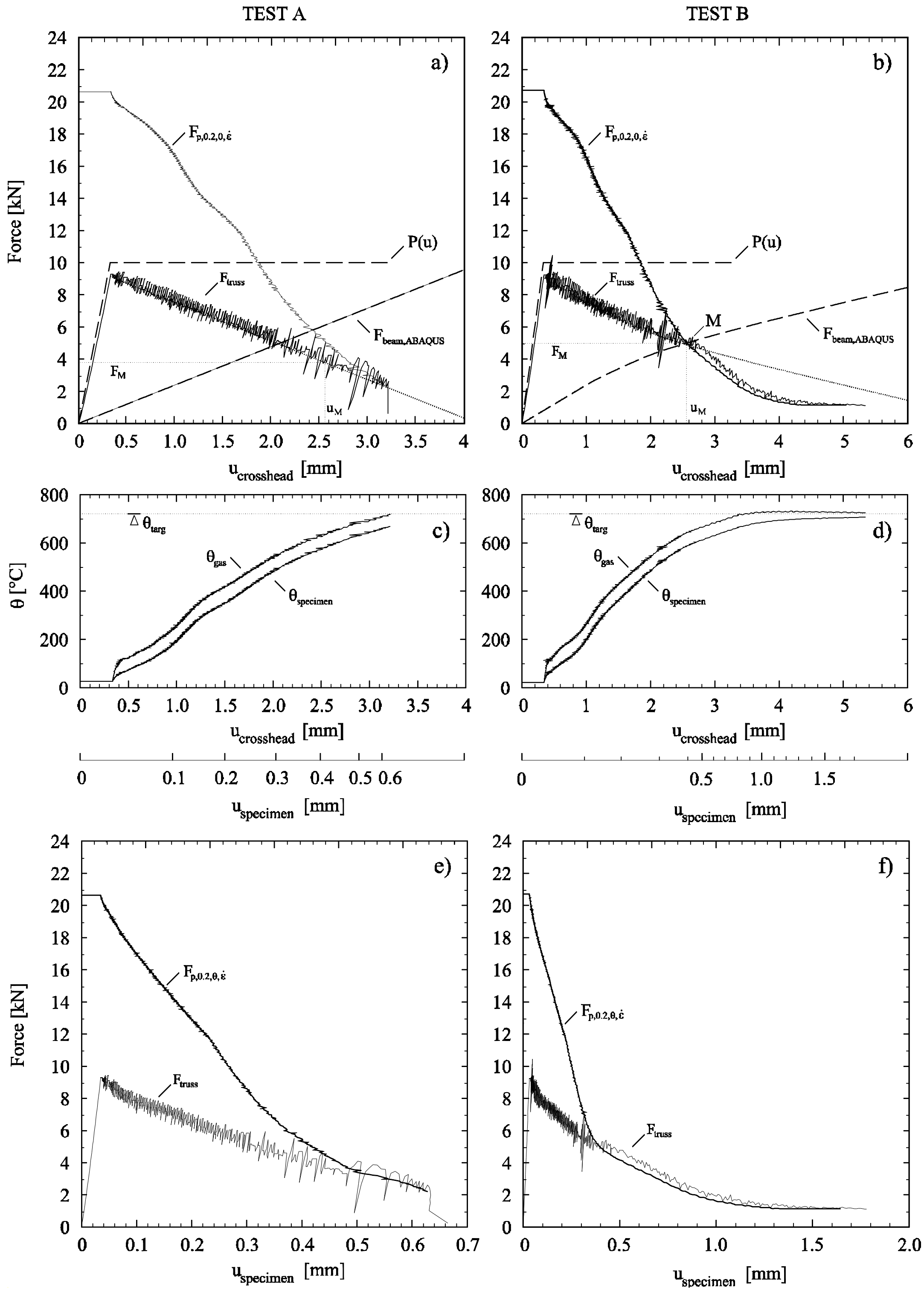

Figure 3. Test results from two CFA; a) F-$u_{crosshead}$ curve for test A; b) F- $u_{crosshead}$ curve for test B; c) θ-$u_{crosshead}$ and θ-$u_{specimen}$ for test A; d) θ-$u_{crosshead}$ and θ-$u_{specimen}$ for test B; e) F-$u_{specimen}$ curve for test A; f) F- $u_{crosshead}$ curve for test B;

SUMMARY, CONCLUSIONS AND OUTLOOK

A testing procedure for consolidated fire analysis has been developed for the analysis of the global behavior of structures in fire. A benchmark problem that can be studied by consolidated fire analysis, pure numerical simulation and sole physical testing has been presented and results from two preliminary fully automated consolidated fire analyses were shown. During the coupled numerical and physical fire analyses, the specimen in the physical sub-model experienced thermally induced strength and stiffness degradation leading to plastic yielding in one of the two tests presented.

The presented study shows the potential of consolidated fire analysis (CFA) and explains the developed testing procedure. The study further shows that the analysis procedure is suitable and could replace difficult to perform and costly large-scale tests by an efficient combination of numerical and local experimental analysis on sub-models. The study of the pure physical test will be used for verification and for the further development of the consolidated fire analysis procedure in the future.

REFERENCES

1. Bailey, C., K. Both, I. Burgess, J. Dowling, B. Kirby, B. Kruppe et al 1999. "The Behaviour of multi storey steel framed buildings in fire", Swinden Technology Center

2. Knobloch, M., J. Pauli, M. Fontana, 2013. "Influence of the strain-rate on the mechanical properties of mild carbon steel at elevated temperatures", Materials and Design, 49:553-565.

3. Knobloch, M., M. Fontana 2014. "Stability of steel structures in fire – State of the art, recent studies in Switzerland and future trends.", Stahlbau 83(4) (2014) 257-264

4. Moore, D. B., T. Lennon, 1997. "Fire Engineering design of steel structures. Progress in Structural Engineering and Materials 1 (1997), 4-9.

5. Mostafei H., 2013. "Hybrid fire testing for assessing performance of structures in fire – Application", Fire Safety Journal, 56:30-38.

6. Schellenberg A., 2008. "Advanced Implementation of Hybrid Simulation," dissertation, University of California, Berkeley.

7. Schulthess P., M. Neuenschwander, M. Knobloch, M. Fontana, 2015. „Consolidated Fire Testing – A Framework for Thermomechanical Modelling" presented at the 6th International Conference on Computational Methods for Coupled Problems in Science and Engineering, Mai 18-20, 2015

8. Takanashi K., M. Nakashima, 1988. "On-line Computer Test Control Method and its Application to Earthquake Response Simulation of Steel Structural Models", Journal of Constructional Steel Research, 11:27-40.

A Static Partitioned Solver for Hybrid Fire Testing

NICOLA TONDINI[1], GIUSEPPE ABBIATI[2],
LUCA POSSIDENTE[1] and BOZIDAR STOJADINOVIC[2]

ABSTRACT

The paper presents the development and the application of a thermomechanical static solver based on the Finite Element Interconnecting Method (FETI) to be employed in hybrid fire tests. Hybrid fire testing is an appealing methodology that intends to test in relatively small furnaces, compared to the whole building, single structural elements or limited parts of the building that exhibit a highly nonlinear fire behaviour whereas the remainder of the structure is modelled numerically with good accuracy. On these premises, the paper comprehensively describes the proposed static solver by highlighting its ability to guarantee compatibility and equilibrium at the interface between the physical substructure (PS) and the numerical substructure (NS), both for non-floating and floating subdomains as well as for nonlinear behaviour of the PS. The algorithm development has been focused on providing a procedure that in principle can be actually used experimentally. Thus, an error propagation analysis that takes into account errors and uncertainties, such delay and measurement noise, is also presented. The validation carried out in a fully numerical framework, i.e. the PS is also numerically modelled, on a steel frame shows promising outcomes for future experimental implementations.

INTRODUCTION

Large-scale structural fire tests are rare because they are costly and require specialized facilities. According to the state of the art, only a few full-scale tests or large-scale tests have been performed [1]. The most of the research regarding the behaviour of structures in fire has been carried out on single structural components, exposed to standard fire curves in order to compare the fire performance under same testing conditions for regulatory purposes. However, they do not represent real fires and building elements, such as beams, floors, walls and columns, are usually tested in fire without taking into account the actual boundary conditions. Especially for statically indeterminate structural assemblies subjected to thermal action, which experience indirect loadings due to restrained thermal deformations, tests on single

[1]Department of Civil, Environmental and Mechanical Engineering, University of Trento, Via Mesiano 77, 38123, Trento, Italy.
[2]Department of Civil, Environmental and Geomatic Engineering (D-BAUG), IBK, ETH Zurich, Wolfgang-Pauli-Strasse 27, Switzerland.

components do not provide insight into the thermomechanical interaction with the remainder of the structure.

In order to run a fire test in a more realistic fashion, the development of dedicated experimental techniques is appealing. Hybrid simulation (HS), extensively investigated in the seismic domain, can be profitably extended to thermal loadings, and thus, the thermomechanical interaction can be accounted for up to collapse. HS is a very effective testing strategy for simulating the dynamic response of structural systems whose dimensions and complexities exceed the capacity of typical testing facilities. The hybrid model of the prototype structural system combines numerical and physical substructures (NSs and PSs). The PSs of the hybrid model are tested in the laboratory because of their strongly nonlinear response and/or lack of a reliable mathematical model, while the NSs are instantiated in a structural analysis software. The first attempts of hybrid fire tests (HFT) were carried out by Korzen [2], Robert et al. [3] and Mostafaei [4]. Some limitations of these works are reported in [5]. In this paper, a numerical partitioned algorithm that provides generality of application and suitability for experimental testing is proposed.

THE PARTITIONED ALGORITHM

Typical civil structures show characteristic heat diffusion times that are much larger than the highest vibration period. As a consequence and in contrast to pure earthquake engineering applications, the thermal action owing to fire can be considered equivalent to a mechanical static load of long duration and, once the failure (local or global) has been triggered, dynamic effects can be significant. From this standpoint, this paper develops an original HFT algorithm that relies on the Finite Element Tearing and Interconnecting (FETI) method. The FETI approach emerged as an efficient technique for solving large linear static problems [6] and it was then extended to dynamic problems. In order to force the continuity of kinematic quantities, an additional force field is defined as further system unknown and applied at the interfaces of both the coupled subdomains. The FETI algorithm that is proposed for HFT calculates the real-time response of the hybrid model of the emulated structure in the fire development phase by considering a pure static force balance of the coupled system. At each simulation step, restoring forces are measured on the PS and the overall displacement solution of the coupled system is calculated via Newton-Raphson's iteration because a nonlinear behaviour of the system is assumed. Lagrange multipliers, which represent the interface force fields, are calculated as additional system unknowns. Finally, the calculated displacements are then applied to the PS. Herein, the static FETI algorithm has been implemented both for systems without floating subdomains, i.e. each subdomain is well restrained and no singular matrices appear, and for systems with floating subdomains, i.e. allowance for rigid body motions has to be taken into account.

The basic algorithm for non-floating subdomains

First, the set of force balance and compatibility equations, which describe the response of the partitioned hybrid system, are presented in Eq. (1). For the sake of clarity, subscripts N and S stand for numerical and physical subdomains, respectively.

$$\begin{cases} \mathbf{r}_N(\mathbf{u}_N) = \mathbf{f}_N + \mathbf{B}_N{}^T\boldsymbol{\lambda} \\ \mathbf{r}_P(\mathbf{u}_P) = \mathbf{f}_P + \mathbf{B}_P{}^T\boldsymbol{\lambda} \\ \mathbf{B}_N\mathbf{u}_N + \mathbf{B}_P\mathbf{u}_P = 0 \end{cases} \tag{1}$$

where, $\mathbf{r}_N$ and $\mathbf{r}_P$ are the restoring force, $\mathbf{f}_N$ and $\mathbf{f}_P$ are the external load, $\mathbf{u}_N$ and $\mathbf{u}_P$ are the displacement fields of the NS and PS, respectively. $\boldsymbol{\lambda}$ is the Lagrange multiplier vector that represents an additional force field which imposes the continuity of the displacement field at the interface between the two subdomains. Finally, $\mathbf{B}_N$ and $\mathbf{B}_P$ are Boolean matrices that localise the interface degrees-of-freedom on each subdomain. A Newton-Raphson's algorithm is selected for the solution of Eq. (1) at each time step of the hybrid simulation. Accordingly, the expression of the residual reads,

$$\mathbf{A}(\mathbf{u}_N, \mathbf{u}_P, \boldsymbol{\lambda}) = \begin{bmatrix} \mathbf{r}_N(\mathbf{u}_N) - \mathbf{f}_N - \mathbf{B}_N{}^T\boldsymbol{\lambda} \\ \mathbf{r}_P(\mathbf{u}_P) - \mathbf{f}_P - \mathbf{B}_P{}^T\boldsymbol{\lambda} \\ \mathbf{B}_N\mathbf{u}_N + \mathbf{B}_P\mathbf{u}_P \end{bmatrix} \tag{2}$$

The entailing minimization problem is solved at each time step.

$$\{\mathbf{u}_N, \mathbf{u}_P, \boldsymbol{\lambda}\} = \underset{\mathbf{u}_N, \mathbf{u}_P, \boldsymbol{\lambda}}{\arg\min}\, \mathbf{A}(\mathbf{u}_N, \mathbf{u}_P, \boldsymbol{\lambda}) \tag{3}$$

Since the modified Newton-Raphson's method the Jacobian of $\mathbf{A}$ is defined as,

$$D\mathbf{A} = \begin{bmatrix} D\mathbf{r}_N & \mathbf{0} & -\mathbf{B}_N \\ \mathbf{0} & D\mathbf{r}_P & -\mathbf{B}_P \\ \mathbf{B}_N & \mathbf{B}_P & \mathbf{0} \end{bmatrix} \tag{4}$$

where $D\mathbf{r}_N$ and $D\mathbf{r}_P$ are the Jacobian of the restoring force vectors of the NS and PS. In the linear case, they correspond to the stiffness matrices. The $D\mathbf{r}_P$ Jacobian is not known a priori because related to the specimen properties that can change during the test. Thus, it was decided to estimate it based on the initial tangent stiffness of the PS without updating it during the test. This is crucial from the HS perspective. In fact, a reliable estimate of the initial $\mathbf{K}_P$ can be obtained before the tests but it cannot be easily updated online at each time step.

From the laboratory standpoint, for each time step i, for each iteration j, the displacement vector $\mathbf{u}_P$ is applied to the specimen and the quantity $\mathbf{r}_P(\mathbf{u}_P) - \mathbf{f}_P$ is measured by the actuator load cells. Such force enter the expression of the residual of Eq. (2) and the modified Newton-Raphson algorithm calculates the next correction. As a result, the hybrid simulation can be conducted in displacement control. The major limitation of the presented approach is that it cannot handle floating subdomains. Therefore, an enhanced version is presented in the following section where floating subdomain can be implemented.

Extension to floating subdomains

Before introducing the algorithm, it is necessary to define the meaning of floating subdomain. A floating subdomain is characterized by a singular stiffness matrix because of insufficient constraint. A non-floating structure can be decomposed in floating subdomains, and therefore, it is crucial to be able to handle such local singularities. In the case of floating subdomains Eq. (1) becomes,

$$\begin{cases} \mathbf{r}_N(\mathbf{u}_N) = \mathbf{f}_N + \mathbf{B}_N{}^T\boldsymbol{\lambda} \\ \mathbf{r}_P(\mathbf{u}_P) = \mathbf{f}_P + \mathbf{B}_P{}^T\boldsymbol{\lambda} \\ \mathbf{B}_N(\mathbf{u}_N + \mathbf{R}_N\boldsymbol{\alpha}_N) + \mathbf{B}_P(\mathbf{u}_P + \mathbf{R}_P\boldsymbol{\alpha}_P) = 0 \\ \mathbf{R}_P^T(\mathbf{f}_P + \mathbf{B}_P{}^T\boldsymbol{\lambda}) = 0 \\ \mathbf{R}_N^T(\mathbf{f}_N + \mathbf{B}_N{}^T\boldsymbol{\lambda}) = 0 \end{cases} \tag{5}$$

where $\mathbf{R}_P$ and $\mathbf{R}_N$ are a column matrices that gather rigid body modes of the PS and the NS, respectively. In this case, the displacement field of each subdomain k-th is split into a deformational component $\mathbf{u}_k$ and a rigid body mode $\boldsymbol{\alpha}_k$. The restoring force of the subdomain depends on the deformational component only, but the interface compatibility must be set in terms of total displacements. The two last equations of Eq. (5) state that the external load cannot produce work with respect to rigid body displacement fields. Similarly to the non-floating case, a minimization problem is solved at each time step

$$\{\mathbf{u}_N, \mathbf{u}_P, \boldsymbol{\alpha}_N, \boldsymbol{\alpha}_P, \boldsymbol{\lambda}\} = \underset{\mathbf{u}_N, \mathbf{u}_P, \boldsymbol{\lambda}, \boldsymbol{\alpha}}{\arg\min}\, \mathbf{A}(\mathbf{u}_N, \mathbf{u}_P, \boldsymbol{\alpha}_N, \boldsymbol{\alpha}_P, \boldsymbol{\lambda}) \tag{6}$$

where the residual **A** now reads,

$$\mathbf{A}(\mathbf{u}_N, \mathbf{u}_P, \boldsymbol{\alpha}_N, \boldsymbol{\alpha}_P, \boldsymbol{\lambda}) = \begin{bmatrix} \mathbf{r}_N(\mathbf{u}_N) - \mathbf{f}_N - \mathbf{B}_N{}^T\boldsymbol{\lambda} \\ \mathbf{r}_P(\mathbf{u}_P) - \mathbf{f}_P - \mathbf{B}_P{}^T\boldsymbol{\lambda} \\ \mathbf{B}_N(\mathbf{u}_N + \mathbf{R}_N\boldsymbol{\alpha}_N) + \mathbf{B}_P(\mathbf{u}_P + \mathbf{R}_P\boldsymbol{\alpha}_P) \\ \mathbf{R}_N^T(\mathbf{f}_N + \mathbf{B}_N{}^T\boldsymbol{\lambda}) \\ \mathbf{R}_P^T(\mathbf{f}_P + \mathbf{B}_P{}^T\boldsymbol{\lambda}) \end{bmatrix} \tag{7}$$

And the Jacobian of **A** is yields

$$D\mathbf{A} = \begin{bmatrix} D\mathbf{r}_N & \mathbf{0} & -\mathbf{B}_N & \mathbf{0} & \mathbf{0} \\ \mathbf{0} & D\mathbf{r}_P & -\mathbf{B}_P & \mathbf{0} & \mathbf{0} \\ \mathbf{B}_N & \mathbf{B}_P & \mathbf{0} & \mathbf{B}_N\mathbf{R}_N & \mathbf{B}_P\mathbf{R}_P \\ \mathbf{0} & \mathbf{0} & \mathbf{R}_N^T\mathbf{B}_N^T & \mathbf{0} & \mathbf{0} \\ \mathbf{0} & \mathbf{0} & \mathbf{R}_P^T\mathbf{B}_P^T & \mathbf{0} & \mathbf{0} \end{bmatrix} \tag{8}$$

where in the case of the NS or the PS is a floating subdomain their respective $D\mathbf{r}_N$ or $D\mathbf{r}_P$ tangent stiffness matrices are singular and consequently $D\mathbf{A}$ cannot be inverted. In order to $D\mathbf{A}$ be non-singular, the subdomain stiffness matrices are modified as follows. First, the null space of each stiffness matrix $D\mathbf{r}_k$ is calculated.

$$\mathbf{T}_k = [\mathbf{T}_{k,1}, \dots, \mathbf{T}_{k,i} \dots, \mathbf{T}_{k,n_k}] = ker(D\mathbf{r}_k) \tag{9}$$

where $\mathbf{T}_{k,i}$ is the i-th rigid body mode of the subdomain k-th normalized to unit maximum value and n_k is the number of its rigid body modes. Then, a complementary stiffness matrix $D\mathbf{r}_{k,c}$ that operates in the null space of $D\mathbf{r}_k$ only, is created and summed to $D\mathbf{r}_k$.

$$D\mathbf{r}_{k,c} = \sum_{i=1}^{n_k} \max\left(\text{diag}(D\mathbf{r}_k)\right) \mathbf{T}_{k,i}\mathbf{T}_{k,i}^T \tag{10}$$

The rank of the complementary stiffness matrix $D\mathbf{r}_{k,c}$ is n_k by construction and the factor $\max\left(\text{diag}(D\mathbf{r}_k)\right)$ ensures a well conditioning of the modified stiffness matrix $D\bar{\mathbf{r}}_k$, which reads,

$$D\bar{\mathbf{r}}_k = D\mathbf{r}_k + D\mathbf{r}_{k,c} \tag{11}$$

By adding contributions that are based on rigid body modes that will not excite the deformational field, the singularity is removed without affecting the deformational modes that are, conversely, the ones that induce restoring forces. The modified Jacobian $\overline{D\mathbf{A}}$ results:

$$\overline{D\mathbf{A}} = \begin{bmatrix} D\bar{\mathbf{r}}_N & \mathbf{0} & -\mathbf{B}_N & \mathbf{0} & \mathbf{0} \\ \mathbf{0} & D\bar{\mathbf{r}}_P & -\mathbf{B}_P & \mathbf{0} & \mathbf{0} \\ \mathbf{B}_N & \mathbf{B}_P & \mathbf{0} & \mathbf{B}_N\mathbf{R}_N & \mathbf{B}_P\mathbf{R}_P \\ \mathbf{0} & \mathbf{0} & \mathbf{R}_N^T\mathbf{B}_N^T & \mathbf{0} & \mathbf{0} \\ \mathbf{0} & \mathbf{0} & \mathbf{R}_P^T\mathbf{B}_P^T & \mathbf{0} & \mathbf{0} \end{bmatrix} \tag{12}$$

In this case, by implementation of the modified Newton-Raphson's method, the numerical static scheme is given below where it is assumed that the initialization occurs after the application of the gravity loads. As for the non-floating subdomain case, a constant Jacobian is used, which is based on the initial tangent stiffness matrices of both subdomains. The algorithm scheme is given below.

$$\mathbf{u}_N^{(1)} = \mathbf{0}, \mathbf{u}_P^{(1)} = \mathbf{0}, \boldsymbol{\lambda}^{(1)} = \mathbf{0}, \boldsymbol{\alpha}_N^{(1)} = \mathbf{0}, \boldsymbol{\alpha}_P^{(1)} = \mathbf{0}$$

$$\mathbf{A}\left(\mathbf{u}_{N,i}^{(k)}, \mathbf{u}_{P,i}^{(k)}, \boldsymbol{\lambda}_i^{(k)}, \boldsymbol{\alpha}_{N,i}^{(k)}, \boldsymbol{\alpha}_{P,i}^{(k)}\right) = \begin{bmatrix} \mathbf{r}_N\left(\mathbf{u}_{N,i}^{(k)}\right) - \mathbf{f}_{N,i} - \mathbf{B}_N{}^T\boldsymbol{\lambda}_i^{(k)} \\ \mathbf{r}_P\left(\mathbf{u}_{P,i}^{(k)}\right) - \mathbf{f}_{P,i} - \mathbf{B}_P{}^T\boldsymbol{\lambda}_i^{(k)} \\ \mathbf{B}_N\left(\mathbf{u}_{N,i}^{(k)} + \mathbf{T}_N\boldsymbol{\alpha}_i^{(k)}\right) + \mathbf{B}_P\left(\mathbf{u}_{P,i}^{(k)} + \mathbf{T}_P\boldsymbol{\alpha}_i^{(k)}\right) \\ \mathbf{T}_N^T\left(\mathbf{f}_{N,i} + \mathbf{B}_N{}^T\boldsymbol{\lambda}_i^{(k)}\right) \\ \mathbf{T}_P^T\left(\mathbf{f}_{P,i} + \mathbf{B}_P{}^T\boldsymbol{\lambda}_i^{(k)}\right) \end{bmatrix}$$

$$
\begin{bmatrix} \Delta\mathbf{u}_{N,i}^{(k)} \\ \Delta\mathbf{u}_{P,i}^{(k)} \\ \Delta\boldsymbol{\lambda}_{i}^{(k)} \\ \Delta\boldsymbol{\alpha}_{N,i}^{(k)} \\ \Delta\boldsymbol{\alpha}_{P,i}^{(k)} \end{bmatrix} = -D\mathbf{A}^{-1}\mathbf{A}\left(\mathbf{u}_{N,i}^{(k)}, \mathbf{u}_{P,i}^{(k)}, \boldsymbol{\lambda}_{i}^{(k)}, \boldsymbol{\alpha}_{N,i}^{(k)}, \boldsymbol{\alpha}_{P,i}^{(k)}\right)
$$

$\mathbf{u}_{P,i}^{(k+1)}$

$$
\begin{bmatrix} \mathbf{u}_{N,i+1}^{(k)} \\ \mathbf{u}_{P,i+1}^{(k)} \\ \boldsymbol{\lambda}_{i+1}^{(k)} \\ \boldsymbol{\alpha}_{N,i+1}^{(k)} \\ \boldsymbol{\alpha}_{P,i+1}^{(k)} \end{bmatrix} = \begin{bmatrix} \Delta\mathbf{u}_{N,i}^{(k)} \\ \Delta\mathbf{u}_{P,i}^{(k)} \\ \Delta\boldsymbol{\lambda}_{i}^{(k)} \\ \Delta\boldsymbol{\alpha}_{N,i}^{(k)} \\ \Delta\boldsymbol{\alpha}_{P,i}^{(k)} \end{bmatrix} + \begin{bmatrix} \mathbf{u}_{N,i}^{(k)} \\ \mathbf{u}_{P,i}^{(k)} \\ \boldsymbol{\lambda}_{i}^{(k)} \\ \boldsymbol{\alpha}_{N,i}^{(k)} \\ \boldsymbol{\alpha}_{P,i}^{(k)} \end{bmatrix}
$$

$$
\mathbf{u}_{N,i+1}^{(1)} = \mathbf{u}_{N,i}^{(iter+1)}, \mathbf{u}_{P,i+1}^{(1)} = \mathbf{u}_{P,i}^{(iter+1)}, \boldsymbol{\lambda}_{i+1}^{(1)} = \boldsymbol{\lambda}_{i}^{(iter+1)}, \boldsymbol{\alpha}_{N,i+1}^{(1)} = \boldsymbol{\alpha}_{N,i}^{(iter+1)}, \boldsymbol{\alpha}_{P,i+1}^{(1)} = \boldsymbol{\alpha}_{P,i}^{(iter+1)}
$$

The splitting of the displacement field into a deformational and a rigid body components is crucial from the hybrid simulation perspective. The floating subdomain cannot be floating anymore once it is tested in the laboratory and some minimal constraint conditions must be introduced. As a result, the only deformational displacement component $\mathbf{u}_P$ is applied to the PS at each iteration. The rigid body coordinate $\boldsymbol{\alpha}_P$ remains a virtual quantity that enters the solution process but it is not applied to the specimen. Since it does not affect the restoring force, it does not influence the force balance.

THE EXPERIMENTAL PROCEDURE

The numerical algorithm was developed to be used in experimental tests that by their nature introduce errors and uncertainties. Thus, the numerical scheme must cope, without exhibiting instability, with noise coming from the load cells and the displacement transducers as well as with delay that inevitably affects the response of the actuators. In addition, the algorithm requires the value of the PS stiffness in order to compute the Jacobian in Eq. (12). As mentioned before, this value will change with time but it is not practical to proceed with an online updating at each time step. Hence, it is kept fixed over the entire duration of the simulation and based on an estimate of the initial tangent stiffness. A wrong estimate of the PS stiffness may cause instability in the numerical algorithm. Therefore, it is necessary to investigate how the error propagates. On these premises, a comprehensive error propagation analysis and a noise analysis that also includes delay are carried out during the validation process on a case study. Moreover, a displacement-control procedure ensure to follow softening branches and enhance lab safety by avoiding instability of actuators at collapse.

VALIDATION ON A CASE STUDY

Figure 1a shows the moment-resisting steel frame that was selected as case study to conduct the validation process of the proposed numerical scheme. The column profiles are HE 200 A and the beam profiles IPE 300. The frame was subdivided into a PS and a NS. In detail, the beam at the first floor located of the second bay was selected as PS, whereas the remainder of the frame is the NS. For simplicity, the frame was not loaded in terms of mechanical loads and only the PS was thermally loaded by a linear temperature gradient in the cross section that linearly increases with time: the intrados of the beam undergoes a temperature increment of 1000 °C in 1000 s whereas the extrados remains at ambient temperature throughout the simulation. The PS is modelled by means of a thermomechanical beam finite element that behaves nonlinearly with respect to temperature because the degradation of the steel elastic modulus according to the EN1993-1-2 model [7] is taken into account. Conversely, plasticity and second order effects were not accounted for. The NS is modelled by means of linear thermomechanical beam elements and remains at ambient temperature. The simulation was performed with the following parameters: simulation time step equal to 1 s; the number of iterations within each time step set to 10; an overestimate of the PS initial elastic stiffness of 50%; delay applied to the displacement application and equal to one sub-iteration, i.e. 100 ms (typically is less than 20 ms); and white noise applied to displacements with range ±2e^{-3} mm and to forces with range ±100 N. The analysis was performed both with a monolithic algorithm, that solves the whole structure, and with the proposed partitioned algorithm that relies on the FETI method.

Figure 1b-d compare the outcomes between the monolithic solution (ML) and the partitioned solutions - NS and PS - in terms of the axial compressive force caused by thermal restraint and of axial displacements of node 1 and 2 of the heated beam. A good agreement is observed and compatibility is satisfied. Moreover, the proposed numerical scheme seems to be less sensitive to noise, delay and errors entailing a good robustness. The nonlinear behaviour owing to the elastic modulus degradation is clearly observed by looking at Figure 1b. The deformed shape illustrated in Figure 1e is consistent with the physical problem.

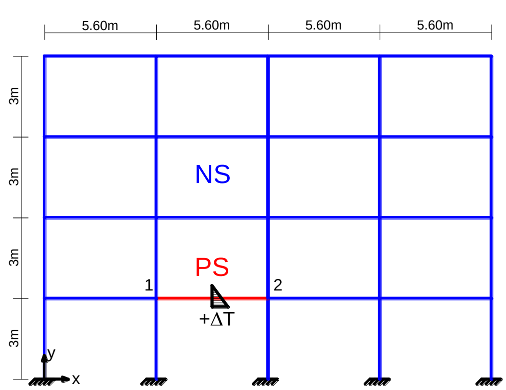

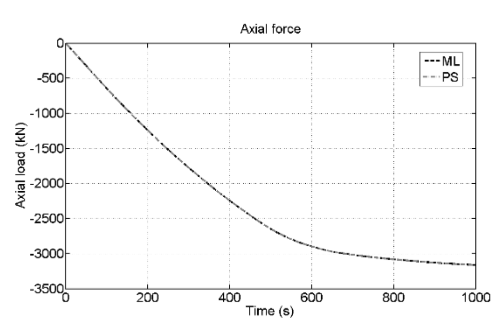

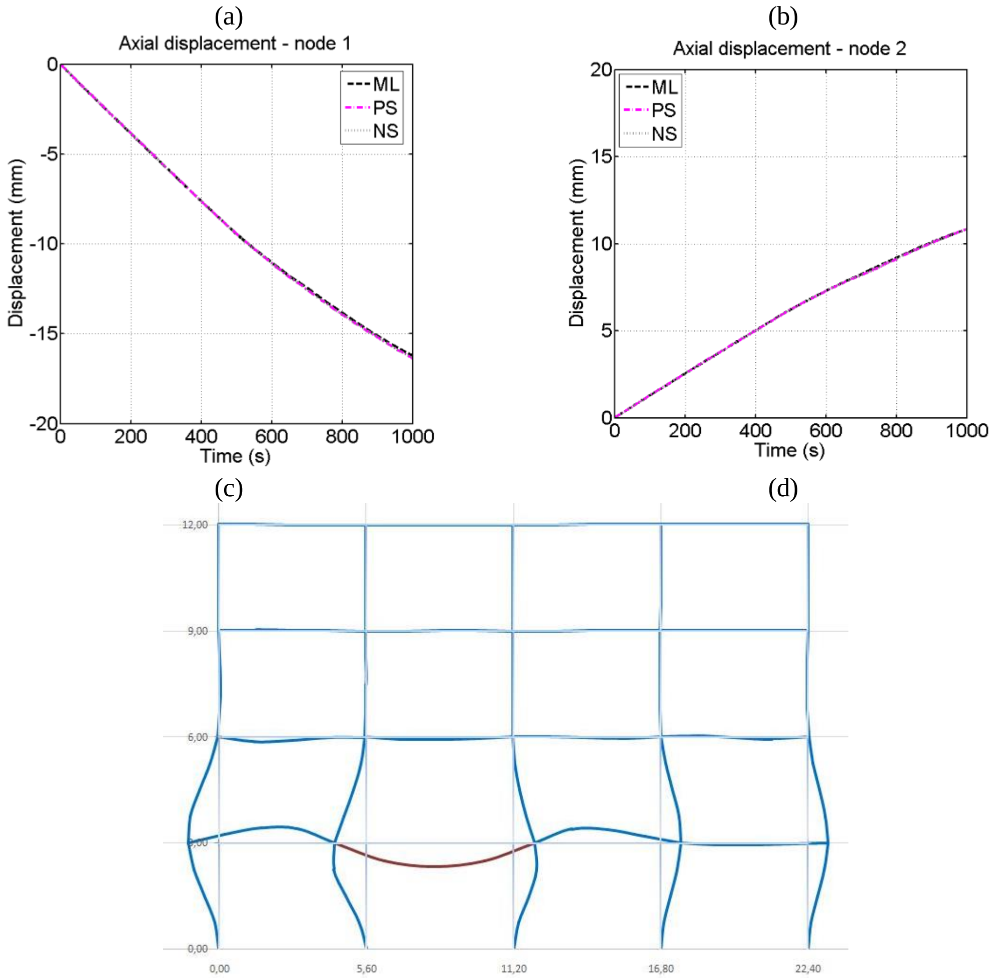

(e)

Figure 1. a) Steel frame; b) evolution of the axial force in the PS; c) evolution of the axial displacement of node 1 of the PS; d) evolution of the axial displacement of node 2 of the PS; e) deformed shape at 1000 s magnified by a factor of 75.

CONCLUSIONS

The proposed static numerical algorithm based on the FETI method showed good outcomes in tackling issues related to hybrid fire testing. In fact, it is a scheme that guarantees compatibility and equilibrium at the end of each time step and general field of application. Moreover, it can handle nonlinear behaviour that appears during the test for both non-floating and floating subdomains by implementing Newton-Raphson's iterations. The numerical algorithm has been developed to be used in displacement control to follow possible softening branches and to avoid actuator instability at collapse. The validation carried out on steel frame confirmed a good agreement between the monolithic solution and the partitioned solutions. Moreover, the proposed numerical algorithm exhibited good robustness with respect typical sources of errors, such noise and delay without undergoing instability. This leads to consider this approach promising for future applications to a real hybrid fire test.

REFERENCES

1. British Steel. 1999. "*The behavior of multi-storey steel frame buildings in fire*" Rotherham: British Steel. 82 pages
2. Korzen M., Magonette G., Buchet Ph., 1999. "Mechanical loading of columns in fire tests by means of the substructuring method," *Zeitschrift für Angewandte Mathematik und Mechanik*, 79: S617-S618.
3. F. Robert, S. Rimlinger, C. Collignon. 2010. Structure fire resistance: a joint approach between modelling and full scale testing (substructuring system), *3rd fib International Congress*.
4. Mostafaei, H. 2013. Hybrid fire testing for assessing performance of structures in fire -Application. *Fire Safety Journal*, 56, 30–38. doi:10.1016/j.firesaf.2012.12.003.
5. Sauca, A., Gernay T., Robert F., Tondini N. and Franssen J.-M. 2016. Stability In Hybrid Fire Testing, *9th International conference on Structures in Fire*, 8-10 June.
6. Farhat, C. and Roux, F.-X. 1991. A method of finite element tearing and interconnecting and its parallel solution algorithm. *Int J Num Meth Engng*, 32: 1205–1227. doi: 10.1002/nme.1620320604.
7. EN1993-1-2. 2005. "*Eurocode 3: Design of steel structures – Part 1-2: General rules – Structural fire design*," CEN, Brussel.

Stability in Hybrid Fire Testing

ANA SAUCA[1], THOMAS GERNAY[1], FABIENNE ROBERT[2], NICOLA TONDINI[3] and JEAN MARC FRANSSEN[1]

ABSTRACT

Hybrid testing is an appealing technique to observe the behavior of an element in an experimental test while taking into account the interaction with the rest of the structure which is modelled numerically. Being widely used in the seismic field, this technique has been recently proposed in the fire field. The purpose of this paper is to demonstrate that the loading control process may be unstable during the hybrid testing when using the methodology applied in former tests presented in the literature. The stability in the latter method depends on the stiffness ratio between the two substructures. For the purpose of discussion, a one degree-of-freedom elastic system is studied. To overcome the stability issues, a new method is presented, independent on the stiffness ratio. Finally, the hybrid testing of a 2D beam being part of a moment resisting frame is analyzed in a virtual environment (both parts being modeled numerically) using the "first generation method" and the new proposed method.

INTRODUCTION

Fire tests are required to observe the behavior of structures exposed to fire. Generally, the tests are performed on single elements, without considering the interaction with the rest of the structure. Entire buildings can also be tested but this approach is very expensive and therefore uncommon.

Using hybrid fire testing (HFT), it is possible to test only selected elements while taking into account the effects of the surrounding structure at the interface.

The methodology is based on substructuring method and it has been widely explored in the seismic field [1]. In fire field, a few hybrid tests have been performed [2]-[5] but the implementation of a method developed from seismic field to the fire field remains a challenge with many aspects to be solved. The principle of HFT is to divide the analyzed structure in two parts, a physical substructure PS (tested in a furnace) and a numerical substructure NS (modelled aside), and to ensure equilibrium and compatibility between these two substructures during the test.

[1]Department ArGEnCO, University of Liege, Bat. B52/3, allée de la Découverte, 9, 4000 Liège, Belgium.
[2]CERIB, Fire Testing Center, BP 30059-28231 Epernon, France.
[3]Departement of Civil, Environmental and Mechanical Engineering, University of Trento, Via Mesiano 77, 38123 Trento, Italy.

At frequent intervals (time step Δt), the displacements or the forces at the interface are measured from the PS and this information is sent to the NS. The reactions (forces or displacements) of the NS at the interface are calculated and then sent back to the PS. There may be an additional delay of time Δt_P requested for the calculation of the NS reaction and for application of the reaction to the PS. The procedure is either called force control procedure FCP or displacement control procedure DCP, when reaction forces or displacements are sent back to the PS.

Korzen [2] presents the hybrid test method applied to a column specimen as part of a simulated building environment. The mode of action between both parts is exemplified on a one degree-of-freedom (DoF) basis, i.e. the axial column force is measured and adjusted continuously to the model force, which is represented through a – not necessarily constant – stiffness, in displacement control.

Robert [3]-[4] presents a hybrid fire test where the PS is a slab, with 3 DoF controlled at the interface i.e. one axial and two rotational. The behavior of the NS is modelled through an elastic predetermined matrix defined before the test.

Mostafaei [5] presents the results of a hybrid test performed on a concrete column (one axial DoF at the interface) extracted from a 3D concrete frame. Unlike the previous cases, the NS is modelled in SAFIR® [6] and a part of the NS is also exposed to fire. The interaction between the PS and NS during the hybrid fire test is done manually by the user.

The methodology presented in previous hybrid fire tests [3]-[5] will be referred in this paper as "first generation method" and is discussed here below.

FIRST GENERATION METHOD FOR HFT

In the case of the first generation method, when updating the interface forces and displacements, only the characteristics of the NS are considered, disregarding the effect of the PS.

The method has been modelled analytically for a simple linear system with a single DoF located at the interface, which is the axial displacement at node 2 (see Figure 1). The temperature in the PS increases with time which induces thermal expansion but, for the sake of simplicity, the stiffness of the PS remains constant. The stiffness of the NS also remains constant during the entire duration of the test. The system is composed of two bars, the PS of length L_P, respectively the NS of length L_N. The heated PS is defined by the axial stiffness K_P and thermal coefficient of the material α whereas the cold NS is characterized by the axial stiffness K_N. In HFT the structure is decomposed and the PS is placed in a furnace, while the NS is modelled via numerical software or characterized by a predetermined matrix.

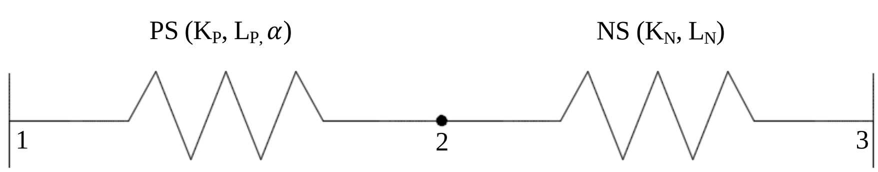

Figure 1. Linear elastic system.

The first generation method using the force control procedure is applied step by step:

a. First, the analysis of the entire system is performed in order to determine the forces and the displacements at the interface between the PS and NS before the fire starts.

b. The PS is placed in the furnace (in a real HFT) and loaded with the exterior loads and interface conditions, while the NS is modeled aside. Herein the exterior loads, the interface forces and displacements are equal to zero.

Note:

$u_x(t_n)$ is the interface displacement of substructure x (P for the PS and N for NS) at time t_n (i.e. displacement of node 2).

$F_x(t_n)$ is the interface force of substructure x (P for the PS and N for NS) at time t_n.

$T(t_n)$ is the temperature of the PS at time t_n.

n is number of the reading.

c. Heating of the PS starts. In force control procedure, the PS is free to expand, and the displacement is measured. In this example, it yields to the value expressed by Eq. (1).

$$u_P(t_1) = \alpha L_P\, T(t_1) \tag{1}$$

d. The measured displacement (1) is imposed on the NS. This generates a reaction force that is computed using Eq. (2).

$$F_N(t_1) = K_N\, \alpha\, L_P T(t_1) \tag{2}$$

e. The new reaction force is imposed on the PS (Eq. (3)). A time delay Δt_P is used to capture the time needed to compute the reaction of the NS and to adjust the force in the jacks, as for a real HFT.

$$F_P(t_1 + \Delta t_P) = -K_N\, \alpha\, L_P T(t_1) \tag{3}$$

f. The new force induces a new displacement of the PS. Meanwhile, heating of the PS has continued and also induces variation in displacement. The updated displacement of the PS at the interface $u_P(t_2)$ is measured (given here by Eq. (4)) and imposed on the NS. This generates a new reaction force $F_N(t_2)$ given by Eq. (5).

$$u_P(t_2) = \alpha L_P\, T(t_2) + \frac{F_P(t_1)}{K_P(t_2)} = \alpha L_P \left(T(t_2) - \frac{K_N}{K_P} T(t_1)\right) \tag{4}$$

$$F_N(t_2) = K_N\, \alpha L_P \left(T(t_2) - \frac{K_N}{K_P} T(t_1)\right) \tag{5}$$

Steps *e* and *f* are repeated in order to maintain equilibrium and compatibility at the interface. For future discussion, the ratio between the stiffness of the NS and PS will be referred in this paper as stiffness ratio $R = \frac{K_N}{K_P}$.

Expanding Eq. (4) and (5), for n time steps, the displacement can be expressed by Eq. (6), while the reaction force generated by the NS, by Eq. (7).

$$u_P(t_n) = \alpha L_P \sum_{i=0}^{n-1} \left[(-R)^i \ T(t_{n-i})\right] \tag{6}$$

$$F_N(t_n) = K_N \ \alpha \ L_P \sum_{i=0}^{n-1} \left[(-R)^i \ T(t_{n-i})\right] \tag{7}$$

The same developments can be made for the displacement control procedure. In this case, the measured reaction force can be determined using Eq.(8), while the displacements can be calculated using Eq. (9).

$$F_P(t_n) = -K_P \ \alpha \ L_P \sum_{i=0}^{n-1} \left[\left(-\frac{1}{R}\right)^i \ T(t_{n-i})\right] \tag{8}$$

$$u_N(t_n) = \frac{1}{R} \alpha L_P \sum_{i=0}^{n-1} \left[\left(-\frac{1}{R}\right)^i \ T(t_{n-i})\right] \tag{9}$$

From the Eq. (6)-(9) it is clear that the results during the HFT, using the first generation method, are influenced by the stiffness ratio R.

In order to avoid instability, the value of the parenthesis which involves the stiffness ratio should be smaller than 1, i.e. $R < 1$, for the force control procedure and $\frac{1}{R} < 1$ or $R > 1$ for displacement control procedure. If not, the value tends toward infinity when the number of iteration i increases, irrespectively of the size of the time steps, and the process becomes unstable.

CONDITIONS FOR STABILITY IN FIRST GENERATION METHOD

It has been shown that the first generation method is sensitive to the stiffness ratio between the substructures. When the NS is more flexible than the PS, i.e. $R < 1$, then the force control procedure FCP is stable, but the displacement control procedure DCP is not. In the case of $R > 1$, the DCP is stable, whereas the FCP is not.

Choosing the right procedure between force control and displacement control is not easy. One of the reasons is that the stiffness of the PS is constantly changing during the HFT. The procedure chosen as appropriate before the test might become inappropriate during the test with the change of the stiffness ratio.

In addition to that, the number of controlled DoFs at the interface can be higher than one. The stiffness ratio of some DoFs may require one procedure, while others would require the other procedure, which makes the method difficult to be applied.
This demonstrates the need of a method that is independent on the stiffness ratio to ensure stability during the whole HFT.

An example of a situation when the FCP is applicable is when the PS consists of a column with the axial DoF to be controlled. A compressed column will generally be stiffer than the surrounding, even when its modulus is reducing due to the fire exposure. This explains why, in the HFT performed by Mostafaei no instability occurred, because the FCP was the good choice. In the case of HFT performed by Robert, the stiffness ratio was always smaller than one during the test, for all the DoFs, which explains why no instability occurred either.

A NEW METHOD TO PERFORM HFT

This section presents a novel method that is unconditionally stable, independently of the stiffness ratio value. The method has been inspired from the finite element tearing and interconnecting method (FETI) [7], and it controls the displacements during the HFT, based on the out of balance forces between the substructures.

During one step, displacements are blocked in the substructures. The variation of temperatures in the heated PS modifies the reaction forces at the interface, due to the thermal expansion and PS's stiffness variation. The reaction forces are measured in the PS and they are not in equilibrium with those that existed at the NS interface at the beginning of the step. The correction of the displacements du is calculated from the out of equilibrium forces dF, based on the stiffness of the PS and NS, as is presented in Eq.(10) .

$$du(t_n) = (K_N + K_P)^{-1}\, dF(t_n) \tag{10}$$

Because the real stiffness value of the PS is unknown, only an estimate of it is used in this equation, for example the value calculated at room temperature. Nevertheless, convergence can be obtained in a Newton-Raphson iteration scheme approach even if the matrix is not exactly equal to the tangent matrix.

In fact, it has been shown by hybrid fire tests performed numerically that it not necessary to apply Eq. (10) iteratively to ensure equilibrium at every time step. During the time that is needed to perform the calculation in the computer and for the testing equipment to apply the corrections of displacements, the temperatures are still increasing and the convergence process is running after an equilibrium that is constantly running away. It is thus not necessary to distinguish between iterations and time steps. The test is performed by applying continuously Eq. (10), with a cycling frequency that is as high as possible, which requires testing equipment that has a short response time. Note that the compatibility is continuously respected, as the same displacements are imposed on the PS and NS at the interface.

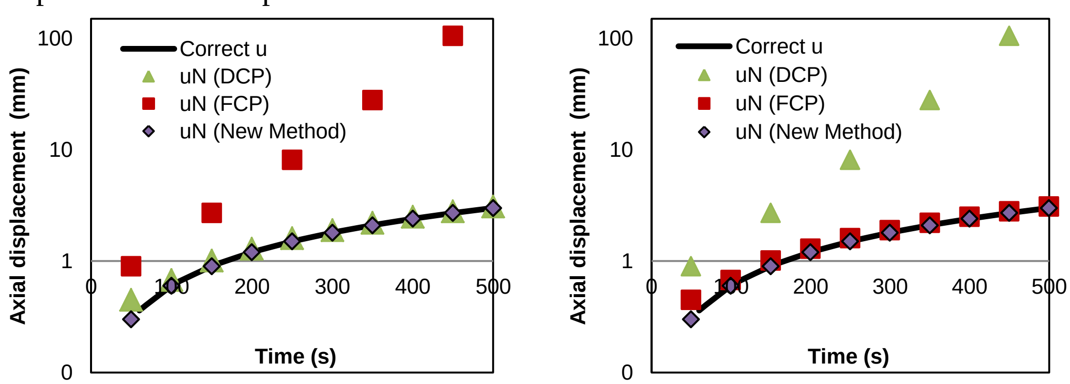

a) Stiffness ratio $R = 2$ b) Stiffness ratio $R = 0.5$

Figure 2. Instability in HFT depending on the stiffness ratio (logarithmic scale).

The results obtained numerically for the system of Figure 1 are used to illustrate this statement. The temperature evolution in the PS is taken as $0.5t_n$.
The evolution of displacements at the interface is presented for different stiffness ratios in Figure 2. The reference solution (correct u) is the one obtained when the entire system is analyzed, without subdivision. For a stiffness ratio $R > 1$, Figure 2 a) shows that the solution diverges from the reference solution when the force control procedure (FCP) is used, while convergence is obtained with displacement control procedure (DCP). Figure 2 b) shows the evolution of displacements for the case of a stiffness ratio $R < 1$, and it can be observed that in this situation the DCP diverges from the correct solution whereas the FCP is stable. In contrast, the new method is stable, independently on the stiffness ratio, as can be seen in Figure 2.

The logarithmic scale is chosen to represent the evolution of displacements in time to be able to plot the divergent solutions, which quickly reach large values. To be noted that in the case of instability, positive and negative values alternate. The negative values cannot be represented in the logarithmic scale, but nevertheless the instability is obvious when looking at the positive values.

Compatibility and equilibrium at the interface are ensured in the case of the new method, as well as in the case of the first generation method provided the correct stiffness ratio is used.

The above discussion addresses the instability induced by using an inappropriate method. The study of other sources of instabilities [8], such as the resolution of actuators and transducers, or effect of the noise, will not be addressed in this paper.

REAL HYBRID FIRE TEST

The new methodology will be implemented and verified on three full scale fire tests in the laboratory of CERIB in France. A concrete beam of 0.25 m x 0.40 m x 5.60 m, which is part of a moment resisting concrete frame, will be tested, where three DOF's, i.e. the axial displacement and the supports rotation will be controlled during the test. Only two of the three tests will be hybrid fire tests. In the hybrid tests, the behavior of the NS will be pre-calculated, using a predefined matrix defined in the software which controls the furnace [9].

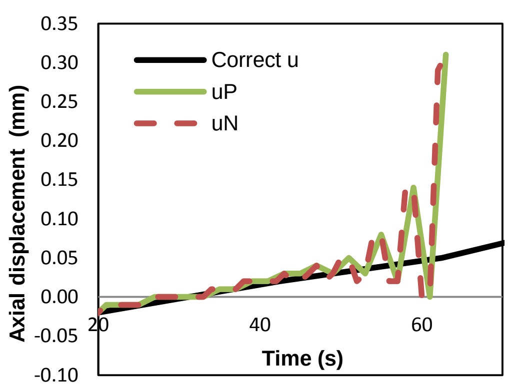

a) The first generation method (FCP)

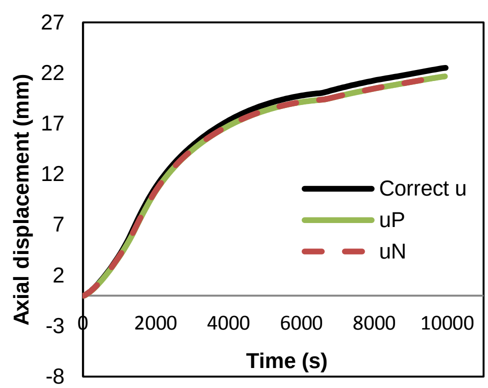

b) The new method

Figure 3. Virtual HFT of a concrete beam part of a frame.

For these hybrid tests, the stiffness ratio of the axial DOF would require a force control procedure, whereas the rotational DOF's would require a displacement control procedure if the first generation method was used. In anticipation of the test, a numerical simulation has been done considering the first generation method (using FCP with $\Delta t = 1$ s and $\Delta t_P = 1$ s), with SAFIR® modelling the PS whereas the stiffness of the NS is pre-calculated and kept constant. Instability occurred right at the beginning of the analysis as can be seen in Figure 3 a). However, by applying the new method the analysis was stable and showing good results (see Figure 3 b)).

The first test (non-hybrid) has been conducted on January 19, 2016, and the effect of the surrounding was constant during the test (constant negative moments applied at the supports and no axial restraint). The purpose of this test is, first, to compare the results with the one of the two following hybrid tests, and to prepare and check the instrumentation (the transducers and the jacks) for the HFT.

Figure **4**Figure 4 a) presents the setup of the traditional test and Figure 4 b) the evolution of the measured and calculated mid-span displacement. Note that failure occurs earlier when the effect of the remainder structure is constant. As can be seen, the test showed a good agreement with the numerical analysis performed with SAFIR®.

a) The setup of the beam

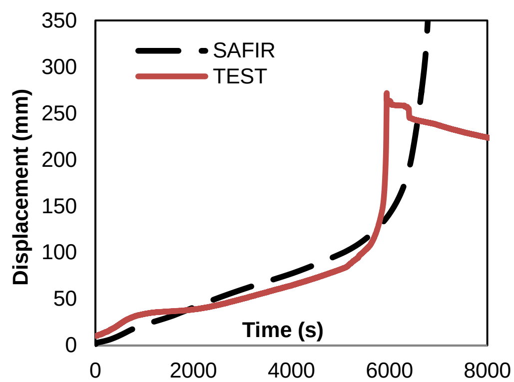

b) The evolution of mid-span displacement

Figure 4. Fire test (non hybrid) performed on a concrete beam.

CONCLUSION

The objective of the paper was to show that the first generation HFT method used in the literature, where the correction of the interface forces/displacements depends only on the characteristics of the NS, is not always stable. It has been shown, using an elastic system as illustrative example, that the stiffness ratio between the NS and PS will dictate the stability of this method. Yet, the stiffness ratio is not easily predictable before a fire test, because the stiffness of the exposed substructures is reduced during the test. Moreover the need of controlling multiple DoFs makes the method impossible to be applied, when different types of procedure should be used for different DoFs.

A new method has been proposed in this paper, unconditionally stable no matter the stiffness ratio, and assumes controlling the displacement during the HFT.

Full scale HFTs are planned on a concrete beam that is part of a moment resisting frame. These tests have been simulated in a virtual environment, i.e. with the PS modeled as substructure in SAFIR®, while the NS was described by the predetermined matrix. The results show that the first generation method cannot be applied due to the fact that the axial DOF requests a force control procedure, while the rotational DOFs request a displacement control procedure. However, the new method succeeds in being stable, ensuring compatibility and equilibrium at the interface.

Prior the HFT a traditional test has been performed, showing good results with the numerical analysis.

REFERENCES

1. Saouma, V.E., and M.V. Sivaselvan. 2008. "*Hybrid simulation: Theory, implementation and application,*" Taylor and Francis, London, UK.
2. Korzen, M., G. Magonette, and Ph. Buchet. 1999. "*Mechanical Loading of Ccolumns in Fire Tests by Means of the Substructuring Method,*" Zeitschrift für Angewandte Mathematik und Mechanik, Vol. 79, pp. S617-S618.
3. Robert, F. 2008. "*Comportement des bétons sous haute température et en cas d'incendie: caractérisation multi-échelle,*"(Unpublished doctoral thesis). L'Ecole Normale Supérieure de Cachan, Cachan, France.
4. Robert, F., S. Rimlinger, C. Collignon. 2010. "*Structure fire resistance: a joint approach between modelling and full scale testing (substructuring system)*", 3rd fib International Congress
5. Mostafaei, H. 2013. "*Hybrid fire testing for assessing performance of structures in fire – Application,*" Fire Safety Journal, 56, 30-38.
6. Franssen J.-M., "*SAFIR, A Thermal/Structural Program Modelling Structures under Fire,*" A.I.S.C. Engineering Journal 42 (3) 143-158.
7. Farhat, C., and F.-X. Roux. 1991. "*A method of finite element tearing and interconnecting and its parallel solution algorithm*," International Journal for Numerical Methods in Engineering, 32:1205-1227.
8. Tondini, N., G. Abbiati, L. Possidente, B. Stojadinovic. 2016. "*A Static Partitioned Solver for Hybrid Fire Testing*", 9th International Conference on Structures in Fire, June 8-10, 2016
9. Sauca, A., T. Gernay, F. Robert, J.M. Franssen. 2015. "*Characteristics and implementation of Hybrid Fire Testing (HFT),*" presented at the Engineering Mechanics Institute Conference, June 16-19, 2015.

Assessment of Concrete Exposed to Elevated Temperatures Using Scanning Electron Microscopy and X-Ray Diffraction

BRUNO FERNANDES, AUGUSTO MASIERO GIL,
FABRICIO LONGHI BOLINA,
EDUARDO ESTEVAM CAMARGO RODRIGUES
and BERNARDO FONSECA TUTIKIAN

ABSTRACT

The microstructure of concrete subjected to high temperature is studied. The aim of this research is to investigate the potentially use of scanning electron microscopy (SEM) and x-ray diffraction (XRD) in the assessment of thermal damaged concrete. A reinforced column was exposed to ISO 834 fire curve for 4 hours. After heating, core samples were obtained and analyzed. Visual observations showed a change in the color of concrete exposed to high temperatures. SEM micrographs presented distinct changes in morphology, like cracks and voids. XRD diagrams showed a reduction of portlandite and presence of larnite as depth increases. The potential use of these techniques in the estimation of damage in concrete exposed to elevated temperatures was confirmed.

INTRODUCTION

Concrete presents a good behavior when exposed to elevated temperatures due to its incombustibility and low thermal diffusivity [1–3], besides, it does not emit any gas or smoke [1]. However, when exposed to high temperatures, concrete suffers physicochemical changes, resulting in loss of mechanical properties, cracking and

Bruno Fernandes, Graduate Student, itt Performance, Av. Unisinos, 950 Bairro Cristo Rei, São Leopoldo 93022-000, Rio Grande do Sul, Brazil
Augusto Masiero Gil, Graduate Student, Universidade do Vale do Rio dos Sinos and itt Performance, Av. Unisinos, 950 Bairro Cristo Rei, São Leopoldo 93022-000, Rio Grande do Sul, Brazil
Fabricio Longhi Bolina (corresponding author), Professor, Universidade do Vale do Rio dos Sinos and itt Performance, Av. Unisinos, 950 Bairro Cristo Rei, São Leopoldo 93022-000, Rio Grande do Sul, Brazil
Eduardo Estevam Camargo Rodrigues, Professor, Universidade do Vale do Rio dos Sinos and itt Performance, Av. Unisinos, 950 Bairro Cristo Rei, São Leopoldo 93 022-000, Rio Grande do Sul, Brazil
Bernardo Fonseca Tutikian, Professor, Universidade do Vale do Rio dos Sinos and itt Performance, Av. Unisinos, 950 Bairro Cristo Rei, São Leopoldo 93 022-000, Rio Grande do Sul, Brazil

spalling [4].

Residual strength of concrete exposed to high temperature is dependent on the heating profile, since in a real fire situation only some of structural element sides are directly exposed to the heating [5]. Besides, due to concrete's low thermal conductivity, a significant temperature gradient may occur inside of the structural element, resulting in a great damage in few centimeters [2,5,6]. Thus, compression tests in core samples pulled-out from concrete structures are not representative [5,7].

Changes in concrete properties are directly related to changes in microstructure [8], thus residual properties of concrete can be assessed by experimental techniques that identify physical, chemical and mineralogical changes. Some techniques, such as scanning electron microscopy [5,9–14], x-ray diffraction [9–11,13,14], thermogravimetric analysis [13–15], mercury intrusion porosimetry [10,12], colorimetry [6,16,17] and petrography [4] are widely used to identify changes in fire-exposed concrete.

Although many experimental investigations have been carried out, the microstructural changes that led macroscopic changes of heated concrete ate not fully explained [14]. Besides that, most of the experimental research are focused in small scale furnace test. Concrete samples used in this kind of experimental program differs from that obtained from full scale tests, usually most representative [18].

Within this context, this research aim to investigate the potentially use of scanning electron microscopy (SEM) and x-ray diffraction (XRD) in the assessment of thermal damaged concrete. For this purpose, a reinforced concrete column was exposed to the ISO 834 fire curve during a period of 4 hours. After natural cooling, the above mentioned techniques were used to investigate microstructural changes.

This research is part of an ongoing research study at Fire Safety Laboratory of itt Performance focused on fire behavior of reinforced concrete columns.

METHOD

An precast reinforced concrete column was fabricated. The column were square cross section (250 mm X 250 mm) and 3000 mm long. Four longitudinal bars (three of 10 mm and one of 16 mm) were tied with 6.3 mm ties with a spacing of 150 mm.

The concrete used were of normal strength. Batch quantities are given in TABLE I. Two kinds of coarse aggregate are used, both basalt. Two kinds of sand are also used, quartzitic natural sand and crushed basalt. The measured compressive strength of the concrete at 28 days was 40.2 MPa.

TABLE I. BATCH QUANTITIES.

Cement content (kg/m^3)	320
Basaltic coarse aggregate 0.15/6.3 (kg/m^3)	320
Basaltic coarse aggregate 2.4/19 (kg/m^3)	745,6
Quartzitic natural sand (kg/m^3)	544
Crushed basalt sand (kg/m^3)	291,2
Water (kg/m^3)	176
Superplasticizer (l)	0,5

To the heating process, a vertical furnace fueled by liquefied petroleum gas, with a chamber that is 2.5 m high, 2.5 wide and 1.0 long, was used. The experimental model consists in a column embedded in a masonry wall build in a frame, in such a way that one side and two corners were exposed to the elevated temperatures. The experimental setup is given at Figure 1 (column studied is highlighted).

The reinforced columns were instrumented with type-K thermocouples. The temperature of every 5.00 cm depth was measured, as well as in the concrete cover and in the non-exposed side. Figure 2 presents the thermocouples locations.

The furnace temperature was also controlled. The columns were subjected to ISO 834 standard fire exposure for 4 hours. Figure 3 presents the temperature measured during heating process.

After natural cooling phase, core samples were pulled out from the concrete column. Core samples from a reference column, using the same concrete mix proportions and not exposed to high temperatures, was also obtained. The concrete cores were sectioned in discs. The samples were dried in oven at 60ºC for 24 hours. After that, the samples were kept in vacuum desiccator with silica gel till experimental tests. TABLE II presents a summary of the analyzed samples.

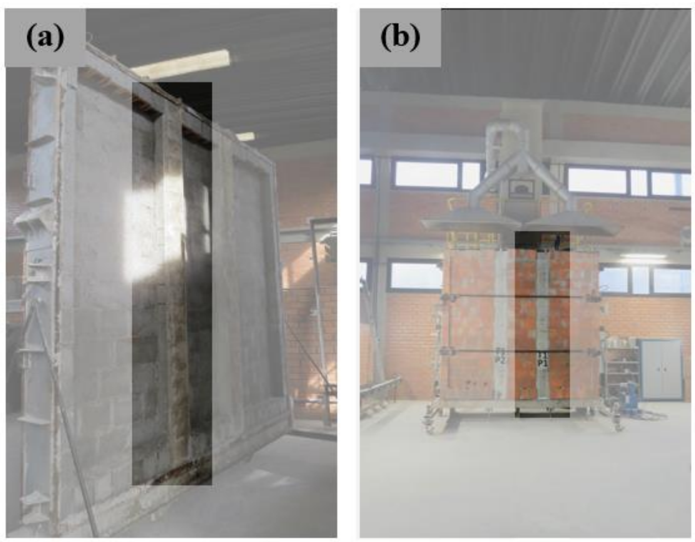

Figure 1. Experimental setup: (a) column embedded in masonry wall/exposed side; (b) frame in the furnace.

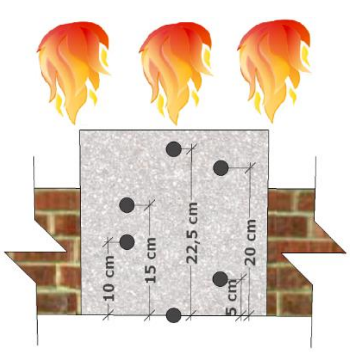

Figure 2. Thermocouple location.

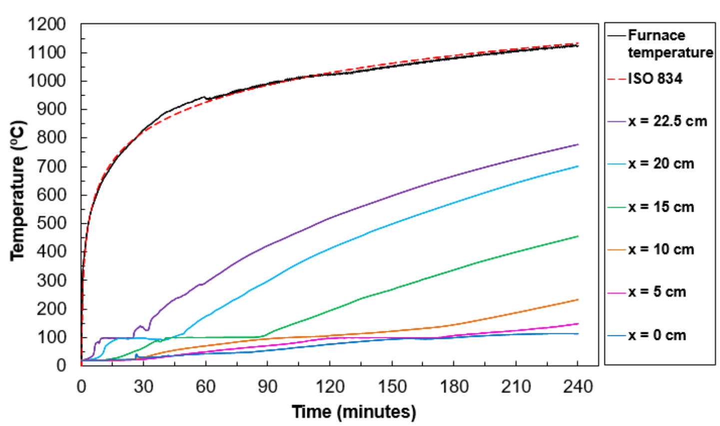

Figure 3. Measured temperatures.

TABLE II. SUMMARY OF ANALYZED SAMPLES.

Depth (cm)*	Temperature (ºC)	SEM	XRD
Reference	23	X	X
0	113.7	X	X
5	149	X	-
10	233.3	X	-
15	455.5	X	-
20	701.2	X	X
25	1123.6	X	X
*Distance from the not-exposed surface			

For SEM tests, samples were fractured for secondary electron analysis. The surfaces of heated concrete were impregnated with gold and the analysis was carried with the scanning electron microscope Zeiss Evo LS 15, 71 days after heating. For XRD tests, samples were crushed into powder and the analysis was carried with the x-ray diffractometer Siemens D500, 49 days after heating.

RESULTS

Macroscopic Observations

The exposed surface of the reinforced concrete column is shown in Figure 4. A yellowish color is verified, indicating that the concrete has reached a temperature above 900ºC [2,16,19]. It is also observed little black dots that can be related with the usage of crushed basalt sand. This is also observed in Figure 5 that shows a piece of concrete cover. In this picture is also verified a change in concrete color as depth increases.

Figure 4. Surface of reinforced concrete column

Figure 5. Piece of concrete cover.

SEM Analysis

SEM micrographs of reference, 0cm, 20 cm and 25 cm depth samples are shown in Figures 6,7,8 and 9. SEM image of concrete from 0 cm depth did not present distinct change in morphology in comparing with the SEM image of reference sample. At this depth, a temperature of 113.7ºC was reached. Increasing temperature at this level only causes dissociation of ettringite [20].

The micrographs of 20 cm depth sample shows similarities with controlled sample, but are coarse and presents little voids. This alteration can be caused by the dehydration of CH (at temperatures above 420ºC [8,20]) and C-S-H (at temperature above 700ºC [8,20,21]). The temperature reached at this depth was of 701.2ºC.

Finally, SEM micrograph of 25 cm depth sample shows strong changes in morphology, like cracks and voids. The temperature reached at this point was of 1123.6ºC and at this temperature level cement paste starts to melt [8].

XRD Analysis

XRD diagrams of reference, 0cm, 20cm and 25cm depth samples are presented in Figure 10. The diagrams shows the presence of portlandite, larnite and quartz due to aggregate used in concrete. Portlandite content is verified until 20cm depth and disappear at depth of 25cm, when a temperature of 1123.6ºC was reached. Similar behavior was observed by Kim, Yun and Park [11]. The larnite (β-C2S) is found at 25cm depth, most probably due to disassociation of C-S-H, as pointed by literature [8,12].

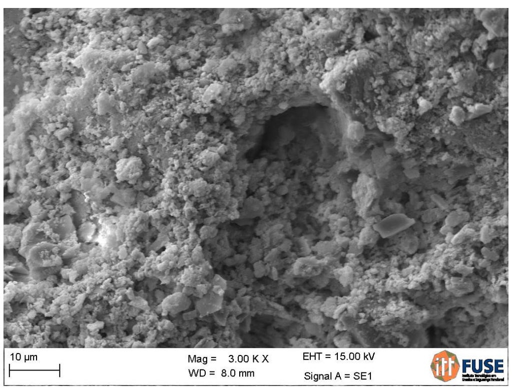

Figure 6. Reference sample (mag. 3000X).

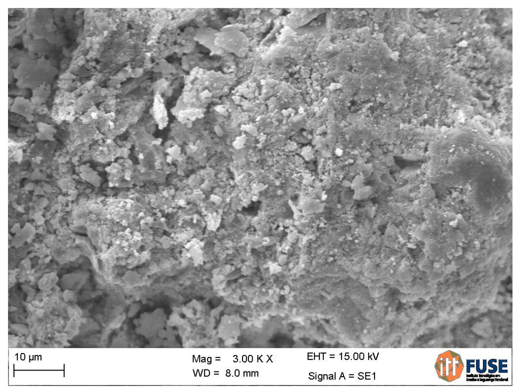

Figure 7. 0 cm depth sample (mag. 3000X).

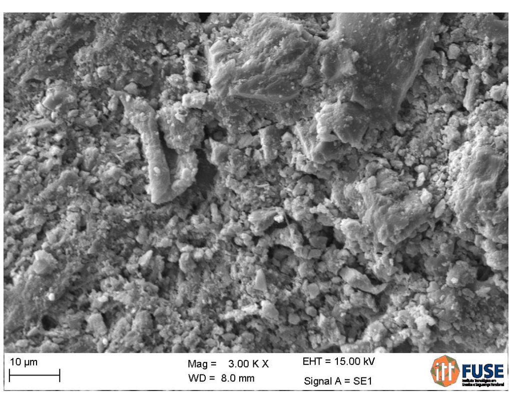

Figure 8. 20 cm depth sample (mag. 3000X).

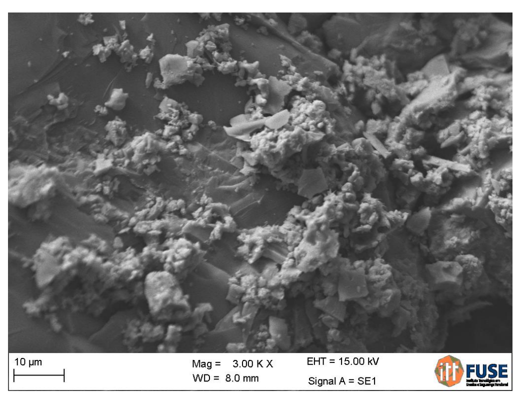

Figure 9. 25 cm depth sample (mag. 3000X).

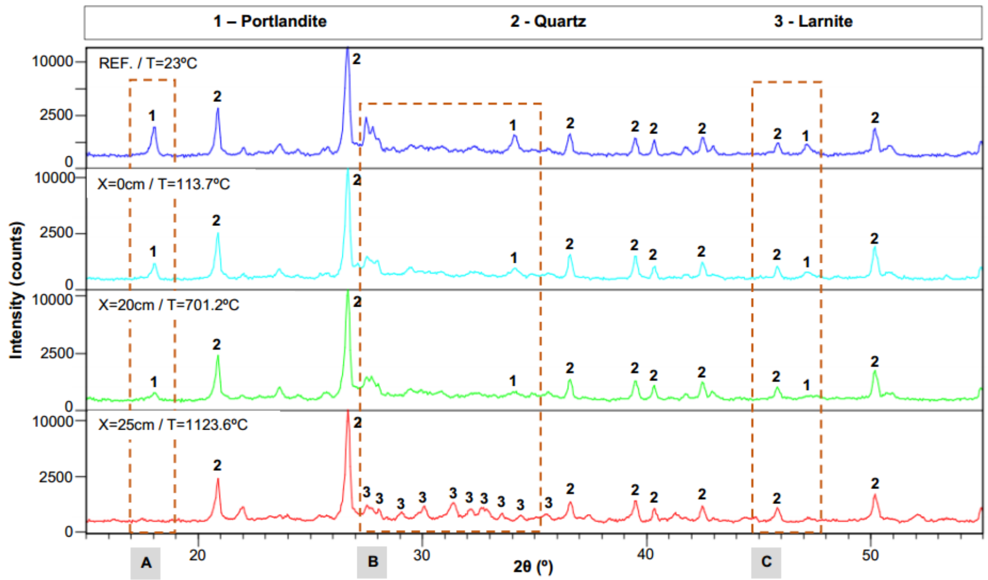

Figure 10. XRD diagrams of reference, 0 cm, 20 cm and 25 cm depth.

DISCUSSION OF THE RESULTS

From the experimental work and existing literature, some conclusions can be drawn. First, macroscopic observations help to determine critical zones of damage, due to color change of concrete. From these observations can be estimated the maximum temperature reached at certain depth.

In addition, experimental techniques provide good information about damage level. SEM micrographs presented distinct changes in morphology, like coarsening of cement paste and presence of cracks and voids. This indicate that a significant degradation of concrete, due to the dehydration of CH and C-S-H. XRD diagrams showed a reduction of portlandite and the presence of larine as depth increases. This can be useful in the estimation of temperature reached and damage level, since CH dehydration at temperatures above 420ºC and C-S-H decomposes into β-C2S at temperatures above 700ºC.

Finally, these informations can be useful in estimation of concrete strength reduction. Khoury (2000) [3] points out that at temperatures above 550-600ºC, concrete becomes not structurally useful. The author also says that only the first centimeters experience this temperature. In fact, the changes above mentioned happened at 20 cm and 25 cm depth (surface of concrete column), were the temperature are above 600ºC.

CONCLUSIONS

The present study confirmed the potential use of scanning electron microscopy and x-ray diffraction in assessment of concrete exposed to elevated temperatures. SEM micrographs presented distinct changes in morphology and XRD diagrams showed a reduction of portlandite and presence of larnite as depth increases. Thus, the simultaneous application of these techniques can be helpful in the estimation of damage in concrete exposed to elevated temperatures, in order to repair the structure or conduct a forensic research.

REFERENCES

1. Fédération Internationale Du Béton. 2008. *fib Bulletin 46: Fire design of concrete structures — structural behaviour and assessment*. fib, p. 209.
2. M. Colombo, R. Felicetti. 2007. "New NDT techniques for the assessment of fire-damaged concrete structures", *Fire Safety Journal*, 42: 461-472.
3. G.A. Khoury. 2000. "Effect of fire on concrete and concrete structures", *Prog. Struct. Eng. Mater*. 2: 429-447.
4. B. Georgali, P.E. Tsakiridis. 2004. "Microstructure of fire-damaged concrete. A case study", *Cem. Concr. Compos*. 27: 255-259.
5. E. Annerel, L. Taerwe. 2009. "Revealing the temperature history in concrete after fire exposure by microscopic analysis", *Cem. Concr. Res.*, 39: 1239-1249.
6. I. Hager. 2013. "Colour Change in Heated Concrete", *Fire Technology:* 1–14.
7. M. Yoshida, Y. Okamura, S. Tasaka, T. Shimode. 1994. "A Study On Temperature Estimation In Concrete Members After Fire", *Fire Saf. Sci.* 4: 1183-1194.
8. Fédération Internationale Du Béton. 2007. *fib Bulletin 38: Fire design of concrete structures - materials, structures and modelling*, fib, p. 97.
9. S.K. Handoo, S. Agarwal, S.K. Agarwal. 2002. "Physicochemical, mineralogical, and morphological characteristics of concrete exposed to elevated temperatures", *Cem. Concr. Res.* 32: 1009-1018.
10. G.F. Peng, Z.S. Huang. 2008. "Change in microstructure of hardened cement paste subjected to elevated temperatures", *Constr. Build. Mater*. 22: 593-599.
11. K.Y. Kim, T.S. Yun, K.P. Park. 2013. "Evaluation of pore structures and cracking in cement paste exposed to elevated temperatures by X-ray computed tomography", *Cem. Concr. Res.* 50: 34-40.
12. Q. Zhang, G. Ye, E. Koenders. 2013. "Investigation of the structure of heated Portland cement paste by using various techniques", *Constr. Build. Mater.*, 38: 1040-1050.
13. G. Wang, C. Zhang, B. Zhang, Q. Li, Z. Shui. 2014. "Study on the high-temperature behavior and rehydration characteristics of hardened cement paste", *Fire And Materials*, 39*: 741-750.*
14. S. Lim, P. Mondal. 2014. "Micro- and nano-scale characterization to study the thermal degradation of cement-based materials", *Mater. Charact*. 92: 15-25.
15. O. Arioz. 2007. "Effects of elevated temperatures on properties of concrete", *Fire Safety Journal*, 42: 516-522.
16. H. Carré, I. Hager, C. Perlot. 2014. "Contribution to the development of colorimetry as a method for the assessment of fire-damaged concrete", *Eur. J. Environ. Civ. Eng.*: 1-15.
17. E. Annerel, L. Taerwe. 2011. "Methods to quantify the colour development of concrete exposed to fire", *Constr. Build. Mater.* 25: 3989-3997.
18. C.A. Britez. 2011. *Avaliação De Pilares De Concreto Armado Colorido De Alta Resistência, Submetidos A Elevadas Temperaturas*, Thesis (PhD), Universidade de São Paulo, p.252.
19. N.. Short, J.. Purkiss, S.. Guise. 2001. "Assessment of fire damaged concrete using colour image analysis", *Constr. Build. Mater.*, 15: 9-15.
20. Q. Zhang. 2013. *Microstructure and deterioration mechanisms of portland cement paste at elevated temperature*, Thesis (PhD), Technische Universiteit Delft, p.175.
21. J.-F.I. Denoël. 2007. *Fire Safety and Concrete Structures*, Febelcem: p. 90.

Pulse-Echo Monitoring of Concrete Damage and Spalling during Fire

ROBERTO FELICETTI and FRANCESCO LO MONTE

ABSTRACT

Monitoring concrete damage and spalling progression in structural members during fire tests (hot conditions) is a central but challenging task, since the high temperatures involved make difficult the implementation of most of the common Non-Destructive evaluation methods. Hence, an advanced ultrasonic technique – Ultrasonic Pulse-Echo (UPE) – was recently adapted for real time survey in fire test, in order to evaluate the material damage during heating. The UPE technique was implemented at the cold (upper) face of concrete slabs (800x800x100 mm) heated at the bottom face according to the Standard Fire and subjected to biaxial compressive membrane loading. Different concretes were tested, with grades ranging from 40 to 60 MPa, with and without different kinds of fibre (monofilament or fibrillated polypropylene, or steel fibres). Furthermore, different load levels were applied, from 0 to 25% of the original compressive strength. During tests, spalling was generally observed in loaded plain concrete (up to 50-60 mm depth), while only slight scaling was experienced on unloaded samples or if polypropylene fibre was added. The method proved to be very effective in recognizing the decay of the Ultrasonic Pulse Velocity (UPV) with temperature and the role played by external loading and fibre type.

INTRODUCTION

Concrete generally exhibits a satisfactory behaviour in fire thanks to its incombustibility and low thermal diffusivity which allows to maintain relatively low temperature in the inner layers, even for long fire durations. A proper design of reinforced concrete structures, however, requires the correct knowledge of material behaviour in order to optimize member sections and mix design accordingly to the needed fire resistance. Unfortunately, concrete response at high temperature is not easy to investigate due to the influence of different aspects such as the dependency of material decay on stress level and fire stage (hot and residual conditions), and spalling phenomenon.

Thermal damage in concrete, in fact, is influenced by the state of stress, since it has been proved that a lower damage is produced if a low/moderate compression is applied during heating. This is probably caused by the reduction of the tensile

Department of Civil and Environmental Engineering, Politecnico di Milano
emails: roberto.felicetti@polimi.it, francesco.lo@polimi.it

stress brought in the cement matrix by the dilation of the aggregate. In addition, there is a difference in the material properties decay between hot and residual conditions because of the further damage introduced by cooling.

Finally, spalling can significantly influence the structural behaviour. Such phenomenon consists in the more or less violent expulsion of chunks from the exposed face and is made particularly complex by the mutual interaction of different influencing factors, namely heating rate, moisture content, pore pressure and stress [1-4]. Spalling ensues from the simultaneous action of: (a) stress induced by thermal gradients and external loads and (b) pore pressure rise caused by water saturation and vaporization.

High-Performance Concrete (HPC) is generally more prone to spalling compared to Normal-Strength Concrete (NSC) due to its denser matrix (that favours higher values of pore pressure) and its higher heat-sensitivity [5]. The common way to reduce spalling risk is to add polypropylene (pp) fibre (1-2 kg/m^3), whose beneficial effect is provided by the further porosity induced by melting and stress intensification around the edges of the channels left free by melted fibres [3,6].

It is worth noting that monitoring the conditions of spalling initiation and propagation, as well as the progression of detachments in fire tests, should be of primary importance in order to fully understand such phenomenon. The quantification of spalling time, depth and extension during a fire is, however, difficult, since most of the available techniques can be hardly implemented in the test furnace.

In the present paper the approach based on Ultrasonic Pulse-Echo (UPE) is discussed. Other examples of Real-Time survey during fire tests can be found in the literature, mostly based on Acoustic Emission (AE), which proved to be rather effective even though distinguishing micro- and macro-cracking from spalling is rather difficult [7,8].

UPE has been considered within a research project recently finalized at Politecnico di Milano (Milan, Italy) in collaboration with CTG-Italcementi Group (Bergamo, Italy) [9]. The experimental campaign was focused on concrete slabs (800x800x100 mm) subjected to heating at the bottom face according to the Standard Fire curve, while a biaxial membrane loading was applied in order to instate a mean compressive stress. Slabs were uniformly heated at the intrados via propane burner and loading was implemented by 8 hydraulic jacks restrained by a steel frame. It is worth noting that the slabs were heated only in the central 600x600 mm area, in order to preserve the hydraulic jacks with a 100 mm unheated concrete rim. In order to limit the confining effect provided by the colder boundary, 16 radial cuts were performed. A section view of slab and loading system (8 hydraulic jacks + restraining frame) above the furnace is shown in Fig.1a, while the specimen geometry is reported in Fig.1b, together with the location of UPE measurements, pressure gauges, thermocouples and displacement transducers.

Firstly, 4 concrete mixes were investigated ($f_c \approx 60$ MPa; calcareous aggregate). The mixes differed only in fibre addition: (1) no fibre, (2) 40 kg/m^3 of steel fibre, and 2 kg/m^3 of (3) monofilament or (4) fibrillated polypropylene fibre. Secondly, also ordinary concrete was studied ($f_c \approx 40$ MPa; calcareous aggregate). The abovementioned Real-Time survey technique was implemented during the tests at the cold face, where the relatively low temperature ($T \leq 150$°C) allowed using the instrumentation.

ULTRASONIC PULSE-ECHO – UPE

The UPE method is based on the reflection/refraction of ultrasonic pulses when crossing a discontinuity within a medium. As shown in Fig.2a, when an ultrasonic source emits pulses on the surface of a member, the elastic waves propagate through the continuum. When a discontinuity is reached, such as a sudden variation of material properties or an interface between two layers, elastic waves are partly transmitted and partly reflected, according to the contrast of acoustic impedance (*acoustic impedance* = *density* x *wave velocity*).

In particular, if reflection occurs due to an impedance reduction, the amplitude sign reverses. A special case is represented by air gap inside concrete. In this case total reflection is observed together with wave sign reversal due to the negligible density and velocity for both compression and shear elastic waves in air. This makes UPE very sensitive to delaminations and voids in concrete members [10,11,12].

As ultrasonic source, a mechanical impact of small hammers or metallic balls (namely, Ultrasonic Impact-Echo) or pulses produced by ultrasonic transducers (namely, Ultrasonic Pulse-Echo) can be used [13]. In the latter case, both compression and shear waves can be generated. Post-processing of data is often non trivial due to the possible influence of the boundary conditions in the propagation of direct and reflected waves. Data can be analyzed in the frequency domain through the Fourier Transform, as well as in the time domain by determining the arrival time of the reflected wave at the receiver or by using other approaches based on Wavelet or Hilbert Transforms [14]. Spectrum analysis, however, requires eliminating "parasitic" effects caused by the global excitation of the specimen and by edge-effects [15].

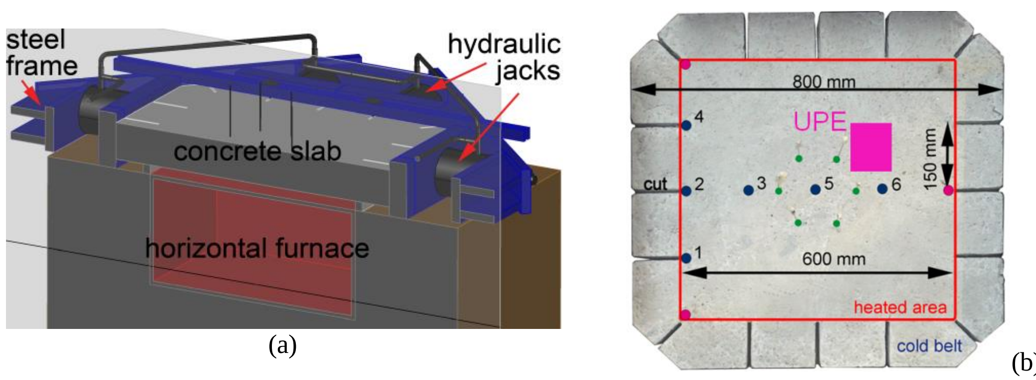

Figure 1. Spalling test on concrete slabs subjected to Standard Fire at the intrados under biaxial membrane loading: (a) slab and loading system on the furnace, and (b) specimens geometry and location of UPE (green dots = pressure gauges and thermocouples, blue dots = displacement transducers).

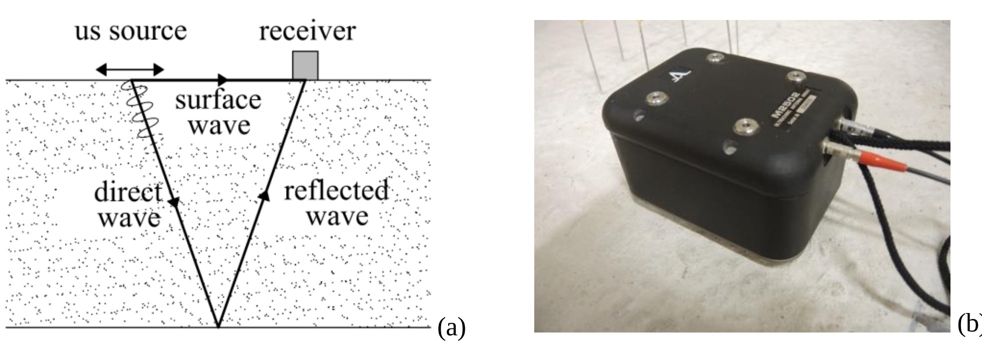

Figure 2. (a) Ultrasonic Pulse-Echo principle and (b) adopted ultrasonic device placed on the slab.

In this research, the ultrasonic flaw detector A1220 by Acoustic Control Systems was used, fitted with the M2502 shear pulse emitter/receiver array (Fig.2b). In Fig.3a the typical ultrasonic waves reflected at the intrados (heated face) and observed at the receiver are shown for different fire durations in a test on plain HPC. In this test, spalling occurred with a single violent event after 35 min of heating.

A reference peak is chosen and highlighted by means of a coloured dot in each wave. By observing the 3 curves related to the measurements before spalling occurred, it is clear that the arrival time of the reference peak at the receiver increases during the test (*time shift* or *echo delay*). This delay takes place, since wave propagation becomes slower due to thermal damage. A reduction of the reflected pulse amplitude is also observed, due to the increased wave attenuation and reduced contrast of acoustic impedance at the exposed face of the slab.

When spalling occurs, on the contrary, a sudden decrease in concrete thickness takes place and the time of reflection instantaneously decreases (echo advance in Fig.3a). Once the echo advance is determined, the spalling depth can be estimated if the pulse velocity (or slowness = 1/velocity) in damaged concrete is known. This requires a preliminary evaluation of the slowness profile along the slab thickness. In the case at hand, the thermal field was known thanks to the continuous measurements of temperature at intrados, extrados and at 6 different depths, while the ultrasonic pulse velocity decay with temperature was not known a priori.

The decay of the compression ultrasonic wave velocity with temperature was evaluated in a previous experimental campaign, conducted on the same concrete mixes on unstressed cylindrical specimens in residual conditions (Fig.3d). At high temperature, however, two main aspects should be taken into account: (a) concrete mechanical properties (and, hence, acoustic impedance) measured after heating and cooling (residual conditions) are generally lower than at high temperature (hot conditions) due to the further damage brought in by cooling; and (b) material damage is lower if a moderate compression is applied during heating.

This consideration explains why the ultrasonic investigations of the previous experimental study performed after cooling on unstressed specimens cannot be used, since a significantly lower decrease of the ultrasonic pulse velocity is expected to take place in the slabs.

To overcome such problem, an inverse analysis was implemented, aimed at evaluating the ultrasonic shear pulse slowness profiles during fire exposure. This was carried out by defining the material slowness as a function of temperature by means of a polynomial function (cubic interpolant), whose coefficients can be determined so to minimize the difference between the observed reflection times (or echo delays) and the slowness integrals in the whole set of steps preceding spalling (if any). The integration of the slowness profile in the depth, in fact, is equal to the time required by ultrasonic waves to cross the slab thickness.

When spalling occurs, the reduction in the reflection time observed via UPE (Fig.3e) is used to evaluate the spalling depth, by determining the thickness reduction required to obtain the same reduction of the slowness integral.

The last crucial point is the precise identification of the Echo Delay – ED, namely the shift of the arrival time of the wave reflected at the intrados. Different procedures have been studied in order to check their sensitivity and effectiveness in defining the ED and the readiness for automation.

Post-processing can be worked out either on time or frequency domain. In the former case, one option is to rescale the time axis of the first acquired waveform until a significant indication (in general the time window 90-120 μs) shows the best correlation with its counterpart in the subsequent waveforms (the probe offset time has been taken as a fixed pivot point). This implies a Time Scale dilation which reflects the average increase of slowness across the slab thickness. The same concept may be more easily implemented by tracking the peak of the Hilbert envelope transform [16].

A similar approach can be implemented in the frequency domain, since the dilation of the signal timescale translates into a contraction of the spectrum, which can be tracked by monitoring the variation of some reference frequency peaks. As abovementioned, the heat-induced damage in concrete makes waves slower, this leading to an increase of the echo delay and to a decrease of the frequency peaks (the rate of peak-frequency decrease is the inverse of relative increase of the arrival time). Such methods are suitable to evaluate an average slowness decay relative to virgin conditions. Since the Time Scale method exhibited a marginally better repeatability among the tests, it has been taken as a reference in the following (further details are given in [17]). Another approach is based on defining the time delay of arrival of the reference peak, providing results in terms of time (μs) and making easier the following evaluation of the spalling depth.

The first set of tests was performed on 4 slabs made of 4 concrete mixes with the same concrete grade and aggregate type ($f_c \approx 60$ MPa, silico-calcareous aggregate) but different fibres (no fibre, steel fibre in the content of 40 kg/m^3 and monofilament or fibrillated polypropylene fibre in the content of 2 kg/m^3). In all cases, the applied membrane compressive stress was 10 MPa. In Fig.3b the increase of echo delay evaluated according to 3 methods is shown for slab Fibrillated B, highlighting their general good agreement, with the exception of the Hilbert envelope method.

The relative increase of the echo delay time obtained via the Time Scale method for the 4 different slabs is reported in Fig.3c, showing a remarkable repeatability among the tests. In Fig.3d, the decay of ultrasonic pulse velocity obtained via inverse analysis on the basis of the echo delay time evaluated via the Time Scale method are compared with those obtained in the previous experimental campaign on unstressed cylindrical specimen in residual conditions. As expected, a more significant damage affects this latter type of specimens. Finally, the comparison between the experimental trend of the echo delay in test Plain B and the numerical values obtained by slowness integration is reported in Fig.3e, showing a satisfactory match both during the smooth damage due to heating and after the sudden detachment of the spalled layer. The total spalled thickness measured after the test was 40 mm which is in fairly good agreement with the layer to be deleted in the slowness integration (35 mm).

In the framework of a joint research project with the Centre Scientifique et Technique du Bâtiment – CSTB, Marne la Vallée (France), a second set of tests was performed on 4 nominally identical slabs made of NSC ($f_c \approx 40$ MPa, calcareous aggregates), but with 4 different levels of biaxial membrane stress (0, 0.5, 5 and 10 MPa), in order to investigate the influence of load on spalling phenomenon and on the decay of ultrasonic pulse velocity with temperature.

Severe spalling was observed for stress levels of 5 and 10 MPa (more than 50 mm of spalling depth), medium spalling depth for 0.5 MPa (about 20 mm) and no spalling for unloaded specimens. Spalling took place after about 8 min of heating. In Fig.4 the results of UPE measurements are reported in terms of Time Shift with respect to the

Reflection Time in virgin conditions. For fire durations shorter than 8 min (before any spalling occurred), a slower increase of time delay is observed for higher values of applied load. This means that the thermal damage depends also on the load level, since it decreases with the applied compression (at least for the investigated range: 0-0.25 f_c).

After spalling occurred, the comparison among the tests becomes more difficult because the decrease of Time Shift observed for 0.5, 5 and 10 MPa is caused by the reduction of thickness, and the results are no more directly comparable in terms of Time Shift. The above described effect agrees with many results in the literature which show as the decay with temperature of the mechanical properties of concrete (both strength and stiffness) are lower if compression is applied during heating.

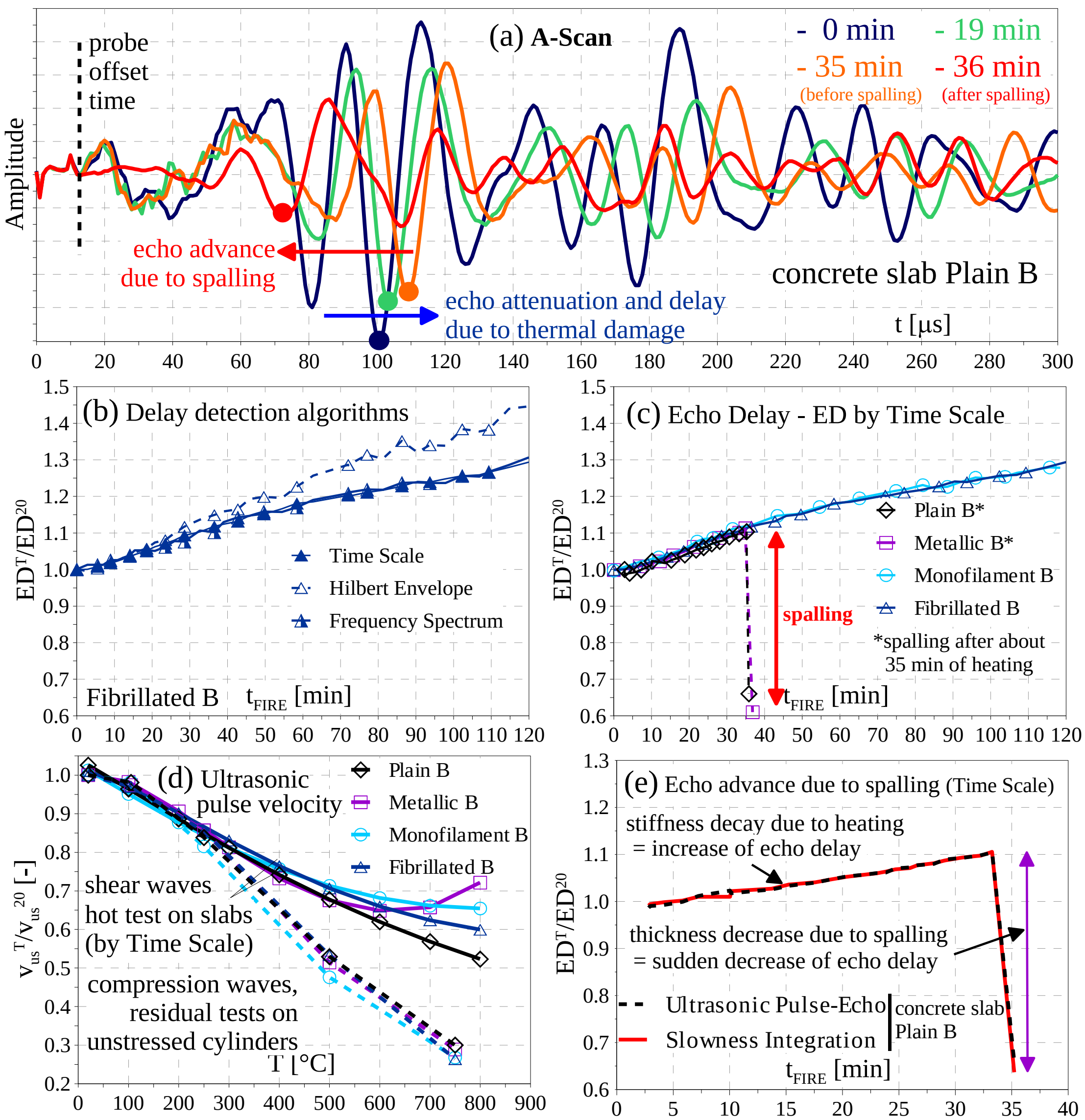

Figure 3. Ultrasonic Pulse-Echo method: (a) waves at the receiver showing the echo delay increase due to heating and the sudden decrease due to spalling; (b) relative Echo Delay – ED according to 3 approaches (Time Scale, Hilbert Envelope and Frequency Spectrum) for the slab Fibrillated B and (c) according to the Time Scale for 4 tested HPC slabs (1 per mix); (d) comparison among the ultrasonic pulse velocity obtained via inverse analyses and that measured in residual conditions on unstressed specimens; and (e) ED evaluated via UPE and Slowness Integration for slab Plain B.

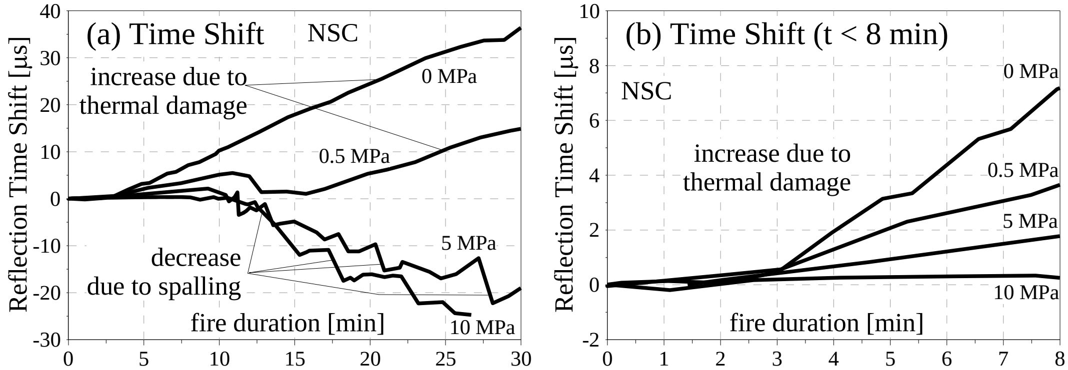

Figure 4: Reflection Time Shift for 4 levels of membrane stress as a function of fire duration: (a) full plot, and (b) plot for $t \leq 8$ min.

This is probably due to the smoothing of the tensile stress induced in the cement paste by aggregate dilation (cement paste-aggregate kinematic incompatibility).

CONCLUDING REMARKS

Two sets of 4 concrete slabs have been tested at the Politecnico di Milano, in order to investigate the influence of different parameters on spalling sensitivity in fire. The specimens were heated at the bottom side according to the Standard Fire curve, while a constant biaxial membrane compression was applied through hydraulic jacks. Spalling monitoring was implemented via an established Non-Destructive Technique, namely Ultrasonic Pulse-Echo. This method, together with the continuous measurement of temperature along the depth of the specimens, is shown to be rather effective in evaluating concrete damage at high temperature and in determining spalling depth.

The original feature allowed by proper post-processing of Ultrasonic Pulse-Echo measurements is the assessment of concrete damage induced by the combined effect of temperature and load. This is something new compared to the results available in the literature, since ultrasonic investigation on heat-damaged concrete is usually performed after cooling (residual conditions) and in unstressed specimens. The investigations clearly show as the decay of ultrasonic pulse velocity with temperature in hot conditions can be significantly lower than in residual conditions; moreover it was proved as the higher the compression stress applied during heating, the lower the thermal damage. These results come together with the effective monitoring of spalling depth during fire tests, a not easy task due to the high temperatures involved.

ACKNOWLEDGEMENTS

The proposed monitoring technique was developed in the framework of PoliNDT, an inter-department laboratory on structural diagnostic and monitoring at Politecnico di Milano. The Authors are grateful to CTG-Italcementi Group (Bergamo, Italy) for the design of the concrete mixes and the preparation of the specimens. Fondazione Lombardi Ingegneria (Minusio, Switzerland) is also thanked for the financial support given to this research project.

REFERENCES

1. Kalifa P., Menneteau F. D. and Quenard D. 2000. "Spalling and pore pressure in HPC at high temperatures", *Cement and Concrete Research*, 30: 1915-1927.
2. Khoury A. G. 2000. "Effect of fire on concrete and concrete structures", *Progress in Structural Engineering and Materials* 2:429-447.
3. Khoury G.A. 2008. "Polypropylene Fibres in Heated Concrete. Part 2: Pressure Relief Mechanisms and Modelling Criteria", *Magazine of Concrete Research* 60 (3): 189-204.
4. Yufang F. and Lianchong L. 2010. "Study on mechanism of thermal spalling in concrete exposed to elevated temperatures", *Materials and Structures* 44: 361-376.
5. Felicetti R. and Gambarova P. G. 1998. "On the Residual Tensile Properties of High Performance Siliceous Concrete Exposed to High Temperature", Special Volume in honour of Z.P. Bazant's 60th Anniversary, Prague (Czech Republic), March 27-28, Ed. Hermes (Paris), pp. 167-186.
6. Pistol K., Weise F., Meng B. and Schneider U. 2011. "The Mode of Action of Polypropylene Fibres in High Performance Concrete at High Temperatures", Proceedings of the 2nd Int. RILEM Work. on Concrete Spalling due to Fire Exposure, 5-7 October, Delft (the Netherlands), pp. 289-296.
7. Grosse C., Richter R., Ozbolt J., Dehn F. and Juknat M. 2011. "Spalling of HPC Evaluated by Acoustic Emission and Numerical Analysis", Proceedings of the 2nd International RILEM Workshop on Concrete Spalling due to Fire Exposure, 5-7 October, Delft (the Netherlands).
8. Pereira F., Pistol K., Korzen M., Weise F., Pimienta P., Carré H. and Huismann S. 2011. "Monitoring of Fire Damage Processes in Concrete by Pore Pressure and Acoustic Emission Measurements", Proceedings of the 2nd International RILEM Workshop on Concrete Spalling due to Fire Exposure, 5-7 October, Delft (the Netherlands), pp. 69-77.
9. Lo Monte F., Rossino C. and Felicetti R. 2015."Spalling Test on Concrete Slabs under Biaxial Membrane Loading", Proceedings of the 4th International Workshop on Concrete Spalling due to Fire Exposure, 8-9 October, Leipzig (Germany).
10. Carino N. J. 2001. "The Impact-Echo Method: an Overview", Proceedings of the 2001 Structures Congress & Exposition, May 21-23, Washington, D.C., American Society of Civil Engineers, Reston, Virginia, Peter C. Chang, Editor, 18 p.
11. Cheng C. and Sansalone M. 1993. "The impact-echo response of concrete plates containing delaminations: numerical, experimental and field studies", *Materials and Structures* 26: 274-285.
12. Lin Y., Sansalone M., and Carino N.J. 1990. "Finite Element Studies of the Impact-Echo Response of Plates Containing Thin Layers and Voids", *J. of Nondestructive Evaluation* 9 (1): 27-47.
13. Krause M., Barmann M., Frielinghaus R., Kretzschmsr F., Kroggel O., Langenberg K. L., Maierhofer C., Muller W., Neisecke J., Schickert M., Schmitz V., Wiggenhauser H. and Wollbold F. 1997."Comparison of pulse-echo methods for testing concrete", *NDT&E Int.* 30 (4): 195-204.
14. Bouden T., Dib S., Aissaous K. and Grimes M. 2009. "Signal Processing Methods for Materials Defects Detection", Ultrasonics Symposium (IUS), 2009 IEEE Int., 20-23 Sept., Rome (Italy).
15. Sansalone M., and Carino N.J. 1987. "Transient Impact Response of Thick Circular Plates", *Journal of Research of the National Bureau of Standards* 92 (6): 355-367.
16. Mayer K., Langenberg K.-J., Krause M., Maierhofer C., Milmann B. and Kohl C. 2006. "Characterization of Ultrasonic and Radar Reflector Types in Concrete by Phase Evaluation of the Signal and the Reconstructed Image", Proceedings of the 9th European Conference on NDT, September 25-29, Berlin (Germany).
17. Lo Monte F., Felicetti R., Lualdi M. and Lombardi F. 2015. "Concrete Damage and Spalling Monitoring in Fire Tests via Ultrasonic Pulse-Echo and Ground-Penetrating Radar", Proc. Int. Symp. Non-Destructive Testing in Civil Engineering – NDT-CE, Berlin (Germany), Sept. 15-17, 2015.

PROBABILISTIC APPROACHES AND APPLICATIONS OF FIRE SAFETY

Towards a Standard Measure of the Ability of a Structure to Resist a Natural Fire

THOMAS GERNAY and JEAN-MARC FRANSSEN

ABSTRACT

Fire brigades face a major threat when intervening in a building in fire: the possibility of structural collapse during the cooling phase of the fire, or soon thereafter. In the current approaches to structural fire engineering, the fire resistance rating (R) is generally the only measure taken into consideration to characterize the fire performance of structural elements, although this measure does not reflect the response in real fire conditions. In this work, a standard measure is proposed to characterize the ability of structural members to resist a natural fire including the decay phases. This measure yields information about the potential occurrence of delayed failure as a function of the duration of the fire before it started to decrease, whether by self-extinction or due to the action of the fire fighters. The paper presents the method to derive this new standard measure as well as results for different typologies of structural elements. Finally, the interpretation and practical consequences are discussed, in particular regarding the safety of fire fighters during an intervention.

INTRODUCTION

In a performance-based approach, a realistic representation of the fire needs to be considered in the analysis. This representation should include the successive fire development stages until burnout. Yet, this demands a shift in perspective on the response of structures to fire, because structural members that perform well under continuously increasing time-temperature curves (such as the standard ISO fire) do not necessarily perform well when subjected to heating-cooling sequence. Meanwhile, collapse of buildings during the cooling phase of a fire occurred in the past, highlighting the importance of filling this lack of knowledge.

Several recent studies have focused on the residual load bearing capacity of structural members after exposure to fire, e.g. [1]. However, the analysis of the transient evolution of capacity during the decay phase has rarely been addressed.

Thomas Gernay, the National Fund for Scientific Research F.R.S.-FNRS, University of Liege, Allée de la Découverte 9, 4000 Liège, Belgium. thomas.gernay@ulg.ac.be
Jean-Marc Franssen, Structural Engineering Department, University of Liege, Liege, Allée de la Découverte 9, 4000 Liège, Belgium, jm.franssen@ulg.ac.be

This aspect needs further investigation as the capacity continues to decrease after the time of maximum gas temperature in a building compartment [2], which particularly endangers the fire fighters and first responders. Other researchers have made contributions to determine equivalent fire resistance based on performance based methods [3]. In this work, the objective is to propose an original and pragmatic concept to characterize the structural fire performance under realistic, natural fires. A novel standard measure is derived and applied to different structural members subjected to natural fire. The goal is also to define a measure that can be helpful for fire fighters education and for increasing their safety on site.

POSSIBILITY OF DELAYED COLLAPSE

Factors Promoting Failure after the Time of Maximum Gas Temperature

When a structural member is exposed to natural fire, its load bearing capacity decreases during the heating phase of the fire, but it also decreases after the maximum gas temperature is attained. As a consequence, structural failure may occur during or after the cooling phase. This delayed decrease in load bearing capacity may be caused by the combination of various phenomena, such as:

- the delayed temperature increase in the sections, due to thermal inertia;
- the non-recovery or additional loss of material properties during cooling;
- the built-up and reversal of thermal forces in a structure subjected to heating-cooling (e.g. tensile forces in connections).

For instance, Figure 1 depicts the evolution of temperature in the section of a reinforced concrete (RC) column exposed to a natural fire. The fire corresponds to the Eurocode parametric fire with a 60-minutes heating phase and a coefficient $\Gamma = 1$ [4]. The maximum temperature in the corner steel rebars (A) is reached after 92 minutes, i.e. during the cooling phase of the fire. In the core of the concrete section (C), the maximum temperatures are reached long after the end of the fire. Hence due to this thermal inertia, the concrete core of the section continues to lose part of its mechanical properties after the gas temperature in the compartment is back to ambient. Besides, concrete material is known to also lose part of its residual strength during cooling [5].

Example: Structural Response of a Column under Natural Fire

The effects of the phenomena listed in the previous section on the possibility of delayed failure are illustrated here for a RC column. Figure 2 shows the evolution of the vertical deflection at the top of a column that is subjected to constant applied load and to natural fire exposure. The column is analyzed under three different values of the load using the nonlinear finite element software SAFIR® [6]. As can be seen, depending on the applied load, structural failures during the cooling phase or even after the end of the fire may be observed. The goal of the standard measure that is introduced in this paper is to quantify the sensitivity to these delayed failures.

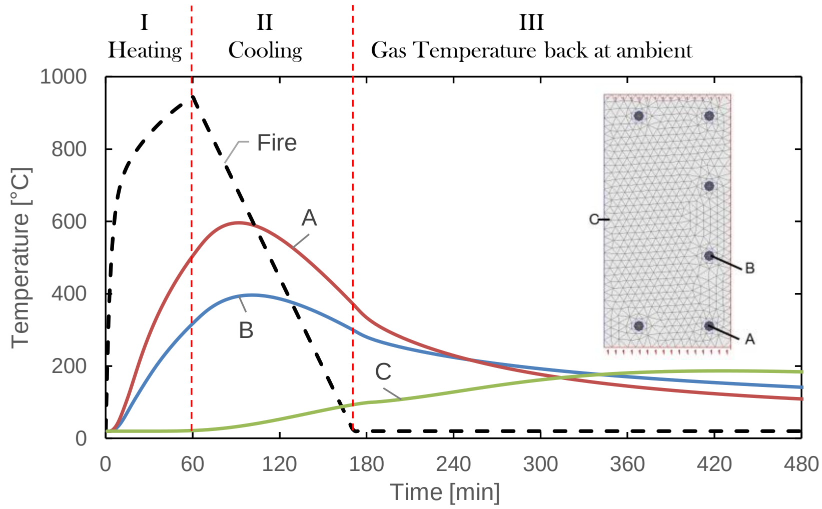

Figure 1. Evolution of temperature in a RC column section exposed to a natural fire (1/2 modeled).

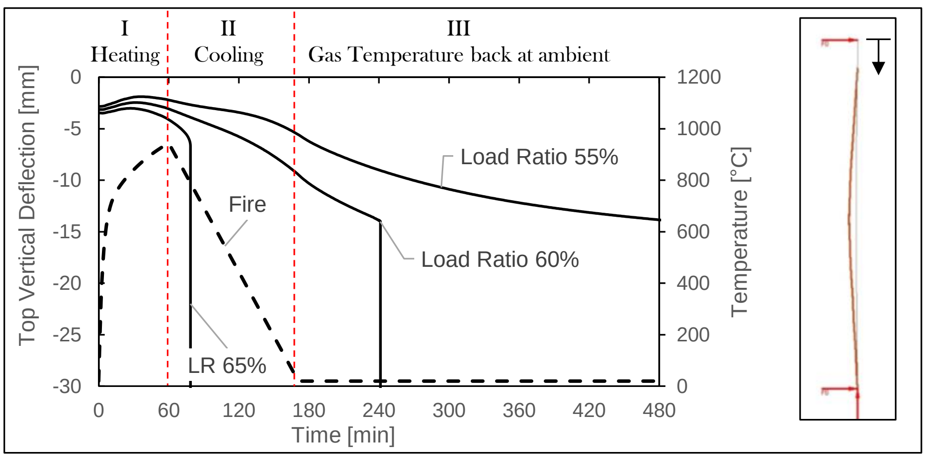

Figure 2. Time evolution of top vertical displacement for a RC column exposed to a 60-minutes heating phase natural fire, for different levels of applied compressive load.

STANDARD MEASURE FOR PERFORMANCE UNDER NATURAL FIRE

Duration of the Heating Phase (DHP)

The fire resistance rating (R) relates the applied load ratio (LR) on a member with the duration of exposure to a standard fire until failure. By similarity, the key idea behind the proposed measure is to relate the applied LR with a duration that is characteristic of a natural fire and that causes failure. It is chosen to work with the duration of the heating phase of the natural fire based on the parametric fire model of Eurocode 1 with $\Gamma = 1$. Selection of this value for Γ makes the heating phase approximate the standard ISO curve.

Using this set of natural fires, a standard measure can then be defined to quantify the response of a structural member under natural fire exposure. This measure is referred to as Duration of Heating Phase (DHP). The DHP of a member under a given applied LR is defined as the minimum exposure time to standard ISO fire (followed by cooling phase in accordance with the Eurocode parametric fire model) that will eventually result in the failure of the structural component, even if the fire stops thereafter. It has a straightforward interpretation for fire brigades: if their intervention (which ends the heating phase) starts earlier than the DHP of the structure, the structure is theoretically safe; if it starts later, they should be particularly careful as the structure is expected to eventually collapse even though the gas temperatures are decreasing. Note that failure can occur several minutes or hours after the time corresponding to the DHP. The DHP only informs about the occurrence of failure (not the time at which it will occur), based on the extent of fire exposure that the member has experienced. The reader is referred to [7] for more details about the theoretical definition of the DHP.

Adopting a measure in time unit is convenient for comparison with the Fire Resistance indicator. Besides, the duration of the heating phase of a natural fire has a direct practical significance and can be easily comprehended by the different stakeholders involved in fire safety. Also, this is a quantity that, to some degree, can be estimated on site during a real fire.

It is recognized that the adopted natural fire model represents a specific type of fire and is not necessarily representative of the real fire that would develop in a building. However, defining a standard natural fire provides significant advantages. It allows quantifying and comparing the performance of different members. The time-temperature relationships that represent the fire are simplified and comprise only one varying parameter, the duration of the heating phase.

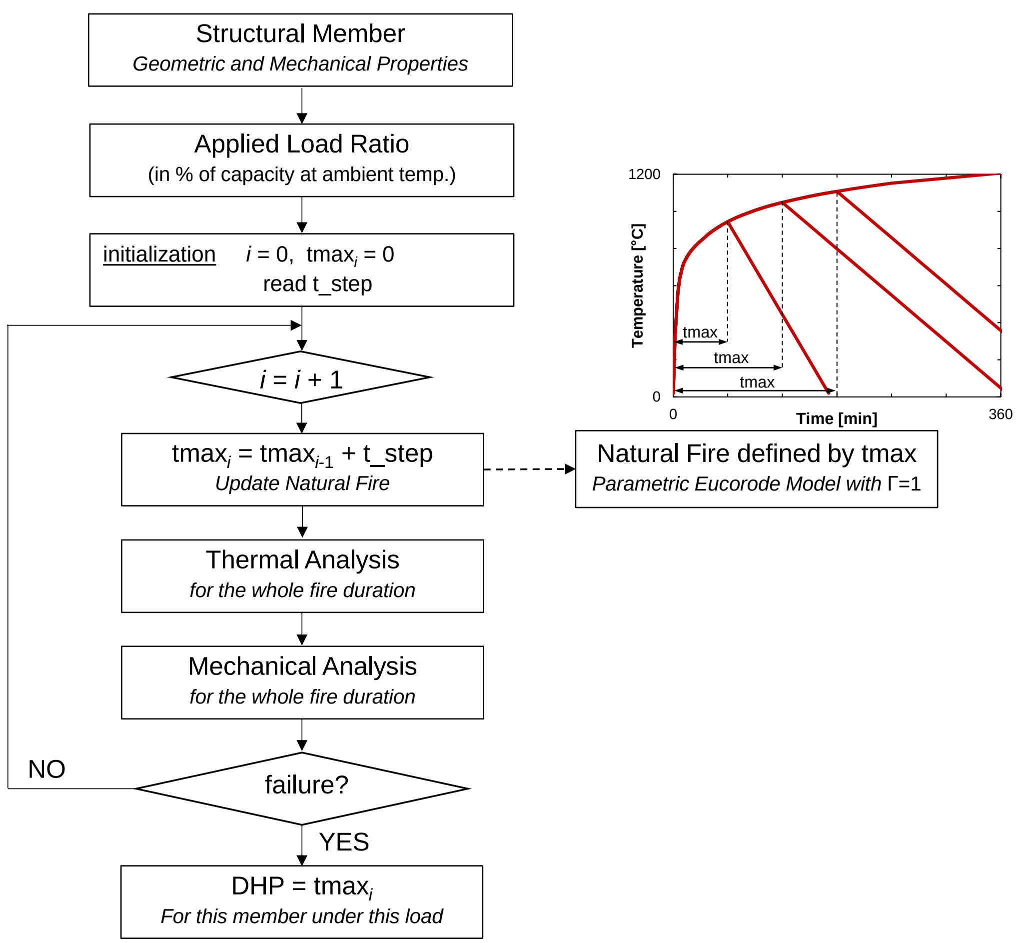

Figure 3. Flowchart to obtain the DHP of a member – fixed load ratio method.

Method to Derive the DHP

The method to obtain the DHP of a structural member subjected to a given LR is illustrated by the flowchart in Figure 3. It can be seen that this method is a more complex operation than the method to obtain the Fire Resistance, for two reasons.

First, searching for the DHP of a member is searching for a fire curve. The process is thus iterative, consisting of several analyses under different applied parametric fires for the search of the minimum value of parameter tmax that leads to structural failure (where tmax is the duration of the heating phase).

Secondly, except for the simplest members, the analysis of a structural member under natural fire necessarily requires a verification in the entire time domain by a step-by-step method, since verification in the load domain at the time of maximum gas temperature does not guarantee against failure at a later stage. Therefore, the "thermal analysis" and "mechanical analysis" in the flowchart need to be transient analyses. These are usually performed by means of advanced numerical methods such as the non-linear FEM. The parameter t_step dictates the degree of accuracy of the process and should not exceed a few percent of the value of DHP.

RESULTS - COMPARISON BETWEEN DHP AND R

Load Bearing Capacity Criterion

For illustration, the DHP and R of various structural members are determined under different applied load ratios. The following members are considered:

- A RC square column of 4 m length and 45 cm side, exposed to natural fire on its four sides;
- A HEB 400 steel column of 4 m length, in S355, exposed to natural fire on its four sides, with a thermal protection designed to provide a fire resistance of 60 minutes under 50% LR (P1);
- The same steel column but with a thermal protection designed to provide a fire resistance of 120 minutes under 50% LR (P2);
- A softwood timber beam, simply supported with 4 m span, exposed to natural fire on 3 sides.

The response of the structural members under natural fire exposure is analyzed using SAFIR® [6]. The material properties are taken according to the Eurocodes. For concrete modeling, the Explicit Transient Creep Eurocode model is adopted to take into account the transient creep strain irreversibility during cooling [8]. Concrete compressive strength is reduced during cooling by an additional 10% of the value corresponding to the maximum temperature according to Eurocode 4.

The fire resistance rating R under standard ISO fire and the DHP under natural fire are obtained for the members. The results are given in Table I. This allows drawing the following main conclusions:

- For all the studied members, the DHP is always lower than the fire resistance R. This reveals the possibility of delayed failure, for any constituting material.
- The difference between the DHP and R is higher for certain members than for others. This is due to the different mechanisms influencing delayed failures,

such as the thermal inertia brought by the insulation in a protected steel member or the delayed charring process in a timber member.

- A member that has a longer fire resistance than another may nevertheless have a shorter DHP.

These conclusions have important implications. In particular, they demonstrate that the fire resistance R is not relevant for estimating the structural performance to fire when considering natural fires. A specific typology and/or material that happens to perform better than another under standardized fire conditions (higher R) might in fact perform worse under a realistic fire (lower DHP).

Insulation Criterion

The discussion so far has focused on the load bearing capacity criterion under fire. Typically, the fire performance of building members may be evaluated based on more than one criterion. For instance, the insulation criterion can also be critical when assessing the fire performance of a concrete slab or wall. It is interesting to examine how this insulation criterion is affected by the cooling phase of a fire.

The Eurocode states that the following requirements apply to the verification of the separation function for the average temperature rise, assuming that the normal temperature is 20°C:

(a) The average temperature of the unexposed side of the construction should be limited to 160°C during the heating phase until the maximum gas temperature in the fire compartment is reached.

(b) The average temperature of the unexposed side of the construction should be limited to 220°C (recommended value) during the decay phase.

Numerical analyses are used to evaluate the heat transfer across the depth of a concrete slab subjected to fire at its lower face. To satisfy the criterion related to the heating phase for 120 minutes, the minimum required thickness is found to be equal to 117 mm. This means that a concrete slab of 117 mm subjected to ISO fire at its lower face reaches an average temperature of 160°C after 120 minutes. If the simulation is continued with the decay phase of the fire (where the cooling phase after 120 min follows the parametric Eurocode fire model), the average temperature of the unexposed side reaches up to 252°C. In order to satisfy the criterion related to the decay phase, the slab thickness needs to be increased to 138 mm, see Figure 4.

Inversely, if the slab has a fixed thickness of 117 mm, the maximum duration of the heating phase that allows satisfying the criterion during the decay phase is 85 min. Therefore, the 117 mm slab has a DHP of 85 min with respect to the insulation criterion (decay phase requirement), whereas it has a R of 120 min (heating phase requirement). Note that those analyses are based on the assumption that the decay phase of the natural fire is according to the Eurocode parametric fire model.

TABLE I. INDICATORS DHP AND R FOR DIFFERENT STRUCTURAL MEMBERS.

Time in min	**RC column**		**Steel Column (P1)**		**Steel Column (P2)**		**Timber Beam**	
Load Ratio	**DHP**	**R**	**DHP**	**R**	**DHP**	**R**	**DHP**	**R**
60%	60	88	35	54	72	108	15	51
50%	89	120	43	61	84	120	26	71
40%	116	164	50	69	97	135	39	92
30%	168	218	60	79	111	153	53	116

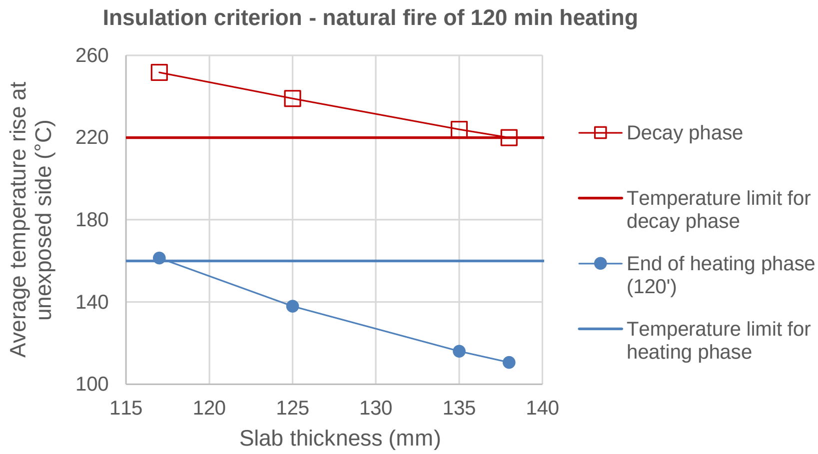

Figure 4. The insulation criterion in Eurocode (average temperature at the unexposed side) for a concrete slab is more severe during the decay phase than during the heating phase.

DISCUSSION

The indicator DHP quantifies the sensitivity of structural members to fire decay phases. The characterization of a structural member by the couple of indicators (DHP, R) can prove useful and have practical implications for the fire brigades.

Figure 5 shows on a timeline the standard measures DHP and R for the steel column (P1) and the timber beam subjected to a 50% LR. The timber beam has a higher R but a lower DHP than the steel column. These measures suggest that, should an intervention of the fire brigade take place between 26 min and 43 min after the time of flashover (scenario b), the timber beam would experience a delayed failure, whereas the steel column would not fail. This conclusion could not be obtained based on the values of R. If R was the only indicator considered, one would disregard entirely the higher sensitivity to cooling phases of the timber beam.

On a conceptual level, the couple of indicators (DHP, R) allows dividing the post-flashover time domain in three parts for a structure in fire:

1) The first part of the time domain starts at the flashover and lasts until the time corresponding to DHP. In this part, the structure is theoretically safe. It is able to withstand the effects of the fire and, should the gas temperature start cooling down in this part, the structure would then survive indefinitely.
2) The second part of the time domain lies between the times corresponding to DHP and R. In this part, the structure is still standing even if the gas temperature has been continuously increasing from the flashover. However, if the fire is still in its heating phase, the structure has been affected to such an extent at that time that it will fail even if the fire starts decreasing soon thereafter.
3) The third part of the time domain starts at the time corresponding to R. In this part, if the gas temperature has not started cooling down yet, the structure is theoretically collapsed.

This means that, for the fire brigades, the DHP of a structure is a key information. When arriving on site, they can relate the DHP with the information they can get about the duration of the fire and use it for mitigating the risk during their intervention.

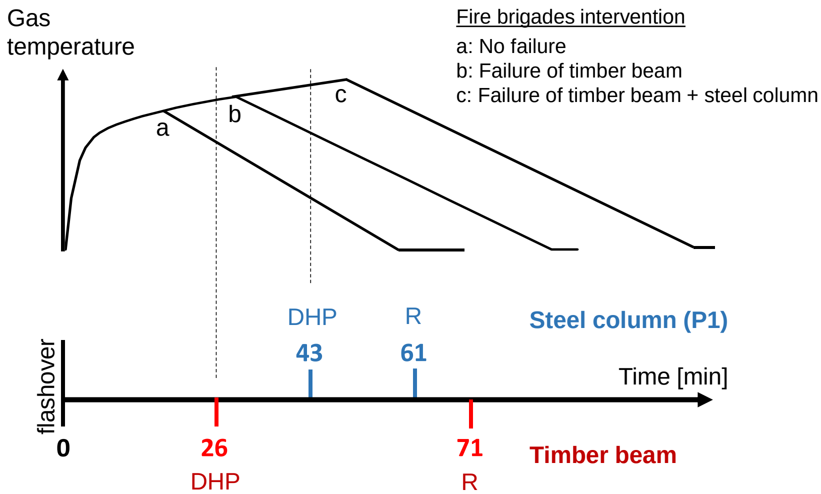

Figure 5. DHP and R for a steel column and a timber beam, for an applied LR of 50% on the members.

CONCLUSION

This research aims at better comprehending and characterizing the fire response of structural members during the decay phases. A methodology has been developed to determine the maximum duration of heating phase of a natural fire that can be withstood by a member without leading to delayed failure. This leads to the definition of a novel standard measure, called Duration of Heating Phase (DHP). The DHP has a straightforward interpretation for fire brigades: if their intervention (which ends the heating phase) starts earlier than the DHP of the structure, the structure is theoretically safe; if it starts later, they should be particularly careful as the structure is expected to eventually collapse even though the gas temperatures are decreasing.

REFERENCES

1. Kodur, V.K.R., Raut, N.K., Mao, X.Y., Khaliq W. 2013. “Simplified approach for evaluating residual strength of fire-exposed reinforced concrete columns”, *Mater Struct*, 46(12):2059-75.
2. Gernay, T., Dimia, M.S. 2013. “Structural behavior of concrete columns under natural fires”, *Engineering Computations*, 30(6):854-872.
3. Kodur, V.K.R., Pakala, P., Dwaikat, M.B. 2010. “Energy based time equivalent approach for evaluating fire resistance of reinforced concrete beams”, *Fire Safety Journal*, 45(4): 211-220.
4. EC1. 2002. *Eurocode 1: Actions on structures – Part 1-2: General actions – Actions on structures exposed to fire*. EN 1991-1-2, Brussels: CEN.
5. Li, Y.-H., Franssen, J.M. 2011. “Test results and model for the residual compressive strength of concrete after a fire”, *Journal of Structural Fire Engineering*, 2(1): 29-44.
6. Franssen, J.M. 2005. SAFIR: A thermal/structural program for modeling structures under fire. *Eng J AISC, 42(3), 143-158.*
7. Gernay, T., Franssen, J.M.. 2015. “A performance indicator for structures under natural fire”, *Engineering Structures*, 100: 94-103.
8. Gernay T, Franssen J.M. 2012. “A formulation of the Eurocode 2 concrete model at elevated temperature that includes an explicit term for transient creep”, *Fire Safety Journal*, 51: 1-9.

Application of Concepts of Fire Resistance of Load Bearing Structural Glass

JOHAN SJOSTROM, DAVID LANGE, MICHAEL DEBUYSER, DANIEL HONFI, DELPHINE SONCK and JAN BELIS

ABSTRACT

The use of glass as a load bearing element in structures is a growing phenomenon. Glass elements cover both beams and shear walls and its use is driven mostly by aesthetical and architectural reasons but brings other benefits considering environmental and financial aspects. Glass is a strong material but with a brittle nature which means a sudden fracture on failure with negative consequences for safety. However, with new techniques of increasing ductile behaviour and with the use of glass elements embedded in a holistic fire safety design strategy there are now several examples of load bearing glass elements in modern construction. This paper highlights some aspects of the use of load bearing glass with recent updates on the general knowledge base and the standardisation work.

INTRODUCTION

Proliferation of Structural Load Bearing Glass Structures

Glass as a building material is seeing a developing interest throughout the world. A few examples are shown in Figures 1-2. Within Europe, companies in e.g. France, Germany, the Netherlands, Switzerland and the UK are all developing techniques for the manufacture of long span building elements comprised almost solely of glass. This is driven by a number of factors, including:

- Cost: transparent glass elements let the natural light in the buildings, making available to reduce the maintenance costs due to artificial lighting. In addition glass is an excellent material for thermal insulation, water proofing and energy conservation.
- Human: glass as a construction material it is both stunning and challenging for the occupants. Furthermore, the natural light penetration into a space is generally believed to promote the wellbeing of the building occupants.
- Sustainability: closely linked with the transparency of glass and its cost. Glass is a relatively low energy material to produce and therefore reduces the entrained CO_2 in a building during the construction phase. Glass is also highly reworkable and recyclable.

All of these factors align themselves well with current trends in both policy and design. Use of glass as a structural load bearing material is therefore increasing throughout the world.

Figure 1. 10m glass cube, Apple Store 5th avenue New York.

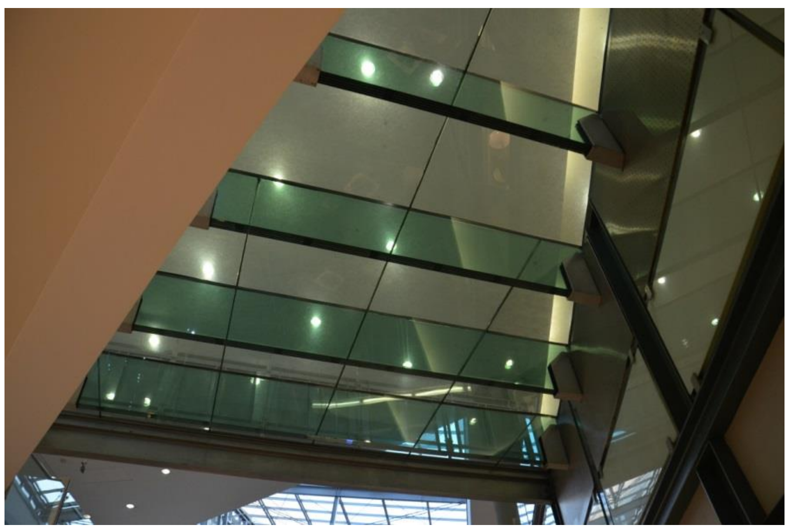

Figure 2. Glass beams supporting a glass floor, WestEnd City Center, Budapest.

Safety of Glass Structures

Glass is approximately 1/3rd of the density, 1/10th the yield strength in tension and 1/3rd of the elastic modulus of steel [1]. As such, for achieving structural design objectives it has a reasonable stiffness and strength to weight ratio. However, glass is perfectly elastic and experiences no ductility [2], fracturing at some critical effective stress rather than undergoing any amount of plastic deformation. Failure of glass is therefore deemed to be a fracture mechanics problem, and in fact glass is one of the classical materials which is used to study and develop fracture mechanics models since it is perfectly elastic up until the point of failure. From this perspective, glass is therefore a rather poor structural material since there is no warning prior to failure, which could be dramatic and have serious consequences for building occupants. Therefore specific safety considerations need to be made.

In order to resolve this issue, modern structural glass construction relies on multiple panes of glass laminated together using a polymer interlayer. This polymer interlayer is typically less stiff than the glass itself and is of much lower thickness. As cracks develop in the glass, the load can be redistributed to adjacent panes via the polymer interlayer. This allows structural load bearing glass elements to be constructed of multiple lamella of glass, whilst still retaining the transparent properties of glass elements in buildings. Using this concept it is possible to construct many different building elements out of glass including: walls, columns, stair cases, façade systems and floors.

With specific concern for fire safety, the polymer constituting the interlayer tends to soften and evaporate at even moderate temperatures. Polyvinyl Butyral (PVB), the most widely used interlayer for structural glass elements, has a glass transition temperature just under room temperature [3]. Thus, with increasing temperature, slow movements of the panes relative to each other are increasingly possible which increases the risk of fracture in a fire situation. With increasing temperature the viscosity of the interlayer decreases significantly. At about 400 ^{o}C the interlayer evaporates [4, and refs. therein], see Figure 3.

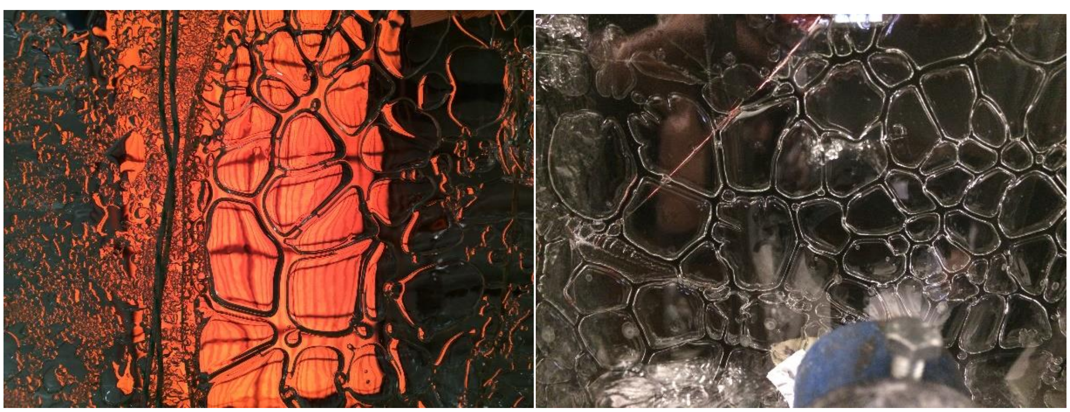

Figure 3. Interlayer gas formation upon heating (left) and post heating (right) of glass beams.

For structural glass beams, a promising concept to enhance structural robustness at component level has been developed in recent years [2], comprising a steel reinforcement bar which is integrated in the layup of the structural glass element. The reinforcement section bridges the cracks as they develop, carrying tensile forces and allowing larger displacements to develop. With subsequent cracking of the glass, the load displacement curve jumps, creating the saw toothed pattern seen in Figure 4. Through this mechanism, a residual load-carrying capacity is generated which enables the glass beam to continue to carry a load even though the glass is broken. This concept, which has some similarities to reinforced concrete, is referred to as reinforced glass beams.

The research into the behaviour of structural glass beams under fire is still in its infancy but early work has been done exploring the fire-testing of laminated glass beams with and without reinforcement [6]. It is expected that the reinforcement section may improve the resistance of the glass beams and that structural failure of the glass beams may be postponed compared to common, or unreinforced, glass beams.

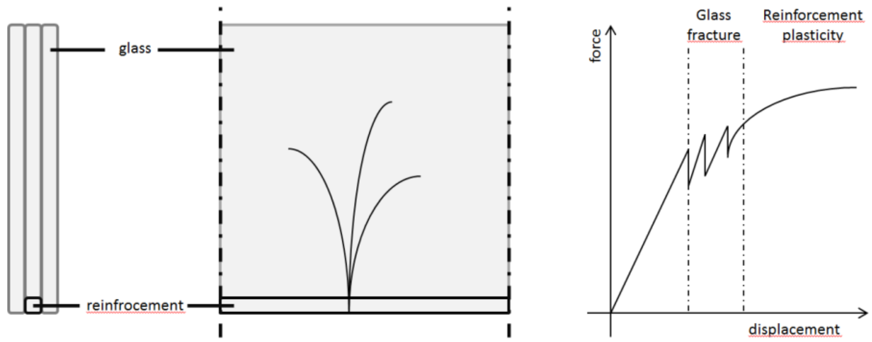

Figure 4. Schematic representation of the functioning of reinforced laminated glass beams: left) cross-section of a laminated glass beam; middle) side-view of a cracked glass beam; right) intended force-displacement diagram, redrawn from [2].

International Research and Standardisation Work

There are several EU-funded projects related to structural glass, for example the Wood-Wisdom project Load-Bearing Timber Glass Composites (LBTGC) [3] which looks at the use of glass elements as the web in composite timber beam sections. Additionally, the recently finished COST Action TU0905 European Research Network on Structural Glass [7] disseminated current knowledge about structural load bearing glass throughout Europe and created a network of experts working in the field of structural glass.

Notably neither the Wood-Wisdom project nor the COST Action specifically addressed fire except for one paper, based on experience from the industry, which discussed fire resistance of glass elements [8]. In this article the fire resistance of glass is discussed only in terms of the integrity and the insulation capability as well as the radiation transmittance. The authors also present initial modelling results of both the heat transfer to and within a glass element as well as the mechanical response of the heated element (which in the case presented appears to be an unreinforced floor section). In a test shown in the paper, the unreinforced glass element failed after 8 minutes of fire exposure.

There is a preliminary European standard on the design of glass elements for loads which act perpendicular to the plane of the plate of glass, such as snow or wind loads on glass roofs or facades, prEN16612 & prEN16613. However this guidance is not representative of the loads which may be expected to be applied to structural load-bearing elements such as beams, floors and columns, further, even in the preliminary standard, there is no guidance as to the fire resistance of this type of element.

At present there is no European standard for structural load bearing glass elements. However, there is on-going work within standardization committees to achieve both in Europe and North America. In Europe CEN TC250 SC11 (Structural glass) [9] works on developing structural design rules for glass components that should result in a new Eurocode on the design of structural glass. Simultaneously a standard committee for the design of structural glass was formed by ASTM [10] The new standard, in contrary to ASTM E1300 [11], will focus on applications where glass is not only used for cladding and where failure of glass causes significant consequences.

A scientific report detailing pre-normative work of CEN/TC 250 WG3 was recently published as a JRC (European Joint Research Centre) scientific and policy report [12], this is a first step prior to publication of this work as a CEN Technical

Specification. After a period for trial use and commenting, CEN/TC 250 will then decide whether the Technical Specification should be converted into an EN. In the draft scientific and policy report, it is stated that loadbearing glass has limited fire-resistance and where fire is a design issue for the component then this can be addressed via e.g. additional redundancy built into the structural design or additional fire safety features to limit the potential heat flux exposure to a glass element. This may be ultimately described as an alternative, or performance based, solution to prescriptive building requirements.

This reflects a significant knowledge gap in the performance of structural load bearing glass elements under fire conditions, and one which must be addressed in order to enable the safe continued growth in the use of structural glass in buildings.

PERFORMANCE IN FIRE OF LOAD BEARING STRUCTURAL GLASS

In order to be able to demonstrate the fire safety of glass elements knowledge about both thermal and mechanical material properties at elevated temperatures are needed. However there is very little information about the material properties of glass at high temperatures. In this section we discuss how some of the relevant properties can be measured, including spectral reflectivity and transmission; as well as conductivity and specific heat. We also discuss how the structural response of glass exposed to fire can be incorporated into a holistic fire safety strategy.

Thermal Properties of Glass

The spectral surface reflectivity and transmission coefficient are measured using spectrophotometers. The reflectivity measures how much of the infrared radiation from a fire that is reflected from the glass. A high reflectivity means a slower heating of the glass due to radiative heat transfer. On the other hand, if the reflectivity remains high also for shorter wavelengths, into the visible spectrum that the glass will look like a mirror which might not be aesthetically acceptable. However, typical window glass is coated with thin layers of metals or metal oxides which increases the reflectivity in the infrared part of the spectrum but with little effect in the visible part of the spectrum. Such coatings are typically used for energy saving purposes but in turn help the fire performance of the glass, without affecting the aesthetical performance.

The spectral transmission coefficient is also measured using spectrophotometers. The difference is that the amount of transmitted light, instead of reflected light, is measured. The spectral transmission coefficient depends both on the reflectivity and the absorbing properties of the material and will determine how the dynamic temperature profile within the profile will look like. Possibly, reflections at the bonding resins between the lamella will complicate the heat transfer.

As mentioned above, we usually consider glass a transparent material. However, for very short UV-wavelengths the transmittance is low, almost zero at wavelengths < 250 nm and a glass thickness of 1 mm. In the near visible and visible spectrum the glass is, as we experience daily, transparent but in the short IR band, above 2500 nm, the transmittance drops sharply and fluctuates between almost optically thick to semi-transparent. These wavelengths correspond to the radiation emitted from flames and hot smoke from fires [4, 13].

The thermal conductivity of borosilicate glass as well as soda lime silicate glass is generally cited as 1.0 W/mK. Recent measurements, using transient plane source techniques (a thin heating spiral sandwiched between to glass surfaces [14]) also show 1.03 (±0.03) W/mk for soda lime glasses at room temperature [13]. Studies concerning properties at higher temperatures generally show an increasing conductivity of 27-30 % from ambient temperature up to glass transition, typically around 500-600 °C. [15-17] Increasing conductivity with temperature is unusual for non-porous materials. The values at higher temperatures are, however, reproduced by different techniques such as glass-metal contact and laser flash technique [18].

The specific heat capacity has more typical temperature dependence. Starting around 800-900 J/kgK at room temperature it increases, with a descending rate, to 1100 J/kgK at the glass transition, where a significant jump in heat capacity occurs due to the new degrees of freedom activated in the supercooled state. The heat capacity is usually measured using a differential scanning calorimeter [19] but similar results have been confirmed by other techniques [13].

Structural Design Considerations

Different surface coatings and different combinations of polymer and glass types are all available and are used in the composition of glass elements for a variety of purposes. These different materials and coatings will have a significant impact not only on the mechanical behaviour of the element in fire but also on the thermal properties and notably on the absorptivity of the glass specimen in fire. The layup of the glass element therefore plays a significant role in the transfer of heat to glass elements. Because of the semi-transparent nature of glass the radiant heat transfer from a fire will be distributed into the glass and will not only take place at the exposed surface but through the thickness of the glass and at each transition between the individual lamella depending upon the different surface coatings, thicknesses and properties of the different glass layers and interlayers.

As a result of any protective surface coatings, the outer lamella therefore may be much more strongly influenced by convective heat transfer in the event of a fire, whereas any steel reinforcement which is included in the element for ductility purposes as described above will be subject to radiative heat transfer, depending upon the absorptivity properties of the glass layers, from the external conditions as well as conductive heat transfer through the glass. In addition to the safety features discussed above, intumescent coatings are also available. There swell upon heat exposure and will create a protective layer around the glass structure, keeping the glass temperature down and mechanical capacity up. Experiments show that this is a feature that brings significant fire resistance to the glass structure while maintaining the transparent behaviour before intumescing [20].

Studying and understanding this complex combination of radiative, convective and conductive heat transfer at the exposed surface, through the lamella, and at the interface between different lamella is therefore critical to understanding the performance of this type of element in fire.

Further, because of the build-up of this type of element from different sheets of glass, shear interaction between the lamella is critical for the structural response at ambient temperature. However, some of the polymer resins which are commonly used to bond the lamella have been shown to lose stiffness at relatively low temperatures, e.g. 60°C [1], which may significantly affect the ability of the lamella to bridge any cracks in adjacent lamella, significantly reducing the capacity of the heated element.

Considering the examples of buildings in which structural glass is used as a material, all of these are typically characterized by occupancies which have low fuel loads and comprise large, open spaces. The concept therefore of testing of fire resistance of structural glass against, e.g. a standard fire therefore seems to be inconsistent with the needs of these buildings. This is because the standard temperature time curve is more representative of a ventilation controlled post-flashover fire in a well-mixed reactor, comprising a compartment of limited size and with effectively unlimited fuel load. Buildings which involve applications of structural glass therefore lend themselves well to fire engineered solutions and may take advantage of concepts of localised or travelling fires.

When considering the response of glass to localised fires, assuming enough redundancy and or robustness in the overall structure to allow for one element to fail, it may be reasonably assumed that the exposure to convective heating of the glass is relatively limited. Any glass elements away from the seat of the fire are therefore only exposed to radiative heating of a relatively low power. Combined with low emissivity coatings, and a combination of thicker panes or more lamella within the layup of the glass this may result in a significant period before failure of any of the glass elements not exposed directly to convection.

The same approach may be true for travelling fires, where the preheating in the far field is equivalent to the heating of elements near to a localised fire and which are not directly exposed to convective currents. However, where the near field is able to move around the compartment it is likely that the glass exposed to the near field heating regime will fail, and so understanding of fire spread rates is important for predicting failure times of glass buildings. Rackauskaite [21], for example, quotes flame spread rates of between 0.1 and 19.3 mm / seconds based on data from experiments and real fires. This suggests that good fuel control may significantly reduce the impact to the structure in the far field for a significant period of time.

CONCLUSIONS

This paper has provided a brief overview of structural glass today, including examples in application, current approaches to ensure robustness of glass structures, as well as current standardisation work ongoing in the field. The paper also gives a short overview of some of the thermal properties needed to understand the heat transfer in such elements, including the transmissivity ad the reflectivity. Finally, the paper discusses some specific issues related to the fire safe use of structural glass.

To conclude, the design for fire of structural glass buildings must be carried out in a completely holistic way, accounting for all aspects of the fire safety strategy of a building. A fuel controlled design solution with good availability of ventilation will lead to localised fires which may damage some of the elements, requiring redundancy and robustness in the structural design. None of this is new, although the performance of structural glass in fire and the relatively low temperatures at which it may be expected to fail means that the incorporation in fire engineered solutions of active protection and incorporating strong fire safety management is critical.

REFERENCES

1. Louter, C.; Belis, J.; Bos, F.; Callewaert, D.; Veer, F.; Experimental investigation of the temperature effect on the structural response of SG-laminated reinforced glass beams; Engineering Structures 32 (2010) 1590-1599.
   Porter, M.; Aspects of Structural Design with Glass; PhD thesis, The university of Oxford 2001
2. Louter C. Fragile yet Ductile – Structural aspects of reinforced glass beams. Dissertation TU Delft, ISBN: 978-90-8570-743-1, April 2011.
3. Dhaliwal, A.K.; Hay, J.N., The characterization of polyvinyl butyral by thermal analysis, Thermochimica Acta 391 (2002) 245-255.
4. DeBuyser, M.., Exploratory investigation of the behaviour of structural glass in fire, MSc Thesis (2015) University of Gent.
5. Wood Wisdom - Load-Bearing Timber Glass Composites (LBTGC); www.glafo.se/projektinformation/12-1/PX10144E1A.htm; accessed 20/2/2014.
6. Louter, C., Presentation at the JCSS Workshop on Structural Glass, 2016.
7. COST Action TU0905 European Research Network on Structural Glass; http://www.glassnetwork.org/; accessed 20/2/2014
8. Bawa, S; Ji, L. and Lenk, P.; Performance of structural glass during fire, Challenging Glass 4 & COST Action TU0905 Final conference – Louter, Bos, Belis and Lebet (edtors); Taylor Francis group London, ISBN – 978-1-138-00164-0.
9. CEN/TC 250/WG3, Document CEN/TC 250 N 1035, Progress report for the period of May-October 2013, 6th November 2013.
10. Green, R. R. A New ASTM Guide for Structural Glass. GPD Glass Performance Days, June 13-15 2013, Tampere, Finland.
11. ASTM1300 Standard Practice for Determining Load Resistance of Glass in Buildings. West Conshohocken, PA: American Society for Testing and Materials, 2012.
12. Dimova, S.; Pinto, A.; Feldman, M. and Densont, S.; JRC Scientific and policy report ‘Guidance for European Structural Design of Glass Components’, 2014. http://publications.jrc.ec.europa.eu/repository/handle/JRC86637
13. DeBuyser, M.; Sjöström, J.; Lange, D.; Honfi, D., Belis, J., Snock, D., Behaviour of monolithic and laminated glass exposed to a radiant heat flux, (2016) in manuscript.
14. Gustafsson, S.E., Transient plane source techniques for thermal conductivity and thermal diffusivity measurements of solid materials. Rev. Sci. Instrum. 62(3) (1991), 797.
15. SCHOTT (2014). Borofloat 33, Technical data sheet.
16. Tempel, L.; Melis, G.P.; Brandsma, T.C., Thermal conductivity of glass: I. Measurement by the Glass- Metal contact, Glass Physics and Chemistry 26 (2000), 606-611.
17. Carwile, L.C.K.; Hoge, H.J., Thermal conductivity of Pyrex glass: selected values, Technical Report 66-14-PR, United States Army (1966).
18. Temple, L.V.D., Thermal conductivity of glass: Empirical model, Glass Physics and Chemistry 28(3) (2002) 147-152.
19. Huang, J; Gupta, P.K., Temperature dependence of the isostructural heat capacity of soda lime silicate glass, Journal of non-crystalline solids 139 (1992) 239-247.
20. Veer, F.A. et al;., Using transparent Intumescent coating to increase the fire resistance of glass and glass laminates, Glass Processing Days, 18-21 June (2001), Tampere, Finland.
21. Rackauskaite, E.; Hamel, C.; Law, A.; Rein, G.; Improved Formulation of Travelling Fires and Application to Concrete and Steel Structures; doi:10.1016/j.istruc.2015.06.001

Performance-Based Fire Engineering: Sensitivity Analysis on Design Parameters

REZA IMANI, PIERRE GHISBAIN and ALI ASHRAFI

ABSTRACT

Performance based fire engineering has recently been the focus of several studies due to its well-known benefits and the short-comings of the traditional prescriptive design methods. However, the method is not often used extensively because of the large number of parameters and decisions involved in the process. This study presents a framework to conduct a number of sensitivity analyses to help the engineer determine which of several parameters used in a performance based design can affect the outcome significantly. A special computational tool is developed to efficiently build several models and conduct analyses by varying different parameters. A simple residential building is used as a case study to show the capability of the tool in conducting sensitivity analysis and identifying key parameters.

INTRODUCTION

Although much has been discussed in research from the last two decades about performance based fire engineering (PBFE) (Meacham and Custer 1995), most of the practical cases in design of fire protection systems for buildings are still handled using the conventional prescriptive methods. This tendency can be explained by several factors, such as a lack of economic incentive due to competition within the fire protection industry to lower the cost of prescriptive design, or shortcomings and inconsistencies in different interpretations of the performance-based approach. Because performance-based design generally leads to more resilient structures (NIST 2010), the development of an industry standard for PBFE remains of critical importance.

While efforts are being made to develop guidelines for PBFE, the performance-based approach is by essence flexible and will continue to grant freedom in the formulation of the performance objectives and the evaluation of whether a given design meets these objectives. The purpose of the research presented in this paper is to understand and quantify how the fire performance of a structure designed through PBFE is affected by the different parameters incorporated in the implementation of the

Reza Imani, Ph.D., P.E., Thornton Tomasetti, 650 California St., Suite 1400, San Francisco, CA 94108
Pierre Ghisbain, Ph.D., Thornton Tomasetti, 40 Wall St., New York, NY 10005
Ali Ashrafi, Ph.D., P.E., Thornton Tomasetti, 40 Wall St., New York, NY 10005

PBFE method. These parameters include the selection of fire scenarios, structural/fire protection design decisions and acceptance criteria.

In order to perform this sensitivity study, a computational tool is developed to simulate the PBFE process multiple times while varying the parameters of the PBFE method or the properties of the structure being designed. This paper presents both the computational tool and a first set of sensitivity studies performed with it. A case study is conducted on a single story of a residential building using the capability of the developed analysis tool for parametric studies. The goal is to identify parameters that have relatively larger impacts on the design outcome, as these parameters shall be fine-tuned when implementing PBFE and become the priorities of PBFE research and development.

PBFE PROCEDURE OUTLINE

In this study, the PBFE process is organized into three main steps integrated in the computational tool: fire hazard analysis, fire simulation and fire performance evaluation.

The first step of PBFE is to conduct a fire hazard analysis to provide a range of possible fire scenarios with their likelihood of occurrence. Although the apparent direction in this step should be towards identifying realistic fire scenarios, a key functionality of the computational tool is to efficiently incorporate numerous scenarios while aiming to identify the ones with major contributions to the outcome. The intent of this study is to develop relatively simple but sufficiently accurate scenarios for practical design purposes. The procedure starts with selection of an appropriate design fire based on the Eurocode 1 guidelines (CEN 2002) and continues by conducting repetitive analyses with systematic changes made in the assumptions leading to the selected design fire.

The second step of PBFE is to perform a fire simulation for each fire scenario and determine a number of response parameters for the structure being designed. An accurate implementation of this step requires computationally expensive thermal and structural analyses to consider the many nonlinearities of the problem, but in this research we rely on simpler and therefore approximate methods to efficiently simulate multiple fire scenarios. Although the structural and thermal analyses are simplified, they retain a number of parameters typically found in the more complex methods and are therefore sufficient to evaluate the effects of these parameters on the outcome of PBFE. The approximate methods may provide inaccurate results for some fire scenarios and yet capture the general picture of the structure's performance in fire conditions. The computational tool is also designed so that more sophisticated thermal and structural analysis methods can be swapped in if the computational effort is rationalized by circumstances.

The third step of PBFE is to turn the fire simulation results into global measures of performance that can be used to inform design decisions. There are two aspects to this step. First the engineering results such as temperature or stress/deformation must be turned into quantities more relevant to decision-makers, such as damage cost, repair time or collapse probability. These practical quantities are determined at the end of each fire simulation and represent the consequences of the corresponding fire scenario. Then the consequences of the different scenarios can be combined into a global risk assessment for the structure. This risk assessment is probabilistic and relates to the first step of PBFE, where different fire scenarios are selected and associated with probabilities of occurrence. This paper attempts to conduct a comparative study based on a few relatively simple performance measures to illustrate the basics of this last step. Note that full implementation of the last step requires a more in-depth thermal/structural analysis as well as access to considerable amount of data (from past real fire incidents, tests or simulations) that are crucial for an appropriate probabilistic loss estimation to serve as a decision-making parameter. Such completeness is out of scope of this work.

DEVELOPMENT OF ANALYSIS TOOL

Overview

The computational tool is implemented in Java, whose object-oriented architecture facilitates the sensitivity study and makes it more consistent by allowing changes in the implementation of any step or sub-step of the PBFE method without affecting the rest. Specialized code is used for the computationally intensive tasks, with the thermal and fire propagation analyses performed in CFAST Version 7 (NIST 2015). Moreover, the code has the ability to conduct the structural analysis either independently (i.e., with simplified member criteria directly defined in the Java code) or through connecting to any general purpose structural analysis tool (e.g., OpenSees) by feeding thermal analysis results as the input.

CFAST Model

The procedure for any given sensitivity study starts with building an initial CFAST model of the building with all of the relevant details (i.e., compartment geometry, materials, ventilation, etc.) subjected to a possible fire scenario defined based on the Eurocode 1 guidelines (CEN 2002). The initial fire curve is the Heat Release Rate (HRR) as function of time which, as shown in Fig. 1, can be divided into three phases: growth, fully developed and decay. This function can be specified as a "t-squared" fire function in CFAST. Standard values for the parameters of the HRR function are provided in Appendix E of Eurocode 1 and summarized in Table I. As also shown in Fig. 1, the HRR curve is modified for ventilation-controlled fires. CFAST handles this effect during the fire simulation.

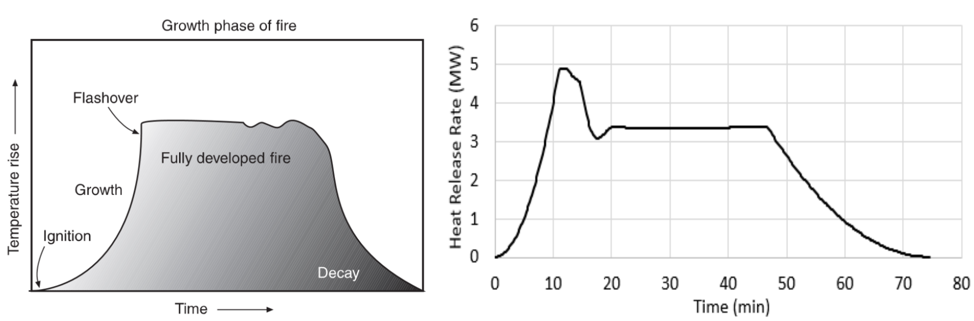

(a) (b)

Figure 1. a) Design fire curve (Hurley and Bukowski 2008), b) HRR curve obtained through CFAST simulation of a ventilation-controlled fire

TABLE I. STANDARD HEAT RELEASE CURVE PARAMETERS (Adapted from CEN 2002)

Occupancy	Fire load density [MJ/ m^2]	Time [s] to reach 1MW	Max. heat flux [kW/m^2]
Dwelling	780	300	250
Hospital (room)	230	300	250
Hotel (room)	310	300	250
Library	1,500	150	500
Office	420	300	250
Classroom of a school	285	300	250
Shopping center	600	150	250
Theater	300	150	500
Transport (public space)	100	600	250

Once the initial CFAST model is complete, the specialized Java tool is used to start several CFAST analyses on different variations of the initial model by updating some of the input parameters in a given range. These parameters may be part of the fire scenario, the openings within the building or to the exterior, and the fire protection systems. The output of each CFAST analysis consists in temperature fields recorded through the fire duration and stored to be used in the subsequent structural analysis or performance criteria checks.

Structural Evaluation

This section of the analysis tool is developed to post-process on the results from various CFAST analyses. These results include the time-histories and peak values of the temperature in all of the main structural members. These temperatures are extracted from CFAST using its "target" feature. Targets are location holders that are defined in various points of the CFAST model to track temperature variations during the fire simulation. Each target can be defined with a specific material and thickness.

The post-processing takes the temperature output for structural elements and evaluates the buildings structural integrity by accounting for the changes in material properties at high temperature levels. This process can be performed in detail by feeding the data to a general structural analysis software, an approach that is being developed for future works of the authors and is out of scope of the current paper. Instead, a set of simplified structural evaluation criteria was directly implemented in the specialized Java code.

One of the simplest approaches that can be used for evaluation of structural performance under fire is checking the maximum recorded temperature values for different structural components against certain predetermined limits (i.e., critical temperatures). These limits usually refer to a state where the integrity of the fully loaded member becomes questionable. The two sets of critical temperatures for steel members used in this study are presented below.

The first set is adopted from ASTM E119 (ASTM 2000) standard, which defines the critical temperature as an approximate limit where steel has lost 50% of its yield stress. These limits are predetermined separately for different member types (e.g. beams, columns, bar joists or reinforcing steel). NIST Technical Note 1681 titled (2010): "Best Practice Guidelines for Structural Fire Resistance Design of Concrete and Steel Buildings" also provides critical temperatures for steel members that are categorized in more detail compared to the ASTM E119 table.

TABLE II. CRITICAL TEMPERATURES FOR STEEL MEMBERS (Adapted from NIST 2010)

Description		**Critical temp. [°C] at load ratios:**					
		0.7	0.6	0.5	0.4	0.3	0.2
Braced member in compression	Slenderness ratio < 70	510	540	580	615	655	710
	Slenderness ratio < 180	460	510	545	590	635	635
Member in bending supporting concrete or composite deck floor	Unprotected	590	620	650	680	725	780
	Protected	540	585	625	655	700	745
Member in bending not supporting concrete or composite floor	Unprotected	520	555	585	620	660	745
	Protected	460	510	545	590	635	690
Member in tension		460	510	545	590	635	690

As shown in Table II, the NIST report, mainly based on works of Lawson and Newman (1990), provides additional description of loading conditions and different critical limits for members with different load ratios. The load ratio represents the level of existing load compared to the capacity of the member at room temperature.

CASE STUDY: RESIDENTIAL BUILDING

Example Building

The selected case study is a residential building with a simple floor plan and framing as shown in Fig. 2. The (10m x 10m) plan consists of four compartments (i.e., living room, kitchen, bedroom and the hall) that are all 3m high. There are four (2m x 1m) doors in the floor. One exterior door from the hall to outside and three interior doors connecting the hall to each of the other three compartments. Four (1m x 1m) windows serve as openings from the kitchen, living room (two windows) and bedroom to outside of the building. The building can be assumed to be single- or multi-story with identical floor plan. A (4m x 2m) opening area shown in the hall serves as an open stair case if the building is assumed to have two or more stories.

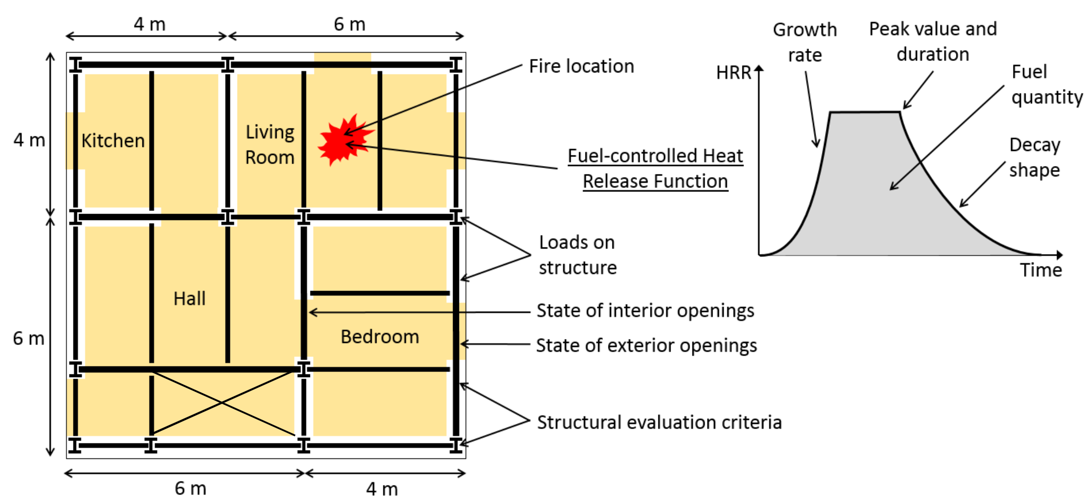

Figure 2: Case study building and parameters varied in the sensitivity study

The initial two-zone CFAST model, hereafter referred to as the "Reference model" was built in CFAST as a single story building with the plan shown in Fig. 2. All compartments were assigned a ½" gypsum material for walls and ceilings, and a 6" concrete material for the floors. The ambient temperature was set to 20 C. Thermal connections were defined between all compartments that shared a boundary wall to account for heat conduction. Several "targets" were defined in the CFAST model to record time-history of all heat transfer result parameters (e.g. temperature, heat flux) at points defined on all beams, girders and columns.

Reference Fire Scenario and Structural Evaluation Method

The reference scenario consisted of a fire starting at the center of the living room (e.g. an armchair catches fire) with all interior doors and living room windows open while the building exterior door and all other windows are closed.

The t-squared HRR curve representing the fire was established based on the Eurocode 1 assumptions (Table I above). Fire duration was determined to be 74 minutes. The Eurocode 1 equations for modifying the fire curve based on the existing openings were ignored in the process. The openings are directly defined in CFAST and the program applies corrections to the fire curve according to ventilation limits. The t-squared fire curve of the reference model after the ventilation-control corrections is shown in Fig. 1b above.

The integrity of the structure is evaluated after each analysis according to the NIST criteria for steel members. A member is assumed to have failed if the maximum average temperature it experiences during the fire exceeds the critical value listed in Table II. The load ratio at ambient temperature is assumed to be 40% throughout the structure.

The developed computational tool was used to generate several additional CFAST models by varying certain selected parameters that can affect the fire scenario and structure's performance during fire. The parameters that were varied in the sensitivity analysis are shown in Fig. 2, and sample results are presented below.

Study 1: Effect of Fire Scenario

Different scenarios were simulated by assuming the fire started in different compartments of the example building. The properties of the HRR curve representing the fire were adjusted based on the properties of each compartment.

Sample results are shown in Fig. 3. On each floor plan, the color scale represents the peak temperature reached on the wall surface of each compartment, and the structural members that have failed are highlighted in red. We observe that a kitchen fire is expected to have a less severe impact on the structure because the room has a single window, or that the inner columns are relatively protected as long as the fire remains confined to a single compartment.

Study 2: Effect of Fire Load and Ventilation

The amount a fuel available in the living room and the state of the doors and windows throughout the building were varied, and sample results are shown in Fig. 4. From Fig. 3.a, 4.b and 4.c, we observe that having the interior door to the fire compartment opened can increase or decrease the peak temperature in that compartment depending on whether the other compartments are opened to the exterior. As shown in Fig. 5, the structural assessment is more sensitive to increasing ventilation than fuel for the scenario considered.

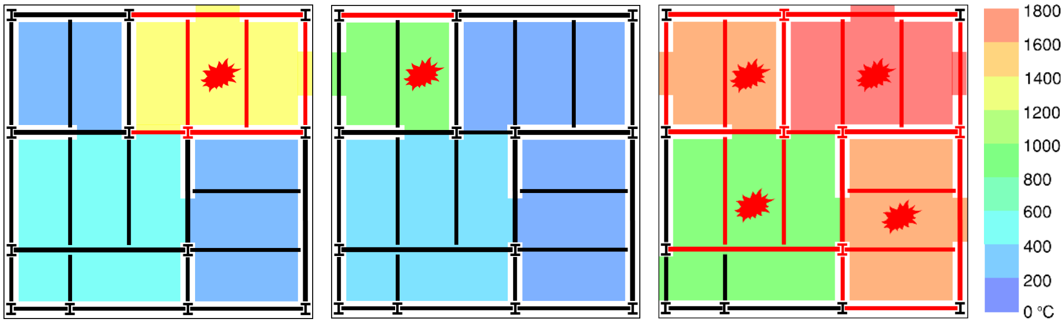

(a) (b) (c)

Figure 3. Room temperatures and member failures for different fire scenarios:
a) Fire in living room (reference), b) Fire in kitchen, and c) Fire in all compartments

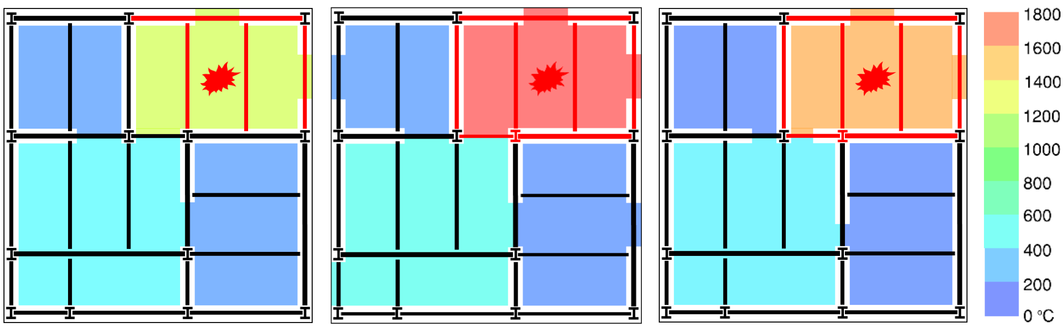

(a) (b) (c)

Figure 4. Room temperatures and member failures for variants of the reference fire scenario:
a) Fire load decreased 30%, b) Windows opened in other rooms, c) Interior doors 50% closed

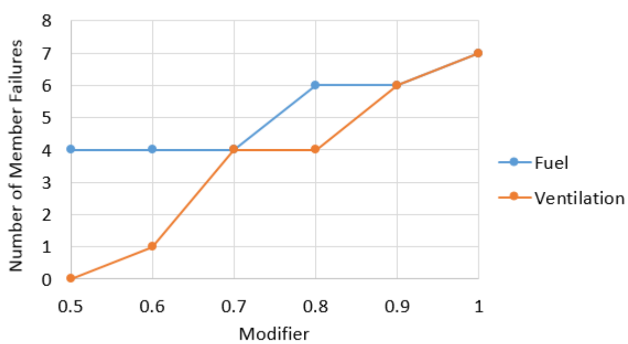

Figure 5 - Sensitivity of structural assessment to fuel and ventilation in fire compartment

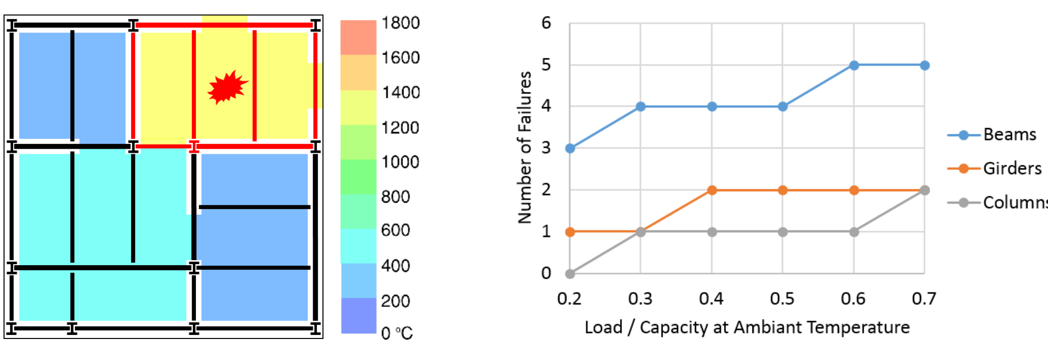

(a) (b)

Figure 6. a) ASTM structural assessment of reference fire scenario
b) structural assessment summary for different loading ratios

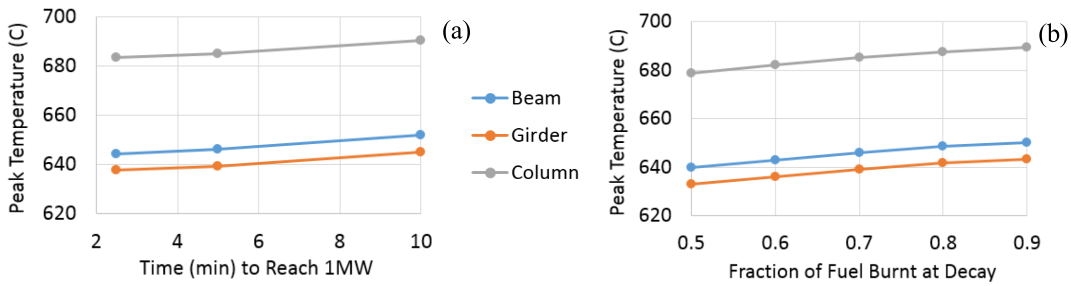

Figure 7: Sensitivity of member temperature to a) fire growth rate, and b) fire decay rate

Study 3: Effect of Structural Analysis Parameters

The reference structural assessment was based on the NIST criteria, with the assumption that the structure was loaded to 40% of its capacity. Fig. 6 shows that an additional member failure is predicted when the ASTM criteria is used instead, and how the number of member failures increases with the load ratio assumed.

Study 4: Effect of Fire Growth and Decay Rates

The growth and decay rates of the fire are controlled by the time to reach a HRR of 1MW and the fraction of fuel that has burnt when decay starts, with reference values of 5 min and 0.7 respectively. Both parameters were varied, and as shown in Fig. 6 their effect on the peak temperature of the structural members was minor.

SUMMARY AND FUTURE WORK

A computational tool was developed to automate the steps of PBFE in order to quantify the sensitivity of the PBFE outcome to its multiple parameters. Preliminary results confirm the relevance of this study, which will continue in two steps. First, the structural assessment will be refined by including finite element analysis and methods to combine the results of several fire simulations into a probabilistic risk assessment. Then the improved tool will be used to study the sensitivity of this risk assessment to the parameters of the PBFE method applied to buildings of various structural systems.

REFERENCES

Meacham, B.J., Custer, R.L.P. (1995). "Performance-Based Fire Safety Engineering: An Introduction of Basic Concepts", Journal of Fire Protection Engineering, Vol. 7, No. 2, pp 35-54.

NIST (2010). “Technical Note 1681: Best Practice Guidelines for Structural Fire Resistance Design of Concrete and Steel Buildings.”, 199p.

CEN (Comité Européen de Normalisation). (2002). Eurocode 1: Actions on Structures – Part 1-2: General Actions – Actions on Structures Exposed to Fire, Brussels, Belgium.

NIST (2015). Technical note 1889 v2: “CFAST – Consolidated Model of Fire Growth and Smoke Transport (Version 7)”, Volume 2: User’s Guide.

Hurley, M.J, Bukowsky, M.W. (2008). “Fire Hazard Analysis Techniques”, Fire Protection Handbook, Volume 2, Section 3.7, National Fire Protection Association.

ASTM (2000), “E119-12: Standard Test Methods for Fire Tests of Building Construction and Materials”, American Society for Testing and Materials, West Conshohocken, PA.

Lawson, R.M., and G.M. Newman (1990), “Fire Resistant Design of Steel Structures - A Handbook to BS5950: Part 8”, SCI Publication 080, U.K.: The Steel Construction Institute.

Shear Breaking of Columns Subjected to Localized Fire

OLIVIER BURNIER

SUMMARY

Resistance to fire of concrete structures is specified with prescriptive rules such as minimal dimensions and concrete cover in Switzerland, in accordance with SIA 262:2003 [1] or Eurocode EN 1992-1 - 2: 2004 [2] standards.

Following a fire in an underground car park, a column underwent a shear force breaking, even though it had the dimensions and concrete cover specified in SIA 262:2003 standard [1] for R60 resistance required by the Association of Public Insurance Companies (APIB) [3] in Switzerland for this type of structure.

After this unusual breaking, that resembles a "short column failure", research was carried out to understand the causes that have led to this situation and develop a calculation method to check resistance of shear force of columns subject to a localized fire.

INTRODUCTION

On the night of 8-9 December 2010, around 2:30 am, a fire involving two cars broke out on the 1st basement of the underground parking of the Ivory Tower in Montreux (CH). This emblematic building of "The Swiss Riviera" with its height of 76 m, is the center of a complex of building with more than 200 apartments. The underground parking is not directly located under the Tower, but surrounds it and links the other apartment buildings located in the periphery.

After bringing the fire under control at around 3:40 am, firefighters noticed that the reinforced concrete structure had been severely damaged. The reinforced concrete ribs slab with a range of 12 m was in relatively good condition despite a few occasional fragments. On the other hand, a large crack was visible on a column located approximately 10 m from the middle of the area of fire.

After this singular breaking, research was undertaken to understand the mechanism that lead to this collapse, by reconstructing the fire's progression. In a second step, a finite element calculation model was created to determine efforts induced by the fire in the structure and to analyses the reasons for this failure.

Olivier Burnier, Civil Engineer HES-UTS, CAS in fire protection. Head of engineering, Etablissement Cantonal d'Assurance Vaud - Switzerland

RECONSTRUCTION OF THE BLAZE

The blaze occurred in the 1st basement of the car park (figure 1) and completely destroyed the two vehicles.

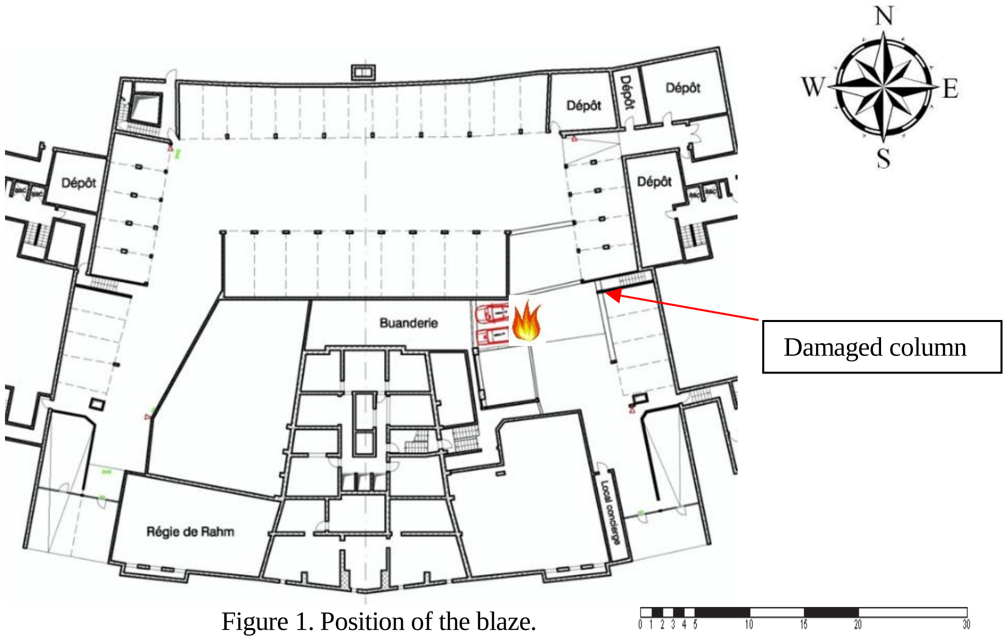

Figure 1. Position of the blaze.

At the sight of the white color of the concrete vertical of the fire, it can be estimated that a temperatures between 600 °C and 900 °C have been reached [4] (figure 2). The column located approximately 10 m from the center of the fire presents a significant crack of shear force. We note the presence on the right of the column of a parapet in reinforced concrete of 1.00 m in height (figure 3).

Figure 2. View of the rib slab.

Figure 3. Column with shear crack.

Hypothesis for the reconstruction

This study will focus on the reconstruction of the blaze, based on the hypothesis that a fire that started in the No. 1 vehicle which has spread to the No. 2 vehicle.

The duration of the fire was about 60 minutes. This data is based on the fact that the peak of HRR (Heat Release Rate) is fixed at 2h50 am, when the Chief of the firefighters heard crackling in the parking during his reconnaissance. The exact timing of this peak power is marred by an uncertainty of ± 10 minutes.

To be able to recreate the fire in the CFD model we have set the course of the various actions (TABLE I) based on the firefighters report and narrative of the witness who gave the alert.

TABLE I. Course of the actions.

Time (hour/minute)	Actions
2 h 15	Beginning of the fire in the n°1 vehicle.
2 h 27	Propagation of the fire to the n° 2 vehicle.
2 h 37	Opening of the parking door on the West side of the building.
2 h 50	Peak of Heat Release Rate.
3 h 15	Firefighters are at the fire.

MODELING WITH NIST FIRE DYNAMIC SIMULATOR

NIST Fire Dynamic Simulation (FDS) is a "Computational Fluid Dynamics" (CFD) model to simulate fluid flows under the laws of Navier-Stockes and analyze blazes [6]. Version 5.5.3 of FDS with the PyroSim 2010 software [7] has been used for the introduction of the data. In order to view the results, "Smokeview», version 5.6 software, has been used [8].

Data for calculating with FDS

The geometry of the car park was modelled in the most accurate way possible, especially in regards to the source of the fire. The influence of the wind has been disregarded in the light of the available weather data for this night.

Subsequent openings that have an essential influence were modelled:

Ramps for access to the lower level, were considered as external openings in the light of the large volume of the two lower floors and the presence of basement windows which allowed supplies of fresh air to those floors.

An opening was modelled on the bottom of the two car park spaces to simulate the laundries ventilation duct. Indeed, even if the ventilation was not working, smoke passed through this duct, as demonstrated by the damage caused by soot in laundries.

The screened opening with a section of 0.45 x 1.00 m, located above the door of access to the second level of the car park, on the East side, has also been modelled.

The front door situated on the West side was modelled as an opening from a time t = 1'320 seconds, to match with the action of the witness who gave the alert.

Fire ignition

The source of inflammation is one of the two vehicles, without being able to determine which caught fire first.

For this simulation, two sources of fire with a surface of 7.0 m² each were modeled. The HRR power for fire is based on sizing curves described in report EUR 18867 [5] for class 3 cars. According to the tests, these curves allowed in Europe for the sizing of fires in car parks cover a wide variety of vehicles. These curves are those proposed for the CFD models, with a level of power at 5.5 MW during 3 minutes (Figure 4). Indeed the CFD models do not properly support the peak to 8.3 MW of the original curve. [9]. A timing of 12 minutes is allowed between the two inflammations, according to tests carried out by the CTICM [5].

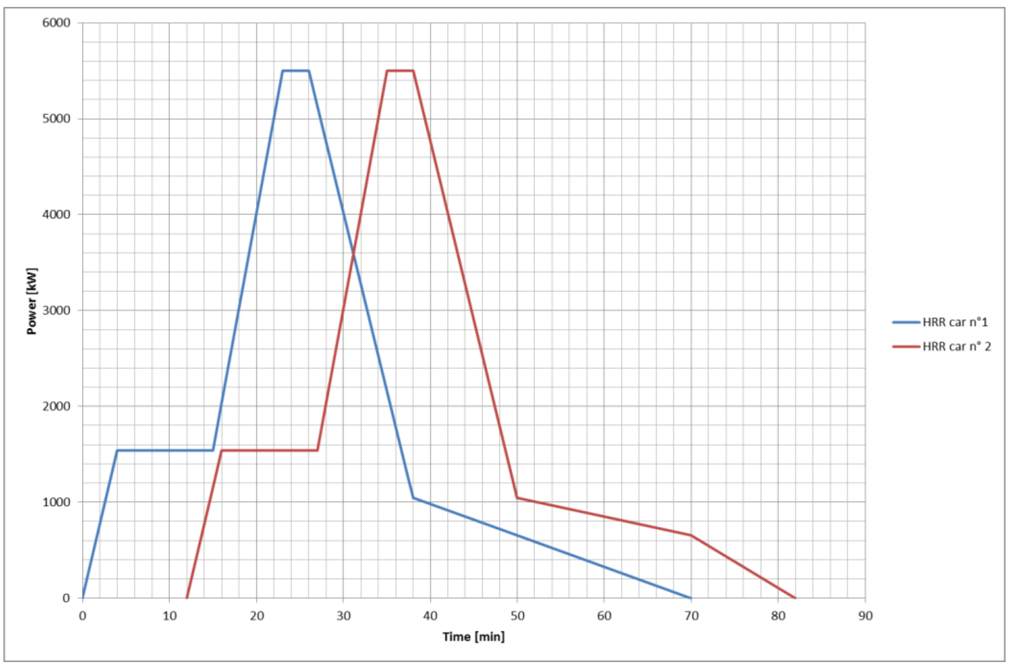

Figure 4. HRR curves.

Results

For measuring temperatures on the bottom of the slab and near the column, virtual thermocouples were placed in the model. THCP 02, 03, 06 and 07 are located above the cars while THCP 05 is located near the top of the column (figure 6). Cuts at different locations were made to check that the progress of the fire corresponded to the findings made on the spot. Modeled smoke-free layers with FDS were compared in several places with traces of soot found on-site, allowing to confirm the validity of the model.

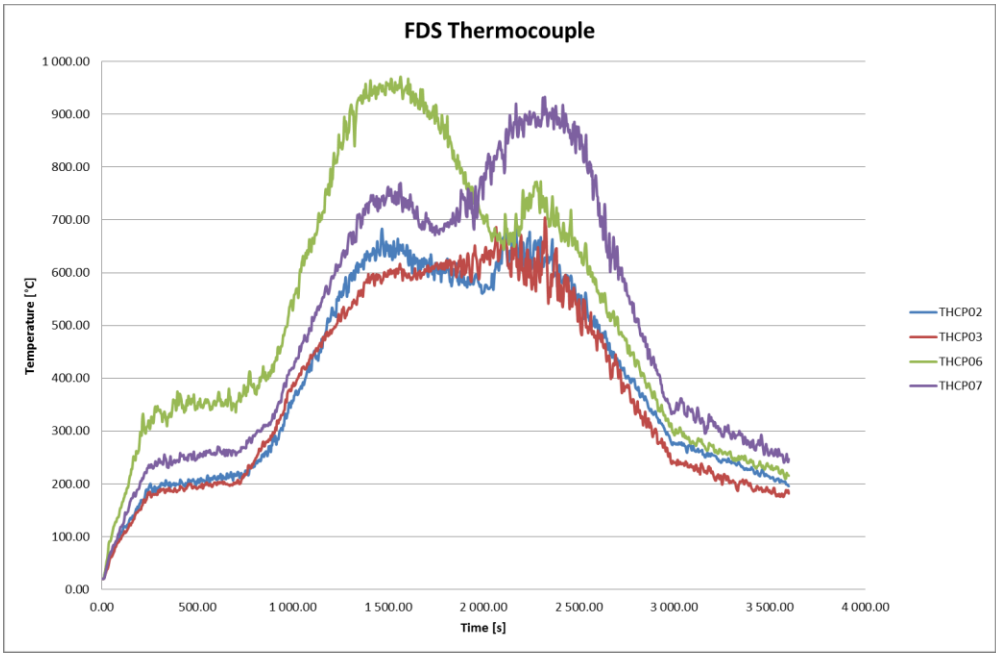

Figure 6. Results of virtual thermocouples located under the slab.

It should be noted that the ceiling temperatures had surpassed the 900 °C which corresponds to the in situ observations. However the temperature near the column was at a maximum of 410 °C.

Comparison between FDS and HASEMI

A comparison with the model of Hasemi for localized fire was also made, with the program "Car Park Fire version 2.1" [10]. The correlation of the results is good (figure 7) especially if we take an average between the thermocouples located at the front and the rear of the car.

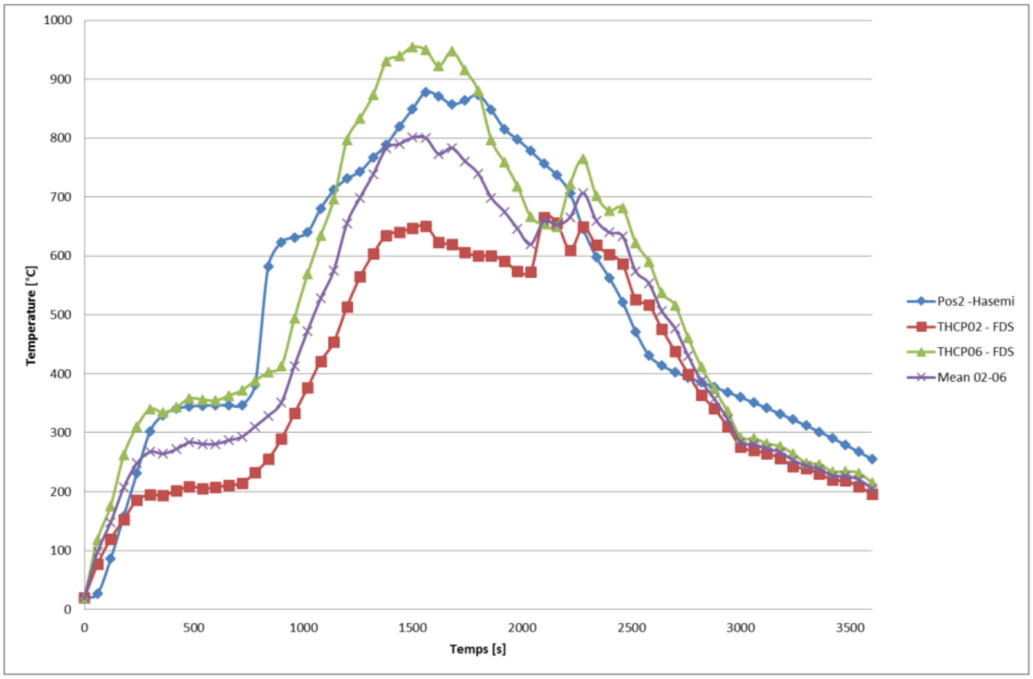

Figure 6. Comparison between FDS thermocouples and Hasemi model.

SIMULATION OF THE COLLAPSE OF THE COLUMN

To better understand what occurred that night, and in particular the collapse of the column by shear force, a model of the concerned grid of beams using the software Safir [11] was made, with conditions of support as close as possible to reality.

To perform this analysis, geometric data from the grid of beams were introduced in the model «Structural_3D» of Safir (figure 7), taking into account for each section their thermal response calculated with the model "Thermal_2D", with temperatures previously obtained from the FDS calculation curves.

The column was subjected to the temperature curve away from the center of the fire (THCP05) on the entire perimeter of the section- Lateral support of the wall has been activated or not, so as to have the two values of the shear force.

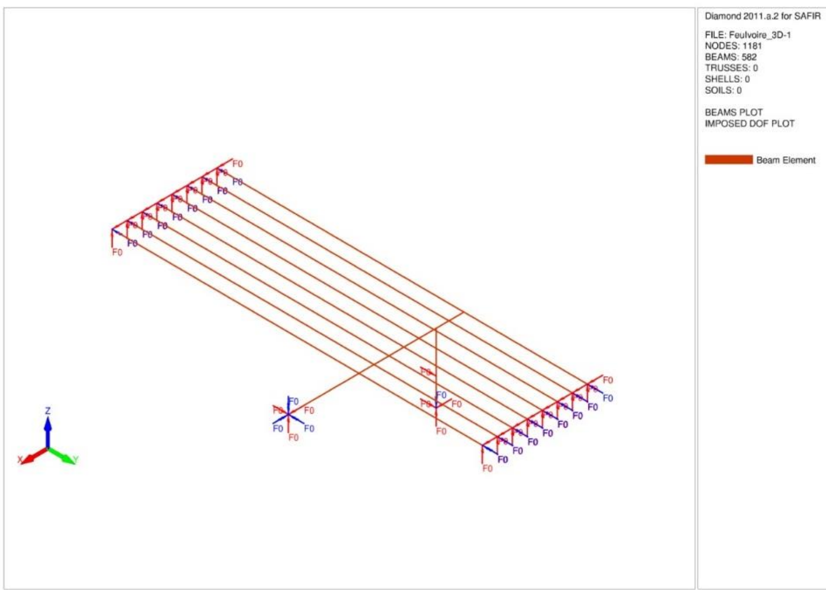

Figure 7. Static system.

To determine the moment of the collapse, the evolution of the shear force $V_{d,z}$, in the bar element of the column located at the right of the parapet was observed. Indeed, even if Safir does not directly determine the collapse by shear force, the observation of the evolution of it, inside the column, shows a significant increase. It is influenced by the deformation of T-beams, which under the effect of heat generated an additional bending moment at the top of the column.

To calculate this value, the research "breaking by shear forces of prestressed beams subjected to fire" [12] was mainly used. For calculating the value of the resistance of shear force V_{Rd}, the 6.2 and 6.8 formulas from the EN 1991-1-1 standard [13] was used. The 6.2 formula was used to calculate the resistance to shear of concrete, taking into account the force of compression N_{Ed}.

$$V_{Rd,c} = [C_{rd,c} \cdot k(100\rho_l f_{ck})^{\frac{1}{3}} + k_1\sigma_{cp}]b_w d$$

The value σ_{cp} is limited in the EN standard to a maximum of $0.2 \cdot f_{cd}$. If this limitation has a meaning in the case of calculation the resistance to shear force on a slab, it is however not realistic in the case of a column subjected to a normal compression force. The maximum value of σ_{cp} has therefore been taken equal to f_{ck}. We also took account of the reduction of the f_{ck} value due to the temperature.

To take into account horizontal Stirrups (10 mm, s = 150) existing in the column, we calculated the $V_{Rd,s}$ effort, with the 6.8 formula [13].

$$V_{Rd,s} = \frac{A_{sw}}{s} \cdot z \cdot f_{ywd} \cdot cot\theta$$

In this case, as the temperature of the reinforcement inside the column did not exceed 100 °C at the moment of breaking, the f_{ywd} value has therefore not been reduced.

These two values were then summed, in order to have resistance to shear force V_{rd} in this section, that we compared to the shear force V_d, obtained by the calculation with Safir. In order to verify the following relationship:

$$V_d \leq V_{Rd}$$

As soon as the value of effort exceeds the resistance, it can be concluded that the ruin of the column is caused by shear force (figure8).

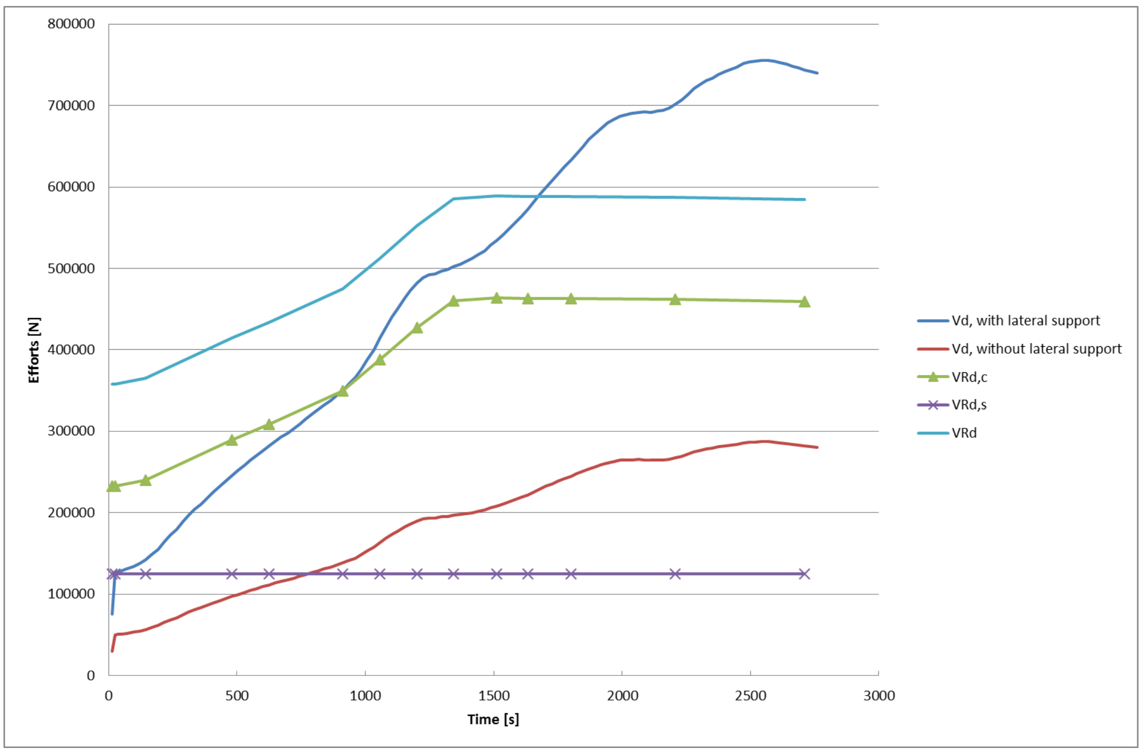

Figure 8. Variation of $V_{d,z}$ effort in column.

Following this result, columns with the minimum size recommended by the EN 1992-1-2 standard [2] have been verified with this method. The results are substantially equivalent in this situation. The collapse of the columns happens each time.

As shown in figure 8, the value of V_{Ed}, exceeds the value of V_{Rd} only where there is a lateral support on the column. Without this support the collapse does not intervene. Thus confirming that we are dealing with a breaking of "short column" type.

CONCLUSION

This study of a real case of fire, demonstrates that despite a reinforced concrete column having been correctly dimensioned with the minimal values for section and concrete cover prescribed in SIA 262 [1] or Eurocode 1992-1-2 [2], a brittle fracture by shear force may occur even though the column is far from the center of the fire. This phenomenon is due to the increase of the bending moment at the top of columns following the expansion of the slab. It is particularly sensitive in the case of short columns while it does not occur in cases where the lateral movement of the column is not impaired

By comparing the model according to Hasemi with a reconstruction of a real case with a CFD model, a simplified model is well suited for design temperatures in this type of structure with a height between 2.00 and 3.00 m. In adapting the formula for the resistance to shear force in a slab from the Eurocode 1992-1-1 [13] to a column, a method was developed to check if such columns are susceptible to ruin in the event of fire.

REFERENCES

1. Swiss Society of Engineers and Architects " SIA 262:2003 standard, Construction in concrete".
2. European Committee of Standardization "Eurocode EN 1992-1-2, Actions on structures – Part 1-2 General actions – Actions on structure exposed to fire".
3. Association of Public Insurance Companies (APIB)" Fire Protection Directive, 14-03, structural systems".
4. Denoël, J-F. 2007. "Sécurité incendie et construction en béton". Febelcem, p. 79.
5. CTICM 2011. "Demonstration of real fire tests in car parks and high buildings.
6. NIST 2004. "Cook County Administration Building Fire, Chicago".
7. Tunderhead 2010. "PyroSim User manual".
8. NIST 2007. "Users' Guide for Smokeview Version 5".
9. Franssen, J-M 1997. "Contribution à la modélisation des incendies dans les bâtiments, chapitre 16".
10. DIFISEK 2011. "Dissemination of Fire Safety Engineering Knowledge".
11. Franssen, J-M 2011. "User's manual for Safir 2011".
12. Franssen, J-M 1997. "Design and Tests of Prestressed Concrete Beams".
13. European Committee of Standardization "Eurocode EN 1992-1-1, Design of concrete structures– Part 1-1 General rules and rules for buildings".

Conversion of Visual Post Fire Measurements into Fire Severity with the Aid of Thermo-Plastic Analysis for Retrofitting

TOM MOLKENS, THOMAS GERNAY and RUBEN VAN COILE

ABSTRACT

At Koksijde in Belgium a severe fire took place in an apartment building in 2015, resulting in the death of a young man and visible structural damage to four balconies. Following the fire, experts were mandated to assess the damage and the need for structural repair. They estimated that the balconies had to be refurbished but that there were no other structural elements affected, in particular the slab inside the apartment could be left in place with only a surface treatment and new plaster finishing. However, the floor slab in the apartment located above the fire apartment exhibited several visual indications that the fire could have had a structural impact, such as residual deformations and cracks in the tiles. This paper presents a methodology to infer the fire severity based on post-fire measurements and non-linear thermo-plastic numerical simulations. Finally, knowing the fire severity, its effect on the structure is evaluated and a reliability-based assessment is made of the residual load bearing capacity of the slab.

CONTEXT OF THE FIRE EVENT

The fire took place at the 3rd floor in an apartment building built in the 1970's at Koksijde (Belgium), see Figure 1.

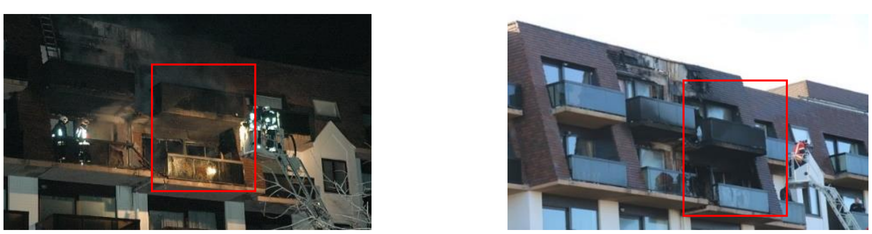

Figure 1. The façade and balconies affected by the fire are framed by the box.

Tom Molkens, StuBeCo bvba, Hoevenstraat 155, 3900 Overpelt, Belgium.
Thomas Gernay, University of Liège, allée de la Découverte 9, 4000 Liège, Belgium.
Ruben Van Coile, Ghent University, Department of Structural Engineering, Technologiepark 904, 9052 Zwijnaarde, Belgium.

A detailed register could be obtained from the fire brigade giving the time delays between the different events. The time between the announcement to the fire brigade and the start of firefighting is about 14 minutes. This value has to be extended with the time between fire ignition, discovering, call to the emergency number, and from the dispatching to the fire brigade. Hence total time is estimated between 20 and 45 minutes.

Geometry of Apartment

A staircase services 3 apartments at each level, two of them are from front to back with 3 sleeping rooms, and one in between these two. The lay-out is identical at each level. Balconies are working in cantilever. Except for a small extract of an original architectural drawing, there was no information available about the structure.

Post-Fire Measurements on Site

Due to a judicial procedure, access to the apartment where the fire took place was not allowed. Furthermore, possibly valuable information stays secret till the end of this procedure (which is still going on). Therefore, we have to focus on post-fire observations and measurements taken from the apartment located above the event.

The wake-up call for the owner from above were cracks which appeared in the finishing tiles in the kitchen after the fire, see the dotted line and detail of the cracks in Figure 2. With an optical instrument, cracks on the slab top surface were measured as between about 0.2-0.3 mm. The tiles were no longer fixed to the underlying layer (hollow sound) and some slight level differences could be observed.

It was also observed that the floor was not horizontal any more, i.e. it exhibited a residual deflection. Using a laser equipment, levels were measured on the spots marked in Figure 2. Assuming that the surface was originally horizontal, the deformations of Table I can be found. The residual vertical deformation was at maximum 11.5 mm.

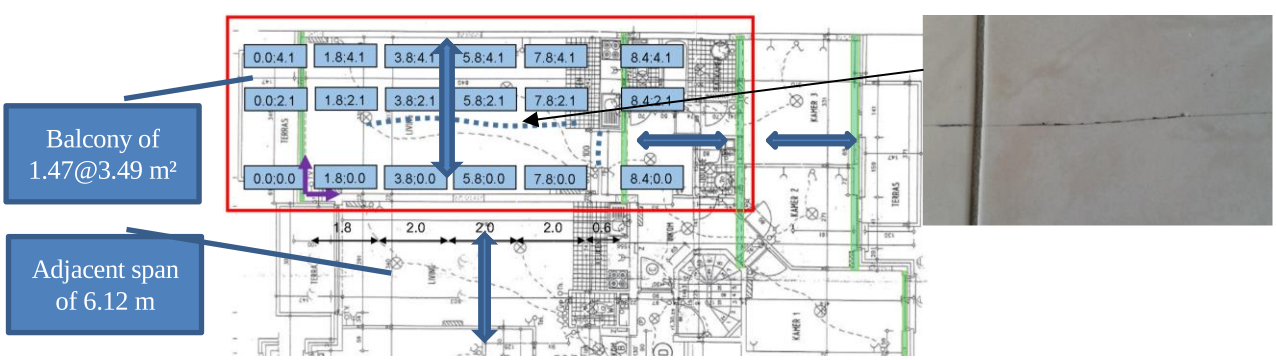

Figure 2. Apartment lay-out, length front room 8.40 m x 4.40 m x 2.42 m + bearing direction.

TABLE I. MEASURED DEFORMATIONS IN M, ORIGIN INDICATED IN FIGURE 2.

Distance in m	0	1.8	3.8	5.8	7.8	8.4
4.1	0.0000	0.0000	0.0000	0.0000	0.0000	0.0000
2.1	-0.0050	-0.0090	-0.0090	-0.0115	-0.0050	-0.0040
0.1	0.0000	0.0000	0.0000	0.0000	0.0000	0.0000

THERMAL DESCRIPTION OF THE FIRE LOAD

Considering the limited information available about the fire, and the features of the compartment where the fire took place, the preferred approach for estimating the fire load consists in building up a 2-zone model.

Two Zone Model

For building up the two zone model by Ozone [1] we took into account the material properties listed up in Table II and dimensions of the apartment as shown in Figure 2 (with a free height of 2.42 m). After calculating a fully developed fire (see Figure 3) we have made a tri-linear simulation of the descending branch, with changes in the cooling rates when the temperature reaches 200°C and 20°C. To simulate the intervention of the fire brigade, it is conservatively assumed that this intervention speeds up the start of the tri-linear descending curve but does not affect the slope of the fire curves (neglecting the effect of the volume of added water). As a reference the well-known ISO 834 standard fire curve has been added as well. Several scenarios are calculated with different intervention times using Eq. (1) for the cooling phase, time t in s and θ in °C.

$$\theta_{i+1} = MAX(IF(\theta_i > 200;\ \theta_i - (t_{i+1} - t_i) \cdot 0.3407;\ \theta_i - (t_{i+1} - t_i) \cdot 0.0165);20) \quad (1)$$

TABLE II. MATERIAL PROPERTIES FOR TWO ZONE MODEL.

Distance in m	Mass (kg/m³)	λ (W/mK)	c (-)	t (m)	Reference
Ceiling	2300	1.6	1000	0.15	EC 2-1-2
Wall	1600	0.7	840	0.14 & 0.19	EC 6-1-2
Glass	Stepwise variation; opening = 10%@ 20°C, 50%@200°C & 90%>400°C				
Screed	1800	1.15	1000	0.08	EC 2-1-2

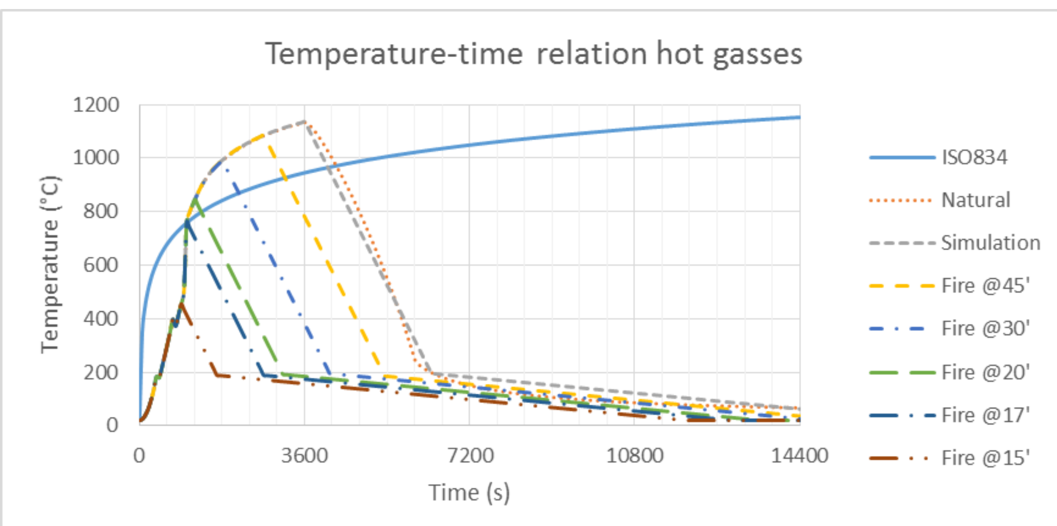

Figure 3. Gas temperature-time relationship for different fire scenarios.

Based on communication with the fire brigade it takes about 30 to 60 minutes to get a fire under control, starting from a fully developed fire. This is in full agreement with the time needed to descend the temperature from the peak value to the previous mentioned 200°C, using the cooling rate of Eq. (1). For instance, a fire that could develop during about 30-60 minutes needs about 40-45 minutes to be brought under control (to a gas temperature below 200°C). It seems that only with a very short reaction time the control time can be substantially reduced.

Localized fire

For furniture it is well known that the peak in heat release takes place always between 120 and 400 s after ignition and this effect is very limited in time. Due to the flash-over, which occurs at about 600 s, we neglected this effect.

MECHANICAL RESPONSE

The concrete slab is a continuous slab supported by load bearing walls of masonry (hollow bricks of 19 cm). Fire took place below an end span which is supported by a (double) wall of 14 cm. Loads are given in Table III. Concrete class is C30/37 and reinforcement strength f_{yk} = 500 N/mm². Using a simple Cross based design and old standards [2], a slab thickness of 150 mm could be derived and also the following main reinforcement ratio's: upper reinforcement of 598 mm²/m (reduced at 85%) above supports and 258 mm²/m for balcony; lower reinforcement of 341 mm²/m (increased proportionally) in the principal direction and 141 mm²/m in the transverse direction. Boundary conditions are simple vertical supports at the location of the joint or beams and clamping at the other supports. The area of the slab incorporated in the thermo-mechanical model is equal to the boxed area of Figure 2.

TABLE III. LOADS ACTING ON THE SLAB.

Load case	Load (kN/m²)	Reference
Mobile load class A (Ψ_{fi}=0.30)	2.00	EC 1-1-1
Partition walls < 3 kN/m	1.20	EC 1-1-1
Screed of 80 mm LC	1.50	EC 1-1-1
Dead load of 150 mm concrete	3.75	EC 1-1-1

Transient thermo-mechanical simulations are run using the software SAFIR®. A plastic-damage model is used for modeling concrete at elevated temperature [3,4]. Different fire exposures are successively considered, corresponding to the scenarios of Figure 3 (i.e. natural fires with cut off at different times). The behavior under a standardized ISO fire is also computed. The results are shown in Figure 4. The level of observed residual deflection, equal to 11.5 mm, is also represented on the graph.

The ISO fire exposure represents a situation where the temperature continuously increases in the compartment, until structural collapse of the slab. In this case, any intervention from the fire brigade is neglected.

In reality, the slab did not collapse owing to the timely intervention of the fire brigades, which resulted in a decrease in the compartment temperature. Numerical analyses for the full fire development (including the decay phase) show that, for natural fires with cut off between 20 min and 60 min, the vertical deflection of the slab increases up to a certain level, then decreases and eventually exhibits a residual value. Considering the computed results of residual deflection, it is possible to estimate the time of cut off and hence the time of fire brigades intervention as approximately 30 minutes after ignition. This estimation is reasonably in line with the registered timeline of the event.

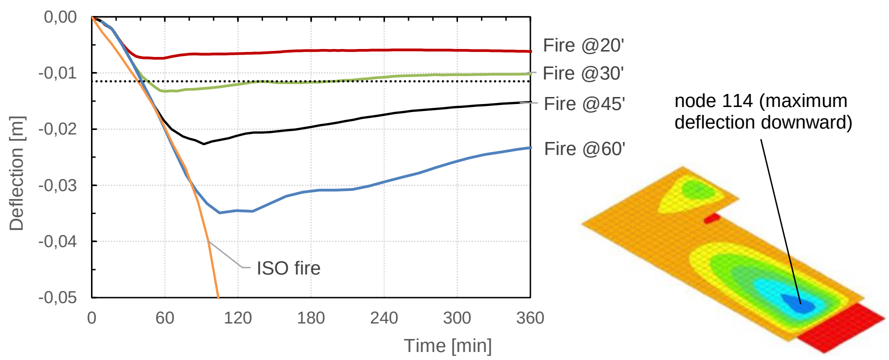

Figure 4. Evolution of vertical deflection at node 114 under different fire exposures (@20' means a cut off after 20 min).

DEFORMATIONS OVER THE SLAB WIDTH

A FEM-based model shows a maximum deflection of 2 mm after finishing and creep before the fire event took place. Residual deformations after fire are taken from the SAFIR® simulation. To explain the cracking in the tiles it is needed to look at the deformations over the width of the slab. For a fire with a cut off time of 30 minutes we have plotted the vertical deformations on a section over the width through point 114 of Figure 4. This deformation line is subsequently approximated by a circle segment with the width of the room and also once with 5/6th of this dimension to obtain a better fitting.

With the circle approximation we can easily adapt the radius of the curve to calculate the effect on top of the tiles instead of at the centerline. For the maximum deformation at 4198 s we derive a shorting of 5 mm on top of the slab, plastic deformations occur at that times and tiles will be pushed loose from the under layer. In the later stage the reversed effect takes place and we obtain 1.3 mm regained length translated in at least 3 cracks (supports and middle) of approximately 0.4 mm. Which can be compared with the measured 0.3 mm.

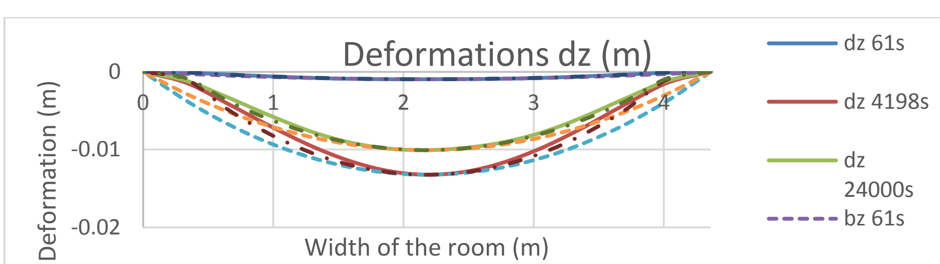

Figure 5. Deformation over the width at starting, maximum and residual deformation.

RELIABILITY OF THE RESIDUAL BEARING CAPACITY OF THE SLAB

A practical reliability based tool for the post-fire assessment of simply supported concrete beams has been presented in [5]. The method considers a general formulation of the strength limit state criterion for structural members, given by:

$$R - E = R - (G + Q) \geq 0 \qquad (2)$$

with R the (lognormal) strength of the structural element (including all model uncertainties), E the load effect, G the (normal) permanent load effect, and Q the (Gumbel) imposed load effect.

Considering a permanent load effect which can be accurately determined as it is mainly made up of self-weight of the structure and finishing's, the method evaluates the maximum allowable characteristic value $Q_{k,max}$ of the imposed load which corresponds with a reliability index (safety level) β of 3.8, which is the target safety level for the design of new structures in accordance with EN 1990 (50 year reference period) [6]. If $Q_{k,max}$ is larger than the value of Q_k required for continued use, the structure is deemed safe for continued use in accordance with the reliability target of the Eurocodes (ULS).

The evaluation is done by using a pre-calculated diagram, called 'Assessment Interaction Diagram' (AID), as given below in Figure 6. The AID is generally applicable to any type of member and presents pre-calculated curves which correspond with β = 3.8 for different load ratios χ, defined by (subscript $_k$ = characteristic value):

$$\chi = Q_k / (Q_k + G_k) \qquad (3)$$

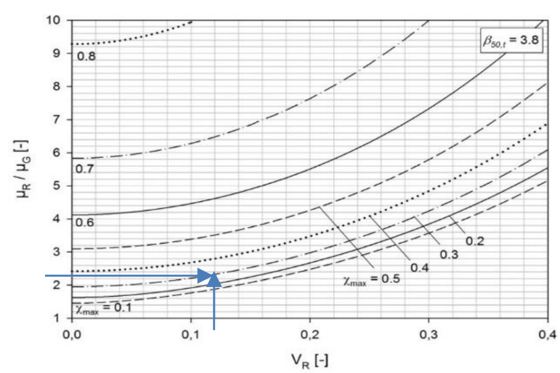

Figure 6. Assessment Interaction Diagram for a reliability index β = 3.8 (50 year reference period).

By evaluating the coefficient of variation V_R and the expected (mean) value μ_R of the resistance effect R, and calculating the ratio of μ_R to $\mu_G = G_k$, a point on the AID is found and the associated maximum allowable load ratio χ_{max} can be read from the diagram (or determined through interpolation). Knowing χ_{max} and G_k, the maximum allowable characteristic value of the imposed load $Q_{k,max}$ is directly defined.

The evaluation of V_R and μ_R can be done through any method. In [5] an analytical model has been used. Here this methodology is extended for continuous concrete slabs. The evaluation of the residual bearing capacity of such a continuous slab is done considering the simple rules out of EC 2-1-2 informative annex I. Based on this concept the span and support capacities should together provide sufficient capacity to fulfil the requirements of static equilibrium, i.e.:

$$\frac{M_{R,support1}+M_{R,support2}}{2}+M_{R,span}\geq\frac{(g+q)l^2}{8} \qquad (4)$$

where $M_{R,support}$ is the (positive) support hogging moment capacity, $M_{R,span}$ is the (positive) field moment capacity, g and q are distributed permanent and imposed load, and l is the span length. Note that in the reliability evaluation model uncertainties are considered as well, as discussed in [5]. As the fire took place underneath the end span of the continuous slab, the assessment is done for this end span with $M_{R,support2} = 0$.

The residual load bearing will be assessed through a simple analytical formula, using a post-fire methodology based on the 500°C method [7], with $k_{fy,res}$ a reduction factor for the residual yield stress as a function of the maximum temperature reached by the reinforcement. The mid span total residual load bearing capacity is given by:

$$M_{R,res} = \cdot A_{si}k_{fy,res}f_{y,20}\left(\left(h-c-\frac{\emptyset}{2}\right)-0.5\frac{A_{si}k_{fy,res}f_{y,20}}{bf_{c,20}}\right) + 1/2\cdot$$
$$A_{ss}f_{y,20}\left(\left(h-c-\frac{\emptyset}{2}-i_{\theta}\right)-0.5\frac{A_{ss}f_{y,20}}{bf_{c,20}}\right) \qquad (5)$$

with parameters as defined in Table IV. A number of uncertainties are associated with the parameters in (5), as is the case for normal design conditions. These uncertain variables are given in Table IV, together with their mean value and standard deviation, literature references are given in [5].

Consequently, the maximum reinforcement temperature and associated factor $k_{fy,res}$ are defined through the nominal reinforcement position. This assumption is robust as for the specific case under investigation the maximum attained reinforcement temperatures remain below 300°C. On the other hand we didn't apply the 0.85 reduction factor for the mechanical analysis because this results in a more conservative result (due to 500°C isotherm).

TABLE IV. STOCHASTIC VARIABLES CONSIDERED FOR THE EVALUATION OF (5).

Variable	**Mean value**	**Standard deviation**
Field bottom reinforcement area A_{si} [mm^2]	223	4.5
Residual steel yield stress reduction factor $k_{fy,res}$ [-]	1.00	0.08
20°C reinforcement yield stress $f_{y,20}$ [MPa]	581	41
Slab thickness h [mm]	150	5
Reinforcement axis position to surface c+Ø/2 [mm]	25	5
Depth of the 500°C isotherm i_{500} [mm]	14.5	-
20°C concrete compressive strength $f_{c,20}$ [MPa]	42.9	6.4
Support top reinforcement area A_{ss} [mm^2]	692	13.8
Total model uncertainty K_T [-]	1.06	0.07
Span length l [m]	4.44	-

For using the AID of Figure 6, $R = K_T \cdot M_{R,res}$. The mean value μ_R and coefficient of variation V_R can be evaluated by any probabilistic method (for example Monte Carlo simulations), but as in [7] Taylor approximations allow to make a very quick analytical assessment based on equation (5). With $\bar{\mu}$ the vector with the mean values for all stochastic variables, X_i indicating any one of the stochastic variables, σ the standard deviation, and $\partial/\partial X_i$ the partial derivative to the variable X_i, a first order Taylor approximation is given by:

$$\mu_R \approx R(\bar{\mu}) = \mu_{KT} [\cdot\, \mu_{Asi}\mu_{kfy,res}\mu_{fy,20}\left(\left(\mu_h - \mu_c - \frac{\mu_\emptyset}{2}\right) - 0.5\,\frac{\mu_{Asi}\mu_{fy,res}\mu_{fy,20}}{\mu_b\mu_{fc,20}}\right) +$$

$$1/2\cdot\mu_{Ass}\mu_{fy,20}\left(\left(\mu_h - \mu_c - \frac{\mu_\emptyset}{2} - \mu_{i\theta}\right) - 0.5\,\frac{\mu_{Ass}\mu_{fy,20}}{\mu_b\mu_{fc,20}}\right)] \qquad (6)$$

$$\sigma_R \approx \sqrt{\sum_{X_i}\left(\frac{\partial R(\bar{\mu})}{\partial X_i}\right)^2 \sigma_{X_i}^2} \qquad \& \qquad V_R = \frac{\sigma_R}{\mu_R} \qquad (7)\ \&\ (8)$$

Evaluating the equations is straightforward using a hand calculator or spreadsheet. Considering the variables given in Table IV, μ_R = 28.3 kNm and V_R = 0.118. Furthermore, g_k is assessed as 5 kN/m^2, giving μ_G = 12.3 kNm. Applying these values in the AID of Figure 6, a maximum allowable load ratio χ_{max} of 0.3 is obtained, resulting in a maximum allowable characteristic value $q_{k,max}$ for the imposed load of 2.14 kN/m^2. This value is more than the 2.00 kN/m² needed for dwellings.

CONCLUSIONS

Based on limited post-fire observations and measurements, which can be done with a minimum of efforts, a method is presented to evaluate the fire load and temperature evolution during a real fire event. This was worked out by transferring results of a two zone fire model into a thermo-mechanical model. Calibration was done by evaluating deformations and crack width and comparing with on-site measurements. The presented method can be useful for post-fire inspection and retrofit of structures.

A simplified reliability based assessment method shows that the post-fire ultimate limit state reliability of the slab is adequate for continued use. Note that this analysis is purely a safety analysis for load bearing capacity and does not incorporate possible serviceability issues as post-fire cracks, displacements and durability issues.

REFERENCES

1. Cadorin J.-F. & Franssen J.-M., "A tool to design steel elements submitted to compartment fires OZone V2. Part 1: pre- and post-flashover compartment fire model", *Fire Safety Journal, Elsevier*, 38 (2003), 395-427, <http://hdl.handle.net/2268/29650>.
2. NBN B15-103: 1977, Design of reinforced concrete, Belgian Institute for Standards BIN.
3. Gernay, T., Millard, A., Franssen, J.-M. 2013. A multiaxial constitutive model for concrete in the fire situation: Theoretical formulation. Int J Solids Struct, 50(22-23): 3659-3673.
4. Gernay, T., Franssen, J.-M. 2015. A plastic-damage model for concrete in fire: Applications in structural fire engineering. Fire Safety J, 71: 268-278.
5. Van Coile R., Caspeele R. and Taerwe. L. June 2015. "Practical reliability-based calculation tool for the post-fire assessment of concrete beams", in *International Conference on Response of Structures Under Extreme Loading*, V.K.R. Kodur, and N Banthia, eds. Lancaster, Pennsylvania, pp 696-703.
6. EN 1990:2002 + National Annex NBN EN 1990-ANB: 2007, "Eurocode 0: Basis of structural design", European Committee for Standardization CEN, 2002.
7. EN 1992-1-2: 2005 + Nationale Annex NBN EN 1992-1-2-ANB: 2010, "Eurocode 2: Design of concrete structures - Part 1-2: General rules - Structural fire design", European Committee for Standardization CEN.

Engineering an Icon or the Probabilistic-based Structural Fire Engineering of the Battersea Power Station

FLORIAN M. BLOCK and TAD-SONG KHO

ABSTRACT

For large compartment floors the assumption of full flashover fire is very unlikely to hold true; instead fires are likely to be localised whilst moving around the floor plate. The paper will describe how a series travelling design fires are developed to assess steel framed structures, in which a probabilistic Monte-Carlo approach is adopted as means of developing design fires that are reflective of the risk associated with the use and height of the building. The Monte-Carlo approach involves a bespoke probabilistic method in which a set of parameters are randomised to produce a large number of possible fires occurring within the floor space; this is a step forward from the deterministic approach in which design fires are often being defined. This paper describes how the above principles are adopted to the structural fire design of the office floors in the refurbishment of the Battersea Power Station – one of the largest redevelopment projects in London in recent years.

INTRODUCTION

The Battersea Power Station, located on the south bank of the river Thames, is an industrial monument, which has been one of the most recognisable and loved London landmarks since the 1930's. The proposed redevelopment will transform the industrial shell into a fully functioning destination offering 2 million square feet of usable space including residential apartments, a 3-storey shopping mall, offices, a hotel, a multiplex cinema and a 2000 seat event space. The historically listed brick building is a true feat of engineering that is now undergoing a similar feat in its transformation, and fire safety engineering used extensively due to the complexity of the building with the large number of occupants of different risk types, which will be occupying this building simultaneously. Where possible the building is designed in accordance with BS9999 and fire engineering applied to others to meet the intent of the Building Regulations (England and Wales) for life safety.

Florian M. Block, BuroHappold Engineering, Florian.Block@BuroHappold.com
Tad-Song Kho, BuroHappold Engineering, Tad-Song.Kho@BuroHappold.com

Figure 1. Overview of Battersea Power Station (left), 3D cut-through of office floors (right).

Due to the complex nature of the project detailed structural fire engineering assessments have been conducted in a number of different areas including existing steel and concrete columns partially encased in brick and highly architectural link bridges. However, this paper will focus on the structural fire engineering design of the office floors. The office floors occupies the entire floor of Level 5-10 of the main building, measuring approximately 150m x 70m in plan and providing almost 8000m^2 of usable floor area. Each floor opens into a central atrium and are bounded by the four iconic wash towers and chimneys at each of the four corners. The internal structure within the office space are new built consisting of composite floor construction, with the steel beams being fabricated with web openings. Lateral stability of the structure does not rely on the four wash towers; instead it is achieved via four internal concrete cores. With an open plan office arrangement in mind, these floor have a typical column grid arrangement of 11.5m x 10.5m.

The standard and parametric fire in EN 1991-1-2 are generally being used to assess the performance of structure due to a fire within a building. However with the demand for buildings with increasingly open floor space with minimal compartment walls, such as the open-plan offices on Level 5-10, the assumption of a compartment fire may no longer be valid. Therefore, travelling fires have been considered in addition to the compartment fires mentioned earlier to ensure that an inherently safe and robust solution is found. The travelling fire in this case study is based on the work done by Stern-Gottfried *et. al* [1].

It has been common practice to adopt a deterministic approach to structural fire engineering, there is however currently a shift away from this to a probabilistic approach. The probabilistic approach allows an acceptable risk level to be quantified based on the usage and occupancy and height of the building. This in turn allows fires, which match this level of risk, to be determined. In this study, the principles behind the work by Kirby *et. al* [2] and Law *et. al* [3] have been adopted.

METHODOLOGY

The structural fire engineering work carried out on the office floor structure is generally conducted using the following methodology:

1. Determine the acceptance criteria of the thermo-mechanical analysis; these are similar to those stated in Block and Kho [4].
2. Establish the fire resistance period of the office and occupancies surrounding it. Based on Table 26 of BS9999, the required fire resistance period of structure within the office space and the residential levels above the office is R75 and R90

(see Figure 1), respectively. Therefore, the main columns running through the office floors which also supports the residential levels above are fire protected to achieve R90. The retail and event space, which are below the office floors, will have a fire rating equal to or exceeding R90.

3. Derive design fires, which are to be imposed onto the structure. This paper covers the derivation of the probabilistic travelling fires only but the office structure has also been subjected to the localised, parametric and the standard fires.
4. Conduct thermo-mechanical analysis of the floor structure for different fire scenarios. Some of the results are presented in this paper.
5. Repeat Step 4 with other structural enhancement until an optimised fire protection layout, which would satisfy the acceptance criteria in Step 1, is found.

THE PROBABILISTIC APPROACH

The probabilistic approach utilises the Monte-Carlo method, which is an algorithm that involves repeated random sampling of parameters to obtain the distribution of a probabilistic outcome. In this case, the Monte-Carlo method is applied to simulate a total of 10,000 possible design fires [2][3]. For each design fire analysed, different variables defining the fire scenarios are chosen at random, within a defined distribution curve, for input into the engineering calculations. This allows the probabilistic element of fire scenarios to be accounted for, which makes up for the shortcomings of traditional deterministic approach that does not account for the uncertainties that prevail in the real world. The proposed size of the compartments are at least $400m^2$ therefore it is assumed that only travelling fires could occur on the office floors. The steps involved in the Monte Carlo analysis is shown in Figure 2; this has been programmed into Microsoft Excel. There would be a total of 15 design fires shortlisted, in which a final three will be selected among the five office configurations based on a similar criteria in in the flow chart below.

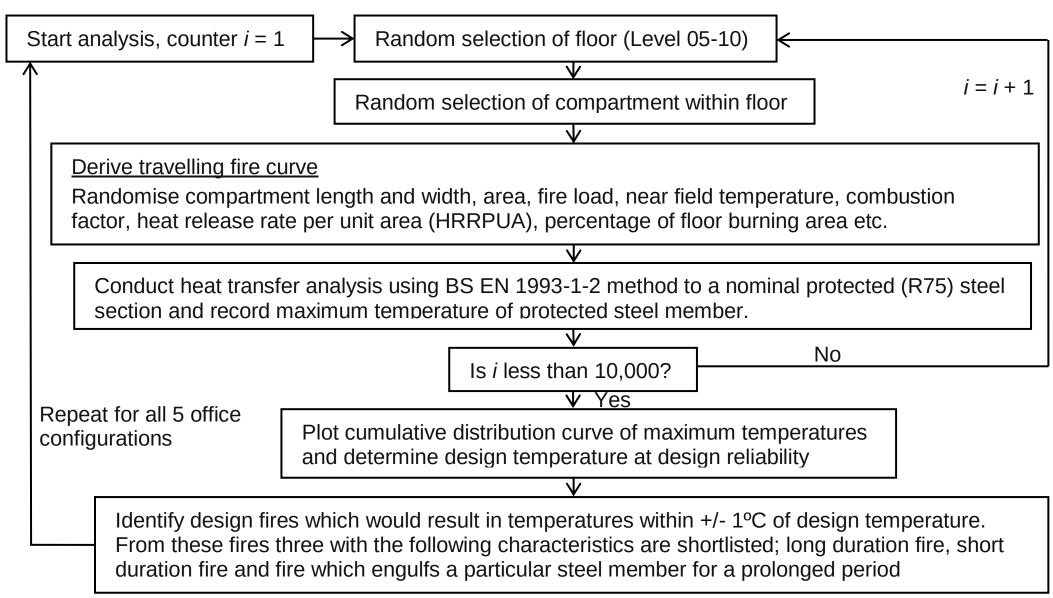

Figure 2. Flow chart of Monte Carlo probabilistic assessment.

Acceptable Level of Risk

An acceptable level of risk is quantified following assumptions outlined by Law *et. al* [3]; readers are directed to their paper for more details about the approach. The quantifiable level of risk (*Risk*) in Eq. (1) is calibrated against Approved Document B assuming building height (*h*) is 18 metres and required reliability (*r*) of the building under fire as 80% [2]. The acceptable risk level is therefore calculated to be 64.8. The required reliability of the Battersea Power Station, being 51.8 metres in height, becomes 97.6%, meaning the building should be able to withstand 97.6% of fires simulated without structural failure occurring.

$$Risk = h \times (1 - r) \times h \quad (1)$$

The presence of sprinklers within the office space is explicitly accounted for [3]; this is done by expressing the contribution of the sprinklers to the structural reliability using the Eq. (2) below. Where r_T is the aggregate reliability of the structure, r_{sp} is the sprinkler reliability and r_{st} is the reliability of the structure in the event of sprinkler failure. From Section 7.1.9 of PD 7974-7 it suggest that the reliability of a new sprinkler system should be taken as 0.8; this assumes that the sprinklers would either control or extinguish 80% of fires in the office space with the remaining 20% of fires being uncontrolled due to the failure of the sprinklers to control the fire effectively either due to human errors or mechanical faults.

$$r_{st} = (r_T - r_{sp}) / (1 - r_{sp}) = (0.976 - 0.8) / (1 - 0.8) = 0.879 \quad (2)$$

Based on the information above the required structural reliability in the event of a sprinkler failure is approximately 87.9%. In other words, the office structure in the Battersea Power Station would have to withstand 87.9% of uncontrolled fires (due to the failure of sprinklers) simulated using the Monte Carlo method without structural failure occurring. From here on the required reliability (*r*) of the building is referred to as the design reliability.

Floor configurations

The architects have presented 6 possible floor layout options which, can accommodate between 1 to 8 tenants on each floor; two possible layouts are shown in Figure 3. However the final floor layout of the office floors has yet to be determined as this is dependent on the number of actual tenants per floor, which at the time of the design is unknown. To account for this uncertainty a few different possible office configurations have been investigated, as shown in Table I below.

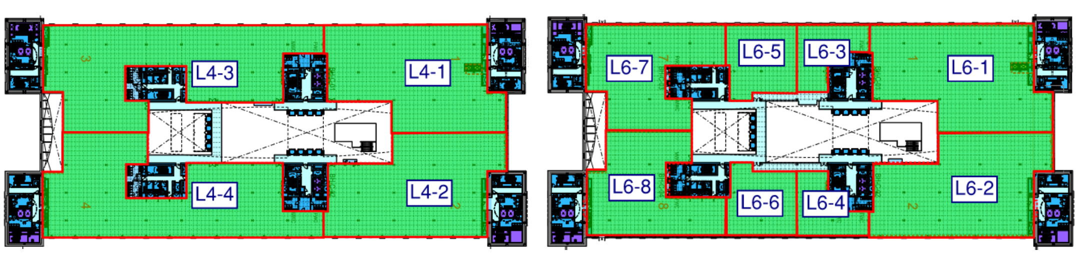

Figure 3. Typical office floor layout assuming 4 (left) and 8 (right) tenants per floor.

TABLE I. OFFICE CONFIGURATIONS USING COMBINATION OF FLOOR LAYOUTS.

	Number of compartments per floor					
Configuration	**Level 5**	**Level 6**	**Level 7**	**Level 8**	**Level 9**	**Level 10**
1	1	1	1	1	1	1
2	8	8	8	8	8	8
3	1	2a	2b	4	6	8
4	4	4	6	6	8	8
5	1	1	2a	2a	2b	2b

Note: 2a: 2 compartments per floor split in the middle along the East-West
2b: 2 compartments per floor split in the middle along the North-South

Travelling Fires Inputs

Most of the parameters such as compartment length and width, plan area, fire load, near field temperature, combustion factor, heat release rate per unit area (HRRPUA), percentage of floor burning area *etc.* for the travelling fire are randomly selected from distribution curves that have been defined based on project experience due to the lack of experimental and statistical data for these parameters except the fire load density (FLD) [2][3]; see Figure 4a. The assumed HRRPUA and Near Field Temperature distribution curves are shown as an example in Figure 4b and 4c. The HRRPUA is taken as 250kW/m^2 as the base value as recommended by the UK National Annex of EN 1991-1-2 but varied +/20% to produce a range of values. The near field temperature is assumed to range from 900-1200ºC which varies linearly. A more scientific way of determining the near field temperature has been carried out in the recent work by Rackauskaite *et al.* [5], however the structural fire engineering design on the office levels of the Battersea Power Station preceded this work.

Selection of Travelling Design Fires

The Monte-Carlo probabilistic analysis conducted on the five configurations explained earlier produces the cumulative distribution curve in Figure 5. It can be seen that the protected steel temperature at design reliability (97.6%) ranges from 604-707ºC. Configuration 1 has the highest design temperature as this configuration consist of the largest compartments with no fire separation on each of the office floors. A fire in a larger compartments means that the steel members are exposed to the travelling fire for a more prolonged period, therefore resulting in generally higher steel temperatures.

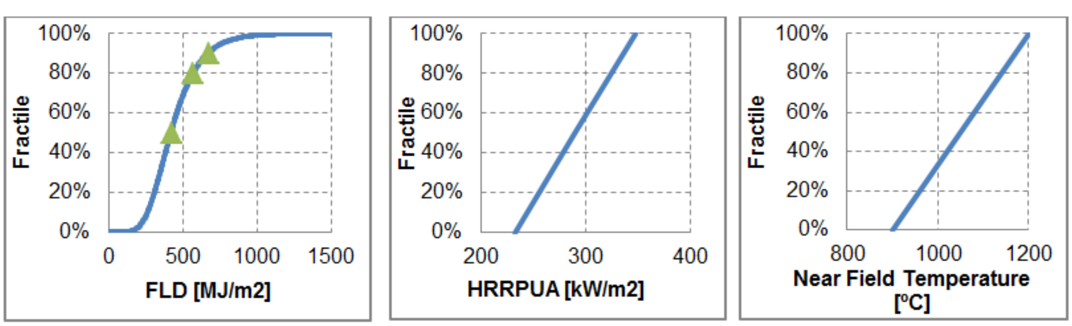

Figure 4. Distribution curves of a) FLD (left), b) HRRPUA (middle) and c) Near Field Temp. (right)

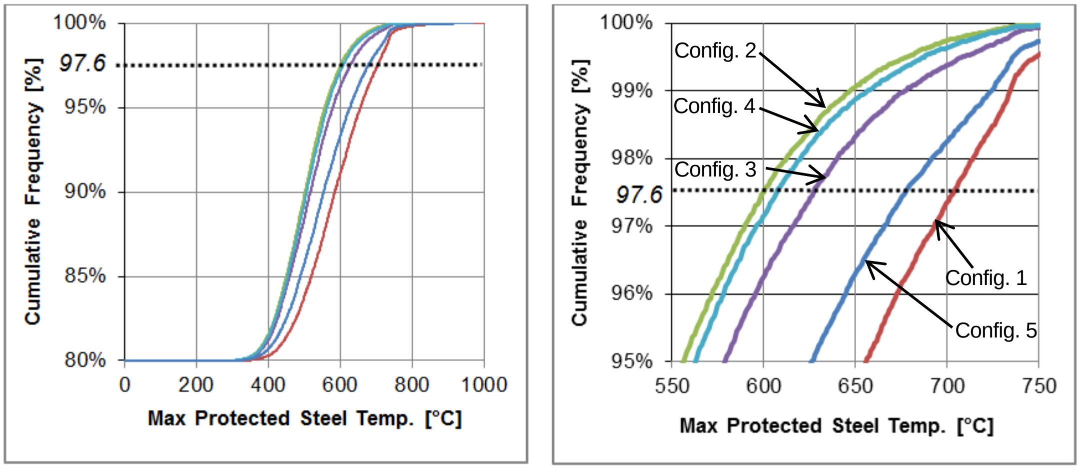

Figure 5. Overview (left) and magnified view (right) of cumulative distribution curves of protected steel.

The shortlisted travelling fires for each configuration are compiled in Figure 6a. The dotted lines highlights the three selected travelling fires, which have been used in the subsequent thermos-mechanical analysis. The fires with a duration exceeding 240 minutes (4 hours) have not been considered as it is likely that some form of fire-fighting intervention or full evacuation of the building would have likely taken place by then. The corresponding steel temperatures response, when subjected to the travelling fires in Figure 6a, are shown in the Figure 6b.

STRUCTURAL ANALYSIS

Due to the scale of the floor structure analysed, a 3D finite element analysis has been conducted using the software Vulcan [6]. Assuming symmetry an approximate quarter of a typical floor plate is modelled, as shown in Figure 7. Due to the regular structural grid of the floor plan, the fire protection to the floor beams has been optimised by omitting fire protection to the off-grid secondary beams; this allows the tensile membrane action to be utilised under fire conditions.

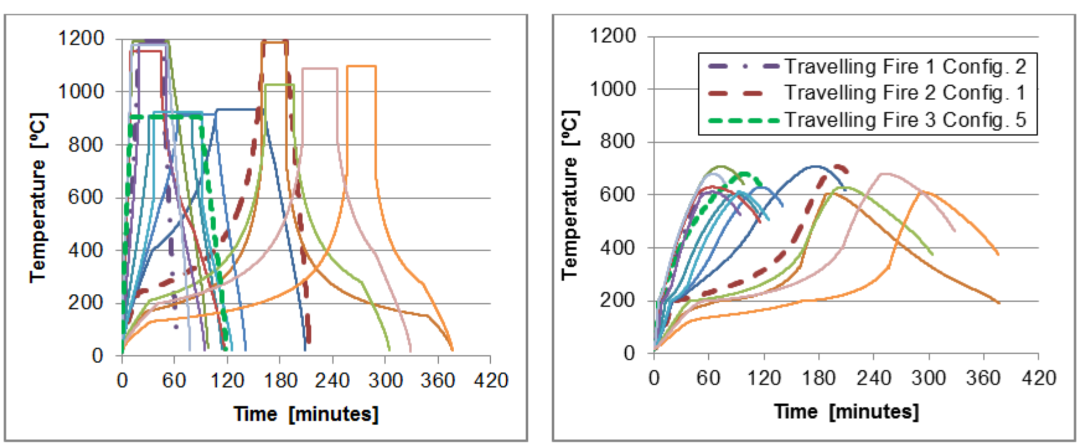

Figure 6. a) Shortlisted traveling fire curves and b) corresponding protected steel temperature response.

Figure 7. a) Approximate quarter of floor plate modelled and b) plan view of Vulcan model.

A total of 10 different scenarios have been investigated, which include looking at 7 different types of design fires (including the three travelling fires defined in this paper). The effect of a single-, two- and three- storey fires have also been investigated as this affects the buckling behaviour of the column by increasing the effective length of the column and therefore its propensity to buckling.

There are currently expansion joints between the wash tower and the main floor plate to allow an uncoupling of movement along the north-south direction at ambient temperature. However, in a fire scenario the thermal expansion of the floor plate is expected to be greater than the what is current allowed for. It is currently not possible to model contact springs elements in Vulcan. Therefore, two scenarios have been modelled; one in which there is free thermal expansion along the north-south direction and the other scenario in which thermal expansion along this direction is restricted. The actual behaviour of the floor would likely be somewhere in between these two modelled scenarios.

The response of the structure at 3 different points in time, when subject to the long travelling fire (Travelling Fire 2 Config. 1 in Figure 5) is shown in Figure 8.

OUTCOME OF SFE ASSESSMENT

The resulting final applied fire protection regime is shown in Figure 9a. To prevent excessive central deflection and excessive cracking/yielding of reinforcement of the slab above some of the primary beams additional reinforcement have been provided in the region highlighted in Figure 9b. The red region indicates where an additional layer

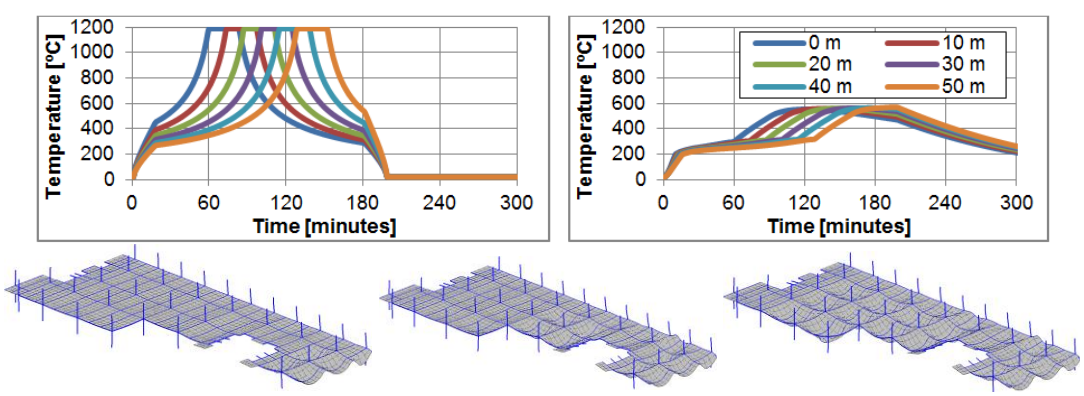

Figure 8. Time temperature curves of travelling fire sampled along length of compartment (top left), corresponding time temperature curves of typical protected steel (top right), thermo-mechanical response of Vulcan model at 75, 120 and 165 minutes scaled by 5x (bottom).

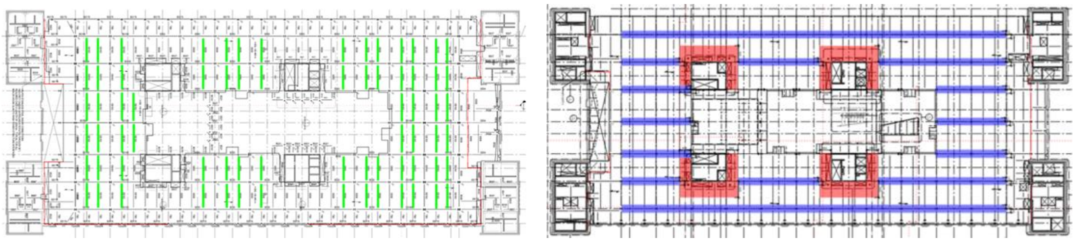

Figure 9. a) Unprotected beams indicated in green and b) additional reinforcement in which the red region indicates where an additional layer of A393 mesh will be required; the blue region indicate H10 reinforcement placed perpendicular to these primary beams at 200mm centre to centre.

of A393 mesh will be required; the blue region indicate H10 reinforcement placed perpendicular to these primary beams at 200mm centre to centre. In addition to prevent connection failure in a fire scenario due to thermal expansion as well as to minimise tensile forces during cooling ductile flush endplates connections have been proposed for the protected beams.

CONCLUSION AND FUTURE WORK

The probabilistic approach described in this paper is a powerful tool which allows the designer to development realistic design fires based on an acceptable calculated risk. With the emerging of increasingly complex and open-plan structures it is imperative that a performance-based approach based on the state of art knowledge in structural fire engineering are adopted to ensure that the resulting solution is inherently robust and safe whilst providing added value to project.

In the future more statistical data on the distribution curves of the fire input and a better understanding of the travelling fire phenomenon would increase the realism of the possible fires defined. Research and a literature review carried out by Rackauskaite *et al.* [5] has closed some of the gap in knowledge with respect to this by providing a more likely range of rate of fire spread and means to determine the near field temperature.

The ability to explicitly model the behaviour of connections in large scale finite element modelling, without the need for significantly more computer resources, would also greatly add value to the design.

REFERENCES

1. Stern-Gottfried, J. and Rein G 2012. “Travelling fires for structural design-Part II: Design methodology”. *Fire Safety Journal* 54 p. 96-112.
2. Kirby B. R., Newman G. M., Butterworth, N., Pagan, J. and English, C 2004. “A new approach to specifying fire resistance periods”. *The Structural Engineer* 84: p. 34-37.
3. Law, A., Butterworth, N., Stern-Gottfried, J 2014. “A Risk Based Framework for Time Equivalence and Fire Resistance”. *Fire Technology*. 51 p. 771-784.
4. Block, F., and Kho, T. 2015. “Engineering the Next Generation of Buildings at Broadgate, London – Combined Assessment for Fire and Progressive Collapse,” in *Conference on Structural Safety Under Fire & Blast*.
5. Rackauskaite, E., Hamel, C., Law, Rein, Rein. “Improved Formulation of Travelling Fires and Application to Concrete and Steel Structures”. *Structures.* 2015, Vol. 3.
6. http://www.vulcan-solutions.com/

Fire Fragility Functions for Community Resilience Assessment

NEGAR ELHAMI KHORASANI, THOMAS GERNAY
and MARIA GARLOCK

ABSTRACT

This work provides a framework to evaluate the response of buildings in a community to fire following earthquake. As part of the framework, the paper discusses two methodologies: (1) how to develop fire fragility functions; (2) how the fire fragility functions can be used in conjunction with an original fire ignition model to estimate the potential losses in a community from fire following earthquake. The paper focuses in particular on the development of fire fragility functions for an entire building to measure the probability of reaching a damage state given a fire scenario. Next, the paper proposes an ignition model to evaluate the probability of fire ignition after an earthquake. The ignition model together with fragility functions measure the probability of damage from fire following earthquake given an earthquake scenario.

INTRODUCTION

Community resilience to extreme events is an issue of increasing concern in our interconnected and urbanized societies. Meanwhile, cascading multi-hazard events, such as fires following an earthquake, can cause major social and economic losses in a community. The problem of evaluating the response of a community to an extreme event involves uncertainties at different levels, and therefore, is generally approached with probabilistic methodologies and risk management formulations. The process can be divided into three steps: evaluating the frequency of a hazard, measuring vulnerability of a community, and quantifying consequences of the event. The three steps together quantify the risk, which provides an estimate of potential losses.

This work provides a framework to evaluate the response of buildings in a community to fire following earthquake. It focuses in particular on the development of fire fragility functions for an *entire building* and their application for measuring the resiliency of a community to fire following earthquake. The work is novel as the fragility functions are developed for the entire building, not just an element or component within the building. The paper includes two parts: (1) how to develop fire fragility functions; (2) how the fire fragility functions can be used in conjunction with an original fire ignition model to estimate the potential losses in a community from

Thomas Gernay, the National Fund for Scientific Research F.R.S.-FNRS, University of Liege, Allee de la Decouverte 9, 4000 Liege, Belgium.
Negar Elhami Khorasani, University at Buffalo, Buffalo, NY, U.S.A.
Maria Garlock, Princeton University, Princeton, NJ, U.S.A.

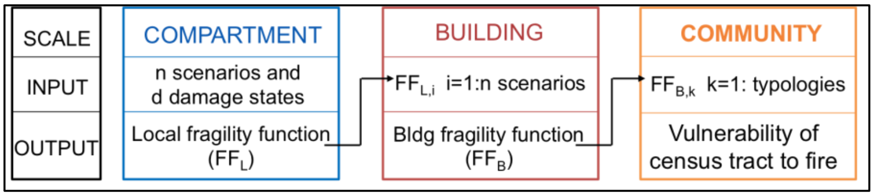

Figure 1. Overview of fire fragility curves for community resilience assessment.

fire following earthquake. Fig. 1 provides an overview of the three scales involved (compartment, building, community of buildings) and how fragility functions fit within these scales. In this framework, local fire fragility functions at the compartment level are combined to obtain fragility functions for entire buildings. Different building topologies in a community demand different fragility functions. Such collection of fragilities can be used to evaluate vulnerability of a community.

FRAGILITY FUNCTIONS

In earthquake engineering, fragility functions are well established to quantify the structural damage due to an earthquake. A fragility function provides the probability of exceeding a damage state for a given intensity measure of a given hazard [1, 2]. The damage states (or limit states) are generally related to the structural performance level. Adopting a similar idea, fire fragility functions can be developed to measure the expected losses based on performance of a building structural system, rather than a single component. Then, different functions can be developed for buildings with different typologies (e.g., high-rise steel with moment resisting frame, low rise concrete with shear walls) to evaluate the vulnerability at the scale of a community.

One important parameter in defining a fragility function is the selected intensity measure for a given hazard. The intensity measure that is used to quantify the effect of an earthquake range from peak ground acceleration (*PGA*), pseudo displacement (S_d), permanent ground deformation (*PGD*) and etc., depending on the type of structure. In the case of a fire scenario, this paper proposes to take the average fire load (in MJ/m^2 of floor area) as the intensity measure, because: (i) the fire load is one of the main parameters affecting the intensity of a fire [3], (ii) the expected value of fire load changes depending the occupancy type, and (iii) it can be easily understood by the different stakeholders involved in fire safety. Therefore, in this paper, a fire fragility function refers to the probability of exceeding a damage state (e.g., column failure, excessive beam deflection, etc.) given the average fire load in a building. Fragility functions yield probabilities conditional to the occurrence of a hazard. In developing the fire fragility functions, it is assumed that a structurally significant fire, i.e. one that is able to endanger the structure, occurs in the building.

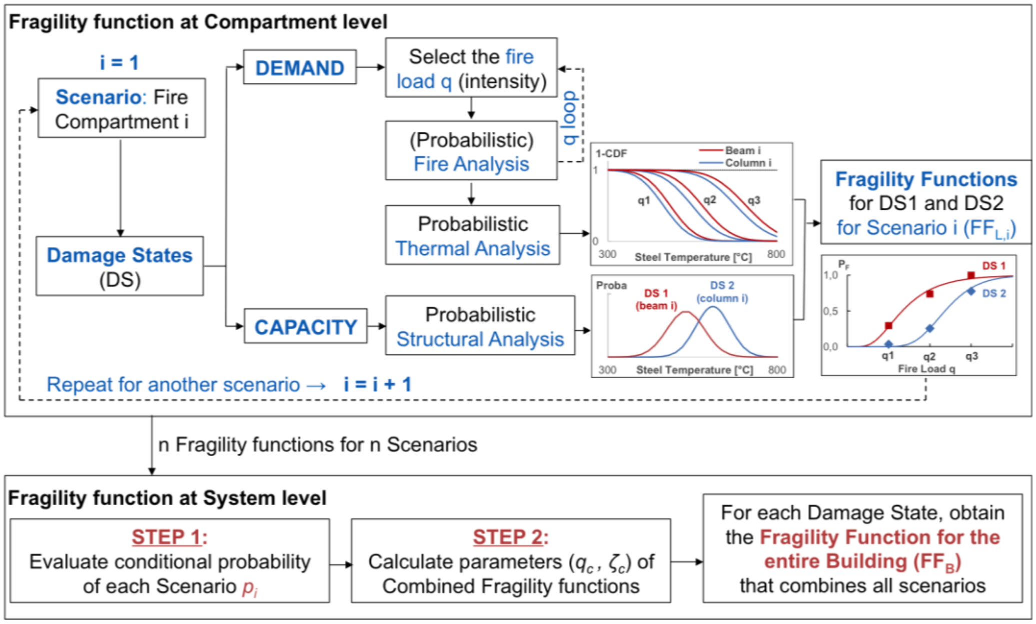

Figure 2. Development of fire fragility curves for a building.

METHODOLOGY

This section provides an overview of the proposed methodology to construct a fire fragility function for a steel building. Developing a fragility function involves the probabilistic assessment of performance of the structure. Designing a member or a structure is traditionally based on comparing demand and capacity. In the context of fragility function, the demand is related to the temperature reached in the structure due to fire, while the capacity for a given damage state is associated to the exceedance of a certain temperature threshold in the sections of a structure, which is referred to as the critical temperature.

The proposed methodology incorporates uncertainties in demand (thermal analysis) and capacity analyses while taking advantage of the critical temperature. The concept of critical temperature is used to decouple the thermal analysis (demand side) from the capacity analysis. Thermal analysis provides the distribution of maximum possible temperatures reached in a section, while the capacity analysis yields a probability distribution function (*PDF*) for the critical temperature associated with a damage state. After both sets of analyses are completed, the results from demand and capacity can be combined and compared to find cases that experience the damage state (demand larger than capacity). The methodology is illustrated in Fig. 2.

Compartment level

For a given compartment in the structure, and focusing on a given damage state, the following procedure is followed to derive fire fragility functions at the compartment level:

(1) A value of fire load is selected and the temperature-time curve of fire is formulated using existing procedures (such as the Eurocode1 parametric fire curves).

(2) Heat transfer analysis is performed considering uncertainties in random variables such as thermal properties of steel or insulating materials, if applicable. The

cumulative distribution function (*CDF*) of the steel temperature in the section is obtained.

(3) Structural analysis at elevated temperature is performed to find the critical temperature in the section. Uncertainties in mechanical properties of steel and the applied gravity loads are considered. The *PDF* of the critical temperature is obtained.

(4) The conditional probability of failure can now be computed using Eq. 1, by convolution of the PDF of capacity and the complementary *CDF* of demand [4].

$$P_{F|H_{fi}} = \int_0^\infty \left[1 - F_{D|H_{fi}}(\alpha)\right] f_C(\alpha) d\alpha \tag{1}$$

In Eq. 1, $P_{F|H_{fi}}$ is the probability of reaching a damage state conditional to the occurrence of a fire H_{fi}, $F_{D|H_{fi}}(.)$ is the *CDF* of the demand relative to the fire H_{fi}, and $f_C(\cdot)$ is the *PDF* of capacity.

The above procedure is repeated for a range of fire load densities (q values) in the same compartment. Repeating the operation for each fire load yields to several outputs relating the fire load q (intensity measure) and the conditional probability of reaching the damage state as shown in Fig. 2. The fragility function is built by fitting a function to the obtained points, assuming a lognormal distribution:

$$F(q) = \Phi\left[\frac{ln(q/c)}{\zeta}\right] \tag{2}$$

where q is the fire load (MJ/m²) and $\Phi[\cdot]$ is the standardized normal distribution function. The two parameters c and ζ characterize the fragility function and are determined by the best fit to the data points. Finally, the same process is applied for deriving the fragility functions relative to the other damage states and other fire compartment locations. Further details about the proposed procedure are provided in [5].

Building level

In a multi-story building, different fire compartments can be defined. As a result, fire fragility functions should first be developed for each compartment, and then combined to derive a fire fragility function for the entire building. The building fragility function should represent the overall vulnerability of the building. Therefore, the procedure discussed at the compartment level should be repeated several times during the fragility analysis of a building, for varying scenarios (where the scenario *i* in Fig. 2 corresponds to a fire located in compartment *i*).

The method for combining fragility functions is adopted from [6] work where fragilities for similar structural attributes are combined. In this procedure, the combined fragility function is also a lognormal function (similar to Eq. 2). The two lognormal parameters for the combined function are calculated on the basis of the corresponding parameters for the individual fragility functions, taking into account the relative likelihood of each fire scenario (Fig. 2). Eq. 3 provides the mean of combined lognormal, where n is the number of “nominally identical but statistically different” fragility curves, c_i is the median associated with each individual fragility curve, and p_i

is the conditional probability for a fire in compartment *i*, given that a fire occurs in the building. The standard deviation of the combined lognormal distribution, ζ_c, is calculated using Eq. 4, where $\boldsymbol{P}$ is the vector of the probabilities p_i, $\mathbf{Z}$ is the vector of the variances ζ_i^2 associated with each individual fragility function, $\boldsymbol{A}$ is the vector of the expected values ($\ln c_i$), and $\boldsymbol{Q}$ is the matrix given by Eq. 5. The reader is referred to [5,6] for more comprehensive information about the procedure.

$$q_c = \prod_{i=1}^{n} c_i^{p_i} \tag{3}$$

$$\zeta_c^2 = \mathbf{P}^{\boldsymbol{T}}\mathbf{Z} + \mathbf{A}^{\boldsymbol{T}}\mathbf{QA} \tag{4}$$

$$\mathbf{Q} = \begin{bmatrix} p_1(1-p_1) & \cdots & -p_1 p_n \\ \vdots & \ddots & \vdots \\ -p_n p_1 & \cdots & p_n(1-p_n) \end{bmatrix} \tag{5}$$

In the proposed methodology, the probability values (p_i) are calculated using the formulation that is applied by Eurocode to develop the prescribed design values for fire load densities [7]. This formulation relates probability of having a severe fire to occupancy type, fire brigade, and active fire protections.

CASE STUDY

The proposed methodology, discussed above, is applied to a 9-story steel building prototype. The building is 45.72 m by 45.72 m in plan, with five bays at 9.144 m in each direction. The structure is composed of four moment resisting frames on the perimeter, and four interior gravity frames. The columns of the interior frames are continuous on the nine-story but the beams have pinned connections (statically determinate beams). The total height of the building is 37.182 m, divided between a first floor of 5.486 m high and eight floors of 3.962 m high. The steel sections (beams and columns) are protected with a sprayed fire-resistive material (SFRM) of nominal thickness 39 mm. The nominal values of the steel yield strength and Young modulus are 345 MPa and 200,000 MPa, respectively. The concrete compressive strength is 28 MPa. The beam sections consist of W21x44 on all floors except a W18x40 at the roof (9^{th} floor). The column sections range from W14x43 at the 9^{th} story to W14x109 at the first floor. Column splices are located at every two floors.

The procedure to develop a fire fragility function for the building is applied to the prototype building. In order to illustrate the procedure, two structural damage states are considered, one relative to the beams and one relative to the columns:

- DS1: when the bending capacity of the beam is exceeded and the mid-span vertical deflection increases dramatically;
- DS2: when the column fails with a sudden increase in transversal deflection, either due to buckling or exceedance of the section plastic capacity under combined compression and bending.

The uncertainties in both demand and capacity analyses are considered. On the demand side, the SFRM thickness is assumed to follow a lognormal distribution with a mean value equal to the nominal value of 39 mm plus 1.6 mm and a coefficient of variation of 0.2 [8]. The probabilistic model proposed by Elhami Khorasani et al. [9] is adopted for the SFRM conductivity. On the capacity side, randomness in the gravity loads and mechanical properties of steel is considered. The factors applied to the dead and live loads are respectively 1.05 and 0.24 and these factors are weighed by probabilistic load factors according to [10]. The reduction in steel mechanical properties with temperature, are modeled using the probabilistic model from [9].

The thermal analyses are performed using the finite difference formula of EN 1993-1-2 Section 4.2.5.2 [11]. Monte Carlo Simulations are conducted using the Eurocode formula and varying the thermal properties of the insulation material (thickness and conductivity) [12]. On the capacity side, the building structure is modeled in the non-linear finite element software SAFIR [13] developed at University of Liege. SAFIR allows conducting a thermal analysis of the sections of the structural members, followed by structural analysis of the building at high temperature. The critical temperature is independent of the particular time-temperature evolution curve in the section. The concept of critical temperature, which was discussed in the previous section and illustrated in Fig. 2, is prescribed in Eurocode [11], and is validated for the specific structure under study. The reader is referred to [5] for details of the study. Therefore, the temperature evolution used as an input in the structural FE analysis, can be any time-temperature relationship. In this work, the ASTME119 fire with no thermal protection on the steel members is used as the input.

Based on the proposed methodology and the inputs, the combined fragility curves associated to the two damage states for the entire building are shown in Fig. 3. Assuming an average fire load of 600 MJ/m² in the building, the figure shows that the probability of exceeding the beam damage state (DS1) is 88% and the probability of exceeding the column damage state (DS2) is 15%. Therefore, the probability of exceeding the damage state in the beam (DS1) but without collapse of the column is 73% (0.88-0.15). The probability of not reaching any of the two considered structural damage state is obtained as the complement of the probability of DS1, i.e. 12%.

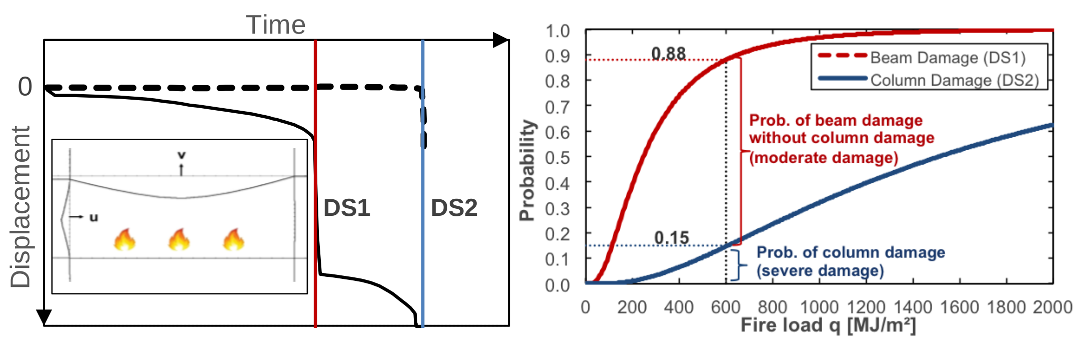

Figure 3. (a) Damage states related to beam and column, (b) Combined fragility curves for the prototype nine-story steel frame building.

IGNITION MODEL

The paper so far discussed a methodology to quantify the vulnerability of a building given that a structurally significant fire occurs in the building. This section provides a model to evaluate the probability of ignition in a building after an earthquake. The two models together can be combined to evaluate the probability of damage due to fire given an earthquake scenario.

The proposed ignition model is developed based on historical ignition data, all of which led to structural ignition fires. The model is based on seven historical earthquake events, all of which occurred in California, U.S.A., between 1983 and

2014: 1983 Coalinga, 1984 Morgan Hill, 1986 North Palm Spring, 1987 Whittier Narrows, 1989 Loma Prieta, 1994 Northridge, and 2014 Napa. Compilation of the inventory of historical data is similar to the work completed by Hazus [14] but updated to include data from the recent Napa earthquake in 2014. Meanwhile, the proposed model takes a different approach than the existing FFE ignition model in Hazus and is based on a probabilistic approach.

The proposed model relates the probability of ignition to the peak ground acceleration *PGA* (as a measure of earthquake intensity), type of building material (number of wood buildings N_W, mobile homes N_{MH}, non combustible buildings N_{NC}), and the main features of the environment in which the buildings are located (the total square footage *SF* and the population density *PD*). The ignition model outputs probability of ignition at a census tract and at individual buildings (Eqs. 6 to 8). Fig. 4 shows the step-by-step procedure to use the ignition model. Eq. 6 uses the characteristics of the area under study and *PGA* to estimate probability of ignition at each census tract P_{Ig_tract}. Then, Eq. 7 uses the complement probability rule to back-calculate probability of ignition P_{Ig} in each building type from P_{Ig_tract}. Finally, Eq. 8 provides the expected number of ignitions in a collection of census tracts given the ignition probability in individual buildings. The model is validated against historical FFE events and shows good agreement with the historical data [15]. In addition, the proposed model has the advantage of providing the breakdown in the number of ignitions for different considered building types.

$$P_{Ig\_tract} = \frac{\exp(-6.755+8.463\times \mathrm{PGA}+98.4\times 10^{-6}\times PD+152.3\times 10^{-6}SF)}{1+\exp(-6.755+8.463\times \mathrm{PGA}+98.4\times 10^{-6}\times PD+152.3\times 10^{-6}SF)} \tag{6}$$

$$P_{Ig\_tract} = 1 - [(1-0.471P_{Ig})|\mathrm{PGA}]^{N_W} \times [(1-1.0P_{Ig})|\mathrm{PGA}]^{N_{MH}} \times [(1-0.411P_{Ig})|\mathrm{PGA}]^{N_{NC}} \tag{7}$$

$$\text{No. of Ignitions} = \sum_{i=1}^{m}\left[N_W \times \left(0.471P_{Ig}\right) + N_{MH} \times \left(1.0P_{Ig}\right) + N_{NC} \times \left(0.411P_{Ig}\right)\right]_i \tag{8}$$

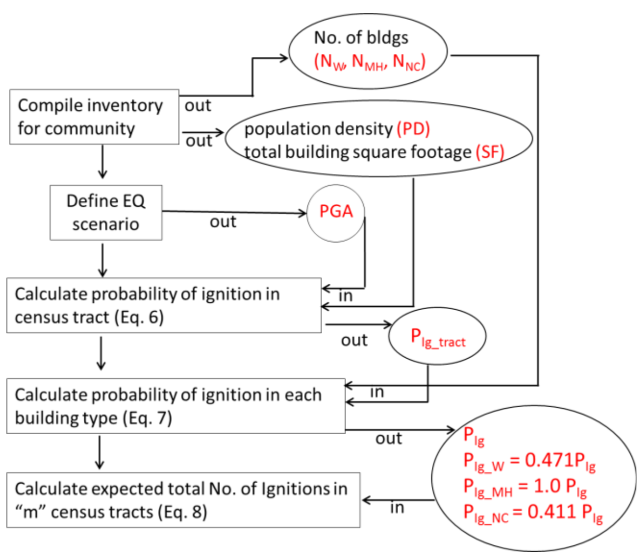

Figure 4. The step-by-step procedure for using the ignition model.

CONCLUSION

This paper provided a methodology to develop fire fragility functions for buildings. The fragility functions are first derived at the compartment level, and then combined to obtain the fragility function for the entire building. The proposed framework employs the concept of critical temperature to decouple the thermal analysis (demand side) from the capacity analysis. The compartment fragility function is obtained by convolution of the PDF of capacity and the complementary *CDF* of demand.

The paper also proposed an ignition model to evaluate probability of fire ignition after an earthquake. The ignition model, combined with the fragility functions, can be implemented in a Geographic Information System (GIS) based risk assessment platform to evaluate social and economical losses in a region from fire following earthquake. The ignition model provides the probability of fire ignition while the fragility function measures the expected structural damage given a fire ignition. The two models together measure the probability of damage from fire following earthquake given an earthquake scenario.

REFERENCES

1. Elnashai, A. S. (2003). "Next generation vulnerability functions for RC structures." *Proc., Response of Structures to Extreme Loading, Elsevier,* Toronto.
2. Pan, Y., Agrawal, A. K., and Ghosn, M. (2007). "Seismic fragility of continuous steel highway bridges in New York State." *J. Bridge Eng.,* 12(6), 689-699.
3. Elhami Khorasani, N., Garlock, M., Gardoni, P. (2014). Fire load: Survey data, recent standards, and probabilistic models for office buildings. *Eng Struct, 58(0), 152-165*.
4. Rota, M., Penna, A., Magenes, G. (2010). "A methodology for deriving analytical fragility curves for masonry buildings based on stochastic nonlinear analyses." *Eng Struc*, 32(5):1312-23.
5. Gernay, T., Elhami Khorasani, N., Garlock, M.E.M. (2016). "Fire fragility curves for steel buildings in a community context: A methodology". *Engineering Structures*, 113: 259-276.
6. Shinozuka, M., Member, H., Member, A., Lee, J., Naganuma, T. (2000). Statistical Analysis of Fragility Curves. *J Eng Mech ASCE, 126(12), 1224-1231*.
7. EC1. (2002). *Eurocode 1: Actions on structures – Part 1–2: General actions – actions on structures exposed to fire*. EN 1991-1-2. Brussels: CEN.
8. Iqbal, S., Harichandran, R. S. (2010). Capacity reduction and fire load factors for design of steel members exposed to fire. *J Struct Eng, 1554-1562*.
9. Elhami Khorasani, N., Gardoni, P., Garlock, M. (2015). Probabilistic Fire Analysis: Material Models and Evaluation of Steel Structural Members. *J Struct Eng.*
10. Guo, Q., Jeffers, A. E. (2014). Finite-Element Reliability Analysis of Structures Subjected to Fire. *J. Struct Eng.*
11. EC3, *Eurocode 3: Design of steel structures – Part 1-2: General rules – Structural fire design*. EN 1993-1-2, Brussels: CEN, 2005.
12. Gernay, T., Elhami Khorasani, N., Garlock, M.E.M. (2015). "Fragility analysis of a steel building in fire", in *Proc. of First Int. Conf. on Structural Safety under Fire and Blast- CONFAB, ASRANet Ltd, Glasgow, UK: 252-261.*
13. Franssen, J.M. (2005). SAFIR: A thermal/structural program for modeling structures under fire. *Eng J AISC, 42(3), 143-158*.
14. FEMA. (2014). *Hazus: MH 2.1 Technical Manual - Earthquake Model*. Developed by the Department of Homeland Security. Federal Emergency Management Agency. Mitigation Division. Washington, DC.
15. Elhami Khorasani, N., Gernay, T., Garlock, M. Modeling Post-Earthquake Fire Ignitions in a Community. Submitted.

Critical Parameters in Deriving Fire Fragility Functions for Steel Gravity Frames

THOMAS GERNAY, NEGAR ELHAMI KHORASANI and MARIA GARLOCK

ABSTRACT

Fire fragility functions can be used to characterize the probabilistic vulnerability of buildings to fire in the context of urban resilience assessment. A methodology has been proposed to develop such functions for multi-story steel buildings. However, a large number of parameters with uncertainties play a role in the process of constructing the fragility functions. The goal of this research is to identify the critical parameters that most affect the global fire safety by investigating the sensitivity of the fragility functions to different input parameters. Sensitivity in parameters affecting the fire model, the heat transfer process and the thermo-mechanical response is examined. The effects of different design assumptions at the system level are also studied. The presented approach is useful for selecting the prevailing parameters in a fire reliability analysis and it provides important information for modeling tools that can be used to evaluate resilience for fire scenarios.

INTRODUCTION

The standard approach in fire design of structures is mainly based on design at the component level using prescriptive approaches, where uncertainties in variables are not explicitly incorporated in the process. However, measured data indicate large uncertainty in the values of the parameters affecting the fire behavior of structures, including for instance fire load and material properties at elevated temperatures. An appealing way to measure these uncertainties is to develop fragility functions.

Fragility functions provide the probability of exceeding a damage state (e.g. column failure, excessive beam deflection, connection failure, etc.) for a given intensity measure of the hazard (fire in this case). The damage states are generally related to the structural performance level and can be grouped in different categories such as ‘no damage’, ‘slight’, ‘moderate’, ‘extensive’, and ‘complete’. Fragility functions can be used for evaluating losses at the scale of a community in the context of disaster resilience assessment [1].

Thomas Gernay, the National Fund for Scientific Research F.R.S.-FNRS, University of Liege, Allee de la Decouverte 9, 4000 Liege, Belgium. thomas.gernay@ulg.ac.be
Negar Elhami Khorasani, University at Buffalo, Buffalo, NY, U.S.A. negarkho@buffalo.edu
Maria Garlock, Princeton University, Princeton, NJ, U.S.A. mgarlock@princeton.edu

In the seismic engineering field, the approach of using fragility functions has been largely adopted. The scientific community has developed a suite of seismic fragility functions for different structural typologies, e.g. [2]. The method generally consists of deriving analytical fragility functions based on stochastic analyses of prototype buildings that are assumed to be representative of a typology. The parameters in the analyses are assumed to be random variables and Monte Carlo Simulations (MCS) are used to generate the distributions. Alternatively, empirical functions can be developed when sufficient historical damage data is available [3].

In this context, the present research aims at developing a framework for constructing fire fragility functions. Over the past years, research in fire engineering has started to progress toward the development of a performance-based framework that explicitly accounts for uncertainties. Contributions notably include the work by Lange et al. to establish a methodology for performance-based fire engineering of structures based on the seismic engineering framework developed in the Pacific Earthquake Engineering Research (PEER) Center [4]. However, the development of fire fragility functions in a system level approach to quantify structural vulnerability has not been addressed yet.

In a previous study [5], the authors developed a novel methodology to generate fire fragility functions, which measure the performance of an entire building system (rather than a single component). The fragility functions can be used to evaluate a city's resilience to fire hazard, including in case of multi-hazard cascading event such as fire following earthquake. However, the process of generating these fire fragility functions raises several important questions. The computational time for thousands of simulations (required by MCS) to model the performance of a building system under fire can be excessive. The large number of input parameters with uncertainty adds to the complexity of analysis and the computational time. For these parameters, probability distributions need to be assumed but rigorous data are often lacking. In order to prioritize the efforts in data collection and limit the complexity of the analyses, it is crucial to identify the parameters that most affect the global fire safety. Furthermore, the sensitivity of the results to different input parameters and assumptions should be quantified. Addressing these issues, this paper aims at identifying the most important input parameters, based on sensitivity analyses, to be considered as random variables when developing fire fragility functions for entire buildings.

METHODOLOGY

Fire Fragility Functions

The methodology for developing the fire fragility functions has been presented in detail in [5]. It requires the probabilistic assessment of the structural system performance under fire. This assessment takes into account uncertainties in the fire model, the heat transfer model and the structural response, in addition to fire scenarios at different locations in the building. The intensity measure selected as the control parameter to characterize the hazard is the fire load. For a given fire load q, MCS can be used to generate the probability density function (PDF) of demand and capacity relative to a given damage state. Convolution of the complementary cumulative distribution function (CDF) of demand $F_{D|q}(\cdot)$ with the PDF of capacity $f_C(\cdot)$ yields the probability of reaching the damage state $P_{F|q}$, according to Eq. 1.

$$P_{F|q} = \int_0^\infty \left[1 - F_{D|q}(T)\right] f_C(T)\,dT \tag{1}$$

The computation is performed for several levels of fire load in order to get the fragility points. Then, a fragility function can be fitted, typically assuming a two-parameter lognormal distribution function.

In this procedure, the random variable representing demand is the maximum temperature in the steel section (for a given fire load). Capacity is the critical temperature in the steel section relative to the given damage state (i.e. temperature at failure). The PDF obtained for demand and capacity are key for constructing the fragility functions. However, these PDF depend on the input parameters and modeling assumptions.

The fragility functions are first built at the component level, assuming a fire scenario in a well-defined compartment. These are referred to as local fragility functions (FFL). Then, building fragility functions (FFB) are built from the combination of the FFL for characterizing the overall vulnerability of the building [5]. In this second step, parameters at the system level may also influence the fire fragility functions (e.g. number of stories).

Building Prototype

For the sensitivity analysis, this paper focuses on a specific typology, namely a multi-story steel frame building. Similarly, a single damage state is considered, i.e. the failure of a frame column. The presented approach can be applied to other building typologies and damage states.

The considered building prototypes consist of steel structures with variable heights, designed based on the FEMA/SAC project for the Los Angeles area. Four prototype buildings are considered with 3, 6, 9, and 12 stories. The four prototype buildings have a similar 45.72 m by 45.72 m plan area, consisting of five bays in both directions (Figure 1). Each structure is composed of four moment resisting frames on the perimeter, and interior gravity frames. The columns of the interior frames are continuous but the beams have pinned connections (statically determinate beams). The work focuses on the vulnerability to fire for columns in an interior frame.

Analytical modeling for probabilistic assessment

This section describes the models that are used to assess the probabilistic fire performance of the building structure. The models are used in MCS for constructing the fire fragility functions. The input parameters in these models that are considered as random are discussed in the next section.

The Eurocode parametric fire model [6] is used to estimate the gas temperature evolution in the fire compartment. The nominal fire compartmentation of the buildings under study is based on a subdivision in compartments of 9.144 m long and 6.096 m wide. It is assumed that the fire remains contained in the compartment where it started.

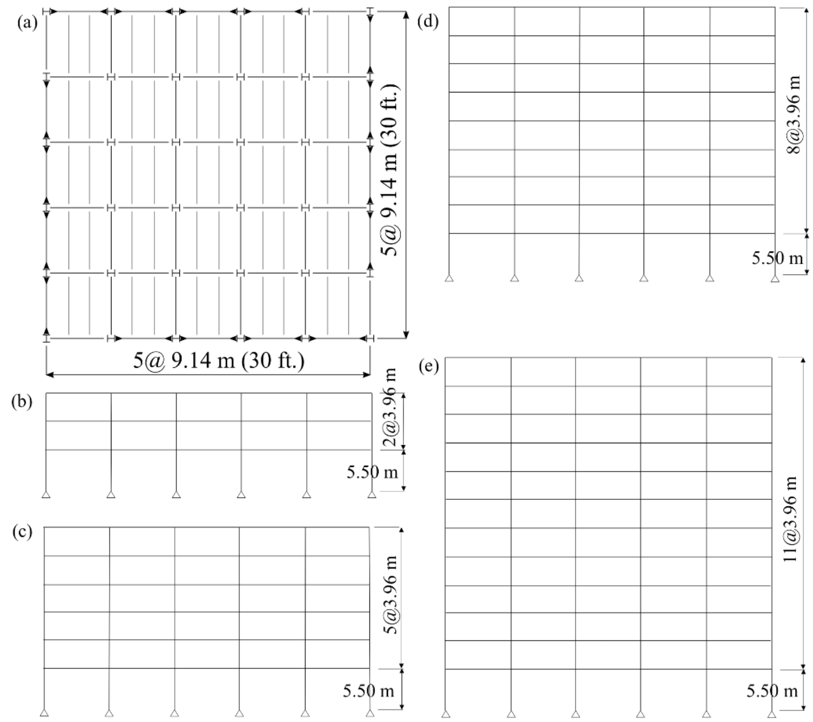

Figure 1. Steel gravity frames (a) plan and elevation of (b) 3-story, (c) 6-story, (d) 9-story, (e) 12-story.

Gypsum plasterboard is assumed as the lining material for walls and ceiling of the prototype building.

For heat transfer analysis, the finite difference formula of Eurocode 3 is adopted [7]. This formula, also referred to as lumped mass approach, yields the uniform temperature in the cross-section of a steel member at each time step and it can be used for insulated and bare steel members. This formula is used to get the maximum temperature reached in the section during the course of the natural fire; this maximum temperature is the demand placed on the member (see Eq. 1).

For structural response, the simple calculation model prescribed in Eurocode 3 is used [7]. This model allows one to calculate the design buckling resistance of a compression member with uniform temperature based on conservative assumptions. The moment of inertia corresponding to the member's weak axis is selected. Knowing the axial load on the column, the model yields the critical temperature at which failure is reached. Selection of a simplified model over a more sophisticated approach (e.g. nonlinear finite element modeling) is motivated by the need to run a large number of realizations for obtaining the PDF of capacity. For the studied prototype, the gravity frame columns are mainly subjected to compression with minor moment, because of the pinned connection with the beams. While thermal gradients create bending in the columns when heated on three faces, this effect does not affect significantly the critical temperature (for the prototype studied here). This has been verified by comparing a selected number of realizations with results of nonlinear finite element simulations.

Parameters with Uncertainty

The parameters with uncertainty considered in the study are listed in Table I. These parameters have been selected because they are expected to be the most significant sources of uncertainties based on literature and engineering judgment. Table I includes parameters affecting the demand and capacity at the component level, as well as different configurations at the system (building) level. Yet this list is not exhaustive and will be completed in further analyses.

TABLE I. LIST OF PARAMETERS WITH UNCERTAINTY.

Fire Fragility Local (FFL): component level		**Fire Fragility Building (FFB): system level**
Demand	**Capacity**	
Compartment geometry	Mechanical properties of steel	Fire resistance rating
Opening factor	Dead load	Fire exposed faces
Thermal conductivity of fireproofing	Live load	Building height
Thickness of fireproofing		Building occupancy

On the demand side, uncertainties in the following parameters of the fire model are considered: compartment geometry and opening factor. Fire load is also a varying parameter but it is a case apart as it is used as the intensity measure for fragility functions. The probabilistic model for thermal conductivity of fireproofing at elevated temperatures is based on experimental data and a Bayesian procedure [8]. A lognormal distribution is assumed for the thickness of fireproofing. On the capacity side, randomness in the mechanical properties of steel and in the applied gravity loads is considered.

At the system level, different fire resistance ratings are considered, which translates into different insulation thicknesses. The ratings range from no insulation to 3-hour fire resistance insulation based on prescriptive design. Note that the case with no insulation is potentially relevant in a cascading multi-hazard scenario, e.g. after an earthquake that would damage the insulation. Different configurations in terms of cross-section fire exposure are analyzed: three sides along the weak or strong axis, or four sides. The considered four building heights allow to span the different classifications (low, medium, and high-rise) based on Building Structure Categories for steel frames defined in Hazus [9]. Finally, the influence of different building occupancy is studied, e.g. re-assigning two stories as dwellings instead of offices.

RESULTS OF SENSITIVITY ANALYSIS

At the Component Level

For a fire in a given compartment, local fragility functions (FFL) are constructed to provide the probability of reaching the column failure as a function of the fire load. The objective is to identify the parameters that must necessarily be considered as random when constructing the FFL. This is done by analyzing the sensitivity of demand and capacity PDF's to the different input parameters.

For the sensitivity analysis, MCS are conducted using mean values for all input parameters except the one for which the values are selected randomly based on its probability distribution. This allows to isolate the effect of the variance of each input parameter on the variance in the output.

On the demand side, the output is the maximum temperature reached in the column section. Figure 2 shows a sample of results for a column section W14x68 protected with a prescriptive 2-hour fire rating. The plots show the mean, plus and minus one standard deviation, of the maximum steel temperature for different selected random parameters. The results are given for fire loads equal to 600 MJ/m² and 900 MJ/m². Each case is based on 200 simulations. The two values of mean and standard deviation provide a reasonable measure of uncertainty since the results follow a normal distribution. The parameters 'compartment geometry' and 'opening factor' influence the fire model, whereas the parameters related to fireproofing influence the heat transfer model. Figure 2 shows that uncertainties in both the fire model and the heat transfer model cause significant variance in demand. The opening factor is the parameter that least influences the demand, yet its influence is not negligible.

On the capacity side, the output is the critical temperature at which the column fails. Figure 3 shows a sample of results for a column section W14x68. The column capacity does not depend on the characteristics of the fire (such as the fire load). However, it depends on the story level, because the story influences the load on the column. The results are given for columns at the fifth and sixth story of the nine-story building. The randomness in steel mechanical properties at elevated temperature contributes the most to the variance of the capacity. In contrast, the influence of live load is negligible. For the studied prototype, live load could be considered as deterministic.

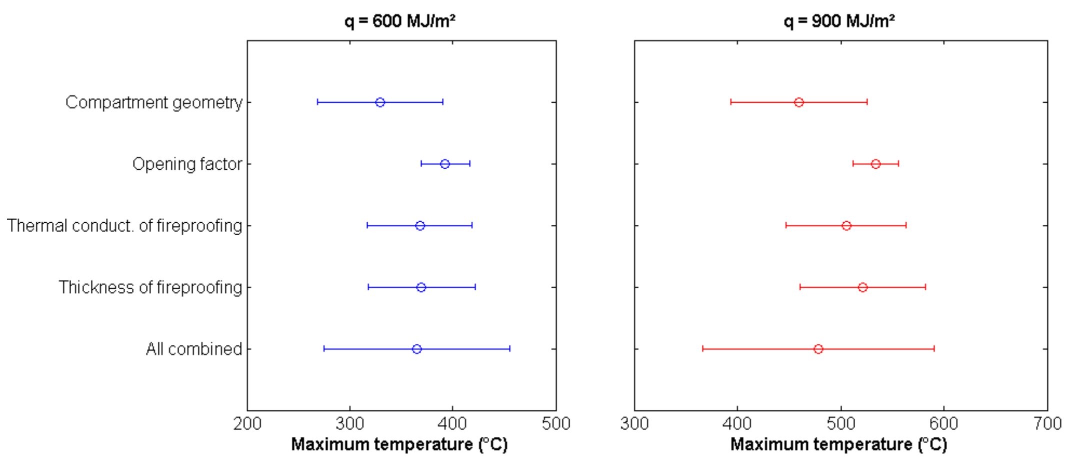

Figure 2. Sensitivity of maximum steel temperature to demand parameters for a W14x68 section.

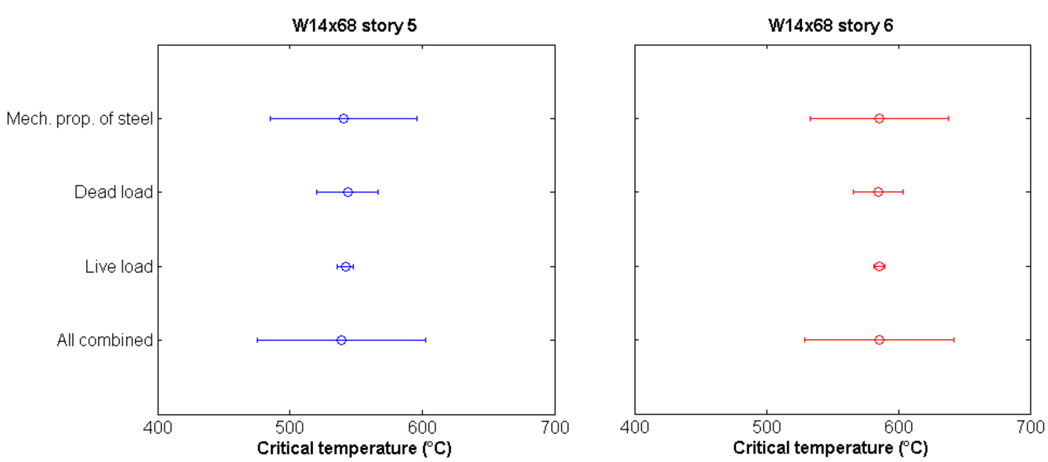

Figure 3. Sensitivity of steel temperature at failure to capacity parameters for a W14x68 section.

At the System Level

At the system level, the FFL constructed for each different compartment fire locations in the building are combined to obtain the building fragility functions (FFB) representative of the vulnerability of the entire building. At this scale, the objective is to investigate the sensitivity of the FFB to different design assumptions for the prototype building. This allows one to discuss the effects of various parameters on the global fire safety of the building.

In constructing the fragility functions, all parameters listed in Table I at the component level are assumed as probabilistic. The functions are successively built for different values of the system level parameters (e.g. for different building heights).

Figure 4 shows a sample of results. Fig. 4a shows that the number (3 or 4 sided fire) and orientation of fire-exposed faces (along weak or strong axis) of the columns influences the fragility curve of the building for column damage state. The building is more vulnerable if the columns are exposed on four faces than on three faces, because of the faster temperature increase that the former generates. Note that the results are given for a fireproofing thickness design independent of the number of fire-exposed faces (for instance the compartmentation layout may vary during the lifetime of the building, without retrofit of the fireproofing). Interestingly, Fig. 4a shows that a building whose columns are exposed on four faces needs a 3h fireproof rating to reach the same reliability level as a building with a 2h fireproof rating whose columns are exposed on three faces along the weak axis. Hence, the fire safety can be improved by reducing the number of fire exposed faces of columns, as an alternative to adding more fire protection.

Fig. 4b shows that the fire rating influences the building fragility curves. However, the building height does not have any significant influence. It should be noted that when the height of a building increases, the probability to have a fire ignition increases, but the conditional vulnerability should a fire start is approximately unchanged. For the considered prototype building, the fire rating requirement for the frame columns is typically 2h (it is 3h for the 12-story building). According to the obtained results, this requirement allows to reach low probability of failure for typical values of the fire load (in the range 300-800 MJ/m²).

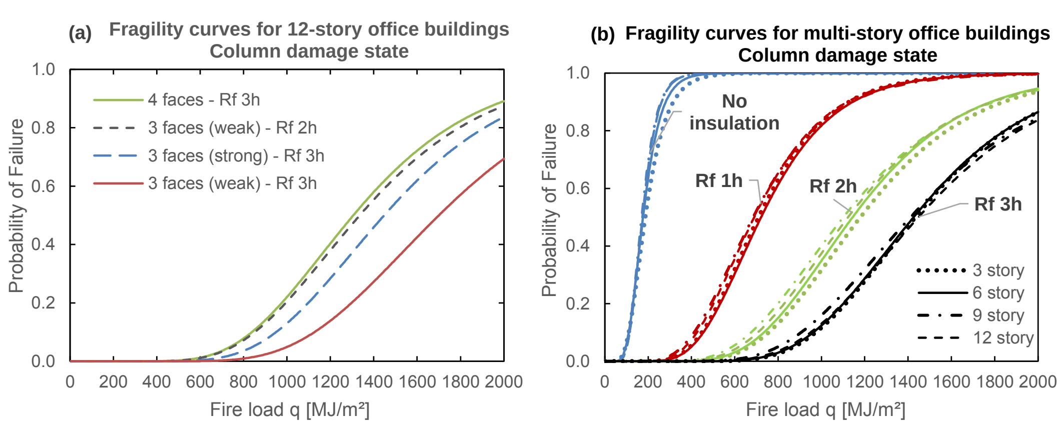

Figure 4. Sensitivity of fire fragility curves to (a) fire exposed faces of column (b) fire resistance rating and building height.

The building occupancy influences the probability of fire occurrence. This has no effect on the FFB when the occupancy is homogeneous in the building, because FFB gives conditional probabilities. Hence, changing the occupancy of a whole building from offices to dwellings does not affect at all the fragility functions of this building. However, the occupancy may affect the FFB when a different occupancy is assigned to part of the building only. In that case, the relative likelihood of a fire event is modified in that part of the building. This leads to assigning different weights to some of the FFL in the process of constructing combined functions. If a part of the structure is particularly vulnerable and its occupancy is such that the relative likelihood of a fire event in this part increases, then the overall vulnerability of the building to fire increases as well.

CONCLUSION

The sensitivity of fire fragility functions is quantified with regards to the effects of the uncertainties in the prevailing parameters. The presented approach allows one to evaluate which parameters should consider randomness and which could be assumed as deterministic. This approach is important in order to prioritize the efforts in data collection and limit the complexity of the probabilistic analyses. The obtained results have implications for modeling tools that can be used to evaluate community resilience for fire scenarios.

The study focuses on a specific building typology consisting in a multi-story steel frame structure. Fire fragility functions should be developed for other building typologies and similar sensitivity analyses should be conducted to identify the parameters that affect global fire safety for these different typologies.

REFERENCES

1. Cimellaro, G. P., A.M. Reinhorn, and M. Bruneau. 2010. "Framework for analytical quantification of disaster resilience", *Engineering Structures*, 32(11): 3639-3649.
2. Rota, M., A. Penna, and G. Magenes. 2010. "A methodology for deriving analytical fragility curves for masonry buildings based on stochastic nonlinear analyses", *Eng Struct*, 32(5): 1312-1323.
3. Shinozuka, M., M.G. Feng, J. Lee, and T. Naganuma. 2000. "Statistical Analysis of Fragility Curves", *Journal of Engineering Mechanics*, 126(12): 1224-1231.
4. Lange, D., S. Devaney, and A. Usmani. 2014. "An application of the PEER performance based earthquake engineering framework to structures in fire", *Engineering Structures*, 66(0): 100-115.
5. Gernay, T., N. Elhami Khorasani, and M. Garlock. 2016. "Fire Fragility Curves for Steel Buildings in a Community Context: A Methodology", *Engineering Structures*, 113: 259-276.
6. EC1. 2002. *Eurocode 1: Actions on structures – Part 1-2: General actions – Actions on structures exposed to fire*. EN 1991-1-2, Brussels: CEN.
7. EC3. 2005. *Eurocode 3: design of steel structures – Part 1–2: General rules – structural fire design*. EN 1993-1-2. Brussels: CEN.
8. Elhami Khorasani N, P. Gardoni, and M. Garlock. 2015. "Probabilistic fire analysis: material models and evaluation of steel structural members", *J Struct Eng ASCE*, 141(12):04015050.
9. NIBS National Institute of Buildings Sciences. 1999. *HAZUS, earthquake loss estimation technology*, FEMA, Washington, DC.

Applying Uncertainty Quantification in Modelling of a Steel Beam Exposed to Fire

JOHAN ANDERSON, DAVID LANGE and LARS BOSTROM

ABSTRACT

Modelling of structures exposed to fires is prone to be heavily influenced by uncertainties in geometrical parameters, thermal material data as well as uncertainties in the boundary conditions. Assessing the effects and influences in variations of all the uncertain parameters is often cumbersome and traditional methods are impractical thus modelling of the total uncertainty is needed. Uncertainty Quantification with deterministic sampling is one possible way ahead to accommodate and evaluating the effects of uncertainties with as few repeated simulations as possible. In this paper the uncertainties stemming from error in the input data and boundary conditions on one example of a steel beam under four point bending exposed to fire is evaluated.

INTRODUCTION

Due to the lack of knowledge of the precise details of the system, seemingly random behavior can be governed by deterministic, though non-linear models. Thus, in such systems small variations may have a significant change in the outcome. Most of the calculations both numerical and analytical are often performed with very little thought given to these uncertainties and thus designs are many times based on potentially inaccurate information. Moreover, modelling is often performed in stages by different numerical or analytical tools where the uncertainties may propagate through the system without much control [1]. It is usually a very difficult task to objectively establish the confidence levels in numerical predictions. Uncertainty Quantification (UQ) is the science of quantitative characterization and reduction of uncertainties in numerical studies and real world experimentation. UQ aims at determining how likely certain outcomes are if some aspects of the system are unknown.

Examples in fire engineering which account for uncertainties mostly rely on brute force Monte Carlo simulation to evaluate the uncertainties in models of, e.g. reinforced concrete columns [2], prestressed concrete beams [3], of reinforced concrete slabs [4], or of steel beams [5]. Methods which have been developed for reliability analysis have been incorporated within the OpenSEES software to add probabilistic hazard analysis and reliability calculation of structures for fire [6]. Furthermore, development of fragility curves of steel buildings for fire loading [7], and the application of the PEER PBEE framework to structures in fire [8, 9] have been investigated.

Deterministic Sampling (DS) [10] is a relatively new method used for Uncertainty Quantification (UQ), is employed in this paper to offer an efficient alternative to other methods of UQ such as, e.g. random sampling. The method is based on the idea that a continuous probability density function can be replaced by an ensemble of discrete deterministic samples, provided that the two representations have the same statistical moments.

In this paper one framework for working on uncertainties and probabilistic modeling of uncertainties in the input data as well as boundary conditions is applied. In the numerical investigation uncertainties will be associated with a number of input parameters regarding the tolerances in the geometry, boundary conditions and the thermal material models. More specifically we further investigate this case by quantifying the errors stemming from the uncertainties in the input data.

DETERMINISTIC SAMPLING

DS has been demonstrated in the past as a means for quality assurance in CFD simulations [11, 12]. In such applications it is of great importance in order to provide reliable simulations and the possibility of validation against experimental results. In this section a short summary of the theoretical background that is the basis for the explicit choices of ensembles used in this work is given.

In the absence of correlations, the ensemble of m samples is given by,

$$\Sigma = \langle\theta\rangle \otimes 1^{1\times m} + \mathrm{diag}\left(\langle\theta\rangle \circ \mathrm{std}\left(\frac{\theta}{\langle\theta\rangle}\right)\right)\cdot \hat{V} \tag{1}$$

where $1^{1\times m}$ denotes a row vector of m 'ones', $\otimes$ outer product, $\circ$ element-wise multiplication, and $\mathrm{diag}(\mathrm{X})$ is the diagonal matrix with the vector X on its diagonal. The excitation matrix $\hat{V}$ contains all variations which will be applied in the deterministic sampling procedure; each column describes one 'normalized' model sample variation from its mean.

In the example which will be given, seven parameters are considered as uncertain in the model. The suggested ensembles may be formed in a number of ways, for example, for $n = 7$ uncertain parameters the standard (STD) ensemble can be used,

$$\hat{V}_{STD} = \sqrt{n} \cdot \left(I_{n\times n} \quad - I_{n\times n} \right) =$$

$$\begin{pmatrix}
\sqrt{7} & 0 & 0 & 0 & 0 & 0 & 0 & -\sqrt{7} & 0 & 0 & 0 & 0 & 0 & 0 \\
0 & \sqrt{7} & 0 & 0 & 0 & 0 & 0 & 0 & -\sqrt{7} & 0 & 0 & 0 & 0 & 0 \\
0 & 0 & \sqrt{7} & 0 & 0 & 0 & 0 & 0 & 0 & -\sqrt{7} & 0 & 0 & 0 & 0 \\
0 & 0 & 0 & \sqrt{7} & 0 & 0 & 0 & 0 & 0 & 0 & -\sqrt{7} & 0 & 0 & 0 \\
0 & 0 & 0 & 0 & \sqrt{7} & 0 & 0 & 0 & 0 & 0 & 0 & -\sqrt{7} & 0 & 0 \\
0 & 0 & 0 & 0 & 0 & \sqrt{7} & 0 & 0 & 0 & 0 & 0 & 0 & -\sqrt{7} & 0 \\
0 & 0 & 0 & 0 & 0 & 0 & \sqrt{7} & 0 & 0 & 0 & 0 & 0 & 0 & -\sqrt{7}
\end{pmatrix}$$

Another example is the binary (BIN) ensemble,

$$\hat{V}_{BIN} = \begin{pmatrix}
+1 & -1 & +1 & -1 & +1 & -1 & +1 & -1 \\
+1 & +1 & -1 & -1 & +1 & +1 & -1 & -1 \\
-1 & +1 & +1 & -1 & -1 & +1 & +1 & -1 \\
+1 & +1 & +1 & +1 & -1 & -1 & -1 & -1 \\
-1 & -1 & +1 & +1 & +1 & +1 & -1 & -1 \\
-1 & +1 & +1 & -1 & +1 & -1 & -1 & +1 \\
+1 & -1 & +1 & -1 & -1 & +1 & -1 & +1
\end{pmatrix}$$

The maximum variation of the standard ensemble is $\sqrt{7}$, while it is only 1 for the binary. By varying all parameters in all samples of the binary ensemble, its maximum variation is minimized. The risk of 'saturating' the model is thereby minimal with the BIN ensemble. The standard ensemble is easily generalized, but the binary ensemble has a more complex construction. The model ensemble can be calculated by evaluating the model H for every sample (column) of Σ, producing the row vector $H(\Sigma)$ of m results. The expected result is given by,

$$\langle H \rangle = \langle H(\Sigma) \rangle = H(\Sigma) \cdot (1/m)^{m\times 1} \tag{2}$$

Compare with $H(\langle \theta \rangle)$ (ordinary deterministic result) to have an idea about non-linear effects. If the difference is large, non-linear effects are significant. If the difference is small, it is not sure that the model can be approximated to be linear, even though it is likely.

The variance of the model result is given by:

$$\mathrm{var}(H) = \left\langle \left(H(\Sigma) - \langle H(\Sigma) \rangle \right)^2 \right\rangle = \left(H(\Sigma) - \langle H(\Sigma) \rangle \cdot 1^{1\times m} \right)^2 \cdot (1/m)^{m\times 1}$$ 3)

Assuming a coverage factor $k = 2$ for also the result, the modeling uncertainty will be:

$$\mathrm{unc}(\mathrm{H}) = 2\sqrt{\mathrm{var}(H)} \tag{4}$$

In summary, the confidence interval of the modeling result is given by:

$$\left[\langle \mathrm{H} \rangle - 2\sqrt{\mathrm{var}(H)}, \langle \mathrm{H} \rangle + 2\sqrt{\mathrm{var}(H)}\right] \tag{5}$$

The methodology will now be utilized to assess uncertainties in a structural model of a HEB beam exposed to the standard fire.

UNCERTAINTY QUANTIFICATION OF A STEEL BEAM

A Round Robin (RR) exercise of modelling of a loaded steel beam exposed to a standard fire test was recently carried out and which showed large deviations in modelling results [13]. The object of the study was an HEB 300 steel beam of grade S355. The beam had a total length of 5400 mm, and a span of 5200 mm between the supports. Loading was applied at two points, 1400 mm from either support. At both the supports and the points of loading application web stiffeners were welded to the steel beam. The stiffeners had a thickness of 15 mm. Separately to the modelling round robin a testing round robin was also carried out on the same subject [14]. This example is used to illustrate the DS technique since it is a good source of experimental data as well as a good illustration of both the modelling uncertainty and the testing uncertainty.

For the DS procedure, the test was modelled using the Abaqus Standard Finite Element solver, using 30 Timoshenko beam elements. The stiffeners are not accounted for. Boundary conditions were simply supported and the material properties were based on those in Eurocode 3 Part 1-2 [15]. Thermal loading was calculated assuming lumped capacitance and this was applied as a uniform temperature to the cross section of the beam. The applied loads, created a uniform bending moment of 140 kNm between the loading points. The steel beam was exposed to the standard fire until failure. One peculiar observation was that seemingly similar physical models yielded large variations in the output failure times.

In order to be able to make comparisons between random sampling and DS an efficient simulation strategy was needed, involving a reduced set of uncertain parameters in models with low computational cost where both brute force Monte Carlo (MC) simulations could be used as well as DS with propagation of moments. In particular the effect on the failure time of variations in the thermal input data is studied. It has been shown that the proposed method is more efficient in reducing the number of samples needed to accommodate for adequate propagation of moments in a non-linear system [11-12].

The modelling approach described above is fast and suitable for both DS and MC analyses. The analysis was performed in steps where all parameters were sorted into the groups: 1. tolerances in geometry and loading; and 2. mechanical and thermal properties and the fire load. The uncertain parameters in the model are summarized in Table 2.

TABLE 1. THE PARAMETERS WITH UNCERTAINTY CONSIDERED IN THE UQ.

Parameter set	1	Parameter set	2
Length between supports	5200 – 5210 mm	Emissivity	0.7 ± 0.2
Flange width	300 ± 0.1mm	Heat transfer coeff.	25 ± 10 W/(K m)

Flange thickness	19 ± 0.1 mm	Yield stress	355 ± 7 MPa
Web depth	262 ± 0.1mm	Density	7850 ± 150 kg/m^3
Web thickness	11 ± 0.1mm	Elongation	14e-6 ± 2%
Load position 1	1400 ± 10mm	Load	10 000 ± 10 kg
Load position 2	3800 ± 10mm	Youngs modulus	210 ± 5 GPa

The temperature – time relation is assumed to be the standard temperature time curve with no variation. The variation of the steel properties with increased temperature is taken from the Eurocode [15]. Failure criteria of a maximum allowed deflection and a maximum rate of deflection as specified in the standard for testing of fire exposed structures was used to allow a comparison between the model of the failure time of the structure: the maximum deflection is $D = L^2/(400\ d) = 225$mm and the maximum of the rate of deflection is $dD/dt = L^2/(9000d) = 10$mm/min.

The resulting failure times of the analysis using DS and MC are summarized in Table 2. Two sets of deterministic sampling were performed, one for parameter set 1 (DS1) and one for parameter set 2 (DS2) and the combined result (DS) in comparison to the MC case with 2000 samples with uncertainties stemming from parameter set 2. The results show that the mean failure time is slightly overestimated by about one minute and the standard deviation is larger for the combined set and in a direct comparison of the analysis of parameter set 2. Note in the DS methodology the variations with the standard deviations are used whereas in the random sampling a large amount of the samples have significantly smaller variations.

TABLE 2. FAILURE TIMES FROM DETERMINISTIC SAMPLING AND RANDOM SAMPLING.

Method	Mean [min]	StDev	Number of samples
DS	23.4	3.17	16
DS1	22.8	1.82	8
DS2	23.9	2.61	8
MC	22.5	1.93	2000

In order to elucidate on the differences between the two approaches of sampling the time histories of the deflections, the probability density functions (PDFs) and the convergence of mean and standard deviation are evaluated.

In Figure 1a, the deflection as a function of time displayed for the eight samples where the parameters in set 1 is modelled uncertain corresponding to DS1 is shown. Along with the distinct samples also the mean and mean value plus/minus one standard deviation are shown. Note that, although the maximum deflection failure criterion is shown as a horizontal dashed line the second criterion of rate of deflection is participating in determining the failure times. Most of the time histories are approximately within one standard deviation from the mean, with some exceptions. A comparison between the PDFs from deterministic sampling (DS2), random sampling and the distribution between different models as found in the above referenced robin study on the same example [13] is shown in Figure 1b.

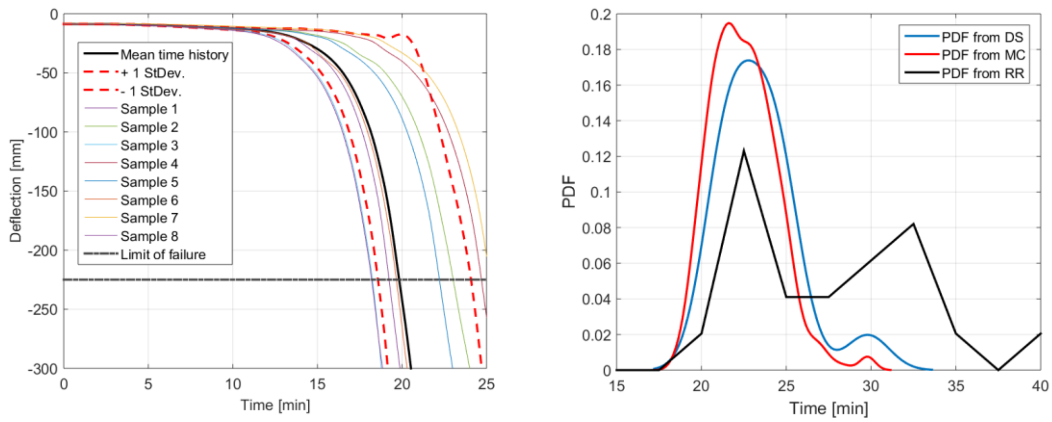

Figure 1a and 1b. The time history [minutes] of the deflection [mm] (left) and the probability distribution of the failure times from 8 samples DS, 2000 samples MC and from the Round Robin of calculations performed on the same system.

In the round robin 17 models were submitted using different modelling strategies such as simple calculation tools and several different FE models using a variety of FE softwares. As can be seen the spread from this exercise was rather large however a rather comprehensive result is obtained which has a peak which corresponds well with the result of variations in the input data from this particular model. Note that similar FE models were included in the round robin. Any other similarities in the distributions, however, can only be considered to be coincidence since the input data for the round robin study largely corresponded with the average values used as input for the modelling done in this paper. A quite remarkable resemblence between the PDFs obtained by 8 samples and 2000 samples is visible although the method of DS cannot give a good represention of the full PDF in the same manner as with random sampling. Furthermore, additional samples to the deterministic method would efficiently increase the accuracy of the the mean and variance as is it gives a slightly higher mean value of around one minute. Thus the failure time prediction would be slightly higher in this case by only using 8 samples. To increase the accuracy of the modelling it is important to investigate if parameters influence each other (correlation) in a study of covariancies of the system, which can be used to determine a minimal set of extra simulations.

In all cases where random sampling is used, the convergence of the results is of great interest. The convergence of mean and standard deviation of failure times in the MC analysis is shown in Figures 2a and 2b. It is found that the mean converges quite fast however the standard deviation is only approximately converged after 400 samples. Thus the random sampling method slowly converges to a stable PDF. Here it is pertinent to remind the reader that it is usually only the mean value and the spread that is of interest when predicting failure times and not the full PDF.

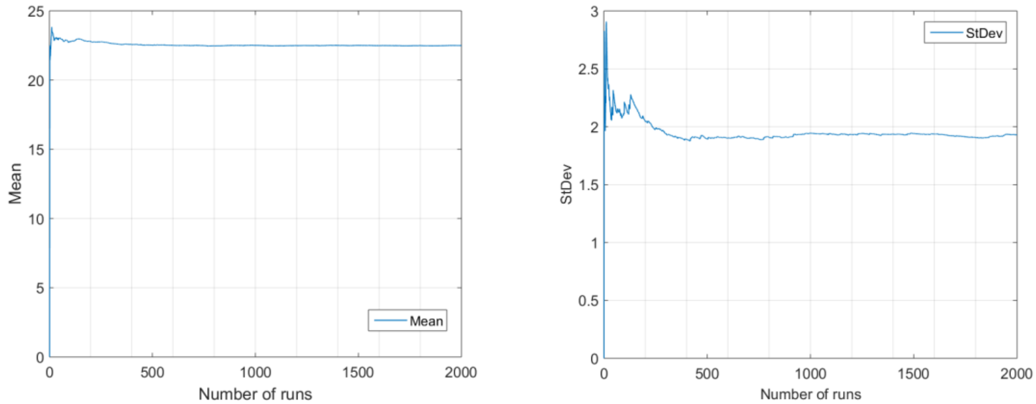

Figure 2a and 2b. The convergence of mean and standard deviation (StDev) with number of runs/samples.

SUMMARY

This paper has illustrated how to use deterministic sampling to assess uncertainties stemming from unknown errors in the input data and boundary conditions. An alternative way to carry out a sensitivity analysis to estimate the total uncertainty in the failure time analysis of a steel beam exposed to fire is shown. In the paper two different modelling strategies of uncertainties using DS and MC are compared. The propagation of uncertainties in a FE model consisting of beam elements with lumped heat assumption is evaluated.

The example took advantage of a relatively simple model with beam elements which had short computation times, although it could equally be applied to a more complex example. Additional sources of uncertainties not accounted for in the study presented include the parameters in the material models at high temperature where rather large variations may be expected. However, the temperature dependencies are kept constant in this work.

It was here possible to assess the differences between this particular deterministic sampling process with a random sampling approach. It is shown that by a very limited set of samples we can obtain similar quantitative information as per random sampling however in a much more efficient way. The mean values were slightly larger however good correspondence was found.

One other possible way to restrict the number of samples is to utilize stratified sampling methods such as Latin Hypercube Sampling (LHS), however this was out of the scope of the present study. It has been seen that the efficiency of the proposed deterministic sampling method is usually higher than using LHS since fewer simulations are needed, however a comparison between the DS methods and the LHS method may constitute future work.

Moreover these types of analyses can point out sources of uncertainty that can be reduced, leading to more reliable simulations. More accurate input from modeling is invaluable as background information for decision making as it result in great benefits to society. Such benefits include safer and better functioning products, reduced prices, reduction in usage of raw materials and reduced environmental impact.

In the future we will investigate the effects of 2D and 3D thermal modeling and structural modelling as well as detailed comparison of the effects of variations in the thermal boundary conditions, thermal material models as well as the grade of the steel.

In the structural analysis we will compare variations stemming from using beam and shell elements as well as implementations in different software such as, e.g. SAFIR and OpenSEES.

REFERENCES

1. Quality Management in Engineering Simulation, A Primer for NAFEMS QSS, NAFEMS 2014.
2. Christopher D. Eamon, Elin Jensen; Reliability analysis of reinforced concrete columns exposed to fire; doi:10.1016/j.firesaf.2013.10.002
3. Christopher D. Eamon, Elin Jensen, Reliability analysis of prestressed concrete beams exposed to fire, doi:10.1016/j.engstruct.2012.05.016
4. Ruben Van Coile, Robby Caspeele, Luc Taerwe, Reliability-based evaluation of the inherent safety presumptions in common fire safety design; doi:10.1016/j.engstruct.2014.06.007
5. Qianru Guo, Kaihang Shi, Zili Jia, Ann E. Jeffers, Probabilistic Evaluation of Structural Fire Resistance, 10.1007/s10694-012-0293-6
6. Negar Elhami Khorasani, Maria E.M. Garlock, Spencer E. Quiel, Modeling steel structures in OpenSees: Enhancements for fire and multi-hazard probabilistic analyses, doi:10.1016/j.compstruc.2015.05.025
7. Thomas Gernay, Negar Elhami Khorasani, Maria Garlock, Fire fragility curves for steel buildings in a community context: A methodology, doi:10.1016/j.engstruct.2016.01.043
8. Shaun Devaney, Development of Software for Reliability Based Design of Steel Framed Structures in Fire, Doctor of Philosophy The University of Edinburgh 2014.
9. David Lange, Shaun Devaney, Asif Usmani; An application of the PEER PBEE framework to Structures in Fire, 10.1016/j.engstruct.2014.01.052
10. Jan Peter Hessling, “Deterministic sampling of propagating model covariance.” SIAM/ASA J. Uncertainty Quantification Vol. 1, pp 297-318 (2013).
11. P. Hedberg and P. Hessling, “Use of deterministic sampling for uncertainty quantification in CFD”, submitted for publication 2015.
12. J. Anderson, Lars Boström, Robert Jansson McNamee and Bojan Milovanović, Uncertainties in Façade Fire Tests – Measurements and Modelling, The second international seminar for fire safety of façades, Lund 11-13 May 2016.
13. David Lange and Lars Boström, “Round robin on calculations: Steel beam with standard fire exposure”, SP Report 2015:25 (2015).
14. Dumont, F.; Boström, L.; Lukomski, M.; van den Berg, G.; Summary report of the EGOLF round robin ntr. TC2 14-1 in fire resistance testing; the European Group of Laboratories for Fire Testing (EGOLF); 2015; available from http://www.egolf.org.uk/
15. Eurocode 3: Design of steel structures- Part 1 and 2. SS-EN 1993 – 1 – 2:2005/AC:2009.

Intensity Measures for Probabilistic Structural Fire Engineering

PETER MOSS, ANTHONY ABU and RAJESH DHAKAL

ABSTRACT

A framework for probabilistic structural fire engineering has recently been proposed. It is based on the Pacific Earthquake Engineering Research Center Performance-Based Earthquake Engineering approach which performs a hazard analysis, structural analysis and loss analysis to assess a building's performance as a result of ground motions. Similar to earthquake engineering, the assessment in fire requires the calculation of intensity measures, engineering demand parameters, damage measures and decision variables for a full assessment of the fire effects, the structural response, the extent of damage and the resulting loss. A number of fire intensity measures have been proposed by a few authors. However, these have been found to only partially reflect the severity of the fire, thereby not uniquely capturing the consequent structural response. For realistic assessments of damage and costs of reinstatement, more appropriate intensity measures are required. Using a two-span reinforced concrete beam as an example, the present research identifies ideal intensity measures by investigating several alternatives and selecting the one with the least dispersion of results with engineering demand parameters.

INTRODUCTION

Traditional design of structures for fire conditions tends to concentrate on a worst case scenario fire which the structure should adequately resist. Depending on the jurisdiction of the particular building this fire could be simply interpreted as a fire resistance rating (FRR) – the minimum fire resistance required - or a well-defined fire with a growth phase and a decay phase. With the advent of sophisticated analysis tools, a deeper appreciation of the benefits of global structural behavior under fire conditions and structural optimization the design of structures for fire conditions increasingly investigates a number of potential fire scenarios, as different components of the structure would be challenged differently under each fire scenario.

Peter Moss, University of Canterbury, Private Bag 4800, Christchurch 8140, New Zealand.
Anthony Abu, University of Canterbury, Private Bag 4800, Christchurch 8140, New Zealand.
Rajesh Dhakal, University of Canterbury, Private Bag 4800, Christchurch 8140, New Zealand.

As none of these fires are guaranteed to occur in a building, it is prudent to develop probabilistic methodologies to assess structural response in fire conditions. A probabilistic approach will account for the likelihood (i.e. probability) of different fire characteristics in addition to accurate predictions of structural behavior (temperature, deflection, failure time, etc.), currently provided by the deterministic process. Apart from the obvious advantages in structural assessment these tools will also aid in financial loss estimation of buildings subjected to fires.

A methodology for probabilistic structural fire engineering has already been proposed. This is based on the Pacific Earthquake Engineering Research (PEER) Center's approach for probabilistic assessment of buildings subjected to earthquake ground motions. The approach performs a hazard analysis, structural analysis, a damage assessment and a loss assessment. These assessments are linked by pinch variables that assess the likelihood of an event based on the occurrence of another. In the PEER framework they are identified by the annual probabilities of exceedance of an event. The variables associated with each of the four stages are: intensity measure (IM), engineering demand parameter (EDP), damage measure (DM) and decision variable (DV), respectively. A suitable intensity measure (IM) is a variable which efficiently and sufficiently describes the severity of an event, such as spectral acceleration, peak ground acceleration and peak ground velocity. Engineering demand parameters (EDPs) are variables which quantify the response of the structure. Some EDPs are inter-story drift ratios, inelastic deformations, strains and floor acceleration. Damage measure (DM) is a variable which provides information about the level of damage that has occurred to the structure. DM helps to quantify the required repairs and functionality of the structure. Finally, decision variables (DVs) are described based on the performance of the facility of greatest interest to stakeholders, in terms of cost or downtime [1].

The framework in structural fire engineering is the same, except that the hazard here is fire [2, 3]. As such, ideal pinch variables (IM, EDP, DM and DV) need to be identified to make the process robust. Examples of potential intensity measures include fire duration, peak fire temperature, fuel load, total heat energy (i.e. cumulative radiant and convective heat), heat release rate, normalized heat release rate, etc. For a given type and value of IM, several time temperature profiles can exist but, unlike the earthquake situation, a single fire profile cannot be scaled to cover a wide range of the IM from a small value that results in no damage to a large value that causes structural collapse. Instead, a suite of fires need to be simulated based on a range of different fuel loads, lining factors, and ventilation factors. The next interrelation required in the process is between the IM and an engineering demand parameter (EDP). Examples of potential EDPs are maximum deformation, maximum section temperature, time of failure and maximum bending moment. The EDP needs to be correlated with a damage measure (DM), such as no damage, spalling, collapse, etc., which will be indicative of loss/cost.

The focus of the current study therefore is on the identification of ideal intensity measures. Following research in earthquake engineering ideal intensity measures must meet the following criteria: efficiency, sufficiency, scaling robustness, hazard computability and predictability [4, 5]. An efficient IM provides relatively smaller dispersion of the response of the structure. It reduces the number of analyses required to achieve a desired level of confidence in the response of the EDP. A sufficient IM is independent of hazard characteristics. In fire engineering terms a sufficient IM would not distinguish between a short duration high-temperature fire and a long-duration low-temperature fire, if they produced the same structural response. Another property of a good IM is that when records are scaled to a target IM, the value results in an unbiased structural response compared to an unscaled fire. However, as mentioned earlier it is unreasonable to scale fires, as a change in either duration or peak temperature affects the whole shape of the time-temperature curve. The choice of an IM is also based on hazard computability. It is defined as the level of effort required to calculate the proposed IM. IMs such as peak temperature and the area under a fire curve are readily available while others like rebar temperatures require considerable effort to obtain. The predictability of an IM is the accuracy with which it can be predicted. If the predictability of an IM is poor, then the accuracy in predicting the structural response will also be poor. While all these properties are important, and will be investigated in detail in subsequent studies, the current paper focuses on efficiency only.

The study examines a relatively simple problem of a loaded two-span reinforced concrete beam subjected to a variety of Eurocode parametric fires. The analysis calculates the temperatures of the beam components and estimates the structural response of the beam on exposure to each of the fires. As the selection of intensity measure (IM) depends on the choice of engineering demand parameter (EDP), the study investigates four EDPs: maximum displacement, maximum reinforcing temperature, maximum concrete temperature and maximum and minimum bending moments. Nine IMs (maximum fire temperature, maximum reinforcing temperature, maximum concrete temperature, total heat energy, time of maximum displacement, time to maximum fire temperature, time to maximum reinforcing temperature, fire duration and fuel load) are also investigated. As mentioned earlier, the most efficient IM, given a particular EDP, is the one that produces the least dispersion in the EDP results. This is an extension of the work by Moss et al. [6], which only investigated two intensity measures.

PROBLEM: TWO-BAY CONTINUOUS BEAM

A series of SAFIR analysis of a simple two span reinforced concrete beam (see Figure 1) subjected to different fire profiles were conducted. The beam has one support horizontally restrained, with the other supports free to move longitudinally. Both bays of the three-side-exposed beam were subjected to a four-hour parametric fire following Eurocode 1 Part 1.2 [7]. The beam was designed according to the rules of DIN 1045-1. The possibility of the occurrence of a fire was not taken into account during the design process [8]. The top reinforcement was curtailed following the given design rules. The bottom reinforcement was continuous through the beam and was not curtailed. As is observed from Figure 1 the individual spans of the beam were 6.0 m with a depth of 600 mm and width 300 mm. It was designed for total dead and live loads of 34.0 kN/m and 9.0 kN/m respectively with concrete compressive strength of 30 MPa and 16 mm diameter cold-worked steel reinforcement of yield strength 500 MPa.

A series of parametric fires were generated using six fuel loads: 200, 500, 750, 1000, 1250 and 1500 MJ/m^2, three lining factors: 500, 1250, and 2000, and six ventilation factors: 0.065, 0.092, 0.119, 0.146, 0.173 and 0.200. The resulting fire curves (time-temperature relationships) peaked at different times, reaching different peak temperatures. This series produced 108 fires.

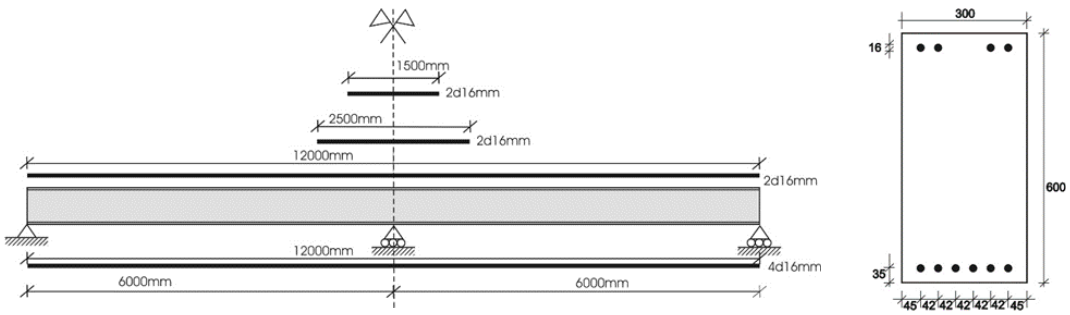

Figure 1. Continuous two-bay beam profile and cross-section, showing rebar arrangement.

Incremental Fire Analysis

Structural fire analysis is required to calculate the EDPs due to a given fire profile (i.e. for a given value of IM). By conducting fire analyses on a structure with a suite of fire profiles, several different values of EDPs can be generated for each discrete value of IM, and these data can be probabilistically interpreted in terms of medians and standard deviations. The authors have proposed that this process be called incremental fire analysis (IFA) [6], analogous to incremental dynamic analysis (IDA) in earthquake engineering. Once sufficient fire profiles had been generated, the loaded continuous beam was subjected to each of these fires. The maximum value of the vertical displacement of the beam during the fire duration (including cooling phase), together with the minimum span bending moment and the maximum bending moment at the central support were extracted from the results as possible EDPs in addition to the maximum reinforcing temperature and the maximum concrete temperature. This EDP data was processed statistically to check the distribution they follow. In earthquake engineering, displacement or drift related EDPs have been proved to conform to lognormal distribution. Assuming a lognormal distribution, the median and the dispersion of the EDPs at a given IM value were estimated. The larger the number of fire profiles used, the less the bias of the database. The abovementioned process was repeated for different levels of IM to cover the whole possible range of fire severity. In the IM-EDP plot, connecting the median response points corresponding to thin bands of IM levels resulted in the IFA curve corresponding to that fire profile.

RESULTS AND DISCUSSION

Figures 2-10 show results from a typical analysis. They show the scatter of IM plots against the maximum displacement EDP. They are the only results shown due to space limitations. A suggested failure displacement of span/66 was used to help extract results. In three cases the analyses ended in a run-away failure of the beams; the results from these analyses are shown by triangles. It is observed that one of the triangle results has an overall displacement less than span/66, but was adjudged to have failed because the displacement increased from 0.088 mm to 0.181 mm over a time step of 18 seconds, at which stage the beam geometry changed significantly. The dispersion (assuming lognormal distribution) of the maximum displacement at different fire intensity (represented by IMs) is shown beside the IFA plots.

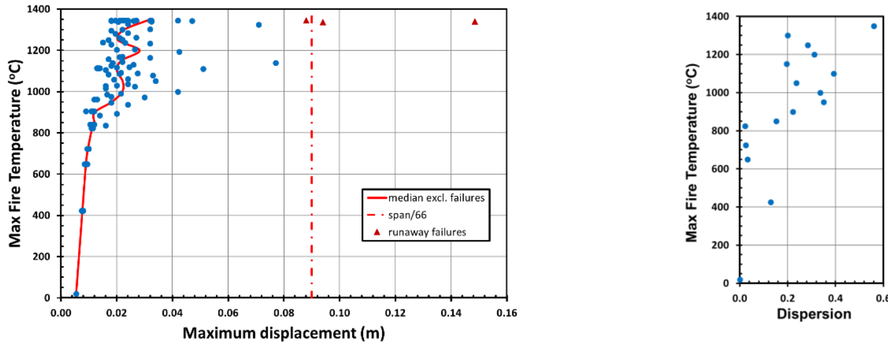

Figure 2. Plot of maximum displacement and dispersion against maximum fire temperature.

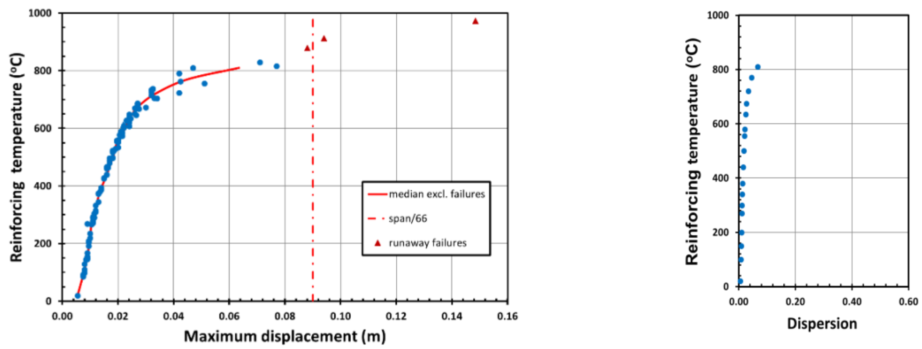

Figure 3. Maximum displacement and dispersion against maximum reinforcing temperature.

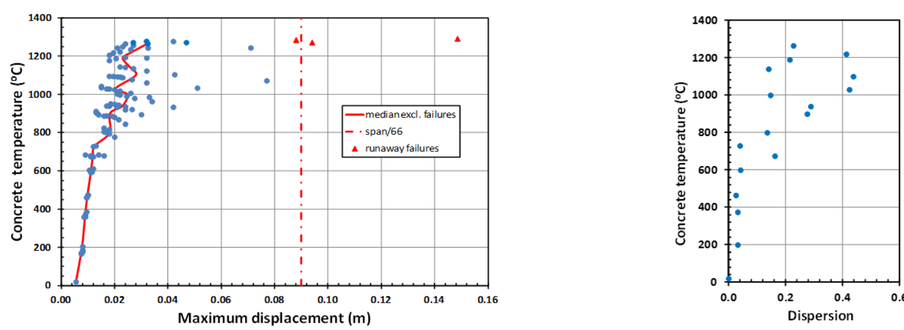

Figure 4. Maximum displacement and dispersion against maximum concrete temperature.

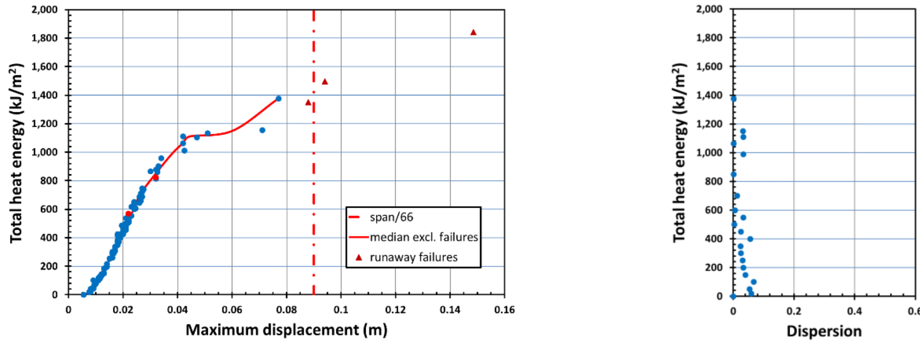

Figure 5. Maximum displacement and dispersion against total heat energy.

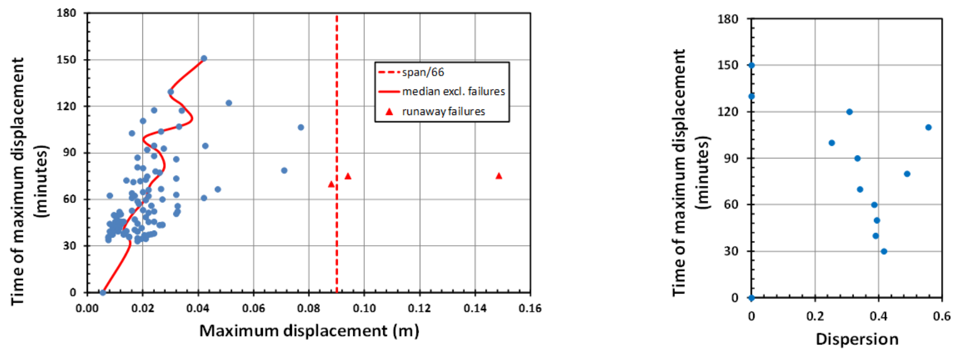

Figure 6. Maximum displacement and dispersion against time to maximum displacement.

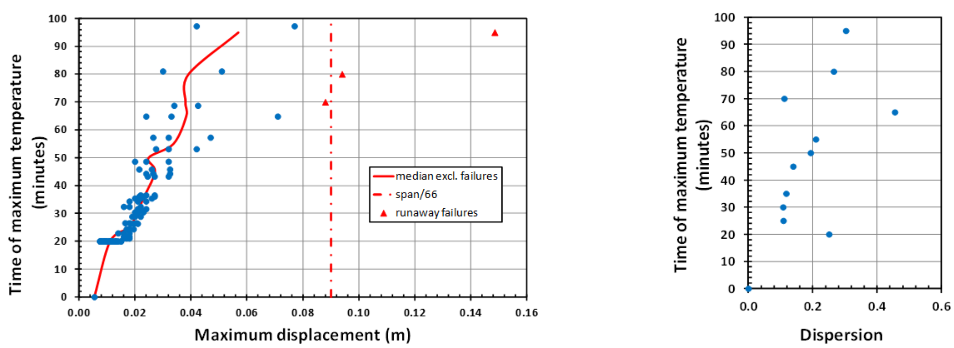

Figure 7. Maximum displacement and dispersion against time to maximum fire temperature.

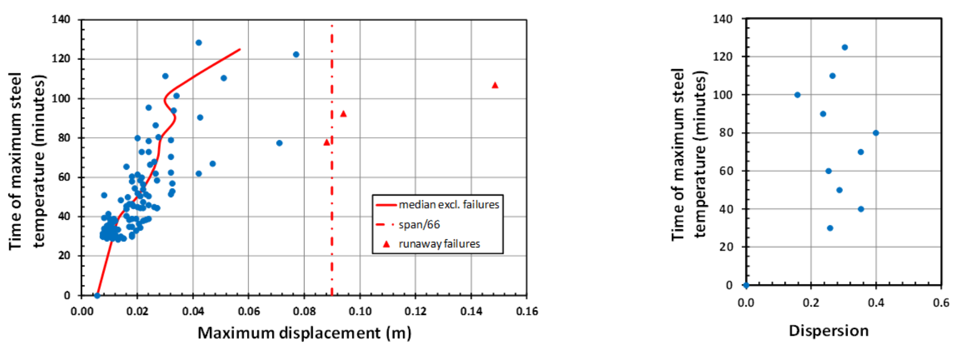

Figure 8. Maximum displacement and dispersion against time to maximum reinforcing temperature.

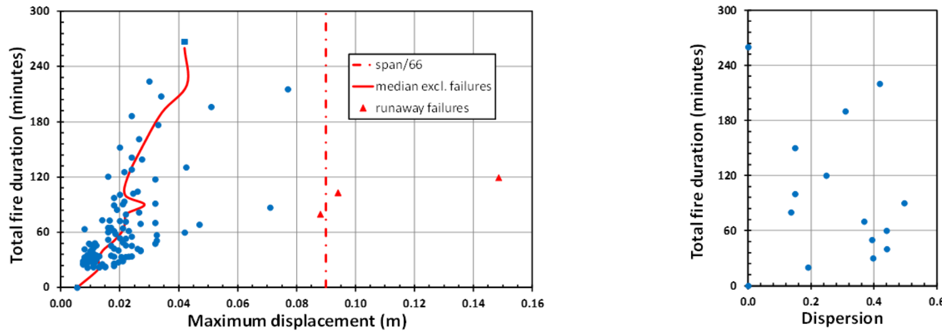

Figure 9. Maximum displacement and dispersion against total fire duration.

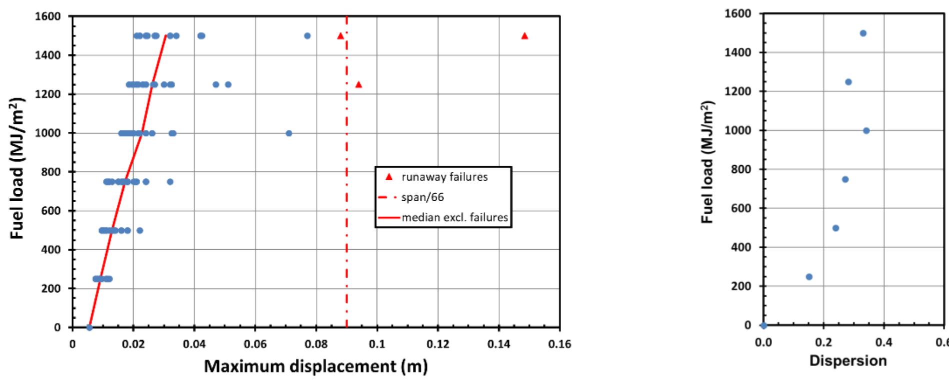

Figure 10. Maximum displacement and dispersion against fuel load.

It can be seen that when the maximum fire temperature (MFT) is used as an IM (Figure 2), there is increasing scatter of the EDP as the temperature increases. This is a feature of the fact that low temperature fires have less effect on the material properties of the concrete and steel reinforcing. Figure 3 shows that when the steel temperature is used as the IM, there is much less scatter even at the higher temperatures; whereas Figure 4 shows that there is considerable scatter in the results at higher temperatures when the maximum concrete temperature is used as the IM. When the total heat energy is used as an IM (Figure 5), there is moderate scatter in the results. In Figure 6, when the time at which the maximum displacement occurs is used as the IM, there is considerable scatter in the results; unlike the cases in Figures 2 and 4, the dispersion is greater for fires that cause the maximum displacement to occur at earlier times, while there are few fires that cause the maximum displacement to occur after longer periods of time. In Figure 7, there is a concentration of results for the shorter times (less intense fires) with larger scatter for the longer times (more intense fires). The results shown in Figure 8 for maximum displacement plotted against the time taken to reach the maximum temperature in the reinforcing, and in Figure 9 for the plot of displacement against the total fire duration, also show a concentration of results for the shorter times (less intense fires) with larger scatter for the longer times (more intense fires). When the fuel load is taken as the IM as shown in Figure 10, there is no longer any random scattering but the scattering and the dispersion increase with increasing fuel load. Also, the hotter fires at each level of fuel load produce much greater deflections than the cooler fires for the same fuel load.

For maximum reinforcement temperature as an EDP the data is generally more scattered than what is observed for maximum displacement. The scatter in results increases with increasing reinforcement temperature. For maximum concrete temperature as an EDP the results are more scattered than what was observed for maximum displacement, but is less scattered in comparison to those with maximum reinforcement temperature, and increase with increasing concrete temperature. For maximum or minimum bending moments as EDPs it is observed that there is not much scatter in the data as plastic hinges form at particular moments. The scatter and dispersion both reduce with increasing moment (maximum or minimum).

CONCLUSION

Incremental fire analysis (IFA), which is an integral part of probabilistic fire risk assessment methodology, has been used in this paper to investigate ideal intensity measures. Nine IMs (maximum fire temperature, maximum reinforcing temperature, maximum concrete temperature, total heat energy, time of maximum displacement, time to maximum fire temperature, time to maximum reinforcing temperature, fire duration and fuel load) and four EDPs (maximum displacement, maximum reinforcing temperature, maximum concrete temperature and maximum and minimum bending moments) were investigated. IFA was conducted on a two-span continuous RC beam using a range of parametric fire profiles. From the results, median IFA curves as well as the associated dispersion profiles were generated, which showed that reinforcement temperature and the total heat energy were more efficient IMs as they result in less variation of the predicted maximum vertical displacement. Using the same set of IMs against other EDPs showed more variations in comparison to the vertical displacement EDP, except for maximum and minimum bending moments, which showed less dispersion. However, that observation was due to the fact that plastic moments formed in the two-span beam. More investigations are underway to scrutinize different aspects of the IFA process and to assess the suitability of other potential IM and EDP variables.

With the identification of ideal intensity measures (IM), engineering demand parameters (EDP), damage measures (DM) and decision variables (DV), probabilistic assessments of structural behavior will become common, and will ensure that buildings are adequately constructed to suit to the worst probable fire that may occur in their lifetimes.

REFERENCES

1. Deierlein, G. G., H. Krawinkler, and C. A. Cornell. 2003. "Framework for Performance-Based Earthquake Engineering", *Pacific Conference on Earthquake Engineering, Christchurch, New Zealand*.
2. Hamilton, S. R. 2011. *Performance-based fire engineering for steel framed structures: a probabilistic methodology*, PhD Thesis, Stanford University, Stanford (CA), USA.
3. Lange, D., S. Devaney and A. Usmani. 2014. "An application of the PEER performance based earthquake engineering framework to structures in fire', *Engineering Structures* 66, 100-115.
4. Tothong, P. and C. A. Cornell. 2007. "Probabilistic Seismic Demand Analysis Using Advanced Ground Motion Intensity Measures, Attenuation Relationships, and Near-Fault Effects, PEER

Report no. 2006/11". *Pacific Earthquake Engineering Research Center*, University of California Berkeley, CA. USA.

5. Giovenale, P., C. A. Cornell and L. Esteva. 2004. "Comparing the adequacy of alternative ground motion intensity measures for the estimation of structural responses", *Earthquake Engineering & Structural Dynamics*, 33 (8), 951-979.
6. Moss, P. J., A. K. Abu and R. P. Dhakal. 2014. "Incremental Fire Analysis (IFA) for probabilistic fire risk assessment", *Proceedings of the 23rd Australasian Conference on the Mechanics of Structures and Materials (ACMSM23)*, 707-712.
7. European Standards Commission. 2002. *Eurocode 1: Actions on structures, EN 1991-1-2: Actions on structures exposed to fire*, European Committee for Standardization, Brussels.
8. Bernhart, D., A. Buchanan, R. Dhakal and P. Moss. 2005. "Effect of Top Reinforcing on the Fire Performance of Continuous Reinforced Concrete Beams", *Proceedings of the Eighth International Symposium on Fire Safety Science (IAFSS 2005)*, Beijing, China, 259-270.

A Probabilistic Study on Concrete Columns Exposed to Biaxial Bending at Elevated Temperatures

LIJIE WANG, RUBEN VAN COILE ROBBY CASPEELE and LUC TAERWE

ABSTRACT

Fire, as one of the most severe accidental load situations, has an important effect on concrete columns. Furthermore, this effect is more pronounced in case an eccentricity is associated with the axial load. Since this situation occurs very frequently, it is significant to investigate the fire performance of concrete columns subjected to biaxial bending. Additionally, differences due to initial imperfections on configurations, cover thickness, as well as the common variability in the concrete compressive strength might cause significant differences to interaction diagrams. Therefore, a probabilistic evaluation is required as a first step to evaluate the safety of concrete columns during fire exposure. In this paper a column subjected to a 4-sided fire exposure in case of a symmetric biaxial load is investigated and Monte Carlo simulations are applied to evaluate probabilistic interaction diagrams for columns in case of fire.

INTRODUCTION

Columns are commonly subjected to bending caused by eccentric axial forces introduced by adjacent beams and slabs. In order to investigate reinforced concrete columns subjected to combinations of an axial load and a moment applied about one or both principal axes, assumptions and hypotheses for performing the cross-sectional analysis and design have been proposed [1]. Bresler [2] first presented a formula for design of columns with rectangular cross-sections subjected both to compression and biaxial bending, by comparing test results with computed values. Afterwards, Parme et al. [3] further developed the formula proposed in [2] and adopted it in an approximate procedure to determine the required size for columns subject to biaxial bending. Then, Marín [4] addressed the biaxial bending of L-shaped sections. More recently, Gil-Martín et al. [1] introduced a model which could determine optimal reinforcement solutions for the design of column reinforcement in case of biaxial bending. However, the applicability of these methods has not been proven in case of fire. With respect to columns subjected to fire combined with biaxial bending, parameters such as the variability of the cover thickness and concrete compressive strength could have

---

Wang L. J., Van Coile R., Caspeele R. & Taerwe L. Ghent University, Department of Structural Engineering, Technologiepark-Zwijnaarde 904. B-9052 Ghent, Belgium.

important effects on interaction curves. Hence, the effect of the stochastic nature of variables in case of concrete columns exposed to fire combined with biaxial bending is investigated in this paper.

As a first step in the calculation, a cross-sectional method is adopted to obtain the relationship between bending moments and curvatures for a certain column. Then, an iterative approach is presented with respect to second-order effects of the column. As a result, interaction curves are obtained in case of columns for different slenderness ratios. In order to validate this analytical tool, the time-dependent deflection curves are compared with tests from Tan and Nguyen [5]. It is shown that this method enables the prediction of the structural resistance of columns subjected to biaxial bending at elevated temperatures. Finally, a probabilistic study on the effects of the variability of the cover thickness and the concrete compressive strength on the column interaction diagram is presented.

BASIC CALCULATION MODEL

A numerical calculation model is proposed to calculate the combined effect of an axial force (N) and a total bending moment (M) on columns exposed to fire in case of biaxial bending, taking into account material strength reduction and thermal strains. This model is based on a cross-sectional calculation and is further extended to predict second-order effects of columns exposed to fire.

Material model and basic assumptions

The stress-strain relationships of concrete and reinforcing bars provided in EN 1992-1-2 [6] are adopted to calculate interaction curves. The following assumptions are made: 1) plane sections remain plane; 2) the tensile strength of concrete is not considered; 3) there is no bond-slip between steel reinforcement and concrete; 4) spalling of the concrete cover is not an issue.

Thermal analysis and structural calculation

The basic calculation includes two parts: first a transient thermal analysis and subsequently a structural analysis. As the first step in the calculation process, the cross-section is discretized into small elements. For the examples described in this paper, a 1 mm × 1 mm square mesh is chosen as the basic element size.

The same cross-sectional discretization is used for the structural analysis. Both the thermal and structural calculation are executed by an own developed calculation tool which has been presented in [7]. The mechanical strain is expressed as follows:

$$\varepsilon_{mech} = \varepsilon_0 + k_0\eta + k_0'\eta' - \varepsilon_{th} \tag{1}$$

where ε_{th} is the thermal strain, ε_0 is the strain at the centroid and k_0, k_0' are the curvature about both axes, η, η' are variables related to the distance from the calculated point to the centroid along both axes respectively.

In this paper, only columns with four-sided exposure in case of a distributed fire combined with an axial force in the diagonal axis are considered. As such, $k_0 = k_0'$ and the formula (1) can be written as:

$$\varepsilon_{mech} = \varepsilon_0 + k_0 (\eta + \eta') - \varepsilon_{th} \quad (2)$$

The virtual work principle is used to calculate the deflection considering first order effects. Next, additional bending moments caused by the defection are calculated with an iterative calculation method adopting the bending moment-curvature curves based on the cross-sectional calculation. Consequently, these are taken into account to calculate the adjusted interaction diagrams when considering the reduced capacity due to second-order effects.

VALIDATION OF THE CALCULATION MODEL

The temperature distributions, interaction curves as well as deflections of columns in case of fire have been compared with experimental data and numerical simulations in [7]. Based on this analysis, the calculation model has been validated for uniaxial bending during fire.

Here, one more example is given to show the prediction under biaxial bending in case of fire. The results obtained for a specific column with three typical sets of equal biaxial eccentricities, i.e., $\eta = \eta'$ = 25 mm, 40 mm and 60 mm are compared to the experimental data from Tan and Nguyen [5]. The following configuration was investigated: the height equals 2700 mm and the cross-section equals 300 mm×300 mm, 4 reinforcement bars with diameter 25 mm are positioned in the corners of the square column, and the concrete cover equals 30 mm. The 20°C concrete compressive strength f_c = 29.3 MPa, reinforcement yield strength f_y = 554 MPa and Young's modulus of steel $E_s = 2.01\times10^5$ N/mm^2. Considering the same fire condition and setups, the curves of the mid-height lateral deflection of columns with time are presented in Figure 1.

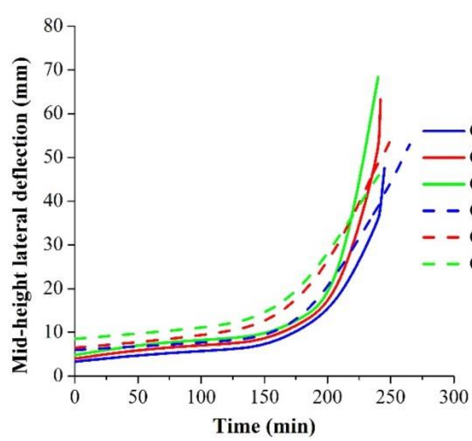

Figure 1. The curves of the mid-height lateral deflection of columns with time.

Figure 1 shows the time-dependent mid-height lateral deflection curves of the investigated columns. The deflections of selected nodes increase slowly and are constantly lower than tests before the fire duration of 210 minutes. The main reason is that spalling was observed in the tests but is not considered in the analytical model. Spalling makes the heat transfer more rapidly, which causes more significant deterioration in stiffness [8]. As a result, second-order effects are more explicit in reality and involve larger deflections than results based on the analytical model. It is worth noting that the deflection grows very fast after 210 minutes due to the reduction in the strength of the reinforcing bars when temperatures of bars are over 400 °C. Meanwhile, the analytical lateral deflection of these columns begin to catch up with the observed deflection. Finally, all of these three columns fail before the fire reaches 250 minutes. The prediction based on the analytical model is quite close to the reality. As it is proven to be applicable also in case of biaxial bending during fire, the tool is further implemented for a probabilistic analysis.

A PROBABILISTIC STUDY

A probabilistic evaluation is made to investigate the effect of the variability of the basic model parameters. The same cross-section is considered as in the parameter study, with probabilistic models for the basic variables as given in Table 1, in accordance with [9] and [10]. As it is explained in [11], a normal distribution may result in physically impossible negative values for the reduction factors of the concrete compressive strength and the reinforcement yield stress at elevated temperatures. Hence, a Beta distribution is proposed which is bounded by three times the standard deviation and the mean value is taken as the nominal value given in EN 1992-1-2 [6].

TABLE I. Probabilistic models for basic variables, based on [9] and [10]: property, dimension, distribution, mean value μ, standard deviation σ and coefficient of variation V.

Property	Dim.	Distr.	μ	σ	V
20°C concrete compressive strength $f_{c,20}$ (f_{ck} = 55 MPa)	MPa	LN	$\frac{f_{ck}}{1-2V_{fc}}$	$\mu \cdot V$	0.15
20°C reinforcement yield stress $f_{y,20}$ (f_{yk} = 500 MPa)	MPa	LN	$\frac{f_{yk}}{1-2V_{fy}}$	$\mu \cdot V$	0.07
Concrete compressive strength reduction factor $k_{fc}(\theta)$ at temperature θ	-	Beta	EN 1992-1-2	$\mu \cdot V$	[11]
Reinforcement yield stress reduction factor $k_{fy}(\theta)$ at temperature θ	-	Beta	EN 1992-1-2	$\mu \cdot V$	[11]
Concrete cover c	mm	Beta	25	5	σ/μ
Column width z	mm	DET	z_{nom}	300	-

EN 1990 [12] states that the design value of the resistance R_d should be defined such that the probability of having a more unfavorable value is as follows:

$$P(R \leq R_d) = \Phi(-\alpha_R \beta) \tag{3}$$

where β is the target reliability index, α_R is the value of sensitivity factor of resistances.

As a simplification, α_R may be taken as 0.8. Hence, Eq. (3) is written as:

$$P(R \leq R_d) = \Phi(-0.8\beta) \tag{4}$$

Regarding to the ultimate limit state and probability of failure of structural members at ambient temperature, a target reliability index $\beta_{t,50}$ of 3.8 is adopted when considering a 50 year reference period [12]. Hence, the curve of $P(R \leq R_d) = \Phi(-0.8 * 3.8) = 0.12\%$ is used for reliability design at ambient temperature here.

In the present study, 10000 Monte Carlo simulations of the interaction diagram are evaluated. The variability of the obtained first-order interaction diagram can be visualized by the 5%, 50%, and 95% values. This is applied in Figure 2 as well as the curve of $P(R \leq R_d) = 0.12\%$ for ambient temperature (i.e. prior to fire), in Figure 3 for 30 minutes of ISO 834 standard fire exposure and in Figure 4 for 90 minutes of ISO 834 standard fire exposure. In all the figures, a comparison is made with the interaction diagram obtained when considering characteristic values for the basic parameters (designated the reference interaction diagram), i.e. f_{ck} for the concrete compressive strength, and f_{yk} for the reinforcement yield stress, with $n = \frac{N_c+N_s}{0.7(A_c f_{cd} + A_s f_{yd})}$ and $m = \frac{M_c+M_s}{0.7(A_c f_{cd} + A_s f_{yd})h}$,where N_c, M_c, N_s, M_s are maximum axial forces and bending moments respectively for concrete and reinforcement, b is the width of the column and h is the height of the cross-section.

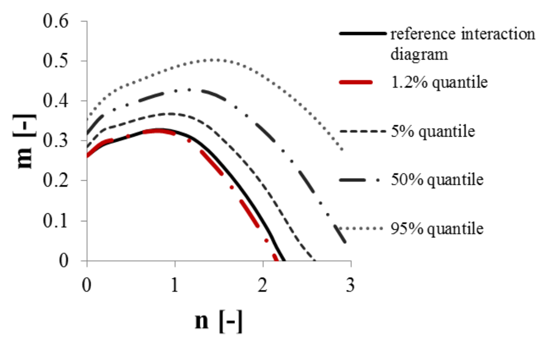

Figure 2. Interaction diagrams of a column at ambient temperature considering a probabilistic study on the effects of the variables mentioned in Table 1.

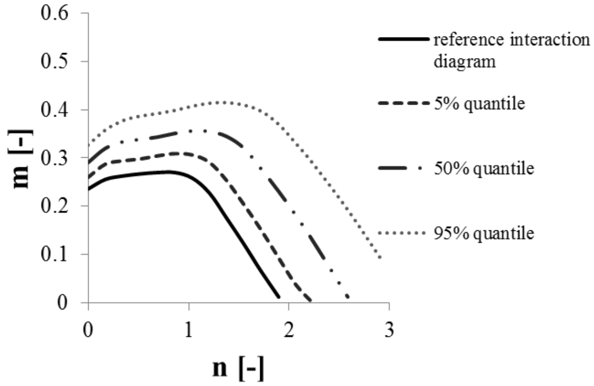

Figure 3. Interaction diagrams of a column exposed to an ISO 834 fire of 30 minutes considering a probabilistic study on the effects of variables mentioned in Table 1.

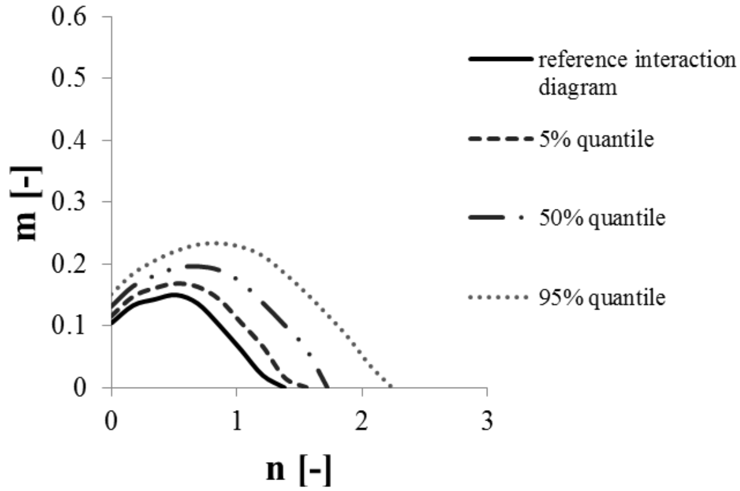

Figure 4. Interaction diagrams of a column exposed to an ISO 834 fire of 90 minutes considering a probabilistic study on the effects of variables mentioned in Table 1

Based on the results presented in Figure 2, Figure 3 and Figure 4, it is clear that a very large variability exists with respect to the interaction diagram for concrete columns, both at ambient conditions and during fire exposure. The comparison of the probabilistic visualization (i.e. 5%, 50% and 95% curves) with the full line representing the nominal calculation in accordance with the normal Eurocode design methodology indicates that the interaction diagram adopting material and mechanical properties provided by Eurocode 2 [6] is situated below the 5% curve. This is in good agreement with the semi-probabilistic design concept of the Eurocodes where the design value should correspond with a low quantile of the resistance effect. Furthermore, compared to 1.2% curve in Figure 2, the reference interaction diagram at ambient temperature is slightly higher only when the respective value of n is more than 0.7. It proves that the reference interaction diagram obtained with the calculation tool holds true with the reliability-based design target related to ultimate limit state and probability of failure of structural members [12]. However, when calculating the observed quantile of the stochastic interaction diagram which corresponds with the analytical value of the Eurocode design methodology in case of an ISO 834 standard fire, a quantile of 0.20% at 30 minutes (Figure 3) and a quantile of 0.21% at 90 minutes of an ISO 834 fire exposure (Figure 4) are obtained based on the calculation tool.

CONCLUSION

Comparing the reference interaction diagram with the probabilistic evaluation at ambient temperature, it is seen that they are in a good agreement. Since there is no explicit target of reliability available for the case of fire, the tool is an important step to evaluating the Eurocode reliability performance during fire. Furthermore, this evaluation tool could be implemented in calculations for a risk assessment of concrete columns exposed to fire and provide references for the fire resistance design of columns.

AKNOWLEDGMENTS

The authors would like to thank the China Scholarship Council (CSC) for the financial support to the first author.

REFERENCES

1. Gil-Martín L. M., Hernández-Montes E., Aschheim M. 2010. "Optimal reinforcement of RC columns for biaxial bending," *Materials and Structures* 43(9): 1245-1256.
2. Bresler B. 1960. "Design criteria for reinforced columns under axial load and biaxial bending," *ACI Journal Proceedings*, 57(11), 481-490.
3. Parme A, Nieves J, Gouwens A. 1966. "Capacity of reinforced rectangular columns subject to biaxial bending," *ACI Journal Proceedings*, 63(9):911-924.
4. Marín J. 1974. "Resistencia de las secciones de concreto armado sometidas a flexo compresión: un método algorítmico general y sus aplicaciones en el diseño de columnas," *tesis de Doctor de Ingeniería*, Univeristy of Central Venezuela, Caracas.
5. Tan K. H., Nguyen T. T. 2013. "Experimental behaviour of restrained reinforced concrete columns subjected to equal biaxial bending at elevated temperatures," *Engineering Structures*, 56, 823-836.
6. CEN. 2004. "EN 1992-1-2: Design of concrete structures - Part 1-2: General rules - Structural fire design," *European Committee for Standardization*, Brussels, Belgium.
7. Wang L. J., Caspeele R., Van Coile R.& Taerwe L. 2015. "Extension of tabulated design parameters for rectangular columns exposed to fire taking into account second-order effects and various fire models". *Structural Concrete*,16(1): 17-35.
8. Nguyen T. T., Tan K. H. 2014. "Thermal-induced restraint forces in reinforced concrete columns subjected to eccentric loads," *Fire Safety Journal*, 69, 136-146.
9. Holický, M., Sýkora, M. 2010. "Stochastic models in analysis of structural reliability," *Proceedings of the International Symposium on Stochastic Models in Reliability Engineering, Life Sciences and Operation Management*. Beer Sheva, Israel.
10. JCSS. 2007. "Probabilistic Model Code," *The Joint Committee on Structural Safety*. available online at www.jcss.byg.dtu.dk.
11. Van Coile R. Reliability-based decision making for concrete elements exposed to fire. Ph.D. dissertation, Ghent University, Belgium, 2015.
12. CEN. 2002. "EN 1990: Eurocode 0: Basis of structural design," *European Standard*.

Reliability of Reinforced Concrete Walls Subjected to Standard Fire Using Advanced and Simplified Methods

MARCUS ACHENBACH and GUIDO MORGENTHAL

ABSTRACT

The probability of failure of concrete walls subjected to a standard fire on both surfaces is examined. The samples are chosen to match the parameters recommended in the tabulated values of Eurocode 2, which allow a classification of the fire resistance. The probabilities of failure are calculated by means of a Monte Carlo simulation considering the Advanced Calculation Method according to Eurocode 2. To examine the accuracy of a simplified method, the Extended Zone Method is also taken into account. The calculated failure rates of both methods are close to each other, which confirms, that the Extended Zone Method is suitable to determine the reliability of reinforced concrete walls subjected to fire. The calculated probabilities of failure indicate that the tabulated values are mean values with small additional safety elements.

INTRODUCTION

The fire resistance of reinforced concrete walls subjected to a standard fire can be checked by different methods. According to EN 1992-1-2 [1] the use of tabulated data, simplified and advanced methods is possible. The tabulated values given in section 5 of EN 1992-1-2 are based on laboratory tests and widely accepted, also the Advanced Calculation Method is state of the art. Simplified methods like the Extended Zone Method (EZM) [2] are under development and the results of the calibration [3] show, that the proposed method is able to predict the time of failure of concrete columns with satisfying accuracy.

But it is not clear, which level of safety is achieved by those methods for concrete walls. Especially it is not known, if the safety level of EZM is comparable to the Advanced Method and which safety is contained in the tabulated data.

Marcus Achenbach, LGA KdöR, Tillystraße 2, 90431 Nürnberg, Germany, marcus.achenbach@lga.de
Guido Morgenthal, Bauhaus Universität Weimar, Marienstraße 13, 90431 Weimar, Germany, guido.morgenthal@uni-weimar.de

A Monte Carlo simulation [4] of reinforced concrete walls heated on both sides by a standard fire is set up. The parameters of the simulated examples are chosen in accordance with the tabulated values provided by EN 1992-1-2. The calculation of the failure rates allows to judge on the safety level of the tabulated values.

The Advanced Calculation Method according to EN 1992-1-2 is considered as reference. The uncertainties of the thermal analysis and the resistance model are taken into account. To evaluate the reliability of a simplified method, the Extended Zone Method – also with the consideration of model uncertainties – is examined. Finally, the effect of model uncertainties on the failure rates is examined by "freezing" the involved variables to deterministic values.

APPLIED METHODS

Calculated examples

Pin ended walls with a constant eccentricity of the applied loads are examined. The structural system and cross section are displayed in Figure 1, the corresponding parameters are given in Table I. The simulated walls have a fire rating R90 according to the tabulated values given in Table 5.4 of EN 1992-1-2. The chosen area of reinforcement is just sufficient to carry the load $P_d = 1.35G_k + Q_k$. The applied load P_d is determined by the method of nominal curvature [5] and a ratio of $Q_k / G_k = 0.7$ is assumed. Hot rolled reinforcement and siliceous aggregates are modelled in the simulation.

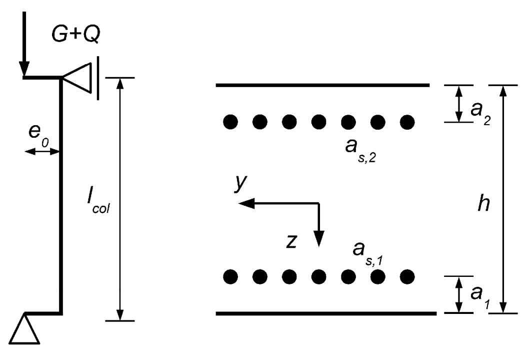

Figure 1. Structural system and cross section of simulated concrete walls

TABLE I. PARAMETERS OF SIMULATED CONCRETE WALLS

nr.	t_f (min)	h (cm)	l_{col}/h (-)	a_1=a_2 (cm)	$(a_{s,1}+a_{s,2})/h$ (%)	f_{yk} (MPa)	f_{ck} (MPa)	G_k (kN)	Q_k (kN)	e_0/h (-)
1	90	20	25	3.0	1.0	500	20	630	440	0.0
2	90	20	25	3.0	1.0	500	20	480	330	0.1
3	90	20	25	3.0	1.0	500	20	230	160	0.5
4	90	20	40	3.0	1.0	500	20	210	150	0.0
5	90	20	40	3.0	1.0	500	20	180	130	0.1
6	90	20	40	3.0	1.0	500	20	120	80	0.5

TABLE II. STOCHASTIC BASIC VARIABLES

variable	distribution	parameters of distribution	reference
l_{col}	N	$\mu = lcol$, $\sigma = 2 / 1.645$ cm	[6]
h	N	$\mu = h$, $\sigma = 0.4$ cm + $0.006 \cdot h$	[7]
a_i	N	$\mu = a_i$, $\sigma = 0.5$ cm	[7,8]
$a_{s,i}$	N	$\mu = a_{si}$, $v = 0.02$	[7,8]
f_c	LN	$\mu = f_{ck} + 0.8$ kN/cm² , $\sigma = 0.5$ kN/cm²	[8,9]
f_y	N	$\mu = f_{yk} + 2\sigma$, $\sigma = 3$ kN/cm²	[7,9]
G	N	$\mu = G_k$, $v = 0,1$	[8,9]
Q	G	Q_k: 98%-quantile , $v = 0.4$	[8]
e_0	N	$\mu = e_0$, $\sigma = l_{col} / 1000$	[7]
e_f	N	$\mu = 0$, $\sigma = l_{col} / 1000$	[7]
X_t	N	$\mu = 1.0$, $v = 0.2$	[10]
X_m	N	$\mu = 1.4$, $v = 0.2$	[10]
$X_{m,EZM}$	N	$\mu = 1.0$, $v = 0.2$	[3]

(N = normal, LN = log-normal, G = Gumbel)

Basic variables

The considered stochastic basic variables are given in Table II. In lack of more detailed data it is assumed that the probabilistic model of concrete strength at room temperature is also valid at elevated temperatures. The calculated temperatures are multiplied by the basic variable X_t to consider the uncertainty of the thermal analysis. The uncertainty of the resistance models is considered by X_m. Both variables have been derived from the recalculation of laboratory tests [3, 10]. A total number of k = 5000 samples is generated. Each sample can be interpreted as one single “numerical” experiment.

Thermal analysis

A finite difference method [11] is implemented to calculate the temperature distribution in each sampled concrete wall. The thermal properties according to EN 1991-1-2 [12] and EN 1992-1-2 [1] are considered: an emissivity $\varepsilon = 0.7$, a heat transfer coefficient $\alpha = 25$ W/m²K, a moisture content $u = 3$ %, a density $\rho = 2400$ kg/m³ and the thermal conductivity λ_c with its lower limit. Both surfaces are exposed to a standard fire [12] for the fire duration given in Table I.

Resistance models

The moment-curvature diagram for the given fire resistance t_f is calculated for each sample and considered resistance model. The principles of the applied Advanced Method and the Extended Zone Method (EZM) are explained briefly.

ADVANCED METHOD

The stress-strain curves according to EN 1992-1-2 are used for the implementation of the Advanced Method in this paper. Transient thermal strains of concrete are included in the material models for reinforcing steel and concrete. The total strain ε of each fiber consists of the thermal strains ε_{th} and the mechanical strains ε_m.

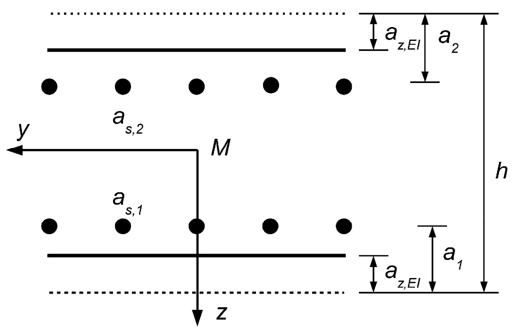

Figure 2. Cross section for the Extended Zone Method

EXTENDED ZONE METHOD (EZM)

The Zone Method proposed by Hertz has been extended by Achenbach and Morgenthal [2] from a scheme for manual calculation towards a method suitable for implementation in design software. Hertz assumes that thermal strains can be neglected and that the loss of stiffness at elevated temperatures can be expressed by means of a reduced cross section.

For a concrete wall heated on both surfaces as displayed in Figure 2, the mean strength of the concrete can be calculated by:

$$k_{c,m} = \frac{\int_{-h/2}^{h/2} k_c(\theta)\,\mathrm{dz}}{h}\ , \tag{1}$$

with $k_c(\theta) = f_{c,\theta} / f_{ck}$, $f_{c,\theta}$ = concrete strength at temperature θ. The height of the zone $a_{z,EI}$ simulating the loss of stiffness is calculated by the empiric equation:

$$a_{z,EI} = \frac{b}{2} \cdot \left(1 - \left(\frac{k_{c,m}}{k_c(\theta_M)} \right)^{4/3} \right)\ . \tag{2}$$

The assumptions and limits of this approach are discussed by Achenbach and Morgenthal [2].

In the Extended Zone Method, the concrete is modeled with constant material properties using the stress-strain curves of EN 1992-1-2. The temperature θ_M at the center is used as reference and a peak strain of the concrete $|\varepsilon_{c1,\theta}| \geq 3.5$ ‰ is considered. The stress-strain curves of EN 1992-1-2 are used for the reinforcement and the strength of the compressed reinforcement reduced by $\eta_s\,(\theta)$ to model the effect of hindered thermal strains. The factor $\eta_s\,(\theta)$ can also be interpreted as reduction of the area of the compressed reinforcement and is definded by

$$\eta_s(\theta) = \begin{cases} 1.0 \text{ for } \theta \leq 100\ °\mathrm{C} \\ 0.5 \text{ for } \theta \geq 400\ °\mathrm{C}\,, \end{cases} \tag{3}$$

where values for 100 °C < θ < 400 °C can be interpolated linearly. The strength of reinforcement under tension is not reduced.

The benefit of the proposed Extended Zone Method is its suitability for design. The concrete is modelled with constant material properties. The application of the stress-strain curves of EN 1992-1-2 introduces strain limits, which are needed for the design of the area of reinforcement. The proposed method is close to a nonlinear calculation method at room temperature and can be implemented in design software.

Limit state function

The deflection in the middle of the compressed concrete wall is calculated in dependence from the curvature κ. For a parabolic shape – as displayed in Figure 3 – the deformation e^{II} including second order effects can be calculated by

$$e^{II}(\kappa)=\left(\frac{l_{col}}{2}\right)^2\cdot\left(\frac{4}{10}\cdot\kappa - \frac{1}{10}\cdot\kappa_0\right) \tag{4}$$

as recommended by Kordina and Quast [13]. The limit state function is defined by

$$G= \max\left(M_R(\kappa)\text{-}M_E(\kappa)\right), \tag{5}$$

where results $G < 0$ indicate a failure of the simulated wall. The limit state function is evaluated for the given fire resistance t_f and the number n of failed walls is counted.

Calculation of failure rates

The probability of failure can be estimated in a Monte Carlo simulation [4] by

$$p_f \approx \frac{n}{k}, \tag{6}$$

where k is the number of samples and n is the number of failed walls. The standard deviation of this estimation is described by [4]:

$$\sigma_{p_f} = \sqrt{\frac{p_f - p_f^2}{k}}. \tag{7}$$

For an estimated probability of failure $p_f = 0.5$ and a number of $k = 5000$ samples the standard deviation is 0.007.

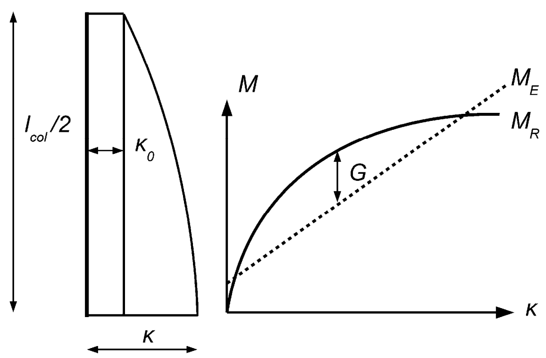

Figure 3. Shape of curvature (left) and qualitative limit state function (right)

RESULTS

The calculated probabilities of failure p_f for the Advanced Method with the uncertainties of the thermal analysis and the resistance model are given in Table III. The corresponding sensitivity analysis of the limit state function against the probabilistic input parameters has been published by Achenbach and Morgenthal [10]. The values for p_f are in a range of 0.24 to 0.54 and are a measure for the reliability of the tabulated values for concrete walls. The calculated failure rates decrease with increasing eccentricities. The mean value of p_f is close to 0.4. Assuming a symmetric, unknown distribution, it can be concluded that the tabulated values are mean values with small additional safety elements. This is in accordance with the background information given by Henke [15].

The effect of the model uncertainties on the failure rates becomes obvious, if they are fixed to a deterministic value: $X_t = X_m = 1.0$. The calculated failure rates $p_{f,det}$ are displayed in Figure 4. Disregarding these uncertainties leads to failure rates up to 89 %, though the samples have been chosen in accordance with the tabulated values. The failure rates are overestimated and conservative results are obtained. – But this statement is not true for concrete columns [14], where deterministic model uncertainties can lead to an overestimation of the reliability. Therefore the question of additional safety factors is discussed by Achenbach and Morgenthal [14].

TABLE III. PROBABILITIES OF FAILURE

nr.	e_0/h (-)	p_f (-)	$p_{f,det}$ (-)	$p_{f,EZM}$ (-)
1	0.0	0.532	0.781	0.502
2	0.1	0.537	0.892	0.500
3	0.5	0.235	0.217	0.309
4	0.0	0.424	0.571	0.451
5	0.1	0.411	0.587	0.468
6	0.5	0.298	0.387	0.416

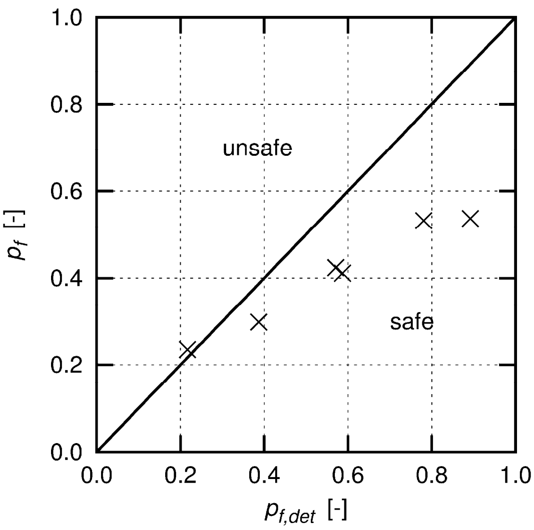

Figure 4. Probabilities of failure p_f for the Advanced Method with probabilistic model uncertainties, $p_{f,det}$ for the Advanced Method with deterministic model uncertainties

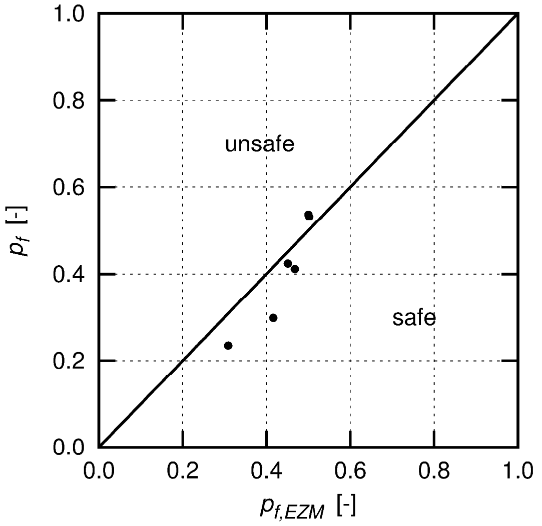

Figure 5. Probabilities of failure p_f for the Advanced Method and $p_{f,EZM}$ for EZM with probabilistic model uncertainties

The calculated failure rates $p_{f,EZM}$ for the Extended Zone Method with the uncertainties of the thermal analysis and the resistance model are contained in Table III and plotted in Figure 5. The calculated failure rates of the Extended Zone Method $p_{f,EZM}$ are close to the results of the Advanced Method p_f for walls with relative eccentricities $e_0 / h \leq 0.1$. For larger eccentricities of the applied loads, the Extended Zone Method becomes more conservative, the probabilities of failure of the Advanced Method are overestimated. This can be explained by the reduction of the height of the wall by $a_{z,EI}$ given by Equation (2). The height of the "damaged zone" has been chosen to simulate the mean loss of stiffness, which is bigger than the mean loss of the concrete compressive strength described by $k_{c,m}$ / $k_c(\theta_M)$. But for walls with larger eccentricities of the applied loads, the ultimate load becomes more determined by the cross section resistance compared to the buckling load limited by the stiffness.

CONCLUSIONS

The Monte Carlo simulation of reinforced concrete walls subjected to a Standard Fire confirms that the probabilities of failure calculated with the Extended Zone Method are comparable to the Advanced Method according to EN 1992-1-2. Therefore the Extended Zone Method can be regarded as "safe" by comparison with the Advanced Method.

The calculated failure rates also indicate that the tabulated values for concrete walls given in EN 1992-1-2 are mean values with small additional safety elements. It can be observed, that the failure rates are dependent on the eccentricity of the applied loads.

REFERENCES

1. EN 1992-1-2. Eurocode 2: Design of concrete structures - Part 1-2: General rules - Structural fire design, December 2004.
2. Achenbach, M. and Morgenthal, G. Extension of the Zone Method of Eurocode 2 for reinforced concrete columns subjected to standard fire. *Journal of Structural Fire Engineering*. Accepted for publication.
3. Achenbach, M. and Morgenthal, G. Recalculation of laboratory tests with the Extended Zone Method. In F. Wald, I. Burgess, M. Jelčić Rukavina, D. Bjegović, and K Horová, editors, *Applications of Structural Fire Engineering - Proceedings of the International Conference in Dubrovnik, 15-16 October 2015*, pages 31–36. Czech Technical University, 2015.
4. Melchers, R. E. *Structural Reliability Analysis and Prediction*. John Wiley & Sons, Chichester, 2ndedition, 1999.
5. EN 1992-1-1. Eurocode 2: Design of concrete structures - Part 1-1: General rules and rules for building, December 2004.
6. EN 13670. Execution of concrete structures, 2000.
7. JCSS. Probabilistic model code, 2001.
8. Six, M. *Sicherherheitskonzept für nichtlineare Traglastverfahren im Betonbau*. PhD thesis, Technische Universität Darmstadt, 2001.
9. Hosser, D., Weilert, A., Klinzmann, C., Schnetgöke, R. and Albrecht, C. Sicherheitskonzept zur Brandschutzbemessung. Abschlussbericht, Institut für Baustoffe, Massivbau und Brandschutz, Braunschweig, 2008.
10. Achenbach, M. and Morgenthal, G. Vollprobabilistische Analyse von Stahlbetonwänden unter Brandeinwirkung. *Bauingenieur*, 89:478–486, 2014.
11. Baehr, H. D. and Stephan, K. *Wärme- und Stoffübertragung*. Springer, Berlin, 3. Auflage, 1998.
12. EN 1991-1-2. Eurocode 1: Actions on structures - Part 1-2: General action – Actions on structures exposed to fire, November 2002.
13. Kordina, K. and Quast, U. Bemessung von schlanken Bauteilen - Knicksicherheitsnachweis. In *Betonkalender 1997, Teil I*, pages 479–575. Ernst & Sohn, Berlin, 1997.
14. Achenbach, M. and Morgenthal, G. Reliability of reinforced concrete columns subjected to standard fire. In Asif Usmani, Yong Lu, and Purnendu Das, editors, *Proceedings of The First International Conference on Structural Safety under Fire & Blast - CONFAB 2015*, pages 244–251. ASRANet Ltd., 2015.
15. Comité Euro-International du Béton. Fire design of concrete structures. CEB Bulletin d'Information N° 208, 1991.

NUMERICAL MODELING

Implementation of a New Design Travelling Fire Model for Global Structural Analysis

XU DAI[1], LIMING JIANG[2], JAMIE MACLEAN[1], STEPHEN WELCH[1] and ASIF USMANI[2]

ABSTRACT

This paper presents a new conceptual framework for travelling fires in large compartments with fire resistant islands in order to ensure that the structure so designed is able to resist more realistic fire exposures expected in such compartments, commonly found in modern office buildings. In addition, this paper also presents the implementation of this new travelling fire model in the SIFBuilder framework [1], which is an OpenSees based integrated computational tool for performing automated thermo-mechanical analyses for large structures subjected to a broad range of idealised design fires.

INTRODUCTION

Many studies of large compartments in fire carried out over the past two decades show that fires in such compartments have a great deal of non-uniformity, unlike the homogeneous compartment temperature assumption commonly made in the current fire safety engineering practice. In general, large compartment fires burn locally and tend to move across entire floor plates over a period of time. This kind of fire scenario is beginning to be idealized as travelling fires. Two representations of travelling fires can be found in literature, hereinafter referred to as: Clifton's model [2]; and Rein's model [3]. However, both models neglect important aspects of fire dynamics. For instance the accumulation of a hot smoke layer is ignored in both models, while in Clifton's model, all elements in one 'firecell' (one compartment) share the same time fire exposure history. In Rein's model, Alpert's correlation is adopted to calculate far field temperature and a uniform temperature ($800^oC-1200^oC$) is assumed for the near field, which seems overly prescriptive. Furthermore, due to the reasons of computational complexity, neither of the travelling fire models have been coupled to the global structural response.

In 2009, OpenSees [4] was adopted at the University of Edinburgh to further develop it to perform structural fire analysis. Significant contributions in terms of heat transfer and fire modules have been made to the framework in developing the

[1]BRE Centre for Fire Safety Engineering, the University of Edinburgh, Edinburgh, EH9 3JL, UK
[2]Department of Mechanical, Aerospace and Civil Engineering, Brunel University London, Uxbridge, Greater London, UB8 3PH, UK

‘Thermal’ version of OpenSees [5]. Temperature dependent formulations have been incorporated for basic element types, primarily beam-column elements and shell elements to account for the thermal effects [6]. Material library of the original framework has also been updated by adding new temperature dependent material models for steel and concrete based on Eurocodes [7].

In order to move towards a more comprehensive solution for a unified analysis, development of an OpenSees based research tool named SIFBuilder was started in 2014 [8], which aims to perform automated thermo-mechanical analyses for large structures under a wide range of idealised fires, some of which mimic realistic fire exposures (such as localized and so-called travelling fires). The special features of SIFBuilder includes: large model generation with minimal input; rapid heat transfer analysis for a range of idealized-uniform and idealized-nonuniform fires; automatic coupling of the heat transfer output with the structural model to perform thermo-mechanical analyses.

This paper introduces a new travelling fire model, which mobilises Hasemi’s localized fire model [9] and hence create a new kind of travelling fire, and combines it with a simple smoke layer calculation for the areas of the compartment not involved in burning. The heat fluxes received by each structural member in a large compartment using this approach should provide greater fidelity with realistic conditions than any other model currently proposed. Furthermore, this new travelling fire model is programmed into SIFBuilder based on previous work [1] and [8], and would enable rapid testing of multiple travelling fire scenarios. Therefore we believe that this approach also offers a great deal of flexibility for designing structural fire resistance in large compartments and, if properly used, should ensure that worse case scenarios are discovered.

NEW TRAVELLING FIRE MODEL

The proposed design fire is idealized as a localized fire plume with characteristics that include: a predetermined plume propagation trajectory along which it travels; variable fuel load distribution along the trajectory; and consideration of smoke accumulation in the ceiling cavity.

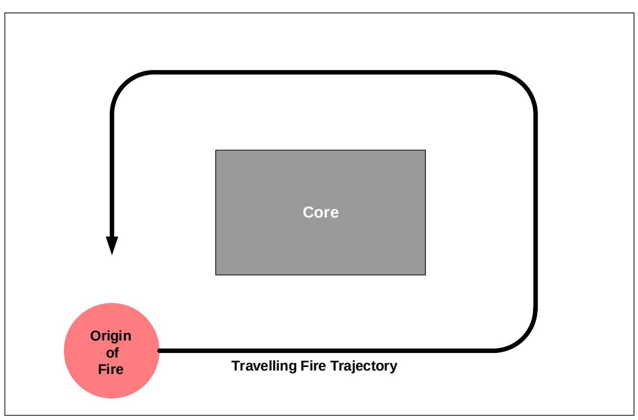

Figure1. New travelling fire model on open plan office floor

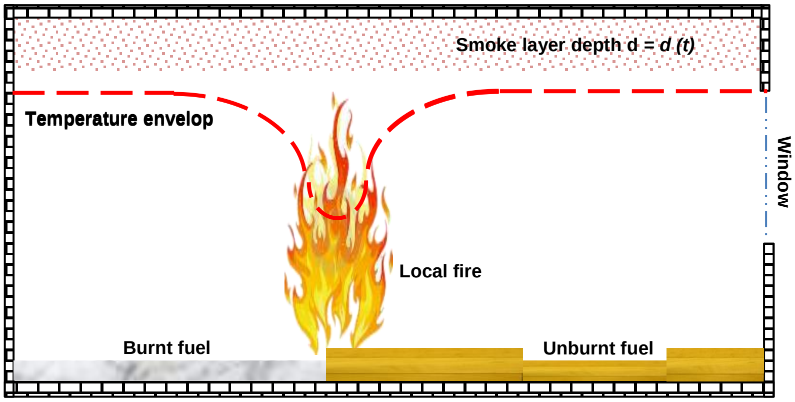

Figure 2. Elevation view - new travelling fire model.

It is proposed here to combine Hasemi's model for determining the temperature evolution in structural members close to the plume location, with a simple smoke layer calculation for predicting the temperatures of structural members away from the burning region. Figures 1 and 2 schematically illustrate the proposed scheme.

Near field: Hasemi localized fire model

For quantifying the local effect of the travelling fire on adjacent structural members, Hasemi's localized fire model is utilized here. When the fire plume is impinging the ceiling, the net heat flux $\dot{h}$ (W/m^2) is given in EC1 as,

$$\dot{h} = 100000 \qquad \text{if } y \leq 0.30 \tag{1a}$$

$$\dot{h} = 136300 - 121000y \qquad \text{if } 0.30 < y \leq 1.0 \tag{1b}$$

$$\dot{h} = 15000 y^{-3.7} \qquad \text{if } y \geq 1.0 \tag{1c}$$

The parameter y is obtained by calculating the following equation:

$$y = \frac{r + H + z'}{L_h + H + z'} \tag{2}$$

Where r (m) is the horizontal distance between the vertical axis of the fire and the point along the ceiling where the heat flux is calculated, H (m) is the distance between the fire source and the ceiling, z' (m) is the vertical distance between the virtual fire origin and the fire source, L_h (m) is the horizontal flame length.

Far field: simple smoke layer calculation

The combination of energy conservation and smoke generation is brought into the travelling fire model in an elementary way, considering different fuel distributions along the trajectory. The depth of the smoke layer is assumed to be time dependent and uniform over the whole ceiling. The rate of air entrainment is determined using a number of different models. Meanwhile, smoke will be generated as more and more local lumped fuel is consumed. This feature would reproduce preheating and post heating effects for the structural analysis, which is the hallmark of travelling fires.

Combination of the two models

Since Hasemi's equation is applicable to localized fires in an unconfined space and smoke accumulation is not considered in his model, this may lead to the far field predicted temperature based on Hasemi's localized fire calculation in a confined space lower than the actual temperature. Therefore, it is proposed here to combine Hasemi's model with a hot smoke layer calculation. In other words, the radiant and convective heat fluxes to structural surface can be calculated based on the summation of heat flux from Hasemi's localized fire, and heat flux from the hot layer of the smoke (see Figures 3).

Fire trajectory

As the final objective of this new travelling fire model is for applications in structural analysis, the travelling fire trajectory is assumed to be the worst case of the structural response: under the mid-span of the main beams (see Figures 1).

Ignition Point

The ignition point of the travelling fire could be anywhere in the compartment. However, a fully developed localized fire will be the initial state of this travelling fire model, at which point it becomes mobile. From the structural design point of view, the development phase of the localized fire is not considered important, just as the pre-flashover stage is ignored in compartment fires

Regulatory minimum fuel depth (RMFD)

The concept of a regulatory minimum fuel depth (RMFD) is introduced corresponding to a reference travelling fire velocity in the model. This RMFD is a layer of fuel uniformly distributed over the entire floor plate, and contributes to the total heat fluxes calculation.

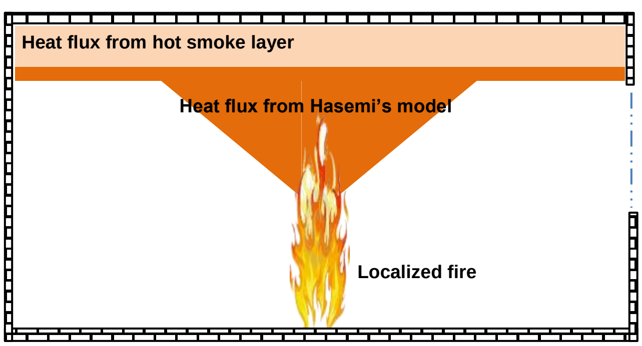

Figure 3. Heat fluxes superposition from two models.

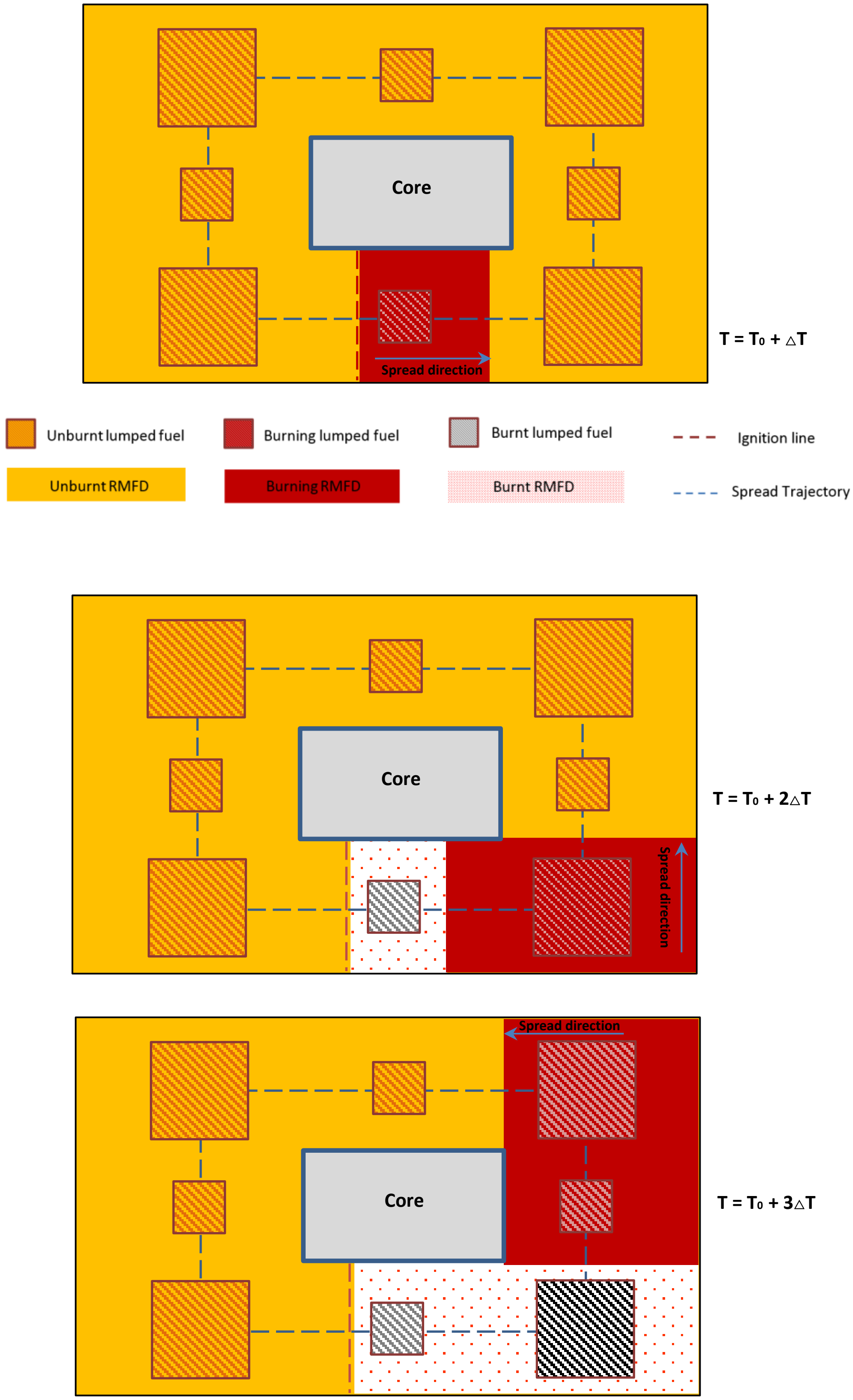

Figure4. Plan view - RMFD concept in 1D Travelling fire with one trajectory.

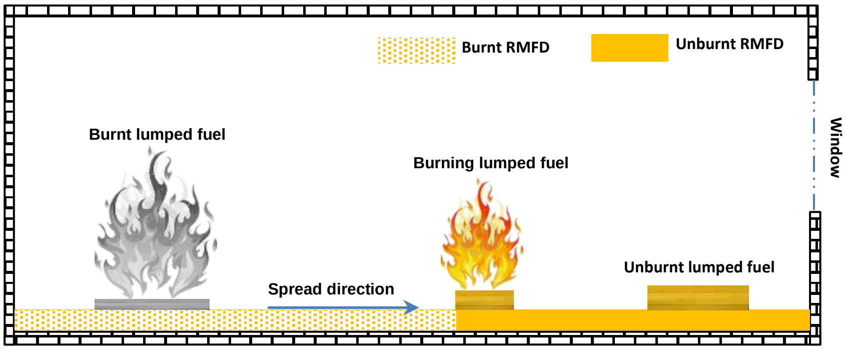

Figure 5. Elevation view - RMFD concept in 1D Travelling fire with one trajectory.

Moreover, an agreed quantity of additional lumped fuel is placed next to the most critical and/or most vulnerable parts of the structure identified in consultation with the structural engineer according to performance-based design principles. Figure 4 & 5 illustrate how the fire travels based on the RMFD concept.

Other key assumptions

The proposed design fire is fuel controlled based on the assumption that sufficient air is available at the beginning and subsequently the glazing adjacent to the fire plume breaks. All fuel is assumed to be consumed over the design fire duration with: non-uniform burning rates of the travelling fire along the trajectory; changing fuel load density; and variable heat release rates.

A flashover scenario arises naturally in this model and the fire transitions from a localized travelling fire to a whole compartment fire when the temperature of the hot smoke layer reaches $500^{o}C$ [10].

IMPLEMENTATION IN SIFBUILDER

This new travelling fire model is programmed into SIFBuilder based on previous work [1] and [8], which is mainly about the development of OpenSees for integrating the heat transfer and thermo-mechanical analysis for modelling localized fire in structures. The implementation of this new travelling fire model in SIFBuilder follows the same workflow as the localized fire model. After inputting basic structural information for generating the structural model, the user defines the structural loading and thereafter the fire loading information.

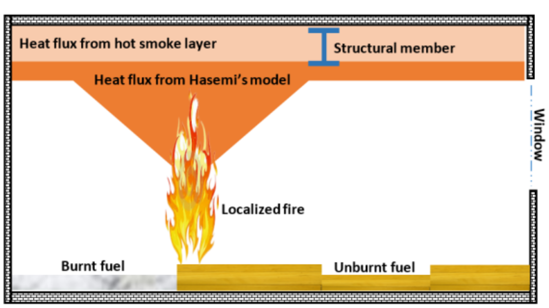

Figure 6. Heat flux at time t_0.

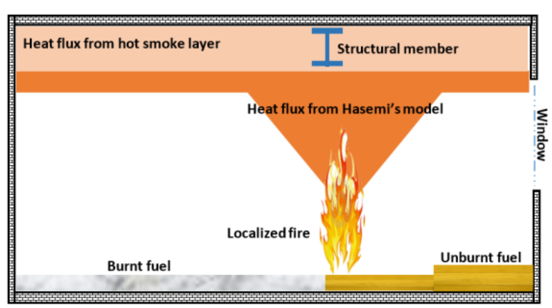

Figure 7. Heat flux at time $t_0 + \Delta t$.

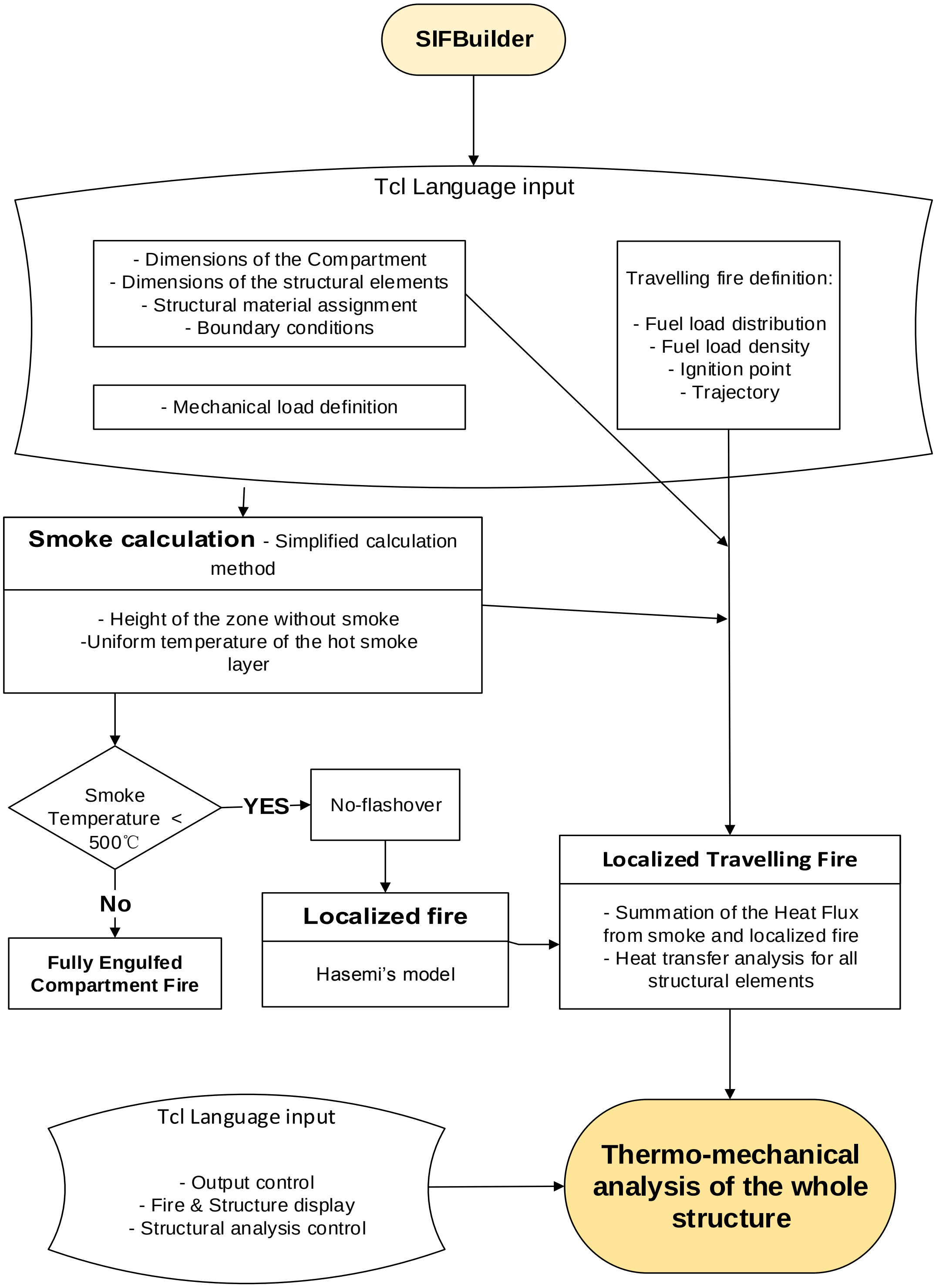

Figure 8. Flow chart of implementing new travelling fire model in SIFBuilder.

The travelling fire module interacts with the heat transfer module through their respective interfaces at each time step in order to determine the transient fire imposed boundary conditions adjacent to the structural surfaces.

Unlike the localized fire model in SIFBuilder, both spatially and temporally non-uniform heat fluxes for different structural elements produced from the summation of the heat flux from the hot smoke layer and Hasemi's model, are updated at each time step according to the travelling fire location in the compartment (see Figures 6 and 7, only one structural element showed for clarity).

Subsequently, the heat transfer analysis module launches and the nodal temperature histories are automatically mapped to the fibers of the structural mesh for each structural member. Following the heat transfer analysis the thermo-mechanical analysis module is invoked to determine the structural response history for the whole frame including all heating phases for each structural member. This may include the effects of preheating, direct heating, post-heating and cooling.

Ultimately, the new tool will provide a flexible approach for examining the impact of fire on structural behavior under realistic design fire scenarios, at greatly reduced cost in the analysis time and user effort than currently possible. Figure 8 shows how the new travelling fire model is implemented in SIFBuilder.

CONCLUSIONS

Although it is still early in the life of this work to make definite conclusions, a good start has been made in developing a conceptual idea of the travelling fire model, a possible programming scheme, and also a set of case studies for the framework verification and validation (which is not illustrated in this paper due to the paper length limitation).

REFERENCES

1. L. Jiang, X. Dai, A. Usmani, and P. Kamath, "OpenSees-based Integrated Tool for Modelling Structures in Fire," *in The First International Conference on Structural Safety under Fire & Blast,*Glasgow, Scotland, UK, 2015, pp. 461-468.
2. Clifton CG, "Fire models for large firecells. HERA Report R4-83." 1996.
3. E. Rackauskaite, C. Hamel, A. Law, and G. Rein, "Improved Formulation of Travelling Fires and Application to Concrete and Steel Structures," *Structures*, vol. 3, pp. 250-260, 2015.
4. F. T. McKenna, "Object-oriented finite element programming: Frameworks for analysis, algorithms and parallel computing," University of California, 1997.
5. Y. Jiang, "Development and application of a thermal analysis framework in OpenSees for structures in fire," The University of Edinburgh, 2012.
6. J. Jiang and A. Usmani, "Thermo-mechanical Analysis of Steel Frame Structures Using OpenSees" no. April, pp. 209-212, 2011.
7. J. Zhang, "Developing OpenSees Software Framework for Modelling Structures in Fire," no. February, 2014.
8. L. Jiang, Y. Jiang, J. Jiang, A. Usmani, and S. Chen, "AN OPENSEES-BASED INTEGRATED TOOL FOR MODELLING STRUCTURES IN REALISTIC DESIGN FIRES," in 8th International Conference on Structures in Fire, Shanghai, China, 2014, pp. 987-994.
9. T. Wakamatsu and Y. Hasemi, "Heating Mechanism of Building Components Exposed to a Localized Fire -FDM Thermal Analysis of a Steel Beam under Ceiling-," *Aofst 3*, no. m, pp. 335-346, 1988.
10. Commission of the European Community (CEC) (1997a), Development of design rules for steel structures subjected to natural fires in large compartments, Draft Fina., no. CEC Agreement 7210-SA/210/317/517/619/932. 1999.

Global Structural Behavior of Steel-Concrete Composite Floor Systems under Traveling Fires

JASON MARTINEZ and ANN E. JEFFERS

ABSTRACT

This paper presents a computational investigation aimed at better understanding the global structural behavior of a steel-concrete composite (SCC) floor system subjected to single-story 1D traveling fires. Using the traveling fire methodology (TFM), a range of spatially and time-varying fire exposures are applied to a three-dimensional (3D) finite element (FE) macro-model of a SCC floor system designed following US design standards and practices. The sequentially coupled thermal-mechanical simulations were carried out using *ABAQUS*, where the structural modeling approach was verified using experimental test data from the Cardington fire test. Essential factors influencing the fire resistance of SCC floor systems, namely the passive fire protection scheme of the floor beams, and the traveling fire burning size, were varied to investigate and characterize the global structural response. Simulation results were analyzed and useful trends were observed, in particular the dependency of the slab vertical displacement rate and the maximum vertical displacement to both the distance from the fire origin and traveling fire burning size. Particularly interesting was the observation of high tensile forces generated in the beam-to-column connections during the heating phase of the traveling fire.

INTRODUCTION

Structural fire safety is a key consideration in design of buildings, as a properly designed building can reduce the hazard to both life and property loss during unwanted accidental fires. Typically, large floor spaces are compartmentalized into smaller compartments (< 500 m^2) with walls and partitions aligning with fire protected primary floor beams. However, structural innovation and evolving architectural trends are resulting in large open spaces becoming a common feature of modern building design, and moreover there are instances where large open spaces are functionally required (e.g., open office space, airport entrance halls, exhibition halls, library space, etc.). The lack of compartmentation in large open spaces results in conditions not favorable for flashover, producing fires in which the spatial variances of temperature

Jason Martinez, Department of Civil and Environmental Engineering, University of Michigan, Ann Arbor, MI, USA.
Ann E. Jeffers. Department of Civil and Environmental Engineering, University of Michigan, Ann Arbor, MI, USA.

are significant. These fires burn locally and travel across the floor, igniting additional fuel in their path of travel, and resulting in spatially and time-varying fire exposures that can last for hours and span across large floor areas [1].

The degree to which structural fire design codes are capable of ensuring structural safety during a traveling fire exposure is poorly understood. This results from the fact that the global structural response and performance of structures under traveling fire exposures is also poorly understood. This study aims to address the knowledge gap pertaining to the global system-level response of structures under horizontally traveling fires by numerically examining the behavior of a code-compliant steel-concrete composite (SCC) floor system, previously used by Agarwal and Varma [2], under a host of single-story 1D traveling fires. The traveling fire methodology (TFM) developed by Stern-Gottfried and Rein [1] is used to characterize the spatial and temporal gas phase temperature distributions of the 1D traveling fire.

STUDY OVERVIEW

The test structure is a generic steel framed building with composite slabs supported by steel floor beams via headed shear stud connectors. Gravity frames are used to resist gravity loads, while an interior rigid core, representing an elevator shaft made of reinforced concrete (RC) shear walls, is used as the main lateral load resisting system. The structural framing plan is 5 bays wide and 3 bays deep, with a plan dimension of 38.1 m x 22.9 m as shown in **Figure 1**. Single-plate shear tab connections are used for beam-to-beam and beam-to-column connections, and are marked as small dots in **Figure 1** below. Further details regarding the composite floor system are found in ref. [2].

Two passive fire protection scheme (FPS) for the steel floor beams will be investigated in this study, differing only on whether intermediate floor beams are protected or not: (1) **FPS1** - all floor beams are fire protected to have a FRR of 1 h; and (2) **FPS2** - only primary beams are fire protected to have a FRR of 1 h, with secondary beams left unprotected. Gravity loads acting on the composite floor system during the traveling fire exposure follow the *ASCE 07-10* [3] critical load combination recommended for fire exposed structures:

$$U = 1.2D + 0.5L + T \tag{1}$$

where U is the overall factored gravity load; D is the gravity dead load; T is the load resulting from the fire scenario, and L is the gravity occupancy live load. Uniform live loads for typical office buildings are taken from ASCE 07-10 as 2.4 kN/m^2, while gravity dead load is computed from the density of steel and concrete as 3.1 kN/m^2.

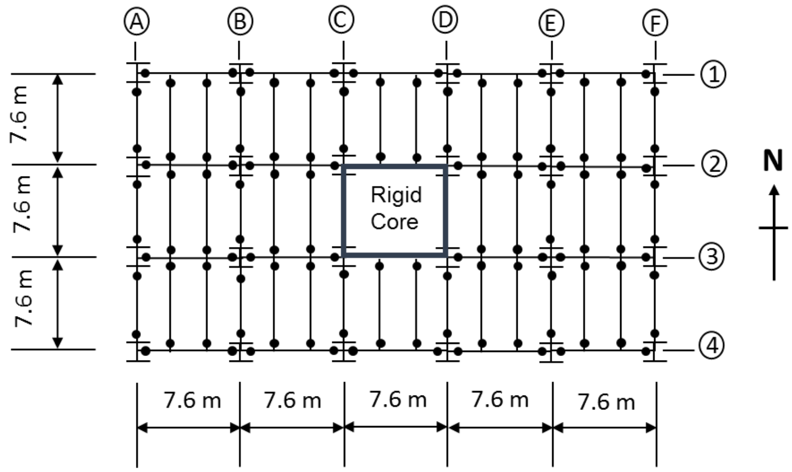

Figure 1. Structural plan layout of the SCC building used in the study.

METHODOLOGY

The sequentially coupled fire-thermal-mechanical analyses entailed three main steps: (1) modeling the appropriate gas-phase temperature-time histories in the large open space using the TFM; (2) carrying out 2D transient thermal analysis to predict internal nodal *T-t* within structural members; and (3) carrying out 3D structural analysis to predict structural responses using predicted nodal *T-t* histories (see **Figure 2(a) to Figure 2(c)**). All of the sequentially coupled thermal-mechanical simulations are carried out using the commercial finite element (FE) analysis package *ABAQUS*. Explicit dynamic analysis is carried out in order to capture response beyond the numerical instability encountered in an implicit static analysis.

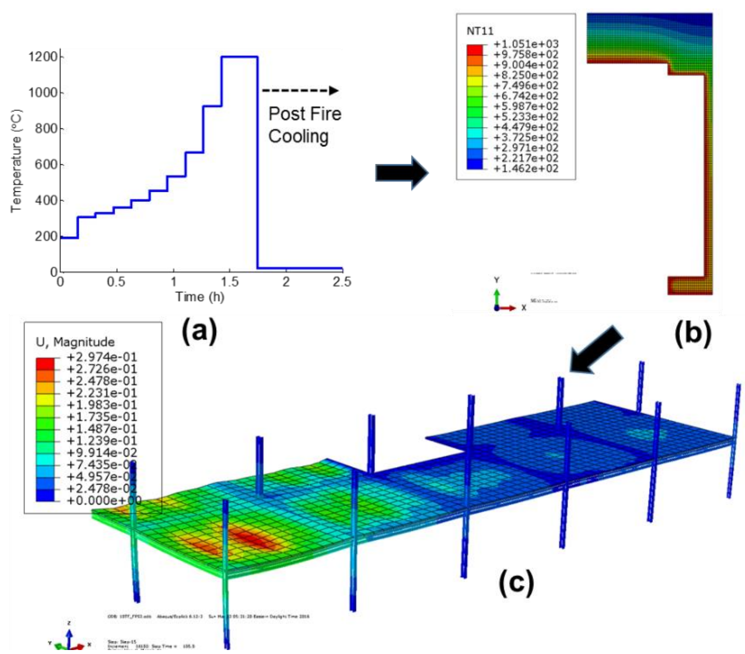

Figure 2. Sequential coupled fire-thermal-mechanical analysis utilized in this study.

The TFM provides the gas-phase temperatures on the underside of the heated floor system (or ceiling). Because the TFM accounts for a whole family of possible traveling fires ranging on the size of the near field (i.e., flaming or burning) region, the fire size will vary between 10 %, 20 %, 30 %, 50 %, and 70 % of the total floor area of the compartment. To treat the traveling fire as one-dimensional (1D), we make the assumption that the fire extends the whole width of the compartment and travels in a single linear path. For this type of fire, the compartment floor length (in the direction of fire travel) is discretized into nodes, each with a fixed width Δx, called the grid size.

A grid size Δx of 3.81 m is utilized so that the spatial discretization resolves the fire travel with adequate resolution. Lastly, the near field region is taken to be a constant 1,200 °C to represent the worst case condition.

The typical 2D thermal model of a composite beam cross-section used in this study is shown in **Figure 2**. Four node plane quadrilateral heat transfer elements *DC2D4*, available in ABAQUS, are used to model the cross-sections. It is assumed that the fire-exposed portions of the members are fully enveloped by the hot gases and are heated with radiative and convection boundary conditions in the heat transfer analysis. Non-heated boundaries (such as the top of the slab) are treated in similar fashion as heated boundaries, but prescribed an ambient temperature condition to simulate the exchange with cold air.

The macro-model of the floor system, consisting of an assembly of beam, shell, and connector elements, to represent steel I-beams, reinforced concrete (RC) slab, and shear stud connectors, respectively, is shown in **Figure 2**. Beam elements of type *B31* with shear-flexible element control are used to model the steel beams and columns, while linear 4-node doubly curved thin/thick type *S4R* general-purpose quadrilateral shell elements are used to model the RC slab. Full composite action between the composite shells representing the reinforced concrete (RC) slab and beam elements representing the steel I-beams is assumed. Both material and geometric non-linearity are considered in the analyses, with σ-ε-T constitutive model of steel and concrete taken from the structural Eurocodes [4, 5]. Given the symmetrical nature of the problem, only half of the floor is modeled.

The accuracy of the proposed modeling approach is validated by comparing recorded test results from the Cardington fire test 3, with results of a replica FE model of the Cardington frame. Structural members are heated using recorded nodal *T-t* data from the Cardington test. The plot in **Figure 3** below shows a good agreement with the experimentally recorded data and shows that the numerical modeling approach is capable of predicting experimentally recorded deflection-time histories in both the RC slab section and composite beam section.

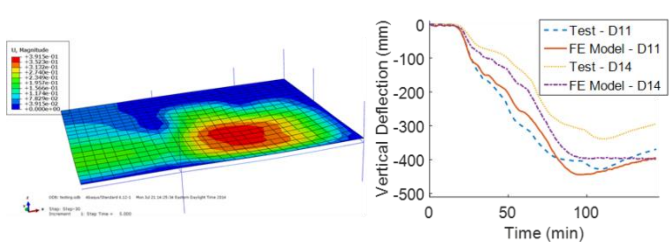

(a) (b)

Figure 3. Validation of the structural modeling approach using the Cardington fire test data. Figure 3(a) shows the finite element model of a quarter of the floor, while Figure 3(b) shows the validation of vertical displacement at two locations within the fire compartment.

RESULTS

For brevity, discussion of the global structural responses are limited here to: (1) displacement time histories (*U3-t*) at the center of two slab panels, labeled *S1* and *S2*, (2) horizontal in-plane displacement time histories (*U1-t*) at the exterior edge of the slab, labeled *S3* and *S4*, and (3) axial force time histories (*P-t*) at the end of floor beams labeled *B1* and *B2*. All labels are shown in **Figure 4** below. Since FPS1 represents the case where all the floor beams are fire protected, the limit of span/20 is appended to each of the vertical displacement time histories to help gauge the severity in magnitude of the displacements. Vertical downward displacements are taken as positive and upward displacements are negative, while for axial force, tensile axial force is taken as positive while compressive axial force is taken as negative.

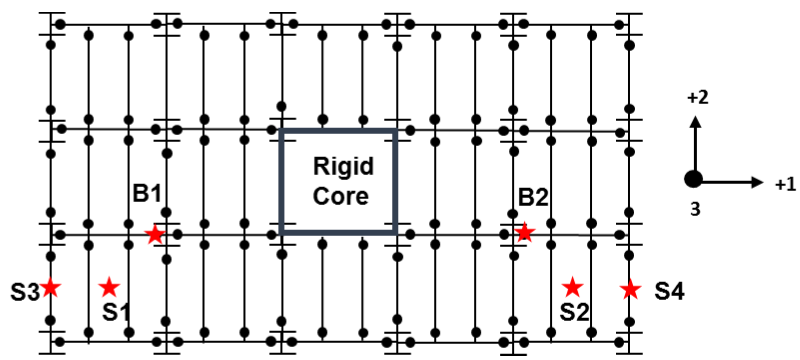

Figure 4. Labels of output interest.

Examining the vertical displacement time histories at slab location S1 in **Figure 5(a)** for fire protection scheme FPS1 reveals that the initial rate of vertical displacement is invariant on the burning size of the traveling fire. **Figure 5(a)** also reveals that the maximum vertical displacement is inversely dependent on the burning size. A larger maximum vertical displacement is associated with a smaller burning size. For the FPS1 case, the limit span/20 of 380 mm is surpassed only for a 10% burning traveling fire. Similar findings are observed for the fire protection scheme FPS2. These figures are omitted for brevity.

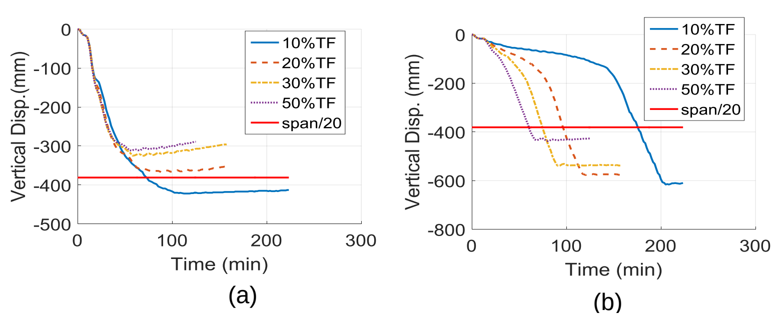

Figure 5. Vertical displacement time histories at (a) slab point S1 and (b) slab point S2, for the fire protection scheme FPS1 and various traveling fire sizes.

An examination of vertical displacement time histories at slab location S2 in **Figure 5(b)** reveals that larger deflections occur in the slab panel furthest from the origin of the 1D traveling fire. In this slab panel, vertical displacements surpass the span/20 limit of 380 mm for all of the traveling fire burning size. Interestingly enough, the initial rate of vertical displacement depends on the burning size of the traveling fire, with the displacement rate increasing as the fire size increases.

The observed trends are particularly important for determining the fire resistance rating of the composite floor system in a performance-based design environment. Using a displacement based criteria the shortest time to failure, defined as the time for which vertical displacements surpass the span/20 limit is governed by the slab panel furthest from the origin of the traveling fire, for the larger traveling fire.

One consequence of having an increase in the spatial extent of a fire is the increase in lateral displacement resulting from thermal expansion of the floor slab. This can result in column buckling due to the composite nature of the floor system—a phenomenon that was not observed in the limited traveling fire analysis carried out. Traveling fires are unique in that the spatial extent of the fire can be large, and for this reason, consideration is given to quantify the extent of this thermal expansion. **Figure 6** below shows the horizontal in-plane displacement at slab points *S3* and *S4* for the fire protection scheme FPS1. It is observed that the expansion of the floor slab can be as high as 200 mm, with the maximum in-plane displacement occurring in the edge slab panel furthest from the fire origin. This is significant since large displacement can cause damage to fragile exterior curtain walls, creating the potential for vertical fire spread to the above story.

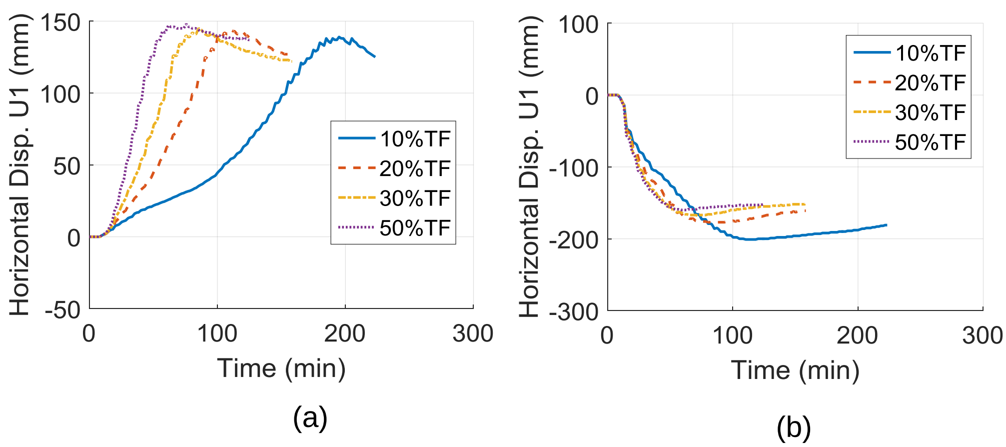

Figure 6. Horizontal in-plane displacement time histories at (a) slab point S3 and (b) slab point S4, for fire protection scheme FPS1 under various traveling fire sizes.

High tensile forces in the shear tab connections are generated during the heating phase of the traveling fire as shown in **Figure 7**. This differs from a uniformly burning small compartment fire in that high tensile forces are usually generated during cooling phase of the fire as thermal contraction occurs. The plot of axial force time histories at beam locations *B1* and *B2* in **Figure 7** reveal that tensile forces significantly surpass the tensile strength of the shear tab connections of ~250 kN. Similar observations are observed for fire protection scheme FPS2. More concerning is the excessive tensile forces generated during the cooling phase of the fire, which are theoretically in the range of ~ 1,500 to 2,000 kN, given that connection failure is prevented. The robustness of beam-to-column and beam-to-beam shear tab connections needs to be investigated further using a macro-based model to represent the shear tab connections. Such a model is capable of capturing failure of the connection, and can account for relaxation of the tensile force in the floor beam after failure of the shear tab connection occur.

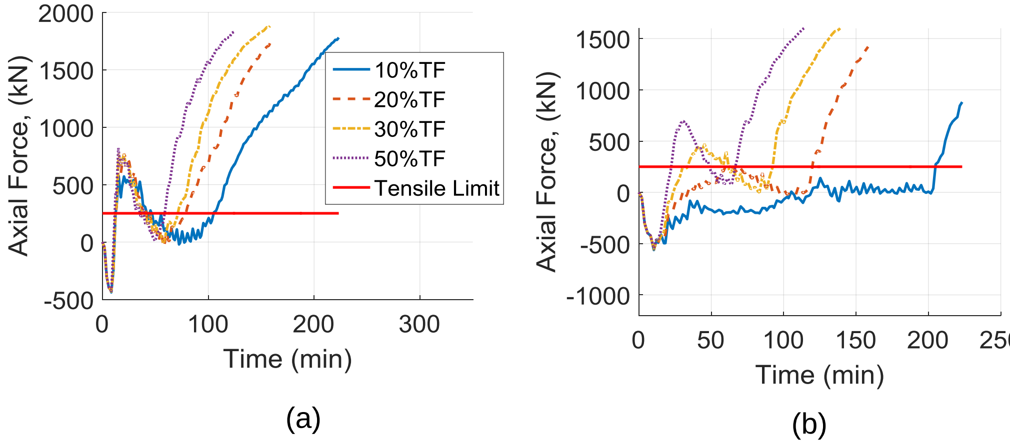

Figure 7. Axial force time histories at (a) beam point B1 and (2) beam point B2, for fire protection scheme FPS1 under various traveling fire sizes.

CONCLUSION

Based on the results presented, the following conclusions are drawn about steel-concrete composite floor systems under 1D traveling fires:

- The initial rate of vertical displacement in a heated slab panel is invariant of the burning size for slab panels closest to the fire origin, and variant on the burning size for slab panels furthest from the fire origin;
- Larger vertical displacements are observed to occur in slab panels furthest from the fire origin and are inversely related to burning fire size;
- Large in-plane horizontal displacements of up to 200 mm occur as a result of large scale thermal expansion of the floor slab. Such lateral floor expansions can be damaging to fragile exterior curtain walls;
- Large tensile forces are generated in the beam-to-column connections during the heating phase of a traveling fire, and even larger theoretical tensile forces are generated during the cooling phase.

ACKNOWLEDGMENTS

The work presented was supported in part by University of Michigan Rackham Engineering Award (REA) and the National Science Foundation (NSF) through Grant No. DGE 1256260 and Grant No. CMMI-253440. This research was also supported in part through computational resources and services provided by the University of Michigan's Advanced Research Computing (ARC) Flux HPC cluster.

REFERENCES

1. Stern-Gottfried, J. and G. Rein. 2012. "Travelling fires for structural design-Part I: Literature review", *Fire Safety Journal*, 54:74-85.

2. Agarwal, A. and A.H. Varma. 2014. "Fire induced progressive collapse of steel building structures: The role of interior gravity columns," *Journal of engineering structures*, 58:129-140.

3. American Society of Civil Engineers (ASCE). 2010. "Minimum Design Loads for Buidlings and Other Structures," ASCE 07-10, Reston, VA.

4. European Committe for Standardization (CEN). 2002. "Eurocode 2: Design of Concrete Structures – part 1-2: General rules – Structural fire design," EN 1992-1-2, Brussels, Belgium.

5. European Committe for Standardization (CEN). 2005. "Eurocode 3: Design of steel structures – Part 1-2: General rules – Structural fire design," EN 1993-1-2, Brussels, Belgium.

Structural Response of a Generic Steel Frame Exposed to Travelling Fires

EGLE RACKAUSKAITE, PANAGIOTIS KOTSOVINOS, ANN JEFFERS and GUILLERMO REIN

ABSTRACT

A design tool called Travelling Fires Methodology (TFM) [1] has been developed in recent years to account for travelling fires in large open-plan compartments. However, there has been little research carried out to understand the structural response of buildings subjected to such fires. The aim of this study is to investigate the behavior of a 10-story steel frame under travelling fires and compare it to the behavior under standard design fires. Each floor of the frame is subjected to four travelling fire scenarios and two Eurocode parametric temperature-time curves ('short-hot' and 'long-cool') using finite element software LS-DYNA. In total 60 fire scenarios are considered. Results show oscillations of axial forces and bending moments for the smallest travelling fire sizes, which are not observed for the parametric fires. In general the development of stresses and displacements within heated beams is found to follow similar trends irrespective of the frame level at which a fire occurs. For the investigated frame the critical fire scenarios are found to occur on the upper floors of the frame where column sections reduce in size. It has been found that depending on the structural metric examined both travelling fires and parametric fires can result in the most severe scenario. Therefore, it is highlighted that in the structural design for fires, in addition to the standard tools it is important to consider more realistic fire scenarios associated with travelling fires as they might trigger previously unnoticed structural mechanisms.

INTRODUCTION

Most of the current understanding of building behavior in fire is based on the adoption of the standard and parametric time-temperature fire curves. However, these design fires are based on small scale tests and assume flashover and therefore an idealized uniform thermal environment in a compartment. Thus, they are only valid in small enclosures. In large open-plan compartments, fires have been observed to travel resulting in a highly non-uniform temperature distributions within the enclosure [2]. Examples of such accidental events include the World Trade Centre Buildings 1, 2 & 7 (2001) and Windsor Tower fire in Madrid (2006).

Egle Rackauskaite and Guillermo Rein, Department of Mechanical Engineering, Imperial College London, London, SW7 2AZ, UK.
Panagiotis Kotsovinos, Arup, UK.
Ann Jeffers, Department of Civil and Environmental Engineering, University of Michigan, Ann Arbor, MI 48109-2125, U.S.A.

Non-uniform temperature variations on structures have been shown to have a significant impact on the failure mechanism and time to failure. In previous studies on steel [3], reinforced concrete [4] and post-tensioned concrete frames [5] where a travelling fire was considered, large distortions and cyclic behavior of stresses have been observed. However, to represent a travelling fire in some of these studies [3, 5] parametric curves were used and shifted from one bay to another after an arbitrary time. Such representation ignores the preheating of structural elements by hot smoke and spatially varying temperatures within the compartment.

The aim of this study is to assess the structural response of a generic multi-story steel frame subjected to a more realistic travelling fire exposure [6], which unlike previously identified studies [3, 5] accounts for spatially varying temperatures in the compartment. Another aim of this work is to investigate how varying the building level that the fire occurs on influences the structural response of the frame.

FINITE ELEMENT MODEL

Investigated frame

The multi-story steel frame considered in this study is based on the moment resistant frame design published by NIST [7]. It is a 10-story 5-bay frame representative of a generic office building with a floor layout of 45.5 m x 30.5 m, as shown in Figure 1. The frame is designed in accordance to the American Society of Civil Engineers (ASCE 7-02) standard. In this study the structural fire response of a two dimensional internal frame with a beam span of 9.1 m is investigated.

Steel beams support a lightweight concrete floor slab and act compositely. Design loads on the floor beams are 3.64 kN/m^2 (dead) and 4.79 kN/m^2 (live). For the roof design loads are 2.68 kN/m^2 (dead) and 0.96 kN/m^2 (live). The same loading on the frame is considered in this study. Beam sections are W14x22 at all levels. Column sections on floors 0 to 3, floors 4 to 6, and floors 7 to 8 are W18x119, W19x97, and W18x55, respectively. ASTM A992 structural steel with the yield strength (F_y) of 344.8 MPa is considered for all beams and columns.

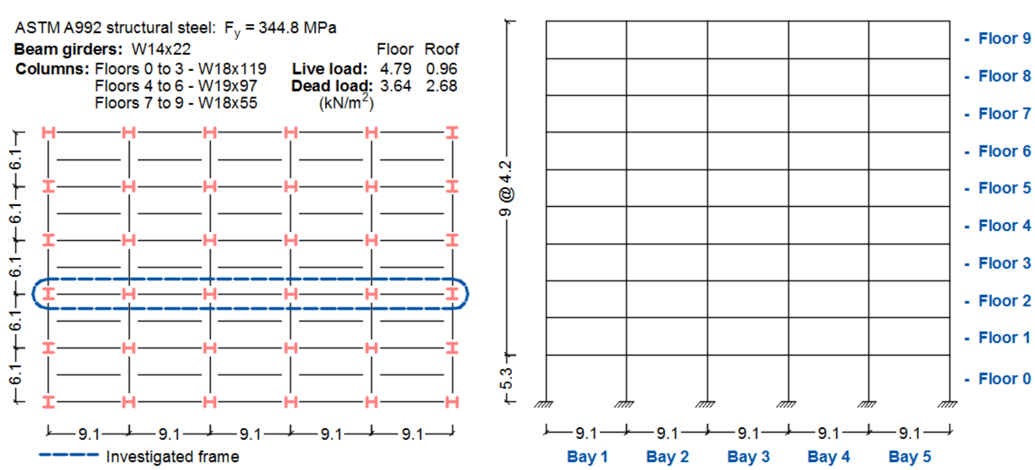

Figure 1. Plan layout and elevation of the investigated frame.

It should be noted that due to the 2D representation of the building the composite action between beams and concrete floor slab are not taken into account, which has been shown to have a beneficial effect to the structural response during fire. 2D analysis has been chosen for reasons of computational time, in order to allow comparison of many different fire exposures and due to the fact that the Improved Travelling Firs Methodology (iTFM), which is used to represent travelling fires, defines fires spreading along a linear path. Uniform thermal profile in the perpendicular side to the travel direction is assumed.

Fire scenarios

In this study the structural response of the frame subjected to travelling fires (TF) and standard design fires such as parametric temperature-time Eurocode (EC) [8] curves is investigated. To represent a travelling fire exposure iTFM [6] is used. It is the most recent version of the Travelling Fires Methodology (TFM), which was developed by Stern-Gottfried, Law and Rein [2, 4, 1] to account for the travelling nature of fires. iTFM considers non-uniform temperature distribution in the compartment and long fire durations observed in previously identified accidents. Illustration of a travelling fire is shown in Figure 2. Each floor of the frame is subjected to four TF scenarios, 2.5%, 10%, 25%, and 48% of the floor area (which effectively represent different fire spread rates [6]), generated using iTFM as well as short-hot and long-cool parametric temperature-time curves. Therefore, in total 60 fire scenarios are considered.

Travelling fires are assumed to travel from Bay 1 to Bay 5 (see Figure 1). Fuel load density and heat release rates are assumed to be 570 MJ/m^2 and 500 kW/m^2, respectively. EC parametric curves were generated assuming the same fuel load density as for travelling fires and opening factors of 0.176 m$^{0.5}$ (short-hot) and 0.044 m$^{0.5}$ (long-cool) to represent different exposures.

Beams and columns are designed for 60 min and 120 min fire resistance respecttively based on a limiting temperature of 550°C. Steel insulation properties are taken as for high density perlite (thermal conductivity k_i = 0.12 W/m.K, density ρ_i = 550 kg/m^3, and specific heat c_i = 1200 J/kg.K) [9]. Heat transfer to the structural members was carried out using lumped capacitance for separate parts of the sections (i.e. web and flanges) according to [9]. For beams the effect of the slab acting as a heat sink was taken into account. The convective heat transfer coefficient, density of steel

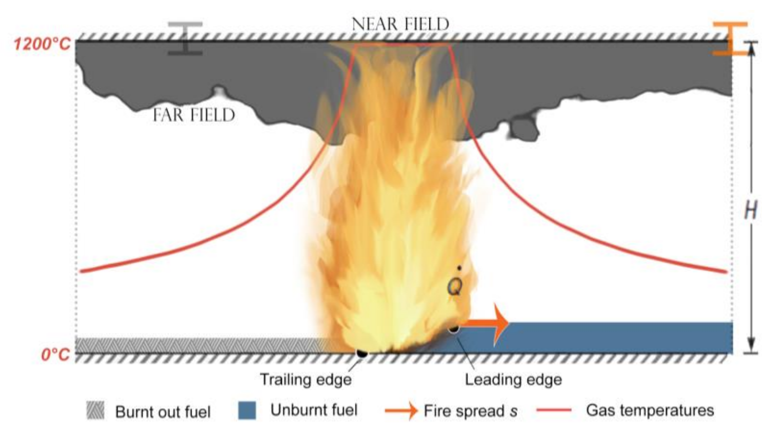

Figure 2. Illustration of a travelling fire and distribution of gas temperatures [6].

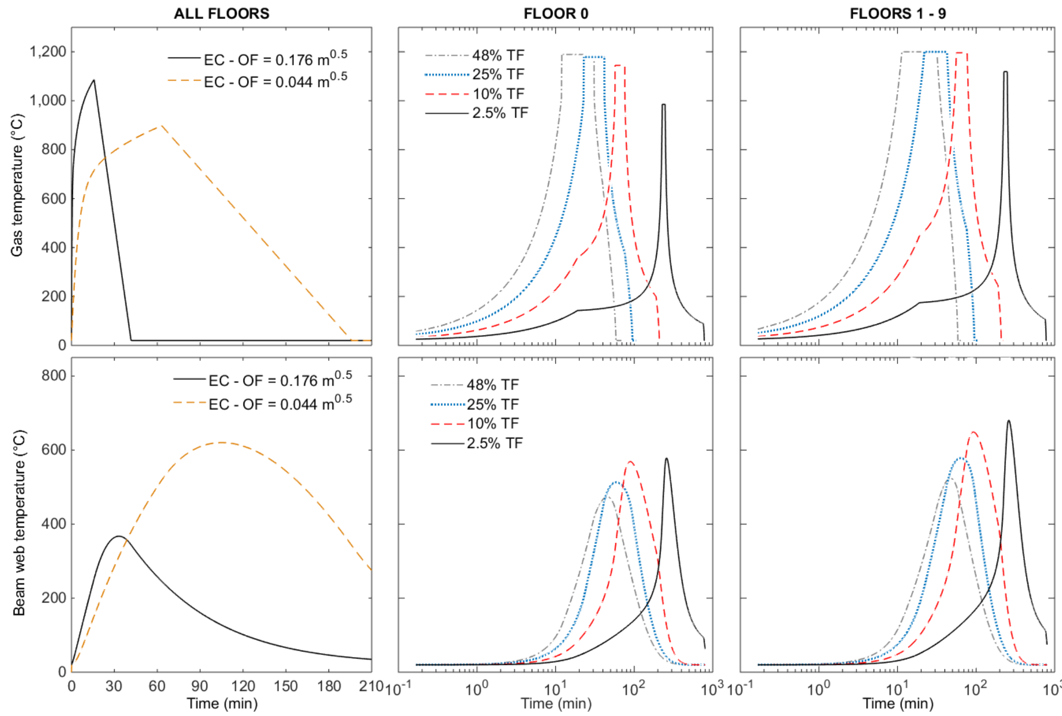

Figure 3. Gas temperature (top) and corresponding steel beam web temperature (bottom) development at mid-span of Bay 2 for six fire scenarios each floor of the frame was subjected to.

and radiative emissivity are assumed to be 35 W/m^2.K, 7850 kg/m^3 and 0.7, respectively [9]. The time step used for heat transfer calculations satisfying the stability criteria is 10 s. Gas temperatures and corresponding beam temperatures for all fire scenarios at the mid-span of Bay 2 are shown in Figure 3. Gas temperatures for Floor 0 are lower in comparison to the other floors because of the higher floor height (floor 0 – 5.3 m, floors 1 to 9 – 4.2 m).

LS-DYNA model

The multi-story steel frame is modelled using general purpose finite element software LS-DYNA. Steel beams and columns are modelled using Hughes-Liu beam formulation with an integration refinement factor of 5. Beams, Floor 0 columns, and Floor 1 to 9 columns are divided into 36, 22, and 16 beam elements, respectively. Corresponding beam element length is approximately 0.25 m. Supports for the ground floor columns are assumed to be fixed, and the beams and columns are assumed to be rigidly connected.

*MAT_STEEL_EC3_(202) material formulation is used for both steel beams and columns with default Eurocode [10] temperature dependent material properties. Steel with initial yield stress of 345 MPa, Young's modulus of 210 GPa, Poisson's ratio of 0.3, and density of 7850 kg/m^3 is assumed for all members. Mechanical, gravity and thermal loading identified in the previous sections is applied using *BEAM_SET, *BODY_Z, and *THERMAL_VARIABLE_BEAM_SET cards respectively. The latter allows the application of the non-uniform temperature distribution through the beam section. Temperatures are assigned to the members on the heated floor only. The remainder of the frame is assumed to be at room temperature. Simulations are carried out using the explicit solver of LS-DYNA. Therefore, in order to reduce the computational time, the temperature developed within heated members is scaled by a factor of 100. This means that parametric curve which would last 120 min in 'real' life in the simulation would be applied in 1.2 min.

RESULTS AND DISCUSSION

Location of the fire floor

Development of the beam mid-span displacements and axial forces with time for a frame subjected to 48% travelling fire is shown in Figure 4. Shaded areas represent a range of the displacements and axial forces which develop within the specific beam in relation to the fire location (i.e. fire floor) with varying fire exposure floor. Numbers 0 and 9 indicate that fire is located on ground floor and top floor, respectively. Development of mid-span displacements and axial forces within these floors is slightly different compared to fire occurring on the intermediate levels due to the reduced number of floors above or below the fire floor, i.e. different level of restraint.

The results indicate that in general the development of stresses and displacements within members follows a similar trend even though the fire occurs on different floors. The lowest limiting axial force values correspond to fire occurring on Floor 8. As the fire floor level reduces, the axial force that develops within the beams increases (by approx. 60 kN). On the other hand, higher displacements (by approx. 30 mm) develop within beams when fire occurs on the top floors of the building rather than the bottom. This is because heated beams on the top floors of the frame are supported by weaker column sections than beams on the bottom floors. Thus, the restraint to thermal expansion and redistribution of stresses is reduced in the upper floors. Results indicate that in the cases when the fire occurs in the upper floors initiation of yielding within the heated beams occurs up to 6 min later than in the cases when fire occurs on the lower floors of the frame. Analogous results of displacement, axial force, and bending moment development with varying fire floor were observed for all scenarios (i.e. 2.5%, 10%, and 25% travelling fires and EC curves).

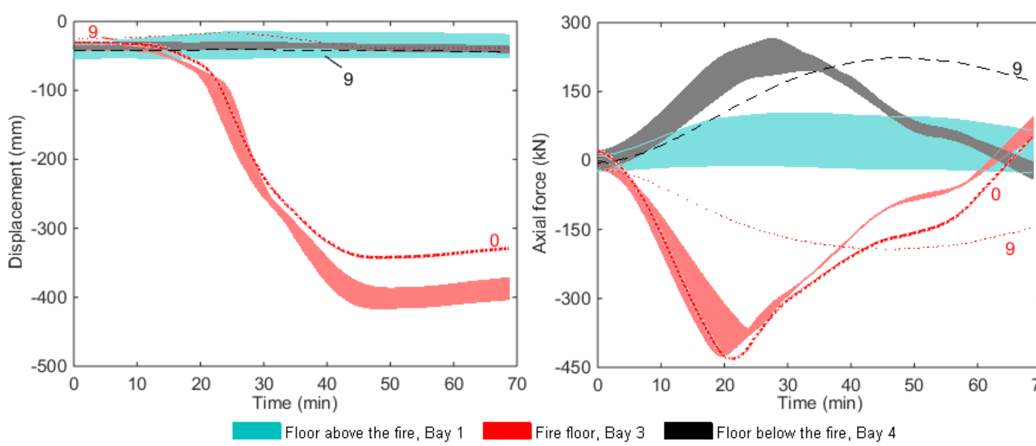

Figure 4. Variation of displacement and axial force development within beams with different levels of the building exposed to a 48% travelling fire (shaded areas). Numbers indicate axial force and displacement development when fire occurs on ground floor (0) and top floor (9).

Effect of fire scenario – travelling fires and parametric curves

The typical deflected shape of the frame and comparison of axial force, bending moment and mid-span displacement development within heated beams for different fire exposures are shown in Figure 6 and Figure 7, respectively. For all travelling fire (TF) scenarios beam displacements in Bay 1 are relatively low in comparison to other bays. Once the cooling begins the displacements remain constant while in the other bays there is a small recovery. However, the peak displacement reached in Bay 1 keeps on increasing with decreasing fire size as the beam is exposed to near-field for a longer duration. Higher displacements initially develop in Bay 3 for the EC fires and in Bays 1 or 2 for the travelling fires. For the 'short-hot' EC fire and 48% TF, displacements develop more rapidly at the early stages of the fire. However, the peak values reached are at least 20 cm lower than for other fire scenarios.

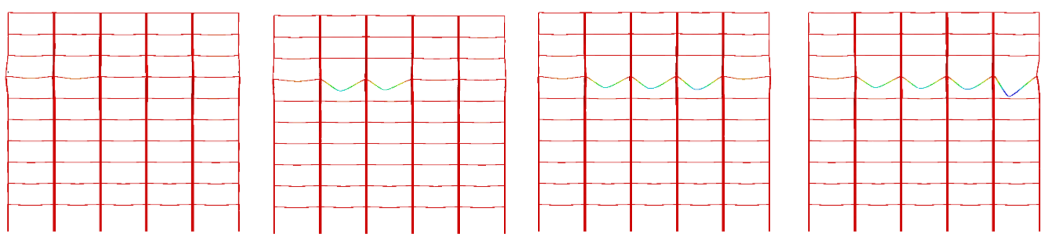

Figure 6. Deflected shape of the frame subjected to the 10% travelling fire during different times of fire exposure. Displacement scale factor is 5.

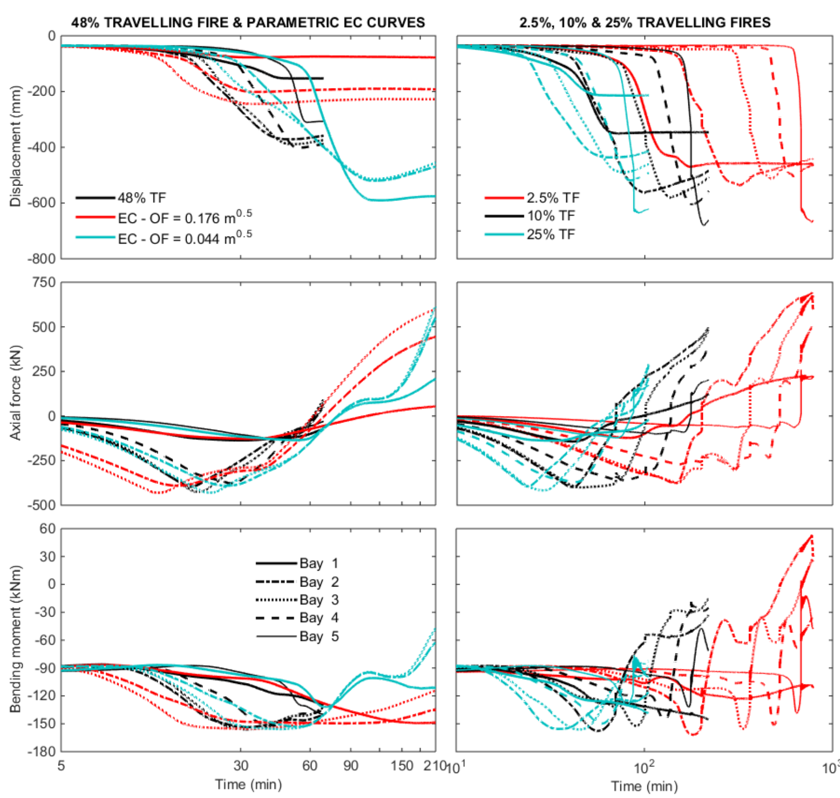

Figure 7. Development of mid-span displacements, axial forces and bending moments within heated beams for EC parametric fire exposure and travelling fire scenarios.

For all fire scenarios compressive axial forces within heated beams in edge bays are significantly lower than in internal bays. The highest axial forces seem to develop when the frame is subjected to large fire sizes (e.g. EC fires and 48% TF) with more uniform temperature distributions. Axial forces under these fires are 20 kN and 50 kN higher in comparison to 25% and 10%, and 2.5% travelling fires respectively. Under EC fires and 48% TF all beams in the floor are either in compression or tension at the same time, while under smaller travelling fire exposures this is not the case.

Peak beam mid-span bending moments for all fire scenarios are in the same range up to 160 kNm. Larger bending moments tend to develop first in Bay 2 for travelling fire scenarios, and Bay 3 for EC parametric fires. Figure 7 also shows small oscillations of bending moments and axial forces for 2.5% and 10% travelling fires. This appears to happen because fire length for these cases is shorter than the bay length. Therefore any column in the frame is exposed to high near-field temperatures when the fire crosses from one bay to another bay. This results in the change of restraint level to the heated beams and redistribution of bending moments. In other fire scenarios at least one column is always in the near-field region.

Failure

Two failure modes are considered based on the stability and deflection criteria. The stability criterion refers to the exceeded section capacity of the first element as reported by LS-DYNA. The deflection criterion refers to the maximum beam length to displacement ratio of L/20 as typically considered in standard fire tests. High deflections might cause damage to fire protection, fire suppression systems or compartmentation leading to faster heating or further fire spread. Results of different failure times for all fire scenarios are shown in Figure 8. Based on the stability criterion failure occurs only when the floors 5 to 8 are exposed to fire and times range from 1.5 h to 13 h (2.5% TF). On these floors, heated beams are connected to the weakest column sections, which are not able to resist development of high forces. Failure occurs by the pull-in of the edge columns. Failure times increase with decreasing fire size and are similar for EC 'long-cool' and 25% travelling fires.

No failure is observed for EC 'short-hot' and 48% travelling fires based on both failure criteria. Due to relatively short fire durations in these cases, members do not reach very high temperatures as in other fire scenarios. Based on the critical deflections, failure occurs for all remaining fire scenarios except for the fires on top

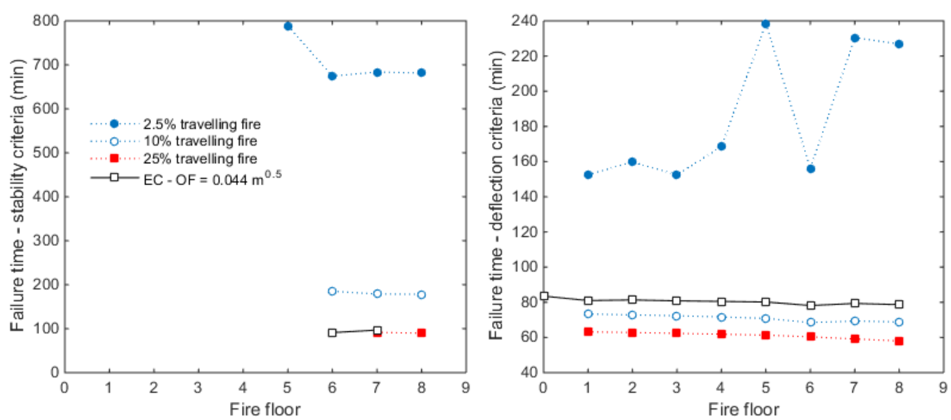

Figure 8. Variation of frame failure time based on stability and deflection (L/20) criteria for all cases.

and bottom floors of the frame. The failure times for the EC ‘long-cool’ fire, 10% and 25% TF seem to be similar with varying fire level in the building with a slight decrease for the floors 6 and above due to the smaller column section. According to the deflection criterion, the 25% TF appears to be the worst with failure occurring after 60 min of fire exposure, followed by the 10% TF (70 min), the EC ‘long-cool’ fire (80 min), and the 2.5% TF (2.5 h to 4h).

CONCLUSIONS

In this study, structural response of a generic steel frame exposed to travelling fires and the parametric fire curves on different levels of the building has been investigated. Results indicate that when different levels of the frame are subject to the same fire exposure, the development of displacements and stresses within heated beams is similar, except for fires on ground floor and top floor. Higher displacements and lower axial forces develop within beams in the upper floors. Peak axial forces and bending moments are in a similar range for both travelling fires and parametric fire curves. When the frame is subject to small travelling fire scenarios small oscillations of axial forces and bending moments is observed. These oscillations are linked to the fire size in relation to the width of the bay.

Critical fire scenarios based on the failure times for stability and deflection criteria have occurred on the upper levels of the building where column section reduces in size. This indicates that column section sizes and their change on different levels of the frame are important in defining the weakest floors. For the investigated frame the most severe fire scenarios in the terms of failure time have been found to be 25% travelling fire (deflection and stability) and Eurocode ‘long-cool’ fire (stability). Thus in the structural fire design of modern buildings it is important to consider both travelling fires and standard fire exposures such as defined in Eurocodes as they may lead to different structural failure mechanisms.

REFERENCES

1. Stern-Gottfried, J., and G. Rein. 2012. "Travelling fires for structural design - Part II: Design methodology," *Fire Saf J* 54:96-112.
2. Stern-Gottfried, J., and G. Rein. 2012. "Travelling fires for structural design - Part I: Literature review," *Fire Saf J* 54:74-85.
3. Bailey, C.G., I.W. Burgess, and R.J. Plank. 1996. "Analyses of the effects of cooling and fire spread on steel-framed buildings," *Fire Saf J* 26:273-291.
4. Law, A., J. Stern-Gottfried, M. Gillie, and G. Rein. 2011. "The influence of travelling fires on a concrete frame," *Eng Struct* 33:1635-1642.
5. Ellobody, E., and C.G. Bailey. 2011. "Structural performance of a post-tensioned concrete floor during horizontally travelling fires," *Eng Struct* 33:1908-1917.
6. Rackauskaite, E., C. Hamel, A. Law, and G. Rein. 2015. "Improved Formulation of Travelling Fires and Application to Concrete and Steel Structures," *Structures* 3:250-260.
7. Sadek, F., J.A. Main, H.S. Lew, et al. 2010. "NIST Technical Note 1669. An Experimental and Computational Study of Steel Moment Connections under a Column Removal Scenario."
8. BSI. 2002. Eurocode 1: Actions on structures. General actions. Actions on structures exposed to fire, European Standard BS EN 1991-1-2:2002.
9. Buchanan AH (2001) Structural Design for Fire Safety. John Wiley & Sons, Ltd.
10. BSI. 2005. Eurocode 3. Design of steel structures. General rules. Structural fire design, European Standard BS EN 1993-1-2:2005

Numerical Calibration of Hydrocarbon Localised Fire Tests by Means of Fire Dynamics Simulator

NICOLA TONDINI[1], CHRISTOPHE THAUVOYE[2], FRANCOIS HANUS[3] and BIN ZHAO[2]

ABSTRACT

The paper describes the Computational Fluid Dynamics (CFD) numerical simulations performed with the aim to reproduce the experimental outcomes of hydrocarbon pool fire tests carried out at the University of Liege (B) and at the University of Ulster (UK) within the European RFCS LOCAFI project. In detail, several pool fire tests of different dimensions (0.7 m ÷ 2.2 m) and fuels (heptane and diesel) were simulated by exploiting the CFD software Fire Dynamics Simulator (FDS). Tests without steel column, with steel column inside/outside of the pool fire and without/with ceiling were analysed. Calibration of numerical models was mainly focused on providing a good match between experimental and numerical heat flux. Hence, useful information on the parameters that influence most the numerical simulations is given in the paper.

INTRODUCTION

Localised fires are an important issue for building typologies where a generalised fire cannot develop, as well as for any fire, except some cases of arson, in its early stage. Examples of these typologies are external structures, open car parks, atria, large industrial halls or large transportation halls. One of the main issues for considering the effects of such localised fires on the structure is the calculation of the thermal profile in the structural elements depending on the fire location and its development during time. For horizontal elements located under the ceiling, various research works have already led to the development of analytical design methods which demonstrated their validity when compared with experimental data [1,2]. The so-called Hasemi model relies on such studies and it is included in the Eurocode EN1991-1-2 [3] for flames impacting the ceiling. However, for vertical members, such as columns in buildings, there is still a shortage of analytical models able to calculate the temperature field

[1]Department of Civil, Environmental and Mechanical Engineering, University of Trento, Via Mesiano 77, 38123, Trento, Italy.
[2]CTICM, Espace technologique l'Orme des Merisiers, 91193, Saint-Aubin, France.
[3]Long Product R&D, Arcelormittal, 66 Rue de Luxembourg, 4009, Esch-sur-Alzette, Luxembourg.

the complexity of the problem, that at the moment is tackled by means of complex and time-consuming numerical methods (such as Computational Fluid Dynamics).

On these premises, the European LOCAFI project was funded with the aim to provide designers with scientific evidence, used to develop design models that will allow them to design steel columns subjected to localised fires.

In this respect, a comprehensive series of experimental tests on pool fires characterised by different size, fuel, layout, with/without- engulfed/not engulfed steel column, with/without ceiling was envisaged. Experimental tests were carried out at the University of Liege (ULG) and at the University of Ulster (ULSTER). A detailed description of the tests is given in the Final report [4]. In this paper, the development of numerical models able to reproduce the experimental evidence is thoroughly reported. Then, they served as a means to conduct parametric analyses for developing simplified design methods.

NUMERICAL MODELLING

The CFD software that was employed for numerical simulations is FDS developed by the National Institute of Standards and Technology (NIST) [5]. The numerical calibration was based on the following steps:

1) identification of the main parameters that allow to calibrate with good accuracy the experimental tests based on a large sample;

2) detailed analysis of a limited number of meaningful experimental tests in order to calibrate the numerical models in the most accurate way;

3) simulation of several experimental tests based on Step 2 conclusions.

IDENTIFICATION OF THE MAIN PARAMETERS FROM A LARGE SAMPLE

The FDS version 6.1.1 was used throughout the calibration process. This version includes improved models for the turbulent viscosity: Deardorff (default), Dynamic Smagorinsky, and Vreman. All turbulent models were employed in the numerical simulations. The Constant Smagorinsky model with constant C_s equal to 0.1 provided better results. C_s typically varies from 0.1 to 0.24. With respect to fuel properties, if not specifically provided by the supplier, they were taken from literature, preferably for overventilated conditions. In particular, since combustion is typically not complete, in addition to CO_2 and H_2O, production of soot and CO occurs. Moreover, generally speaking, higher soot content entails lower flame temperature and soot is the primary emitter and absorber of thermal radiation; thus, it provides the mechanism of radiative heat loss. This phenomenon was actually observed in the numerical simulations and the selection of an appropriate soot yield was based on literature [6]. Conversely, the CO production was found to be negligible and it was not considered in the remainder of the study as well as the baroclinic torque. The Number of Radiation Angles (NRA) was an additional parameter that influenced the results (default value equal to 100). In fact, the Radiative Transfer Equation (RTE) is solved by means of a finite volume method according to a finite number of directions. If this number is too small and the measurement distance is too large with respect to the diameter of the fire source, no uniform distribution of heat flux at equal distances in an axisymmetric problem, like a circular pool fire, is observed. This non-uniformity can be significant. In this respect, in order to even out this numerical discrepancy by keeping a reasonable computational effort, the number of radiation angles was increased up to 200. In any case, different measurement points were placed in the CFD domain in order to compute the average heat flux by also taking into account possible wind effects. This numerical effect was more evident in ULG tests where the heat flux gauge was located at 3.75 m from the axis of small pool fires (diameter = 1÷1.4 m); whereas in ULSTER tests being the radiometer placed closer to the fire source (max at 1.5 m), the radiative heat flux was more uniform for similar pool fire diameters (0.7 m). It was found that the radiative loss fraction χ_{rad} was another parameter that influenced the results in terms of flame temperature and heat flux. Typical χ_{rad} values are comprised between 0.3 – 0.4 for typical sooty fuels with diameters of about 1 m. However, when the diameter increases smoke tends to shroud the flame and the radiative fraction progressively decreases until values as low as 0.05 for pool fires of diameter 50 m [6]. Values of radiative fractions were selected based on literature [6] by taking into account the type of fuel and the size of the fire.

DETAILED ANALYSIS OF A LIMITED NUMBER OF TESTS

The selection of the tests to be accurately simulated was based on the following criteria:

- in order to compute a meaningful average value of the measured air temperatures and heat fluxes, tests that exhibited long steady state conditions were preferred;
- tests with pool fires ranging from small to large diameters;
- tests with different combustibles;
- tests without column;
- tests with column engulfed/not engulfed in the pool fires and without/with ceiling.

Therefore, the following tests were selected and numerically simulated with FDS:

- ULG T06: diameter 1.0 m, heptane, without column;
- ULG T19: diameter 2.2 m, diesel, without column;
- ULG T14: diameter 1.4 m, heptane, with a HE 300 A column positioned in the middle of the pool fire.
- ULSTER I7: diameter 0.7 m, diesel, with an IPE 300 column located 0.5 m from the pool fire axis, without ceiling.
- ULSTER O11: 4 pans of diameter 0.7 m, diesel, with a CHS 219x10 located in the middle of the pool fire, without ceiling.
- ULSTER O29: diameter 0.7 m, diesel, with a CHS 219x10 located at 1 m from the pool fire axis, with ceiling placed at 3.5 m from the floor.

It was observed that wind effects had to be included in order to obtain a good agreement between experimental and numerical values, above all for air temperatures and flame height. This was consistent with experimental evidence where tilting of the flame was observed. Wind speed was introduced as dynamic pressure. Moreover, possible uneven vaporization of fuel due to uneven radiant heat flux feedback to the fuel surface could be also a contributing cause of tilting.

When a steel column was included in the CFD domain, its thermal properties, i.e. thermal conductivity and specific heat, were assigned according to EN1993-1-2 [7]. The fire was located at a height consistent with tests. The pan was not modelled in ULG tests as the fuel level was always kept close to the edges. Conversely, in ULSTER tests, the pan was modelled because the fuel level was well below the pan edges. In order to measure the heat flux, several devices were employed; however, the device "Radiative Heat Flux Gas" was mainly used because of its versatility. In FDS 6, "Radiative Heat Flux Gas" provides the radiative heat flux re-emitted at ambient temperature and with respect to any orientation without being attached to any surface. In the absence of a substantial contribution of the convective part, the comparison with a heat flux gauge used in the tests is justified. Air temperatures were measured with FDS "Temperature" and "Thermocouple" quantities. The "Temperature" quantity provides the actual gas/air temperature whereas the "Thermocouple" quantity takes also into account the thermal properties of the bead such as emissivity, diameter, density, specific heat etc. For the ULG tests, the default values of the "Thermocouple" quantity were considered, whereas for the ULSTER tests "Thermocouple" devices with the bead emissivity equal to 1.0 and bead diameter equal to 0.0025 m were also added. The thermocouples were located in the same positions of the tests and some others were added in order to capture the temperature evolution. Model parameters were varied within their range of applicability and based on literature so that a meaningful model calibration could be achieved.

Results of numerical simulations

For brevity here only results of test ULSTER O29 are shown. The O29 test was performed with a 0.7-m diesel pool fire located 1 m away from a steel tube CHS219x10 and with the presence of a ceiling. The pool fire characteristics used in FDS are reported in Table I. The clearance between the floor and the ceiling was 3.5 m. The ceiling was made of plaster boards 10-mm thick and an IPE 300 connected to top of the column was instrumented with thermocouples. The whole compartment was modelled. Thus, the CFD domain was 7 m x 7 m x 3.5 m discretized with a mesh grid 5 cm x 5 cm x 5 cm. The adequacy of the mesh grid was checked against the R* value computed according to Ma and Quintiere [8], that suggested R* to be close to 0.05 with upper limit 0.1. In the optimised analysis R* = 0.0692. All beams were included into the model as they act as barriers influencing the smoke flow, as depicted in Figure 1c. The ceiling was modelled by means of thermal properties of plaster (c_p = 1.7 kJ/kgK, ρ = 800 kg/m^3 [6]). From the photos supplied by the University of Ulster, see Figure 1a, it was noted that cross-wind could have a significant influence in numerical modelling. Therefore, wind was included into the model in the direction consistent with experimental evidence – resultant wind speed = 0.76 m/s -.

TABLE I. ULSTER O29. POOL FIRE CHARACTERISTICS USED IN THE FDS MODEL.

Diameter D	0.7 m
Fuel type	Diesel
RHR	1277 kW/m^2
Fuel density $\rho_{heptane}$	823 kg/m^3
Soot yield	0.10
Ideal heat of combustion ΔH_c	44000 kJ/kg
Radiative loss fraction χ_{rad}	0.45

Two levels of “Radiative Heat Flux Gas” were located at 1 m from the pool fire axis and at 1 m and 2 m from the floor. In order to investigate the radiative heat flux variation around the pool fire, several angles were spanned. The orientation of the gauges points was towards the pool fire centre. In the test two gauges (GG) – at 1 m and at 2 m from the floor, were placed at an angle equal to -45°, as shown in Figure 1d. Comparing Figure 1a with Figure 1b the numerical and experimental flame shapes well agree. Moreover, from Figure 1b and c it is possible to observe both the effect of the ceiling and the influence of the beams on the smoke flow. By comparing numerical (CFD) and experimental (EXP) air temperature values, the agreement is fairly good. In this respect, the evolution of the air temperature at 3 m from the floor along the IPE 300 is given in Figure 2a. The radiative heat flux is overall well captured by the CFD analyses with error less than 15%, as depicted in Figure 2b. The agreement between experimental and numerical outcomes is overall good.

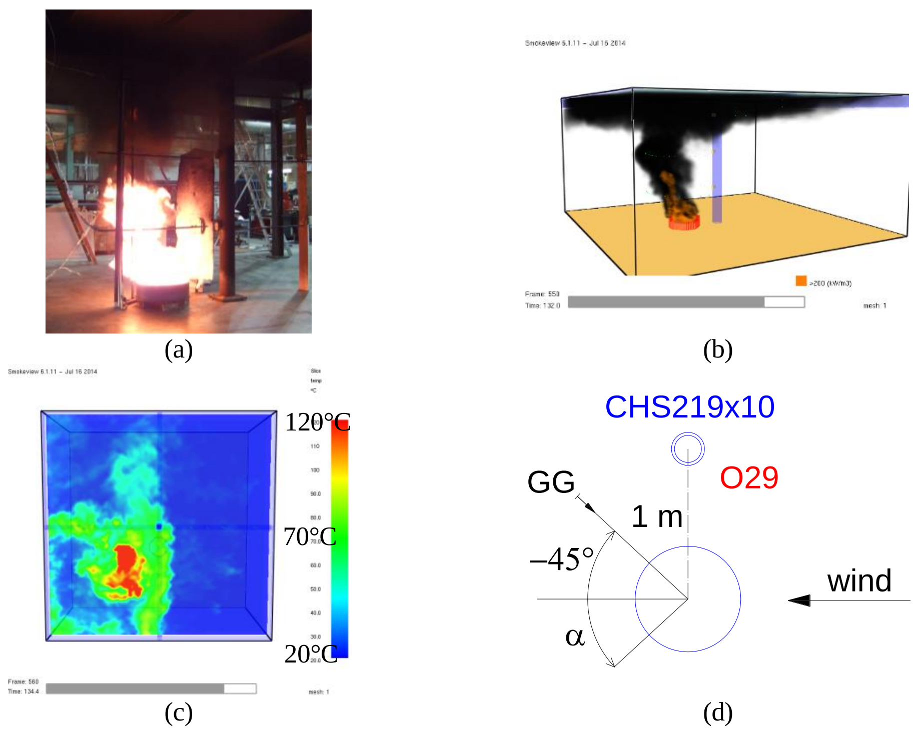

Figure 1. ULSTER O29. a) flame shape: experimental; b) flame shape: numerical; c) temperature field at 3 m from the floor; d) plan configuration.

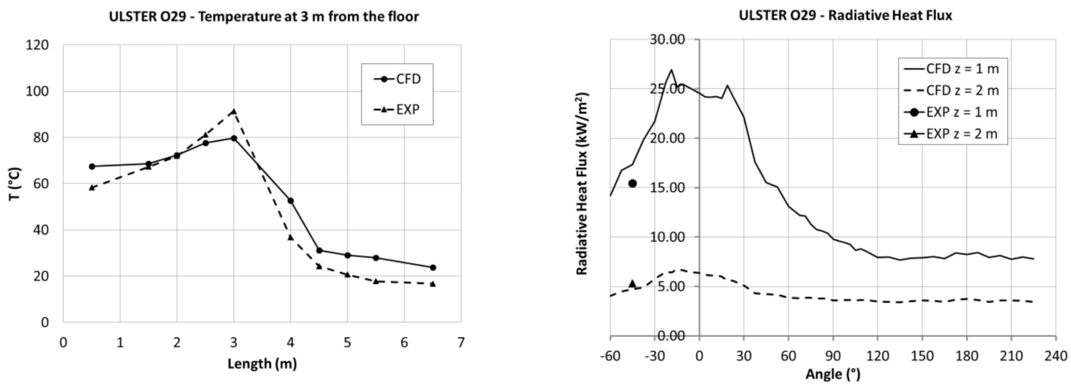

(a) (b)

Figure 2. ULSTER O29. a) comparison of average air temperatures along the length of the beam at 3 m from the floor b) evolution in space of the average radiative heat flux in a range -60° ÷ 225° at a distance of 1.0 m from the centre of the pool fire where α = -45° is the position of GG.

SIMULATION OF LARGE NUMBER OF EXPERIMENTAL TESTS

More than 60 experimental tests were performed by ULSTER and 45 tests were reproduced using the previous numerical parameters. In terms of behaviour, experimental tests are always subjected to small perturbations that influence them in a specific way. For example, the efficiency of combustion can be influenced by fuel impurities; atmospheric pressure variations will influence the flow through cross-wind effect. Moreover, turbulent flows have the specificity to be highly influenced by these small variations and have a tendency to amplify them. Thus, it is more relevant to perform an analysis on a statistical basis. The simulations were analysed by grouping them according to two criteria: first the type of column and second the position of the pan(s). For example, tests involving an I-shape column are put into the 5 following groups:

- Group 1: Tests I1, I3, I5, I7 and I13 corresponding to a unique 0.7 m pan at 0.5 m from the column,
- Group 2: Tests I2, I4, I6, I8, I14 and I15 corresponding to a unique 0.7 m pan at 1.0 m from the column,
- Group 3: Tests I12 and I16 corresponding to two 0.7 m pans at 0.5 m from the column,
- Group 4: Test I11 corresponding to three 0.7 m pans at 0.5 m from the column,
- Group 5: Tests I9 and I10 corresponding to a unique 1.6 m pan centred on the column.

Many configurations were studied by ULSTER and some are specific to a column-shape. It is the case of the H-column for which two additional pan positions were considered leading to more groups, e.g. Group 6 and 7.

Figure 3 shows the flame shape for the numerical simulations (bottom) compared with the experimental evidence (top) for Group 1 in case of an I-shape column. A simple comparison of the flame length can be done by taking into account that the simulation devices are clearly identifiable at 1 m, 2 m and 3 m from the floor that correspond to the two horizontal sticks visible in the photos taken during the tests. We observe that the simulations give a good agreement in terms of flame length. In fact, the flame length is in the range of 1.8 m – 2.0 m in the experiments and in the range of 1.9 m – 2.1 m in numerical simulations.

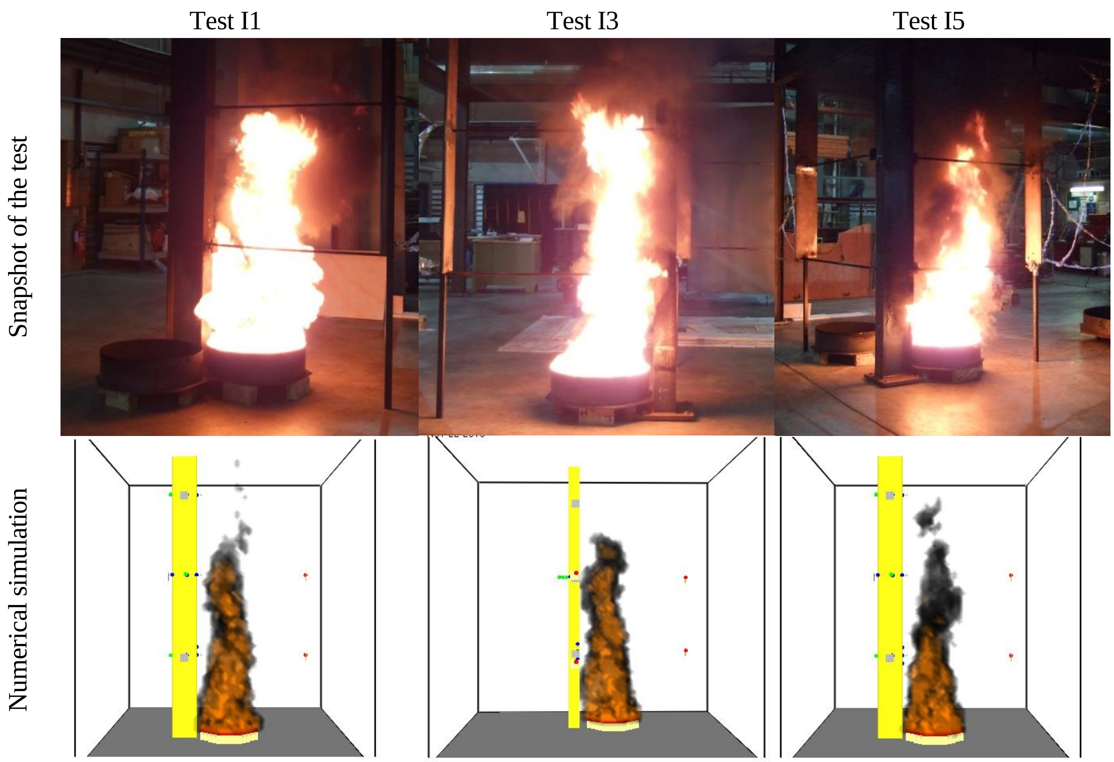

Figure 3. Numerical and experimental flame shape for tests I1, I3 and I5 of group 1.

This kind of analysis, done for each group, has demonstrated the ability of the model to reproduce the experimental tests. Complementary to this, a global analysis is also performed in a statistical way for the heat fluxes. Figure 4 provides results for tests with an I-shape column, an H-shape column, an O-shape column and an O-shape column with a ceiling. For heat fluxes, results are very close to the experiment and it confirms that the numerical model is able to reproduce the tests.

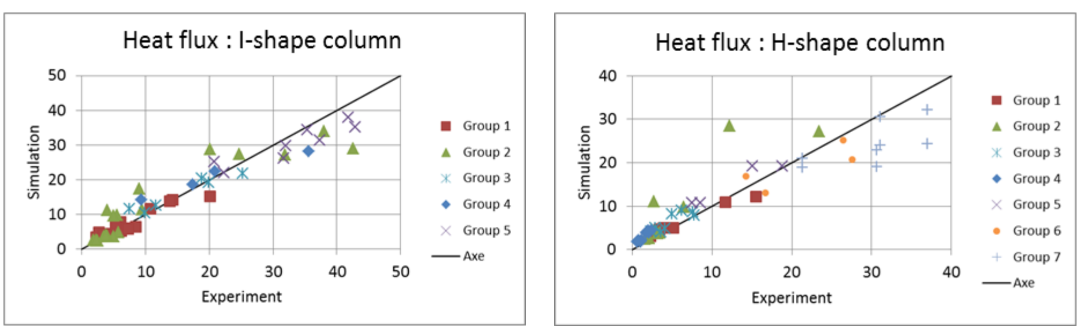

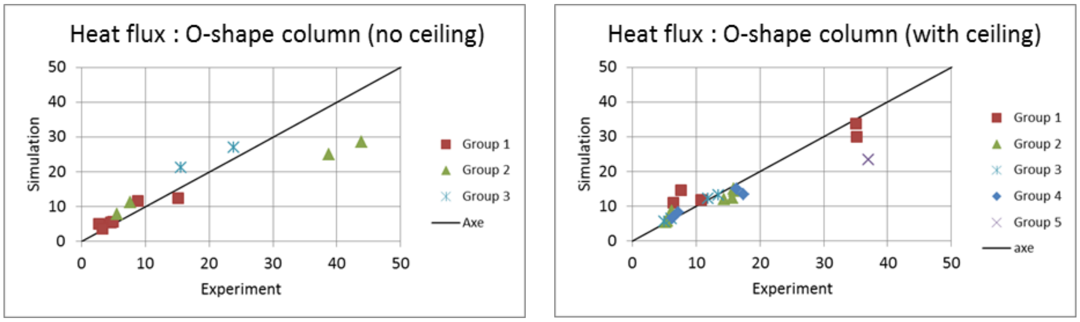

Figure 4. Heat flux: comparison Experiment-Simulation for different shape of columns.

CONCLUSIONS

A large number of numerical simulations were performed with the aim to develop numerical models that were then used to conduct parametric analyses for developing simplified design methods capable of predicting the impinging flux to a vertical structural member.

The numerical simulations have shown that the main parameters to be considered when calibrating the models of the localised fires under study were:

- The turbulence model. The Constant Smagorinsky with C_s = 0.1 allowed a better representation of the flame shape in time and in space.
- The radiative loss fraction. An appropriate value of radiative loss fraction that depends on the type of fuel and pool fire dimensions is important for obtaining a good agreement between experimental and numerical values of radiative heat flux.

The number of radiation angles can be also important owing to numerical effects introduced by FDS in solving RTE and it should be increased if the measurement point is located fairly away from the fire source. Roughly speaking, from simulations with NRA = 200 it was observed that if the ratio between the pool fire diameter and distance of the heat flux gauge from the centre of the fire was more than 0.6 this numerical effect was not particularly significant, whereas if the ratio was less than 0.4 this effect was not negligible. The introduction of cross-wind effects can be significant for accurately reproducing the experimental outcomes. These results were used in order to reproduce a large amount of experimental tests and a good agreement was achieved in terms of flame shape, flame height and heat fluxes.

ACKNOWLEDGEMENTS

This work was carried out with a financial grant from the Research Fund for Coal and Steel of the European Community, within the LOCAFI project: "Temperature assessment of a vertical steel member subjected to localised fire ", Grant N0 RFSR-CT-2012-00023.

REFERENCES

1. Hasemi, Y. and T. Tokunaga. 1984. “Flame Geometry Effects on the Buoyant Plumes from Turbulent Diffusion Flames,” *Fire Science and Technology*, Vol. 4, N°1.
2. Pchelintsev A., Y. Hasemi, T. Wakamatsu and Y. Yokobayashi. 1997. “Experimental and numerical study on the behaviour of a steel beam under ceiling exposed to a localized fire,” *Fire Safety Science* 5: 1153-1164.

3. EN1991-1-2. 2002. "*Eurocode 1: Actions on structures – Part 1-2: General actions – Actions on structures exposed to fire*," CEN, Brussel.
4. Vassart, O., M. Brasseur, F. Hanus, J.-M. Franssen, A. Scifo, B. Zhao, C. Thauvoye, A. Nadjai, H. Sanghoon, 2016. '*LOCAFI project – Midterm Report*," Research Fund for Steel and Coal.
5. Mcgrattan, K., S. Hostikka, K. Mcdermott, J. Floyd, C. Weinschenk, K. Overholt. 2013a. "*Fire Dynamics Simulator User's Guide*," National Institute of Standards and Technology, Special Publication 1019, April.
6. SFPE. 2008. *The SPFE Handbook of Fire Protection Engineering*, 4th Edition, National Fire Protection Association, Quincy, MA, USA.
7. EN1993-1-2. 2005. "*Eurocode 3: Design of steel structures – Part 1-2: General rules – Structural fire design*," CEN, Brussel.
8. Ma, T.G. and J.G. QUINTIERE, 2003, "*Numerical simulation of axi-symmetric fire plumes: accuracy and limitations*", *Fire Safety Journal*, 38:467-492.

FDS-FEM Simulation Method and Its Application to Model Localized Fire Tests on Steel Members

CHAO ZHANG

ABSTRACT

Fire Dynamics Simulator (FDS) is an open source CFD code, developed by NIST. It has been widely used in fire engineering for modeling the gas phase environment (temperature, heat flux, velocity, species concentrations, etc.) in fires. Recently, there has been increased research in the application of FDS for structural fire analysis. Fire-structure interface tools for transferring data from FDS to particular FEM codes (such as ANSYS, ABAQUS, SAFIR) have been developed. Although both FDS and FEM codes have been separately validated, there needs to be a direct validation for the integrated FDS-FEM simulation methodology. This paper validates the integrated FDS-FEM simulation methodology against a number of localized fire tests reported in literature. Localized fire tests on steel columns and on ceiling steel beams were simulated using the FDS-FEM method. The concept of adiabatic surface temperature used for transferring data from FDS to FEM was presented and the limitation of the concept was discussed. The FEM program ANSYS was used to conduct the heat transfer analyses and thermo-mechanical analyses to get the temperature and structural responses of the tested steel beams and steel columns.

INTRODUCTION

Advanced simulation methods are needed to predict the complex behavior of structures exposed to realistic fires. Fires in the open or in large enclosures are characterized as localized fires, e.g. vehicle fires in transportation infrastructure, small shop fires in transport terminal halls, and workstation fires in open plan office buildings. Compartment fires begin with localized burning. The current structural fire design approaches are developed for fully-developed compartment fires that gas temperatures in the compartment can be approximated as uniformly distributed. In localized fires, the gas temperature distributions are spatially non-uniform. Because of the thermal gradient, the failure model and failure temperature of structural members in a localized fire might be different than those of the members in uniform heating conditions (e.g. the standard fire condition) [1-3]. Consideration of localized fires is

chao.zhang@nist.gov; Engineering Laboratory, National Institute of Standards and Technology, Gaithersburg, MD 20899, U.S.A

important for safety of structures in the modern buildings with large enclosures. From literature [4], realistic fire test data for model validation are quite limited, especially for modeling structure response to non-uniform heating conditions. The localized fire tests reported by Hasemi et al. [5-6] were selected for model validation because of the applicability to real-world thermal conditions and because the test was well controlled (e.g. the heat release rate of the fire was controlled by computer), and well instrumented (e.g. temperatures were measured by series of thermocouples).

INTEGRATED FIRE-STRUCTURE SIMULATION

FDS-FEM approaches

With increase in complexity, the FDS-FEM approaches may be classified into four categories (Figure 1):

- **Level 1**: FDS models which omit structural members are first used to predict the gas (fire) temperatures; then, the gas temperatures are used in simple thermal models (e.g. the Eurocode 3 equation) to predict the temperatures of the structural members; and, finally, the temperatures of the structural members are imported to the FE structural models to predict the structural responses.
- **Level 2**: FDS models which include structural members are first used to predict the temperatures of the members; and then the FDS predicted (solid) temperatures are imported to the FE structural models.
- **Level 3**: FDS models which include structural members are first used to predict the thermal boundary conditions (e.g. adiabatic surface temperatures, AST) at the exposed surfaces of the members; then, the thermal boundary conditions are imported to the FE thermal model to conduct heat transfer analysis to predict the temperature of the members; and finally, the FE predicted temperatures of the structural members are mapped to the structural models.
- **Level 4**: FDS models which include structural members are used to predict the thermal boundary conditions. The real time thermal boundary condition data are imported to the FE thermal model to predict the temperatures of the members which are then mapped to the FE structural models to predict deformations, strains, stress, etc. The deformations are transferred and used to update the geometry of the FDS model for the next time increment calculation.

The **Level 1** approach is the simplest one and implicitly assume that the presence of the structural members (e.g. steel beams, steel columns), or in other words the heat sink effect of the structural members, has negligible effect on the predicted (average) fire temperature (because the heat absorbed by the structural members are quite small compared to the heat released by combustion), and also assume that the load capacity of a structural member is solely determined by the maximum (average) temperature. The author's previous work [7-8] investigated the heat sink effect of steel members on the predicted fire temperature by a modified one zone model and found that even the heat sink effect was not important on the predicted fire temperature, ignoring that effect could yield an over-design of fire protection for about 16%. As shown in Fig.1, in a (fully-developed) compartment fire neither the gas temperature distribution nor steel temperature distribution is uniform, and the steel columns with the same cross section but at different locations have different temperatures. Because thermal gradient might have important negative effect on the failure temperature of steel members, as found in the authors' previous studies [1-2], the **Level 1** approach, which ignores the effect of temperature gradient, might be unsafe for structural fire safety design.

The **Level 2** approach is theoretically inaccurate by the one-dimensional (1D) heat conduction assumption within the solid in FDS. The **Level 4** approach is the most complex one and is regarded to be the most accurate one. However, because FDS cannot consider solid deformation at this moment, artificially changing the geometry of solid in FDS in order to match the FEM predicted deformation will cause calculation errors. Before failure, the deformation of a structure is usually very small and could be ignored in a CFD calculation. Therefore, the **Level 3** approach is more preferable than the other approaches and is recommended for engineering usage.

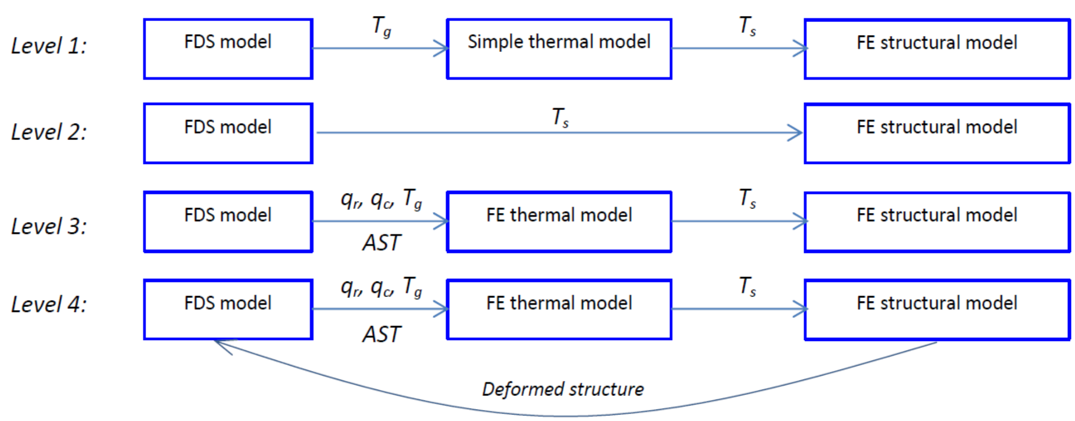

Figure 1. FDS-FEM simulation approaches.

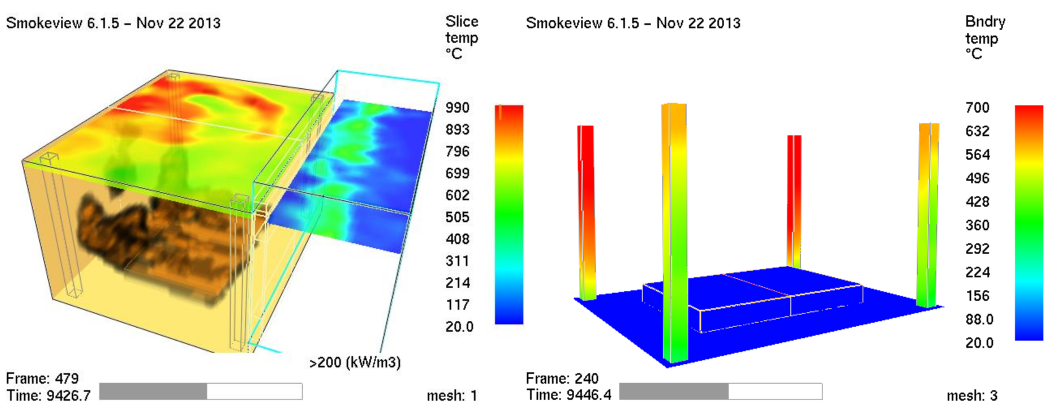

Figure 2. FDS predicted gas temperature (left) and steel temperature (right) distributions for a compartment with 4 steel columns.

Adiabatic surface temperature

The concept of adiabatic surface temperature is used to transfer thermal boundary data from a FDS model to a FEM model. Consider an ideal adiabatic surface exposed to a heating condition; the net heat flux to the surface is by definition zero, thus

$$\varepsilon_{AS}(\dot{q}''_{in} - \sigma T_{AS}^4) + h_{c,AS}(T_g - T_{AS}) = 0 \quad (1)$$

where ε_{AS} is emissivity of the adiabatic surface; T_{AS} is temperature of the adiabatic surface or adiabatic surface temperature; and $h_{c,AS}$ is film coefficient between the adiabatic surface and the surrounding gas. From Eq. (1), the incident radiative flux to a surface can be calculated from an adiabatic surface temperature,

$$\dot{q}''_{in} = \frac{h_{c,AS}(T_{AS} - T_g)}{\varepsilon_{AS}} + \sigma T_{AS}^4 \quad (2)$$

Consider a real surface exposed to the same heating condition, the net heat flux to the surface can be calculated by

$$\dot{q}'' = \varepsilon_s \sigma (T_{AS}^4 - T_s^4) + \frac{\varepsilon_s}{\varepsilon_{AS}} h_{c,AS}(T_{AS} - T_g) + h_c(T_g - T_s) \quad (3)$$

If the emissivity of the adiabatic surface is taken as the emissivity of the real surface ($\varepsilon_{AS} = \varepsilon_s$), and the film coefficient between the adiabatic surface and the surrounding gas is equal to the film coefficient between the real surface and the surrounding gas ($h_{c,AS} = h_c$), we get

$$\dot{q}'' = \varepsilon_s \sigma (T_{AS}^4 - T_s^4) + h_c(T_{AS} - T_s) \quad (4)$$

Eq. (4) shows that the net heat flux to a surface can be approximately calculated by using a single parameter T_{AS} . Consider the case at high temperature (above about 400 ^{o}C [9]), where convection is not the dominant mode of heat transfer in fire; from Eq. (3) or (4) the adiabatic surface temperature measured by a plate thermometer can be used to predict the net heat flux to a surface with a different emissivity. FDS includes an output quantity of adiabatic surface temperature calculated by Eq. (4) according to the idea proposed by Wickstrom [9]. It should be noted that the calculated adiabatic temperature of a surface is fundamentally influenced by the convection.

APPLICATION TO MODEL REAL FIRE TESTS

Thermo-structural response of a steel column subjected to a localized fire

Fig.3 shows the experimental setup in the localize fire test on a axially loaded steel column reported by Kamikawa et al. [5]. A 0.25 m height, 0.3 m square propane burner with HRR of 52.5 kW was located just beside a square steel column (STKR400, 0.1 m × 0.1 m × 3.2 mm thick and 1.6 m tall). Four tests (cases) with various loading and restraint conditions were conducted. In all cases, the column was fixed at the base. In Zhang et al. [10], case 1 and case 4 were considered. In case 1, the structure was unrestrained except for the base. The fire was extinguished after 60 min, when the column behavior (temperature and displacement) reached steady-state. In case 4, the horizontal displacement toward the fire source was restrained (see Fig.3). Also, a vertical force was applied and increased gradually after the steel temperature in the column became steady (about 52 min after ignition); the column buckled about 90 min after ignition with a vertical force of approximately 374 kN. The fire was extinguished only after the column buckled. Fig.3 also shows the FDS and FEM models [10]. Fig.4 shows some numerical results.

The FDS-FEM approach gives well prediction of both the thermal and structural responses of the steel column subjected to the localized fire, as shown in Fig. 5. The predicted buckling time was about 88.5 min after ignition, which means that the error was about 1.7%.

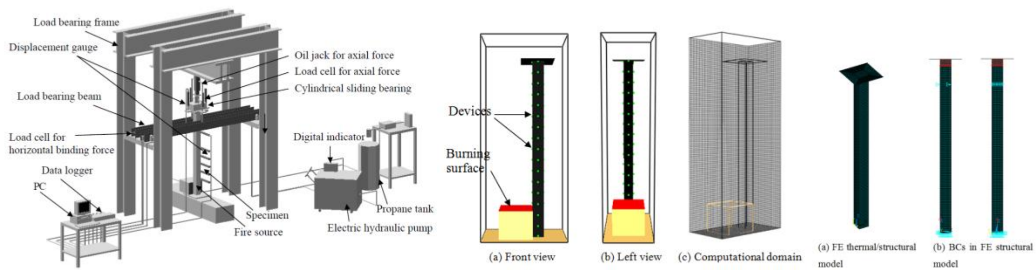

Figure 3. Experimental setup, FDS model and FEM model for Kamikawa et al.'s test [10].

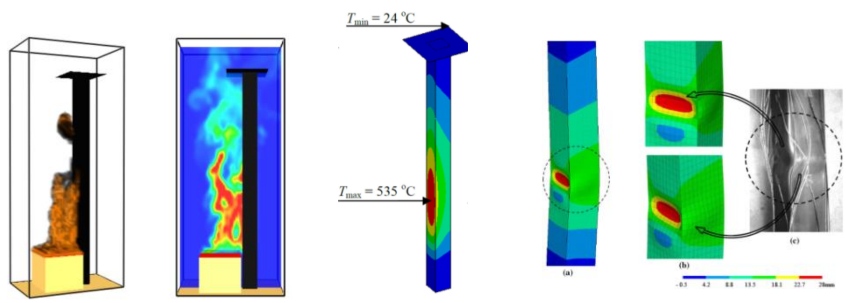

Figure 4. Predicted fire behavior, gas temperature, steel temperature and structural response [10].

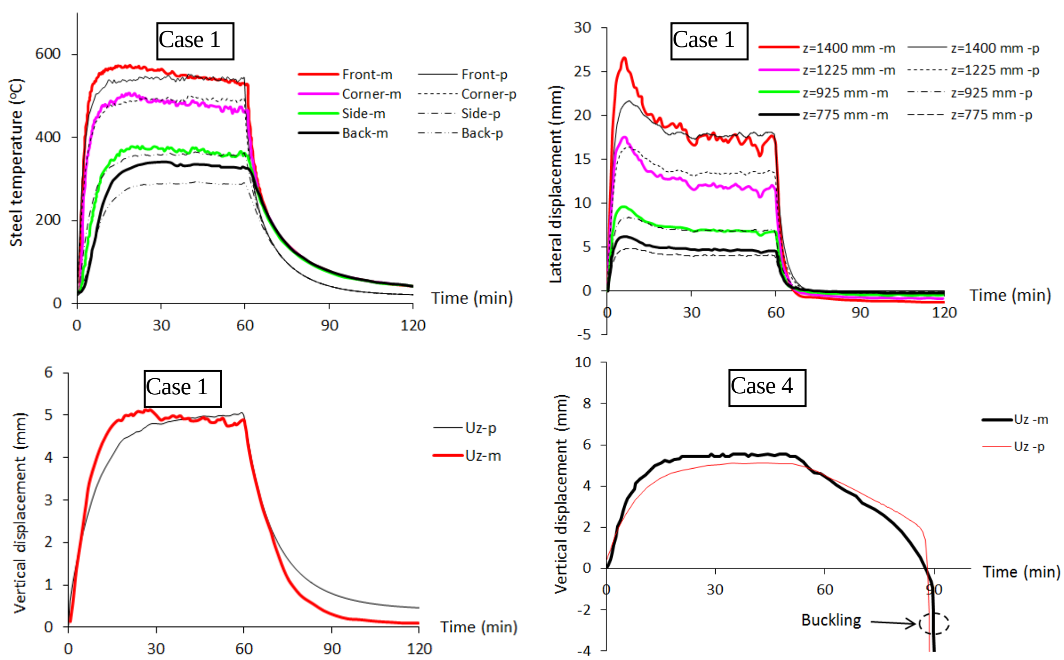

Figure 5. Comparisons of measured and FDS-FEM predicted results for steel column tests [10].

Heating of a steel ceiling beam subjected to a localized fire

Fig.6 shows the experimental layout in Yokubayashi et al.'s experiments [6]. The rectangular flat ceiling consists of two layers of 12 mm thick mineral fiber Perlite board with dimensions 1.83×3.60×0.024 m. The ceiling is reinforced by a steel frame and is horizontally placed over the beam held by two steel vertical posts at the ends. H-section bare steel beam with the following dimensions was used: 3.6 m long, 75 mm width, 150 mm height, 5 mm (thickness of web), 6 mm (thickness of flange). The height of the beam and the ceiling was adjusted by lifting these specimens up and down the posts. Heat flux measurements were made at nine horizontal distances from the stagnation point of the beam. The heat flux to the upper flange, web and also lower and upper surfaces of the lower flange was measured. Temperature measurements were made with thermocouples at 27 points, arranged symmetrically to the points of the heat flux gauges with regard to the center of the beam. Thermocouples were 0.2 mm K-type and were installed 0.5 mm from the beam surface. A 0.5 m diameter round and a 1.0 m square porous propane burner were used as the fire source. The case with 900 kW square burner and distance from the burner to the bottom of the beam of 1.2 m was considered. Fig.6 also shows the FDS and FEM models.

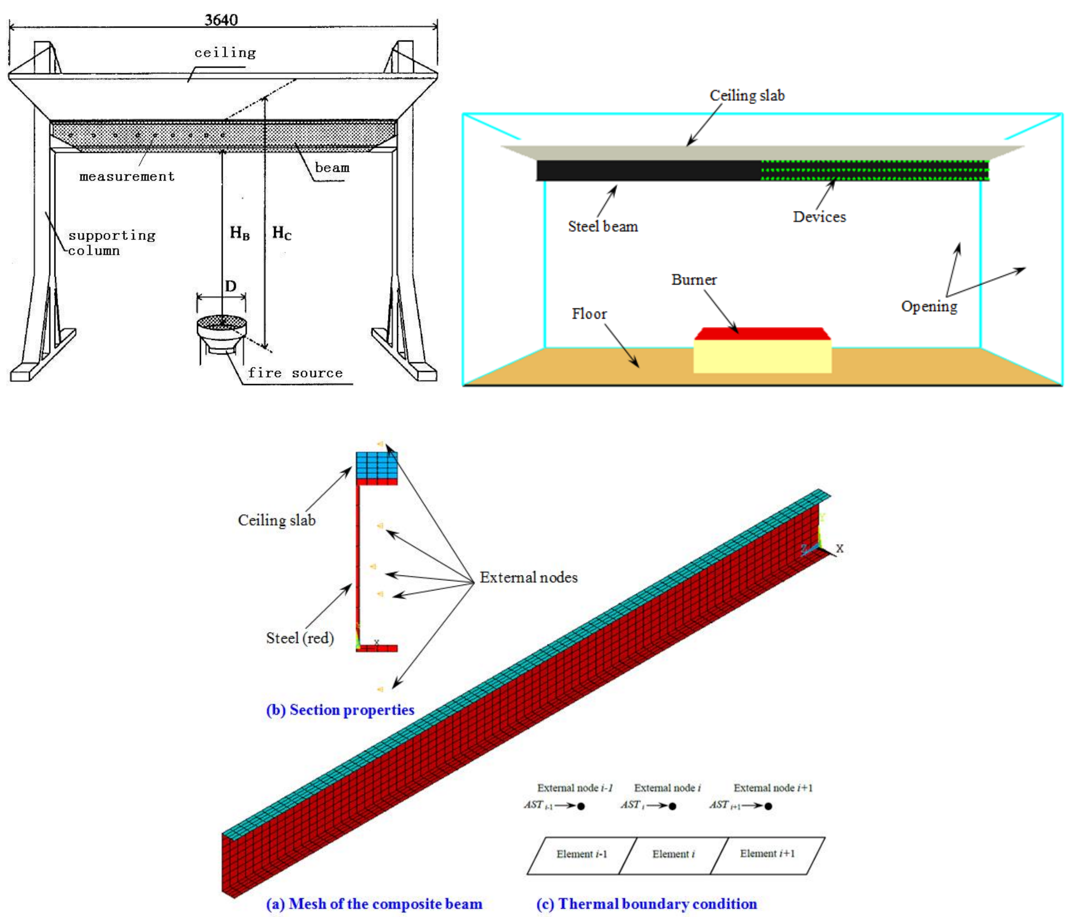

Figure 6. Experimental setup, FDS model and FEM model for Yokubayashi et al.'s test.

Fig. 7 shows the FDS predicted time-history curves for heat fluxes and adiabatic surface temperatures. Fig.8 compares the FDS-FEM predicted steel temperatures with the test data. For the lower flange and the web of the steel I beam, the predicted steel temperatures agree very well with the test data. The over-prediction of maximum steel temperature for the lower flange is about 60 °C (about 11%) and for the web is about 44 °C (about 8%). The under-prediction of the upper flange steel temperature is caused by the ignoration of the horizontal heat conduction between the nearby slab to the steel section.

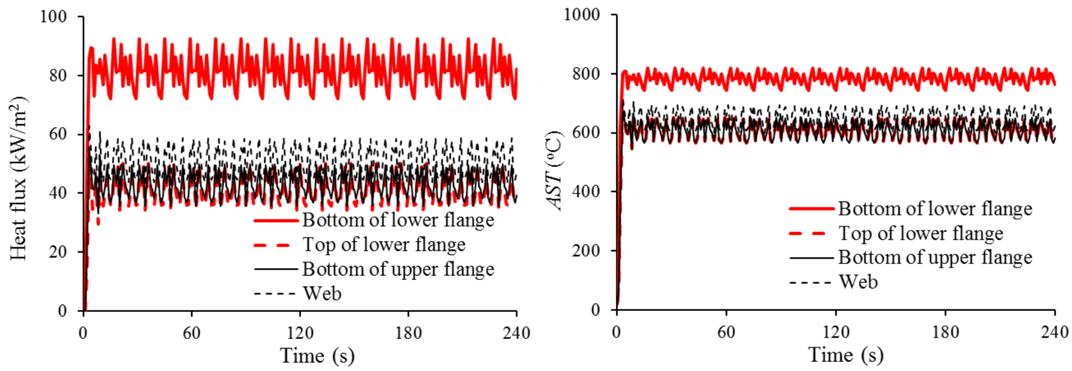

Figure 7. Time history of FDS predicted heat fluxes and ASTs (900 kW case).

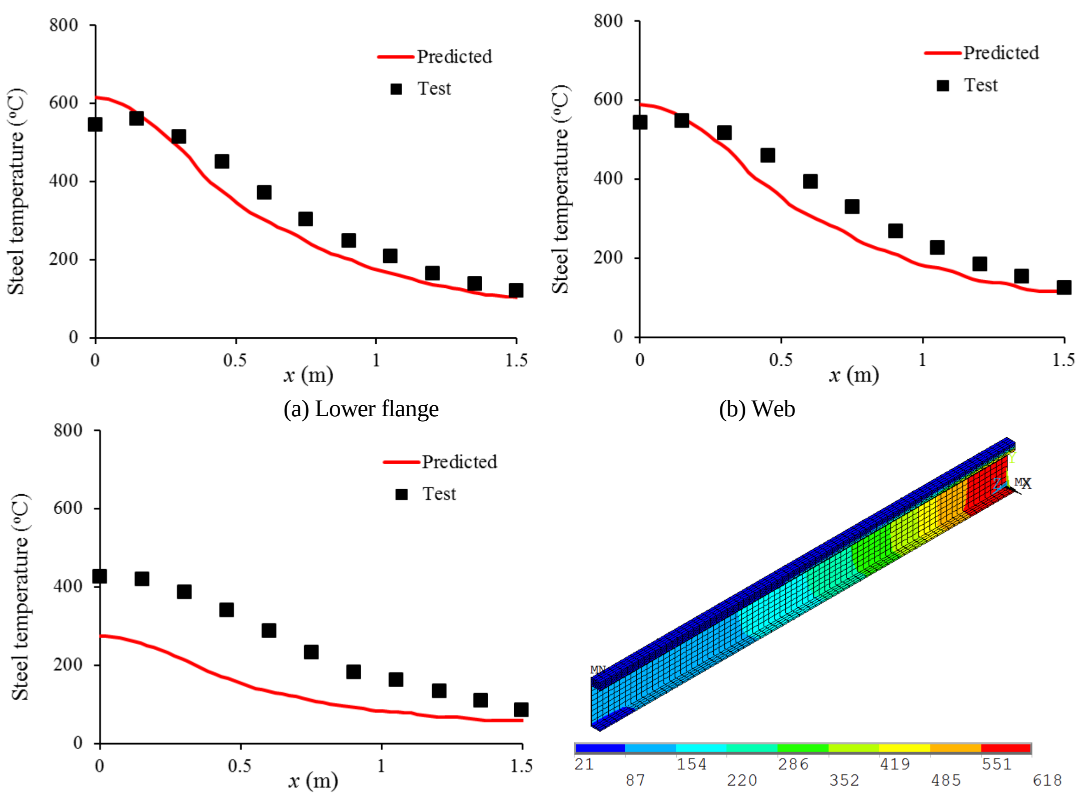

Figure 8. FDS-FEM predicted steel temperatures for the investigated case with HRR of 900 kW.

CONCLUSIONS

This paper discusses the FDS-FEM simulation approaches for performance based fire safety design. A fire-structure interface, named adiabatic surface temperature, was applied to transfer data from FDS to ANSYS. By comparing the predicted and measured thermal and structural responses of steel members subjected to localized fire, the FDS-FEM method was tested. The FDS-FEM method gave good prediction of the temperatures of steel ceiling beams subjected to a localized fire. The over-prediction of maximum steel temperature was within 11% for the investigated case. The FDS–FEM method predicted both the thermal and structural responses of a steel column in a localized fire test. The column buckling time was predicted with a maximum error of 7.8%. The methods described in this study provide a feasible way to study the complex behavior of structures in realistic fires.

DISCLAIMER Certain commercial entities, equipment, or materials may be identified in this document in order to describe an experimental procedure or concept adequately. Such identification is not intended to imply recommendation or endorsement by the National Institute of Standards and Technology (NIST), nor is it intended to imply that the entities, materials, or equipment are necessarily the best available for the purpose. Any opinions, findings, and conclusions expressed herein are those of the author and do not necessarily reflect the view of the NIST.

REFERENCES

1. Zhang, C., Gross, J., McAllister, T., and Li, G.Q. (2014). "Behavior of Unrestrained and Restrained Bare Steel Columns Subjected to Localized Fire." *Journal of Structural Engineering-ASCE*, 10.1061/(ASCE)ST.1943-541X.0001225, 04014239.
2. Zhang C., Li G.Q., Usmani A. (2013). “Simulating the behavior of restrained steel beams to flame impinged localized fires.”*Journal of Constructional Steel Research*, 83:156-165.
3. Zhang C., Gross J.L., McAllister T. (2013). “Lateral torsional buckling of steel w-beams to localized fires.”*Journal of Constructional Steel Research*, 88:330-308.
4. Bisby L., Gales J., Maluk C. (2013). “A contemporary review of large-scale non-standard structural fire testing.”*Fire Science Reviews*, 2:1-27.
5. Kamikawa D., Hasemi Y., Yamada K., Nakamura M. (2006). “Mechanical response of a steel column exposed to a localized fire.”*SiF’06*, pp. 225-234.
6. Yokubayashi Y., Hasemi Y., Wakamatsu T. (1997). “Experimental study on the heating mechanism and thermal response of a steel beam under ceiling exposed to localized fires”. *Journal of Structural and Construction Engineering*, 498:169-175. (in Japanese).
7. Zhang C., Li G.Q. (2013) “Modified one zone model for fire resistance design of steel structures.” *Advanced Steel Construction*, 9:282-297.
8. Zhang C., Usmani A. (2015) “Heat transfer principles in thermal calculation of structures in fire.” *Fire Safety Journal*, 78:85-95.
9. Wickstrom U., Duthinh D., McGrattan K.B. (2007). "Adiabatic surface temperature for calculating heat transfer to fire exposed structures." Proceedings of the 11th International Interflam Conference, pp. 943-953, London, England.
10. Zhang C., Silva J.G., Weinschenk C., Kamikawa D., Hasemi Y. (2016). “Simulation Methodology for Coupled Fire-Structure Analysis: Modeling localized fire tests on a steel column.” *Fire Technology*, 52:239-262.

Results of a Post Test Round Robin of the Calculated Response of a Loaded Steel Beam to a Furnace Test

DAVID LANGE and LARS BOSTRÖM

ABSTRACT

Calculations or simulations are often used as an alternative means of evaluating the fire resistance of elements and structures as opposed to fire resistance testing. Indeed, in Europe, calculations carry the same credibility as testing for the certification of certain building products. However, while for testing there are accreditation requirements of the test laboratory, this is not the case for calculations. In other words, when evaluating building products for certification based on testing there is a formal control system that must be followed and this is not the same when doing the same job based on calculations.

This paper details the second stage of a round robin study of the calculated response of structures in fire. In this instance, the study is based on a fire test which was conducted on two steel beams at SP's fire resistance laboratory in Sweden. We describe the different approaches taken to the prediction and how the additional information provided to the participants was taken into account. We also compare the predicted deflection histories with the deflection history during the test.

Finally, we compare the calculation round robin with the results of a fire resistance testing round robin of the same object, which illustrates the relative certainties in testing results compared with calculation results.

INTRODUCTION

One of the requirements for accreditation of fire testing laboratories in Europe is the participation in round robins to determine the scatter of results between laboratories. Some public summaries of these round robins are available from the European Group of Laboratories for Fire Testing's (EGOLF) website [1]. Very few round robins of calculations are however carried out in fire safety engineering, with few notable examples, e.g. [2, 3, 4]. One of the conclusions of the recent NIST R&D Roadmap project for structural fire engineering was that there was a need to carry out additional round robins within the field [5].

This paper present the second stage results from a recent round robin study in fire safety engineering where participants were asked to predict the response of an unprotected steel beam loaded in 4 point bending and exposed to a fire test carried out according to EN 1365-3. The first stage results were presented at the PROTECT conference in 2015 [6] and showed a surprising variation in the predicted deflection histories, and the reported failure times of the beams. They also highlighted significant differences in the failure criteria used for the determination of failure times. However, the biggest variation in the analysis of the beam arose during the temperature calculation, where a remarkably wide spread in predicted temperatures will have influenced the spread in the first stage deflection histories and failure times significantly.

For the second stage round robin, the participants were provided with additional information including the measured tensile strength of the steel; as well as the measured temperatures from the furnace plate thermometers and the measured temperatures at the midspan of the steel beam during the test. The participants were then invited to revise their models and the prediction of the failure time accounting for this additional information. This meant that the uncertainties surrounding the temperature of the steel beam were effectively removed since all participants were able to either use the recorded temperatures or adjust their heat transfer analysis to account for them.

This paper describes the problem which was set to the participants of the round robin, and gives a very short overview of the first stage round robin results before describing in detail the second stage round robin results and comparing those with the results of a testing round robin.

ROUND ROBIN PROBLEM

The exercise was designed to mimic a round robin as it would be carried out by EGOLF. The test object which was used for comparison was an HEB 300 steel beam, grade S355. In the test which was performed the beam had a total length of 5400 mm, and a span of 5200 mm between the supports. Loading is applied at two points, 1400 mm from either support. At both the supports and the points of loading application web stiffeners were welded to the steel beam. The stiffeners had a thickness of 15 mm.

The applied loads, P, created a uniform bending moment of 140 kNm between the loading points.

During the testing the deflection was measured at mid span, as well as 700 mm from either of the supports, and the temperature of the beam was measured at 5 locations: in the middle of each of the flanges and in the middle of the web. These temperature measurements were made at the mid-span of the beam; and in the middle of one each of the top and bottom flanges and the web at 1200 mm from the supports.

The configuration of the beam is shown in Figure 1a. The position of the thermocouples at mid span of the steel beam is shown in Figure 1b. At the temperature measurement points 1200 mm from the supports temperatures were not measured at locations 1b and 3b.

The beam was unprotected and exposed to fire in a horizontal fire resistance furnace on 3 sides (bottom and the two sides – the top was not exposed to fire and continuity of the top of the furnace was ensured by covering the top of the beam with light weight concrete blocks). The test was carried out in accordance with EN 1365-3 [7] and the fire was an EN 1363-1 (ISO 834) standard fire [8].

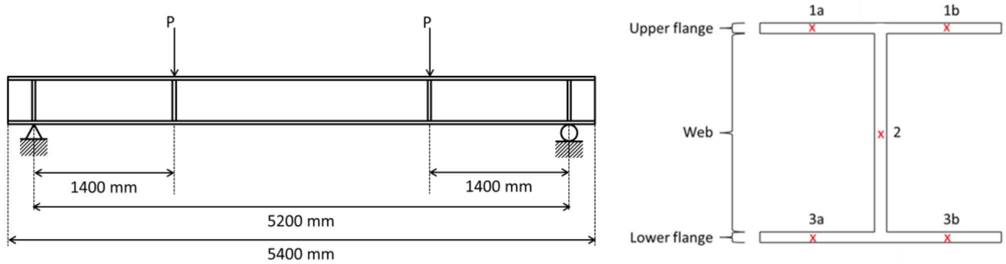

Figure 1. Geometry of the test specimen

PARTICIPANTS

Participants for the study were invited from several fields and represent a cross section of the fire engineering community who are involved in research, certification, and consultancy and may be considered to be among experts in the field. Of the 22 invited, 12 participants agreed to contribute to the study, with some of them submitting more than one solution to the problem using different calculation tools. These additional solutions are treated as further participants in the overview of the data. In total 19 submissions were made to the first stage. One of the participants, however, contributed with only the thermal analysis to the first stage, and another asked for their data to be withdrawn after finding an error in the calculation.

One of the participants declined to contribute to the second stage, however one of the other participants contributed with an additional submission, meaning that in total we received at least one submission from 10 different groups and in total 18 different submissions to the second stage.

For anonymity the submissions were all assigned an identification number and the identities of the participants was disclosed only to the participants responsible.

FIRST STAGE RESULTS SUMMARY

An overview of the first stage results was presented in [6]. In the majority of cases, the participants used the finite element method to model the fire test, basing the thermal exposure on EN 1991-1-2 and the material response on EN 1993-1-2. Different numerical codes were used and different assumptions were made with regards to the approach which was taken. 5 of the 18 solutions presented assumed lumped capacitance for the temperature distribution. 4 of the submissions accounted for the shadow effect, and 3 accounted for the heat transfer through the concrete when determining the temperatures of the beam. For the structural analysis, participants either used the simplified methods presented in EN 1993-1-2 or finite element software packages, including Abaqus, Ansys, Sofistik, OpenSEES, SAFIR and Infograph. Different approaches were taken when developing the solutions, including using beam elements, shell elements and solid elements. Some of the solutions relied on symmetry, including quarter symmetry. The solutions which used beam elements necessarily ignored the stiffeners.

The reported deflection histories from the simulations are shown in Figure 2.

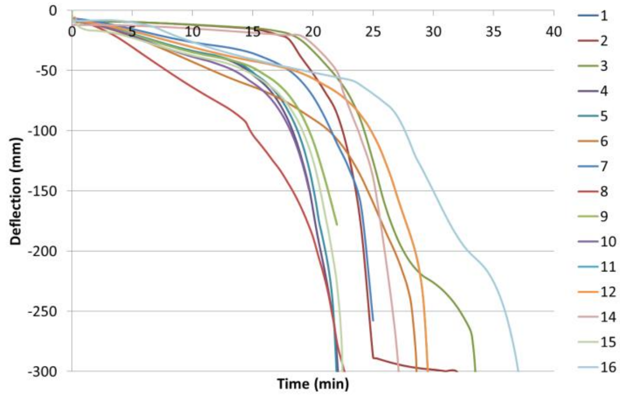

Figure 2. Calculated midspan deflection histories in the first stage round robin

The participants were also asked to report the failure times of the steel beams in their models, as well as the criteria which they used for this. This resulted in fact in many different failure criteria being used, making it impossible to compare the results. In order to allow a comparison, the results were 'corrected' according to the failure criteria described in EN 13501-2 [9]: "*failure of loadbearing capacity shall be deemed to have occurred when both of the following criteria have been exceeded:*

a) deflection $D = L^2/400\,d$ *(mm) and*

b) rate of deflection $dD/dt = L^2/9000\,d$ *(mm/min)*

where L is the clear span of the test specimen in mm and d is the distance from the extreme fibre of the cold design compression zone to the extreme fiber of the cold design tension zone of the structural section, in mm."

A comparison of the corrected and the uncorrected results is shown in Figure 3. Figure 3 a) shows the frequency of different failure times, and Figure 3 b) shows the CDF of failure times. The results highlighted two issues. First of all, that the spread in calculated response is significant, and secondly that the failure criteria is not consistent between the participants.

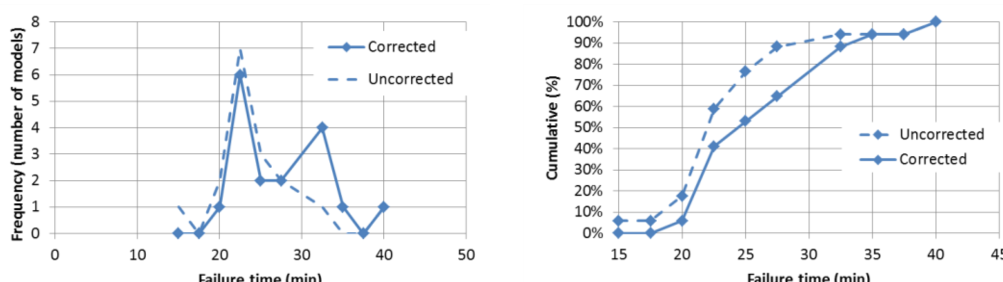

a) b)

Figure 3. a) frequency and b) cumulative percentage of the corrected failure times, including a comparison with the reported failure times in the first stage round robin

SECOND STAGE ROUND ROBIN

Additional Information Provided

In the instructions for the second stage of the study the participants were furnished with additional information which would allow them to improve their estimation of the fire resistance of the steel beam. This information included the tensile strength of the steel; as well as the measured temperatures from the furnace plate thermometers and the measured temperatures at the midspan of the steel beam during the test.

By means of tensile testing of the steel, the elastic limit was determined to be 447.5 MPa, based on 6 samples tested according to ISO 6892-1[10]. The standard deviation was below 2 %. This elastic limit is notably higher than the elastic limit implied by the steel grade of 355 MPa.

Average plate thermometer temperature measurements and measured temperatures from the steel beam were provided in tabular format. The temperatures which were provided to the participants were extended with estimated temperature values since the test was terminated when the beam failed, and by only giving the measured temperatures we would be informing the participants of the actual failure time. Therefore the temperatures provided between the failure time and 45 minutes are estimated values. Figure 4 summarises the temperature data provided to the participants.

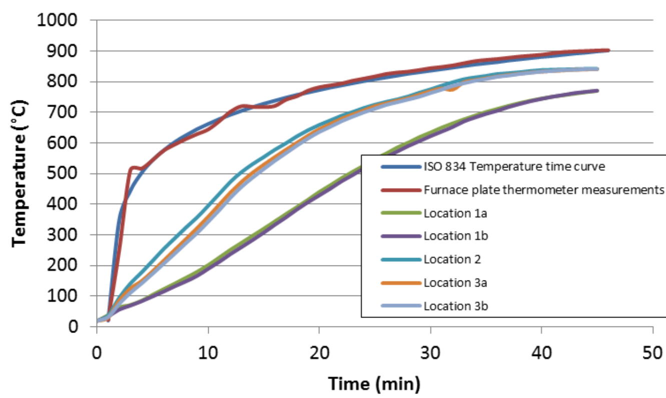

Figure 4. Summary of temperature data provided to the participants

Changes to the Modelling Approach

Participants responsible for submissions 2, 3, 6, 8, 11, 12, 13 and 14 applied the measured temperatures to the relevant parts of the beams, with no smoothing of the temperatures at the transitions between web and flange (i.e. three temperature histories were applied, one to the upper flange; one to the web; and one to the bottom flange). In submission 2 the temperatures were applied across the entire length of the beam, whereas in submission 3 the measured temperatures were applied at the midpsan and the temperature (in °C) was decreased linearly to 80% of the midspan temperature at the ends of the beam. In both submissions 2 and 3 the average of the reported temperature was applied to the stiffeners. Submission 6 applied the temperature of the web to the stiffeners.

The participant responsible for submission 7 changed the convective heat transfer coefficient from 25 kW/m^{2}K in stage 1 to 35 kW/m^{2}K. They also changed the surface emissivity of the steel to 0.6 from 0.7. The measured furnace temperatures (plate thermometer measurements) were then used as the radiation temperature and the gas temperature in the heat transfer calculation. The use of the measured furnace temperatures in this way was also the case for submission 9.

Submission 10 did not account for the additional information provided regarding the temperatures.

For submission 15, the participant also adjusted the convective heat transfer coefficient and the surface emissivity of the steel in order to make the temperatures in the simulation better fit the measured temperatures. In this case they used a convective heat transfer coefficient of 12 kW/m^2K on the upper flange and 15 kW/m^2K everywhere else; the emissivity was changed to 0.5 throughout.

Submission 16 used the reported temperature data to recalculate the emissivity of the element, and used the reported plate thermometer temperature as the radiation and gas temperature for the heat transfer calculation.

Participants responsible for submissions 4, 5 and 19 applied the measured temperatures to the steel directly. The top flange temperature was the average of the measured temperature at both stations in the upper flange and the bottom flange temperature the average of both stations on the bottom flange.

Participants responsible for submissions 2, 3, 4, 5, 6, 7, 8, 9, 10, 11, 12, 13, 14, 15 and 19 adjusted the temperature dependent stress-strain curve to reflect the measured value of the elastic limit which was reported to the participants.

The participant responsible for submission16 did not adjust the stress-strain curve to reflect the measured value of yield strength of the steel reported.

Second Stage Results

The deflection history reported by the participants is shown in Figure 5. The dashed line indicates the results from the fire test. The deflection history of submission 12 has a rather difficult to explain response where there is some relaxation of the deflection at about 25 minutes. By comparison of Figure 5 with Figure 2, it can be seen that overall the spread has been significantly reduced by incorporating the measured temperatures in the majority of models.

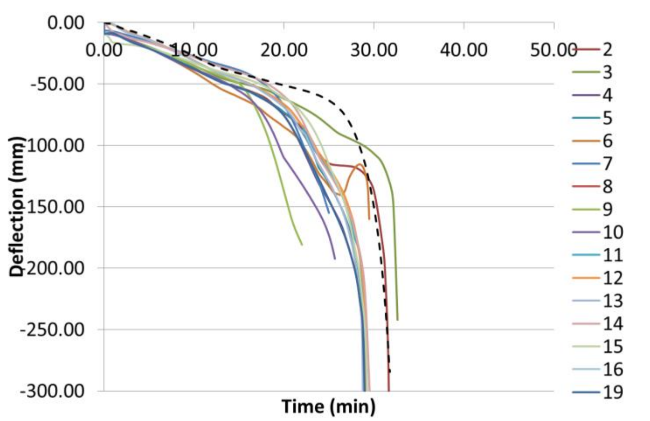

Figure 5. Deflection histories at midspan in the second stage round robin.

As with the first stage, the submissions in the second stage used a variety of different failure criteria in their reports, and these were corrected to allow a comparison between the failure times. The corrected and uncorrected failure times from the second stage round robin are shown in Figure 6.

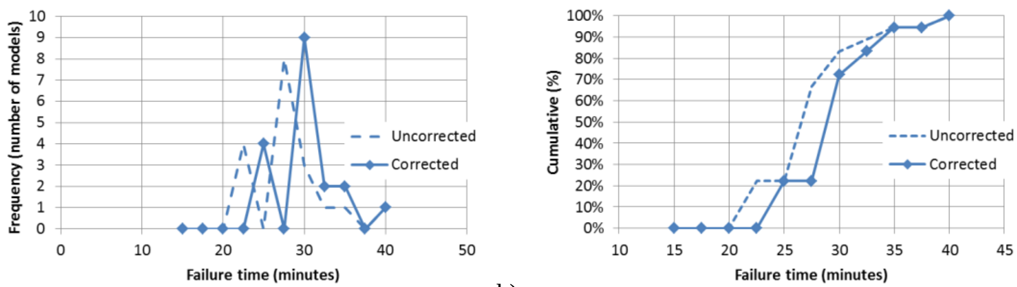

a) b)

Figure 6. a) frequency and b) cumulative percentage of the corrected failure times, including a comparison with the reported failure times in the second stage round robin

COMPARISON WITH EXPERIMENTAL ROUND ROBIN

The test which was used for the comparison in the calculation round robin was a part of an experimental round robin which was conducted by EGOLF, where each laboratory undertook 2 tests, and all of the steel beams came from the same cast flow from the steel mill. The public report into the experimental round robin [11] conducted across different testing laboratories in Europe provides a summary of the mean of the failure times based on the limiting rate of deflection and the absolute deflection arising from the tests in different laboratories.

A comparison between the calculated results and the results arising from testing is provided in table 1. This is based on the standard deviation of the reproducibility limit reported in the testing report, and on the values reported from the 2nd stage round robin, omitting the simple calculation methods. This highlights the collective conservativeness of the calculations performed. However, in both of the criteria of limiting deflection and limiting rate of deflection the calculation round robin has a larger variance than the testing round robin.

TABLE 1 COMPARISON BETWEEN THE 2ND STAGE CALCULATION ROUND ROBIN RESULTS AND THE EXPERIMENTAL ROUND ROBIN RESULTS

		Calculation		Test	
Limiting deflection	**Mean value**	28.15	minutes	31.37	minutes
	Std dev	2.34	minutes	1.47	minutes
	CoV	9	%	6	%
Limiting rate of deflection	**Mean value**	22.11	minutes	27.17	minutes
	Std dev	4.15	minutes	1.27	minutes
	CoV	19	%	5	%

The distributions of the results from the calculation and the test round robin are shown in Figure 18 a) and b). The series *p(C, def)*, for example, denotes the probability density function of the calculated, *"C"*, results for the limiting deflection, *"def"*, criterion; the label *"T"* denotes the test result, and *"rate"* denotes the results for the limiting rate of deflection. In these figures the width of the distributions serve to illustrate the relative spread of the results, in both cases for the limiting criteria the calculation has a clearly wider spread, although this is notably wider for the criterion of limiting rate of deflection.

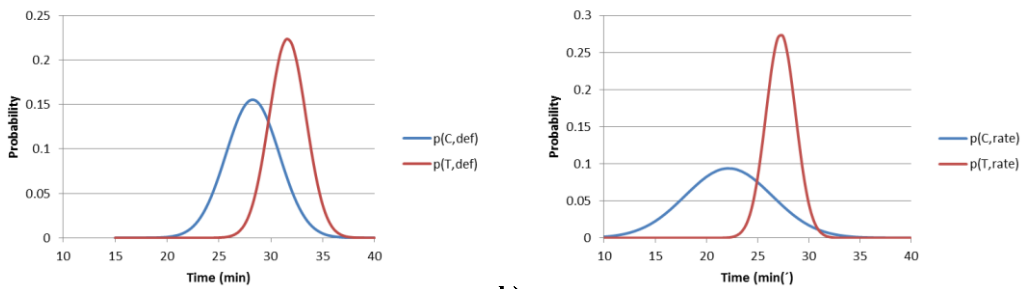

a) b)

Figure 18. Distributions of the failure times in the test and the calculation for the criteria limiting deflection (a), and limiting rate of deflection (b)

CONCLUSIONS

The results of the study highlight the fire research and testing community's ability to model this simple case as well as the uncertainty in the calculation results. Regarding the spread in the calculated deflection histories and calculated times to failure the scatter in results suggests that the relative performance of the design tools or of the designers has some inherent variation which should perhaps be taken account of when using calculations for design or certification.

A comparison between variation in calculations and variations in testing conducted by different groups suggests a greater certainty in the results from testing than from calculation.

The different failure criteria used by the participants highlights a potential issue when calculations are relied upon for certification or design. There is no common consensus or approach to determining the point or time of failure in calculations.

REFERENCES

1. EGOLF; http://www.egolf.org.uk/; accessed 18th December 2015
2. G Rein, C Abecassis Empis and R Carvel, The Dalmarnock Fire Tests: Experiments and Modelling, University of Edinburgh, November 2007. ISBN 978-0-9557497-0-4NRC CFD Validation Studies
3. C. Abecassis-Empis, S. Higginson, G. Morris, M. Krajcovic, J.L. Torero; Modelling heat transfer to a steel beam exposed to a localised pool fire, Proceedings of 2nd CILASCI, Portugal 2013
4. Emmons, H.W.; Fire research abroad; Fire Technology; 1967(3) 225-231
5. Yang, J.C.; Bundy, M.; Gross J.; Hamins, A.; Sadek, F.; Raghunathan, A.; International R&D Roadmap for Fire Resistance of Structures Summary of NIST/CIB Workshop; NIST Special Publication 1188; 2015;
6. Lange, D.; Boström, L.; A priori round robin study of the calculated response of a loaded steel beam to a furnace test; presented at the Fifth International Workshop on Performance, Protection & Strengthening of Structures under Extreme Loading (PROTECT), Michigan, June 28-30, 2015
7. EN 1365-3: 000 Fire resistance tests for loadbearing elements. Beams
8. EN 1363-1: 999 Fire resistance tests. General requirements
9. Dumont, F.; Boström, L.; Lukomski, M.; van den Berg, G.; Summary report of the EGOLF round robin ntr. TC2 14-1 in fire resistance testing; the European Group of Laboratories for Fire Testing (EGOLF); 2015; available from http://www.egolf.org.uk/
10. EN 13501-2:2007 Fire classification of construction products and building elements. Classification using data from fire resistance tests, excluding ventilation
11. ISO 6892-1:2009 Metallic materials -- Tensile testing -- Part 1: Method of test at room temperature

A Unified Rheological Model for Analysis of Steel Behaviour at High Temperature

NENO TORIC[1], IAN W. BURGESS[2], JOSIP BRNIC[3], IVICA BOKO[1], GORAN TURKALJ[3], MARKO CANADIJA[3], ALEN HARAPIN[1], VLADIMIR DIVIC[1] and IVANA UZELAC[1]

ABSTRACT

This paper presents the theoretical background for development of a unified rheological model (URM) for low-carbon steel which is sensitive to the temperature and strain-rate effects during fire exposure. The proposed URM consists of a serial connection of two Kelvin-Voight (KV) rheological elements. Each KV element is used to simulate a particular material strain (stress-related and creep strain) in fire-affected steel. The first KV element is capable of taking into account strain-rate-governed change of yield strength and the second is sensitive to variation of heating rate. A verification of the proposed URM by using test data from transient coupon tests of steel Grade 275 is also presented.

INTRODUCTION

A traditional representation of a material model for fire-affected steel [1-3] is based either on an analytical description of the test results from a set of stationary or transient coupon tests conducted at high temperature. These coupon tests are generally conducted by using a prescribed strain or stress rate at given temperatures in a stationary test, or by using a prescribed heating rate at constant stress in a transient test. In both cases, the material model obtained only captures a limited range of material effects (and behaviour patterns) which occur during high-temperature exposure, depending on the test parameters used.

An example of a material model based on a fixed heating rate, which is widely used in Europe, is the Eurocode 3 material model [1]. This model was determined on the basis of series of transient tests conducted at 10°C/min [4-6]. The test parameter used for his particular model left an open question about its validity in accounting for steel creep which occurs below the test heating rate.

Some recent experimental/numerical studies [7-9] have pointed out that the Eurocode 3 material model has limitations in modelling creep in the case of heating rates lower than 10°C/min. These studies have suggested that an explicit-creep

---

[1]University of Split, Faculty of Civil Engineering, Architecture and Geodesy, Matice Hrvatske 15, 21000 Split, Croatia
[2]University of Sheffield, Department of Civil and Structural Engineering, Sir Frederick Mappin Building, Mappin Street, Sheffield, S1 3JD, UK
[3]University of Rijeka, Faculty of Engineering, Vukovarska 58, 51000 Rijeka, Croatia

analysis should be incorporated when analyzing fire response in the case of low heating rates. Considering the traditional testing procedures for determining steel's mechanical properties, two distinct test parameters can be identified.

The first is the heating-rate, which is generally considered as a factor that governs the level of creep strain evolution in fire-affected steel [7-9]. The second is the strain-rate, which is considered [10] as influencing the yield strength of steel, which tends to increase with the increase of strain-rate. Therefore, a universal material model which is sensitive to these crucial parameters cannot be created if relying solely on either of the traditional test procedures used for determining material properties. A unified rheological model, such as the one presented in this paper, represents a way of taking into account the complex response of the material and its dependence on the crucial heating and loading boundary conditions.

THEORETICAL BACKGROUND

Three strain components for steel at any temperature can be defined according to [11]:

$$\varepsilon_{\mathrm{tot}} = \varepsilon_{\mathrm{th}}(T) + \varepsilon_{\sigma}(\sigma, T) + \varepsilon_{\mathrm{cr}}(\sigma, T, t) \tag{1}$$

in which: $\varepsilon_{\mathrm{tot}}$ is the total strain, $\varepsilon_{\mathrm{th}}(T)$ is the thermal strain, $\varepsilon_{\sigma}(\sigma, T)$ is the stress-related strain and $\varepsilon_{\mathrm{cr}}(\sigma, T, t)$ is the creep strain. As is generally appreciated, thermal strain is temperature-dependent, stress-related strain depends on the applied stress σ and temperature T, and creep strain depends on stress, temperature and time. The stress-related and the creep strains are the most complex to define, due to their dependency on a large number of thermo-mechanical variables. The thermal strain will not be considered in the following representation of the rheological model since it can be modelled with relative ease. The proposed URM consists of a series connection of two Kelvin-Voight (KV) rheological elements. Each KV element is used to simulate a part of the material strain.

The first KV element represents a stress-related strain component which defines the strain-rate governed change of yield strength. The second KV element represents a creep strain component which is sensitive to variation of heating rate. The differential equation describing the strain calculation procedure for a series connection of KV elements is:

$$\frac{\sigma}{\mathrm{c_i}} = \frac{\mathrm{k_i}}{\mathrm{c_i}}\varepsilon_{\mathrm{i}} + \dot{\varepsilon}_{\mathrm{i}}\,;\ \mathrm{i}=1,2 \quad ; \quad \dot{\varepsilon} = \mathrm{const} = \dot{\varepsilon}_1 + \dot{\varepsilon}_2 \quad or \quad \sigma = \sigma_{el1} = \sigma_{el2} \tag{2}$$

In which $\dot{\varepsilon}_{\mathrm{i}}$ represents the first strain derivative of the i-th KV, and k_i and c_i represent the spring and damper functions. These nonlinear functions are stress-, temperature- and strain-rate dependent, so they which can be written as:

$$\sigma_1 = \mathrm{k_i}\left(\sigma, \mathrm{T}\right)\varepsilon \quad ; \quad \sigma_2 = \mathrm{c_i}\left(\dot{\varepsilon}, \mathrm{T}\right)\dot{\varepsilon} \quad ; \quad \mathrm{i}=1,2 \tag{3}$$

Figure 1 shows the rheological model and its constitutive components.

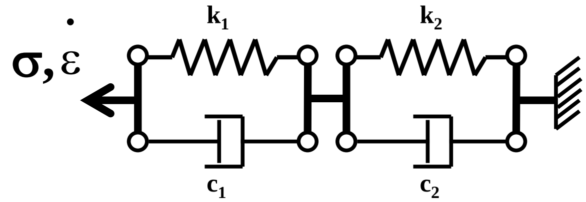

Figure 1. Unified rheological model and its constitutive components.

The solution of two differential equations (2) can be obtained using Euler integration with the appropriate increment for time integration. Two types of solver (strain-rate or stress-rate) can be employed, depending on the type of test which is being analyzed. The principle of a stress-rate solver is illustrated in Figure 2. This type of solver is appropriate for modelling transient tests, in which stress is a fixed test parameter. A different type of solution scheme has to be employed for modelling strain-rate-controlled tests.

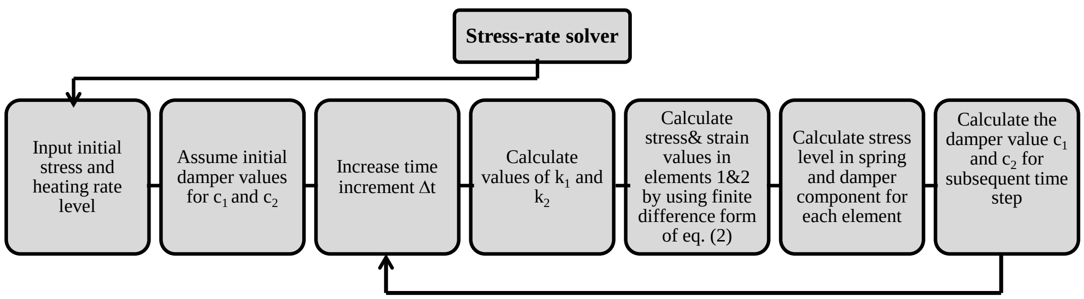

Figure 2. Principle of a stress-rate solver.

COMPONENT MODELS

Prior to the utilization of the unified rheological model, constitutive material laws need to be provided for all four components of the URM. The spring component model is based on a previously developed [8, 12] creep-free Eurocode 3 stress-strain model. Essentially, its shape and analytical form is identical to the original Eurocode 3 model, except that the yield strain value has been modified, and in the creep-free version the yield strain amounts to 1% instead of the original 2%. This is the constitutive model for the spring component belonging to the first KV. The constitutive model for the second spring has the same shape and form as the model for the first, except for the modified value of yield strength (f_y) which amounts to 80% of that used for the first spring. This was arranged in order to take into account the experimentally observed reduction in yield strength at very low strain-rate high-temperature tests [10]. The shapes of the creep-free stress-strain models for both springs are presented in Figure 3.

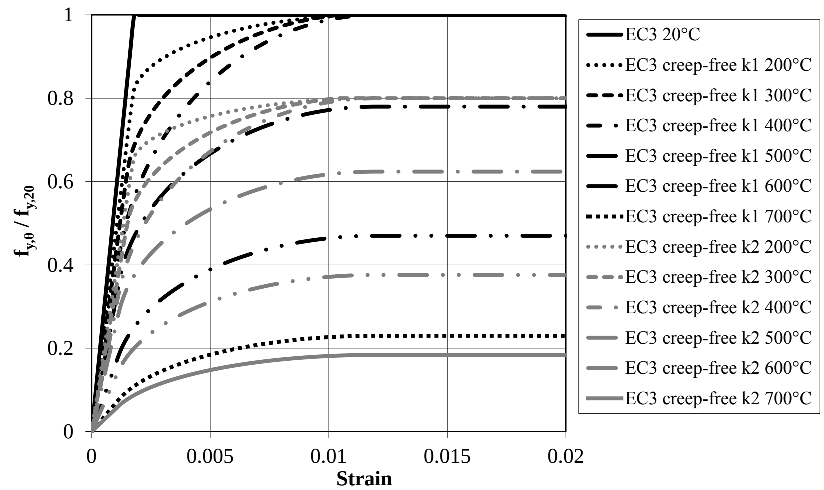

Figure 3. Graphical representation of constitutive material models for spring 1&2.

The constitutive model for the damper component of the first KV has been determined with the help of strain-rate test results from study [10]. The constitutive model for the second damper was created with the help of an existing creep model developed by Harmathy [13] and the corresponding material parameters for American steel A36 [14]. This creep model has proved sufficiently accurate in representing the creep-strain behaviour of European steel grades, which was analyzed in previous research studies [7-9] by the authors. The damper value for both KVs is calculated by the URM using the following expression:

$$c_i = \frac{\sigma_{d_i}}{\dot{\varepsilon}_i}\,;\ i = 1,2 \tag{4}$$

where σ_{d_i} is the damper stress and $\dot{\varepsilon}_i$ is the strain rate of the corresponding KV element. In the case of damper c_1 of the first KV, the damper stress is determined from an experimentally-derived function, and the strain rate can be determined after the calculation of strain of the first KV is completed. The damper stress of the first KV is a function of both strain rate and temperature. This relationship has been determined experimentally, using data from study [10] for slow, medium and fast strain-rate tests. For the second damper, the damper stress is determined using the value of c_2 from the previous time step. The strain rate of the second KV (which in this case represents the creep strain rate) is determined as a function of temperature and stress (defined on a logarithmic scale). The values of c_1 and c_2 which are calculated in the current time step are stored for use in the subsequent time step.

MODEL VERIFICATION

The overall performance of the unified rheological model is compared with the test results published by Kirby *et al.* [4, 5], using the results of transient tests conducted at heating rate of 5°C/min for steel S275 and at 2.5°C/min for S355.

Selected results are given in Figures 4 and 5, in which a comparison is given between the predictions of the URM and the transient coupon study [4, 5]. The unique feature of the proposed URM is, as specified in Equation (3), that the spring and damper components are temperature-, stress- and strain-rate-dependent. Therefore, by providing adequate calibration of the constitutive models for springs and dampers, it is possible to take into account the effects of variable strain- and heating-rate on the strain output. The comparisons from Figures 4 and 5 show that the URM can adequately model the development of stress-related and creep strains by using the proposed material models for each of the constitutive components.

A discrepancy can be observed from Figure 4 at higher stress levels, which can be attributed to the fact that the yield strength increase has been taken into account up to a certain strain-rate level (the fastest strain-rate from study [10]). In cases where steel is stressed close to its yield strength, the occurrence of a very high strain rate is possible, especially at and beyond the steel's yield strain. This is why the URM shows some discrepancy in predicting strain evolution after the yield strain which is used in the URM (1% strain in Figure 3) is exceeded.

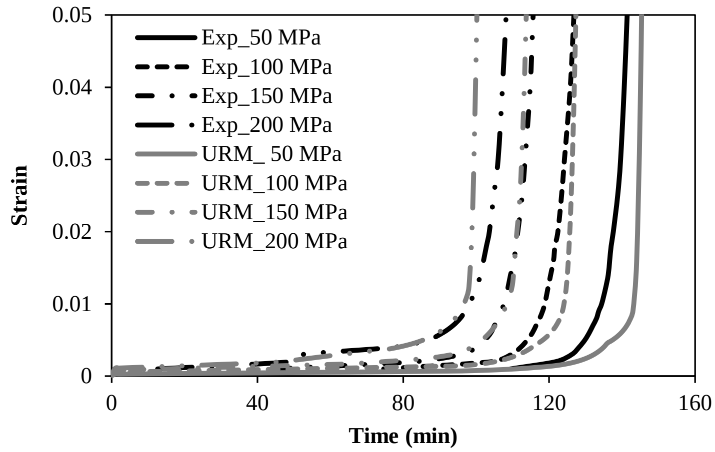

Figure 4. Selected comparison of results between the URM and the coupon experiments - grade S275 [4,5] – 5°C/min.

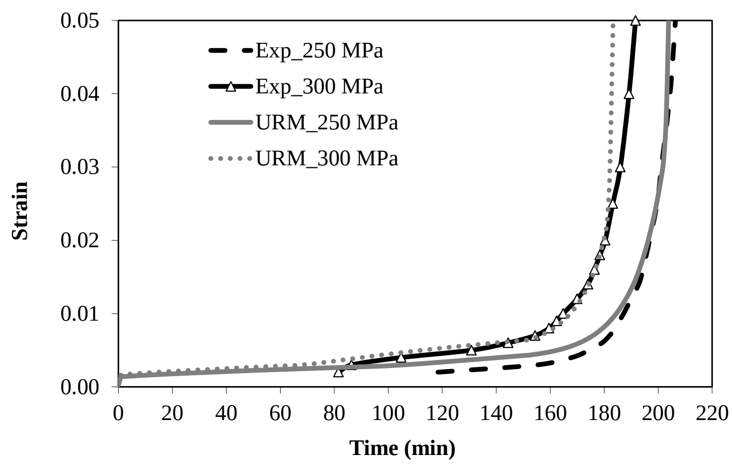

Figure 5. Selected comparison of results between the URM and the coupon experiments - grade S355 [4,5] – 2.5°C/min.

Figure 6 presents the values of damping constant c_2 calculated by the URM for transient testing at 5°C/min, where a coupon of steel S275 is exposed to a stress of 100 MPa. The main logic behind the interaction of two dampers as strain-rate-sensitive components is that the initial value of c_1 is very low in comparison to the value of c_2. This is to ensure the activation of damper c_1 at higher strain-rates, when the change of yield strength occurs, and the activation of damper c_2 at later stages of fire exposure when creep starts to develop. The functionality of the damper c_2 is illustrated in Figure 6, where the initial damping value is initially very high (no creep strain), and after 140 minutes a sudden drop in the value is observed (which corresponds to the start of creep strain development).

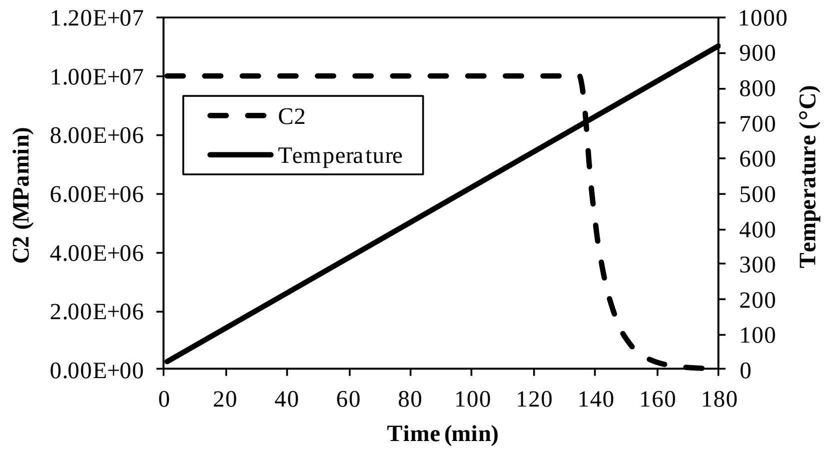

Figure 6. Reduction of the value of c_2 with respect to time – S275, 100 MPa at 5°C/min.

A comparison between the explicit creep analysis using the original Eurocode 3 material model and the predictions of the URM is given in Figure 7. This analysis was conducted by utilizing the *Vulcan* research code and its force-controlled solver, which can run the analysis up to the onset of the yield strain of original Eurocode 3 model (2%).

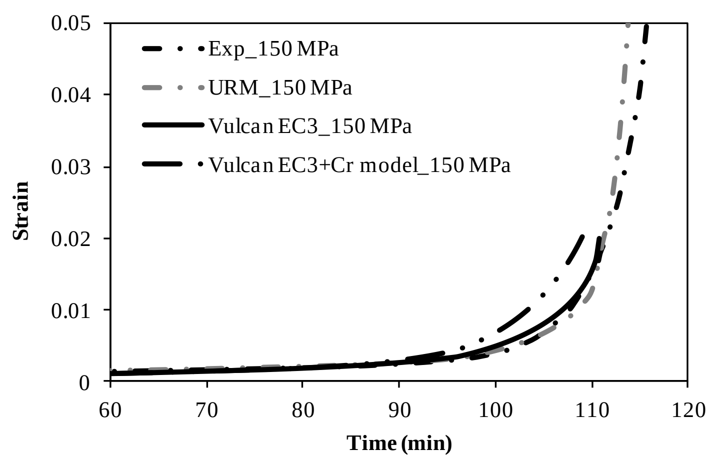

Figure 7. Comparison of different modelling approaches – URM vs. Vulcan explicit creep modelling for grade S275, 5°C/min.

It can be seen from Figure 7 that the analysis which uses the original EC3 model in combination with an explicit creep model provides imprecise predictions of the total strain if compared to the experimental values, with the predictions of the URM being closest to the experimental values. In addition, the URM provides good predictions of total strain over a range of 1%, indicating its validity over the entire strain range.

Table 1 presents a comparison of results between the predictions obtained by the URM and the experimental values.

TABLE I. COMPARISON OF TOTAL STRAIN PREDICTION – URM AND THE EXPERIMENT.

Temperature (°C)	**Exp [4,5] 5°C/min, S275 (%)**	**URM (%)**
558	1.00	0.9
563	1.20	1.04
567	1.40	1.19
572	1.60	1.60
574	1.80	1.78
577	2.00	2.13

CONCLUSION

Variation of both strain- and heating-rates is generally expected in fire-affected steel structures. Therefore, a versatile material model is necessary in order to take into account all the effects which occur in the structure when exposed to variable mechanical and thermal boundary conditions. The main advantage of the proposed URM is that it can take into account the change of crucial thermo-mechanical variables, since a classical material model based either on a test conducted with a unique strain- or heating-rate cannot be considered as representative for all aspects of overall material strain output during fire exposure. Future research will involve an in-depth verification of the URM by using published test studies [4, 5], including other available test sources, whether these are based on stationary or transient test data.

Acknowledgement

This work has been fully supported by Croatian Science Foundation under the project: Influence of creep strain on the load capacity of steel and aluminium columns exposed to fire (UIP-2014-09-5711).

REFERENCES

1. EN 1993-1-2:2005, Eurocode 3 - Design of Steel Structures - Part 1-2: General Rules - Structural Fire Design, *European Committee for Standardization*, Brussels, 2005.
2. ASCE 1992. “Structural fire protection,” ASCE committee on fire protection, Manual No. 78, ASCE, Reston, Va., 1992.
3. Poh, K. W. 2001. “Stress-Strain-Temperature Relationship for Structural Steel”, *Journal of Materials in Civil Engineering*, 13(5):371-379.
4. Kirby, B.R. and Preston, R.R. 1988. “High Temperature Properties of Hot-Rolled, Structural Steels for Use in Fire Engineering Design Studies,” *Fire Safety Journal*, 13:27-37.
5. Wainman D. E. and Kirby B. R. 1988. “Compendium of UK Standard Fire Test Data: Unprotected Structural Steel – 1 & 2,” *British Steel Corporation*.
6. Rubert A. and Schaumann P. 1985. “Temperaturabhaengige Werkstoffeigenschaften von Baustahl bei Brandbeanspruchung,” *Stahlbau*, 3, 81-86.
7. Torić, N., Harapin, A. and Boko, I. 2013. “Experimental Verification of a Newly Developed Implicit Creep Model for Steel Structures Exposed to Fire,” *Engineering Structures*, 57:116-124.
8. Torić, N., Sun R.-R., Burgess, I.W. 2015. “Creep-free fire analysis of steel structures with Eurocode 3 material model,” *Journal of Structural Fire Engineering*, Accepted for publication.

9. Torić N., Sun R. R. and Burgess I.W. 2015. "Performance of different creep models in the analysis of fire exposed steel members", presented at the 4th International Conference on Applications of Structural Fire Engineering, 15-16 October, 2015, Dubrovnik, Croatia, pp. 313-318.
10. Latham D. and Kirby, B.R 1998. "Elevated temperature behaviour of welded joints in structural steels," *European commission, Technical steel research-final report*, 58-60.
11. Anderberg Y. 1988. "Modelling Steel Behaviour," *Fire Safety Journal*, 13(1):17-26.
12. Torić, N., Sun R.-R., Burgess, I.W. 2015. "Development of a creep-free stress-strain law for fire analysis of steel structures," *Fire and Materials*, DOI: 10.1002/fam.2347
13. Harmathy, T. Z. 1967. "A Comprehensive Creep Model," *Journal of Basic Engineering*, 89(3):496-502.
14. Harmathy, T. Z. and Stanzak, W.W. 1970. "Elevated-Temperature Tensile and Creep Properties of Some Structural and Prestressing Steel", National Research Council of Canada, Division of Building Research, Ottawa.

Scaling of Reaction Forces in a Displacement Controlled Steel Beam, Transitioning From Elastic to Plastic Behaviour

KIM OLSSON, DAVID LANGE and LARS BOSTROM

ABSTRACT

Fire resistance testing of structural elements and components is limited by the scale of fire resistance furnaces. Certification of long span or large structural systems may not be verified based on the results of full scale furnace tests but instead computer simulations.

The response of structures exposed to fire depends on a number of different mechanisms which scale differently over different mechanical regimes. Consider the simple case of a fire exposed steel beam with a fixed point load, pinned at both ends. During the early period of fire exposure, it is the elastic behaviour which governs the flexural response. As the fire exposure increases, the beam starts to behave plastic and the axial response will be dominant.

Dimensional analysis is applied to accurately create two different scale models of a prototype beam. The prototype and the models are modelled using Abaqus. We have shown that the total reaction force at displacements where a tensile mechanism is mobilised scales to the ratio of cross sectional areas of model to prototype. The total reaction force at low displacements under flexural behaviour scales with the ratio of the length of the model to the length of the prototype.

Using a scale model to predict the response of a prototype exhibiting flexural and catenary mechanisms is therefore possible. There is a transition region between the elastic and the plastic region which does not scale with either length or area.

It is our long term intention to develop scaling laws which could be used to help to 1) validate numerical models of structures exposed to fire; and 2) to better support extended application of test results.

Kim Olsson, David Lange, Lars Boström, SP Fire Research, Sweden
e-mails: kim.olsson@sp.se, david.lange@sp.se, lars.bostrom@sp.se

NOMENCLATURE

L	beam length
t_f	flange thickness
t_w	web thickness
b	width of I-section
h	height of I-section
E	Young's modulus
P	point load
u	lateral displacement
A	cross sectional area
R_F	reaction force
ν	Poisson ratio
σ_Y	yield stress
ε	strain

INTRODUCTION

Fire resistance testing of structural elements and components is limited by the scale of fire resistance furnaces, typically these are of the order of 3 x 3 m in the case of vertical furnaces, and 4 or 5 x 3 m in the case of horizontal furnaces. This means that certification of elements with larger dimension than this is based on extended field of application of fire test results [1]. However the rules for this extended field of application limit the extent of this to no more than typically 10 or 20 % in excess of the original dimensions which were tested.

This is an issue for certification of long span or large structural systems which may not be verified based on the results of full scale furnace tests but instead computer simulations [2].

However, the response of structures exposed to fire depends on a number of different mechanisms which scale differently. For example, consider the simple case of a fire exposed steel beam with a fixed point load, pinned at both ends. The mid span deflection of such a floor system is shown schematically in Figure 1. During early stages of fire exposure and at low deflections, the response is primarily governed by the flexural behaviour of the floor. During the early period of fire exposure, it is the elastic behaviour which governs the mid span deflection of the beam. As the fire exposure and the mid span deflection increases, the plastic capacity of the section decreases until it is no longer sufficient to support the applied load and a hinge forms allowing a rapid increase in the deflection. A new equilibrium is then finally obtained at some larger deflection as the beam adopts a catenary mechanism. There are four mechanisms which scale differently here, the elastic flexural response of the steel; the ultimate plastic moment of the cross section, the axial behaviour of the cross section once it adopts the catenary mechanism and finally the thermal response of the cross section.

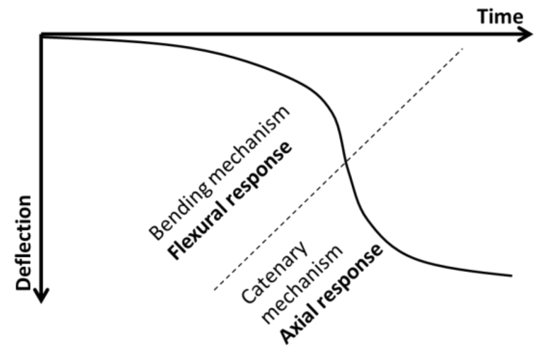

Figure 1. The governing mechanism, and thus the scaling laws varies with time during fire exposure.

To satisfactorily scale the behaviour of a fire test, or to determine the scaling laws needed to be applied to a model of a structural system in order to allow for extended application of the fire test results, each of these different scaling behaviours has to be taken into account, and the correct application of them in either interpreting or defining fire test results is needed.

In paper [3] a strategy for reduced scale structural models in fire testing, is presented. The paper deals with scaling of the thermo-structural behaviour where both considerations to the dynamical, static and thermal aspects of the problem are given. The strategy is validated for low temperatures where the structural response is in the elastic region.

One example of scaling of structures exposed to fire was presented at SiF '06 [4]. However this focussed on scaling of the fire and the heat transfer within the model, and when the model was exposed to a large fire the change from linear to non-linear mechanical response of the model reduced the effectiveness of the small scale model in describing the response of the large scale model.

The work presented in this paper focuses on investigating scaling of reaction forces as a steel beam transitions from elastic to plastic region.

THEORY

In order to understand a full scale system by testing a geometrically scaled system; it is important to know under which circumstances the scaled system should be tested. It is also necessary to know what to measure in the model scale test in order to fully understand the full scale system. The answers to these types of questions are found in dimensional analysis [5].

Dimensional analysis is a way to reduce and simplify the number of variables and parameters that describes a physical system. It also gives valuable insight to the problem without knowing the governing equations [6].

The core of dimensional analysis is the Buckingham-π theorem. The Buckingham theorem describes the procedure of acquiring the so called dimensionless π – groups. An appropriate scaled model *(m)* of a prototype *(p)* will be satisfied if all relevant dimensionless groups are set equal for both model and prototype i.e.

$$(\pi_i)_m = (\pi_i)_p \; \forall \; i \in N^1 : i \; \leq n \tag{1}$$

where n is the number of dimensionless groups.

Considering the example given above and illustrated in Figure 1, there are, as discussed two principal mechanisms which govern and which scale differently: a flexural mechanism and a tensile catenary mechanism. When the system is acting in bending then the structural similitude in the elastic region is relatively straightforward and basically means that all dimensions of the prototype model will be scaled by the ratio of the length of the prototype and the model.

$$\left[b, h, t_f, t_w, L\right]_m = L_m/L_p\left[b, h, t_f, t_w, L\right]_p \tag{2}$$

In the elastic region the reaction force to the displacement is proportional to the length due to the flexure nature of the problem. Analogous to this, when the system is in the catenary or axial response region then the behaviour is governed by the axial stiffness and this the structural similitude becomes proportional to the cross sectional area of the beam.

Thus two different scale factors for the geometry need to be considered to describe the behaviour of the model by scaling of a prototype for the entire deflection history. These are the length ratio between the prototype and the model

$$S_L = L_m/L_p \tag{3}$$

and the area ratio

$$S_A = A_m/A_p \tag{4}$$

In this paper, both a prototype and a model of the system described above are analysed in a displacement controlled analysis. The intention in the analysis is to push the models through both of the relevant regimes, from a flexural mechanism through to the catenary mechanism. Under a load controlled analysis, the point load would normally be scaled according to S_L^2 due to the fact that the π-group representing the point load P is

$$\left[\frac{P}{EL^2}\right] = 1 \tag{5}$$

However, this is under the assumption that the scaled model will deflect half of the prototype. Since in our displacement controlled analysis we apply the same displacement to the model and the prototype, twice the model load is needed which will be the same as scaling the load on the prototype with S_L.

NUMERICAL MODELING

In order to demonstrate these scaling factors, numerical simulations were carried out using the Abaqus standard finite element solver. Three steel I-beams were modelled: the prototype which represents the full scale specimen, a 3/4 scale model and a half scale model. A schematic of the cross sectional dimensions of the I-section are seen in Figure 2. All of the dimensions of the models were scaled accordingly to the relationship in equation (2).

The FEM models were all comprised of 3-dimensional linear Timoshenko beam elements of length 100 mm. The beams were pinned at both ends. The material was assumed to be ideal elastic plastic with a modulus of elasticity of 210 GPa and a yield stress of 355 MPa.

Each of the models was subjected to an applied displacement at the mid span which was ramped linearly over an analysis step from 0 to 40 mm. A schematic of the FEM model is seen in Figure 3.

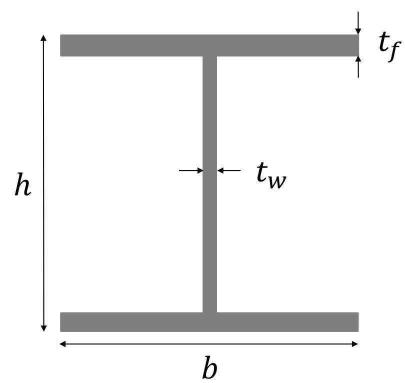

Figure 2. Schematic of cross sectional dimensions of the I-sections.

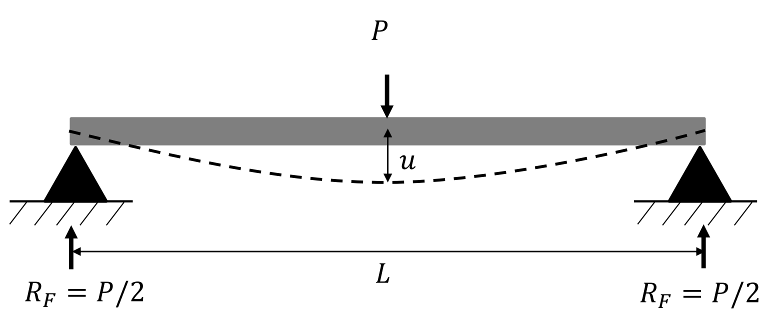

Figure 3. A schematic of the boundary conditions, imposed displacement $\boldsymbol{u}$ and reaction forces $\boldsymbol{R_F}$ in the FEM model.

The dimensions of the prototypes and the models are shown in Table 1.

TABLE I. DIMENSIONS OF THE PROTOTYPE, THREE QUARTER SCALE AND HALF SCALE MODELS.

Dimension (mm)	Prototype	¾ Model	½ Model
L	4000	3000	2000
b	200	150	100
h	200	150	100
t_f	15	11.125	7.5
t_w	9	6.75	4.5

A picture of the prototype is seen in Figure 4 with the beam section rendered.

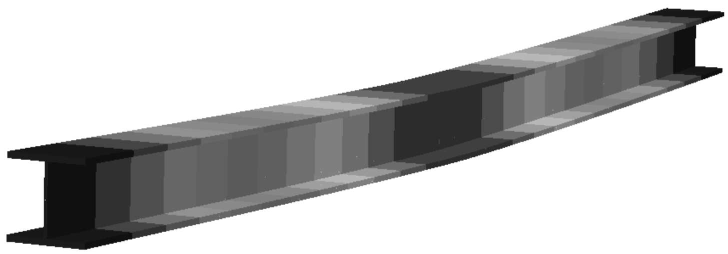

Figure 4. A picture of the prototype.

RESULTS

The point load P required inducing displacements of 10 and 40 mm in the prototype and the models is given in Table 2, along with the scaling ratio for the two mechanisms between the prototype and the two models. This scaling ratio is determined from equations (3) and (4) above.

TABLE II. POINT LOAD ***P*** IN THE ELASTIC AND PLASTIC REGION AND SCALE FACTORS FOR THE PROTOTYPE, THIRD AND HALF SCALE MODELS.

		Prototype	¾ Model	½ Model	u (mm)
Flexural	P (kN)	83.8	62.3	41.9	10
	S_L	1	3/4	1/2	
Catenary	P (kN)	225.6	125.8	56.4	40
	S_A	1	0.5625	1/4	

The application of the scaling ratios is shown in Figure 5, below. This shows the point load P as a function of the displacement for the prototype and the half scale model, as well as the scaled results from the half scale based on both the ratio of the length and the ratio of the areas. The scaling of the half scale model with the length is seen to give a good agreement with the prototype at low deflections, up to around 12 mm when the model begins to behave inelastically. The load scaled at this deflection with the area ratio then agrees well with the final load in the prototype in the inelastic region.

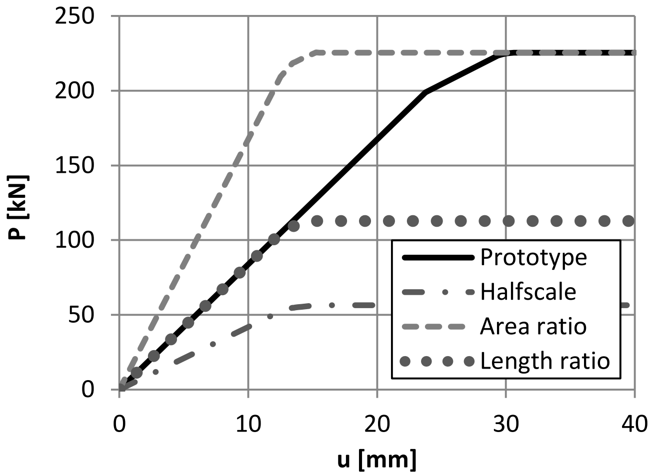

Figure 5. The induced point load $\boldsymbol{P}$ as a function of the displacement $\boldsymbol{u}$ for the prototype and the half scale model. Results from the half scale model scaled using length ratio $\boldsymbol{S_L}$ and area ratio $\boldsymbol{S_A}$.

The same results are shown for the ¾ scale model in Figure 6. Again, good agreement is seen scaling the results with the length until the model begins to behave inelastically, after which the results scale better with the area.

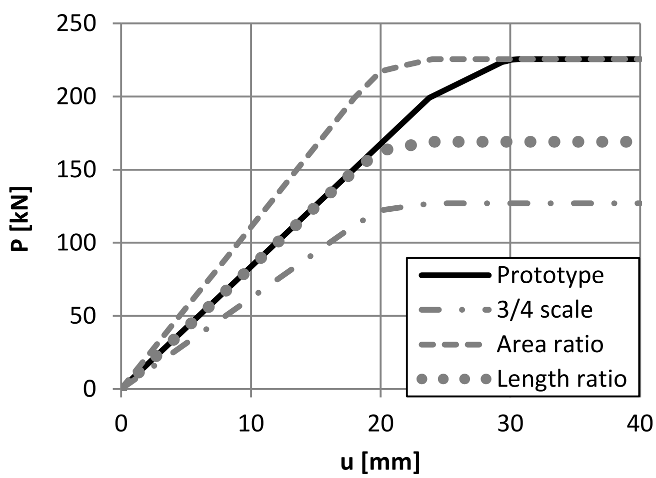

Figure 6. The induced point load $\boldsymbol{P}$ as a function of the displacement $\boldsymbol{u}$ for the prototype and the ¾ scale model. Results from the scaled model scaled using length ratio $\boldsymbol{S_L}$ and area ratio $\boldsymbol{S_A}$.

Based on the ratios in Table 4 we can predict the load P needed to create a displacement u of 10 mm in the elastic region based on a scaling factor determined according to equation (3). The point load P needed to create a displacement u of 40 mm in the plastic region, is scaled accordingly to S_A, determined from equation (4). However in Figures 5 and 6 it can be seen that there is a transition region between the elastic and the plastic region which does not scale with either length or area. Scaling in this region certainly needs to be better understood to be able to scale the results of either numerical models or test results, however based on the study above we believe that it is possible to scale both the early behaviour and the late behaviour of fire exposed horizontal elements

CONCLUSIONS

In the example which is shown here, we have shown that the total reaction force at displacements where a tensile mechanism is mobilised scales to the ratio of cross sectional areas of model to prototype. However the total reaction force at low displacements under flexural behaviour scales with the ratio of the length of the model to the length of the prototype. In order for these conclusions to hold, it is not possible to have a half scale model of the same length as the prototype and only divide the cross sectional dimensions in half. All dimensions must be scaled according to (2).

Using a scale model to predict the response of a prototype exhibiting flexural and catenary mechanisms is therefore possible. However, since the scaling rules for the different mechanisms differ, the correct scaling laws need to be applied to the model analysis to evaluate the prototype under different regimes.

This requires an understanding of the mechanisms which are being mobilised over the entire history of response of a structural element exposed to fire.

This paper has concentrated on describing the background to structural similitude and demonstrating it applied to mechanisms relevant to structural fire engineering. However, the models are very simple representations and were not, in the instance shown, exposed to heating. There are two effects which therefore need to be included in the analysis in the future to address this, and those are the thermal expansion of the model and the prototype and the temperature dependent material properties. These effects will be considered in future work.

It is our long term intention to develop scaling laws which could be used to help to 1) validate numerical models of structures exposed to fire; and 2) to better support extended application of test results.

REFERENCES

1. EN 15725:2010. Extended application reports on the fire performance of construction products and building elements.
2. International maritime organisation (IMO), International Code for the Application of Fire Test Procedures (2010 FTP Code) mandatory from 1 July 2012, recommendation for the evaluation of fire performance and approval of large fire doors IMO ref. T4/4.01.
3. D.J.O'Connor, G.W.H. Silcock. 1992. A strategy for the fire testing of reduced scale structural models. Fire Technology. 28(1):48-69.
4. Wang, M.; Chang, P.; Quintiere, P.; Scale modelling of insulated steel framed structure testing in fire; Proceedings of the 4th international workshop of Structures in Fire '06; Aveiro, Portugal, May 2006.
5. Ain A. Sonin. 2001. The physical basics of dimensional analysis. Department of mechanical engineering, Cambridge MIT.
6. Daniella Calvetti. 2013. Computational mathematical modelling.

Factors Governing the Fire Response of Reactive Powder Concrete Simply-Supported Beams

XIAOMENG HOU, PENGFEI REN, WENZHONG ZHENG, QIN RONG and YAO ZHAN

ABSTRACT

Reactive powder concrete (RPC) is a kind of new cementitious composite material with super high performance and high toughness, which has extensive application prospect. A numerical model for tracing the fire response of RPC simply - supported beams is developed using finite element analysis software. The validity of the numerical model is established by comparing the predictions from the computer program with results from reinforced concrete (RC) beams under fire. Results show that as compared with normal strength concrete (NSC), the thermal conductivity of RPC is higher and its compressive strength decreases faster at elevated temperature. With same reinforcement ratio, concrete cover thickness and cross section, the moment bearing capacity and deflection of reinforced RPC beams decreased faster than that of RC beams at elevated temperature. The analysis variables included load level, reinforcement ratio, concrete cover thickness. Results show that reinforcement ratio, concrete cover thickness and load level have significant influence on the fire resistance performance of reinforced RPC beams. It should be mentioned here that fire resistance of RPC simply-supported beams increases at the beginning and then decreases with the increase of reinforcement ratio. This is mainly because that the stress of longitudinal steel bar increases at the beginning and then decreases with the increase of heating time.

Keywords: Reactive powder concrete, simply-supported beam, fire performance, numerical model.

Xiaomeng Hou, Key Lab of Structures Dynamic Behavior and Control, Ministry of Education, Harbin Institute of Technology, Harbin 150090, China. Email: houxiaomeng_hit@126.com

Pengfei Ren, School of civil engineering, Harbin Institute of Technology, Harbin 150090, China.

Wenzhong Zheng, Key Lab of Structures Dynamic Behavior and Control, Ministry of Education, Harbin Institute of Technology, Harbin 150090, China.

Qin Rong, School of civil engineering, Harbin Institute of Technology, Harbin 150090, China.

Yao Zhan, School of civil engineering, Harbin Institute of Technology, Harbin 150090, China.

INTRODUCTION

Fire is one of the most high frequency disasters[1]. There are over 150 thousand and 3.6 million building fires in China and in the world, respectively. Fire safety is one of the key considerations in building design.

A review of literature indicates that many experiments have been conducted to evaluate fire resistance of Reinforced Concrete (RC) members. Kodur[2-3] analyzed the fire response of HSC (High Strength Concrete) columns and beams. Yi[4] researched the performance of prestressed concrete slab. Wu [5]and Gao[6] researched the fire resistance of RC beams under fire. Ellingwood[7] studied flexure and shear behavior of RC beams during fire.

Reactive powder concrete (RPC) is a kind of new cementitious composite material. Therefore, the fire resistance performance of RPC members is envisioned to be different as compared with RC members. Simply-supported beams are important member in structures. However, there is lack of test data on the behavior of RPC beams under fire conditions. To overcome some of the current limitations in fire resistance for RPC beams and to develop a better understanding, fire resistance simulation were carried out by ANSYS. Analysis data are utilized to discuss the effect of load level, concrete cover thickness, reinforcement ratio on fire response of RPC simply-supported beams.

THERMAL AND MECHANICAL PROPERTIES OF RPC

The temperature distribution of RPC beams under fire is simulated by the software ANSYS. Heat conductivity coefficient, specific heat capacity and mass density have significant influence on temperature distribution.

Thermal properties of RPC

The heat conductivity coefficient λ_c of RPC is expressed as8:

$$\lambda_c = 1.44 + 1.85\exp\left(-T/242.95\right) \quad 20℃ < T \le 900℃ \tag{1}$$

The specific heat capacity C_c of RPC is expressed as8:

$$C_c = \begin{cases} 950 & 20℃ \le T \le 100℃ \\ 950 + (T-100) & 100℃ < T \le 300℃ \\ 1150 + (T-300)/2 & 300℃ < T \le 600℃ \\ 1300 & 600℃ < T \le 900℃ \end{cases} \tag{2}$$

Where, T is temperature in Eq.1 and Eq.2.

The density of RPC is adopted as $\rho_c = 2500 kg/m^3$.

The thermal expansion coefficient of RPC[9] is given in Table1.

Table 1. Thermal expansion coefficient of RPC.

Temperature(℃)	20	200	400	600	800
Thermal expansion coefficient	0.0131	0.0131	0.0182	0.0188	0.0155

Relation for stress-strain response

Stress-strain tests of RPC at elevated temperatures (20, 200, 400, 600 and 800 C) were conducted by Zheng [10]. Utilizing the developed test data, a stress-strain curve is proposed for RPC at elevated temperatures(Eq. 3). For fire resistance analysis of RPC beams using computer models, temperature dependent strain-stress curves of RPC is provided as input data.

$$y = \begin{cases} 1.3x + 0.4x^2 - 0.7x^3, & 0 \le x \le 1, \\ \dfrac{x}{8(x-1)^2 + x}, & x \ge 1. \end{cases} \tag{3}$$

Where $x = \dfrac{\varepsilon}{\varepsilon_{c,T}}$, $y = \dfrac{\sigma}{f_{c,T}}$.

The compressive strength of RPC at elevated temperature is expressed as:

$$\frac{f_{c,T}}{f_{c,20}} = \begin{cases} 1.032 - 1.58(\dfrac{T}{1000}), & 20℃ \le T \le 200℃ \\ 0.857 - 0.712(\dfrac{T}{1000}), & 200℃ \le T \le 800℃ \end{cases} \tag{4}$$

Where $f_{c,20}$, $f_{c,T}$ is compressive strength at ambient and at elevated temperature, respectively, $f_{c,20} = 160MPa$.

The peak strain at of RPC at elevated temperature is expressed as:

$$\frac{\varepsilon_{c,T}}{\varepsilon_0} = 0.696 + 12.1(\frac{T}{1000}) - 39.7(\frac{T}{1000})^2 + 48.8(\frac{T}{1000})^3 \quad 20℃ \le T \le 800℃ \tag{5}$$

Where ε_0, $\varepsilon_{c,T}$ is peak strain at ambient and at elevated temperature, respectively, $\varepsilon_0 = 3185\mu\varepsilon$.

The predicted stress-strain response of RPC by Eq. 3 together with test data by Zheng[10] is shown in Fig.1. A comparison of the measured and calculated stress-strain response indicates that the predicted results and measured data are in good agreement.

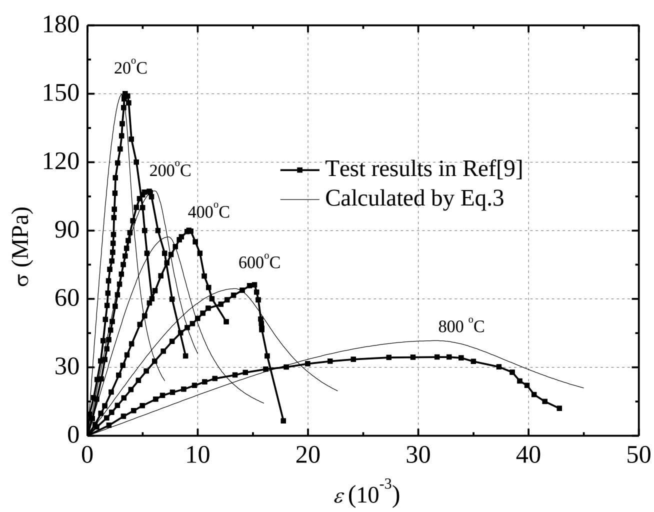

Figure 1. Stress-strain response of RPC at elevated temperatures.

NUMERICAL MODEL AND MODEL VALIDATION

Element PLAN55 was used to simulate he temperature field by ANSYS software. Because the rule of fire-induced spalling of RPC is not clear, the effect of spalling on the temperature field calculation is neglected. Reinforcement steel bars are simulated by element LINK8 and RPC by element SOLID65. A smeared crack model was adopted to study the cracking of the RPC beams subjected to fire. It is assumed that each of the steel bar elements and its corresponding RPC element share the same nodes in order to satisfy displacement compatibility.

The temperature field in the beam could be analyzed separately. After the temperature field was analyzed, the temperatures needed for structural analysis were written into the input file, and then imposed the temperatures on the structural cross section as action. Then time-dependent structural analysis was carried out to find the deflection of the RPC beams during fire. More details about the numerical model can be found in Ref11.

Validation of temperature field

Temperatures of RC beams were measured by Wu[5] and the test results are utilized to validate the numerical model. Details of the beam dimensions and material properties are listed in Table 2.

Table 2. Detail of RC beams used in temperatures analysis.

Property	Wu[5]
Description	RC beams
Cross section	200mm×400mm
Length(m)	5.1
Concrete cover thickness (mm)	25
Heating curve	ISO834
Number of side exposed to fire	3
Reinforcement	2Φ10 top bars 2Φ12+1Φ14 bottom bars
$f_c(MPa)$	24.2
$f_y(MPa)$	240
Load method	Uniformly distributed load

Note: f_c is test prism strength of concrete, f_y is yield strength of steel bars.

Arrangement of thermocouples is given in Fig.2(a). The comparison between the calculated values and the measured values is given in Fig.2(b). A comparison of the measured and calculated temperatures indicates that the predicted results and measured data are in good agreement.

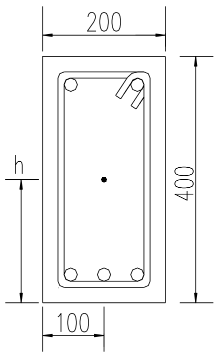

(a) Arrangement of thermocouples

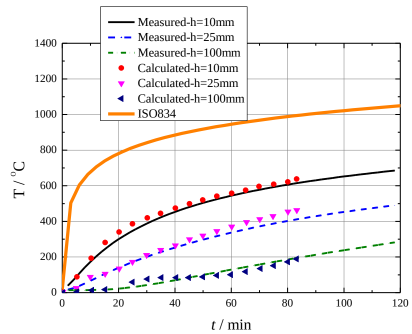

(b) Comparison between calculated and the measured temperatures

Figure 2. Validation of temperature field.

Validation of deflection

The fire resistance test of NSC simply-supported beams were conducted by Zheng[1] and the test results are utilized to validate the numerical model. According to Ref[1],details of the beam dimensions and material properties are listed in Table 3.

Test results of NSC simply-supported beams (B-1) under fire were utilized to validate the numerical model. The comparison between the calculated measured deflections is given in Fig.3. It shows that the calculated values by numerical model and the measured values in test are in good agreement.

Table 3. Detail of RC beam(B-1) used in deflection analysis.

Property	Zheng
Description	NSC simply-supported beam B-1
Cross section	190mm×300mm
Length(m)	4.9
Concrete cover thickness (mm)	25
Heating curve	ISO834
Number of side exposed to fire	3
Reinforcement	2Φ20 top bars 2Φ20 bottom bars
$f_c(MPa)$	52.1
$f_y(MPa)$	410
Load method	Uniformly distributed load

It should be mentioned that the heat conductivity coefficient of RPC is relatively big, its compressive strength degrades fast at elevated temperature. Hence, as compared with same RC beams, the stiffness and flexural capacity of RPC beam at high temperature drops faster.

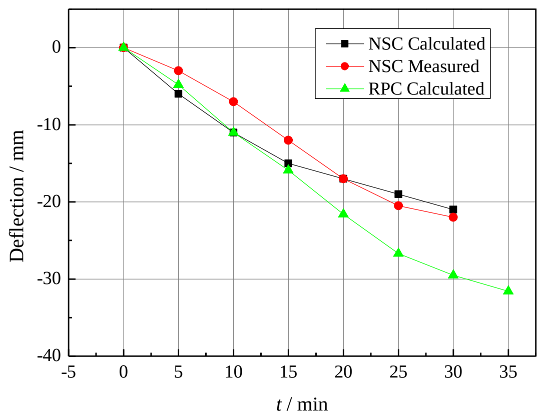

Figure 3. Comparison between mid-span deflection by ANSYS and the measured values.

PARAMETRIC STUDIES

The validated model was applied to evaluate the effect of factors on the fire response of RPC beams during fire. The factors considered in the study include load level (defined as the ratio of the applied static load to the beam capacity), reinforcement ratio and concrete cover thickness.

Concrete cover thickness

The influence of concrete cover thickness of deflection-time curve of the mid-span of RPC simply-supported beam is shown in Fig. 4, with various concrete cover thickness at 25mm, 35mm and 45mm. Results show that beams with higher concrete cover thickness undergo smaller mid-span deflection. The mid-span deflection of beams is reduced by increasing the concrete cover thickness from 25mm to 45mm.The concrete cover thickness has significant influence on the maximum mid-span deflection of beams.

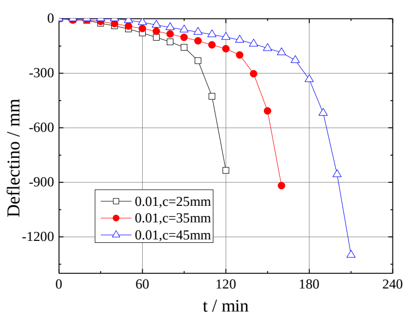

b(width)=600mm, *h*(depth)=900mm,*l*(calculation span)=12000mm, ρ(reinforcement ratio) =0.01, M/Mu(load level)=0.2

Figure 4. Deflection of RPC simply-supported beams varied with concrete cover thickness.

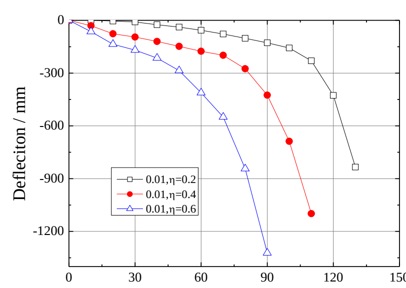

b(width)=600mm, *h*(depth)=900mm, *l*(calculation span)=12000mm, ρ(reinforcement ratio) =0.01,*c* (concrete cove thickness)=25mm

Figure 5. Deflection of RPC simply-supported beams varied with load level.

Load level

The influence of load level on deflection-time curve of the mid-span of RPC simply-supported beam is shown in Fig. 5, with various load level at 0.2,0.4 and 0.6. Results show that beams with higher load level undergo higher mid-span deflection. The load level has significant influence on the mid-span deflection of beams.

Reinforcement ratio

The influence of reinforcement ratio of deflection-time curve of the mid-span of RPC simply-supported beam is shown in Fig. 6, with various reinforcement ratios at 1%, 2%, 4%, 6% and 8%. It can be seen that beams with larger reinforcement ratio undergo smaller mid-span deflection.

The fire resistance of RPC simply-supported beams increases at the beginning (when reinforcement ratio is less than 6%) and then decreases with the increase of reinforcement ratio. This is mainly because that the stress of longitudinal steel bar increases at the beginning and then decreases with the increase of heating time. The reinforcement ratio has significant influence on the maximum mid-span deflection.

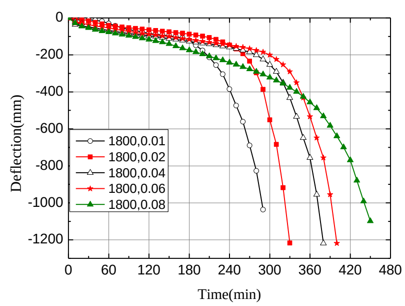

b(width)=600mm, *h*(depth)=1800mm, *l*(calculation span)=12000mm, *c*(concrete cove thickness)=35mm, M/Mu(load level)=0.4

Figure 6. Deflection of RPC simply-supported beams varied with reinforcement ratio.

CONCLUSIONS

Based on the results of this study, the following conclusions can be drawn:

1. An approach for modeling RPC simply-supported beams during fire is presented. The validity of the model is established by comparing predictions from numerical analysis with relative test results. As compared with RC beams, the thermal conductivity of RPC is higher, the degradation of compressive strength is faster, which cause a worse fire performance of RPC beams.
2. Load level, concrete cover thickness and reinforcement ratio, have significant influence on the fire resistance of RPC beams. Lower load level and larger concrete cover lead to higher fire resistance in RPC beams.
3. Fire resistance of RPC simply-supported beams increases at the beginning and then decreases with the increase of reinforcement ratio.

4. Additional tests on fire response of RPC beams under fire will be conducted in further research.

ACKNOWLEDGEMENTS

The study presented in this paper, is supported by the National Natural Science Foundation of China (No. 51578484, 51408167) and the Specialized Research Fund for the Doctoral Program of Higher Education of China (No. 20122302120084).

REFERENCE

1. Zheng Wenzhong, Hou Xiaomeng, Yan Kai. Fire resistance and fire safety design of Prestressed concrete structures[M]. Harbin, Harbin Institute of Technology Press, 2012.(in Chinese)
2. VKR Kodur, TC Wang, FP Cheng, Predicting the fire resistance behaviour of high strength concrete columns[J]. Cement & Concrete Composites, 2004, 26(2): 141-153.
3. Dwaikat M B, Kodur V K R. Response of restrained concrete beams under design fire exposure[J]. Journal of structural engineering, 2009, 135(11): 1408-1417.
4. Na-Hyun Yi, Seung-Jai Choi et al., Failure behavior of unbonded bi-directional prestressed concrete panels under RABT fire loading [J]. Fire Safety Journal 71(2015)123-133.
5. Wu HJ, Lie TT, Hu JY. Fire resistance of beam-slab specimens–experimental studies. Internal Report No. 641, Institute for Research in Construction, National Research Council Canada, Canada, 1993.
6. W.Y. Gao, Jian-Guo Dai, J.G. Teng, G.M. Chen. Finite element modeling of reinforced concrete beams exposed to fire[J]. Engineering Structures, 2013(52): 488-501.
7. Ellingwood B, Lin TD. Flexural and shear behaviour of concrete beams during fires. J Struct Eng-ASCE 1991;117(2):440-458.
8. Zheng Wenzhong, Wang Rui, Wang Yin.Experimental study on thermal parameter of reactive powder concrete[J]. Journal of Building Structures, 2014,35(9): 107-114. (in Chinese)
9. Luo Baifu. Study on explosive spalling rules and mechanical properties of reactive powder concrete at elevated temperatures[D]. Harbin institute of technology, 2013
10. Zheng Wenzhong, Luo Baifu, Wang Ying. Stress-strain relationship for reactive powder concrete with steel fibres at elevated temperatures[J]. Materials and Structures,2015,48(7):2299-2314
11. Zheng WZ, Hou XM. Experiment and Analysis on the Mechanical Behaviour of PC Simply-supported Slabs Subjected to Fire[J]. Advances in Structural Engineering. 2008,11(1):71-89.

Numerical Analyses for Precast RC Structures at Fire Condition in Underground Space

J. X. LIU and K. H. TAN

ABSTRACT

To create sustainable urban development, it is widely recognized that underground space development is a long-term solution to cater for future economic growth. In urban cities, many underground projects have been constructed to mitigate the increasing demand for land and infrastructure.

For structures in very deep underground construction, prescriptive fire codes require 4-hour rating for structures. In this paper, a typical 2 hour-rating RC frame structure is designed for underground space. Standard fire curve (ISO-834) is applied to affected RC members under certain fire scenarios. Numerical results show that with the help of tensile membrane action, even a 2-hour fire rating RC beam-slab system can achieve satisfactory result.

INTRODUCTION

Due to growing shortage of urban land, utilization of underground space is gaining momentum all over the world, despite the initial higher capital outlay. For a small city-state, deployment of mega underground space is a viable and attractive option for housing laboratories, factories, warehouses for storage of non-combustible goods [1].

Among man-made or natural disasters such as fire events, explosions, earthquakes and floods, fire is of the greatest concern in most underground buildings. The number of guidelines or fire codes that address underground space is rather limited, such as the standards established by National Fire Protection Association (NFPA) [2], Kansas City (USA) [3], China [4], Hong Kong [5] and Singapore [6]. Besides the requirements for pre-flashover fire safety such as detector, engineered smoke control and suppression system, structural fire resistance requirement has significant impact on construction cost for underground structures. However, structural fire resistance requirement for underground caverns varies significantly among the codes mentioned. While NFPA 520 [2] specifies 2-hour fire rating for structural components, Chinese code [4] requires 3-hour rating for columns and load bearing walls; Hong Kong [5] requires 4-hour requirement for caverns that are four or more levels. Singapore Fire Code Appendix 23 [6] stipulates 4-hour fire rating for underground structures.

Compared with 2-hour fire requirement for aboveground structures, structural design for 4-hour rating will generally result in significant increase in cross-sectional dimensions and cost. This paper presents a case study in which tensile membrane action was utilized to enhance performance of reinforced concrete (RC) frames in fire situation to justify a lower fire resistance requirement of the structure using performance-based method.

School of Civil and Environmental Engineering, Nanyang Technological University, Singapore 639798, Singapore

E-mails: LIUJ0055@e.ntu.edu.sg, ckhtan@ntu.edu.sg

DESIGN OF UNDERGROUND STRUCTURE

An internal structure for underground cavern is shown in Figure 1 in which the precast beam-column frame is designed based on 2-hour fire resistance with a concrete cover of 35mm. To simplify the analysis procedure, a 150mm thick one-way precast slab with Φ12mm rebar at 100mm spacing is designed to span 5.4m. The precast slab will be constructed with a 50mm topping (A142 anti-crack mesh). One precast slab of 2m width is modelled as a one-way beam element by SAFIR [7] as shown in Fig 2. This underground RC-framed structure is used for office with an imposed load of 3 kPa according to EN1991-1-1[8].

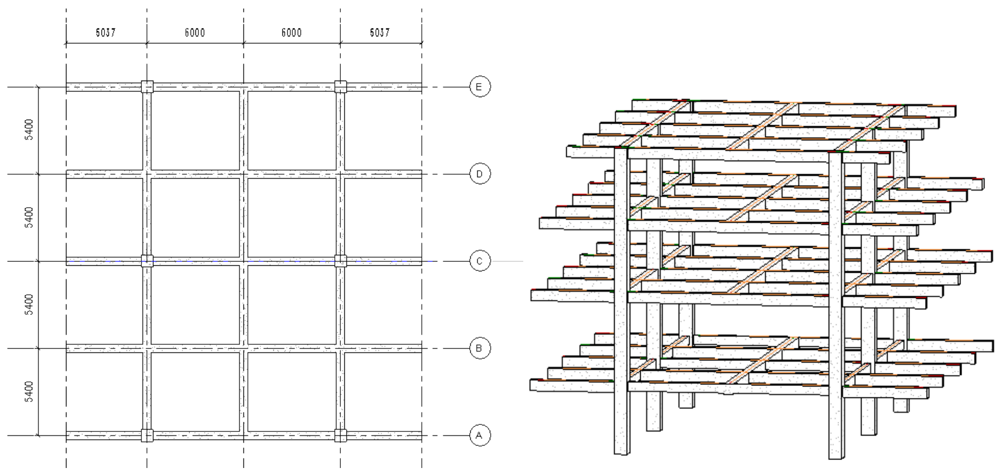

(a) Plan View (b) 3D view

Figure 1. Typical underground RC frames.

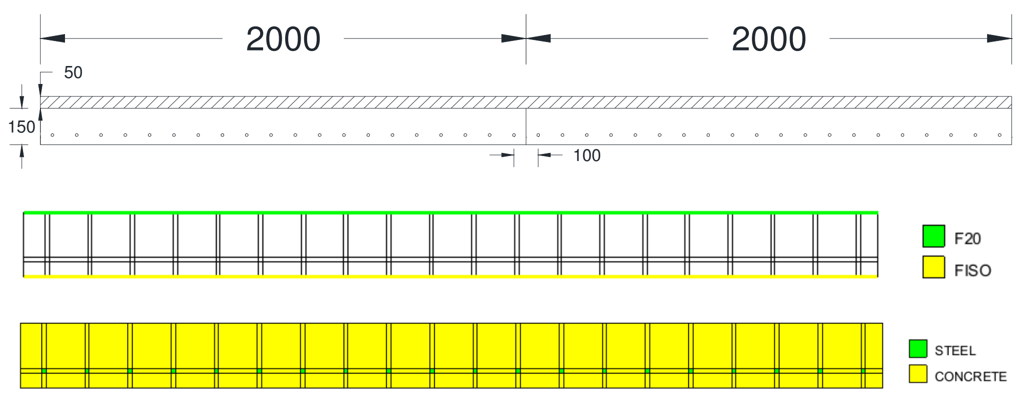

Figure 2. One way precast slab (non-prestressed).

Precast slab planks are supported by RC frames (along gridline ABCDE in Figure 1(a)). Maximum hogging and sagging moments in beam and column sections of RC frames are designed and modelled in SAFIR as shown in Figure 3.

A typical slab-beam-column system is established in SAFIR as shown in Figure 4. 150mm precast slabs are resting on the primary beams and 50mm topping is modelled as shell element which is not shown. Due to limitation in shell elements, shear failure in slabs is not considered. The whole system is supported by four fixed columns.

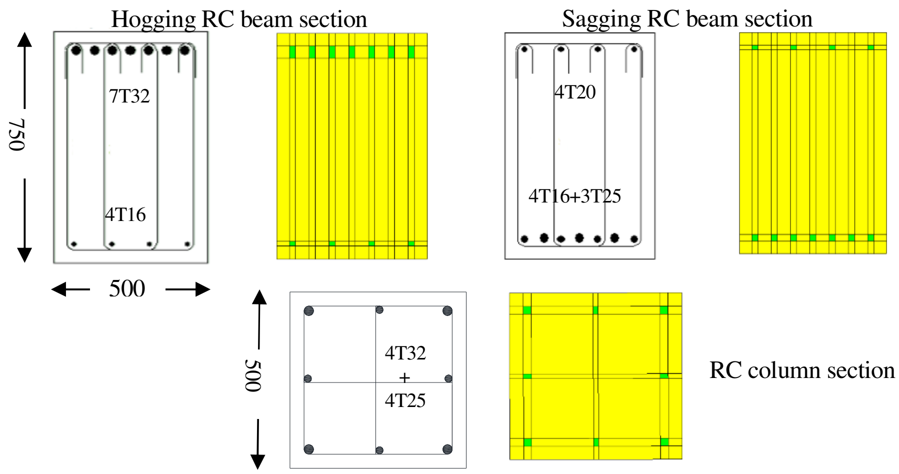

Figure 3. Reinforcement details in beam and column sections.

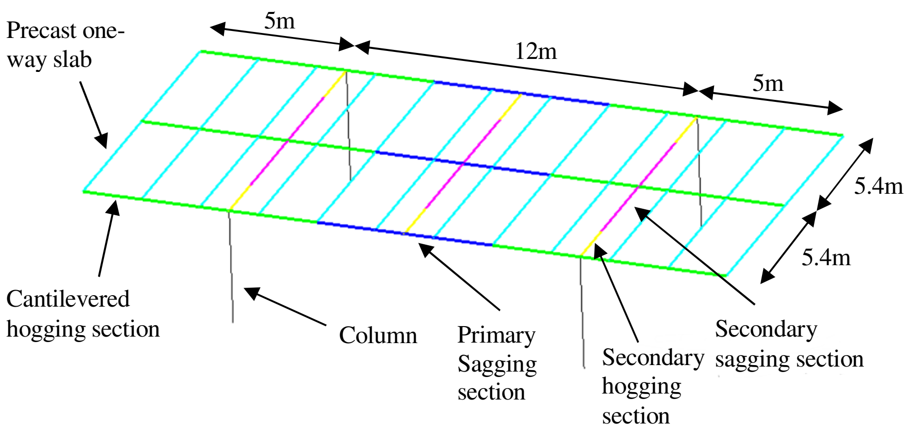

Figure 4. SAFIR modelling for precast RC frame with hogging and sagging beam sections (without topping).

RESULTS OF ANALYSES

Standard fire ISO-834[9] is applied to all members to simulate the worst fire scenario. Thermal boundary conditions for slab, beam and column sections are one-side, three-side and four-side heated, respectively.

A simply supported 150mm thick precast slab panel with 50mm topping is analyzed as shown in Figure 5. The deflection limit according to EN1363-1[10] is determined through either Eq. 1 or 2 (whichever is greater), where D is the deflection limit, *L* is the clear span and *d* is the effective depth of flexural members.

$$\mathrm{D} = \frac{L^2}{400d} \tag{1}$$

$$\frac{d\mathrm{D}}{dt} = \frac{L^2}{9000d} \tag{2}$$

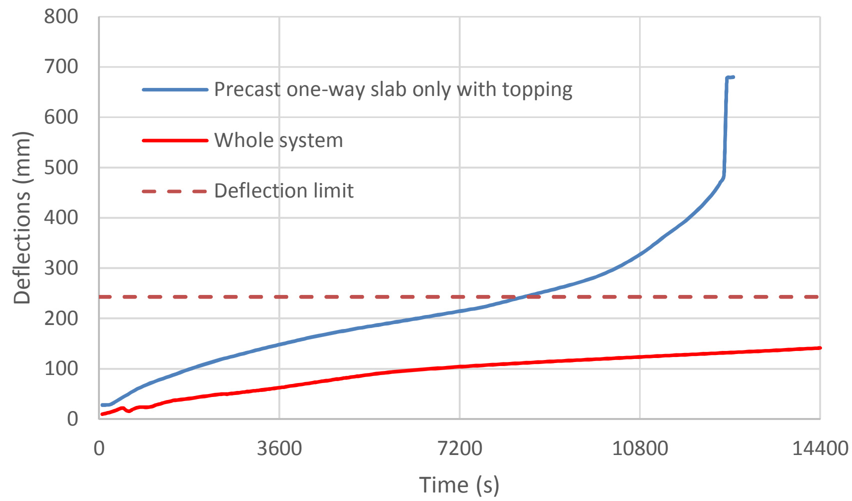

Figure 5. Comparison between precast one-way slab only versus slab-beam system.

It can be seen that for the isolated precast one-way slab with topping, the fire resistance period is slightly greater than 2-hour, which is the duration when the maximum deflection exceeds the allowable deflection limit as shown in Figure 5. However, when the slab-beam-column system is considered, the deflection is much smaller (Figure 6) and the fire resistance period can be greatly enhanced.

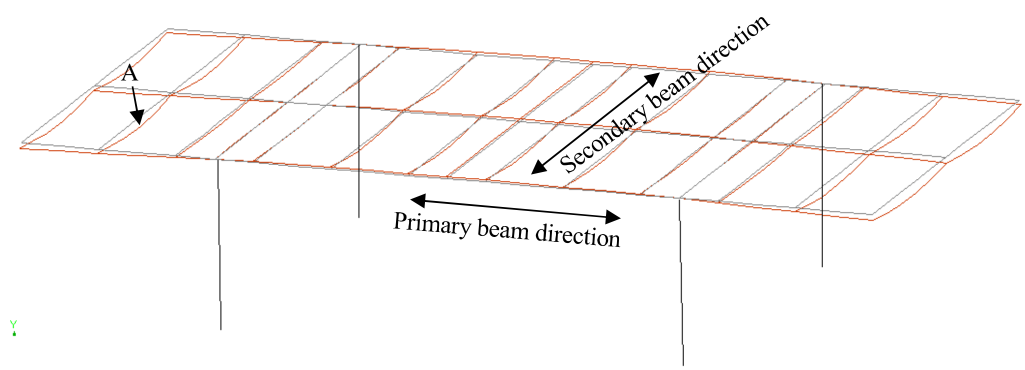

Figure 6. Deflection shape for slab-beam-column system (50mm topping shell elements not shown).

Additionally, the element A with the largest deflection at the mid-span of the precast one-way slab is investigated further. Membrane forces are extracted along both the primary and the secondary beam directions as shown in Figure 6, where the precast one-way slab is supported by the secondary beams which in turn are supported by the primary beams.

At the beginning stage, the slab element resists the applied mechanical load based on flexure. With increasing temperature, the membrane forces become compression due to restrained thermal expansion from the physical boundary conditions.

With further increase in temperature, the membrane forces change from compression to tension, which is the starting point of tensile membrane action stage. It can also be seen that the tensile membrane forces along the primary beam direction are larger than those in the secondary direction. This implies the 50mm topping improves the overall performance of one-way precast slab panels, which in turns mobilizes tensile membrane forces with larger magnitudes along the primary beam direction. Since shell elements are placed on top of the precast slab planks, temperature effects on these shell elements are negligible. Hence, membrane forces are stable after half an hour.

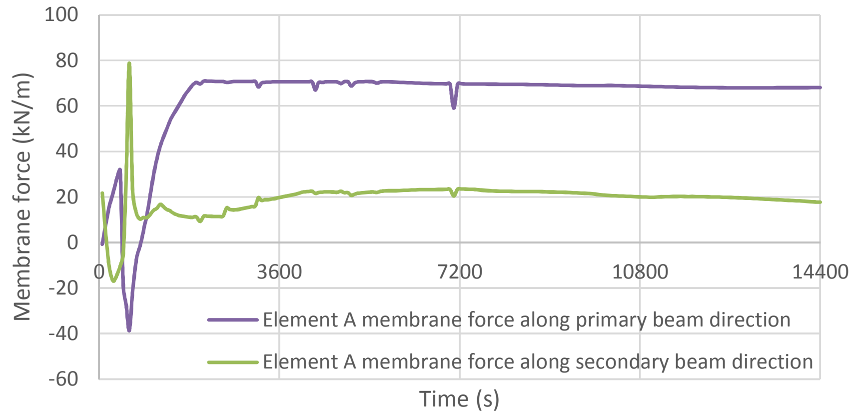

Figure 7. Membrane forces along primary and secondary beam directions at A.

UNDERGROUND FIRE

For underground space, the most effective solutions is to control the fire within the compartment. According to EN1991-1-2[11], for a typical 10.8m×22m×4m (length×width ×height) office compartment (whole compartment in fire as shown in SAFIR model in Figure 4) with a given fire load 550 MJ/m^2, the temperature versus time can be calculated based on Eq. 3 as shown in Figure 7.

$$T_f = 20 + 1325(1 - 0.324e^{-0.2t^*} - 0.204e^{-1.7t^*} - 0.427e^{-19t^*}) \quad (3)$$

$$t^* = t\left(\frac{O}{b}\right)^2\left(\frac{0.04}{1160}\right)^2 \quad (4)$$

In Eq. 3, parameter t^* can be determined through Eq. 4, where O stands for opening factor. It can be seen that the overall temperature for the compartment fire is smaller than that from the standard fire curve. After about 1.34 hour (80 min), the temperature within the compartment starts to drop due to ventilation-controlled fire. Therefore, even if the whole structure is designed with a 2-hour fire resistance period, so long as the fire is confined within this compartment, the overall stability can still be maintained.

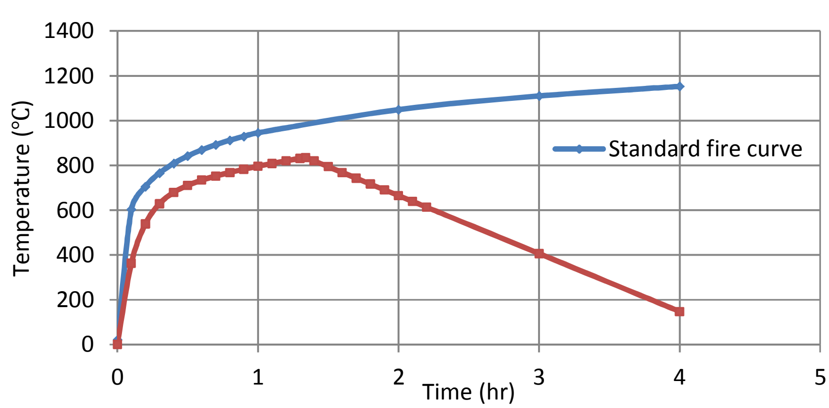

Figure 8. Compartment fire versus ISO-834 standard fire curve.

CONCLUSIONS

Current prescriptive design method of RC structures in fire, such as EN1992-1-2[12], relies on single-member behavior through fire resistance tests, which is very conservative and does not reflect the whole structural behavior under fire conditions. Interactions among all members of a structure should be included in structural fire analysis to optimize structural design even if standard fire curve is adopted.

Through numerical analyses, the performance of a 2-hour RC frame structure is greatly improved with the help of tensile membrane action as compared with that of isolated one-way slab member. Based on parametric studies, the duration of a compartment fire is shorter compared with the standard fire curve. This is a performance-based approach following the recommendations of EN1991-1-2 [12].

ACKNOWLEDGEMENT

This material is based on research/work supported by the Land and Livability National Innovation Challenge under L2 NIC Award No. L2NICCFP1-2013-4.

DISCLAIMER

Any opinions, findings, and conclusions or recommendations expressed in this material are those of the author(s) and do not necessarily reflect the views of the L2 NIC

REFERENCES

1. Carmody, J., R.L. Sterling, and R. Sterling, *Underground space design: Part 1: Overview of subsurface space utilization Part 2: Design for people in underground facilities*. 1993: University of Texas Press.
2. National Fire Protection Association, *NFPA 520: Standard for subterranean spaces*. 2005: United States of America.
3. Kansas City Council, *Building and Rehabilitation Code*. 2012, Kansas City, MO 64106: Kansas City Planning and Developement.
4. China Association for Engineering Construction Standardization, *Fire resistance design of underground structures*. 2014.
5. Building Authority & Fire Services Department, *Guide to Fire Safety Design for Caverns.* . 1994: Hong Kong.
6. Singapore Civil Defence Force, *Singapore Fire Code, Appendix 23: Amendments to the fire code - Fire safety requirements for mega underground developments*. 2012.
7. Franssen, J., *User's manual for SAFIR 2011 a computer program for analysis of structures subjected to fire.* University of Liege, Belgium, 2011.
8. CEN, E., *Eurocode 1: Actions on structures—Part 1-1: General actions-Densities,self-weight,imposed loads for buildings*, in *Commission of European Communities ENV*. 1991.
9. Tests, I., *Elements of Building Construction, ISO-834.* International Organization for Standardization. Geneva, 1975.
10. Standard, B., *Fire resistance tests, Part 1: General requirements (BS EN 1363-1)*. 1999, Brussels.
11. CEN, E., *Eurocode 1: Actions on structures—Part 1-2: General actions—Actions on structures exposed to fire*, in *Commission of European Communities ENV*. 1991.
12. CEN, E., *Eurocode 2: Design of Concrete Structures, Part 1-2: Structure fire design*, in *Commission of European Communities ENV*. 1992. p. 1-1.

Numerical Modelling of Load-Induced-Thermal-Strain of Prestressed Concrete Pressure Vessels

GIACOMO TORELLI[1], MARTIN GILLIE[1], PARTHA MANDAL[1] and VAN-XUAN TRAN[2]

ABSTRACT

This paper presents the implementation of a 3D Load-Induced-Thermal-Strain (LITS) model in an isotropic linear thermoelastic material law to be used for modelling concrete under transient thermal conditions. A new approach for extending to 3D uniaxial temperature-LITS curves has been proposed and adopted, capable of capturing the experimentally demonstrated dependency of LITS on the confinement of the stress state. A stress dependent confinement coefficient which amplifies uniaxial LITS curves in the case of multiaxial stress confinement was defined to capture such a dependency. Besides, a novel practice-oriented bilinear LITS model has been defined and proved to reproduce experimental curves better than the existing models in the case of triaxial stress states and temperatures up to 250°C. The model was verified, validated and calibrated by modelling experiments performed on concrete specimens. In the last part of the paper, the model has been employed to assess the effects of LITS on a Prestressed Concrete Pressure Vessel (PCPV) subjected to an accidental heating-cooling cycle. It was found that LITS plays a key role for this sort of structure, and that significant aspects of structural behavior are missed if no confinement dependency is modelled.

INTRODUCTION

Load induced thermal strain (LITS) is a phenomenon seen in heated concrete where the degree of thermal expansion depends on the stress-state. LITS has been studied experimentally for many years [1–3], however most of the literature focuses on LITS in uniaxial loading conditions using experimental or analytical approaches. This provides a good basis for understanding the behavior of framed structures but leaves many questions about the multiaxial behavior of heated bulk concrete structures, such as the pre-stressed concrete reactor vessels (PCRVs) used in the nuclear industry, unanswered. This article presents the first numerical approach to modelling confinement-dependent multi-axial LITS behavior and applies it to bulk concrete structures in fire conditions.

[1]School of MACE, The University of Manchester, Manchester M13 9PL, UK
[2]EDF Energy, R&D UK Centre, 40 Grosvenor Place, London SW1X 7EN, UK

LITS MODELLING APPROACH

A common approach for extending uniaxial LITS models to 3D is to assume that concrete behaves independently of stress confinement when heated under mechanical load [4–9]:

$$\dot{\varepsilon}_{ij}^{lits} = \frac{\beta(T)}{\sigma_{u0}}\left(-\upsilon_{lits}\sigma_{kk}^{-}\delta_{ij} + (1+\upsilon_{lits})\sigma_{ij}^{-}\right)\dot{T} \tag{1}$$

Where $\beta(T)$ is the LITS function, i.e. a generic function of temperature aimed at fitting the uniaxial temperature-LITS curve, σ_{u0} the compressive strength of the material, σ_{ij}^{-} the *i*-th *j*-th component of the negative projection of the stress tensor and υ_{lits}, a material parameter analogous to the elastic Poisson's modulus υ. However, this approach does not fully match the few experimental works on concrete heated under multiaxial stress conditions, which suggest LITS is a confinement-dependent phenomenon [10,11].

In the light of this, the approach described in (1) has been modified here by making LITS dependent on the confinement state. This has been achieved by introducing a confinement coefficient η. Additionally a variable T_{MAX} is introduced. T_{MAX} stores the maximum temperature reached by the material, allows LITS to be formulated in a way that it develops only upon first heating under compressive load (as observed experimentally). The confinement coefficient η and the internal variable T_{MAX} are discussed in detail below before the numerical implementation of this new LITS model is presented.

Confinement coefficient

The derivative of the LITS over time has been assumed to be directly proportional to a confinement coefficient η as follows:

$$\dot{\varepsilon}_{ij}^{lits} = \eta\frac{\beta(T)}{\sigma_{u0}}\left(-\upsilon_{lits}\sigma_{kk}^{-}\delta_{ij} + (1+\upsilon_{lits})\sigma_{ij}^{-}\right)\dot{T} \tag{2}$$

The confinement coefficient η is automatically evaluated at each time step as a function of the negative projections of principal stresses σ_1^{-}, σ_2^{-} and σ_3^{-} and of a user-defined triaxiality scaling factor γ:

$$\eta = 1 + (C_m - 1)\gamma \tag{3}$$

$$C_m = \frac{\sigma_1^{-}+\sigma_2^{-}+\sigma_3^{-}}{\sqrt{(\sigma_1^{-})^2+(\sigma_2^{-})^2+(\sigma_3^{-})^2}} \tag{4}$$

TABLE I. TRIAXIALITY INDEX AND CONFINEMENT COEFFICIENT.

Stress state	$\boldsymbol{C_m}$	$\boldsymbol{\eta(\gamma = 0.5)}$	$\boldsymbol{\eta(\gamma = 1)}$	$\boldsymbol{\eta(\gamma = 1.5)}$
Uniaxial	1	1	1	1
Equal Biaxial	1.41	1.21	1.41	1.62
Hydrostatic	1.73	1.37	1.73	2.10

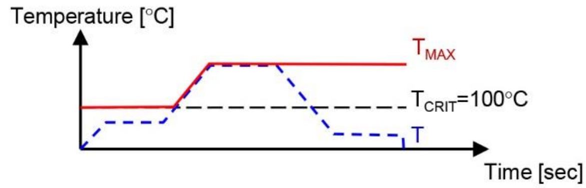

Figure 1. Schematic evolution of the internal variable T_{MAX}, given a hypothetical temperature history T and a user-defined initial value T_{CRIT}=100°C.

Where C_m is a triaxiality index aimed at capturing the multiaxiality of a compressive stress state. Table I shows how C_m and η grow with the multiaxiality, and how η increases for increasing triaxiality scaling factor γ.

Irrecoverability in terms of temperature

In order to model the irrecoverability of LITS on cooling, an internal variable named maximum temperature T_{MAX} has been defined in the behavior law, aimed at storing the maximum temperature ever reached by the material at each point. The derivative of the LITS over time is assumed to be zero when the temperature is less than the critical temperature T_{CRIT}:

$$T < T_{MAX} \;\; \Rightarrow \;\; \dot{\varepsilon}_{ij}^{lits} = 0 \tag{5}$$

As shown from Figure 1, T_{MAX} has been defined so as to enable the user to define its initial value, named T_{CRIT}.

Integration of the implemented models

The new LITS model was added to an isotropic linear thermoelastic material law in Code_Aster [12]. Various LITS curves $\beta(T)$ were represented. First the Anderberg and Thelandersson model [3] was implemented in 3D following the classic approach described in equation (1), leading to the following expression for the increment in LITS in a given time step:

$$\Delta\bar{\bar{\varepsilon}}_{lits} = \frac{\alpha(T)k_{tr}}{\sigma_{u0}}\left[(1+\upsilon_{lits})(\bar{\bar{\sigma}}_m^-) - \upsilon_{lits} tr(\bar{\bar{\sigma}}_m^-)\bar{\bar{I}}\right]\Delta T \tag{6}$$

Where $\alpha(T)$ is the thermal expansion coefficient and k_{tr} is a material parameter defined in the proportionality between uniaxial LITS and free thermal strain.

Then, an original bilinear LITS model was formulated and extended to 3D as irrecoverable and confinement dependent, following the approach described by equation (2):

$$\Delta\bar{\bar{\varepsilon}}_{lits} = \begin{cases} 0 & for\ T \le T_{CRIT} \\ \eta\left[\dfrac{\beta}{\sigma_{u0}}\right]\left((1+\upsilon)\bar{\bar{\sigma}}_m^- - \upsilon tr(\bar{\bar{\sigma}}_m^-)\bar{\bar{I}}\right)\Delta T & for\ T \ge T_{CRIT} \end{cases} \tag{7}$$

Where β is a material parameter, called LITS slope coefficient, which does not depend on temperature, therefore leading to a linear development of LITS with temperature when the user defined critical temperature T_{CRIT} is exceeded.

VERIFICATION AND VALIDATION STUDIES

The implemented constitutive models were verified and validated by modelling the effect of heating-cooling cycles on concrete specimens subjected to various mechanical boundary conditions.

In order to qualitatively verify the modelling approach in the general case of a varying stress state, a test case was considered, where the stress relaxation due to the development of LITS in a uniaxially constrained concrete specimen was evaluated. A constant thermal strain coefficient and the bilinear LITS model described in equation (7) were adopted. Figure 2 shows that up to 100°C, the value of the user-defined T_{CRIT}, the stress increases linearly, due to the constrained thermal strain. Above this temperature, LITS develops together with additional constrained thermal strain, producing an overall stress relaxation. On cooling LITS does not recover, leading to the development of tensile stresses due to the perfect recoverability of the thermal strain component.

Then, a series of LITS tests performed at the University of Sheffield, whose results have been reported in [10], were reproduced in order to validate the implementation of the confinement factor η, calibrate the material parameters γ and υ_{lits}, and identify the most suitable LITS function $\beta(T)$ for temperatures up to 250°C. The tests were performed by heating concrete specimens up to 250°C while applying constant uniaxial, biaxial and triaxial compressive stress states. In order to verify the irrecoverability on re-heating, a complete heating-cooling-heating cycle was modelled numerically. Figure 3 illustrates the applied thermo-mechanical load and total strain obtained in case of uniaxial compressive load. It is worth noting that during first heating LITS develops in the direction of the load, while on cooling only the thermal strain recovers, producing an overall contraction of the specimen after a heating cooling cycle.

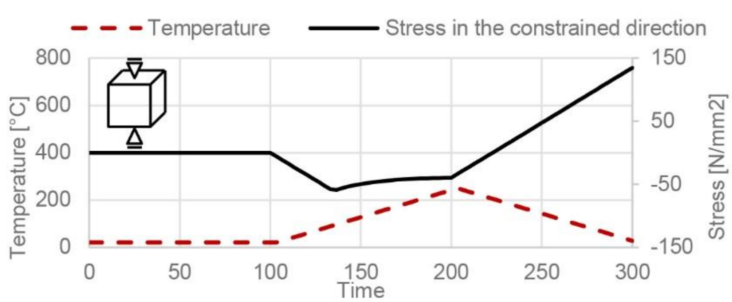

Figure 2. Uniaxially constrained specimen: applied thermal load and evolution of the stress in the constrained direction obtained with the bilinear LITS function.

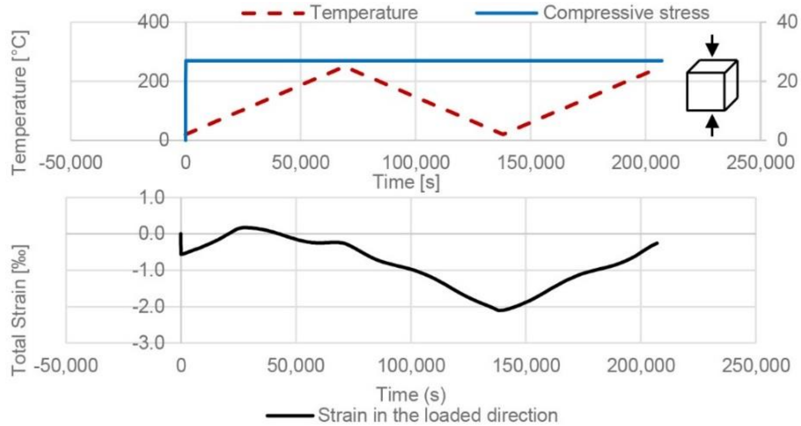

Figure 3. Uniaxially loaded specimen: applied thermo-mechanical load (a) and evolution of the strain in the loaded direction obtained with the bilinear LITS function (b).

Figure 4 shows the experimental results of LITS reported in [10], and the numerical predictions obtained by implementing the Anderberg and Thelandersson LITS model [3] and the confinement-dependent bilinear model proposed here. The material parameters were calibrated to the uniaxial LITS curves and then used in the cases of biaxial and hydrostatic compressive stress states (Table 2).

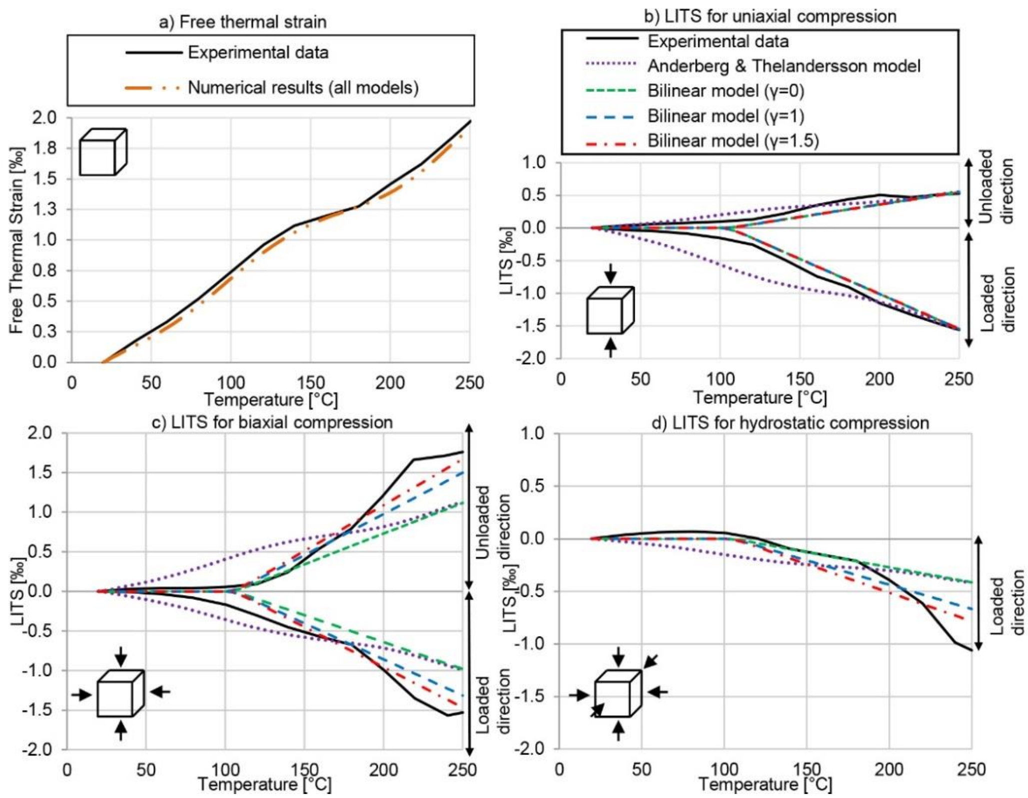

Figure 4. Developments of LITS with temperature in the loaded and unloaded directions, for specimens subjected to biaxial and hydrostatic compression.

TABLE 2. MATERIAL PARAMETERS ADOPTED FOR THE DIFFERENT MODELS.

Parameter	**Anderberg & Thelandersson**	**Bilinear (γ=0)**	**Bilinear (γ=1)**	**Bilinear (γ=1.5)**
E	47000 MPa	47000 MPa	47000 MPa	47000 MPa
ν	0.25	0.25	0.25	0.25
k_{tr}	1.78	-	-	-
β	-	$2.33x10^{-5}°C^{-1}$	$2.17x10^{-5}°C^{-1}$	$2.10x10^{-5}°C^{-1}$
γ	-	0	1.0	1.5
σ_{u0}	57 MPa	57 MPa	57 MPa	57 MPa
ν_{lits}	0.37	0.37	0.37	0.37
T_{crit}	20°C	100°C	100°C	100°C

The bilinear model gives a better approximation to experimental LITS curves for all the loading conditions. Moreover, in contrast to the classical approach, the method proposed here allows the dependency of LITS on the confinement to be captured. In particular, it was found that a triaxiality scaling factor γ=1.5 gives the best fit to the LITS curves in case of biaxial and hydrostatic compression.

The present model treats LITS as only stress and temperature history dependent; it neglects the influence of the moisture content and its time-dependent movement throughout the material. This allowed the formulation of robust and practice-oriented LITS model, which has been demonstrated to be suitable for modelling concrete subjected to partially sealed conditions [10]. The design of experiments to assess the effect of sealing conditions on the development of LITS, would provide the necessary data to model such dependency and refine the model.

TEST CASE: PCPV SUBJECTED TO HEATING-COOLING CYCLE

The validated model was next used to evaluate the loss in prestress due to LITS in the wall of a hypothetical nuclear reactor vessel subjected to a heating-cooling cycle (Figure 5). The study aimed to assess the stress redistribution occurring at mid-height in the lateral wall of a typical nuclear PCPV, assumed to be 4.5m thick. In that area of the vessel, the horizontal restraining effects of top cap and foundation may be considered negligible, therefore justifying the analogy with an infinite cylinder [13].

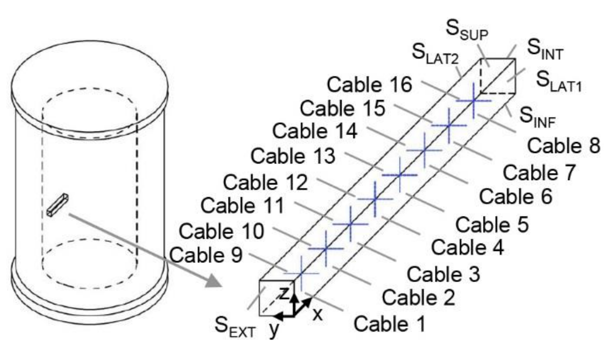

Figure 5. Schematic illustration of a typical PCPV and model of the studied representative portion.

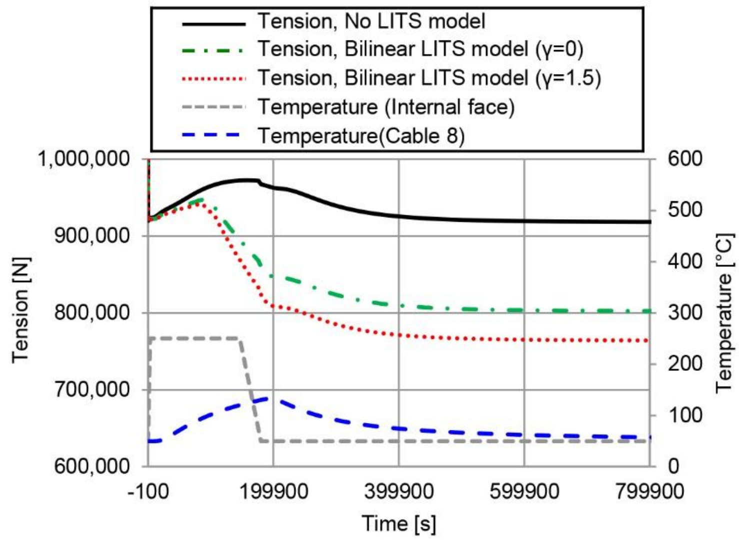

Figure 6. Temperature histories at the internal surface and in Cable 08 obtained without LITS, with the bilinear model with γ=1, and with the bilinear model with γ=1.5.

Based on this assumption a parallelepiped-shaped portion of the vessel was studied, representative of a region extending through the whole thickness of the wall, 0.5m high and 0.5m wide (Figure 5). The effects of the relatively large radius of the vessel were omitted from the model. Displacements normal to S_{INT}, S_{LAT} and S_{INF} (Figure 5) were prevented. A prestressing system composed of 8 vertical and 8 tangential tendons was considered, bearing an initial tension of 1266 kN each.

A hypothetical design scenario was considered, where a partial fault of the cooling system made the internal face of the vessel reach 250°C for 48h (Figure 6). This condition was imposed to S_{INT}, while zero heat flux was imposed on all the other external surfaces. A thermal analysis showed that, for that particular design scenario, the first meter of thickness is significantly influenced by the fault condition. The loss in prestress of the most internal cable, Cable 08 in Figure 5, is therefore analyzed. The results reported in Figure 6 show that if LITS is not taken into account, the heating-cooling cycle produces a temporary increase in the tension of cable which tends to disappear as the temperatures returns to 50°C throughout the entire thickness of the wall. However, if the bilinear LITS model is activated, the increase in tension during heating is reduced, due to concrete relaxation resulting from LITS, while the drop in tension due to the recovery of the thermal strain still occurs. This results in a significant loss in prestress at the end of the heating-cooling cycle, which cannot be captured if LITS is not taken into account. Specifically, a drop in tension of 16.80% is obtained with γ=1.5.

CONCLUSIONS

The following conclusions can be drawn from this study:

- For temperatures up to 250°C, the bilinear LITS model proposed here reproduces the general trend of the LITS curves better than the Anderberg and Thelandersson model.

- In order to extend uniaxial LITS behavior laws to 3D it is crucial to take into account confinement dependency. The confinement factor η introduced here captures this dependency in an intuitive and robust manner.
- The inclusion of LITS in concrete behavior laws is essential when assessing the behavior of prestressed bulk concrete structures subjected to multiaxial compressive stress states. In the case of PCPVs subjected to partial fault conditions, the development LITS can produce a loss in prestress of about 15-20% in the tendons located in proximity to the internal surface of the vessel.

REFERENCES

1. Khoury GA, Grainger BN, Sullivan PJE. Transient thermal strain of concrete; literature review, conditions within specimen and behaviour of individual constituents. Mag Concr Res 1985;37:131-44.
2. Schneider U. Concrete at high temperatures - A general review. Fire Saf J 1988;13:55-68.
3. Anderberg Y, Thelandersson S. Stress and deformation characteristics of concrete at high temperature: 2. Experimental investigation and material behaviour model. Bull. No. 46, Lund: 1976, p. 86.
4. De Borst R, Peeters PPJM. Analysis of concrete structures under thermal loading. Comput Methods Appl Mech Eng 1989;77:293-310. doi:10.1016/0045-7825(89)90079-0.
5. Gawin D, Pesavento F, Schrefler BA. Modelling of deformations of high strength concrete at elevated temperatures. Mater Struct Constr 2004;37:218-36.
6. Khennane A, Baker G. Thermoplasticity Model for Concrete under Transient Temperature and Biaxial Stress. Proc R Soc London A Math Phys Eng Sci 1992;439:59-80.
7. Thelandersson S. Modeling of combined thermal and mechanical action in concrete. J Eng Mech 1987;113:893-906.
8. Pearce CJ, Nielsen C V., Bićanić N. Gradient enhanced thermo-mechanical damage model for concrete at high temperatures including transient thermal creep. Int J Numer Anal Methods Geomech 2004;28:715-35. doi:10.1002/nag.376.
9. Gernay T, Millard A, Franssen J-M. A multiaxial constitutive model for concrete in the fire situation: Theoretical formulation. Int J Solids Struct 2013;50:3659-73. doi:10.1016/j.ijsolstr.2013.07.013.
10. Petkovski M, Crouch RS. Strains under transient hygro-thermal states in concrete loaded in multiaxial compression and heated to 250 °C. Cem Concr Res 2008;38:586-96.
11. Kordina K, Ehm C, Schneider U. Effects Of Biaxial Loading On The High Temperature Behaviour Of Concrete. Fire Saf Sci 1986;1:281-90. doi:10.3801/IAFSS.FSS.1-281.
12. De Soza T. Code_Aster: guide de lecture de la documentation de référence 2013.
13. Granger L. Comportement différé du béton dans les enceintes de centrales nucléaires. Analyse et modélisation - Thèse de doctorat de l'ENPC. 1996.

ABSTRACT REVIEWERS'S COMMENTS

Comment 1: Authors should provide full details of the new model so interested researchers could implement in their codes. The model clearly seems to be improvement on existing practice but it would be useful if a good discussion of merits and demerits are discussed particularly in the context of the many uncertainties associated with concrete subjected to high temperature, such as severe moisture gradients.

Comment 2: This paper proposes a 3D model for considering Load induced thermal strain (LITS) on the prestressed concrete pressure vessels. The results are very interesting. It may be interesting to compare the cases without considering the effect of LITS in the paper.

Comment 3: Accept.

Structural Behavior Under Localized Fire Action—Modelled Using an Integrated Computational Tool

LIMING JIANG, SUWEN CHEN and ASIF USMANI

ABSTRACT

An integrated computational tool 'SIFBuilder' was developed to model the global behaviour of structures subjected to various fire scenarios. This OpenSees based tool is currently capable of performing weakly coupled sequential analyses and able to automatically apply idealised fire actions to the structure including localised fires. A few illustrative cases are thereafter conducted to demonstrate the usage of SIFBuilder, presenting the global response of a generic 2×2×2 frame building subjected to different fire actions. Two types of idealised fire scenarios are considered for the building, which include an idealised uniform fire (one hour standard fire) occurring in one confined compartment, and an idealised non-uniform fire (0.5 hour Eurocode 1 localised fire) assumed to wrap symmetrically around the central column. Greater slab deflections are observed in the case of confined compartment fire, whereas collapse may occur in the central column due to the exposure to localized fire.

INTRODUCTION

In a prescriptive design approach regime, the global behaviour of structures is largely ignored, while traditional design strategy for structural fire safety was based on Standard Fire tests with respect to the performance of isolated members. However, performance-based engineering or PBE approaches have gained enormous popularity in structural fire safety engineering, which often requires a comprehensive simulation for fire action and fire induced structural behaviour. SIFBuilder [1] is developed for this purpose, and is based on OpenSees [2] as an open source framework (Open System for Earthquake Engineering Simulation), which was initially designed to simulate non-linear response of structural frames subjected to seismic excitations. It is written in C++ and adopts an object-oriented architecture, which breaks up a finite

Liming Jiang, Department of Mechanical, Aerospace and Civil Engineering, Brunel University London, Kingston Lane, Uxbridge, UB8 3PH, UK

Suwen Chen, College of Civil Engineering, Tongji University, Shanghai, 200092, P.R. China

Asif Usmani, Department of Mechanical, Aerospace and Civil Engineering, Brunel University London Kingston Lane, Uxbridge, UB8 3PH, UK

element source code into objects like elements, materials, sections and solution algorithms, making it a lot easier to maintain the software and add new capabilities to it. In 2009, 'Structures in fire' modelling capabilities were added into OpenSees at the University of Edinburgh [3,4]. The early-stage work focused on the main topics as: (1) modelling of the fire action and analysis of the fire induced heat transfer to the structural components; (2) thermo-mechanical analysis for modelling structural response to the thermal actions produced by a fire. In order to move towards a more comprehensive solution for a unified analysis, development of an OpenSees based research tool (SIFBuilder) was started in order to provide an automated environment for modelling large structures under a range of idealised design fires. In addition to automated computation, minimum input is expected to create a *SIFModel* (building information model) which supplies the data for the heat transfer analysis and the thermo-mechanical analysis.

The major task of SIFBuilder is to deal with two types of fires: idealised uniform fires and idealised non-uniform fires. The former category of fire models are associated with the post flashover stage of fires, which are typically described analytically, such as the widely adopted standard fire curve and the Parametric Fire curves [5] that account for the fuel load and compartment configuration parameters. The latter category is typically referred to as the localised fire models, which may be extended to the so-called "travelling fires" [6]. Interest in idealised non-uniform fires has developed specifically for buildings with large open plan spaces, where a fuel controlled fire may remain in the pre-flashover stage as the fuel distribution is extremely localised so that it is unlikely to cause the spread of fire (localised fires) [5]. Travelling fires can be used to address the non-uniform distribution of gas temperatures in a large open plan space found in modern office blocks [7]. To implement idealised non-uniform fires, it is desirable to perform three dimensional (3D) heat transfer analyses for structural members, which increases the computational cost and adds significant complexity due to the data communication required between heat transfer model and structural model in the context of the unified approach being developed. However, heat transfer analyses in OpenSees facilitated with SIFBuider can be automatically performed for each member by taking advantage of the dimensional reduction concept and rapid temperature interpolation approaches which have been explained in [1] and briefly introduced in this paper.

To compare the responses of framed structures subjected to different design fire scenarios, two illustrative cases are conducted to demonstrate the SIFBuider powered 'structures in fire' analysis. A generic 2×2×2 frame building was modelled and subjected to two types of localised fire scenarios considered for the building, which include an idealised uniform fire (one hour standard fire) occurring in one confined compartment, and an idealised non-uniform fire (0.5 hour Eurocode 1 localised fire) assumed to wrap symmetrically around the central column. The thermal and structural responses are discussed later in this paper. Although the steel beams in the first scenario are only partially heated by uniform fire exposure (as the effect of partitions in partially protecting structural members is also automatically accounted for in SIFBuilder), the structural member temperatures are higher than that in the second fire scenario, where no partition wall exists. For the fire protected steel columns, temperatures remain relatively low in both scenarios. The thermo-mechanical behaviour of the structure also differs, as severe but localised deflections are seen in the confined fire case, and a lower level of deformation can be found in the second case which will be discussed later in this paper.

OPENSEES BASED SIFBUILDER

As an integrated computational tool, SIFBuilder could enable structural engineers to obtain the structural response automatically with the application of the fire load on the structure in the same manner as any other form of load and so provide a performance-based structural fire engineering tool. It would potentially also become a testbed to foster a wide range of future developments, which may be new fire models featuring advanced characteristics in terms of fire science, or new thermo-mechanical constitutive models for materials, sections and elements to improve the accuracy and efficiency of integrated simulations.

Unlike commercial packages, neither OpenSees nor SIFBuilder have a graphical user interface (GUI). However, there is a script based user input capability based on Tcl, which provides considerable flexibility and scope due to its programmable nature. Similar to other commonly used FEM software, SIFBuilder requires the user to input basic structural information for generating the structural model. Procedural scripts are written to specify geometry, materials, loads, heat transfer parameters, fire type, analysis procedures, solution algorithm and output requirements using Tcl commands. A *SIFModel* is first created to store the building information, for which the typical user input script includes: (1) model type definition (2D or 3D); (2) geometry of the structure; (3) cross section and its embedded materials; (4) boundary conditions; (5) structural and fire loadings; (6) mesh control parameters; and (7) output request supported by *SIFRecorders*. A typical input may be defined as shown in Figure 1.

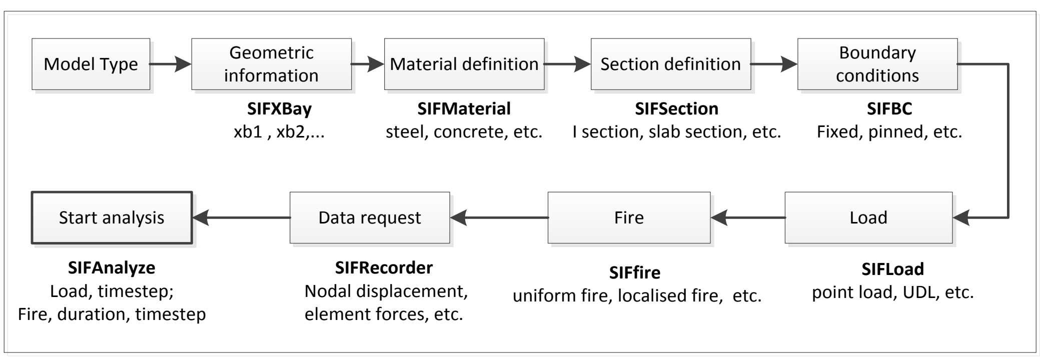

Figure 1. Work flow of using SIFBuilder in OpenSees

A so-called *SIFModel* that actually comprises many objects defined for building components is programmed to hold the building configuration throughout the structural analysis, allowing further operations which may include removal of members to create variations of the building model, such as atrium spaces or large compartments. In addition to the ordinary structural loads such as self-weight and live load, a wide variety of well-established fire models are integrated into SIFBuilder, which include idealised uniform fires and non-uniform fires. Fire load calculations are succeeded by the heat transfer analysis using a dimensionally reduced scheme to address the non-uniform thermal response induced by localised fire action, which adopts a few 2D section analyses to represent the 3D temperature distribution of a beam, and a number of 1D through thickness analyses to represent the thermal response of a slab. These temperature histories are calculated with the consideration of partial exposure as a result of partition walls. *NodalThermalAction* is responsible to store these nodal temperature histories, and then being submitted to polynomial approximations to obtain thermal response at arbitrary locations in a structural member. The dimensional reduction scheme for heat transfer analysis can be found from author's other paper and graphically described in Figure 2.

Following the heat transfer analysis, structural analysis is performed on the building, accounting for the thermally induced deformation and the degraded material properties. A finite element (FE) model is generated from the *SIFModel*, which comprises Nodes and beam-column elements and shell elements (for slabs) as shown in Figure 3. Fibre based sections are correspondingly defined for beams and columns based on the information stored in *SIFModel*, while uniaxial steel or concrete materials are assigned to fibres in each section. Additionally, concrete slab can be discretised into shell elements of multi-layer plate section. In OpenSees, these thermo-mechanical elements have been adapted for considering localised thermal action and capable of receiving non-uniformly distributed temperature data from the heat transfer module. Uniaxial materials for steel and concrete are defined in accordance with Eurocodes [8, 9], while multi-axial material for concrete in slab is currently defined using plane stress material which can be potentially improved to be more sophisticated. Steel reinforcement has been considered in orthogonal directions, for which uniaxial materials are assigned.

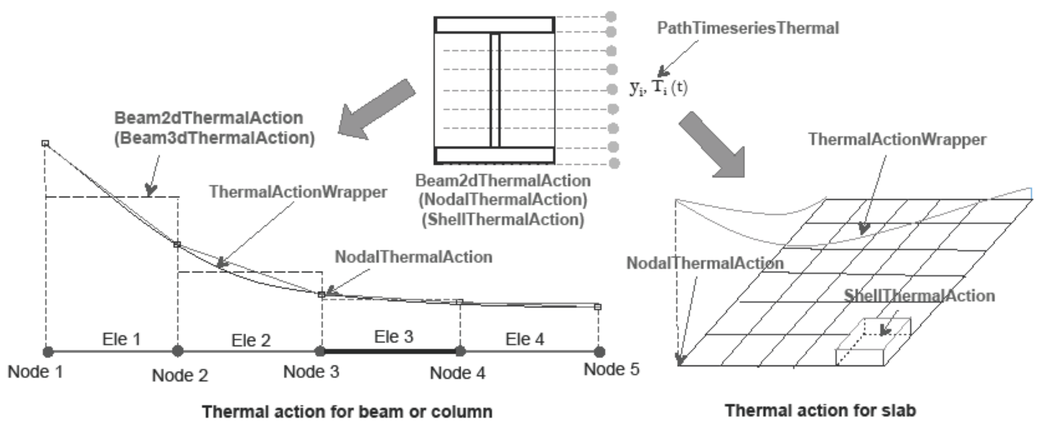

Figure 2. Implementation of non-uniform thermal action

GENERIC MODEL OF A FRAME BUILDING

A generic steel frame structure is modelled using SIFBuilder, where a schematic overview of the structure is shown in Figure 4(a). The configuration of this two-storey frame structure is similar to the small frame used by Lamont et al. [10] which was to investigate the behaviour of a small structure resulting from different design fires (`short hot' or `long cool' fire). The *y* axis of the global coordinate system is set as the default along vertical direction (this is convenient to create a 2D model in the *xy* plane). The plan layout of this idealised building is shown in Figure 4(b) which consists of two bays (6m and 9m span) along each axis. A grid line system is used to describe the layout with tags ranging from 1 to 9, along both the x and z axes (last number refers to the storey tag). Using this tag system, the compartment could be numbered in accordance with the left upper column as Figure 4(b) shows. Such a numbering system is only suitable for modelling small frames as the number of grid lines cannot exceed 9. For larger frames, the components of a building model are identified using its *x* (*XBay*), *y* (*YStorey*), *z* (*ZBay*) coordinates in SIFBuilder.

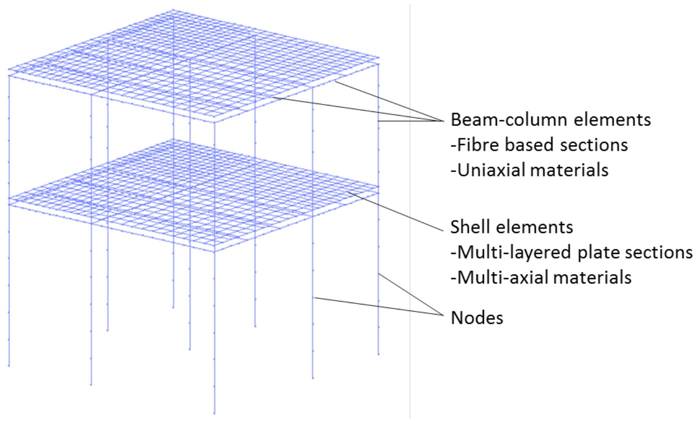

Figure 3. FE model of framed structure

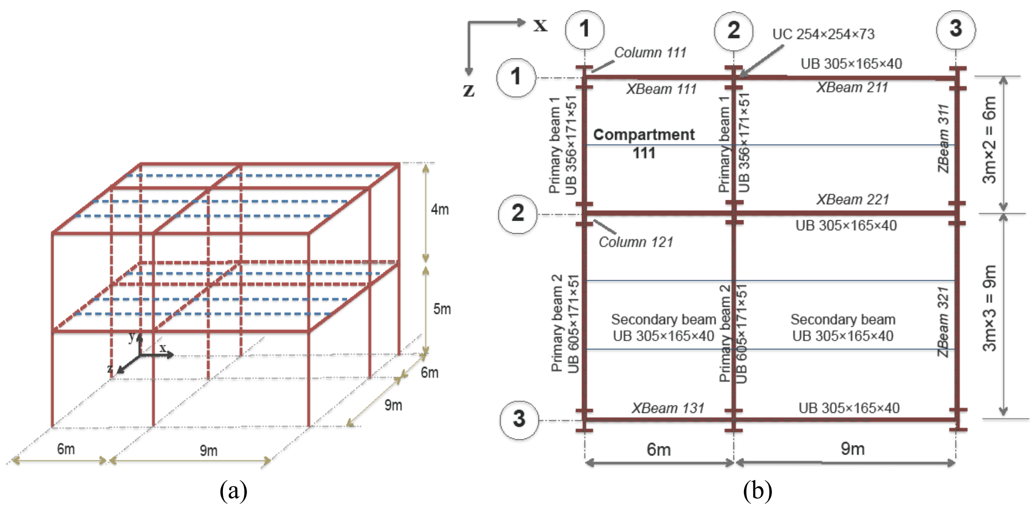

Figure 4. Configuration of the generic frame building: (a) schematic view; (b) plan layout

Two different sizes of primary beams are used in the framing system, including a UB356×171×40 steel beam for the 6m span, and a UB610×228×101 for the 9m span. Secondary beams with a spacing of 3m are assigned to the floor system, using a UB305×165×40 section. All the steel section beams are assumed to be of yield strength 275 MPa. Instead of using the usual profiled decking, a flat slab is used for simplicity with double reinforcement layers and with a 20mm thick concrete cover. The reinforcement layers are assumed to be constructed of A142 standard mesh

(141mm^2/m) of yield strength 600 MPa. Normal weight concrete for the slab of compressive strength 30MPa is adopted for the floor slab. All the beam and column joints are assumed to be rigidly connected, and no bracing members are included in this model.

All the steel beams and concrete components are left unprotected, whereas all the steel columns are protected by 20mm thick Spray-applied Fire Resistive Material (SFRM) coatings. The contribution of SFRM coatings to the load bearing capacity is ignored because of its extremely low strength and modulus. Thermal properties of SFRM are considered constant during the fire, while the corresponding parameters can be adopted as thermal conductivity λ=0.05 W/m/K, density ρ= 350 kg/m^3, and specific heat c_p = 1100 J/K/kg. A uniform distributed load is applied to the slabs to represent the dead and imposed loading, which was adopted to be 4.95 kN/m^2 as in the Cardington tests.

GENERIC BUILIDING SUBJECTED TO LOCALISED FIRES

Two different fire scenarios are examined for this generic steel framed structure. The first scenario is an idealised uniform fire occurring in the confined compartment (Compartment111), where the time-temperature relationship is chosen to conform to the standard fire curve. It is assumed that during the fire, flames and smoke remain confined to the compartment by the wall partitions therefore structural members are only partially exposed, which shall result in a non-uniform temperature distribution across the section of the beams and columns, all of which is automatically accounted for by SIFBuilder. The second fire scenario is a localised fire defined according to the Eurocode 1 model, which is assumed to be a fire source surrounding the central column at the ground floor. Considering the 5m high ceiling and to simulate a relatively large fire, the rate of heat release is chosen as 5MW, while the nominal diameter of the fire source is assumed to be 1m. In this fire scenario, the building may be considered as a car park which does not allow build-up of a smoke layer because of the open perimeter. It has to be pointed out that ignoring the effect of smoke layer usually underestimates the degree of incident heat flux and overestimates the non-uniformity of the fire action, especially for buildings with facades.

Thermal responses to different localised fires

Thermal responses of different structural members within the fire compartment have been presented in Figure 5. Due to the insulation effect of SFRM layers, the columns experience much lower temperatures than beams. While the uniform fire is confined in the compartment, different temperature increases can be found across the column section. The column flange temperature goes up to 150^{o}C at the interior face, as much lower temperatures up to 47.8 ^{o}C appear at the exterior face. For primary beams that are located at the edge of the compartment, the steel section is also partially exposed to the hot gas, which results in lower temperatures (up to 528 ^{o}C) as shown in the figure, compared with the temperatures appearing in the secondary beams and at the bottom surface of the concrete slab. For the case of localised fire occurring at the central column, the effect of spatial decay is significant. Above the fire source, primary beam may experience a temperature as high as 669 ^{o}C, and the temperature at the concrete slab goes up to 528.3 ^{o}C. In the contrast, temperatures drop radically at the mid-span of beam and slab, and also in the secondary beams.

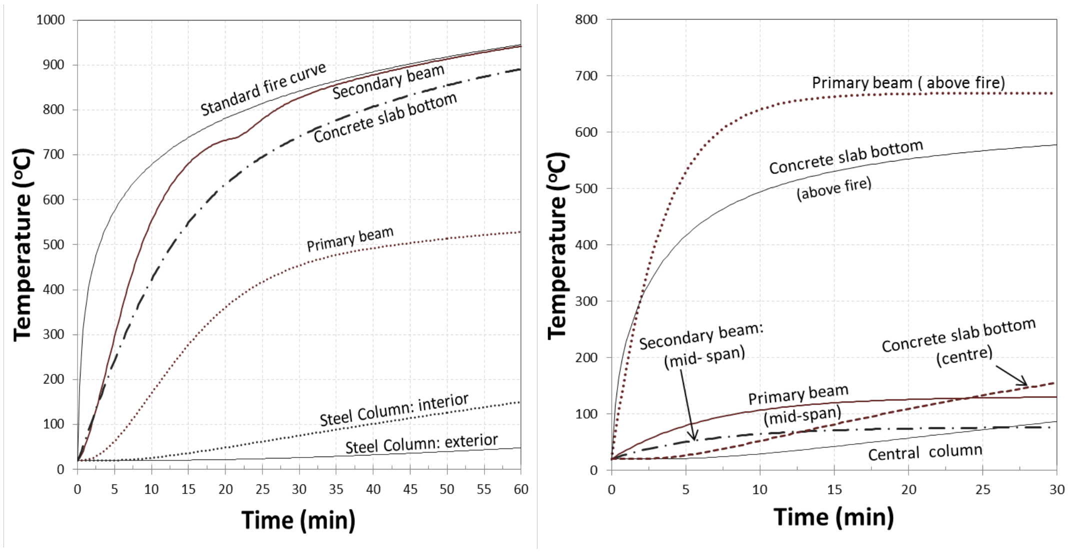

(a) (b)

Figure 5. Thermal response of structural members: (a) 1hr standard fire; (b) 0.5h localised fire

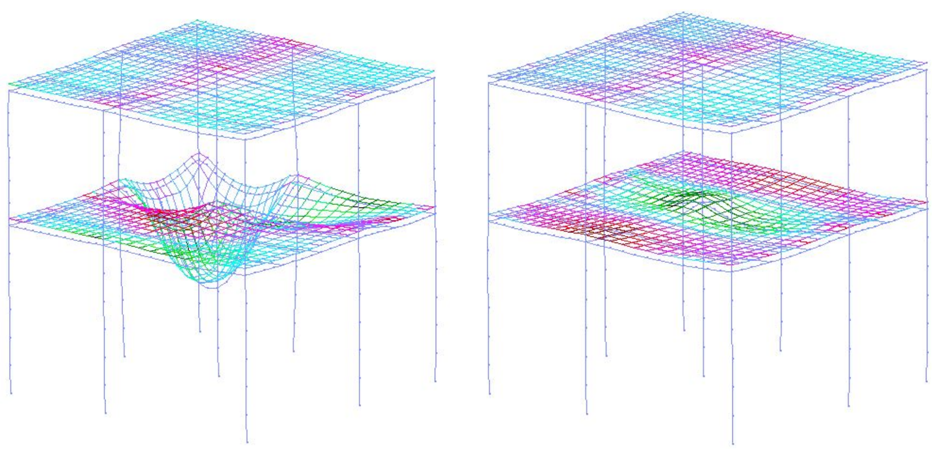

(a) (b)

Figure 6. Deformed shape of the generic frame building: (a) after 1hr Standard Fire in corner compartment; (b) after 0.5h Localised Fire surrounding central column

Thermo-mechanical responses to different localised fires

The deformed shapes (factorized by 10) of the generic building subjected to the two different localised fire scenarios are shown in Figure 6. In the case of compartment uniform fire, large deflections are seen in the slab 111 especially at the center (up to 0.31m), which is a combined action of thermal bowing and material degradation. As the edge beams are concurrently heated, the neighboring slab system is affected by the fire but with relatively small deflections (not exceeding 0.1m). When the generic building is subjected to localised fire surrounding its central column, only small deflections are seen in the members, and limited to the area adjacent to the column. Very slight increases of deflections are observed in the beams connected to the central column as a result of thermal expansion in the heated column. The average magnitude of deflections in the Slab 111 is significantly lower compared to the Standard Fire case, whilst a slightly larger deflection (up to 0.015m) can be seen in Slab 221 (9m×9m). The largest deflection is found in the ZBeam 211, which is connected to the two large span compartments and as a primary beam bears the load transferred from the slab and secondary beams. A maximum deflection of 0.035m is observed at 20 minutes of fire exposure,, whereas no significant deflections are developed in the other beams. However, the locally heated beams and slabs may redistribute the load to the columns. It is found that the axial force in central column keeps increasing because of its thermal elongation. Meanwhile the axial forces in adjacent columns (Column 121, 211, 231, 321) decrease as the softening of secondary beams around the central column decreases the load carried by the middle primary beams.

CONCLUSIONS

An integrated computational tool for modelling structures in fire is presented that can potentially truly revolutionize performance-based structural fire engineering. However at this stage this tool is primarily meant for researchers to explore the structural response to previously unfeasible but realistic fire scenarios.

A 2×2×2 framed structure is modelled to demonstrate the usage of SIFBuilder and is assumed to subject an idealised uniform fire confined in one compartment, and a localised fire surrounding the central column, separately. Large deflections are observed from the slab directly exposed to standard fire, while non-uniform temperature distribution appear in the beams and columns due to the partial exposure to the confined fire. Much lower deflections are observed in localised fire case as the temperature increases show great spatial difference. An increase of axial force is found in the central column, which may threaten the fire safety of the structure.

REFERENCES

1. Jiang, L. et al., 2015. OpenSees-based integrated tool for modelling structures in fire. In *The First International Conference on Structural Safety under Fire & Blast*. Glasgow, pp. 461–468.
2. McKenna, F.T., 1997. *Object-oriented finite element programming: frameworks for analysis, algorithms and parallel computing*. University of California, Berkeley.
3. Jiang, J. et al., 2015. OpenSees Software Architecture for the Analysis of Structures in Fire. *Journal of Computing in Civil Engineering*, 29(1), 1–13.
4. Jiang, Y., Usmani, A. & Welch, S., 2011. Development of heat transfer modelling capability in OpenSees for strctures in fire. In *Applications of Structural Fire Design*.
5. CEN, 2002. BS EN 1991-1-2:2002: Eurocode1: Actions on Structures. General actions-actions on structures exposed to fire.
6. Stern-Gottfried, J. & Rein, G., 2012. Travelling fires for structural design–Part I: Literature review. *Fire Safety Journal*, 54, pp.74–85.
7. Stern-Gottfried, J. & Rein, G., 2012. Travelling fires for structural design-Part II: Design methodology. *Fire Safety Journal*, 54, pp.96–112.
8. CEN, 2004. BS EN 1992-1-2:2004: Eurocode 2: Design of concrete structures. Generic rules-structural fire.
9. CEN, 2005. BS EN1993-1-2:2005: Eurocode 3: Desgin of Steel structures. General rules-structural fire design.
10. Lamont, S., Usmani, A.S. & Gillie, M., 2004. Behaviour of a small composite steel frame structure in a "long-cool" and a "short-hot" fire. *Fire Safety Journal*, 39(5), 327–357.

Optimal Tuning of Thermomechanical Hybrid Simulation Parameters

CATHERINE A. WHYTE[1], KEVIN R. MACKIE[2],
GIUSEPPE ABBIATI[1] and BOZIDAR STOJADINOVIC[1]

ABSTRACT

According to current engineering practice, the fire performance qualification of structural elements relies on single component tests, where specimens are exposed to standard fire curves. As a result, the interactions between elements within the overall structural assembly are lost. This situation has motivated researchers to extend the hybrid simulation method, which has been deeply investigated in the seismic domain, to structures-in-fire testing. By linking numerical and physical substructures, hybrid simulation offers a flexible, cost-effective approach. Purely mechanical hybrid simulation tests are often performed slower than real-time (extended time scale), dictated by actuator capacity limitations, quality of displacement tracking, and synchronization among computational and experimental drivers. This practice is generally not acceptable when a rate-dependent response of the specimen is expected, as is often the case in fire (e.g. creep strain occurs when steel is subjected to high temperatures). In this scenario, the proper selection of the testing time scale must balance the laboratory testing capacity requirements (operating too close to real-time compromises the test stability if the equipment is not suited for this) and the expected rate-dependency of the structural response (operating at an extended time scale could reduce the solution accuracy if the specimen undergoes excessive creep). From this perspective, it is crucial to accurately tune the testing time scale to minimize experimental approximation. Thus the optimal tuning of the time integration scale in thermomechanical hybrid simulation (TMHS) is presented herein. Furthermore, updates to the TMHS experimental element, newly implemented in the OpenFresco hybrid simulation middleware, provide the ability to fully simulate a TMHS test prior to experimentally substructuring the physical specimen in the laboratory.

INTRODUCTION

In order to develop performance-based standards for fire engineering and to investigate the structural response to complex and dynamic loading scenarios, there

---

1 ETH Zürich, Department of Civil, Environmental and Geomatic Engineering, Institute of Structural Engineering, HIT F43, Wolfgang-Pauli-Strasse 27, 8093 Zürich, Switzerland.
2 University of Central Florida, Department of Civil, Environmental and Construction Engineering, Engr II 402, 4000 Central Florida Blvd., Orlando FL 32816, USA.

is a need for extensive experimentation beyond standard single structural component fire tests [1, 2, 3]. Barring accessibility to full-scale testing facilities, which are generally prohibitively expensive for both time and financial reasons, hybrid simulation (HS) is the ideal approach for understanding global structural response in a flexible and efficient way. HS [4, 5, 6] originated as a method for simulating dynamic structural response to earthquake loads, where a hybrid model of a prototype structural system combines numerical and physical substructures (NSs and PSs). The PSs of the hybrid model are tested in the laboratory because of their strongly nonlinear responses and/or lack of reliable mathematical models, while the NSs are instantiated in structural analysis software. The dynamic response of the hybrid model is solved using a time-stepping response history analysis with reduced costs and effort.

In general, the thermal response time of a structure subjected to fire is quasi-static. Accordingly, a static force balance was pursued during a breakthrough experiment by Korzen and co-workers [7] that extended HS to fire loads and simulated a steel frame with a single column PS. Later, Mostafaei [8, 9] tested a 6-story reinforced concrete building with a 3D NS modeled in SAFIR [10] and a single column PS in a furnace. At 5 minute intervals, the interface boundary conditions between NS and PS were adjusted by a human operator.

In order to study combined dynamic mechanical loads and fire loads, there was a need for implementing a finite element (FE) code with a transient integrator and automatic data transfer between the substructures as the core solver of the hybrid simulator. With these objectives in mind, Whyte et al. [11] extended the Open-source Framework for Experimental Setup and Control (OpenFresco) [12] middleware to the thermal domain by adding temperature degrees of freedom (DOFs) and thermal control capabilities. They verified and validated the thermomechanical hybrid simulation (TMHS) developments with proof-of-concept tests in conjunction with the Open System for Earthquake Engineering Simulation (OpenSees) [13] software framework.

Purely mechanical HS tests are often performed with an extended time scale that is slower than real-time (RT). This is the so called pseudodynamic (PsD) testing method. In this case, oil flow limitations in the hydraulic network, actuator control accuracy, and synchronization among computational and experimental drivers determine the optimal testing time scale [14]. However, a PsD approach is not acceptable when a rate-dependent specimen response is expected. Such a situation occurs, for example, when a steel structure is subjected to high temperatures and creep strain is involved [15]. As a result, the proper selection of the testing time scale is a trade-off between simulation accuracy and laboratory testing capacity. From this perspective, this paper discusses the testing time scale tuning in the recent TMHS test campaign conducted by Whyte et al. [11]. Furthermore, modifications to the TMHS experimental element in OpenFresco are presented that allow for fully simulating a TMHS test prior to substructuring the PS in the laboratory.

SUBSTRUCTURING OF THE THERMOELASTIC EQUATIONS

The thermomechanical substructuring framework is introduced for a generic spatially discretized thermoelastic system [16],

$$\begin{bmatrix} M_{uu} & 0 \\ 0 & 0 \end{bmatrix} \begin{bmatrix} \ddot{u} \\ \ddot{\theta} \end{bmatrix} + \begin{bmatrix} C_{uu} & 0 \\ 0 & C_{\theta\theta} \end{bmatrix} \begin{bmatrix} \dot{u} \\ \dot{\theta} \end{bmatrix} + \begin{bmatrix} K_{uu} & K_{u\theta} \\ 0 & K_{\theta\theta} \end{bmatrix} \begin{bmatrix} u \\ \theta \end{bmatrix} = \begin{bmatrix} F_u \\ F_\theta \end{bmatrix} \tag{1}$$

The matrix partitioning refers to displacement and temperature DOFs, i.e. u and θ, respectively, and their derivatives. M_{uu}, C_{uu}, and K_{uu} are the mass, damping, and stiffness matrices. $K_{\theta\theta}$ and $C_{\theta\theta}$ are the heat conduction and capacity matrices. F_u and F_θ are the mechanical external forces and the thermal fluxes. Positive thermal fluxes supply power to the system. Because the off-diagonal sub-matrix, $K_{u\theta}$, represents the internal forces due to thermal deformations, its inclusion is crucial to account for TM structural interactions. Now, by applying the HS technique, each matrix can be split into numerical (N) and physical (P) components, respectively.

$$\begin{aligned} &\begin{bmatrix} (M_{uu}^N + M_{uu}^P) & 0 \\ 0 & 0 \end{bmatrix} \begin{bmatrix} \ddot{u} \\ \ddot{\theta} \end{bmatrix} + \begin{bmatrix} (C_{uu}^N + C_{uu}^P) & 0 \\ 0 & \left(C_{\theta\theta}^N + C_{\theta\theta}^P\right) \end{bmatrix} \begin{bmatrix} \dot{u} \\ \dot{\theta} \end{bmatrix} \\ &+ \begin{bmatrix} (K_{uu}^N + K_{uu}^P) & \left(K_{u\theta}^N + K_{u\theta}^P\right) \\ 0 & \left(K_{\theta\theta}^N + K_{\theta\theta}^P\right) \end{bmatrix} \begin{bmatrix} u \\ \theta \end{bmatrix} = \begin{bmatrix} F_u^N + F_u^P \\ F_\theta^N + F_\theta^P \end{bmatrix} \end{aligned} \tag{2}$$

The first row block of Equation 2 represents the equation of motion of the system, whilst the second row block describes the heat transfer problem. In the case of a cold NS, the heat transfer problem is confined to the PS, and therefore only the equation of motion enters the time stepping scheme of the hybrid simulator. Then a classical mechanical time stepping algorithm is sufficient to conduct the test. In the PsD case with a cold NS, rate-dependent components of the PS restoring force are simulated numerically, and the system of equations defined by Equation 2 reduces to:

$$\begin{gathered} (M_{uu}^N + M_{uu}^P)\ddot{u} + (C_{uu}^N + C_{uu}^P)\dot{u} + K_{uu}^N u = F_u^N \text{-} R_u^P \\ R_u^P = K_{uu}^P u + K_{u\theta}^P \theta \text{-} F_u^P \end{gathered} \tag{3}$$

On the other hand, in the RT case with a cold NS, the following system of equations holds:

$$\begin{gathered} M_{uu}^N \ddot{u} + C_{uu}^N \dot{u} + K_{uu}^N u = F_u^N \text{-} R_u^P \\ R_u^P = M_{uu}^P \ddot{u} + C_{uu}^P \dot{u} + K_{uu}^P u + K_{u\theta}^P \theta \text{-} F_u^P \end{gathered} \tag{4}$$

DESCRIPTION OF THE PROOF-OF-CONCEPT CASE STUDY

The hybrid model used for the TMHS proof-of-concept tests of Whyte and co-workers [11] is retained for the simulations in this paper. The prototype structure is a long-span girder fixed at both ends and supported at mid-span by a hanger exposed to a fire. By utilizing symmetry, one half of the prototype girder (NS) and one half of the prototype hanger (PS) comprise the scaled hybrid model, shown in Figure 1.

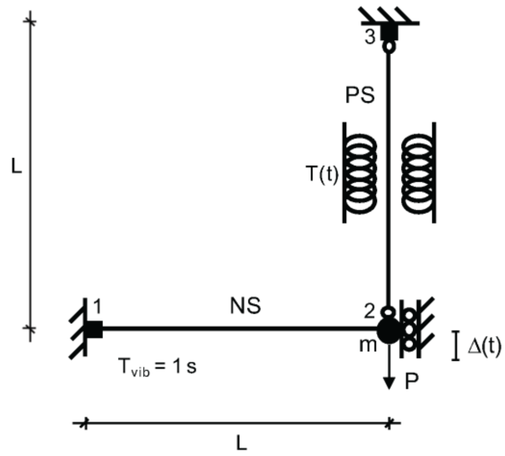

Figure 1. Hybrid model.

The vertical displacement at node 2 is the only free DOF of the hybrid model. The steel beam NS is assumed to be insulated from the fire and from the PS, so it is modeled as an unheated *elasticBeamColumn* element in OpenSees. The steel truss PS is modeled using the recently developed OpenFresco *thermalTruss* experimental element. In the basic coordinate system, this experimental element has one mechanical DOF (element elongation) and two temperature DOFs (one at each node). The cross-sectional dimensions of the PS are 9.78 mm x 3.31 mm, and the length, L = 40 mm. The Young's modulus of the steel material is modeled as E = 200 GPa. The thermal expansion coefficient is estimated from the experimental data to be α = 10E-06 [1/˚C]. The numerical mass, applied to node 2, is tuned to obtain an overall vibration period of T_n = 1 s. The cross-sectional moment of inertia of the NS and the mechanical and thermal load ranges are chosen such that the PS remains linear elastic, and changes in steel parameters due to temperature variations do not occur. The mechanical tensile force, P(t), is applied at node 2 as a linear load ramp from 0 to 15 kN. Simultaneously, the surface temperature of the PS is heated in the furnace with a scaled version of the international standard ISO 834 temperature-time fire curve, as defined in Eurocode 1 Part 1-2 [17], and as shown in Equation 5.

$$T(t) = 20 + 345\log_{10}(8t+1) \tag{5}$$

where T(t) is temperature [˚C] in the fire compartment and t is time [min]. A scaling factor multiplies T(t) and is adjusted with respect to the starting room temperature so that a final temperature of 200˚C is achieved at the end of the TMHS test. All of the following simulations refer to this benchmark case study.

OPTIMIZATION OF THE TESTING TIME SCALE

PsD HS uses an extended testing time scale that results in a simulation that is slower than RT. The testing time scale, λ, is defined as:

$$\lambda = \frac{dt_{sim}}{dt_{\text{int}}} \tag{6}$$

where dt_{sim} is the wall-clock time required to accomplish one analysis time step in the laboratory, and dt_{int} is the numerical integration time step length. λ=1 in a RT-HS, and λ>1 in a PsD HS.

Increasing the testing time scale is an acceptable approach when the restoring force measured on the PS is rate-independent. However, high temperature loads induce creep, which is inherently a rate-dependent phenomenon. For example, in the final Cardington test [18], the maximum steel temperature occurred after 57 min, and the duration of the test was 150 min. With such a long test duration involving high temperatures, even relatively small testing time scales (e.g. λ = 2-5) can bias the results.

As can be observed in Equation 6, a reduction of the testing time scale can be achieved by either reducing dt_{sim} or increasing dt_{int}. Therefore, the combination of the lower bound of dt_{sim} and the upper bound of dt_{int} dictate the minimum allowable, and thus most preferential, testing time scale. In particular, dt_{sim} relates to the performance of the experimental and the computational equipment, and can be reduced by increasing the communication network speed, reducing the actuation delay, or boosting the computational driver [6]. On the other hand, the maximum allowable dt_{int} is limited by numerical integration method stability and accuracy criteria [19].

In the present case study, the minimum value for dt_{sim} allowed by the experimental setup in the laboratory is 6 s, due to the slow reaction time of the furnace. The size of dt_{int} is established by the following error analysis, where both an implicit and an explicit variant of the Newmark algorithm [20] are considered. For the explicit algorithm, the upper bound of dt_{int} is further constrained by the stability limit and is equal to T_n/π = 0.32 s.

In order to define the optimal testing time scale, the thermomechanical response of the hybrid model presented in the previous section is simulated in Matlab. Gaussian noise with a root mean square (RMS) value of 50 N, which is significantly smaller than the maximum applied load of 15 kN, is added to the restoring force to simulate measurement errors. A reference solution is obtained considering a sufficiently small integration time step, dt_{int} = 0.01 s, and no restoring force noise. RMS errors between the displacement history of the TMHS simulation and the reference solution are calculated for a range of dt_{int} between 0.01 s and 0.3 s and averaged over 1000 simulations. The values obtained are normalized by the difference between the maximum and minimum displacement values of the reference solution and are presented in Figure 2.

As can be appreciated from Figure 2, the normalized RMS error remains small even for coarse integration time step values. This can be intuitively justified by the quasi-static character of the hybrid system response. As a result, dt_{int} = 0.25 s is selected for conducting the HS tests, which is satisfactory for both the explicit and implicit cases. Together with dt_{sim} = 6 s, a testing time scale of λ = 24 is obtained. Because these proof-of-concept tests remain at low-temperatures up to 200˚C, creep is not a concern. In order to accurately perform TMHS tests with smaller testing time scales, the laboratory equipment would need to be optimized significantly.

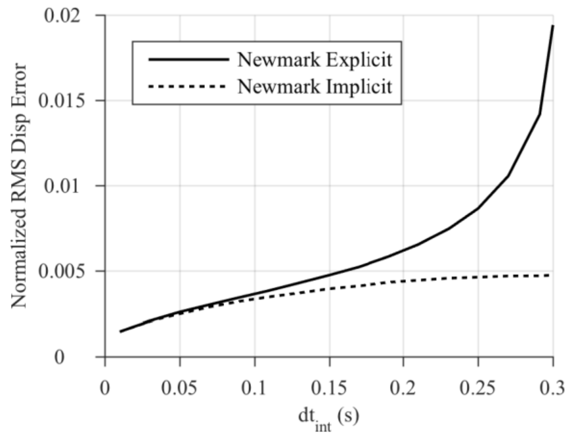

Figure 2. Normalized RMS error curves calculated for the hybrid system response.

OPENFRESCO TMHS EXPERIMENTAL ELEMENT

Before describing the details of the implementation of the OpenFresco experimental element, it is important to focus on the TM loading process on the PS. The mechanical side of the hybrid simulation is performed in displacement control, meaning that the equation of motion governing the behavior of the hybrid model is solved for a target displacement in each time step. This value is converted to a target total strain, ε_{total}, which is applied by the actuator to the PS through extensometer control over a gage length, L = 40 mm, which coincides with the PS length. A positive displacement command corresponds to specimen elongation and thus to a positive total strain, ε_{total}. When thermal expansion is involved, ε_{total} is the sum of the mechanical, ε_m, and thermal, ε_{th}, strain components. It is noteworthy that actuator imposes ε_{total} relatively quickly and then holds the specimen in that position for the remainder of the time step, while the furnace takes longer to heat the specimen. As the specimen heats, ε_{th} increases within that time step. To maintain the fixed ε_{total}, ε_m correspondingly decreases within the time step. Because the force is proportional to ε_m, the PS restoring force also decreases within each simulation time step. Therefore, the force feedback value is sampled only when the temperature setpoint is achieved.

In order to enable TMHS in OpenFresco, a new *thermalTruss* experimental element has been recently implemented [11]. An upgraded version of *thermalTruss* is presented in this paper, which allows for simulating the thermomechanical response of the PS numerically. In detail, an optional thermal expansion parameter, alpha (α) [1/˚C], is included to model the thermoelastic material behavior. The syntax to instantiate the upgraded *thermalTruss* reads:

expElement thermalTruss $tag $iNode $jNode -site $siteTag <-alpha $alphaVal> -initStif $K <-iMod> <-rho $rho>

In a TMHS, the temperature history, T, is provided as a command to the furnace. When α is included, the experimental element calculates ε_{th} and then the displacement due to thermal strain, u_{th}, in each step as:

$$\varepsilon_{th} = \alpha\,\Delta T \qquad (7)$$
$$u_{th} = \alpha\,\Delta T\,L$$

where ΔT is the difference between the current temperature and the initial temperature. Then, u_{th} is subtracted from the command displacement in each step. The resulting updated command displacement is passed to the OpenFresco *SimUniaxialMaterials* experimental control object [21], which returns a simulated force response based on an assigned OpenSees uniaxial material model. With this upgraded *thermalTruss*, it is possible to fully simulate the TMHS in OpenFresco, including the effect of the middleware. This implementation has been validated with Matlab simulations and the proof-of-concept test results. Figure 3 compares the displacement and force responses of the hybrid system obtained from the TMHS experiments with those simulated in OpenFresco and Matlab using the same simulation parameters as presented in the previous section.

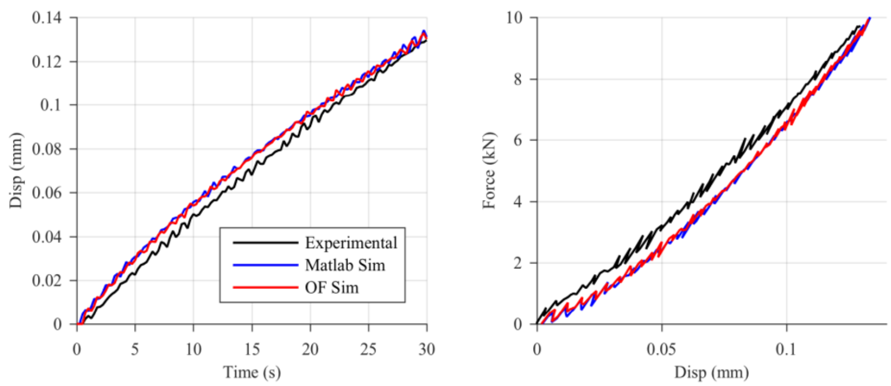

Figure 3. Validation of the *thermalTruss* OpenFresco element.

As can be appreciated from Figure 3, the OpenFresco simulation matches the Matlab simulation, and both models agree very well with the experimental test.

CONCLUSIONS

The hybrid simulation technique, which has been extensively investigated in the seismic domain, has been recently enhanced to combine mechanical and thermal loads. The thermomechanical hybrid simulation paradigm offers a deep insight into the responses of large and complex structural systems subjected to fire loadings. In this context, particular care must be devoted to the proper selection of the testing time scale. When high temperature and long duration thermal loads are involved, rate-dependent material creep becomes a concern and restricts the use of extended simulation time scales. While real-time tests would be ideal in these situations, laboratory equipment is often not capable of attaining real-time speeds. As a result, the optimal testing time scale is a trade-off between simulation accuracy and testing capacity. To investigate this problem, an upgraded OpenFresco *thermalTruss* experimental element is presented, which allow full simulation of a TMHS prior to implementation in the laboratory. This element enables evaluation of the suitability of experimental approximations, and is of paramount importance for validating test settings before laboratory implementation. Future developments will include the possibility to simulate physical substructures with rate-dependent behavior.

REFERENCES

1. Dwaikat, M.M.S., V.K.R. Kodur, S.E. Quiel, and M.E.M. Garlock. 2011. "Experimental behavior of steel beam-columns subjected to fire-induced thermal gradients," *Journal of Construction Steel Research*, 67(1): 30-38.
2. Martins, A.M.B. and J.P.C. Rodrigues. 2010. "Fire resistance of reinforced concrete columns with elastically restrained thermal elongation," *Engineering Structures*, 32(1): 3330-3337.
3. Tondini N., B. Rossi, and J.-M. Franssen. 2013. "Experimental investigation on ferritic stainless steel columns in fire," *Fire Safety Journal*, 62: 238-248.
4. Takanashi, K., K. Udagawa, M. Seki, T. Okada, and H. Tanaka. 1975. "Non-linear earthquake response analysis of structures by a computer-actuator on-line system," *Bulletin of Earthquake Resistant Structure Research Center*, Institute of Industrial Science, University of Tokyo, Tokyo.
5. Mahin, S.A. and M.E. Williams. 1981. "Computer controlled seismic performance testing," 2nd ASCE-EMD Specialty Conference on Dynamic Response of Structures, Atlanta.
6. Stojadinovic, B., G. Mosqueda, and S.A. Mahin. 2006. "Event-Driven Control System for Geographically Distributed Hybrid Simulation," *ASCE Journal of Structural Engineering*, 132(1): 68-77.
7. Korzen, M., G. Magonette, and P. Buchet. 1999. "Mechanical loading of columns in fire tests by means of the substructuring method," *Zeitschrift für Angewandte Mathematik und Mechanik*, 79: S617-S618.
8. Mostafaei, H. 2013. "Hybrid fire testing for assessing performance of structures in fire – Application," *Fire Safety Journal*, 56: 30-38.
9. Mostafaei, H. 2013. "Hybrid fire testing for assessing performance of structures in fire – Methodology," *Fire Safety Journal*, 58: 170-179.
10. Franssen, J.M., et al. 1995. "A simple model for the fire resistance of axially-loaded members according to Eurocode 3," *Journal of Construction Steel Research*, 35(1): 49-69.
11. Whyte, C. A., Mackie, K.R. and Stojadinovic, B. 2016. "Hybrid Simulation of Thermomechanical Structural Response," *Journal of Structural Engineering*, 142(2): 04015107-1 – 04015107-11.
12. OpenFresco 2016. "Open Framework for Experimental Setup and Control." <http://openfresco.neesforge.nees.org> (Feb. 4, 2016).
13. OpenSees 2016. "Open System for Earthquake Engineering Simulation." <http://opensees.berkeley.edu> (Feb. 4, 2016).
14. Bursi O.S. and D. Wagg, eds. 2008. "Modern testing techniques for structural systems," International Centre for Mechanical Sciences, CISM Courses and Lectures, 502, Vienna: Springer.
15. Anderberg, Y. 1988. "Modelling steel behavior," *Fire Safety Journal*, 13(1): 17-26.
16. Hetnarski, R.B., M.R. Eslami, and G.M.L. Gladwell. 2009. "Thermal stresses: advanced theory and applications," 41, New York: Springer.
17. CEN (European Committee for Standardization). 2002. "Eurcode 1: Actions on structures – Part 1-2: General actions – Actions on structures exposed to fire," *EN1991-1-2*, Brussels, Belgium.
18. Wald, F. et al. 2006. "Experimental behavior of a steel structure under natural fire," *Fire Safety Journal*, 41(7): 509-522.
19. Griffiths, D., H. Griffiths, and J. Desmond, 2010. "Numerical Methods for Ordinary Differential Equations: Initial Value Problems," Springer Science and Business Media.
20. Newmark, N.M. 1959. "A method of computation for structural dynamics," *Journal of Engineering Mechanics*, ASCE, 85(EM3): 67-94.
21. Schellenberg, A., S. Mahin, and G. Fenves. 2009. "Advanced implementation of hybrid simulation," *PEER Center Research Report* No. 2009/104: 1-266.

FIRE PROTECTION

Experimental Study of the Behavior of Steel Structures Protected by Different Intumescent Coatings and Exposed to Various Fire Scenarios

ANDREA LUCHERINI, RAZVAN-IOAN COSTA,
LUISA GIULIANI and GRUNDE JOMAAS

ABSTRACT

Three different experimental setups corresponding to three different fire scenarios were used to investigate how different heating conditions and heating rates affect the behavior of two different thin intumescent coatings (solvent-based and water-based paints, respectively). The results confirm that the current procedure for the design of intumescent coatings has shortcomings, as different paints have different performances according to the heating conditions and, in particular, according to the fire's heating rate. The tested water-based paint had better performance for low heating rates, while the tested solvent–based paint had better performance for high heating rates. However, for really low heating rates the solvent-based paint did not activate or provide proper insulation.

INTRODUCTION

Thin intumescent coatings have become the dominant passive fire protection system used to protect structural steel from fire [1]. These coatings swell on heating to form a highly insulating foamed char, hence preventing steel from reaching critical temperatures that could cause structural failure. The increasing growth of intumescent coatings in the built environment is associated with the low impact in the attractive appearance of bare steel structure, with their ability to be applied off site, and with their potential for offshore applications [1]. Intumescent coatings are thermally reactive fire protection materials and they are usually composed of a combination of organic and inorganic components bound together in a polymer matrix [2, 3].

Current design procedures for assessing the amount (i.e. thickness) of intumescent coating needed to protect steel profiles exposed to fire are based on standard fire tests, in particular the cellulosic standard fire curve [4, 5]. However, several studies have highlighted that the behavior of intumescent coatings not only depends on the temperature, but it can be highly influenced by other conditions of any given fire event, for example the heating rate [2, 3, 6, 7]. As a consequence, the current design procedures used for intumescent coatings are fundamentally based on the standard fire exposure, and hence cannot be

Lucherini A., Costa R.I., Giuliani L. and Jomaas G., Technical University of Denmark, Brovej, Building 118, 2800 Kgs. Lyngby, Denmark; email: grujo@byg.dtu.dk

applied to other fire conditions due to the fire-dependent nature of these organic fire protection materials. Therefore, the standard fire exposure does not necessarily replicate the worst-case scenario.

In the literature several research studies have proposed various approaches and methodologies to analyze the performance of intumescent coatings exposed to different fire conditions. Anderson et al. [8] developed a one-dimensional model to evaluate the effective thermal conductivity of the intumescent char. Li et al. [2] proposed a simple approach to assess the equivalent thermal resistance of intumescent coatings subjected to the ISO834 cellulosic fire [4]. Dai et al. [9] carried out some experiments on steel joints partially protected by intumescent coatings and subjected to standard fires. Wang et al. [3] performed some furnace tests on steel plates coated by intumescent paints and exposed to non-standard fire curves. Still, despite the process made in these studies, the performance of intumescent coatings subjected to different fire scenarios is still not fully understood due to the complexity of the intumescing process and the huge variety of different products and possible fire conditions.

The insulation properties and behavior of intumescent coatings exposed to eight different fire conditions were studied. Steel samples coated by two commercial intumescent paints were tested in three different experimental set-ups, representing different types of heating exposure. The current study highlights the limits of the current design methodology and provides some suggestions for a safer design method accounting for the various parameters that affect the intumescent coatings insulating performance, such as the heating rate and heating conditions.

EXPERIMENTAL INVESTIGATIONS

Two different types of samples were used throughout the project. In the first and second sets of experiments, the test specimens were 400mm-long sections of standard IPE400 steel profiles, with a resulting section factor A_s/V_s equal to 175 m^{-1}. In the third set of experiments, the test specimens were carbon steel plates of size 100 mm by 100 mm and having a thickness of 10 mm, with a resulting section factor A_s/V_s equal to 100 m^{-1}. All the samples were painted with either a solvent-based (Paint A) or a water-based (Paint B). Both commercially available paints were professionally applied to a dry film thickness (DFT) of approximately 1 mm.

In the first set of experiments, intumescent coatings were tested in an electric oven with internal dimensions of the heating chamber of 72x82x97 cm. One IPE400 steel profile sample per test was placed in horizontal position at half distance along the main axes of the oven. The steel samples were exposed to different non-standard fire curves with heating rates lower than the ISO834 standard fire curve [4]. The four temperature-time curves were characterized by different durations and heating rates, but similar target temperatures (900-1000°C). They were qualitatively denoted as “fast”, “medium”, “slow” and “very slow”, according to the heating rates. A total of thirteen experiments (four "very slow", three "slow", two "medium" and four "fast" – six with Paint A and seven with Paint B) were conducted [11, 12].

In the second set of experiments, the IPE400 steel profile specimens were tested in a gas furnace with internal dimensions of the heating chamber of 150x150x150 cm. The furnace temperature was monitored by eight plate thermocouples placed throughout the heating chamber and it can be controlled

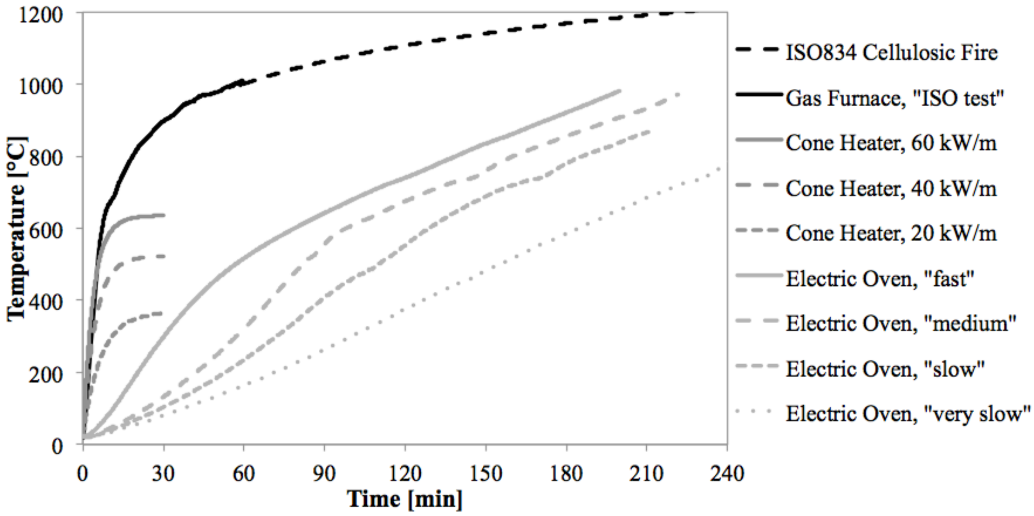

Figure 1: Unprotected steel temperature curves for all the different experimental set-up and the corresponding fire scenarios

both manually and automatically. Five steel profile samples in horizontal position (one unprotected, two coated by Paint A and two by Paint B) were tested at the same time, placed in a symmetrical configuration. The steel samples were exposed to the ISO834 cellulosic standard fire curve [4] and the test lasted 60 minutes, reaching a final temperature of 1000°C [11, 12].

In the third set of experiments, the intumescent coatings were tested in a cone heater, where a steel spiral located in the cone above the sample generated incident irradiance up to 100 kW/m^2. The distance between the bottom surface of the cone heater and the upper surface of the samples was set equal to 60 ± 1 mm, according to the standard ISO 5660 for dimensionally unstable materials [13]. The back of the steel plate was in contact with a layer of 20 mm thick mineral wool to minimize heat loss to the surrounding environment. The coated steel plates were exposed to different incident irradiances (20, 40, 60 kW/m^2) that provided temperature-time curves with heating rates similar to the ISO834 standard fire curve [4] for 30 minutes [11, 12].

In each experiment several thermocouples (NiCr-Ni, 1.4 mm, type K) were inserted into the steel specimens through holes and fixed using droplets of ceramic glue. Two to five thermocouples were placed into the each steel specimen in order to monitor the temperature distributions at different locations; thermocouples were also placed inside the heating chamber in order to control and evaluate the electric oven or the gas furnace temperature [11, 12].

Figure 1 shows the unprotected steel temperature curves for all the fire exposures implemented in the three different experimental set-ups. Each of the eight temperature-time curves is characterized by a different duration, heating rate and amount of energy provided to the steel specimens. In particular, one can observe the strong similarity between the initial branch of the temperature-time curves in the cone heater and the gas furnace tests.

INSULATING PERFORMANCE ASSESSMENT

The insulating performance of the intumescent coatings was assessed by considering two different parameters that evaluate the ability of this passive fire protection system to prevent or reduce the heat penetration.

The first parameter is the thermal resistance $R(t)$[m^{2}K/W] of the paint. Using an analogy with dry insulation, this value can be preliminary evaluated at each time interval by using the steel heating formula from EN1993-1-2 [14] for insulated steel sections and it can be defined as:

$$R(t) = \frac{d_p(t)}{\lambda_p(t)} = \frac{1}{\rho_s c_s} \frac{T_g - T_s}{\Delta T_s} \frac{A_s}{V_s} \Delta t \tag{1}$$

where $d_p(t)$[m] is the intumescent coating thickness, $\lambda_p(t)$[W/mK] is the intumescent paint thermal conductivity, $\rho_s c_s$[J/m^{3}K] is the volumetric specific heat of the steel, T_g[K] is the average fire temperature, T_s[K] is the average steel temperature, A_s/V_s[m^{-1}] is the steel section factor and Δt[s] is the time increment.

The second parameter estimates the ability of this passive fire protection system to lower the temperature of the coated samples $T_{s,prot}$[K] with respect to the temperature of unprotected steel specimens $T_{s,unpr}$[K]. The intumescent coating efficiency η_p[-] can be defined as:

$$\eta_p = \frac{T_{s,unpr} - T_{s,prot}}{T_{s,unpr}} \tag{2}$$

RESULTS AND DISCUSSION

The first results were obtained by evaluating the thermal resistance of the intumescent coatings according to equation (1), which enables assessment of the effectiveness of the fire protection material throughout the entire fire scenario. By collecting all the values, a common trend was observed for both the two intumescent paints in all the electric oven and gas furnace experiments. As suggested by Andersen [15], the thermal resistance curve (Fig. 2) was divided into four phases, identified according to four critical points.

The activation point marks the beginning of the intumescent chemical process and the paint swelling. It also represents the end of the inert phase, phase in which the coating is slowly melting and increasing its viscosity. In order to have a univocal definition of phase, the activation point was conventionally identified as the minimum value of the thermal resistance before the intumescent reaction. The next phase, the transient phase, is composed of a

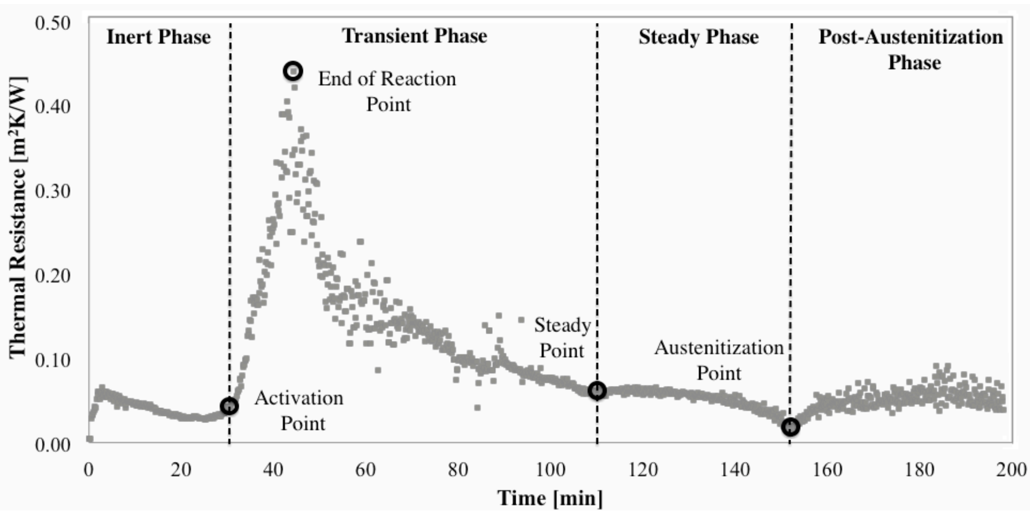

Figure 2: General trend of the thermal resistance of intumescent coatings and definition of the four general phases in its development, identified according to the four critical points

growing branch and a declining branch. In the first part, the paint starts swelling and increasing its volume. The chemical reaction stops in correspondence of the end of reaction point, which marks the thermal resistance peak. At this point the intumescent char has reached the maximum expansion and the highest insulating properties. Afterwards, the gradual decline of the thermal resistance is due to the gradual consumption of the carbon binder, the main component responsible for the cohesion and dark color of the char structure. When all combustibles have been burned, the thermal resistance reaches a steady value, which is approximately kept constant during the steady phase. The beginning of this phase, called steady point, was conventionally identified as the point of maximum curvature of the hypothetical trend curve of the thermal resistance values during the steady phase and the decreasing branch of the transient phase. Finally, the austenitization point refers to a particular phenomenon which takes place in steel at about 730°C-735°C [10]. At this temperature a molecular transformation of the steel occurs and the thermal capacity of steel increase due to this endothermic transformation. After this point the so-called post-austenitization phase starts: the carbon binder is completely combusted and, as a consequence, the intumescent char is white and very brittle. Moreover, the cracks begin to occur and they slowly decrease the insulating properties of the char structure.

Figures 3 (Paint A) and 4 (Paint B) show the thermal resistance development of the two intumescent coatings subjected to two different heating rates. The general trend with the four phases can be easily recognized in all the curves for both paints and all the five heating rates. However, it was found that the water-based Paint B had better insulating properties than the solvent-based Paint A, something which is also highlighted by the different scales of the vertical axes. Furthermore, the two paints have an opposite behavior with respect to the heating rates: the water-based Paint B has higher values of the thermal resistance at low heating rates, while the solvent-based Paint A is more efficient at high heating rates and does not activate properly for very slow heating rates.

As a conclusion, the current procedure for the design of intumescent coatings has certain limitations, as different paints have different performances according to the composition and the fire scenario. Nevertheless, the two intumescent coatings were designed according to the same standard exposure. However, according to the results obtained during this research study, this exposure characterized by really high heating rates produced the worst scenario for the solvent-based Paint B's insulating performance and, therefore, the best design case. On the contrary, the standard fire curve represented the best scenario for the solvent-based Paint A's insulating performance and, as a result, Paint A thermal resistance turned out as overestimated, representing a mistaken design on the non-conservative side.

In contrast to the electric oven and the gas furnace experiments, the cone heater experimental set-up did not allow for measurements of the intumescent coating's surface temperature, and thus the thermal resistance was not also obtainable. As a consequence, in this case the paint effectiveness was related to the intumescent coating efficiency (2). In general, similar considerations to the thermal resistance results can be also drawn from the paint efficiency developments. However, the two parameters are basically defined in a different way and they represent two slightly different aspects of the same problem. In particular, it was confirmed that the water-based paint usually has better insulation properties than the solvent-based paint. Moreover, both the paints have an increasing efficiency with increasing heat fluxes and their performances

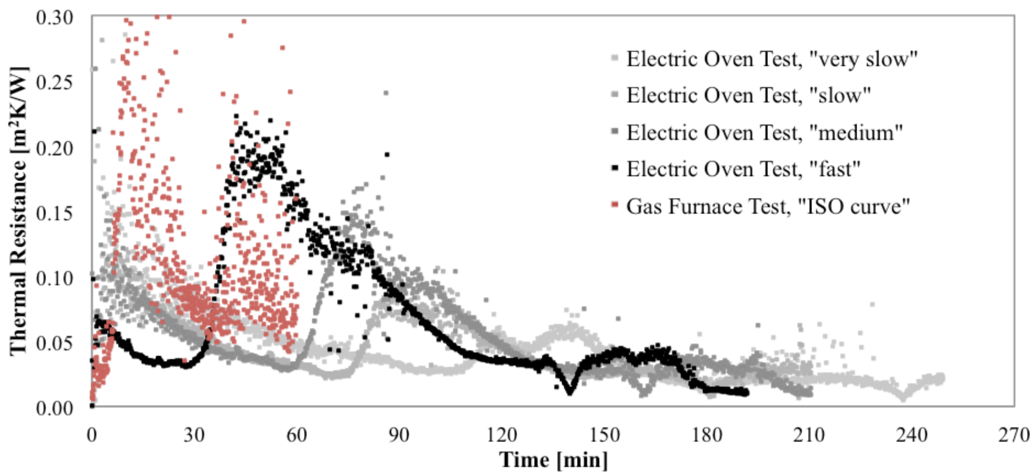

Figure 3: Paint A - thermal resistance developments for five different fire curves (electric oven and gas furnace)

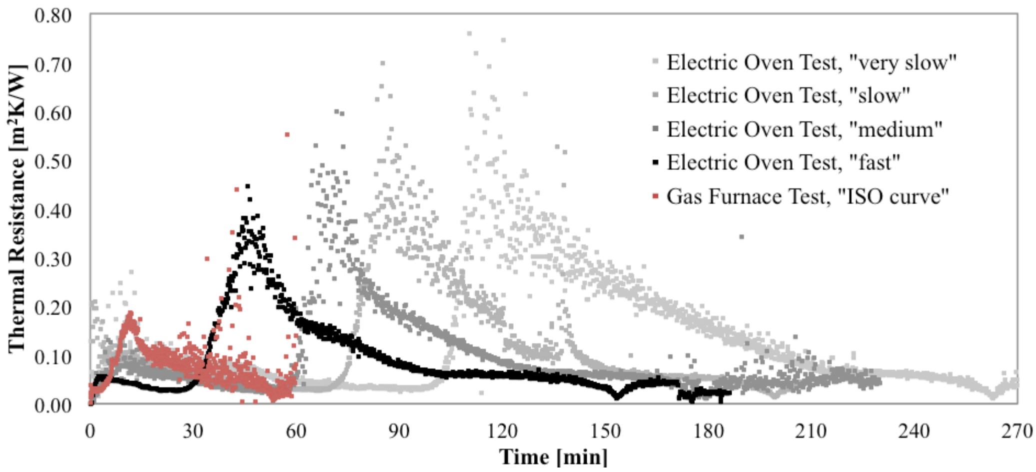

Figure 4: Paint B - thermal resistance developments for five different fire curves (electric oven and gas furnace)

become similar to each other with increasing heat fluxes (i.e. heating rates), similarly to the thermal resistance case.

Figure 5 shows all efficiencies curves for both paints for all the cases of the three different fire scenarios. As seen, Paint B had higher efficiency values than Paint A in the electric oven set-up, while for a higher heating rate in the gas furnace, Paint A's performance was better than Paint B's. However, this statement was not verified by the efficiency curves corresponding to similar fire curves in the gas furnace and the cone heater experimental set-ups. The heating rates in these two fire scenarios were really similar, as shown in Fig. 1. It should be noted that for the same heating rate, Paint A had a better performance than Paint B in the gas furnace set-up, while Paint B was always more efficient than Paint A in the cone heater experiments. The main reason of this difference may be related to the different natures of the two fire exposures. Moreover, it underlined the influence of the heating rate on the performances of Paint A and Paint B. Once again, the graph shows that Paint A had lower efficiency values at low heating rates. In particular, Paint A did not have an evident activation at low heating rates, as the maximum efficiency value within the transient phase is lower than the corresponding value for the virgin paint layer.

Finally, the maximum intumescent coating efficiency values were collected and compared for the three different experimental set-ups. Figure 6 shows the influence of the heating rate on the maximum paint efficiency value.

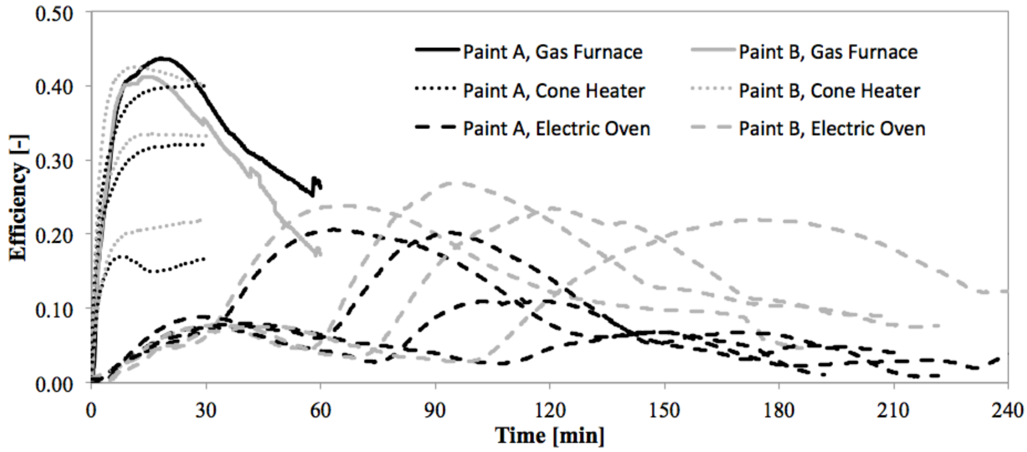

Figure 5: Intumescent coatings efficiencies for the three different experimental set-ups

Moreover, the maximum efficiency values of Paint A and Paint B were compared to the theoretical efficiency of a 1 mm non-reactive paint coating (estimated equal to 0.08). The results highlighted that the maximum efficiency values of the two coatings increased with increasing heating rates, but each of the intumescent paints had a different sensitivity to low heating rates. Regarding Paint B, its performance decreased gradually with decreasing heating rates and the paint developed good insulating properties also at really low heating rates. On the contrary, Paint A's performance decreased fast with decreasing heating rates. In particular, at really low heating rates the paint did not activate and expand at all: the maximum efficiency value is lower than the theoretical efficiency of the non-reactive paint layer. Therefore, the exposure of Paint A to slow fires leads to a degradation procedure.

CONCLUSION

Results from an experimental study on the insulation properties of two different intumescent coatings (a solvent-based and a water-based paint) exposed to eight different standard and non-standard fire conditions showed clear differences between the two paints and highlighted the importance of the heating rates when assessing the performance of intumescent paints. The insulating performance of the tested intumescent coatings was assessed by considering the variation of thermal resistance. Its development followed a

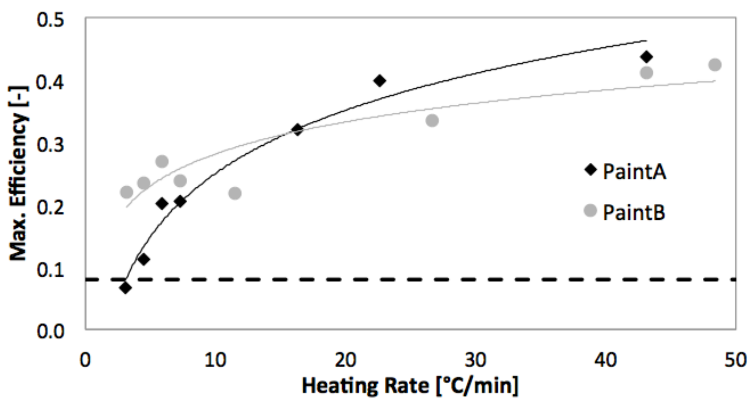

Figure 6: Influence of the heating rate on the maximum efficiency of Paint A and Paint B intumescent coating for all the three experimental set-ups, compared to the theoretical efficiency of the 1 mm non-reactive paint layer (black dashed line)

certain trend that can be divided into four general phases, identified according to four critical points on the thermal resistance curve. In addition, it was confirmed that the current procedure for the design of intumescent coatings has certain shortcomings, as different paints have different performances according to the heating conditions. In particular, different products have different sensitivity to the fire heating rates: the tested water-based paint had better performances at low heating rates, while the tested solvent-based paint had better performances at high heating rates and at really low heating rates the paint does not activate and provide insulation at all. Further studies are needed in order to confirm or contradict the exposed theories to the huge variety of different products and possible fire conditions.

ACKWNOWLEDGEMENTS

This study was partially financed by COWI Fonden.

REFERENCES

[1] Dowling J., “Fire protection costs for structural steelwork”, New Steel Construction, United Kingdom, 2003.

[2] Li G.Q., Lou G.B., Zhang C., Wang L. and Wang Y., “Assess the fire resistance of intumescent coatings by equivalent constant thermal resistance”, Fire Technology, vol.48, pp. 529-546, 2012.

[3] Wang L., Dong Y., Zhang D., Zhang D. and Zhang C., "Experimental study of heat transfer in intumescent coatings exposed to non-standard furnace curves", Fire Technology, vol. 51, no.1, pp. 627-643, 2015.

[4] International Organization for Standardization (ISO), “ISO834-1, Fire resistance tests - Elements of building construction - Part 1: General requirements for fire resistance testing”, Geneva, Switzerland, 1999.

[5] Comité Europeén de Normalization (CEN), “EN 13381-4, Test methods for determining the contribution to the fire resistance of structural members - Part 4: Applied protection to steel members”, Brussels, Belgium, 2002.

[6] Zhang Y., Wang Y., Bailey C.G. and Taylor A.P., "Global modelling of fire protection performances of an intumescent coating under different furnace fire conditions", Journal of Fire Science, vol. 31, no.1, pp. 51-72, 2012.

[7] Bartholomai M., Schriever R. and Schartel B., "Influence of external heat flux and coating thickness on the thermal insulation properties of two different intumescent coatings using cone calorimeter and numerical analysis", J. of Fire Materials, vol. 27, pp. 151-162, 2003.

[8] Anderson C.E., Ketchum D.E. and Mountain W.P., "Thermal conductivity of intumescent chars", Journal of Fire Science, vol. 16, pp. 390-410, 1988.

[9] Dai X.H., Wang Y.C. and Bailey C., “A simple method to predict temperatures in steel joints with partial intumescent coating fire protection”, Fire Tech., vol.46, pp. 19-35, 2010.

[10] Reed-Hill R. and Abbaschian R., "Physical metallurgy principles", PWS-Kent Publishing, 3rd edition, Boston, 1991.

[11] Lucherini A., “Experimental study of the behaviour of steel structures protected by different intumescent coatings and exposed to various fire scenarios”, MSc thesis, Civil Engineering Department, Technical University of Denmark, 2016.

[12] Costa R.I., “Thermal resistance of steel profiles protected with intumescent coatings”, MSc thesis, Civil Engineering Department, Technical University of Denmark, 2016.

[13] International Organization for Standardization (ISO), "ISO 5660-1: International Standard, Fire tests - Reaction to fire - Part 1: Rate of heat release from building products (Cone Calorimeter Method)", Geneva, Switzerland, 1993

[14] European Committee for Standardization (CEN), "Eurocode 3: Design of steel structures - Part 1-2: General rules - Structural fire design", EN 1993-1-2, April 2005.

[15] Andersen J.H., “Experimental study of the thermal resistance of intumescent coatings exposed to different heating rates,” MSc thesis, Technical University of Denmark, 2015.

An Improved Method for Thermal Analysis of Intumescent Coatings

ANITA TREVEN, TOMAŽ HOZJAN and MIRAN SAJE

ABSTRACT

Intumescent coating is a popular fire protection material for steel structural elements with beneficial temperature dependent thermal and mechanical properties. The analysis of the heat flux through the intumescent coating appears to be complicated, due to expansion and chemical reactions in material. In the paper an improved numerical method for the thermal analysis of intumescent coatings is presented. Temperature dependency on both the thermal and the mechanical properties of intumescent coating, expansion of the material and the chemical reaction are taken into account. The method is validated by comparing numerical and experimental results for two different intumescent coatings.

INTRODUCTION

In the performance-based analysis of behaviour of steel structures in fire, it is important to determine the time variation of the temperature in a structural element as accurate as possible. This is not an easy task, if the steel structure is protected with an intumescent coating. The most notable change is a large increase of the coating thickness during the intumescence process, which occurs over a short period of time right after the condition for the expansion has been met [1]. The expansion factor, F_{exp}, is specific to each type of the intumescent coating, and can reach values over 40 [2]. As can be seen from the results in [1], density of the coating decreases simultaneously as the consequence of both the expansion and the chemical and thermal decomposition. The rate of the density loss due to the chemical reactions appears to be governed by the Arrhenius equation [1, 3]. Intumescence and chemical reactions also effect the thermal conductivity and the heat capacity. These properties are thus temperature and deformation dependent and vary across the thickness of the coating. This is why thermal properties of intumescent coatings can rarely be found in literature.

University of Ljubljana, Faculty of Civil and Geodetic Engineering, Jamova 2, 1000 Ljubljana, Slovenia.

In many mathematical models for the thermal analysis of intumescent coatings, the so called 'effective thermal properties' are used [3, 4], determined by fitting the numerical to the experimental results (e.g. in [5, 6]) or by solving formulae from the Eurocode 3 for temperature increments in protected steel sections, as in [7]. However, this approach is not the most appropriate in the performance-based analysis, since the progress of the intumescent process and, consequently, the change of the thermal properties depend on the heating regime. A somewhat more detailed approach is to treat the intumescent coating as being a mixture of several material phases, and to determine experimentally properties of each phase. These properties are mixed in ratios, which vary with depth of the coating and depend on the progress of the intumescent process. Asaro et al. [1] assume three material phases. One is the virgin material, where intumescence or chemical reactions have not taken place yet. Intumesced material phase is defined as the material after the intumescence is completed, i.e. roughly prior to the chemical reactions occur. The third material phase represents charred material, after both the intumescence and the chemical reaction are completed.

The mathematical model for predicting the thermal response of intumescent coating based on the 1-D energy equilibrium and mass equation was first proposed in Henderson and Wiecek [8] assuming the constant volume and zero-gas accumulation. The assumption of a constant volume of a 1-D coating can only be satisfied, if the material under consideration is not expandable [9, 10], which is not the case with intumescent materials, or if the expansion from the initial to the final thickness of entire layer of coating is assumed to be instantaneous. Here, virgin density ρ_V and virgin thermal conductivity k_V prior to the actual expansion need to be scaled accordingly with F_{exp} [1]. After the actual expansion, temperatures between the coating and the substrate obtained match nicely with the experimental results [1]. Their numerical results for temperatures are too low at temperatures prior to the actual expansion takes place, however.

The aim of this paper is to present an improved numerical method for thermal analysis of intumescent coatings. The present method is in principle based on the numerical model of Asaro et al. [1], but enhanced with a step-by-step progress of the front of expansion within a coating related to the instant of time, when the condition for the expansion is met. The appropriate virgin, intumesced and charred thermal properties of the coating in each material phase, i.e. before and after the expansion, are introduced and discussed. Both the method presented in [1], later on referred to as the method-A, and our newly proposed method are implemented in a computer software for the planar thermal analysis, Heatko [11]. Two different commercial intumescent coatings are analysed. Comparisons between the obtained numerical and experimental results are presented as well.

NUMERICAL MODEL

A mathematical model for the thermal analysis of intumescent coating presented by Henderson and Wiecek [8] and modified by Asaro et al. [1] is based on the energy and mass equilibrium equation (1)

$$\rho c_p \frac{\partial T}{\partial t} - \frac{\partial}{\partial x}\left(k\left(\frac{\partial T}{\partial x}\right)\right) + \frac{\partial \rho}{\partial t} Q + \frac{\partial \rho}{\partial t}(c_p - c_{pg})T - \int_x^{l_x}\left(\frac{\partial \rho}{\partial t}\right) dx\, c_{pg} \frac{\partial T}{\partial x} = 0. \quad (1)$$

Here, ρ, c_p, k are the density, the heat capacity and the thermal conductivity of the coating, determined from virgin and charred properties by the rule of mixtures. c_{pg} denotes the heat capacity of decomposition gases, T is the temperature, and Q is the heat of decomposition. The first and the second term in Eq. (1) represent classical heat equation, and the rest of the terms are specific to reactive materials. The third term describes an internal heat source or sink, caused by exothermic or endothermic chemical reactions, respectively. Q is negative for endothermic reactions, such as those in intumescent coating. The fourth term stands for transformation of solid material into gaseous state and the last term, based on assumption of zero gas accumulation within the intumescent coating, describes cooling due to removal of hot gasses [1].

A density loss is mathematically sufficiently well described with Arrhenius rate equation

$$\frac{\partial \rho}{\partial t} = -A(\rho_V - \rho_{CH})\left(\frac{\rho - \rho_{CH}}{\rho_V - \rho_{CH}}\right)^n e^{-\frac{E_a}{RT}}. \quad (2)$$

Here A, E_a and n are the pre-exponential factor, the activation energy and the order of the reaction, respectively. These constant kinetic parameters can be fitted to the experimental results of thermo-gravimetric analysis. R is the gas constant and indices $\bullet_V$ and $\bullet_{CH}$ denote, respectively, the virgin and the charred material. With given densities of the coating in virgin and charred states, which are in general temperature dependent, known kinetic parameters and an initial density ρ_0, differential equation (2) can be integrated for density of the intumescent coating, ρ, as a function of time *t*. The mass fraction of the virgin material, F, can be determined from equation

$$a = F a_V + (1 - F) a_{CH}, \quad (3)$$

where a stands for any of the properties of the intumescent coating (either ρ, c_p or k), and used for calculation of other properties.

Asaro et al. [1] assume that the expansion of an intumescent coating to its final thickness occurs instantaneously at $t = 0$; hence, all the equations are set and solved with respect to the final thickness. Consequently, the volume remains constant during the heat transfer, and the thermal and mechanical fields at material points are scaled with F_{exp} earlier than the actual expansion takes place. The resulting values of temperature obtained by integrating the differential equation (1) without accounting for a current extension, are found to be too low when compared to experimental results.

In order to avoid this theoretical deficiency of the model, we propose new, and more precise model, where the expansion of a small material region of the coating during the heat transfer process occurs only when the condition for the onset of expansion is met. In the numerical integration of Eq. (1) this requirement is realized by introducing finite elements to model these small expendable regions. We assume

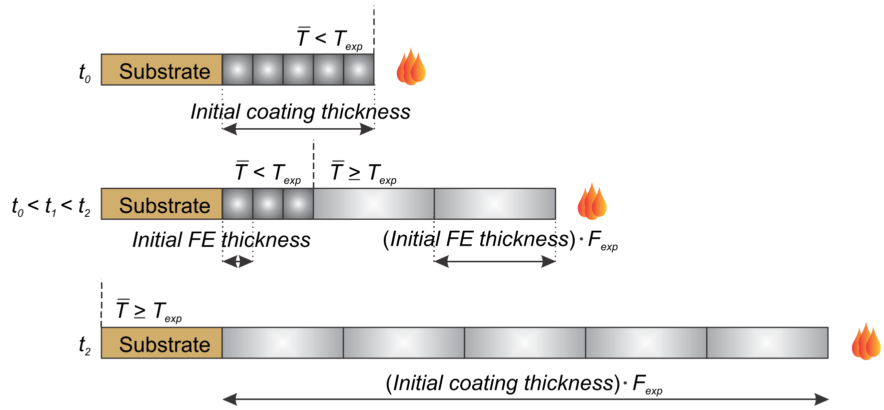

Figure 1. Expansion process.

that a finite element expends instantly. This, however, requires dense finite-element meshes and small time increments to be applied.

Following the above ideas, Eq. (1) was rewritten in a way to describe the planar heat transfer problem for intumescent materials. The new algorithm was implemented in our computer programme Heatko for the planar thermal analysis, see [11]. Heatko uses the standard 4-node iso-parametric finite elements and employs a well-known implicit one-step time integration method. The expansion of the intumescent coating is expressed with displacements of the element nodes. Consequently, the finite element mesh deforms during the analysis, yet the number of finite elements remains constant, see Fig. 1. The condition for sudden expansion of a finite element is assumed to be met when an average temperature, $\bar{T}$, based on the four Gaussian points of the finite element equals or exceeds the temperature of expansion, T_{exp}. In general, the condition for a sudden expansion of a finite element is satisfied at different time step for different finite elements. Thus the expansion of the entire layer of coating can be completed only within a finite time span. The finite element model of the process of the expansion of a typical layer of an intumescent material is schematically presented in Fig. 1.

The density, the thermal conductivity and the heat capacity prior to the expansion of the layer are determined from Eqs. (2)–(3). Once the expansion starts developing, the form of the equations remains the same, only that the virgin properties $\bullet_V$ are replaced by the intumesced properties $\bullet_{INT}$.

NUMERICAL EXAMPLES

Two different types of intumescent coatings, both sufficiently well documented in literature, were numerically analysed with Heatko. First, an example presented by Asaro et al. [1] is discussed and the results of the method-A and of our improved method are compared. Furthermore, in order to validate our method as generally applicable, an experiment conducted by Bartholmai et al. [5] is also analysed.

Both experiments were designed as a 1-D heat transfer problem. Our planar numerical model of the tested specimens consists of 31 x 1 elements; i.e. 31 elements in the direction of the heat flux, of which the first one models a non-intumescent substrate, while the remaining elements represent an intumescent coating, and 1 finite element in the direction perpendicular to the heat flux. A linear heat transfer in accordance with the experiments is ensured by boundary condition of zero heat flux. On the unexposed end of the model (backside of the substrate), a zero heat flux boundary condition is also prescribed, assuming an ideal thermal insulation of the specimen. Boundary conditions on the exposed end of the model are specific to each example. The time step in both analyses was chosen to be 2s.

Example 1

In the first example an experiment conducted by Asaro et al. [1] was analysed. They investigated a 1mm thick aluminium substrate with properties according to the Eurocode 9 [12]. An initial thickness of the intumescent coating was 3.94 mm, hence each finite element representing the coating was 0.13133 mm thick initially. In accordance with [1], the following constants were used: $F_{exp} = 4$, $A = 30$ s^{-1}, $E_a = 5.1 \cdot 10^7$ J/gmol, $n = 2$ and $Q = -240$ kJ/kg.

Three sets of thermal conductivities of the intumescent coating were tested. Properties in set 1 were determined such, that the method-A could be simulated with our model as best as possible. Sets 2 and 3 differ in k_{INT} and in $c_{p\,INT}$, which are temperature independent and dependent, respectively. Densities, heat capacities and thermal conductivities for each material phase and each set are presented in Table I. Material properties according to [1] are added for comparison.

The boundary condition at the exposed end was a time-dependent temperature, measured in the experiment [1], and shown in Fig. 2, together with the experimentally and numerically obtained temperatures at the interface between the coating and the aluminium substrate. The comparison between the results of the method-A and the results obtained with the present method using assumptions from set 1 is reasonably good. The results within the time range before and during the actual expansion, obtained with assumptions from the sets 2 and 3, match the experimental results very well. The numerical results, obtained with the temperature-dependent k_{INT}, agree even much better also on the post-expansion interval.

TABLE I. ASSUMED MATERIAL PROPERTIES

	Material	**Method-A [1]**	**Set 1**	**Set 2**	**Set 3**
k_V [W/mK]	0.4	0.4	1.6	0.4	0.4
k_{INT} [W/mK]	0.1 + 0.000286T	/	k_V/F_{exp}=0.4	k_V/F_{exp}=0.1	0.1 + 0.0015T
k_{CH} [W/mK]	0.1 + 0.0005T	0.1 + 0.0005T	0.1 + 0.0005T		
$c_{p\,V}$ [J/kgK]	2200	2200	2200		
$c_{p\,INT}$ [J/kgK]	1.5T + 3000	/	2200		1.5T + 3000
$c_{p\,CH}$ [J/kgK]	2T + 2800	2T + 2800	2T + 2800		
ρ_V [kg/m^3]	1392	348	1392		
ρ_{INT} [kg/m^3]	ρ_V/F_{exp}=348	/	348		
ρ_{CH} [kg/m^3]	ρ_{INT} ·0.47=163.56	163.56	163.56		
Expansion at	$T_{exp} \cong 120$ °C	$t = 0$	$t = 0, T_{exp} = 20$°C	$t > 0, T_{exp} = 120$°C	

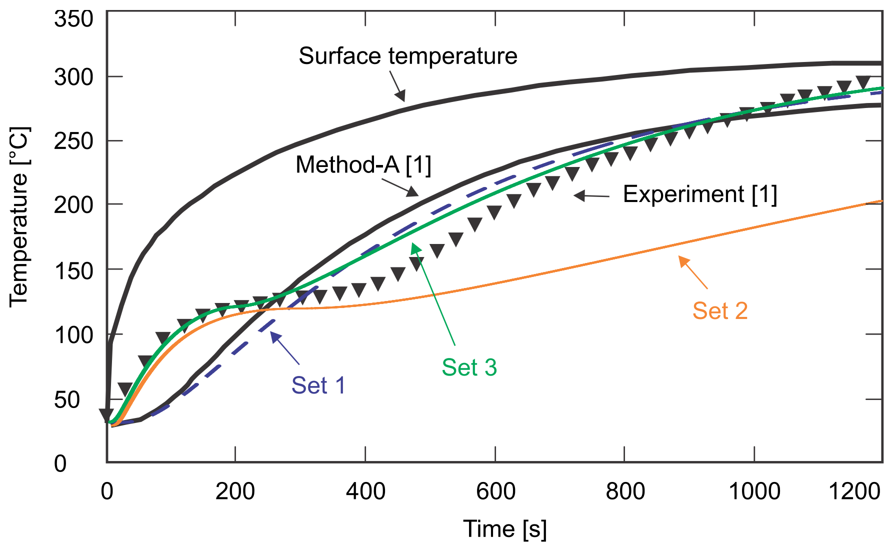

Figure 2. Comparison of experimental and numerical results – example 1.

Example 2

The experiment in Bartholmai et al. [5] was carried out in a small-scale test furnace, where the temperature of air followed the standard temperature-time curve [13]. Accordingly, these temperatures of air were the boundary condition on the exposed edge in the second example, with the coefficient of the heat transfer by convection and the emissivity of the surface being, respectively, 25W/m^{2}K and 0.95. The properties of the steel substrate were taken in accord with the Eurocode 3 [14] and its thickness is 5 mm. Kinetic parameters A, E_a and n were fitted to the TGA curve, given in [5], with the least squares method. The obtained values were 0.2291 s^{-1}, $2.7529 \cdot 10^7$ J/gmol and 1.00001, respectively. Some properties of the analysed epoxy resin-based intumescent coating were obtained from the manufacturer. While the virgin density was exactly defined to be $\rho_V = 1000$ kg/m^3, other properties needed to be estimated from charts of the effective thermal conductivity and the time-history of factor of expansion for two fire curves distinct from the standard temperature-time curve [13]. The estimated properties were chosen as: $T_{exp} = 250$°C, $F_{exp} = 3.5$, $k_V = 0.235$ W/mK, $k_{INT} = 0.013$ W/mK and $k_{CH} = (0.013 + 0.0001115T)$ W/mK. Furthermore, the calculated values of intumesced and charred density were 500 kg/m^3 and 190 kg/m^3, respectively. Unfortunately, no data for the heat of decomposition and heat capacity were available; therefore the assumptions from the set 3 in the first example were used for these quantities as only rough approximations.

In [5] the experimentally obtained time-history of the temperatures at the backside of the substrate is given for the initial thicknesses of the intumescent coating 5 mm, 10 mm and 15 mm. Comparisons of experimental and our numerical results are shown in Fig. 3. In general the curves match reasonably well, with the maximum error being less than 60°C. A possible further reason for the differences, beside, of course, guessing the missing data for some quantities, is the use of the Arrhenius equation, which describes only one-step chemical reaction and not the two-step one, as clearly indicated by the two peaks on the mass loss rate curve [5].

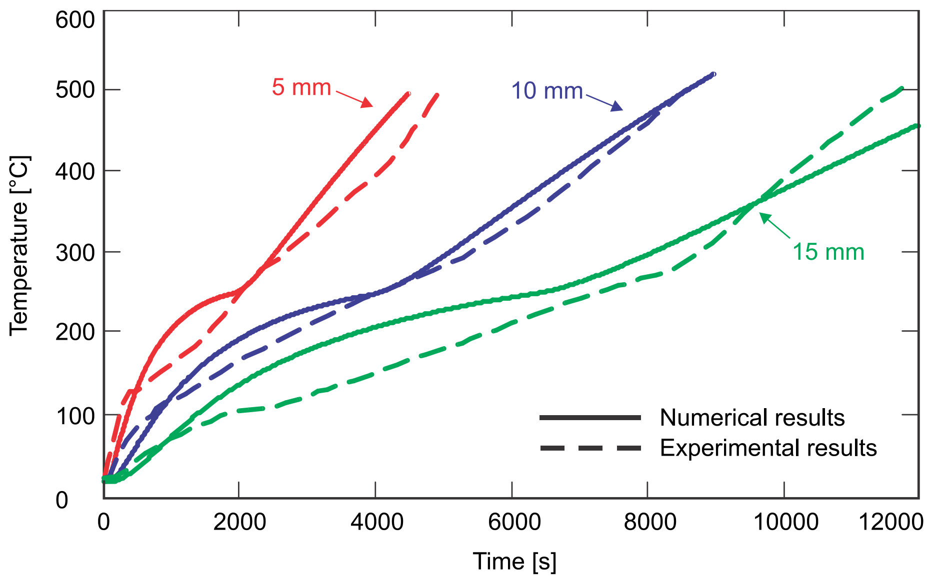

Figure 3. Comparison of experimental and numerical results – example 2.

CONCLUSIONS

An improved method for the thermal analysis of intumescent coating was presented and validated with experimental results. The results of the first example have proved that the proposed numerical model is suitable for the thermal analysis of the metal structures insulated by the intumescent coating, particularly at times before and during the insulation expansion. Temperatures after the expansion has fully developed are highly dependent on the assumed intumesced thermal conductivity. This issue needs a further research. In the second example, the numerical model was validated for another type of intumescent coating; this analysis showed a much better agreement between the experimental and the present numerical results.

For the presented method to be practically applicable, the following data about the intumescent coating are necessary: (i) a TGA curve, from which the kinetic parameters A, E_a and n can be determined, (ii) virgin density ρ_V and the factor of expansion F_{exp} (intumesced and charred density can then be determined from the data (i) and (ii)), (iii) a good approximation of the thermal conductivity for the three phases of the material. Note that the results of the second example suggest that the model is not very sensitive to the heat capacity and the heat of decomposition. Yet a further research is still needed for confirmation.

Although the presented numerical examples are 1-D only, the present formulation and the related computer programme are not limited to 1-D problems. Of a special interest for a structural engineer is the 2-D formulation because it enables us also to predict the temperature distribution in variously shaped metal cross-sections protected with intumescent coating. The related analyses will be presented elsewhere.

ACKNOWLEDGEMENTS

The work of A. Treven was supported by the Slovenian Research Agency through grant 1000-14-0510 in accordance with decision No. 1240-1/2013-49. The support is gratefully acknowledged.

REFERENCES

1. Asaro, R.J., Lattimer, B., Mealy, C., Steele, G. 2009. "Thermo-physical performance of a fire protective coating for naval ship structures," *Composites: Part A*, 40: 11-18.
2. Wang, L.L., Wang, Y.C., Li, G.Q. 2013. "Experimental study of hydrothermal aging effects on insulative properties of intumescent coating for steel elements," *Fire Safety Journal*, 55: 168-181.
3. Gomez-Mares, M., Tugnoli, A., Landucci, G., Barontini, F., Cozzani, V. 2012. "Behavior of intumescent epoxy resins in fireproofing applications," *Journal of Analytical and Applies Pyrolysis*, 97: 99-108.
4. Wang, Y., Göransson, U., Holmstedt, G., Omrane, A. 2005. "A Model for Prediction of Temperature in Steel Structure Protected by Intumescent Coating, based on Tests in the Cone Calorimeter," *Fire Safety Science – Proceedings of the eighth international symposium*: 235-246.
5. Bartholmai, M., Schartel, B. 2007. "Assessing the performance of intumescent coatings using bench-scaled cone calorimeter and finite difference simulations," *Fire and Materials*, 31: 187-205.
6. Kolšek, J., Češarek, P. 2015. "Performance-based fire modelling of intumescent painted steel structures and comparison to EC3," *Journal of Constructional Steel Research*, 104: 91-103.
7. Piloto, P.A.G., Mesquita, L.M.R. 2005. "Thermal behaviour of reaction intumescent paint used for passive protection of steel structures," presented at 7º Congreso Interamericano de Computación Aplicada a la Industria de Procesos, September, 2005.
8. Henderson J.B., Wiecek T.E. 1987. A mathematical model to predict the thermal response of decomposing, expanding polymer composites. *Journal of Composite Materials* 21: 373-393.
9. Looyeh, M.R.E., Bettess, P., Gibson, A.G. 1997. "A one-dimensional finite element simulation for fire-performance of GRP panels for offshore structures," *International Journal of Numerical Methods for Heat & Fluid Flow*, 7(5/6): 609-625.
10. Krysl, P., Ramroth, W.T., Stewart, L.K., Asaro, R.J. 2004. "Finite element modelling of fibre reinforced polymer sandwich panels exposed to heat," *International Journal for Numerical Methods and Engineering*, 61: 49-68.
11. Hozjan T. 2009. "Software Heatko: 2-D analysis of heat transfer through solid materials," Ljubljana, University of Ljubljana, FGG.
12. EN 1999-1-2, "Eurocode 9, Design of aluminium structures - Part 1-2: Structural fire design," Brussels: European Committee for Standardisation, 2007.
13. EN 1991-1-2, "Eurocode 1, Actions on Structures – Part 1-2: General actions – Actions of structures exposed to fire," Brussels: European Committee for Standardisation, 2002.
14. EN 1993-1-2, "Eurocode 3, Design of steel structures – Part 1-2: General rules - structural fire design," Brussels: European Committee for Standardisation, 2005.

Experimental Tests on Intumescent Coating for Protecting Steel Structures

DONATELLA DE SILVA, ANTONIO BILOTTA and EMIDIO NIGRO

ABSTRACT

Intumescent coatings (IC) are fireproof materials that provide the thermal insulation of steel structures. When exposed to fire, IC generally expand in thickness by 15 to 30 times in a standard test, forming a thick layer of foam that protects the steel by thermally insulating it. As part of the expansion process, many coatings generate an outer ash-like char layer. Moreover, during the process the IC change their chemical, physical and also thermal properties. This work shows an ongoing experimental program that could allow to characterize the thermal properties of the IC, based on the measurements of thickness variation during the fire and highlighting the parameters which influence the thermal behavior of IC-protected steel members. The ongoing research is aimed to allow analytical or numerical modelling of steel members protected by IC through a finite element thermal analysis. This modelling could be useful for the fire designers, since it allows to take into account the presence of the IC also when the Structural Fire Safety Engineering approach (SFSE) is applied, according to the modern fire regulations. The experimental results show that (i) small thickness of IC (500 μm) do not react homogeneously for all the section factors and (ii) the equivalent thermal conductivity depends on both the initial thickness and the section factor.

INTRODUCTION

An increase of the fire resistance time for steel structures can be reach by applying fire protection materials, preventing the achievement of high temperatures in the steel members during fire. The protection materials can be divided into two main categories: passive materials, as the incombustible boards, and reactive materials, as the intumescent coatings (IC). The IC are solvent- or water-based systems and are generally applied with a thickness ranging between 400μm and 3000μm. The advantages of this protection include reduced invasiveness compared to other materials, an easy application and a good surfaces finishing.

To date the design of IC thickness for protected steel members is possible only using data provided by the manufacturer, according to prescriptive approach (standard fire curve), whereas no information are provided for analytical or

---

Department of Structures for Engineering and Architecture, University of Naples, via Claudio 21 80125, Naples, Italy

numerical thermal modelling of IC protected steel members. Hence, a detailed investigation in the high-temperature thermal properties of IC for protected structural steel members is important for advanced calculation models (performance-based procedure). Indeed, although the performance-based approach is now well established and already worldwide applied to practical engineering problems, often it is not used with the IC. With the performance-based methods, the knowledge of the time evolution of steel temperature is required and the data provided by the manufacturer are not adequate to this scope [4].

EXPERIMENTAL PROGRAMME

Test instrumentation

The furnace has a volume of 1 m^3; 1m wide and 1m long; it has a front door that can be removed indeed, in this case, the opening was closed with mineral fiber, on which a hole was created in order to observe the specimen during the tests (Figure 1).

The furnace has two burners that keeps the temperature uniform inside it during the tests. The input curve was the ISO834, as the Figure 1(b) shows. Each test was stopped when the temperature of 700°C is reached in the steel specimen.

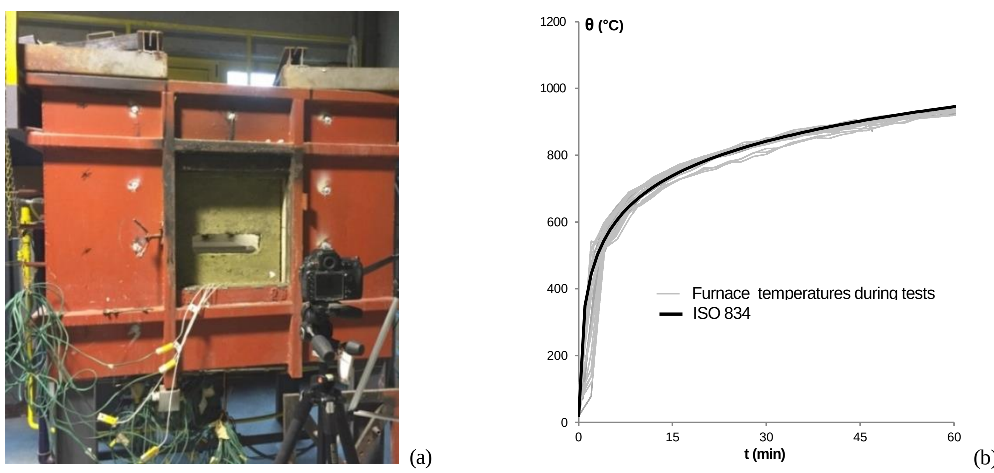

Figure 1. Furnace and input curve.

Test samples and setup

The specimens tested are steel plates with dimensions 30×30 cm and several thicknesses in order to obtain different section factors. The plates were protected with different thicknesses (500µm, 1000µm, 1500µm, 2000µm) of water-based commercial IC only on the top surface (the exposed surface). In addition, three plates with A/V=250 m^{-1}, A/V=125 m^{-1}, A/V=67 m^{-1} without protection were tested. The details are contained in Table 1.

The plates were placed on an insulating support, which is composed by a ceramic fiber mat 25,4 mm thick. Each sample was protected on the perimeter by ceramic board strips, so that only the upper surface of the plate is exposed to fire (see Figure 2a); in this way, the possible deformation of the plate during the test is limited.

The plate and the insulating system are placed on a support consisting of bricks of cellular concrete (Figure 2b).

TABLE I. TESTS MATRIX.

Samples	n°	ID	Dimension (mm)	A/V (m^{-1})	IC (µm)	Input Curve
	1	S_300x300x4-260_500_ISO_1			500	
	2	S_300x300x4-260_500_ISO_2			500	
	3	S_300x300x4-260_1000_ISO_1			1000	
8 plates 300x300x4	**4**	S_300x300x4-260_1000_ISO_2	300x300x4	250	1000	ISO834
	5	S_300x300x4-260_1500_ISO_1			1500	
	6	S_300x300x4-260_1500_ISO_2			1500	
	7	S_300x300x4-260_2000_ISO_1			2000	
	8	S_300x300x4-260_2000_ISO_2			2000	
	9	S_300x300x8-150_500_ISO_1			500	
	10	S_300x300x8-150_500_ISO_2			500	
	11	S_300x300x8-150_1000_ISO_1			1000	
8 plates 300x300x8	**12**	S_300x300x8-150_1000_ISO_2	300x300x8	125	1000	ISO834
	13	S_300x300x8-150_1500_ISO_1			1500	
	14	S_300x300x8-150_1500_ISO_2			1500	
	15	S_300x300x8-150_2000_ISO_1			2000	
	16	S_300x300x8-150_2000_ISO_2			2000	
	17	S_300x300x15-80_500_ISO_1			500	
	18	S_300x300x15-80_500_ISO_2			500	
	19	S_300x300x15-80_1000_ISO_1			1000	
8 plates 300x300x15	**20**	S_300x300x15-80_1000_ISO_2	300x300x15	67	1000	ISO834
	21	S_300x300x15-80_1500_ISO_1			1500	
	22	S_300x300x15-80_1500_ISO_2			1500	
	23	S_300x300x15-80_2000_ISO_1			2000	
	24	S_300x300x15-80_2000_ISO_2			2000	

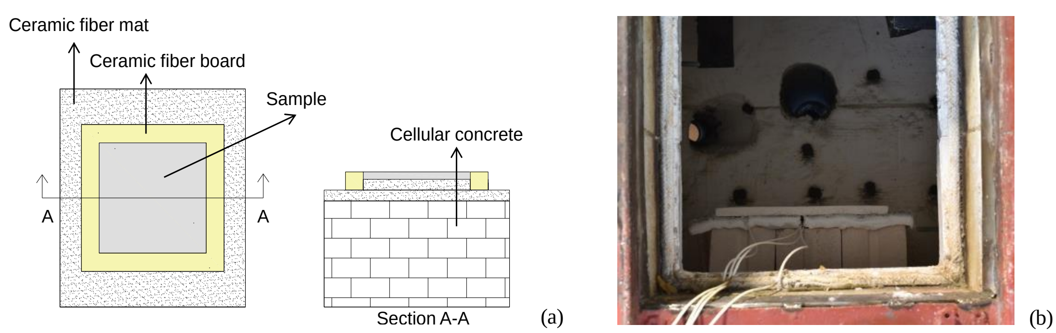

Figure 2. (a) Test setup and (b) Sample in the furnace.

Instrumentation

Four K-type thermocouples were placed on each plate, according to the scheme of Figure 3. In particular, four holes were made in the ceramic fiber mat under the plate in order to introduce four metallic platelet (0.6 mm) to which the thermocouples are welded. The platelet were used to ensure the contact between the thermocouple and the specimen (Figure 3).

The test setup involves the insertion of a camera in front of the opening of the furnace in order to take a series of pictures of the specimen during the test. The photos were shot with five-second time interval during all tests and then were used to obtain the variation of IC thickness by means of the Digital Image Correlation technique (DIC).

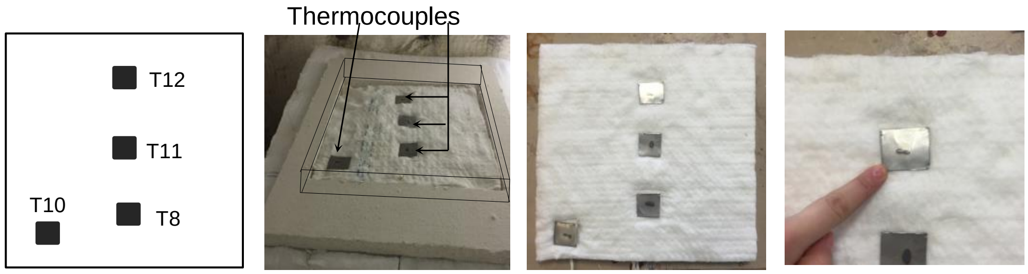

Figure 3. Position of the thermocouples.

RESULTS

IC are materials characterized by a swelling behaviour when exposed to high temperatures, due to the generation of gaseous compounds during thermal decomposition of the organic matrix [5], [6]. The swelling phenomenon contributes in retarding the heat transfer to the protected surface.

Figure 4 shows the temperatures for the samples with A/V=67 m-1. The temperature recorded by the four thermocouples of the unprotected specimen are very close to each other, the same is for the specimen with 2000 μm, while a variability is observed for the sample protected with 500 μm. This difference could be related to the IC swelling phenomenon, which in the case of protection 2000 μm is more regular than that observed for the 500 μm case.

Generally a fast increase of thickness is observed between 150 °C and 300°C, then it becomes stable until the end of the test. This trend was observed for all the tests with 1000 μm, 1500 μm and 2000 μm. Figure 5 shows the thickness increase registered during tests 6 through DIC technique. The maximum value of thickness is recorded at about 280°, then a slight decrease in thickness is recorded (e.g. 40 mm is the thickness at 600°C).

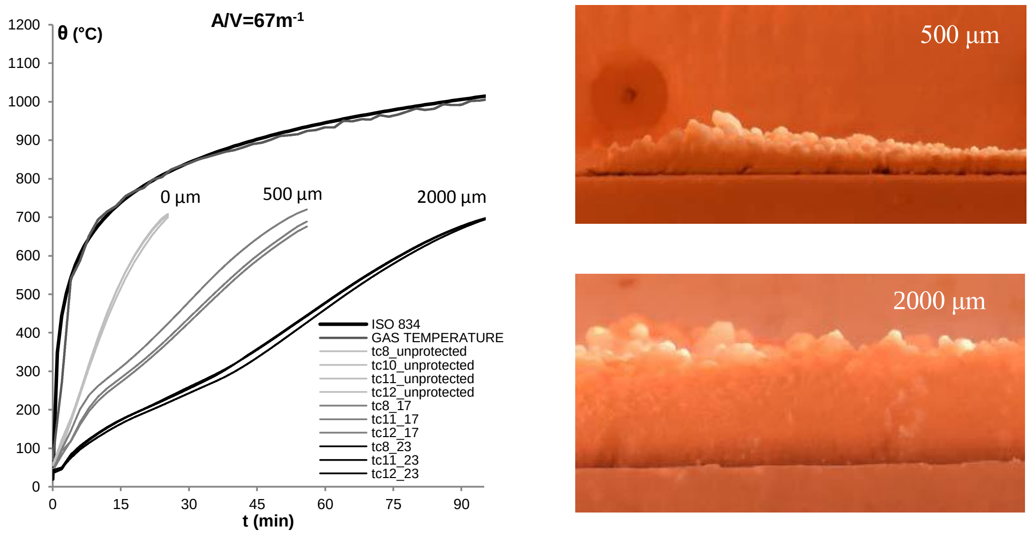

Figure 4. Temperatures and IC swelling for samples with A/V=67 m^{-1}.

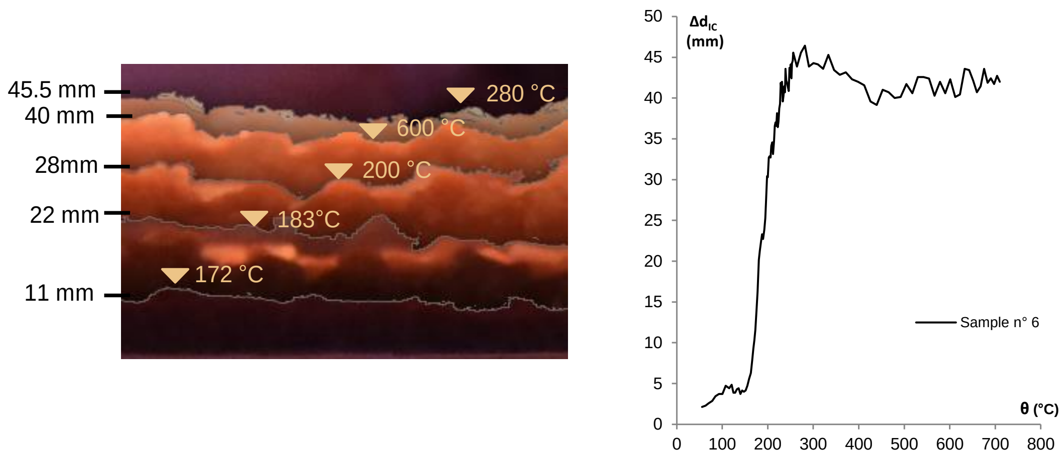

Figure 5. Thickness increase registered during tests 6 through DIC technique.

Because the response of reactive coatings to heating is complicated by the various chemical reactions, phase transitions, thermal expansion, and charring phenomena, developing holistic models which account for all relevant parameters to predict their thermal insulating properties under different heating regimes is fraught with complications [7]. As a result, it is typical to treat the thermal conductivity of reactive coatings using an empirically informed procedure called the "Variable λ Method" which is set out in Annex E of EN 13381-8 [8]. This method is intended for evaluating the equivalent thermal conductivity of fire protection systems and is defined by the following expression:

$$\lambda_{p,t} = d_p \times \frac{V}{A_p} \times c_a \times \rho_a \times \frac{1}{\left(\theta_t - \theta_{a,t}\right) \times \Delta t} \times \Delta\theta_{a,t} \qquad (1)$$

where:

d_p= dry film thickness of reactive product, in metres;

V/A_p= inverse of the steel section factor, in metres;

c_a= temperature dependant specific heat capacity of steel at θ_a, in J/kgK;

ρ_a= density of the steel, in kg/m^3;
θ_t= furnace temperature, in Celsius degrees;
$\theta_{a,t}$= steel temperature, in Celsius degrees;
Δt = time step, in seconds;
$\Delta\theta_{a,t}$= steel temperature rise over time step Δ_t, in Kelvin degrees.

Eq. 1 derives from an energy balance taken during a given time interval during heating. It was applied to all the tested plates, and as such it assumes an adiabatic condition between the furnace gases and the surface char 9.

After reading the thickness variation Δd_{IC} and calculating the equivalent conductivity λ_{IC} , a comparison between the several test results was carried out.

In the following Figure 7, Figure 8, Figure 9, Figure 10, for each couple of equal samples, the value of Mean Thickness (M.T.), Mean Conductivity (M.C) and Mean Temperature (M.θ.) are shown.

The Figure 6 shows a comparison in terms of temperatures, conductivity and swelling between samples with different section factors but protected with the same IC thickness (1000μm). The samples with the highest section factor have the highest temperature, but they have also the biggest swelling; correspondingly the equivalent conductivity is the lowest. The same considerations can be done by observing Figure 7, which refers to specimens having the same IC thickness (1500 μm) but different section factors. These results show that both the swelling and equivalent conductivity of IC depend on the section factor of the protected steel plate.

Figure 8 and Figure 9 show the trends of the swelled thickness and the "specific equivalent conductivity" (λ_{IC}/d_{IC}) versus the temperature, for samples having equal section factor but different dry thicknesses of IC. The "specific equivalent conductivity" is the calculated as ratio between equivalent conductivity λ_{IC} and IC dry thickness d_{IC}.

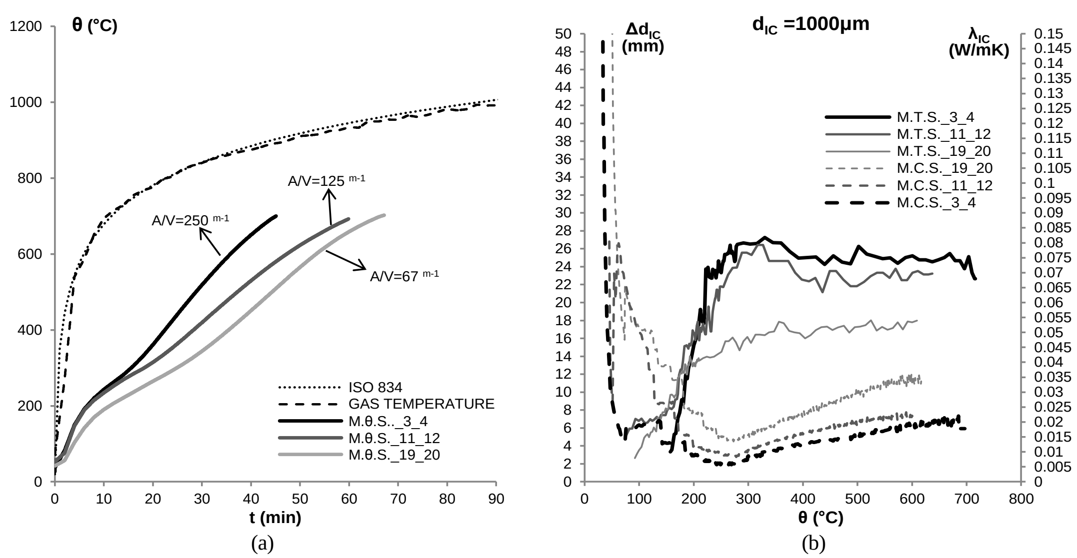

Figure 6. Results for samples with 1000 μm of IC - (a) temperatures, (b) thickness and conductivity.

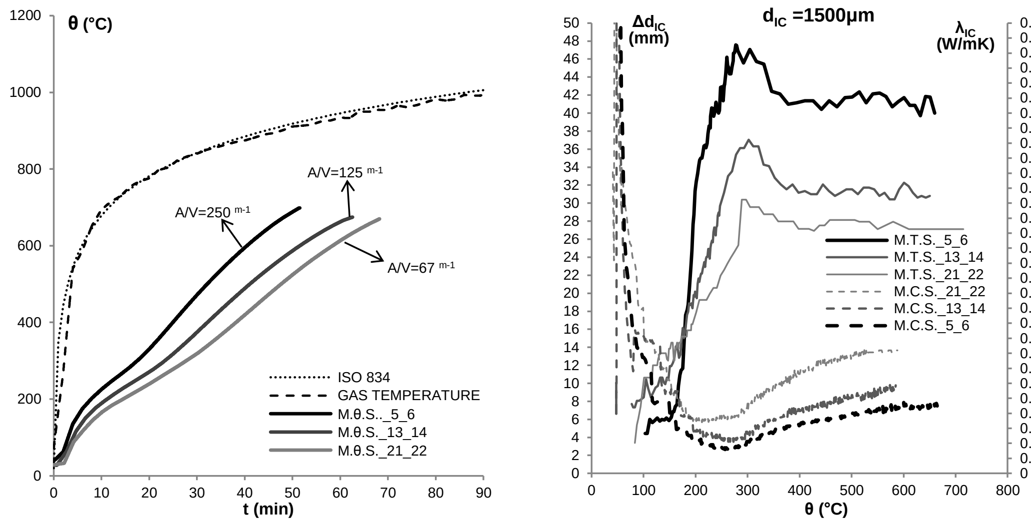

(a) (b)

Figure 7. Results for samples with 1500 μm of IC- (a) temperatures, (b) thickness and conductivity.

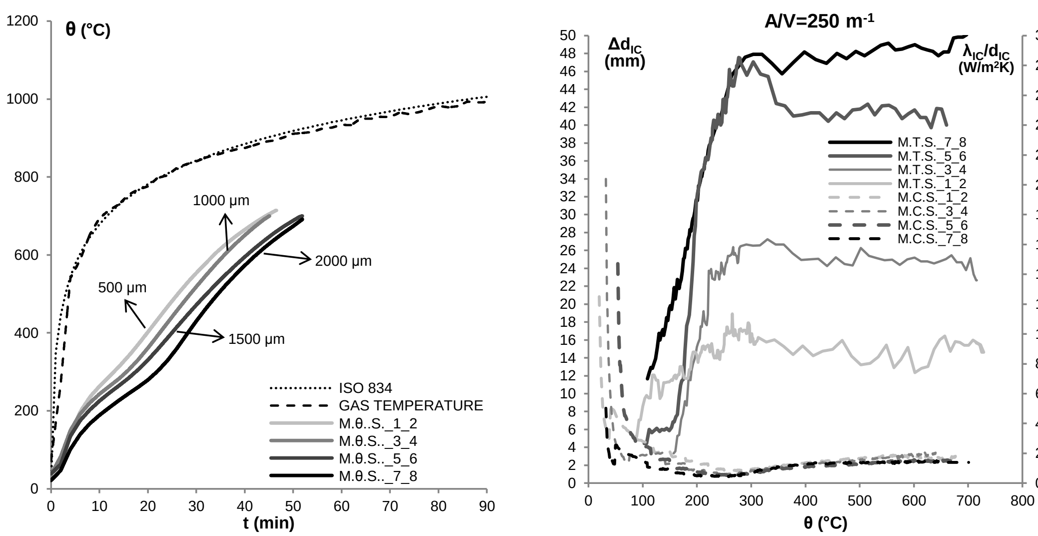

(a) (b)

Figure 8. Results for samples with A/V= 250 m^{-1} -(a) temperatures, (b) thickness variation Δd_{IC} and specific conductivity λ_{IC}/d_{IC}.

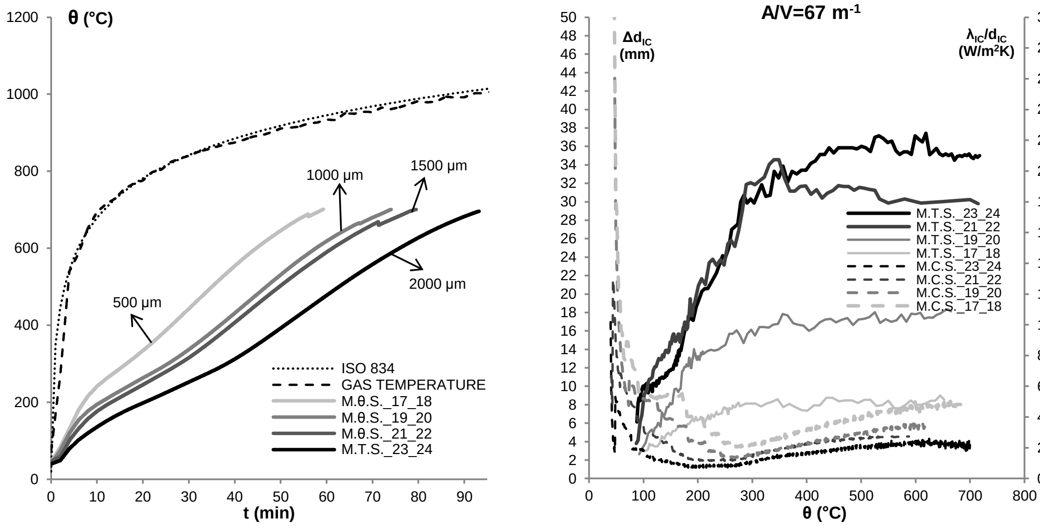

(a) (b)

Figure 9. Results for samples with A/V=67 m^{-1} -(a) temperatures, (b) thickness variation Δd_{IC} and specific conductivity λ_{IC}/d_{IC}.

Figure 8 shows that, for A/V=250 m^{-1}, there is no significant dependence between specific equivalent conductivity and swelled thickness, obtaining an unique trend of conductivity with temperature. However this result is not completely confirmed for A/V=67 m^{-1} (Figure 9). In both cases (Figure 8 and Figure 9), the results show that, although the thickness after about 300°C stabilizes, the equivalent conductivity is not constant with the increase of temperature.

CONCLUSIONS

This work presents an ongoing experimental program to characterize the thermal properties of the IC, starting from the temperatures measured during the tests by thermocouples and thermoplates and from the measurement of the IC thickness variation made during the tests through the Digital Image Correlation (DIC) technique. The experimental results show that:

- small thickness of IC (500 μm) do not react homogeneously for all the section factors
- the equivalent thermal conductivity depends on both the initial thickness and the section factor.

Although the latter outcome could depend on the formula used for the calculation of equivalent conductivity, the direct reading of the thicknesses during the tests allows to verify the real dependency between the swelling phenomenon of IC and the section factors.

The future developments of the experimental program foresee fire tests of specimens with other section factors (e.g. varying the shape of the sample) and also tests with different temperature curves (i.e. the smouldering curve or natural fire curves).

ACKNOWLEDGMENTS

The authors thanks the J.F. AMONN SPA - Divisione Color for the support in performing the experimental tests, and the precious assistance of Giovanni Nava and Mauro Banfi.

REFERENCES

1. Susan M. Neiningera, J.E.J. Staggs, A.R. Horrocks, N.J. Hill, A study of the global kinetics of thermal degradation of a fibre-intumescent mixture. Polymer Degradation and Stability 77 (2002), 187–194.
2. Bilotta A., de Silva D., Nigro E., Ponticelli L., 2015, Tests on intumescent paints for fire protection of existing steel structures. International Fire Safety Symposium IFireSS_2015, 20-22 April 2015, Coimbra, Portugal.
3. Bilotta A., de Silva D., Nigro E. "Structural fire safety of existing steel buildings:possible general approach and application to the case of the intumescent coatings" Applications of Structural Fire Engineering (ASFE), 15-16 October 2015, Dubrovnik, Croatia 80-85.
4. J. Kolšek, P. Češarek, Performance-based fire modelling of intumescent painted steel structures and comparison to EC3. Journal of Constructional Steel Research 104 (2015), 91-103.
5. Jimenez M., Duquesne S. and Bourbigot S., 2006a, Characterization of the performance of an intumescent fire protective coating, Surface&Coatings Technol 201, 979-987.
6. Jimenez M., Duquesne S. and Bourbigot S., 2006b, Intumescent fire protective coating: Toward a better understanding of their mechanism of action, Thermochimica Acta 449, 16-26.
7. Rush D. I., Bisby L. A., Jowsey A. Evaluating design guidance for intumescent fire protection of concrete filled steel hollow sections. Structures in Fire (SIF) Shanghai, China (2014), 1071-1078.
8. EN 13381-8-June 2013-Test methods for determining the contribution to the fire resistance of structural members. Applied reactive protection to steel members.
9. Elliott A., Temple A., Maluk C., and Bisby L. "Novel testing to study the performance of intumescent coatings under non-standard heating regimes" Fire safety science-proceedings of the eleventh international symposium pp. 652-665 copyright © 2014 international association for fire safety science/ doi: 10.3801/iafss.fss.11-652

An Experimental Study of the Damage Modes of Fireproof Coatings Under Complex Loads

S. W. CHEN, Y. J. WANG, L. M. JIANG and A. S. USMANI

ABSTRACT: Fire proof coatings used as passive fire protection in steel structures may sustain damage when subjected to seismic, blast or impact action. Complex states of stress exist within the coating as well as at the interface between the coating and the surface of the steel member. This paper reports an experimental study on damage modes of different fireproof coatings when steel columns under complex loads. Behavior of cementitious coating and intumescent coating are compared. Different failure modes of these two coatings are observed.
Keyword: Cementitious fireproof coating; intumescent fireproof coating; complex loads; failure modes

1 Introduction

Post-earthquake fire is believed to be one of the main secondary disasters after an earthquake[1]. It may cause greater losses than the loss caused by the earthquake itself [2~3]. Steel structures are generally considered to be sustainable because of their light weight, recyclability, good seismic performance and speed of erection, however they are perceived to possess poor fire resistance as at 550℃, the yield strength and ultimate strength may drop to half of those at room temperature[4]. Therefore steel structures unprotected against fire are considered to be vulnerable to elevated temperatures and liable to failure or collapse [4],. The traditional approach to mitigate this vulnerability has been to insulate steel structural members from the effect of fire by using appropriate form of passive fire protection (PFP) material.

Cementitious fireproof coating[5] is one of the most widely used PFP, usually spray applied to structural members to protect steel frames buildings because of its low density, low thermal conductivity (around 0.1 W/m K), low cost and non-toxic emissions in fire. However, this type of fireproofing material is brittle and fragile with a low tensile strength and a great deal of variation in its mechanical properties. Thus, cracking and interfacial debonding may occur under the action of seismic, blast or impact action leading to impaired fire resistance of steel structures [6,7]. Dwaikat and Kodur [8] present parametric studies conducted for modelling the fracture and delamination of cementitious coating on insulated steel plates subjected to static and impact loads based on a mixed 2D cohesive zone finite element (CZFE) scheme.

In recent years, a programme of fundamental research[9-13] has been undertaken by the authors at Tongji University in order to develop a method for evaluating the damage in cementitious coatings on structural steel members subjected to external

Corresponding author: Suwen Chen, PhD, Associate Professor, State Key Laboratory for Disaster Reduction in Civil Engineering, College of Civil Engineering, Tongji University, Shanghai, 200092, P.R. China. Tel: +86-21-65982975-16, Fax: +86-21-65983431, Email:swchen@tongji.edu.cn

Yanjun Wang, MA.Eng, College of Civil Engineering, Tongji University, Shanghai, 200092, P.R. China. Email: 1332732@tongji.edu.cn

Liming Jiang, PhD, Post-Doctoral Research Assistant, Brunel University London, UK. Email: liming.jiang@ed.ac.uk

Asif Usmani, PhD, Professor, Brunel University London, UK. Email: asif.usmani@brunel.ac.uk

loading, including: tests on the mechanical properties of cementitious materials; adhesive properties of the coating to the steel substrate; interlaminar stress analyses on axially and flexurally loaded steel members; monotonic loading tests on cementitious coated steel members under axial loads and under pure bending; and detailed numerical studies.

Cementitious coatings have also been used in industrial environments, such as oil and gas installations, petrochemical and power plants and offshore platforms, however, because of the extreme nature of the fire hazard in such environments, intumescent fireproof coatings are gaining favour. There is very little research data or understanding of the damage mechanisms of intumescent coatings under the action of earthquake, blast or impact loads. In order to assess the residual fire resistance of, say a steel frame having been exposed to some arbitrary seismic action, it is necessary to first understand the damage mechanisms of different types of fireproof coatings under realistic loading conditions. This paper presents an experimental study on this topic.

2 Test set-up

Tests are conducted to study the damage mechanisms of different types of fireproof coatings on steel columns under monotonic loading and under low-frequency cyclic loading. For each type of loading, two types of fireproof coating, cementitious and intumescent, are applied and compared.

2.1 Specimen

Welded Q235 steel columns with a section of H200×150×6×10 (mm) are tested, as shown in Figure 1. The column is rigidly fixed at the end and strengthened with stiffeners to prevent plate buckling at the bottom. A jack is installed at the top of the column to apply lateral load. The height from the loading point to the base of the column is 1.5m.

The cementitious fireproof coating used in the experiment is YC-1 type indoor cementitious fireproof coating provided by Shanghai YiChuan Fireproof Coating Co. Ltd. It is a mixture of vermiculite, perlite, kaolinite, light calcium carbonate, mica, cement, and additive materials. The ratios by weight for coating and the interfacial layer are suggested as, (1) YC-1:water = 1:0.86, and (2) specific interfacial agent: YC-1:water = 1:3:2.5, respectively.

The intumescent fireproof coating used adopts Chartek 1709 provided by the Akzo Nobel International Paint Co. Ltd, which is a thick slurry, solvent-free, two-component coating material, provides both functions of corrosion protection and fire protection and is said to have excellent durability. This coating is applied by professional workers from the company. Specimens with the two different types of coatings used in the tests are shown in Figure 2.

2.2 Experiment device and loading protocol

The experiment was carried out using the 200kN large-scale multi-function structural testing machine at Tongji University. The loading principle and the loading set-up are shown in Figure 3 (a) and (b).

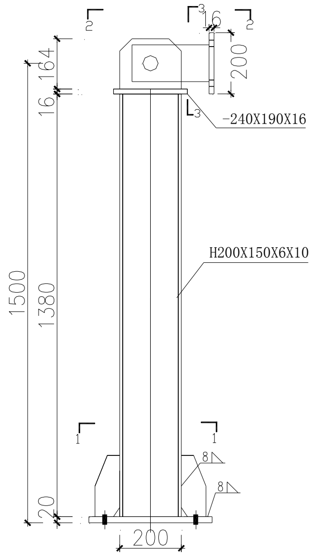

Figure 1. Experimental specimen

Figure 2. Specimens with different types of coating

For monotonic loading, a lateral load P is applied at the top of the column. At first, force control is adopted with each load level incremented by 10kN and maintained for 2 minutes. After the yielding of the steel section at the edges, displacement control loading of 2mm/min is adopted.

Low-frequency cyclic loading is applied according to the FEMA 461 Interim testing protocols for determining the seismic performance characteristics of structural and nonstructural components, using displacement control at the top of the column as shown in Fig. 3(c). The first level of the loading displacement is 7mm, and the displacement value of the following level is 1.4 times of the previous level. When the tested column starts to yield, the growth factor is reduced to 1.3 until the failure of the column. Each displacement load level is repeated three times, and the loading rate is controlled at 45-60min for each level to ensure quasi-static response.

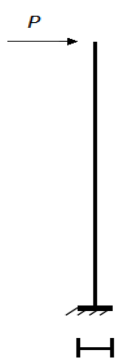

（a）Loading principle

（b）Site photo

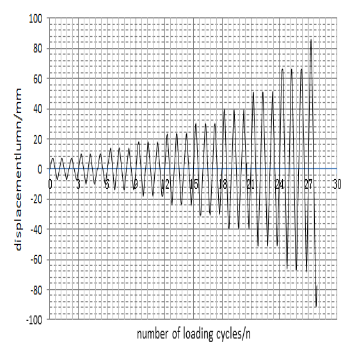

（c）Cyclic loading protocol

Figure 3. Loading set-up

3 Experimental observation and analysis

3.1 Monotonic loading test

The damage occurrence and propagation have been detailed in Table 1 in accordance with story drift ratio Φ, which is defined as $\Phi = \Delta / H$. H is the effective height of the column and the story drift Δ is the displacement measured at the loading point. At first, a full-length diagonal crack appears on the stiffened rib on the compression-side of the specimen when the story drift ratio reaches 0.0041 (as shown in Fig. 4(a)), followed by a number of small transverse cracks of regular spacing on the tension-side flange at level 4 (as shown in Fig. 4(b)). When the story drift ratio reaches 0.0098 (level 6), a large number of transverse cracks appear and a main full-length crack forms at the bottom of the tested column (as shown in Fig. 4(c)). Meanwhile, vertical cracks also appear through the thickness of the compression-side flange. After this the loading method was changed to displacement control at level 7 with story drift ratio of 0.0121. No new cracks appear when the story drift ratio reaches 0.0228 (level 10). With a further increase of story drift ratio, transverse cracks continue to propagate and two main full-length cracks form, and a part of the coating strips on the compression-side flange at bottom due to the buckling of the compression flange of the tested column at the story drift ratio of 0.0449 (level 12). The maximum crack width reaches 1.0mm. The final failure mode is that the coating fractures into several segments with the largest crack appearing at the bottom of the tension-side, and a part of the coating strips and peels off due to the buckling of the compression flange (as shown in Fig. 4(d)).

For the intumescent fireproof coating, there is no damage before the story drift ratio reaches 0.0241 (level 10) when several small cracks appear at first on the stiffened rib of the tension-side (as shown in Fig. 5(a)). When the story drift ratio reaches 0.0483 (level 12), a number of small transverse cracks appear at the bottom of the tension-side flange. Following this, a large number of small horizontal cracks appear and the compression flange of the tested column starts buckling (as shown in Fig. 5(b)). A main full-length crack forms at the bottom of the tested column at the Story drift ratio of 0.0723 (level 14), while the maximum crack width reaches 1.0mm. In the mean time, the compression flange already starts buckling with no visible crack. As the story drift ratio continues to increase, many small transverse cracks connect with each other, forming more full-length cracks (as shown in Fig. 5(c)). Finally, due to the buckling at the compression flange of the tested column, the test was terminated (as shown in Fig. 5(d)). During the whole test, there is no obvious change at the top of the tested column.

（a）diagonal crack （Φ=0.0041） （b）transverse cracks （Φ=0.0057） （c）crack developing （Φ=0.0098） （d）coating peels off （Φ=0.0449）

Figure 4. Damage observation of the cementitious fireproof coating under monotonic loading (Φ means the story drift ratio)

（a）small cracks （Φ=0.0241） （b）flange buckling （Φ=0.0483） （c）full-length crack （Φ=0.0723） （d）buckling （Φ=0.0901）

Figure 5. Damage observation of the intumescent fireproof coating under monotonic loading (Φ means the story drift ratio)

Table 1. Damage propagation related with Story drift ratio under monotonic loading

Load level	Story drift ratio	Damage propagation of cementitious fireproof coating
3	0.0041	Diagonal crack appears at first on the stiffened rib
4	0.0057	Many small transverse cracks appear at regular intervals
6	0.0098	Full-length transverse crack form and vertical cracks appear
7	0.0121	Loading method is changed to displacement control
10	0.0228	Cracks develop completely
12	0.0449	Cracks propagates and a part of the coating peels off
Load level	Story drift ratio	Damage propagation of intumescent fireproof coating
10	0.0241	Some small cracks appear at first on the stiffened rib
12	0.0483	A number of small transverse cracks appear
14	0.0723	Full-length crack formed
15	0.0901	Cracks connect with each other forming full-length cracks

3.2 Low-frequency cyclic loading test

In order to facilitate the description, the two surfaces of the specimen are here denoted as A and B (A refers to the front flange and B is the back flange in forward loading). Each load level has also been numbered. For an example, 4-2-F means forward loading to the second cycle of the fourth level (Surface A is in compression and Surface B is in tension), and 5-3-B means backward loading to the third cycle of the fifth level (Surface A is in tension and Surface B is in compression).

The damage propagation for the case of cyclic loading test has been detailed in Table 2. When the story drift ratio reaches 0.0056 (level of 2-1-F), a number of small transverse cracks with regular intervals rapidly appear at the bottom of surface B (as shown in Fig. 6(a)) but with no cracks on surface A. When loading to the level of 2-1-B, the cracks appearing at surface B in forward loading are fully closed, new transverse cracks appear at regular intervals at the bottom of surface A and continue to expand with the widest crack of about 0.1mm width appearing at the bottom of the tested column. When the story drift ratio reaches 0.0101(level 4-3-B), three vertical cracks appear at the bottom of surface B and the cracks on surface A develop completely with no new cracks appearing. With further loading, cracks continue to expand. When the story drift ratio reaches 0.0425 (level 9), the coating cut by the largest transverse crack at the bottom and the two vertical cracks formed on both sides of the compression flange peels off, at the same time, the coating along the thickness of the compression-side flange break (as shown in Fig. 6(b)). The final failure mode is similar to those of the cementitious coatings under monotonic loading except that cracks appear at lower load levels (as shown in Fig. 6(c)) under cyclic loading.

For the intumescent fireproof coating, there is no visible crack before the story drift ratio reaches 0.0173 (level 6). Then, some small cracks (about 0.1mm) appear at first on the stiffened rib of the tension-side, which will close completely when compressed. With a further increase of story drift ratio, cracks continue to develop slowly. Finally, the tension-side flange of the tested column is damaged with an obvious tearing sound, which leads to a rapid decrease of load bearing capacity. Hence the test was terminated. During the whole loading period, only a few small cracks appear at the bottom of the tested column (as shown in Fig. 6(d)).

（a） transverse cracks （Φ=0.0056） （b） coating peels off （Φ=0.0425） （c） broken （Φ=0.0425） （d） broken （Φ=0.0425）

Figure 6. The coating damage phenomenon under low-frequency cyclic loading (Φ means the story drift ratio)

Table 2. Damage propagation related with Story drift ratio under low-frequency cyclic loading

Load level	Story drift ratio	Damage propagation of cementitious fireproof coating
2-1	0.0056	Transverse cracks appear at regular intervals at B surface
2-(1)	0.0056	Transverse cracks appear at regular intervals at A surface
4-(3)	0.0101	Three vertical cracks appear at the bottom of B surface
5	0.0130	Cracks develop completely and expanding
9	0.0425	Peel off of coatings
Load level	Story drift ratio	Damage propagation of intumescent fireproof coating
6	0.0173	Some small cracks appear at first on the stiffened rib
9	0.0425	Flange fracture

3.3 Analysis of the experiment results

The load-displacement curve in Figure 7 illustrates the complete monotonic loading process. From the curve, it is found that the displacement increases linearly at the initial stage of loading. The specimen begins to yield when the lateral load increases to 80kN(story drift ratio of 0.0150), as the ultimate load bearing capacity is 104.9kN (story drift ratio of 0.0701).

For the cementitious fireproof coating, the strains in the coating at the bottom of the column flange surface change linearly with the loading at first (as shown in Fig. 9), regardless of whether it is in the compression zone or in the tension zone. As the story drift ratio reaches 0.0041(about 30kN)，the strains on the tension side of the coating surface begin to decrease due to cracks in the coatings. After yielding of the steel specimen (80kN), the strains on the compression-side also change but no longer linearly.

For the intumescent fireproof coating, because of its good mechanical properties, the strains of coating agrees well with the strains at the bottom of the column flange surface (as shown in Fig. 8). The strains, whether it is in the compression zone or in the tension zone, change linearly before the yield load, followed by rapid increases until the strain gauges get damaged when the load reaches the ultimate load.

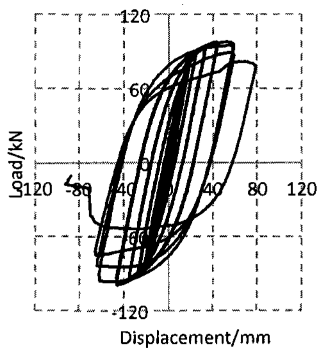

Fig7. Load-displacement curve

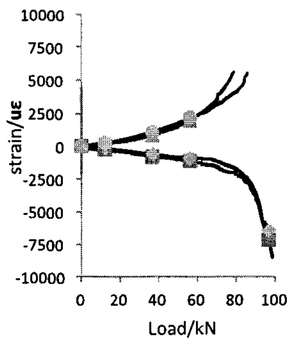

Fig8. Strain-load curve of steel

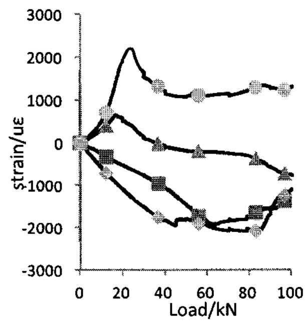

Fig9. Strain-load curve of cementitious coating

The hysteretic curve in Fig.10 illustrates the complete low-frequency cyclic loading process. The strains at the bottom of the intumescent coating surface vary in a similar manner to those of the column flange surface (as shown in Fig. 11), which change linearly with the load at low load levels. In the subsequent loading cycles, the curve shows a good hysteretic phenomenon. The strains at the bottom of the cementitious fireproof coating surface don't show a hysteretic phenomenon (as shown in Fig. 12).

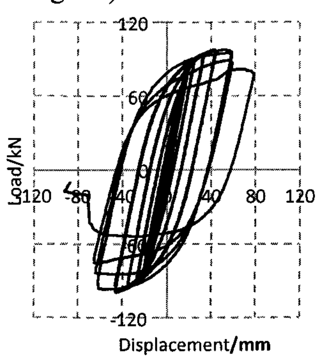

Fig10. Hysteretic curve

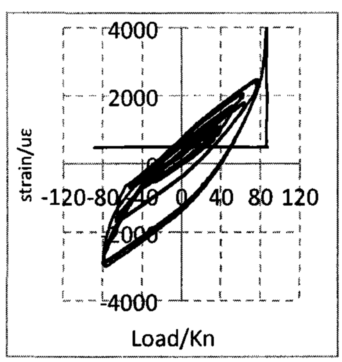

Fig11. Strain-load curve of steel

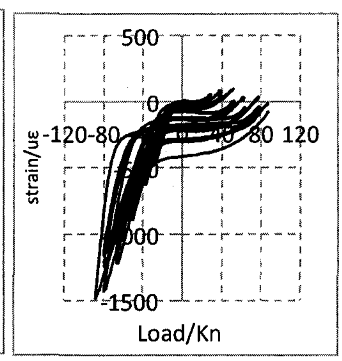

Fig12. Strain-load curve of coating

4 Summary

Experiment based studies have been conducted for investigating the damage mechanisms of two different types of fireproof coatings on steel columns under complex and realistic loads. The main findings are listed as follows.

1) Under monotonic loading for cementitious fireproof coating, cracks appear at first at regular intervals on the tension-side flange and continue to develop until the largest crack appears at the bottom of the tested column. It is followed by vertical cracks which occur on the compression-side flange at the bottom. The final failure mode is that the coating fractures into several segments with the largest crack

appearing at the bottom of the tension-side, and a part of the coating strips and peels off due to the buckling of the compression flange of the tested column. For intumescent fireproof coating, the damage modes are similar to those of the cementitious coating except that the crack widths are smaller and no coating peels off on the compression side due to the ductility of this coating.

2) Under low-frequency cyclic loading, the final failure mode of cementitious coatings is similar to the case of monotonic loading except that cracks appear at lower load levels. A better performance is again observed for the intumescent coatings compared to the cementitious coatings.

Findings from this study lay down the foundation for developing practical methods to determine the condition of both cementitious fireproof coatings and intumescent fireproof coatings on steel framed structures after a short duration extreme loading event, which may result in minimal external damage to the building (earthquake, blast, windstorms) or long duration cumulative damage from routine and moderate levels of repeated non-monotonic loading.

REFERENCES

1. Li J, Li GQ. A research on the prediction model of earthquake-aroused fire disaster. Earthquake research in China,1992,Vol.8(1):76~82（in chinese）
2. Izuru Takewaki. Preliminary report of the 2011 off the Pacific coast of Tohoku Earthquake. Journal of Zhejiang University-Science A,Vol.12(5):327~334
3. NIED (National Research Institute for Earth Science and Disaster Prevention). 2011 Off the Pacific Coast of Tohoku earthquake. (in japanese),2011
4. Li GQ, Han LH, Lou GB, Jiang SC. 2006. Fire resistant design for steel structure and steel-concert composite structure, China Architectural Building Press. （in chinese）
5. Falconer D F & Cihomsky J. Intumescent fire protection adds. decorative flair to steel structures1Paint & Coatings Ind. , 1993 ,9 (10) :38～401
6. Chen SW, Jin C, Li GQ. A study on damage mechanism of thick fireproof coating for steel member subjected to monotonic loading. In: Structures in fire: proceedings of the sixth international conference; 2010, p. 130.
7. Braxtan NL and Pessiki S (2011) Bond performance of SFRM on steel plates subjected to tensile yielding. Journal of Fire Protection Engineering 21(1): 37–55.
8. Dwaikat M, Kodur V. Modeling fracture and delamination of spray-applied fire-resisting materials under static and impact loads. J Eng Mech 2011;137(12):901–10.
9. Jin C. Research on the failure mode and damage mechanism of the thick fireproof coating for steel member under monotonic loading (MSc thesis). College of Civil Engineering, Tongji University (in Chinese); 2011.
10. Jiang LM. Numerical simulation and study on the damage of the thick fireproof coating for steel member under monotonic loading (MSc thesis). College of Civil Engineering, Tongji University (in Chinese); 2012.
11. Chen SW, Jiang LM, Asif Usmani, Li GQ. Experiemental and numerical studies on damage mechanisms in cementitious coatings on structural steel members. 8th International Conference on Strutures in Fire Shanghai, China, June 11-13, 2014.
12. Chen SW, Jiang LM, Asif Usmani, Li GQ, Jin C. Damage mechanisms in cementitious coatings on steel members under axial loading. Construction and Building Materials 90 (2015) 18 – 35.
13. Chen SW, Jiang LM, Asif Usmani, Li GQ. Damage mechanisms in cementitious coatings on steel members in bending. Structures and Buildings, Volume 168 Issue SB5 May 2015, 351 – 369

Fire Tests of Reactive Fire Protection Systems Applied to Steel Tension Members with Solid Circular Section

DUSTIN HÄßLER and SASCHA HOTHAN

ABSTRACT

In civil engineering, steel tension members are normally used for bracings, suspensions and underbracing systems. Typically, slim circular solid sections (CSS) are used for such tension members. However, sufficient knowledge about the performance of reactive fire protection systems (RFPS) applied to solid steel tension members has so far been missing. The application of RFPS on such members was not covered by national German approvals (abZ) as well as European technical assessments (ETA) and therefore only possible by approvals in individual case by the building authority. This paper describes the world's first scientifically investigated fire tests of RFPS applied to steel tension members with CSS. The influence of various parameters such as profile geometry, dry film thickness of the RFPS, level of the load utilization as well as member orientation was tested. In addition, the foaming and cracking behaviour and thermal protection of the RFPS used are investigated and failure mechanisms are identified. To measure the steel temperature of the tension member without weakening the cross-section a special method for the application of thermocouples was developed. The fire tests show that an application of RFPS on steel tension members with solid section is generally possible. However, due to the slim cross-sections and the missing possibility of load distribution within the tension member, high requirements are placed particularly on the effectiveness and reliability of the RFPS. In particular, the testing of mechanically loaded tension members is essential, since the necessary three-dimensional foaming results in the highest stress level for the RFPS. The findings obtained from the performed fire tests are of general nature. Recommendations for the testing and assessment of RFPS applied to steel tension members with solid section are briefly described in this paper and explained in detail in [1] and [2]. Based on this research, the German building authority (DIBt) has defined national approval guidelines for the testing and the assessment of RFPS applied to tension members with solid section. Since November 2015, a general building approval for a RFPS is available in Germany [3].

Bundesanstalt für Materialforschung und –prüfung (BAM), Unter den Eichen 87, 12200, Berlin, Germany.

INTRODUCTION

Reactive fire protection systems (RFPS) are used to increase the fire resistance of steel members. The architectural appearance of the construction can be maintained. The use of these products is usually regulated by abZ in Germany and ETA in Europe. However, the application of RFPS on steel tension members with solid section is currently not regulated in Germany or Europe [4] and [5], as normative guidelines for the testing of steel tension members with RFPS do not exist. So far the performance of RFPS applied to steel tension members with solid sections has not been analysed, and test data are not available.

In this paper, the world's first scientifically investigated fire tests of RFPS applied to steel tension members with circular solid section (CSS) are described. The fire tests are part of a research project [2] that aims to give recommendations for the testing and the assessment of RFPS applied to steel tension members with solid section. Thus the research serves as a basis for an extension of the scope of application of RFPS for such members. The results are provided in [1] and [2] that are currently only available in German. This paper intends to share the new findings with interested researchers internationally and to contribute to the current on-going development of the international standardization for the testing and the assessment of RFPS on solid steel members in tension, i.e. pr ISO/IEC WD 834-14 [6] and pr EN 13381-10 [7].

The paper focuses on the description of the experimental setup, testing procedure as well as the assessment of the performed fire tests. In particular, the influence of the diameter of the tension member, the dry film thickness of the RFPS and tensile stress level are investigated. Moreover, the cracking, crack healing and foaming behaviour of the RFPS as well as the heating and the steel temperatures are analysed. Material testing for the steel used in the fire tests as well as numerical simulations is addressed in [1] and [2].

DESCRIPTION OF THE FIRE TESTS

Specimens

The fire tests were carried out in real scale. Because relatively filigree profiles are generally used for tension members and expected high demands of the RFPS at curved surfaces, steel members with CSS and a diameter of 20 and 30 mm (D20 and D30) were tested. The solid sections consist of cold-drawn steel of strength class S355. The dimension and material properties of the steel sections are given in Table I.

TABLE I. STEEL MEMBERS USED IN THE FIRE TESTS

Profile type	CSS D20	CSS D30
Rod diameter	20 mm	30 mm
Section factor	200 m^{-1}	133 m^{-1}
Material	cold-drawn steel S355 J2C +C	cold-drawn steel S355 J2C +C
Strength at 20°C	585 N/mm² / 679 N/mm²	570 N/mm² / 661 N/mm²
Note: Steel members with the same profile are taken from the same batch and have therefore identical material properties. The steel strength is determined by small-scale material tests. The first strength value refers to the 0.2%-proof strength and the second value to the tensile strength.		

TABLE II. TESTING PROGRAMME FOR THE FIRE TESTS

Profile	Test series (TS)	Mechanically unloaded tension members	Mechanically loaded tension members
CSS D20	TS a (DFT = 1.5 mm)*	4 specimens	8 specimens, μ_{fi} = 0.15 - 0.45
	TS b (DFT = 2.5 mm)	4 specimens	8 specimens, μ_{fi} = 0.15 - 0.65
	TS c (DFT = 3.5 mm)	4 specimens	8 specimens, μ_{fi} = 0.15 - 0.65
CSS D30	TS d (DFT = 2.5 mm)	4 specimens	6 specimens, μ_{fi} = 0.15 - 0.65
	TS e (DFT = 3.5 mm)	4 specimens	6 specimens, μ_{fi} = 0.15 - 0.65

* A number of three mechanically loaded specimens were tested with an increased DFT of 3.0, 4.0 and 4.5 mm and μ_{fi} = 0.45.
μ_{fi} is the load utilisation factor in case of fire. A fully utilised tension member has a load utilisation factor of μ_{fi} = 0.65.
In each TS two unloaded specimens are tested in vertical direction and all other loaded and unloaded specimens are tested in horizontal direction.
Information regarding the name and specification of each specimen is given in the research report [2].

For comparability, all fire tests were carried out with the same RFPS that is a water-based conventional product with a valid European technical assessment [8]. The experimental program was designed such that the different factors that influence the behaviour of the RFPS, i.e. profile geometry of the tension member, dry film thickness (DFT) of the RFPS and the tensile stress level in terms of the load utilization factor in case of fire μ_{fi}, can be specifically examined and evaluated. Specimens with the same dry film thickness of the RFPS are summarised in a test series (TS). An overview of the testing programme is given in Table II. To analyse the effect of the tensile stress level, two types of specimens were tested: mechanically loaded and unloaded tension members. In total, 36 mechanically loaded and 20 unloaded steel tension members with RFPS were tested. In general, the tension members are tested in horizontal orientation. However, in order to identify the effect of the orientation of the tension members two mechanically unloaded specimens of each test series are tested in vertical direction.

Because negative effects of the mechanical tensile load on the performance of the RFPS are expected, the test programme consists mainly of mechanically loaded specimens. The load utilisation of the loaded tension members is varied from μ_{fi} = 0.15 (low capacity) to 0.65 (full capacity) at an interval of usually 0.1. In addition to the amount of the applied tensile load, also an influence of the timing of the load is suspected. In the fire tests the tension members are first coated with the RFPS, i.e. factory coating, and after curing the mechanical tensile load is applied. In addition to various practical considerations, such as the better application conditions of the coating at the factory, it is suspected that the application of the tensile load results in the formation of micro-cracks in the hardened intumescent coating, which can have a negative effect on the foaming behaviour of the RFPS and thus represents the most critical case.

Application of the thermocouples for the temperature measurement

To assess the thermal protection of the RFPS and thus the fire resistance of the tension members, thermocouples (TC) were attached to the steel surface in a longitudinal distance of 150 mm to measure the steel temperature during the fire test. The attachment is done before the application of the RFPS. The measuring point is designed in such a way that the foaming behaviour and the thermal protection of the RFPS is only marginally influenced. To measure the steel temperature usually mineral-insulated stainless steel sheathed thermocouples are used. These thermocouples are attached to the steel member by small bore holes. For steel beams and columns in general, relatively large profiles are used and thus the cross-sectional weakening at the measurement points can be neglected. However, for the slim profiles typically used for tension members, this type of application of thermocouples result in a local defect that can affect the time and location of the fracture of the mechanically loaded specimens. In addition, due to the higher stiffness of these cables, it is very difficult to remove the surplus RFPS from the mineral-insulated stainless steel sheathed thermocouple cables before the fire test. Furthermore, the missing strain relief of this application method carries also the risk of a dissolution of the cable from the specimen.

In order to consider the points mentioned above, a special technique for the application of thermocouples was developed. Conventional type K thermocouple cables with a fire resistance up to 1200 °C, a wire diameter of 0.5 mm and a ceramic fibre sheath are used. To minimise interferences of the thermocouple cable to the foaming behaviour of the RFPS, a relatively compact cable with a small total diameter, i.e. about 2.2 to 2.8 mm, is selected. A heat shrink tubing at the end of the cable prevents unravelling of the ceramic fibres. The thermocouples are attached to the surface of the steel member by using a spot welder. This method has the advantage that the cross-section of the steel member remains undamaged. To avoid a breaking of the thermocouple cable from the steel member a tight-fitting thin wire is winded and welded over a length of about 3 cm along the thermocouple cable (see Figure 1). The wire serves as a strain relief and fixes the thermocouple. In order to minimize the influence on the foaming of the RFPS, the thermocouple cable is led away after the strain relief perpendicular from the steel member. At the tension member, the temperature measurement stations are positioned in a row along the rod axis of the tension member. Due to the good thermal conduction of steel and the small diameter of the selected CSS it can be assumed that the surface temperature is equal to the core temperature of the specimen. Therefore, one thermocouple per measurement station is sufficient. To detect local temperature differences along the steel tension member, which can result from the foaming and cracking behaviour of the RFPS, the distance between the thermocouples is defined to 150 mm (see Figure 2). For additional measurement of the steel temperature of the mechanically loaded tension member outside of the furnace, additional four thermocouples (TC 8 – TC 11 according to Figure 1) are attached.

To obtain representative results of the steel temperature, a concentration of RFPS at the measurement station must be avoided. Therefore, prior to the fire test, the RFPS is removed from the thermocouple cable (see Figure 3). Due to the flexible structure of the thermocouple cable sheathed with ceramic fibre and the strain relief at the measuring station, the surplus RFPS can be easily removed without risking a breakage of the cable from the specimen. Fire tests of steel tension members showed that the foaming of the RFPS at the area of the measurement station is hardly affected by the thermocouple (see Figure 3). Therefore, the developed method for attaching thermocouples sheathed with ceramic fibres at the surface of steel member has proved its applicability. Detailed information regarding the application method and the performed fire tests are described in [1] and [2].

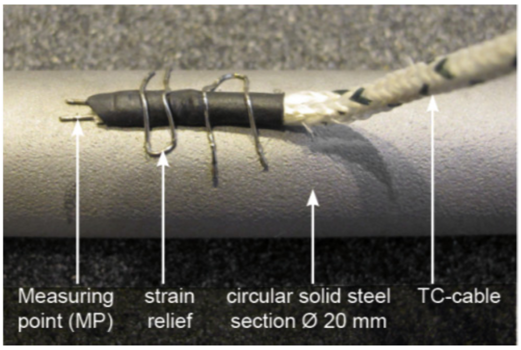

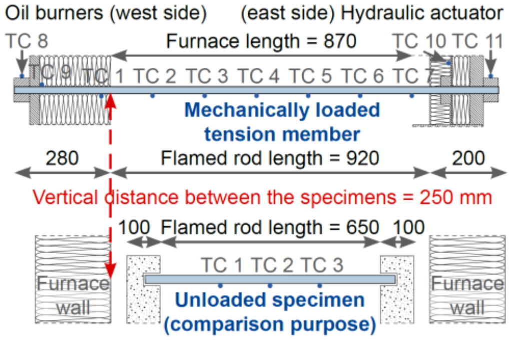

Figure 1. Thermocouple application method for steel members with solid section [1]

Figure 2. Drawing of mechanically loaded and unloaded tension members in horizontal position [1]

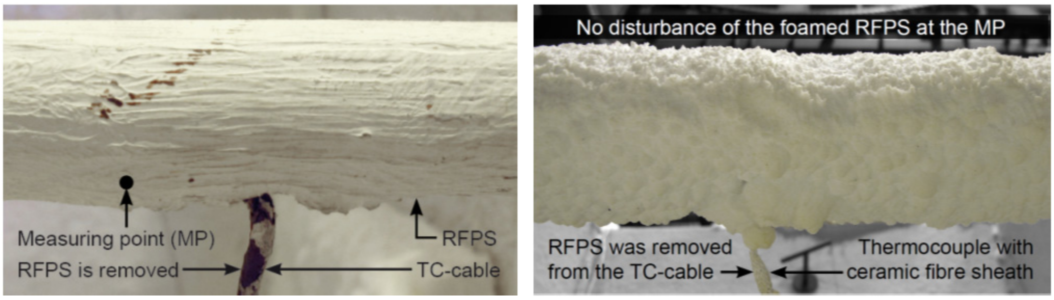

Figure 3. Steel temperature measuring point before (left) and after (right) the fire test [1]

Experimental setup

To perform the mechanically loaded and unloaded fire tests on tension members a special testing bay was developed and mounted within the horizontal furnace of BAM (see Figure 4). The device consists of a horizontal steel frame, i.e. load frame, and a furnace of about 1.0 × 1.5 × 1.5 m. For applying the tensile force to the specimen, at one side of the steel frame a servo-hydraulic actuator with a maximum tensile force of 400 kN is attached. By using special connections the mechanically loaded tension member can be attached to the actuator (east side) and the load frame (west side). Due to the self-contained load frame, the furnace remains unstressed. The testing bay is designed such that steel tension members with different profile sections, e.g. solid, open and closed cross-section can be tested. The tension members can be exposed to standard ISO fire curve [9] over a length of about 1 m. Two oil burners are used to heat the furnace. The oil burners are located at the west side of the furnace.

The mechanically loaded specimen is located between the axes of the burners to direct impingement. To avoid shadowing effects unloaded specimens in horizontal direction are installed parallel to the mechanically loaded tension member in a horizontal and vertical distance of 250 mm. This also complies with the regulations in DIN EN 13381-8 [10]. In order to minimize an influence on the formation of longitudinal cracks on the top of horizontally installed tension members and an associated possible sliding down of the RFPS during the fire test, the thermocouples are generally arranged at the bottom of the rod. Unloaded specimens in vertical direction are located in a vertical distance of the 150 mm from the mechanically loaded specimen.

The combustion gases are exhausted through ducts at the bottom of the furnace. A heat-resistant window at the south side of the furnace allows the observation of the specimens during the fire tests. The top of the furnace is sealed by three reinforced cellular concrete slabs. The gas-temperatures are measured according to DIN EN 1361-1 [9]. Two plate thermocouples are positioned along each specimen in a horizontal distance of about 100 mm. Due to the existing dimensions of the furnace the lateral distance between the plate thermocouples and the furnace wall as well as the distance between the two plate thermocouples, which is according to the standard 450 mm, is reduced to about 300 mm.

Performance of the fire tests

After installing the specimens, the thermocouples are connected to the measuring system. Before the start of the fire test, the specimens are checked for damages or abnormalities. The applied tensile load (F) is calculated using the actual 0.2%-proof stress ($f_{p0.2}$) at room temperature of the steel used for the tension members, the rod diameter (d) and the selected load utilisation factor in case of fire (μ_{fi}) (see Equation 1). Since the fire tests on mechanically loaded tension members with RFPS are comparable with in-stationary tensile tests at elevated temperature, the applied tensile load is kept constant over the entire test. During the fire test, the amount of the applied tensile load as well as the gas and specimen steel temperatures is measured. Furthermore, the foaming of the RFPS is recorded on video. Fire test with a loaded specimen tested alone end with the rupture of the member. Tests including an unloaded specimen also have to reach a maximum steel temperature of 750 °C. This requirement is based on the fact that for temperatures exceeding 750 °C, the strength of the steel is very low and thus the tension member most likely loses its static function within the structure. After the fire test, by the help of a thin wire, the height of the foamed RFPS is measured and documented along the specimens. Furthermore, the change in length and the necking area of the tension member are measured. Detailed information regarding the results of the fire tests can be found in [1] and [2].

$$F = f_{p0.2} \cdot \mu_{fi} \cdot \pi \cdot d^2 / 4 \qquad (1)$$

RESULTS OF THE FIRE TESTS

The assessment of the fire tests has shown that the profile geometry, the dry film thickness of the coating, the tensile stress and the orientation direction of the tension member have a significant influence on the thermal protection of the RFPS. In addition, these factors interact with each another. The effect of the different factors is schematically shown in Figure 5. Generally, the fire resistance of the tension member can be improved by an increase of the rod diameter or a reduction of the profile factor, a higher dry film thickness of the intumescent coating or by lowering the tensile stress level. Moreover, the thermal protection of the RFPS is usually better at horizontally than vertical orientated tension members.

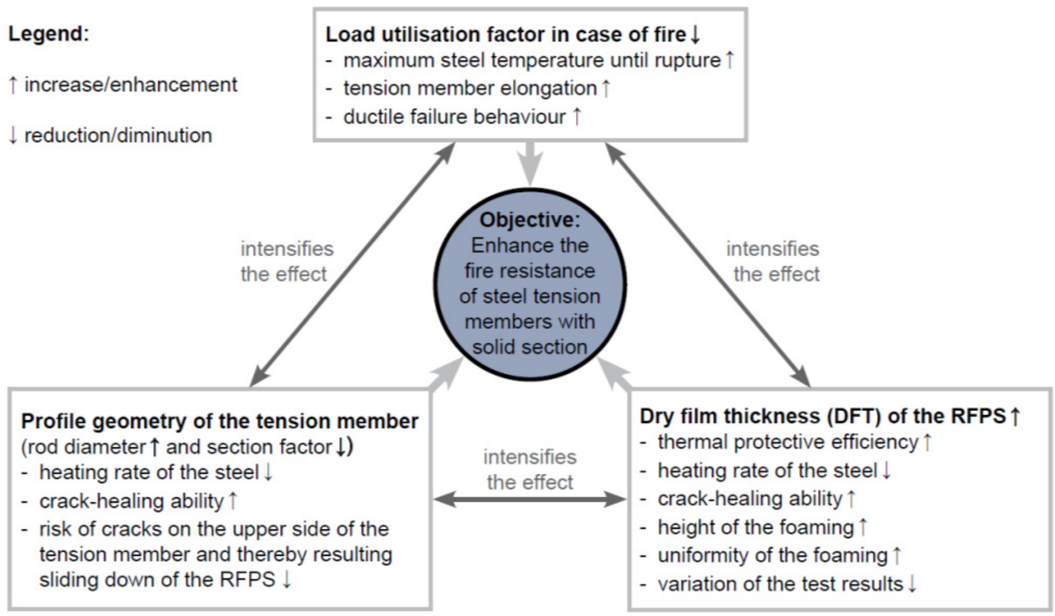

Figure 5. Effect of the dry film thickness, profile geometry and load utilization in case of fire to the fire resistance of steel tension members with solid section [1]

The fire tests also show that an application of RFPS to tension members with CSS is basically possible. Furthermore, the fire resistance of such members can be significantly increased. However, due to the relatively slim cross-sections typically used for steel tension members and the missing possibility of load redistribution within the tension member, high requirements are placed particularly on the effectiveness and reliability of the RFPS. In the fire tests, especially the cracking and foaming behaviour and the thermal protection of the RFPS as well as the time til rupture and the heating rate of the tension members are analysed. Due to the curved surface and the tensile stress, mechanically loaded tension member with CSS in case of fire requires a three-dimensional extension of the RFPS, which represents the highest stress level on the system. As a result in the fire tests, mechanically loaded tension members show a more distinctive cracking of the RFPS (see Figure 6). The longitudinal and transverse cracks reduce the thermal protection of the foamed RFPS. At some mechanically loaded specimens also a partial sliding down of the foaming RFPS occurred (see Figure 7). Due to the cracks in the foamed RFPS, mechanically loaded tension members have generally higher temperatures than unloaded specimens that were simultaneously tested (see Figure 8). Therefore, the fire resistance of loaded tension members is reduced more significantly. In order to analyse and assess the fire resistance of RFPS fire tests on mechanically loaded tension members are essential.

ACKNOWLEDGEMENTS

The German Institute for Building Technology (DIBt) is gratefully acknowledged for the financial support of the research project [2].

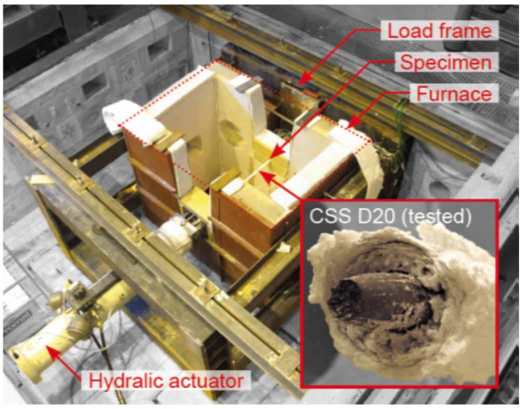

Figure 4. Experimental setup of the rod-testing furnace; tension member with foamed RFPS [1]

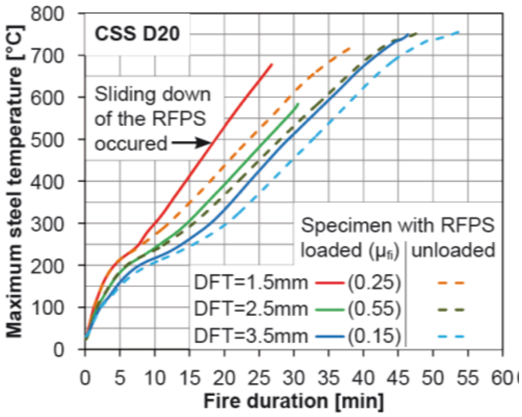

Figure 8. Max. steel temperature of mech. loaded and unloaded specimens [1]

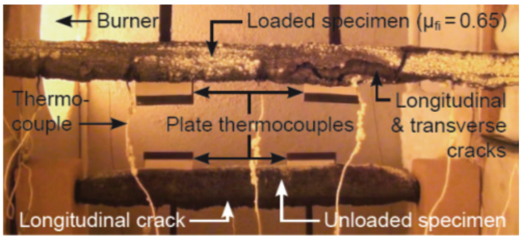

Figure 6. Foaming and cracking behaviour of the RFPS on tension members with CSS [1]

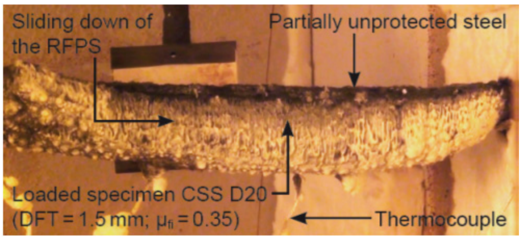

Figure 7. Partially sliding down of the RFPS on a mechanically loaded tension member [1]

REFERENCES

1. Häßler, D. 2016. "Verhalten reaktiver Brandschutzsysteme auf kreisrunden Zuggliedern aus Blank- und Baustahl," Dissertation, Leibniz Universität Hannover, Hannover, submitted January 2016.
2. Hothan, S. and D. Häßler. 2015. "Numerische und versuchstechnische Untersuchung zur Anwendung von reaktiven Brandschutzsystemen auf Zuggliedern aus Stahl," Research report, Berlin, Bundesanstalt für Materialforschung und –prüfung (BAM).
3. AbZ Nr. Z-19.11-2194. November 2015. "Allgemeine bauaufsichtliche Zulassung für das reaktive Brandschutzsystem "Hensotherm® 420 KS" zur Anwendung auf Stahlzuggliedern," DIBt, Berlin.
4. Hothan, S. and D. Häßler. 2012. "Zur Anwendung reaktiver Brandschutzsysteme auf Stahlzuggliedern. Bauphysik," Vol. 6, pp. 275-285, Berlin, Ernst & Sohn.
5. Häßler, D. and S. Hothan. 2013. "Numerical and experimental analysis of reactive fire protection systems applied to solid steel rods in tension," Applications of structural fire engineering conference, pp. 454-460, Prague.
6. pr ISO/IEC WD 834-14. October 2015. "Fire resistance tests - Elements of building constructions – Part 14: Specific requirements for the testing and assessment of applied fire protection to solid steel bar," International Organization for Standardization: Technical Committee ISO/IEC TC92/SC 2.
7. pr EN 13381-10. November 2015. "Test methods for determining the contribution to the fire resistance of structural members – Part 10: Applied protection to solid steel rods," CEN – European Committee for Standardization: Technical Committee CEN/TC 127.
8. ETA-12/0050. March 2013. "European Technical Approval for the reactive fire protection system „HENSOTHERM® 420 KS". Warrington Certification Limited, Warrington.
9. DIN EN 1363-1. October 2012. "Fire resistance tests. Part 1: General Requirements," Beuth, Berlin.
10. DIN EN 13381-8. August 2013. "Test methods for determining the contribution to the fire resistance of structural members. Part 8: Applied reactive protection to steel members," Beuth, Berlin.

Numerical Investigation of Plasterboard Partitions Subjected to Fire: Confrontation between Numerical and Experimental Results

GUILLAUME CUEFF and GILDAS AUGUIN

ABSTRACT

Plasterboard partitions which are widely used in construction have to satisfy technical approval for fire safety requirements from regulations. These fire safety approvals are generally evaluated from fire resistance tests performed in accredited laboratory. The dimensions of fire resistance furnace are a limitation to test and to approve high rise plasterboard partitions. In this context, a research program was initiated by Efectis whose main objective is to develop a numerical model for simulating a fire resistance test on plasterboard partitions. Based on simulated temperature field and estimation of the global bending of the partition wall, the model can predict collapse of height extension plasterboard partition in order to validate the fire resistance of high partition walls. In this paper, a thermo-mechanical model applied to plasterboard partitions is first presented. Simulation results of fire resistance tests on two plasterboard partitions under standard fire curve ISO-834-1 are detailed. Then, application of the model to height extensions and evaluation of fire performance are presented.

INTRODUCTION

Plasterboard partitions, widely used in building construction, have to satisfy technical approvals, but also fire requirements for the safety regulations [1]. The fire resistance of plasterboard partition walls is generally assessed thanks to tests in laboratory [2]. Fire resistance tests are based on a complex protocol: full size samples are placed in large furnaces able to reproduce severe fire aggressions. During this test, criteria such as load-bearing stability, thermal insulation and integrity of the plasterboard partition are evaluated. The multiplication of such tests is not an easy task and could be costly to finalize new products. Moreover, the limited dimensions of fire resistance furnaces are a restraint to validate high-rise partition walls.

In that context, the use of simulation tools can be a complement to experimental

Guillaume Cueff, Efectis France, 19/23 Quai de Paludate, F-33800 Bordeaux, France.
Gildas Auguin, Efectis France, Route de l'Orme des merisiers, Espace Technologique, F-91193 Saint-Aubin France

tests. The concept of "Virtual Furnace" is therefore developed in some laboratories in order to model a fire resistance test and to predict thermo-mechanical behavior of the tested product. Using a "virtual furnace" permits exhaustive analyze and to evaluate a large number of technical alternatives. Notably, this approach allows to validate dimensional extensions of a partition wall on the basis of a conclusive fire resistance test with standard dimensions.

The work presented in this paper is a part of the R&D project so-called VIRGILE (Virtual Facilities of Fire Resistance Testing) of Efectis France (A French fire safety laboratory), and based on PhD works [3]. VIRGILE aims to create simulation tools to reproduce standard fire resistance tests of products by taking into account interaction between products and furnace. The main objective of the thesis was to develop a numerical model able to simulate the thermo-mechanical behavior of plasterboard partitions under fire tests. Plasterboard partitions are designed by considering regularly spaced steel studs, fixed in one or both ends to the side wall, on which one or two facings of plasterboard (each composed of a single or a double layer of plasterboard) are fixed with screws. Steel studs, usually with a C-section or I-section, play the role of a supporting frame and the plasterboard is use to compartmentalize space. The main benefits of these products are: lightweight, easy to install and high fire resistance performances.

In the first part of the paper, the thermo-mechanical model is presented. In the second part, simulation results are compared to experimental results from real fire resistance tests carried out in Efectis France Laboratory where products were exposed to the standard fire ISO curve 834-1 in a vertical furnace [1]. Two different fire resistance tests are performed: one plasterboard partition with a height of 4.9 m and a second one of 3 m high. In the third part of the paper, the reference model is applied to height dimension extension of plasterboard partitions to evaluate fire performance of high-rise partition walls. Collapse phenomena of these extension cases are determined thanks to failure criteria established from initial partition wall simulations.

NUMERICAL MODELS

The model takes into account evolution of physical and mechanical properties of materials (gypsum and steel) at high temperatures. The thermal model used to simulate heat transfer through plasterboard at high temperature is first presented. If needed, interspace void between facings can be simulated, as well as the fall of facings, to adapt the model to the real plasterboard partition configuration. Then a mechanical model is exposed that takes into account a specific procedure to simulate screw stiffness evolutions between plasterboard and steel studs as a function of mechanical strain.

Calculations are performed on the finite element code CAST3M [4] in which specific procedures can be added for modelling the physical-chemical transformations of a material at high temperature, and their effects on its thermo-mechanical properties.

Heat Transfer Model

The heat transfer by conduction inside the solid is resolved using the Fourier law (1).

$$\rho C_p \frac{\mathrm{dT}}{\mathrm{dt}} = \nabla(\lambda \nabla T) \tag{1}$$

For simulation of thermal transfers through plasterboard partition, following assumptions are made: i/ The temperature field is uniform throughout the height of the plasterboard partition. This assumption leads to a 2D thermal model instead of a 3D one, which reduces largely the computation time. ii/ Double plasterboard layers constituting facings can be considered as an equivalent homogeneous material. iii/ Contacts between the different elements of the partition wall are assumed to be perfect and the fixing system (screws) is not modelled. iv/ The variation of water content of plasterboards, water vaporization and mass transfers are not predicted. All these phenomena are simply taking into account by adapting the specific heat C_p of the material.

The thermo-physical properties of steel are those given in Eurocode 3 [5], while those of the plasterboards versus temperature were identified by a characterization program [3].

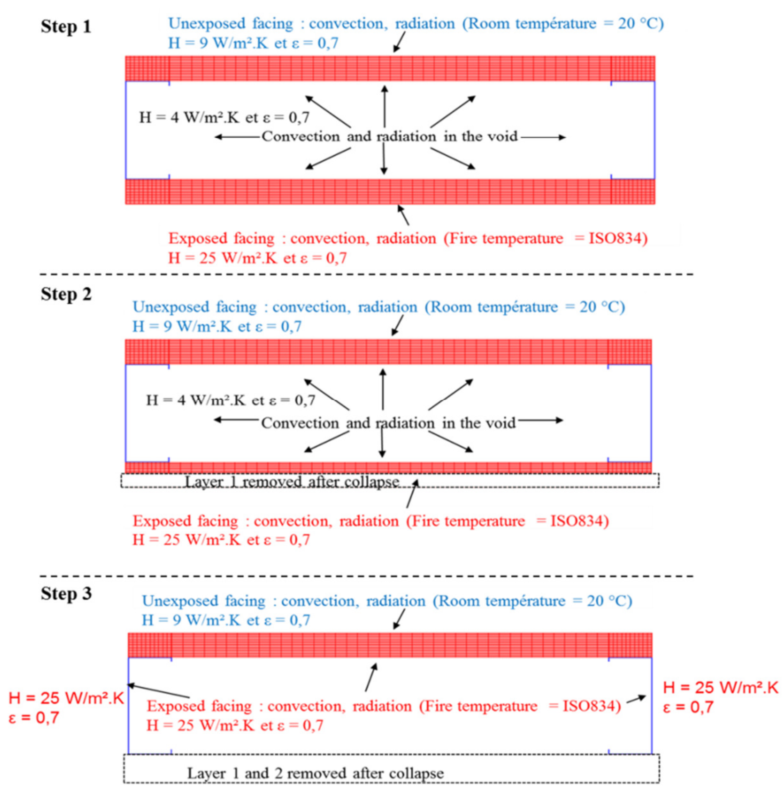

Figure 1. Simulation steps and boundary conditions used for thermal transfer analyses.

Thermal analyses are conducted on a 2D model using 4-node linear elements. A thermal analysis is divided in two or three steps to take into account the facing collapse inside the fire resistance furnace (two steps for single layer facing with one collapse and three steps for a double layer facing with two collapses). The first step is the thermal analysis on the overall thickness of the partition wall, the second step is the heat transfer after the first layer of exposed plasterboard has collapsed and the third step is the heat transfer after all the exposed facing is ruined. At this time, the steel stud and one face of the unexposed facing are directly exposed to the fire curve ISO-834-1. Figure 1 shows the different three steps for a thermal analysis and the boundary conditions used in thermal simulations. Thermal heat transfers inside partition wall's void are also calculated by the use of convection and radiation boundaries with the average temperature of the void.

Collapse's times of exposed facing layers are determinate by analyzing the test report and experimental temperature measurements. A layer of plasterboard is to remove in simulation at the time when experimental temperatures are rapidly increasing due to a plasterboard collapse inside the furnace. When a layer is removed in simulation, the thermal loading is applied to the new boundary with a small delay of 5-10 min (linear increase to the ISO-834-1 curve) to reproduce the progressive fall of the plasterboard layer.

Thermo-Mechanical Model

The thermo-mechanical simulation of a plasterboard partition is realized using results of the thermal analysis. Assumptions made for the mechanical analysis are as follows: i/ Facings are considered as a continuous membrane without interruption along the full height (no horizontal joints between boards of a same facing). ii/ Double layers of plasterboard are simulated as an equivalent homogeneous material and the progressive collapse of the exposed facing is not simulated. iii/ The exposed facing is supposed to remain in place during the simulation. Its loss is taking into account in the simulation by a drastic reduction of its thermo-mechanical properties.

The plasterboard partition is modelled in 3D as an assembly of finite multi-layer shell and interface elements: two shell meshes are used for plasterboard facings and one for a steel stud [3]. Only one steel stud of the plasterboard partition is simulated and a width of gypsum corresponding to a section between two studs is fixed to it. By this mean, just the part of plasterboards supported by the stud is simulated (Figure 2). Non-linear mechanical elastoplastic model are used to reproduce mechanical strain of the partition wall due to thermal transfer. Mechanical properties (elastic modulus, yield strength and thermal expansion coefficients) are respectively from [5] for steel stud and from characterization tests at different temperatures for plasterboard [3]. Elastic modulus and yield strength of gypsum were measured by 4-points bending tests at different temperatures up to 400 °C. After this temperature, mechanical properties have drastically reduced and can be assumed to decrease down to zero at 1 200°C. Thermal expansion coefficients of the plasterboard were measured by dilatometry from 20 °C to 1 000 °C.

Screws connection between the two facings and the steel stud are modelled by using interface elements (JOINT3D) of CAST3M [3] [6] with an elastic behavior. Shear stiffness and normal stiffness used for these connections were measured at 20 °C and are from [3].

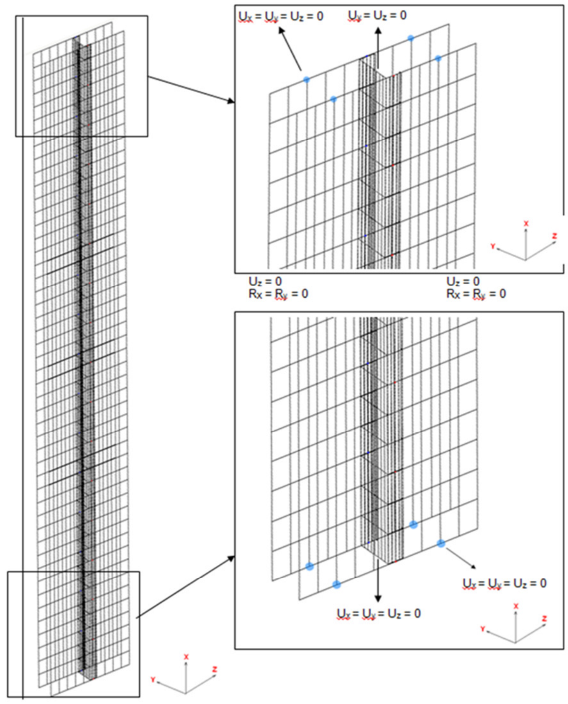

Figure 2. Shell mesh and mechanical boundaries used for mechanical simulation.

Mechanical boundaries applied to the plasterboard partition are as follows:

- 8 nodes at the upper and lower parts of plasterboard facings are blocked in three directions to simulated screw connections to the supporting frame (blue nodes in Figure 2).
- 1 node at the lower end of the steel stud is blocked in three directions to simulated screw connection at the base of the steel stud.
- 1 node at the upper end of the steel stud is blocked in two directions (height's direction remain free) to simulated connection between the top of the steel stud and the supporting frame.
- Depending of the partition wall, a dilatation clearance is applied at the upper end of the steel stud.

In addition to this, the weight of the structure is taking into account for mechanical simulations but the reduction of this weight due to water removing or plasterboard collapse is not simulated.

SIMULATION RESULTS

In this part, we present thermal and thermo-mechanical results of plasterboard partition simulations. Firstly, results from simulations of two standard plasterboard partitions tested at Efectis France Laboratory are discussed. Secondly, results from height extensions of these partition walls and fire performances are presented.

Simulations of Reference Plasterboard Partitions

Two plasterboard partitions tested at Efectis France Laboratory are considered here. The first test (Test n°1) was a partition wall with 4.9 m height made of two facings. Each facing was composed by two layers of BA15 plasterboard (BA15 thickness = 15 mm). Steel studs with C-shape were used with following dimensions: 50 x 120 x 50 mm and a thickness of 0.6 mm. Screw connections between facings and steel studs every 300 mm were used and a dilatation clearance of 50 mm was applied.

The second test (Test n°2) was a 3 m high plasterboard partition made of two facings. Each facing was composed by two layers of BA13 plasterboard (BA13 thickness = 13 mm). Steel studs with C-shape were used with following dimensions: 35 x 48 x 35 mm and a thickness of 0.6 mm. Screw connections between facings and steel studs every 150 mm were used and a dilatation clearance of 10 mm was applied.

For the test n°1 a collapse time at 92 min for the first exposed BA15 layer and 106 min for the second one were observed. For the test n°2, collapse times are respectively 89 min and 135 min for the first and second layers of exposed plasterboard facing layers.

Numerical temperatures on steel stud and unexposed facing for test n°1 and n°2 are presented in Figure 3 and Figure 4. As it can be seen, the model gives quite good agreement with experimental temperatures and impacts of exposed facing collapses are well taken into account.

Figure 5 presented numerical and experimental out of plane displacements at mid-height of the steel stud for both test n°1 and n°2. Displacements are well simulated during all the duration of fire resistance tests. Numerical model also allows to reproduce the decrease of displacements after the collapse of plasterboard partitions (around 100 min for test n°1 and 121 min for test n°2). From these results, numerical model will be applied to height extensions of plasterboard partitions in the next section.

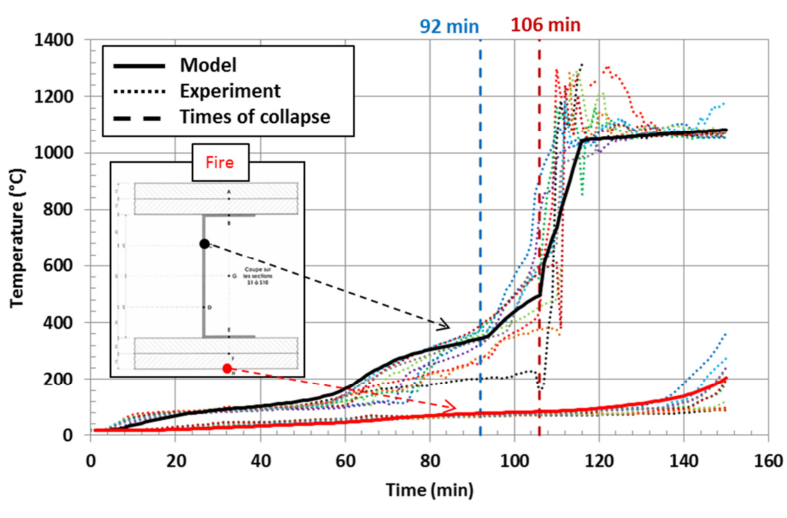

Figure 3. Experimental and numerical temperatures on steel stud and unexposed facing - Test n°1.

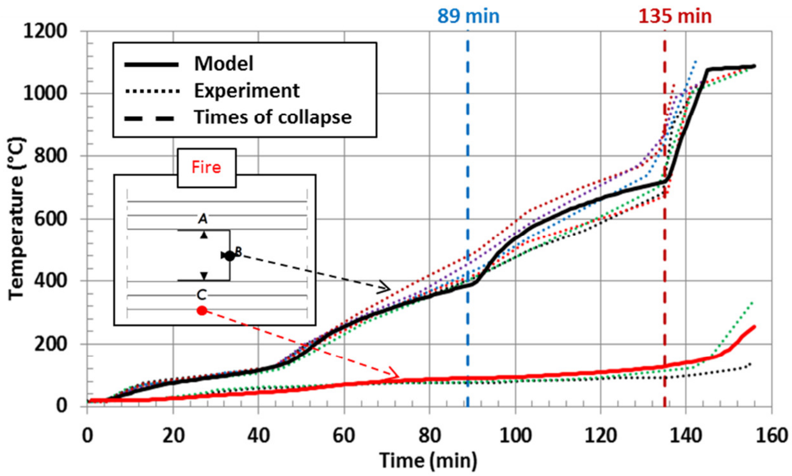

Figure 4. Experimental and numerical temperatures on steel stud and unexposed facing - Test n°2.

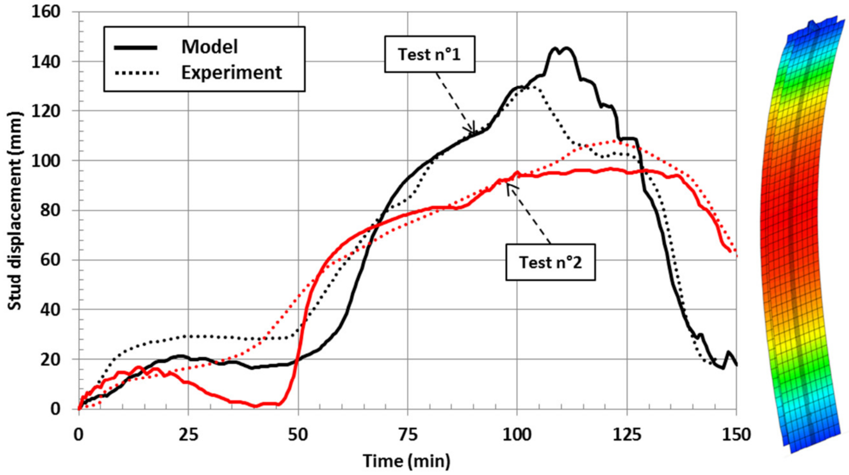

Figure 5. Experimental and numerical displacements at mid-height of the steel stud - Tests n°1 and n°2.

Simulations of Height Dimension Extensions of Plasterboard Partitions

The model, verified previously in standard dimensions configurations, is now applied for height extensions. Two tested partition walls with height of 9 m or 11 m for the test n°1 and steel stud's dimensions of 50 x 150 x 50 mm, and 5 m or 7 m for the test n°2 with C-section studs doubled and fixed together in I-section by screw connections every meter, are considered.

Same thermal histories from standard height simulations are applied to extension cases. Out of plane displacements at mid-height and a deformed steel stud are presented in Figure 6.

To evaluate the fire resistance of extension cases, two criteria are used: the relative elongation of steel stud and the rotation angle between the lower end and the out of plane displacement at one fifth of the height of the steel stud where the displacement is the most important after collapse (see Figure 6). In both cases, a height extension is considered to be validated if both criteria are achieved after 120 min of simulation to validate a 2h fire resistance performance [2]. Results for height extension cases here are presented in Table 1. It can be seen that both height of 9 m and 11 m are validated for extension of the test n°1 but only the 5 m height is validated for extension of the test n°2.

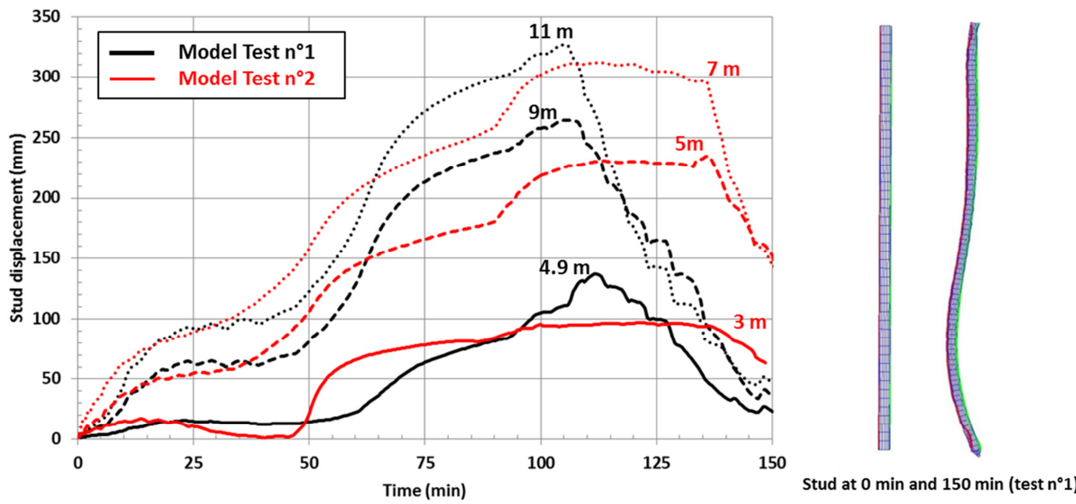

Figure 6. Experimental and numerical displacements at mid-height of the steel stud for extension cases—Tests n°1 and n°2.

TABLE I. CRITERIA AND VALIDATION TIMES FOR EXTENSION CASES.

Criteria	Values	Test n°1 - Time of collapse	9 m	11 m
Relative elongation (-)	1.0088	140 min	134 min	132 min
Rotation angle (°)	5.235	140 min	137 min	132 min

Criteria	Values	Test n°2 - Time of collapse	5 m	7 m
Relative elongation (-)	1.0202	141 min	121 min	116 min
Rotation angle (°)	8.760	141 min	121 min	112 min

CONCLUSION

The fire safety laboratories have to validate fire resistance of products that cannot be tested in fire resistance furnace due to over-size dimensions. Based on the VIRGILE approach (Virtual Facilities of Fire Resistance Testing) a thermo-mechanical model has been developed to evaluate the fire performance of high-rise plasterboard partitions. The model is based on the simulation of temperature field and mechanical behavior of a tested plasterboard partition in standard configurations. Then it is possible to determine failure criteria to evaluate performance of height extensions cases on the basis of real fire resistance tests.

Simulation results show good agreements with both thermal and mechanical test results. The thermo-mechanical model has been validated on two different partition walls and its application to extension cases seems conclusive. A next step will be to validate extension cases based on real extension tests.

REFERENCES

1. AFNOR, 2000. *NF-EN-1363-1, Fire resistance tests, Part1: General requirements*. French standard.
2. AFNOR, 2000. *NF-EN-1364-1, Fire resistance tests on non-structural products Part1: walls*. French standard.
3. H. Tran, 2012. *Etude numérique et expérimentale du comportement au feu des éléments séparatifs en plaques de plâtre à ossature acier*. PhD thesis, ENS Cachan.
4. CAST3M-2013, 2013. Finite element software, CEA, www-cast3m.cea.fr.
5. AFNOR, 2005. *EN-1993-1-2, Eurocode 3: Design of steel structures - Part 1.2: General rules - Structural Fire Design*. European standard.
6. P. Pegon, A.V. Pinto, M. Géradin. 2001. "Numerical modelling of stone-block monumental structures", *Computers and Structures.* 79: 2165-2181.

Material Characterisation and Numerical Modelling of Gypsum Plasterboards in Fire

MANEESHA THARINDI DODANGODA, MAHEN MAHENDRAN, KEERTHAN POOLOGANATHAN and RAY L. FROST

ABSTRACT

The fire resistance characteristic of LSF wall systems mainly depends on the protective linings in use, commonly gypsum plasterboards. However, unclassified boards with varying composition and more notably with ambiguous thermal properties are increasingly becoming available in the market. Therefore a study was undertaken with an aim to set minimum standards for fire protective boards used in LSF wall applications. This paper presents the details of this study based on material characterisation and finite element thermal modelling of the most commonly used fire protective board, gypsum plasterboards, to address these critical issues related to fire safety design. In the material characterisation phase of this study, thermal properties of three different gypsum plasterboards manufactured in Australia were measured, analysed and compared. Subsequently, it proposes a thermal property based "k-factor" capable of giving an overall measure of the fire performance of boards, so that it can be used in appropriately classifying fire protective boards. As it is not known how this factor relates to the overall fire performance of LSF wall systems, numerical models were also developed and used to simulate the performance of LSF walls exposed to the standard fire. Finally, a correlation between time-temperature profiles from numerical analyses and calculated k-factors was established.

INTRODUCTION

Buildings must be designed and constructed to meet acceptable standards of structural adequacy, safety, health and services. Fire safety is considered as one of the most important criteria of a building. In the Building Code of Australia [1] light gauge steel framed (LSF) wall systems protected with plasterboards are identified as continuous fire rated barriers for compartmentalising buildings against fire incidents. The code requires certain Fire Resistance Level (FRL) for them to be used as construction elements. AS 1530.4 [2] provides suitable guidelines for determining this FRL of construction elements. FRL is expressed in minutes and is determined based on three criteria; structural adequacy, integrity and insulation.

The steel frame of LSF wall systems is made of thin-walled cold-formed lipped

Science and Engineering Faculty, Queensland University of Technology (QUT)
2, George Street, Brisbane, QLD 4000, Australia

channel section (LCS) studs and unlipped channel section tracks. When exposed to fire conditions, these thin-walled steel stud sections heat up rapidly and reach their failure temperatures quickly. It will eventually lead to structural instability of the building. Therefore, fire resistance of load bearing LSF wall systems mainly depend on the protective linings in use, i.e. fire protective boards, which keep the steel stud temperatures from reaching their limits. Fire rated gypsum plasterboards are the most commonly used type of boards as protective lining for LSF wall systems.

However, unclassified plasterboards with varying composition and more notably with ambiguous thermal properties are increasingly being used in recent times. Hence there is a need to set minimum standards for fire protective boards based on their thermo-physical properties in order to ensure appropriate fire protective boards are used to enhance fire safety. There is also a need to study the effect of these thermal properties on the FRL of LSF walls and develop a method to calculate FRL based on thermal properties. Hence a study was undertaken based on material characterisation and finite element thermal modelling of the most commonly used fire protective board, gypsum plasterboards, to address these critical issues on fire safety design.

MATERIAL CHARACTERISATION

The main constituents of gypsum plasterboard is Calcium Sulphate Di-hydrate ($CaSO_4 \cdot 2H_2O$). The percentage of pure gypsum (i.e. $CaSO_4 \cdot 2H_2O$) within can vary between 60 – 100% depending on the manufacturer [3]. This pure gypsum contains approximately 20.9% chemically bound water. Additionally, about 3–4% free moisture content is present within the pores of gypsum core [4]. Fire retarding property of gypsum plasterboards is mainly related to its delayed temperature evolution across the depth of plasterboard due to the energy absorption for evaporation of free water and crystalized water of gypsum ($CaSO_4 \cdot 2H_2O$). Supplementary to gypsum, the composition of commercial plasterboards consists of three other categories of constituents which are accountable for adjusting shrinkage, maintaining integrity, and providing low thermal conductivity of the end product exposed to fire. Vermiculite, glass fibres and fillers are used respectively under the above categories.

In this material characterisation phase of the study, chemical composition and thermal properties of three different gypsum plasterboards manufactured in Australia were measured, analysed and compared.

Chemical Composition Characterisation

As the amount of gypsum varies among different boards, and specific chemical identity and/or exact percentage of composition are not available, the powder X-ray diffraction (PXRD) analysis was undertaken in this study. X-ray diffraction patterns were collected with a PANalytical X'Pert Pro diffractometer using cobalt Kα radiation, and the data was analysed using JADE and Highscore Plus for phase identification, and TOPAS for quantitative phase analysis using the Rietveld method. Table 1 shows the composition analysis from PXRD analysis at ambient temperature. It reveals significant differences in the composition of the three boards although they are considered equivalent in terms of FRL. Scanning electron microscopy (SEM) images from TM3000 was used to view the crystalline structure of the constituents of gypsum plasterboards. The specimens were freshly cracked to obtain best images.

TABLE I. COMPOSITION FROM PXRD ANALYSIS.

Components	Board 1	Board 2	Board 3
Quartz	0.6	1.2	1.4
Aragonite	2.4	3.3	3.4
Anhydrite	1.5	1.3	1.9
Bassanite	2.2	8.8	1.2
Gypsum	83.9	65.0	84.4
Vermiculite	1.7	0.8	
Sepiolite	5.7	7.0	
Non-diffracting/unidentified	2.0	12.7	7.8

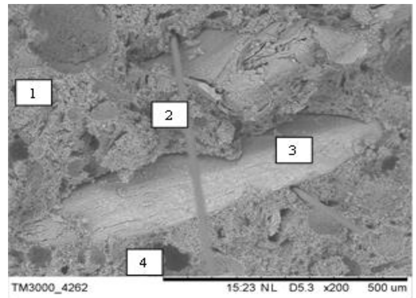

Figure 1. Crystalline structure 1) gypsum, 2) glass fibre, 3) vermiculite, 4) pores/voids.

Thermo-physical Characterisation

Specific heat (C_p), mass loss/relative density, thermal conductivity and linear thermal expansion variations with temperature were measured for thermo-physical characterization of the three gypsum plasterboards. Simultaneous thermal analyzer (NETZSCH STA 449, F3), laser flash apparatus (NETZSCH LFA 457) and dilatometer (NETZSCH DIL 402C) were used to measure these thermal properties. For the first three properties 20 ºC/min heating rate was used while linear thermal expansion was measured at 5 ºC/min heating rate (maximum for the instrument). Powdered samples were used in STA measurements (Pt crucibles with pin holed lids) while solid board samples were used in both LFA and DIL. Figures 2 to 5 show the measured thermal properties as functions of temperature for the three boards.

All the samples exhibited similar specific heat versus temperature characteristics with two peaks. The dehydration process of the chemically bound water contributes to these peaks. The board with the largest gypsum content (Board 3) shows the highest peak values of 13,080 J/kg/ºC at 148 ºC and 9,200 J/kg/ºC at 172 ºC. The higher the peak specific heat the more energy the gypsum plasterboard can absorb, and thus the heat transfer across the wall will be delayed. Thus Board 3 is likely to perform better, however, the overall thermal performance will depend on all three thermal properties. A mass reduction of 16-17% occurs with dehydration reactions at temperatures between 115 and 180ºC, while another 6-8% mass reduction occurs at 650ºC following an almost constant relative density. As seen in Figure 3, the mass loss of these plasterboards is small and thus the effects of cracking and shrinkage will be minimised beyond 650ºC. The boards that exhibit rapid reduction in density are likely to cause premature integrity and insulation failures, and must be avoided. Further, thermal expansion results (Figure 5) of Boards 1 and 2 show that overall cracking and shrinkage characteristics will be improved due to the expansion of vermiculite in these boards. Test results showed that thermal conductivity at room temperature is 0.25 W/m/ºC. The thermal conductivity values decreased to 0.12 W/m/ºC at about 200ºC due to dehydration reactions with hardly any variation among the three boards. Beyond this, the thermal conductivity increases due to the ablation process caused by burning of plasterboard outer layers and exhibit a sudden increase at about 900ºC due to intense cracking.

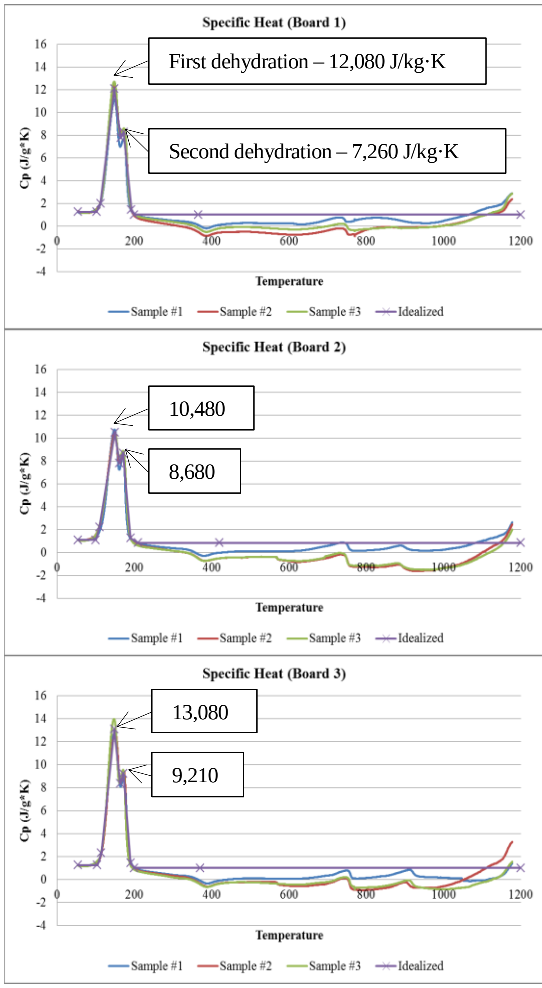

Figure 2. Specific heat variation.

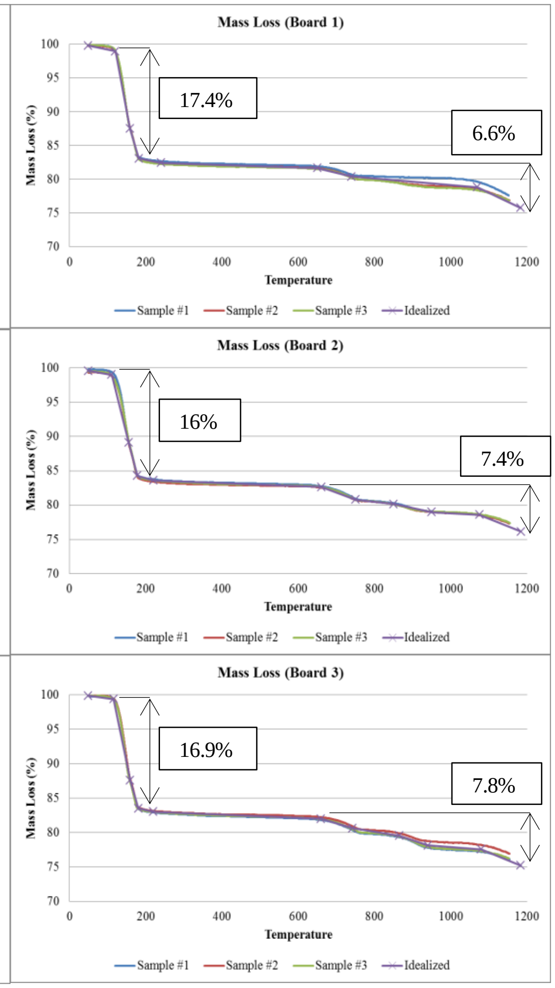

Figure 3. Mass loss variation.

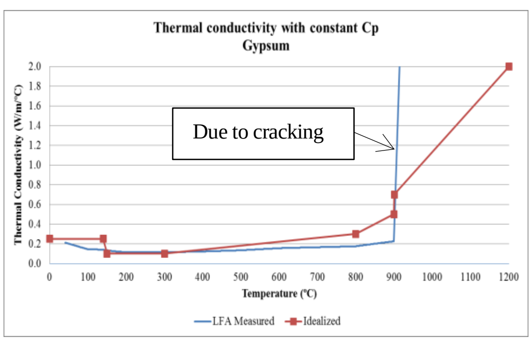

Figure 4. Thermal conductivity variation.

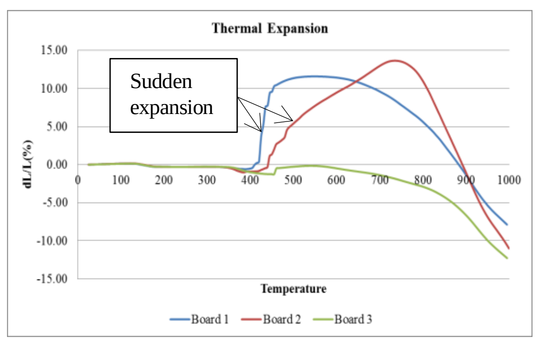

Figure 5. Thermal expansion.

Overall Fire Performance Index (k-factor)

As discussed above, the overall fire performance of a certain gypsum plasterboard depends on all the three thermal properties. Hence this paper proposes a "k-factor" and its variation with temperature as an overall measure of the fire performance of boards that can be used as a standard to appropriately classify fire protective boards. The k-factor (Equation 1) is based on thermos-physical properties and is defined as a function of specific volumetric enthalpy ($E(T)$ in J/m^3), specific heat ($C_p(T)$ in J/(kg°C)), density ($\rho(T)$ in kg/m^3) and thermal conductivity (λ in W/m/K) at temperature T (T_A - ambient temperature). However, this does not account for the extensive ablation and subsequent integrity failure of plasterboards due to excessive mass loss. Therefore, using the results given in Figure 3, it is proposed that the total mass loss by 1200 °C and the mass loss by 200 °C are limited to 25% and 20% from the initial value, respectively.

$$k = \frac{E(T)}{\lambda} = \frac{\int_{T_A}^{T} C_p(T)\rho(T)dT}{\lambda} \qquad (1)$$

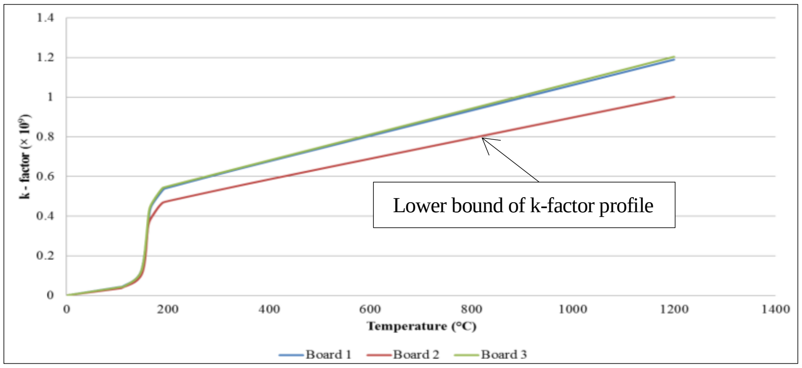

Figure 6. Variation of k-factor with temperature.

As illustrated in Figure 6, the k-factor profiles of the three boards calculated based on Equation 1 showed a similar trend with increasing temperature, however, it is not known how they relate to the overall fire performance (FRL). Therefore numerical models were developed to simulate the performance of LSF walls exposed to the standard fire to establish a relationship between k-factor profiles and FRL.

FINITE ELEMENT THERMAL MODELLING

Finite element (FE) thermal modelling has been widely used for predicting the thermal performance of LSF wall systems instead of the expensive and time consuming full-scale fire tests. In this study, 3-D FE heat transfer model was developed as shown in Figure 7 to simulate the performance of LSF walls exposed to the standard fire. For this purpose the LSF wall with single 16 mm plasterboard lining was simulated using the heat transfer model developed with Abaqus/CAE Version 6.14-2 [5] and was validated using Kolakar's [4] fire test results. The simulated wall configuration was of single plasterboard (1 x 16 mm) and lipped channel section studs of 90×40×15×1.15 mm. The model development was undertaken using 8-node linear heat transfer brick elements (DC3D8) and a global mesh density of 20 mm was used with solid sections. Tie constraints were defined at the interface to facilitate the solid to solid heat transfer. The thermo-physical properties proposed in Keerthan and Mahendran [6] for Australian manufactured gypsum plasterboards and properties given in the Eurocode 3 Part 1-2 for steel were used as the inputs for FE heat transfer model validations. The three heat transfer modes viz. conduction, convection and radiation are integrated in FE modelling. The conduction was defined under material properties as thermal conductivity. The effects of convection and radiation for heat transfer were defined by assigning appropriate convective film coefficients (exposed =

25, unexposed = 10 W/m^2°C) and emissivity values (exposed, unexposed, cavity = 0.9). The standard fire curve was assigned to the fire exposed side as a boundary condition using an amplitude curve of time-temperature profile of ISO 834 standard fire curve. The temperature of fire exposed side was allowed to follow the amplitude curve by assigning unity to sink temperature. The initial temperature of the models was assigned by defining a pre-defined field for entire model at ambient temperature, 23°C. Further, the Stefan-Boltzmann constant of 5.67×E^{-8} and absolute zero temperature of -273 °C was assigned to the models. As illustrated in Figures 8 and 9 FE analysis results showed a good agreement with Kolakar's (2010) results.

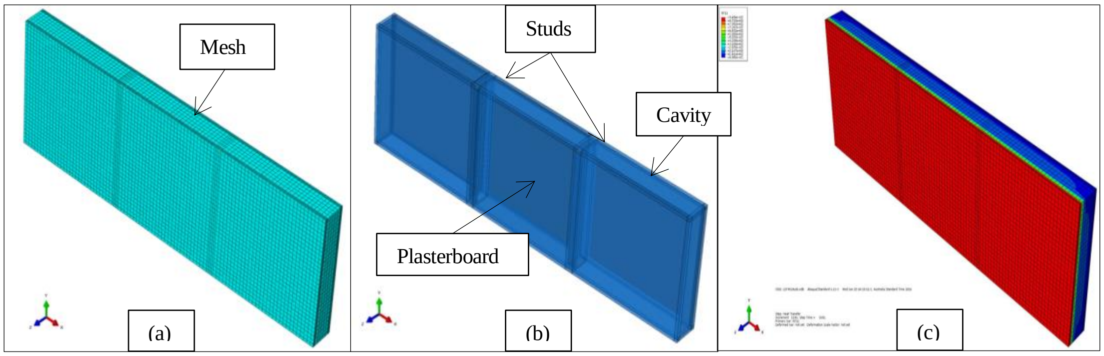

Figure 7. 3D FE model of LSF wall (a) mesh details, (b) wall model (c) temperature contours 60 min.

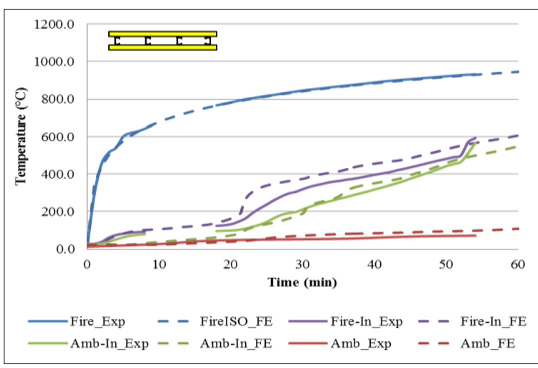

Figure 8. Model validation for plasterboard.

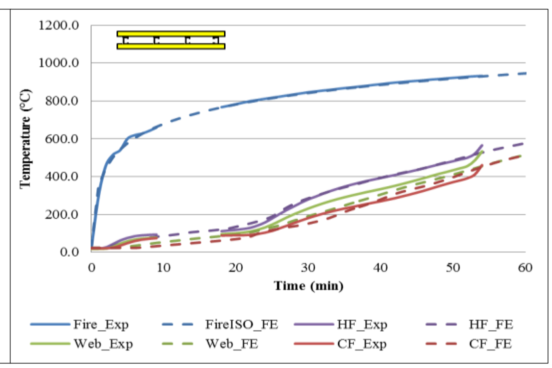

Figure 9. Model validation for studs.

FRL of LSF Walls

The validated 3-D FE heat transfer model was used to predict the time-temperature profiles for the steel stud hot flange (HF) and the ambient side plasterboard (Amb) of LSF wall panels lined with single 16 mm lining made of the three gypsum plasterboards considered in this study. The idealized thermal properties proposed in Figures 2 to 4 for these three plasterboards were used as the thermal property inputs. The time-temperature profiles obtained from thermal FE analysis (Figure 10) show that the LSF wall panels lined with these three boards are likely to produce similar FRLs for load bearing and non-load bearing walls based on a hot flange limiting temperature of 500°C and an ambient side limiting temperature of 200°C.

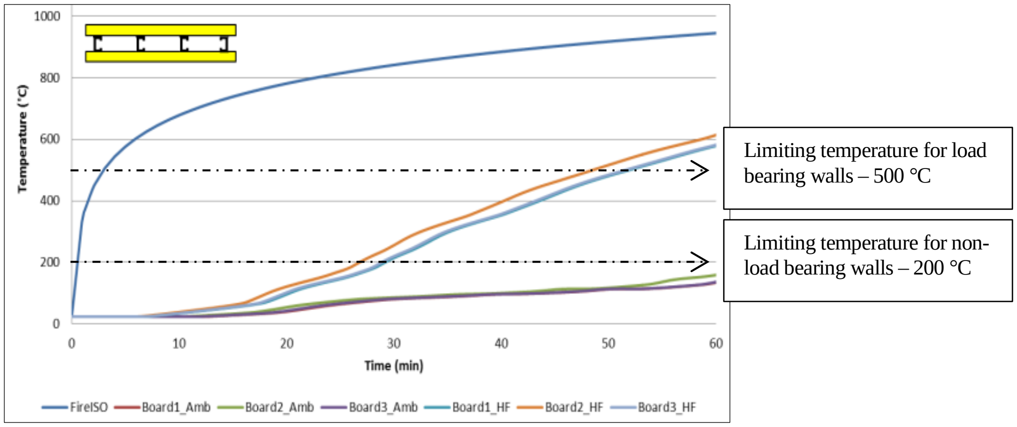

Figure 10. Time-temperature profiles of steel stud hot flange and ambient side plasterboard.

DISCUSSION

The predicted time-temperature curves for LSF wall panels in Figure 10 show that the differences in time-temperature curves are small and appear to correlate well with the calculated k-factor profiles in Figure 6, i.e. k-factor profiles shifts up for LSF walls with higher FRL. Although all three board manufacturers claimed the same FRL, time-temperature profiles from FE analysis depicts that FRL of Board 2 is slightly lower compared to the other two. This corresponds to the lower most k-factor profile in Figure 6. Therefore, lower bound k-factor profile of Board 2 is proposed as the standard for the overall measure of the fire performance of plasterboards in LSF wall applications. The mass loss limitations stated earlier should also be considered when comparing any plasterboard against this proposed standard of k-factor profile.

The k-factor profile of any fire rated plasterboard, calculated using Equation 1, should lie above the curve proposed in Figure 11 for it to be used as lining material for LSF wall systems exposed to fire conditions. If part of the k-factor profile of a given plasterboard lies below the proposed standard in Figure 11, LSF walls lined with those boards should be tested according to the standard fire testing procedure given in AS 1530.4 [2] to determine the suitability for fire design applications. The plasterboards with the entire k-factor profile located above the proposed standard can be considered safe to use in LSF wall applications for fire design.

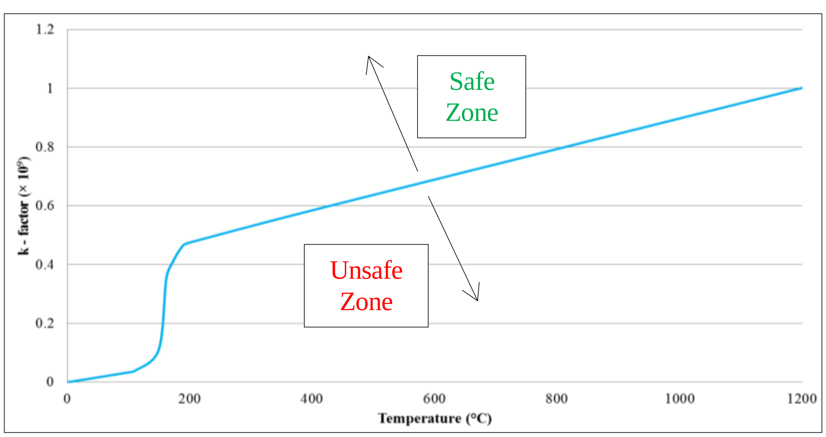

Figure 11. Proposed k-factor profile as a standard.

CONCLUSIONS

This paper has presented the details of an investigation on setting minimum standards for fire protective boards used in load bearing and non-load bearing LSF wall panels. It included the chemical composition and thermal property characterisation of commonly used gypsum plasterboards from three Australian manufacturers. As an overall measure of the fire performance of plasterboards for LSF wall applications, a "k-factor" is proposed as a function of specific volumetric enthalpy, specific heat, density and thermal conductivity at elevated temperatures based on measured thermal properties. To investigate the relationship of the k-factor to the fire performance of LSF wall panels, a 3-D FE heat transfer model was developed and validated using fire test results. The k-factor profiles and the time-temperature curves from FE analysis showed a similar behaviour and hence it was concluded that FRL of LSF wall panels lined with the three gypsum plasterboards correlated well with the proposed k-factor. Finally, the lower bound of k-factor profiles for the three gypsum plasterboards was proposed as the standard of fire performance of plasterboards for use in LSF wall applications in fire design. Supplementary conditions on mass loss have also been proposed in this paper to allow for the extensive ablation and subsequent integrity failure of plasterboards due to excessive mass loss.

Further numerical studies and tests are currently under way using other boards with considerable differences in thermal properties to verify the suitability of the proposed k-factor profile.

ACKNOWLEDGEMENT

The data reported in this paper were obtained at the Central Analytical Research Facility (CARF) operated by the Institute for Future Environments (QUT). Access to CARF is supported by generous funding from the Science & Engineering Faculty. Financial support was provided by QUT and an Australian Research Council Grant.

REFERENCES

1. Australian Building Codes Board. 1996. *Building Code of Australia*. Canberra, Australia.
2. Standards Australia. 2014. *AS 1530.4 Methods for fire tests on building materials, components and structures*. Sydney, Australia.
3. Kolarkar, P. and Mahendran, M. 2014. "Experimental studies of gypsum plasterboards and composite panels under fire conditions." *Fire and Materials* 38 (1): 13-35.
4. Buchanan, A. H. and J. T. Gerlich. "Fire Performance of Gypsum Plasterboard, *Wellington, N.Z, 1997*, edited, 160-166: Institution of Professional Engineers New Zealand.
5. Dassault Systems Simulia Corporation. 2013. "Abaqus/CAE User's Guide, Abaqus 6.13."
6. Keerthan, P. and Mahendran, M. 2012. "Numerical studies of gypsum plasterboard panels under standard fire conditions." *Fire Safety Journal* 53: 105-119.

Performance of Gypsum-Protected CLT and NLT in Natural and Standard Fires

MARC JANSSENS, JASON HUCZEK and NATASHA ALBRACHT

ABSTRACT

Two large-scale tests were conducted to evaluate the performance of CLT and NLT construction protected with two 16 mm sheets of type X gypsum board in the pre-flashover, post-flashover and cool-down phases of a severe living room fire. Since minimal or no charring was observed in the room test, additional small-scale furnace tests were performed on gypsum-protected CLT and NLT specimens using standard and simulated natural thermal exposures. The furnace tests indicate that the wood continues to char for some time at a decreasing rate during the cool-down-phase. The corresponding reduction in the load-bearing section needs to be accounted for in the assessment of the fire performance of CLT and NLT structures.

INTRODUCTION

Wood is a renewable resource when produced by sustainable forestry techniques. It has significant advantages over other construction materials in terms of the impact of its use on the environment. This has been demonstrated, in recent life cycle assessment studies [1][2].

In recent years the renewable and sustainable nature of the materials has resulted in the construction of an increasing number of mid- and high-rise wood buildings in Europe and other parts of the world. These structures use cross-laminated timber (CLT) panels and other types of massive engineered wood members such as glued-laminated (glulam) beams and columns. A substantial amount of fire testing and computer fire modeling has been (and continues to be) conducted to demonstrate that tall wood buildings can provide an acceptable level of safety in case of fire.

U.S. building codes currently do not allow wood structures higher than four stories. However, several tall wood buildings up to 12 stories in height are now being constructed based on case-by-case acceptance by the local authority having jurisdiction (AHJ). This paper describes the results of two room fire tests and four furnace tests that were conducted to support a more general acceptance of engineered wood products such as CLT in tall buildings in the U.S.

Southwest Research Institute, 6220 Culebra Road, San Antonio, TX 78238, U.S.A.

ROOM TESTS

The two room fire tests were conducted at Southwest Research Institute (SwRI) to evaluate the performance of CLT and nail laminated timber (NLT) construction protected with two layers of 16 mm type X gypsum board when exposed to the thermal environment of a severe living room fire.

First Test

The first test was conducted on September 3, 2015. The interior dimensions of the test room were approximately 4.11 × 3.60 × 2.38 m. The front narrow wall of the compartment was provided with an open doorway, measuring approximately 1.87 × 2.07 m. In this test the walls of the test room were constructed from CLT panels, which consisted of five layers of spruce-pine-fir (SPF) lumber stacked at right angles and glued together into nominally 0.175 m thick panels. The ceiling consisted of 4.27 m long 2 by 6 Southern pine floor joists nailed together one-by-one using 89 mm long 3.33 mm diameter nails. Concrete blocks were placed on top of the ceiling to impose a distributed structural load of 1.9 kN/m^2. No additional load was imposed on the walls of the structure.

The room was generously furnished with typical residential non-FR treated living room furniture as shown in Figure 1. The corresponding fire load density was equal to the 90^{th} percentile of the fire load density frequency distribution for living rooms developed from surveys by the National Research Council of Canada [3]. The intent was to maximize the intensity of the fire at the expense of the duration of exposure since a loaded CLT wall panel protected with a single layer of 16 mm Type X gypsum board had already achieved a 3-hour fire resistance rating in a standard ASTM E119 furnace test.

The test was started by igniting a sofa seat cushion with a small flame source (BS 5852 Source 2). Flashover occurred in approximately four minutes (see Figure 2), and the peak heat release was measured at approximately 5.5 MW. Figure 3 compares the room temperatures measured at five locations 0.1 m below the ceiling to the standard ASTM E119 time-temperature curve. With the exception of some heavy pieces of furniture (a bookcase and an armoire in the rear corners, and a heavy bookcase in the front left corner), the contents were largely consumed in less than 15 minutes. The test was terminated after three hours to ensure that any continued heating and potential charring of the wood structure during the cool-down phase was captured.

The highest recorded temperature between the two layers of gypsum board was 269°C. The thermocouple temperatures between the base layer gypsum board and the wood (CLT and NLT) did not exceed 100°C at any time during the three-hour test. The gypsum board face layer sustained limited damage, except for the pieces that fell from the ceiling during the test and some pieces that fell down during cool-down (see Figure 4). The base layer remained largely intact although there was some noticeable damage in the three corners where solid furniture items burned for a long time. The wood structure was also intact except for the same three corners. Some superficial charring was observed in the back corners, while a maximum char depth of approximately 6 mm was measured in the front corner where the heavier bookcase was located (see Figure 5).

Figure 1. Furnished room for Test 1.

Figure 2. Four min into Test 1.

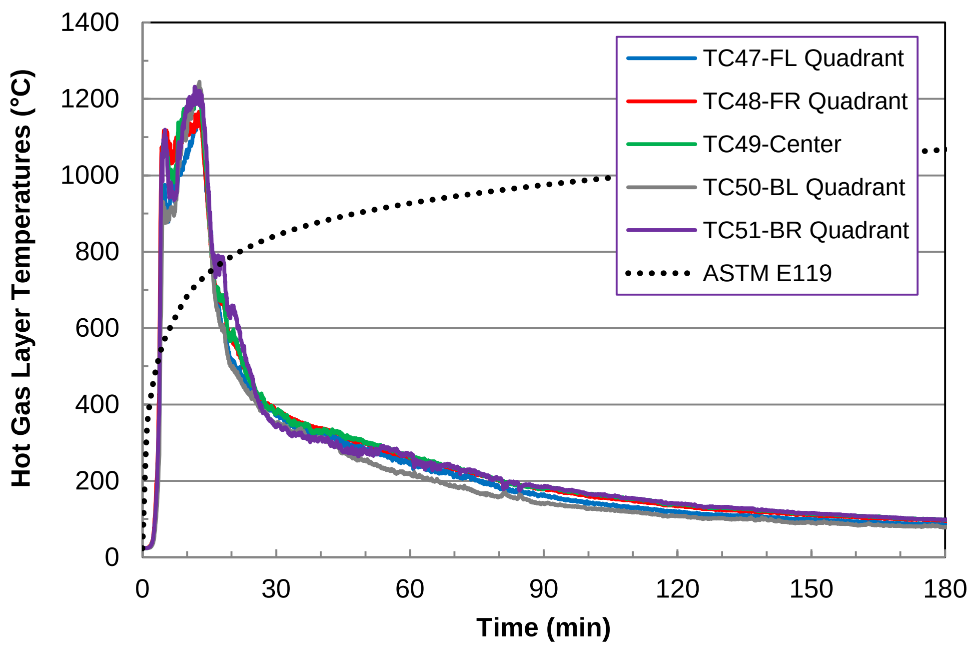

Figure 3. Hot gas layer temperatures compared to standard ASTM E119 curve.

Figure 4. Gypsum board post-test condition.

Figure 5. Area of maximum charring.

Second Room Test

The second test was conducted on September 15, 2015. The interior dimensions of the test room were approximately 4.46 × 3.25 × 2.38 m. The dimensions of the doorway were the same as in Test 1. In this test the walls and ceiling of the test room were constructed from CLT panels. Concrete blocks were again placed on top of the ceiling to impose a distributed structural load of 1.9 kN/m^2.

The room furnishings and contents were similar to those in Test 1. The corresponding fire load density was equal to the 94^{th} percentile of the Canadian fire load density frequency distribution. Flashover again occurred in about four minutes, and the peak heat release was approximately 4.9 MW. Room temperatures were similar as in Test 1. The test was terminated after 2 hours and 15 minutes.

The highest recorded temperature between the two layers of gypsum board was recorded in the ceiling (231°C). The thermocouple temperatures between the base layer gypsum board and the CLT again never exceeded 100°C. The damage to the gypsum board was similar as in Test 1. The wood structure was intact except for some superficial charring in the front left corner where the heavier bookcase was located.

FURNACE TESTS

Since there was minimal charring of the CLT, and no charring of the NLT very limited information was gained from the room tests about the performance of the wood structure during cool-down. A series of fire resistance furnace tests were therefore conducted in which 0.6 × 0.6 m slabs of CLT and NLT protected with one 16 mm layer of type X gypsum board were exposed to the standard ASTM E119 and high intensity UL 1709 time-temperature curves. In these tests the furnace burners were turned off shortly after the char front progressed 13 mm into the wood to simulate cool-down following room burnout.

The ASTM E-119 time-temperature curve is shown in Figure 3. In a UL 1709 test the furnace temperature is ramped to 1093°C in 5 min, and then maintained at that temperature. The UL 1709 curve was chosen because it is reasonably representative of the very severe thermal environment that was observed in the room tests. The modified ASTM E119 and UL 1709 tests were conducted in the small horizontal furnace at SwRI (see Figure 6). Four 0.6 × 0.6 m slabs, two CLT slabs and two NLT slabs, were exposed in each test as shown in Figure 7. The test matrix is presented in Table I. Test 2 is a duplicate of Test 1.

Figure 6. Small Horizontal Furnace at SwRI.

Figure 7. Tests specimens after Test 4.

TABLE I. SMALL FURNACE TEST MATRIX.

Test No.	Date	Thermal Exposure	Gypsum Board Protection
1	11/02/15	ASTM E119	Single 13 mm layer
2	11/04/15	ASTM E119	Single 13 mm layer
3	11/06/15	UL 1709	Single 13 mm layer

The test specimens were instrumented with thermocouples to measure the temperature along the centerline at the exposed surface of the gypsum, in between the layers of gypsum and wood, and at 13 mm, 25 mm, and 38 mm from the surface of the wood surface facing the furnace. To minimize conduction losses along the thermocouple wires, thermocouples were inserted in holes that were drilled from the edge to the center of each CLT or NLT slab. Since the distance between the edges and the center is 0.3 m and the drill bit is approximately 1 mm in diameter, this technique introduced significant uncertainty in the exact location of the thermocouple junction, which partly explains the scatter in the temperature data presented below.

Figures 8 and 9 are examples of the measured temperatures for each of the two conditions; ASTM E119 and single layer gypsum protection (Tests 1 and 2), and UL 1709 and single layer gypsum protection (Test 3).

Figure 8 indicates that CLT protected with a 13 mm layer of type X gypsum board and exposed to the standard ASTM E119 fire continues to char, but that the char front eventually ceases to advance (in this case at 80 min, when the char depth is about 13 mm). This same behavior is expected for the UL 1709 exposure, although this is not evident from Figure 9 as the test was terminated prematurely.

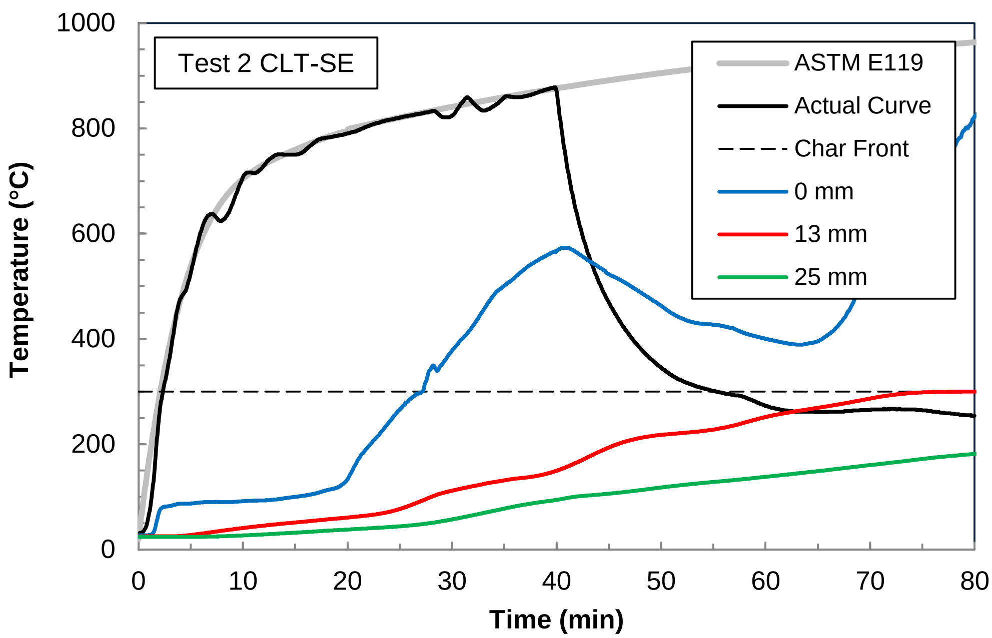

Figure 8. Example of measured temperature profiles for ASTM E119 and single layer of gypsum board.

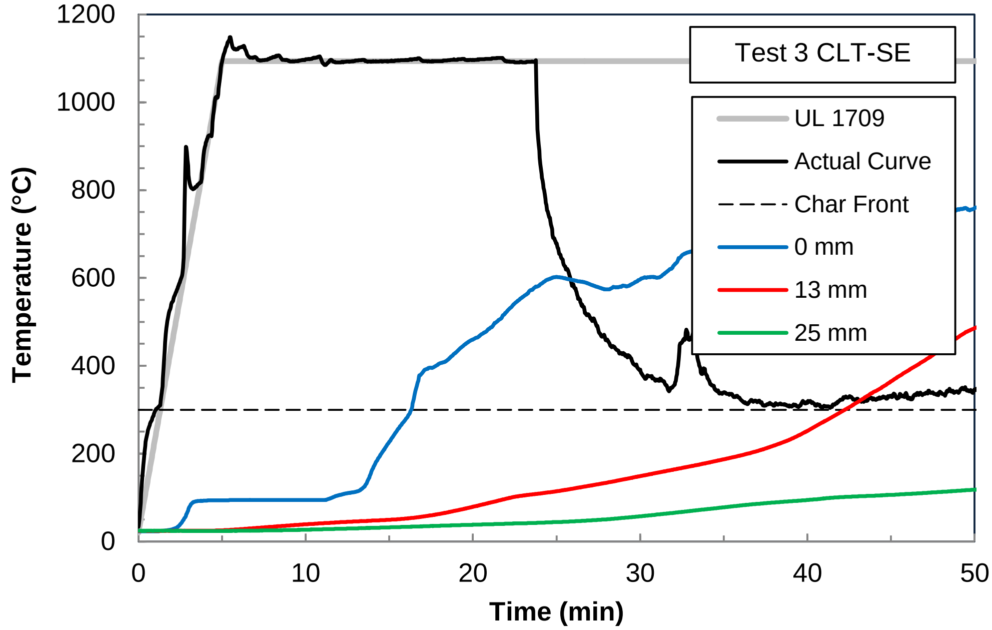

Figure 9. Example of measured temperature profiles for UL 1709 and single layer of gypsum board.

Based on a comparison between Figures 3 and 9, it can be determined that the UL 1709 furnace exposure is significantly more severe than that in the room fire tests because the protected CLT and NLT specimens were exposed to peak temperatures for about 5 min longer in the furnace (~20 min) than in the room tests (~15 min). Given that the fire load density in the room tests was in the 90-95% range, it is therefore extremely unlikely that a living room fire will be as severe as the UL 1709 furnace exposure that was used here.

Table II gives the times for Tests 1 and 2 when the thermocouples at and below the wood surface reached 300°C ($t_{300°C}$), which is generally assumed to coincide with the location of the char front. The time when the wood surface facing the furnace reaches 300°C is quite repeatable (28 min ± 9%). Two of the eight $t_{300°C}$ values at 13 mm are clearly outliers; Test 1 NLT-NW and Test 2 CLT-SW. Eliminating the outliers leads to averages of $t_{300°C}$ at 13 mm and $\beta_{0\text{-}13mm}$ (charring rate) of 74 min ± 7% and 0.28 mm/min ± 11%, respectively.

TABLE II. TIMES FOR WOOD THERMOCOUPLES TO REACH 300°C IN TEST 1 AND 2.

Test No.	Specimen	Start of cooling (min)	$t_{300°C}$ at 0 mm (min)	$t_{300°C}$ at 13 mm (min)	Charring rate, $\beta_{0–13mm}$ (mm/min)	$t_{300°C}$ at 25 mm (min)	$t_{300°C}$ at 38 mm (min)
1	NLT-NW	48	27	37	1.34	77	87
1	NLT-NE	48	29	81	0.24	--	--
1	CLT-SW	48	26	67	0.31	--	--
1	CLT-SE	48	26	67	0.30	--	--
2	NLT-NW	40	27	77	0.25	--	--
2	NLT-NE	40	34	74	0.31	--	--
2	CLT-SW	40	27	31	3.26	--	--
2	CLT-SE	40	27	76	0.26	--	--

TABLE III. TIMES FOR WOOD THERMOCOUPLES TO REACH 300°C IN TEST 3.

Test No.	**Specimen**	**Start of cooling (min)**	**$t_{300°C}$ at 0 mm (min)**	**$t_{300°C}$ at 13 mm (min)**	**Charring rate, $\beta_{0–13mm}$ (mm/min)**	**$t_{300°C}$ at 25 mm (min)**	**$t_{300°C}$ at 38 mm (min)**
3	NLT-NW	24	18	46	0.46	--	--
3	NLT-NE	24	16	36	0.64	--	--
3	CLT-SW	24	16	27	1.12	43	48
3	CLT-SE	24	16	42	0.49	--	--

Table III gives the $t_{300°C}$ values for Test 3. Based on the data in Table III for UL 1709 exposure and a single layer of gypsum board, eliminating the single outlier leads to average values of $t_{300°C}$ at 13 mm and β_{0-13mm} of 41 min ± 12% and 0.53 mm/min ± 18%, respectively.

USE OF THE TEST DATA FOR MODEL DEVELOPEMENT

The charring rates derived in the previous sections are not very useful for structural fire design purposes because they are a function of when the cool-down period is initiated. The intent is to use the data described in this paper for model development and validation.

Fire Dynamics Simulator (FDS), [4] a CFD code developed at NIST in Gaithersburg, MD, is used to simulate the response of the protected CLT and NLT in the two room fire tests and the furnace experiments. FDS includes a detailed pyrolysis sub-model that predicts the heat transfer through and thermal degradation of a solid slab exposed in a fire.

The kinetic parameters for the pyrolysis model have been obtained from an analysis of TGA (thermogravimetric analysis) data obtained for specimens taken from the gypsum board, CLT, and NLT. SwRI is currently estimating the remaining properties from an inverse heat transfer analysis of pyrolysis experiments conducted in the Cone Calorimeter (ASTM E1354) on protected and unprotected CLT and NLT specimens instrumented with thermocouples at various depths from the exposed surface.

Using a pyrolysis model has an advantage over a simple heat transfer model that simulates the thermal degradation of wood based on thermo-physical properties (thermal conductivity, specific heat, and density) such as those specified in Eurocode 5 [5]. The latter assumes that the temperature continuously increases, but if that is not the case (as, for example, in the cool-down phase of a fire) the property values may not be correct because the thermal degradation is not reversible (although some adjustments can perhaps be made to indirectly address this problem).

ACKNOWLEDGEMENT

The authors wish to express their gratitude to the American Wood Council for sponsoring the room fire project, and the Advisory Committee of Research at SwRI for providing the funds for the furnace and material characterization tests.

REFERENCES

1. Lippke, B., J. Wilson, J. Perez-Garcia, J. Bowyer, and J. Meil, 2004. "CORRIM: Life-Cycle Environmental Performance of Renewable Building Materials," *Forest Products Journal*, 54: 8-19.
2. John, S., N. Nebel, N. Perez,, and A. Buchanan. 2009. “Environmental Impacts of Multi-Storey Buildings Using Different Construction Materials,” Research Report 2008-02, University of Canterbury, Christchurch, New Zealand, 2009.
3. Bwalya, A., G. Lougheed, A,, Kashef,., and H. Saber. 2011. "Survey Results of Combustible Contents and Floor Areas in Canadian Multi-Family Dwellings," *Fire Technology*, 47:1121-1140.
4. McGrattan, K., R. McDermott, S. Hostikka, J. Floyd., C. Weinschenk, and K. Overholt, 2015. *Fire Dynamics Simulator User’s Guide,* NIST Special Publication 1019, Sixth Edition, NIST, Gaithersburg, MD.
5. “EN 1995-1-2:2004: Eurocode 5: Design of timber structures - Part 1-2: General - Structural fire design,” European Committee for Standardization (CEN), Brussels, Belgium.

Study on Residual Flexural Performance of Precast Prestressed Hollow Core Slabs After Exposure to Fire

LINGZHU CHEN[1], QINGFENG XU[1], XIANGMIN LI[1], CHONGQING HAN[2], ZHENLONG CHEN[2] and XI CHEN[1]

ABSTRACT

The structural performance of precast prestressed hollow core slabs after exposure to fire was experimentally and numerically investigated in this paper. Four levels of fire duration were considered in the experiments. All specimens both loaded without heating and after exposure to fire exhibited flexural failure. The initial stiffness, cracking loads and ultimate loads were observed to degrade with increasing levels of fire duration. A numerical model was developed to predict the response of precast hollow core slabs after fire using ABAQUS. The user subroutine USDFLD available in ABAQUS was employed to consider the effect of the maximum temperature experienced by the concrete and cold worked wires on their material properties. The predicted temperature and load-deflection relationships from the numerical model were in good agreement with the experimental results. Calculation method was proposed for the precast prestressed hollow core slabs after exposure to fire based on the plastic analysis to predict their ultimate moment capacity. The predicted moment capacity compares well with the experimental results.

1 INTRODUCTION

Precast prestressed hollow core slabs are widely used in concrete and masonry buildings because of their advantages including cost effectiveness, convenient installation and low maintenance costs compared to other floor systems[1]. The fire performance of precast hollow core slabs has been studied by many researchers through full-scale furnace tests [2-5]. The fire resistance rating and shear behaviour of the precast hollow core slabs were carefully investigated. Numerical models were also developed to predict the structural performance of precast hollow core slabs in fire [1, 4, 6]. Tabulated data method and 500 ^{o}C isotherm method [7] were proposed to calculate the fire rate of hollow core slabs. Despite the extensive work carried out to

[1]Shanghai Key Laboratory of Engineering Structure Safety, Shanghai Research Institute of Building Sciences, Shanghai 200032, China.
[2]Architects & Engineers Co., LTD of Southeast University, Nanjing 210096, China

investigate the performance of precast hollow core slabs exposed to fire, only limited studies are currently available in the literature on their performance after exposure to fire. However, the structural performance of the precast hollow core slabs after exposure to fire was crucial to the repair and restoration of the slabs after fire. Hence, the objective of this paper is to study the flexural behaviour of the precast hollow core slabs after exposure to fire. Experimental study consisted of four levels of fire duration was carried out. A new three-dimensional finite element model was developed in ABAQUS and validated against the test results reported in this study. A design method was proposed to calculate the ultimate capacity of the precast hollow core slabs after exposure to fire.

2 EXPERIMENTAL STUDY

2.1 Test Specimens

Seven pieces of precast hollow core slabs with cold worked wires were tested either at ambient temperature or after exposure to fire, with the heating duration specified in Table I. Three slabs referred to as CB1 to CB3 were tested at ambient temperature, while the other four specimens, referred to as B20, B40, B60 and B80 respectively, were tested after different fire exposure durations. The hollow core slabs were prepared following the design guide in Shanghai, China. The thickness of the slab was 120 mm and the diameter of the cold worked wires was 4 mm. The detail geometry of the specimens was illustrated in Figure 1. A layer of cement mortar with a thickness of 10 mm was applied to the bottom of the specimens (B20, B40, B60 and B80) to be loaded after exposure to fire before heating process. Each cold worked wire was pre-tensioned with a load around 7 kN.

The measured cube compressive strength of the concrete was 52.4 MPa and the measured tensile strength of cold worked wires was 773 MPa.

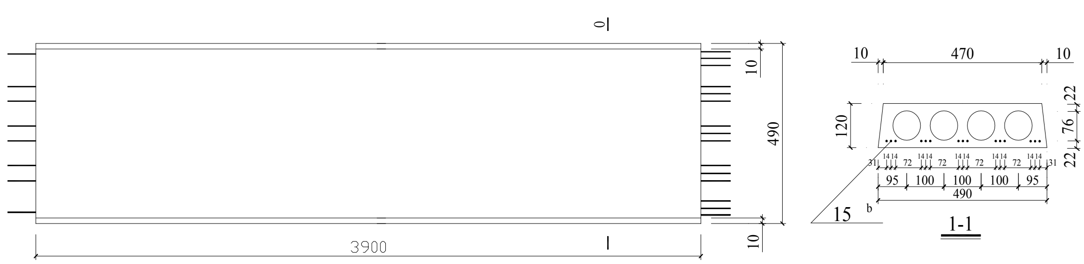

Figure 1. Geometry of the precast hollow core slab.

2.2 Instrumentation

Vertical displacement at the mid-span and two boundaries were measured with LVDTs in load tests labelled as DG-1, DG-2 and DG-3 respectively (Figure 2a). K-type thermocouples named T1 to T4 were installed in the holes and top surface of the precast slabs to record the temperature development, as shown in Figure 2b. The thermocouples were inserted into the holes until below the loading points, and then both ends of the holes were sealed with rock wool and cement mortar, which prevented the cold air going into the holes during the heating.

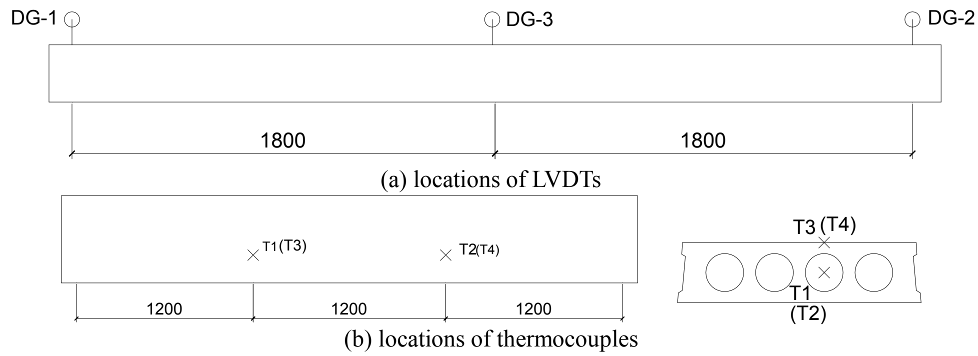

Figure 2. Layout of the instrumentation for displacement and temperature measurements.

2.3 Test Procedure

The experiments were carried out in the horizontal furnace at Southeast University, Nanjing, China, with the test setup shown in Figure 3. The precast hollow core slabs were simply-supported on the top of the furnace. Loads were applied at the one-third points though a distribution beam. For the specimens without heating, they were loaded to failure directly. For the experiments conducted after exposure to fire, specimens were loaded to failure after exposure to specified time of ISO 834 standard fire. During the fire, no load was applied on the slabs.

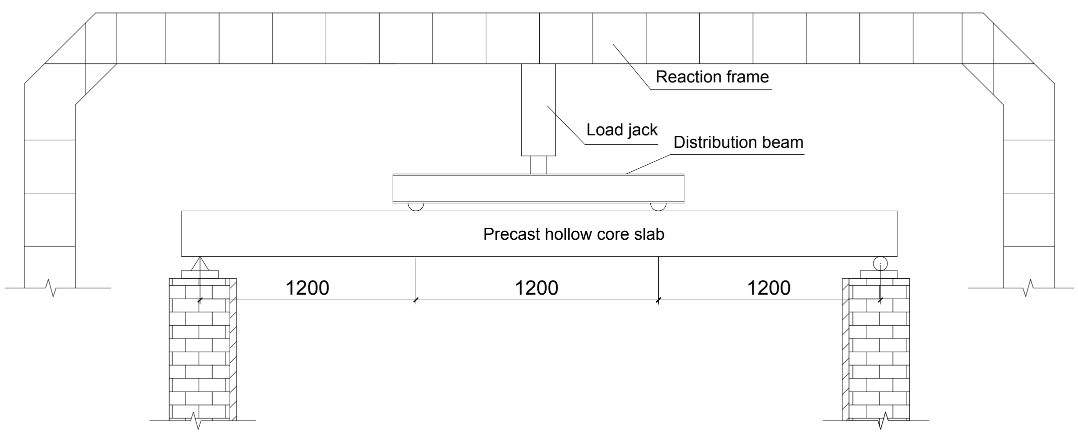

Figure 3. Test setup and loading arrangement.

2.4 Test Results

The flexural failure was observed for specimens tested without heating, i.e. CB1, CB2 and CB3. The measured cracking loads were 15.7 kN, 15.1 kN and 14.7 kN respectively, while the ultimate loads were 20.1 kN, 22.1 kN and 21.3 kN respectively. Figure 4 presents the measured load deflection curves for CB1, CB2 and CB3.

After exposure to fire for specified time, no visible crack was observed on the top surface of the slabs. Falling down of the mortar layer was not observed. The color of the concrete at the bottom of the slab turned to light yellow, while the color of the concrete at the side of the slab turned to purple red. No spalling was observed for all specimens.

The temperature development rule during the heating and cooling process of all specimens were similar. Large temperature gradient was observed along the cross-section, with the temperature at the top surface of the slab was still under 200 ^{o}C. Only the temperature development of specimen B80, which was heated with the longest time, was presented in Figure 5.

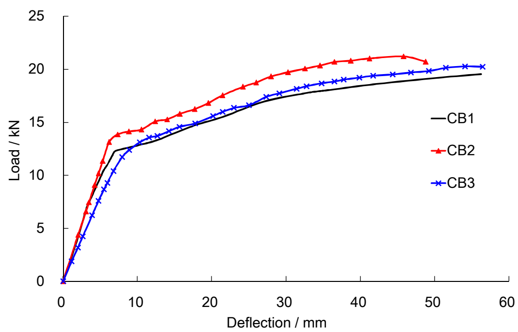

Figure 4. Load-deflection relationship for specimens tested without heating.

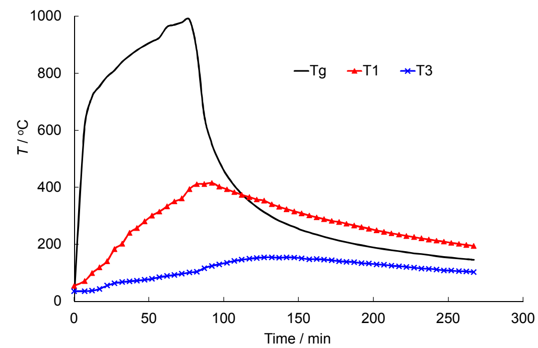

Figure 5. Temperature development of specimen B80.

The flexural failure was also observed for specimens loaded after exposure to fire. The recorded load-deflection curves for B20, B40, B60 and B80 were provided in Figure 6. Table I summarized the cracking loads and ultimate loads of all specimens. The initial stiffness, cracking loads and ultimate loads were observed to decrease with the fire exposure duration.

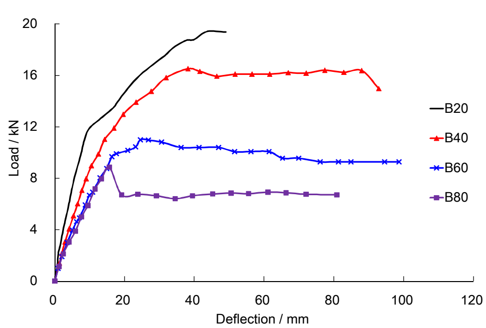

Figure 6. Load-deflection relationship for specimens tested after exposure to fire.

TABLE I. SUMARRISE OF THE EXPERIMENTAL RESULTS.

Specimen ID	Fire duration/min	Cracking load/ kN	Ultimate load / kN
CB1	0	15.7	20.1
CB2	0	15.1	22.1
CB3	0	14.7	21.3
B20	20	13.8	20.4
B40	40	10.9	17.5
B60	60	9.7	12.0
B80	80	7.9	9.9

3 NUMERICAL SIMULATION

A three-dimensional finite element model was developed using the commercial software ABAQUS to predict the mechanical behaviour of the precast hollow core slabs after exposure to fire. To consider the influence of the fire exposure on the material property of concrete and the prestress of cold worked wires, heat transfer analysis was conducted first to evaluate the temperature distributions within the sample when subjected to fire. A mechanical analysis was then implemented with

ABAQUS Standard to simulate the structural response of the sample, in which case the precast hollow core slab was subjected to fire (here defined in terms of a temperature history obtained from the previous heat transfer analysis) before the applied loads. Taking advantage of the symmetry of the specimen, the finite element model represented only half of the slab.

3.1 Thermal Analysis

A typical finite element model used for the precast hollow core slab simulation is illustrated in Figure 7. The 8-node linear heat transfer brick element (DC3D8) was adopted to simulate the concrete slab and mortar layer. To consider the influence of the air inside the holes of the slab, the air inside the holes was also represented with brick element. The cold worked wires were simulated with a 2-node linear heat transfer line element (DC1D2).

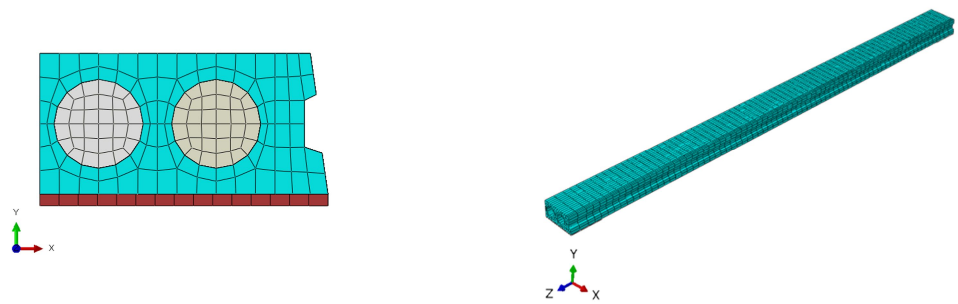

(a) cross-section of the model (b) Overview of the model

Figure 7. Typical finite element model.

The contact between the concrete slab and mortar layer, air and concrete slab was implemented making use of the surface to surface interaction. A convection coefficient value of 25 W/m^2K and an emissivity of 0.5 were used for the mortar surfaces exposed to the fire, as recommended in EC1. The sink temperature option in SFILM and the ambient temperature option in SRADIATE were taken from the measured furnace temperature during the experiments. A convection coefficient of 9 W/m^2K was assigned to the top and lateral surfaces of the slabs (i.e. those not exposed to the higher temperatures) with SFILM, with the sink temperature taken as room temperature.

The temperature-dependent thermal properties of both concrete and steel materials recommended in EC4 were used in the analysis. The moisture evaporation in concrete was modelled specifying a peak value of specific heat at 115 ^{o}C as suggested in EC4. The suggested thermal properties for light weight concrete in EC4 were taken for the mortar.

3.2 Mechanical Analysis

The precast hollow core slab was described in the numerical model with the C3D8R element, while the cold worked wires were simulated with the T3D2 element. In the mechanical analysis, the air and mortar layer were not included in the model. Based on this, the overall arrangement of the mechanical model was similar to the one already illustrated in Figure 7 for the thermal analyses.

The boundary conditions were applied on reference points and the precast slab was simply-supported with a roller support and a pinned support. The load was applied by enforcing pressure on the precast slab. The embedment technique was used to describe for the bond between the reinforcement and the concrete slab. The pretension of the cold worked wires was simulated with the predefined stress.

A bi-linear stress-strain curve was adopted for the steel of the cold worked wires, and the failure of the steel relied in the Von-Mises failure criteria. An initial linear-elastic range up to 40% of the compressive strength was applied after which the Concrete Damage Plasticity model available in ABAQUS was adopted. The non-linear stress-strain curve both at elevated temperatures and after cooling down to ambient temperature suggested in EC4 was adopted for the material model of concrete under uniaxial loading condition. Following heating to a maximum temperature and subsequent cooling down to ambient temperature, concrete does not recover its initial compressive strength, and the material properties of concrete depends greatly on its maximum temperature experienced during the heating process. Due to the thermal inertia of concrete, concrete at different thickness of slab reaches the maximum temperatures at different time. To consider the effect of the heating before the cooling, the maximum temperatures experienced at integration points were recorded with user subroutine USDFLD embedded in ABAQUS [8] and the material of concrete was defined to be dependent on this maximum temperatures. Reductions in the material properties of the cold worked wires at elevated temperatures and after cooling down to ambient temperature were based on EC2 recommendations [9] and referrence [10] respectively.

3.3 Model Validation against Experimental Results

The results obtained with the proposed numerical heat transfer and mechanical model were validated against those measured in the experiments. Representative comparisons carried out between the calculated temperature values and load-deflection relationships with those measured experimentally are illustrated in Figure 8, and highlights the good predictions of the numerical model.

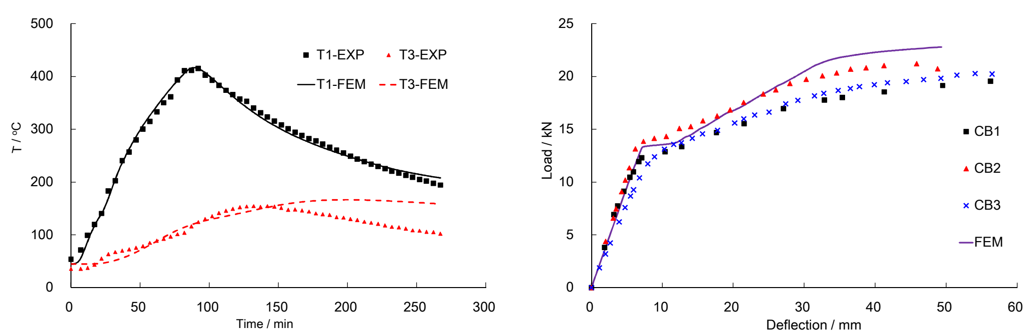

(a) Temperature development (b) CB1-3

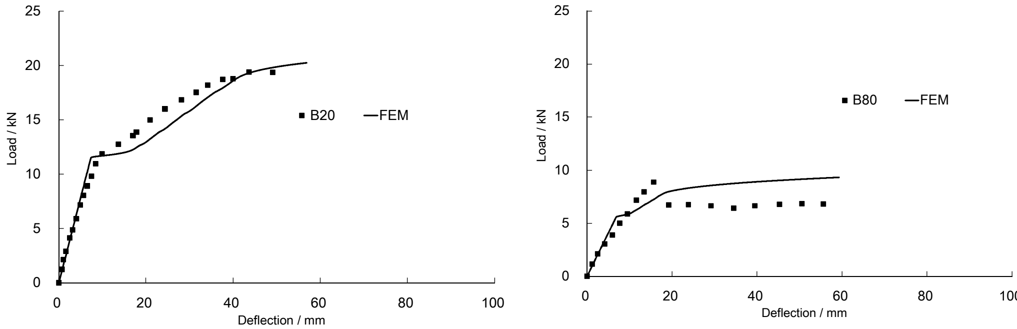

(c) B20 (d) B80

Figure 8. Comparison between the simulation and experimental results.

4 CALCULATION METHOD OF ULTIMATE MOMENT CAPACITY

For the ultimate limit state design at room temperature, the cross-section of precast hollow core slab can be equivalent to I-section based on the area and moment of inertia, as shown in Figure 9. And the moment capacity of the slab can then be conveniently calculated according to the plastic analysis, as shown in Equation 1.

$$\begin{cases} A_p f_{py} = \alpha_1 f_c bx \\ M_u = \alpha_1 f_c bx\left(h_0 - 0.5x\right) \end{cases} \tag{1}$$

Where, A_p is the area of the cold worked wires, mm^2; f_{py} is the tensile strength of the cold worked wires, MPa; α_1 is a coefficient; f_c is the compressive strength of concrete, MPa; b is the width of the slab, mm; x is the height of the compressive zone, mm; M_u is the ultimate moment capacity, N.mm; h_0 is the distance between the cold worked wires and the compressive edge of the slab, mm.

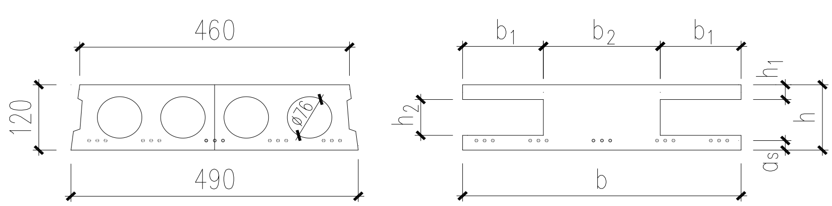

Figure 9. Equivalent cross-section.

For the precast hollow core slabs after exposure to fire, the similar method may be applied, only that the properties of concrete and cold worked wires should be replaced by the properties after heating to high temperatures. The maximum temperatures of concrete and cold worked wires can be approximately taken from the suggestions in EC4 for solid slabs. For cold worked wires, the predicted temperature at the time when the furnace temperature begins to decrease may be employed, while for concrete, temperature may be higher than the temperature predicted at the time when the furnace temperature stops increasing due to the effect of thermal inertia of concrete. However, as only the bottom side of the slab was exposed to fire, the concrete compression block was rarely affected by the fire, as can be seen in Table II. The comparison between the predicted ultimate capacity and experimental results was listed in Table II. The maximum temperature and the degradation factor of concrete T_c and cold worked wires T_p were also presented in Table II. The comparison highlights a good agreement between the theoretical and experimental ultimate capacity.

TABLE II. COMPARISON BETWEEN THE PREDICTED ULTIMATE CAPACITY AND EXPERIMENTAL RESULTS.

Specimen ID	T_p / °C	k_p	T_c/ °C	k_c	P/ kN	P_{test} / kN	Deviation / %
CB*	20	1.00	20	1.00	21.5	21.2	1.2
BP20	266	0.92	60	1.00	19.6	20.4	-4.1
BP40	446	0.69	73	1.00	14.3	17.5	-18.2
BP60	559	0.55	100	0.95	11.0	12.0	-8.7
BP80	626	0.47	160	0.89	8.9	9.9	-9.8

* the average of specimens CB1, CB2 and CB3 was listed.

5 CONCLUSIONS

This paper presents experimental results of ultimate tests carried out on precast hollow core slabs after exposure to fire. Four levels of fire duration were considered, and all specimens both without heating and after exposure to fire exhibited flexural failure. The initial stiffness, cracking loads and ultimate loads were observed to degrade with increasing levels of fire duration. A numerical model was developed to predict the flexural performance of precast hollow core slabs after fire. The predicted temperature and load-deflection relationships from the numerical model were in good agreement with the experimental results. Calculation method was also proposed for the precast hollow core slabs after exposure to fire based on the plastic analysis to predict their ultimate moment capacity. Comparison between the theoretical and experimental results shows that the proposed calculation method was able to predict the moment capacity of precast hollow core slab with acceptable accuracy.

This work was financially supported by the Program of Shanghai Subject Chief Sci entist (B type) (No.15XD1522600)

References

[1] Shakya, A. M. and V. K. R. Kodur. 2014. "Behaviour of prestressed concrete hollowcore slabs under standard and design fire exposure, " in *Proceeding of 8th International Conference on Structures in Fire,* G. Q. Li, V. K. R.Kodur, S. C. Jiang, et al., eds. Shanghai:Tongji University Press, pp. 199-208.

[2] Cooke, G. M. E. 2001. "Behaviour of precast concrete floor slabs exposed to standardised fires," *Fire Safety Journal,* 36: 459-75.

[3] Bailey, C. G. and T. Lennon. 2008. "Full-scale fire tests on hollowcore floors," *The Structural Engineer*, 86(6): 33-39.
[4] Venanzi, I., M. Breccolotti, A. D'Alessandro, A. L. Materazzi. 2014. "Fire performance assessment of HPLWC hollow core slabs through full-scale furnace testing," *Fire Safety Journal*, 69: 12-22.
[5] Aguado, J. V., A. Espinos, A. Hospitaler, J. Ortega, M. L. Romero. 2012. "Influence of reinforcement arrangement in flexural fire behavior of hollow core slabs," *Fire Safety Journal*, 53: 72-84.
[6] Chang, J. J., P. J. Moss, R. P. Dhakal, A. H. Buchanan. 2009. "Effect of Aspect Ratio on Fire Resistance of Hollow Core Concrete Floors," *Fire Technology*, 46(1): 201-16.
[7] EN1994-1-2. 2005. "Eurocode 4: Design of composite steel and concrete structures—Part 1-2: General rules - Structural fire design," Brussels, European committee for standardization.
[8] Tan Q. H., L. H. Han. 2013. "Post-fire and post-strengthening analysis of steel reinforced concrete columns subjected to fire," *Journal of Tsinghua University (Science and Technology)*, 53(1): 12-17.(in Chinese)
[9] EN1992-1-2. 2004. "Eurocode 2: Design of concrete structures -Part 1-2: General rules - Structural fire design," Brussels, European Committee for Standarization.
[10] Shen R., L. Y. Feng, K. Rong. 1991. "Assessment of the mechanical performance of steel reinforcement after fire," *Sichuan Construction Science Research,* 2: 5-9.(in Chinese)

Author Index